Proceedings of the International Congress of the Mexican Hydrogen Society XIV, Cancun, Mexico, 2014

September 30 - October 4, 2014
In Honor of Prof. Ernesto R. González

INFORMACIÓN LEGAL

PROCEEDINGS OF THE INTERNATIONAL CONGRESS OF THE MEXICAN HYDROGEN SOCIETY DERECHOS DE AUTOR Y DERECHOS CONEXOS, **Año 1, No. 1, 2014**, es una publicación anual editada por la Sociedad Mexicana del Hidrogeno A. C., Calle Monte Bello No. 108, Col. Colinas del Padre, C. P. 98085, Zacatecas, Zacatecas, México, Teléfono (614) 4394815, Editor responsable: Alejandro López Ortiz., **ISSN: 2448-7120**, otorgado por el Instituto Nacional del Derecho de Autor. Responsable de la última actualización de este Número, Dr. Alejandro López Ortiz, Cordillera de Guanacaste, 6435, Frac. Cordilleras, C.P. 31124, Chihuahua, Chihuahua, México, teléfono (614) 4394815, correo electrónico lalejan@gmail.com, fecha de última modificación, 8 de Septiembre 2016.

Instituto Tecnológico de Cancún

XIV International Congress of the Mexican Hydrogen Society

September 30 - October 4, 2014

In Honor of Prof. Ernesto R. González

This conference will address important aspects of the hydrogen technologies, from fundamentals, applications, policies and environmental aspects.

Topics will include but are not limited to:

1. Nanostructured materials
2. Hydrogen production, storage and applications
3. Direct Oxidation Fuel Cells
4. Fuel Cells components and stacks
5. Modelling and design
6. Renewable energy systems
7. Control and power conditioning
9. Policies, economy and market strategies
10. Codes, standards and safety issues
11. Environmental aspects

Committee

Co-Chairs:
Dr. Javier Rodríguez Varela
Centro de Investigación y de Estudios Avanzados del IPN (Cinvestav Unidad Saltillo). Saltillo, Coahuila, México.

Dr. Ysmael Verde Gómez
Instituto Tecnológico de Cancún. Cancún, Quintana Roo, México

Organizing Committee:

Dr. Javier Rodríguez Varela
CINVESTAV-IPN Saltillo, México

Dr. Sergio Durón Torres
Universidad Autónoma de Zacatecas, México

Dra. Beatriz Ruiz Camacho
Universidad Politécnica de Guanajuato, México

Dra. Virginia Collins Martínez
CIMAV, México

Dr. Ysmael Verde Gómez
Instituto Tecnológico de Cancún, México

Dra. Beatriz Escobar Morales
Instituto Tecnológico de Cancún, México

Dra Ana María Valenzuela Muñiz
Instituto Tecnológico de Cancún, México

Dra. Ivonne Liliana Alonso Lemus
Instituto Tecnológico de Cancún, México

Dr. Romeli Barbosa Pool
Universidad de Quintana Roo, México

Invited speakers

>> Prof. Ernesto Rafael González
Instituto de Química de São Carlos da Universidade de São Paulo, Brazil

>> Prof. Edson A. Ticianelli
Instituto de Química de São Carlos da Universidade de São Paulo, Brazil

>> Prof. Gerri. G. Botte
Ohio University, USA

>> Prof. Enza Passalacqua
Institute for Advanced Energy Technologies (ITAE), Italy

>> Prof. Arumugam Manthiram
Materials Science and Engineering Program and Texas Materials Institute The University of Texas at Austin, USA

>> Prof. Nicolas Alonso-Vante
University of Poitiers, France

>> Prof. Di-Jia Liu
Argonne National Laboratory, USA

Invited speakers

>> Prof. Ernesto Rafael González
Instituto de Química de São Carlos da Universidade de São Paulo, Brazil

Abstract: There is much interest in the production of pure hydrogen by water electrolysis, but the main problem of this method is the high cost of the hydrogen produced. The most common way of implementing the electrolysis system is the use of non-noble metal cathodes, like nickel or nickel alloys, in alkaline medium. In order to reduce the operational cost in this system it is essential that the electrolyser operates with a potential difference between the electrodes as small as possible. This requires a good electrocatalytic activity of the cathode for the hydrogen evolution reaction (HER). And in order to improve the electrocatalytic activity it is essential to know the mechanism of the reaction. In earlier times, the mechanism of the HER was studied by recording “Tafel slopes” that were then compared with theoretical predictions. As this method is not very reliable we discuss in this presentation the application of electrochemical impedance spectroscopy (EIS) to the study of the HER. As this implies the use of a modelistic approach, we also discuss a possible way of validating the approach using the experimental results. Considering the use of hydrogen, the oxidation of pure hydrogen in proton exchange membrane fuel cells (PEMFC) is easy on platinum catalysts. But it is a problem when the hydrogen is contaminated with carbon monoxide, as is the case of the cheap hydrogen obtained by reforming other fuels. We present here some platinum based catalysts that reduce this problem and a new approach that consist of operating the PEMFC at higher temperatures by using an alternative membrane. This allows the use of hydrogen obtained by reforming of other fuels in PEMFC.

>> Prof. Edson A. Ticianelli
Instituto de Química de São Carlos da Universidade de São Paulo, Brazil

Abstract: The direct or indirect use of ethanol in fuel cells is of high interest because it is a liquid fuel, which reduces storage, distribution and hazard problems associated to gas fuels such as hydrogen, although this last provides higher practical energy conversion efficiency. Moreover, ethanol is a renewable and distributed fuel, factors that are of great importance for the development of a sustainable economy. In this lecture aspects associated with the use of ethanol in proton exchange membrane fuel cells (PEMFC) in the form of hydrogen obtained by its dehydrogenation and reform, as well in solid oxide fuel cells (SOFC) by its direct oxidation will be discussed. The specific issues to be addressed are: 1) the electrocatalysis of the CO tolerance of Pt-based anodes when working in the presence of carbon monoxide in the fuel, particularly when reformate hydrogen is fed to the anode in PEMFC operating at around 80 °C; (2) the description of a system comprising an ethanol dehydrogenation catalytic unit coupled to a conventional PEMFC; and (3) the problems associated with coke formation and consequent deactivation of the anode that occurs when the direct oxidation is promoted in solid oxide fuel cells (SOFC) that operate around 800-900 °C.

In this context, the performance of H_2/O_2 PEMFCs fed with hydrogen contaminated with CO, such as that generated by the reforming of ethanol, will be discussed for anode electrocatalysts containing nanoparticles of Pt, Ru, PtW and PtMo dispersed on carbon and metal carbides (tungsten and molybdenum). Aspects related to CO tolerance mechanisms, particularly involving the shift and methanation reactions of CO, as well as the stability of the catalyst materials, will be specifically considered. Next, the performance of a system in which ethanol is first dehydrogenated over a Cu/ZrO_2 catalyst bed, and then the gaseous effluent is trapped in a simple cold condenser enabling a gas current rich in H_2 to feed a PEMFC will be discussed. Here chromatographic analyses are used to show that the condensed effluent is formed essentially by ethyl acetate which has heat of combustion between ethanol and gasoline. Finally, the effects of coating a conventional Ni/YSZ SOFC anode (electrolyte formed by two layers YSZ/YDC and a cathode of LSFCO where YSZ = yttria stabilized zirconia; YDC = yttria doped ceria and LSFCO = Ferrite strontium doped lanthanum and cobalt) with a Ni-Cu/CGO (CGO = $Ce_{0.9}Gd_{0.1}O_2$) cermet layer will be treated. In this case, the possibility of the Ni- Cu/CGO pre-layer to convert the flow of ethanol into a useful fuel such as H_2 and CO, as well as its influence on the accumulation of coke will be analyzed.

>> Prof. Gerri. G. Botte
Ohio University, USA

Abstract: Typically, water is the source for the electrochemical production of hydrogen, using alkaline or proton exchange membrane electrolysis. However, there are limitations with water electrolysis such as high-energy consumption, high capital costs, and high purity of the source (water). To circumvent these problems, the Center for Electrochemical Engineering Research (CEER) at Ohio University has been working in the development of novel, simple, suitable, and environmentally friendly electrochemical technologies to produce hydrogen from nonconventional sources such as urea.

The electrolysis of urea for hydrogen production takes place in alkaline media. In the process, the electrochemical oxidation of urea to nitrogen and carbon dioxide takes place at the anode of the electrolytic cell in nickel-based electrodes, while hydrogen evolves at the cathodic compartment [1,2]. The process, with a theoretical cell voltage of 0.37 V at standard conditions, is thermodynamically more favorable than water electrolysis. Because of its low energy consumption and the use of inexpensive catalysts, the technology finds applications for the production of hydrogen on demand requiring only the storage of urea.

In addition to direct production of hydrogen on demand, urea-rich wastewaters can be remediated via urea electrolysis to prevent toxic ammonia emissions and nitrate contamination that currently results from leaving these waters untreated.

In this talk, Dr. Botte will present a summary of the technology including catalysts, oxidation rates, and progress on understanding of the reaction mechanism.

>> Prof. Enza Passalacqua
Institute for Advanced Energy Technologies (ITAE), Italy

Abstract: The polymer electrolyte fuel cells (PEFCs) are a highly efficient technology and an environmentally attractive source for power generation for various applications such as automotive, stationary, military or portable devices. Proton exchange membrane (PEM) is the key component in a fuel cell system and in the recent years the research activity have focused to obtain membranes with high proton conductivity, low permeability to fuel, good chemical/thermal stability, good mechanical properties in a wide window of operative conditions of temperature, pressure and relative humidity. These features must be achieved by ensuring good performance, long durability, and low cost, for these reasons several polymers and membranes have been proposed as an alternative to conventional Nafion® membranes, especially for working at temperatures above 80°C. In this work is described the experience and progress made on the development of membranes based on two different approaches: − Composite membranes prepared by addition of inorganic oxides to improve hygroscopic and mechanical properties or by addition of heteropolyacids (phosphotungstic acid) immobilized on inorganic oxides to improve the proton conduction through the acid functionality. − Reinforced membranes obtained through the introduction of a reinforcement to improve the mechanical properties. The polymeric films, obtained by cast of the dispersion of the polymers in the solvent, have been tested in a range of temperature between 80 and 120°C with different gas humidity. Results on swelling characteristics, proton conductivity and long-term degradation of the membranes are reported. Finally, the application of composite MEAs, in a 1500W stack, especially designed for cogeneration systems, is shown and discussed.

>> Prof. Arumugam Manthiram
Materials Science and Engineering Program and Texas Materials Institute The University of Texas at Austin, USA

Abstract: Batteries power most of the modern portable electronic devices such as cellphones and laptops, and they are being intensively pursued for electric vehicles and stationary storage of electricity produced from renewable sources like solar and wind. However, their adoption for transportation and large-scale grid storage applications requires significant reduction in cost, long cycle life, increase in energy and power, and improvement in safety, which are in turn controlled by the battery chemistry adopted. Clearly, development of new battery chemistries at an affordable cost with long life is needed to address our future energy needs. Accordingly, this presentation will focus on the development of next-generation battery chemistries. Specifically, after providing an overview of the current status of lithium-ion battery technology, the presentation will focus on high-energy, high-power lithium-sulfur and hybrid lithium-air batteries. With the lithium-sulfur batteries, novel sulfur-carbon nanocomposite electrode structures as well as new cell configurations with a carbon-paper interlayer between the cathode and the separator or carbon-coated bifunctional separators that offer high energy, high power, and long cycle life will be presented. With the hybrid lithium-air batteries in which the lithium-metal anode in a nonaqueous electrolyte is separated from the air cathode in an aqueous catholyte by a ceramic lithium-ion conducting electrolyte membrane, optimum catholyte systems as well as development of inexpensive electrocatalysts for the oxygen reduction reaction (ORR) and oxygen evolution reaction (OER) will be presented. Particularly, nanocarbon architectures as ORR catalysts and oxide nanostructures as OER catalysts will be presented.

>> Prof. Nicolas Alonso-Vante
University of Poitiers, France

Abstract: The photocurrent response of mesoporoustitania generated via the sol–gel process was investigated in the presence of different hole scavenger species, e.g. alcohols (methanol, ethanol, isopropanol) and water.The photocurrent of the oxidephotoelectrode was enhanced in the presence of alcohol. The extent of the response of the photocurrent was a function of the nature of the alcohol used, namely, methanol ≈ethanol >isopropanol > H2O. Absorption of the visible light through the reactor allowed us to monitor, in real time, the photodeposition process of platinum nanoclusters on titania (Anatase phase). The photodeposition kinetics was correlated with the magnitude of the photocurrent response observed in a photoelectrochemical environment. The outcome of this investigation, besides allows envisioning future developments concerning plasmonicphotocatalysis, opens interesting perspectives concerning the control of the size of photodepositedplatinum nanoparticles in order to study the role of the interaction of the metal cluster influencing the nature of the catalytic sites for a multi-electron charge transfer process, e. g. the oxygen reduction reaction (ORR). This talk will discuss various aspects regarding the effect of substrate modification to enhance the catalytic activity of metal nanoparticles.

>> Prof. Di-Jia Liu
Argonne National Laboratory, USA

Abstract: Finding inexpensive replacements for the platinum group metals (PGMs) has been the ultimate goal for proton exchange membrane fuel cell catalyst research. Among all the non-PGM candidates, transition metal doped nitrogen-carbon (TM-N-C) composites appear to be the most promising in promoting oxygen reduction reaction (ORR) at cathode. Since non-PGM catalysts are known to have lower turn-over frequency per catalytic site when compared to platinum, their active site densities must be substantially higher to deliver a comparable performance. At Argonne National Laboratory, we recently developed several new approaches using metal-organic frameworks (MOFs) and porous organic polymers (POPs) as the precursors for the non-PGM catalyst preparation. For example, we demonstrated that MOF could produce the “support-free” non-PGM electrode catalysts, taking the advantages of its 3-dimensional metal-N4 coordination structure, high volumetric active site density and high surface area. Both single and binary MOF-based catalysts have been developed in our laboratory with excellent ORR activities. More recently, we developed a method of preparing non-PGM catalyst using POPs containing high density of metallated N-coordination sites evenly distributed in highly porous networks. POPs with both two-N coordinated (polybipyridine-spirobifluorene) and four-N coordinated transition metals (Tetrakis-(3,5-di-thiophen-2-yl-phenyl)-polyporphyrin) were investigated. In this presentation, we will discuss the design, synthesis and activation strategies of MOF and POP based non-PGM catalysts and their physical/chemical properties obtained from various characterization techniques.

Sponsors


H2


CONACYT


ECS


ISASA
INSTRUMENTACION


BioLogic
Science Instruments


Princeton
Applied
Research
solartron
analytical


PINE
RESEARCH INSTRUMENTATION

INDEX

			Incipient Wetness Impregnation Method		
HC013	Sanchez	Luis	Preparation of a Solid Catalyst by Sulfonation Superacids from Mesoporous Carbon Material	X	X
HC014	Oliver Tolentino	Miguel Angel	Paramagnetic behavior of Ni-Fe Layered Double Hydroxide and their effect over the Electrocatalytic Activity towards Oxygen Evolution Reaction in Alkaline Media	X	X
HC015	Guevara López	Eliane	Evaluation of different support materials used with a photo-fermentative consortium for hydrogen production	X	X
HC016	Castro Luna	Ana	Research on Methanol-Tolerant Catalysts for the Oxygen Reduction Reaction	X	X
HC017	Hernandez Flores	Giovanni	Derivation of mathematical model based on Taffel equation explains microbial fuel cell performance	X	X
HC018	Hernandez Flores	Giovanni	Characteristics of a single chamber microbial fuel cell fitted with low cost membrane	X	X
HC019	Hernandez Flores	Giovanni	Alternative Proton Exchange Membrane Fitted in a Microbial Fuel Cell in Batch Operation	X	X
HC020	Altamirano Gutierrez	Alejandro	Development and Characterization of Pd-CeO2 Electrocatalysts for the Formic Acid and Glycerol Oxidization Reactions in Acid Medium	X	
HC021	Siller	Adriana	Theoretical Study of Ru-organometallic Compounds-Functionalized Grapheneas Catalyst Supports for Low-Temperature Fuel Cells.	X	
HC022	Baque	Laura	Characterization of Cathode/Electrolyte Interphases for IT-SOFCs	X	X
HC023	Suarez Alcantara	Karina	Mg-M-Li Alloys Prepared by Mechanical Alloying and their Hydrogen Storage Characteristics	X	X

HC024	Suarez Alcantara	Karina	In-situ XRD Studies of H2 Sorption/ Desorption on CaH2+MgB2 Reactive Hydride Composite Doped with Fluorinated Compounds	X	
HC025	Zeferino Gonzalez	Isaias	Influence of the Synthesis Parameters in CNT Doped with Nitrogen Towards the Electroreduction of Oxygen	X	X
HC026	Benavides	Roberto	Electrochemical Studies of Poly(styrene-co-acrylic acid) PEM Membranes Synthesized by two different Methods	X	X
HC027	Suarez Alcantara	Karina	Towards the Hydride Tank for Hydrogen Storage	X	
HC028	Suarez Alcantara	Karina	Developing our Hydrogen Technology, Design and Construction of a Sieverts type Equipment for Hydrogen Sorption/ Desorption Characterization.	X	
HC029	Palacios Hernandez	Guadalupe	Mg-EVA Composites with Selective Permeability as an Hydrogen Storage Material	X	
HC030	Oliver Tolentino	Miguel Angel	Hematite Thin Films Produced by Spray Pyrolysis Method for Water Splitting	X	
HC031	Cabanas Moreno	Jose	The Analysis of Hydridying and Dehydriding Kinetics	X	
HC032	Sathish Kumar	Kamaraj	Novel Microbial Fuel Cell Design for Real Time High Organic Load Waste Water Treatment	X	X
HC033	Camacho Perez	Beni	Production of Electricity in an Electrobiochemical Slurry Reactor used for the Bioremediation of Pesticide Contaminated Soil	X	X
HC034	Moreno Andrade	Ivan	Biohydrogen Production from Organic Solid Waste in a Discontinuous Process	X	X
HC035	Breton Deval	Luz	Metallic Nanoparticles for the Treatment of Effluents Contaminated with Chlorinated Organic Compounds: a Review	X	X
HC036	Patino	Rodrigo	Hydrogen Production from Renewable Energy in Yucatan	X	

HC037	Escamilla Alvarado	Carlos	Saccharification of Fermented Solids for a Hydrogen Producing Biorefinery	X	X
HC038	Godinez Salomon	Jose Fernando	Core-Shell Ni@Pt Supported on Carbon Nanotubes as cathode-catalyst for Fuel Cell Application	X	
HC040	Reyes Rodriguez	Jose Luis	The effect of physicochemical pretreatment of supported Pt nanoparticles for the ORR. A novel carbon from natural source.	X	X
HC041	Escobar	Beatriz	The Outreach Program of Renewable Energy for High School in Quintana Roo, Mexico	X	
HC042	Munoz Paez	Karla Maria	Evaluation of Biohydrogen Production from Cheese Whey and Assessment of the Associated Microbial Community	X	X
HC043	Lopez	Manuel	An approach for Fuel Cell Balance of Plant design and its electronic control for modular flexibility	X	
HC044	Rodriguez Martinez	Victor Hugo	Performance Study of Carbon Supported Co@Pt/C Core-Shell Nanocatalyst for Oxygen Reduction Reaction in a PEMFC	X	
HC045	Tellez Cruz	Miriam Marisol	Y@Pt/C Core-Shell Electro-Catalyst for Oxygen Reduction Reaction	X	X
HC046	Hernandez	Anayantzin	Pt-NiTiO3-C Catalyst Synthesized by the Microwave Assisted Method for Direct Alcohol Fuel Cell Applications.	X	
HC047	Lopez Martinez	Juan Eduardo	Synthesis of CeO2/C and Pt-CeO2/C Nanoparticles by the Microwave Assisted Polyol Method and Evaluation of their Electrocatalytic Activity.	X	
HC048	Rosado Ortiz	Gabriel	Synthesis of Ni@Pt Core-Shell Nanoparticles Supported on MWCNTs for Hydrogen and Methanol Electrooxidation	X	
HC049	Gonzalez Quijano	Diego	Effects of Solvent Properties on the Electrocatalytic Response	X	

			of Highly Active Pt-Sn/C and Pt-Ru/C Catalysts for the EOR		
HC050	Vega Villalobos	Diana	NiO@Pt/C Core-Shell Nanocatalyst for Oxygen Reduction Reaction	X	X
HC051	Ordonez Lopez	Luis Carlos	Catalytic layer location in MEA and air supply influence on the performance of an Open-Cathode Direct Ethanol Fuel Cell	X	X
HC052	Alba	Gerardo Isaac	Microstructural analysis of modified gas diffusion layer for a water PEM electrolyzer.	X	
HC053	Melendez	Perla	Pd-Fe3O4/MWCNT Nanomaterials as Novel Anode Catalysts for the Formic Acid Oxidation Reaction	X	
HC054	Sanchez Padilla	NM	Magnetite-Platinum Core-shell Nanoparticles Using a Two-step Method for the Oxygen Reduction Reaction	X	
HC055	Ramirez	Jorge	Microstructural Analysis and Electrochemical Performance of a PEMFC Electrode	X	
HC056	Maya Cornejo	J	Enhancement of the Glycerol electrooxidation reaction using PdCu/XC-72 as electrocatalyst	X	
HC057	Arjona	N	Pd Synthesized by Electrochemical Techniques in three-dimensional carbon electrodes	X	
HC058	Sandoval	JM	Bi-directional DC-DC Converter to Charge/Discharge a Supercapacitor Modulein a Hybrid Renewable Energy System.	X	X
HC059	Pineda	Jose Luis	Performance membrane study on an Electrochemical Hydrogen Compressor	X	X
HC060	Mora	Edgar	Preparation of Nickel Catalysts Deposited on Gamma Alumina to Process Hydrodeoxygenation First Generation Biodiesel	X	
HC061	Medina	Juan	Electrochemical Impedance Studies of Co-based	X	X

			Nanomaterials for Hydrogen Evolution Reaction		
HC062	Perez Viramontes	Nicte Julieta	Novel (IrxSnySbz)Ow Material as Catalyst for the Oxygen Evolution Reaction.	X	X
HC063	Altamirano Perez	Sandra Cesia	Effects of Ball Milling Conditions on the Hydrogen Sorption of Mg and Cr2O3 Nanopowders	X	
HC064	Sanchez	Victor	A PEM Fuel Cell Model Based on Artificial Neural Network and Particle Swarm Optimization	X	
HC065	Sanchez	Victor	Multi-Objective Optimization of a Hybrid Generating System	X	X
HC066	Ruiz Camacho	Beatriz	Nanoparticles of Pt and Ag-Pt Synthesized by Ultrasonic for Oxygen Reduction Reaction	X	X
HC067	Quechulpa Perez	Pompeyo	Development and Application of Hybrid Membranes obtained by the Sol-Gel Process for the Enrichment of Hydrogen and Methane Gases Produced in Biodigesters	X	X
HC069	Martinez Salazar	Ana Lidia	High H2 Production from the Reforming of CH4 by Hydrogen Sulphide Using Mo-Cr Supported on Heterogeneous Catalysts	X	X
HC070	Martinez Salazar	Ana Lidia	Kinetics and Modelling Study of the Catalytic Reaction of Methane and Hydrogen Sulphide over Mo/La2O3-ZrO2 Catalyst	X	X
HC071	Villullas	Hebedelas Mercedes	On the Role of Electronic Properties of Nanostructured Catalysts on the Reaction Pathways of Ethanol Oxidation	X	
HC072	Alva Rojas	Elvia	Hydrogen Production from CH4 and NO Treatment with non Thermal plasma	X	X
HC073	Estevez Martinez	Yoxkin	Synthesis and Characterization of Chitosan-Starch Polymer Reinforced with Functionalized Multiwalled Carbon Nanotubes as Electrolyte for Lithium Batteries	X	X

HC074	Galicia	Jade	MOFs as Natural Gas Storage Materials	X	
HC075	Ortega Martinez	AC	A Microbial Fuel Cell Equipped with a Denitrifying Biocathode Effectively Degrades the Toxic Carbon Tetrachloride	X	X
HC076	MaciasFerrer	David	Pt-based Linked Monometallic Nanoparticles Supported on Nanostructured Carbon for Electro-oxidation of Methanol	X	
HC077	RODRIGUEZ CASTELLANOS	ANDRES	Hybrid Electric Vehicle (NAYAA II) Batteries - Fuel Cell	X	X
HC078	Avila Vazquez	Veronica	ATO Nanoparticles as Support for Reduction and Evolution Oxygen Reactions in PEM Electrolysers	X	X
HC079	Oseguera	Edwin	Synthesis and Characterization of Pt/NTC/WOx Electrocatalysts for Oxygen Reduction Reaction	X	X
HC080	Montiel Macias	Elizabeth	Nanoestructured Carbon Doped with Heteroatoms as Electrocatalyst in Fuel Cells	X	
HC081	Benavides	Roberto	Influence of Metal Nanoparticles in Proton Conductivity and Water Absorption of Polymeric Membranes for Fuel Cells	X	
HC082	Lopez Perez	Pablo A	Kinetic Modeling and Virtual Sensor for Renewable Hydrogen Estimation in an Anaerobic Reactor	X	
HC083	Campos Roldan	Carlos Augusto	Influence of Exfoliation on Multi-walled Carbon Nanotubes in their Performance as Electrode Support Material	X	X
HC085	Pacheco	Joel	Greenhouse Gas Treatment and H2 Production, by Warm Plasma Reforming	X	X
HC086	Citalan Cigarroa	Hebedelas Mercedes	Design, Construction and Evaluation of Performance a SPE electrolyzer using Virtual Instrument Developed with LabVIEW	X	X

HC087	IturbeGarcia	Jose Luis	Synthesis of Mg2Cu Alloy as a Precursor of MgH2 by Mechanical Alloying and its Characterization Using XRD and SEM	X	
HC088	Diaz Guillen	Alonso	Electrical Properties of Gd2Hf2-xZrxO7 Solid Electrolytes Synthesized by Mechanical Milling	X	X
HC089	Sierra	Juan Manuel	Numerical Study of Fluid Dynamics and Heat Transfer in a PEM Fuel Cell Stack	X	X
HC090	Armenta Gonzalez	Angelica	Pd/MWCNT and PdAg/MWCNT Electrocatalysts for Ethanol Oxidation in an Air-breathing Microfluidic Fuel Cell	X	
HC091	Patino Carachure	Cristobal	Hydrogen Generation Using Different Morphologies of Recycled Aluminum with Alkaline Substance	X	
HC092	Moreno Andrade	Ivan	Effect of Persian Lime on Hydrogen Production from Food Organic Solid Waste	X	
HC093	Castillo Hernandez	Alfonso	Start-up of a Continuous Stirred-Tank Reactor for Biohydrogen Production from Restaurant Organic Waste	X	X
HC094	Videa	Marcelo	Evaluation of the electrocatalytic activity of Nickel-Molybdenum Nanoparticles for Hydrogen Production	X	
HC095	Jesus Christopher	Jaime	Modeling and Optimization of Hybrid Nafion Membranes Modified with Oxides Based on Artificial Neural Networks and Genetic Algorithms	X	X
HC096	Ramos Sanchez	Victor	Analysis of Microbial Communities Associated with Hydrogen Production Obtained from Wastewater	X	X
HC097	Ramos	Guadalupe	Organic Molecule-Functionalized Zn3P2 Nanowires for Photochemical H2 Production: DFT and Experimental Analyses	X	

HC099	Morales	Lizbeth	Effect of Ptx-Ruy-Irz Electrocatalyst Composition for Oxygen Electrode in an Unitized Regenerative Fuel Cell	X	
HC100	Yunez Cano	Armando	Implementation of a Hydrogen Control System, Using PLC Applied to a Sustainable Housing	X	
HC101	Cruz Torres	Armando	A DFT study of O2 adsorption on periodic Ga1-xNx (100) surface	X	
HC103	Olmedo	Jorge	Control and Automation System of Power Generation through Photovoltaic-Hydrogen Technology to Lighting	X	X
HC104	Valdez	Idania	Implications of the Heat Shock Treatment During the Bioconversion of Crystalline Cellulose into Hydrogen by a Microbial Consortium	X	
HC105	Figueroa Torres	Mayra Zyzlila	Ni and Ru Loading on Sr2Ta2O7 by Electroless to Enhance its Photocatalytic Hydrogen Evolution from water	X	X
HC106	Lardizabal	Daniel	Synthesis of Carbon Fiber Electrocatalysts Obtained by Pyrolysis of Polymeric Fiber	X	
HC107	Palacios	A	Effect of the Palladium Content on the Oxidation of Ethylene Glycol Oxidation	X	
HC109	Padmasree	KP	Electrical and Optical Characterization of NdAlO3 Nanoparticles	X	
HC110	Padmasree	KP	Molten Salt Synthesis of Doped Ceria-Na2CO3 Nanocomposites	X	
HC111	Padmasree	KP	Molten Salt synthesis and characterization studies of co-doped ceria electrolytes for IT-SOFCs	X	
HC112	Perez Alvarez	Jonatan	XPS study of mixed valence Titanium-Cobalt oxides and it´s electrocayalitic activity for the OER	X	
HC113	Barbosa	Romeli	Criteria of optimization theoretical and experimental of a renewable energy system with hydrogen storage	X	

HC114	Sanchez	Manuel	Strategies for implementation of fuel cells in Quintana Roo, short technical-economic analysis	X	
HC115	Matencio	A.A.	Effect of the different TiO2 nanostructures in PtRu/C-TiO2 catalysts on the catalytic activity for methanol oxidation	X	
HC116	Fortuna	Javier	New Catalytic Technology Implementation on the Hydrogen Production Industry	X	
HC117	Fortuna	Javier	Project to implement a heat recovery system, for steam generation, to an existing SMR Hydrogen production plant	X	
HC118	Valdivia	J.C.	Synthesis and Characterization of 2,1,3-benzothiadiazole derivatives for solar cell applications	X	
HC119	Lopez	G.G.	Synthesis and characterization of discotic liquid-crystalline semiconductors based on [1,3,5]-triazine	X	
HC120	Fernandez Loyola	R	Selective decomposition of urea by enzyme immobilization, for electrolysis of ammonium	X	
HC121	Fernandez Loyola	R	Effect of size of carbon nanotubes on the electrochemical activity in basic medium	X	
HC122	Ramaswamy	Monohara n	NixMo1-xO3 ($x \leq 0.4$) as Electrocatalysts for Electrochemical Hydrogen Production from Acid Water	X	X
HC123	Navarro Diaz	Marcelo	Differences in Ecological Structure Between Hydrogen Producing and Anaerobic Digestion Consortia	X	X
HC124	Alonso Lemus	Ivonne	Sulfur Doped Carbon Nanotubes as Electrocatalyst in Pem Fuel Cells	X	
HC125	Samaniego Benitez	E	Comparison of Structural and Electrochemical Properties of Doped and Superficially Modified Multiwall Carbon Nanotubes	X	

HC126	Uicab	E.M.	Comparison of Two Methods of Synthesis of Byfunctional Platinum-Iridium Electrocatalyst for Unitized Regenerative Fuel Cells	X	
HC127	Carbone	Alessandra	Composite sPEEK-TPyP Membranes Development for Portable Applications	X	X
HC128	Pedicini	R	Performance Assessment of an Integrated PEFC and an Hydrogen Storage Device Based on Innovative Material	X	X
HC130	Pech Rodriguez	Wilian Jesus	Functionalization of Vulcan XC-72 by IMH and its Effect as Support for Pt Electrocatalysts for the EOR	X	X
HC131	Alamilla	Zulma R	Richness, Composition and Predominance in Undefined Mixed Cultures for Fermentative Hydrogen Production	X	
HC132	Mendoza	Hector Daniel	Development of an electronic device for impedance measurements for online PEMFC failure diagnostic applications	X	
HC133	Loyola	Felix	Flooding and dehydration processes in a PEM fuel cell. A phenomenological analysis based on EIS measurements	X	
HC134	Lopez Ortiz	Alejandro	Thermodynamic and Kinetics Modeling of H2 Production by Dry Reforming of Ethanol with CaCO3 as CO2 Source	X	X
HC135	Lopez Ortiz	Alejandro	Na2ZrO3 Stability under Reforming/Regeneration Cycles during the Steam Reforming of Ethanol with CO2 Absorption	X	
HC136	Paraguay Delgado	Francisco	W1-xMoxO3?0.33H2O Solid Solutions with Tunable Band Gap for Hydrogen Production	X	X
HC137	Lara Romero	Javier	Microwave-assisted synthesis and electrocatalytic activity of Pt-CeO2 nanoparticles supported on carbon nanotubes	X	

HC138	Collins Martinez	Virginia	Kinetic Study of the Pyrolysis of Pinus Cooperi and Quercus Sideroxyla for the H2 production combined with CO2 capture	X	
HC139	Tufino	Miguel	A hybrid approach based on a solar PV-hydrogen system for household electric energy supply in Mexico	X	X
HC140	Ruiz Camacho	Beatriz	Pt/TiO2?C electrocatalysts prepared by chemical vapor deposition with high tolerance to methanol in oxygen reduction reaction	X	X
HC141	Sanchez	M Esther	Hydrogen adsorption on beryllium-C60 fullerene: a theoretical study	X	
HC142	Arenas	Rosita	Electrocatalytic Oxidation of Glycerol in Alkaline Media on Pd-Au/MWCNT Nanocatalysts Prepared by the Polyol Method	X	
HC143	Collins Martinez	Virginia	Enhanced Photocatalytic Hydrogen Production Under Visible Light over Ag Doped TiO2	X	X
HC144	Collins Martinez	Virginia	Synthesis Method Effect of CoFe2O4 on its Photocatalytic Properties for H2 Production from Water and Visible Light	X	X
HC145	Collins Martinez	Virginia	Photocatalytic Hydrogen Production under Visible Light over Magnesium Ferrite	X	X
HC146	Collins Martinez	Virginia	KNbO3 as Photocatalyst for Hydrogen Production	X	X
HC147	Bedolla	Zaira	Sonochemical Synthesis of Pt/CNT/TiO2 Anode Catalyst for Direct Methanol Fuel Cells	X	X
HC148	Morales Acosta	Diana	Ordered Mesoporous Carbon Synthesized via Self-Assembly in Aqueous Phase as Support for ORR Pt Electrocatalyst	X	
HC149	Vazquez Larios	A.L.	Bioelectricity from Recalcitrant Municipal Leachate in a Microbial Fuel Cell	X	X
HC150	Vazquez Larios	A.L.	Effect of Type of Inoculum and Application of RuxMoySez on	X	X

			Microbial Fuel Cell Performance		
HC151	Navarro	P.	Control of agitation and temperature of a reactor for biodiesel production	X	
HC152	Garcia	I.J.	Study of electrocatalysts for the ORR based on nanocomposites of polypyrrole-CoSe2 supported on nitrogen-doped graphene	X	

Abstracts

Behavior of Ionic Species in Sulfonated PEI Using DFT Simulations: A Study to Determine Ionic Conductivity.

Ernesto López-Chávez *[1], Yesica A Peña-Castañeda[1], José M Martínez-Magadán[2], Raúl Oviedo-Roa[3], Fray de Landa Castillo-Alvarado[4].

[1]Colegio de Ciencia y Tecnología de la Universidad Autónoma de la Ciudad de México, Av. Fray Servando Teresa de Mier 92-110. Col. Centro. México D.F. 06080. México.

[2]Programa de Ingeniería Molecular, [3]Programa de recuperación de Hidrocarburos, Instituto Mexicano del Petróleo, Eje Central Lázaro Cárdenas Norte 152, Col. San Bartolo Atepehuacán, Deleg. Gustavo A. Madero, México. D.F. 07730. México.

[4]Escuela Superior de Física y Matemáticas del Instituto Politécnico Nacional, Unidad Profesional Adolfo López Mateos. Col. Lindavista. Deleg. Gustavo A. Madero. México, D. F., 07738. México.

ABSTRACT

Compared with internal combustion engines, proton exchange fuel cells (PEMFC) are able to operate without polluting emissions. Increasing the operating temperature of the fuel cell above 100 º C is one of the major objectives in this field as it would facilitate the commercial development of electric vehicles powered by fuel cells. To achieve this objective, it is important to develop new types of membranes to replace Nafion. The poly (ether imide) sulfonated are presented as a new alternative in order to use as an electrolyte in PEMFC. In this work, DFT theory has been used to study the interaction between ionic species charged of hydrogen as hydroxyl ((OH)-) or hydronium ((H3O)+) and sulfonated poly(ether imide). The analysis of molecular reactivity through frontier MO (HOMO and LUMO) allows to determine the mechanism of ionic conductivity which takes place over the polymeric membrane. This study is addressed to improve the efficient of PEM fuel cells.

Keywords:Fuel cell, conductivity, ionic species

XIV International Congress of the Mexican Hydrogen Society
Cancun, Mexico, 2014

A Theoretical Study of Oxygen Reduction Reactivity on Disordered Binary Alloy Surfaces

Ernesto López-Chávez[1], Yesica A. Peña-Castañeda[1], Alberto García-Quiroz[1], Gerardo González-García[1], Fray de Landa Castillo-Alvarado[2], José A. I. Díaz-Góngora[3]

[1]Colegio de Ciencia y Tecnología de la Universidad Autónoma de la Ciudad de México. Av. Fray Servando Teresa de Mier 92-110. Col. Centro Histórico, Del. Cuauthémoc, CP 06080 México, D.F.

[2] Escuela Superior de Física y Matemáticas del Instituto Politécnico Nacional, Unidad Profesional Adolfo López Mateos. Col. Lindavista. Deleg. Gustavo A. Madero. México, D. F., 07738. México.

[3]Centro de Investigación de Ciencia Aplicada y Tecnología Avanzada del Instituto Politécnico Nacional. Calzada Legaria No. 694 Col. Irrigación, Del. Miguel Hidalgo, México D.F., C.P.11500.

ABSTRACT

In the present paper, Pd_xCu_{1-x} disordered binary alloys with promising properties for the ORR were studied. The approach suggested by Nørskov et al. was applied in order to obtain the free energies of different reaction intermediates on (111) surface of Pd_xCu_{1-x} disordered binary alloys, with values of 0.80, 0.85, 0.90, and 0.95 of Pd concentration. The free-energy differences take solvation, entropic, and zero point energies into account. Subsequently, we construct the hybrid free energy diagrams (FED) by also including the activation energy barriers for different O–O bond scission steps in the ORR network. Finally, by performing a Sabatier analysis, the free energy changes and activation energy barriers for relevant steps are used to estimate the relative activity of these catalysts at cell potentials of 0 V, 0.80 V and 1.23 V.

Keywords: Pd_xCu_{1-x}; disordered; binary.

XIV International Congress of the Mexican Hydrogen Society
Cancun, Mexico, 2014

Calculations of Water Uptake and IEC Parameters of Ionic Exchange Membranes with Applications in Fuel Cells

Ernesto López-Chávez[*a], Yesica A. Peña-Castañeda[a], Gerardo González-García[a], Patsi Montserrat Perales-Enciso[b], Fray de Landa Castillo-Alvarado[c], Alberto García-Quiroz[a]

[a]Colegio de Ciencia y Tecnología de la Universidad Autónoma de la Ciudad de México. Av. Fray Servando Teresa de Mier 92. Col. Centro. México. D. F, 06080. México.

[b] Ingeniería en Sistemas de Transporte Urbano de la Universidad Autónoma de la Ciudad de México. Av. Fray Servando Teresa de Mier 92. Col. Centro. México. D. F, 06080. México.

[c] Escuela Superior de Física y Matemáticas del Instituto Politécnico Nacional, Unidad Profesional Adolfo López Mateos. Col. Lindavista. Deleg. Gustavo A. Madero. México, D. F., 07738. México.

ABSTRACT

The water uptake (WU) and ion exchange capacity (IEC) are two important parameters for PEMs, which represent their water retention and the proportion of exchangeable protons in the membrane, respectively. According to the vehicle mechanism of proton transport, an appropriate amount of water content and a suitable value of IEC in PEMs is necessary for achieving high proton conductivity. In this work, studies based on Density Functional Theory (DFT), Molecular Mechanics and Dynamics Simulations were realized in order to develop a theoretical methodology to obtain water uptake and ionic exchange capacity parameters. Unlike other methods, our proposal considers the molecular structure of the monomers of the membrane, the solvation medium and the various interactions between the monomer and water molecules. The methodology is applied to structures of sulfonated poly (ether-imide) (SPEI) with $(-SO_3H)_n$ (n=1,…6) groups. These structures were built and optimized aiming to obtain above properties as a function of the number of sulfonyl groups. The comparative study demonstrates that the SPEI with four sulfonyl groups in its backbone is the polymer having better properties for successful operation in fuel cells.

*Keywords:*water uptake; IEC; PEM.

Thermochemical Study of Ca $(OH)_2$-$CaCO_3$ Cycle for CO_2 Capture from Air and Co-Produce H_2

T. Ramírez-Rodríguez[1] , F. de Landa Castillo-Alvarado[1]

[1]Instituto Politécnico Nacional, Av. Instituto Politécnico Nacional s/n, San Pedro Zacatenco, Gustavo A. Madero, D.F, México, 07738.
e-mail: teresa.ramirez7715@gmail.com

ABSTRACT

The combination of the release of CO_2 from the decomposition of $CaCO_3$, with the CO_2-consuming dry reforming of CH_4, it is possible to simultaneously co-produce CaO and syngas in a single reaction. The benefit of such a combination is the considerable decrease of CO_2 emissions vis-à-vis the separate production of these two valuable commodities. Catalytic effects of decomposition/reforming of hydrocarbons using Ca-components have been studied with regard to coal gasification processes. Both CaO-producing reactions, reverse reaction, are highly endothermic and proceed at temperatures above 1300K. So that, they are attractive candidates for the use of concentrated solar energy as the source of high-temperature process heat, avoiding emissions such as COx, NOx, SOx and other pollutants derived from the combustion of fossil fuels.

This paper examines thermochemically a Ca $(OH)_2$-$CaCO_3$ cycle led to the capture of CO_2 from the air using concentrated solar energy. Open cycle material that co-produces hydrogen is analyzed. The equilibrium composition of the relevant reactions, temperature requirements and energy balances are calculated based on operating conditions, and the main sources of irreversibility are identified.

Keywords: CO_2 capture; Hydrogen; Methane reforming

Synthesis and Characterization of Poly {styrene-co-crylonitrile} for Application in Fuel Cells

L.F. Vieira[1], A.G. Dal-Bó[1], M.M.S. Paula[1], R. Benavides[2], T. A. Frizon[1]
L. da Silva[1, *]

[1]Universidade do Extremo Sul Catarinense (Unesc), Av. Universitária, 1105 - Cx.P. 3167, 88.806-000, Criciúma (SC), Brasil

[2] Centro de Investigación en Química Aplicada, Blvd. Enrique Reyna H. 140, Saltillo, Coah., México.

*Corresponding author. Tel.: + 55 48 91026649; FAX: + 55 48 34312674

E-mail address: luciano.silva@unesc.net (Luciano da Silva)

ABSTRACT

The growing demand for energy and concern about the high level of pollution caused by the emission of gases associated with fossil fuels has been significantly contributed to the development of alternative sources of power generation. Fuel cells have received considerable attention due to the direct conversion of chemical into electrical energy with high efficiency. In this context, Polymer Electrolyte Membrane Fuel Cells (PEMFCs) stand out due to their high performance, low emissions and low temperature operation, but these systems require hydration for use, which limits the operating temperature of the system. However, the development of polymer electrolytes to allow the use of temperatures higher than 130 ^{o}C, will open the type of catalyst used and hence reduce the degree of purity required for the fuel. Among the most commonly used membranes Nafion dominates the market for ionomer membranes, reaching the requirements of high proton conductivity below 100 º C. However, it has a high cost and is limited due to high permeability to methanol, for its use in direct methanol fuel cell. Alternatively, the proton conducting membranes of sulphonated aromatic based hydrocarbons, exhibit excellent thermal and chemical stability, reasonable mechanical strength and film-forming ability. In this work, the synthesis and characterization of membranes derived of poly{styrene-co-acrylonitrile} (SAN) is described. In order to enhance proton conductivity and thermal stability, sulfonation treatment and doping with nano metal particles (silver, gold and copper) were also carried out. Membranes were prepared by outside spin coating technique and evaluated for chemical structure, thermal stability, mechanical properties and proton conductivity. Results show doping increases thermal stability and ionic conductivity is similar to materials obtained commercially.

Keywords: Fuel cell, poly{styrene–co-acrylonitrile}, polymer electrolyte.


Sociedad Mexicana del Hidrógeno A. C.
Mexican Hydrogen Society


CONACYT


ITC

Synthesis and Properties of the Copolymer Styrene-5-(4-Oxipentenylfenil)-2-Octyltetrazol to use as Electrolyte.

C. Guralski[1], J.L. Westrup[1], R. Benavides[2], T. A. Frizon[1], A.G. Dal-Bó[1], U. Cano-Castillo[3], M.M.S. Paula[1], L. da Silva[1,*]

[1]Universidade do Extremo Sul Catarinense (Unesc), Av. Universitária, 1105 - Cx.P. 3167, 88.806-000, Criciúma (SC), Brasil

[2]Centro de Investigación en Química Aplicada, Blvd. Enrique Reyna 140, Saltillo, Coah., México

[3]Grupo de Hidrógeno y Celdas de Combustible, Reforma 113, col. Palmira C.P. 62490 Cuernavaca, Mor. México

*(luciano.silva@unesc.net)

ABSTRACT

Sustainable growth requires increasing alternative sources of power generation and such task has been undertaken in the majority of research centers around the world. The high levels of pollution caused by the burning of fossil fuels used for power generation, especially in the use of vehicles in general, causes attention and is directed towards clean sources of power generation. In this respect, fuel cells appear as magnificent sources of clean energy generation. However, these materials have limitations on their application and durability, mainly related to the dependence of water, which limits the operating conditions of the cells; as well as problems with fuel permeation. This work aims to elucidate the relationship between structure and properties of new materials that can be used as solid electrolytes in fuel cells. Copolymers from comonomers styrene and 5-(4-oxipentenylfenil)-2-octyltetrazol were synthesized and characterized in a 92:8 molar ratio. Copolymers prepared were evaluated in their chemical structure, thermal stability and thin film morphology. The effect of material structure on physical properties and conductivity were also investigated.

***Keywords**:* 5-(4-oxipentenefenil)-2-octiltetrazol; fuel cells, polyelectrolyte.

Electrochemical Evaluation of Membranes of poly-[styrene-co-acrylic acid] for use in PMFC

M. M. S. Paula[1,*], C. Burigo [1], H. J. de Souza[1], L. W. Oenning[1], L. da Silva[1], F. S. Notoya[1], A. G. Dal-Bó[1], T. E. A. Frizon[1], R. Benavides[2], J. C. O. Rodriguez[2]

[1]Universidade do Extremo Sul Catarinense (Unesc), Av. Universitária, 1105 - Cx.P. 3167, 88.806-000, Criciúma (SC)
[2] Centro de Investigación en Química Aplicada, Blvd. Enrique Reyna 140, Saltillo, Coahuila, México 25294
*E-mail address: bocaocao@gmail.com

ABSTRACT

Nanotechnology allows to create and implement materials, structures and systems by mounting and manipulating in atomic and molecular scale. New effects observed on the nanometer scale are explored in this study for the development of membranes for application in fuel cells (PMFC). It has been observed that the incorporation of metal nanoparticles of gold, silver, among others, in polymeric matrices increases the thermal stability of the membranes. This is desirable since the catalytic activity of the catalysts employed in cells is associated with operating temperature. In this study we report the preparation and electrochemical characterization of polymeric membrane of poly-[styrene-co-acrylic acid] sulfonated for application in PMFC. Poly-[styrene-co-acrylic acid] was prepared in the ratio 92:8, followed by sulfonation with H_2SO_4. Electrodes of Pt//poly-[styrene-co-acrylic acid] sulfonated were prepared by slow evaporation from a polymer solution deposited on its surface. The polymer films were characterized by cyclic voltammetry and electrochemical impedance spectroscopy in acidic and neutral media environment. Cyclic voltammograms were recorded in solutions 0.5 mol.dm^{-3} and revealed the presence of redox processes attributed to the H^+ ions. The thermal stability was evaluated by TGA and the microstructural characterization conducted by atomic force microscopy.

Keywords: Electrochemistry; metal nanoparticles; fuel cells

Incorporation of Carbon Vulcan Metal Nanoparticles for Catalytic Application in Fuel Cells (PMFC)

M. M. S. Paula[1,*], E. T. Zanoni[1], T. E. Frizon[1], A. G. Dal-Bó[1], U. Cano-Castillo[2], B. Escobar-Morales[3], L. da Silva[1]

[1]Universidade do Extremo Sul Catarinense (Unesc), Av. Universitária, 1105 - Cx.P. 3167, 88.806-000, Criciúma (SC)
[2] Grupo de Hidrógeno y Celdas de Combustible, Reforma 113, Col. Palmira, C.P. 62490 Cuernavaca, Mor., México
[3]Instituto Tecnológico de Cancún, Av. Kabah, Km 3, Cancún, Quintana Roo, México.
*E-mail address: bocaocao@gmail.com

ABSTRACT

Currently there is great interest in finding new ways to generate clean, renewable energy aimed at environmental preservation by reducing greenhouse gas emissions such as fossil fuels. Much has been done in this field of research and one of the main focuses in the area of non-polluting energy production are called polyelectrolyte membrane fuel cells (PMFC). Metallic nanoparticles are objects of study to serve as catalysts in these cells producing electricity. Materials at the nanoscale have different physicochemical properties when compared in macro-scale due to their high surface area. These particles when embedded in ceramic or polymeric materials can provide new catalytic properties, originating functionalized materials. In this study we report the preparation of metal nanoparticles of gold, silver, copper and ruthenium and, subsequent incorporation in Vulcan carbon or carbon nanotubes. The products were characterized using spectroscopic and analytical techniques. The evaluation of catalytic activity according to the method of preparation of Vulcan carbon||metallic nanoparticles and carbon nanoTubes||metallic nanoparticles system was investigated.

Keywords: Catalysts; metal nanoparticles; carbon Vulcan; cabon nanotubes.

XIV International Congress of the Mexican Hydrogen Society
Cancun, Mexico, 2014

Experimental Validation of a Coupled Nonlinear Observer in a Hydrogen Production Dark Fermenter

A. Villa-Leyva[1], A. Zhang[1], I. Torres-Zúñiga[1], A. Vargas[1], G. Buitrón[1,*]

[1]Laboratorio de Investigación en Procesos Avanzados de Tratamiento de Aguas, Unidad Académica Juriquilla, Instituto de Ingeniería, Universidad Nacional Autónoma de México, Blvd. Juriquilla 3001, Querétaro, Qro. C.P. 76230, Mexico.
[*]Tel: +524421926165; e-mail: gbuitronm@ii.unam.mx

ABSTRACT

In order to optimize the production of hydrogen from glucose in a continuous dark fermenter, an existing and already experimentally validated strategy is to modify the organic loading rate (OLR) by manipulating the inflow rate, based on an output-feedback control algorithm that aims at maximizing the hydrogen productivity, obtained through on-line measurements of the biogas composition and flow rate. However, the validation was made with a known and constant inflow substrate concentration (Sin) and thus the OLR was proportional to the dilution rate. To realistically implement the controller, real time knowledge of this concentration is needed. Since it cannot be measured on-line, the coupling of a second-order sliding-mode observer and a linear robust Luenberger observer can be used to estimate the substrate at the reactor input. Although a validation of the proposed estimator has already been done using numerical simulations based on a mathematical model that was calibrated with past experimental data, a further experimental validation of the proposed estimator was still needed. This work presents these results, with data obtained for 10 combinations of hydraulic retention times (HRT) and inflow substrate concentrations according to a Latin hypercube experimental design, leading to different values of OLR. Upon changing the OLR, sufficient time was allowed for reaching steady state conditions, and then returned to a standard operating condition of HRT=8 h and Sin=15 g/L before testing a different condition. The collected data allowed testing the proposed nonlinear observer in open loop after the experimentation period and the results are encouraging, leading to good estimations of the inflow substrate concentration, but being sensitive to perturbations that lead to an erroneous estimation of the biomass concentration with the Luenberger observer. Nevertheless, the observer may be suitable to complement the output-feedback control strategy previously proposed.

Keywords: bio-hydrogen production; nonlinear observer; bioprocess control

Optimization of Photo-Fermentative Hydrogen Production using Volatile Fatty Acids

R. Cardeña[1], G. Moreno[1], G. Buitrón[1]

[1]Laboratory for Research on Advanced Processes for Water Treatment, Instituto de Ingeniería, Unidad Académica Juriquilla, Universidad Nacional Autónoma de México, Blvd. Juriquilla 3001, Querétaro, Qro, México, 76230
Tel: +52 442 192 6165; e-mail: gbuitronm@ii.unam.mx

ABSTRACT

Biohydrogen yield can be incremented by using the volatile fatty acids, generated in the dark fermentation process, in a photo-fermentation process. In the present study, the optimum concentration of mixtures of volatile fatty acids for hydrogen production was evaluated using a response surface methodology (Box Behnken and Central Composite designs). A phototrophic hydrogen-producing consortium obtained from a bio-electrochemical system was enriched and used for experiments. The tests were conducted in serological bottles with a nitrogen-free environment. Bottles were mixed at 100 rpm and, 100 mg L^{-1} of biomass (as volatile suspended solids) was used. Temperature was maintained at and 35 °C and the reactors were illuminated under a constant radiation of 5000 lux. It was observed that high propionic acid concentrations caused inhibition of hydrogen production. A decrease on hydrogen production with the increase pH, due to ammonia formation (from 0.4 to 10.8 mg L^{-1}), was observed. The optimal conditions were found when acetic, propionic and butyric acids concentrations were 1200 mg L^{-1}, 715 mg L^{-1} and 1571 mg L^{-1}, respectively. Under such conditions hydrogen production rate was as much as 6.5 mmol d^{-1} L^{-1} and the maximal amount of hydrogen produced was 108.8 mmol L^{-1}.

Keywords: Photo-fermentation, hydrogen, volatile fatty acids

Hydrogen Production in a Microbial Electrolysis Cell Fed with Volatile Fatty Acids

I. Rivera[1] and G. Buitrón[1]

[1]Laboratory for Research on Advanced Processes for Water Treatment, Instituto de Ingeniería, Unidad Académica Juriquilla, Universidad Nacional Autónoma de México, Blvd. Juriquilla 3001, Querétaro, Qro, México, 76230
Tel: +52 442 192 6165; e-mail: gbuitronm@iingen.unam.mx

ABSTRACT

The organic matter consumption and the hydrogen production rate were evaluated in a two chamber microbial electrolysis cells (MEC). Three chemical oxygen demand concentration (COD) levels (400, 600 and 1200 mg/L) were tested. The COD was composed of a mixture of volatile fatty acids (VFAs) present in the effluent of a dark fermentation process containing. Two levels of voltage were studied: 350 mV and 550 mV. The MEC were operated in 120-hours batches. The performance of the MFC was evaluated using either an anionic (AEM) or a cationic exchange membrane (CEM). The robustness of the MEC was tested using a real dark fermentation effluent and another spiked with 1100 mg/L glucose. The highest production rates (81 mL/L/d) were obtained with 550 mV and 85% of COD consumption was attained. No significant differences on hydrogen production rate were observed when the COD was increasing from 400 to 1200 mg/l and using 550 mV. However, maximal hydrogen production rates were obtained with the lower COD concentration using 350 mV. No significant differences in the performance of the MEC were found by using AEM or CEM and also no significant differences of hydrogen production rates were found when real substrate o synthetic substrate was fed to the MFC. The substrate spiked with glucose was more slowly degraded since glucose was first transformed into VFAs (first 48 h) then the VFAs were consumed to produce hydrogen. In this case, methane and carbon dioxide were found after 120 h.

Keywords: microbial electrolysis cells; hydrogen; volatile fatty acids

Characterization of Catalysts Pt / γ-Al2O3 Prepared by Incipient Wetness Impregnation Method

M. Sanchez[1], J. Medina[2], J. Rodriguez[3], D. González[3], E. Mora[1]

[1]Universidad Politécnica de Aguascalientes, Calle Paseo, San Gerardo, 207, 20342, Aguascalientes, Ags., México, 20342.
[2] Instituto Tecnológico de Aguascalientes, Av. Adolfo López Mateos #1801 Ote.
Fracc. Bona Gens, Aguascalientes, Ags., México, 20256.
[3] Cinvestav Unidad Saltillo, Av. Industria Metalúrgica 1062, Zona Industrial, Ramos Arizpe, Coahuila de Zaragoza, México, 25900.
[1]Tel: +524494421400; e-mail: manuel.sanchez@upa.edu.mx

ABSTRACT

A platinum catalyst supported on gamma alumina was prepared by incipient wetness impregnation method, using as a precursor Platinum II acetylacetonate salt, because the precursor salt is soluble in water, a variant of the method, consisting of a milling is applied and physical mixing boehmite precursor salt with platinum, once the homogeneous physical mixture drops of a solution of nitric acid 1:16 dissolved in water was added, this was achieved by modifying the surface pH of the boehmite and achieve impregnation salt. They were anchored platinum particles by a controlled, to obtain oxides of platinum calcination method finally the metal oxide catalysts were reduced by exposure to a flow of hydrogen at 400°C, obtaining as a product a Pt /γ-Al_2O_3 can accelerate and direct the hydrodeoxygenation reaction of oxygenated organic compounds for converting a first generation biodiesel on a second generation biodiesel. The catalysts were characterized by Raman spectroscopy, X-ray diffraction, scanning electron microscopy, IR analysis and EDS. With the interpretation of the results the effectiveness of the process of preparation and the catalytic action to direct and accelerate ensures hydrodeoxygenation reaction.

Keywords: Pt/ γ-Al_2O_3; biodiesel, oxygenated organic compounds.

Preparation of a Solid Catalyst by Sulfonation Superacids from Mesoporous Carbon Material

L. Sanchez[1], J. Medina[2], J. Rodriguez[3], D. González[3]

[1]Universidad Politécnica de Aguascalientes, Calle Paseo, San Gerardo, 207, 20342, Aguascalientes, Ags., México, 20342.
[2] Instituto Tecnológico de Aguascalientes, Av. Adolfo López Mateos #1801 Ote.
Fracc. Bona Gens, Aguascalientes, Ags., México, 20256.
[3] Cinvestav Unidad Saltillo, Av. Industria Metalúrgica 1062, Zona Industrial, Ramos Arizpe, Coahuila de Zaragoza, México, 25900.
[1]Tel: +524494421400; e-mail: luis.sanchezo@upa.edu.mx

ABSTRACT

A new solid super acid catalyst was functionalized using H_2SO_4 as catalyst supports a mesoporous carbon from tire rubber. The method of sulfonation in liquid phase was through direct immersion incipient coal 98.3 % concentrated H_2SO_4 in a flask under reflux. The carbonization temperature of tire rubber pyrolysis was performed with a flow of N_2 at low temperature to obtain a mesoporous carbon and achieve effective sulfonation. The mesoporous carbon was functionalized with the group $-SO_3H$, CMHL520 -SO3H, was characterized by XRD, SEM, EDS, IR and elemental analysis, indicating the presence of polycyclic disordered carbon plates in structure extremely high surface area and large pores that provided more acidic surface sites. The high catalytic activity and stability of this catalyst is related to the acid site density by -OH, Bronsted acid sites, hydrophobicity preventing hydration of hydrophilic -OH and $-SO_3H$ functional groups.

Keywords: Solid super acid catalyst, mesoporous carbon, pyrolysis.


Sociedad Mexicana del Hidrógeno A. C.
Mexican Hydrogen Society


CONACYT


ITC

Paramagnetic behavior of Ni-Fe Layered Double Hydroxide and their effect over the Electrocatalytic Activity towards Oxygen Evolution Reaction in Alkaline Media

Miguel A. Oliver Tolentino[a]*, Arturo Manzo-Robledo, Juvencio Vázquez-Samperio[b], Ariel Guzmán-Vargas[b]

[a]Instituto Politecnico Nacional, UPIBI-Departamento de Bioingeniería. Av. Acueducto s/n, Barrio La Laguna, Col. Ticomán, México, D.F. 07340, Mexico
[b]Instituto Politécnico Nacional, ESIQIE-Departamento de Ingeniería Química, Laboratorio de Investigación en Materiales Porosos, Catálisis Ambiental y Química Fina, UPALM Edif. 7 P.B. Zacatenco, GAM, México, DF 07738, Mexico
*otma_iq@hotmail.com

ABSTRACT

In the present work the hydrotalcite like materials know as Layered Double Hydroxide (LDH) Ni-Fe with different Ni/Fe relationship were synthesized by co-precipitation method to constant pH, the LDH obtained were labeled H/Ni-Fe1 and H/Ni-Fe2, the hexagonal lattices with R3m rhombohedral symmetry, characteristic for this materials was verify by XRD, No secondary phases are observed for any materials. On the other hand, the electronic properties were evaluated by Electronic Paramagnetic Resonance (EPR), the results suggested that H/Ni-Fe1 exhibited a ferromagnetic behavior as a result of the combined action of NiII-OH-NiII and FeIII-OH-NiII and FeIII-OH-FeIII pairs across the layers and ferromagnetic dipolar interactions operating between layers. Whereas, the H/Ni-Fe2 presented a Paramagnetic behavior due to intralayer magnetic superexchange between metal centers through the OH bridges across the cationic sheets and dipole–dipole interaction in sites of less distorted octahedral field which operating through the space between the magnetic layers. These materials were evaluated as electrocatalyst in the Oxygen Evolution Reaction (OER) in alkaline media, the results showed that OER begin c.a. to 1.4V/NHE, the tafel plots for both materials were around to 39mV dec-1 which is comparable with IrO in same media. However, the Turn Over Number (TON) value was 9.9 s-1 for H/Ni-Fe1 and 38.1 s^{-1} for H/Ni-Fe2, indicating the higher electrocatalytic behavior in H/Ni-Fe2 than H/Ni-Fe1, this interesting result were discusses by electronic properties determinate in EPR experiments.

Keywords: LDH, Paramagnetic, Turn Over Number

XIV International Congress of the Mexican Hydrogen Society
Cancun, Mexico, 2014

Evaluation of Different Support Materials used with a Photo-Fermentative Consortium for Hydrogen Production

E. Guevara-López[1], G. Buitrón[1*]

[1]Laboratory for Research on Advanced Processes for Water Treatment, Instituto de Ingeniería, Unidad Académica Juriquilla, Universidad Nacional Autónoma de México, Blvd.J uriquilla 3001, Querétaro, Qro, México, 76230
Tel: +52 442 192 6165; *e-mail: gbuitronm@ii.unam.mx

ABSTRACT

Four different support materials were evaluated for immobilization of a consortium of purpur non-sulfur bacteria (PNS) producing hydrogen gas. The inoculum was enriched from a microbial fuel cells. Tested materials were acrylic bars, silica gel, high-density polyethylene cylinders and luffa (dispersed fibers and cubes). The area/volume ratio, volatile solids per area and the amount of hydrogen produced using volatile fatty acids as substrate were determined. The experiments were conducted in serological bottles of 120 mL, continuously illuminated at 7 kilolux, mixed at 100 rpm and 32 °C. It was found that the PNS bacteria generated 16.7 ± 2.6 mLH_2/gVS-h. The highest biomass quantity (as volatile solids, VS) was found in dispersed luffa fibers (8.0 ± 1.7 $mgVS/cm^3$) followed by luffa in cubes, high-density polyethylene cylinders and acrylic bars. Dispersed luffa allowed a better light distribution and contact with the media than luffa in cubes. Silica gel was not suitable for the immobilization and hydrogen production. Experiments with the colonized supports indicated that no significant differences regarding specific hydrogen production were observed among luffa, acrylic bars and polyethylene. In conclusion the luffa in the form of fibers is a suitable support for purpur non-sulfur consortium because of this provide the highest area/volume ratio and the highest attached quantity of VS per volume. After several batches the biomass remained attached to the support.

Keywords: Hydrogen, cell immobilization, photo-fermentation

XIV International Congress of the Mexican Hydrogen Society
Cancun, Mexico, 2014

Research on Methanol-Tolerant Catalysts for the Oxygen Reduction Reaction

M Asteazaran[1,2], G Cespedes[2], S Bengió[3], MS Moreno[3], WE Triaca[1], AM Castro Luna[1,2*]

[1]Instituto de Investigaciones Fisicoquímicas Teóricas y Aplicadas (INIFTA), Facultad de Ciencias Exactas, UNLP- CONICET
[2]Centro de Investigación y Desarrollo en Ciencia y Tecnología de Materiales (CITEMA) Facultad Regional La Plata,UTN
[3]Centro Atómico Bariloche, Comisión Nacional de Energía Atómica (CAB-CNEA) – Argentina
[*]Tel: +542214257430; e-mail: castrolu@gmail.com

ABSTRACT

Direct methanol fuel cells (DMFCs) represent an interesting alternative to obtain electricity in a clean and efficient way, potentially valuable to substitute traditional environmentally harmful technologies.

Portable power sources are one of the most promising applications of passive DMFCs. One of the requirements in these devices is to use high alcohol concentration. Unfortunately, the methanol permeation across the polymer electrolyte membrane (methanol crossover) causes a considerable loss of the fuel cell efficiency because both the oxygen reduction reaction (ORR) and the methanol oxidation reaction (MOR) occur simultaneously in the cathode.

In order to develop methanol tolerant cathodes with suitable activity at low temperature, different PtM, PtMRu and PtMPd catalysts, with M = Co or Fe were prepared either via poliol reduction (*EG catalysts*) or alloy (*AL catalysts*) methods, the latter followed by a thermal treatment in a reducing atmosphere.

All cathode-catalysts were studied to determine the role of the components in enhancing the ORR and discouraging the MOR, simultaneously.

The physical characterization of the synthesized materials was accomplished by TEM, XPS and EDS. According to the synthesis procedure, XPS spectra showed that the amount of metal oxides on the catalyst varies. Small and well distributed particles on the carbon support were shown by TEM.

The catalysts electrochemical characterization was accomplished in a three electrodes electrochemical cell with a glassy carbon rotating disk electrode covered with a thin catalytic layer as the working electrode. Linear sweep voltammetry, chronoamperometry and electrochemical impedance spectroscopy were employed.

Electrochemical results showed that the AL catalysts have better activity for the ORR. However, the enhanced activity of *AL catalysts* is completely lost when the ORR is accomplished in presence of methanol. On the other hand, binary or ternary *EG catalysts* showed higher methanol tolerance, the role of metal oxides according the synthesis method is discussed.

Keywords: ORR; Methanol Crossover; DMFCs

XIV International Congress of the Mexican Hydrogen Society
Cancun, Mexico, 2014

Derivation of Mathematical Model Based on Tafel Equation Explains Microbial Fuel Cell Performance

G. Hernandez-Flores[a], O. Solorza-Feria[b], M. T. Ponce Noyola[c], T. Romero-Castañon[d], N. Rinderknecht-Seijas[e] and H. M. Poggi-Varaldo[a*]

[a] Environmental Biotechnology and Renewable Energies R&D Group, Dept. of Biotechnology and Bioengineering, Centro de Investigación y de Estudios Avanzados del Instituto Politécnico Nacional. Av. Instituto Politécnico Nacional 2508, Col. San Pedro Zacatenco, Delegación Gustavo A. Madero, México D.F., C. P. 07360 Apartado Postal: 14-740, 07000 México, D.F. Tel: +52 (55) 5747 3800 ext 4321 & 4324
[b] Dept. of Chemistry, *ibídem.* Av. Instituto Politécnico Nacional 2508, Col. San Pedro Zacatenco, Delegación Gustavo A. Madero, México D.F., C. P. 07360 Apartado Postal: 14-740, 07000 México, D.F.
[c] Dept. Biotechnology and Bioengineering, *ibídem.* Av. Instituto Politécnico Nacional 2508, Col. San Pedro Zacatenco, Delegación Gustavo A. Madero, México D.F., C. P. 07360 Apartado Postal: 14-740, 07000 México, D.F.
[d] Electric Research Institute. Reforma 113, Col. Palmira, C. P. 62490 Cuernavaca, Morelos, México.
[e] ESIQIE del IPN, Division of Basic Sciences. Escuela Superior de Ingeniería Química e Industrias Extractivas, ESIQIE. Edificio N° 7, Unidad Profesional Adolfo López Mateos. Colonia Lindavista, Delegación Gustavo A. Madero, México D.F., C. P. 07738.

*Author for correspondence: r4cepe@yahoo.com

ABSTRACT

The aim of this work was to establish a mathematical model based on Tafel equation to quantitatively relate the maximum volumetric power ($P_{V,max}$) as well as the internal resistance (R_{int}) in a Microbial Fuel Cell (MFC), with the specific surface area of the graphite anodes (A'_s), and either their conductance C or electrolytic conductivity σ of the material.
The *MFC* consisted of a horizontal cylinder built in Plexiglas 80 mm long and 57 mm internal diameter. The anodic chamber was packed with the different anodic materials (graphite rod (*GR*), triangles of graphite (*GT*) and graphite flakes (*GF*))
The R_{int} were 795, 410 and 273 Ω for *GR*, *GT* and *GF*, respectively, whereas the $P_{V,max}$ were 1326, 2108 and 3052 mW/m^3 for *GR*, *GT* and *GF*, respectively. There was a correspondence of either the decrease of R_{int} or the increase of $P_{V,max}$ with the increase of the log of A'_s of the graphite anodic materials. Here we show the detailed derivation of a mathematical model for the $P_{V,max}$ and R_{int} based on Tafel equation for the cell potential; it lead to equations that exhibited a good correlation with experimental results.
The best fitting models for $P_{V,max}$ were $P_{V,max} = a_0' + a_1' * \log A'_s$ and $P_{V,max} = a_0' + a_1' * \log A'_s + a_2' * \log C$ with determination coefficients 0.8872 and 0.9810, respectively. On the other hand for R_{int} the best fitting models were $R_{int} = b_0' + b_1' * \log A'_s$ and $R_{int} = b_0' + b_1' * \log A'_s + b_2' * \log C$, with determination coefficients 0.8850 and 0.8904, respectively. In general, the inclusion of the electrolytic conductivity did not improve model fitting, whereas the inclusion of conductance lead to a higher determination coefficient in the P_V model but not in the model of R_{int}.

Keywords: Mathematical Model, Volumetric Power, Microbial Fuel Cells

Characteristics of a Single Chamber Microbial Fuel Cell Fitted with Low Cost Membrane

G. Hernandez-Flores[a], O. Solorza-Feria[b], M. T. Ponce Noyola[c], T. Romero-Castañon[d], N. Rinderknecht-Seijas[e], J. Galíndez-Mayer[f], H. M. Poggi-Varaldo[a*]

[a] Environmental Biotechnology and Renewable Energies R&D Group, Dept. of Biotechnology and Bioengineering, Centro de Investigación y de Estudios Avanzados del Instituto Politécnico Nacional. Av. Instituto Politécnico Nacional 2508, Col. San Pedro Zacatenco, Delegación Gustavo A. Madero, México D.F., C. P. 07360 Apartado Postal: 14-740, 07000 México, D.F. Tel: +52 (55) 5747 3800 ext 4321 & 4324

[b] Dept. of Chemistry, *ibídem.* Av. Instituto Politécnico Nacional 2508, Col. San Pedro Zacatenco, Delegación Gustavo A. Madero, México D.F., C. P. 07360 Apartado Postal: 14-740, 07000 México, D.F.

[c] Dept. Biotechnology and Bioengineering, *ibídem.* Av. Instituto Politécnico Nacional 2508, Col. San Pedro Zacatenco, Delegación Gustavo A. Madero, México D.F., C. P. 07360 Apartado Postal: 14-740, 07000 México, D.F.

[d] Electric Research Institute. Reforma 113, Col. Palmira, C. P. 62490 Cuernavaca, Morelos, México.

[e] ESIQIE del IPN, Division of Basic Sciences. Escuela Superior de Ingeniería Química e Industrias Extractivas, ESIQIE. Edificio N° 7, Unidad Profesional Adolfo López Mateos. Colonia Lindavista, Delegación Gustavo A. Madero, México D.F., C. P. 07738.

[f] ENCB del IPN, Division of Basic Sciences. Escuela Nacional de Ciencias Biológicas, ENCB. Unidad Profesional Lázaro Cárdenas, Prolongación de Carpio y Plan de Ayala s/n, Col. Santo Tomas C. P. 11340 Delegación Miguel Hidalgo México, D.F.

*Author for correspondence: r4cepe@yahoo.com

ABSTRACT

Proton exchange membrane (*PEM*) is a key component of microbial fuel cells (*MFC´s*) design and configuration, and determines both performance and the cost of the device.

On the one hand, the membrane acts as a channel in *MFC* that allows the transport of protons to the cathode. On the other hand, the *PEM* avoids, at the same time, the oxygen back diffusion to the anodic chamber. Currently, Nafion is the most common membrane used due its good transport properties; however its cost is high and it determines about 40 % of the microbial fuel cell total cost.

Thus, the aim of this research was *(i)* to test a new organic membrane (*NOM*) based on agar in an air-cathode, single chamber *MFC*, and *(ii)* to compare its characteristics with the *MFC* performance fitted with a Nafion® 117 membrane (*NF*).

The *MFC* consisted of a horizontal cylinder built in Plexiglas 80 mm long and 57 mm internal diameter. The anodic chamber was packed with graphite flakes as anodic material The *MFC* was seeded with a sulfate-reducing inoculum. The *MFC* performance was determined using the polarization curve method, by varying the external resistances and recording both the voltage and the current intensity.

The internal resistances (R_{int}) were 192 and 110 Ω using *NOM* and *NF*, respectively, whereas the maximum volumetric powers ($P_{v,max}$) were 2120 mW/m^3 and 14,181 for *NOM* and *NF*, respectively. The relatively low value of R_{int} of *NOM*-fitted *MFC* was encouraging, although it was twice the value of the NF-fitted MFC. Power delivered with *NOM* was 15% of that with Nafion 117. However, the cost ratio *NOM*/Nafion was quite low, (US$ 14/m^2)/(US$ 1733/m^2) ~ 1/120 ~ 1%. These results point out to a trade-off between sacrificing some power output of the cell (85%) but achieving outstanding savings on membrane costs (99%).

Key words: New Organic Membrane, Nafion 117 Membrane, Microbial Fuel Cell

Alternative Proton Exchange Membrane Fitted in a Microbial Fuel Cell in Batch Operation

G. Hernandez-Flores[a], O. Solorza-Feria[b], T. Romero-Castañon[c], E. Ríos-Leal[d], J. Galíndez-Mayer[e], F. Esparza-García[f], H. M. Poggi-Varaldo[a*]

[a] Environmental Biotechnology and Renewable Energies R&D Group, Dept. of Biotechnology and Bioengineering, Centro de Investigación y de Estudios Avanzados del Instituto Politécnico Nacional. Av. Instituto Politécnico Nacional 2508, Col. San Pedro Zacatenco, Delegación Gustavo A. Madero, México D.F., C. P. 07360 Apartado Postal: 14-740, 07000 México, D.F. Tel: +52 (55) 5747 3800 ext 4321 & 4324

[b] Dept. of Chemistry, *ibídem.* Av. Instituto Politécnico Nacional 2508, Col. San Pedro Zacatenco, Delegación Gustavo A. Madero, México D.F., C. P. 07360 Apartado Postal: 14-740, 07000 México, D.F.

[c] Electric Research Institute. Reforma 113, Col. Palmira, C. P. 62490 Cuernavaca, Morelos, México.

[d] Dept. Biotechnology and Bioengineering, *ibídem.* Av. Instituto Politécnico Nacional 2508, Col. San Pedro Zacatenco, Delegación Gustavo A. Madero, México D.F., C. P. 07360 Apartado Postal: 14-740, 07000 México, D.F.

[e] ENCB del IPN, Division of Basic Sciences. Escuela Nacional de Ciencias Biológicas, ENCB. Unidad Profesional Lázaro Cárdenas, Prolongación de Carpio y Plan de Ayala s/n, Col. Santo Tomas C. P. 11340 Delegación Miguel Hidalgo México, D.F.

[f] Dept. Biotechnology and Bioengineering, *ibídem.* Av. Instituto Politécnico Nacional 2508, Col. San Pedro Zacatenco, Delegación Gustavo A. Madero, México D.F., C. P. 07360 Apartado Postal: 14-740, 07000 México, D.F.

*Author for correspondence: r4cepe@yahoo.com

ABSTRACT

It is recognized that performance and cost of microbial fuel cells (*MFC*) depend substantially on the proton exchange membrane (*PEM*) used. At present, Nafion is the most commonly used membrane in *MFC* due its good transport properties. Yet, its commercial price is up to US $ 1470/m^2 and it determines *ca.* 40 % of the *MFC* total cost. In recent years, there has been an increased interest in finding suitable replacements for Nafion as *PEM* material. Therefore, the objective of this work was to compare the effect of membrane type on the performance of *MFC* operated in long batch process. The tested *PEMs* were Nafion 117 (*NF*) and a new organic membrane (*NOM*). The treated influent was a very recalcitrant, actual leachate from Mexico City sanitary landfill.

The *MFC* was seeded with an inoculum previously enriched in electrochemically-active bacteria using a selective medium of Fe(III) salts and acetate. The batch lasted 15 days.

MFC characteristics improved with time of operation; this suggested an in-cell enrichment process or acclimation of inoculum. Indeed the values of internal resistance (R_{int}) were 650 y 350 Ω at 0 d for *NOM* and *NF*, respectively, whereas the maximum volumetric power ($P_{v,max}$) were 9 and 1100 mW/m^3 at 8 d for *NOM* and *NF*, respectively.

During the batch operation, the cell fitted with *NOM* outperformed the one fitted with *NF*. Average volumetric powers (P_Vs) were 14 and 5 W/m^3 for *MFC* fitted with *NOM* and *NF*, respectively. Considering the subperiod from 9 to 15 d when external resistances were adjusted, the average P_Vs were 18.9 and 5.1 W/m^3 for *NOM* and *NF*, respectively. At the end of the operational period, deposits of dry salts appeared on the external side of the cathode carbon cloth of the cell fitted with *NF*. This effect was not observed for the cell with *NOM*. Presumably, these deposits could be responsible for the decrease of power output during 9 to 15 d in the cell fitted with *NF*.

Key words: Natural Polymer Organic Membrane, Batch Operation, Microbial Fuel Cell, Leachate

XIV International Congress of the Mexican Hydrogen Society
Cancun, Mexico, 2014

Development and Characterization of Pd-CeO_2 Electrocatalysts for the Formic Acid and Glycerol Oxidization Reactions in Acid Medium

A. Altamirano-Gutiérrez[1], A.M. Fernández[1], F.J. Rodríguez Varela[2,*], Aruna K Kunhiraman[3], Ramasamy Manoharan[3], P. Karthikeyan[4]

[1]Instituto de Energías Renovables, Universidad Nacional Autónoma de México, Privada Xochicalco S/N, Temixco, Morelos, C. P. 62580, México.
[2]Grupo de Sustentabilidad de los Recursos Naturales y Energía, Cinvestav Unidad Saltillo, Av. Industria Metalúrgica 1062, Parque Industrial Ramos Arizpe. Ramos Arizpe, Coahuila, C.P. 25900, México.
[3]Electrochemical Energy Materials Laboratories
Nanotech Research Facility, PSG Institute of Advanced Studies, Coimbatore, India, 641 004
[4]Department of Automobile Engineering, PSG College of Technology, Coimbatore, India, 641 004
[*]Tel: +52 844-438-9612; e-mails: alexalgtz@gmail.com, javier.varela@cinvestav.edu.mx

ABSTRACT

In this work, Pd-CeO_2 and Pd-CeO_2/C electrocatalysts were synthesized by pyrolysis at 300 and 600 ^oC during 5 hours, in a reducing atmosphere of H_2/N_2 (50:50), in order to study their catalytic activity for the formic acid oxidation reaction (FAOR) and the glycerol oxidation reaction (GOR). The reactions were carried out in acid medium. The electrocatalysts were characterized by XRD, HRTEM, EDS, and electrochemical techniques such as CV. The XRD results indicated the formation of polycrystalline materials with particles sizes ranging from 10 to 48 nm. The unsupported materials showed no catalytic activity as anodes for the FAOR or the GOR. Also, supported Pd-CeO_2/C synthesized at 300 and 600 ^oC showed no activity for the GOR. However, the Pd-CeO_2/C electrocatalysts showed a high catalytic activity for the electro-oxidation of formic acid. The results suggested that the chemical surface composition of Pd-CeO_2/C differs from that of Pd-CeO_2 due to an effect of the carbon support during the synthesis. Such modification gave the supported material a high catalytic activity towards the FAOR. Therefore, the Pd-CeO_2/C electrocatalysts could be considered as candidate anodes for direct formic acid fuel cells (DFAFCs).

Keywords: Pd-CeO_2/C electrocatalysts, nanomaterials, formic acid oxidation reaction, DAFCs.

XIV International Congress of the Mexican Hydrogen Society
Cancun, Mexico, 2014

Theoretical Study of Ru-Organometallic Compounds-Functionalized Grapheneas Catalyst Supports for Low-Temperature Fuel Cells.

A. Siller-Ceniceros[1*], E. Sánchez Castro[2], F.J. Rodríguez Varela[1,2,*], M. Sánchez Vázquez[3]

[1]Programa de Nanociencias y Nanotecnología, Cinvestav Unidad Saltillo, Av. Industria Metalúrgica 1062, Parque Industrial Ramos Arizpe. Ramos Arizpe, Coahuila, C.P. 25900, México.
[2]Grupo de Sustentabilidad de los Recursos Naturales y Energía, Cinvestav Unidad Saltillo, Av. Industria Metalúrgica 1062, Parque Industrial Ramos Arizpe. Ramos Arizpe, Coahuila, C.P. 25900, México.
[3]Centro de Investigación en Materiales Avanzados, S.C. Alianza Norte 202, PIIT, Carretera Monterrey-Aeropuerto Km. 10, Apodaca NL 66600, México.
[*]Tel: +52(844)438-9600ext 8612; e-mails: adriana.siller@cinvestav.edu.mx, javier.varela@cinvestav.edu.mx

ABSTRACT

Nanostructured compounds such as carbon nanotubes (CNT), graphene (Gr) and ordered mesoporous carbon (OMC) have proven to be excellent supports to homogenously disperse electrocatalyst for fuel cell applications. However, the surface of these carbon materials has to be functionalized in order to properly anchor nanoparticles. Typically, aqua regia has been used to chemically modify the surface of the supports. In this work, the functionalization of graphene with ruthenium organometallic compounds (OM-Ru) has been studied using density functional theory (DFT) calculations. The OM-Ru complexes have ligands such as η^6-arene, -OH, -NR_2, -COOH and other polar groups that can promote the formation of surface functional groups on the graphene support to anchor Pt nanoparticles. Furthermore, it has been hypothesized that metallic Ru nanoparticles can be formed after functionalization and interact with Pt to create bimetallic phases. Thus, a synergetic effect at the graphene surface can be expected. The Pt/Gr electrocatalysts will be tested as anode materials for the Methanol and Ethanol Oxidation Reaction.

Keywords: Graphene supports; ruthenium organometallic compounds; functionalization; DFT; fuel cells.

XIV International Congress of the Mexican Hydrogen Society
Cancun, Mexico, 2014

Characterization of Cathode/Electrolyte Interphases for IT-SOFCs

A.Soldati[1], K. Padmasree[2], L. Baqué[1], A. F. Fuentes[2], A. Serquis[1,*]

[1]CONICET-Centro Atómico Bariloche, CNEA, Av. Bustillo 9500, S. C. Bariloche, Río Negro, Argentina, R8402AGP.
[2]Sustentabilidad de los Recursos Naturales y Energía, Cinvestav Unidad Saltillo, Coahuila, México, 25900.
[*]Tel: +542944445100; e-mail: aserquis@cab.cnea.gov.ar

ABSTRACT

Solid oxide fuel cells (SOFCs) represent an efficient and environmental friendly technology to convert directly hydrogen and fossil fuels into electrical power and heat. These devices require high operation temperature to allow the transport of oxygen ions through the ceramic components of the cell, challenging the long term stability and inducing rapid degradation of the cell. In recent years, a considerable research effort has been done in order to decrease the operation temperature from 800-1000ºC to the 500-800ºC range in the so-called Intermediate Temperature (IT)-SOFCs. One of the materials of choice for IT-SOFCs electrolytes is the ceria based oxides because they present higher oxygen ion conductivities at lower operation temperatures. Nevertheless, the main drawback of using intermediate temperatures is the increase of the cathode overpotential, which limits the overall performance of the cell. This issue can be overcome with the use of nanostructured mixed conducting oxide cathodes. It is also important to note that the performance of the whole cell depends not only of each individual component but also of the interphase between them. In this work, we studied symmetrical cells composed by high performance nanostructured $La_{0.4}Sr_{0.6}Co_{0.8}Fe_{0.2}O_3$ (LSCFO) cathodes deposited by spin coating on $Ce_{0.8}Y_{0.2}O_2$ (CYO) electrolytes. LSCFO cathodes were synthetized by an acetic acid based method, while the CYO electrolytes were synthesized by mechanical milling. The assemblies were studied by Electrochemical Impedance Spectroscopy, X-Ray Diffraction and Transmission and Scanning Electron Microscopy. The correlation between the electrochemical behavior within the 300-600ºC range, and the bulk and interfacial characteristics will be discussed.

Keywords: Solid oxide fuel cells; electrolyte; interphase

XIV International Congress of the Mexican Hydrogen Society
Cancun, Mexico, 2014

Mg-M-Li Alloys Prepared by Mechanical Alloying and their Hydrogen Storage Characteristics

K. Suárez-Alcántara[1], A.F. Palacios-Lazcano[2], J. G. Cabañas-Moreno[3]

[1]UNAM-IIM Morelia, Antigua carretera a Pátzcuaro 8710, Col. Ex-hacienda de San José de la Huerta, Morelia, Michoacán, México, 58190.
[2]ESIME Zacatenco, Miguel Othón de Mendizábal S/N Col. La escalera, Del. Gustavo A Madero, México. 07320.
[4]Centro de Investigación y de Estudios Avanzados, IPN, Av. Instituto Politécnico Nacional 2508, D.F. México, 07360.

ABSTRACT

$Mg_{96}M_2(LiH)_2$ (M=Y, Zn, Al, Ag), $Mg_{98}(LiH)_2$ and $Mg_{96}(LiH)_4$ powder alloys were produced by ball milling and deliberately air-exposed by 12 hours in order to investigate their hydrogen storage properties. The addition of LiH at the level of 2 mol % had a beneficial effect on the kinetics of the hydriding and dehydriding processes at 300 and 350 °C compared to mechanically milled Mg powders. However, the additions of Al, Ag, Zn and Y mostly had an opposite effect. Only the addition of aluminum seems to have provided an advantage of a different sort, in reducing the susceptibility of the Mg powders to become oxidized during the course of processing and of the hydriding and dehydriding treatments.

Keywords: hydrogen storage; Mg alloys; PCI curves.

In-situ XRD Studies of H_2 Sorption/ Desorption on CaH_2+MgB_2 Reactive Hydride Composite Doped with Fuorinated Compounds

K. Suárez-Alcántara[1*]

[1]UNAM-IIM Morelia, Antigua carretera a Pátzcuaro 8710, Col. Ex-hacienda de San José de la Huerta, Morelia, Michoacán, México, 58190.
e-mail: karina_suarez@iiu.unam.mx

ABSTRACT

The reactive hydride composites (RHC) $9CaH_2 + 10MgB_2 + CaF_2$, $10Ca(BH_4)_2 + 9MgH_2 + MgF_2$ and $9Ca(BH_4)_2 + Ca(BF_4)_2 + 10MgH_2$ were prepared by ball milling. Their properties towards hydrogenation were tested by means of manometric measurements. The highest reversible hydrogen storage capacity was obtained at $9CaH_2 + 10MgB_2 + CaF_2$ (7.6 wt. %). The effects of fluorine source and its mobility on the dehydrogenation reaction were studied by means of in situ time-resolved synchrotron radiation powder X-ray diffraction (SR-PXD), differential scanning calorimetry (DSC), and attenuated total reflection infrared (ATR-IR) techniques. Independently of the F source, the formation of CaF_2 was observed after cycling. SR-PXD studies indicate the formation of a complex mixture of phases. In these RHC systems, the formation of hydrided Mg-Ca compounds and losing of Boron can hinder the hydrogen sorption/ desorption reversibility.

Keywords: Hydrogen storage; reactive hydride composites; fluorine.

Influence of the Synthesis Parameters in CNT Doped with Nitrogen Towards the Electroreduction of Oxygen

Isaías Zeferino González, Ivonne Alonso Lemus, Beatriz Escobar Morales, Ana María Valenzuela Muñiz, Ysmael Verde Gómez[a].

[a] *Instituto Tecnológico de Cancún, Av. Kabah Km. 3, Cancún, Q.R., México, 77500. yverde@yahoo.com*

ABSTRACT

One of challenges in the commercialization of fuel cells is the high cost and scarcity of platinum based catalysts. In addition, there is also the slow kinetics problem in the oxygen reduction reaction (ORR). Therefore, alternative electrocatalysts are needed. Systems based on doped carbon nanostructures (without the use of active metals) have been proposed as a good option to solve both of the drawbacks before mentioned. In the present study, nitrogen doped carbon nanotubes (N-CNTs) were by a chemical vapor deposition method. Pyridine was used as carbon and nitrogen precursor and ferrocene as a metal catalyst for the nanotubes growth. Different synthesis conditions such as temperature of the reactor, carrier gas flow, concentration of the reactants, and vaporizer temperature were studied. The purpose of this variation of parameters was to found the optimal conditions in which the material achieves the best catalytic activity. The electrocatalytic performance was evaluated towards the ORR by linear sweep voltammetry measurements. A catalyst-coated rotating disk electrode at different rotation rates in 0.5 M H_2SO_4 solution was performed. The results show that the reactor temperature and gas flow significantly influence the characteristics of the materials and hence the electrocatalytic activity for ORR. The factors that determine the high electrocatalytic activity of the N-CNTs are discussed.

Keywords: Nanotubes; Carbon; Synthesis.

Electrochemical Studies of Poly(styrene-co-acrylic acid) PEM Membranes Synthesized by two different Methods

J.C.O. Rodriguez[1], L. Melo[1], R. Benavides[1]*, M. M. S. Paula[2] , L. da Silva[2]

[1] Centro de Investigación en Química Aplicada, Blvd. Enrique Reyna H. 140, Saltillo, Coahuila, México.

[2] Universidade do Extremo Sul Catarinense (UNESC), Av. Universitária, 1105 - Cx.P. 3167, Criciúma, SC. Brazil, 88.806-000

.*Corresponding author. Tel.: + 52 01 844 438 9830 ext. 1322

E-mail address: roberto.benavides@ciqa.edu.mx (Roberto Benavides)

ABSTRACT

The synthesis of two alternatives to Nafion random copolymers was carried out by radical copolymerization. Poly(styrene-co-acrylic acid) (PSAA) in a 94:6 styrene-acrylic acid molar relation, partially cross-linked with trimethylol propane trimethacrylate (TMPTMA) was synthesized by mass polymerization. The PSAA obtained was sulfonated (PSAAS-m) with sulphuric acid, considering the 100 % molar substitution of styrene benzene rings. Separately, same random PSAA was synthesized by solution polymerization, but cross-linked with Divinylbenzene (DVB) and sulfonated (PSAAS-s) with acetyl sulphate at a 20 % molar substitution with respect to benzene rings. Copolymers, including non sulfonated blanks, were dissolved in THF and used to coat a platinum (Pt) electrode by "deep coating" and studied electrochemically by the voltamperometric cycle technique in H_2SO_4 0.5 M. Both non-sulfonated PSAA copolymers showed only a baseline signal, indicating no proton conductivity through them. Similarly was observed for the PSAAS-s copolymer, suggesting no proton conductivity as well. On the other hand, the copolymer synthesized in mass and highly sulfonated (PSAAS-m) showed the corresponding signals of Pt reduction, as observed in the experiment carried out for the Pt electrode without any coating.

Keywords: sulfonated PSAA , fuel cells, Pt electrode.

Towards the Hydride Tank for Hydrogen Storage

J.C. Carranza-García [1, 2], A.M. Castañeda-Lopez[1, 2], F. Reyes-Calderon[1], M. Valdovinos-Lombera[1], K. Suarez-Alcantara[2,*]

[1]Instituto Tecnológico de Morelia. Avenida Tecnológico No. 1500 Lomas de Santiaguito, Morelia, Michoacán, México, 58120.
[2]UNAM-IIM Morelia, Antigua carretera a Pátzcuaro 8710, Col. Ex-hacienda de San José de la Huerta, Morelia, Michoacán, México, 58190.
* e-mail: karina_suarez@iiu.unam.mx

ABSTRACT

TiFe-Ni/C-nanotubes alloy was prepared by high-energy ball milling. The alloy was characterized for hydrogen storage purposes by SEM, hydrogen storage capacity/ kinetics and DSC. A 1 kg hydride tank was designed and constructed in stainless steel 316L. This tank operates at room temperature and low hydrogen pressure (15 bar); however the design and construction allows changing the hydride material for higher operational-temperature materials. This hydride tank is our first prototype for mobile applications.

Keywords: hydrogen storage; hydride tank, prototype.

Developing our Hydrogen Technology, Design and Construction of a Sieverts Type Equipment for Hydrogen Sorption/ Desorption Characterization.

K. Suárez-Alcántara

UNAM-IIM Morelia, Antigua carretera a Pátzcuaro 8710, Col. Ex-hacienda de San José de la Huerta, Morelia, Michoacán, México, 58190.
e-mail: karina_suarez@iiu.unam.mx

ABSTRACT

A Sieverts type equipment was designed and constructed to determine the hydrogen uptake in hydrogen-storage materials. This equipment can operate up to 600°C and 100 bar hydrogen pressure. The equipment was constructed in stainless steel 316L and is capable of recording pressure-temperature data set each second. The parameters pressure, temperature, volume and compressibility factor are correlated by real gases function state equations to give the gain or loss of hydrogen in a storage material. Detailed calibration and validation was performed using high purity hydrogen and nanometric Pd and Mg as reference materials.

Keywords: hydrogen storage, Sieverts equipment, hydrogen technology.

Mg-EVA Composites with Selective Permeability as an Hydrogen Storage Material

G. Palacios Hernández [1], M. Valera Zaragoza [2], E. A. Juarez-Arellano [2*]

[1]División de Estudios de Posgrado, Universidad del Papaloapan, Campus Tuxtepec, Circuito central 200, Col. Parque Industrial, Tuxtepec, Oax. México. C.P. 68301 lupitapalher@hotmail.com
[2]Instituto de Química Aplicada, Universidad del Papaloapan, Campus Tuxtepec, Circuito central 200, Col. Parque Industrial, Tuxtepec, Oax. México C.P. 68301. eajuarez@unpa.edu.mx

ABSTRACT

Hydrogen (H_2) is considered one of the most promising sources of renewable energy. Hydrogen is the most abundant element in nature and one the lightest. Currently different hydrogen storage alternatives have been explored: high pressure, carbon nanotube, metal hydrides, composite materials, organic molecules, etc. From the wide range of alternatives for hydrogen storage, in this study we consider MgH_2 as one of the safest, most efficient and compact way to store hydrogen. Magnesium is one of the most abundant elements on earth and it has a great gravimetric storage capacity of hydrogen (7.6 wt%). The problem of the magnesium is its high reactivity with oxygen and moisture. Once the oxide is formed the hydrogen absorption - desorption process is inhibited. One possible solution to the problem is to generate a composite material with selective permeability. In this study is explored the selective permeability, the behavior and interaction of the composite magnesium – ethylene vinyl acetate copolymer (EVA). Using EVA copolymer at 28% vinyl acetate. The study and characterization of this nanocomposite is great promise for hydrogen storage.

Keywords: Composite, ethylene vinyl acetate copolymer, magnesium

XIV International Congress of the Mexican Hydrogen Society
Cancun, Mexico, 2014

Hematite Thin Films Produced by Spray Pyrolysis Method for Water Splitting

T. Mariño-Otero[1,2], M.A. Oliver-Tolentino[1] E. Pérez-Cappe[2], M.A. Aguilar-Frutis[1], G. Contreras-Martínez [1,2] E. Reguera[1*]

[1]Centro de Investigación en Ciencia Aplicada y Tecnología Avanzada-Unidad Legaria, Instituto Politécnico Nacional, Legaria 694, Col. Irrigación, Del. Miguel Hidalgo, C.P. 11500, México DF, Mexico
[2] Institute of Materials Science and Technology, Havana University, 10400 Havana, Cuba.
*edilso.reguera@gmail.com

ABSTRACT

The increasing demand for clean energy sources is driving research for the development of alternative energy technologies. Based on the requirement for clean, preferably carbon-neutral technologies, hydrogen is considered as an ecologically benign green fuel with high energy density. The natural photosynthesis process has served as source of inspiration for the design of artificial photosystems. With these systems the water splitting occurs, produced H_2. In this context, semiconductors have the primary role in these systems, because in this materials occurs the charge separation (e^--h^+) leading to the redox processes of interest. In particular, the hematite (α-Fe_2O_3) is one of the most promising materials for water splitting, due to its availability and its good light absorption of the solar spectrum with a band gap about 1.9−2.2 eV. Moreover, this material is obtained from inexpensive reagents, is relatively easy to synthesize, is not harmful and is very stable in contact with aqueous solutions. Previous works have not been reported of good efficiency of these materials in the process of converting light energy. The present work aims to obtain thin films of hematite over a conductive substrate, by the Spray Pyrolysis, structural characterization and photoelectrochemical behavior for the films obtained was discussed as a function of thickness.

Keywords: Water splitting, Photoelectrochemistry,

The Analysis of Hydridying and Dehydriding Kinetics

J. G, Cabañas-Moreno[1,*], G. García-Pacheco[2]

[1]Centro de Investigación y de Estudios Avanzados del IPN, Av. Instituto Politécnico Nacional núm. 2508, México, D. F., MEXICO 07360
[2]Instituto Politécnico Nacional, ESIME-Ticomásn, Col. Lindavista, México D.F., MEXICO.07338
[*]Tel: +525557473800 ext 1409; e-mail: jcabanasm@cinvestav.mx

ABSTRACT

The kinetics of hydriding and dehydriding (H/D) in hydrogen storage materials are important for practical as well as fundamental reasons. On the one hand, any applications involving the use of hydrogen stored in solid media must consider the rate at which hydrogen gas can be liberated from a storage medium under a given set of temperature and pressure conditions, so that hydrogen fluxes can be adjusted to the requirements of the specific application; in addition, the rate at which the hydrogen charge can be replenished may be a relevant consideration for the intended practical purposes. On the other hand, the analysis of the kinetics may allow to determine the physic-chemical mechanisms controlling the processes of hydrogen uptake by and release from the storage medium; such knowledge, in turn, could be used to the design or discovery of new storage materials with improved properties. With a few exceptions, the kinetic data of (H/D) in solids has been customarily treated with scant consideration to the fact that the storage materials are far from fulfilling the premises set up by well-known transformation or reaction theories (for example, size uniformity), despite the fact that it has been known for a long time that these inconsistencies may well turned irrelevant any conclusions drawn from the kinetics analysis. The present work deals with the kinetics of H/D in magnesium-based materials in order to illustrate the effects on the kinetics analysis of parameters such as particle size, MgO content, and temperature on the results derived from conventional theoretical treatments. The final results are conveyed as a set of guidelines intended to provide a methodology to obtain a better understanding of the actual microstructural evolution during the H/D processes and an improved capacity for modelling the uptake and release of hydrogen in nanostructured, Mg-based materials.

Keywords: hydrogen storage, kinetics analysis, Mg-based alloys

XIV International Congress of the Mexican Hydrogen Society
Cancun, Mexico, 2014

Novel Microbial Fuel Cell Design for Real Time High Organic Load Waste Water Treatment

A.R. Montes-Ochoa[1], A. Esqueda-Rivera[1], O. Solarza-Feria[2], J. Tapia-Ramírez[3], K. Sathish-Kumar[1*]

[1] Universidad Politécnica de Aguascalientes, Ingeniería en Energía Calle Paseo San Gerardo No. 207. Fracc. San Gerardo. Aguascalientes, Ags. México, 20342.
[2] Centro de Investigación y de Estudios Avanzados del Instituto Politécnico Nacional, Departamento de Química, Av. Instituto Politécnico Nacional 2508, Col. San Pedro Zacatenco, Delegación Gustavo A. Madero, México D.F. 07360.
[3] Centro de Investigación y de Estudios Avanzados del Instituto Politécnico Nacional, Departamento de Genéticas y Biología Molecular
[*]Tel: +52 4491156589 ; e-mail: sathish.bot@gmail.com, sathishkumarkamaraj@hotmail.com

ABSTRACT

Microbial fuel cells (MFCs) provide new prospects for a sustainable production of energy from organic waste water. Most of the results obtained so far from the field of MFCs research can be exploited to design MFCs. From this context, we proposed novel simplified MFC. The graphite rod (4.2 cm) could act as anode besides submerged with wooden portion (4.2 cm) into the waste water, remained wooden portion (4.2 cm) bound with Pt/Carbon cloth (Cathode) exposed to air. Proton can migrate up with the culture liquid on the wood and react with oxygen in the air, to generate water as final by-product. Up to now there is limited information available about the use of real time high concentrated waste water (41.38 ± 9.6 g/L) as source in MFC application. In this frame work, real wastewater collected from a Universidad Politécnica de Aguascalientes (UPA) was used. Waste waters were used both as inoculum to form electrochemically active biofilm on graphite based anode and also as the medium to be treated. Above mentioned configuration of novel MFC was produced maximum power density of 0.028 mW/m^3. Later we performed the overnight treatment of wooden portion with distilled water and sulfuric acid. Interestingly, maximum power density was higher for sulfuric acid treated wooden material (200.98 mW/m^3) than the distilled water treated wooden material (1.52 mW/m^3). Such enhancements might be attributed to the anchored sulfonyl group on wood material which would enhance the proton mobility, as confirmed by pre-luminary power density curve. To the best of our knowledge, this is the first times that successfully demonstrate wooden material exhibit the capillary migration of proton transfer exploited in MFC for high concentrated real time waste water application.

Keywords: Microbial fuel cells; Capilary migration; Waste water.

XIV International Congress of the Mexican Hydrogen Society
Cancun, Mexico, 2014

Production of Electricity in an Electrobiochemical Slurry Reactor used for the Bioremediation of Pesticide Contaminated Soil

B. Camacho-Pérez [1], H.M. Poggi-Varaldo [1]*, J. Garcia-Mena [2], O. Solorza-Feria[3], E. Ríos-Leal [4], N. Rinderknecht-Seijas [5]

[1]Environmental Biotechnology and Renewable Energies R&D Group, Dept. of Biotechnology and Bioengineering, CINVESTAV del IPN, México D.F., México, P.O. Box 14-740, 07000
[2]Dept. of Genetics and Molecular Biology, CINVESTAV del IPN, México D.F., México, P.O. Box 14-740, 07000
[3]Dept. of Chemistry, CINVESTAV del IPN, México D.F., México, P.O. Box 14-740, 07000
[4]Central Analítica, CINVESTAV del IPN, México D.F., México, P.O. Box 14-740, 07000
[5]ESIQIE del IPN, Mexico D.F., México.
*Author for all correspondence: r4cepe@yahoo.com

ABSTRACT

It is recognized that mass transfer of lindane from soil to liquid phase is the limiting process in biodegradation processes used for soil bioremediation. Surfactants are used due to their ability to increase water solubility and mass transfer. On the other hand, electrobiochemical slurry reactor (EBCR) constitutes a promising technology that could remove organic matter, phenol, petroleum hydrocarbons, and pesticides in contaminated soils with simultaneous electricity output. The aims of this research were *(i)* to evaluate the desorption of lindane from soil with Tween 80 at different concentrations; *(ii)* to determine the power output and removal of lindane in an electrobiochemical slurry reactor; and (*iii*) to characterize the dominant microorganisms in the electrobiochemical slurry reactor using 16S rRNA and denaturing gradient gel electrophoresis. The EBCR consisted of a Plexiglass cylinder approximately 6 cm in diameter and 8 cm in length, fitted with two anodes and two cathodes.

Addition of 2000 mg /L Tween 80 removed 9.61% of lindane in *in vitro* desorption experiments. The internal resistance of the EBCR determined by polarization curve was 820 Ω; a moderate volumetric power activity was recorded (374 mW/m^3) along with a potential of 600 mV when the two-electrode sets were connected in parallel. During the batch operation, the EBCR showed a 56% lindane removal whereas the reduction in the abiotic control was 3%. Unexpectedly the removal efficiency of lindane ($\eta_{lindane}$) in the EBCR was lower than that in an EBCR operated without surfactant in a previous experiment. This could be ascribed to the increased degradable organic matter supply related to Tween in our EBCR that possibly shifted microbial metabolism from lindane degradation to degradable matter uptake. An average volumetric power of 685 mW/m^3 and average voltage of 420 mV were achieved. Results from the DGGE analysis and further sequencing, indicate the presence of *Trichococcus palustris* strain DSM 9172 (99% sequence identity). This bacterium has been reported in autotrophic biocathodes of other bioelectrochemical systems. Finally, the energy output obtained in our EBCR allows for the recovery of 20% of the power required for mixing, thus paving the way to sustainable bioremediation of soils.

Keywords: Electrobiochemical slurry reactor, lindane, Tween 80

Biohydrogen Production from Organic Solid Waste in a Discontinuous Process

I. Moreno-Andrade*, M.C. Bujanos-Adame

[1]Universidad Nacional Autónoma de México, Instituto de Ingeniería, Academic Unit Juriquilla, Laboratory for Research on Advanced Processes for Water Treatment, Blvd. Juriquilla 3001, Juriquilla, C.P. 76230, Querétaro, Mexico
*Tel: +524421926171; e-mail: imorenoa@ii.unam.mx

ABSTRACT

The organic solid waste (OSW) represents more than 60% of total urban waste and include 75% of easy-to-degrade matter. Using a fermentative process, the organic matter is transformed into H_2, CO_2 and organic acids and alcohols, this make feasible the biological production of H_2. There exist several parameters that affect the H_2 production as the hydraulic residence time (HRT). In order to optimize the process is necessary to determine the HRT where the H_2 production is maximized. The objective of this study was to evaluate the effect of HRT on H_2 production form OSW in a Sequencing Batch Reactor (SBR). Different HRT (72, 24, 12 and 6 h) were evaluated in an SBR of 1.25L (with a head space of 250 mL and an exchange volume of 50%). Each HRT was maintained in the reactor at least 10 degradation cycles. OSW at 5gVS/L was filled as substrate at each degradation cycle. The reactor was inoculated with fermentative H_2 producers selected by a thermal shock pre-treatment (103-105 °C during 1 h). H_2, CO_2, methane and Volatile Fatty acids (VFA) were determined by gas chromatography. Kinetics of H_2 production was adjusted to the Gompertz model. The results showed that the values for H_2 in biogas varied from 22 to 48% depending the HRT. The highest H_2 production was obtained applying an HRT of 24 followed by the HRT of 12 h. The maximum H_2 percentage in gas (48 ± 6 %), maximum volumetric H_2 production (757 ± 391 mL H_2) and the maximum H_2 production rate (328 ±144 mL H_2/h) were obtained at HRT of 24 h. Acetic acid was the main VFA obtained. Higher propionic acid production was observed at HRT of 6h, reducing the maximal H_2 generation to 282 ± 24.

Keywords: Bio-hydrogen; HRT;organic solid waste.

XIV International Congress of the Mexican Hydrogen Society
Cancun, Mexico, 2014

Metallic Nanoparticles for the Treatment of Effluents Contaminated with Chlorinated Organic Compounds: a Review

L. Breton-Deval[1], O. Solorza-Feria[1], F. Godinez-Salomon[1], H.M. Poggi-Varaldo[1*]

[1]Centro de Investigación y de Estudios Avanzados del Instituto Politécnico Nacional, Av. Instituto Politécnico Nacional No. 2508, Ciudad de México, México, 07360.
[*]Tel: +555747 3800 ext 4321; e-mail: r4cepe@gmail.com

ABSTRACT

Nanomaterials are the core of a promising technology that can be used to accelerate and improve the transformation and detoxification of chlorinated organic compounds (COCs). Hence this review will cover topics such as efficient nanomaterials for COCs treatment, supports and stabilizers that improve the process, interactions of nanomaterials with the microorganisms involved, and emerging fields. The most common material used for treatment of waters polluted with COCs has been zero-valent iron (ZVI) because of its efficiency and low cost. However, there are concerns on the stability and long term durability of ZVI nanoparticles (NP). For this reason there are some works with other materials such as Pd, Zn or Ni and with combination of materials in the fabrication of NP. The bimetallic NPs allow for a lower cost of production, since one of the materials could be the most economic but not the most efficient whereas the second metal, the most expensive, provides the degradation capability. Alloyed and *crochet* types of bimetallic NP have been tested. The process with NP can be made more efficient by using a support that prevents the aggregation of NP during reaction and in some cases can facilitate the recovery of the NP afterwards. Currently, the application of NP in bioreactors and *in situ* treatments is gaining momentum. Another significant issue especially for hybrid treatments is the interaction between NP and the microbial community harbored in bioreactors and devices, ranging from toxicity issues to biosynthesis of NP. There has been attempts to incorporate metal NP onto the microbial cells for COC treatment, although more research is needed. Furthermore, there is increased interest on biosynthesis of NP with microorganisms in order to have true "nanoparticle-ized biomass" with increased degradation capability of pollutants. Among important emerging fields we can highlight the environmental impact assessment as well as life cycle analysis of the NP fabrication and use.

Keywords: chlorinated organic compounds, nanoparticles, pollutant treatment

Hydrogen Production from Renewable Energy in Yucatan

C. Sosa, E. Us, J. Chi, R. Patiño*

Departamento de Física Aplicada, Cinvestav – Unidad Mérida, A.P. 73 Cordemex, 97310 Mérida, Yucatán, México
*Tel: +52(999)9429438; e-mail: rtarkus@mda.cinvestav.mx

ABSTRACT

An estimation of the solar and wind energy resources was performed in four locations of the Yucatan state in Mexico: Mérida, the capital city, and three coastal towns, Sisal, Chelem and Telchac. These renewable resources were evaluated from meteorological stations having an automatic data registration every 10 min, during at least 4 years. Hourly averages were used with the SAM-NREL software to calculate the annual production of electrical energy in 500-kW installation plants with photovoltaic cells or wind turbines. In addition, the same plants were evaluated with monthly averages of the solar and wind resources using the HOMER software, obtaining similar results by both methods. Then, the hydrogen production through electrolysis was estimated using the electricity produced from solar and wind energy, and it is proposed here to use this hydrogen for a local transportation network. On the other hand, the methane production was evaluated from urban organic wastes in Mérida and from wastes in agricultural and livestock in the Yucatan state, mainly corn, poultry and pigs production. These estimations were performed using simple models with a number of different results, but it is possible to find that both urban and agricultural wastes have similar small amounts of methane production, while livestock wastes are much more important for biogas production. This biogas could be also transformed to hydrogen production for the transportation network, although it can be used directly by the farms. Therefore, using organic wastes, the methane is also proposed here as energy vector, being avoided the natural emissions to the atmosphere together with its contribution to the greenhouse effect in the planet.

Keywords: solar energy, wind energy, Yucatan

XIV International Congress of the Mexican Hydrogen Society
Cancun, Mexico, 2014

Saccharification of Fermented Solids for a Hydrogen Producing Biorefinery

C. Escamilla-Alvarado[1], H.M. Poggi-Varaldo[1], T. Ponce-Noyola[2,*], E. Ríos-Leal[3], F. Esparza-García[4], J. Barrera-Cortez[5], J. García-Mena[6], N. Rinderknecht-Seijas[7]

[1]Environmental Biotechnology and Renewable Energies R&D Group, Dept. of Biotechnology and Bioengineering, Centro de Investigación y de Estudios Avanzados del IPN, P.O. Box 14-740, 07000 México D.F., México.
[2]Microbial Genetics Group, ibidem.
[3]Central Analítica, ibidem.
[4]Biochemical Ecology, ibidem.
[5]Intelligent Control, ibidem.
[6]Dept. of Genetics and Molecular Biology, ibidem.
[7]Escuela Superior de Ingeniería Química e Industrias Extractivas del IPN, Mexico D.F., México.

*Author for all correspondence: tponce@cinvestav.mx.

ABSTRACT

Biorefineries are being devised as an effort to find solutions to multiple problems, i.e. decreased dependence on fossil fuels, new bioproducts development and commodities satisfaction. The production of hydrogen has been successfully coupled to a biorefinery model coined H-M-Z, providing advantages such as the generation the environmental friendly clean fuel hydrogen, and surprisingly an intermediate organic by-product coined as fermented solids (FS) that showed interesting properties for more biofuel and enzymes production. This biorefinery model is comprised by an in-series process for hydrogen and methane production and by a parallel process for holocellulases production. The main substrate was the organic fraction of municipal solid wastes (OFMSW). The objective in this work was to add a new stage for the saccharification of lignocelullosic substrates in a hydrogen producing biorefinery model.

Two saccharification experiments were performed. In the first one (SS-1) two factors were evaluated: type of substrate and type of holocellulolytic enzymes according to a 2x3 factorial design. The substrates were OFMSW, FS, and filter paper Whatman No. 1 (FP). As holocellulolytic enzymes, we used the enzyme extract from Z-stage (*Trichoderma reesei* extract) of the biorefinery model and the commercial enzyme Celluclast (Sigma-Aldrich, USA). In the second experiment (SS-2), the FS was subjected to evaluation at four different levels of enzyme:substrate ratio [40, 60 80, 100 and 120 FP units (g volatile solids)$^{-1}$].

In SS-1 all substrates were best saccharified with the *T. reesei* extract, whereas the most saccharified substrate, independently of the enzyme used, was the FP [up to 18 g of glucose and xylose (L)$^{-1}$]. The FS had up to 34 % higher saccharification than OFMSW, with up to 13.09 g of gluc + xyl (L)$^{-1}$. The highest saccharification efficiency for FS was 75 % on holocellulose basis. In the SS-2, we found that contrary to what expected, the highest enzyme:substrate ratio had no significant positive effect on saccharification yield. Indeed, the ratio 40 FP units (g volatile solids)$^{-1}$ had the highest saccharification yield [11 mg sugars (filter paper unit)$^{-1}$].

In conclusion, the hydrogen production in a biorefinery is transcendental because on the one hand, it provides a renewable clean fuel, and on the other hand, it provides a pre-degraded substrate (saccharified liquors) easily convertible into valuable bioproducts, or even into more biofuels.

Keywords: biohydrogen; cellulases; municipal organic solid wastes; saccharification.

Core-Shell Ni-Pt Supported on Carbon Nanotubes as cathode-catalyst for Fuel Cell Application

F. Godinez-Salomón[1], C. Mercado-Zúñiga[2], J.R. Vargas-Garcia[2], H. A. Calderon[3], O. Solorza-Feria[1*]

[1] Centro de Investigación y estudios Avanzados del IPN, Depto. Química, Av. IPN 2508. A. P. 14-740, CP. 07360, México-D.F. México.
[2]Depto. Ing. Metalurgia y Materiales,ESIQIE-IPN, Zacatenco México-D.F. CP. 07738, México.
3 Depto. de Ciencia de Materiales, ESFM-IPN, Zacatenco México-D.F. CP. 07738, México.
[*]Tel: +52 (55) 57473715; e-mail: osolorza@cinvestav.mx

ABSTRACT

In recent years, outstanding advances have been done in increasing the performance of polymer electrolyte membrane fuel cells (PEMFC). However, together with high activity and low cost catalysts, some issues related to durability should be overpass to assure massive application. Slow kinetic for the oxygen reduction reaction (ORR) and the acidic nature of polymer electrolyte, straiten the use of catalyst to noble metal, like platinum, which impose a considerable increase in production cost. Added to this, the inefficient use of Pt in the catalyst layer (CL), and low stability of both catalyst and carbon, commonly used as support material, makes its application even more complicated. Core-shell catalysts (M-Pt), have attracted considerable attention owing to the possibility to have both, specific and mass activity higher than that of commercial Pt/C materials. On the other hand, the use of carbon nanotubes as support material instead of amorphous carbon could increases the stability of the catalysts in normal operating conditions. In this work we propose the design of Ni-Pt core-shell nanoparticles, highly dispersed on multiwall carbon nanotubes (MWCNT) as cathode-catalyst for fuel cell application. The catalysts will be physical characterized by X-ray diffraction, electronic microscopies, X-ray photon spectroscopy and electrochemical techniques, using a rotating ring disk electrode setup (RRDE) and in a single-cell assembly.

Keywords:Core-Shell catalysts; Carbon Nanotubes; Polymer Electrolyte Fuel Cells

Knowledge: This project was supported by Conacyt (grant FOINS 75/2012) and SIP 20144667.

XIV International Congress of the Mexican Hydrogen Society
Cancun, Mexico, 2014

The Effect of Physicochemical Pretreatment of Supported Pt Nanoparticles for the ORR. A Novel Carbon from Natural Source.

J.L. Reyes-Rodríguez[1], S. Kumar-Kamaraj[2], O. Solorza-Feria[1,*]

[1] Departamento de Química, Centro de Investigación y Estudios Avanzados del IPN, Av. IPN 2508, Col. San Pedro Zacatenco, A. Postal 14-740, 07360 México D.F., México.
[*]Tel: 011 +52 +55 5747-3715 ; osolorza@cinvestav.mx

[2]Universidad Politécnica de Aguascalientes, Calle Paseo San Gerardo No. 207, Fracc. San Gerardo, C.P. 20342 Aguascalientes, Aguascalientes, México.

ABSTRACT

Materials used as nanoparticles supports play an important role in the performance, efficiency and stability of catalysts applied in polymer fuel cells. Carbon supports have been employed for their excellent properties like good electronic conduction, high surface area, relative crystallinity and resistance to acids and alkalis moderate. The surface modification of carbon by physical-chemical treatment (functionalization) has a favorable effect on the performance and stability of the catalyst to improve the metal-support interaction through anchoring sites which in turn favor the distribution of the metal particles on the carbon matrix. The shape and particle size are influenced by the properties of the support and these characteristics are directly related (together with the diffusion of gases and ionomer interaction conductor) with the catalytic activity towards the reactions of interest. Pre-treated Carbon Vulcan with nitric acid is the most used support for nanoparticles in polymer fuel cell. However its origin derived from the combustion of waste oil (non-renewable energy source) makes it unattractive for future applications by issues of environmental pollution, furthermore the sulfur content and other impurities can degrade and decrease the lifetime of the metal catalysts. In this study we present the research for a new type of carbon obtained by a simple process from natural sources. This carbon was treated by different physicochemical methods and then Pt nanoparticles were synthesized and supported by chemical reduction with $NaBH_4$ on the different pre-treated carbons. This work plan is performed with the main target to evaluate the potential use of natural carbon as a novel support material and to analyze the effect of different treatments on the catalytic activity of nanoparticles towards the ORR. The study is complemented by physical characterization techniques like TEM, SEM, EDAX, Raman, FTIR and electrochemical techniques by RDE in acid medium. All the results are compared with Pt/Vulcan Carbon pre-treated.

Keywords: Novel natural carbon; Oxygen reduction reaction; Physicochemical pretreatment to carbon.

Acknowledgments: This project was supported by Conacyt (grant FOINS 75/2012).

The Outreach Program of Renewable Energy for High School in Quintana Roo, Mexico

B. Escobar Morales[1,*], Romeli Barbosa[2], I. Bojorquez[2], J. C. Cruz[3]

[1]Instituto Tecnológico de Cancún, Av. Kabah Km. 3, Cancun, Q. Roo, Mexico, 77500.
[2]Universidad de Quintana Roo, Boulevard Bahía s/n, Chetumal, Q. Roo, Mexico, 77019.
[3]Instituto Tecnológico de Chetumal, Av. Insurgentes 330, Chetumal, Q. Roo, Mexico, 77013.
[*]Tel: +529981428487; e-mail: bem08@hotmail.com

ABSTRACT

The increase of the international concern about global warming has led to a need to inform young generation about natural disaster risks and the impact of climate change. The renewable energy is a very attractive option to reduce the greenhouse gasses effect, but is necessary to organize information and educational campaigns which highlight their ecofriendly impact. At the present paper, main activities about hydrogen technology demonstration in Quintana Roo's high schools were reviewed, in order to find out the level of knowledge as well as awareness of students concerning hydrogen energy technologies. Because the textbooks do not mention about the role of hydrogen technologies in the development of a secure and sustainable energy, consequently, at this workshop designed for high school students, disseminate about the importance of hydrogen technologies through the hands-on energy demonstrations, conferences and short-courses were crucial. This work presents the results of surveys applied to participants and didactic prototypes built for this purpose.

Keywords: Greenhouse Gasses, Hydrogen Energy, Outreach Education. Didactic Prototypes

XIV International Congress of the Mexican Hydrogen Society
Cancun, Mexico, 2014

Evaluation of Biohydrogen Production from Cheese Whey and Assessment of the Associated Microbial Community

K. M. Muñoz- Páez [1], H. M. Poggi-Varaldo[1*], J. García-Mena [2],

[1]Environmental Biotechnology and Renewable Energies R&D Group, Dept. Biotechnology and Bioengineering. CINVESTAV-IPN. P.O. Box 14-740, México D.F.; [2]. Dept. Genetic and Molecular Biology, ibidem.

*Author for all correspondence: r4cepe@yahoo.com

ABSTRACT

Biological H_2 production could be an attractive alternative for cheese whey (CW) treatment and reclaiming. In principle H_2 production at ambient temperature could lead to energy savings in heating both the feed and bioreactor. On the other hand, it is important to study the microbial communities associated to biological processes in order to find eventual relationships between process performance and biocatalysts. Therefore the aim of this work was to evaluate the H_2 production in lab scale anaerobic fluidized bed reactors at ambient temperature using CW as substrate as well as the related changes in the microbial community. There were 3 stages of operation with an organic volumetric load (Bv) of 10 g/(L.day) using: (i) sucrose, (ii) CW, and (iii) CW with 1 g/L of NaCl. The main response variables were: H_2 productivity (NmLH2/Lbed.day), Jaccard similarity index (IJ) and Poggi's discrete divergence index ΔP . In experiment with sucrose the H_2 productivity was 1 011 $NmLH_2$/Lbed.day. In the CW stage, H_2 productivity was 101 NmLH2/(Lbed.day), 10 fold lower than in the first stage with sucrose. We detected moderate concentration of lactic acid in the effluent that suggested the presence of lactic acid bacteria (LAB). LABs are microorganisms related to low H_2 production due to two main effects: substrate competition and excretion of bacteriocins. Some studies showed that the effect of bacteriocins diminish with the presence of NaCl. So, we run a third period of operation with CW plus 1 g/L of NaCl and heat treatment to the bioparticles. In this period we observed that the H_2 productivity increased 3 times (316 NmL H_2/(Lbed. day) compared to the value with only CW. The IJcw-CWNaCl was 0.18 and the ΔP was 0.35, this indicates that the community profiles are almost completely different, maybe due to the NaCl addition and the heat treatment to the bioparticles. One of the identified microorganisms was *Propionibacterium cyclohexanicum*, this strain is considered to be a competitor of hydrogen-producing microorganisms in dark fermentation. We could conclude that the addition of NaCl had a positive effect on H_2 productivity.

Keywords: Biohydrogen production, cheese whey, microbial community

XIV International Congress of the Mexican Hydrogen Society
Cancun, Mexico, 2014

An approach for Fuel Cell Balance of Plant design and its electronic control for modular flexibility

M. López[1], F. Loyola[1,*], U. Cano[1]

[1]Instituto de Investigaciones Eléctricas. Reforma 113, Col. Palmira, Cuernavaca, Morelos, México, 62490.
Tel: +527773623811; e-mail: felix.loyola@iie.org.mx

ABSTRACT

A fuel cell stack operating for a specific application needs a particular additional stage for its control and instrumentation known as balance of plant (BoP). In this work, the design of a BoP and its electronic control for a fuel cell stack is proposed. The main components in a BoP are typically sensors and actuators. The sensors acquire electronic signals to know system parameters such as: temperature, voltage, electric current and hydrogen gas pressure. Actuators on the other hand, drive actions on process elements, such as turning on or turning off input/output valves. Also, they manage velocity of oxidant gases and cooling fans.

The approach in the BoP design and control proposed in this article resides in the versatility approach used for fuel cells with potentially different electric power capacity. This is possible by changing a minimum of electronic components. The BoP design also is includes a communication port where a graphic interface is connected to monitor and change operating parameters of the fuel cell stack. Moreover, with a master control is possible to connect more than one fuel cell stack providing flexibility for modularity. This configuration allows varying the power plant capacity. In this work the BoP and electronic control of a four stack system is developed, where each stack has a 750 watts capacity to supply electric power in a hybrid all-electric utility vehicle.

Keywords: Balance of plant; Control; Fuel Cells.

Performance Study of Carbon Supported Co@Pt/C Core-Shell Nanocatalyst for Oxygen Reduction Reaction in a PEMFC

V.H Rodríguez-Martínez[1], J. L. Reyes-Rodríguez[1], F. Godínez-Salomón[1], L. Lanturdo-Rojas[2], O. Solorza-Feria[1].*

[1]Departamento de Química, Centro de Investigación y Estudios Avanzados del IPN, Av. IPN 2508, Col. San Pedro Zacatenco, A. Postal 14-740, 07360 México D.F., México.
[2]Centro de Nanociencia y Micro y Nanotecnologías-IPN, UPALM, Zacatenco México-D.F. 07738, México.
*Tel: 011 +52 +55 5747-3715 ; e-mail: osolorza@cinvestav.mx

ABSTRACT

In this study carbon supported Co-Pt core-shell nanocatalysts, with different Co:Pt ratio, were synthesized and characterized for evaluating their performances in a rotating disk electrode (RDE) setup, and in membrane electrode assemblies (MEAs) configuration, for the oxygen reduction reaction (ORR). In first instance Co cores were obtained from the chemical reduction of $CoCl_2$ with $NaBH_4$ using TBAB as surfactant and in an ultrasound probe system. Subsequently through a galvanic displacement process Co atoms were replaced by Pt atoms to make a shell. TEM and SEM analysis have showed highly dispersed nanoparticles with size averaged between 4-10 nm. XRD diffractograms showed peaks related to Pt phase little shifted to higher angles compared with pure Pt nanoparticles used as reference. Electrochemical results don't show Co phase segregation, which is characterized by the presence of a wide peak around 0.4 V/RHE, during the first cycle. Results of RDE show that both catalysts presented superior current density, of at least three folds of specific activity than that of commercial 20% Pt/C Etek® catalyst, however the mass activity is still below obtained by the commercial catalyst, which we must continue to work in order to eradicate this problem attributed to agglomeration of nanoparticles. The catalyst with higher specific activity was selected for preparing a membrane electrode assembly (MEA) and their performance evaluated in a PEM single cell. Optimization of catalytic materials loading was carried out and final results showed superior performance in mW/mg Pt to commercial catalysts. The SEM analysis showed that MEAs of more porous films provide higher performance compared to the most compact films.

Keywords: Synthesis of Co@Pt /C; Oxygen reduction reaction; Membrane electrode assembly.

Acknowledgments: This project was supported by Conacyt (grant FOINS 75/2012).

Y@Pt/C Core-Shell Electro-Catalyst for Oxygen Reduction Reaction

M.M. Tellez-Cruz[1], J.F. Godínez-Salomón[1], O. Solorza-Feria[1].*

[1]Departamento de Química, Centro de Investigación y Estudios Avanzados del IPN, Av. IPN 2508, Col. San Pedro Zacatenco, A. Postal 14-740, 07360 México D.F., México.
*Tel: 011 +52 +55 5747-3715 ; e-mail: osolorza@cinvestav.mx

ABSTRACT

The catalyst for oxygen reduction reaction (ORR) plays an important role in determining the performance of a fuel cell. At present, platinum (Pt) is still the best ORR catalyst. However, the prohibitive price of Pt limits the commercialization of fuel cells. To reduce the amount of the Pt used in fuel cells, one approach is to introduce an additional metal to form Pt based alloy as a substitute for pure Pt. Because it, Pt–M alloys (M is the transition metals) have been extensively investigated as cathode electrocatalysts. However, the loss of the guest metal from the Pt based alloy is a significant problem in an acidic fuel cell operation environment. In the last years, it has been shown that by forming a monolayer–submonolayer of Pt on other metal, the Pt usage could be reduced considerably without scarifying the activity. In this work the synthesis and characterization of the yttrium decorated platinum core-shell nanocatalyst supported on carbon Vulcan for the oxygen reduction reaction (ORR) in acid media was evaluated. The core was synthesized by chemical reduction with $NaBH_4$ of the precursor salt, while the shell was deposited by galvanic displacement in the surface atoms of Y in the particles. The material was characterized by XRD, TEM and EDAX. The electrochemical performance of Pt@Y/C is evaluated by cyclic voltammetry, CO stripping and RDE.

Keywords: Y@Pt / C; ORR; core-shell.

Acknowledgments: This project was supported by Conacyt (grant FOINS 75/2012).

XIV International Congress of the Mexican Hydrogen Society
Cancun, Mexico, 2014

Pt-$NiTiO_3$/C Catalyst Synthesized by the Microwave Assisted Method for Direct Alcohol Fuel Cell Applications.

A. Hernández-Ramírez[1], F.J. Rodríguez-Varela[1,2,*]

[1]Programa de Nanociencias y Nanotecnología, Cinvestav Unidad Saltillo,
Av. Industrial Metalúrgica No. 1062, Parque Industrial Saltillo-Ramos Arizpe,
Ramos Arizpe, Coah., México, 25900.
[2]Grupo de Sustentabilidad de los Recursos Naturales, Cinvestav Unidad Saltillo,
Av. Industrial Metalúrgica No. 1062, Parque Industrial Saltillo-Ramos Arizpe,
Ramos Arizpe, Coah., México, 25900.
[*]Tel: +528444389600; e-mail: javier.varela@cinvestav.edu.mx

ABSTRACT

Pt-$NiTiO_3$ catalyst supported on Vulcan XC-72 (Pt-$NiTiO_3$/C) was prepared by microwave-assisted polyol method. Nickel titanate ($NiTiO_3$) powders were synthesized by wet-chemical method using nickel acetate and titanium isopropoxide as metal sources and citric acid as complexing reagent. The precursors werecalcinated at 700°C for 3h in air atmosphere. Results from TEM characterization revealed $NiTiO_3$ nanoparticles having homogeneous morphology with particle size in the rangeof 30 to 50 nm. To obtain the Pt-$NiTiO_3$/C catalyst, $NiTiO_3$ nanoparticles and Vulcan were mixed by magnetic stirring in an ethylene glycolsolution. Afterwards, $H_2PtCl_6 \cdot 6H_2O$ was added maintaining stirring. The mixture was submitted to microwave irradiation under on/off pulses. The Pt-$NiTiO_3$/C catalyst was evaluated as cathode in acid and alkaline medium.

Keywords: Pt-$NiTiO_3$catalyst; microwave-assisted polyol method; Oxygen Reduction Reaction; Direct Alcohol Fuel Cells.

XIV International Congress of the Mexican Hydrogen Society
Cancun, Mexico, 2014

Synthesis of CeO_2/C and Pt-CeO_2/C Nanoparticles by the Microwave Assisted Polyol Method and Evaluation of their Electrocatalytic Activity.

J. E. López Martínez[1], F.J. Rodríguez-Varela[1,2,*]

[1]Programa de Nanociencias y Nanotecnología, Cinvestav Unidad Saltillo,
Av. Industrial Metalúrgica No. 1062, Parque Industrial Saltillo-Ramos Arizpe,
Ramos Arizpe, Coah., México, 25900.
[2]Grupo de Sustentabilidad de los Recursos Naturales, Cinvestav Unidad Saltillo,
Av. Industrial Metalúrgica No. 1062, Parque Industrial Saltillo-Ramos Arizpe,
Ramos Arizpe, Coah., México, 25900.
[*]Tel: +52 844 4389600; e-mail: javier.varela@cinvestav.edu.mx

ABSTRACT

Cerium oxide has been usually obtained by pyrolisis at temperatures as high as 600 °C, in a H_2 atmosphere during experiments lasting 3 – 6 h. In this work Vulcan-supported CeO_2nanoparticles (CeO_2/C) were synthesized by the intermittent microwave assisted polyol method, in a 20 min on/off pulses procedure. In order to obtain the Pt-CeO_2/C electrocatalyst, CeO_2/C powders and $H_2PtCl_6 \cdot 6H_2O$ were dispersed by magnetic stirring and submitted to microwave irradiation during 5 min. CeO_2/C and Pt-CeO_2/C were characterized by XRD, SEM-EDS and TEM. The catalytic activity of the electrocatalysts for the Ethanol and Methanol Oxidation Reaction (EOR and MOR, respectively) in acid and alkaline medium was evaluated by cyclic and linear scan voltammetry.

Keywords:CeO_2 nanoparticles, Pt-CeO_2/Celectrocatalyst, Intemittent Microwave Heating, DAFC.

Synthesis of Ni@Pt Core-Shell Nanoparticles Supported on MWCNTs for Hydrogen and Methanol Electrooxidation

G. Rosado[1], B. Escobar[1], R. Barbosa[2], A.M. Valenzuela-Muñiz[1], I. Alonso[1], Y. Verde-Gómez[1].

[1]Instituto Tecnológico de Cancún, Av. Kabah Km 3 s/n, Cancún, Q. Roo, México, 77515.
[2]Universidad de Quintana Roo, Boulevard Bahía s/n Esq. Ignacio Comonfort, Col. del Bosque Chetumal, Q. Roo, México, 77019.

ABSTRACT

Platinum has been used in fuel cell because have a good electrocatalytic activity for hydrogen oxidation. However, the platinum is a precious metal, therefore is expensive and affects the final cost of a fuel cell. The use of Pt in Direct Alcohol Fuel Cells (DAFCs) has been affected by low tolerance to CO poisoning, an intermediate produced during the oxidation of methanol. In these cases have been used bimetallic catalysts such as PtRu, but Ru is an expensive transition metal too. A solution is to use Pt nanoparticles with cheaper metals such as Ni, Co and Fe in core-shell configuration. This helps to optimize the amount of Pt, covering metal nanoparticles (Ni, Co or Fe) with a few layers of Pt. The presence of a second metal affects the electronic structure of Pt, decreasing the binding energy with the intermediates produced during the oxidation of methanol (mainly CO), avoiding poisoning. In this work we have synthesized Ni-Pt nanoparticles supported on multiwall carbon nanotubes (MWCNT) at different Ni:Pt atomic ratios. The synthesized materials were characterized physically and chemically by Scanning Electron Microscopy (SEM), High Resolution Transmission Electron Microscopy (HRTEM), X-ray diffraction (XRD), Energy Dispersive Spectroscopy (EDS) and Fourier Transform Infrared Spectroscopy (FTIR). For the study of the hydrogen oxidation, three electrode cell was used, with Ni-Pt/MWCNT deposited on a glassy carbon working electrode, with Ag/AgCl (KCl sat) reference and Pt wire counter electrode, in 0.5M H_2SO_4 electrolyte. The study of methanol oxidation reaction, the same cell configuration was employed with a 0.5M H_2SO_4 + 0.5M CH_3OH electrolyte.

Keywords: core-shell; nanoparticles; platinum

Effects of Solvent Properties on the Electrocatalytic Response of Highly Active Pt-Sn/C and Pt-Ru/C Catalysts for the EOR

D. González-Quijano[1], W.J. Pech-Rodríguez[1], J.I. Escalante-García[1,2], G. Vargas-Gutiérrez[1,2], F.J. Rodríguez-Varela[2,3*]

[1]Ingeniería Metalúrgica e Ingeniería Cerámica
[2]Sustentabilidad de los Recursos Naturales y Energía
[3]Programa de Nanociencias y Nanotecnología
Cinvestav Unidad Saltillo, Av. Industria Metalúrgica 1062, Parque Industrial Ramos Arizpe.
Ramos Arizpe, Coahuila, C.P. 25900, México
[*]Tel: +52(844)438-9600 ext. 8526; e-mail: javier.varela@cinvestav.edu.mx

ABSTRACT

Pt-M/C catalysts (where M: Sn and Ru) with nominal Pt:Mratio of 1:1 (at. %) were synthesized by a polyol reduction process. The metal: Vulcan support ratio was 20:80 (wt. %). The effects of different ethylene glycol:ethanol:water (EG:EtOH:H_2O) volume ratios as solvent on the physicochemical characteristics of the Pt-Sn/C and Pt-Ru/C catalysts was evaluated. Afterwards, the electrocatalytic activity of the alloys for the Ethanol Oxidation Reaction (EOR) was studied in acid media. XRD characterization for Pt-Sn/C catalysts showed that the degree of alloying calculated by using Vegard's law ranged from about 15 % (synthesis in the presence of water) to roughly 49 % (synthesis in the absence of water). The average particle size was calculated with the Scherrer equation to be within 1.8-4.7 nm, with the smaller sizes obtained in the absence of water. The XRD patterns of Pt-Ru/C showed a material with low crystallinity, which prevented the estimation of the particle size and degree of alloying for these catalysts.Chemical analysis by EDS indicated the formation of oxides for both alloy systems regardless of the presence or not of water during the synthesis, attributed to the presence of tin and ruthenium oxide phases in the materials. The electrochemical characterization showed that the synthesis conditions have an important effect on the electrocatalytic activity of the Pt-Sn/C and Pt-Ru/C catalysts for the EOR. In general, the alloys synthesized in the absence of H_2O delivered higher performances for the EOR. Overall, the Pt-Sn/C catalysts obtained without water showed higher current densities than Pt-Ru/C and Pt/C catalysts. The Pt-Ru/C catalysts showed current densities roughly similar to those of Pt/C. However, the onset of the reaction and the peak current density at the alloy were at lower potentials compared to Pt/C.

Keywords: Pt-Sn/C; Pt-Ru/C; Ethanol Oxidation Reaction.

NiO@Pt/C Core-Shell Nanocatalyst for Oxygen Reduction Reaction

D. Vega-Villalobos[1], F. Godínez-Salomón[1], J. L. Reyes-Rodríguez[1], L. Lartundo-Rojas[2], O. Solorza-Feria[1*].

[1]Departamento de Química, Centro de Investigación y Estudios Avanzados del IPN, Av. IPN 2508, Col. San Pedro Zacatenco, A. Postal 14-740, 07360 México D.F., México.[2]Centro de Nanociencias y Micro y Nanotecnologías-IPN, UPALM, Col. San Pedro Zacatenco; A. Postal 07738 México D.F., México.
[*]Tel: 011 +52 +55 5747-3715 ; e-mail: osolorza@cinvestav.mx

ABSTRACT

Nowadays catalysts based on Pt and Pt-M alloy (M = Co, Ni) are materials of great interest to be applied as cathodes in proton-exchange membrane fuel cells; however the common problem in the alloys is the easily degradation of the element non-noble in acidic media, decreasing significantly its stability and performance. Currently intense investigation has been focused on the synthesis of core-shell materials, where cores of different non-noble metals have been decorated with Pt. This procedure could deeply reduce the amount of Pt used; decreasing the catalyst cost and improving catalytic activity towards oxygen reduction reaction (ORR), respect to benchmark Pt/C catalysts. These features have been related with changes on geometrical and/or electronic properties owing to M-Pt interactions. In this work, we present the synthesis, as well physical and electrochemical characterization of the nickel oxide supported in Ketjenblack carbon decorated platinum core-shell nanocatalyst for the oxygen reduction reaction (ORR) in acid media. The core was synthesized by chemical reduction with $NaBH_4$ of $Ni(NO_3)_2.6H_2O$, while the shell was deposited by galvanic displacement on the surface of Ni nanoparticles. The presence of Pt in the core was proved by XRD. On the other hand, TEM micrographs have showed highly dispersed nanoparticles with an average between 2-20nm. The presence of Ni and Pt on 71 and 29 wt. % respectively was confirmed by EDAX while XPS and Raman spectroscopy confirms the presence of NiO. The electrochemical performance of NiO@Pt/C is evaluated by cyclic voltammetry, CO stripping and using rotating disk electrode setup, was carried out for the ORR in HClO4 electrolyte; indicated that have more catalytic activity than that of commercial 20% Pt / C-Etek® catalyst, used as reference.

Keywords: NiO:Pt core-shell nanoparticles; oxygen reduction reaction, electrochemical analysis.

Acknowledgments: This project was supported by Conacyt (grant FOINS 75/2012).

Catalytic Layer Locationin MEA and Air Supply Influence on the Performance of an Open-Cathode Direct Ethanol Fuel Cell

D.A. Moreno J, Daniella E. Pacheco C., L.C. Ordoñez*

Centro de Investigación Científica de Yucatán, A.C. Unidad de Energía Renovable, Centro de Investigación Científica de Yucatán, C. 43 No. 130 Col. Chuburná de Hidalgo, Mérida, Yucatán, 97200. México. Tel +52-999-9428330, e-mail: lcol@cicy.mx

ABSTRACT

The influence of the catalytic layer location on the performance of an open-cathode DEFC was investigated using three different methods of preparation ofMEAs. A catalytic loading of 1mgPtcm^{-2} of a commercial catalysts of PtRu/C was used in bothanode and cathodeelectrodes.In MEA1, catalyst layers (CL)were deposited directly on the Nafion® membrane surface. MEA2consisted of two CL´s: an inner layer placed on the member surface and an outer CL located onto the carbon clothdiffuser (GDL). MEA3 was prepared using Pt-Black as the inner CL and PtRu/C or PtSn/Cas the outer CL.Additionally, we report two approach of the open-cathode DEFC operation: air-self breathing and forced-air convection at two temperatures: RT and 60°C. Results show an improvement on the cell performance with the combination of the inner and outer CL. The best activity was recorded with the outer CL prepared withPtSn/C. There is a strongly dependence between air supply to the cathode and cell performance, however, our Open-Cathode DEFC design shows a small decrease about24.6 % in the power density while the cell was working in air-self breathing mode respect to forced-air convection modeat RT.

Keywords: DEFC;Open-Cathode desing;MEA preparation

XIV International Congress of the Mexican Hydrogen Society
Cancun, Mexico, 2014

Microstructural Analysis of Modified Gas Diffusion Layer for a Water PEM Electrolyzer

G. I. Alba[1], R. Barbosa[3], B. Escobar[4], Y. Verde-Gomez[4], L.G. Arriaga[1], J. C.Cruz[2,*]

[1]Centro de Investigación y Desarrollo en Electroquímica S.C., Parque Tecnológico Querétaro s/n, Sanfandila, Pedro Escobedo, Qro., México, 76703.
[2]Instituto Tecnológico de Chetumal, Av. Insurgentes 330, Chetumal, Q. Roo, México, 77013.
[3]Universidad de Quintana Roo, Boulevard Bahía s/n, Chetumal, Q. Roo, México, 77019.
[3]Instituto Tecnológico de Cancún, Av. Kabah Km. 3, Cancún, Q. Roo, México, 77500.
[*]Tel: +529831043002; e-mail: jcca12345@hotmail.com

ABSTRACT

The water electrolysis is a process capable of producing high purity hydrogen (H2 ≈ 100%), due to its electrochemical conversion of hydrogen and oxygen. However, the operating conditions required materials that can resist aggressive environmental as high overpotencials and low pH values. The composition and structure of the elements that constituting the gas diffusion layer (GDL) of a Proton Exchange Membrane Electrolyzer (EPEM), affects the global performance of the cell itself. But also in the mass transport of the reactants due to reaction. In this work are presented the results of a morphologic and modified titanium porous matrix. The analysis includes the determination of the microstructural influence for the mass transport through numerical simulation and statistical characterization techniques. Two different etching attacks were performed to modify the porous matrix, these chemical etchings corresponds to a: one mix acidic solution of HCl/H_2SO_4 17 and 27 %v/v respectively, and attached by a oxalic acid solution 0.1 M both were performed a different times. Therefore, the GDL were characterized by SEM at different magnifications to determine the microestrutural statistical differences among the three matrix (two modified and one without modification) and its stochastic reconstruction. Subsequently a surface area characterization was performed by BET absorption technique to calculate the porosity on the different matrix.

Keywords: Microstructural Analysis; Gas Difussion Layer; Etching attack.

Pd-Fe_3O_4/MWCNT Nanomaterials as Novel Anode Catalysts for the Formic Acid Oxidation Reaction

P.C Meléndez González[1], F.J. Rodríguez Varela[1,2]

[1]Programa de Sustentabilidad de los Recursos Naturales y Energía, Cinvestav Unidad Saltillo, Av. Industria Metalúrgica 1062, Parque Industrial Ramos Arizpe. Ramos Arizpe, Coahuila, C.P 25900, México.
[2]Programa de Nanociencias y Nanotecnología, Cinvestav Unidad Saltillo, Av. Industria Metalúrgica 1062, Parque Industrial Ramos Arizpe. Ramos Arizpe, Coahuila, C.P 25900, México.
*E-mail: javier.varela@cinvestav.edu.mx

ABSTRACT

In this work, novel 20% Pd-Fe_3O_4/MWCNT nanomaterials have been evaluated as anode catalysts for the Formic Acid Oxidation Reaction (FAOR) in alkaline medium. The catalysts were synthesized using $NaBH_4$ as a reducing agent. The Pd:Fe_3O_4 atomic ratio was 3:1, 2:1 and 1:1. For comparison purposes, a 20% Pd/MWCNT catalysts was also synthesized. The electrochemical evaluation showed high catalytic activity of the bimetallic material for the FAOR. Such performance suggests that Pd-Fe_3O_4/MWCNT may be considered as anode catalyst for alkaline DFAFCs.

Keywords: Pd-Fe_3O_4 catalysts, formic acid oxidation reaction, MWCNTs

Magnetite-Platinum Core-shell Nanoparticles Using a Two-step Method for the Oxygen Reduction Reaction

N.M. Sánchez-Padilla[1], S.M. Montemayor[2],F.J. Rodríguez Varela[1,3*]

[1] Programa de Sustentabilidad de los Recursos Naturales y Energía, Cinvestav Unidad Saltillo, Av. Industria Metalúrgica 1062, Parque Industrial Ramos Arizpe. Ramos Arizpe, Coahuila. C.P 25900, México.
[2]Facultad de Ciencias Químicas, Universidad Autónoma de Coahuila. Blvd. V. Carranza s/n, República Oriente, Saltillo, Coahuila. C.P. 25280, México.
[3]Programa de Nanociencias y Nanotecnología, CinvestavUnidad Saltillo, Av. Industria Metalúrgica 1062, Parque Industrial Ramos Arizpe. Ramos Arizpe, Coahuila. C.P 25900, México.
[*]E-mail: javier.varela@cinvestav.edu.mx

ABSTRACT

Direct Alcohol Fuel Cells (DAFCs) are a promising alternative to replace energy devices that use fossil fuels. To reach this objective, it is necessary to enhance the catalytic activityand reduce the cost of cathode catalysts. Decreasing the Pt loadingon the electrode is a viable approximation to achieve lower catalyst costs. Also, the use of cheap co-catalysts helps to accomplish this goal. This is the reason for the research carried out in this work, on new nanostructures and materials as cathodes for DAFCs. It has been proved that iron oxides have a synergetic interaction with Pt to form highly active and stable anode and cathode materials. In this study, wehave synthesizedFe_3O_4@Pt and Fe_3O_4@Pd core-shell cathode catalysts supported on Ordered Mesoporous Carbon (OMC),a novel material applied as a support on fuel cells. The synthesis has been performed in a two step procedure.First, the formation of the ferric-ferrous oxide as core material via the reduction of the Fe precursor, using$NaBH_4$ as reducing agent. Second, the deposition of the Pt (or Pd) shell, followed by the dispersion of the core-shell nanoparticles on OMC, using the polyolmethod. The Fe_3O_4@Pt/OMC and Fe_3O_4@Pd/OMCcatalytshave been characterized by XRD, SEM-EDS andtested as cathode materials for Oxygen Reduction Reaction (ORR) in acid medium.

Keywords:two step synthesis, core-shell nanocatalyst,Oxygen Reduction Reaction.

Microstructural Analysis and Electrochemical Performance of a PEMFC Electrode

J. Ramírez[1], R. Barbosa[2]*, E. Escobedo[1], D. Pacheco[1], B. Escobar[3], Y. Verde[3]
[1]Centro de Investigación Científica de Yucatán, calle 43 no. 130 Chuburná de Hidalgo, Mérida Yucatán, México C.P. 97200
[2]Universidad de Quintana Roo, Boulevard Bahía s/n, Chetumal, Q. Roo, México, 77019.
[3*]Instituto Tecnológico de Cancún, Av. Kábah Km. 3, Cancún, Q. Roo, México, 77500.
Tel: +529831566032; e-mail: romelix1@gmail.com

ABSTRACT

In Proton Exchange Membrane Fuel Cell (PEMFC) there are many factors which may affect the global performance of the cell itself such as the manufacturing technique, composition and structure of the elements that constituting the catalytic layer (CL) of a PEMFC. This work summarizes the results of a morphological and electrochemical studies made with manufactured electrodes using the electro-spray method. The analysis includes the determination of the microstructure influence related to the electrochemical response through statistical characterization techniques. Also, three different manufacturing techniques were performed: electrocatalyst deposited on the membrane, electrocatalyst deposited on the diffuser and electrocatalyst deposited both on the electrode and the membrane. The assemblies were characterized by SEM at different magnifications and AFM to determine the morphology and distribution of the CL over the diffuse layer among and their relation with electrochemical performance of the three different manufacturing electrodes techniques. Electrochemical characterizations were performed by electrochemical impedance spectroscopy and polarization curves.

Keyword: Microstructural, electrocatalitytic layer, PEMFC.

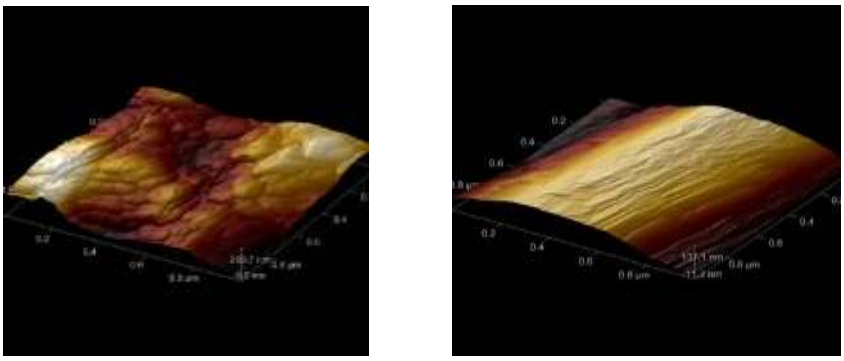

a) with electrocatalyst deposited b) without electrocatalyst deposited

Figure 1: AFM images corresponding to diffuser (1µm of carbon paper) with and without electrocatalyst deposited

Enhancement of the Glycerol Electrooxidation Reaction Using PdCu/XC-72 as Electrocatalyst

J. Maya-Cornejo[1], N. Arjona[1], M. Guerra-Balcázar[2], L. Alvarez-Contreras[3], J. Ledesma-García[2] and L.G. Arriaga[1]*

[1]Centro de Investigación y Desarrollo Tecnológico en Electroquímica, 76703 Querétaro México
[2]División de Investigación y Posgrado, Facultad de Ingeniería, Universidad Autónoma de Querétaro, 76010 Querétaro México.
[3]Centro de Investigación en Materiales Avanzados, 31109 Chihuahua, México
*Tel: +524422116069 larriaga@cideteq.mx;

ABSTRACT

Pd-Cu electrocatalyst was synthesized by chemical reduction method using $CuSO_4$ and K_2PdCl_4 as metallic precursors in the presence of ethylene glycol as surfactant and sodium borohydride as reducing agent. This electrocatalyst was electrochemically and physicochemically characterized by means of cyclic voltammetry, chronoamperometry, X-Ray Diffraction (XRD), X-Ray Fluorescence (XRF) and Transmission Electron Microscopy (TEM). The electrocatalyst presented a homogeneous distribution, with an average particle size around 5 nm. According to XRF results, the mass content of active phase is Pd 80%, Cu 20% for a catalyst with a composition of 60-40 (PdCu / Vulcan XC-72 as support). The electrocatalytic activity of Pd-Cu was evaluated in terms of glycerol electrooxidation reaction at three concentrations (0.1, 1 and 3M) in 0.3 M KOH aqueous solution. The results obtained from voltamperometric studies showed that the current density achieved with Pd-Cu electrocatalyst is 3 times higher than that reached with commercial Pd (30% from ETEK) and a shift to negative values for electrooxidation potential about 100mV.

Keywords: Glycerol electrooxidation, chemical reduction, Pd-Cu electrocatalyst.

XIV International Congress of the Mexican Hydrogen Society
Cancun, Mexico, 2014

Pd Synthesized by Electrochemical Techniquesin Three-Dimensional Carbon Electrodes

N. Arjona[1], M.-A. Goulet[2], M. Guerra-Balcázar[3], J. Ledesma-García[3], E. Kjeang[2,**], L. G. Arriaga[1,*]

[1]Centro de Investigación y Desarrollo Tecnológico en Electroquímica, Querétaro, México, 76703.
[2]School of Mechatronic Systems Engineering, Simon Fraser University, 250-13450 102 Av., Surrey, BC, Canada, V3T 0A3
[3]División de Investigación y Posgrado, Facultad de Ingeniería, Universidad Autónoma de Querétaro, Querétaro, México, 76010.
[*]Tel: +524422116069 larriaga@cideteq.mx; [**]Tel: +17787828791 ekjeang@sfu.ca

ABSTRACT

One of the main strategies to enhance the electrocatalytic activity is related to the use of supports with high surface area. In this sense,we used three-dimensional Toray carbon paper. The electrochemical properties of this material as substrate-electrode were evaluated with and without thermal treatment using potassium ferrocyanide as target molecule. Without thermal treatment the electrode exhibited a poor reversibility of the ferrocyanide specie. With the thermal treatment the Toray paper showed good electrochemical properties which could be attributed to the enhancement of the electrode wettability. After that, Pd materials as electrocatalysts were synthesized using two different electrochemical techniques in the heat treated Toray paper as working electrode: cyclic voltammetry (namely Pd_1) and differential pulse voltammetry (Pd_2). The electrochemical active surface area (ECSA) was determined by cyclic voltammetry in 0.5 M H_2SO_4resulting in areas of 16 and5.7-fold higher than the geometrical area for Pd_1 andPd_2, respectively. The electrocatalytic activity was tested toward the 0.1 M formic acid electrooxidation reaction in basic medium (0.3 M KOH). The current density was of 1.76, and 0.6 mA cm^{-2}, respectively. The potentials for the formic acid oxidation were located at -0.38 and -0.40 V *vs*. NHE.

Keywords: Toray paper, three-dimensional electrode, formic acid electrooxidation.

Bi-directional DC-DC Converter to Charge/Discharge a Supercapacitor Modulein a Hybrid Renewable Energy System.

J.M. Sandoval[1], I. Domínguez[2], Y. Verde[3], D.E. Pacheco[1*],J.L. Durán[2]

[1]Centro de Investigación Científica de Yucatán A.C., Calle 43 No.130, Colonia Chuburná de Hidalgo, Mérida, Yucatán, México, CP 97200.
[2]Instituto Tecnológico de Chihuahua, Ave. Tecnológico #2909, Chihuahua, Chih., México. C.P. 31310.
[3]Instituto Tecnológico de Cancún, Av. Kábah Km. 3, Cancún, Q. Roo, México, CP77500.
*email: dpacheco@cicy.mx

ABSTRACT

This paper presents an interconnected integrated bidirectional dc-dc flyback converter and its application to charge (and discharge) a supercapacitor module (SC) froma +24V dc-bus energized by renewable energy sources such as: photovoltaic (PV) panels and a wind turbine. The SC module is interconnected to the rest of the hybrid system by a dc-dc integrated bi-directional flyback converter (IBFBC). The dc-bus voltage in the hybrid system is supplied from two renewable energy sources: a+60V, 2.4kW photovoltaic array, a low voltage/low power wind turbine at +48V, 250kW, and a battery bank (+24V). In this paper, the development of a dc-dc flyback converter for charge and discharge at165F +48V, 2.48Wh/kg supercapacitor module is presented. A design example will illustrate the feasibility of the proposed bidirectional flyback converter to charge the SC module from the +24V dc-bus voltage to store energy, as well as to supply the energy demand of required loads connected to the dc-bus voltage. Extensive analysis, simulation and experimental results are presented to validate the theory. A design example will be presented to demonstrate the performance of charge/discharge functions of the proposed IBFBC.

Keywords: Bidireccional; Flyback; Hybrid System; Supercapacitor.

Performance Study of Membranes on an Electrochemical Hydrogen Compressor

J. L. Pineda[a].,M. P. Gurrola[a], S. Rivas[b]., B. Bahar[c].,J. Ledesma-García[b]., L.G. Arriaga[a]., A. U. Chávez-Ramírez[a]

[a]Centro de Investigación y Desarrollo Tecnológico en Electroquímica S. C., Parque Tecnológico Querétaro s/n, Sanfandila, Pedro Escobedo, C.P. 76703. Querétaro, México.
[b]Universidad Autónoma de Querétaro, División de Investigación y Posgrado, Facultad de Ingeniería. 76010. Querétaro, México.
[C]Xergy Incorporated. 310 North race Street. Georgetown. DE 19947, USA.

ABSTRACT

The electrochemical hydrogen compression (EHC) is a scarcely explored alternative to conventional hydrogen compression methods. The EHC uses the transport phenomena presented in the operation of Proton Exchange Membrane (PEM) technologies, provides important advantages such as low energy demand to reach high compression rates, it is noiseless, low maintenance is required, and unpolluted hydrogen can be obtained. Like in a PEM fuel cell or PEM electrolyzer, the core of the compressor is a Membrane-Electrode Assembly (MEA). One of the main challenges is to find a membrane with a high ionic conductivity and capable of withstand a high pressure between anode and cathode. This work shows the evaluation of four different membranes Nafion, S-PEEK, F>N1, F>S in an EHC system based on an Electrochem PEMFC (5 cm^2). Potential pulses from 100 to 800 mV were applied to the EHC while the pressure increase in the compression chamber was monitored.

Keywords: Hydrogen; Electrochemical Hydrogen Compressor; Fuel Cell;

Preparation of Nickel Catalysts Deposited on Gamma Alumina to Process Hydrodeoxygenation First Generation Biodiesel

E. Mora, J. Medina[2], J. Rodriguez[3], D. González[3], M. Sanchez[1]

[1]Universidad Politécnica de Aguascalientes, Calle Paseo, San Gerardo, 207, 20342, Aguascalientes, Ags., México, 20342.
[2] Instituto Tecnológico de Aguascalientes, Av. Adolfo López Mateos #1801 Ote.
Fracc. Bona Gens, Aguascalientes, Ags., México, 20256.
[3] Cinvestav Unidad Saltillo, Av. Industria Metalúrgica 1062, Zona Industrial, Ramos Arizpe, Coahuila de Zaragoza, México, 25900.
[1]Tel: +524494490720; e-mail: up110014@alumnos.upa.edu.mx

ABSTRACT

Due to the current problems in the consumption of fossil fuels nowadays; by the wet impregnation method incipient, a nickel catalyst supported on gamma alumina was prepared using as precursor salt Nickel acetate tetrahydrate, because the precursor salt is not soluble in water, a variant of the method, consisting of a grinding and physical blending of boehmite precursor to nickel salt, once the homogeneous physical mixture drops of a solution of nitric acid dissolved 1:16 in water was added, was applied in this possible to modify the pH of the boehmite surface and achieve the impregnation of the salt. They were anchored nickel particles by a controlled, to obtain nickel oxide, calcination method finally the metal oxide catalysts were reduced by exposure to a flow of hydrogen at 400 ° C, obtaining as a product catalyst Ni/γ -Al_2O_3 can accelerate and direct the hydrodeoxygenation reaction of oxygenated organic compounds for converting a first generation biodiesel second generation biodiesel.

Keywords: Ni/ γ-Al_2O_3; second generation biodiesel, oxygenated organic compounds.

XIV International Congress of the Mexican Hydrogen Society
Cancun, Mexico, 2014

Electrochemical Impedance Studies of Co-based Nanomaterials for Hydrogen Evolution Reaction

J.V. Medina, E. M. Arce, J. G. López

Instituto Politécnico Nacional. ESIQIE. Departamento de Ingeniería en Metalurgia y Materiales, México, D.F.

ABSTRACT

The electrocatalytic activity for hydrogen evolution reaction (HER) of cobalt based nanomaterials synthesized by high energy mechanical milling was studied to use in PEM electrolyzers. X-ray diffraction, scanning electron microscopy and transmission electron microscopy were used to characterize the synthesized powders. Their composition was established by means of energy dispersive spectroscopy, showing the presence of iron which was caused by the wear of grinding medium. Analysis SEM and TEM showed the formation of agglomerates of 1-7 microns, constituted by particles close to 20 nanometers. The electrocatalytic activity of the materials $Co_{80}Ru_{20}$ and $Co_{80}Ru0_{15}Pt_5$ in acid medium was evaluated in 0.5 M H_2SO_4 at 25 °C using linear polarization technique and electrochemical impedance spectroscopy (EIS). From polarization curves was possible to determinate the mechanism of HER. Nyquist diagrams were obtained in a frecuency range from 100 kHz to 10 mHz at selected overpotentials in order to avoid the formation of bubbles on the surface of electrode, these diagrams were characterized by the presence of two semicircles, the diameter of the first one, at high frequency, remained constant at all overpotentials, while the diameter of the second one, at low frequency, decreased when overpotential increased. Electrical equivalent circuit 2-CPE was used for the purpose of explaining the electrochemical response. The kinetic parameters for HER obtained from analysis of polarization and impedance data showed that both materials exhibit good performance as electrocatalysts toward to HER. The material with the best performance was $Co_{80}Ru0_{15}Pt_5$.

Keywords: Impedance; linear polarization; hydrogen evolution reaction

XIV International Congress of the Mexican Hydrogen Society
Cancun, Mexico, 2014

Novel $(Ir_xSn_ySb_z)O_w$ Material as Catalyst for the Oxygen Evolution Reaction.

N. J. Pérez-Viramontes[1], C. Guzmán-Martínez[1], M. Galván-Valencia[1,] S. M. Durón-Torres[1*]

[1]Universidad Autónoma de Zacatecas, Programa de Maestría en Ciencias de la Ingenieria, Campus Siglo XXI, Carretera Zacatecas-Guadalajara Km. 6.0, Ejido la Escondida, Zacatecas, Zacatecas, México, 98160.
[*]Tel: +524929256690 Ext. 4655; e-mail: duronsm@prodigy.net.mx

ABSTRACT

The synthesis of a novel material of general composition $(Ir_xSn_ySb_z)O_w$ for use in solid polymer electrolyte water electrolysers (SPEWE) was accomplished from the simultaneous synthesis of the electrocatalyst and the support by means of thermal decomposition of chlorides precursors H_2IrCl_6 , $SnCl_2{\cdot}2H_2O$ and $SbCl_5$ in ethanol . Different H_2IrCl_6 proportions in the reaction mixture were tested to observe their effect on the amount and electrocatalytic activity of the material obtained. The electrochemical properties of the different syntheses were measured by using: cyclic voltammetry (CV), linear voltammetry (LV), rotating disk electrode (RDE), chronoamperometry (CA) and electrochemical impedance spectroscopy (EIS). Electrochemical tests were conducted using as support electrolyte H_2SO_4 0.5 M in a conventional three-electrode cell. A mechanical mixture of IrO_2 with Vulcan carbon and iridium oxide with antimony doped tin oxide were also tested respect to the oxygen evolution reaction to compare the properties of catalyst/support obtained. The results indicate that synthesized materials could represent a suitable candidate to be used use as anode in SPWE to catalyze the oxygen evolution reaction (OER).

Keywords: Water Electrolysis, Electrocatalyst, Oxygen Evolution Reaction.

Effects of Ball Milling Conditions on the Hydrogen Sorption of Mg and Cr_2O_3 Nanopowders

S. C. Altamirano-Pérez[1], A. Martínez-García[1], E. Reguera[2], E. A. Juarez-Arellano[3,*]

[1]División de Estudios de Posgrado, Universidad del Papaloapan, Campus Tuxtepec, Circuito central 200, Tuxtepec, Oax., México, 68301.
[2]Centro de investigación en Ciencia Aplicada y Tecnología Avanzada,CICATA-IPN Legaria, México D.F. 11200.
[3] Instituto de Química Aplicada, Universidad del Papaloapan, Campus Tuxtepec, Circuito central 200, Tuxtepec, Oax. México, 68301.
[*]Tel: 01(287)8759240; e-mail: eradjuar@hotmail.com

ABSTRACT

Mg powders with 1%wt of Cr_2O_3 and 1%wt of Boro powders catalysts were obtained by high energy ball milling. A continuous particle size reduction was observed by SEM as result of grinding time and it was confirmed by XRD. However, the superficial area values obtained by BET show a reduction in the superficial area with increasing grinding time. The hydrogen sorption studied at -198°C showed a pour hydrogen storage capability in the samples treated at 80 minutes of grinding. The low hydrogen adsorption could be due to the formation of MgO and $Mg(OH)_2$ and due to the sintering processes of powder particles generating agglomerates. Therefore, although the particle size decreased with grinding time, the superficial areal decrease as a consequence of the formation of agglomerates. However, increasing the milling time, for instance 280 min, the hydrogen adsorption increased which can be associated with the destruction of the agglomerates. The incorporation of boron improved the hydrogen adsorption.

Keywords: Hydrogen, ball milling, Mg.

A PEM Fuel Cell Model Based on Artificial Neural Network and Particle Swarm Optimization

Miguel Gonzalez[1], Victor M. Sanchez[1], F. Chan[1], R. Barbosa[1]

[1]Universidad de Quintana Roo, Boulevard Bahía s/n, Chetumal, Q. Roo, México, 77019.
Tel: +5298350300; e-mail: vicsan.huerta@gmail.com

ABSTRACT

This paper presents a proton exchange membrane fuel cell (PEMFC) model obtained from a neural network trained by a particle swarm optimization algorithm (PSO). Although in the open literature there are several works using neural networks for PEMFC modeling, backpropagation or gradient training algorithms are used in them. PSO is a stochastic population-based search method which has been shown as powerful method for optimization global in several applications. In this work, neural network is employed for modeling the internal processes of the PEMFC such as the gas pressure, temperature, humidity in order to produce a response that fits to the real performance of the fuel cell. The results shown that the PEMFC model obtained by the neural network trained by PSO obtains the best response, outperforming traditional training algorithms for neural networks. The PEMFC model obtained can be used to research the influence of internal process variables for the optimal design of cells or stacks of PEMFC.

Keywords: fuel cells; neural-networks, particle swarm optimization.

XIV International Congress of the Mexican Hydrogen Society
Cancun, Mexico, 2014

Multi-Objective Optimization of a Hybrid Generating System

Miguel Hernan[1], Victor M. Sanchez[1], R. Barbosa[1], J. Hernandez, Juan M. Ramirez[2,*]

[1]Universidad de Quintana Roo, Boulevard Bahía s/n, Chetumal, Q. Roo, México, 77019.
Tel: +5298350300; e-mail: vicsan.huerta@gmail.com
[2]CINVESTAV Guadalajara, Av. del Bosque 1145, Zapopan, Jalisco, México, 45019.
[*]Tel: +523337773600; e-mail: jramirez@gdl.cinvestav.mx

ABSTRACT

Renewable generating systems are a sustainable solution for the electrical energy production; however the costs associated with the initial investment and that usually these kind of electrical generating systems are over-sized with the aim of satisfying the electrical load connected to them, implies an increase in the costs of investment, maintenance and operation as well as a reduction of their overall efficiency. Therefore, sizing is an important issue in the design of renewable generation systems, in order to reach an efficient relationship between cost and benefit. Likewise, the random nature of the renewable sources increases the complexity for sizing a renewable generating system with regard to a conventional system. This paper is aimed to estimate the cost/sizing relationship of a hybrid energy solar-wind-diesel generator system using solar irradiation and wind data. The hybrid energy system uses the hydrogen as storage vector, so that it employs a fuel cell and electrolyzer for such task. The formulation is made up as a multi-objective optimization problem, solved by a genetic algorithm. The optimizer calculates the best system configuration to meet the commitment between the energy supply reliability and cost. Moreover, the optimizer allows an easy way for optimal sizing without depth knowledge of the relationship between the hybrid system costs and the generated power. Results are presented for a domestic installation load located in the south-east region of Mexico (Chetumal city).

Keywords: fuel cells; genetic algorithm, multi-objective optimization.

Nanoparticles of Pt and Ag-Pt Synthesized by Ultrasonic for Oxygen Reduction Reaction

M.E. Beltrán-Perez[1], F.M. Hernández-Mendoza[1], O. Martínez-Alvárez[1], B. Ruiz-Camacho[1,*]

[1]Ingeniería en Energía, Universidad Politécnica de Guanajuato, Av. Universidad Norte s/n, Juan Alonso Cortázar Guanajuato, México, 38438

[*]Tel: +524624414307; e-mail: beatrizr@upgto.edu.mx

ABSTRACT

This paper presents the synthesis of nanoparticles of Pt, Ag and Pt-Ag using ultrasonic irradiation at room temperature. The metal nanoparticles were supported on carbon substrates. A concentration study of alcohol was carried out to determine the kinetics of reduction metallic using UV-vis spectroscopy. The materials synthesized (Pt/C , Ag/C and Pt-Ag/ C) were evaluated on the oxygen reduction reaction (ORR) for be applied as cathodes in a Proton Exchange Membrane Fuel Cell (PEMFC). The electrochemical evaluation of the materials synthesized was performed using a cyclic and linear voltammetry technique in acidic medium and room temperature conditions. The kinetic reaction study indicates that the higher alcohol concentration favors the reduction of the metal precursor. Preliminary results demonstrate that the bimetallic electrocatalyst exhibits greater catalytic activity for the ORR compared to the monometallic sample. Pt-Ag/C electrocatalyst can be used as a cathode in a fuel cell.

Keywords: Ag-Pt electrocatalyst, ultrasonic, oxygen reduction reaction, fuel cell

Development and application of hybrid membranes for the enrichment of hydrogen gas produced in biodigesters

P. Quechulpa-Pérez[1], JF. Pérez Robles[1], AF Pérez-de Brito[2], LM. Avilés-Arellano[1], J. Pineda Piñón[3]

[1]Centro de Investigación y de Estudios Avanzados del Instituto Politécnico Nacional Unidad Querétaro, Libramiento Norponiente No.2000. Frac. Real de Juriquilla Querétaro, Qro. C.P. 76230, Tel: +52 (442) 2 11 99 00. E-mail: martin.pompeyo@hotmail.com

[2]Grupo de tribología y superficies. Facultad de minas. Universidad Nacional de Colombia Sede Medellin,

[3]Centro de Investigación en ciencia Aplicada y Tecnología Avanzada del IPN, Unidad Querétaro, C.P. 76090, Cerro Blanco No. 141. Colinas del Cimatario, Querétaro, Qro., México

ABSTRACT

The production of renewable energies is an important topic in our present-day society. Many researchers are currently working in processes for the production of biofuels and also the use of them. Among biofuels the production of hydrogen and methane from different wastes play an important role today. Normally biohydrogen and methane biogas are produced in anaerobic biodigesters using different organic wastes. Nevertheless the produced gas in both cases has undesirable gases like carbon dioxide and sulphur compounds among others. Then it is necessary to decrease the concentration of undesirable gases and at the same time to increase the quantity of hydrogen and methane gas.

Taking into account the aforementioned, our research group has made an extensive work for the development of some hybrid membranes to separate the hydrogen and methane from carbon dioxide and in general from undesirable gases. The hybrid membranes were prepared using colloidal silica by the sol-gel process and polyvinyl acetate, PVac. The membranes were characterized by Thermogravimetric Analysis, Optical Microscopy, Scanning Electron Microscopy and Raman Spectroscopy. Also mechanical tests like tensile strength, penetration and superficial hardness were performed on the hybrid material used for the production of the membranes.

A homemade device was fabricated for testing the diffusion of gases through the membranes. It was demonstrated that that the best performance of the membranes was attained using a ratio silica/PVac of 35/65 %w/w, methanol as solvent and annealed at room temperature. From the results it was fabricated a device of three columns of 6” for using it in a biodigester prototype of 7.0 tons that will be used for the production of hydrogen and methane.

Keywords: Biohydrogen, membranes, sol-gel.

High H_2 Production from the Reforming of CH_4 by Hydrogen Sulphide Using Mo-Cr Supported on Heterogeneous Catalysts.

A. L. Martínez-Salazar[1,*], J. A. Melo-Banda[1], J. M. Domínguez- Esquivel[2], M. A. Coronel-García[1], A. I. Reyes de la Torre[1]

[1]Instituto Tecnológico de Ciudad Madero, 1° de mayo s/n col. Los Mangos, Cd. Madero, Tamaulipas, México, 89440.
[2]Instituto Mexicano del Petróleo, Eje Central Lázaro Cárdenas 152, San Bartolo Atepehuacan, Gustavo A. Madero, Ciudad de México, Distrito Federal, México, 07730.
[*]Tel: +528332111039; e-mail: analidiams@gmail.com

ABSTRACT

Catalytic steam reforming has been for a long time the principal method for the production of hydrogen. According to this method, hydrogen is generated by the reaction of steam with methane (CH_4) at quite high temperatures from 923 to 1223 K requiring the removal of hydrogen sulphide (H_2S) present in natural gas streams or light hydrocarbons.

Alternative processes for hydrogen production have been studied. A proposed method is the reforming of CH_4 by H_2S. With this process, the removal of H_2S in natural gas streams is no longer necessary and sulfur, usually considered as a strong pollutant on liquid fuels in refineries, is used as a reagent in H_2S form of hydrodesulphurization processes.

This research involved the synthesis of modified SBA-15 support with zirconia dioxide; achieving the mechanical resistance, chemical stability and redox properties of zirconia improving the textural characteristics. Furthermore, lanthanum oxide incorporation in zirconia was carried out allowing increase of its surface area with enhanced thermal stability. The supports were impregnated with molybdenum as active phase and chromium as promoter.

The materials were evaluated in a quartz reactor at range temperatures of 873 – 1123 K, feed molar ratio CH_4:H_2S of 1:12. Synthesized materials were characterized before and after reaction by X-Ray diffraction, nitrogen physisorption, transmission electronic microscopy and thermogravimetry techniques. All techniques confirm the mechanical and thermal stability of the supports and their textural properties.

Molybdenum supported on zirconia-lanthanum catalyst showed better catalytic performance, achieving high selectivity to hydrogen (64%).

Keywords: reforming, hydrogen, modified supports

XIV International Congress of the Mexican Hydrogen Society
Cancun, Mexico, 2014

Kinetics and Modelling Study of the Catalytic Reaction of Methane and Hydrogen Sulphide over Mo/La_2O_3-ZrO_2 Catalyst

A. L. Martínez-Salazar[1,*], J. A. Melo-Banda[1], J. M. Domínguez- Esquivel[2], M. A. Coronel-García[1], M. A. Meraz-Melo[3]

[1]Instituto Tecnológico de Ciudad Madero, 1° de mayo s/n col. Los Mangos, Cd. Madero, Tamaulipas, México, 89440.
[2]Instituto Mexicano del Petróleo, Eje Central Lázaro Cárdenas 152, San Bartolo Atepehuacan, Gustavo A. Madero, Ciudad de México, Distrito Federal, México, 07730, [3]Instituto Tecnológico de Iztapalapa, Av. Telecomunicaciones s/n Col. Chinampac de Juárez, Del. Iztapalapa, Ciudad de México, Distrito Federal, Mexico, 09208.

[*]Tel: +528332111039; e-mail: analidiams@gmail.com

ABSTRACT

In recent times the availability of liquid fuels reserves is constantly declining. This reality has triggered research for the discovery of new solutions using other energy resources.

Catalytic steam reforming is a widely used method today either to produce hydrogen or to give syngas as the first step for the conversion of methane into liquid fuels through the Fischer-Tropsch synthesis.

The reforming of CH_4 by H_2S can be considered as the first step of an alternative route to produce light hydrocarbons from methane. With this process, the removal of H_2S in natural gas streams is no longer necessary and sulfur, usually considered as a strong pollutant on liquid fuels in refineries, is used as a reagent in H_2S form of hydrodesulphurization processes. Furthermore, this alternative produces hydrogen, a valuable chemical and clean energy source, and carbon disulphide as a secondary petrochemical.

The open literature concerning the kinetic study of the methane-hydrogen sulphide reaction is very poor. In this research the reaction of CH_4 and H_2S over zirconia catalyst modified with lanthanum oxide impregnated with molybdenum has been studied in a fixed bed tubular reactor varying the inlet CH_4 flowrate over a temperatures range of 1023 – 1323 K and feed molar ratio CH_4:H_2S of 1:12. The Langmuir-Hinshelwood theory has been used to determine kinetic models. Model discrimination has been performed by using statistical and thermodynamic constraints.

Finally, the simulation process of reforming CH_4 by H_2S has been developed in which separation of the reaction product and H_2S involves absorption through diethanolamine. A tubular reactor from kinetic parameters was designed. Aspen Plus ® 11.1 simulation software was used. Preliminary results showed a high H_2 produced by this route, also; low temperatures where considered to performance this reaction.

Keywords: reforming, hydrogen, kinetics

XIV International Congress of the Mexican Hydrogen Society
Cancun, Mexico, 2014

On the Role of Electronic Properties of Nanostructured Catalysts on the Reaction Pathways of Ethanol Oxidation

F. G. Freitas, D. R. M. Godoi, H. M. Villullas*

Instituto de Química, Universidade Estadual Paulista - UNESP, Rua Francisco Degni, 55 - Araraquara (SP) 14800-900 Brasil.
*Tel: +551633019653; e-mail: mercedes@iq.unesp.br

ABSTRACT

Studies of the distribution of reaction products carried out by *in situ* FTIR and the evaluation of the Pt 5d band vacancy by *in situ* XAS measurements performed around the Pt L_3 edge were combined aiming to unravel the influence of electronic properties on the reaction mechanism of ethanol electrooxidation on PtSn-based catalysts. These studies were carried out for nanocatalysts containing PtSn nanoparticles supported on carbon and on carbon-TiO_2 nanocomposites. All catalysts were prepared with 20 wt.% load of PtSn nanoparticles and characterized by several ex situ techniques (X-ray diffraction, transmission electron microscopy and X-ray photoelectron spectroscopy). The catalytic activities for ethanol oxidation were determined by linear potential sweeps and chronoamperometry, while the ability of the catalysts for promoting the bifunctional mechanism was evaluated by measuring the stripping curves of adsorbed CO. It was observed that the presence of TiO_2 has little effect on the activity for CO oxidation, which remains nearly unchanged, at the time that it produces an enhancement of the ethanol oxidation current density. *In situ* FTIR results indicate that larger amounts of acetaldehyde (and therefore smaller quantities of acetic acid) are produced on PtSn/TiO_2-C catalysts than on PtSn/C. At first glance an increase in the yield of acetaldehyde, which involves the exchange of a lower number of electrons per ethanol molecule than the formation of acetic acid, may seem inconsistent with an enhancement of the measured currents. However, data can be rationalized based on the increase in the turnover frequency for the acetaldehyde formation pathway, which would result from an easier acetaldehyde desorption caused by the decrease of the Pt 5d band vacancy promoted by the oxide.

Keywords: electronic effects; reaction mechanism; ethanol oxidation.

Hydrogen production from CH_4 and NO treatment with non thermal plasma

E Alva[b], M Pacheco[a], A Colín[b], V Sánchez[b], J Pacheco[a], R Valdivia[a], H. Frías[a], G. Soria[a,c], S. Darío[a,c], F. Ramos[a], M. Duran[a], M. Hidalgo[a]

[a]Instituto Nacional de Investigaciones Nucleares, Carretera México-Toluca s/n, La Marquesa, Ocoyoacac, México, C.P.52750
[b]Universidad Autónoma del Estado de México, Instituto Literario # 100. Col. Centro Toluca, México, C.P.50000
[c]Instituto Tecnológico de Toluca, Av. Instituto Tecnológico s/n, Metepec, México, C.P.52140
E-mail: marquidia.pacheco@inin.gob.mx

ABSTRACT

In this project chemical kinetics model and its experimental demonstration to produce hydrogen from NO and CH_4 treatment with a dielectric discharge barrier is proposed.
The research was carried out in 2 phases: The first was the analysis of simulation degradation of NO and CH_4. The second step was the development of the experimental methodology to treat the mixture (NO and CH_4).

To produce the non-thermal plasma, an AC power source was developed. This energy source works with a high frequency series resonant inverter in the range of 20 kHz to 180 kHz, able to generate a voltage of 15 kV. The discharge can be sustained at atmospheric pressure. The experimental conditions of this special case were: 36V, 2-5A and 160 kHz.

Chemical model elucidates the degradation of NO and CH_4, however theoretical results concerning hydrogen production are overestimated when they are compared to experimental results; therefore a set of additional equations are then proposed. Results obtained from the model, illustrate that in a mixture of NO in humid air, the main path for the NO removal is the oxidation to NO_2 and, soon after, to HNO_3. Concerning the diminution of CH_4 the electron impact reactions are crucial.

Keywords: Hydrogen, non-thermal plasma, toxic gases treatment

Synthesis and Characterization of Chitosan-Starch Polymer Reinforced with Functionalized Multiwalled Carbon Nanotubes as Electrolyte for Lithium Batteries

Y. Estévez-Martínez[1,2], C. Guzmán-Martínez[2], D. Alaníz-Lumbreras[3], M. Mendoza-Duarte[4], V.M. Castaño-Meneses[5] , S.M. Durón-Torres[2,*].

[1]Nano Coating Technologies SA de CV, Paseo de las Palmas 555, Lomas de Chapultepec I Seccion, Miguel Hidalgo, CP 11000, Distrito Federal, México.
[2]U. A. Ciencias Químicas, Universidad Autónoma de Zacatecas, CU Siglo XXI Edificio 6, Km 6 Carr. Zac-Gdl, La Escondida Zacatecas, CP 96160, Zacatecas, ZAC, México
[3]Facultad de Ingeniería Eléctrica, Universidad Autónoma de Zacatecas, Avenida Ramón López Velarde No. 801, CP 98000, Zacatecas, ZAC, México.
[4]Centro de Investigación en Materiales Avanzados CIMAV, Ave. Miguel de Cervantes 120, Complejo Industrial Chihuahua, C.P. 31109 Chihuahua, Chih., México
[5]Departamento de Ingenieria Molecular de Materiales, Centro de Fisica Aplicada y Tecnologia Avanzada, Universidad Nacional Autónoma de México, Boulevard Juriquilla 3001, CP 76230, Querétaro, Qro., México.
*Tel.: +524929256690 ext 4655, duronsm@prodigy.net.mx

ABSTRACT

In recent years, it has been reported that solid electrolytes are considered promising materials in store energy field, due to their unique properties such as high ionic conductivity, physical flexibility and their ability to provide good electrode / electrolyte contact. Compared to the liquid state, the production of leak and gas formation during the decomposition of the solvent is avoided, in addition to being small, lightweight and safe.

In this work is reported the synthesis and the physical and electrochemical characterization of chitosan-starch polymers modified with carbon nanotubes and lithium. For obtain the structural and physicochemical properties of polymers were used the thecniques of: Dynamical Mechanical Analysis, Scanning Electronic Microscopy, FTIR and Raman spectroscopy. The electrical and electrochemical properties were determinated by using Electrochemical Impedance Spectroscopy and Conductivity Measurements. The results obtained indicate that the polymeric material is a viable candidate to be used as electrolyte for lithium batteries.

Keywords: Nanocomposite-Biopolymer; Electrolyte; Lithium Batteries.

MOFs as Natural Gas Storage Materials

Jade A. Galicia[1*], Erick A. Juarez-Arellano [2]

[1] División de estudios de posgrado, Universidad del Papaloapan Campus Tuxtepec. Av. Circuito Central No.200. Tuxtepec, OAX. C.P 68301.
[2] Instituto de Química Aplicada, Universidad del Papaloapan, Circuito Central No. 20, Col Parque Industrial, Tuxtepec, Oaxaca. C.P. 38301, México.
[*]Tel: 287 87 5 92 40; e-mail: jeder_22@hotmail.com

ABSTRACT

The need for alternative fuels is greater now than ever. Therefore, natural gas is promising fuel source due to their availability and low contamination factor, which make it a natural choice as a substitute for oil in cars and other mobile applications. However, due to the lack of efficient storage methods it has not been fully implemented in the automotive industry. Advanced porous materials, such as metal-organic frameworks, have been explored as methane storage systems due to their exceptionally high surface areas and chemically tunable structures. MOFs are infinite networks formed by metal units (isolated atoms or clusters) that are joined together by at least di-coordinated organic ligands. The strong metal-ligand bonds provide a great mechanical and thermal stability, and a well-defined crystal structure. The structural versatility nature and composition of the MOFs opens a new possibility of controlling the chemical properties of the functional groups as well as the geometry and dimensions of the pores, channels and windows of the structure, making them an interesting alternative to the specific adsorption of gases. Therefore, in this work will be shown the preliminary results of the solvothermal synthesis of Zn- 1,4-bencenodicarboxilato which will be tested as a methane storage materials.

Keywords: metal-organic materials (MOF), adsorption, methane, affinity, porosity, Nanostructures.

XIV International Congress of the Mexican Hydrogen Society
Cancun, Mexico, 2014

A Microbial Fuel Cell Equipped with a Denitrifying Biocathode Effectively Degrades the Toxic Carbon Tetrachloride

A.C. Ortega-Martínez[1]; O. Solorza-Feria[2]; E. Ríos-Leal[3]; M. T. Ponce-Noyola[4]; H. M. Poggi-Varaldo[1]; K. Juárez-López[5]; J. Galíndez-Mayer[6]; N. F. Rinderknecht-Seijas[7]

[1]Environmental Biotechnology and Renewable Energies R&D Group, Dept. Biotechnology & Bioengineering, Centro de Investigación y de Estudios Avanzados del I.P.N., P.O. Box 14-740, C.P. 07000 México, D.F., México
[2]Dept. of Chemistry, Centro de Investigación y Estudios Avanzados del I.P.N., México
[3]Central Analítica Dept. of Biotechnology & Bioingineering, Centro de Investigación y Estudios Avanzados del I.P.N., México
[4]Microbial Genetic Group, Dept. of Biotechnology & Bioingineering, Centro de Investigación y Estudios Avanzados del I.P.N., México
[5]Depto. Ingeniería Celular y Biocatálisis, Instituto de Biotecnología, Universidad Nacional Autónoma de México, Cuernavaca, Mor., México
[6]Escuela Nacional de Ciencias Biológicas, Depto. De Ingeniería Bioquímica, Instituto Politécnico Nacional, México, D.F., México
[7]Escuela Superior de Ingeniería Química e Industrias Extractivas, Instituto Politécnico Nacional, México, D.F., México

ABSTRACT

Carbon tetrachloride (CT) is one of the toxic chlorinated solvents frequently observed at many contaminated sites. While a number of bioreactors have been developed for CT reduction, reduction using a biologically active cathode (biocathode) within a microbial fuel cell (MFC) is a novel and potentially cost-effective approach. Biocathodes harness the capacity of specific microorganisms to accept electrons from a solid surface (cathode). High-rate oxygen reduction without a platinum catalyst has been accomplished using biocathodes, as well as reduction of chlorinated groundwater pollutants. An advantage of such a process would be the oppotunity for electrical energy recovery from the treatment process. The aim of this work was to design and operated a MFC equipped with a denitrifying biocathode (MFC-DN) in the perspective of carbon tetrachloride reduction from polluted effluents.

The MFC-DN consisted of two plexiglass cubic chambers of 3 cm. Each electrode compartment was filled with small graphite cubes (3 mm x 3mm). The anode and cathode compartments were separated by a proton exchange membrane (Nafion 117). The anode chamber was loaded of 12 mL of biocatalyst (enriched inoculum, E-In) that was cultured in an acetate-ferric citrate medium. The cathode chamber was seeded with a mixed culture of denitrifying bacteria sampled from a denitrifying lab-scale reactor acclimated to CT. A synthetic wastewater containing potassium buffer salts, Na_2CO_3, and KNO_3 was fed to the cathode chamber. The CT concentration within the cathode of the MFC-DN was 10 mg/L.

In the characterization experiment, the R_{int} of MFC –DN was 1450 Ω with a maximum cell voltage of 230 mV. This relatively high value of R_{int} is typical in two-chamber MFCs. The values of P_v and P_S of the MFC were 772 mW/m^3 and 23 mW/m^2, respectively, where P_S is the power density expressed on the basis of projected surface area of membrane.

During the batch operation the average voltage of the MFC-DN was 132 mV, whereas average P_v and P_S were 11 620 mW/m^3 and 35 mW/m^2. A 100% CT depletion in the cathodic liquor was observed in the first 12 h of the run, which is equivalent to a removal rate higher than 20 mg CT/(L.d). In both experiments. abiotic removal of CT by sorption to the electrode graphite cubes (anodic and cahtodic) was negligible as determined by headspace GC-FID. We can conclude that a MFC-DN shows promise for the bioelectrochemical remediation of waters polluted with CT.

Keywords: Biocathode, Carbon Tetrachloride, Microbial Fuel Cell

Pt-based Linked Monometallic Nanoparticles Supported on Nanostructured Carbon for Electro-Oxidation of Methanol

D. Macias-Ferrer[1*], J. A. Melo-Banda[1], J. Y. Verde-Gómez[2], R. Silva-Rodrigo[1], P. del Angel-Vicente[3]

[1]División de Estudios de Posgrado e Investigación, Instituto Tecnológico de Ciudad Madero,. Juventino Rosas y Jesús Urueta S/N, Col. Los Mangos, Cd. Madero, Tamaulipas, C.P. 89440, México
[2]División de Estudios de Posgrado e Investigación, Instituto Tecnológico de Cancún. Av. Kabah Km. 3, S/N, Cancún, Quintana Roo, C.P. 77500, México
[3]Instituto Mexicano del Petróleo, Dirección de Investigación y Posgrado, Eje Central Lázaro Cárdenas 152, México D. F. 07730, Mexico
[*] e-mail: maestro_macias@hotmail.com

ABSTRACT

In this work, electrocatalysts as nanostructured carbon (NC) supported pt-based linked monometallic nanoparticles Pt, PtFe and PtCo (with different atomic ratios) samples have been prepared by sequential impregnation reduction method in which Pt, Co and Fe precursors are reduced by sodium borohydride, ammonium hydroxide, citric acid and Ar-H_2 atmosphere. SBA-15 was prepared via sol gel using pluronic 123 as surfactant and TEOS as silica precursor. NC sample was synthesized via nanomolding method and pyrolysis at 1273 K using SBA-15 as hard template and purified sucrose as carbon source. The prepared materials were characterized by means of N_2 physisorption analysis, XRD, FT-IR, RAMAN, SEM and TEM. The performance of electrocatalysts for methanol oxidation reaction was measured by CV. The characterization techniques revealed that SBA-15 sample having a high specific surface area, a large channels with high degree of hexagonal mesoscopic organization and a rope-like morphology characteristic of mesoporous silica materials. NC proved to be a negative replica of SBA-15 having hard template morphology with carbon nanopipes surrounded turbostratic carbon. On the other hand, all the electrocatalysts exhibit high dispersion of spherical nanoparticles with average particle sizes of 12, 6 and 3.5 nm respectively. Three transition metals show face cubic centered crystalline structures. In the case bimetallic nanoparticles a linked monometallic system of nanoparticles is confirmed. In comparison with commercial Pt/XC-72 and PtRu/XC-72, Pt/NC, PtFe/NC (1:1.2), PtFe/NC (1:3.5), PtCo/NC (1:1.1) and PtCo/NC (1:3.3) exhibit higher electrocatalytic specific activity and better resistance to carbonaceous intermediate poison for electro-oxidation of methanol.

Keywords: Electrocatalysts, SBA-15, nanoparticles

Hybrid Electric Vehicle (NAYAA II)

Batteries – Fuel Cell

A. Rodríguez-Castellanos, J. C. Magallón Martínez, S. Citalán-Cigarroa, C. Castro-Morales, O. Solorza-Feria.

Centro de investigación y de Estudios Avanzados del I.P.N., Av. IPN 2508, D.F., México, 07360.
Tel: 57473800; e-mail: acastella@cinvestav.mx

ABSTRACT

Worldwide, the trucking sector emits about 25% of all CO2 emissions and is projected to increase to 50% by 2030 and more than 80% by 2050, according to the International Energy Agency (IEA, info. 2009).

The use of hybrid vehicles can significantly reduce the amount of emission of polluting gases into the atmosphere. A hybrid electric vehicle (HEV) can have two or more power sources on board and depending on system configuration; two or more sources of energy are used to drive the vehicle. The interest in reducing the emission of pollutants in automobiles has created the need to develop and build a wide variety of systems and devices for this purpose.

This experimental work presents the design, construction and performance evaluation of a hybrid electric vehicle (Nayaa), powered by a generator with PEM fuel cell and / or rechargeable batteries. The generator design was done using AutoCAD software, construction of fuel cells using a CNC router and CNC laser cutter.

The characterization of the cell was performed by potentiostatic polarization tests.

The operation conditions of generator with fuel cell was: feeding the fuel (H2) and oxidant (air) at room temperature and a pressure of 0.1 atm (1.5psi), operating temperature of 20 º C at 70 º C.

Keywords: Design; Stack Fuel Cell; Electric Vehicle.

ATO Nanoparticles as Support for Reduction and Evolution Oxygen Reactions in PEM Electrolysers

V. Ávila -Vázquez[1], C. Guzmán-Martínez[1], M. Galván-Valencia[1], V. H. –Collins[2], S. M. Durón-Torres[1].

[1] Universidad Autónoma de Zacatecas, U. A. Ciencias Químicas, Km 6 Carr. Zac-Guad, Ejido la Escondida, C.P. 98160, Zacatecas, Zac. México.
[2] Centro de Investigación en Materiales Avanzados, S.C. Dpto. de Materiales Nanoestructurados, Miguel de Cervantes 120, Complejo Industrial Chihuahua, Chihuahua, C.P. 31190
*Tel: 4929256690 ext. 4655, mail:duronsm@prodigy.net.mx

ABSTRACT

Sb was used as dopant of SnO2 to prepare a powder of conductive nanoparticles with the aim to be used as a support for PEM electrolysers and fuel cells, the support were prepared by a chemical coprecipitation method. In this work it is reported the physicochemical characterization and evaluation of the electrochemical response of the powder of antimony doped tin oxide as catalytic supports for ORR and OER. Pt and IrO2 were used as catalysts in the electrochemical oxygen reactions. The ATO was characterized by X-ray Diffraction (XRD), High Resolution Transmission Electron Microscopy (HRTEM) and Energy Dispersive Spectrometry (EDS) techniques. The resistivity of SnO2 Sb doped conductive nanoparticles was measured by using a Milliohmeter system, The electrochemical properties respect to the oxygen reactions were obtained by using CV, LV, RDE, EIS and chronoamperometry techniques. The material obtained presented nanoparticles sizes of 6-8 nm and the electrochemical results indicate that ATO nanoparticles synthesized can be used as support in electrolysers and fuel cells.

Keywords: ATO, OER, Coprecipitation

Synthesis and Characterization of Pt/NTC/WOx Electrocatalysts for Oxygen Reduction Reaction

Edwin R. Oseguera[1*], C. A. Cortés[1] and Rosa de G. González[2]

1 Laboratorio de Energías alternas CIITEC IPN, Cda. Cecati s/n, Azcapotzalco, Mexico D.F.
2 Laboratorio de Foto-Electrocatálisis, ESIQIE- IPN UPALM, México, DF.
*E-mail: eosegueraiqi@hotmail.com Telephone: 57296000 ext 54246

ABSTRACT

Recent research has been developed on electrocatalysts for ORR in which decomposition of the support and particularly in the cathode side was found. This phenomena is compromising the useful life of the fuel cells, since the carbon vulcan is oxidized to CO_2 in the operating conditions of the cell. In order to improve operation, carbon support has been combined with a semiconductor in different proportions to increase stability and catalytic activity. In particular, on this work Pt and different compositions of WOx were used to know the optimal composition and obtain greater potential difference and current in a PEM fuel cell, in addition to increasing the useful life of the same cell.

Results on cathode electrocatalysts synthesis by the the polyol method are shown. This method was chosen in order to obtain particle sizes of less than 10nm, because according to the literature, smaller particle size produce enhanced catalytic activity by increasing contact area. A solution of diethylene glycol (DEG) with platinum chloride and multiwalled carbon nanotubes was refluxed for 4 hours at 214 ° C. Resulting solution after reflux process was filtered and washed with ethanol to remove DEG excess. Nanotubes underwent an exfoliation treatment to increase the surface area and get a higher dispersion of the active phase, which allow oxygen diffusion and improvement of reaction kinetics.

A tungsten salt was added into Pt/ NTC catalyst suspension to form the Pt/NTC/WO_X catalyst. The results are shown by means of linear sweep voltammetry (LSV), scanning electronic microscopy (SEM), transmission electronic microscopy (TEM) and X-ray diffraction (XRD) and compared with the performance of catalyst 10% Pt/90% NTC.

Keywords: Electrocatalyst, PEM fuel cell, polyol mediated synthesis.

XIV International Congress of the Mexican Hydrogen Society
Cancun, Mexico, 2014

Nanoestructured Carbon Doped with Heteroatoms as Electrocalyst in Fuell Cells.

E. Montiel-Macias[1,*], I. Alonso-Lemus[1], P.B. Balbuena[2], Y.Verde-Gómez[1]

[1]Instituto Tecnológico de Cancún, Av. Kábah Km. 3, Cancún, Q. Roo, México, 77500.
[2]Department of Chemical Engineering, Texas A&M University, TAMU 3122, College Station, TX, USA, 77843.
[*]Tel: +529988807432; e-mail: elizabethmontielmacias@hotmail.com

ABSTRACT

The importance of finding new options for generation of energy that are friendly to the environment has taken more relevance in recent years. In this context, hydrogen fuel cell has been recognized as a promising option to produce clean energy. One of the most important components in fuel cell consists are the electrocatalyst for anode and a cathode, respectively. Platinum supported on carbon (Pt / C), is conventionally as electrocatalyst due to its stability and high electrocatalytic activity, principally in the oxygen reduction reaction (ORR). However, due to the shortage and consequently the high cost of platinum: Alternatives have been developed to replace or decrease the amount of Pt in the electrocatalyst. Recent research has shown that free platinum electrocatalyst based on supported carbons doped with heteroatoms (e.g. B, N, P and S) have similar electrocatalytic activities to the conventional Pt/C for ORR. On the other hand, carbon nanotubes have unique properties that make them excellent candidates for using as electrocatalyst support. This work present a review from the state of art of synthesis and evaluation of free platinum catalysts materials based on nanoestructured carbon doped with heteroatoms in fuel cells applications.

Keywords: heteroatoms doped carbons, free platinum elctrocatalysts, hydrogen fuell cells.

Influence of Metal Nanoparticles in Proton Conductivity and Water Absorption of Polymeric Membranes for Fuel Cells

L. W. Oenning[2], R. Benavides[1*], M. M. S. Paula[2], L. da Silva[2]

[1]Centro de Investigación en Química Aplicada, Blvd. Enrique Reyna Hermosillo 140, Saltillo, Coahuila, México.
[2]Universidade do Extremo Sul Catarinense, Av. Universitária 1105, Criciúma, Santa Catarina, Brasil.
[*]Tel: +52(844)4389830 xt. 1322; e-mail: roberto.benavides@ciqa.edu.mx

ABSTRACT

Polymeric membrane fuel cells (PEMFC) are a reality nowadays in several popular applications, although, their massive use is still not achieved due to the high cost of some components. One of the most expensive components is the proton exchange membrane, where NAFION® has proved to have high performance. Such performance has been associated, apart of the membrane chemical nature, to its capacity to absorb water and hence influence its proton conductivity. Alternative membranes of sulfonated poly(styrene-co-acrylic acid) copolymers were prepared, as well as gold and silver nanoparticles through their salts reduction. The water absorption and proton conductivity of the membrane were evaluated after addition of such metal nanoparticles into the copolymer at 3 different concentrations. Water absorption increased independently of quantity or nature of the nanometal, comparing with a non-doped membrane. Such result can be associated to a deformation of the ionic clusters in charge of the proton conductivity. However, proton conductivity measured through electrochemical impedance spectroscopy (EIS) show a reduction of their values after addition of nanparticles; independently of nature and concentration in the copolymer. On the other hand, a charge transfer resistance, related to the resistance to transfer electrons at the membrane/electrode interface, was enhanced for the nanoparticle doped membranes. Considering that nanoparticles can migrate to the membrane surface during preparation, the reduction in proton conductivity values could be associated to the specific electron clouds for the evaluated metals, which in turn improve conduction of the electrons involved during the process.

Keywords: Fuel Cells, nanoparticles, protonic conductivity.

Kinetic Modeling and Virtual Sensor for Renewable Hydrogen Estimation in an Anaerobic Reactor

P. A. López Pérez [1], B. Ruiz Camacho [2], P. B. Zárate Segura[3], R. Aguilar López[4] and M. I. Neria-González[5]

[1]Department of Energy Universidad Politécnica Metropolitana de Hidalgo, Boulevard de acceso a Tolcayuca No. 1009, Ex hacienda San Javier, Tolcayuca, Hgo. México, 43860

[2]Universidad Politécnica de Guanajuato, Antiguo Camino a Pavieleros SN, La Joya, 36130 Silao, Guanajuato México

[3]Unidad Profesional Interdisciplinaria de Biotecnología, IPN, Luis Enrique S/N, Unidad Profesional Adolfo López Mateos, Zacatenco, México

[4] Department of Biotechnology & Bioengineering, CINVESTAV-IPN, Av. Instituto Politécnico Nacional, No. 2508, San Pedro Zacatenco, D.F. México

[5] Chemical and Biochemical Engineering División, Tecnológico de Estudios Superiores de Ecatepec, Tecnológico, 55210, Valle de Anáhuac, Estado de México.

[*]Tel: +529831566032; e-mail: save1991@yahoo.com.mx

ABSTRACT

In this study, the kinetics of hydrogen production was discussed from the point of view of energetic sustainability based in the reusing of toxic residues in effluents contaminated by cadmium and sulfate in a batch bioreactor under anaerobic conditions, whereas the products of bacterial metabolism such as the sulfide (H_2S) and cadmium sulfide (CdS) in the presence of light allowed the hydrogen production. The proposed mathematical model was suitable for predicting concentrations of sulfate, sulfide, biomass, cadmium, CdS and production hydrogen. The model was subsequently calibrated with experimental data from the bioreactor. The experiments showed that the concentrations of hydrogen production increased with increasing sulfide hydrogen concentration. The proposed virtual sensor demonstrated monitoring the concentrations in the hydrogen production process. The sensor consists of a model-based state observer (nonlinear) to infer the (unmeasured) hydrogen, cadmium, cadmium sulfide and biomass concentrations, considering only on-line measurements of sulfate and sulfide concentrations. The software sensor performance is showed with experimental data from a real process and it is compared versus an others observers, obtaining good estimated concentrations of the proposed virtual sensor. The solution of using a virtual sensor gives promising guidelines to tackle in the future the problem of real time control of hydrogen production

Keywords: Nonlinear observer; Photocatalytic; kinetics

XIV International Congress of the Mexican Hydrogen Society
Cancun, Mexico, 2014

Influence of Exfoliation on Multi-walled Carbon Nanotubes in their Performance as Electrode Support Material

C. A. Campos Roldán[1,2*], R. G. González Huerta[1], J. R. Vargas García[2], E. Franco Martínez[3]

1 Laboratorio de Foto-Electrocatálisis, ESIQIE- IPN UPALM, México, DF.
2 Departamento de Ingeniería Metalúrgica y Materiales, ESIQIE- IPN UPALM, México, DF.
3 Laboratorio de Energías alternas CIITEC IPN, Cda. Cecati s/n, Azcapotzalco, Mexico D.F.

*E-mail: charly1909@hotmail.com
Telephone: 57296000 ext 54246

ABSTRACT

In this work, we report the physic and electrochemical characterization of multi-walled carbon nanotubes (MWCNT) after exfoliation, where is evident the development of the properties which are of interest for hydrogen technologies. So we compare these results with carbon Vulcan. High Resolution Scanning Electron Microscopy micrographics show the increment of dimensions in the exfoliated MWCNT (e-MWCNT), suggesting a surface area increment. Cyclic voltammetry measurements confirmed the enhance active electrochemical surface in e-MWCNT, showing higher current density (four orders of magnitude) than untreated MWCNT. Capacitance determination confirmed that e-MWCNT have more active electrochemical surface (26866, 370 and 280 mF cm^{-2} for e-MWCNT, carbon Vulcan and MWCNT, respectively). In addition, voltammograms exposed two symmetric signals which are attributed to functional groups onto e-MWCNT´s surface. Infrarred Spectroscopy measurements were used to determinate that there are carbonyl and carboxyl groups. According to references, these functional groups are nucleation sites to catch platinum nanoparticles.

Keywords: Multi-walled Carbon Nanotubes, Exfoliation, Functional Groups

Greenhouse Gas Treatment and H_2 Production, by Warm Plasma Reforming.

J. Pacheco[1], G. Soria[2], R. Valdivia[1], M. Pacheco[1], F. Ramos[1], S. Darío[2], H. Frías[1], M.Durán[1], M. Hidalgo[1].

[1] Instituto Nacional de Investigaciones Nucleares. Km 36.5 Carretera México-Toluca, La Marquesa Ocoyoacac, México CP 52750
[2]Instituto Tecnológico de Toluca, Av. Instituto Tecnológico, S/N, Ex- Rancho la Virgen, Metepec, México

E-mail: joel.pacheco@inin.gob.mx
Tel 53297200 ext. 12646

ABSTRACT

Carbon dioxide (CO_2) and methane (CH_4) have been identified as the most significant greenhouse gas (GHG) arising from anthropogenic activities affecting the climatic global change. It is of great importance to reduce GHG emissions in order to counteract global warming.
This paper considers dry GHG reforming, involving synthesis gas generation followed by the production of some other solid by-products. CO_2 and CH_4 are both relatively stable compounds with low potential energies. The dry reforming reaction is highly endothermic and external energy must to be provided in order to drive it in the forward direction. More recently, applications of plasma gas reforming are highlighted as promising technique for energy saving and environment safe purposes with increasing demand of hydrogen and synthesis gas. In the case of plasma reforming, high energy electron must provide not only radical species, but also enthalpy required for endothermic reaction. The conversion of hydrocarbon in by-products with high added value, is mainly contributed by dissociation and ionization, when a plasma discharge processes is used; therefore, the more energy consumed by these two kinds of reactions, the more energy-effective for hydrocarbon reforming. Although the low pressure plasma, such as radiofrequency or microwave plasma could achieve high hydrocarbon conversion and good H_2 selectivity, the low H_2 production rate and extra energy requirement for vacuum device restrict its practical use, therefore, the plasma reactor here proposed must fulfill two principal characteristics: Environment-friendly and Auto-sustainable. Warm plasma is a transitional discharge which has low specific energy requirement (1-3eV) but still maintaining enough high temperature (2000-3000K) to produce excited species supporting subsequent chemical reactions. Such plasma discharges have significant advantages: Do not require extra cooling systems, since they work with reduced current flows and high voltages, this avoid electrodes erosion and stainless steel walls in the reactor designs can be used.

Keywords: Plasma Reforming, Greenhouse gas, Synthetic gas

Design, Construction and Performance Evaluation of a Solid Polymeric Electrolyzer

S. Citalán-Cigarroa, A. Rodríguez-Castellanos, C. Castro-Morales, O. Solorza-Feria.

Centro de investigación y de Estudios Avanzados del I.P.N., Av. IPN 2508, D.F., México, 07360.
Tel: 57473800 ext. 4473, e-mail: scitalan@cinvestav.mx

ABSTRACT

In this paper the design, construction and characterization of a Solid Polymer Electrolyte (SPE) as water electrolyzer is presented. As anode, titanium grade 2 with geometric surface area of 12 cm^2 impregnated with a mixture of oxides of RuO-IrO2/Ti was used. This material offer advantages in terms of stability, resistance to extreme corrosion and good electrical conductivity, determined by chronoamperometry experiments. Commercial carbon black supported Pt (Pt/C 20wt%) was used as a cathode electrode. The electrolyzer uses DC power which was supplied by a 30W solar panel. The hydrogen produced was fed to a 5W PEM fuel cell.

Keywords: Design; Electrolyzer; Stack Fuel Cell;

Synthesis of Mg_2Cu Alloy as a Precursor of MgH_2 by Mechanical Alloying and its Characterization Using XRD and SEM

J.L. Iturbe García[1], B.E. López-Muñoz[1] and L. Escobar Alarcón[2]

[1]Departamento de Química

[2]Departamento de Física

Instituto Nacional de Investigaciones Nucleares, Km 36.5 Carretera México-Toluca s/n, la marquesa

C.P. 52045, Ocoyoacac, Estado de México, Tel: (01-55) 53297200 ext. 12274, fax: (01-55) 53297301

mail: joseluis.iturbe@inin.gob.mx

ABSTRACT

In this work the synthesis of intermetallic Mg_2Cu is presented. Elemental particles of magnesium with a purity of 99.8% and Cu 99.9% were mixed in the desired quantity to reach a nominal composition from 40-60 up to 90 – 10 wt% respectively. The synthesis of compound was carried out by mechanical alloying technique with a high energy ball mill type spex which was constructed in our Institute. Then the Mg and Cu particles were put into a stainless steel vial and three stainless steel balls of 12.7 mm in diameter for milling and methanol as process control agent were used. The ball to particles weight ratio was 10:1. The milling time is a parameter essential in the preparation of materials for which a time period was defined only between 1 to 5 h, at room temperature. To avoid overheating of the milling system a ventilator was placed on the container, the temperature at the end of milling was 28C. The metal powders were analyzed before and after milling by X-ray diffraction and electron scanning microscopy. The results obtained by XRD shows the formation of only phase Mg_2Cu. These results show that due to the high impact between the milling media, material and the control agent can be obtained this alloy easily and fast by mechanical alloying technique continuously. This compound is the precursor for the preparation of magnesium hydride compound which can absorb hydrogen up to 6.7wt%.

Keywords: Mg_2Cu Intermetallic, mechanical alloying, XRD-SEM techniques.

Electrical Properties of $Gd_2Hf_{2-x}Zr_xO_7$ Solid Electrolytes Synthesized by Mechanical Milling

N.M. Cepeda-Sánchez[1], A.F. Fuentes[1], F.A. López-Cota[2], M. Rodríguez-Reyes[2] and J.A. Díaz-Guillén[2,*]

[1]Cinvestav Saltillo, Apartado Postal 663, 25000-Saltillo, Coahuila, México.
[2]División de Estudios de Posgrado e Investigación, Instituto Tecnológico de Saltillo, 25280-Saltillo, Coahuila México.
*Tel: +528444389539; e-mail: j.a.diazguillen@gmail.com

ABSTRACT

Gadolinium hafnates $Gd_2Hf_2O_7$ belong to a family of complex oxides with general formula $A_2B_2O_7$ which can show two different structural arrays, pyrochlore and non stoichiometric fluorite. These materials are known by their interesting electrical and thermal properties; thus, some of them are good oxygen ion conductors at high temperatures and can be used as solid electrolytes in SOFC's (Solid oxide Fuel Cells). Some others show low thermal conductivity and high thermal stability which make them attractive materials for TBCs (Thermal Barrier Coatings) to protect metal components of gas turbines and diesel engines.

The properties of these materials are significantly affected by the presence of defects such as vacancies and structural disorder. Therefore, their electrical and thermal properties can be modified by single or multiple chemical substitutions or by processing.

The ceramic method to obtain lanthanides hafnates usually involves thermal treatments at temperatures higher than 1500°C by long periods of time. This work deals with the mechanochemical synthesis and characterization of advanced ceramics of general formulae $Gd_2Hf_{2-x}Zr_xO_7$ (x = 0, 0.4, 0.8, 1.2, 1.6 and 2). This powder processing method allows obtaining metastable phases at room temperature that include a large number of structural defects, which will have an interesting effect on their electrical properties for their use as solid electrolytes. We also analyze the effect of substitution of Hf by Zr on the crystal structure and electrical properties of the gadolinium hafnate.

Results show that solid solutions $Gd_2Hf_{2-x}Zr_xO_7$ can be obtained by mechanical milling, by using a planetary mill and Yttria Stabilized Zirconia vials and balls. Their electrical properties, analized by impedance spectroscopy, reveal that these oxides are potential candidates to be used as solid electrolytes in SOFC's.

Keywords: SOFC's, pyrochlores, hafnates

Sociedad Mexicana del Hidrógeno A. C.
Mexican Hydrogen Society

CONACYT

ITC

XIV International Congress of the Mexican Hydrogen Society
Cancun, Mexico, 2014

Numerical Study of Fluid Dynamics and Heat Transfer in a PEM Fuel Cell Stack

S. J. Figueroa-Ramírez[1], C. Patiño-Carachure[1], S. Díaz[1], O. Meza[1], M. A. Meza[1], J. M. Sierra[1,*]

[1] Facultad de Ingeniería, Universidad Autónoma del Carmen, Cd. del Carmen, Campeche, México, 24115.
*Tel: +52(777)1843585; e-mail: juanmsg@live.com.mx

ABSTRACT

In this research, a numerical study of fluid dynamics and heat transfer in the flow distributor of a PEM fuel cell is presented. The aim of this work is focused on studying the pressure drops and temperature variations presented by stacks with serpentine channels. Different fuel cells with flow fields of 1, 2 and 3 parallel channels; active areas of 5, 10 and 25 cm^2; and stacks with 2, 3 and 5 assemblies were evaluated. From simulation results, it was found that the use of parallel channels improves the gas distribution inside of the fuel cell, increasing of this way the utilization of fuel and oxidant. In addition, it was observed that the relationship between the channel width and the active area of the fuel cell is considered as an important factor in the design of the flow field. If this relationship is not taken into account, the pressure drops that occur in the flow channels will affect the overall performance of the stack. Moreover, based on the heat transfer study were identified the spots with more temperature variation in fuel cell. From the simulation results, different solutions are proposed to obtain a more uniform temperature distribution in the bipolar plates. These solutions include changes in the plates design, modifications on flow field and the way of supply the gases to the fuel cell.

Keywords: Fluid Dynamics; Heat Transfer; PEM Fuel Cell

Pd/MWCNT and PdAg/MWCNT Electrocatalysts for Ethanol Oxidation in an Air-breathing Microfluidic Fuel Cell

A. J. Armenta-González[1], A. Moreno-Zuria[1], F. M. Cuevas-Muñiz[1], R. Carrera-Cerritos[2], L. Álvarez-Contreras[3], J. Ledesma-García[4], L. G. Arriaga[1]*

[1]Centro de Investigación y Desarrollo Tecnológico en Electroquímica, 76703, Pedro Escobedo, México.
[2]Departamento de Ingeniería Química, División de Ciencias Naturales, Universidad de Guanajuato, 36050, Guanajuato, México.
[3]Centro de Investigación en Materiales Avanzados, 31109 Chihuahua, México.
[4] División de Investigación y Posgrado, Facultad de Ingeniería, Universidad Autónoma de Querétaro, 76010, Santiago de Querétaro, México.
*Tel: +524422116000 Ext 6069; e-mail: larriaga@cideteq.mx

ABSTRACT

In this work, two electrocatalysts based in Pd (Pd/MWCNT and PdAg/MWCNT) were used for ethanol oxidation into a fuel cell. Pd and PdAg nanoparticles (NPs) were synthesized by reverse microemulsion and supported on multiwalled carbon nanotubes (MWCNT). The average nanoparticle size was estimated using TEM resulting in 5-6 nm for both electrocatalysts. TGA showed that both electrocatalysts have similar metallic loading (24% for Pd and 22% wt. for PdAg). Both materials were tested toward the ethanol electro-oxidation reaction in alkaline media (1 M ethanol + 1 M KOH). 50 cycles using the cyclic voltammetry technique were performed with the aim to evaluate the stability of the Pd-based electrocatalysts. Fuel cell experiments were carried out in a closed microfluidic fuel cell (µFFC) feeding with 1 M ethanol in KOH as fuel and oxygen-saturated KOH as oxidant at 12 mL h^{-1} flow rate in both channels. Commercial Pt/C was used as cathodic catalyst. The results were compared with those obtained using an air-breathing microfluidic fuel cell (ABµFFC), where the oxygen is taken from the air improving the cathodic reaction performance. In this device, two streams were injected, one with fuel and other with electrolyte (1 M KOH) at 12 mL h^{-1} flow rate. The ABµFFC that use PdAg/MWCNT as anodic electrocatalyst exhibited better performance (almost 70% more power harvested) compared to that obtained using Pd/MWCNT. The power density harvested from ABµFFC is 4 times higher than that obtained with the µFFC.

Keywords: PdAg Nanoparticles, Multiwalled carbon nanotubes, Ethanol Oxidation Reaction, microfluidic fuel cell, Air-Breathing.

Hydrogen Generation Using Different Morphologies of Recycled Aluminum with Alkaline Substance

C. Patiño-Carachure*, I. E. Castro, J. M. Sierra, M. Abatal, S. Martinez-Vargas, S.J. Figueroa-Ramírez.

Facultad de Ingeniería, Universidad Autónoma del Carmen, Campus III,
Fracc. Mundo Maya, C.P. 24115, Ciudad del Carmen, Campeche, México.
*Tel: +52(938)3811018 ext.1702; e-mail: cpatino@pampano.unacar.mx

ABSTRACT

Different morphologies of recycled aluminum were used to produce a hydrogen flow sufficient to supply a fuel cell. The morphologies of recycled aluminum were powders, ingots, and cracked rings containing 1 g for all specimens. Different concentrations of NaOH, $Ca(OH)_2$, KOH were employed into solution of 100 ml distilled water and sea water. The results indicate that the hydrogen generation is faster to powders during 40 minutes of reaction time employing water distilled. The process of reaction to water sea is slower to produce hydrogen. The specimens threated by alkaline solutions with sea water were recovered by a layer of saline particles. During the 10-40 minutes the production of hydrogen was 5 ml/min. These results can be manipulate to producing enough hydrogen that can be used in fuel cells.

Keywords: Recycled aluminum, hydrogen generation, alkaline substance.

Effect of Persian Lime on Hydrogen Production from Food Organic Solid Waste

I. Mar-Alvarez, A. Castillo-Hernández, I. Moreno-Andrade

Universidad Nacional Autónoma de México, Instituto de Ingeniería, Academic Unit Juriquilla, Laboratory for Research on Advanced Processes for Water Treatment, Blvd. Juriquilla 3001, Juriquilla, C.P. 76230, Querétaro, Mexico
*Tel: +524421926171; e-mail: imorenoa@ii.unam.mx

ABSTRACT

The organic solid waste (OSW) can be used as a substrate for hydrogen production applying a hidrolitic-acidogenic reactor. In Mexican dishes the Persian lime is wide used. The Mexican production of lime in 2013 was 2,095,000 tons approximately. It has been observed that high percentage of lime in OSW can reduce the methane production in ananerobic digestion process. No reports about the effect of lime content in OSW on the hydrogen production in fermentative reactor. For this reason, the objective of this study was to evaluate the effect of different percentages of lime (from 1.25 to 6.25%) in OSW from a restaurant. The waste characterization showed the next composition: fruits and vegetables 38±8% (including a percentage of 15% of lime), meat 10±3%, flours 30±8 and other fermentative waste 22±7%. Hydrogen production was evaluated in serum bottle test. Inoculum was pre-treated by a thermal shock pre-treatment (103-105 °C during 1 h). H_2, CO_2, methane and Volatile Fatty acids (VFA) were determined by gas chromatography. Kinetics of H_2 production was adjusted to the Gompertz model. The results showed that the hydrogen percentage in biogas comprised between 25 to 60%. The higher H_2 production was observed when 3.1% of lime are present in OSW (120 $mLH_2/L_{reactor}/h$). In this case the lime was metabolized without any adverse effect. At 6.3% of lime in OSW, showed a decrease in H_2 production. The presence of lime in OSW increase the lag time (96 to 180 h).

Keywords: Bio-hydrogen; lime; organic solid waste.

XIV International Congress of the Mexican Hydrogen Society
Cancun, Mexico, 2014

Start-up of a Continuous Stirred-Tank Reactor for Biohydrogen Production from Restaurant Organic Waste

A. Castillo-Hernández[1], I. Mar-Alvarez[1], I. Moreno-Andrade[1*],

[1]Universidad Nacional Autónoma de México, Instituto de Ingeniería, Academic Unit Juriquilla, Laboratory for Research on Advanced Processes for Water Treatment, Blvd. Juriquilla 3001, Juriquilla, C.P. 76230, Querétaro, Mexico
[*]Tel: +524421926171; e-mail: imorenoa@ii.unam.mx

ABSTRACT

Recently, continuous stirred-tank reactor (CSTR) has been applied to degrade organic solid waste (OSW) in anaerobic digestion. If the anaerobic process is separated in two phases (hydrolytic-acidogenic and methane production steps), it is possible to increase the energy production due to the hydrogen (H_2) generation in the first step. The objective of this study was to star up a CSTR to generate H2 from OSW of a restaurant in order to determine the operational conditions for increase the H_2 production. The start-up was obtained in three phases: 1) Inoculum activation with glucose, 2) Acclimation of inoculum to H2 production in a discontinuous process and 3) CSTR operation. The reactor was constructed by acrylic with a total useful volume of 2L with a headspace of 0.3 L. The HRT was fixed in 24 h. The OSW was fed in a concentration of 20 $gTS/L_{reactor}/d$. The reactor was inoculated with anaerobic sludge from a brewery. Fermentative H_2 producers selected by a thermal shock pre-treatment (103-105 °C during 24 h). H_2, CO_2, methane and Volatile Fatty acids (VFA) were determined by gas chromatography. The results showed that inoculum activation with glucose was obtained in 3 d (H_2 percentage in biogas of 38%). The reactor was operated during two cycles of 24h. After, the CSTR was operated with H2 percentages comprised between 33 to 51%. The reactor production begins in 59 $mLH2/L_{reactor}/d$, and increase as the reactor was continually operated. The COD removal was 66%, and the digestate showed a remnant concentration of carbohydrates and proteins of 0.7 g/L and 2.7 g/L, respectively.

Keywords: CSTR; bio-hydrogen; organic solid waste.

XIV International Congress of the Mexican Hydrogen Society
Cancun, Mexico, 2014

Evaluation of the Electrocatalytic Activity of Nickel-Molybdenum Nanoparticles for Hydrogen Production

M. Videa*, D. Castillo

Departamento de Química, Tecnológico de Monterrey, Av. E. Garza Sada 2501 Sur, Monterrey, N. L., México, 64849.
*Tel: +528183284489; e-mail: mvidea@itesm.mx

ABSTRACT

Nickel -molybdenum nanoparticles as electrocatalyst for hydrogen reaction evolution (HER) were electrodeposited on glassy carbon and carbon felt electrodes under short constant current density pulses. Their electrocatalytic activity was determined analyzing the Tafel parameters obtained from experiments of cathodic polarization in diluted sulfuric acid. The catalytic activity of the nickel-molybdenum deposits were evaluated by comparing their Tafel parameters with those obtained for platinum nanoparticles prepared in this work following a similar methodology as for the NiMo deposits. Additionally, the corrosion stability against of the nanoparticles of nickel-molybdenum as a function of molybdenum was measured by cyclic voltammetry. It was observed that the concentration of molybdenum in the electrolytic bath affects the electrocatalytic efficiency of nanoparticles, since at higher concentrations higher currents for hydrogen evolution are observed reaching 100 mAcm $^{-2}$ at −0.75V vs. SCE . It was also concluded that as the molybdate concentration in the electrolytic bath was increased, the oxidation potential of the deposit is increasingly positive, indicating that a greater stability was conferred. The total charge under the anodic process corresponding to the oxidation of the deposit observed in cyclic voltammetry is proportional to the current pulse applied during its electrodeposition. In the experiments of electrodeposition on carbon felt, multiple pulses of current of 170 and 250 mA cm^{-2} were applied for the synthesis of the nanoparticles. Comparison of the electrocatalytic activities of Ni-Mo and Pt deposits demonstrate that similar values can be obtained varying the particle density of the deposits.

Keywords: HER, Nickel-Molybdenum, nanoparticles

XIV International Congress of the Mexican Hydrogen Society
Cancun, Mexico, 2014

Modeling and Optimization of Hybrid Nafion Membranes Modified with Oxides Based on Artificial Neural Networks and Genetic Algorithms

J.C. Jaime-Domínguez[1], C. K. Gutiérrez Beltrán[2], S. Martínez Montemayor[2], S.M. Durón-Torres[1], A.U. Chávez-Ramírez[3].

[1] Universidad Autónoma de Zacatecas, Programa de Maestría en Ciencias de la Ingeniería, Campus Siglo XXI, Carretera Zacatecas-Guadalajara Km. 6.0, Ejido la Escondida, C.P. 98160, Zacatecas, Zacatecas, México.
[2]Universidad Autónoma de Coahuila, Facultad de Ciencias Químicas, Blvd. Venustiano Carranza s/n, Colonia República, C.P. 25280, Saltillo, Coahuila, México.
[3] Centro de Investigación y Desarrollo Tecnológico en Electroquímica S.C., Parque Tecnológico Querétaro, Sanfandila, C.P. 76703 Pedro Escobedo, Querétaro, México.

ABSTRACT

Recent studies have demonstrated the successful application of artificial intelligence tools in modeling, optimization and design of new materials (Sahoo and Ray 2006.) (Madaeni, Hasankiadeh et al 2010.). This paper describes the application of a Backpropagation Multilayer Perceptron (MLP-BP) neural network based on Levenberg-Marquardt learning algorithm in combination with evolutionary models based on genetic algorithms (GA) to find the optimal operation conditions to provide the highest proton conductivity from a set of hybrid membranes in fuel cell applications. A total of six membranes were analyzed, each one fabricated from a polymer matrix of Nafion and then modified with several oxides (N-HfO2, N-ZrO2, N-La2O3, N-(HfO2, ZrO2), N-(HfO2-La2O3) and N-(ZrO3-La2O3)). The experimental conditions considered for optimization were: temperature of the humidifier (Th) [30-100] ° C, the cell temperature (Tc) [30-120] ° C, voltage [0.05-0.8] (V), relative humidity (RH) [50% -100%] and the membrane thickness (σ). Four-electrode method was employed in fuel cell mode and pulse voltammetry were obtained. The pressure was kept at 15 psi and the nitrogen flow at 500ml/min.

The MLP-BP -GA combination throws the following optimal condition for the Hf-La membrane 1% wt: with 100% of relative humidity and temperatures around 80 ° C in the humidifier and cell. This model also provides the best conditions where the highest conductivity is achieved for every membrane; these estimations were compared against experimental tests obtaining a variation of less than 10%.

Keywords: Artificial Neural Network, Genetic Algorithm, hybrid membranes

Analysis of Microbial Communities Associated with Hydrogen Production Obtained from Wastewater

Chacón-Carrera, R.A.[1], Zavala-Díaz de la Serna, F.J.[1], Ramos-Sánchez, V.H.[1], Camacho-Dávila, A.[1], Robles-Venzor, J.C.[1].

(1) Universidad Autónoma de Chihuahua, Facultad de Ciencias Químicas, Circuito No. 1, Nuevo Campus Universitario s/n, Chihuahua, Chih. C.P.31125, México. Tel: 6142366000 Ext.4298 email: vramos@uach.mx

ABSTRACT

Microbial Fuel Cells (MFCs) are devices capable to supply energy from organic substrates. Although MFCs offer low current densities, they have proven to be a feasible option for wastewater treatment. When a suitable overpotential is applied to MFCs, hydrogen is produced, these devices are known as Microbial Electrolysis Cells (MECs). México has a huge potential for solar energy, particularly Chihuahua exhibits a solar irradiance of 18kJ/m^2. Bearing this in mind, this project aims to feed the overpotential for a MEC through a solar cell, in order to assess the potential to produce hydrogen through wastewater effluents in public universities. The microorganisms responsible of hydrogen production in these devices have not been fully characterized, as a matter of fact; the occurrence of microbial consortia able to optimize the operation of MECs is still under study. Therefore, at this stage of research, a representative wastewater sample was growth in differential cultures; and communities were compared by molecular techniques using a Polymerase Chain Reaction - Denaturing Gradient Gel Electrophoresis (PCR-DGGE) in order to compare their electrochemical performance and hydrogen yield within a MEC.

Keywords: wastewater, MEC, PCR-DGGE

XIV International Congress of the Mexican Hydrogen Society
Cancun, Mexico, 2014

Organic Molecule-Functionalized Zn_3P_2 Nanowires for Photochemical H_2 Production: DFT and Experimental Analyses

G. Ramos-Sanchez,[1] M. Albornoz[1], Y-H. Yu,[4] Z. Cheng,[1,4] V. Vasiraju,[4] S. Vaddiraju,[1,4] F. El Mellouhi[2,3], and P. B. Balbuena[1,4,*]

[1]Artie McFerrin Department of Chemical Engineering,
Texas A&M University, College Station TX, 77843, USA
[2]Physics Department, Texas A&M University at Qatar,
Texas A&M Engineering Building, Education City, Doha, Qatar
[3]Qatar Energy and Environment Research institute, P.O. Box 5825 Doha, Qatar
[4]Department of Materials Science & Engineering,
Texas A&M University, College Station, TX 77843,USA
*e-mail: balbuena@tamu.edu

ABSTRACT

Hydrogen production via photochemical reactions in water/methanol solutions containing Zn_3P_2 nanowires functionalized with an organic molecular layer is shown to be between 217 and 405 times higher than that obtained in absence of the molecular layer. Combined surface characterization and theoretical analyses are used to elucidate aspects of the photochemical reaction process. It is found that the protective layer exerts a passivation role decreasing the rate of nanowire degradation, while facilitating electron transfer for the hydrogen evolution reaction.

Keywords: Hyudrogen production, density functional theory, functionalized nanowires

XIV International Congress of the Mexican Hydrogen Society
Cancun, Mexico, 2014

Effect of Pt_x-Ru_y-Ir_z Electrocatalyst Composition for Oxygen Electrode in an Unitized Regenerative Fuel Cell

L. Morales S[1], S. Rivas[1], Y. Gochi-Ponce[2], A.M. Fernández[1*]

[1] Instituto de Energías Renovables. Universidad Autónoma de México. Privada Xochicalco s/n, Temixco, Morelos, C. P. 62580
[2] Instituto Tecnológico de Oaxaca, Av. Ing. Víctor Bravo Ahuja No. 125, esq. Calzada Tecnológico Oaxaca, Oaxaca, C.P. 68030

[*] Tel/fax direct 5622-9742 ext 29705; e-mail: afm@ier.unam.mx

ABSTRACT

The effect of variations in the composition for the type Pt_x-Ru_y-Ir_z ternary catalysts toward Oxygen Reduction Reaction and Oxygen Evolution Reaction (ORR and OER, respectively) is reported. According to the formula, there are variations in x and z values with 4.5, 3.5, 2.5, 1.5 and 0.5. The catalysts were prepared by chemical reduction method with a constant amount of Ruthenium (y=4) in the five compositions and characterized by X-Ray Diffraction (XRD),Transmission Electron Microscopy (TEM), Scanning Electron Microscopy (SEM) and energy dispersive X-Ray (EDX) analyses. A displacement of the diffraction patterns were observed on the materials by the formation of alloys between Pt, Ru and Ir. A conventional three electrode cell was used to evaluate the materials in 0.5 M solution of H_2SO_4 and tested in a Proton Exchange Membrane Fuel Cell (PEMFC) in FC and WE mode. Cyclic voltammograms shows an inhibition of the hydrogen adsorption/desorption peaks and ORR activity due to the presence of Ruthenium. $Pt_{1.5}Ru_4Ir_{3.5}$ and $Pt_{0.5}Ru_4Ir_{4.5}$ material shows a similar mechanism like Iridium. Repetitive Steady-state polarization experiments (Tafel plots) showed that the $Pt_{3.5}$-Ru_4–$Ir_{1.5}$ material is the most stable bifunctional catalysts for oxygen electrode.

Keywords: Oxygen Reduction Reaction; Oxygen Evolution Reaction, PEMFC

Implementation of a Hydrogen Control System Using PLC Applied to a Sustainable Housing

Armando Yunez Cano[1*], Rosa de G. González Huerta[2], Miguel Tufiño Velázquez[3], Domingo de Jesús Cortés Rodríguez[4]

1 Laboratorio de Energías Alternas CIITEC IPN, Cda. Cecati s/n, Azcapotzalco, México D.F.
2 Laboratorio de Foto-Electrocatálisis, ESIQIE- IPN UPALM, México, DF.
3 ESFM- IPN UPALM, México, DF.
4 ESIME- IPN Unidad Culhuacán, México, DF.
*E-mail: eosegueraiqi@hotmail.com
Telephone: 57296000 ext 54246

ABSTRACT

At present the necessity to incorporate new ways of generating clean energy applied to the housing sector has become more relevant in the last decade, in as much as the rapid population growth which requires people to take responsibility for the environment and at the same time that they can enjoy the benefits to strengthen the delivery of basic services of a home, being one of the most important, electrical supply.

This paper deals with the implementation of a programmable logic controller (PLC) applied to the " Sustainable Housing " of IPN which today has been installed with two photovoltaic systems (SFV), the "SFV A" has a power of 1080 watt with polycrystalline silicon technology, the " SFV B" has a power of 600 watts with amorphous silicon technology, the proposed PLC aims to control the electric parameters between two SFV's and System PEM fuel Cells 500 W.

The control system discussed above, provides the foundation and restrictions for automatizing the hybrid power system of electric energy generation, Solar-hydrogen, in a future.

Keywords: PEM Fuel Cell, Sustainable Housing, PLC

XIV International Congress of the Mexican Hydrogen Society
Cancun, Mexico, 2014

A DFT Study of O_2 Adsorption on Periodic $Ga_{1-x}N_x$ (100) Surface

L.C. de la Portilla-Maldonado[1], R. Mendoza-Pérez[2], G. Contreras-Puente[3], F de L. Castillo-Alvarado[3], A. Cruz-Torres[3,*], M. López-López[4]

[1]Departamento de Ciencias Básicas, División de Ciencias Básicas e Ingeniería, Universidad Autónoma Metropolitana-Azcapotzalco, Av. San Pablo 180 Col Reynosa Tamps, Azcapotzalco, 02200, México D. F.,

[2]Universidad Autónoma de la Ciudad de México; Av. Prolongación San Isidro 151; Col. San Lorenzo Tezonco; C. P. 09790; México, D. F.

[3]Escuela Superior de Física y Matemáticas. IPN, Edificio 9 U: P: Adolfo López Mateos, Col. San Pedro Zacatenco. Del. Gustavo A. Madero, 07738, México D. F.

[4]Departamento de Física, Centro de Investigación y Estudios Avanzados del IPN, México DF.

[*]Tel: 5563667484; e-mail: acruztorres@yahoo.com.mx

ABSTRACT

The adsorption of molecular oxygen on $Ga_{1-x}N_x$ (100) surface has been explored. This work was achieved using Accelrys Material Studio software for material modeling and simulation applying CASTEP library. With that kind of library it was obtained the geometry optimization. Moreover, this job is done by density functional theory (DFT) model using generalized gradient approximations (GGA) an enhanced with 1996 gradient-corrected correlation functional of Perdew, Burke and Ernzerhof. With this software we also calculated the density of states, the number of electrons, up and down number of spins, chemisorption and repulsion energies for O_2 on $Ga_{1-x}N_x$ (100), etc. We compare our results with theoretical and experimental data obtained in the literature.

Keywords: Electronic band stucture; Ab initio calculations; Nitrides

Control and Automation System of Power Generation through Photovoltaic-Hydrogen Technology to Lighting

J. Olmedo-González[1], R.G. González-Huerta[1], M. Tufiño-Velázquez[2], L.A.Loera-Cervantes[3]

[1] ESIQIE-IPN, Laboratorio de Electroquímica y Corrosión, UPALM, CP 07738, México, D.F.
[2]ESFM-IPN, Laboratorio de Física Avanzada, UPALM, CP 07738, México, D.F.
CECyT 3-IPN, Laboratorio de Maquinas Eléctricas, CP 55119, México, Edo.Mex
Tel: 5527092864; e-mail: jolmedog0900@alumno.ipn.mx

ABSTRACT

At present, it is very important study new power generation systems, like a photovoltaic-hydrogen. This is a hybrid system where the photovoltaic modules are used to provide power to the electrolyzer for producing hydrogen and oxygen through the water electrolysis. Gases produced are stored to be supplied when they are required into a fuel cell to generate electrical power.

The prototype was integrated by solar photovoltaic modules to generate 2.49 KWh day^{-1}. PEM electrolyzer is used to produce hydrogen from 100 to 300 cm^3 min^{-1} at 0-120 psi. The prototype has a variable volume storage system at atmospherically conditions (25°C and 585 mm Hg) and fuel cell stack can be operated in a range of 50 W to 150 W.

The system is able to operate with different fuel cells in a range of 10 to 1000 cm^3 min^{-1} hydrogen flow. In order to be a safe system and make easier the regulation flow, it is really important to develop a control and automation system. In this project, it is proposed a closed loop system where the hydrogen and oxygen needed is selected in a panel control. Gasses flow is controlled by pumps and proportional electrovalves that use a recirculation system which is monitored by flow sensors. Algorithm main aspect is the flow regulation, because the gases are storage in a variable volume system where the flow is not constant. Also, the project includes a monitoring system where power energy behavior can be reviewed.

Keywords: Fuell Cells; Automation; Renewable Enegy

XIV International Congress of the Mexican Hydrogen Society
Cancun, Mexico, 2014

Implications of the Heat Shock Treatment During the Bioconversion of Crystalline Cellulose into Hydrogen by a Microbial Consortium

Zulma L Alamilla[1], Ana E Escalante[2], Gustavo Hernandez[1], Idania Valdez Vazquez[1]*

[1] DICIVA Universidad de Guanajuato CIS. Irapuato, México
[2] Instituto de Ecología, UNAM. México
*e-mail: valdez_idania@yahoo.com

ABSTRACT

The fermentative hydrogen production using microbial communities (MC) as inoculum has advantages such as high production rates, the use of organic waste as substrate, and the reactor operation under unsterile conditions which decrease the operation costs. These MC are obtained from sources such as anaerobic digester sludge, sewage treatment plants, wastewater, ruminal fluids, and composts, among others. In most studies using these inocula, the heat-shock treatment (hst) is applied to enrich with *Clostridium* species and kill the rest of microorganisms. This hst is highly effective when the substrate consist of easily fermentable sugars. On the other hand, agricultural residues also called lignocellulosic substrates, have a high potential for its conversion into biohydrogen. Its composition shows up to 70% polysaccharides (cellulose and hemicellulose), and its bioconversion has been mainly reported with the use of physical-chemical pretreatments, and/or enzyme which negatively affect the operation costs. The aim of this work was to study the conversion of crystalline cellulose into hydrogen by MC derived from anaerobic digester sludge. Inocula tested were complete MC, and a heat-shocked MC (boiling in a water bath for 60 min). such as a control, a culture of *Clostridium acetobutilicum* was used. The assays were performed in mini-reactor with a working volume of 100 ml with 6 g / L of crystalline cellulose (SIGMA) in PYG medium and initial pH of 5.5. Mini-reactors were statically incubated at 37 °C. The parameters measured were volume and composition of biogas, cellulose consumption and cell growth. The results showed that biogas production from cellulose was higher using the complete MC (151 mL), while the heat-shocked MC produced 42 mL and *C. acetobutilicum* 19 mL. These results show that the sht negatively affects the cellulose conversion into hydrogen due to the reduction of microorganisms needed for the efficient hydrolysis and fermentation of the cellulosic substrate.

Keywords: cellulose, hydrogen, fermentation.

Ni and Ru Loading on $Sr_2Ta_2O_7$ by Electroless to Enhance its Photocatalytic Hydrogen Evolution from water

C.L Compean-González[1], V. M. Arredondo-Torres[2], M.E Zarazúa-Morin[1], M.Z Figueroa-Torres[1*]

[1]Departamento de Ecomateriales y Energía, Facultad de Ingeniería Civil, Universidad Autónoma de Nuevo León, Av. Universidad s/n Ciudad Universitaria San Nicolás de los Garza Nuevo León, México. CP. 66451.
[2]Facultad de Químico Farmacobiología, Universidad Michoacana de San Nicolás de Hidalgo, Tzintzuntzan #173, Col. Matamoros, Morelia, Michoacán, México. C.P. 58240
*Tel: +5214424421; e-mail: m_zyzlila@yahoo.com.mx

ABSTRACT

Hydrogen has been recognized as an important energy carrier, especially for use it in fuel cell. Clean and sustainable hydrogen production is still a challenge for scientists to solve energy and environmental problems. Therefore, water splitting using a photocatalyst is one of the most attractive alternatives for hydrogen production. However, most semiconductors cannot give high H_2 evolution activities without a cocatalyst even in the presence of sacrificial electron donor. This work evaluates the effect of textural characteristics of the strontium tantalate on its surface modification with nickel and ruthenium nanoparticles by electroless deposition. The material with smooth texture was synthesized by solid state reaction and porous texture by combustion synthesis. Nitrogen adsorption isotherms indicate that the material present a mesoporous structure. The energy band gab values calculated from Kubelka-Munk formula were 4.6 and 3.8 eV for smooth and porous materials respectively. Specific surface areas were estimated by the BET equation. The porous material exhibited a surface area 2.1 times greater than the smooth material. Ni and Ru nanoparticles deposited onto $Sr_2Ta_2O_7$ are highly dispersed, they present spherical shape and a narrow size range between 3-8 nm. It was found that hydrogen evolution under UV irradiation was significantly increased when a suitable amount of nanoparticles is dispersed, which dependent of the texture properties.

Keywords: texture; photocatalysts

Synthesis of Carbon Fiber Electrocatalysts Obtained by Pyrolysis of Polymeric Fiber

Daniel Lardizábal G [*1], Ivonne Alonso L.[1], A. Aguilar Elguezabal. [2] Ysmael Verde Gomez[1]

[1]Instituto Tecnológico de Cancún, Av. Kábah Km. 3, Cancún, Q. Roo, México, 77500.
[2]Centro de Investigación en materiales avanzados, Miguel de cervantes No. 120, Chihuahua, Chihuahua, México, 31109.
e-mail: daniel.lardizabal@cimav.edu.mx

ABSTRACT

One of main barriers to the production of fuel cells is the high price of platinum. Several studies propose solutions based on the decrease of platinum amount; e.g. enhance the support an dispersion, decreasing their particle size, mix with other metals, etc. Since 2009, Dai et al reported a different path to synthesize electrocatalysts, using nitrogen doped nanotubes, creating a branch of metal-free catalysts with activities very close to platinum for ORR. Recent studies are shifting towards to carbon derivatives with a graphitic lattice limited, such as activated carbon, carbon black, carbon fibers and amorphous graphite doped with nitrogen, which yields similar to compounds of highly ordered structures used as electrocatalysts, getting great economic advantages due to its simplicity in the synthesis of these materials. This study, proposes the synthesis of carbon fibers from pyrolysis of commercial polymeric fibers (Kevlar and Nylon). These fibers are aramids and polyamides, which contain nitrogen in its structure. According to studies made by Bradley et al (1997), the nitrogen bonds with carbon produce nitrogenated quaternary structures. The polymers fibers were subjected to heating in an argon gas atmosphere with a flow of 200cm^3/min during 2 h., then they were subjected to a carbon dioxide atmosphere by 1 h, as an activation process. Raman spectra show the typical Raman-active band D and G of carbonaceous materials. The samples were characterized by TGA and BET. SEM images show that fibers diameter were from 8 to 10µm. Catalytic activity was evaluated by electrochemistry techniques (cyclic voltammetry and rotated disk electrode). The obtained results show that the electrocatalysts have catalytic activities comparable to graphene and CNTs doped with nitrogen.

Keywords: Electrocatalysts, carbon, nitrogen

References:

1. - R.H. Bradley et al “Chemical transformations resulting from pyrolysis and carbon dioxide activation Kevlar” Carbon (1997).

2.-Marta E.G. Mosquera, Marielle Jamond, Amelia Martinez-Alonso and Juan M.D. Tasconi, “Thermal Transformations of Kevlar Aramid Fibers during Pyrolysis: Infrared and Thermal Analysis Studies “Chem. Mater (1994).

Effect of the Palladium Content on the Oxidation of Ethylene Glycol Oxidation

A Palacios[1], N. Arjona[2], J. Ledesma-García[1], M. Guerra-Balcázar[1**], L. G. Arriaga[2,*]

[1]División de Investigación y Posgrado, Facultad de Ingeniería, Universidad Autónoma de Querétaro, Querétaro, México, 76010.
[2]Centro de Investigación y Desarrollo Tecnológico en Electroquímica, Querétaro, México, 76703.
[*]Tel: +524422116069 larriaga@cideteq.mx; [**]Tel: +5244221921200 minbalca@yahoo.com.mx

ABSTRACT

AuPd/Polyaniline was synthetized by a chemical/electrochemical method at various Pd content and used as anode for ethylene glycol (EG) oxidation. The AuPd/Polyaniline composites were characterized by means of cyclic voltammetry, SEM, EDS, and XRD. The results show some dependence of the electrocatalytic properties related with the metal content. The composites were used in a in a novel microfluidic fuel cell (MFC) operated at room temperature. The device exhibited high electrocatalytic performance and stability for the conversion of cheap and fully available EG as fuel.

Keywords: bimetallic catalyst, poyianiline, ethileneglycol

Electrical and Optical Characterization of $NdAlO_3$ Nanoparticles

M. Harilal[1,2], V. Manikantan Nair[1], P.R.S. Wariar[1], K. P. Padmasree[3*], M.M. Yusoff[2,4], R. Jose[2]

[1]Department of Physics, University College, University of Kerala, Trivandrum, India, 695101.
[2]Faculty of Industrial Sciences & Technology, Universiti Malaysia Pahang, Pahang, Malaysia 26300.
[3]CINVESTAV unidad Saltillo, Coahuila, Mexico, 25900.
[4]Central Laboratory, Universiti Malaysia Pahang, Malaysia, 26300.
[*]Tel: +52-8444389600-8521; e-mail: padma512@yahoo.com

ABSTRACT

Nanocrystals of neodymiumaluminate ($NdAlO_3$) are synthesized using an optimized single step auto-ignition citrate complex combustion process. The combustion product was characterized by X-ray diffraction, transmission electron microscopy, Fourier transform infrared spectroscopy, Raman spectroscopy and Ultraviolet–visible reflection spectroscopy. The combustion product is single phase and composed of aggregates of nanocrystals of sizes in the range 20–40 nm. The $NdAlO_3$ crystallized in rhombohedral perovskite structure with lattice parameters a = 5.3223 Å and c = 12.9292 Å. The absorption spectrum of the $NdAlO_3$ nanocrystals shows characteristic absorption bands of the Nd atom. The polycrystalline fluffy combustion product is sintered to high density (~97%) at ~1450 °C for 4 h and the microstructure was characterized by scanning electron microscopy. The electrical properties of the sintered product were studied using dielectric measurements. The sintered $NdAlO_3$ has a dielectric constant (ε_r) and a dielectric loss (tan δ) of 21.9 and ~10−3 at 5 MHz, respectively.

Keywords: electronic ceramics; nanocrystals; optical properties

XIV International Congress of the Mexican Hydrogen Society
Cancun, Mexico, 2014

Molten Salt Synthesis of Doped Ceria-Na_2CO_3 Nanocomposites

A.L. Mendoza Villa[1], K.P. Padmasree[2*], J.A. Diaz-Guillen[1], A.F.Fuentes[2]
[1]Ingeneria en Materiales, Instituto Tecnológico de Saltillo, Coahuila, México
[2]Sustentabilidad de los Recursos Naturales y Energía, CINVESTAV unidad Saltillo, Coahuila, Mexico, 25900.
[*]Tel: +528444389600-852; e-mail: padma512@yahoo.com

ABSTRACT

Solid oxide fuel cells (SOFCs) are considered as one of the most promising power generation technologies which convert the energy of chemical reactions directly into electrical energy and heat with high efficiency. Recently, ceria-based composite materials, especially ceria-carbonate composites, have been developed as competitive electrolyte candidates for intermediate temperature (600-800°C) operation of SOFCs. Composite electrolytes composed of Sm^{3+}, Gd^{3+}, Y^{3+} doped ceria and sodium carbonates (Na_2CO_3) were synthesized via a facile and environmental friendly molten salt method. Hydrated metal nitrates, sodium hydroxide and sodium carbonate are used as the raw materials. The proposed procedure consists of a mechanically induced metathesis reaction and short firing above the melting point of sodium nitrate. The purpose of mechanically induced metathesis reaction is to generate in situ $NaNO_3$ flux and to obtain a suitable precursor for the synthesis of target materials in molten nitrates. The prepared materials were then characterized by X-ray diffraction, thermal analysis, infra-red analysis, transmission electron microscopy, scanning electron microscopy, electrical properties etc.

Keywords: ceria nanocomposites, solid oxide fuel cells, solid electrolytes

Molten Salt Synthesis and Characterization Studies of co-doped Ceria Electrolytes for IT-SOFCs

V. Ramirez-Salazar[1], K.P. Padmasree[2*], J.A. Diaz-Guillen[1], A.F.Fuentes[2]
[1]Ingeneria en Materiales, Instituto Tecnológico de Saltillo, Coahuila, México
[2]Sustentabilidad de los Recursos Naturales y Energía, CINVESTAV unidad Saltillo, Coahuila, Mexico, 25900.
[*]Tel: +528444389600-852; e-mail: padma512@yahoo.com

ABSTRACT

Solid oxide fuel cells (SOFC) have attracted extensive attention due to their high-energy conversion efficiency, fuel flexibility and environment safety. Yttria stabilized zirconia (YSZ) solid electrolytes have been extensively investigated for SOFCs because of their high ionic conductivity and chemical stability in reducing anodes and oxidizing cathode atmospheres. But it requires high operating temperature (~1000°C) to gain high enough conductivity which limits the selection of component material for SOFC. Lowering the operating temperature would increase the lifetime of the cell, SOFC stability, widen the selection of the electrodes, interconnect and other construction materials which reduce the overall cost of the fabrication of SOFC system. Doped CeO_2 based solid electrolyte exhibits high ionic conductivity than the conventional YSZ at intermediate temperature (600-800°C). Rare earth doped ceria exhibit good ionic conductivity in the intermediate temperature region. One of the approaches to further improve the ionic conductivity and other properties is to dope ceria with two or more components (co-doping). Many methods have been developed for the synthesis of nanocrystalline doped ceria systems. In this work, we are going to present a low temperature synthesis of nanostructured system of co-doped ceria ($Ce_{0.8}Gd_{0.1}Nd_{0.1}O_{2-\delta}$) doped with transition metal elements like (Cu and Co) via a facile and environmental friendly molten salt method. Hydrated metal nitrates and sodium hydroxide are used as the raw materials. The proposed procedure consists of a mechanically induced metathesis reaction and short firing above the melting point of sodium nitrate. The purpose of mechanically induced metathesis reaction is to generate in situ $NaNO_3$ flux and to obtain a suitable precursor for the synthesis of target materials in molten nitrates. The prepared materials were then characterized by X-ray diffraction, thermal analysis, infra-red analysis, transmission electron microscopy, electrical properties etc.

Keywords: solid oxide fuel cells, ionic conductivity, molten salt synthesis

XIV International Congress of the Mexican Hydrogen Society
Cancun, Mexico, 2014

XPS Study of Mixed Valence Titanium-Cobalt Oxides and it´s Electrocayalitic Activity for the OER.

J. Pérez Alvarez[1, 2,*], S.M. Fernández Valverde[3], L. Escobar Alarcón[2], A. Contreras Ramírez[3]

[1]Departamento de Física, Instituto Nacional de Investigaciones Nucleares, Apdo. Postal 18-1027, México DF, México.11801
[2] Centro Conjunto de Investigación en Química Sustentable UAEM-UNAM, Carretera Toluca-Atlacomulco Km 14.5, Unidad San Cayetano, Toluca, Estado de México, México 50200.
[3]Departamento de Química, Instituto Nacional de Investigaciones Nucleares, Apdo. Postal 18-1027, México DF, México.11801

* jonatan3101@yahoo.com.mx

ABSTRACT

Recently the electrocatalytic performance for the oxygen evolution reaction (OER) where correlated to the absorption energies OH and HOO* on oxide surfaces [1]. Co:TiO_2 thin films were deposited using two interacting plasmas produced from different targets [2], TiO_2 and cobalt. By keeping constant the laser ablation conditions on the TiO_2 target and changing them on the Co target, it was possible to vary in a controlled way the Co content in the films. The cobalt plasma parameters, such as the ion kinetic energy and plasma density, were determined for each deposition condition in an attempt to correlate them with the material's properties. The cobalt ion mean kinetic energy was varied from 36 to 789 eV, resulting in films with Co content from 1.2 up to 5.1 at.%, respectively, revealing that the cobalt content can be controlled by the Co^+ kinetic energy. The study of the optical properties showed that the optical band gap decreased from 2.9 to 2.0 eV as the Co content increased. Raman spectroscopy was use to characterize the microstructure of the deposits and the obtained results suggest the formation of two coexisting phases: TiO_2 in its rutile phase and $CoTiO_3$. It was found that as the Co^+ energy increases, the $CoTiO_3$ phase develops in a greater quantity. XPS measurements confirm the Raman spectroscopy results [3]. XPS study of the thin films with different cobalt content. The films where tested for the OER [4], the over potential, and the current density could be attributed to the different oxidation states of the Ti and Co present in the films. The presence of the different states since to change the distance between O-Ti-O-Co and consequently by electro catalytic activity for the oxygen evolution reaction. The obtained results be compare and discussed.

Keywords: Thin films ; Oxygen evolution reaction OER ; Xray Photoelectron Spectroscopy XPS

References.

[1] Isabela C. Man,Hai-Yan Su, Federico Calle-Vallejo, Heine A. Hansen,José I. Martínez, Nilay G. Inoglu, John Kitchin, Thomas F. Jaramillo, Jens K. Nørskov,and Jan Rossmeisl; *Universality in Oxygen Evolution Electrocatalysis on Oxide Surfaces*; **ChemCatChem**, 3, 1159–1165 (2011).

[2] Jonatan Pérez Alvarez; *Películas delgadas de TiO_2 modificado con Co para su aplicación en sistemas electrocatalíticos y fotocatalíticos*; **Tesis de Doctorado**, UAEMex, 2014.

[3] L. Escobar-Alarcón, J. Pérez- Alvarez, D. A. Solís-Casados, E. Camps, S. Romero, J. Jiménez-Becerril; *Preparation of Co:TiO_2 thin films by Crossed Beam Pulsed Laser Deposition*. **Applied Physics: A** 110 (4), 909-913 (2013).

[4] S. M. Fernández, J. Pérez Alvarez, J. Jimenéz, L. Escobar Alarcón; *TiO_2/Co_3O_4 Films Obtained by Pulsed Laser Deposition and sol-gel for the Oxygen Evolution Reaction in Alkaline Media* ; Proceedings of the 17th World Hydrogen Energy Conference; 601-604, (2008).

Criteria of Optimization Theoretical and Experimental of a Renewable Energy System with Hydrogen Storage

R. Barbosa[1], V. Sánchez[1], B. Escobar[2], J. Hernández[1], H. Toral[1], A. Allanes[1], D. Cámara[1]

[1]Universidad de Quintana Roo, Boulevard Bahía s/n, Chetumal, Q. Roo, México, 77019.
[*]Tel: +529831566032; e-mail: romelix1@gmail.com
[2]Instituto Tecnológico de Cancún, Av. Kábah Km. 3, Cancún, Q. Roo, México, 77500.

ABSTRACT

In this paper a computational tool to assist in the sizing and automatic control of a hybrid renewable system with energy storage in the form of hydrogen is presented. The tool is based on an algorithm programmed in language C++. The philosophy of the algorithm consists to analyze the effectiveness and efficiency of the system according to operating conditions planned and actual experimental data. An energy balance based in analytical models of each component is used for previously dimension the installation of the hybrid system. Afterwards when a real requirement is generated in the hybrid system, an optimization strategy is implemented with the same philosophy and previously applied mathematical models

Keywords: computational tool; fuel cells; hydrogen

Strategies for Implementation of Fuel Cells in Quintana Roo, Short Technical-Economic Analysis

Manuel Sánchez[1], Romeli Barbosa[1], B. Escobar[2], Inocente Bojórquez[1], Roberto Acosta[1], Victor Sánchez[1]

[1]Universidad de Quintana Roo, Boulevard Bahía s/n, Chetumal, Q. Roo, México, 77019.
[*]Tel: +529831566032; e-mail: romelix1@gmail.com
[2]Instituto Tecnológico de Cancún, Av. Kábah Km. 3, Cancún, Q. Roo, México, 77500.

ABSTRACT

In the near future the world's energy demand will have to be supplied using energy sources different from fossil fuels. Within such scenario hydrogen fuel could be playing an important role as an energy vector. In this paper a short socio-technical-economic analysis of the implementation of hydrogen-based energy systems in the state of Quintana Roo is presented. Implementation of this technology is fully justified in the first instance, also the main local features are highlighted and a range of possible applications are described. Subsequently a quantitative analysis of the implementation of the hydrogen technology in communication networks projected for the northern region of the state was developed; ground transportation system specially designed for purpose and wireless communication networks in Cancun, Q. Roo is analyzed.

Keywords: hydrogen economy; communication networks; fuel cells

XIV International Congress of the Mexican Hydrogen Society
Cancun, Mexico, 2014

Effect of the Different TiO_2 Nanostructures in PtRu/C-TiO_2 Catalysts on the Catalytic Activity for Methanol Oxidation

A. A. Matencio[1], A. L. Ocampo[1,*], J. A. Toledo[2] and J. de Gyves[1]

Facultad de Química, Departamento de Química Analítica, Universidad Nacional Autónoma de México, México D.F. 04510, México
Instituto Mexicano del Petróleo, Programa de Ingeniería Molecular, Eje Central Lázaro Cárdenas # 152, C.P. 07730 México D.F., México
*e-mail: analof@unam.mx, Tel. +525556223791

ABSTRACT

Direct methanol fuel cells (DMFC) are attractive as power sources due to the high energy density and easy handling of the liquid methanol fuel. However, the further development of DMFCs faces serious problems such as low activity of methanol electrooxidation catalysts and poor durability. Among the various bimetallic combinations that have been studied, PtRu has been accepted as the best electrocatalyst for the methanol oxidation reaction (MOR). To obtain a high surface area, PtRu nanoparticles have been synthesized, supported and mixed with different carbon materials; however, the carbon support degrades over time due to electrochemical corrosion. To improve the stability of the support, the addition of metal oxide supports such as WO_3, SnO_2, TiO_2, CeO_2 and SiO_2 has been reported. The characteristics of TiO_2 materials include excellent corrosion resistance in various electrolyte media, electrochemical stability, cost-effective, non-toxic and easily available. Furthermore, titania can enhance catalytic activity of platinum due to a metal-support interaction, nevertheless, the mechanism has not yet been identified.

In this work TiO_2 is used in different structured forms: as nanoparticles (anatase nanoparticles, anatase/rutile nanoparticles), nanowires and nanotubes in combination with Vulcan carbon to serve as support of PtRu catalysts with the aim of evaluating their performance. Chemical reduction method was used to synthesize the catalysts, being ethanolic $NaBH_4$ the reducing agent. XRD and TEM were used for the characterization of the catalysts morphology, while catalytic activity was studied by chronoamperometry and cyclic voltammetry. Results indicate that different TiO_2 nanostructures show different catalytic activities, in all cases higher than the catalyst without TiO_2. Effects on the crystallinity of the Pt fcc structure are also observed which might modify the electronic properties of the catalysts and help to improve the catalytic activity.

Keywords: Direct methanol fuel cell; metal oxide supports.

XIV International Congress of the Mexican Hydrogen Society
Cancun, Mexico, 2014

New Catalytic Technology Implementation on the Hydrogen Production Industry

J-Fortuna-Espinosa

[1]Total Energy, Consultoría en Hidrogeno,
Guillermo Ortega Vargas, Manzana 3, Lote 25, Casa 4,
Fraccionamiento Los Héroes 2ª Sección,
Toluca, Estado de México, C.P. 50246
[*]Tel: 722 1995108, fax 722 1995108, javier.fortuna@totalenergyh2.com

ABSTRACT

Presenting a real case, where it was possible to implement a new catalytic technology for hydrogen production at industrial level, in a SMR (Steam Methane Reforming) plant type. Details relating to the technical and commercial part are presented, and the approach related to the economic benefits to be obtained by using this new technology. At the end, the final tests and results are shown from a technical and commercial perspective.

Keywords: Industrial application; New Catalytic technology; Hydrogen Production.

Project to Implement a Heat Recovery System, for Steam Generation, to an Existing SMR Hydrogen Production Plant.

J-Fortuna-Espinosa

[1]Total Energy, Consultoría en Hidrogeno,
Guillermo Ortega Vargas, Manzana 3, Lote 25, Casa 4,
Fraccionamiento Los Héroes 2ª Sección,
Toluca, Estado de México, C.P. 50246
[*]Tel: 722 1995108, fax 722 1995108, javier.fortuna@totalenergyh2.com

ABSTRACT

A real case for a project to design, manufacture and assembly of a heat recovery system for steam generation, which will be adapted to existing SMR (Steam Methane Reforming) hydrogen production plant. Details relating to the detection of the need and the technical and economic opportunity to justify the project. Subsequently, the technical and financial details related to the development of this project and the engineering involved areas, with the specific scopes are described for each area. At the end, the summary, with obtained results from the technical and economical perspective.

Keywords: Industrial application; Heat Recovery System; Hydrogen Production.

Synthesis and Characterization of 2,1,3-benzothiadiazole Derivatives for Solar Cell Applications

J. C. Valdivia[1], L. Werncke[1], T. Frizon[1], A. G. Dal Bó[1], M. Marques[1], R. Benavides[2], L. da Silva[1]*.

[1] Universidade do Extremo Sul Catarinense (UNESC), Av. Universitária, 1105 - Cx.P. 3167, Criciúma, SC. Brazil, 88.806-000

*Tel: e-mail: luciano.silva@unesc.net

[2].Centro de Investigación en Química Aplicada (CIQA), Blvd. Enrique Reyna Hermosillo, No. 140, C.P. 25294, Saltillo, Coahuila. México

*Tel:844.4389830, e-mail: robciqa@gmail.com

ABSTRACT

Over the past two decades, fluorescent organic compounds have important applications in several fields, like organic light emitting diodes (OLEDs), electro-optic devices and solar cells. Due to the low cost of manufacture and feasibility to control their properties according to their chemical structure, organic materials have more advantages comparing with inorganic materials. Organic compounds of 2,1,3-benzothiadiazole derivatives have fluorescence when combined with others compounds, for example substituted aromatic rings with alkoxy chains. The central unit in these compounds is the heterocyclic 2,1,3-benzothiadiazole; an excellent acceptor of electrons, which facilitates the intra-molecular charge transfer and consequently reducing and adjusting the band-gap of molecules in π-conjugated polymers to the visible region in the solar radiation spectrum. In this paper, we report the synthesis and characterization of compounds 2,1,3-benzothiadiazole derivatives, designed to assure molecular planarity. All the synthesized compounds were chemically characterized by spectrometric techniques as FTIR, ^{1}H NMR and ^{13}C NMR. Thermal properties were evaluated through DSC studies, optical properties were carried out by analysis of absorption spectroscopy (UV) and finally, the electrochemical properties were evaluated by measurements of cyclic voltammetry.

Keywords: fluorescence; benzothiadiazole, band-gap;

Synthesis and Characterization of Discotic Liquid-Crystalline Semiconductors Based on [1,3,5]-triazine.

G. G. López[1], L. F. Vieira[1], T. A. Frizon[1], A. G. Dal-Bo[1], M. M. S. Paula[1], R. Benavides[2], L. da Silva[1]*.

[1]Universidade do Extremo Sul Catarinense (UNESC), Av. Universitária, 1105 - Cx.P. 3167, Criciúma, SC. Brazil, 88.806-000.

[2] Centro de Investigación en Química Aplicada, Blvd. Enrique Reyna H. 140, Saltillo, Coahuila, México.

*Corresponding author. Tel.: + 55 48 91026649; FAX: + 55 48 34312674

E-mail address: luciano.silva@unesc.net (Luciano da Silva)

ABSTRACT

Compounds with liquid-crystalline properties are studied because of the wide application as information displays, also named Liquid Crystal Displays (LCDs), and widely used in many devices that are essential part of our everyday life. In particular, the liquid crystals with disk like molecular geometry (discotic liquid crystals) have a wide range of applications in molecular electronics, such as: photoconductors, OLEDs, solar photovoltaic cells and chemical sensors. The previous due to its highly organized structure, excellent charge transportation and thermal stability. Compounds with liquid-crystalline properties containing [1,3,5]-triazine structures are good candidates for using as discotic functional materials with luminescence. This self-organization can be used for orientation of charge transportation ducts, with potential application in organic electrolytes for fuel cells. In this study, it is described the synthesis and characterization of compounds based on the heterocycle tris-[1,2,4] triazol [1,3,5]-triazine (TTT), designed to obtain self-organizing liquid crystalline state. The materials were characterized by FTIR and ^{1}H and ^{13}C NMR. The thermal properties were measured by TGA (Thermogravimetric Analysis) and DSC (Differential Scanning Calorimetry). Membranes were prepared by the spincoating technique and electrochemical conductivity evaluated. The optical properties were obtained by absorption spectroscopy (UV) and fluorescence analysis. The results show great potential for application of these materials in electrolyte for fuel cells.

Keywords: discotic liquid crystals; electrical conductors; heterocycles.

Selective Decomposition of Urea by Enzyme Immobilization, for Electrolysis of Ammonium.

R. Fernández-Loyola[1], F. Pérez-Robles[1], A. Pizaña-Hernández[2], T.Z. Juárez-Montoya[2], R. Monroy-Solís[2], U. Granados-Macías[2].

[1] Centro de Investigación y de Estudios Avanzados del IPN, Querétaro, Qro. México.76230.
[2] Universidad del Valle de México, Campus Querétaro, Qro. México. 76230
Tel: +524422119900 Ext 1527; email: rfernandez@qro.cinvestav.mx

ABSTRACT

It was realized and studied the enzymatic activity of urease, as well as immobilization for the decomposition of urea, by working with concentration of 20 g of urea per liter, simulating the urea contained in urine of animal origin. It was found an increased enzyme activity and reaction rate at neutral pH (7.2), work temperature of 50 ° C and a time of 30 minutes for these parameters; the point of maximum enzyme concentration on enzyme activity was 4687.5U. The enzyme immobilization was carried out using alginate as encapsulating matrix, which showed good chemical kinetics. Electrochemical measurements for electrolysis of ammonium produced by urease selective break down were carried out by the technique of cyclic voltammetry (CV) using a potentiostat (Volta Lab 80 Radiometer Analytical Model PGZ402) and multi wall carbon nanotubes (MWCNT) as catalyst material, synthesized by the technique of chemical vapor deposition (CVD), doped in situ with different metals (Co, Pt and Ru) obtaining greater activity in the anode region for hydrogen formation with multi wall carbon nanotubes doped with Ruthenium.

Keywords: Urease, Immobilization, MWCNT.

Effect of Size of Carbon Nanotubes on the Electrochemical Activity in Basic Medium

R. Fernández-Loyola[1], E. Samaniego-Benitez[1], F. Perez-Robles[1], O. Solorza-Feria[2].

[1] Centro de Investigación y de Estudios Avanzados del IPN, Querétaro, Qro. México.76230.
[2] Centro de Investigación y de Estudios Avanzados del IPN, Zacatenco, México D.F. 7360.
Tel: +524422119900 Ext 1527; email: rfernandez@qro.cinvestav.mx

ABSTRACT

The electro-oxidation in alkaline solution (0.5M KOH) of multi-walled carbon nanotubes (MWCNT) with different sizes (85, 45, 35 and 25 nm respectively) was studied. The catalyst for carbon nanotubes was synthesized from a sol-gel suspension in a homemade rod mill applying at the same time a temperature of 350 °C for one hour. The carbon nanotubes were synthesized using the chemical vapor deposition (CVD) process. The structure and composition of the surface of the MWCNT was examined by scanning electron microscopy (SEM), transmission electron microscopy (TEM) and Raman spectroscopy, observing differences in the diameters of the obtained MWCNT. SEM and TEM images confirmed the formation of carbon nanotubes of different diameters and Raman Spectroscopy revealed changes in the structure of the carbon nanotubes. The electrocatalytic activity of the material was measured by cyclic voltammetry, which shows that the activity depends on the behavior proportional to the diameter of the MWCNT obtained, showing activity in the region of the cathodic peak for the formation of oxygen and a slight increase in the anodic region for the formation of hydrogen.

Keywords: MWCNT, Sizes, cyclic voltametry.

XIV International Congress of the Mexican Hydrogen Society
Cancun, Mexico, 2014

$Ni_xMo_{1-x}O_3$ ($x \leq 0.4$) as Electrocatalysts for Electrochemical Hydrogen Production from Acid Water

K. K. Aruna and R. Manoharan*

Electrochemical Energy Materials Laboratories
Nanotech Research Facility, PSG Institute of Advanced Studies, Coimbatore, India 641 004
Phone: 0422- 4344000 x 4322
*email: krsmano@gmail.com

ABSTRACT

Solar electricity powered water splitting is an important scheme for solar energy conversion and storage. For this, electrochemical production of hydrogen from water electrolyzers seems to be one of the promising and sustainable solutions. This hydrogen can be converted back to electricity as in hydrogen driven fuel cell and it can also be used directly in several other applications. Conventional noble metal based electrocatalysts used in the electrolysis of water in devices like proton exchange membrane water electrolyzer (PEMWE) have very limited use due to their high cost and scarcity. Identification of an apt non noble electrocatalyst will be a breakthrough in this field. In this work, we have tried to dope Ni in cheaper MoO_3 nano belt materials and examined the resulting materials as electrocatalysts for the cathodic hydrogen evolution reaction (HER). X- ray diffraction analysis of our synthesized materials indicated that Ni enters into the orthorhombic structure of $\alpha - MoO_3$ up to x = 0.2. Nanobelt morphologies have been observed in TEM analysis and with the increase in the Ni concentration, presence of broken belts has been observed along with few spherical particles. The HER catalytic studies have been performed on these particles using 2.5 M H_2SO_4 solution as the electrolyte in a three electrodes cell assembly. The HER evolving rates as inferred from the linear sweep voltammograms recorded at the 500^{th} cycle for $Ni_{0.1}Mo_{0.9}O_3$, $Ni_{0.2}Mo_{0.8}O_3$, $Ni_{0.3}Mo_{0.7}O_3$ and $Ni0_{.4}Mo_{0.6}O_3$ are compared. The data suggest that the HER current densities increase several times on $\mathbf{Ni_{0.2}Mo_{0.8}O_3}$ and with further increase in the doping concentration beyond x = 0.2, the HER activities decrease. A Tafel slope value of 126 mV/dec has been noticed for $Ni_{0.2}Mo_{0.8}O_3$ from the recorded Tafel curves.
It appears that the adsorption of hydrogen (Volmer reaction) $Mo^{6+}\ OH^- + H_{aq}^+ + e^- \longrightarrow Mo^{5+}OH_2$ is the slow rate determining step during the occurrence of the cathodic HER on this oxide material.

Keywords: Hydrogen evolution reaction, Ni doped MoO_3, Catalytic studies.

XIV International Congress of the Mexican Hydrogen Society
Cancun, Mexico, 2014

Differences in Ecological Structure Between Hydrogen Producing and Anaerobic Digestion Consortia

Marcelo Navarro Díaz[1], Idania Valdez-Vazquez[2], Ana E. Escalante[1*]

[1]Laboratorio Nacional de Ciencias de la Sostenibilidad (LANCIS), Instituto de Ecología, Universidad Nacional Autónoma de México
* anaelena.escalante@gmail.com
[2]Depto. Ciencias Ambientales, Universidad de Guanajuato, Irapuato, Gto. México.

ABSTRACT

To date, high hydrogen yields by dark fermentation has been challenging because tight control of methanogenic microbial populations is needed and rarely achieved. This control is commonly achieved through aggressive pretreatments of the inocula (e.g. activated sludge, agricultural disposal). Despite this approach has been somewhat successful it is still unclear what are the effects of these pretreatments in the microbial communities composition and dynamics. Moreover, stability of production and up-scaling remain a challenge. We propose that a better, systemic description of microbial communities composition and modeling of their dynamics and interactions among members is key to a sustainable biohydrogen production. In this work we inferred the ecological (co-occurrence) networks of anaerobic digestion (methanogenic) and dark fermentation (/hydrogen production) prokaryotic communities based on published information from 100 experimental settings of each kind. We compared both networks in terms of their robustness, modularity and other topological aspects in order to unravel important interactions between populations of these communities and unknown roles of some groups. In addition, we performed multivariate and indicator species analyses to relate performance and culture conditions with key species in these communities.

Keywords: dark fermentation; ecological networks; biohydrogen production

XIV International Congress of the Mexican Hydrogen Society
Cancun, Mexico, 2014

Sulfur Doped Carbon Nanotubes as Electrocatalyst in PEM Fuel Cells

I. Alonso-Lemus[1], E. Montiel Macias[1], Y. Verde-Gómez[1]

[1]Instituto Tecnológico de Cancún, Av. Kábah Km. 3, Cancún, Q. Roo, México, 77500.
*Tel: +529988807432; e-mail: ivalemus@gmail.com

ABSTRACT

Fuel cells are attractive devices for the generation of clean energy. However, the main obstacle found for large-scale commercialization is the high cost of platinum, which is used as electrocatalyst for high performance and activity. Recently there have been studies on free-platinum electrocatalysts based on carbon materials doped with heteroatoms (N, S, P, B, etc.), which exhibit electrocatalytic activity similar to platinum but with a significantly lower cost. Furthermore, carbon nanotubes have unique properties such as high resistance to corrosive atmospheres and good electrical conductivity, making these excellent candidates for use in the hostile operation environment of the fuel cell. In this study sulfur doped carbon nanotubes were synthetized by chemical vapor deposition technique. Sulfur was incorporated from the carbon nanotubes synthesis using as precursor thiophene. Influences of parameters as temperature and carrier flow gas were studied in order to find the optimal synthesis conditions. The morphology was analyzed by Scanning Electron Microscopy and High Resolution Transmission Electron Microscopy. Morphology results show that carbon nanotubes with several diameters were obtained (between 70 to 500 nm). Elemental mapping show a homogenous distribution of sulfur on the carbon nanotube surface. However the formation of FeS in the core of nanotubes was corroborated by elemental mapping and X-Ray diffraction analysis. The electrocatalytic activity of these novel platinum-free electrocatalysts will be evaluated by the rotating disk electrode technique to determine its feasibility for use in this application.

Keywords: Carbon nanotubes, electrocatalyst, heteroatom

Comparison of Structural and Electrochemical Properties of Doped and Superficially Modified Multiwall Carbon Nanotubes

E. Samaniego Benitez[1], R. Fernández Loyola[1], E. Flores Rojas[2], J. F. Pérez Robles[1], O. Solorza Feria[2],

[1]Centro de Investigación y Estudios Avanzados del IPN unidad Querétaro; Libramiento Norponiente #2000; Fracc. Real de Juriquilla; C.P. 76230; Queretaro Mexico
[2]Centro de Investigacion y Estudios Avanzados del IPN unidad Zacatenco; Av. Instituto Politécnico Nacional No. 2508, Colonia San Pedro Zacatenco, CP 07360, Ciudad de México D.F., México.
*Tel: +529831566032; e-mail: esamaniego@qro.cinvestav.mx

ABSTRACT

One of the most active fields of research is currently the synthesis, characterization and application of carbon nanotubes (Carbon Nanotubes: CNTs). In the particular case of the family of technologies related to hydrogen, CNTs and proton exchange membranes are candidates for improving the performance of fuel cells, as well as to resolve many of the difficulties related to the storage of hydrogen. In this work the structural and electrochemical differences of both doped CNT's and superficially modified with transition metals was studied. The CNT's used in this work were produced by the chemical vapor deposition (CVD) process and purified by an acid route. The structural properties were studied by Raman spectroscopy to determine the purity of the material. Scanning and transmission electron microscopy were used to characterize the morphology of the samples. The chemical composition was determined by Inductively Coupled Plasma Mass Spectrometry with which it was possible to determine the amount of dopant metal of the samples. Cyclic voltammetry and chronoamperometry in acid medium were used to determine the electrochemical behavior and stability of the samples respectively. A great number of imperfections were determined in the doped samples compared with a sample of pure CNT. The study of the morphology showed the presence of the tubular structure characteristic CNT's in all samples. The study showed that electrochemical AACVD sample exhibits better electrochemical activity as well as a higher stability despite having a lower amount of doping material compared to the other two samples.

Keywords: Carbon Nanotubes; doping; electrochemical

Comparison of Two Methods of Synthesis of Bifunctional Platinum-Iridium Electrocatalyst for Unitized Regenerative Fuel Cells

E. M. Uicab[1, 2], E. Escobedo[2], L.C. Ordoñez[2], D. Pacheco[2*], M. Smit[2]

[1] Universidad Autónoma de Yucatán, Facultad de Ingeniería Química.
Periférico Norte Kilómetro 33.5, Tablaje Catastral 13615, Col. Chuburna de Hidalgo Inn.
[2]Centro de Investigación Científica de Yucatán (CICY), Calle 43 No. 130,
Col. Chuburná de Hidalgo, C.P. 97200, Mérida, Yucatán, México.
[*]Tel: +999-9428330 ext:322; e-mail: dpacheco@cicy.mx

ABSTRACT

The Unitized Regenerative Fuel Cell (URFC) is an electrochemical device that generates hydrogen and oxygen through electrolysis, and produces an electric current when operated in fuel cell mode using the gases obtained by electrolysis. For the URFC, it is necessary to use an electrocatalyst without carbon-support, since the high voltages during the oxidation processes, causes carbon degradation leading to rapid cell performance decrease. An alternative, is to use bifunctional electrocatalysts which combine the properties of two metals resulting in an increased performance.

In this work, two methods of the synthesis of bifunctional electrocatalysts of Pt supported on IrO_2 were compared. In the first method, platinum was supported onto IrO_2 by a reduction of chloroplatinic acid (H_2PtCl_6) with sodium hydroxide (NaOH), dissolved in ethyleneglycol. For the second method, deionized water was used to dissolve the sodium hydroxide, and pH was adjusted to 9 by adding sodium carbonate ($NaCO_3$), with formaldehyde being used as reducing agent. The obtained materials were mixed with platinum black to a 1:1 ratio.

The iridium oxide support material was synthesized by reduction of an iridium salt (H_2IrCl_6) in the presence of NaOH. Pt black was synthesized from H_2PtCl_6 mixed with sodium nitrate ($NaNO_3$) dissolved in water and reducing with sodium borohydrate ($NaBH_4$).

The materials obtained were characterized by EDS for evaluation of the elemental composition of the components, and by XRD to determine its structure. The electrocatalytic performance was evaluated electrochemically by cyclic voltammetry. The electrochemically active area and specific power were determined from these methods.

Finally, the best-performing electrocatalytic materials of Pt-IrO_2 were used as a catalyst in the oxygen side of an URFC, with Pt black in the hydrogen side, and the URFC performance was evaluated.

Keywords: **IrO_2; electrocatalysts; URFC.**

XIV International Congress of the Mexican Hydrogen Society
Cancun, Mexico, 2014

Composite sPEEK-TPyP Membranes Development for Portable Applications

A Carbone[1*], M.A. Castriciano[2], A. Saccà[1], R. Pedicini[1], I. Gatto[1], L. Monsù Scolaro[3]

[1]Istituto di Tecnologie Avanzate per l'Energia "Nicola Giordano", via S. Lucia sopra Contesse 5, 98126 Messina , Italy.
[2]Istituto per lo Studio dei Materiali Nanostrutturati, c/o Dipartimento di Scienze Chimiche Viale Ferdinando Stagno D'Alcontres n.31, 98166 Villaggio S. Agata, Messina, Italy.
[3]Dipartimento di Scienze Chimiche, University of Messina Viale Ferdinando Stagno D'Alcontres n.31, 98166 Villaggio S. Agata, Messina, Italy.
[*]Tel: +39090624273; e-mail: alessandra.carbone@itae.cnr.it

ABSTRACT

Composite membranes based on sulphonated Polyetheretherketone (sPEEK) and 5,10,15,20-tetra(4-pyridyl)porphyrin (TPyP) were developed for portable applications. A sulphonation degree of 65% and different weight percentages (0-5%) of TPyP porphyrin were used. The membranes were realized with a standardized doctor-blade method, thermally and chemically treated. Physical-chemical characterizations were carried out in terms of ionic exchange capacity, water uptake, dimensional variations and swelling, structural and morphological analyses. Moreover, proton conductivity measurements at a temperature useful for portable applications, were performed. SEM analyses of composite membranes highlight a similar morphology to the pristine sPEEK membrane. XRD profiles of composite membranes correspond to the amorphous pattern of sulphonated polymer, while the fundamental peaks of TPyP were completely suppressed. This effect indicates that a good interaction occurs between the filler and the polymer matrix. This interaction, in particular between nitrogenous groups of porphyrin and sulphonic groups of polymer, leads to unaltered physico-chemical properties and a proton conductivity respect to the sPEEK membrane, used as a reference. In particular, the membrane with the lowest loading (1 wt%) of TPyP, shows higher water uptake and λ values than the reference membrane, resulting in an increased proton conductivity. This behavior could be attributed to an additive protonation and, consequently, hydration of porphyrin groups able to contribute to the proton conduction mechanism. In addition, the developed membranes were characterized in a PEFC 25cm^2 single cell to verify their applicability in portable devices.

Keywords :Sulphonated PEEK; TPyP; PEFC.

Performance Assessment of an Integrated PEFC and a Hydrogen Storage Device Based on Innovative Material

R.Pedicini[1*], F.Matera[1], G.Giacoppo[1], I. Gatto[1], E.Passalacqua[1]

[1]CNR-ITAE, via S. Lucia sopra Contesse 5, 98126, Messina, Italy.
[*]Tel: +39090624277; e-mail: rolando.pedicini@itae.cnr.it

ABSTRACT

Storage of hydrogen in solid materials has the potential to become a safe and efficient way to store energy, both for stationary and mobile applications. An integrated small scale system, integrating a small hydrogen tank and a 25 cm^2 PEFC single cell, has been tested to assess the performance of an innovative hydrogen storage material based on manganese oxide anchored to a polymeric matrix. A prototype small hydrogen tank, with a capacity of 18 cm^3 made of a stainless steel tube, has been filled with the hydrogen storage material, previously characterized and reaching an hydrogen storage capacity of about 1 wt%. The system included a temperature and pressure sensors and a mass flow to control the desorption rate. A Labview software application has been developed for data logging and control of the test set-up. Sorption process has been achieved by fixing the charging time and recording pressure vs time. The electrochemical tests were performed at 80°C (PEFC cell temperature) and several discharge-charge cycles have been performed at different pressure and two discharge rates (i.e. 100 and 200 ml/min). The nominal power produced by the PEFC cell has been between 6-10 W, with an average discharge time of 400-500 s, depending on charging time and pressure. This material, which adsorbs H_2 in no drastic condition and safe as inert when in contact with ambient air, has demonstrated both a good cycle reversibility in terms of H_2 charge and discharge and, moreover, not affected by the packing in the tank.

Keywords: Hydrogen storage material; H_2 tank and Fuel Cell integration; electrochemical tests.

XIV International Congress of the Mexican Hydrogen Society
Cancun, Mexico, 2014

Functionalization of Vulcan XC-72 by IMH and its Effect as Support for Pt Electrocatalysts for the EOR

W.J. Pech-Rodríguez[1], D. González-Quijano[1], G. Vargas-Gutiérrez[1,2], J.I. Escalante-Garcia[1,2], F.J. Rodríguez-Varela[2,3,*]

[1]Ingeniería Metalúrgica e Ingeniería Cerámica
[2]Sustentabilidad de los Recursos Naturales y Energía
[3]Programa de Nanociencia y Nanotecnología
Cinvestav Unidad Saltillo, Av. Industria Metalúrgica 1062, Ramos Arizpe, Coahuila, México, 25900.
[*]Tel: +528444389600 Ext. 8526; e-mail: javier.varela@cinvestav.edu.mx

ABSTRACT

In this study, Vulcan XC-72 was functionalized by an intermittent microwave heating (IMH) method in two different soft chemical agents, namely citric acid (CA) and methanol (MeOH). The specific surface area and pore structure of the treated carbons were investigated by BET and FTIR studies were achieved to investigate their surface state. The results showed physical and chemical changes in the structure of functionalized Vulcan. Also, Pt/C electrocatalysts were synthetized by pulse-microwave assisted polyol method using the treated carbons as support. The electrochemical activity and stability of the Pt/C materials were investigated by cyclic voltammetry and chronopotentiometry measurements. The electrochemical results showed higher catalytic activity and stability for Pt nanocatalyst supported on some of the functionalized carbons for the Ethanol Oxidation Reaction (EOR) compared to a Pt/C electrocatalysts dispersed on unmodified Vulcan. The higher performance of Pt/C electrocatalysts on functionalized supports may be due to: i) a better distribution of the nanoparticles, and ii) an enhanced interaction between Pt nanoparticles and the oxygenated species present on the surface of the treated carbon. The results showed in this work suggest that functionalization of Vulcan with MeOH and CA using the IMH method is a promising process for the development of highly active Pt/C catalyst toward the EOR due to its simplicity and low cost.

Keywords: functionalization of Vulcan; citric acid and methanol; EOR

XIV International Congress of the Mexican Hydrogen Society
Cancun, Mexico, 2014

Richness, Composition and Predominance in Undefined Mixed Cultures for Fermentative Hydrogen Production

Zulma Lizzette Alamilla[1], Ana E Escalante[2], Idania Valdez-Vazquez[1*]

[1] Depto. Ciencias Ambientales, Universidad de Guanajuato, Irapuato, Gto. México.
[2] Laboratorio Nacional de Ciencias de la Sostenibilidad (LANCIS), Instituto de Ecología, Universidad Nacional Autónoma de México
* valdez_idania@yahoo.com

ABSTRACT

The fermentative hydrogen production has many approaches including those reports using monocultures or those reports using undefined microbial consortia. The last one has as advantages, high hydrogen production rates, operation under unsterile conditions and use of unrefined substrates such as a great variety of organic wastes. The metabolic capacities of undefined microbial consortia are higher than that of a monoculture, and therefore it is possible to convert very complex substrates into hydrogen, for instance, lignocellulosic substrates composed by cellulose microfibrils embedded in a matrix of hemicellulose and lignin. Several types of undefined microbial consortia have been used to produce hydrogen derived from sludge of hot-springs, beaches, anaerobic digesters, composts, wastewater treatment plants (WWTP). The objective of this work was to know the ecological attributes of richness, composition and predominance of these H_2-producing consortia (HPC). For that, a total of 90 papers were reviewed in which the microbial structure was studied by molecular methods. An inventory of the reported species in the operation time with the highest hydrogen production was done. The results showed the HPC derived from the anaerobic digesters were those with the highest richness with a total of 109 species followed by those derived from composts with 78 species, WWPT with 68 species, hot-springs with 34 species and beaches with 12 species. The genera with the highest number of species reported were *Clostridium, Bacillus, Thermoanaerobacterium, Lactobacillus, Klebsiella, Magasphaera* y *Streptococcus.* All these genera belong to the phyla Firmicutes and Proteobacteria. The information presented in this review will be useful to understand the ecological relationships between the members of the HPC and therefore contribute to the better operation of the bioreactors at large scale.

Keywords: Clostridium, consortia, microbial ecology.

Development of an Electronic Device for Impedance Measurements for Online PEMFC Failure Diagnostic Applications

H. D. Mendoza[1], F. Loyola[2, *], U. Cano[2], C. Morales[1], M. López[2]

[1]Universidad Politécnica del Estado de Morelos, Boulevard Cuauhnáhuac 566, Col. Lomas del Texcal, Jiutepec, Morelos. CP 62550
[2]Instituto de Investigaciones Eléctricas. Reforma 113, Col. Palmira, Cuernavaca, Morelos, México, 62490.
[*]Tel: +527773623811, Ext. 7140; e-mail: felix.loyola@iie.org.mx

ABSTRACT

In this work, the design and construction of a small and low cost impedance measurement device is presented. The device was developed for online dehydration and flooding PEMFC's diagnostic applications, therefore, its design allows interaction through a SPI communication protocol with the PEMFC´s control system. Applying a sinusoidal signal at two pre-set frequencies, this device based on analog circuits, has the ability of negligibly disturb the PEMFC's stable operation point and measure the current, voltage, and phase angle of the signal response. Then, based on these measurements, the imaginary and real impedance components as well as the impedance magnitude are calculated. The device also has the ability to perform electrochemical impedance measurements online at open circuit (no current generation) or in operation (during current generation) and it is applicable to every electrochemical cell, capable of generating an output potential in the 1.01 – 60 V range and at least 150 mA current.

Keywords: EIS; PEMFC; Online diagnostic.

XIV International Congress of the Mexican Hydrogen Society
Cancun, Mexico, 2014

Flooding and Dehydration Processes in a PEM Fuel Cell. A Phenomenological Analysis Based on EIS Measurements

F. Loyola[1, *], U. Cano[1]

[1]Instituto de Investigaciones Eléctricas. Reforma 113, Col. Palmira, Cuernavaca, Morelos, México, 62490.
[*]Tel: +527773623811, Ext. 7140; e-mail: felix.loyola@iie.org.mx

ABSTRACT

In this work a study on the phenomena occurring within a PEM fuel cell during the flooding and dehydration processes is presented. The study consisted of voltage control electrochemical tests on a 50 cm^2 geometrical active area fuel cell, under controlled conditions to promote flooding or dehydration. During the chronoamperometric tests, electrochemical impedance spectroscopy (EIS) measurements were carried out. The EIS analysis was based on the use of a Randles-type electric equivalent circuit. This circuit, represent through its electrical components, the characteristic properties of the electrochemical system and their variation when the experimental conditions change as a result of the catalysis layer flooding or dehydration of the electrolyte. The results, allowed us to explain phenomena as the interfacial and the charge and mass transport occurring within the fuel cell. In addition, through a sensibility analysis, the electrical parameters directly related with the flooding and dehydration processes were identified; as well as the conditions under which they can be used as control variables in the design of strategies for failure diagnostics and prediction in PEM fuel cells.

Keywords: EIS; PEMFC; Flooding-Dehydration.

XIV International Congress of the Mexican Hydrogen Society
Cancun, Mexico, 2014

Thermodynamic and Kinetics Modeling of H_2 Production by Dry Reforming of Ethanol with $CaCO_3$ as CO_2 Source

R. B. Pallares Sámano[1], M. R. Baray Guerrero[1], J. Salinas Gutiérrez[1], V. Guzmán Velderrain[1], V. Collins-Martínez[1], A. López Ortiz[1*]

[1] Departamento de Materiales Nanoestructurados, Centro de Investigación en Materiales Avanzados, S.C., Miguel de Cervantes 120, Chihuahua, Chih., México, 31109, México.
*Tel: +526144394815 mail: alejandro.lopez@cimav.edu.mx

ABSTRACT

A viable alternative to fossil fuels is to make use of H_2 from renewable sources as an energy carrier or as a clean fuel. Steam reforming of hydrocarbons is the conventional process to produce H_2, with the drawbacks that presents low efficiency combined with high operational costs and CO_2 being emitted into the atmosphere. An alternative to this process is the dry reforming of hydrocarbons, which employs CO_2 to produce hydrogen-syngas and the use of ethanol as a renewable feedstock which would prevent CO_2 emission into the atmosphere. One innovative approach is the use of a solid carbonate to serve as a source of CO_2 for this process. Thus, exposing the solid carbonate to high temperatures (reaction temperature), this decomposes emitting CO_2, which is used as raw material along with ethanol (ETOH) to produce hydrogen-synthesis gas. The present work aims to perform a thermodynamic and kinetic simulation study to explore reaction conditions close to equilibrium for a high syngas-H_2 production, under the dry reforming of ETOH. $CaCO_3$ was used as source of CO_2 for the reaction system. The thermodynamic study was performed using the HSC software and the studied conditions were: T = 300-1000 °C, $CaCO_3$/ETOH molar ratio = 1-5. Results showed that at T ≥ 755 °C and $CaCO_3$/ETOH ≥ 3, a free carbon formation syngas is produced. Maximum H_2 production was obtained at 855 °C and $CaCO_3$/ETOH ≥ 3, while the highest concentration of H_2 was produced at 755 °C. Furthermore, a process and kinetics simulations were performed through ASPEN-Plus and CKS, respectively and based on experimental data taken from the literature for the dry reforming of ETOH. Results indicate that at 900 ºC and $CaCO_3$/ETOH = 0.9 ratio, the estimated value of H_2 purity was very similar to that obtained by the thermodynamic equilibrium analysis.

Keywords: CO_2 dry reforming; thermodynamic analysis; kinetics modelling.

XIV International Congress of the Mexican Hydrogen Society
Cancun, Mexico, 2014

Na_2ZrO_3 Stability under Reforming/Regeneration Cycles during the Steam Reforming of Ethanol with CO_2 Absorption

M. A. Escobedo Bretado[1], V. Collins Martínez[2], J. Salinas Gutiérrez[2], L. I Gracia Campos[2], R. H. Lara Castro[1], A. López Ortiz[2]*

[1] Facultad de Ciencias Químicas, Universidad Juárez del Estado de Durango, Av. Veterinaria s/n, Circuito Universitario, Durango, Dgo., México, 34120.
[2] Departamento de Materiales Nanoestructurados, Centro de Investigación en Materiales Avanzados, S.C., Miguel de Cervantes 120, Chihuahua, Chih., México, 31109.
*Tel: +52 614 4394815; e-mail: alejandro.lopez@cimav.edu.mx

ABSTRACT

In this work Na_2ZrO_3 and a Ni-Al_2O_3 catalyst were used to evaluate the hydrogen production by the steam reforming of ethanol in combination with CO_2 absorption. The Na_2ZrO_3 was synthesized by the solid state method with a Na_2CO_3/ZrO_2 = 1:1 molar ratio and calcined at 900 °C in air. A 25% W Ni-Al_2O_3 catalyst was synthesized by incipient impregnation and calcined at 900 °C in air. During reforming, operating conditions were: H_2O/C_2H_5OH = 6:1 molar ratio, T = 600 °C, SV = 414 h^{-1}, with a reactor loading of Ni-Al_2O_3/Na_2ZrO_3 = 0.2g/3.7g. Results of the X-ray absorbent confirmed the Na_2ZrO_3 crystalline phase. While, the catalyst shown NiO and Al_2O_3 phases with a surface area of 125 m^2/g. TGA CO_2 absorption tests by Na_2ZrO_3 reached 84.3% of the theoretical absorption value. Ethanol steam reforming without absorbent reached a maximum concentration of 69.1% H_2 (dry basis). After reaction X-ray results shows Ni and Al_2O_3 phases, while maintaining its initial surface area. Regeneration of the absorbent was carried out by separating this from the catalyst followed by calcination in air at T = 900 ° C by 4 hours. For the following reaction cycle the regenerated absorbent was remixed with the catalyst and reloaded to the reactor for a new step of reforming completing a reforming-regeneration cycle (R-Reg). 10 R-Reg cycles were performed resulting an excellent thermal and chemical stability of the Na_2ZrO_3 absorbent. While, during the reforming step an average of 92% H_2 (dry basis), together with 8% CO_2, and CO free with an absorbent carbonation of 17.7% W. These observed values are close to the thermodynamic equilibrium and show excellent compatibility between the reforming and carbonation kinetics, and a great thermal stability of materials resulting in an attractive process for hydrogen production

Keywords: Absorption enhanced reforming; Na_2ZrO_3; Reforming/regeneration cycles

$W_{1-x}Mo_xO_3 \cdot 0.33H_2O$ Solid Solutions with Tunable Band Gap for Hydrogen Production

A. Arzola-Rubio[a], J. Camarillo[a], V. Collins-Martínez[a], L. De la Torre-Sáenz[a], F. Paraguay-Delgado[a*]

A Departamento de Materiales Nanoestructurados, Centro de Investigación en Materiales Avanzados S. C., CIMAV
Miguel de Cervantes 120, Chihuahua, Chih. México. CP 31109.
*Tel: +526144391107; e-mail: francisco.paraguay@cimav.edu.mx

ABSTRACT

A series of $W_{1-x}Mo_xO_3 \cdot 0.33H_2O$ (x = 0, 0.25, 0.50, 0.75) nano/microstructures and $MoO_3 \cdot 0.55H_2O$ microamorphous structures have been prepared by hydrothermal synthesis starting from aqueous hydrate ammonium metatungstate ($(NH_4)6H_2W_{12}O_{40} \cdot xH_2O$) and tetrahydrate ammonium heptamolybdate ($(NH_4)_6Mo_7O_{24} \cdot 4H_2O$) acidified solutions. The $WO_3 \cdot 0.33H_2O$ lattice can be substituted with Mo up to 75% without structural alterations of the orthorhombic host structure. With the increase of the Mo content (x) from 0 to 0.75, the band gap of the as-prepared $W_{1-x}Mo_xO_3 \cdot 0.33H_2O$ nano/microstructure is narrowed from 2.74 to 2.31 eV. The increased M^{5+} (M = Mo and W) fraction and thus enhanced intervalency-transition are responsible for the narrowing of the band gap and presumably making hydrogen production feasible through the photocatalytic water splitting.

Keywords: H_2 production; water splitting; W/Mo solid solutions.

Microwave-Assisted Synthesis and Electrocatalytic Activity of Pt-CeO_2 Nanoparticles Supported on Carbon Nanotubes

M. Velasco-Plascencia[1], J.M García-Hernández[1], J. Lara-Romero[1,*], A.M. Valenzuela-Muñíz[2], Y. Verde-Gomez[2]

[11]Facultad de Ingeniería Química, Universidad Michoacana, Morelia, México,58060
[2]Instituto Tecnológico de Cancún, Av. Kábah Km. 3, Cancún, Q. Roo, México, 77500.
[*]Tel: +524433273584; e-mail: jlara_romero@hotmail.com

ABSTRACT

Carbon nanotubes have been successfully used as support for the dispersion and stabilization of metal and oxide nanoparticles due to their large chemical active surface and thermal stability. Among many techniques to produce these composites, microwave processing has emerged as a novel method for this purpose. Microwave-assisted deposition offers the advantage of uniform heating of the sample resulting in a better particle size control and distribution of the metal nanoparticles produced as well as a substantial synthesis time reduction. The use of surfactants as stabilizers is an important parameter to achieve uniform distribution and size control of the nanoparticles on the surface of the carbon nanotubes.

In this work, we study the deposition of Pt-CeO_2 nanoparticles on MWCNTs by microwave irradiation and its application as fuel cell electrocatalyst. Dioctil sodium sulfosuccinate (AOT) was used as surfactant. $NaBH_4$ was used as a reducing agent. MWCNTs were produced by spray pyrolysis of alpha-pinene and purified by a conventional acid treatment. The microwave synthesis was performed in a Synthos 3000 microwave reactor. The produced composites were characterized by HRTEM, Raman spectroscopy, TGA and XRD. Electrochemical experiments were carried out in a conventional three cell electrode to evaluate the electrochemical active area and the oxygen reduction reaction. The Pt-CeO_2/MWCNTs electrochemical results will be discussed and compared with traditional Pt/C.

Keywords:Pt-CeO_2 /MWCNTs composite, microwave synthesis, oxygen reduction reaction.

Sociedad Mexicana del Hidrógeno A. C.
Mexican Hydrogen Society

CONACYT

ITC

Kinetic Study of the Pyrolysis of *Pinus Cooperi* and *Quercus Sideroxyla* for the H_2 Production Combined with CO_2 Capture

M. A. Escobedo Bretado[1], R.I. Gándara Terrazo[2], B. C. Escobedo Bretado[2], J. A. Nájera Luna[2], R. H. Lara Castro[1], M. R. Baray Guerrero[3], J. Salinas Gutiérrez[3], A. López Ortiz[3], V. Collins Martínez[3*]

[1] Facultad de Ciencias Químicas, Universidad Juárez del Estado de Durango, Av. Veterinaria s/n, Circuito Universitario, Durango, Dgo., México, 34120.
[2]Instituto Tecnológico de El Salto, Mesa del Tecnológico s/n, El Salto, P.N., Durango, México, 34942.
[3]Departamento de Materiales Nanoestructurados, Centro de Investigación en Materiales Avanzados, S.C., Miguel de Cervantes 120, Chihuahua, Chih., México, 31109.
[*]Tel: +526144391129; e-mail: virginia.collins@cimav.edu.mx

ABSTRACT

Pyrolysis of forestry residues is currently of great interest because bio-oil compounds are produced and these can be employed for the hydrogen production from steam reforming. The objective of the present research was to perform a kinetic study and to determine the optimum reaction conditions for the pyrolysis of the Mexican species *Pinus cooperi* and *Quercus sideroxyla* to achieve the greatest amount of volatile matter (condensable and non-condensable). Furthermore, a thermodynamic analysis was made to evaluate its possible application towards the steam reforming of the volatile matter combined with CO_2 absorption (AERS). Samples of forest biomass were crushed and sieved to particle sizes between 300 to 710 µm and evaluated in a pyrolytic reactor under a N_2 flowrate of 50, 100 and 150 ml/min, at heating rates of 1, 5, 10, 15, 20 and 25 °C/min from room temperature to 700 °C. Results show that at a particle size of 300 microns, 100 ml/min and SV = 33000 h^{-1} and heating rate of 20 °C/min, allowed to obtain the greatest amount of volatile matter in both species. Proximate analysis (wt%) for *Pinus cooperi* resulted in 3.01% moisture, 78.01% volatile matter, 12.35% fixed carbon, 0.42% ash and 6564 J/g of calorific value, while for *Quercus sideroxyla* specie was 2.39% moisture, 78.69% volatile matter, 18.24% fixed carbon, 0.45% ash and a 7322 J/g of calorific value. Kinetic study of the pyrolysis shown an activation energy of Ea = 201.24 kJ/mol for *Pinus cooperi* and 141.97 kJ/mol for *Quercus sideroxyla*, respectively with an apparent reaction order of 1 for both species. Finally, through the thermodynamic analysis, it was found that the obtained volatile species showed a high potential for the production of hydrogen under the steam reforming combined with CO_2 absorption reaction scheme (AESR).

Keywords: hydrogen production; biomass pyrolysis; kinetic study

A Hybrid Approach Based on a Solar PV-Hydrogen System for Household Electric Energy Supply in Mexico

M. Tufiño Velázquez[1*], R.G. González Huerta[2], A. Yunez Cano[2,3], G.S. Contreras Puente[1], D. Jiménez Olarte[1]

[1]Laboratorio de Física Avanzada, ESFM.IPN, UPALM, México, DF
[2]Laboratorio de Electroquímica y Corrosión, ESIQIE- IPN UPALM, México, DF.
[3]Laboratorio de Energías alternas CIITEC IPN, Cda. Cecati s/n, Azcapotzalco, Mexico D.F.
Email: mitufinovel@gmail.com
Telephone: 57296000 ext 46138

ABSTRACT

Mexico as the world has a 90% energy production based on fossil fuels. Billions of CO_2 tons are emitted to the atmosphere; greenhouse gas emissions are generated causing side effects as global warming. The oil peak production was already reached in 2005 and oil production is decreasing every day. Fossil fuels are non-renewable resources and reserves are being depleted much faster than new ones are being made; besides, domestic energy consumption demand is rising steadily. Therefore the use of renewable energy sources is under way to help meet increasing energy needs. On the other hand, every day conventional energy sources increase their cost, while renewable ones become cheaper; this goes hand in hand together with technology progress. In this work we present a hybrid approach based on a solar PV -hydrogen system for household electric energy supply. A mobile house was designed and dimensioned to be powered by this hybrid system to be used as a demonstration household. This would make possible to show this prototype house to more people as we can move it to different locations for making them aware of the feasibility and benefits of using renewable sources of energy. A 1 kW PV system was installed in the roof of the mobile house and a hydrogen system made out of an electrolyzer, a hydrides storage tank and a two-500 W fuel cell system will be installed to be used as a back up system. The capacity of the PV-hydrogen system was calculated from the average electric power consumption of a typical Mexican family living in a CFE 01 rated house by the Electricity Federal Agency in Mexico (CFE: Comisión Federal de Electricidad). House rating by CFE is made according to its bimonthly average energy consumption; CFE 01 rated house has an established baseline day average consumption of 2.2 kWh/day. The implementation of renewable energy is currently growing in Mexico at a moderate pace, as some government programs encouraging investment in these technologies begin to appear. A direct impact is achieved when renewable energy sources are interconnected to the grid so they cause a reduction in the cost of electricity tariffs, thus benefiting the citizens economy.

This work was partially supported under grant SECITI-DF agreement ICYTDF/127/2012 and CONACYT under grant 47587.

Keywords: hybrid approach; photovoltaic; hydrogen; fuel cell; household

Pt/TiO_2–C Electrocatalysts Prepared by Chemical Vapor Deposition with High Tolerance to Alcohols in Oxygen Reduction Reaction

F.M. Hernández-Mendoza[1], M.E. Beltrán-Perez[1], O. Martínez-Alvárez[1], V. Granados Alejo[1], B. Ruiz-Camacho[1,*]

[1]Ingeniería en Energía, Universidad Politécnica de Guanajuato, Av. Universidad Norte s/n, Juan Alonso Cortázar Guanajuato, México, 38438

[*]Tel: +52-462-4414307; e-mail: beatrizr@upgto.edu.mx

ABSTRACT

Pt nanoparticles were synthesized by chemical vapor deposition and were deposited on carbon and TiO2–C substrates. The Pt/C and Pt/TiO2–C catalysts synthesized were characterized by TEM and XRD techniques. Cyclic voltammetry and rotating disk electrode measurements for the Oxygen Reduction Reaction (ORR) were investigated in acid medium in presence of alcohols as methanol and ethanol. A Pt/C commercial sample was tested at the same conditions for comparison purposes. It was found that the catalyst nanoparticles were homogenously distributed over the carbon and TiO2–carbon substrates with a mean particle size about 3 nm. Significant differences in the electrochemical results and alcohols tolerance are observed in the samples prepared in comparison whit Pt/C commercial catalyst. The methanol tolerance of the catalysts synthesized was higher compared to the ethanol tolerance. The electrochemical activity of Pt/TiO2–C catalyst prepared with TiO2 rutile phase was not affected by the presence of alcohols in comparison with Pt/C samples. It is explained by the thermal treatment over Pt/TiO2–C during the synthesis process that produces a synergetic effect caused by the formation of the interface between the platinum and oxide materials where titanium oxide acts as a protecting agent of platinum nanoparticles

Keywords: Pt nanoparticles, chemical vapor deposition, DMFC

XIV International Congress of the Mexican Hydrogen Society
Cancun, Mexico, 2014

Hydrogen Adsorption on Beryllium-C_{60} Fullerene: a Theoretical Study

M. E. Sánchez-Castro[1], I. F. Hernandez-Ahuactzi[2], M. Sanchez[2,*]

[1]Centro de Investigación y de Estudios Avanzados del IPN, Unidad Saltillo, Av. Industria Metalúrgica No. 1062, Parque Industrial, Ramos Arizpe, Coahuila, México 25900
[2] Centro de Investigación en Materiales Avanzados, Alianza Norte #202. Parque PIIT, Apodaca, NL, México, 66600.
[*]Tel: +52 (81) 11560812; e-mail: mario.sanchez@cimav.edu.mx, esther.sanchez@cinvestav.edu.mx

ABSTRACT

Nowadays chemists have focused their efforts in the design and preparation of new materials capable of storing gases responsible for the greenhouse effect, such as CO, CO_2, N_2O, SO_2. Also, there is great interest in the design of materials capable of storing H_2 molecules due to their potential application as an alternative energy source for hydrocarbons. These efforts are complemented by theoretical studies using, computational chemistry. Based on the above, we have explored the potential energy surface of $[C_{60}]$-Be_n complexes to find how many beryllium atoms can interact with the fullerene. Results with the B3LYP/def2-TZVP method suggest that fullerene can accommodate up to 20 beryllium atoms on its surface. Complexes of the type $[C_{60}]$-Be_nH_{2n} (n = 1-20) also were calculated at the same level of theory, in order to find the maximum number of hydrogen molecules coordinated to each beryllium atom. Results show that metallic atoms are η^2 bonded on the fullerene surface. On the other hand, beryllium atoms can coordinate up to two hydrogen molecules with two-electron three-center bonds. Be-H and H-H bond lengths have values from 1.45-1.51 and 0.81-0.85 Å, respectively. The availability of those complexes, for hydrogen storage, will be discussed in more detail during the congress of hydrogen.

Keywords: fullerene, beryllium, DFT

Electrocatalytic Oxidation of Glycerol in Alkaline Media on Pd-Au/MWCNT Nanocatalysts Prepared by the Polyol Method

R. Arenas-Carmona[1], D. Morales-Acosta[2,3], A. Martinez-Luevanos[1], B. Escobar Morales[4], Y. Verde-Gomez[4], F. J. Rodríguez-Varela[2,3]

[1] Facultad de Ciencias Químicas, Universidad Autónoma de Coahuila. Blvd. V. Carranza s/n, República Oriente, Saltillo, Coahuila, México. C.P. 25280.
[2] Grupo de Sustentabilidad de los Recursos Naturales y Energía, CINVESTAV-IPN, Unidad Saltillo, Av. Industria Metalúrgica 1062, Parque Industrial Ramos Arizpe. Ramos Arizpe, Coahuila, México, 25900.
[3] Programa de Nanociencias y Nanotecnología, CINVESTAV-IPN, Unidad Saltillo, México.
[4] Instituto Tecnológico de Cancún, Kabah Km 3, Cancún, Quintana Roo, México, 77500.
Phone: (844) 438-9600 ext. 8526
[*]E-mail: dmoralesacosta@gmail.com; javier.varela@cinvestav.edu.mx

ABSTRACT

Several alcohol molecules have been studied with the purpose of replacing hydrogen in fuel cell for portable applications. Among them, glycerol represents a very promising alternative. Glycerol is a by-product of biodiesel production, has high energy content, low flammability, low volatility, and high boiling point. Moreover, glycerol is less toxic than methanol and has a relatively high theoretical energy density (5.0 kWh kg^{-1}, close to that of methanol of 6.1 kWh kg^{-1}). However the glycerol oxidation reaction (GOR) is slow and its utilization as a fuel therefore requires the development of efficient catalysts. Au and Pd catalysts have shown a high catalytic activity for the GOR, outperforming Pt in alkaline solution. Even more, it is generally accepted that the interaction of metal nanoparticles with the carbon support is beneficial to the improvement of catalytic activity and durability of the electrocatalysts. In this work, the synergetic effect between Pd and Au supported on multiwalled carbon nanotubes in the catalytic activity for the GOR in KOH electrolyte has been investigated. Pd-Au/MWCNT catalysts with several chemical compositions have been synthesized by the polyol reduction method. The catalysts exhibited a more negative anodic potential for the oxidation of glycerol compared to monometallic Au and Pd catalyst. Beside, the oxidation mechanism observed clearly depends on the composition and structure of the Pd-Au/MWCNT catalyst. Such electrocatalyts offer potential possibilities for application in Alkaline Glycerol Fuel Cells.

Keywords: Glycerol Oxidation Reaction, Direct Alcohol Fuel Cells, Au and Pd nanoparticles.

Sociedad Mexicana del Hidrógeno A. C.
Mexican Hydrogen Society

CONACYT

ITC

Enhanced Photocatalytic Hydrogen Production Under Visible Light over Ag Doped TiO_2

V. Guzmán-Velderrain[1], M. Meléndez Zaragoza[1], E. Medina-Henandez[2], P. Gutiérrez Rivera[3], Y. Ortega-López[1], J. Salinas Gutiérrez[1], A. López Ortiz[1], V. Collins-Martínez[1*]

[1]Centro de Investigación en Materiales Avanzados S. C., Laboratorio Nacional de Nanotecnología, Depto. de Materiales Nanoestructurados, Miguel de Cervantes 120, C. P. 31109, Chihuahua, Chih. México
[2]Universidad Autónoma de Chihuahua, Facultad de Ciencias Químicas, Campus Universitario # 2 C.P. 31125, Chihuahua, Chih, México
[3]Universidad Tecnología Junta de los Ríos, Carretera Aldama, Km 3, C. P. 31313, Chihuahua, Chih. México
. Tel: +52 (614)439 11 29 *e mail: virginia.collins@cimav.edu.mx

ABSTRACT

TiO_2 is the most widely used photocatalyst for water and air purification, and for hydrogen production, due to its good properties such as chemical and photo-corrosion resistance and low cost. One disadvantage of this material, resides in its bandgap energy (3.2eV), which lies in the UV spectrum. For this reason, studies have been conducted to modify TiO_2 bandgap into the visible light range. Doping elements used for this purpose are noble metals such as Au, Pt and Ag. However, Au and Pt are expensive and scarce materials, leaving Ag as a preferred candidate. TiO_2 and doped TiO_2 were synthesized via Sol-Gel/hydrothermal (SGH) named TiO_2-F and TiO_2Ag-F, respectively, while under the Sol-Gel/hydrothermal/thermal (SGHT) technique was named as TiO_2Ag-C, using titanium butoxide as a precursor and ethanol as solvent. XRD characterization resulted in the presence of the anatase phase in all three synthesized samples as well as the characteristic signals for Ag in TiO_2Ag-F. Samples crystal sizes were determined by the Scherrer equation, and were ~ 10 nm. Light absorption exhibited a shift in the Eg value from 3 eV for TiO_2-F to 1.98 eV for TiO_2Ag-F. TGA indicates the presence of residual organic material for samples synthesized through the SGH technique. BET surface area for the SGH and SGHT photocatalysts were of 140 and 90 m^2/g, respectively. SEM images presented particle agglomerates of irregular morphology. Photocatalytic evaluation for hydrogen production was performed using a 250 W mercury light lamp, filtering the UV spectrum. TiO_2Ag-F was the only sample that showed activity, producing 175 µmol of H_2/g catalyst over an 8-h irradiation period. This activity can be mainly attributed to the ability of this material to be activated under the visible light spectrum.

Keywords: TiO_2 doped Ag;, Water splitting; Hydrothermal method.

Sociedad Mexicana del Hidrógeno A. C.
Mexican Hydrogen Society

CONACYT

ITC

Synthesis Method Effect of $CoFe_2O_4$ on its Photocatalytic Properties for H_2 Production from Water and Visible Light

Y. Ortega-López[1], J. Salinas Gutiérrez[1], V. Guzmán Velderrain[1], A. López Ortiz[1], V. Collins Martínez[1*]

[1]Centro de Investigación en Materiales Avanzados S. C., Laboratorio Nacional de Nanotecnología, Depto. de Materiales Nanoestructurados, Miguel de Cervantes 120, C. P. 31109, Chihuahua, Chih. México
. Tel: +52 (614)439 11 29 *e mail: virginia.collins@cimav.edu.mx

ABSTRACT

More efficient materials, which work under the visible light spectrum (energy bandgap from 1.5 to 3.0 eV) are the trends for today's new photocatalysts in the field of hydrogen production. Within this criteria, some transition metal ferrites are ideal. Since, the development of a ferrite-based photocatalytic material will help to address the need for a stable photocatalysts, activated under visible light and with high application potential due to their low cost. In particular, this paper reports cobalt ferrite ($CoFe_2O_4$) as a photocatalyst for hydrogen production, activated under visible light. A comparison between two methods of synthesis; chemical co-precipitation (CP) and milling ball (BM) is presented based on its photocatalytic properties. Furthermore, the influence of the synthesis method over the observed activity is presented. Characterization of $CoFe_2O_4$ was performed by X-ray diffraction (XRD), scanning electron microscopy (SEM), transmission electron microscopy (TEM), BET surface area, UV-Vis spectroscopy and water adsorption/desorption tests. Evaluation of the photocatalytic activity under visible light was followed by gas chromatography. Results indicate that crystalline materials with nanometer sizes were obtained (dp < 25nm). BET areas of 21 and 4 m^2/g and band gap energies of 1.3 eV and 1 eV were found for $CoFe_2O_4$ synthesized by CP and BM techniques, respectively. Water adsorption tests shown an adsorption capacity of 39 for the CP and only 0.3 mg-adsorbed-H_2O/g-catalyst for the BM synthesis. The substantial decrease in surface area and adsorption capacity of the ferrite obtained by BM is attributed to a possible sintering process that the material undergoes during its synthesis. Photocatalytic activity results showed better yields for $CoFe_2O_4$ obtained through the CP synthesis. These results are associated with a higher water absorption capacity and greater surface area of this ferrite, properties that the CP synthesis method, which is based on soft and wet chemistry, provides to the material.

Keywords: cobalt ferrite, visible light photocatalyst, hydrogen producton.

Sociedad Mexicana del Hidrógeno A. C.
Mexican Hydrogen Society

CONACYT

ITC

Photocatalytic Hydrogen Production under Visible Light over Magnesium Ferrite

V. Guzmán-Velderrain[1], M. Meléndez Zaragoza[1], E. Medina-Henandez[2], P. Gutiérrez Rivera[3], L. García Campos[1], Y. Ortega-López[1], J. Salinas Gutiérrez[1], A. López Ortiz[1], V. Collins-Martínez[1*]

[1]Centro de Investigación en Materiales Avanzados S. C., Laboratorio Nacional de Nanotecnología, Depto. de Materiales Nanoestructurados, Miguel de Cervantes 120, C. P. 31109, Chihuahua, Chih. México
[2]Universidad Autónoma de Chihuahua, Facultad de Ciencias Químicas, Campus Universitario # 2 C.P. 31125, Chihuahua, Chih, México
[3]Universidad Tecnología Junta de los Ríos, Carretera Aldama, Km 3, C. P. 31313, Chihuahua, Chih. México
. Tel: +52 (614)439 11 29 *e mail: virginia.collins@cimav.edu.mx

ABSTRACT

Magnesium ferrite ($MgFe_2O_4$) was synthesized by the hydrothermal technique and was found to be an active photocatalyst for hydrogen production from water under visible light. The structural, morphological, and optical properties of the material were characterized by powder XRD, SEM, TEM, and UV-Vis diffuse reflectance spectroscopy. Iron and magnesium aqueous nitrate solutions were used as precursors under hydrothermal conditions of 200 °C for 3.5 h. $MgFe_2O_4$ photocatalytic activity towards the H_2 production was determined by gas chromatography, using a batch-type quartz photoreactor and irradiated using a 250 W mercury lamp. XRD results from the synthesized sample found the $MgFe_2O_4$ crystalline structure. The optical properties revealed semiconducting properties with a band gap energy of 1.9 eV (653nm) showing an efficient visible light absorption. SEM images found particles with a morphology in the form of agglomerates composed of hemispherical particles, while TEM images revealed particles with an average of 9.3 nm in size. Furthermore, the solid exhibited a high photoactivity toward the reduction of water, which is attributed to the efficient separation and transportation of the photogenerated charge carriers. This ferrite material exhibited a production of 650 μmol $H_2/g_{catalyst}$ over an irradiation period of 8 h, thus exceeding the H_2 generation obtained by TiO_2, which was of 14 μmol $H_2/g_{catalyst}$. This increase in H_2 production is attributed to the fact that $MgFe_2O_4$ exhibits a band gap, which is activated under the visible light range.

Keywords: Hydrogen production, $MgFe_2O_4$, Water splitting

XIV International Congress of the Mexican Hydrogen Society
Cancun, Mexico, 2014

$KNbO_3$ as Photocatalyst for Hydrogen Production

M.A. Rodríguez-Villa[1,2], A. López-Ortiz[1], M.Y. Luna-Porres[1], K. Aguilar-Collins[1], J. Silva-Aceves[2], J. R. Farías-Mancilla[2], J. T. Elizalde-Galindo[2], V. Collins-Martínez[1,*]

[1]Centro de Investigación en Materiales Avanzados S. C., Laboratorio Nacional de Nanotecnología, Depto. de Materiales Nanoestructurados, Miguel de Cervantes 120, C. P. 31109, Chihuahua, Chih. México
[2]Universidad Autónoma de Ciudad Juárez, Ave. Plutarco Elías Calles, Alfa, C. P. 32317, Ciudad Juárez, Chih. México
. Tel: +52 (614)439 11 29 *e mail: virginia.collins@cimav.edu.mx

ABSTRACT

Semiconductor photocatalytic water splitting to produce hydrogen from solar energy has been considered as one of the most important approaches in achieving an energy based sustainable development. A large number of semiconductor materials have been proposed as photocatalysts for water splitting to hydrogen. The pervoskite-structure compounds have attracted wide attention over the past half a century. $MNbO_3$ (M = Li, Na or K) is a pervoskite oxide with unique physical and chemical properties such as low density, high sound velocity, photorefractive effect and photoactivity. These materials have presented remarkable photocatalytic activity for water splitting and environmental purification. Moreover, potassium niobate ($KNbO_3$) submicro-crystals were prepared by a soft chemical method and characterized by powder X-ray diffraction, nitrogen adsorption–desorption, diffuse reflectance UV–visible spectroscopy, and scanning electron microscopy. The photocatalytic performance was evaluated toward H_2 generation from an aqueous methanol solution (2%Vol) under UV and Vis light using a 250 W mercurial lamp as an irradiation source. XRD results found that synthesized $KNbO_3$ presented an orthorhombic rhombohedral phase. Crystallite size was estimated using the XRD data and the Debye-Scherrer equation, reaching ~43.4 nm. From UV–visible spectroscopy it was found that $KNbO_3$ exhibited a band gap energy of 2.98 eV. The BET surface area of the synthesized sample was 1.80 m^2/g. Photocatalytic activity of potassium niobate presented a hydrogen production of 350 µmol/$g_{catalyst}$ using a reactor loading of 200 mg of photocatalyst under a 5 h irradiation time. Results from this study indicate that $KNbO_3$ perovskite is potentially applicable for the production of H_2 through photocatalytic water splitting.

Keywords: $KNbO_3$; Hydrogen production; Photocatalysis

Sonochemical Synthesis of Pt/CNT/TiO_2 Anode Catalyst for Direct Methanol Fuel Cells

Z. I. Bedolla-Valdez[1,*], Y. Verde[2], Y. Gochi-Ponce[3], M. T. Oropeza-Guzman[4], G. Alonso-Núñez[1]

[1]Centro de Nanociencias y Nanotecnología-UNAM, Km. 107 carretera Tijuana-Ensenada, Ensenada, B. C., México, 22800.
[2]Instituto Tecnológico de Cancún, Av. Kábah Km. 3, Cancún, Q. Roo, México, 77500.
[3]Instituto Tecnológico de Oaxaca, Av. Ing. Víctor Bravo Ahuja 125, México, 68030.
[4]Centro de Investigaciones y Desarrollo Tecnológico en Electroquímica, Km. 126.4 carretera Tijuana-Tecate, Tijuana, B.C., México, 22253
[*]Tel: +526461750650 ext. 450; e-mail: zairabe@cnyn.unam.mx

ABSTRACT

Electrocatalytic materials are a major challenge for Direct Methanol Fuel Cells (DMFC) commercialization. To improve the properties of supported Pt anode catalysts several metal oxides are used to enhance the methanol oxidation performance [1-3]. Currently, titanium oxide is widely studied as electrocatalytic promoter due to its low cost and stability in acid media [1-3].

In this research, Pt/CNT/TiO_2 anode catalysts were prepared by a sonochemical method using a high-intensity probe during each synthesis step. In first instance, the system CNT/TiO_2 was synthesized at controlled temperature. Finally, 7 wt.% of Pt nanoparticles were incorporated to CNT/TiO_2 using $NaBH_4$ as a reducing agent . Pt/CNT and Pt/TiO_2 catalysts were prepared as reference samples.

The chemical composition of the systems was determined by ICP and EDS analysis. Structural properties and specific surface area of anode catalysts were examine by XRD and nitrogen adsorption by BET method, respectively. The electrochemical study was performed by cyclic voltammetry in a three-electrode half-cell at room temperature.

Pt/CNT/TiO_2 electrocatalysts were successfully synthesized by a short time synthesis method. The results of cyclic voltammetry test for methanol oxidation suggest that the incorporation of TiO_2 improves the catalyst tolerance to carbonaceous species. The Pt/CNT/TiO_2 anode catalyst exhibited better oxidation of methanol to carbon dioxide than Pt/CNT.

The authors acknowledge CONACyT project 174689 and PAPIIT IN104714.

Keywords: Carbon nanotubes; Titanium dioxide; Methanol oxidation

References

[1]W. Xiuyu, Z. Jingchang, Z. Hong, Chin. J. Catal., 32 (2011), 74-79.
[2]W. Wang, H. Wang, J. Key, V. Link, *et al.*, Ionics, 19 (2013), 529-534.
[3] P. Kolla, A. Smirnova, Int. J. Hydrogen Energy, (2013), 1-8.

Ordered Mesoporous Carbon Synthesized via Self-Assembly in Aqueous Phase as Support for ORR Pt Electrocatalyst

D. Morales-Acosta[1,2], F. J. Rodríguez-Varela[1,2]

[1] Grupo de Sustentabilidad de los Recursos Naturales y Energía, CINVESTAV-IPN, Unidad Saltillo, Av. Industria Metalúrgica 1062, Parque Industrial Ramos Arizpe. Ramos Arizpe, Coahuila, México, 25900.
[2] Programa de Nanociencias y Nanotecnología, CINVESTAV-IPN, Unidad Saltillo, México.
Phone: (844) 438-9600 ext. 8526
[*]E-mail: dmoralesacosta@gmail.com; javier.varela@cinvestav.edu.mx

ABSTRACT

Carbon-supported Pt or Pt-alloys are generally used as cathode electrocatalysts in Direct Oxidation Fuel Cells (DOFCs) in order to promote an enhancement of the oxygen reduction reaction (ORR) kinetics. Ordered Mesoporous Carbon (OMC) has received great attention to be used as support for fuel cell electrocatalysts due to its relatively large pores and high surface area, which allows a high concentration of catalytic active sites, facilitating the mass transport process. In this work, OMC has been synthesized via self-assembly in aqueous phase using a mixture of resorcinol/formaldehyde as carbon precursor. Afterwards, Pt/OMC electrocatalysts have been obtained by deposition of metal nanoparticles using the polyol reduction process. The materials have been characterized by BET, XRD and TEM analysis. The catalytic activity for the ORR of the Pt/OMC electrocatalysts has been evaluated by linear scan voltammetry under potenciodynamic conditions in acid media. The results have been compared with those obtained from a Pt/C (C=Vulcan) electrocatalysts synthesized by the same method. The effect of the home-developed OMC on the Pt structure and how the metal-support interaction influences its catalytic activity for the ORR has been evaluated. Structural characterization has revealed a BET surface area of OMC of nearly ~530 $m^2 g^{-1}$, while TEM studies of Pt/OMC have indicated a Pt particle size around 2.5 nm. The results have shown that the type of carbon support has a positive effect on the Pt particle size and that the specific activity of the Pt/OMC electrocatalysts is comparable to that of Pt/C.

Keywords: Ordered Mesoporous Carbon, Oxygen Reduction Reaction, Pt nanoparticles.

Sociedad Mexicana del Hidrógeno A. C.
Mexican Hydrogen Society

CONACYT

ITC

XIV International Congress of the Mexican Hydrogen Society
Cancun, Mexico, 2014

Bioelectricity from Recalcitrant Municipal Leachate in a Microbial Fuel Cell

A.L. Vázquez-Larios[a], H.M. Poggi-Varaldo[a]*, O. Solorza-Feria[b], M.T. Ponce-Noyola[c], R. de G. Gonzalez-Huerta[d], E. Ríos-Leal[c], N. Rinderknecht-Seijas[d]

[a] Environmental Biotechnology and Renewable Energies Group, Dept. Biotechnology and Bioengineering, CINVESTAV del IPN, P.O.Box 14-740, Mexico D.F., 07000, Mexico
[b] Dept. of Chemistry, CINVESTAV del IPN, P.O.Box 14-740, Mexico D.F., 07000, Mexico
[c] Dept. Biotechnology and Bioengineering, CINVESTAV del IPN, P.O.Box 14-740, Mexico D.F., 07000, Mexico
[d]ESIQIE-IPN, Mexico D.F., Mexico
*Author for correspondence, r4cepe@yahoo.com

ABSTRACT

The objective of this work was to evaluate the effect of several inocula on the treatment and bioelectricity production from municipal leachate in a two-face microbial fuel cell equipped with graphite flakes as anode and (*MFC-G*) and Pt as cathodic catalyst at a dose of 0.5 mg/cm^2 Pt. Inocula tested were: two enriched in Fe(III)-reducing bacteria (i.e., one was started with soil, *In-E*$_{Fe(III)-S}$, the other was started from a sulphate-reducing bioreactorn, *In-E*$_{Fe(III)-SR}$), one enriched in Mn(IV)-reducing bacteria (*In-E*$_{Mn(IV)}$), and a plain sulphate-reducing inoculum (*In-SR*).. Each face (I and II) of the *MFC-G* was characterized by separate, in series, and parallel connection. Parallel connection of faces increased the maximum volumetric power up to 14 954, 24 319, 28 112 and 28 113 mW/m^3 for the *In-SR*, *In-E*$_{Fe(III)-S}$, *In-E*$_{Fe(III)-SR}$ and *In-E*$_{Mn(III)}$ respectively. In general parallel connection of electrode faces significantly decreased the R_{int}. In the batch operation where the cells were connected to an external resistance of 100 Ω, the average volumetric powers $P_{V\text{-}ave}$ were 26 424, 25 548, 25 752 and 13 379 mW/m^3 for the *In-E*$_{Fe(III)-S}$, *In-E*$_{Fe(III)-SR}$, *In-E*$_{Mn(IV)}$, and *In-SR* respectively. The high $P_{V\text{-}ave}$ achieved in our work with enriched inocula could be attributed to the combined effects of increased concentrations of exoelectrogenic bacteria as well as the high total anodic surface area by the use of granular graphite. This, in turn, could have improved the electron transfer microbe-to-anode. The power values registered in this work (26 W/m^3) were in the range of power yields typical of the anaerobic digestion of municipal wastewaters (5 to 50 W/m^3). To the best of our knowledge, it is the first time that volumetric powers as high as 26 W/m^3 are reported in the treatment of recalcitrant, actual leachate in *MFC*. Our results constitute a firm step towards sustainable remediation of this problematic effluent.

Keywords: enriched inocula; leachate; microbial fuel cell

Sociedad Mexicana del Hidrógeno A. C.
Mexican Hydrogen Society

CONACYT

ITC

XIV International Congress of the Mexican Hydrogen Society
Cancun, Mexico, 2014

Effect of Type of Inoculum and Application of $Ru_xMo_ySe_z$ on Microbial Fuel Cell Performance

A.L. Vázquez-Larios[a], O. Solorza-Feria[b], H.M. Poggi-Varaldo[a*], M.T. Ponce-Noyola[c], R. de G. González-Huerta[d], E. Ríos-Leal[c], J. Barrera Cortés[c], José I. Tapia- Ramírez[e]

[a] Environmental Biotechnology and Renewable Energies Group, Dept. Biotechnology and Bioengineering, CINVESTAV del IPN, P.O.Box 14-740, Mexico D.F., 07000, Mexico
[b] Dept. of Chemistry, CINVESTAV del IPN, P.O.Box 14-740, Mexico D.F., 07000, Mexico
[c] Dept. Biotechnology and Bioengineering, CINVESTAV del IPN, P.O.Box 14-740, Mexico D.F., 07000, Mexico
[d] ESIQIE-IPN, Mexico D.F., Mexico
[e] Dept. Genetics and Molecular Biology, CINVESTAV del IPN, P.O.Box 14-740, Mexico D.F., 07000, Mexico
*Author for correspondence, r4cepe@yahoo.com

ABSTRACT

This research aimed at evaluating the effect of inoculum type and the application of $Ru_xMo_ySe_z$ as a cathode catalyst on the treatment and bioelectricity production of a microbial fuel cell fed with recalcitrant, municipal leachate. The device was an air-cathode, two-face microbial fuel cell fitted with graphite flakes as anodic material (*MFC-G*). The cathode was painted with $Ru_xMo_ySe_z$ at a dose of 0.5 mg/cm^2. The inocula assayed in our work were a plain sulphate-reducing inoculum (*In-SR*), an enrichment in Mn(IV)-reducing bacteria (*In-*$E_{Mn(IV)}$), and two enrichments in Fe(III)-reducing bacteria, namel, *In-*$E_{Fe(III)-S}$ and *In-*$E_{Fe(III)-SR}$.

Each face (I and II) of the *MFC-G* was characterized by separate (I and II), in series and parallel connection. We found that parallel connection of electrode faces lead to significantly lower values of the internal resistnace. In the batch operation where the cells were operated with the faces connected in parallel and loaded with an external resistance of 100 Ω, enrichment of the inocula had a significant, positive effect of cell performance. The average volumetric powers $P_{V\text{-}ave}$ observed were 4 376, 9 555, 11 249, and 13 303 mW/m^3 for the *In-SR*, *In-*$E_{Mn(IV)}$, *In-*$E_{Fe(III)-SR}$, and *In-*$E_{Fe(III)-S}$, respectively. The high $P_{V\text{-}ave}$ registered with the enriched inocula in our work could be attributed to the synergism of increased concentrations of exoelectrogenic bacteria as well as the high total anodic surface area by the use of granular graphite that could have facilitated the electron transport to the anode. The first issue was confirmed by molecular characterization of enriched inocula. In general, values of $P_{V\text{-}ave}$ obtained with the chalcogenide catalyst were 30-40% lower than those registered with Pt catalyst. Yet, the cost of the chalcogenide is 80% lower than that of platinum. We conclude that the application of inocula enriched in Fe(III) and Mn (IV)-reducing bacteria significantly improved the performance of cells that used $Ru_xMo_ySe_z$ as a cathodic catalyst for the ORR

Keywords: $Ru_xMo_ySe_z$ cathodic catalyst, leachate, microbial fuel cell, enriched inocula

Control of Agitation and Temperature of a Reactor for Biodiesel Production.

P. Navarro[1], J. Ramirez[1], M. Sanchez[1].

[1]Universidad Politécnica de Aguascalientes, Calle Paseo, San Gerardo, 207, 20342, Aguascalientes, Ags., México, 20342.
Tel: +524494421400; e-mail: perla_navarro@live.com.mx

ABSTRACT

A control system embodying the hydrodeoxygenation reaction of first generation biodiesel in a reactor containing the conditions of pressure and operating temperature to obtain a biofuel. The temperature control system can work so as to contain the features that are required to work to keep the biodiesel temperature to 450 ° C. Circuit in which you conditioned temperature sensors to capture the temperature conditions in the reactor is to send this information to a "$PIC18F4550_1$" programmed "assembly" language that receives sensor data was used to maintain the temperature to 450 ° C. By stirring system used as a single-phase induction motor, with horsepower ¼ which is conditioned a capacitor for starting, and a circuit built with solid state switches "Transistors", since their lifetimes and frequencies switching are much higher. Moreover the switches are associated with diodes connected to them in parallel to allow the currents circulating in the opposite direction that is provided each time the voltage is switched, since the motor comprises windings for a short period of time it will oppose the current varies, plus a power implementing "$LM317_2$" and capacitors to achieve the engine start half turns so you can get the 20 bar hydrogen to which biodiesel is maintained conditioned.

Keywords: $PIC18F4550_1$: Microcontroler; $LM317_2$: adjustable voltage regulator three terminal.

Sociedad Mexicana del Hidrógeno A. C.
Mexican Hydrogen Society

CONACYT

ITC

Study of Electrocatalysts for the ORR Based on Nanocomposites of Polypyrrole-$CoSe_2$ Supported on Nitrogen-Doped Graphene

I.J. García R.[a,*], M.A. Smit[a], N. Alonso-Vante[b], Y. Verde-Gómez[c]

[a] *Centro de Investigación Científica de Yucatán (CICY), Calle 43 No. 130, Col. Chuburná de Hidalgo, 97200 Mérida, Yucatán, México.*
[b] *IC2MP, UMR-CNRS 7285, University of Poitiers, 4 rue Michel Brunet, 86022 Poitiers, France.*
[c] *Instituto Tecnológico de Cancún, Av. Kabah km. 3, 77500 Cancún, Q. Roo, México.*
**e-mail: ismag@cicy.mx*

ABSTRACT

The cathodic oxygen reduction reaction (ORR) is key and an important factor in the performance of low-temperature fuel cell (PEMFC), since a major voltage loss takes place at the cathode. The use of traditional, high cost, platinum-based catalytic materials is one of the barriers for successful large-scale introduction of PEMFC in the energy market. An interest exists in developing alternative catalytic materials.

In this project a novel catalytic material is proposed. First, graphite oxide was prepared by a modified Brodie's method and then treated with thermal reduction and surface nitrogen doping. The treatment consisted of synthesizing polypyrrole nanoparticles, as the nitrogen source, by chemical polymerization on the graphite oxide surface, which then was thermally treated under argon atmosphere over a period of time at high temperatures.

Cobalt-Selenium ($CoSe_2$) is proposed as the metal catalyst to further increase ORR activity. Polypyrrole nanoparticles synthesized by chemical polymerization on the nitrogen doped graphene with a specific proportion (ca. 12 wt%), is expected to aid the ORR activity in the composite.

The nitrogen doping proposed for the catalyst support showed an increase in ORR activity, with no further modifications, during the cyclic voltammetry (CV) experiments, indicating that the doping was successful. X-Ray Diffraction (XRD) showed that the (002) carbon peak for the graphite oxide was displaced to lower 2-theta angles as compared to its graphite precursor, an evidence for the successful addition of oxygen groups on the graphite inter-laminar surface. SEM and EDX analyses also showed the reduction of oxygen content after doping with nitrogen and a morphology indicative of exfoliated graphene sheets. Additionally BET analysis showed an increase in surface area for the catalyst support after the nitrogen doping and thermal reduction.

Keywords: ORR; Graphene; Nitrogen doping.

Full Papers

Behavior of ionic species in sulfonated PEI using DFT simulations: A study to determine ionic conductivity

E. López-Chávez*[1], Y. Peña-Castañeda[1], J. Martínez-Magadán[2], G. González-García[1], F. Castillo-Alvarado[3], J. Díaz-Góngora[4]

[1] Colegio de Ciencia y Tecnología de la Universidad Autónoma de la Ciudad de México, Av. Fray Servando Teresa de Mier 92-110. Col. Centro. México D.F. 06080. México.

[2] Programa de Ingeniería Molecular, Instituto Mexicano del Petróleo, Eje Central Lázaro Cárdenas Norte 152, Col. San Bartolo Atepehuacán, Deleg. Gustavo A. Madero, México. D.F. 07730. México.

[3] Escuela Superior de Física y Matemáticas del Instituto Politécnico Nacional, Unidad Profesional Adolfo López Mateos. Col. Lindavista. Deleg. Gustavo A. Madero. México, D. F., 07738. México.

[4] Centro de Investigación en Ciencia Aplicada y Tecnología Avanzada, Instituto Politécnico Nacional, Legaria 694, Col Irrigación. Deleg. Miguel Hidalgo, 11500 Ciudad de México, Distrito Federal.

ABSTRACT

Compared with internal combustion engines, proton exchange fuel cells (PEMFC) are able to operate without polluting emissions. Increasing the operating temperature of the fuel cell above 100 º C is one of the major objectives in this field as it would facilitate the commercial development of electric vehicles powered by fuel cells. To achieve this objective, it is important to develop new types of membranes to replace Nafion®. The poly (ether imide) sulfonated are presented as a new alternative in order to use as an electrolyte in PEMFC. In this work, DFT theory has been used to study the interaction between ionic species charged of hydrogen as hydroxyl ($(OH)^-$) or hydronium ($(H3O)^+$) and sulfonated poly (ether imide). The analysis of molecular reactivity through frontier MO (HOMO and LUMO) allows determine the mechanism of ionic conductivity which takes place over the polymeric membrane. This study is addressed to improve the efficient of PEM fuel cells.

Keywords: Ion conductivity, DFT Theory, sulfonated poly (ether imide)

*Corresponding autor: email: elopezc_h@hotmail.com

1. Introduction

The polymer exchange membrane (PEM) is the heart of the fuel cell. Based on the research, it has been determined that protonic exchange membrane fuel cell (PEMFC) has a huge variety of applications like: portable, mobile and stationary power [1-4].

Because of their importance new polymers st**r**uctures have been studied with the promise of enhance the disadvantages that the membrane perfluorosulfonic acid called Nafion® does have. New proposals are, **sulfonated poly(arylene ether sulfone)s**[5-6], **poly(**arylene ether ketone)s[7], **poly(arylene** ether) [8], polyimides[9-12], polyphosphazenes[13], chitosan[14], polybenzimidazoles[15] and other polymers[16-17].

All the materials proposed for the development of PEM must have a high protonic conductivity, and, at the same time must avoid the electron transport through of its structure. A high chemical, mechanical and thermal stability are required in conditions of operation of the PEMFC [18].

In a previous work, we proposed polymers based on sulfonated ether imide (SPEI) with sulfonic groups different ($(SO_3H)\,n \quad n = 1, \ldots, 6$) [19-21]. These sulfonic groups at the matrix of the SPEI provide charge sites that produced and guided the ionic species as hydronium $(H_3O)^+$ and hydroxyl $(OH)^-$ in its conduction throughout membrane. The SPEI have been studied both theoretical and experimental, they were found to have chemical, mechanical and thermically stable and these became themselves in a perfect candidate for development of the PEMFC's with properties equals or better than Nafion®[22-23].

In this paper, we present some theoretical results regarding the behavior between ionic species and the SPEI's. These results give us information about the intermolecular interactions like van der Waals, ionic and electrostatic interaction which determine the mechanism of ionic conductivity throughout membrane. The Mulliken population analysis is an important factor to charge sites localized in the membranes that guide some species with hydrogen charge.

Finally, results give us information about which chemical structure will do much better the protonic conductivity in order to improve the efficiency of PEMFC's.

2. Methodology and computational details

Both computational simulations and theoretical studies of the mechanism of the protonic conductivity in a lot of membranes have been studied for many scientific groups into different research centers[24-27] .The polymers based on sulfonated ether imide (SPEI) with sulfonic groups are the structures that we proposed to develop proton exchange membranes.

For the study of interaction between SPEI and ionic species, we took one after another the polymers sulfonated, then, we obtained their frontier orbitals HOMO-LUMO. Subsequently, the hydronium molecule was placed near the highest occupied molecular orbital of each SPEI and hydroxyl molecule was putted close to the lowest unoccupied molecular orbital of each SPEI.

When the ionic structures were put, the geometry optimization took place. We used the Denstiy Functional Theory (DFT) with general gradient approximation (GGA) of Perdew and Wang PW91 and DFT semi-core pseudopotentials as approximation for treating core electrons, the DPN (double numerical plus polarization) atomic orbital basis set was used in the calculation [28-29].

In order to determine the stability and the grade of the reactivity for each group (between each ionic specie and each SPEI), we calculated HOMO and LUMO energy differences for each single molecule, E_{LUMO}-E_{HOMO} terms and between pairs of molecules E_{LUMO} (ionic species)- E_{HOMO} (SPEI's) and conversely.

To obtain another parameter that confirm us the chemical interactions, we calculated the Mulliken population analysis [30-32]

3. Results and discussion

As mentioned above, in general Membrane is the core component of the PEM fuel cell. Triple roles of the polymeric membrane in the PEM fuel cells are as follows: charge carrier for protons, to separate of the reactant gases, and electronic insulator for not passing of electrons through the membrane (due to have a negative charge from SO_3H and electron repelling).

In this work, chemical reactivity was studied in terms of frontier orbital HOMO-LUMO between each SPEI and ionic species. In Figure 1, the frontier orbitals of each SPEI are presented in conjunction with energy corresponding. For each SPEI these frontier orbitals are built from sulfur 3p, carbon 2p, nitrogen 2p and oxygen 2p atomic orbitals; thus, the corresponding molecular orbital type is the type pπ.

From Figure 1, we can observed, for polymers from 1 to 4 sulphonyl groups, the HOMO orbital is bonding-type, while polymers with 5 and 6 sulfonyl groups is antibonding-type. The lowest unoccupied molecular orbital is antibonding for all SPEI's. Hybridization of the ionic species is sp^2 y sp^3 for the hydroxyl and hydronium respectively; based on hybridization,both ions have σ-type molecular orbitals. Since the LUMO antibonding character in all cases of the polymers, it appears that this region is suitable for interacting with the ionic species and promote the proton conduction.

SPEI_1

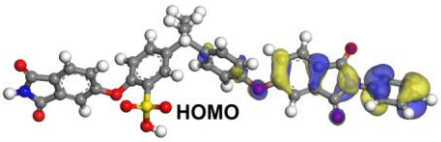

E= -5.843 eV

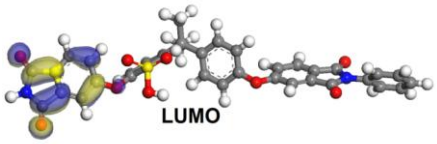

E= -3.245 eV

SPEI_2

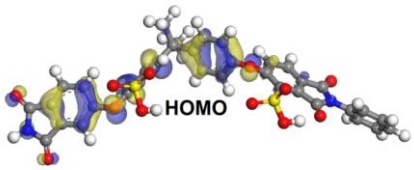

E= -5.053 eV

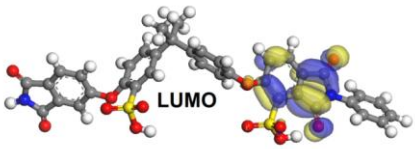

E= -4.052 eV

SPEI_3

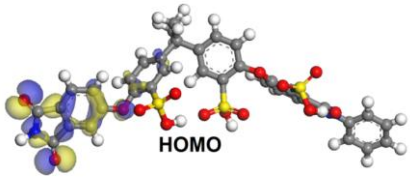

E= -5.080 eV

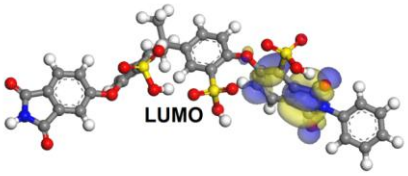

E= -4.049 eV

SPEI_4

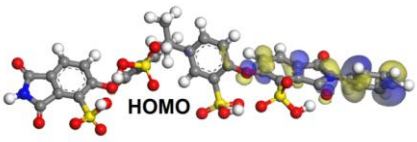

E= -5.295 eV

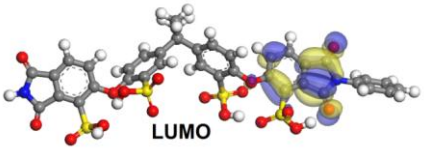

E= -4.443 eV

SPEI_5

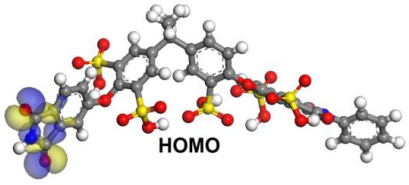

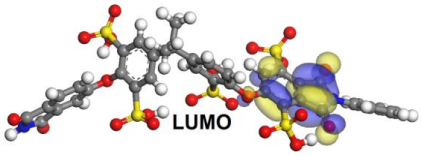

E= -5.356 eV

E= -4.508 eV

SPEI_6

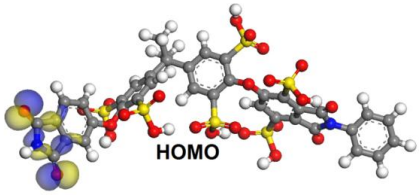

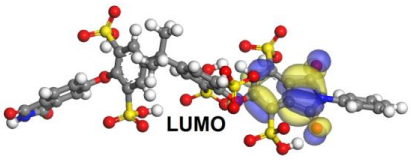

E= -5.350 eV

E= -4.508 eV

Figure1. Frontier molecular orbital of SPEI

HOMO and LUMO orbitals for the hydroxyl and hydronium are plotted in Figure 2. The forms of these frontier orbitals illustrate type bonds in each molecule, these are σ bonds. Both HOMO-LUMO for hydroxyl turn out to be antibonding σ bonds, this indicate that hydroxyl will have low reactivity with each SPEI, therefore, the interactions determining hydroxyl mobility inside of each SPEI will be electrostatic-type or Van der Waals-type; this characteristic is an indication that, at a molecular level, the ionic transport of hydroxyl in the hydrated polymeric matrices is in general is a vehicular mechanism. In this mechanism ion $(OH)^-$ diffuses through the aqueous medium in response to the electrochemical difference. In vehicular mechanism, the water connected ions in the result of the electroosmotic drag carry the one or more molecules of water through the membrane and itself are transferred with them [33].

HOMO for hydronium is antibonding while LUMO is bonding σ-type, this characteristic favors the mechanism "proton hopping" or "Grotthus mechanism" type, since, in proton hopping mechanism, protons hop from one hydrolyzed ionic site ($(SO_3)^-$, $(H_3O)^+$) to another across the membrane. The produced proton by oxidation of hydrogen in anode adheres to water molecule than the provisional hydronium ion is

formed and one different proton from same hydronium ion hops on the other water molecule. In this mechanism, ionic clusters were swelled in presence of water and formed the percolation mechanism for proton transferring. The simple scheme of the hydronium hopping mechanism has been shown in Figure 3[34].

To have an indicator of the interaction between the SPEI and ionic species, were calculated the energy differences between pairs $E_{LUMO}(hidronio) - E_{HOMO}(SPEI_n)$ y $E_{LUMO}(hidroxilo) - E_{HOMO}(SPEI_n)$ and viceverza. They are specified in Table 1.

Table1. Energy differences (in eV) among LUMO and HOMO for pairs of molecules

Molecule	E_{LUMO}(Hydronium)-E_{HOMO}(SPEI)	E_{LUMO}(Hydroxyl)-E_{HOMO}(SPEI)	E_{LUMO}(SPEI)-E_{HOMO}(Hydronium)	E_{LUMO}(SPEI)-E_{HOMO}(Hydroxyl)
SPEI_1	-2.083	15.949	10.898	-10.441
SPEI_2	-2.873	15.159	10.091	-11.248
SPEI_3	-2.846	15.186	10.094	-11.245
SPEI_4	-2.631	15.401	10.012	-11.327
SPEI_5	-2.570	15.462	9.635	-11.704
SPEI_6	-2.576	15.456	9.7	-11.639

Hydroxyl

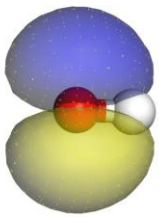

HOMO

E= 71.96 eV

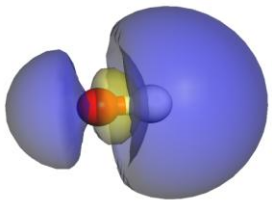

LUMO

E= 10.106 eV

Hydronium

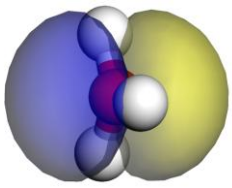

HOMO

E= -14.143 eV

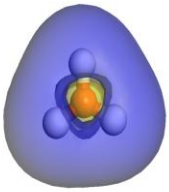

LUMO

E= -79.26 eV

Figure2. Frontier molecular orbital for ionic species

According to the results of Table 1, for that an electron is transferred from the hydroxyl at SPEI must release a large amount of energy of about 11 eV which would require very strong collisions between hydroxyl and SPEI, while it is required very high energies, around 15 eV, to excite an electron from the hydroxyl to SPEI. This indicates that there is little possibility that the hydroxyl and SPEI can form chemical bond, which favors the diffusion mechanism of the hydroxyl in the membrane, as mentioned above.

Moreover, in Table 1, we can see that the hydronium have greater difficulty in moving through the membrane because the released energy for transfer an electron from the SPEI to this ionic specie is relatively low, about 2 eV, so that there is some likelihood of the ionic specie form a chemical bond with SPEI so that the hydronium be anchored in the membrane structure. However, the interaction will not be so strong, because the electron require high relatively energy, at least 10 eV, to be transferred from hydronium to SPEI, so there is the probability that a hydrogen atom is apparent from the hydronium and this could lead to proton conduction type "proton hopping" or "Grotthus mechanism" that is consistent with those found in the analysis of the frontier orbitals.

Based on these results, we carried out a qualitative analysis of the mechanism of ion conductivity of hydronium inside different SPEI. For this, the hydronium was placed close LUMO of each SPEI, then the geometry optimization was performed. The final state of interactions hydronium-SPEIs is seen in Figure 3. In this figure, dipole-dipole interactions and electrostatic interactions at the final state of interactions hydronium-SPEI's are too observed.

For the polymer with a group SO_3H (Figure 3a) shows that because the nitrogen atom is more electronegative than hydrogen atom H_3, it gives up electron and consequently N atom attracts H_3.

In Figure 3b (SPEI_2), we observe an interesting effect: as a result of the different interactions between hydronium and SPEI_2, the atom H_3 is attracted to the atom O_2 because it has the same feature that the nitrogen atom, under this process, H_3 belongs to the sulfonyl group, and, in turn the hydrogen atom H_4 is detached from sulfonyl group and attracted to the atom O_3. Similar process occurs in Figures 3c and 3d (SPEI_3 and SPEI_5 respectively).

In SPEI_4 (Figure 3e) follows the same mechanism, the difference is the involvement of two groups SO_3H. In the three cases we have a good indication that the conduction mechanism is much closer to the type of mechanism Grotthus, as predicted above.

In Figure 3f a C_1-S_1 bond break is observed and no detachment of atoms from hydronium.

Table 2 contains information on atomic charges distribution on atoms indicate in figure 3 corresponding to the initial and final states of the optimization, since this quantity is not only an index of ionicity of a bond,

but can also be considered as an index of reactivity when charged species are involved in a chemical process like the one we are studying here. The mechanism of chemisorption and further breaking is revealed from both Mulliken electron population on atoms [32] (Table 2) and the analysis of interaction of frontier orbital HOMO-LUMO between hydronium and SPEI (Figure 3)

3a. SPEI_1 y H_3O^+

3b. SPEI_2 y H_3O^+

3c. SPEI_3 y H_3O^+

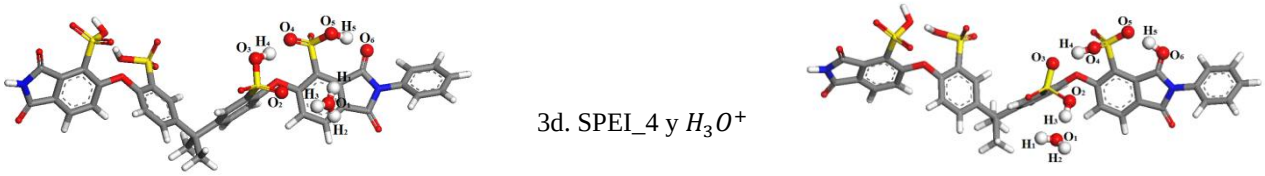

3d. SPEI_4 y H_3O^+

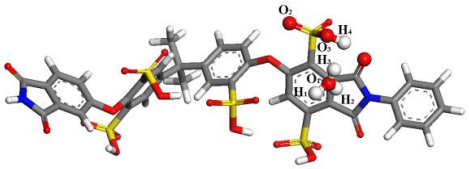

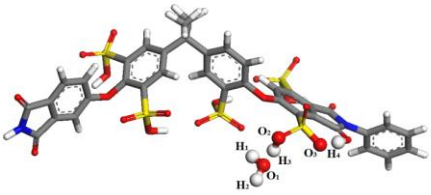

3e. SPEI_5 y H_3O^+

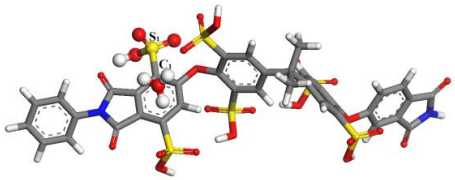

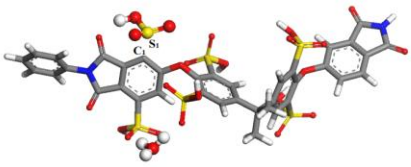

3f. SPEI_6 y H_3O^+

Figure 3.Interaction between ion hydronioum with each SPEI's

Table2. Charge distribution on atoms of figure 3

atom SPEI_1	Initial State (e)	Final State (e)
H_1	0.357	0.326
H_2	0.369	0.326
H_3	0.224	0.373
H_4	0.284	0.302
O_1	-0.275	-0.595
N	0.351	-0.543

atom SPEI_2	Initial State (e)	Final State (e)
H_1	0.243	0.328
H_2	0.349	0.326
H_3	0.378	0.398
H_4	0.366	0.379
O_1	-0.197	-0.576
O_2	-0.461	-0.582
O_3	-0.471	-0.401

atom SPEI_3	Initial State (e)	Final State (e)
H_1	0.315	0.341
H_2	0.331	0.324
H_3	0.364	0.386
H_4	0.366	0.377
O_1	-0.335	-0.589
O_2	-0.415	-0.418
O_3	-0.461	-0.517

atom SPEI_4	Initial State (e)	Final State (e)
H_1	0.212	0.325
H_2	0.327	0.319
H_3	0.342	0.357
H_4	0.353	0.367
H_5	0.375	0.377
O_1	-0.255	-0.580
O_2	-0.484	-0.460
O_3	-0.396	-0.385
O_4	-0.434	-0.385
O_5	-0.422	-0.505
O_6	-0.463	-0.386

atom SPEI_5	Initial State (e)	Final State (e)
H_1	0.250	0.337
H_2	0.344	0.326
H_3	0.351	0.389
H_4	0.357	0.376
O_1	-0.173	-0.587
O_2	-0.456	-0.417
O_3	-0.487	-0.512

Conclusion

Theoretical studies based on density functional theory provide valuable information on mechanism of proton conductivity in sulfonated poly (ether imide). Our results indicate that the hydroxyl presents a vehicular mechanism. In this mechanism ion $(OH)^-$ diffuses through the aqueous medium in response to the electrochemical difference. In this vehicular mechanism, we can infer that the water may connect ions in the result of the electroosmotic drag carry the one or more molecules of water through the membrane and itself are transferred with them. On other hand, proton specie $(H_3O)^+$ meets all of the features to perform a mechanism of proton transport "proton hopping" or "Grotthus mechanism" since the results of this study show the detachment of hydrogen atoms from the hydronium and other hydrogen hop from one hydrolyzed ionic site to another across the sulfonated poly(ether imide). These results show that sulfonated poly (ether imide) is a promising material for development of proton exchange polymeric membranes.

Acknowledgements

We greatly acknowledge the financial support provided by the SECITI and UACM by 060/2013 agreement through PI2011-23R project. We also acknowledge to CONACyT – Mexico and to Sistema Nacional de Investigadores.

References

[1] S.J. Peighambardoust, S. Rowshanzamir, M. Amjadi, International Journal of Hydrogen Energy, 35 (2010).

[2]K. D. Kreuer, Chem Mater, 8 (1996)

[3]S. Gottesfeld, T. A. Zawodzinski, Advances in electrochemical science and engineering, Winheim:Wiley/VCH, New York (1994)

[4]B. Smitha, S. Sridhar, A. A. Khan, J Membr Sci, 259 (2005)

[5] F. Wang, M. Hickner, Y.S. Kim, T. A. Zawodzinski, J. E. McGrath, J. Membr Sci 197 (2002)

[6] K. Miyatake Y. Chikashige, E. Higuchi, M. Watanabe, J Am Chem Soc 129 (2007)

[7] T. Mikami, K. Miyatake, M. Watanabe, ACS Appl Mater Interfaces, 2 (2010)

[8] K. Miyatake, Y. Chikashige, M. Watanabe, Macromolecules 36 (2003)

[9] Y. Yin, J. H. Fang, T. Watari, K. Tanaka, H. Kita, K. Okamoto, J Mater Chem 14,6 (2004)

[10] S. Chen, Y. Yin, H. Kita, K. I. Okamoto, J Poly Sci Part a Poly Chem, 45 (2007)

[11] N. Asano, M. Aoki, S. Suzuki, K. Miyatake, H. Uchida, M Watanabe, J Am Chem Soc 128 (2006)

[12] S. Li, X. Zhi, Y. Qian, S. Hang, W. Shu, X. You J Appl Polym Sci, 92 (2004)

[13] D. Meng, G. K. Sangamesh, W. Yuging, S. T. Udaya, R. A. Harry, T. L. Cato, Soft Matter, 6 (2010)

[14] Y. Zhao, Z. Jiang, L. Xiao, T. Xu, S. Qiao, H. Wu, Solid State Ionics 187, 1 (2011)

[15] L. Qingfeng, O. Jens, F. S. Robert, J. B. Niels, Prog Polym Sci, 34 (2009)

[16]Z. Javaid, T. Matsuura, Polymer membrane for fuel cells, Springer, New York (2009)

[17]Z. Shuangling, C. Xuejun, F. Tiezhu, N. Hui, J Power Sourc, 180, (2008)

[18]T.Higashihara, K. Matsumoto, M. Ueda, Polymer, 50 (2009)

[19]B. Peres, L. Santa Mariam M. Sena, Mater Lett, 61 (2007)

[20]S. Yao, C. Fu T. Wen, C. Jing, G. Chunli, W. Sheng, J Appl Polym Sci, 107, 5 (2008)

[21]C. S. Fu, T. Wen, C. Jing, G. Chunli, W. Sheng, J Appl Polym Sci, 108 (2008)

[22]P. C. Rieke, N. E. Vanderborgh, Journal of Membrane Science, 32 (1987)

[23]S. C. Yeo, A. Eisenberg, Journal of Appl Polym Sci, 21 (1977)

[24]J. Ennari, I. Neelov, F.Sundholm, Polymer, 42 (2001)

[25]J. Ennari, L. Pietilä, V. Virkkunen, F. Sundholm, Polymer, 43 (2002)

[26] E. López, J. M. Magadán, R. Oviedo, J. Guzmán, J. Ramírez, J. Marín, Polymer, 46 (2005)

[27]E. López, R. Oviedo, G. Contreras, J. Martínez, F. Castillo, International Journal of Hydrogen Energy, 35, 21 (2010)

[28]J. M. Martínez, R. Oviedo, P. García, R. Martínez, Fuel Processing Technology, 97 (2012)

[29] R. Oviedo, J. M. Magadán, F. Illas, The journal of Physics Chemistry B, 110 (2010)

[30]C. Gruber, V. Buss, Chemosphere, 19, (1989)

[31]J. N. Murrell, S. F. Kettle, J. M. Tedder, The Chemical Bond, John Wiley & Sons, Chichester (1985)

[32]R. S. Mulliken, Journal of Chemical Physics, 23 (1955)

[33] K. D. Kreuer, S. J. Paddison, E. Spohr, M. Schuter, Chem Rev, 104 (2004)

[34] N. W. Deluca, Y. A. Elabd, J Polym Sci Part B Polym Phys, 44 (2006)

Theoretical Methodology for Calculating Water Uptake and IEC Parameters of Ionic Exchange Membranes with Applications in Fuel Cells

E. López-Chávez[*a], Y. Peña-Castañeda[a], G. González-García[a], P. Perales-Enciso[b], A. García-Quiroz[a], J. Irán Díaz-Góngora[c]

[a]*Colegio de Ciencia y Tecnología de la Universidad Autónoma de la Ciudad de México. Av. Fray Servando Teresa de Mier 92. Col. Centro. México. D. F, 06080. México.*

[b]*Ingeniería en Sistemas de Transporte Urbano de la Universidad Autónoma de la Ciudad de México. Av. Fray Servando Teresa de Mier 92. Col. Centro. México. D. F, 06080. México.*

[c]*Centro de Investigación en Ciencia Aplicada y Tecnología Avanzada del InstitutoPolitécnico Nacional. Legaria 694, Col Irrigación, Miguel Hidalgo, 11500 Ciudad de México, Distrito Federal, Mexico.*

ABSTRACT

The water uptake (WU) and ion exchange capacity (IEC) are two important parameters for PEMs, which represent their water retention and the proportion of exchangeable protons in the membrane, respectively. According to the vehicle mechanism of proton transport, an appropriate amount of water content and and a suitable value of IEC in PEMs is necessary for achieving high proton conductivity. In this work, studies based on Density Functional Theory (DFT), Molecular Mechanics and Dynamics Simulations were realized in order to develop a theoretical methodology to obtain water uptake and ionic exchange capacity parameters. Unlike other methods, our proposal considers the molecular structure of the monomers of the membrane, the solvation medium and the various interactions between the monomer and water molecules. The methodology is applied to structures of sulfonated poly (ether-imide) (SPEI) with $(-SO_3H)_n$ (n=1,…6) groups. These structures were built and optimized aiming to obtain above properties as a function of the number of sulfonyl groups. The comparative study demonstrates that the SPEI with four sulfonyl groups in its backbone is the polymer having better properties for successful operation in fuel cells.

Keywords: Sulfonation, Poly (ether-imide), polymers.

*Corresponding autor: email: elopezc_h@hotmail.com

1. Introduction

Polyelectrolyte membranes have been extensively investigated lately due to their potential applications in different types of electrochemical devices such as ion conducting membranes in fuel cells [1]. Since years ago, polymer electrolyte membrane fuel cells (PEMFCs) are regarded as a source of clean energy because of features such as high efficiency, high energy density, and environmental friendliness [2]. The perfluorinated sulfonic acid membrane, which is known as DuPont™ Nafion®, has been used for years as electrolyte in PEMFC. However, despite great successes with this membrane, it presents many disadvantages during the operation mechanism of the PEMFC [3], and besides they are expensive.

Hydrogen and fuel cells technology is facing three main challenges related to new polymeric materials for membranes: reducing the high cost of production, increasing durability and chemical and mechanical stability at temperatures above 100 ºC, and improving proton conductivity at temperatures above 120 ºC.

Nowadays, many efforts are being directed towards developing new non-DuPont™ Nafion® electrolyte polymers, possessing excellent overall properties in order to build proton exchange membranes for fuel cell [4]. However, most of the efforts have been focused on the experimental developments, thereby neglecting the development of theoretical methods. A theoretical methodology is necessary, since it could significantly contribute to guide the experimental work, which would reduce the experimental time and resource savings. Some of the main problems that the ionic membranes, for use in PEM cells, have presented are the low proton conductivity at low relative humidity and the low mechanical properties at high temperatures and humidities. Ion conduction is a thermally activated process and its magnitude varies dramatically from one material to the other. The type of electrolyte, which may be either liquid or solid, determines the temperature at which the fuel cell may be operated. The main limitation to obtain a polymeric material with a high value of conductivity at high temperatures is necessary to maintain the polymeric membrane hydrated, since their ionic conductivity increase [5-17]. Two of the parameters which determine and predict the proton conductivity of the membrane are water uptake (WU) and ion exchange capacity (IEC). The rapid increase in computing resources and the progress in software offer new possibilities to rapidly gain new information from molecular modeling and simulation of the conductivity phenomena.

In the present approach, studies based on Density Functional Theory (DFT), Molecular Mechanics and Dynamics Simulations were realized in order to develop a theoretical methodology to obtain water uptake and ionic exchange capacity parameters. The methodology was applied to structures of sulfonated poly (ether-imide) (SPEI) with $(-SO_3H)_n$ (n=1,…6) groups. Poly (ether imide)s modified by sulfonation are particularly interesting as PEMs because the sulfonide groups $(-SO_3H)_n$ show good water retention and excellent adhesive ability with polymides and inorganic materials [18-22]. These structures were built and optimized aiming to obtain above properties as a function of the number of sulfonyl groups.

Our theoretical results are in good agreement with experimental values reported in literature for similar structures to those studied here [23, 24].

2. Methodology and computational details

Repeat unit structure of poly(ether imide) (Ultem-type), Figure 1, was used in this work in order to build molecular computer models of sulfonated poly(ether imide), PEI–$(SO_3H)_n$, n = 1, 2, 3, 4, 5, 6. Once the structures were built, it is necessary to carry out the geometry optimization or energy minimization since after they have been sketched, they are often in high energy configurations. Starting dynamics simulations from such unoptimized structures can lead to simulations of systems at temperatures much higher than room temperature. In this work three aspects were considered to select a geometry optimization method and quality level: system size, convergence threshold and basis set used. In this study, the calculations were carried out using functional GGA PW91, DFT semi-core pseudopotentials as approximation for treatment of core electrons. This treatment replaces core electrons by a single effective potential, reducing the computational cost; the DNP (Double Numerical plus polarization) atomic orbital basis set was used in the calculation. In order to obtain structural, vibrational, reactivity, selectivity and thermodynamics properties of each PEI–$(SO_3H)_n$, the following computational scheme was performed: (a) building of the structures, (b) determination of the lowest energy structure of each structure, and (c) calculation of physical properties.

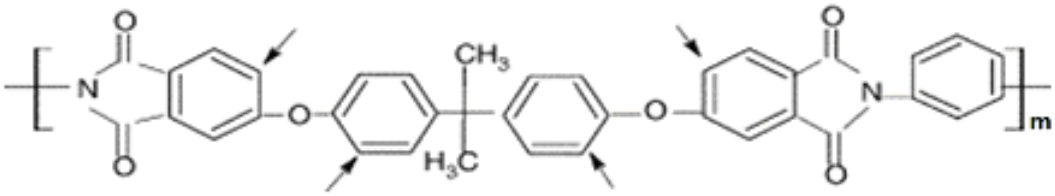

Figure 1. Backbone of repeat unit structure of poly(ether imide). Arrows indicate sites where sulfonyl groups are inserted

The next step was to obtain properties of water uptake and ion exchange capacity (IEC) of each polymer SPEI. The simulated water uptake was calculated using the following equation:

$$\text{Water uptake} = \frac{W_{\text{wet}} - W_{\text{dry}}}{W_{\text{dry}}} \times 100 \qquad (1)$$

where, W_{wet} and W_{dry} are molecular weight of wetted and dried polymers, respectively. The IEC is the equivalents per gram of dry polymer, and it can be calculated using the following equation:

$$\lambda = \frac{\text{Water uptake}}{18 \times \text{IEC}} \qquad (2)$$

where 18 is the molecular weight of water and λ is the number of water molecules per sulfonic group.

The λ parameter was calculated using computational simulation following the next procedure: for each SPEI, a 3D simulation cell containing a single SPEI molecule was built by using the interface of Materials Studio (MS) from Accelrys Inc [28]. Each simulation cell was first minimized through molecular mechanics using the steepest-descents method up to 10,000 steps and using the Compass forcefield, as included in the MS Discover module. Then, water molecules were added, one by one to each simulation cell and the minimization process was repeated until it is found the hydrated cell possessing the lowest energy, being the number of water molecules at this step the value of λ parameter.

In order to obtain molecular weight and water uptake for each SPEI, molecular dynamics was carried out in two stages: equilibration and production. The duration of each stage depends on the system, as well as on the purpose of the run. The purpose of equilibration stage is to lead the system to the most probable configuration consistent with the target temperature and pressure, obtaining in this way the cell density. Equilibration stage was carried out using an NPT ensemble with a target temperature of 298 K, and an external hydrostatic pressure of 0 GPa (i.e., the simulation cell is not under compression). The time step was 1 fs and total simulation duration time was 30,000 fs. Integration method used in this process was Velocity Verlet method [29]. After equilibrating the system, we setup the production stage, during which data and statistics are collected. The molecular dynamics during the production stage was made using the NVT ensemble and the Berendsen method [30] for temperature control. The temperature used was 298 K. Simulation duration time was 80,000.00 fs. We use the automatic method of calculating charges from COMPASS forcefield [31, 32].

Once MD simulations were made, the cell volume V_P and the density of each polymer SPEI (ρ), were then estimated. The molar volume V_M and the molecular weight W for (both wet and dry) models were obtained as follows [33]:

$$V_M = N_A V_P \qquad (3)$$

$$W = \rho V_M \qquad (4)$$

where N_A is Avogadro number.

3. Results and discussion

3.1Geometry structural properties and stability

The chemical structures of minimum energy for each simulated SPEI, along with atom numbering, are showed in Figure 2. These structures are constituted by a combination that had both polyimide and polyether units in the backbone. SPEIs were obtained by sulfonation of the PEIs on the electron-rich benzene rings.

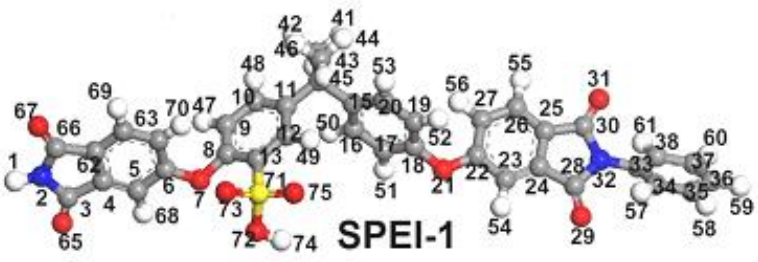

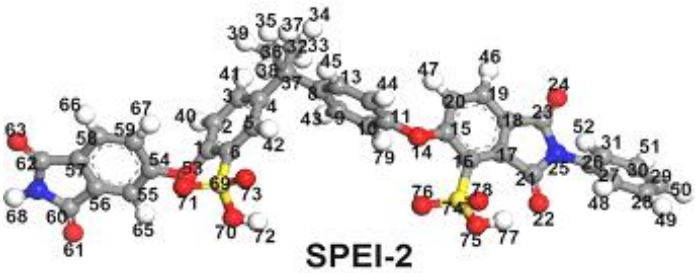

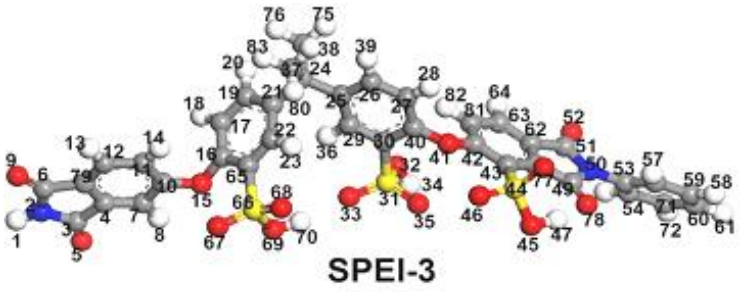

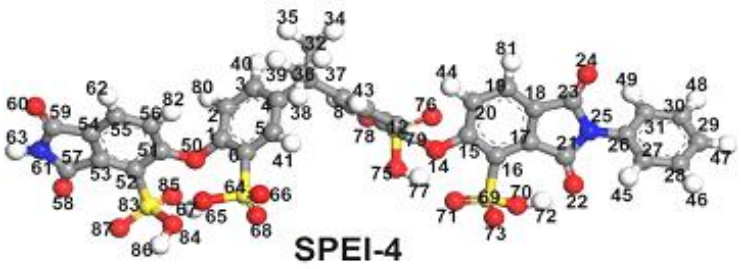

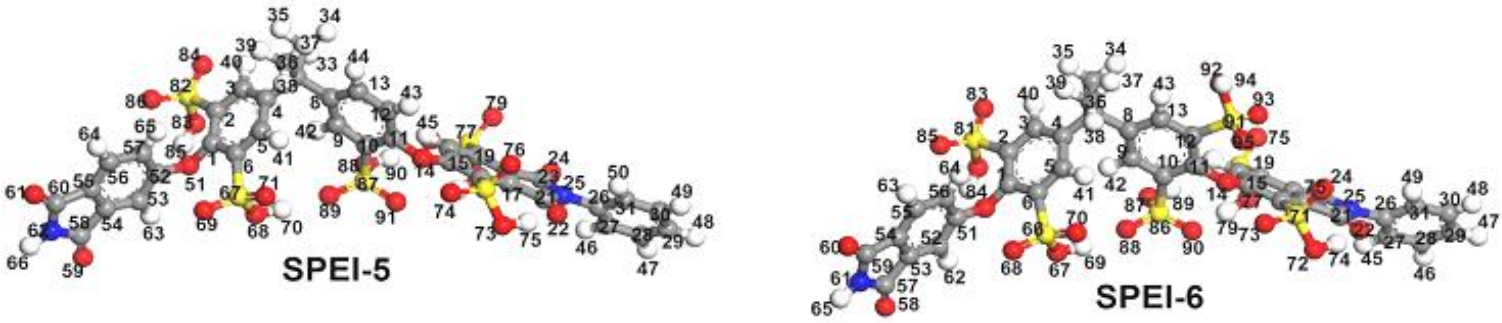

Figure 2 Chemical structures at minimum energy for each SPEI simulated in this work, along with atom numbering.

The SPEIs contain twelve different kinds of bonds, namely: (C-C in imide ring, C-C in benzene ring, C-C connecting two aromatic rings, C-O at diphenyl-ether groups , C═O at carbonyl groups, C-N at imide, C-H at diphenyl-ether groups, C-S at ortho position of diphenyl ether, N-H at imide, O-S at sulfonic groups, O═S at sulfonic groups and O-H sulfonic groups), whose DFT-calculated lengths are listed in Table 1. The lengths obtained are in agreement with those typical reported in the literature [34]. For example, the know C–C covalent-bond-lengths in molecules such like C_2H_6, C_2H_4, C_2H_2 and C_2 (ethane, ethylene, acetylene and C-diatomic molecules, respectively), are correspondingly 1.54 (single bond), 1.34 (double bond), 1.21 and 1.24 Å (triple bonds) bonds, respectively. In particular, at aromatic rings in SPEIs, the calculated bond lengths are slightly lower than the one in single C-C bonds of benzene, 1.4 Å.

Table1. Most relevant bond lengths for the six different polymers studied

SPEI	C-C Imide ring (Å)	C-C Benzene ring (Å)	C-C Connected two aromatic rings (Å)	C-O Diphenyl-ether groups (Å)	C=O Carbonyl groups (Å)	C-N Imide (Å)	C-H Diphenyl-ether groups (Å)	C-S Ortho position diphenyl (Å)	N-H Imide (Å)	O-S Sulfonic groups (Å)	O=S Sulfonic groups (Å)	O-H Sulfonic groups (Å)
1	1.456	1.396	1.540	1.385	1.222	1.416	1.093	1.782	1.021	1.634	1.449	0.988
2	1.457	1.400	1.540	1.383	1.226	1.413	1.093	1.801	1.021	1.608	1.448	1.012
3	1.457	1.415	1.542	1.378	1.225	1.412	1.093	1.798	1.021	1.617	1.449	1.005
4	1.443	1.395	1.530	1.382	1.224	1.409	1.092	1.797	1.021	1.615	1.448	1.013
5	1.460	1.397	1.541	1.383	1.224	1.411	1.093	1.411	1.021	1.610	1.448	1.004
6	1.460	1.351	1.541	1.383	1.224	1.411	1.093	1.803	1.021	1.616	1.447	0.999

Bonds lengths may give some information about both mechanical and chemical stability of each SPEI structure [35]. The shorter bonds are those requiring more energy to break it, thereby the structure degradation is hard. According to Table 1, the SPEI containing four SO_3H groups is that which have greater chemical stability because among all of the twelve types of bonds shown by the structures, it has greater number of bonds with lowest bond lengths in comparison with the ones of the other five structures.

3.2 Water Uptake and Ionic Exchange Capacity Parameters

The λ, IEC and water uptake values are important parameters because they are related to the proton conductivity of the membranes when they are used in fuel cell. In this work, these parameters were obtained according to methodology described in section 2. In Figure 3 are showed simulation cell of all SPEIs in conjunction with λ water molecules number which energy minimize of system.

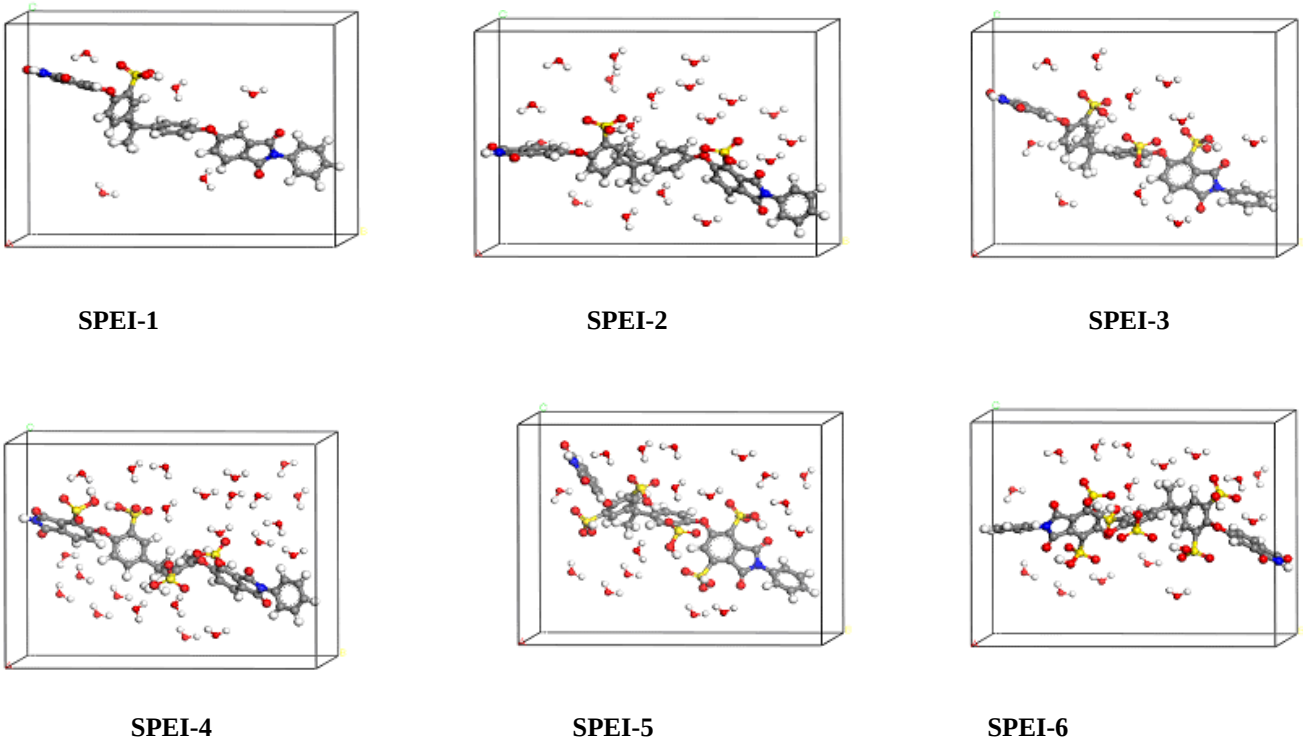

Figure 3 Simulation cell of wetted polymer in ground state for each SPEI

Table 2 presents theoretical values of V_P, ρ, V_M, W_M, parameters in dry and wet, besides of λ, IEC and water uptake values for SPEI-n (n=1,2,3,4,5,6), they were calculated according to methodology described in section 2. In all cases, the theoretical value of both λ, IEC and water uptake are agree with the experimental ones [18], indicating that our theoretical methodology is reliable. It is observe from Table 2 that IEC value decreases as number of sulfonyl groups in PEI increases, this indicate that as more sulfonyl groups are added to the backbone of PEI, the material will go losing the ability to undergo displacement of ions of (SO_3H), previously attached and loosely incorporated into its structure, by oppositely charged ions present in the surrounding solution, such as OH^- or H_3O^+. However, the results of IEC show also that, for all cases, the sulfonyl groups were successfully incorporated into polymer backbone.

Table 2. λ, IEC and water uptake values in conjunction with values of density, and cell volume, molecular volume, molecular weight in conditions wet and dry

SPEI-n	V_p(cc)x10^{-21}		ρ (g/cc)		V_M(cc/mol)		W_M (g/mol)		λ	Water absorption	IEC (meqH/gPol)
	Dry	Wet	Dry	Wet	Dry	Wet	Dry	Wet			
1	1.85	1.22	0.60	1.05	1116.6	732.0	675	**766**	5.06	13.5	1.48
2	2.04	1.68	0.61	1.06	1229.0	1010.5	755	1072	17.62	42.0	1.32
3	2.24	1.55	0.62	1.09	1347.2	935.4	835	1019	10.21	22.0	1.20
4	2.42	1.98	0.63	1.12	1454.9	1193.7	915	1340	23.64	46.5	1.09
5	2.62	1.91	0.63	1.13	1577.1	1151.5	995	1303	17.14	31.0	1.01
6	2.79	1.95	0.64	1.14	1679.9	1175.0	1075	1338	14.63	24.5	0.93

From the water uptake data, it can be concluded that the hydrophilicity of PEI was improved by the incorporation of sulfonyl groups. The ability to take up water is one of the important properties of sulfonated polymers that enable them to be used in fuel cells. The proton conductivity of the polymer generally increases with water uptake: the uptake of more water improves the formation of the hydrophilic domain that conducts protons [12]. The water uptake of the polymer can be increased by an increase in the ionic group content in the polymer chain, but most often, the uptake of more water increases the swelling of a membrane, leading to the loss of the mechanical stability of membranes and high methanol permeability.

Therefore, from Table 2, we can observe the SPEI with n=4 is the polymer who better optimize properties of IEC and water uptake for successful operation in fuel cells. Similar phenomenon was also observed in the literature [7, 12, 18].

Conclusion

We have presented general ideas to develop a theoretical methodology, based on molecular simulations and considering a great number of atoms for obtaining water uptake and ionic exchange capacity parameters of ionic exchange membranes with applications in Fuel Cells. The methodology was applied to poly (ether imide) with different degrees of sulfonation. Processes of geometry optimization and energy minimization yielded results on the chemical stability of all SPEIs. The SPEI with n=4 is the polymer who better optimize properties of IEC and water uptake for successful operation in fuel cells. Similar phenomenon was also observed in the literature. We found that the SPEI-4 presents shorter average bond lengths than SPEI-n (n=2, 3, 5, 6). So, SPEI-4 is the polymer that will have better characteristics for ionic conductivity than others SPEI-n. From the water uptake data, it can be concluded that the hydrophilicity of PEI was improved by the incorporation of sulfonated group. The methodology can be applied to others molecular structures for polymeric membranes in fuel cell.

Acknowledgements

The authors acknowledge the financial support of the following national institutions that made possible the realization of this study: Ministry of Science, Technology and Innovation (SECITI) of the Government of the Federal District, through the agreement 060/2013 and projects: PI2011-23R and PI2013-35. Furthermore, we also recognize the invaluable support of the National System of Researchers of the National Council of Science and Technology (CONACYT-SNI) and the Autonomous University of Mexico City (UACM).

References

[1] H.G. Bohn, T. Schober, J. Am. Ceram. Soc. **83**, 768 (2000).

[2] T. Higashihara, K. Matsumoto, M. Ueda, Polymer **50**, 5341 (2009).

[3] Y. Wan, K. A. M. Creber, B. Peppley, V. Bui J. Membrane Sci., **280**(1–2), 666 (2006).

[4] S. Subianto, M. K. Mistry, N.R. Choudhury, N.K. Dutta, R. Knott, *ACS* Appl. Mater Interfaces **1**(6), 1173 (2009).

[5] F. Wang, M. Hickner, Y. S. Kim, T. A. Zawodzinski, J.E. McGrath, J. Membrane Sci. **197**, 231 (2002).

[6] K. Miyatake, Y. Chikashige, E. Higuchi, M. Watanabe, J. Am. Chem. Soc. **129**, 3879 (2007).

[7] T. Mikami, K. Miyatake, M. Watanabe, *ACS* Appl. Mater Interfaces **2**, 1714 (2010).

[8] K. Miyatake, Y. Chikashige, M. Watanabe, Macromolecules **36**, 9691 (2003).

[9] Y. Yin, J. H. Fang, T. Watari, K. Tanaka, H. Kita, K. Okamoto, J. Mater Chem. **14**(6), 1062 (2004).

[10] S. Chen, Y. Yin, H. Kita, K.I. Okamoto, J. Polym. Sci. **45**, 2797 (2007).

[11] N. Asano, M. Aoki, S. Suzuki, K. Miyatake, H. Uchida, M. Watanabe, J. Am. Chem. Soc. **128**, 1762 (2006).

[12] S. Li, X. Zhi, Y. Qian, S. Hang, W. Shu, X. You, J. Appl. Polym. Sci. **92**, 1709 (2004).

[13] D. Meng, G. K. Sangamesh, W. Yuging, S. T. Udaya, R. A. Harry, T. L. Cato, Soft Matter **6**, 3119 (2010).

[14] Y. Zhao, Z. Jiang, L. Xiao, T. Xu, S. Qiao, H. Wu, Solid State Ionics **187**(1), 33 (2011).

[15] K . Hyoung, A. Seong, K. Ju, M. Jin, C. Sung, E. Yeong, Y. Hae, P .Youngmi, K. Ho, S. Eun, Macromol. Rapid. Comm. **25**(15), 1410 (2004).

[16] Z. Javaid, Takeshi Matsuura, *Polymer membranes for fuel cells* edited by Javaid SM, Matsuura T. (Springer, New York, 2009).

[17] S. Swier, M. Shaw, R. A. Weiss, J. Membrane Sci. **270**, 22 (2006).

[18] B. Peres, L. Santa Maria, M. Sena, Mater Lett. **61**, 2540 (2007).

[19] S. Yao, C. Fu, T. Wen, C. Jing, G. Chunli, W. Sheng, J. Appl. Polym. Sci. **107**(5), 2963 (2008).

[20] S, Fu C, Wen T, Jing C, Chunli G, Sheng W. J Appl Polym Sci. **108** 1783 (2008).

[21] D. Loredo, M. Paredes, M. Sena, Mater Lett. **62**(19), 3319 (2008).

[22] R. T. P. S. M. Lakshmi, S. Bhattacharya, I. K. Varma, High Perform. Polymers **18**, 115 (2006).

[23] H. Mark, N. Bikales, C. Overberger, G. Menges, J. Kroschwitz , *Encyclopedia of polymer science and engineering* edited by Mark H, Bikales N, Overberger C, Menges G, Kroschwitz J, (Wiley, New York, 1988).

[24] L. Fu, G. Xiao, D. Yan, *ACS* Appl. Mater Interfaces **2**(6), 1601 (2010).

[25] R. G. Parr, W. Yang, *Density-functional theory of atoms and molecules* edited by R. G. Parr, W. Yang, (Oxford Science Publications; New York, 1989).

[26] P. K. Chattaraj, S. Nath, B. Maiti, *Reactivity Descriptors in Computational Medicinal Chemistry for Drug Discovery*, edited by J. Tollenaere, P. Bultinck, H. D. Winter, W. Langenaeker, (Marcel Dekker Inc, New York, 2003).

[27] R. Parthasarathi, J. Padmanabhan, U. Sarkar, B. Maiti, V. Subramanian, P. K. Chattaraj, Internet Electron J. Mol. Des. **2**, 798 (2003).

[28] M. Meunier, J. Chem. Phys. **123**, 134906 (2005).

[29] E. Hairer, C. Lubich, G. Wanner, *Acta Numerica* 399 (2003).

[30] H. J. C. Berendsen, J. P. M. Postma, W. F Van Gunsteren, J. R. DiNola A. Haak *J. Chem. Phys.* **81**(8), 3684 (1984).

[31] A. K. Rappe, W. A. Goddard, J. Chem. Phys. **95**, 3358 (1985).

[32] T. Schlick, *Molecular Modeling and Simulation: An Interdisciplinary Guide* (Springer-Verlag, New York, 2002).

[33] M. S. Diallo, T. Cagin, J. L. Faulon, W. A. Goddard, *Thermodynamic properties of asphaltenes: a predictive approach based on computer assisted structure elucidation and atomistic simulations* edited by T. F. Yen, G. V. Chilingirian, (Elsevier Science, Amsterdam, 2000).

[34] Handbook of Chemistry & Physics edited by R. Weast, (CRC Press; 1984).

[35] J. Martínez, R. Oviedo, P. García, R. Martínez, Fuel Process Technol **97**, 24 (2012).

[36] W. Sułkowski, k. Nowak, A. Sułkowska, A. Wolińska, W. Bajdur, D. Pentak, B. Mikuła, Pure Appl. Chem. **81**(12), 2417 (2009).

[37] S. Swier, V. Ramani, J. M. Fenton, H. R. Kunz, M. T. Shaw, R. A. Weiss, J. Membrane Sci. **256**, 122 (2005).

[38] A. J. Reuvers, C. A. Smolders, J. Membrane Sci. **34**, 67 (1987).

[39] F. Lingchao, X. Guyu, Y. Deyue, *ACS* Appl. Mater Interfaces **2**(6), 1601 (2010).

[40] V. M. Chetan,G. Venkat, J. Phys. Chem. B **114**, 8367 (2010).

Electrochemical evaluation of membranes of poly-[styrene-co-acrylic acid] for use in PMFC

M. M. S. Paula[1,*], C. Burigo [1], H. J. de Souza[1], L. W. Oenning[1], L. da Silva[1], F. S. Notoya[1], A. G. Dal-Bó[1], J. T. Langbehn[1], T. E. A. Frizon[1], R. Benavides[2], J. C. O. Rodriguez[2]

[1]Universidade do Extremo Sul Catarinense (Unesc), Av. Universitária, 1105 - Cx.P. 3167, 88.806-000, Criciúma (SC)
[2] Centro de Investigación en Química Aplicada, Blvd. Enrique Reyna 140, Saltillo, Coahuila, México 25294
Tel: +55 48 34312577; E-mail address: bocaocao@gmail.com

ABSTRACT

Nanotechnology allows to create and implement materials, structures and systems by mounting and manipulating in atomic and molecular scale. New effects observed on the nanometer scale are explored in this study for the development of membranes for application in fuel cells (PMFC). It has been observed that the incorporation of metal nanoparticles of gold, silver, among others, in polymeric matrices increases the thermal stability of the membranes. This is desirable since the catalytic activity of the catalysts employed in cells is associated with operating temperature. In this study we report the preparation and electrochemical characterization of polymeric membrane of poly-(styrene-co-acrylic acid) *sulfonated (*poly-(StS-co-AA)) for application in PMFC. Poly-(styrene-co-acrylic acid) (poly-(St-co-AA)) was prepared in the ratio 92:8, followed by sulfonation with H_2SO_4. Electrodes of Pt//poly-(StS-co-AA) were prepared by casting from a polymer solution deposited on its surface. The polymer films were characterized by cyclic voltammetry and electrochemical impedance spectroscopy in acidic and neutral environment. Cyclic voltammograms were recorded in 0.5 mol.dm^{-3} KCl solutions and was observed the presence of redox processes attributed to the H^+ ions. The microstructural characterization was performed by atomic force microscopy

Keywords: Electrochemistry; membranes; fuel cells

1. Introduction

Many researchers are studying alternative technologies for the production of energy efficient and low cost, due to a future crisis in the energy sector. By a search for ways of generating clean and sustainable energy, the study and production of fuel cells is very promising, with several models developed and described in literature [1-8].

Fuel cells are electrochemical devices that consume hydrogen and oxygen to produce electricity [2,6]. Also called continuous battery operation, they produce direct current by electrochemical cold combustion of a gaseous fuel, usually hydrogen, being viable for stationary power generation [9]. Cells with low operating temperature, using a polymer membrane as the electrolyte, also called PEMFC (Proton Exchange Membran Fuel Cell), are promising as an alternative to research and development of techniques derived from clean technology with low emissions, high chemical, efficiency electric conversion, robustness, easy to drive and shutdown [9,10].

In a fuel cell system type PEMFC, supplied with hydrogen and oxygen are conducted two partial electrochemical reactions in two electrodes separated by a polymer electrolyte, forming water as a product of the overall reaction and generating electric and thermal power with high efficiency [3].

The development of membranes produced with nano polymeric materials for application in fuel cells, is increasingly being investigated for the generation of clean energy is a challenge to be pursued [5, 11, 12]. By having a low operating temperature, it is possible to emit zero NOx as the use of these cells.

Aiming at technological interest is possible to combine the electrical conductivity of conducting polymers with the mechanical properties of conventional polymers [13]. The use of polystyrene (PS) is due to the fact that it is one of the most known thermoplastic in the plastics industry and the sulfonating process has been used for efficiency and versatility for obtaining polymers seen introducing polar substituents capable of increasing the hydrophilicity and conductivity of the membrane [4, 14, 16]. Therefore, this work describes the preparation and characterization of conducting membranes poly [styrene-co-acrylic

acid] sulfonated for use in fuel cells as alternative energy source. The Figure 1 illustrates a fragment of chain poly-(StS-co-AA).

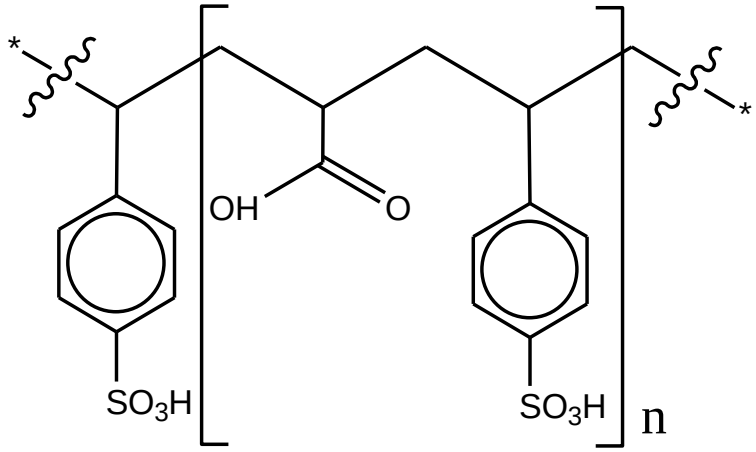

Fig 1. Schematic representation of poly-(StS-co-AA).

2. Experimental

Reagents and solvents were purchased from various commercial sources and used without further purification. The only exception was the Styrene (Sigma-Aldrich) that was previously purified by adding 10 ml of 2 mol.dm^{-3} solution of NaOH in 100 mL of monomer under stirring. This procedure was repeated until the styrene became transparent. After, the styrene was washed with distilled water until pH 7.0. Then, the monomer was dried with $CaSO_4$ under stirring for 3 hours and filtered. The procedure was repeated three times. Finally, the styrene was distilled under reduced pressure and protected from light.

The poly-(St-co-AA) was prepared by radical chain copolymerization in bulk, using benzoyl peroxide as initiator and 98:2 molar ratio of styrene and acrylic acid, respectively, as described previously [17]. The reaction medium was precipitated in methanol, washed with distilled water and dried under reduced pressure for 24 h. The poly-(St-co-AA) was sulfonated using H_2SO_4 as sulfonating agent and purified as previously described [17].

Polymer films surface were characterized by atomic force microscopy employing a Scanning Probe Microscope - SHIMADZU, model SPM-9700. The vibrational spectra of the films were recorded with a FT-IR – Shimadzu, model IRAffinity-1

Modified electrodes were prepared by casting, depositing 10µl of a copolymer solution (10mg/mL) in THF on the surface of a Pt disk electrode and allowed to dry at room temperature for 24 h to complete evaporation of the solvent. Previously, the electrode was mechanically polished followed by electropolishing in H_2SO_4 0.5 mol.dm-3 using cyclic voltammetry technique. All electrochemical experiments were performed with a potentiostat / galvanostat - Biologic, model SP-200, using a typical three-electrode cell. All measurements

carried out on inert argon atmosphere.A commercial Pt disc electrode (0.018 cm^2) was used as working electrode; Saturated Calomel Electrode (SCE) as reference electrode; a Pt wire as auxiliary electrode . All datas were acquired and treated with EC-Lab ® software V10.23.

To evaluate the electrochemical properties of modified electrodes were used aqueous solutions of KCl 0.1 mol.dm-3 and H_2SO_4 0.5 $mol.dm^{-3}$ as electrolytic medium. The modified electrodes were kept in KCl solution and the E_{oc} was monitored until achieve the equilibrium between Pt | | film | | solution interfaces

3. Results and discussion

The yields for the synthetized poly-(St-co-AA) and poly-(StS-co-AA) were 40.5% and 80.0%, respectively. Comparing the vibrational spectra FTIR between poly-(St-co-AA) and poly-(StS-co-AA), was observed the maintenance of the main vibratio

nal modes relative to styrene and acrylic acid after the sulfonation reaction. However, the sulfonated copolymer shows a stretching which υ in 3500-3100 cm^{-1} corresponding to -SO_3H groups in the polymer matrix.

The atomic force microscopy images of poly-(St-co-AA) and poly-(StS-co-AA) films showed marked morphological differences, as can be seen in Figure 2.

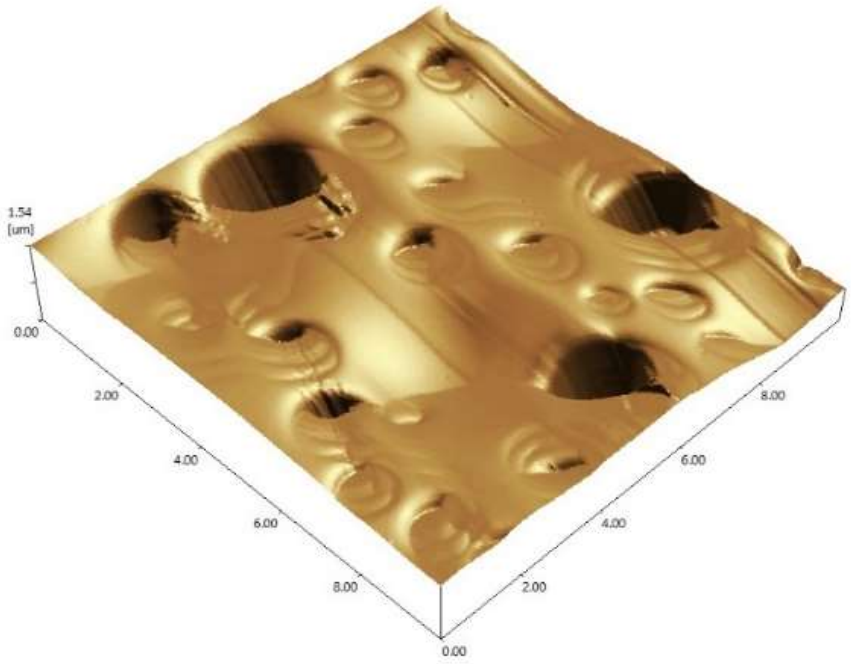

A

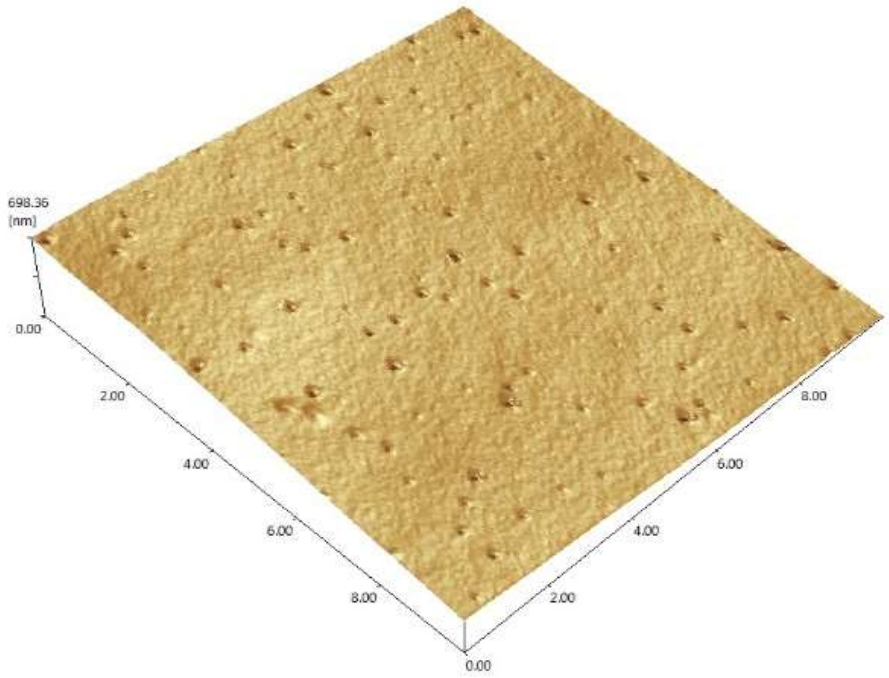

B

Fig 2. Pictures of films of poly-(St-co-AA) (A) and poly-(StS-co-AA) (B) from Atomic Force Microcopy.

The sulfonated copolymer (Fig. 2B) shows a much more regular and uniform surface, without the presence of "craters", when compared to non-sulfonated copolymer (Fig. 2A). A possibly explanation about it is the presence of sulfone groups increases the hydrophilicity of the material, reducing the rate of evaporation of the solvent. This leads to the formation of a layer more homogeneous and uniform than in the case of poly-(St-co-AA).

A Pt electrode coated with poly-(St-co-AA) was maintained in KCl 0.1 mol.dm^{-3} and the E_{oc} vs time monitored until to achieve the equilibrium in the Pt || Film || Solution interface. Then, the voltammetric profile was recorded in the range of 1.0 V to -1.0 V *vs.* SCE at a scan rate of 50 mV.s $^{-1}$. No redox process could be observed in this range, even after 24 h of immersion. This is an indicative of the film stability in solution.

The ionic permeability through the film was measured by transferring the electrode into a $K_3[Fe(CN)_6]$ 0.05 mol.dm^{-3} + KCl 0.1 mol.dm^{-3} solution. Differences between the E_{pa} and E_{pc} values and the respective I_{pa}

and I_{pc} are observed in the voltammetric profiles recorded at different immersion times and presented in Figure 3.

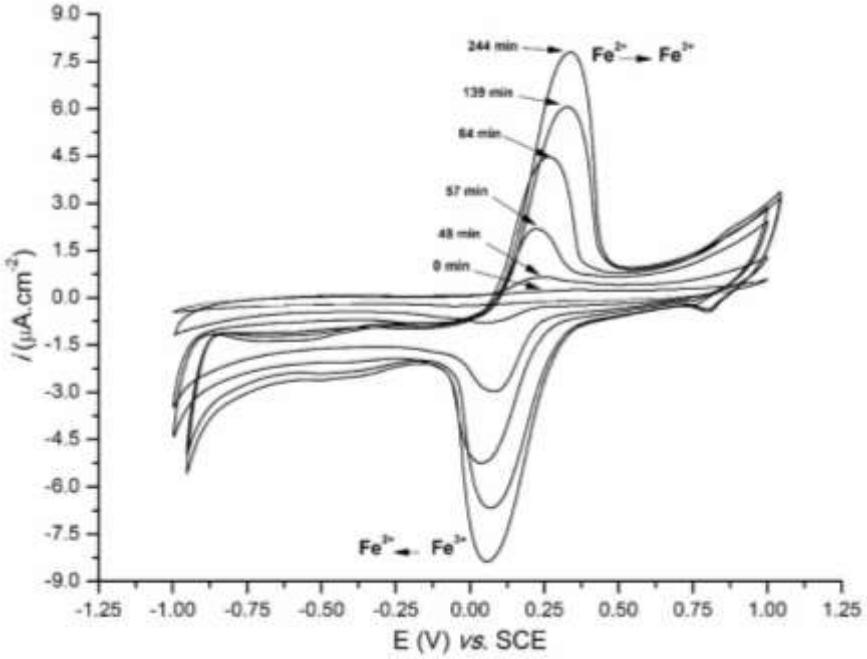

Fig 3. Cyclic voltammograms of $K_3[Fe(CN)_6]$ 0.05 mol.dm-3 KCl 0.1 mol.dm^{-3} of Pt electrode modified by poly-{ST-co-AA}. Reference: SCE. Scan rate 50 mV.s^{-1}.

The current of cathodic and anodic peak increases with the immersion time, but more sharply in the first hour. The $E^{1/2}$ remains constant and independent of immersion time. The ΔEp is 280 mV, well above the value observed for the voltammetric profile for the $K_3[Fe(CN)_6]$ recorded on a Pt electrode unmodified.

In part, this should be associated to the uncompensated film resistance. Additionally, one may take into account, possible concentration gradients near to the Film || Electrode interface, where the concentration of

electroactive species is greater. Such differences in the chemical environment can influence the diffusion processes of the oxidized and reduced species within the polymer matrix.

A study of the scan rate dependence was performed in the range of 25 to 500 $mV.s^{-1}$ and the obtained cyclic voltammograms are shown in the Figure 4.

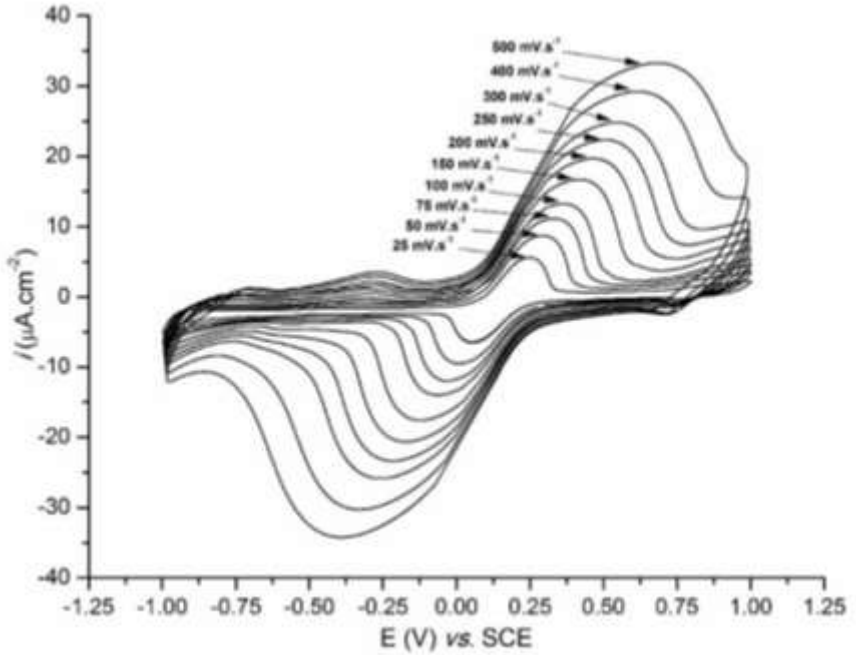

Fig 4. Cyclic voltammograms of $K_3[Fe(CN)_6]$ 0.05 mol.dm-3 KCl 0.1 $mol.dm^{-3}$ of Pt electrode modified by poly-{ST-co-AA} recorded at different scan rates. Reference: SCE.

The plot of Ipa and Ipc vs. the square root of the scan rate is linear and with intercepts at zero, ie, follows Randles-Sevcik equation, as can be seen in Figure 5. This is typical for a limited diffusion system. In addition,

the $E^{1/2}$ is constant and independent of the scan rate. However, ΔEp increases with increasing scanning speed [18].

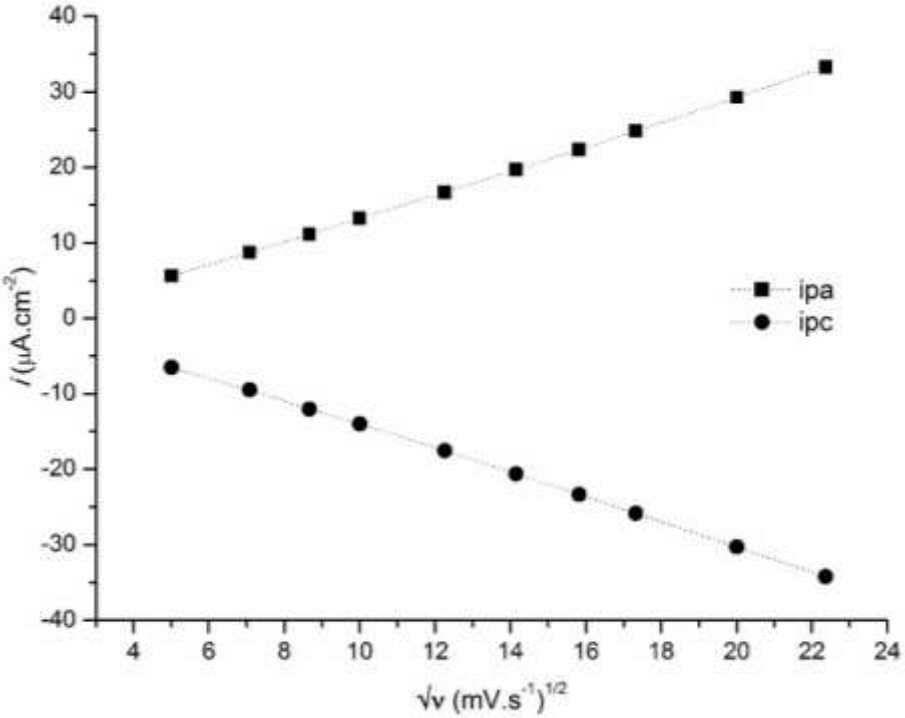

Fig 5. Plot of current of anodic and cathodic peak as a function of the square root of the scan rate corresponding to the cyclic voltammograms shown in Figure 4.

In order to evaluate the protonic permeability, cyclic voltammograms of electrodes modified by poly-(St-co-AA) and poly-(StS-co-AA) were recorded in H_2SO_4 0.5 mol.dm^{-3} solution and compared to a voltammetric

profile of unmodified Pt electrode. Figure 6 corresponds to CV of the three electrodes and clearly show five distinct regions.

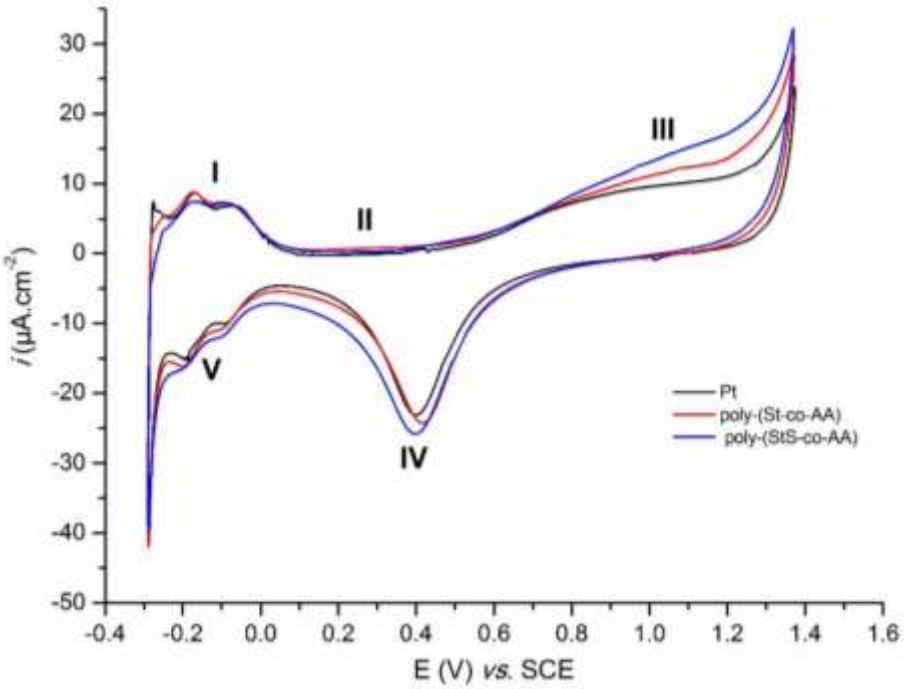

Fig 6. Cyclic voltammograms of (——) Pt, (——) poly-(ST-co-AA) and (——) poly-(STS-co-AA) electrodes in H_2SO_4 0.5 mol.dm^{-3}. Scan rate 50 mV.s^{-1}.

The regions I and V corresponding to oxidation and redeposition of atomic hydrogen; Region IV is attributed to the formation of surface oxide on platinum. Region II corresponds to the double charge layer and the region III corresponds to adsorption of OH- and its respective oxidation [18]. By comparing the three curves, it turns out that the regions II, III and IV does not show substantial differences. In addition, differences in regions I and V are very subtle, indicating that the active sites of platinum were not blocked. The relationship between the charges involved in redox processes attributed to oxidation and reduction of atomic hydrogen (I and V) are preserved in the three electrodes and are close to unity, even after more than 50 scan cycles. This shows that both copolymers are permeable to H^+ ions and stable in acid medium, which is

desirable to membranes for use in fuel cells. These results are in agreement with images of atomic force microscopy, showing an excellent surface coating of the electrodes.

In order to demonstrate that the presence of sulfone group enhance proton conductivity, there was a cyclic voltammogram of an electrode modified by poly-(StS-co-AA) in KCl 0.1 mol.dm^{-3}.

The modified electrode by poly-(St-co-AA) shows no redox process in KCl solution in the range between -1.0 V and 1.0 V vs. SCE. By other hand, the redox processes for the modified electrode with poly-(StS-co-AA) can be seen in the Figure 7.

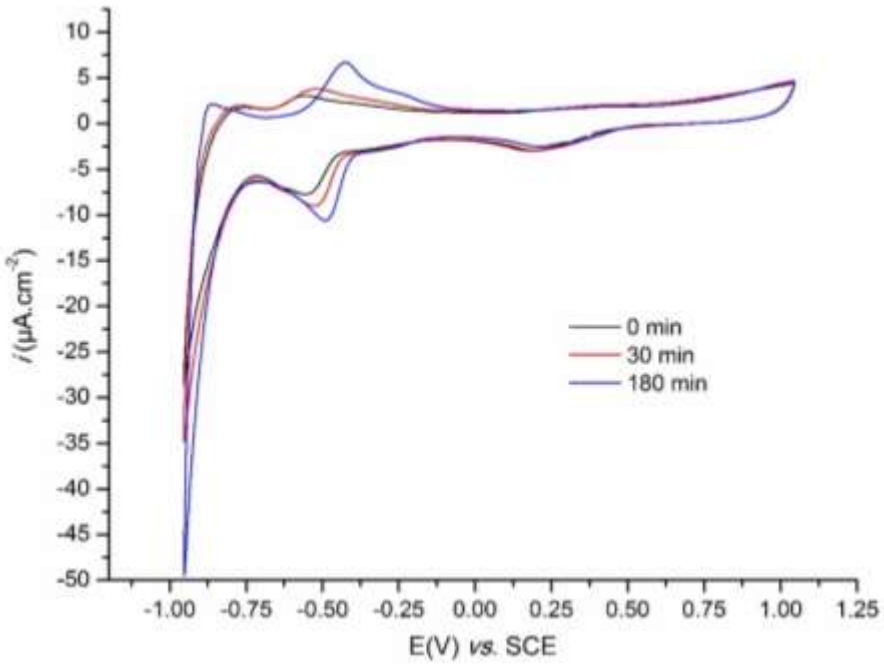

Fig 7. Cyclic voltammograms for a film of poly-(StS-co-AA) in KCl 0.1 mol.dm^{-3} in different immersion times. (——) 0 min., (——) 30 min. and (——) 180 min. Scan rate 50 mV.s^{-1}.

Shortly after KCl immersion, the voltammetric profile showed a redox process with $E^{1/2}$ in -0.55 V and ΔEp = 0.3 mV, which is much lower than expected by the Nernst equation for a reversible redox process. In this case, the shape of the voltammetric sine wave is characteristic of monolayer adsorption processes. It is reasonable to assume that these processes result from the ionization of protons from the -SO_3H groups. After 30 minutes of dipping, the $E^{1/2}$ shifts to the more positive potential region, close to -0.52 V and presenting ΔEp = 8 mV. Finally, after 180 min of immersion the $E^{1/2}$ stabilizes at -0.46 V and ΔEp = 66 mV. This change in the voltammetric profile can be explained by the slow ionization of the -SO_3H groups.

To confirm this hypothesis, the modified electrode was transferred to a basic solution of NaOH. After 30 minutes of immersion, the electrode was rinsed in distilled water and a new cyclic voltammogram was

recorded in KCl. One could note the suppression of the voltammetric waves observed in the Figure 8, regenerating a characteristic voltammetric profile of an electrode modified by poly-(St-co-AA).

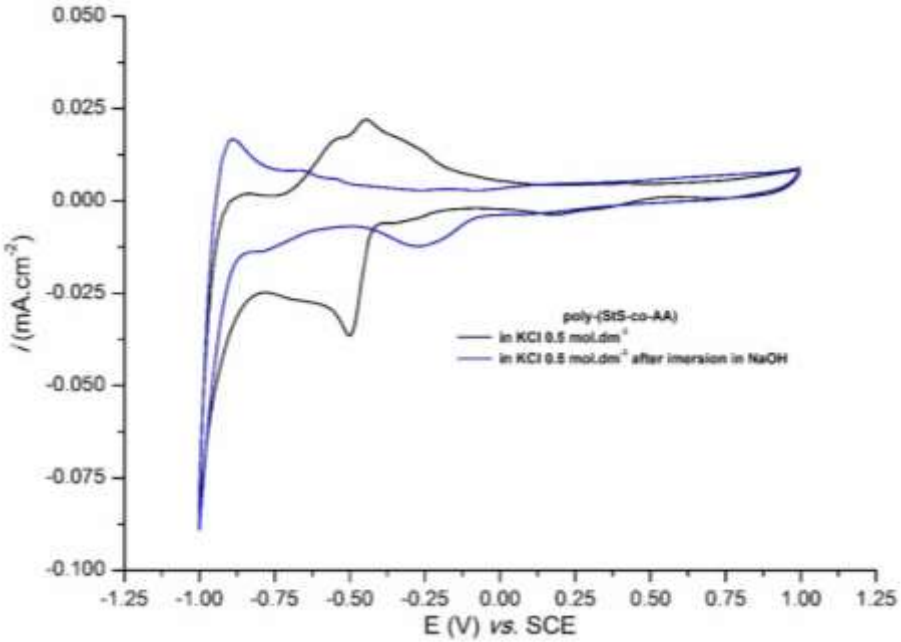

Fig 8. Cyclic voltammograms for a film of poly-(StS-co-AA) in KCl 0.1 mol.dm^{-3} (——) and in KCl 0.1 mol.dm^{-3} after immersion in NaOH (——). Scan rate 50 mV.s^{-1}.

The impedance diagrams of an electrode modified by poly-(StS-co-AA) in KCl 0.1 mol.dm^{-3} recorded in the potential E = 0.0 V vs. E_{oc}, E = -1.0 V and 1.0 V vs. SCE can be observed in Figure 9.

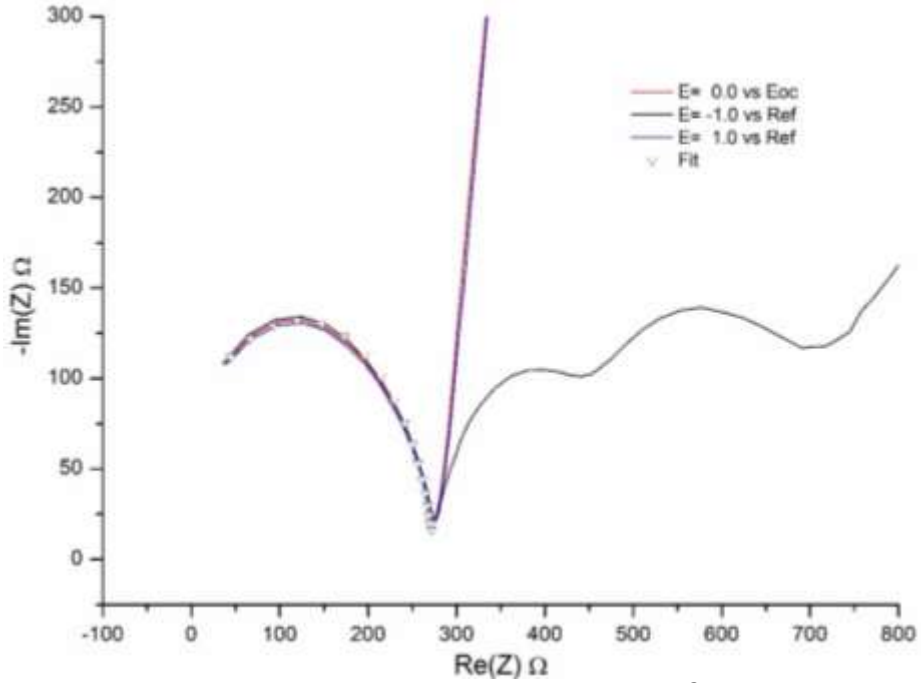

Fig 9. Nyquist Plot for a film of poly-(STS-co-AA) in KCl 0.1 mol.dm^{-3} at different potentials: 0.0 V *vs.* E_{oc} (——); -1.0 V *vs.* SCE (——); 1.0 V vs. SCE (——) and fit (Δ).

In all Nyquist impedance occurs the presence of capacitive arc in the region of high frequencies, that can be adjusted to the equivalent circuit showed in Figure 10. The circuit consists of a resistor R_1 in series with a resistor R_2 which is in parallel with a constant phase element Q2.

The impedance of Q_2 is obtained by equation: $Z(Q_2) = Q_2^{-1} i\omega^{-a}$, where Q_2 is a factor of proportionality, and "a" expresses the phase shift. When the value of "a" assumes values between 0.8 and 1, the element of

constant phase Q_2 corresponds a capacitance distortion due to surface roughness or a distribution/accumulation of charge carriers.

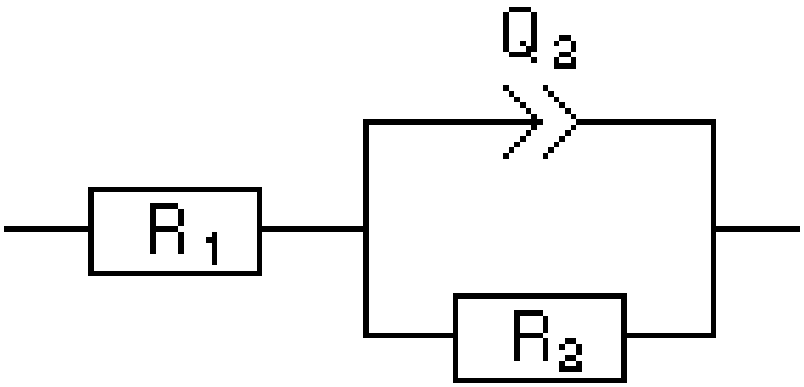

Fig 10. Schematic representation of the proposed equivalent circuit.

The values of the elements of circuit of Figure 10, obtained from the mathematical fit, are: R_1 = -32.09 Ohm; R_2 = 307.00 Ohm; Q_2 = 2.33 nF.s$^{(a-1)}$, where a = 0.90.

Finally, the two capacitive arcs shows in the low frequency region can be attributed to the electrochemical diffusional process that occurs between the Pt||Film and Film||Solution interfaces.

4. Summary and perspectives

In this work we show that poly-(StS-co-AA) is an electroative polymeric material and can be used like permeable membrane fuel cell due the considerable protonic conductivity.

Acknowledgements

This work was supported by grants from the Conselho Nacional de Pesquisa e Desenvolvimento (CNPq), Coordenação de Aperfeiçoamento de Pessoal de Nível Superior (CAPES) and Universidade do Extremo Sul Catarinense UNESC). The authors would also like to thank CNPq and UNESC for their fellowship support.

References

[1] Villalobos, L.F., et al., Poly-thiosemicarbazide/gold nanoparticles catalytic membrane: In-situ growth of well-dispersed, uniform and stable gold nanoparticles in a polymeric membrane. Catalysis Today, 2013(0).

[2] Breeze, P., Chapter 7 - Fuel Cells, in Power Generation Technologies (Second Edition), P. Breeze, Editor. 2014, Newnes: Boston. p. 129-152.

[3] Bonifácio, R.N., M. Linardi, and R. Cuenca, Desenvolvimento de processo de produção de conjuntos eletrodo-membrana-eletrodo para células a combustível baseadas no uso de membrana polimérica condutora de prótons (PEMFC) por impressão a tela. Química Nova, 2011. 34: p. 96-100.

[4] Wang, B.-Y., et al., Polytetrafluoroethylene (PTFE)/silane cross-linked sulfonated poly(styrene–ethylene/butylene–styrene) (sSEBS) composite membrane for direct alcohol and formic acid fuel cells. Journal of Membrane Science, 2014. 464(0): p. 43-54.

[5] Njomo, N., et al., Graphenated tantalum(IV) oxide and poly(4-styrene sulphonic acid)-doped polyaniline nanocomposite as cathode material in an electrochemical capacitor. Electrochimica Acta, 2014. 128(0): p. 226-237.

[6] Sousa Jr, R. and E.R. Gonzalez, Mathematical modeling of polymer electrolyte fuel cells. Journal of Power Sources, 2005. 147(1–2): p. 32-45.

[7] Mann, R.F., et al., Development and application of a generalised steady-state electrochemical model for a PEM fuel cell. Journal of Power Sources, 2000. 86(1–2): p. 173-180.

[8] Benavides, R.O., Leonardo W.; Paula, MMS, da Silva, Luciano ; Kotzian, C.; (2013) O uso de um tri-funcional reticulação Agente em estireno / acrílico copolímeros do ácido para melhorar as propriedades mecânicas para uso como membranas em células a combustível. . Jornal de novos materiais para sistemas eletroquímicos 16, 157-162.

[9] Wendt, H., M. Götz, and M. Linardi, Tecnologia de células a combustível. Química Nova, 2000. 23: p. 538-546.

[10] Mahapatra, M.K. and P. Singh, Chapter 24 - Fuel Cells: Energy Conversion Technology, in Future Energy (Second Edition), T.M. Letcher, Editor. 2014, Elsevier: Boston. p. 511-547.

[11] Punyawudho, K., et al., Identification and quantification of performance losses for PEM fuel cells as determined by selective chemisorption and ESA measurements. International Journal of Hydrogen Energy, 2014. 39(21): p. 11110-11119.

[12] Wang, X., et al., Ultra-low platinum loadings in polymer electrolyte membrane fuel cell electrodes fabricated via simultaneous electrospinning/electrospraying method. Journal of Power Sources, 2014. 264(0): p. 42-48.

[13] Segala, K., et al., Characterization of poly-{trans-[RuCl2(vpy)4]-styrene-4-vinylpyridine} impregnated with silver nanoparticles in non aqueous medium. Journal of the Brazilian Chemical Society, 2006. 17: p. 1679-1682.

[14] Melo, L., et al., Degradation reactions during sulphonation of poly(styrene-co-acrylic acid) used as membranes. Polymer Degradation and Stability, (0).

[15] da Silva Paula, M.M., et al., Synthesis, characterization and antibacterial activity studies of poly-{styrene-acrylic acid} with silver nanoparticles. Materials Science and Engineering: C, 2009. 29(2): p. 647-650.

[16] da Silva, L., et al., Humidity and pH sensor based on sulfonated poly-{styrene–acrylic acid} polymer.: Synthesis and characterization. Materials Science and Engineering: C, 2009. 29(2): p. 599-601.

[17] Franco, César Vitorio ; PRATES, P. B. ; MORAES JR, Volni Nunes de ; PAULA, MMS . Oxidative formation of Electroative Film from Polypyridinyl Complexes of Ruthenium(II)- containing 3-(pyrrol-1-ylmethil)-pyridine). pmp=3-(pyrrol-1-ylmethil)-pyridine). Synthetic Metals, v. 90, p. 81-88, 1997.

[18] Conway, B.E. et al., Ultrapurification of water for electrochemical and surface chemical work by catalytic pyrodistillation. *Anal. Chem.*, 1973, *45* (8), p. 1331–1336.

Experimental validation of a coupled nonlinear observer in a hydrogen production dark fermenter

A. Villa-Leyva[1], Axue Zhang[1], I. Torres-Zúñiga[1], A. Vargas[1], G. Buitrón[1],*

[1]*Laboratorio de Investigación en Procesos Avanzados de Tratamiento de Aguas, Unidad Académica Juriquilla, Instituto de Ingeniería, Universidad Nacional Autónoma de México, Blvd. Juriquilla 3001, Querétaro, Qro. C.P. 76230, México.*
**Tel: +524421926165; e-mail: gbuitronm@iingen.unam.mx*

ABSTRACT

In order to maximize the production of hydrogen from glucose in a continuous dark fermenter by modifying the OLR, specifically manipulating the inflow rate, the real knowledge of the substrate concentration at the reactor input is needed. Since it cannot be measured on-line, a Luenberger observer coupled to a Super-Twisting one can be used to estimate the substrate concentration at the reactor input. This study aimed to demonstrate the experimental validation of the proposed observer, which was tested by numerical simulations based on a mathematical model calibrated by experimental data in a previous research. Five conditions with different combinations of hydraulic retention time (HRT) and inflow substrate concentration were performed in the fermentative reactor for calibrating the mathematical model of the observer. These conditions were chosen based on Latin hypercube experimental design. The collected data allowed testing the proposed nonlinear observer and the results are encouraging, showing good estimations of the inflow substrate concentration. However the model is sensitive to perturbations, which leads to an erroneous estimation of the VSS concentration with the Luenberger observer. Nevertheless, the observer may be suitable to complement an optimization strategy previously proposed.

Keyword : bio-hydrogen production; nonlinear observer; bioprocess control

1. Introduction

The continued usage of fossil fuels is threatened the environment by increasing concentration of greenhouse gases and causing serious pollution problems in the atmosphere. Moreover gasoline, diesel and natural gas, with nearly 80% of global energy demand supplied are finite sources and are rapidly becoming scarcer and more expensive [1]. Hydrogen has been introduced as a potential replacement for energy resource due to its low generation of pollutants and high energy density [2].

Currently, most hydrogen is produced form non-renewable sources such as oil, natural gas and coal; about 50% is obtained using thermocatalytic techniques and gasification of natural gas, heavy oils, cola and naphtha [3]. On the other hand, the biological processes for the hydrogen production are presented as an alternative. These processes can be classified into three types [4]: bio-photolysis, photo-fermentation and dark-fermentation. Fermentative hydrogen production has been received increasing attention in recent years, it has the advantage of rapid hydrogen production rate and simple operation, moreover it can use organic solid wastes and the organic compound in the wastewater as substrate [5].

In fermentative hydrogen production the operation parameters have a crucial role on the metabolic pathway of the microorganisms, as a result, influence the process efficiency, product gas quality and energy inputs. Many researchers have been focusing on optimal operation parameters (pH, temperature, hydrogen partial pressure, and inoculum) to obtain the maximum hydrogen yield and hydrogen production rate. One of the operational conditions that affect the hydrogen production rate (HPR) in a dark fermenter reactor is the organic loading rate (OLR). According to [6] and [7] an optimum OLR exits in which the HPR is maximum, moreover this optimum OLR is close to the overloading one. In order to maximize the HPR, the OLR should be maintained optimal. The OLR depends on inflow rate and substrate concentration at the reactor input, a controlled variable and an uncontrolled one, respectively.

In order to optimize the productivity of hydrogen in a continuous dark fermenter by modifying the OLR, specifically manipulating the inflow rate, based on an optimization strategy proposed in [13], the real knowledge of the substrate concentration is needed. Since it is unpractical to measure on-line, a coupled observer is proposed [11]. It is able to estimate the substrate concentration at the reactor input by measuring the hydrogen flow rate at the reactor output. Although a validation of the proposed estimator has already been done using numerical simulations based on a mathematical model that was calibrated with previous experimental data, an experimental validation of the proposed estimator is needed as well. This work presents the results of this experimental validation.

2. Experimental

2.1 Inoculum, feed water composition and start-up of reactor

The inoculum was obtained from a UASB reactor used for treating the wastewater of a brewery plant. The sludge was subjected to a heat treatment described by [8]. The granular sludge was heated at 104°C during

24h in order to select the hydrogen-producing spore forming anaerobes and inhibit the activity of hydrogen consumers. The heated material was broken down in a mortar and sieved with a # 20 mesh (850µm). Glucose was used as organic substrate. For every gram of glucose 104 mg NH_4Cl and 50 mg K_2HPO_4 were added. For every liter of feed solution, the following amounts of mineral salts were added: 0.4 mg; $MnCl_2 \cdot 4H_2O$, 20 mg; $MgCl_2 \cdot 6H_2O$, 20 mg; $FeSO_4 \cdot 7H_2O$, 2 mg; $CoCl_2 \cdot 6H_2O$, 2 mg; $Na_2MoO_4 \cdot 2H_2O$, 2 mg; H_3BO_4, 2 mg; $NiCl_2 \cdot 6H_2O$, 2 mg; $ZnCl_2$, 2 mg. The experiment was carried in a continuous stirred tank reactor (CSTR) of 1.2 L with a working volume of 0.9 L equipped with a ez-biocontroler (Applikon Biotechnology, Schiedam, The Netherlands). The biocontroler allowed to keep the following operating conditions: temperature of 35 °C, stirring velocity at 100 rpm and the pH at 5.5. A lever sensor was set in the reactor to maintain the liquid volume.

The culture was started in batch mode with glucose and volatile suspended solids (VSS) concentration of 15 g/L and 4 g/L, respectively. After 5 cycles of 12 h the reactor was switched to continuous system. The feed solution was fed into the reactor by a peristaltic pump (Masterflex, Barnann, Illinois, USA).

2.2 Data acquisition system

Biogas flow was measured using a flow meter ADM 2000 (Agilent Technologies, Inc.) connected at a serial port of a personal computer. The percent of hydrogen in the biogas was measured with a HY-OPTIMA analyzer model 7000 (H2scan), which was connected to the personal computer using a device DAQ NI-USB-6008 (National Instrument Inc.).

2.3 Analytical method

The concentration of glucose at the influent and the effluent were determined according to the Dubois method [9]. The VSS concentration was determined according to the standard method [10]. To identify the biogas composition a gas chromatograph (SRI-8610C) was used, equipped with a thermal conductivity detector and two stainless steel columns packed. The carrier gas used was nitrogen at a flow rate of 20 ml/min. The temperatures of operation at the injector and the detector were 90 °C and 150 °C, respectively. The concentration of volatile fatty acids (VFA), acetic, propionic and butyric, and ethanol were measured using another gas chromatograph (Varian 3300) equipped with a flame ionization detector and a silica capillary column (Zebron ZB-FFAP) of 15 m long and 0.53 mm internal diameter. The samples were filtered firstly in glass fiber filter and then a nitrocellulose filter (0.45 µm), and later on acidified with hydrochloric acid. Nitrogen was used as carrier gas at flow of 9.5 ml/min. Injector and detector temperatures were maintained at 190 and 210 °C, respectively.

2.4 Coupled observer to estimate the glucose concentration at the reactor input.

The hydrogen production bioreactor has two inputs, the substrate concentration Glu_{in} (an uncontrolled input) and the flow rate Q_{in} (a controlled input). On the other hand, the total gas flow rate Q_{gas} and the hydrogen fraction $\%H_2$ at the reactor output are measured. Using both measurements, the hydrogen flow rate at the reactor output $q_{H2,gas}$ can be calculated.

In order to estimate the glucose concentration at the reactor input, the coupled observer proposed in [10] and shown in figure 1, is considered. The observer consists of a Luenberger observer followed by a super-twisting observer. By measuring the hydrogen flow rate at the reactor output the Luenberger observer estimates the glucose and the biomass concentrations inside the reactor. Then, the super-twisting observer uses these estimations to estimate the glucose concentration at the reactor input.

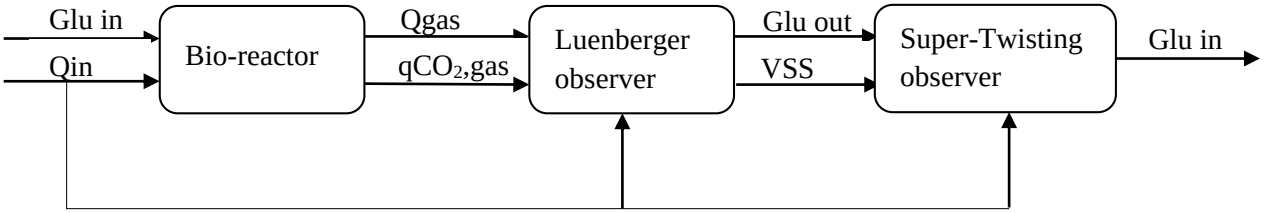

Figure 1. Coupled observer to estimate the glucose at the reactor input.

Since the coupled observer is based on the model of the process, firstly, the parameters of the model are computed. The model considered in [11] has two kinds of parameters: the pseudo-stoichiometric and the kinetic ones. On the other hand, the model has ten state variables, eight in liquid phase: glucose, acetate, propionate, butyrate, ethanol, biomass, carbon dioxide and hydrogen; and two in gas phase: carbon dioxide and hydrogen.

The biohydrogen production reactor was then operated in five nominal conditions resulting of the combination of hydraulic retention times (HRT) and inflow substrate concentrations according to a Latin hypercube experimental design [12] (see Table 1). Once the steady state was reached for each operation condition the analyses were performed, and then the reactor returned to the standard operation condition (HRT=8h and Glu_{in}=15g/L) before test the next condition.

Table 1. Nominal conditions of operation reactor according to Latin hypercube experimental design.

Number of condition	Glucose concentration (g/L)	HRT (h)
1	15	8
2	10	10
3	20	8
4	15	10
5	25	6

A variance analysis was performed to determine that two reactions explain 88% of the total variance of the experimental data measured between days 1 and 63. By considering three reactions 94% of the variance can be explained. This analysis shows that adding a third reaction would account for only 6% of the variance of the experimental data, which is lower than the 100/8 = 12.5 % of the variance of each state variable in liquid phase. In this way, the pseudo-stoichiometric parameters are grouped in an 8x2 matrix K. The reactions considered are based on the Monod model. Therefore, the kinetic parameters are grouped

in two 2-dimension column-vectors μmax and KGlu.

The Luenberger observer considers only the dynamics of the glucose, the biomass and the hydrogen in liquid and gas phases. Thus, the Luenberger observer correction term is a 4-dimension row-vector LL.

The super-twisting observer considers the dynamics of the glucose inside the reactor and the glucose at the reactor input. The super-twisting observer correction term is then a 2-dimension row-vector LST.

In order to compute the matrix K an optimization Non-Linear Problem (NLP) to minimize the product of the kernel of KT and the matrix of experimental data is solved by using the MATLAB function fmincon with the SQP algorithm [11]. In order to compute the vectors max and KGlu a NLP to minimize the difference between experimental data and simulation results is solved by using the MATLAB function RegNonO [10]. The parameters computed are then:

$$K^T = \begin{bmatrix} -1 & 0.3238 & 0.0174 & 0.2737 & 0.0219 & 0.1135 & 0.0087 & 0 \\ -1 & 0 & 0.0205 & 0.3028 & 0.0242 & 0.0934 & 0.0049 & 0.0351 \end{bmatrix}$$

$$\mu_{\max} = [37.32 \quad 27.24]$$

$$K_{Glu} = [0.29 \quad 0.26]$$

On the other hand, in order to compute the correction term LL, an optimization semi-definite problem (SDP) to decrease the influence of a disturbance (the unknown input Glu_{in}) on the estimation error is solved [11]. In order to compute the correction term LST, a SDP to decrease the influence of the uncertainties related to both the glucose and the input glucose dynamics on the estimation error is solved [11]. Both SDP are solved using the SEDUMI solver over the YALMIP toolbox in the MATLAB environment. The correction terms computed are then:

$$L_L = \begin{bmatrix} 108.93 \\ 0.67 \\ 0.06 \\ 0.08 \end{bmatrix}$$

$$L_{ST} = \begin{bmatrix} 0.43 \\ 1.79 \end{bmatrix} x10^6$$

The coupled observer is implemented in the MATLAB environment. The hydrogen flow rate at the reactor output is measured each 10 seconds. After 10 minutes, the mean is calculated and it is used together with the current input flow rate Qin to compute the current estimations of the glucose and the biomass inside the reactor, and the glucose at the reactor input.

3. Results and discussion

Once the model has been calibrated and both correction terms, from the Luenberger observer and the super-twisting observer, have been computed, the observer was validated on-line by using real-time hydrogen flow rates measured at the bioreactor output. In order to validate the observer, the reactor was operated for 15 days in three different nominal conditions of substrate concentration and HRT: on days 1-7 at 20 g/L and 6 h, on days 7-13 at 15 g/L and 4 h, and on days 13-15 at 10 g/L and 4 h, respectively.

Figures 1, 2 and 3 show the estimated VSS concentration in the reactor, glucose concentration at the effluent and at the influent, respectively. During the first condition (days 1-7) the estimation of the VSS was very close to the analytical method. After the day seven, in the second condition (15 g/L), the VSS concentrations estimated for the observer were below 1 g/L. Similar behavior was observed in the estimation of the substrate concentration at the input. During the operation at 20 g/L the value estimated was close to the value obtained with the analytical method, and at 15 g/L (days 7-13) the estimation of the substrate at the input was lower than the real concentration. Apparently, the disturbance (the unknown input) was not correctly rejected by the Luenberger observer because of the uncertainty on the glucose dynamics grew, the glucose at the reactor input was not correctly estimated as well. In order to have a better estimation the operating point of the Luenberger observer was modified in the ninth day of the bioreactor operation. Nevertheless, even if the error estimation decreased, the coupled observer performance was not satisfactory. Then, the condition of operation was changed to 10 g/L of substrate concentration. In this condition the estimation of substrate concentration at the input was very close to the real concentration despite the error estimation of VSS concentration, demonstrating the robustness of the super-twisting observer.

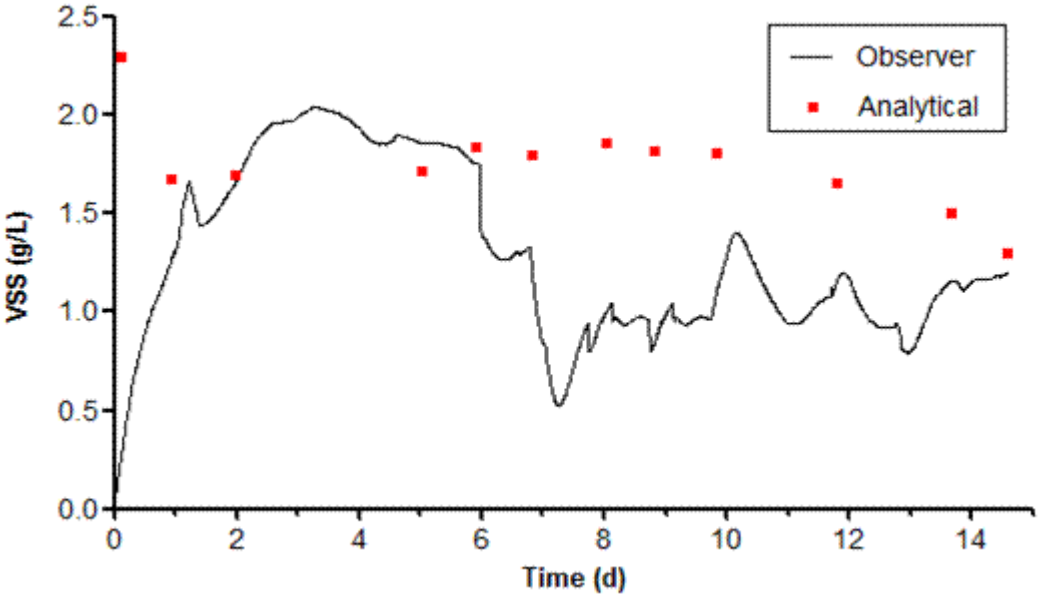

Figure 1. Estimation of VSS and the result of analytical method.

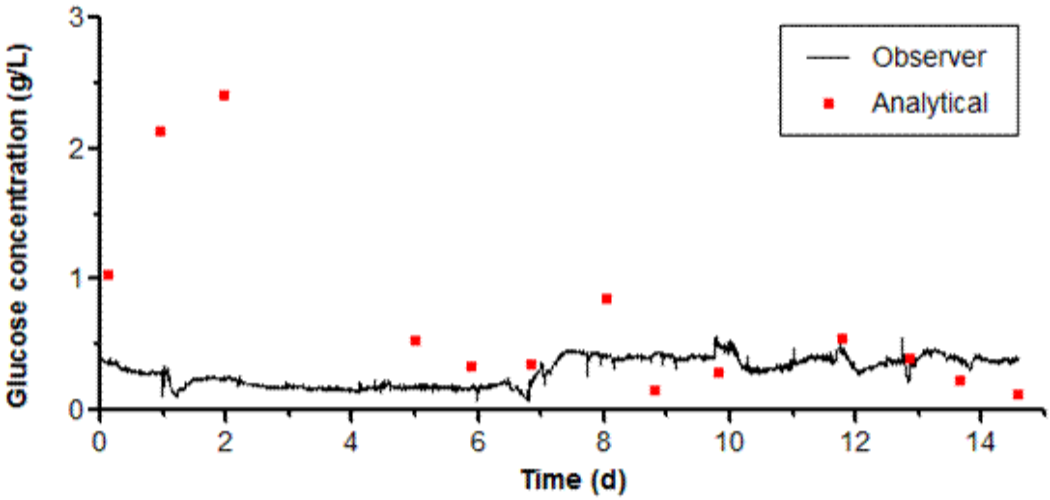

Figure 2. Estimation of substrate concentration inside the reactor.

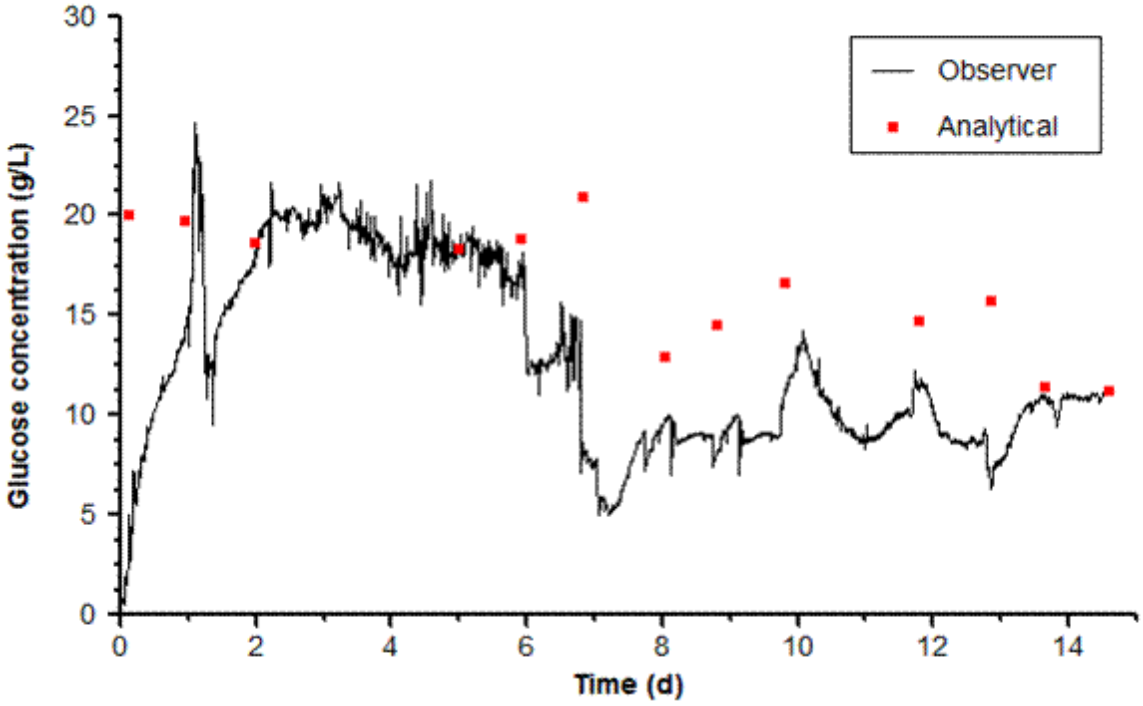

Figure 3. Estimation of substrate concentration at the input of the reactor.

4. Conclusions

This study presented the results of experimental validation of a Luenberger observer coupled to a Super-Twisting for the estimation of substrate concentration at the input of the reactor. When the glucose concentration was 20 and 10 g/L, the observer was able to estimate the concentration to close to the real. The result was not completely successful at 15 g/L, although the operating point of the Luenberger observer was modified, the error estimation was not sufficiently decreased.

Therefore, further experimental implementation of the coupled observer must be carried out in order to compute the observer gains to correctly estimate the substrate at the reactor input for any operation condition.

Once the observer correctly estimates the glucose at the reactor input, the optimization strategy will be implemented to compute the optimal flow rate at the reactor input for maximizing the hydrogen productivity rate.

Acknowledgements

This research was supported through FOMIX CONACYT project (192341). The authors are grateful to Jaime Perez for the technical support and fruitful discussions.

References

[1] R. L. Evans. Fueling our future: An introduction to Sustainable Energy. 1st ed. Cambridge University Press. N. Y. 2007.

[2] B. Rohland, J. Nitsch, H. Wendt. Hydrogen and fuel cells: the clean energy system. J. of power source. 1992; 37: 271-277.

[3] Mohan, S. V., Bhaskar, Y. V. Sarma, P. Bio-hydrogen production from chemical wastewater treatment in biofilm configured reactor operated in periodic discontinuous batch mode by selectively enriched anaerobic mixed consortia. Water Research. 2007; 41: 2652–2664.

[4] K. K. Ilgi, K. Fikret. Bio-hydrogen production from waste materials. Enzyme and Microbial Technology. 2006; 38: 569-582.

[5] J. Wang, W. Wan. Factors influencing fermentative hydrogen production: Areview. Int. J. of Hydrogen Energy. 2009: 799-811.

[6] H. Hafez, G. Nakhla, M. Hesham, E. Elbeshbishy, B. Baghchehsaraee. Effect of organic loading on a novel hydrogen bioreactor. Int. J. of Hydrogen Energy. 2010; 35: 81-92.

[7] L. Shen, D. M. Bagley, S. N. Liss. Effect of organic loading rate on fermentative hydrogen production from continous stirred tank and membrane bioreactor. Int. J. of Hydrogen Hydrogen Energy. 2009; 34: 3689-3696.

[8] G. Buitrón, C. Carbajal. Biohydrogen production from Tequila vinasses in an anaerobic sequencing batch reactor: Effect of initial substrate concentration, temperature and hydraulic retention time. Bioresource Technology. 2010; 101: 9071–9077.

[9] M. Dubois, K. A. Gilles, P. A. Rebers, F. Smith. Colorimetric method for determination of sugar related substrate. Analytical Chemistry. 1956; 28: 350-356.

[10] APHA. Standard Methods for the Examination of Waters and Wastwater. 11th ed. Port City Press. Baltimore. 2005.

[11] I. Torres-Zúñiga, J. E. Ramírez, A. Vargas, E. Latrille and G. Buitrón. Coupled robust observer to estimate the substrate at the input of a biohydrogen production reactor. Submitted to Chemical Engineering Journal. 2014.

[12] A. Saltelli, M. Ratto, T. Andres, F. Campolongo, J. Cariboni, D. Gatelli, M. Saisana, S. Tarantola, Global sensitivity analysis, John Wiley and Sons, Ltd, 2008.

[13] J. E. Ramírez, I. Torres Zúñiga, G. Buitrón. Real time optimization for fermentative hydrogen production in a continuous reactor. Submitted to Process Biochemistry.

Optimization of photo-fermentative hydrogen production using volatile fatty acids

R. Cardeña[1], G. Moreno[1], G. Buitrón[1]

[1]Laboratory for Research on Advanced Processes for Water Treatment, Instituto de Ingeniería, Unidad Académica Juriquilla, Universidad Nacional Autónoma de México, Blvd.Juriquilla 3001, Querétaro, Qro, México, 76230
Tel: +52 442 192 6165; e-mail: gbuitronm@iingen.unam.mx

ABSTRACT

A combination of photofermentation with dark fermentation is an ideal option for efficient hydrogen production. In the present study, the optimum concentration of substrates for the hydrogen production was found by response surface methodology. The optimum combination of three individual fatty acids was determined by Box Behnken design and Central Composite design. The influence of a mixture of volatile fatty acids was evaluated using the Phototrophic Hydrogen-Producing Mixed Bacterial Consortium obtained from bio-electrochemical system used to produce hydrogen. For these experiments, 100 mg VSS L^{-1} were used. The serologic bottles were then sparged with argon for a period of 30 s to remove dissolved oxygen and to create an oxygen free microenvironment prior to closing with rubber septum**.** The tests were placed on the shaker plate at 100 rpm and operated at 30-35 °C and illuminated under a constant radiation of 5000 lux. It was observed an inhibition of hydrogen production by the propionic acid. Also was presented the decrease in hydrogen production with the increase pH that occurred in the tests during the experimentation. The ammonium formation was responsible for pH changes. The concentrations of ammonia nitrogen formed at the tests ranged between 0.4 and 10.8 mg L^{-1}. From the ANOVA analysis the both experimental designs resulted significant, as it is evident from the Fischer's F-test with a high F-values ($p<0.001$-$p<0.017$). The R^2 values near to 1 (0.9766-0.9089) in both cases suggests good correlation between experimental and predicted values. The results showed that a maximum hydrogen production rate of 6.5 mmol d^{-1} L^{-1} and maximal amount of hydrogen produced of 108.8 mmol L^{-1} were obtained when the concentrations of acetic acid, propionic acid and butyric acid were 1200 mg L^{-1}, 715 mg L^{-1} and 1571 mg L^{-1}, respectively.

Keywords: Photofermentation, hydrogen, volatile fatty acids

1. Introduction

At present, fossil fuels are considered the main source of energy supply. However, because of its growing demand and limited availability an alternative source of energy is needed [1]. Hydrogen (H_2) is considered to be one of the most promising fuels of the future due to high energy content (122 kJ g^{-1}) which is 2.72 times that for gasoline [2-3]. Hydrogen gas is also a clean fuel with no CO_x, SO_x and NO_x emissions. Besides, H_2 is an important energy carrier and can be used in fuel cells for generation of electricity [4-5]. However, hydrogen gas is not readily available in nature like fossil fuels and natural gas, but can be produced from renewable materials such as biomass [2] and water [6]. The biological production of hydrogen is considered environmentally friendly. In particular, this process can use a variety of organic substrates as carbon sources, including wastes [7]. So, there exists a double benefit: the waste reduction and the energy production.

The combination of photosynthetic bacteria with fermentative bacteria can provide a system for hydrogen photo production from residual carbohydrates such as organic wastes. Photosynthetic non-sulfur (PNS) bacteria have the ability to convert volatile fatty acids (VFAs) to H_2 and CO_2 under anoxygenic conditions [5, 8]. PNS bacteria also have the ability to use carbon sources like glucose, sucrose, succinate rather than VFA for H_2 production [9-11]. The most widely known PNS bacteria used in photo-fermentative H_2 production are *Rhodobacter sphaeroides O.U001*, *Rhodobacter capsulatus*, *R. sphaeroides-RV*, *Rhodobacter sulfidophilus*, *Rhodopseudomonas palustris* and *Rhodospirillum rubrum* [12]. Both hydrogenase and nitrogenase enzymes were detected in PNS bacteria [5, 13]. However, nitrogenase is the main enzyme responsible in molecular H_2 production under anoxygenic conditions [13-14]. The photofermentation culture is very promising because of the purity of the generated biogas (H_2:80%) [15]. However, it must be considered the different potential of substrates. For example, during dark fermentation are produced acetate, propionate and butyrate mainly [16].

The one factor-at-a-time design has two main drawbacks, one is it does not take into consideration the interactions among different factors; it involves a relatively large number of experiments, which makes it laborious and time-consuming to carry out the experiments, especially when the number of factors is large [17]. On the contrary, factorial design is able to study the effects of more than one factor at two or more levels. The experimental design generally includes various combinations of different factor levels, which enables it to depict the interactions among different factors and to be more efficient to deal with a large number of factors. Factorial design can be classified into two categories: full factorial design and fractional factorial design.

The number of runs for a full factorial design increases geometrically as the number of factors increases, when the effects of a large number of factors are to be studied simultaneously, a great many runs of experiment are required. Generally, this will constitute a larger experiment that is not economically and practically feasible [18]. Fractional factorial design provides an alternative when the number of runs for a full factorial design is too large to be practicable. Taguchi design, Plackett–Burman design, central composite design and Box–Behnken design are fractional factorial designs that were used a lot for fermentative hydrogen production processes provides an economical alternative [19].

The use of the consortium photofermentative can to be better than a pure strain because it isn't need sterilized and the operation conditions are easier of controller. Also the consortium mixed obtained can present good resistance to inhibitions produced for variations in the system. In the present study, Box-Behnken design and Central Composite design were used for evaluate the effect of a mixture of acetic, propionic and butyric acids on the hydrogen production rate using photobacteria. The individual maximum

substrate concentration for acetic acid, propionic acid and butyric acid were already found by literature review. The optimum concentration of volatile fatty acids for maximum hydrogen production is found by applying response surface methodology.

2. Experimental

2.1 Inoculating and enriching the microbial consortium

The Phototrophic Hydrogen-Producing Mixed Bacterial Consortium (PHPMBC) was obtained from bio-electrochemical system used to produce hydrogen. Firstly, the sludge was the growth tests, bacteria plus 150 mL of medium and the organic acid and glutamate were placed in 250 mL glass bottles. Then, argon gas was purged in the headspace to ensure the anaerobic conditions. The culture medium was supplemented with acetate (2.46 g L^{-1}), butyrate (3.30 g L^{-1}) and sodium glutamate (0.37 g L^{-1}). The initial pH was adjusted to 6.8 with NaOH (1 N). The bottle was incubated about at 30-35 °C illuminated by 4 fluorescent lamps (20 W) and 4 tungsten lamps (60 W). After growing for 100 hours, the biomass with the purple non-sulfur photosynthetic bacteria was harvested.

2.2. Operation of the batch reactors

The basal medium [20] was constituted of 0.75 gL^{-1} K_2HPO_4, 0.85 gL^{-1} KH_2PO_4, 0.2 gL^{-1} $MgSO_4$, 11.78 mg L^{-1} $FeSO_4 \cdot 7H_2O$, 2.8 mg L^{-1} H_3BO_3, 0.75 mgL^{-1} $Na_2MoO_4 \cdot 2H_2O$, 0.24 mg L^{-1} $ZnSO_4 \cdot 7H2O$, 2.1 mg L^{-1} $MnSO_4 \cdot 4H_2O$, 0.04 mg L^{-1} $CuCl_2 \cdot 2H_2O$, 0.75 mg L^{-1} $CaCl_2 \cdot 2H_2O$, 2.0 mg L^{-1} EDTA-Na, 3.78 mg L^{-1}, B1 vitamin and 3.57 mg L^{-1} de biotin. For this stage a C/N ratio of 16. The influence of a mixture of VFAs was evaluated using the PHPMBC. For these experiments, 100 mg VSS L^{-1} were used. The serologic bottles were then sparged with argon for a period of 30 s to remove dissolved oxygen and to create an oxygen free microenvironment prior to closing with rubber septum. All the bottles were placed on the shaker plate at 100 rpm. Was operated at 30-35 °C and illuminated under a constant radiation of 5000 lux.

2.3 Box-Behnken design

Box–Behnken design (BBD) is a three-level fractional factorial design developed by Box and Behnken. The design can be thought of as a combination of a two-level factorial design with an incomplete block design. In each block, a certain number of factors are put through all combinations for the factorial design, while other factors are kept at the central levels. BBD provides an economical alternative to the central composite design, because it has less factor levels than the central composite design and does not contain extreme high or extreme low levels. BBD matrix was used to investigate the effect of VFAs concentration on photofermentative hydrogen production. The variables designated were acetic acid concentration (X_1), butyric acid concentration (X_2) and propionic acid concentration (X_3) on hydrogen production. The factors X_1, X_2 and X_3 were considered as an independent variables and maximal amount of hydrogen produced (H_{max}) and maximum hydrogen production rate (R_{max}) were the response (dependent variable). The low, middle and high level of each variable were coded as −1, 0 and +1 respectively. The coded and actual values were given in Table 1.

The following second order polynomial equation was adopted to study the effects of variables to the response.

$$H_{max}, R_{max} = \beta_0 + \beta_1 X_1 + \beta_2 X_2 + \beta_3 X_3 + \beta_{11} X_1^2 + \beta_{22} X_2^2 + \beta_{33} X_3^2 + \beta_{12} X_1 X_2 + \beta_{13} X_1 X_3 + \beta_{23} X_2 X_3 \quad (1)$$

where H_{max} and R_{max} are the response, β_0 is the constant term; β_1, β_2 and β_3 are the coefficient of linear terms; β_{11}, β_{22} and β_{33} are the coefficient of quadratic terms; β_{12}, β_{13} and β_{23} are the coefficient of cross product terms respectively. A statistical design package, Minitab 15 is used for regression analysis of the data obtained and to estimate the coefficients of the second-degree polynomial equation.

The estimated second-order polynomial model can be displayed as a surface plot and a contour plot, by varying only two factor levels, while keeping other factor levels constant. The surface plot and contour plot will visually show the response over a region of interesting factor levels. In addition, they will indicate how sensitive the response is to the change of each factor levels and to what degree the factors interplay as they affect the response. Based on the analysis of variance (ANOVA) of the estimated model, terms which have significant effects on the response can be determined. It is important to note that all interactions higher than second order have been neglected in Eq. (1). A total of 15 experiments were needed to estimate of the model.

Table 1. Experimental range, level and code of independent variables for the optimization of hydrogen production

Independent variables	Symbol coded	Range and levels		
		-1	0	1
Acetic acid concentration (mg L^{-1})	X_1	125	1235	2345
Butyric acid concentration (mg L^{-1})	X_2	50	160	270
Propionic acid concentration (mg L^{-1})	X_3	175	672.5	1170

2.4 Central composite design

The BBD presented only the optimized value of propionic acid. A two-level central composite design (CCD) was used to construct second-order models for hydrogen production (Table 2). The CCD consisted of three types of experimental points: cube points, axial points, and center points. The center points were used to calculate the experimental error, and the distance of axial points from the center points in this work was fixed at 1.414 [21]. The experimental factors taken into consideration were the acetic acid concentration and butyric acid concentration. The maximal amount of hydrogen produced (H_{max}) and maximum hydrogen production rate (R_{max}) were selected as the model response. The experimental runs were analyzed to fit second-order polynomial equation, as shown in Eq. (2).

$$H_{max}, R_{max} = \beta_0 + \beta_1 X_1 + \beta_2 X_2 + \beta_{11} X_1^2 + \beta_{22} X_2^2 + \beta_{12} X_1 X_2 \quad (2)$$

where H_{max} and R_{max} are the response, β_0 is the constant term; β_1 and β_2 are the coefficient of linear terms; β_{11} and β_{22} are the coefficient of quadratic terms; β_{12} is the coefficient of cross product terms respectively. A statistical design package, Minitab 15 is used for regression analysis of the data obtained and to estimate the coefficients of the second-degree polynomial equation. The adequacy of the proposed model was verified using analysis of variance (ANOVA), R^2 and adjusted R^2.

New concentrations of acetic acid and butyric acid (Table 2) were proposed based on data Nan-Qi [22]. The propionic acid concentration remained fixed at 715 mg L^{-1} for the 13 tests.

Table 2. Experimental range, level and code of independent variables for the optimization of hydrogen production

Independent variables	Symbol coded	Range and levels				
		-1.414	-1	0	1	1.414
Acetic acid concentration (mg L^{-1})	X_1	85.8	500	1500	2500	2914.2
Butyric acid concentration (mg L^{-1})	X_2	85.8	500	1500	2500	2914.2

2.5 Analytical methods

Hydrogen, carbon dioxide and methane were analyzed with a gas chromatograph (Agilent 6890 N) equipped with a thermal conductivity detector and a 30 m long (0.53 mm id) Carboxen 1010 Plot column. The temperature of the injection port, column and detector, were 200, 100 and 230 °C, respectively. Nitrogen was used as the carrier gas at a flow rate of 4 mL min^{-1}. Liquid samples were taken at the end of the run for the analysis of VFAs and solvents. To analyze VFA, alcohols and acetone, 1 mL of sample was centrifuged at 600 g during 10 min. Concentration of these by-products was determined using a chromatograph (Varian 3300) fitted with a FID detector and a 15 m long (0.53 mm id) Zebron ZB-FFAP column. Injector and detector temperatures were maintained at 190 and 210 °C, respectively. The temperature of the column was maintained at 45 °C for 1.5 min; then, it was increased to 135 °C at a rate of 8 °C min^{-1}. The carrier gas was nitrogen at 9.5 ml min^{-1}. Biogas was monitored daily using a pressure transducer. Hydrogen content, from the head space of the bottles, was analyzed twice a week, VSS concentration, COD and N–NH_3 were determined according to standard methods [23].

2.6 Kinetic analysis

The cumulative hydrogen volume in the tests followed he modified Gompertz Eq. (3) was used to fit the kinetics of biohydrogen production using Microsoft's software Excel 2010. This equation has been widely used to model gas production data [24]:

$$H = H_{max} exp\left\{-exp\left[\frac{R_{max}\times e}{H_{max}}(\lambda - t) + 1\right]\right\} \quad (3)$$

where, H(t) (mL) is the total amount of hydrogen produced at culture time t (h); H_{max} (mL) is the maximal amount of hydrogen produced. R_{max} (mL h^{-1}) is the maximum hydrogen production rate; λ (h) is the lag time before the exponential hydrogen production.

3. Results and discussion

3.1 Box-Behnken design approach for optimization of hydrogen production

Multiple regression analysis of the experimental data yielded the following regression equations for the hydrogen production (Eqs. 4 and 5).

$$H_{max} = -0.2017 + 4.526\times10^{-4}X_1 - 6.845\times10^{-3}X_2 + 1.146\times10^{-2}X_3 - 2.203\times10^{-7}X_1^2 + 1.721\times10^{-5}X_2^2 - 6.51\times10^{-6}X_3^2 + 2.285\times10^{-6}X_1X_2 + 2.427\times10^{-7}X_1X_3 + 2.056\times10^{-7}X_2X_3 \quad (4)$$

$$R_{max} = 1.002 + 2.096 \times 10^{-4}X_1 + 8.421 \times 10^{-4}X_2 - 8.201 \times 10^{-4}X_3 + 5.675 \times 10^{-8}X_1^2 - -7.714 \times 10^{-6}X_2^2 + 1.279 \times 10^{-8}X_3^2 - 1.009 \times 10^{-6}X_1X_2 + 2.852 \times 10^{-8}X_1X_3 + 2.695 \times 10^{-6}X_2X_3 \quad (5)$$

where H_{max} is the maximal amount of hydrogen produced, R_{max} is the maximum hydrogen production rate, X_1 is the initial acetic acid concentration, X_2 is the initial butyric acid concentration and X_3 is the initial propionic acid concentration.

BBD matrix of independent variables in coded units along with experimental and predicted values for hydrogen production was shown in Table 3. According to BBD, batch experiments were carried out with different combinations of the independent variables in order to find the combined effects of these factors toward hydrogen production.

Table 3. The Box-Behnken experimental design with Gompertz values.

Run	X_1	X_2	X_3	H_{max} of H_2			R_{max} of H_2		
				Observed (mmol)	Predicted (mmol)	Error (%)	Observed (mmol/d)	Predicted (mmol/d)	Error (%)
1	0	0	0	5.00	4.81	3.9	0.84	0.85	-2.1
2	0	0	0	5.00	4.81	3.9	0.99	0.85	16.3
3	-1	1	0	4.06	4.16	-2.3	0.57	0.61	-6.4
4	-1	0	-1	1.38	1.06	23.4	0.96	0.88	9.6
5	0	1	1	5.13	5.11	0.5	0.64	0.63	2.6
6	-1	0	1	3.88	3.82	1.7	0.54	0.51	4.4
7	0	0	0	4.42	4.81	-8.7	0.73	0.85	-14.3
8	0	1	-1	1.83	2.06	-12.5	0.62	0.67	-6.9
9	0	-1	-1	1.70	1.72	-1.7	1.18	1.20	-1.3
10	0	-1	1	4.96	4.73	4.6	0.61	0.57	8.1
11	1	0	-1	1.70	1.76	-3.9	1.29	1.31	-1.7
12	1	0	1	4.73	5.06	-6.8	0.92	1.01	-8.4
13	1	1	0	5.98	5.69	4.9	0.89	0.82	8.3
14	1	-1	0	4.87	4.77	2.0	1.34	1.30	3.0
15	-1	-1	0	4.06	4.36	-7.3	0.53	0.59	-11.5

The statistical significance of the polynomial equation was checked by F-test. Analysis of variance (ANOVA) for response surface quadratic model is given in Table 4. Significance of model terms is checked by their respective p values. P-value less than 0.05 suggests model terms are significant and less than 0.0001 are highly significant. The goodness of fit of the model was checked by determination of coefficient (R^2) and adjust R^2. The R^2 value varies from 0 to 1.0 and R^2 value close to 1.0 implies better accuracy of the model. But incorporation of large number of insignificant variables in the model may result high R^2 value but model become erroneous and there by predict poor response. So the term adj R^2 was introduced which corrects R^2 value according to the sample size and number of terms in the model. Ideally adjust R^2 should be close to R^2 value. Large difference between R^2 and adj R^2 gives a warning that model contain too many insignificant terms [25].

Table 4. Analysis of variance (ANOVA) for the hydrogen production.

Source of variation	H_{max}					R_{max}				
	DF[a]	SS[b]	MS[c]	F-value	P	DF[a]	SS[b]	MS[c]	F-value	P
Regression	9	30.925	3.436	23.16	0.001	9	0.960	0.010	7.98	0.017
Linear	3	20.243	6.812	45.92	0.000	3	0.757	0.252	18.88	0.004
Square	3	10.104	3.368	22.71	0.002	3	0.054	0.018	1.36	0.357
Interaction	3	0.383	0.123	0.86	0.518	3	0.148	0.049	3.71	0.096
Residual	5	0.741	0.148			5	0.066	0.013		
Lack-of-fit	3	0.517	0.172	1.54	0.417	3	0.032	0.011	0.62	0.664
Pure error	2	0.224	0.112			2	0.034	0.017		
Total	14	31.667				14	1.027			

H_{max}:R^2=0.9766, Adjust R^2=0.9344 R_{max}:R^2=0.9349, Adjust R^2=0.8178

[a] Degrees of freedom

[b] Sum of squares

[c] Mean square

For H_{max} (maximal amount of hydrogen produced) the model was found to be significant, as it is evident from the Fischer's F-test with a high F-value 23.16 ($p<0.001$). The high R^2 value (0.9766) suggests good correlation between experimental and predicted values and 97.66 % variability of the response could be explained by the model and about only 2.34 % of the total variation cannot be explained by this model. Adjust R^2 value (0.9344) was found to be very close to R^2. The lack of fit test, measures the failure of the model to represent experimental data in the experimental domain at point which are not included in regression analysis. Lack of fit was found to be non-significant (P value 0.417) and it suggests that the model equation was adequate to predict the maximal amount of hydrogen produced under any sets of combination of the variables. In the case of R_{max} (maximum hydrogen production rate) the model was found to be significant, as it is evident from the Fischer's F-test with a high F-value 7.98 ($p<0.017$). The high R^2 value (0.9349) suggests good correlation between experimental and predicted values and 93.49 % variability of the response could be explained by the model and about only 6.51 % of the total variation cannot be explained by this model. Adjust R^2 value (0.8178). Lack of fit was found to be non-significant (p value 0.664) and it suggests that the model equation was adequate to predict the maximum hydrogen production rate under any sets of combination of the variables.

P-value serves as a tool for checking the significance of each coefficient. P-value less than 0.05 indicate model terms are significant. It can be concluded from Table 5 that, for H_{max} the coefficient of linear effect of initial acetic acid concentration (X_1) and initial propionic acid concentration (X_3) were significant on amount of hydrogen produced. The coefficient of quadratic term of initial propionic acid concentration (X_3*X_3) was found to be highly significant. On R_{max} the coefficient of linear effect of each model terms (X_1, X_2 and X_3) were significant on hydrogen production rate. 3D plot represents response surface of two independent variables where remaining variables are fixed at their respective zero level. It helps to understand the main and their interaction effect and also to determine optimum level of each variable [26]. The response surface 3D plots for H_{max} and R_{max} have been shown in Fig. 1(a–c) and Fig. 2(a-c), respectively.

Table 5. Significance of regression coefficient with codified values (BBD)

Model term	H_{max}			R_{max}		
	Parameter estimate (coefficients)	T	P	Parameter estimate (coefficients)	T	P
Constant	4.806	21.616	0.000	0.853	12.790	0.000
X_1	0.485	3.564	0.016	0.230	5.633	0.002
X_2	0.178	1.312	0.247	-0.116	-2.853	0.036
X_3	1.512	11.107	0.000	-0.167	-4.095	0.009
$X_1 * X_1$	-0.271	-1.354	0.234	0.069	1.162	0.298
$X_2 * X_2$	0.208	1.039	0.346	-0.093	-1.551	0.182
$X_3 * X_3$	-1.611	-8.038	0.000	0.003	0.053	0.960
$X_1 * X_2$	0.279	1.449	0.207	-0.123	-2.132	0.086
$X_1 * X_3$	0.134	0.696	0.518	0.015	0.272	0.796
$X_2 * X_3$	0.011	0.058	0.956	0.147	2.552	0.051

Applying an optimization model was performed with the program Minitab 15. The optimum values of test variables corresponding to the maximum hydrogen production (4.9 mmol y 1.27 mmol d^{-1}) in uncoded units X_1=2345 mg L^{-1}, X_2=50 mg L^{-1} y X_3=715 mg L^{-1}. A maximal amount of hydrogen produced of 4.9 mmol and maximum hydrogen production rate of 1.27 mmol d^{-1} were obtained under optimum conditions. However an optimal concentration of 715 mg L^{-1} of propionic acid was found. This behavior suggests an inhibition of hydrogen production by the propionic acid.

The maximum hydrogen production rate and amount of hydrogen produced obtained was 1.34 mmol H_2 d^{-1} and 5.98 mmol H_2 respectively. Ammonia nitrogen concentrations formed during the experimentation ranged between 0.63 and 2.62 mg L^{-1}. The COD removal varied, the best removal was 87.80 % and the lowest was 41.63 %, have been reported COD removals over 80 % were obtained using purple non-sulfur bacteria named ZX-5 [27]. The pH remained stable throughout the test in 7 approximately. The amount of biomass was measured indirectly by optical density at 660 nm and the results were in the range of 541 and 913 mg VSS L^{-1}. The 15 different bottles were incubated during 400 hours.

3.3 Central Composite design approach for optimization of hydrogen production

CCD matrix of independent variables in coded units along with experimental and predicted values for H_{max} and R_{max} were shown in Table 6. According to CCD, batch experiments were carried out with different combinations of the independent variables in order to find the combined effects of these factors toward hydrogen production. The second order quadratic model expressed by the following equation represents maximal amount of hydrogen produced (H_{max}) and maximum hydrogen production rate (R_{max}) as a function of initial acetic acid concentration (X_1) and is the initial butyric acid concentration (X_2).

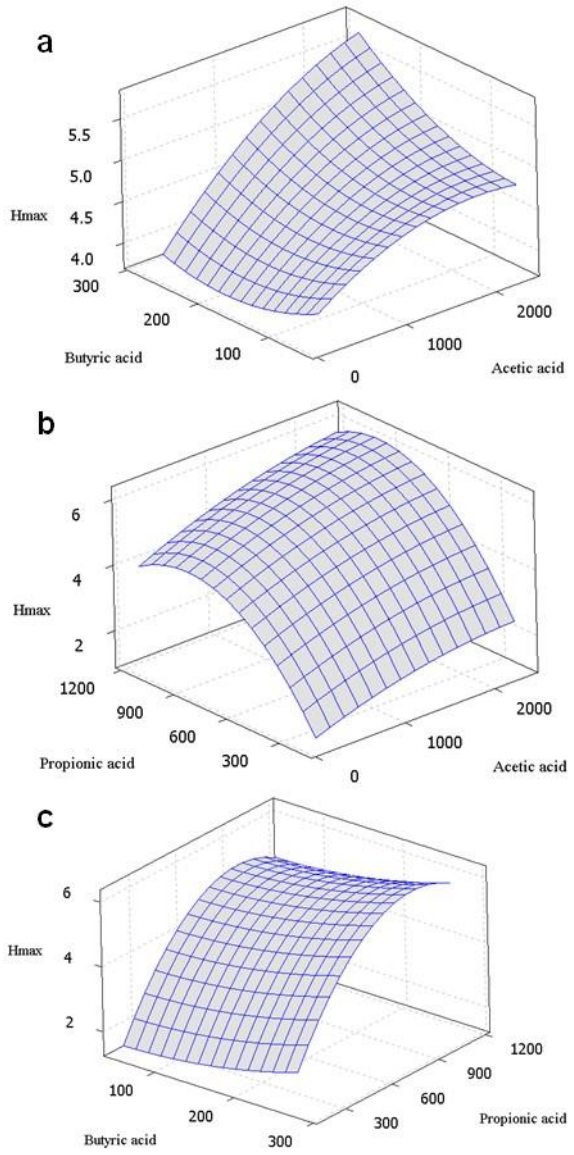

Fig. 1. (a) Response surface plot showing the effect of two variables acetic acid concentration (X_1) and butyric acid concentration (X_2) on amount of hydrogen produced. (b) Response surface plot showing the effect of two variables acetic acid concentration (X_1) and propionic acid concentration (X_3) on amount of hydrogen produced. (c) Response surface plot showing the effect of two variables butyric acid concentration (X_2) and propionic acid concentration (X_3) on amount of hydrogen produced.

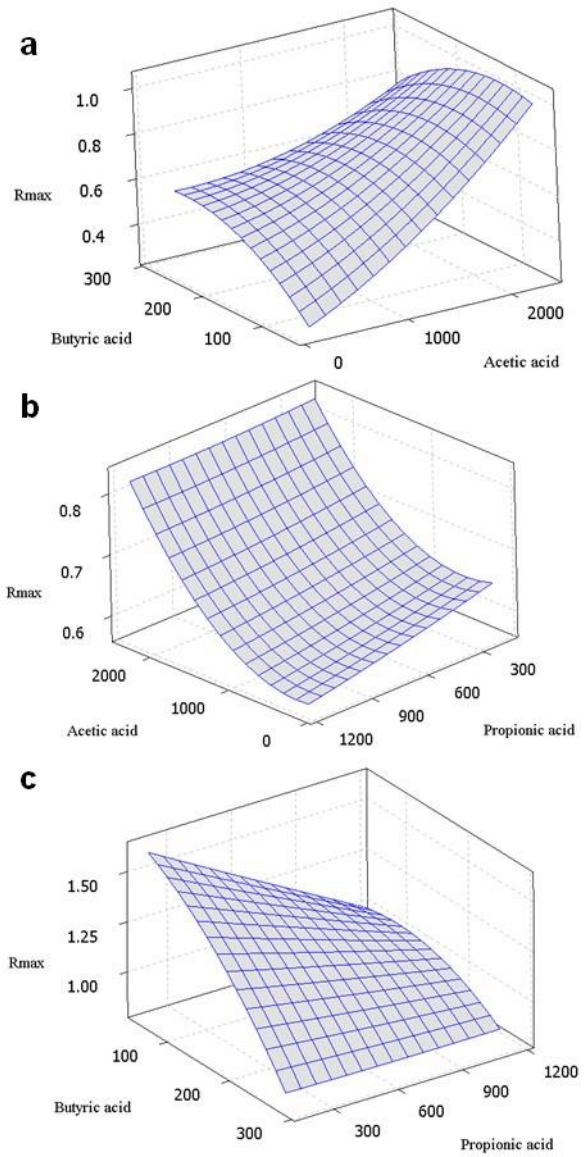

Fig. 2. (a) Response surface plot showing the effect of two variables acetic acid concentration (X_1) and butyric acid concentration (X_2) on hydrogen production rate. (b) Response surface plot showing the effect of two variables acetic acid concentration (X_1) and propionic acid concentration (X_3) on hydrogen production rate. (c) Response surface plot showing the effect of two variables butyric acid concentration (X_2) and propionic acid concentration (X_3) on hydrogen production rate.

$$H_{max} = 5.074 + 3.108 \times 10^{-3} X_1 + 5.038 \times 10^{-3} X_2 - 1.156 \times 10^{-6} X_1^2 - 1.681 \times 10^{-6} X_2^2 - 1.116 \times 10^{-6} X_1 X_2 \quad (6)$$

$$R_{max} = 0.428 + 4.598 \times 10^{-5} X_1 + 2.205 \times 10^{-4} X_2 - 4.781 \times 10^{-8} X_1^2 - 7.192 \times 10^{-8} X_2^2 + 2.679 \times 10^{-8} X_1 X_2 \quad (7)$$

Table 6. The Central Composite experimental design with Gompertz values.

Run	X_1	X_2	H_{max} of H_2			R_{max} of H_2		
			Observed (mmol)	Predicted (mmol)	Error (%)	Observed (mmol/d)	Predicted (mmol/d)	Error (%)
1	0	-1.414	7.72	7.55	2.2	0.39	0.41	-6.8
2	1	-1	7.68	7.70	-0.3	0.44	0.37	15.6
3	0	0	11.21	10.88	2.9	0.66	0.62	6.8
4	-1	1	8.13	8.41	-3.6	0.57	0.57	-1.3
5	0	1.414	7.63	7.49	1.9	0.50	0.54	-7.0
6	-1.414	0	9.46	9.11	3.8	0.63	0.60	4.3
7	1	1	7.63	7.64	0.0	0.51	0.51	12.8
8	0	0	10.22	10.88	-6.5	0.58	0.62	-7.0
9	0	0	11.47	10.88	5.1	0.65	0.62	5.2
10	0	0	10.63	10.88	2.4	0.61	0.62	-15.6
11	-1	-1	8.13	8.43	-3.8	0.53	0.54	-2.6
12	1.414	0	7.99	8.04	-0.6	0.44	0.44	-25.2
13	0	0	10.89	10.88	0.1	0.66	0.62	6.8

Table 7. Analysis of variance (ANOVA) for the selected quadratic model.

Source of variation	H_{max}					R_{max}				
	DF[a]	SS[b]	MS[c]	F-value	P	DF[a]	SS[b]	MS[c]	F-value	P
Regression	5	27.011	5.402	28.77	0.000	5	0.094	0.018	13.97	0.002
Linear	2	1.144	0.572	3.05	0.112	2	0.031	0.015	11.67	0.006
Square	2	25.866	12.933	68.87	0.000	2	0.062	0.031	23.18	0.001
Interaction	1	0.001	0.001	0.00	0.960	1	0.0002	0.0002	0.17	0.696
Residual	7	1.314	0.188			7	0.009	0.001		
Lack-of-fit	3	0.360	0.120	0.50	0.700	3	0.003	0.001	0.74	0.581
Pure error	4	0.954	0.238			4	0.006	0.001		
Total	12	28.325				12	0.103			

H_{max}:R^2=0.9536, Adjust R^2=0.9204 R_{max}:R^2= 0.9089, Adjust R^2=0.8439

[a] Degrees of freedom

[b] Sum of squares

[c] Mean square

Analysis of variance (ANOVA) for response surface quadratic model is given in Table 7. F-values for H_{max} and R_{max} the model were found to be significant, as it is evident from the Fischer's F-test with a high F-value 28.77 and 13.97 ($p<0.000$, $p<0.002$), respectively. Because the R^2 values ($R^2_{Hmax}=0.9536$, $R^2_{Rmax}=0.9089$) and adjust R^2 values ($R^2adj_{Hmax}=0.9204$, $R^2adj_{Rmax}=0.8439$) are in reasonable agreement, the quadratic models (Eqs. 6 and 7) satisfactorily describe the process behaviors within the proposed experimental range. The model adequacy was tested through lack of fit F-tests. The lack of fit, which had a F-value of 0.50 and 0.74 and a P-value of 0.700 and 0.581 in sets H_{max} and $_{Rmax}$, respectively, showed that they were not significant. This implies that all the models had a good fit for prediction.

Table 8. Significance of regression coefficient with codified values (CCD)

Model term	H_{max}			R_{max}		
	Parameter estimate (coefficients)	T	P	Parameter estimate (coefficients)	T	P
Constant	10.883	56.161	0.000	0.633	38.568	0.000
X_1	-0.377	-2.465	0.043	-0.051	-3.993	0.005
X_2	-0.021	-0.139	0.893	0.035	2.718	0.030
$X_1 * X_1$	-1.156	-7.037	0.000	-0.043	-3.136	0.016
$X_2 * X_2$	-1.680	-10.230	0.000	-0.089	-6.401	0.000
$X_1 * X_2$	-0.011	-0.052	0.960	0.007	0.407	0.696

It can be concluded from Table 8 that, for H_{max} the coefficient of linear effect of initial acetic acid concentration (X_1) was significant on amount of hydrogen produced. The coefficient of quadratic terms of all initial substrate concentration (X_1*X_1, X_2*X_2) was found to be highly significant. On R_{max} the coefficient of linear effect of each model terms (X_1 and X_2) were significant on hydrogen production rate. The coefficient of quadratic terms of all initial substrate concentration (X_1*X_1, X_2*X_2) was found to be significant. The response surface 3D plots for H_{max} and R_{max} have been shown in Fig. 3(a–b).

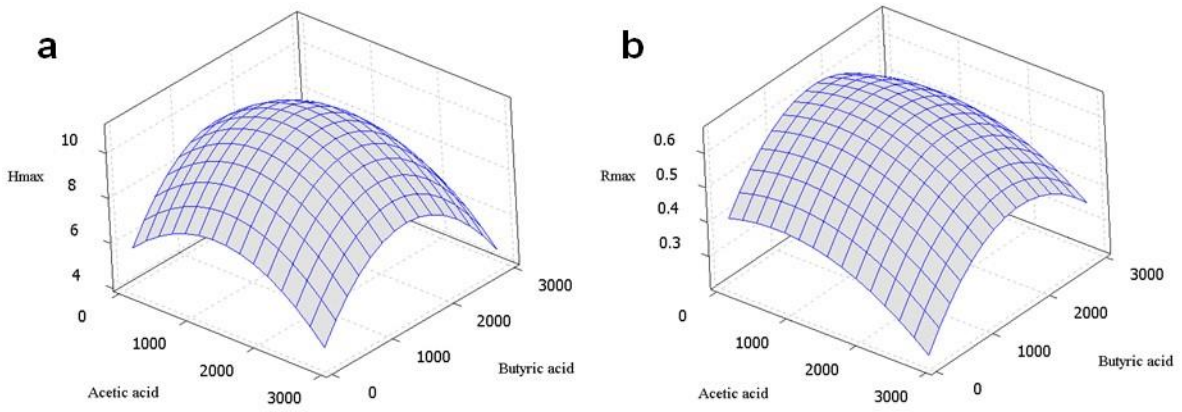

Fig. 3. (a) Response surface plot showing the effect of two variables acetic acid concentration (X_1) and butyric acid concentration (X_2) on amount of hydrogen produced. (b) Response surface plot showing the effect of two variables acetic acid concentration (X_1) and butyric acid concentration (X_2) on maximum hydrogen production rate.

The optimum conditions for the selected parameters were predicted by Minitab 15 software. The maximum hydrogen production was predicted could be achieved with the following concentration conditions; acetic acid of 1200 mg L^{-1} and butyric acid of 1571 mg L^{-1}. Under these conditions, the predicted H_{max} was 10.88 mmol H_2 and R_{max} was 0.65 mmol H_2d^{-1} with a desirability value of 0.99. The optimum concentrations corresponding to the maximum hydrogen production were acetic acid 1200 mg L^{-1}, propionic acid 715 mgL^{-1} and butyric acid1571 mg L^{-1}.

Have been reported that the optimum concentrations of VFAs in the hydrogen production found between 1800 and 2500 mg L^{-1} [28-30]. During the experimentation were obtained the maximum hydrogen yields were to average concentrations at 3500 mg L^{-1} of VFAs. Shi and Yu [31] reported its optimal condition at 1800, 200 and 1000 mg L^{-1} of acetic acid, propionic and butyric respectively using *Rhodopseudomonas capsulata*.

The 13 different bottles were incubated during 700 hours. Hydrogen content in the biogas was comprised from 77 to 87 %; hydrogen purity from 95 % were obtained using a pure culture of *Rhodobacter sphaeroides* O.U.001 when malate was used as the substrate [32-33]. On the other hand have been reported hydrogen purities between 80 and 90 % using a phototrophic sludge [20]. The amount of biomass was measured indirectly by optical density at 660 nm and the results were in the range of 1.19 and 3.76 mg VSS L^{-1}. The COD removal varied, the best removal was 69.67 % and the lowest was 37.58 % and total VFAs concentration in the effluent was 58-21% after photofermentation.

Hydrogen yields were obtained ranging between 76.3 and 114.7 mmol H_2 L^{-1} culture, Nan- Qi et al. [22] reported hydrogen yields that varied between 26.8 and 84.8 mmol H_2 L^{-1} culture using a pure strain of *Rhodopseudomonas faecalis RLD-53* when remained constant acetate concentration at 2051 mg L^{-1} and the concentration of butyrate varied at intervals of 1.38, 2.75, 5.50, 8.26 and 11.0 g L^{-1}. Other studios [34] reported hydrogen yields in a range of 5.6 to 13.9 mmol H_2 L^{-1} culture using various organic acids (acetate, butyrate, citrate, lactate and malate) with Phototrophic Hydrogen-Producing Bacterial Consortium. Hydrogen production rates obtained ranging between 0.35 to 1.34 mmol H_2 d^{-1}; similar range to reported by Fang et al. [35] (0.03 to 1.37 mmol H_2 d^{-1}). The maximum hydrogen production rate obtained was 6.6 mmol H_2 d^{-1} L^{-1}, the specific hydrogen production rate was 0.66 mmol H_2 d^{-1} g-VSS^{-1}.

3.4 Influence of pH in the hydrogen production

The decrease in hydrogen production rates is related to the long lag phase that occurred during the tests; for all the cases the activation time "lambda" was comprised between 1 and 177 h. The longer latency phases were associated with pH changes that occurred during the experimentation, these changes pH depended on the formation of ammonium in the medium. The concentrations of ammonia nitrogen formed at the end of the test ranged between 0.4 and 10.8 mg L^{-1}, inhibition for this compound is reported from concentrations of 0.36 mg L^{-1} [14,32]. Have been reported to excess of ammonia and other nitrogen compounds usable repress the synthesis of nitrogenase in purple non sulfur bacteria [36]. The first increase pH occurred at 144 h after the test started. The pH increased in average of 6.8 at 7.1 -8.7. A very high pH values was decrease

and even inhibited hydrogen production. Optimal pH reported for the production of hydrogen is 6.8-7.5 [12, 13] thus pH was adjusted to 6.8 with 1N HCl twice at 144 and 288 h after test started.

4. Conclusions

Effect of volatile fatty acids on hydrogen production by Phototrophic Hydrogen-Producing Mixed Bacterial Consortium was investigated in batch tests and the optimization was done by response surface methodology with a Box-Benhken and Compost Central designs. It was observed an inhibition of hydrogen production by the propionic acid. Also was presented the decrease in hydrogen production with the increase pH that occurred in the tests during the experimentation. The ammonium formation was responsible for pH changes. The concentrations of ammonia nitrogen formed at the tests ranged between 0.4 and 10.8 mg L^{-1}. The results showed that a maximum hydrogen production rate of 0.65 mmol H_2 d^{-1} and maximal amount of hydrogen produced of 10.88 mmol H_2 were obtained when the concentrations of acetic acid, propionic acid and butyric acid were 1200 mg L^{-1}, 715 mg L^{-1} and 1571 mg L^{-1}, respectively.

Acknowledgements

This research was supported through DGAPA-UNAM (PAPIIT IT100113). The authors are grateful to Jaime Perez for the technical support and fruitful discussions.

References

[1] D. Das, T. Veziroğlu. Advances in biological hydrogen production processes. Int. J. Hydrogen Energy 2008; 33: 6046-6057.
[2] I. Kapdan, F. Kargi. Bio-hydrogen production from waste materials. Enzyme Microb. Technol. 2006; 38: 569-582.
[3] H. Argun, F. Kargi, F. Bio-hydrogen production by different operational modes of dark and photo-fermentation: An overview. Int. J. Hydrogen Energy 2011; 36: 7443-7459.
[4] A. Ohnishi, Y. Bando, N. Fujimoto, M. Suzuki. Development of a simple bio-hydrogen production system through dark fermentation by using unique microflora. Int. J. Hydrogen Energy 2010; 35: 8544-8553.
[5] D. Das, T. Veziroğlu. Hydrogen production by biological processes: survey of literature. Int. J. Hydrogen Energy 2001; 26: 13-28.
[6] J.R. Bartels, M.B. Pate, N.K. Olson. An economic survey of hydrogen production from conventional and alternative energy sources. Int. J. Hydrogen Energy 2010; 35: 8371-8384.
[7] X. Shi, H. Yu. Continuous production of hydrogen from mixed volatile fatty acids with *Rhodopseudomonas capsulate*. Int. J. Hydrogen Energy 2006; 31: 1641-1647.
[8] D. Levin, L. Pitt, M. Love. Biohydrogen production: prospects and limitations to practical application. Int. J. Hydrogen Energy 2004; 29: 173-185.
[9] T. Jeong, G. Ch, S. Yeom, S. Choi. Comparison of hydrogen production by four representative hydrogen-producing bacteria. J. Ind. Eng. Chem. 2008; 14: 333-337.
[10] H.H. P. Fang, H. Zhu, T. Zhang. Phototrophic hydrogen production from glucose by pure and co-cultures of Clostridium butyricum and *Rhodobacter sphaeroides*. Int. J. Hydrogen Energy 2006; 31: 2223-2230.
[11] X. Li, Y. H. Wang, S. L. Zhang, J. Chu, M. Zhang, M. Z. Huang et al. Enhancement of phototrophic hydrogen production by *Rhodobacter sphaeroides* ZX-5 using a novel strategy shaking and extra-light supplementation approach. Int. J. Hydrogen Energy 2009; 34: 4517-4523.
[12] N. Basak, D. Das. The prospect of purple non-sulfur (PNS) photosynthetic bacteria for hydrogen production: the present state of the art. World J. Microbiol. Biotechnol. 2007; 23: 31-42.
[13] C. Dasgupta, J. Gilbert, P. Lindblad, T. Heidorn, S. Borgvang, K. Skjanes. Recent trens on the development of photobiological processes and photobioreactors for the improvement of hydrogen production. Int. J. Hydrogen Energy 2010; 35: 10218-10238.
[14] H. Koku, I. Eroglu, U. Gündüz, M. Yücel, L. Türker. Aspects of the metabolism of hydrogen production by *Rhodobacter sphaeroides*. Int. J. Hydrogen Energy 2002; 27: 1315-1329.
[15] A. Hidayet, K. Fikret. Photo-fermentative hydrogen gas production from dark fermentation effluent of groun wheat solution: Effects of light source and light intensity. Int. J. Hydrogen Energy 2010; 35: 1595-1603.
[16] H. H. Fang, H. Yu. Mesophilic acidification of gelatinaceous wastewater. J. Biotechnol. 2002; 93: 99-108.
[17] M. Kennedy, D. Krouse. Strategies for improving fermentation medium performance: a review. J. Ind. Microbiol. and Biotechnol. 1999; 23: 456-475.

[18] J. T. Luftig, V. S. Jordan. Design of experiments in quality engineering, McGraw-Hill, New York, 1998.
[19] J. Wang, W. Wan. Experimental design methods for fermentative hydrogen production: a review. Int. J. Hydrogen Energy 2009; 34: 235-244.
[20] Ying Li, R., Zhang, T., Fang, H., 2008. Characteristics of a phototrophic sludge producing hydrogen from acetate and butyrate. Int. J. Hydrogen Energy 2008; 9: 2147-2155.
[21] R. Myers, D. Montgomery. Response Surface Methodology: Process and Product Optimization using designed experiments, John Wiley & Sons, USA, 2002.
[22] R. Nan-Qi, L. Bing-Feng, D. Jie, G. Wan-Qian, C. Guang-Li, X. Guo-Jun. The effect of butyrate concentration on photo-hydrogen production from acetate by *Rhodopseudomonas fecalis* RLD-53. Int. J. Hydrogen Energy 2008; 33: 5981-5985.
[23] APHA, AWWA and WPCF. Standard methods for the examination of water and wastewater. In: Eaton, A.D., Clesceri, A.E., Rice E.W., Greenberg, A.E. (Eds.), American Public Health Association, 21st ed. American Water Works Association and Water Environment Federation, Washington D.C., 2005.
[24] G. Buitrón, C. Carvajal. Biohydrogen production from Tequila vinasses in an aerobic sequencing batch reactor: Effect of initial substrate concentration, temperature and hydraulic retention time. Bioresource Technol. 2010; 101: 9071-9077.
[25] P.D. Haaland. Experimental Design in Biotechnology. Marcel Dekker, New York, 1989.
[26] K. Yetilmezsoy, S. Demirel, R. J. Vanderbei. Response surface modeling of Pb (II) removal from aqueous solution by Pistacia vera L: Box–Behnken experimental design. J. Hazard. Mater. 2009; 171: 551–562.
[27] Y. Tao, Y. He, Y. Wu, F. Liu, X. Li, W. Zong. Characteristics of a new photosynthetic bacterial strain for hydrogen production and its application in wastewater treatment. Int. J. Hydrogen Energy 2008; 3: 963-973.
[28] C. Chen, W. Lu, J. Wu, J. Chang. Enhancing phototrophic hydrogen production of *Rhodopseudomonas palustris* via statistical experiment design. Int. J. Hydrogen Energy 2007; 32: 940-949.
[29] T. V. Laurinavichene, D. N. Tekucheva, K. S. Laurinavichus, M. L. Ghirardi, M. Seibert, A. A. Tsygankoc. Towards the integration of dark and photo fermentative waste treatment. 1. Hydrogen photoproduction by purple bacterium *Rhodobacter capsulatus* using potential products of starch fermentation. Int. J. Hydrogen Energy 2008; 33: 7020-7026.
[30] J. Lee, D. Klaus, P. C. Maness, J. Spear. The effect of butyrate concentration on hydrogen production via photofermentation for use in a Martian habitat resource recovery process. Int. J. Hydrogen Energy 2007; 32: 3301-3307.
[31] X. Shi, H. Yu. Optimization of glutamate concentration and pH for H_2 production from volatile fatty acids by *Rhodopseudomonas capsulata*. Letters in Applied Microbiol. 2005; 40: 401-406.
[32] H. Argun, F. Kargi. Bio-hydrogen production by different operational modes of dark and photo-fermentation: An overview. Int. J. Hydrogen Energy 2011; 36: 7443-7459.
[33] I. Eroglu, A. Tabanoglu, U. Gündüz, E. Eroglu, M. Yücel. Hydrogen production by *Rhodobacter sphaeroides O.U.001* in a flat plate solar bioreactor. Int. J. Hydrogen Energy, 2008; 33: 531-541.
[34] C. Zampol Lazaro, D. Vital Vich, J. Sumiko Hirasawa, M. Amâncio Varesche. Hydrogen production and consumption of organic acids by a phototrophic microbial consortium. Int. J. Hydrogen Energy 2012; 37: 11691-11700.
[35] H. Fang, H. Liu, T. Zhang. Phototrophic hydrogen production from acetate and butyrate in wastewater. Int. J. Hydrogen Energy 2005; 30: 785-793.
[36] A. Tsygankov. Hydrogen photoproduction by purple bacteria: Immobilized vs. suspension cultures. En J. Miyake, T. Matsunaga, & A. San Pietro, Biohidrogen II, Pergamon, 2001: 229-243.

Hydrogen production in a microbial electrolysis cell fed with volatile fatty acids

I. Rivera[1] and G. Buitrón[1]

[1]Laboratory for Research on Advanced Processes for Water Treatment, Unidad Académica Juriquilla, Instituto de Ingeniería, Universidad Nacional Autónoma de México, Blvd. Juriquilla 3001, 76230 Querétaro, México,
Tel: +52 442 192 6165; e-mail: gbuitronm@iingen.unam.mx

ABSTRACT

The organic matter consumption and the hydrogen production rate were evaluated in a two chamber microbial electrolysis cells (MEC). Three chemical oxygen demand concentration (COD) levels (400, 600 and 1200 mg/L) were tested. The COD was composed of a mixture of volatile fatty acids (VFAs) present in the effluent of a dark fermentation process containing. Two levels of voltage were studied: 350 mV and 550 mV. The MEC were operated in 120-hours batches. The performance of the MFC was evaluated using either an anionic (AEM) or a cationic exchange membrane (CEM). The robustness of the MEC was tested using a real dark fermentation effluent and another spiked with 1100 mg/L glucose. The highest production rates (81 mL/L/d) were obtained with 550 mV and 85% of COD consumption was attained. No significant differences on hydrogen production rate were observed when the COD was increasing from 400 to 1200 mg/l and using 550 mV. However, maximal hydrogen production rates were obtained with the lower COD concentration using 350 mV. No significant differences in the performance of the MEC were found by using AEM or CEM and also no significant differences of hydrogen production rates were found when real substrate o synthetic substrate was fed to the MFC. The substrate spiked with glucose was more slowly degraded since glucose was first transformed into VFAs (first 48 h) then the VFAs were consumed to produce hydrogen. In this case, methane and carbon dioxide were found after 120 h.

Keywords: microbial electrolysis cells; hydrogen; volatile fatty acids

1. Introduction

Environmental and economic issues related with fossil fuels become the research for alternative fuels into a necessity. Hydrogen has the highest combustion heat of all fuels. It is a good energy carrier, but its current main production processes are thermochemical processes that consume fossil fuels [1]. Biological processes are able to produce hydrogen from wastewater and other residues so they are attractive subjects for research.

Dark fermentation is a favorable biological process for hydrogen production. In comparison to other options, the main advantage of dark fermentation is that the H_2 production rate is orders of magnitude larger than those achieved by other biological means [2]. It is known that dark fermentation effluent contains a high concentration of volatile fatty acids (VFAs) which are considered as organic pollutants and need treatment before been discharged to the environment. There are biological processes that are capable of utilizing VFAs and produce value products.

The bioelectrochemical systems are electrochemical cells where certain microorganisms produce electric current while oxidize organic matter on a biofilm over an electrode called anode. Their organic matter sources are substances such as acetate, cellulose, starch and wastewater [3]. The most studied electrogenic bacteria belong to the families of *Shewanella* and *Geobacteraceae* [4]. There are two kinds of bioelectrochemical systems. The difference between them is the reaction on the cathode:

Microbial fuel cells (MFCs) produce electric current via redox reactions. Electrons travel through an external circuit to the cathode. At the same time, protons travel to the cathode through the electrolyte and through a membrane that divides cathode chamber from anode chamber. Electric current is produced because of oxygen reduction on the cathode [5]. Microbial electrolysis cells (MECs) are modified MFCs that produce hydrogen. Its cathode is anaerobic and without oxygen spontaneous electricity production is not possible since the free Gibbs energy of the reaction is ΔG_r = + 104.6 kJ/mol [6]. To drive electrons from the anode to cathode an external voltage is applied to the circuit. Hydrogen is produced by proton reduction on the cathode [5].

Equations 1 to 3 describe the reactions occurring in the cell when using acetate as a model:

Anode:

$$CH_3COO^-{}_{(ac)} + 4H_2O_{(l)} \rightarrow 2HCO^-{}_{3(ac)} + 9H^+{}_{(ac)} + 8e^- \quad (1)$$

Cathode:

$$8\left(H^+{}_{(ac)} + e^- \rightarrow \frac{1}{2}H_{2(g)}\right) \quad (2)$$

Global reaction:

$$CH_3COO^-{}_{(ac)} + 4H_2O_{(l)} \rightarrow 2HCO^-{}_{3(ac)} + H^+{}_{(ac)} + 4H_{2(g)} \quad (3)$$

At standard conditions of temperature and pressure, the voltage required is 0.14 V using acetate as substrate. However, in reality voltage required is over 0.25 V due to internal system resistances. Nevertheless this voltage is lower than that of the water electrolysis, 1.8-2.0 V [7].

For this paper organic matter consumption and the hydrogen production rate were evaluated in a two chamber microbial electrolysis cells (MEC) using as substrate dark fermentation the effluent containing VFAs. Voltage, COD and substrate composition were evaluated.

2. Experimental

2.1 System operation

Four MECs were constructed using a two-chamber configuration (163 mL/chamber) with a distance between electrodes of 3.7 cm. The anode was made of graphite cloth (Brunsen de Occidente S.A. de C.V., Guad., Jal., Mex.) whereas the cathode was constructed of carbon paper with Pt (5 cm × 5 cm, 0.5 mg Pt/cm2, ElectroChem, Inc., Woburn, MA). Internal connections were made using titanium wire, 10 cm, (Sigma-Aldrich Co., St. Louis, MO). External connections were made of copper wire. Two input voltages (0.35 and 0.55 V) were applied using a power source (GWInstek, model GPS-4303).

The anode was colonized operating the cell in MFC mode with 48-hour batches. Cycles were conducted until the generated voltage reached by the cell was maximum and reproducible during at least three cycles. A mixture (75:25) of municipal wastewater (wastewater treatment plant of Campus Juriquilla, UNAM) and sodium acetate (20 mM) in 100 mM phosphate buffer solution and vitamins and minerals [8] was used as the inoculum source and cell fuel. The chambers were separated by a cationic exchange membrane (CEM) (CMI 7000, Membranes International, Glen Rock, NJ). Temperature was 25° C maintained constant in a water bath with a submersible heater.

For the electrolysis cells, the synthetic substrate was prepared with a mixture of FVAs based in the composition of a dark fermentation effluent. The pH was set at a value of 7 with 1M HCl and 1M NaCl. The purpose of the synthetic mixture was to have only VFAs (which the cell is supposed to consume) in the substrate and exclude other substances from the dark fermentation effluent such as glucose or ethanol, which can interfere with the hydrogen production via electrolysis. VFA percentage in the mixture was 26% acetic, 12% propionic y 63% butyric. Three levels of synthetic substrate COD were used: 1200, 600 y 400 mg/L. The cells were operated in batch during 120h until a stable hydrogen production was observed. The COD consumption was also evaluated at the end of each cycle.

Once the synthetic substrate study was completed, the cell was fed directly with a real dark fermentation effluent, to compare the hydrogen production vs. the synthetic substrate. Next, the robustness of the system was evaluated. For that, a dark fermentation effluent containing a high concentration of glucose (simulating a malfunctioning of the dark fermentation process) was tested in the MEC using first 120 h batches, and then reducing the cycle time to 48 h in order to inhibit the methane formation. The performance of the system with the CEM vs. an anionic exchange membrane, AEM, (AMI-7001, Membranes International, Glen Rock, NJ) was also studied.

The dark fermentation reactor used to obtain the substrate was a continuous 2-liter UASB reactor, operated under the following conditions: pH 4.5, 35° C and 16 h of hydraulic retention time. Glucose was used as a carbon source. The reactor operated with three glucose concentrations: 5 g/L; 0.6 g/L (for real vs. synthetic and membranes comparison) and 10 g/L (for the robustness study).

2.2 Measurements

Voltage was monitored with a DAQ USB 6008 (National Instruments Inc., Austin, TX) and LABVIEW 7 software. pH was measured after every batch with an OAKION pH 510 Series potentiometer with a pH Orion 9156BNWP electrode. COD was measured by using an spectrophotometer (Hach 435 and 430 methods).

VFAs were identified and quantified with a gas chromatograph Varian 3300 equipped with a flame ionization detector according to [9] and gas composition in the cathode chamber was measured with a SRI8610C gas chromatograph equipped with a thermal conductivity detector as described in [10]. All experiments were performed

using duplicate cells and the reported data are the average of at least six values (three cycles for each cell). In all cases, hydrogen volume was measured in an inverted cylinder filled with water.

3. Results and discussion

3.1 Synthetic substrate

No traces of CO_2 or CH_4 were found in the MEC cathode. Figure 1 shows the hydrogen production rate as a function of the applied voltage and the initial COD fed to the reactor. The maximum hydrogen production rate was 81±5 $mLH_2/L/d$ and it has the same order of magnitude as other results reported in the literature as can be seen in table 1.

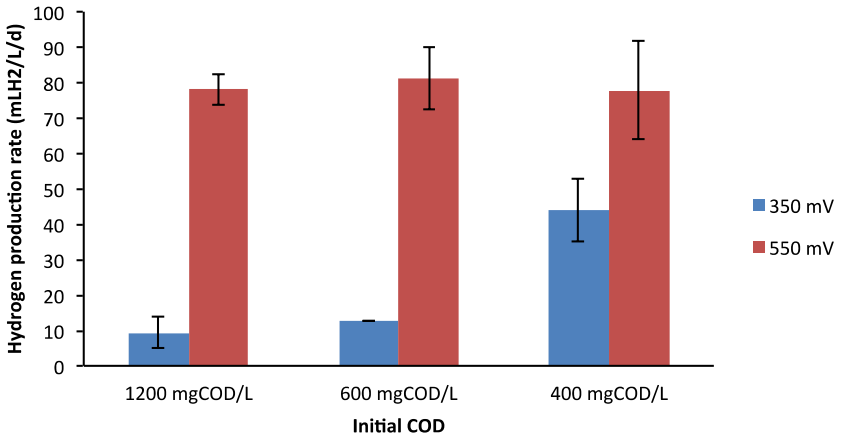

Figure 1. Hydrogen production rate versus the applied voltage and initial COD.

Table 1. Hydrogen production rate in two chamber system using low voltages

Substrate	Anode	Cathode	Membrane	Voltage	Max. H_2 prod. Rate	Reference
Acetate	Carbon paper	Carbon paper with Pt	PEM	0.4 V	18 $mLH_2/L/d$	[11]
Domestic wastewater	Graphite felt	Carbon paper with Ni	Cellulose cloth	0.2-1.4 V	45 $mLH_2/L/d$	[12]
Domestic wastewater	Graphite felt	Stainless steel	Polyethylene membrane	0.6 V	15 $mLH_2/L/d$	[13]
Sodium acetate	Carbon paper	Carbon paper with Pt	CEM	0.418 V	14 $mLH_2/L/d$	[14]
Fermented activated sludge	Graphite fiber brush	Carbon cloth with Pt	CEM	0.6 V	68 $mLH_2/L/d$	[15]
Mixture of acetate, propionate, butyrate	Graphite cloth	Carbon paper with Pt	CEM	0.550 V	81 $mLH_2/L/d$	This study

ANOVA analysis indicated that there exists a significant influence on hydrogen production rate of the applied voltage and the initial COD. When a high input voltage is applied, there not exists a significant influence on the production rate, when the initial COD was increased from 400 to 1200 mg/L, but with the low input voltage, the productivity increases when concentration decreases.

Figure 2 shows the organic matter consumption as a function of the applied voltage and initial COD. COD removal was in the interval of 38 - 85%. Higher COD removals were observed with lower initial COD. In this case, no significant influence of the applied voltage was found. This behavior indicates that the organic matter consumption is not the limiting factor for hydrogen production (Fig. 1). The pH changes were evaluated (table 2). It was found that the higher the substrate concentration, the higher the pH difference between the two chambers and the required voltage for electrolysis increases. With the high voltage there is enough energy to compensate this pH change, so there is a high production rate. At the low voltage, the production rate was higher at low COD concentration; however low COD were observed after the cycle indicating that the MEC is not enough for organic matter removal generating residual organic matter that needs to be further removed.

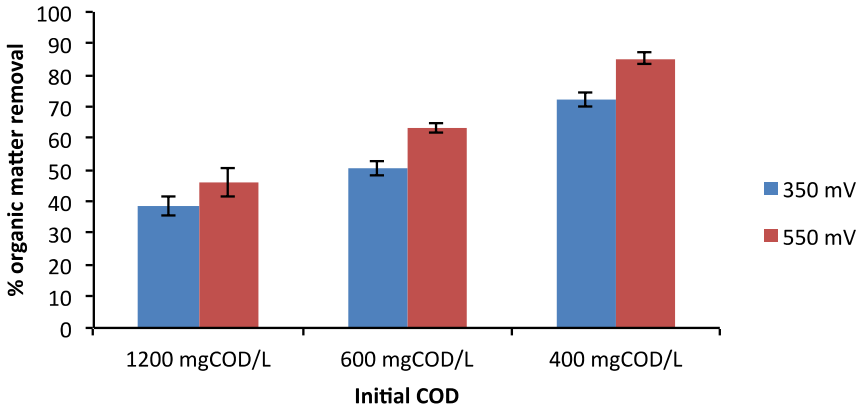

Figure 2. Organic matter removal measured as COD in a 120 hours batch using synthetic substrate.

Table 2. pH values at the end of a 120 hours batch measured in the anodic and cathodic chambers.

	Cathode		Anode		ΔpH	ΔpH
	350 mV	550 mV	350 mV	550 mV	350 mV	550 mV
1200 mg COD	7.43	7.69	6.61	6.07	0.82	1.62
600 mg COD	7.26	7.53	6.60	6.22	0.66	1.31
400 mg COD	7.16	7.24	6.56	6.29	0.6	0.95

3.2 Real substrate

The effluent obtained from the dark fermentation reactor presented the following composition (in mg/L): Glucose (10±2), ethanol (66±8), acetate (100±5), propionate (32±15) butyrate (57±7), COD (420±14). The hydrogen production rate and the organic matter removal obtained with the synthetic substrate and the real effluent are presented in figures 3 and 4. The ANOVA analysis indicates that there were not significant differences, despite 38% of the COD in the real substrate was formed by other compounds different to the VFAs as was the case for the synthetic substrate.

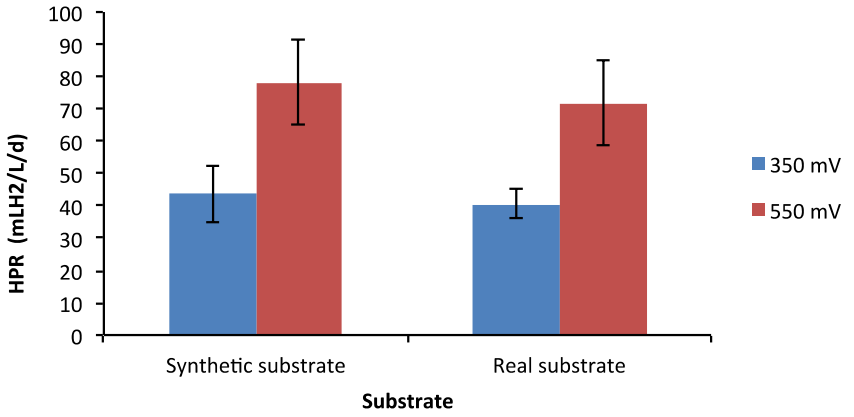

Figure 3. Hydrogen production rate in a MEC fed with synthetic and real substrate.

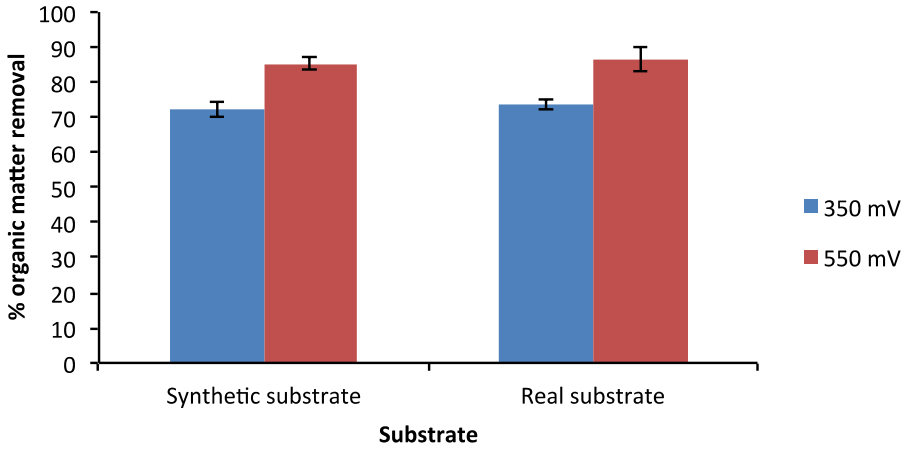

Figure 4. Organic matter consumption in a MEC fed with synthetic and real substrate.

3.2.2 Performance of the MEC using cationic (CEM) and anionic exchange membranes (AEM).

It has been reported [16] that an AEM (Fumasep FAA, FuMa-Tech GmbH, Germany) allows higher production rates than a CEM (Fumasep FKE, FuMa-Tech GmbH, Germany). This increment was attributed to the differences of ionic transport in the membranes [16]. The importance of the phosphate buffer anions diffusion through the AEM membrane has already been explained by Sleutels et al. [16]. The HPO_4^{2-} ion diffuses to the cathode and the PO_4^{-} ion does to the anode. The transport of buffer anions is equivalent to the transport of H^+/OH^-, which are the main charge carriers in the electrolysis system. On the other side with a CEM all the cations travel to the cathode chamber. H^+ exists in a lower concentration than the other cations, so its diffusion to the cathode is lower. Because of this transport and acidity the CEM eventually has a positive charge on the anode side and reflects the cations. Thus, it is more difficult to the protons produced on the anode to reach the cathode.

In order to evaluate the effect of the type of membrane on the hydrogen production rate, the cells were tested using an anionic exchange membrane (AMI-7001). Real substrate was used. As can be seen in figure 5 no significant differences were found by using an AEM or a CEM, independently of the voltage supplied. ANOVA indicates there is no important difference when the control variable is the membrane. The materials used for the membranes can explain the difference with the previous study. The membranes used for this study presented higher electric resistance (40 $\Omega.cm^2$ for the anionic membrane and 30 $\Omega.cm^2$ for the cationic membrane) than the membranes already reported [16] (1.9 $\Omega.cm^2$ for the anionic membrane and 3 $\Omega.cm^2$ for the cationic membrane). Thus, although the ionic transport reported in literature exists, the electric resistance of the membranes of this study dissipates energy instead of favoring hydrogen production. Another important factor is the input voltage since in the present study lower input voltages were applied than the values reported by Sleutels et al. [16], which conducted the experiments using 1000 mV.

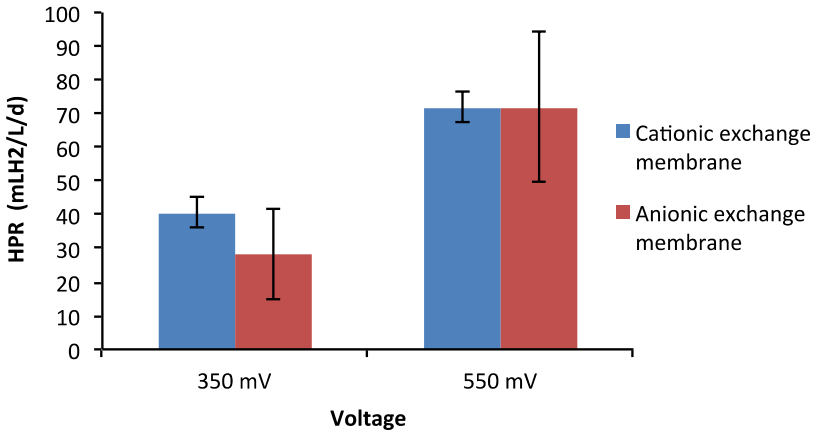

Figure 5. Hydrogen production rate in a MEC with two ionic exchange membranes.

3.3 Robustness of the System

To evaluate the robustness of the MEC a real effluent containing a high glucose concentration was study. The substrate composition was (in mg/L): glucose (1137±25), ethanol (8.1±3), acetate (397±19), propionate (75±7),

butyrate (363±23) and COD (3700±20). When the cells were operated under that condition, the biogas production stopped after 48 h and after 120h, when the cycle was completed methane was detected in the biogas (60% for 550 mV and 70% for 350 mV) the rest was CO_2. No H_2 was found. It is possible that glucose passed through the membrane to the cathodic chamber favoring the growth of Archea. To avoid the methane formation the cycle duration was reduced to 48 h. In this case, no CH_4 was found and H_2 percentage was 80% for 350 mV and 90% for 550 mV. Decreasing the time of the batch was enough to avoid growth of Archea and methane production. The production rate obtained with this substrate was compared to the high COD level in the synthetic substrate. Hydrogen production rate was similar for both substrates at 350 mV, but it was clearly inferior at 550 mV (Figure 6). The maximum production rate with this real substrate containing glucose in excess was 28±3 mL/L/d; almost three times lower than a substrate containing only VFA. The reason for this behavior can be explained considering that microorganisms present in the MEC first transform the glucose into VFAs, and then these are utilized to generate hydrogen.

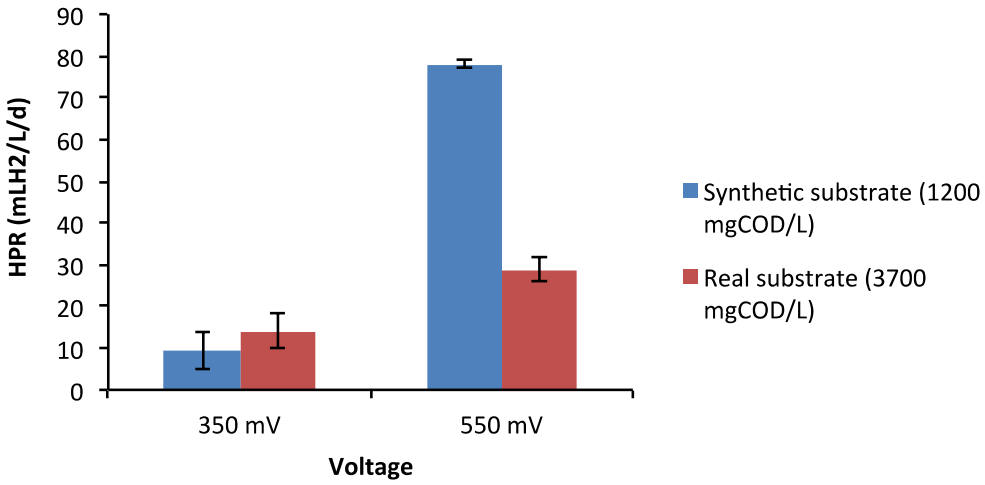

Figure 6. Hydrogen production rate in a MEC fed with synthetic and real substrate with carbohydrates.

Figures 7 and 8 present the evolution of the substrate as a function of time in the anodic chamber when the 120h cycle was operated. It is possible to observe that glucose is degraded as the VFAs are produced. The maximum VFAs production was reached at 24 hours for 550 mV and at 48 hours for 350 mV after this time concentration decreases. It was found an important COD consumption of 59% for 350 mV and 66% for 550 mV. Indicating that some of the fuel was not directly utilized for hydrogen production and explaining the lower hydrogen production rates.

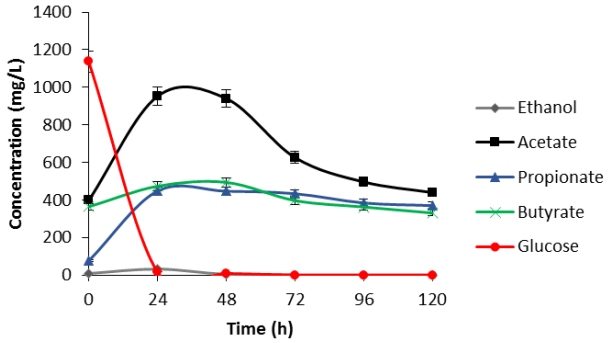

Figure 7. VFAs, ethanol and glucose evolution for 550 mV.

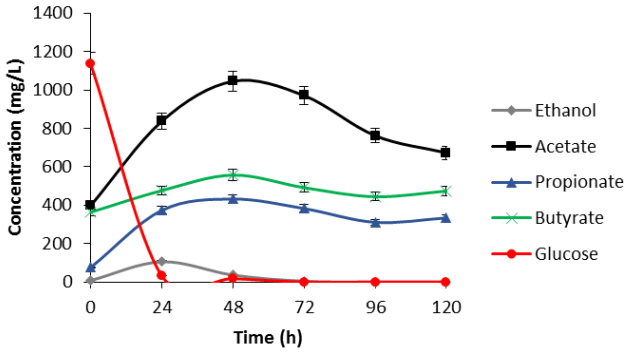

Figure 8. VFAs, ethanol and glucose evolution for 350 mV.

4. Conclusions

Best local conditions for the operation of a microbial electrolysis cell for hydrogen production using volatile fatty acids were obtained using an input voltage of 550 mV, cycles of 96 h, and initial COD from 400 to 1200 mg/L. Under these conditions, maximum hydrogen production rate was 81 mLH_2/L/d and maximum organic matter removal was 85 %. In general, low organic matter levels are recommended for the operation of the system. When a dark fermentation effluent was utilized, similar results to the synthetic substrate were obtained. Under the condition operated with the system no significant differences were found when an anionic exchange membrane or a cationic exchange membrane were used. When the substrate fed to the cell contains carbohydrates, the hydrogen production rate decreases significantly and some methane can be produced. It is important for the correct performance of the microbial electrolysis cell, when coupling to a dark fermentation process, that no carbohydrates are present in the effluent.

Acknowledgements

This study was supported by the International Found of the Instituto de Ingeniería-UNAM and DGAPA-UNAM (PAPIIT IN104710). This research work is part of the master supported by the Conacyt scholarship.

References

[1] K.Y. Show, D.J. Lee, J.H. Tay, C.Y. Lin, J.S. Chang, Biohydrogen production: Current perspectives and the way forward. *Int. J. Hydrogen Ener*. 2012; 30: 1-16.

[2] H. S. Lee, W. F.J. Vermaas, B. E. Rittmann, Biohydrogen production: Current perspectives and the way Forward. Trends in Biotechnology 2010; 28 (5): 262-271.

[3] T.H.J.A. Sleutels, A. Ter Heijne, C.J.N. Buisman, H.V.M. Hamelers, Bioelectrochemical Systems: An Outlook for Practical Applications. *Chemsuschem* 2012 5: 1012-1019. DOI: 10.1002/cssc.201100732.

[4] N. Wrana, R. Sparling, N. Cicek, D. B. Levin, Hydrogen gas production in a microbial electrolysis cell by electrohidrogénesis. *J. Clean. Prod*. 2010; 18: S105-S111.

[5] D. Pant, A. Singh, G. Van Bogaert, S.I. Olsen, P.S. Nigam, L. Diels, K. Vanbroekhoven, Bioelectrochemical Systems (BES) for sustainable energy production product recovery from organic wastes and industrial wastewaters. *RSC Adv*. 2012; 2: 1248-1263.

[6] B.E. Logan, D. Call, S. Cheng, H.V.M. Hamelers, T.H.J.A. Sleutels, A.W. Jeremiasse, R.A. Rozendal, Microbial Electrolysis Cells for High Yield Hydrogen Gas Production from Organic Matter. *Envorin. Sci. Technol*. 2008; 42(23): 8639-8640.

[7] B.E. Logan, Microbial fuel cells. Willey Interscience 2007; 127.

[8] D. Lovley, E. Phillips, Novel mode of microbial energy metabolism: organic carbon coupled to dissimilatory reduction of iron or manganese. Appl. Environ.Microbiol. 1988; 54: 1472–1480.

[9] G. Buitrón & C. Carvajal, Biohydrogen production from Tequila vinasses in an anaerobic sequencing batch reactor: effect of initial substrate concentration, temperatura and hydraulic retention time. Bioresource Technol. 2010; 101: 9071-9077.

[10] C.E. Hernández-Mendoza, G. Buitrón, Suppression of methanogenic activ-ity in anaerobic granular biomass for hydrogen production. J. Chem. Technol.Biotechnol 2014; 89: 143–149.

[11] Y. Zhang, I. Angelidaki, Innovative self-powered submersible microbial electrolysis cell (SMEC) for biohydrogen production from anaerobic reactors. Water Res. 2012; 46: 2727-2736.

[12] L. Gil-Carrera., A. Escapa, R. Moreno, A. Morán, Reduced energy consumption during low strength domestic wastewater treatment in a semi-pilot tubular microbial electrolysis cell. J. Environ. Manage. 2013; 122: 1-7

[13] E.S. Heidrich, J. Dolfing, K. Scott, S.R. Edwards, C. Jones, T.P. Curtis, Production of hydrogen from domestic wastewater in a pilot-scale microbial electrolysis cell. Appl. Microbiol. Biotechnol. 2013; 97(15): 6979-6989

[14] M. Sun, G.P. Sheng, Z.X. Mu, X.W. Liu, Y.Z. Chen, H.L Wang., H.Q. Yu, Manipulating the hydrogen production from acetate in a microbial electrolysis cell–microbial fuel cell-coupled system. J. Power Sources. 2009; 191(2): 338-343.

[15] L. Lu, N. Ren, D. Xing, B.E. Logan, Hydrogen production with effluent from an ethanol–H2-coproducing fermentation reactor using a single-chamber microbial electrolysis cell. Biosens. Bioelectron. 2009; 24: 3055-3060.

[16] T.H.J.A. Sleutels, H.V.M. Hamelers, R.A. Rozendal, C.J.N. Buisman, Ion transport resistance in Microbial Electrolysis Cells with anion and cation exchange membranes. Int. J. Hydrogen Ener. 2009; 34: 3612-3620.

Characterization of Catalysts Pt / γ-Al2O3 Prepared by Incipient Wetness Impregnation Method

M. Sanchez[1], J. Medina[2], J. Rodriguez[3], D. González[3], E. Mora[1]

[1]Universidad Politécnica de Aguascalientes, Calle Paseo, San Gerardo, 207, 20342, Aguascalientes, Ags., México, 20342.
[2] Instituto Tecnológico de Aguascalientes, Av. Adolfo López Mateos #1801 Ote.
Fracc. Bona Gens, Aguascalientes, Ags., México, 20256.
[3] Cinvestav Unidad Saltillo, Av. Industria Metalúrgica 1062, Zona Industrial, Ramos Arizpe, Coahuila de Zaragoza, México, 25900.
[1]Tel: +524494421400; e-mail: manuel.sanchez@upa.edu.mx

ABSTRACT

A platinum catalyst supported on gamma alumina was prepared by incipient wetness impregnation method, using as a precursor Platinum II acetylacetonate salt. Because the precursor salt is not soluble in water, a variant of the method, consisting of a milling was applied by mixing boehmite and a platinum salt. Once the physical mixture was homogeneous, drops of a solution of nitric acid 1:16 were added, this was achieved by modifying the pH of the surface of the boehmite, thus achieving impregnation the salt. Then platinum particles were anchored. To obtain oxides of platinum the calcination method was utilized; finally, the catalysts of metal oxides were reduced by exposure to a flow of hydrogen at 400 °C, obtaining as a product a Pt /γ-Al_2O_3, which can accelerate and direct the hydrodeoxygenation reaction of oxygenated organic compounds to make them into second generation biodiesel departing from first generation biodiesel. The catalysts were characterized by Raman spectroscopy, X-ray diffraction, scanning electron microscopy, IR analysis and EDS. With the interpretation of the results, the effectiveness of the preparation process was guaranteed, also their catalytic action to accelerate and direct the reaction of hydrodeoxygenation.

Keywords: Pt/ γ-Al_2O_3; biodiesel, oxygenated organic compounds.

1. Introduction

At present, about 80% of world energy demand is obtained by burning fossil fuels. This leads to a depletion of fossil energy resources, which are limited. This, in turn, has led scientists to think that the use of fossil fuels is the main cause of global climate change: the emission of pollutants as a result of combustion [1].
One option to reduce the consumption of fossil fuels and their impact on the environment is the use of renewable biofuels based on biomass processing, because they have a huge energy potential and can contribute to the reduction of greenhouse emissions. Such is the case of Biodiesel. The method of application of biodiesel and its blends with diesel fuel based on oil can be used in diesel engines without the need to perform significant engine modifications in them [2]. Disadvantages encountered in the application of first generation biodiesel are: susceptibility to oxidation under low temperature and high emissions of NOx [3]. In order to solve these drawbacks, there has been an increasing interest on the part of investigators in the development of methods of preparation of Pt catalysts for their application in catalytic processes of hydrodeoxygenation of methyl esters from vegetable oils and animal fats, so that they can transform the biofuel molecules from polyunsaturated into monounsaturated. This new biodiesel is known as second generation biodiesel.

In different publications, several methods have been reported that help obtain catalysts of palladium, platinum and nickel, among which we can mention: sulfurized NiMo catalysts prepared by incipient wetness impregnation method; catalysts of Pd on SiO_2 deposited by incipient wetness impregnation method; Pd/ImS3-12 catalysts on γ-Al_2O_3 deposited by the method of adsorption of palladium nanoparticles. This paper presents an effective method of preparation of catalysts for Pt/γ-Al_2O_3 by the wet incipient impregnation method, also the results of the characterization of the catalyzers that guarantee their catalytic action to manage and accelerate the reaction of hidrodesoxigenacion.

2. Experimental

- The necessary amounts of boehmite and Platinum II acetylacetonate, in order to obtain the percentages of active metal phase sought (3%, 5% and 7%) are weighed.
- A physical mixing of the catalyst support and the precursor salt are blended and subjected to a fine grinding process by mixing quantities of boehmite and Platinum II acetylacetonate.
- A solution volume ratio of 1:16 (water : acid) nitric acid is prepared.
- Once the mixture has been produced, the solution of nitric acid is added through a dripping process, until a smooth paste is formed.
- The paste is allowed to dry at room temperature for 48 hours.
- Once the paste is dry, an extrusion process is performed in order to obtain pellets cut to the same size, making sure that they won't be pulverized, since if this happens, the catalyst cannot be recovered after hydrodeoxygenation process.
- Subsequently all pellets are calcined at 510 °C in the presence of oxygen. The purpose of the calcination of the catalyst is for the water to be removed from the boehmite in order to obtain γ-

Al_2O_3; another aim of this calcination is for the acetylacetonate and the nitric acid to burn, in order to obtain the end oxides of platinum on γ-Al_2O_3 deposited.

- Finally the catalysts are subjected to a reduction process with hydrogen flow at 400 °C, through this, the conversion the oxides of platinum is achieved, eliminating all oxygen from all platinum oxides, obtaining Pt deposited on γ-Al_2O_3, ready to be used in the process hydrodeoxygenation.

3. Results and discussion

The characterization of catalysts Pt/γ-Al_2O_3 with 3%, 5% and 7% weight active phase was performed through Raman spectroscopy, X-ray diffraction, scanning electron microscopy and EDS. Then the results of these characterizations and the interpretation and discussion of results obtained are here included:

Figure 1 shows Raman spectra, which were used to monitor the preparation process of the catalysts of platinum on γ-Al_2O_3. The blue spectrum is the one that corresponds to the precursor platinum salt (II platinum acetylacetonate, PTACAC). The green spectrum shows the Raman signal of the mix in coordination (PTACAC + Boehmite = PTACACBO5), corresponding to obtain a 5 wt% platinum on gamma alumina, this indicates that the process of deposition of the precursor salt by the incipient wetness impregnation method was adequate, and pH modification helped the impregnation of salt, a new mix in coordination was obtained with very different peaks to those showed by the single precursor salt. This clearly shows that the catalyst of platinum oxide on gamma alumina OPTGA5 (preparation to obtain 5% by weight of Pt) doesn't show Raman characteristic peaks; this is due to the fact that the amount of platinum oxide deposited on the γ-Al_2O_3 is very small. It was also demonstrated that the process of calcination at 510 °C is suitable, because the characteristic peaks disappeared from the organic components of the mixture in coordination. Finally, the spectrum of the catalyst 5% by weight of platinum on gamma alumina (PTGA5) which was reduced to 400 °C and a pressure of 20 bar of hydrogen, doesn't show the characteristic Raman peaks, this is because Raman doesn't detect pure metals, regardless of the percentage of metal that the substance may contain.

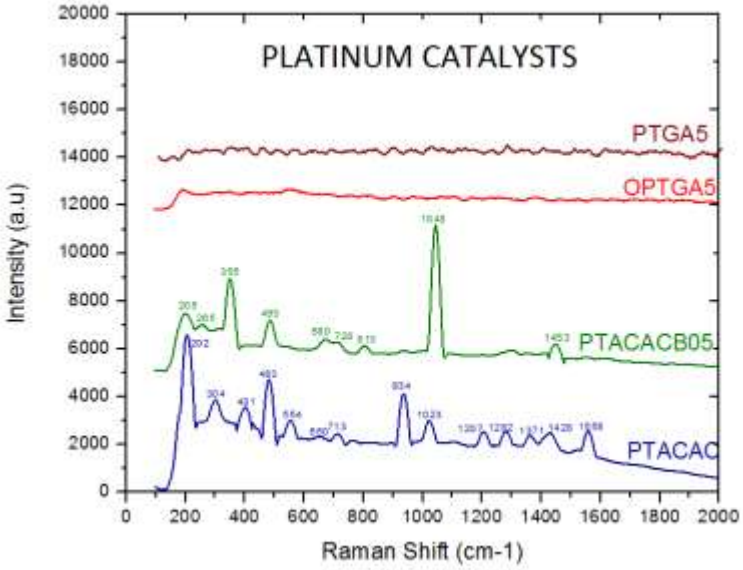

Figure. 1. Monitoring of the preparation process of platinum catalysts on γ-Al2O3 by Raman spectroscopy.

In Figure 2, the patterns of X-ray diffraction of the catalysts of platinum deposited on gamma alumina with 3% weight (PTGA3 display) show reflections in 2 θ of 32.6 °, in 37.2 °, in 39.8 °, in 46.25 ° and in 67.1 °. These reflections are characteristic of the gamma alumina phase (GA). Still an indication of the presence of metal particles of Pt can be noticed in the growth of the intensity of the reflections at 2 θ of 39.8 ° and 46.25 °. This phenomenon is consistent with several works published before [4], [5].

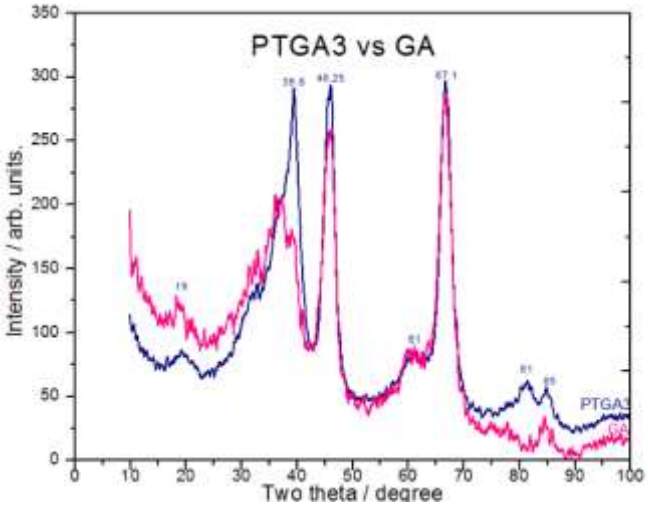

Figure 2. XRD patterns of the platinum catalyst on γ-Al_2O_3 with 3 wt% (PTGA3) and γ-Al_2O_3 catalyst support (GA).

Figure 3 shows the image of scanning electron microscopy of platinum catalysts deposited on gamma alumina with 3% weight. It is possible to observe crystals or clusters ranging in size from nanoscale and up to 7 μm.

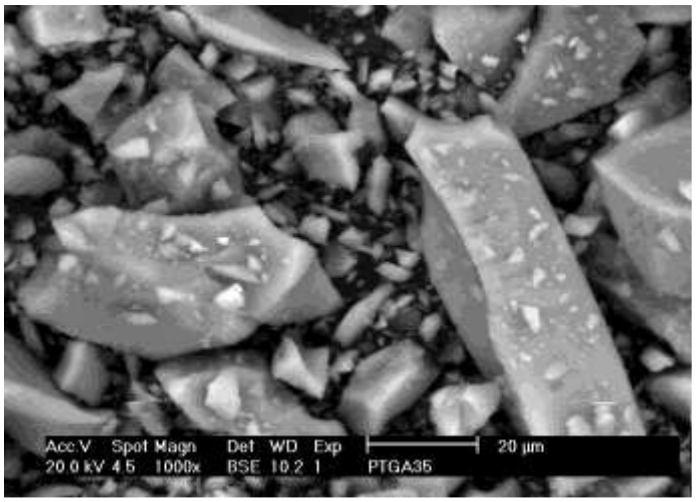

Figure 3. Image of scanning electron microscopy of platinum catalysts deposited on gamma alumina with 3% weight of active phase.

Table 1 shows the percentages of weight and the atomic percentage of platinum deposited on gamma alumina with a 3% weight of active phase. The data show that the amounts of reactants mixed and the preparation process of the catalysts were appropriate.

Table. 1. Average chemical composition by EDS for the platinum catalyst deposited on gamma alumina with 3% weight of active phase.

Catalyst	O		Al		Pt	
	Wt %	At %	Wt %	At %	Wt %	At %
PTGA3	38.995	53.465	56.59	46.035	4.41	0.495

4. Summary and perspectives

Through Raman spectroscopy it was found that the deposition process of the precursor salt of platinum carried out using the incipient wetness impregnation method was adequate; also the calcination process. Through the interpretation of patterns of X-ray diffraction, the presence of metal particles of Pt was proved, and the results of chemical composition by EDS showed that the amounts of reactants mixed and the preparation process of the catalysts were suitable.

With the results of characterization of the catalysts, it can be assured that these catalyzers will direct and accelerate the reaction of hydrodeoxygenation of oxygenated organic compounds in order to obtain second-generation biodiesel. The next stage of the project is to test the catalysts in a reactor containing first generation biodiesel, at controlled temperature and pressure of hydrogen, in order to determine the conditions under which the highest yield in the hydrodeoxygenation reaction can be obtained.

5. Acknowledgements

Thanks to Dr. Javier Rodríguez Varela CINVESTAV Saltillo Unit for his support in the characterization of materials.

6. References

[1] D. Dasa, T. NejatVeziroglu, ”Hydrogen production by biological processes: a survey of literature‘‘, International Journal of Hydrogen Energy, 2001; 26;13-28.

[2]G. Knothe, J.H. Van Gerpen, J. Krahl, The Biodiesel Handbook, AOCS Press, Champaign, Illinois, 2005.

[3] A.L. Boehman, D. Morris, J. Szybist, E. Eton, The impact of the bulk modulus of diesel fuels on fuel injection timing, Energy Fuel 18 (2004) 1877–1882.

[4] R.M. Rioux, H. Song, J.D. Hoefelmeyer, P. Yang, G.A. Somerjai, Journal of Physical Chemistry B 109 (2005) 2192.

[5] M. Santhosh Kumar, D. Chen, J.C. Walmsley, A. Holmen, Catalysis Communications 9 (2008) 747.

Preparation of a Solid Catalyst by Sulfonation Superacids from Mesoporous Carbon Material

L. Sanchez[1], J. Medina[2], J. Rodriguez[3], D. González[3]

[1]Universidad Politécnica de Aguascalientes, Calle Paseo, San Gerardo, 207, 20342, Aguascalientes, Ags., México, 20342.
[2] Instituto Tecnológico de Aguascalientes, Av. Adolfo López Mateos #1801 Ote.
Fracc. Bona Gens, Aguascalientes, Ags., México, 20256.
[3] Cinvestav Unidad Saltillo, Av. Industria Metalúrgica 1062, Zona Industrial, Ramos Arizpe, Coahuila de Zaragoza, México, 25900.
[1]Tel: +524494421400; e-mail: luis.sanchezo@upa.edu.mx

ABSTRACT

A new solid super acid catalyst was functionalized using H_2SO_4 as catalyst supports a mesoporous carbon from tire rubber. The method of sulfonation in liquid phase was through direct immersion incipient coal 98.3 % concentrated H_2SO_4 in a flask under reflux. The carbonization temperature of tire rubber pyrolysis was performed with a flow of N_2 at low temperature to obtain a mesoporous carbon and achieve effective sulfonation. The mesoporous carbon was functionalized with the group $-SO_3H$, CMHL520, was characterized by XRD, SEM, EDS, IR and elemental analysis, indicating the presence of polycyclic disordered carbon plates in structure extremely high surface area and large pores that provided more acidic surface sites. The high catalytic activity and stability of this catalyst is related to the acid site density by -OH, Bronsted acid sites, hydrophobicity preventing hydration of hydrophilic -OH and $-SO_3H$ functional groups.

Keywords: Solid super acid catalyst, mesoporous carbon, pyrolysis

1. Introduction

The discovery of mesoporous materials with high surface area and pore volumes different in structure, has opened new opportunities for the conversion of large molecules from the catalytic point of view, as they are very applicable in the petroleum industry, pharmaceutical and Industrial [1]. Today is very important catalytic processes employing heterogeneous phase, as an alternative to the traditional homogeneous processes where the use of catalysts such as sulfuric acid, hydrochloric acid and p-toluenesulfonic acid [2] acid is involved.

Activated carbon is a solid material prepared artificially, which is characterized by a well developed pore structure, which gives a high specific surface area and adsorption capacity. [3] It has great versatility due to the possibility to modify and control the size and distribution of pores in the carbonaceous structure and the chemical nature of the surface during the process of preparation [4].

In terms of chemical composition mainly consists of carbon atoms, about 87-97%. The remaining composition includes hetero atoms such as hydrogen, oxygen, sulfur and nitrogen from the feedstock, or incorporated during the preparation process [5].

Its structure consists of graphite microcrystals, formed by a number of aromatic rings as the interlocking structure of graphite, and forming from 5 to 15 layers of graphitic planes with a spacing of 3 to 4 Å therebetween. Aromatic carbon sheets interconnected appear irregularly and randomly, so that not appear perfectly parallel, or even overlap each other [6]. The interstitial spaces between the sheets aromatic result in pore formation, structural defects, unpaired electrons and holes in the system at the edge of the basal planes. In the presence of hetero-atoms in the reaction medium (sulfur, nitrogen, hydrogen and molecular oxygen), can be formed on said active surface groups [7] centers.

Both the random ordering of the layers as the crosslinking prevents the rearrangement of the structure for graphite, even when this material is heated to 3000 °C. This is the characteristic of activated carbon that contributes most to its most important property, the highly developed internal pore structure and accessible for adsorption processes [8].

With the above it was decided to prepare a carbon rubber trowel amorphous mesoporous type for use as a catalyst support and funcionalizarlo with sulfonic groups to obtain a solid catalyst super acid (CMHL520), in order to carry out a more efficient and environmentally friendly processes used esterification and transesterification of vegetable oil.

Activated charcoal (CMHL) was obtained by a pyrolysis process from tire rubber fiber. The method obtained from this material was developed at the Technologic Institute of Aguascalientes of subjecting tire rubber fibers at high temperatures in an atmosphere of N_2 obtaining a carbonaceous material.

As a method of functionalization of CMHL sulfonation with H2SO4 was used. For the sulfonation procedure by which -SO_2OH sulfonic group is introduced as sulfonating agent using concentrated sulfuric acid was performed 98.3%. It is noteworthy that the sulfonation is called when a carbon atom, or sometimes to a nitrogen atom is attached to the sulfonic group -SO_2OH [9].

To characterize the CMHL and CMHL520 the following methods were used: Infra Red Spectroscopy Fourier transforms (FTIR), X-ray diffraction (XRD), scanning electron microscopy and EDS.

.

2. Experimental

2.1 Obtaining CMHL from used tire

a) A thermal pyrolysis which weighed 5 g sample of tire rubber powder in an analytical balance was used.

b) The powder was packed into a micro-reactor of stainless steel, once inside the sample in the micro-reactor, purged with N_2 for 10 min before starting the stage of pyrolysis.

c) In pyrolysis followed rubber which was maintained at a temperature of 515 °C, with a pre-heating ramp of 15 °C / min and N_2 flow of 30 ml / min for 2 hours was begun.

2.2 Activation CMHL.

This pyrolysis process consisted of heating at a temperature of 520 °C in an inert nitrogen atmosphere, to break the bonds between the carbon atoms. Thus, the material is dehydrated and the volatiles are removed, increasing the proportion of carbon atoms and forming a carbonaceous amorphous structure when the hydrocarbon chains lose their hydrogen atoms.

Because the energy provided during the heating process, graphite microcrystals are rearranged into the structure recombined together irregularly and joining the aromatic rings to form graphitic planes, creating free interstitial voids that are blocked as a result of the decomposition and deposition tar. During the carbonization step, the lower the heating rate increases the performance for the materials used.

2.3 Sulfonation of CMHL

- *1*0g were taken of each catalytic support and 100 ml of concentrated H_2SO_4 (98.3%) of solution. Each was placed in a flask of 500 ml and a temperature controlled around 120 °C.
- The mixture was kept under reflux and stirring for 5 hours as shown in Figure 3.3.

- After treatment, the suspension was washed with hot deionized water at 80 ° C to remove any physically adsorbed species to be detected non-sulfonated ion water seepage. That is to have a neutral pH.
- After filtration, the sample was dried at 120 °C for 8 hours to obtain a sulfonated coal or alternatively, the CMHL520 material.

3. Results and discussion

The catalyst support CMHL and CMHL520 catalyst were characterizing by various techniques and the results are shown below:

The FTIR spectra of CMHL showed in the Table 1 a first peak located at 653 cm-1 with a weak intensity corresponding to the functional group C-S, the second at 866 cm-1 with strong intensity corresponding to the aromatic moiety HCC, the third 1140 cm-1 with a weak intensity corresponding to the asymmetric S=O functional group, the fourth at 1420 cm-1 with a strong asymmetric stretching intensity corresponding to the aromatic functional group C-C, the fifth and last at 1636 cm-1 medium intensity corresponding to the functional group C = C.

Table 1. FTIR of the CMHL

Bands (cm-1)	Functional group		Allocation	Intensity of the peak in the spectrum
653	C-S	Sust. Para	Elongation	Weak
866	HCC	Aromatic	Elongation	Strong
1140	S=O	Asymmetric	Elongation	Weak
1420	C-C	Aromatic	Symmetric stretch	Strong
1636	C=C	Aromatic	Elongation	Medium
2829	CH2/CH3		Elongation	Medium

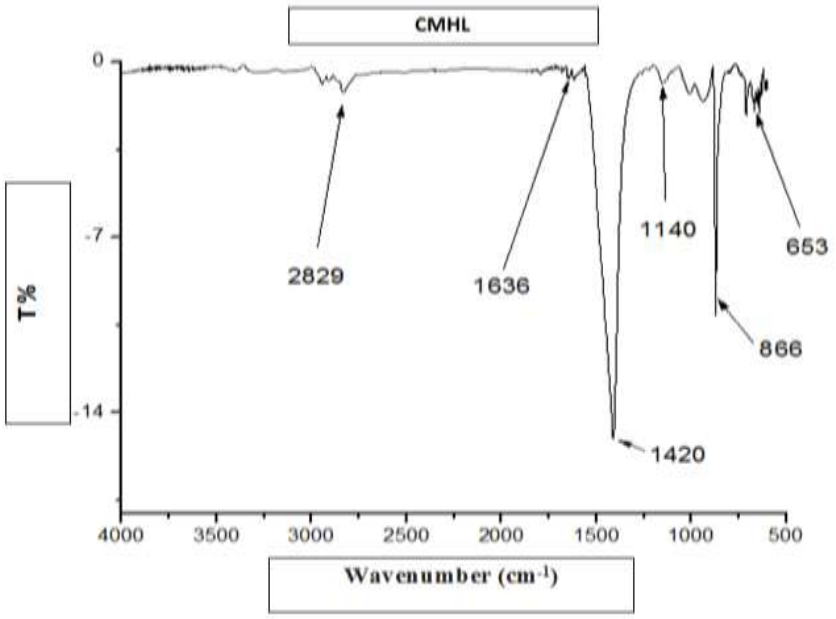

Figure 1. FTIR of the CMHL

The FTIR spectra showed CMHL520 in the Table 2 a first peak located at 617 cm-1 with a weak intensity that corresponds to the S-OH functional group, the second at 642 and 726 cm-1 with an average intensity which corresponds to the aromatic moiety C-H the third at 1254 cm-1 with a weak intensity corresponding to the functional group to the fourth Aromatic C-C 1074 cm-1 with strong intensity corresponding to asymmetric-SO_3H functional group, the fifth to 1447 cm -1 with strong intensity asymmetric stretching corresponding to aromatic C = C functional group, the sixth and last at 1717 cm-1 with an average intensity that corresponds to the functional group conjugated C = O.

Table 2. FTIR of the CMHL520.

Bands (cm-1)	Functional group		Asignación	Intensidad del pico en el espectro
617	S - OH	Sust. Para	Elongation	Weak
726 - 642	C - H	Aromatic	Elongation	Medium
1074	SO_3H	Asimétric	Elongation	Strong
1254	C-C	Aromatic	Symmetric stretch	Weak
1447	C=C	Aromatic	Symmetric stretch	Strong
1717	C=O	Conjugate	Elongation	Medium

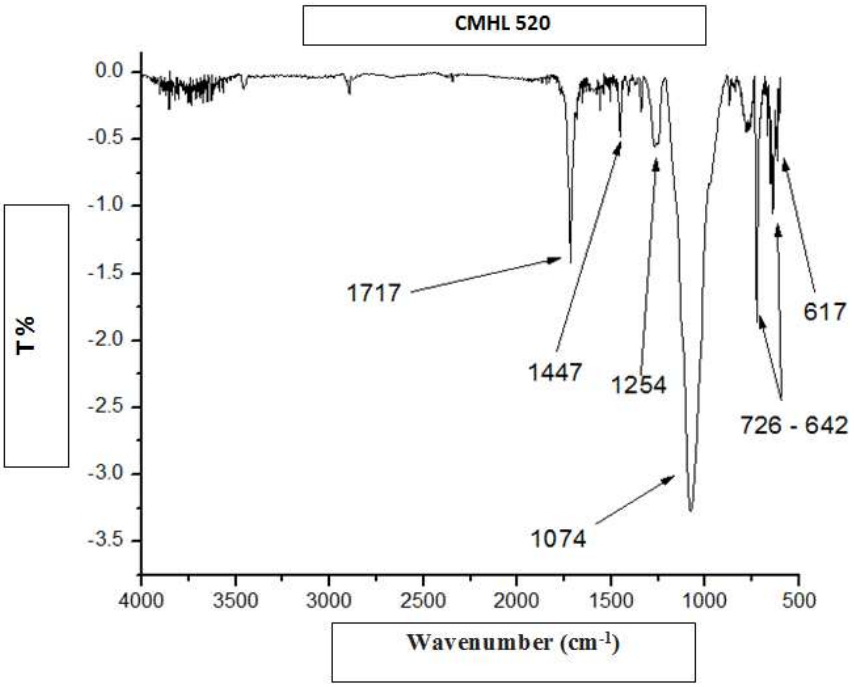

Figure 2. FTIR of the CMHL520.

The XRD diffractogram of CMHL shows the presence of calcite in the activated carbon zincita as shown in Figure 3, and two characteristic peaks at 2θ angle of 10-30 ° and 35-50 ° attributed to the plates amorphous carbon as shown in Figure 4. These results indicated the presence of polycyclic aromatic carbon sheets in the activated carbon of tire rubber.

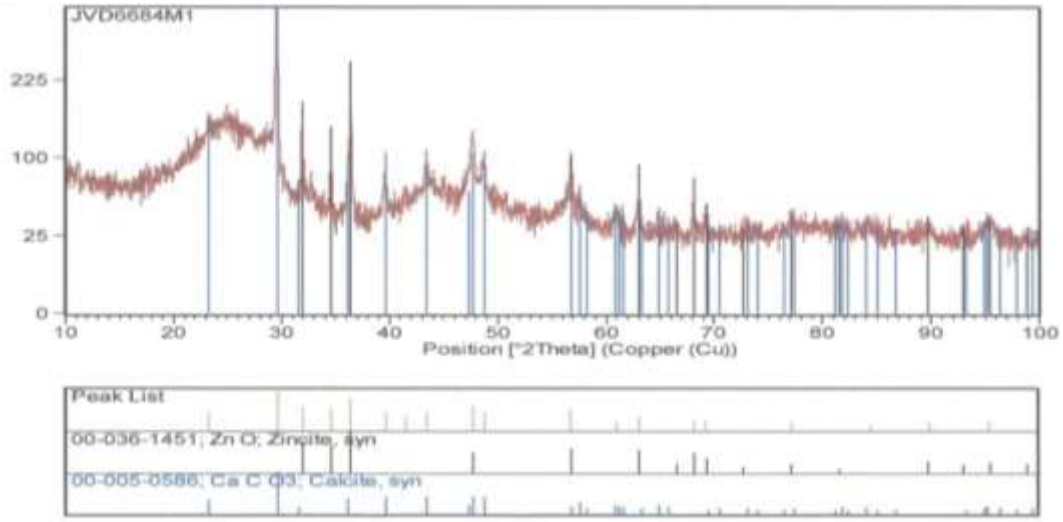

Figure 3. XRD of the CMHL

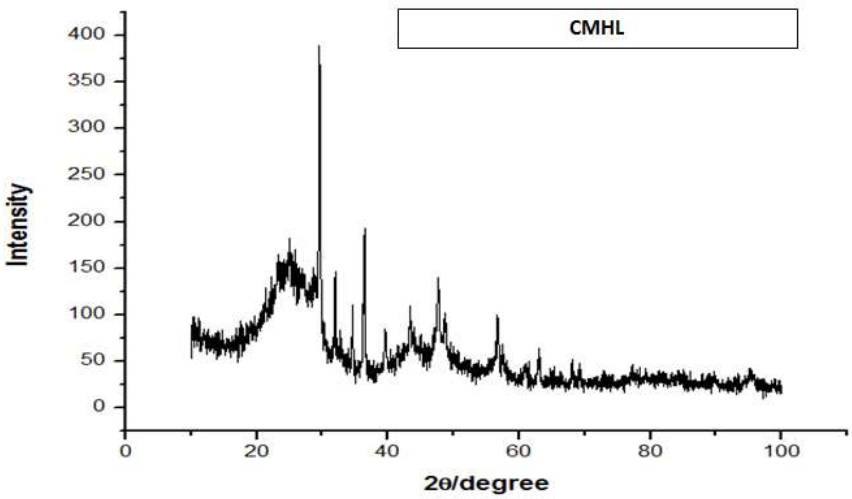

Figura 4. XRD of the CMHL

The XRD diffractogram of CMHL520 not already detected the presence of calcite in CMHL520 zincita as shown in Figure 5, this is attributed to the removal by the contact with sulfuric acid. In Figure 7, the presence of two characteristic peaks shown at the 2θ angle of 10-30 ° and 35-50 ° attributed to amorphous carbon plates. These results indicated the presence of polycyclic aromatic carbon sheets in CMHL520.

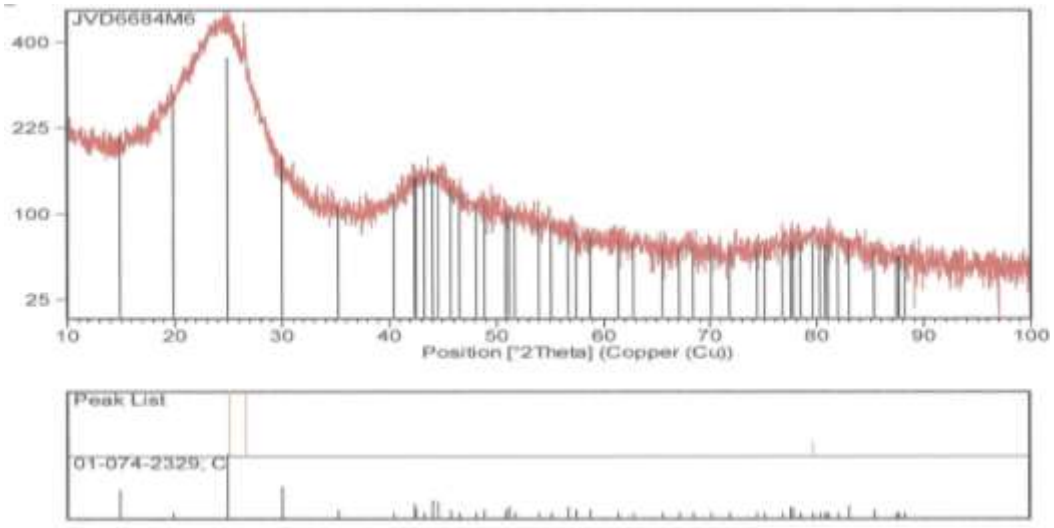

Figure 5. XRD of the CMHL520.

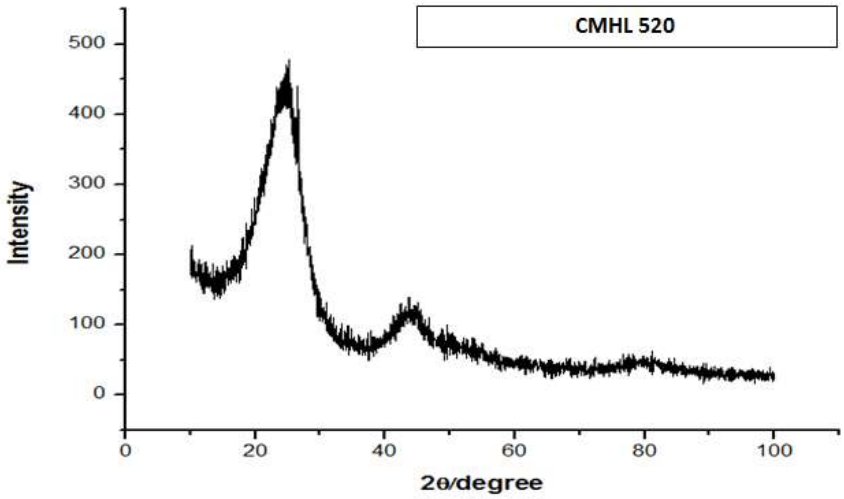

Figura 6. XRD del CMHL520.

EDS analysis to CMHL and CMHL520 was conducted to determine its chemical composition wherein the percentage by weight and the atomic percentage demonstrated an increase in the amount of sulfur in the catalyst. In the Table 3 was observed on the catalyst support a weight percentage of 1.78% of sulfur and on the catalyst was observed by weight percentage of sulfur of 3.82%, which shows increase in sulfur in the coal sulfonated with sulfuric acid. There are 3 sulfur atoms attached to the surface per 200 carbon atoms in the latter case.

Table 3. Elements in the CMHL and CMHL520.

Catalyst	C		O		S	
	Wt %	At %	Wt %	At %	Wt %	At %
CMHL	62.29	74.19	21.46	19.19	1.78	0.79
CMHL520	92.09	95.34	4.09	3.18	3.82	1.48

Quantification of acid functionalization CMHL and CMHL520 held by acid-base titration by titration, resulting in a density of acidic groups of 0.92 mmol / g 2.82 mmol / g, respectively, which are anchored in the layer carbon.

4. Summary and perspectives

The technique used for the sulfonation of the carbon catalyst support tire rubber was performed correctly and that the deposition of sulphone ion was found in the catalytic carbon support for tire rubber from concentrated sulfuric acid.

With the techniques used in the characterization and CMHL520 CMHL are satisfactory and that obtaining a solid catalyst were demonstrated by sulfonation super mesoporous acid from a carbon rubber tire.

CMHL520 with obtaining a density of acidic groups of 2.82 mmol / g the proper functioning in the esterification and transtesterificación of vegetable oil used in an autogenous reactor is guaranteed.

5. Acknowledgements

Thanks to Dr. Javier Rodríguez Varela CINVESTAV Saltillo Unit for their support in the characterization of materials.

6. References

[1] Rodriguez Reinoso, F. El carbón activado como adsorbente universal. En: Sólidos porosos. Preparación, caracterización y aplicaciones. Ed. J.C. Moreno P. Bogotá. Ediciones Uniandes. 2007. pp. 1-42.

[2] Zabaniotou, A.; Madau, P.; Oudenne, P.D. Active carbon production from used tire in two-stage procedure: industrial pyrolysis and bench scale activation with H2O–CO2 mixture. J. Anal. Appl. Pyrol. 2004. 72: 289–297.

[3] Troca-Torrado, C.; Alexandre-Franco, M.; Fernández-González, C.; Alfaro- Domínguez, M.; Gómez-Serrano, M. Development of adsorbents from used tire rubber their use in the adsorption of organic and inorganic solutes in aqueous solution. Fuel Processing Technology. 2011. 92: 206–212.

[4] Ko, D.C.K.; Mui, E.L.K.; Lau, K.S.T.; McKay, G. Production of activated carbons from waste tire – process design and economical analysis. Waste Management. 2004. 24: 875-888.

[5] Kalnes, T., Koers, K., Marker, T., & Shonnard, D. (2009). A technoeconomic and environmental life cycle comparison of green diesel to biodiesel and syndiesel. AIChE Journal 28.

[6] D. Zhao, J. Feng, Q. Huo, N. Melosh, G.H. Fredrickson, B.F. Chmelka, G.D. Stucky, Triblock copolymer syntheses of mesoporous silica with periodic 50–300 angstrom pores, Science 279 (1998) 548–552

[7] Sivasamy, A., Cheah, K., Fornasiero, P., Kemausuor, F., Zinoviev, S., & Miertus, S. (2009). Catalytic applications in the production of biodiesel from vegetable oils. ChemSusChem.

[8] Gerpen, J.V., 2005, Biodiesel processing and production. Fuel Process Technol, 86(10): 1097–1107.

[9] Li Y, Zhang XD, Sun L, Xu M, Zhou WG, Liang XH. Solid superacid catalyzed fatty acid methyl esters production from acid oil. Appl Energy 2010;87:2369–73

Paramagnetic Behavior of Ni-Fe Layered Double Hydroxide and their effect over the Electrocatalytic Activity towards Oxygen Evolution Reaction in Alkaline Media

Miguel A. Oliver-Tolentino[a], Juvencio Vázquez-Samperio[b], Arturo Manzo-Robledo[c], Ariel Guzmán-Vargas[b]*

[a]Instituto Politécnico Nacional, Centro de Investigación en Ciencia Aplicada y Tecnología Avanzada, Calzada Legaria 694, Col. Irrigación, México D.F. 11500, Mexico.
[b]Instituto Politécnico Nacional, ESIQIE-Departamento de Ingeniería Química, Laboratorio de Investigación en Materiales Porosos, Catálisis Ambiental y Química Fina, UPALM Edif. 7 P.B. Zacatenco, GAM, México, DF 07738, Mexico
[c]Instituto Politécnico Nacional, ESIQIE-Departamento de Ingeniería Química, Laboratorio de Electroquímica y Corrosión, Edif. Z-5 3er piso, UPALM, Zacatenco, GAM, México, DF 07738, Mexico

ABSTRACT

In the present work the hydrotalcite like materials know as Layered Double Hydroxide (LDH) Ni-Fe with different Ni/Fe relationship were synthesized by co-precipitation method to constant pH, the LDH obtained were labeled H/Ni-Fe1 and H/Ni-Fe2, the hexagonal lattices with R3m rhombohedral symmetry, characteristic for this materials was verify by XRD, No secondary phases are observed for any materials. On the other hand, the electronic properties were evaluated by Electronic Paramagnetic Resonance (EPR), the results suggested that H/Ni-Fe1 exhibited a ferromagnetic behavior as a result of the combined action of NiII-OH-NiII and FeIII-OH-NiII and FeIII-OH-FeIII pairs across the layers and ferromagnetic dipolar interactions operating between layers. Whereas, the H/Ni-Fe2 presented a Paramagnetic behavior due to intralayer magnetic superexchange between metal centers through the OH bridges across the cationic sheets and dipole–dipole interaction in sites of less distorted octahedral field which operating through the space between the magnetic layers. These materials were evaluated as electrocatalyst in the Oxygen Evolution Reaction (OER) in alkaline media, the results showed that OER begin c.a. to 1.4V/NHE, the tafel plots for both materials were around to 39mV dec-1 which is comparable with IrO in same media. However, the Turn Over Number (TON) value was 9.9 s-1 for H/Ni-Fe1 and 38.1 s-1 for H/Ni-Fe2, indicating the higher electrocatalytic behavior in H/Ni-Fe2 than H/Ni-Fe1, this interesting result were discusses by electronic properties determinate in EPR experiments.

*Keywords:*LDH, Paramagnetic, Turn Over Number

1. Introduction

The electrolysis of water to produced hydrogen and oxygen gas (i.e.,water splitting, $H_2O \rightarrow H_2 + 1/2O_2$) is a key component in the development of future energy storage technologies. The oxygen evolution reaction $4OH^- \rightarrow 2H_2O + O_2 + 4e^-$ (in basic media) is kinetically slow and hence represents a significant efficiency loss. The oxygen evolution mechanism has several steps that have large reaction barriers, which lead to large required overpotentials to drive the reaction at practical rates. The large overpotentials significantly decrease the efficiency, as the extra energy is dissipated as low quality heat, and limit the possibility of large scale production of hydrogen from water splitting. Therefore, considerable research efforts have been made in developing the OER electrocatalysts which are highly active, stable and inexpensive. The oxides of Ru and Ir are considered as the best OER catalysts for use in acid and base respectively, but these metals are amongst the rarest elements on the earth and, hence, are not economical for large-scale applications [1].

Nickel and its alloys have been traditionally the materials of choice for anodes in the process of alkaline electrolysis of water oxygen evolution reaction (OER), it has relatively low overpotentials, low cost, long-term stability and high corrosion resistance. Ni-Al and Ni-Fe LDH catalysts have been shown to be of particular interest because of the lower overpotential of reaction and the stable activity [2].

Layered double hydroxides (LDHs) are a group of inorganic materials that contain positive charged in the layers region. The composition of the main layer can be written as [M(II)1-xM′(III)x(OH)2], with the positive charge on the main layer resulting from the replacement of divalent ions with trivalent ions. Both divalent and trivalent ions are located at the center of octahedral composed of OH- ions; M(OH)6 and M′(OH)6 octahedral units share edges forming 2D layers. The interlayer incorporates anions and water molecules to maintain charge neutrality [3].In this work we report reported the oxygen evolution reaction (OER) using hydrotalcite-like (LDH) materials

2. Experimental

The Ni-Al and Ni-Fe LDH were prepared by coprecipitation as described elsewhere. As an example, Ni-Fe2 was prepared by dissolving 0.117 moles of NaOH (Aldrich) and 0.034 moles of Na_2CO_3 (Aldrich) in 100 mL of deionized water; the pH of this solution was 13.4. A second solution was prepared by dissolving 0.034 moles of $Ni(NO_3)2{\cdot}6H2O$ (Aldrich) and 0.017 moles of $Fe(NO_3)_3{\cdot}9H2O$ (Aldrich) in 100 mL of deionized water. While maintaining the first solution under vigorous stirring the second solution was slowly added by means of a peristaltic pump. After complete addition the resultant slurry was stirred for 2 h at room temperature; the pH of the suspension was 9.5. Finally, the suspension was stirred for 2 days at 50 °C, and then the solid obtained was separated by centrifugation, rinsed thoroughly with warm distilled water, and dried overnight at 80 °C. The solids obtained were labeled H/Ni-Fe1 and H/Ni-Fe2, where the number indicates Ni/Fe ratio.

The modified carbon paste electrode were prepared mixing graphite powder (Alfa Aesar, 99.9995%, USA), silicon oil (Aldrich) and the corresponding LDH at 20 wt.%. The mixture was mechanically homogenized and inserted in 2 mm diameter cylinder (0.0314 cm2). The surface contact on the electrode was made with a platinum wire.

The XRD structural characterization of LDHs was performed in a Philips X'PERTPRO instrument using CuKα1 radiation (λ= 1.542 Å, 45 kV, and 40 mA); Electron Paramagnetic Resonance (EPR)

measurements were carried out at room temperature and 77 K using a JEOL JES-RES3X continuous wave EPR spectrometer. Typical EPR spectral parameters were as follow: X-band frequency = 9.1642 GHz, modulation amplitude = 3.2 G, modulation frequency = 100 kHz.

Electrochemical analyses were carried out at room temperature in a potentiostate–galvanostate VERSASTAT3-400 (Princeton Applied Research). A three-electrode standard electrochemical cell was used for the cyclic voltammetry (CV) measurements at 5 mV s^{-1} with a carbon rod and a Saturated Calomel Electrode (SCE), respectively. For these experiments, the working electrode was made from the synthesized materials, immersed in a carbon paste electrode (CPE) matrix.

3. Results and discussion

Materials Characterization

Lamellar structure of solids was confirmed by X-ray diffraction, infrared spectroscopy and Raman spectroscopy. The powder X-ray diffractograms of the synthesized samples are shown in Figure 1. All samples exhibited the typical signature of hexagonal lattices with R3m rhombohedral symmetry (JCPDS card 22-0700), any secondary phases were observed.

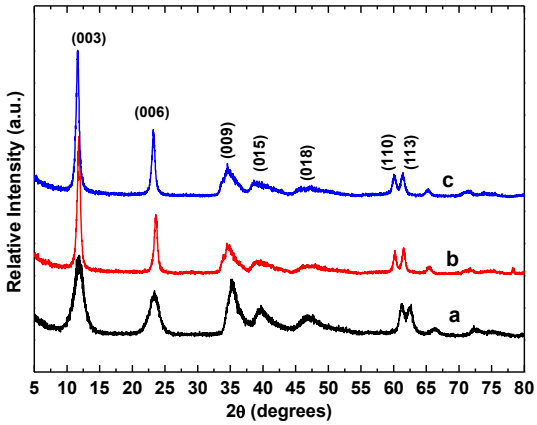

Figure 1. X-Ray Diffraction patterns of a) H/Ni-Al, b) H/Ni-Fe1 and c) H/Ni-Fe2

The H/Ni-Al EPR spectra exhibited a very broad and weak signal around g = 2.2014 (Figure not shown), which has been attributed to the MS=0 and MS=±1 magnetic dipole transition of NiII. This phenomenon is favored by orthogonality of the NiII magnetic orbitals due to NiII-OH-NiII interaction, where the angle in the LDH structure should be close to 90°. On the other hand, the H/Ni-Fe samples showed broad signals around g = 2.0248 (Figure 2B) which are characteristic of FeIII low spin with S=1/2. The line width (Γ) and the morphology of the EPR spectra indicate a strong FeIII-OH-FeIII interaction with an important

contribution of FeIII-OH-NiII interaction. However, due to the composition of LDH materials NiII-OH-NiII interaction could not be discarded.

Both samples presented interesting differences in the EPR spectra. The H/Ni-Fe2 sample shown a weak and broad signal at 300 K (Figure 2) but at 77 K this EPR signal was increased. This behavior suggests that the sample exhibits an antiferromagnetic (AF) interaction with a small contribution of ferromagnetic (F) interaction at 300 K. However, ferromagnetic interaction is increased at 77 K. This fact could be explained due to the Ni-Fe hydrotalcite like materials behave as ferrimagnets, as a result of the combined action of F NiII-OH-NiII and AF FeIII-OH-NiII and FeIII-OH-FeIII pairs across the layers and ferromagnetic dipolar interactions operating between layers.

On the other hand, H/Ni-Fe1 showed an intense EPR signal with line width Γ = 285 Gauss and g = 2.2014 at 300 K, which is characteristic of paramagnetic behavior (Figure 2B curve a). Furthermore, at 77 K the line width of the EPR signal was increased notoriously, indicating the presence of a ferromagnetic behavior among the Fe spins; however, the paramagnetic behavior shown at 300 K can still be seen at this temperature. The paramagnetic behavior of H/Ni-Fe1 could be associated to the increase of iron content. As a result of this increase may be that: 1) an increment in FeIII-OH-FeIII interactions, which generate a spin glass process in this material due to the spin frustration. In addition, these iron interactions could promote the intralayer superexchange interaction between metal centers through the OH bridges across the cationic sheets; 2) a dipole–dipole interaction in sites with distorted octahedral field, which operate through the space between the magnetic layers.

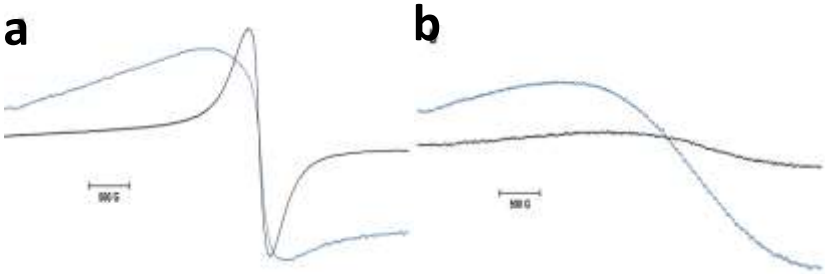

Figure 2. EPR spectra of a) H/Ni-Fe1 and b) H/Ni-Fe2, black line at room temperature and blue line at 77K.

Electrochemical characterization

The current-potential characteristics obtained in 1M KOH solution at 5 mV s^{-1} for LDHs immobilized in a Carbon Paste Electrode (CPE), are displayed in Figure 3. For H/Ni-Al (curve a) an anodic peak at ca. 1.52 V/RHE is observed and might be associated with the oxidation of NiII to NiIII, followed by the OER starting at ca. 1.6 V/RHE. Conversely, for H/Ni-Fe1 and H/Ni-Fe2 samples (curve b and c) the obtained

profiles indicated that only OER is carried out, starting at ca. 1.46 and 1.48 V/RHE, respectively. According to these results, the current magnitude order during oxygen evolution was as follow: H/Ni-Fe1>H/Ni-Fe2>H/Ni-Al.

On the other hand, the current-potential characteristic obtained using cyclic voltammetry (CV) for H/Ni-Al displays well-defined anodic and cathodic peaks associated with redox process for the couple NiIII/NiII with a peak-to-peak potential ΔEp=200 mV, see inset in Figure 3. This electrochemical behavior is well-known and is due to insertion/desertion of OH- ions from the LDH-interlayer space during nickel-sites oxidation/reduction by electron hopping mechanism along the brucite structure inducing electro-neutrality. It is worth to mention that non-faradic processes were observed at CPE free of LDH (Figure not shown).

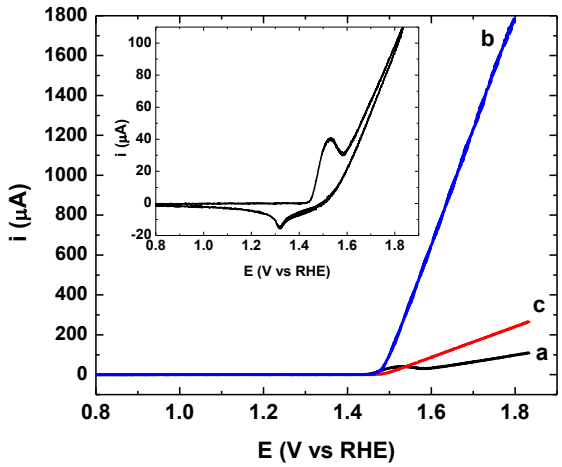

Figure 3. Linear Sweep Voltammetry of a) H/Ni-Al, b) H/Ni-Fe1 and c) H/Ni-Fe2, inset: cyclic voltammetry of H/Ni-Al in 1M KOH.

Tafel plots obtained from polarization curves were fashioned (Fig. 4). The resulting Tafel slopes were ca. 34, 36 and 37 mV dec-1 for H/Ni-Al, H/Ni-Fe2 and H/Ni-Fe1, respectively. These values are smaller than those reported for the system Ir/C which exhibited a Tafel slope of ca. 40 mV dec^{-1}; indicating that, within experimental error, the OER mechanism is similar for all set of these materials. Such reaction mechanism might be related with i) a surface oxidation by one electron electrochemical step; ii) adsorption step; and iii) a one electron-electrochemical rate-determining step for oxygen production.

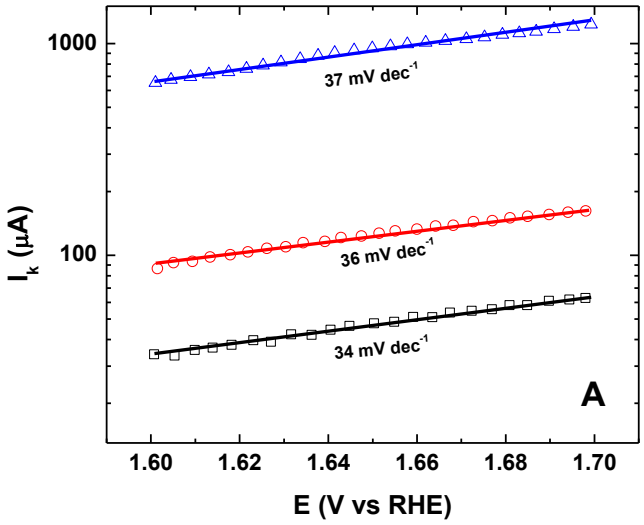

Figure 4. A) Tafel Plots of a) H/Ni-Al, b) H/Ni-Fe1 and c) H/Ni-Fe2 obtained from i-E characteristic of Fig. 3

4. Summary and perspectives

LDH materials with different Ni/Fe ratio using co-precipitation method at variable pH were synthetized. The iron content in the structure of these materials plays an important role on their magnetic properties. It may be postulated that the superexchange interaction is one of the main causes that promotes the enhancement of the H/Ni-Fe1 catalytic activity toward OER. Production of molecular oxygen were confirmed using LSV. Whereas, Tafel slopes were around 40 mV dec-1, indicating that every materials rules out by the same mechanism reaction, where one electron electrochemical is the rate determining step for O_2 production.

Acknowledgements

This work was partially supported by Projects: SIP-IPN 20140793, CONACYT 101319,

References

[1] Coronado-Guinto, J.L.; Cardeño-García, L.; Martínez-Casillas, D.C.; Sandoval-Pineda, J.M.; Tamayo-Meza, P.; Silva-Casarin, R.; González-Huerta, R.G.;Performance of a PEM electrolyzer using RuIrCoOx electrocatalysts for the oxygen evolution electrode. Int. J. Hydrogen Energy 2013, 38, 12667-12673.

[2] Gong, M.; Li, Y.; Wang, H.; Liang, Y.; Wu, J. Z.; Zhou, J.; Wang, J.; Regier, T.; Wei, F.; Dai, H.; An Advanced Ni-Fe Layered Double Hydroxide Electrocatalyst for Water Oxidation. J. Am. Chem. Soc. 2013, 135, 8452-8455.

[3] Oliver-Tolentino, M.A.; Guzmán-Vargas, A.; Manzo-Robledo, A.; Martínez-Ortiz, M.J.; Flores-Moreno, J.L.; Modified electrode with hydrotalcite-like materials and their response during electrochemical oxidation of blue 69. Catal. Today 2011, 166, 194-200.

Evaluation of different support materials used with a photo-fermentative consortium for hydrogen production

E. Guevara-López[1], G. Buitrón[1*]

[1]Laboratory for Research on Advanced Processes for Water Treatment, Unidad Académica Juriquilla, Instituto de Ingeniería, Universidad Nacional Autónoma de México, Blvd. Juriquilla 3001, Querétaro 76230, México
Tel: +52 442 192 6165; *e-mail: gbuitronm@ii.unam.mx

ABSTRACT

Four different support materials were evaluated for immobilization of a consortium of purple non-sulfur bacteria (PNS) producing hydrogen gas. The inoculum was enriched from a microbial fuel cells. Tested materials were acrylic rods, silica gel, high-density polyethylene cylinders and luffa (dispersed fibers and cubes). The area/volume ratio, volatile solids per volume and the amount of hydrogen produced using volatile fatty acids as substrate were determined. The experiments were conducted in serological bottles of 120 mL, continuously illuminated at 7 klux, mixed at 100 rpm and 32 °C. It was found that the PNS bacteria generated 16.7 ± 2.6 mLH_2/gVS-h. The highest biomass quantity (as volatile solids, VS) was found in dispersed luffa fibers (8.0 ± 1.7 $mgVS/cm^3$) followed by luffa in cubes, high-density polyethylene cylinders and acrylic bars. Dispersed luffa allowed a better light distribution and contact with the media than luffa in cubes. Silica gel was not suitable for the immobilization and hydrogen production. Experiments with the colonized supports indicated that no significant differences regarding specific hydrogen production were observed among luffa, acrylic bars and polyethylene. In conclusion the luffa in the form of fibers is a suitable support for purple non-sulfur consortium because of this provide the highest area/volume ratio and the highest attached quantity of VS per volume. After several batches the biomass remained attached to the support.

Keywords: Hydrogen, purple non-sulfur bacteria, cell immobilization

1. Introduction

Hydrogen is the most promising alternative to fossil fuels since it combust cleanly producing only water, can be converted to electricity via fuel cell technology, can be transported for domestic/industrial consumption through conventional means and it is a renewable energy [1,2]. Most importantly, hydrogen has the highest energy content per unit weight (142 kJ/g) [1]. Hydrogen can be produced from renewable sources, even waste materials, by biological processes operated at ambient temperatures and pressures; therefore, less energy intensive than thermochemical and electrochemical ways generally used [3].

Purple non-sulfur (PNS) photosynthetic bacteria are found as the most promising microbial system for biohydrogen production, due to high substrate conversion, lack of oxygen-evolving activity, ability to use a wide wavelength of light and capability to use organic substrates (sugars or volatile fatty acids, derived from wastes) for hydrogen production [4]. Even more, gas produced by PNS bacteria consists of 80-95% (v/v) of H_2. The remaining part is mostly CO_2, which can be removed easily [5]. This biochemical process is catalyzed by nitrogenase in the absence of nitrogen. Sufficient source of ATP is required for efficient hydrogen production. Energy from light enables PNS bacteria to overcome the thermodynamic barrier in the conversion of organic acid into hydrogen [6].

Several studies have been conducted to evaluate the different factors affecting the hydrogen production in the photofermentation process as type of substrate and concentration [7, 8, 9], C/N ratio [10], pH [8], wavelength [11, 12], light intensity [11, 13, 14, 15] and illumination protocols [11, 16, 17]. However, the yields are still low. Hydrogen yields can be improved by maintaining a maximal activity of nitrogenase, a favorable molar C/N ratio and a uniform distribution of light through the culture [6].

Processes with immobilized cells have different advantages: the systems can be operated in exponential growth phase for a long period of time, less space and volume of growth medium are required, higher catalytic stability and resistance against toxins or enzymatic inhibitors, higher concentration of cells per unit volume of the bioreactor than suspended cells process and easier recovery of cells and reuse of these [6, 18].

These advantages have been tested entrapping cells of *R. rubrum* in agar or agarose [19], *R. sphaeroides* in chitosan, polyethyleneimine, trimethylammonium glycol chitosan iodide and poly-L-lysine [20], *R. faecalis* in agar [21] and *R. palustris* in polyvinyl alcohol, sodium alginate and carrageenan powder [12]. However, the surface attachment seems to be more proper for photofermentation because this technique offers less mass transfer resistance, higher operation stability and easier light penetration than entrapment [2, 22]. Different supports have been evaluated for biofilm formation, *R. sphaeroides* on porous glass [23], glass textile fiber [24] and filter porous glasses [18], *R. palustris* on activated carbon, silica gel and clay [25, 26], polymethyl methacrylate [27], glass slide [28], glass beads [2] and optical fiber [22], and *R. faecalis* on activated carbon fibers [29]. Nevertheless, all this studies were conducted with pure cultures. The use of mixed cultures can be beneficial for the treatment of complex substrates [30].

This work evaluates four different support materials for immobilization of a consortium of purple non-sulfur bacteria (PNS) producing hydrogen gas. The main objective was to identify the support that can allow the highest quantity of cells immobilized per volume and the highest production of hydrogen using a synthetic medium containing sodium acetate and sodium butyrate as carbon source. The performance of the hydrogen production using the colonized supports batch cultures was evaluated.

2. Experimental

2.1. Bacterial consortium and media

The hydrogen producing bacterial consortium was isolated from the anode of a bioelectrochemial system used in hydrogen production. Bacteria were grown on basal medium [31] consisting of (g/L) K_2HPO_4 750, $MgSO_4$ 200,

$FeSO_4 \cdot 7H_2O$ 11.78, H_3BO_3 2.80, $Na_2MoO_4 \cdot 2H_2O$ 0.75, $ZnSO_4 \cdot 7H_2O$ 0.24, $MnSO_4 \cdot 4H_2O$ 2.10, $CuCl_2.2H_2O$ 0.04, $CaCl_2.2H_2O$ 0.75, EDTA-Na 2.00, thiamine 3.78 and Biotin 3.57. The medium was supplemented with sodium acetate (2.46 g/L), sodium butyrate (3.30 g/L) and sodium glutamate (0.37 g/L). The C/N ratio was 80 [1]. The initial pH was adjusted to 6.8. Argon was used to obtain anaerobic conditions in the medium. The cultures were conducted to 32°C with continuous illumination to 5 klux in 1 L bottles mixed with a magnetic stirrer. The biomass was collected by centrifugation (Centrifuge Solbat C-40) to 3500 rpm for 15 min.

2.2. Support materials

Four different materials were selected as possible supports for the bacterial consortium. The material were acrylic rods (6 mm diameter and 7 mm length, in average), silica gel (Yamani, JIS Z 0701), high-density polyethylene (PE) cylinders (BCN 009 plus, 2H Germany) and luffa (dispersed fibers and 1 cm^3 cubes). Densities of the support materials was determining by weight in analytical balance (Ohaus Adventurer Pro AV114C) and displacement of water in Falcon tubes. The volume and area of the luffa fibers were determined measuring the diameter and length of the fibers through microscopy (Leica DM 500, Optical Len ICC50 HD). For that, the fibers were previously stained with methylene blue. Plastic materials (acrylic and polyethylene) were immersed in wastewater during three days to oxidize the surface and help to the biofilm formation.

2.3. Immobilization procedure

For the colonization, the supports were placed in 120 mL serum bottles with 75 mL of growth medium and were inoculated with 100 mg/L of inoculum. The bottles were kept, during 29 days, at 32±2 °C, with continuous illumination at 7 klux, and 100 rpm orbital shaking (Barnstead Lab-Line SHKE2000). The cultures were illuminated with yellow LED (590 nm) and tungsten lamps. Bottles inoculated in similar manner but without support material were used as control. During the immobilization period, biogas production was measured and samples of the biogas were taken off to measure the gas composition. At the end of the immobilization period, suspended biomass concentration and fixed biomass were determined. Biomass was separated of the medium by centrifugation and COD and pH of the medium were measured.

2.4. Hydrogen production by immobilized consortium

To evaluate the hydrogen production by the immobilized biomass, a sample of the colonized supports were taken off and washed with fresh medium to eliminate suspended cells. Then, they were transferred to fresh medium, but with the COD diluted ten times (sodium acetate 0.246 g/L, sodium butyrate 0.330 g/L and sodium glutamate 0.037 g/L), to maintain a similar COD/biomass ratio to that used in the colonization experiments. Culture conditions were the same than described in Section 2.3 and they were kept for four cycle cultures with a total time of 18 days. Volume and composition of produced biogas were determined during this time. At the end, pH, COD and biomass concentration were evaluated.

2.5. Analytical methods

Light intensity was measured on bottles surface with a luxmeter (Extech LT300) and pH value with a pH meter (OAKTON 510, probe Orion 9156BNWP). Suspended cell concentrations of the cultures were determined by optical density at 660 nm using a UV-VIS spectrometer (Perkin Elmer, Lambda 25). Calibration curves were previously elaborated to relate this measurements with Volatile Suspended Solids determined according the Standard Methods [32]. The amount of biomass attached to the supports was determined by estimating the protein concentration according to a modified Lowry method [33]. The supports were sonicated during 45 min in a bath (Branson 2510R-DTH) previous the protein determination. COD was measured by dichromate method [34]. A spectrophotometer (HACH DR/2010) was used.

The composition of biogas was measured by a gas chromatograph (SRI 8610C) equipped with a thermal conductivity detector (TCD) and a 1.82 m long silica gel column followed by a 1.82 m long (3.175 mm) molecular sieve column 13x. The initial column temperature was 40°C, which was held for 4 min and then gradually increased 20°C/min up to 110°C. The injector and detector temperatures were 90°C and 150°C, respectively. Nitrogen was used as the carrier gas at a flow rate of 20 mL/min.

Hydrogen production performance was fitted to modified Gompertz equation (1) [29, 35]:

$$H = H_{max} exp\left\{-exp\left[\frac{R_{max}e}{H_{max}}(\lambda - t) + 1\right]\right\} \quad (1)$$

where H (mL/g SVT) is the cumulative amount of hydrogen produced at culture time t(h), H_{max} (mL H_2/g SVT) is the maximum amount of hydrogen produced, R_{max} (mL H_2/g SVT/h) in the maximum hydrogen production rate; λ (h) is the lag phase time.

3. Results and discussion

3.1. Support characterization

Supports materials were selected by choosing a high A/V ratio and the facility to be suspended in the medium. In addition, a suitable light distribution was searched to be present with the supports. Table 1 shows the results for density and A/V ratio for supports evaluated. Silica gel and luffa presented the lowest density and highest A/V ratio, which can provide a high surface for the immobilization and facility for mixing.

Table 1 Characteristics of the support materials.

Support material	Density (g/cm^3)	A/V (cm^2/cm^3)
Luffa	0.82	244.0
Acrylic rods	1.25	9.6
PE cylinders	0.92	68.7
Silica gel	0.70	5000000

3.2. Hydrogen evolution during colonization

The hydrogen production per gram of total volatile solids, VS, (suspended and attachment cells) was fitted to the Gompertz model as shown in Figure 1. Parameters obtained with the model are presented in Table 2. The maximum hydrogen production rate was reached with acrylic rods; however, the maximum specific hydrogen production was similar for luffa fibers, luffa cubes, polyethylene cylinders and control. Cultures with luffa cubes had a lower rate and hydrogen production than luffa fibers. The difference among the two configurations is explained because of the different light distribution between them. Luffa cubes is a more compact structure that can block the light pass through the support. In the case of silica gel, minimal biogas quantity was detected in the first 200 h, after that, production stopped. Although silica gel has been reported like a support for PNS bacteria [25], this has been previously sterilized. In contrast, in this study minimal treatment was used (only washed with deionized water). For all the cultures, a pH increment of 0.3±1 units was observed, which can be associated to the ammonia production. Nevertheless, in the case of silica gel, the pH decreased to 5.6 ± 0 1, which may indicate that other microorganisms non-hydrogen producers (fermentation bacteria) were developed. COD removal percentages (average of 72.2 ± 4.2 %) were similar for luffa, acrylic rods, polyethylene cylinder and control.

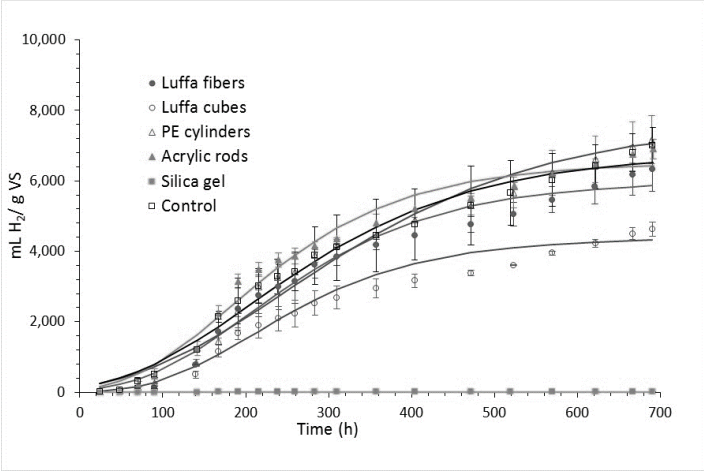

Figure 1. Cumulative hydrogen production and Gompertz fit as a function of time.

Table 2. Gompertz parameters, COD removal and final pH during colonization experiments

Support material	Gompertz parameters			ΔCOD %	Final pH
	$H_{máx}$ (L H_2/g SV)	$R_{máx}$ (mL H_2/g SV/h)	λ (h)		
Luffa fiber	6.0	17.0	73.7	71.6	7.1
Luffa cubes	4.4	14.0	92.0	69.4	7.2
Acrylic rods	6.5	20.2	61.5	70.9	7.2
PE cylinders	7.7	15.7	66.0	79.6	7.2
Control	6.8	16.4	54.1	69.4	7.1

3.3. Immobilized biomass

Figure 2 shows the results for the biomass quantification for the tested supports. After immobilization, a maximum amount of biomass per volume of support was found for the dispersed luffa fibers (8.0 ± 1.7 mg VS/cm^3). The highest amount of attached biomass correlated with the highest A/V ratio. When the supports were transferred to fresh medium to evaluate the hydrogen production by immobilized biomass, the biofilm increased between 2.5 and 4.5 times on the supports. At the end of the experiment, the biomass attached to the luffa fibers was 19.6 ± 1.5 mg SV/cm^3, 1.8 times more than the observed for the luffa cubes, 9.8 times more than PE cylinders and 16.2 times than acrylic rods. This increase in the immobilized biomass had been observed through several cycles of semicontinuous operation for *R. palustris* on filter porous glasses [18], reaching a final concentration of 19 mg/cm^3, similar to founded in the luffa fibers tested in this study. A lower biomass concentration has been found with *R. sphaeroides* in porous glass (11.2 mg/cm^3) [23]. In contrast with this study, porous glass required chemical modification to ensure biofilm formation. Silica gel was not appropriate for immobilizing the hydrogen producer consortium.

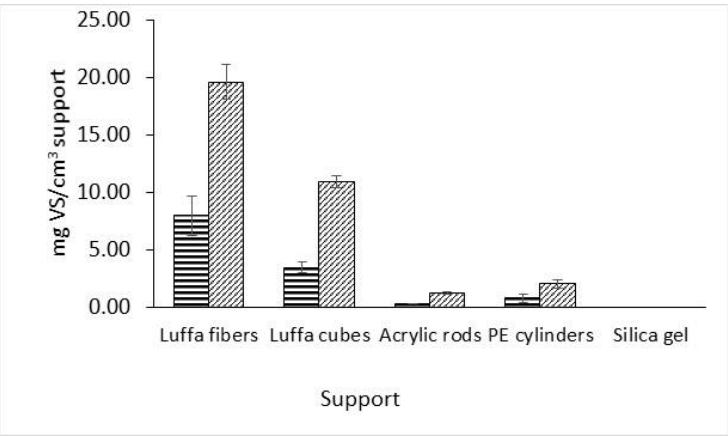

Figure 2. Immobilized biomass quantification. ▤ Immobilization, ▨ Evaluation of supports in hydrogen production.

3.4 Hydrogen production by immobilized consortium

Figure 3 presents the results for the evaluation of hydrogen production using the colonized supports. During the first batch cycle, the cumulative hydrogen production was lower than in subsequent cycles, which can be explained by an adaptation period of the cells. Zagrodnik et al. [18] explained this behavior because of the low bacteria concentration in the biofilm. The maximum specific hydrogen production for the subsequent batch cultures were similar in the different supports. In contrast with colonization experiments, here the luffa fibers and luffa cubes had similar productivities, because the suspended cells were lower than in the colonization experiments, and then the light presented a better distribution. Luffa productivities were slightly higher than with plastic materials, which may indicate a higher affinity of cells by natural materials. Luffa is mainly constituted by cellulose, lignocellulose and lignin. Patel et al. [36] observed the production of H_2 in dark fermentation with cells immobilized in ligno-cellulosic materials and PVC, and they observed that some ligno-cellulosic materials improved the hydrogen productivity in comparison with immobilization with PVC.

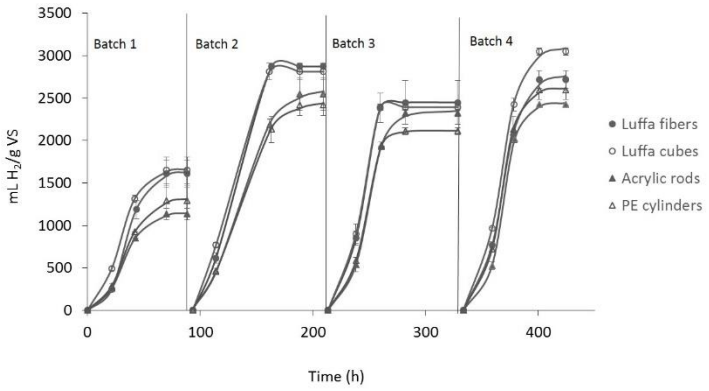

Figure 3. Hydrogen production with immobilized cells during four batch cycles (425 h)

COD removal obtained for all the tests were similar to colonization experiments (76±6.1 %). The results of this study were compared with other studies using immobilized cells in biofilms (Table 3). The obtained maximum hydrogen production rates are in accordance with that reported for other supports materials [18, 25-26, 29]. However, a highest hydrogen production was observed in the present study with the luffa present the additional advantage that sterilization or pre-treatments were no required.

Table 3. Comparison of hydrogen production using different support materials.

Bacteria	Support	R_{H2} (L/L_{cult}-h)	$H_{máx}$ (L/L_{cult})	Ref
R. sphaeroides	Filter porous glasses	0.007-0.059	-	18
R. palustris	Clay	0.038	1.54	25
	Silica gel	0.035	1.79	
	Active carbon	0.029	1.37	
R. palustris	Clay	0.039	3.19	26
R. faecalis	Active carbón fibers	0.033	3.45	29
Bacterial consortium	Luffa fibers	0.014	4.88	This study

4. Conclusions

Maximum hydrogen production rates of 16.7 ± 2.6 mLH_2/gVS-h were obtained with the evaluated supports. Maximal hydrogen production is mainly influenced by the concentration of the cells in the support materials. It was found that luffa fibers is the most suitable support for the hydrogen producer consortium because allowed the highest

amount of attached biomass (19.6 ± 1.5 mg SV/cm^3) and allowed a better light distribution and the highest cell concentration. Percentage of COD removal was 76±6.1 %.

Acknowledgements

This research was supported through DGAPA-UNAM (PAPIIT IT100113). The authors are grateful to Jaime Perez for the technical support and fruitful discussions.

References

[1] D. Das, T. N. Veziroglu, Advances in biological hydrogen production processes, Int. J. Hydrogen Energy 2008; 33: 6046-6057.

[2] X. Tian, Q. Liao, X. Zhu, Y. Wang, P. Zhang, J. Li, H. Wang, Characteristics of a biofilm photobioreactor as applied to photo-hydrogen production. Bioresour. Technol.2010; 101: 977-983.

[3] D. Das, T. N. Veziroglu, Hydrogen production by biological processes: a survey of literature. Int. J. Hydrogen Energy. 2001; 26: 13-28.

[4] N. Basak, D. Das, The prospect of purple non-sulfur (PNS) photosynthetic bacteria for hydrogen production: the present state of the art. World J. Bicrobiol Biotechnol 2007; 23: 31-42.

[5] A. Adessi, R. De Philippis, (2014) Photobioreactor design and illumination systems for H_2 production with anoxygenic photosynthetic bacteria: A review. Int. J. Hydrogen Energy 2014; 39: 3127-3141.

[6] N. Basak, A. K. Jana, D. Das, D. Saikia, Photofermentative molecular biohydrogen production by purple-non-sulfur (PNS) bacteria in various modes: the present progress and future perspective. Int. J. Hydrogen Energy 2014, 39: 6853-6871.

[7] H. Han, B. Liu, H. Yang y J. Shen, Effect of carbon sources on photobiological production of hydrogen using *Rhodobacter sphaeroides* RV. Int. J. Hydrogen Energy, 2012; 37:12167-12174.

[8] H. H. P. Fang, H. Liu, T. Zhang, Phototrophic hydrogen production from acetate and butyrate in wastewater. Int. J. of Hydrogen Energy, 2005; 30: 785-793.

[9] T. Keskin, P. C. Hallenbeck, Hydrogen production from sugar industry wastes using single-stage photofermentation. Bioresour Technol. 2012; 112: 131-136.

[10] P. Hillmer, H. Gest, H_2 metabolism in the photosyntetic bacterium *Rhodopseudomonas capsulata*: H_2 production by growing cultures. J. of Bacteriol. 1977; 129(2):724-731.

[11] B. Uyar, I. Eroglu, M. Yücel, M., U. Günduz, L. Türker, Effect of light intensity, wavelength and illumination protocol on hydrogen production in photobioreactors. Int. J. Hydrogen Energy 2007; 32: 4670-4677.

[12] Y. Z. Wang, Q. Liao, X. Zhu, R. Chen, C. L. Guo, J. Zhou, Bioconversion characteristics of *Rhodoseudomonas palustris* CQK 01 entrapped in a photobioreactor for hydrogen production. Bioresour.Technol. 2013; 135: 331-338.

[13] K. Seifert, M. Waligorska, y M. Laniecki, Hydrogen generation in photobiological process from dairy wastewater. Int. J. Hydrogen Energy 2010; 35: 9624-9629.

[14] C. Pintucci, A. Giovannelli, M. L. Traversi, A. Ena, G. Padovani, P. Carlozzi, Fresh olive mill waste deprived of polyphenols as feedstock for hydrogen photo-production by means of *Rhodopseudomonas palustris* 420L. Renew.Energy 2013; 51: 358-363.

[15] H. Argun, F. Kargi, Photo-fermentative hydrogen gas production from dark fermentation effluent of ground wheat solution: effects of light source and light intensity, Int. J. Hydrogen Energy 2010; 35:1595-1603.

[16] J. Miyake, T. Waayama, J. Schnackenberg, T. Arai, Y. Asada, Simulation of the daily sunlight illumination pattern for bacterial photo-hydrogen production. J. Biosci. Bioeng. 1999; 88(6):659-663.

[17] E. Eroglu, U. Gunduz, M. Yucel, I. Eroglu, Photosynthetic bacterial growth and productivity under continuous illumination or diurnal cycles with olive mil wastewater as feedstock. Int. J. Hydrogen Energy 2010; 35:5293-5300.

[18] R. Zagrodnik, M. Thiel, K. Seifert, M. Wlodarczak, M. Laniecki, Application of immobilized *Rhodobacter sphaeroides* bacteria in hydrogen generation process under semi-continuous conditions. Int. J. Hydrogen Energy 2013; 38: 7632-7639.

[19] P. von Felten, H. Zürrer, R. Bachofen, Production of molecular hydrogen with immobilized cells of *Rhodospirillum rubrum*. Appl, Microbiol. Biotechnol. 1985; 23: 15-20.

[20] H. Zhu, T. Wakayama, T. Suzuki, Y. Asada y J. Miyake, Entrapment of *Rhodobacter sphaeroides* RV in cationic polymer/agar gels for hydrogen production in the presence of NH4+, J. Biosci. Bioen. 1999; 88(5): 507-512.

[21] B. F. Liu, N. Q. Ren, D. F. Xing, J. Ding, Guo. X. Zheng, W. Q. Guo, J. F. Xu, G. J. Xie, Hydrogen production by immobilized *R. faecalis* RLD-53 using soluble metabolites from ethanol fermentation bacteria *E. harbinense* B49. Bioresour. Technol. 2009; 100: 2719-2723.

[22] C. L. Guo, X. Zhu, Q. Liao, Y. Z. Wang, R. Chen., D. J. Lee, Enhancement of photo-hydrogen production in a biofilm photobioreactor using optical fiber with additional rough surface. Bioresour. Techol. 2011; 102: 8507-8513.

[23] A. A. Tsygankov, Y. Hirata, M. Miyake, Y. Asada, J. Miyake, Photobioreactor with photosynthtetic bacteria immobilized on porous glass for hydrogen photoproduction. J. Ferment. Bioeng. 1994; 77(5): 575-578.

[24] D. Tekucheva, T. V. Laurinavichene, M. Seibert, A. A. Tsygankov, Immobilized purple bacteria for light-driven H2 production from starch and potato fermentation effluents. Biotechnol. Prog. 2011; 27(5) 1248-1256.

[25] C. Y. Chen, J. S. Chang, Enhancing phototropic hydrogen production by solid-carrier assisted fermentation and internal optical-fiber illumination. Process Biochem. 2006; 41:2041-2049.

[26] C. Y. Chen, M. H. Yang, M. H., K. L. Yeh, C. H. Liu, J. S. Chang, Biohydrogen production using sequential two-stage dark and photo fermentation processes. Int. J. Hydrogen Energy, 2008; 33:4755-4762.

[27] C. Zhang, X. Zhu, Q. Liao, Y. Wang, J. Li, Y. Ding, H. Wang, Performance of a groove-type photobioreactor for hydrogen production by immobilized photosynthetic bacteria. Int. J. Hydrogen Energy, 2010; 35: 5284-5292.

[28] Q. Liao, Y. J. Wang, Y. Z. Wang, X. Zhu, X. Tian, J. Li, Formation and hydrogen production of photosynthetic bacterial biofilm under various illumination conditions. Bioresour. Tenchol. 2010; 101: 5315-5324.

[29] G. J. Xie, B. F. Liu, J. Ding, D. F. Xing, H. Y. Ren, W. Q. Guo, Enhanced photo-*H_2 production* by *Rhodopseudomonas faecalis* RLD-53 immobilization on activated carbon fibers. Biomass Bioenerg. 2012; 44: 122-129.

[30] C. Zampol Lazaro., D. Vital Vich., J. Sumiko Hirasawa., M. B. Amâncio Varesche, Hydrogen production and consumption of organic acids by a phototrophic microbial consortium. Int. J. Hydrogen Energy, 2012; 37: 11691-11700.

[31] R. Ying Li, T. Zhang, H. Fang, Characteristics of a phototrophic sludge producing hydrogen from acetate and butyrate. Int. J. Hydrogen Energy, 2008; 9(33): 2147-2155.

[32] American Public Health Association) Standard methods for the examination of water and wastewater, APHA, WA, 1999

[33] O. H. Lowry, N. J. Rosebrough, A. L. Farr, R. J. Randall, Protein measurement with the Folin Phenol reagent. The Journal of Biological Chemistry, 1951; 193: 265-275.

[34] HACH (2002) Water Analysis Handbook. HACH Company. CO, 2002

[35] G. Buitrón, C. Carvajal, Biohydrogen production from Tequila vinasses in an anaerobic sequencing batch reactor: Effect of initial substrate concentration, temperature and hydraulic retention time. Bioresour. Technol. 2010; 101: 9071-9077.

[36] S. K. S. Patel, H. J. Puronhit, V. C. Kalia, Dark fermentative hydrogen production by defined mixed microbial cultures immobilized on lingo-cellulosic waste materials. Int. J. Hydrogen Energy 2010; 35: 10674-10681.

Research on Methanol-Tolerant Catalysts for the Oxygen Reduction Reaction

M Asteazaran[1,2], G Cespedes[2], S Bengió[3], MS Moreno[3], WE Triaca[1], AM Castro Luna[1,2*]

[1]Instituto de Investigaciones Fisicoquímicas Teóricas y Aplicadas (INIFTA), Facultad de Ciencias Exactas, UNLP- CONICET – Argentina
[2]Centro de Investigación y Desarrollo en Ciencia y Tecnología de Materiales (CITEMA) Facultad Regional La Plata, UTN – Argentina
[3]Centro Atómico Bariloche, Comisión Nacional de Energía Atómica (CAB-CNEA) – Argentina
Tel: +542214257430; e-mail: castrolu@gmail.com

ABSTRACT

Direct methanol fuel cells (DMFCs) allow obtaining electricity in a clean and efficient way, valuable to substitute traditional environmentally harmful technologies.
Portable power sources are one of the applications of passive DMFCs. One of the requirements in these devices is to use high alcohol concentration. The methanol permeation across the polymer electrolyte membrane (methanol crossover) causes a loss of fuel cell efficiency because the oxygen reduction reaction (ORR) and the methanol oxidation reaction (MOR) occur simultaneously at the cathode.
To develop methanol tolerant cathodes with suitable activity at low temperature, different PtM and PtMRu catalysts, with M = Co or Fe were prepared with the alloying method (**AM**), a variant of the impregnation method (**IM**) and the classic ethylene glycol method (**EG**).
The catalysts synthesized were PtCo/C, PtFe/C and PtFeRu/C and PtCoRu/C and they were studied to determine the role of the components in enhancing the ORR and discouraging the MOR, simultaneously.
The physical characterization of the synthesized materials was accomplished by TEM, XPS and EDS. According to the synthesis procedure, XPS spectra showed that the metal oxides amount on the catalyst varies. Small and well distributed particles for all the catalysts were shown by TEM.
The electrochemical characterization was accomplished by linear sweep and cyclic voltammetry in a three-electrode electrochemical cell with a glassy carbon rotating disk electrode covered with a thin catalytic layer as the working electrode.
AM and **IM** catalysts have better activity for the ORR. However, the enhanced activity of **AM** catalysts is lost when the ORR is studied in presence of methanol. Binary catalysts with a similar composition are resistant to methanol depending on their synthesis method. Ternary catalysts containing Ru showed higher methanol tolerance, regardless of the composition and synthesis method. The role of metal oxides is discussed.

Keywords: Oxygen Reduction Reaction; Methanol Crossover; Direct Methanol Fuel Cells.

1. *Introduction*

Direct methanol fuel cells (DMFCs) are attractive devices to obtain electricity in a clean and efficient way, potentially valuable to substitute traditional environmentally harmful technologies [1]. To make DMFC commercially interesting, it is yet necessary to improve the catalysts employed on both fuel cell electrodes. At the cathode, due to methanol permeation from the anode, a mixed potential is established because of the simultaneous occurrence of the oxygen reduction reaction ORR and the methanol oxidation reaction MOR [2].

To get cathodes resistant to methanol presence, different Pt-base catalysts have been prepared and analyzed. It has been claimed that supported Pt based catalysts containing Cr, Co, Fe are tolerant to methanol, justifying that enough Co or Cr or Fe atoms avoid methanol adsorption and oxidation [3, 4].

However, it is important to pay special attention not only to the catalyst composition but also to the employed method in their preparation, since a complex behavior can be obtained depending on both aspects [5].

In this work ORR catalysts with different compositions obtained by different methodologies are analyzed and the role of catalyst composition and synthesis preparation for the ORR in presence of methanol is discussed.

2. *Experimental*

2.1. Catalysts Preparations

In order to develop methanol tolerant cathodes with suitable activity at low temperature, we have prepared different PtM and PtMRu catalysts, with M = Co or Fe. Different synthesis methods were employed, namely: i) Alloying Method, **AM**, with a thermal treatment in a H_2/N_2 reducing atmosphere, in line with [6] ii) a variant of the Impregnation Method, **IM**, employing $NaBH_4$ as reducing agent [5] iii) the classic Ethylene Glycol Method, **EG**, which uses the alcohol as solvent and reducing agent [7].

A) AM catalysts

In this method, the initial reactants were a given quantity of E-TEK Pt/Vulcan XC-72R, which was dispersed in water and ultrasonically stirred for 15 min. The initial acidic pH was shifted to 8 with NH_4OH solution. At this point, the required amount of $CoCl_2$, or $FeCl_3$ was put into the mixture and then, an HCl solution was added to reach a pH of 5.5. Stirring continued for 1 h and then the solid was isolated by filtering, rinsing with water repeatedly and finally drying at 70 °C in an oven for 12 h. After that, the powder was heat-treated at 900 °C in a H_2/N_2 atmosphere for 1 h to form a binary catalyst. The synthesized electrocatalysts were labeled as PtCo/C **AM** and PtFe/C **AM**.

B) IM catalyst

Following [5], calculated amounts of H_2PtCl_6, $FeCl_3$ and $RuCl_3$ were each of them, dissolved in 5 ml of ethylene glycol. The solutions were ultrasonicated and purged with N_2 for 10 min. After that, a calculated amount of chemically treated carbon support (Vulcan XC-72R) was added to a given volume of ethylene glycol and ultrasonicated for 30 min, under N_2 flow, its pH was adjusted to 10 by adding NH_4OH. Afterward, 0.2 ml of Pt precursor and 2 ml of a freshly prepared 0.1 M $NaBH_4$ solution were added to the carbon suspension under ultrasonication to form Pt seeds. Then, the remaining precursor solutions and a given amount of $NaBH_4$ solution were added to the mixture. Finally, the catalyst suspension was further ultrasonicated for 2 h under N_2 flow. The solid obtained after filtering the suspension, was thoroughly washed with abundant distilled water and dried in an oven overnight at 70 °C. The catalyst was denoted as PtFeRu/C **IM**.

C) EG catalysts

In the classic ethylene glycol method, ethylene glycol is the reducing agent and dissolving medium where the synthesis occurs. Summarizing, ethylene glycol solutions of each metal precursor, H_2PtCl_6, $CoCl_2$ and $RuCl_3$, in the required amount were added to a suspension of a calculated amount of functionalized carbon black support in ethylene glycol, under vigorous stirring. The mixture was stirred for 4 h under N_2 bubbling. Once the stirring was finalized, NaOH in ethylene glycol solution was added to the mixture to adjust its pH to around 13. In order to achieve the complete reduction of the metallic precursors, the mixture was refluxed at 197 °C for 2 h also under N_2 bubbling. The solid was isolated by low pressure filtering, then thoroughly rinsed with water and dried at 70 °C in an oven for 12 h. The synthesized electrocatalysts were labeled as PtCo/C **EG**, PtCoRu/C **EG**.

Additionally the functionalization of the support was achieved after an oxidative treatment in 70% HNO_3 solution at 140 °C for 2 h following [8].

2.2. Catalysts characterization

All synthesized materials were studied in terms of composition and surface chemistry by using energy dispersive X-ray spectroscopy (EDS) and X-ray photoelectron spectroscopy (XPS). The distribution and size particles of the supported catalysts were analyzed by employing high resolution transmission electron microscopy (HRTEM).

The electrochemical characterization was accomplished employing a standard three-electrode electrochemical cell. We used as a working electrode a rotating disk electrode (RDE) of glassy carbon (0.071 cm^2 geometric area) covered with a thin layer of catalyst powder, attached by a 0.1 µm Nafion® thin film. A Pt foil of 1 cm^2 geometric area was used as counter electrode and a saturated calomel electrode (SCE) as reference electrode. In this work, we referred all potentials to that of the reversible hydrogen electrode (RHE). The supporting electrolyte was 0.5 M H_2SO_4 solution and the working solution was an O_2 saturated 0.5 M H_2SO_4 solution with different CH_3OH concentrations. The electrochemical experiments were conducted at room temperature. In order to get a stable voltammetric profile, prior to ORR experiments, we cycled the potential of the working electrode at a rate of 0.1 Vs^{-1} in a N_2 purged 0.5 M H_2SO_4 solution.

3. Results and discussion

3.1. Physicochemical characterization

A) XPS analysis

The surface composition of the catalysts was determined measuring the Pt 4f (not shown) Co 2p, Fe 2p and Ru 3d photoelectron peaks. The Co 2p XPS spectra exhibit signals with binding energies at 778 eV assigned to Co (0) (778.3eV) and at 781 eV assigned to $Co(OH)_2$ (781 eV), Figure 1a.

The Fe 2p XPS spectra of the PtFe/C AM catalyst show a peak at ca 712 eV attributed to Fe_2O_3 (710.9 eV), Figure 1b.

In regard to Ru, the XPS spectra of PtCoRu/C catalysts have been analyzed in the region of the Ru 3d core-level peak, which partially overlaps with the C1s core-level peak. Despite the overlapping, the Ru signal at ca. 281.5 eV can be assigned to RuO_2 (281 eV), Figure 1c.

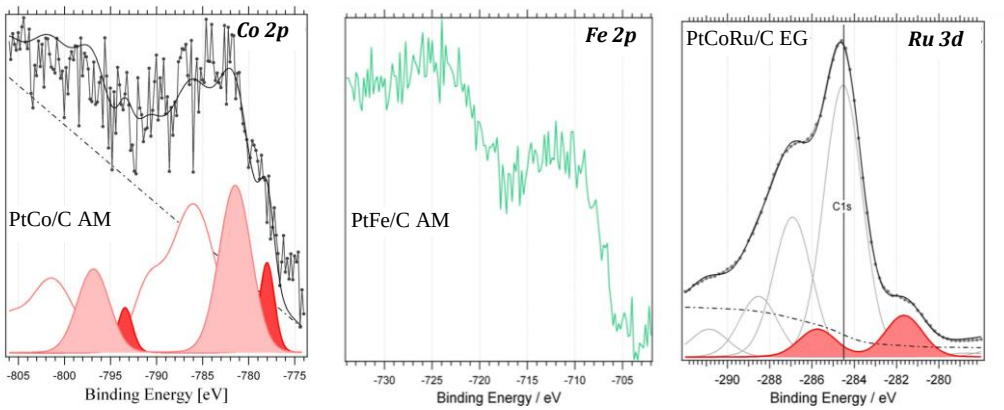

Figure 1- XPS spectra of (a) Co 2p from PtCo/C **AM,** (b) Fe 2p from PtFe/C **AM**, (c) Ru 3d from PtCoRu/C **EG**

B) EDS analysis

In Table 1, the atomic ratio of the components in the prepared catalysts PtCo/C **AM** and **EG**, PtFe/C **AM** and PtCoRu/C **EG** and **AM** have been determined by EDS.

Table 1. EDS composition of the catalysts prepared by different methods

	Pt/Co at. ratio (EDS)	Pt/Ru at. ratio (EDS)	Pt/Fe at. ratio (EDS)	Catalyst label
EG	10.1			PtCo/C EG
AM	10.4			PtCo/C AM
EG	3.1	1.1		PtCoRu/C EG
AM			2.5	PtFe/C AM
IM		1.2	2.3	PtFeRu/C IM

C) TEM images

High resolution transmission electron microscopy (HRTEM) showed for all catalysts, nanoparticles homogenously spread on the carbon support. In order to follow the change in the particle size as consequence of the heat-treatment in AM catalysts, we show in Figure 2a and b TEM images of PtFe/C before (*BHT*) and after (*AHT*) heat-treatment, the average particle size increases from 2.9 nm to 5.8 nm. In Figure 2c, for a ternary PtCoRu EG the average particle size is ca 2.5 nm.

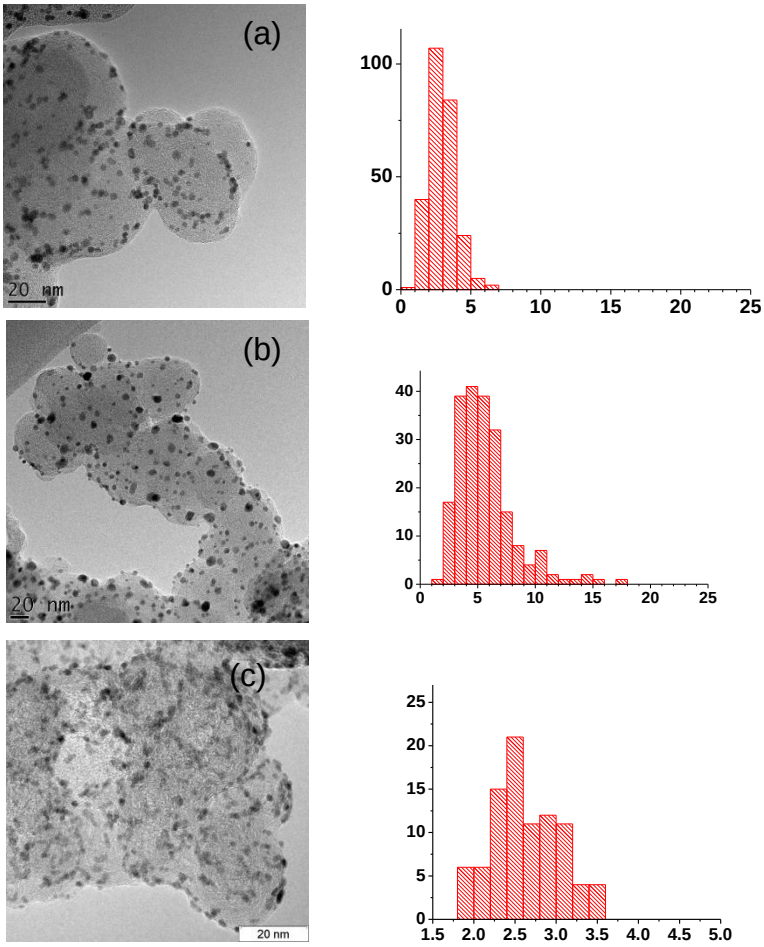

Figure 2- TEM images and particle size distribution of (a) PtFe/C **AM** *BHT*, (b) PtFe/C **AM** *AHT*, (c) PtCoRu/C **EG**

3.2. Electrochemical behavior

Typical polarization curves for ORR on PtCo/C **AM**, PtFe/C **AM** catalysts at a rotating disc rate ω = 2000 rpm without or with 0.1 M CH_3OH solution are shown in Figure 3. The polarization curves using Pt /C ETEK are added as reference for the ORR. It can be noticed that catalysts exposed to a reducing atmosphere at high temperatures, show a better catalytic activity for ORR. However these catalysts resulted less tolerant to methanol presence as shown in Figure 3 a and b.

PtFeRu/C and PtCoRu/C exhibit a similar methanol tolerance degree, although PtCoRu/C catalyst is less active for ORR, Figure 3 c and d.

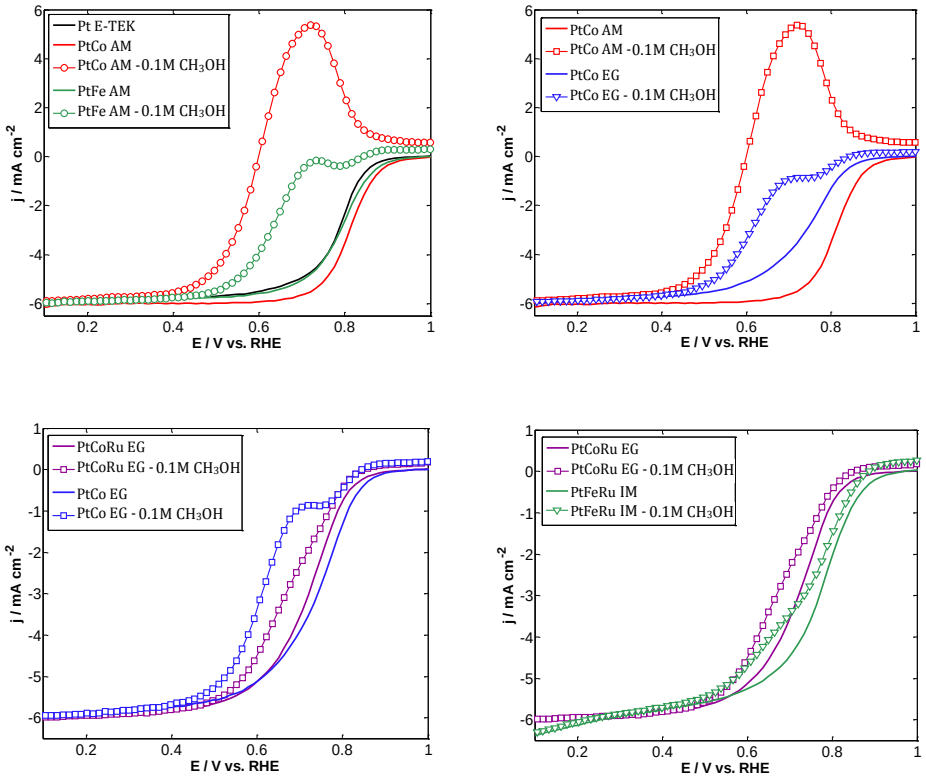

Figure 3- Polarization curves for ORR in O_2 saturated 0.5M H_2SO_4 at v = 0.005Vs^{-1} and ω = 2000 rpm without or with 0.1M CH_3OH for (a) PtCo/C **AM**, PtFe/C **AM** and Pt/C ETEK, (b) PtCo/C **AM** and PtCo/C **EG**, (c) PtCoRu/C **EG** and PtCo/C **EG**, (d) PtCoRu/C **EG** and PtFeRu/C **IM**

Summary and perspectives

- The methanol resistance of the bimetallic catalysts seems to be associated to the synthesis methodology. Consequently, EG catalysts are better.
- For those catalysts containing Ru, the tolerance to methanol regardless of the synthesis method. Thus, the PtCoRu/C **EG** and PtFeRu/C **IM** have similar tolerance degree.

Acknowledgements

This work was supported by Consejo Nacional de Investigaciones Científicas y Técnicas (CONICET), Agencia Nacional de Promoción Científica y Tecnológica, Comisión de Investigaciones Científicas de la Provincia de Buenos Aires (CIC), and Universidad Tecnológica Nacional (UTN-FRLP). AMCL is member of the research career at CIC. GC and MA acknowledge financial support through a Ph.D. fellowship from CIC and CONICET, respectively.

References

[1] HR Corti, ER Gonzalez, Direct Alcohol Fuel Cells Materials, Performance, Durability and Applications. Springer, Netherlands 2014

[2] AS Aricò AS, V Baglio, V Antonucci, Direct Methanol Fuel Cells: History, Status and Perspectives. In: Liu H, Zhang J (eds) Electrocatalysis of Direct Methanol Fuel Cells: From Fundamentals to Applications. Wiley-VCH Verlag GmbH & Co. KGaA, Weinheim, 2009 1-78

[3] AK Shukla, RK Raman, Methanol-Resistant Oxygen Reduction Reaction Catalysts for Direct Methanol Fuel Cells. Annual Review of Materials Research 2003 33:155–168

[4] E Antolini, T Lopes, ER Gonzalez, An overview of platinum-based catalysts as methanol-resistant oxygen reduction materials for direct methanol fuel cells. Journal of Alloys and Compounds 2008 461:253–262

[5] I Spanos, JJK Kirkensgaard, K Mortensen, M Arenz, Investigating the activity enhancement on Pt_xCo_{1-x} alloys induced by a combined strain and ligand effect. Journal of Power Sources 2014 245:908-914

[6] JRC Salgado, E Antolini, ER Gonzalez, Structure and Activity of Carbon-Supported Pt−Co electrocatalysts for Oxygen Reduction. The Journal of Physical Chemistry B 2004 108:17767–17774

[7] C Grolleau, C Coutanceau, F Pierre, J Leger, Optimization of a surfactant free polyol method for the synthesis of platinum – cobalt electrocatalysts using Taguchi design of experiments 2010 195:1569

[8] AR Bonesi, MS Moreno, WE Triaca, AM Castro Luna, Modified catalytic materials for ethanol oxidation. International Journal of Hydrogen Energy 2010 35:5999–6004

Derivation of Mathematical Model Based on Tafel Equation Explains Microbial Fuel Cell Performance

G. Hernández-Flores[1], H. M. Poggi-Varaldo[1,*], O. Solorza-Feria[2], M. T. Ponce Noyola[3], T. Romero-Castañon[4] and N. Rinderknecht-Seijas[5]

[1]Environmental Biotechnology and Renewable Energies R&D Group, Dept. of Biotechnology and Bioengineering, Centro de Investigación y de Estudios Avanzados del Instituto Politécnico Nacional. Av. Instituto Politécnico Nacional 2508, Col. San Pedro Zacatenco, Delegación Gustavo A. Madero, México D.F., C. P. 07360 Apartado Postal: 14-740, 07000 México, D.F.
[2]Dept. of Chemistry, *ibídem.* Av. Instituto Politécnico Nacional 2508, Col. San Pedro Zacatenco, Delegación Gustavo A. Madero, México D.F., C. P. 07360 Apartado Postal: 14-740, 07000 México, D.F.
[3]Dept. Biotechnology and Bioengineering, *ibídem.* Av. Instituto Politécnico Nacional 2508, Col. San Pedro Zacatenco, Delegación Gustavo A. Madero, México D.F., C. P. 07360 Apartado Postal: 14-740, 07000 México, D.F.
[4]Electric Research Institute. Reforma 113, Col. Palmira, C. P. 62490 Cuernavaca, Morelos, México.
[5]ESIQIE del IPN, Division of Basic Sciences. Escuela Superior de Ingeniería Química e Industrias Extractivas, ESIQIE. Edificio N° 7, Unidad Profesional Adolfo López Mateos. Colonia Lindavista, Delegación Gustavo A. Madero, México D.F., C. P. 07738.
*Author for correspondence: Tel: +52 (55) 5747 3800 ext 4321 & 4324; r4cepe@yahoo.com

ABSTRACT

The aim of this work was to establish a mathematical model based on Tafel equation to quantitatively relate the maximum volumetric power ($P_{V,max}$) as well as the internal resistance (R_{int}) in a Microbial Fuel Cell (MFC), with the specific surface area of the graphite anodes (A'_s), and either their conductance C or electrolytic conductivity σ of the material.
The *MFC* consisted of a horizontal cylinder built in Plexiglas 80 mm long and 57 mm internal diameter. The anodic chamber was packed with the different anodic materials (graphite rod (*GR*), triangles of graphite (*GT*) and graphite flakes (*GF*)).
The R_{int} were 795, 410 and 273 Ω for *GR*, *GT* and *GF*, respectively, whereas the $P_{V,max}$ were 1326, 2108 and 3052 mW/m^3 for *GR*, *GT* and *GF*, respectively. There was a correspondence of either the decrease of R_{int} or the increase of $P_{V,max}$ with the increase of the log of A'_s of the graphite anodic materials. Here we show the detailed derivation of a mathematical model for the $P_{V,max}$ and R_{int} based on Tafel equation for the cell potential; it lead to equations that exhibited a good correlation with experimental results. The best fitting models for $P_{V,max}$ were $P_{V,max} = a_0' + a_1' \times \log A'_s$ and $P_{V,max} = a_0' + a_1' \times \log A'_s + a_2' \times C$ with determination coefficients 0.8872 and 0.9842, respectively. On the other hand for R_{int} the best fitting models were $R_{int} = b_0' + b_1' \times \log A'_s$ and $R_{int} = b_0' + b_1' \times \log A'_s + b_2' \times \log C$, with determination coefficients 0.8850 and 0.8904, respectively. In general, the inclusion of the electrolytic conductivity did not improve model fitting, whereas the inclusion of conductance lead to a higher determination coefficient in the P_V model but not in the model of R_{int}.

Keywords: Mathematical Model; Volumetric Power; Microbial Fuel Cells

Introduction

The imminent fossil fuels depletion and their adverse effects on the environment have resurrected the interest in bioenergies as well as other renewable energy sources [1,2]. In processes such as biohydrogen production from fermentation of organic wastes, the complete conversion of wastes to energy is not possible [3]. Dark fermentation of organic substrates effects a partial degradation of the organic matter, and typically a large amount of organic metabolites remain in the spent liquors that can be used as substrate in microbial fuel cells (*MFCs*) [4-6].

In this regard, *MFCs* constitute a promising technology for sustainable production of alternative energy and treatment of wastes such as the spent liquors of dark fermentation. A microbial fuel cell (*MFC*) is an electro-biochemical reactor capable of directly converting organic matter into electricity. In the anodic chamber the microorganisms anaerobically oxidize the organic matter and release electrons and protons. The electrons are transported to the anode that acts as an intermediate, external electron acceptor. The electrons flow through an external circuit where there is a resistor or a device to be powered, producing electricity. Electrons finally react at the cathode with protons and molecular oxygen producing water [5-9].

There are some factors that affect the electric energy production in a *MFC*, such as the nature of the biocatalysts, the type and materials of electrodes, electrode catalysts, cell configuration, and architecture, among others [10-13]. The *MFC* performance is usually restricted by ohmic overpotential, also known as internal resistance (R_{int}).

This translates into a loss of voltage that is required to drive the electron and proton transport processes. The ohmic losses in an *MFC* include both the resistance to the flow of electrons through the electrodes and interconnections and the resistance to the flow of ions through the membrane and the anodic and cathodic electrolytes (only anodic electrolyte in a single chamber *MFC*) [14]. This results in ohmic losses whose reduction or mitigation is crucial for improving the characteristics and performance of the *MFC* [15]. Furthermore, another significant role of R_{int} is related to the eventual operation of the *MFC*, since Jacobi's Theorem demonstrated that the maximum power output of an electromotive force is achieved when it is connected to an external resistance equal to its R_{int} [14-20].

The R_{int} of a *MFC* depends on some factors such as the surface area of electrodes, distance between electrodes, anodic material conductivity, the presence or absence membrane, the type of electrolyte(s), *inter alia* [14,21,22].

Indeed, the anodic material plays an important role on R_{int}. A good anodic material should have the following properties: high electrical conductivity, strong biocompatibility, chemical stability and anti-corrosion, large surface area and appropriate mechanical strength and toughness [13,14].

In order to reduce the R_{int} of the cell some materials and designs have been evaluated, such as new anodic materials, replacement of the salt bridge by membranes, choosing membranes with high protonic conductivity or building membrane-less *MFC*, increasing solution conductivity and reducing the pH, reducing electrode spacing, among others [5,6,23-29].

Regarding the effect of anodic materials, there has been much research on the use of graphite anodes in *MFC* [11-14, 28-35, among others]. However, less has been published on the effect of the specific surface area of graphite anodes on *MFC* characteristics and performance in terms of the volumetric power. On the other hand, to the best of our knowledge there is little information on modelling the effect of the anodic specific surface area on performance of *MFC* [36-38].

For instance, Hsu *et al.* [36] fitted the current intensity i to the anode surface area. This model gave an inverse relationship between the variables.

$$i = \frac{(mE_{anode}+b)}{A_{anode}} \qquad R^2 \text{ not reported} \qquad (1)$$

where i is the current density, E_{anode} is the anodic potential, A_{anode} is the surface area of the anode, m and b are fitting coefficients.

Incidentally, Hsu *et al.* [36] experimentally observed, but did not model, the decrease of the surface power densities P_{An} when the anode surface area was increased. They reported the values of P_{An} but they neither modelled

the effect of the anodic surface area (or the specific surface area) on that variable nor the volumetric power of the cell. To some extent, the decrease of P_{An} with increase of anode area should be expected whenever the increase of P_{MFC} is less than proportional to such an area. Furthermore, the model of Hsu *et al.* [36] was strictly empirical since it was not based upon electrochemical theoretical considerations. The authors did not report statistical parameters of the model, and consequently, it is very difficult to ascertain the goodness-of-fit of the proposed equation.

Dewan *et al.* [37] worked with several anodic areas (graphite plates) in a two-chamber *MFC*. They modelled the P_{An} versus the logarithm of the total surface area of the anode. They found a linear, decreasing relationship (Eq. 2, R^2 = 0.95). It can be seen that the coefficient of the term ln (surface area) is negative, which was consistent with the experimental results of Hsu *et al.* [36]. As we commented above, it is debatable to use P_{An} as a variable for comparison of process intensity. In this regard, volumetric power P_V is the dependent variable of choice. On the other hand, P_{An} is an adequate variable to assess anode performance. The model fitted by Dewan *et al.* [37] was strictly empirical since it was not based upon electrochemical theoretical considerations. No statistical parameters of goodness-of-fit were reported, other than R^2.

$$P_{An} = 0.3371 - 0.0369 \times \ln(surface\ area) \qquad R^2=0.95 \qquad (2)$$

Di Lorenzo *et al.* [38] presented a "Current distribution model" that found a relationship between a variable ν (the so-called 'utilization of the electrode area', (Siemens $^{0.5}$/sec) with a set of independent variables of electrode geometry ('*L*', thickness of the anode; '*a*', specific area of the anode), the slope of the polarization curve '*s*', and the conductivity of the influent κ

$$v = L \times \left(\frac{a \times s}{k}\right)^{0.5} \qquad (3)$$

They departed from theoretical grounds (Butler-Volmer kinetics in the anode) and several simplifying assumptions.

They also defined a new variable efficiency η related to ν by Eq. 4

$$\eta = \frac{\tanh(\nu)}{\nu} \qquad (4)$$

$$\eta = \frac{\text{observed current density}}{\text{current obtained if the electrode potential was equal to the maximum observed at position L in the electrode}} \qquad (5)$$

As a working example of their model, the authors calculated the current density peak i_2 during batch operation of a *MFC* based on a known current density peak i_1, the corresponding values of L (L_1 and L_2), and the corresponding values of η, with an equation (not given by the authors and recreated by us).

$$i_2 = i_1 \times \left(\frac{L_2}{L_1}\right) \times \left(\frac{\eta_2}{\eta_1}\right) \qquad (6)$$

They showed that their model could give reasonable results compared to experimental values of current density peaks in a couple of their experimental cases. However, in their work

(*i*) they did not develop any general fitting of Eq. 3 to 5. Furthermore, they did not report any statistical measure of good fitness (no determination coefficients, no ANOVA of the model equations and predictions, etc.);

(*ii*) they did not fit any model with volumetric power or internal resistance as dependent variable and the specific surface area of the anode as independent variable, *i.e.*, their model was used just to approximately predict current density peaks but not powers (neither P_V nor P_{An}).

(*iii*) the physical meaning of the variable ν given by the authors is vague. Furthermore, in spite of considerable work load to develop an expression for ν, this variable is only used as a 'transition' one in order to calculate the corresponding value of η.

In the end, Di Lorenzo *et al.* [38] concluded that, in spite of several recognized simplifying assumptions, the model could be useful as a starting point in selecting electrode geometries based on basic data of the influent and electrode conductivity.

Interestingly, the use of either *i* or P_{An} in the above mentioned models is very debatable as a means to express the *MFC* performance when the purpose is to compare the process intensity (unit power delivery) of a given *MFC* to the intensity of other competing processes such as other *MFC* configurations, anaerobic digestion, biohydrogen generation, etc., that could use the same influent as the main experiment. Indeed, the volumetric power is the variable to consider for a fair comparison of different processes (39,40).

Thus, the objective of this work was to establish a mathematical model based on Tafel equation to quantitatively relate the maximum volumetric power ($P_{V,max}$) as well as the R_{int} in a *MFC*, with the specific surface area (A'_s) of the graphite anodes and either their conductance *C* or electrolytic conductivity σ of the material.

Experimental

Model development

We describe a full version of the derivation of our model. A typical form of Tafel equation that relates the overpotential with the current density is given by Castellan [41].

$$\Delta V = a + b \times \ln(i) \tag{7}$$

where ΔV is the overpotential, V; *b* is the "Tafel slope", V; *i* is the current density, A/m^2.
It can be shown that

$$a = -b \times \ln(i_0) \tag{8}$$

where i_0 is the "exchange current density", A/m^2
Substituting Eq. 8 into Eq. 7, and taking logarithms in base 10 instead of base e, leads to

$$\Delta V = k \log\left(\frac{i}{i_0}\right) \tag{9}$$

where

$$k = b \times 2.303 \tag{10}$$

The actual potential delivered by the *MFC* can be expressed as the reversible potential minus the overvoltage, as in Eq. 11 (15,20)

$$E = E_{rev} - \Delta V = E_{rev} - k \log\left(\frac{i}{i_0}\right) \tag{11}$$

where *E* is the actual cell voltage; E_{rev} is the reversible potential (thermodynamic potential [41]), in V; ΔV is the overpotential, in V.

Substituting Eq. 9 into Eq. 11 we obtain the following

$$E = E_{rev} - k\ \log\left(\frac{i}{i_0}\right) \tag{12}$$

In turn, the power *P* delivered by the cell is given by [5]:

$$P = \frac{E^2}{R_{ext}} \tag{13}$$

where R_{ext} is the external resistance connected to the cell circuit, in Ω
Substituting Eq. 12 into 13 we obtain the following

$$P = \frac{\left(E_{rev} - k\ \log\left(\frac{i}{i_0}\right)\right)^2}{R_{ext}} \tag{14}$$

Doing the algebra, taking into account that $\Delta V < E_{rev}$, and that $i = I/A_{el}$, plus some simplifications based on order of magnitude of selected terms, leads to

$$P = \frac{E_{rev}^2 - 2klog\left(\frac{i}{i_0}\right) + k^2\left(log\frac{i}{i_0}\right)^2}{R_{ext}} \tag{15}$$

$$P = \frac{E_{rev}^2 - 2k(\log i - \log i_0) + k^2[(\log i)^2 - 2\log i * log\ i_0 + (\log i_0)^2]}{R_{ext}} \tag{16}$$

Since $\Delta V < E_{rev}$, we can neglect the term $(log\ i_0)^2$ in Eq. 16, leading to

$$P \cong \frac{E_{rev}^2 + 2klogi_0 - 2klogi}{R_{ext}} \tag{17}$$

By definition, the current intensity can be expressed as [17,41]

$$i = \frac{I}{A_{el}} \tag{18}$$

where
I is the current intensity in Amperes
A_{el} is the electrode surface area in m^2

Substituting Eq. 18 into Eq. 17 leads to

$$P \cong \frac{E_{rev}^2 + 2klogi_0 - 2klog\left(\frac{I}{A_{el}}\right)}{R_{ext}} \tag{19}$$

and

$$P \cong \frac{E_{rev}^2 + 2klogi_0 - 2klogI + 2klogA_{el}}{R_{ext}} \tag{20}$$

$$P \cong \frac{(E_{rev}^2 + 2klogi_0 - 2klogI) + 2klogA_{el}}{R_{ext}} \quad (21)$$

We recall that the specific area of the electrode A'_s can be determined dividing the electrode surface area A_{el} by the cell volume V_{cell} (the anodic chamber volume in unicameral *MFC*),

$$A'_s = \frac{A_{el}}{V_{cell}} \quad (22)$$

$$A_{el} = V_{cell} A'_s \quad (23)$$

On the other hand, the volumetric power P_V of a *MFC* is given by the Eq. 24 below [28]

$$P_V = \frac{P}{V_{cell}} \quad (24)$$

Substituting Eq. 21 in the Eq. 24

$$P_V \cong \frac{(E_{rev}^2 + 2klogi_0 - 2klogI)}{R_{ext}V_{cell}} + \left(\frac{2k}{R_{ext}V_{cell}}\right) \log A_{el} \quad (25)$$

Now, we substitute Eq. 23 in Eq. 25

$$P_V \cong \frac{(E_{rev}^2 + 2klogi_0 - 2klogI)}{R_{ext}V_{cell}} + \left(\frac{2k}{R_{ext}V_{cell}}\right) \log(V_{cell}A'_s) \quad (26)$$

Regrouping terms leads to

$$P_V \cong \frac{(E_{rev}^2 + 2klogi_0 - 2klogI)}{R_{ext}V_{cell}} + \frac{2klogV_{cell}}{R_{ext}V_{cell}} + \frac{2k}{R_{ext}V_{cell}} \log A'_s \quad (27)$$

$$P_V \cong \frac{(E_{rev}^2 + 2klogi_0 - 2klogI + 2klogV_{cell})}{R_{ext}V_{cell}} + \frac{2k}{R_{ext}V_{cell}} \log A'_s \quad (28)$$

The first term of the left hand member of Eq. 28 is nearly a constant and it will denoted as a_o, whereas the parameters in the logarithmic term will be denoted as the coefficient a_1

$$a_0 = \frac{(E_{rev}^2 + 2klogi_0 - 2klogI + 2klogV_{cell})}{R_{ext}V_{cell}} \quad (29)$$

$$a_1 = \frac{2k}{R_{ext}V_{cell}} \quad (30)$$

So,

$$P_{V,max} \cong a_0 + a_1 \log A'_s \quad (31)$$

Now, to estimate the R_{int}, we know that maximum volumetric power $P_{v,max}$ occurs when the external resistance R_{ext} connected to the circuit of an electromotive force is equal to the value of the internal resistance R_{int}. This is a result of Jacobi's theorem of electromotive forces [17,20,28].

$$R_{int} = R_{ext} \tag{32}$$

By definition of power *P* in direct current circuits and Jacobi's theorem, then

$$P = \frac{(E_{MFC,max})^2}{R_{int}} \tag{33}$$

where

$E_{MFC,max}$ is the cell potential at which the maximum volumetric power is registered. Introducing the volume V_{cell} for converting the power into volumetric power, and solving Eq. 33 for R_{int} leads to

$$R_{int} = \frac{(E_{MFC,max})^2}{V_{cell} P_{V,max} F} \tag{34}$$

V_{cell} is the cell volume or the anodic chamber volume in a unicameral *MFC*

$P_{V,max}$ maximum volumetric power

F is a unit conversion factor that, for example, takes into account that the volumetric power is usually expressed in mW/m^3, etc.

Substituting Eq. 31 into Eq. 34 and rearranging

$$R_{int} = \frac{(E_{MFC,max})^2}{V_{cell} F} \frac{1}{a_0 + a_1 \log A's} \tag{35}$$

$$R_{int} = \frac{(E_{MFC,max})^2}{V_{cell} F a_0 \left(1 + \frac{a_1}{a_0} \log A's\right)} \tag{36}$$

When a given amount β is $\beta < 1$, the following approximation can be used [42]

$$\frac{1}{1+\beta} \cong 1 - \beta \tag{37}$$

This approximation, although simple, is very good. Indeed, it can be shown that when $\beta \leq 0.30$, the error of this formula does not exceed 10%, and when $\beta \leq 0.10$, the error of this formula does not exceed 1% [42]

Using Eq. 37 in Eq. 36 leads to the following approximate result

$$R_{int} \cong \frac{(E_{MFC,max})^2}{V_{cell} F a_0} \left(1 - \frac{a_1}{a_0}\right) \log A'_s \tag{38}$$

Rearranging Eq. 38

$$R_{int} \cong \left(\frac{(E_{MFC,max})^2}{V_{cell} F a_0}\right) - \frac{(E_{MFC,max})^2 a_1}{V F a_0^2} \log A'_s \tag{39}$$

Now, we conveniently rename the constant coefficients of Eq. 39 as follows

$$b_0 = \frac{(E_{MFC,max})^2}{V_{cell} F a_0} \quad (40)$$

$$b_1 = -\frac{(E_{MFC,max})^2 a_1}{V_{cell} F a_0^2} \quad (41)$$

Finally, the equation for R_{int} is in the form

$$R_{int} \cong b_0 + b_1 \log A'_s \quad (42)$$

Experimental design

The first experiment consisted of the characterization of the *MFC* fitted with following anodic materials: graphite rod (*GR*), triangles of graphite (*GT*) and graphite flakes (*GF*) in an *MFC* loaded with a sulfate-reducing inoculum (*SR-In*), with two replicates. The main response variables were the $P_{V,max}$ and the R_{int} of the *MFC*s. The experiments were carried out in a single compartment, air-cathode *MFC*. The cells were operated at ambient temperature.

2.3. Microbial fuel cell

The *MFC* consisted of a horizontal cylinder built in Plexiglas 80 mm long and 57 mm internal diameter. The anodic chamber was packed with the different anodic materials, i.e., *GR*, *GT* and *GF* with corresponding surface areas of 8.89×10^{-4}, 0.06 and 0.28 m^2 (Table 1).

The *GR* was purchased to Lumen S.A. de C.V., Mexico City, Mexico; they report that this material was imported from the Czech Republic. The *GT*s were fabricated by conveniently slicing graphite bars of 38 mm diameter in disks of 5 mm thickness. Each disk, in turn, was cut in 8 similar parts. The graphite bar was purchased to Brunssen de Occidente S.A. de C.V., Guadalajara, Jalisco, Mexico.

For *GF*, we screened a large sample of material and collected the fraction between meshes 10 and 6 (diameters 2 mm and 3.55 mm, respectively). We took and weighed five 20 g subsamples of this fraction; the mass values were annotated. Afterwards, the number of particles in each subsample were determined and annotated. An average number of particles was estimated. With this number, we estimated the average weight of particle of each material. By using the equations shown below, it was possible to calculate the surface area of the mass of material loaded into the *MFC*. The shape factor of the material (also called sphericity factor in other textbooks) was taken into account as described in Perry [43]. For instance, we chose 0.43 for *GF* flakes, and 0.73 for *GAC*.

On the other hand, the net volume of the only chamber in our *MFC*s was calculated as the geometric volume of the chamber minus the physical volume of the anodic material. With the surface area of the anodic material and the net volume, the specific surface area of the anode A'_s was finally calculated with Eq. 43 below

$$A'_s = \frac{\frac{M}{\Phi_s}\left(\frac{6^2 m_p{}^2 \pi^3}{m_p{}^3 \pi^2 \rho^2}\right)^{1/3}}{V} = \frac{\frac{M}{\Phi_s}\left(\frac{36\pi}{m_p \rho^2}\right)^{1/3}}{\left(V_{cell} - \frac{M}{\rho}\right)} \quad (43)$$

where

$\bar{D}_p$ average particle diameter, defined as the diameter of a sphere of the same volume as the particle

Φ_s shape factor of the particle defined as the quotient of the area of a sphere equivalent to the volume of the particle divided by the actual surface of the particle

m_p average weight of a particle of the given size fraction

M total mass of anodic material loaded into the *MFC*
ρ actual density of the material
V_{cell} geometric volume of the cell chamber

The surface area of the graphite rod was calculated by geometric calculations based on diameter and height of the rod. The net volume of the *MFC* necessary for the denominator in the calculation of $A_s^{'}$ was estimated as described above in the denominator of Eq. 43.

Similarly, the surface area of graphite triangles was estimated by geometric calculations. For each triangular piece to be loaded into the *MFC*, the total area was the sum of the areas of the two triangular faces ((base times height/2) ×2) plus the areas of the rims. The overall surface area was estimated as the sum of the areas of the pieces. The specific surface area was finally calculated by dividing by the net volume of the *MFC*.

The cathode of our *MFC* was a flexible carbon-cloth containing 0.5 mg/cm^2 platinum catalyst (Pt 10 wt%/C-ETEK). On the air side, the cathode was limited by a perforated plate of stainless steel 1 mm thickness. In the liquid side, the cathode was in contact with a proton exchange membrane (Nafion® 117) [6,44].

2.4. Sulfate-reducing inoculum SR-In

The *MFC*s were seeded with a *SR-In* sampled from a sulphate-reducing complete mix reactor. The biomass concentration in the inoculum was *ca*. 1280 mg VSS/L. The complete mix bioreactor was operated at 37 °C in a constant temperature room. An influent containing sucrose as carbon source was fed at a flow rate of 120 mL/d to the complete mix sulphate-reducing bioreactor. Its composition was (in g/L): sucrose (5.0), acetic acid (1.5), $NaHCO_3$ (3.0), K_2HPO_4 (0.6), Na_2CO_3 (3.0), NH_4Cl (0.6), Na_2SO_4 (11.0).

2.5. Leachate

The *MFC* was loaded with 6 mL of a leachate similar to that produced in the hydrogen fermentation of the organic fraction of the municipal solid wastes [45]. The model leachate was concocted with a mixture of simple organic acids and solvents (in g/L): acetic, propionic and butyric acids (4 each) as well as acetone and ethanol (4 each) and mineral salts like $NaHCO_3$ and Na_2CO_3 (3 each) and K_2HPO_4 and NH_4Cl (0.6 each) [46,47].

2.6. Determination of internal resistance of the cell

The internal resistance of the cell was determined by duplicate for each anodic material, using the polarization curve method by varying the external resistance and recording both the voltage and the current intensity [6,28].

The *MFC* was operated at open circuit for 1 h; afterwards the R_{ext} was varied from 10 Ω to 1 MΩ and viceversa. After this, the cell was set to open circuit conditions for 1 h in order to check the adequacy of the procedure (values of initial and final open circuit voltages should be close). The voltage was measured and recorded with a Multimeter ESCORT 3146A. The current was calculated by the Ohm's law and the R_{int} was calculated as the slope of the linear section of the curve voltage versus the current intensity [6,14].

The volumetric power (P_V) was calculated according the following equation:

$$P_V = \frac{(E_{MFC})^2}{V_{cell} \times R_{ext}} \quad (44)$$

where V_{cell} is the net volume of the cell; E_{MFC} is the voltage delivered by the cell; R_{ext} is the external resistance connected to the cell.

The initial chemical oxygen demand (COD) and biomass concentration in the cell liquor were *ca.* 1300 mg O_2/L and 1280 VSS/L respectively. The pH and the electrical conductivity were 7.03 and 1385 µS/cm respectively.

2.7. Analyses

The COD and VSS of the liquors of sulphate-reducing seed bioreactor and cells were determined according to the Standard Methods [48]. In addition, the individual concentrations of volatile organic acids and solvents in the model extract were analyzed by gas chromatography in a chromatograph Perkin Elmer Autosystem equipped with a flame ionization detector as described elsewhere [6].

Statistical data processing was performed with the tool Analysis of Data/Regression of Excel software, Microsoft Office 2010 (Microsoft, Seattle, WA, USA). Excel outputs were checked with Minitab 17 (Minitab Inc., State College, PA, USA) outputs as a quality control; the softwares gave identical results.

Results and discussion

Characterization of the cell using the anodic materials and sulphate-reducing inoculums

Table 1 exhibits some properties of the anodic materials whereas Figure 1a shows the characterization of the *MFC* fitted with *GR* as anode. The maximum OCP was 800 mV in the first hour of the characterization; at the end of the procedure the OCP was 600 mV. The R_{int} was obtained from the slope of graph voltage *vs.* current intensity and gave a value of 795 Ω (Table 2). With *GT* as anode, the estimated R_{int} was 410 Ω and the $P_{V,max}$ reached 2108 mW/m^3 (Figure 1b, Table 2), 50% lower than the R_{int} obtained by the *GR*.

Table 1. Selected physical characteristics of anodic materials

Anodic material	Working net volume (m^3)	Anodic actual surface (m^2)	*A's*[a] (m^2/m^3)	Conductance (S)[b]
Graphite rod	2.03×10^{-4}	$8.89\times10^{-4} \pm 2.5\times10^{-5}$	7.3	0.20 ± 0.04
Triangles of graphite	6.64×10^{-5}	0.062 ± 0.001	931	0.61 ± 0.02
Graphite flakes	7.22×10^{-5}	0.28 ± 0.08	1302	0.13 ± 0.04

[a] Relationship between the anode surface area to cell volume, also known as specific surface area of the anode.
[b] Electrical conductance of the materials, expressed in Siemens.

The P_V improved by 60% using the *GT* (Table 2). It is interesting to note that the ratio between specific surface areas of the corresponding anodes (anodic surface/cell volume) increased by 12700% from *GR* to *GT* (a ratio 931/7.3; Table 1). This could partially explain the lower R_{int}, although neither the power increase or the R_{int} decrease was in the same proportion ratio as the anodic surface area increase.

Regarding the *GF* used as anode, the R_{int} and $P_{V,max}$, decreased and increased respectively with respect to *GT* as anode (Fig. 2, Table 2). The R_{int} was 35% lower than *GT* and the $P_{V,max}$ reached 3052 mW/m^3, 45% more than *GT*. It is important to note that in this anode, the relationship anodic surface/cell volume increased 4 times from *GT* to *GF* (Table 1).

The larger surface area of *GF* compared to the other anodic materials would be an advantage since the microorganisms would have a greater anodic surface to colonize and transfer the electrons. In this regard, our results and interpretation are consistent with findings of other researchers [31-35].

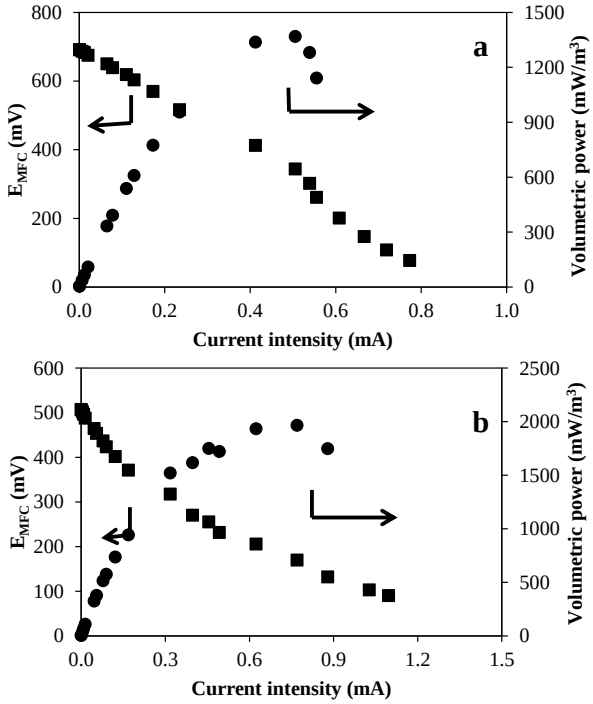

Fig 1. Characterization of the microbial fuel cell fitted either with graphite rod and graphite triangles as anode: (a) Polarization curve and volumetric power for graphite rod as anode; (b) Polarization curve and volumetric power with graphite triangles as anode.

Hays *et al.* [31] found that *MFC* equipped with graphite fiber brush electrodes and modified designs (separators with graphite brush electrodes, to make a more compact design) gave satisfactory power and potential outputs. They ascribed this to high surface areas for exoelectrogenic bacteria growth in graphite-brush-equipped *MFC*s. Feng *et al.* [32] studied the treatment of carbon fiber brush anodes for improving the power output in an air-cathode *MFC*s. They concluded first that carbon brush electrodes provided high surface areas for bacterial growth and high power densities in microbial fuel cells (*MFC*s). Second, they showed that a combined heat and acid treatment of the brush anodes lead to improved power output of the cell, 34% higher than that of the untreated control.

Larrosa-Guerrero *et al.* [33] examined the effect of various carbon anodes (graphite, sponge, paper, cloth, felt, fiber, foam and reticulated vitreous carbon (RVC)) on *MFC* performance. Brewery wastewater diluted with domestic wastewater was the model influent. Biofilms were grown at open circuit or under an external load. The average voltage output was 600 mV at closed circuit when connected to an external resistance of 300 kΩ, and 750 mV at open circuit for all materials, except RVC. They observed a poor performance of RVC compared to the other anodic materials, i.e., power densities as low as 1.3 mW/m^2. The authors concluded that this might be related to lower surface area available and concentration polarization caused by the morphology of the material and the structure of the biofilm.

Table 2. Results of characterization of the microbial fuel cells

Parameters	Graphite rod	Triangles of graphite	Graphite flakes
Inoculum	SR-In [a]	SR-In [a]	SR-In [a]
R_{int} (Ω)	795 ± 147	410 ± 22	273 ± 153
$P_{s,max}$ (mW/m^2)[b]	65.4 ± 0.1	54 ± 0.1	86.4± 0.7
$P_{V,max}$(mW/m^3)[c]	1326 ± 72	2108 ± 174	3052 ± 23
P_{max}(mW)	0.17 ± 0.01	0.14 ± 0.01	0.22 ± 0.01
I_{max} (mA)[d]	1.53 ± 0.3	1.92 ± 0.6	3.50 ± 0.6
$E_{MFC,max}$ (mV)[e]	700 ± 1	500 ± 1	402 ± 1
$E_{MFC,OC}$ (mV)[f]	800 ± 120	600 ± 140	575 ± 33

[a] Sulphate-reducing inoculum.
[b] Maximum power density based on surface area of electrode (cathode).
[c] Maximum volumetric power.
[d] Current intensity value at the maximum power.
[e] Potential value at the maximum power.
[f] Open circuit potential.

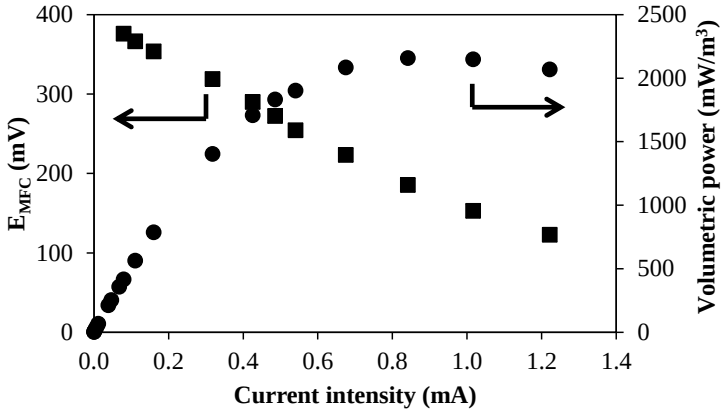

Fig 2. Polarization curve and volumetric power with graphite flakes as anode

Liu *et al.* [34] observed that the achievable maximum current density for mature microbial biofilms in *MFC* treating wastewater was strongly dependent on the electrode material, among other factors. Incidentally, the potential of the active site (-120 mV vs. SHE) was similar for all the electrocatalytically active microbial biofilms in their work, and to that observed for *Geobacter sulfurreducens* in other works. Jin *et al.* [35] tested the effect of using carbon mesh anodes modified by hydrazine hydrate chemical reduction on possible improvement of power generation in an air-cathode *MFC*.

The power densities of *MFC*s using hydrazine-treated anodes were all higher (by 31%) than that of the untreated control; coulombic efficiency increased by 24%. Such improvement in *MFC*s performance correlated with the increased surface area and the change of surface functional groups as revealed by X-ray photoelectron spectroscopy analysis. Also, the authors concluded that the anode material type and surface area are considered key factors influencing the energy conversion in *MFC*s because it links microbiology and electrochemistry. Also, the better characteristics of *MFC* fitted with graphite anodes in this work (*i.e.*, *GR*, *GT* and *GF*) compared to *GAC* could be explained by the high electric conductivity of graphite compared to the low conductivity of *GAC* (Table 1).

Modeling of the maximum volumetric power and internal resistance of microbial fuel cells equipped with graphite anodes in this work

We made an attempt to quantitatively relate the $P_{V,max}$ and R_{int} in this work to the specific surface area A'_s of the graphite anodes as well as either the conductance C or electrolytic conductivity σ of the material. We have used the six datasets for model fitting, *i.e.*, two replicates for each anodic material (2×3). A theoretical development that linked the volumetric power to the cell potential (and the latter, in turn, was expressed as the reversible potential minus the overpotential described by Tafel equation, see Section 2.1 for Model derivation) showed that $P_{V,max}$ and R_{int} could be associated to the log A'_s as follows in the Eq. 31 and 42.

$$P_{V,max} \cong a_0 + a_1 \log A'_s$$

$$R_{int} \cong b_0 + b_1 \log A'_s$$

Consequently, we postulated linear regression models of R_{int} and $P_{V,max}$ in terms of:
-the specific surface area of the electrode A'_s or its logarithm,
-the conductance C of the material of the electrode or its logarithm,
-the electrolytic conductivity σ of the material of the electrode or its logarithm
A family of uni-variable regression models (with log A'_s as the regressor variable) and bi-variable models (with log A'_s and either C or σ as or their logarithms regressor variables, without and with interaction between regressor variables) were fitted to the experimental data (Table 3). The fittings were carried out with the tool Analysis of Data/Regression of Excel 2010, Microsoft Office, Microsoft.

Table 3 shows detailed statistical information on the fitting of several models tested in our work. The selection of the recommended models was based on these criteria:

(i) Among models with similar goodness of fit, we select the one or those that has/have a theoretical basis over the ones that are only empirical.

(ii) Among models with similar or reasonable goodness of fit, we choose the one or those that are more simple (lower number of independent variables, for example) because, in addition to the attractive simplicity, the regression will have higher degrees of freedom.

(iii) We recommmend models that exhibit the lowest value of probability of the Fisher statistic *p(F)*, low values are related to higher significance of ANOVA of the regression).

(iv) Models with high values of determination coefficient are good candidates for final selection, provided that other statistical parameters of the regression are also satisfactory.

(v) Models with higher values of the parameter Ranking will be preferred, provided that other statistical parameters of the regression are also satisfactory. In this regards, we have defined a convenient parameter Ranking as follows:

$$Ranking = \left(\frac{\text{Number of significant coefficients of the regression}}{\text{Number of total coefficients}}\right) \times 100 \qquad (45)$$

In this work, a coefficient of the regression equation is defined as 'significant' (stands for 'this work') when its confidence interval 95% does not contain the zero (0), although the statistical significance of a coefficient is given by the corresponding value *p(T)*. Generally, a low value of *p(T)* indicates a statistically significant coefficient.

Based on the application of these criteria we have chosen five models that could adequately fit our experimental results. Three models for the volumetric power (Eq. 46 to 48; models 1, 3, and 5; Table 3) and two models for the internal resistance of the *MFC* (Eq. 49 and 50; models 2, 16; Table 3).

1.- $P_{V,max} \cong a_0{}' + a_1{}' \log A'_s$ (46)

3. $P_{V,max} \cong a_0 + a_1 \log A'_s + a_2 \times C$ (47)

5. $P_{V,max} \cong a_0' + a_1{}' \times \log A'_s + a_2{}' \times \log C$ (48)

2. $R_{int} \cong b_0{}' + b_1{}' \times \log A'_s$ (49)

16. $R_{int} \cong b_0 + b_1 \times \log A'_s + b_2 \times \sigma + b_{12} \times [(\log A'_s) \times \sigma]$ (50)

Table 3. Model fitting of either maximum volumetric power or internal resistance with the specific area of anodes and other variables this work

Model Regression equation	R^{2a}	a_0' or b_0' [b]	a_1' or b_1' [c]	a_2' or b_2' [d]	a_{12}' or b_{12}' [e]	Ranking[f] (%)	p(F)[g]
1. $P_{V,max}=a_0'+a_1'\times\log A'_s$	0.8872	842.9*	633.2*	NA[h]	NA[h]	100	0.005
2. $R_{int}=b_0'+b_1'\times\log A'_s$	0.8850	933.5*	-211.6*	NA[f]	NA[h]	100	0.005
3. $P_{V,max}=a_0+a_1\times\log A'_s+a_2\times C$	0.9842	1133.66*	660.73*	-1046.79*	NA[h]	100	0.002
4. $R_{int}=b_0+b_1\times\log A'_s+b_2\times C$	0.8865	922.15*	-212.75*	43.69	NA[h]	67	0.038
5. $P_{V,max}=a_0'+a_1'\times\log A'_s+a_2'\times\log C$	0.9810	403.2	629.8*	-738.69*	NA[h]	67	0.003
6. $R_{int}=b_0'+b_1'\times\log A'_s+b_2'\times\log C$	0.8904	968.9*	-211.3*	59.46	NA[h]	67	0.036
7. $P_{V,max}=a_0+a_1\times\log A'_s+a_2\times C+a_{12}\times[(\log A'_s)\times C]$	0.9861	1569.97	493.39	-3387.82	917.61	0	0.021
8. $R_{int}=b_0+b_1\times\log A'_s+b_2\times C+b_{12}\times[(\log A'_s)\times C]$	0.9124	353.21	-4.11	2962.56	-1144.1	0	0.128
9. $P_{V,max}=a_0'+a_1'\times\log A'_s+a_2'\times\log C+a_{12}'\times[(\log A'_s)\times(\log C)]$	0.9833	-402.11	949.48	-1864.23	427.92	0	0.025
10. $R_{int}=b_0'+b_1'\times\log A'_s+b_2'\times\log C+b_{12}'\times[(\log A'_s)\times(\log C)]$	0.9081	1720.77	-509.79	1110.44	-399.57	0	0.135
11. $P_{V,max}=a_0+a_1\times\log A'_s+a_2\times\sigma$	0.9277	-318.23	1026.97*	1.61	NA[h]	33	0.019
12. $R_{int}=b_0+b_1\times\log A'_s+b_2\times\sigma$	0.9052	658.72	-118.45	0.38	NA[h]	0	0.029
13. $P_{V,max}=a_0+a_1'\times\log A'_s+a_2'\times\log\sigma$	0.9732	-3583.09	1507.69*	1423.86	NA[f]	33	0.004
14. $R_{int}=b_0'+b_1'\times\log A'_s+b_2'\times\log\sigma$	0.8918	517.10	-129.35	133.94	NA[f]	0	0.036
15. $P_{V,max}=a_0+a_1\times\log A'_s+a_2\times\sigma+a_{12}\times[(\log A'_s)\times\sigma]$	0.9401	-382.66	1286.00	10.09	-13.47	0	0.089
16. $R_{int}=b_0+b_1\times\log A'_s+b_2\times\sigma+b_{12}\times[(\log A'_s)\times\sigma]$	0.9923	715.79*	-347.90*	-7.13*	11.93*	100	0.012
17. $P_{V,max}=a_0'+a_1'\times\log A'_s+a_2'\times\log\sigma+a_{12}'\times[(\log A'_s)\times(\log\sigma)]$	0.9732	-3581.61	1514.17	1425.54	-5.78	0	0.040
18. $R_{int}=b_0'+b_1'\times\log A'_s+b_2'\times\log\sigma+b_{12}'\times[(\log A'_s)\times(\log\sigma)]$	0.9595	350.38	-857.95	-54.84	649.40	0	0.060

[a] Determination coefficient; [b] independent term of the equation; [c] coefficient of the variable log A'_s; [d] coefficient of the second variable C, σ, log C or log σ; [e] coefficient of the third variable 'crossed product' of the first and second variable; [f] Ranking = (Number of significant coefficients of the regression/Number of total coefficients) *100; 'significant coefficients' are those whose confidence interval does not include zero (0); [g] probability of the Fisher statistics in the ANOVA of the regression; [h] not applicable; *the star on the right side of the coefficient values means that their values were statistically significant and that zero did not belong to their 95% confidence intervals.

Among these models, we feel that the most recommendable are the No 1 and 2 (Eq. 46 and 49) since they show an adequate set of statistical parameters and at the same time are the most simple (one independent variable) and their mathematical forms are based on a theoretical derivation (Tafel equation for overvoltage of the *MFC* plus ancillary concepts). Standardized residuals of our selected models were higher than -2 and lower than 2, which suggests the absence of wild data (outliers) [49].

As a worked example on how the selection process proceeds, let us focus the attention on model 17 for $P_{V,max}$ (Table 3). This model was not chosen to represent our data in spite that the regression shows a high R^2, because

-the model is more complex (3 independent variables, or two independent variables plus their interaction, as one prefers to consider it),

-two terms of the regression are not related to basic electrochemical mechanisms of the device (the second and the third terms of the right member), in fact, these two terms could be considered as empirical "crutches"

-the *p(F)* of the ANOVA of the regression is relatively high compared to those of other models

-the Ranking is 0%, that is, the confidence intervals of all the regression coefficients contain zero (0).

The fitting of our model to data published by Dewan *et al.* [37] was also performed. Their goal was to quantify the relationship, if any, between the surface area of the anode of a two-chamber *MFC* and the anodic power density (surface). Graphite plate electrodes of various sizes were used as anodes. The cathode consisted of Mn-based catalyzed carbon bonded to a Pt mesh that performed as current-collector device. They found that the power density (surface) P_{An} decreased as the surface area of the anode increased; the relationship was decreasingly linear when the P_{An} was plotted against log of the surface area of the anode.

Unfortunately, they neither used the *specific surface area* A'_s of the anode (just the plain surface area) nor performed any study on the relationship between the *volumetric power* P_V and A'_s.

From data in their 'Materials and Methods' section as well as their results from the 'Results and discussion' section (Fig. 2b in their article), we calculated the $P_{v,max}$ and the A'_s. Afterwards, we applied our most simple model $P_{v,max}$ versus log (A'_s) (Model 1 in Table 3, Eq. 46). We found that our model adequately fitted their experimental results (Eq. 51 below)

$$P_{V,max} \cong 0.0348 + 0.01437 \times \log A'_s \qquad (51)$$

with $P_{V,max}$ in mW/cm^3, A'_s in cm^2/cm^3

The statistical parameters were the following:

R^2 = 0.8704; *p(F)* = 0.0022; Ranking = 100%

$0.02347 \leq a_o \leq 0.04469$ at 95% confidence, *p(T)* = 0.00042

$0.00800 \leq a_1 \leq 0.02075$ at 95% confidence, *p(T)* = 0.00216

The largest standardized residual was 1.43, whereas the smallest was -1.22. Thus, all the residuals fell in the interval (-2.0, 2.0) meaning that no outliers were found [55].

At this point, it is worth comparing our model with the previous models available in the literature. They dealt with cell performance and the surface area of the anode but focused on other dependent variables that are not useful indicators of process intensity, such as current intensity [36], peaks of current intensity [38], or P_{An} [36]. This was a first shortcoming, since the use of either *i* or P_{An} is not the most adequate variable to express the *MFC* performance when the purpose is to compare the process intensity with intensity of other competing processes such as other *MFC* configurations, anaerobic digestion, biohydrogen generation, etc.

Two of the three previous models presented in the literature did not report statistical parameters that show the goodness of fit. Only one of them [37] reported the determination coefficient of the regression, but no information on *p(F)*, confidence intervals of the regression coefficients, *etc.*, was included. So, the usefulness of such models as well as their goodness-of-fit is difficult to ascertain.

Only one of the previous models out of the three has been based on electrochemical theoretical grounds [38]. The other two are strictly empirical.

In contrast, our model focuses on the relationship of the volumetric power and internal resistance versus the specific area of anode, and it is based on electrochemical theory (Tafel equation and ancillary concepts). Moreover, thorough statistical evidence of its goodness-of-fit is provided.

Another model (Eq. 52) proposed by us, completely empirical and with no theoretical support so far, was tested for fitting results from literature and our own work (Table 4).

$$\log P_{V,max} \cong a_0 + a_1 \times \log A'_s \quad (52)$$

Table 4. Summary of fitting results of a log-log model given by Eq. 52

Model Regression equation	R^{2a}	a_0 [b]	a_1 [c]	Ranking [d] (%)	p(F) [e]	Reference
$\log P_{V,max} \cong a_0 + a_1 \times \log A'_s$	0.9970	-0.905*	0.840*	100	1.7×10^{-7}	[37]
	0.9683	-0.918	1.152*	50	0.0160	[38]
	0.9430	3.024*	0.137*	100	0.0012	This work

[a] Determination coefficient; [b] independent term of the equation; [c] coefficient of the variable log A'_s; [d] Ranking = (Number of significant coefficients of the regression/Number of total coefficients) ×100; 'significant coefficients' are those whose confidence interval does not include zero (0); [e] probability of the Fisher statistics in the ANOVA of the regression; *the star on the right side of the coefficient values means that their values were statistically significant and that zero did not belong to their 95% confidence intervals.

Transforming the log-log model (Eq. 52) to its potential form, the data from Di Lorenzo *et al.* (2010) [38]

$$\log P_{V,max} = -0.918 + 1.152 \times \log A'_s \quad (53)$$

are represented by

$$P_{V,max} = 10^{-0.918} \times A'_s{}^{1.152} \quad (54)$$

or better

$$P_{V,max} = 0.1208 \times A'_s{}^{1.152} \quad (55)$$

Similarly, data from Dewan *et al.* (2008) [37] are represented by

$$P_{V,max} = 0.1244 \times A'_s{}^{0.8404} \quad (56)$$

Whereas our own experimental data fitted by this second model gives

$$P_{V,max} = 1056.82 \times A'_s{}^{0.1373} \quad (57)$$

The table 4 shows best statistical values for the fitting of the results from literature and our own work in the log-log mathematical model. However, this mathematical model lacks of a theoretical basis. Although the good fit of the model, is not enough evidence to use this model.

Summary and perspectives

The type and size of anodic material have a significant effect on the R_{int} and $P_{V,max}$ of *MFC*s in our work. Comparing the graphite anodes, the $P_{V,max}$ increased and the R_{int} decreased in three materials (*GR*, *GT* and *GF*) with the increase of the log of the specific surface area of the anode. A theoretical model for the $P_{V,max}$ and R_{int} based on the electrochemical performance of the cell lead to equations that satisfactorily fitted the experimental results. The mathematical model leads us to predict the behavior of the performance of the *MFC*s. It is very important in order to scaling of these devices.

Finally, results of this work point out to a promising approach to further tapping bioelectricity from organic wastes that previously have yielded biohydrogen.

Acknowledgements

The authors wish to thank CINVESTAV-IPN and SECITI-GDF (formerly ICYTDF), Mexico, for financial support to this research (PICCO-10-28). Giovanni Hernandez-Flores received a graduate scholarship from CONACYT, Mexico. Also the authors thank Mr. Rafael Hernández-Vera, and technicians of the Environmental of Biotechnology and Renewable Energy R&D Group, CINVESTAV-IPN for their excellent technical help.

References

[1] D. Das, T. N. Veziroglu, Hydrogen production by biological processes: a survey of literature. Int J. Hydrogen Energy 2001; 26:13-28
[2] Y. Cheng-Dar, L. Chung-Ming, E. M. L. Liou, A transition toward a sustainable energy future: feasibility assessment and development strategies of wind power in Taiwan. Energy Policy 2001; 29: 951-963
[3] I. Valdez-Vázquez, E. Ríos-Leal, F. J. Esparza-García, F. Cecchi, H. M. Poggi-Varaldo, Semi-continuous solid substrate anaerobic digestors for H_2 production from organic waste: Mesophilic versus thermophilic regime. Int. J. Hydrogen Energy 2005; 30: 1383-1391
[4] I. Valdez-Vazquez, E. Rios-Leal, A. Carmona-Martinez, K. Muñoz-Páez, H. M. Poggi-Varaldo, Improvement of biohydrogen production from solid wastes by intermittent venting and gas flushing of batch reactors headspace. Environ. Sci. Technol. 2006; 40: 3409-3415
[5] H. M. Poggi-Varaldo, A. Carmona-Martínez, A. L. Vázquez-Larios, O. Solorza-Feria, Effect of inoculum type on the performance of a microbial fuel cell fed with spent organic extracts from hydrogenogenic fermentation of organic solid wastes. J. New Mater. Electrochem. Syst. 2009; 12: 49-54
[6] A. L. Vazquez-Larios, O. Solorza-Feria, G. Vazquez-Huerta, F. J. Esparza-Garcia, E. Rios-Leal, N. Rinderknecht-Seijas, H. M. Poggi-Varaldo, A new design improves performance of a single chamber microbial fuel cell. J. New Mater. Electrochem. Syst. 2010; 13: 219-226
[7] Z. Du, H. Li, T. Gu, A state of the art review on microbial fuel cells: A promising technology for wastewater treatment and bioenergy Biotechnol. Adv. 2007; 25: 464–482
[8] O. Lefebvre, A. Al-Mamun, W. K. Ooi, H. Y. Ng, Z. Tang, D. H.C. Chua, An insight into cathode options for microbial fuel cells. Water Sci Technol. 2008; 57: 2031–2037
[9] S. Ouitrakul, M. Sriyudthsak, S. Charojrochkul, T. Kakizono. Impedance analysis of bio-fuel cell electrodes. Biosens. Bioelectron. 2007; 23: 721-727
[10] P. Belleville, P. J. Strong, P. H. Dare, D. J. Gapes. Influence of nitrogen limitation on performance of a microbial fuel cell. Water Sci. Technol. 2011; 63: 1752-1757
[11] B. E. Logan, J. M. Regan, Microbial challenges and harnessing the metabolic activity of bacteria can provide energy for a variety of applications, once technical and cost obstacles are overcome. Environ. Sci. Technol. 2006; 5172–5180
[12] Y. Yang, G. Sun, M. Xu, Microbial fuel cells come of age. J. Chem. Technol. Biotechnol. 2010; 86: 625-632
[13] M. Zhou, M. Chi, J. Luo, H. He, T. Jin, An overview of electrode materials in microbial fuel cells. J. Power Sources 2011; 196: 4427-4435
[14] B. E. Logan, B. Hamelers, R. Rozendal, U. Schröder, J. Keller, S. Freguia, P. Aelterman, W. Verstraete, K. Rabaey, Microbial fuel cells: Methodology and technology. Environ. Sci. Technol. 2006; 40: 5181-5192
[15] H. Rismani-Yazdi, S. M. Carver, A. D. Christy, O. H. Tuovinen, Cathodic limitations in microbial fuel cells: an overview. J. Power Sources 2008; 180: 683-694
[16] D. Halliday, R. Resnick, J. Walker, *Fundamentals of Physics.* 7th ed. John Wiley & Sons, Inc. New York, ISBN:978-0-471-21643-8, 2005
[17] D. Halliday, R. Resnick, J. Walker, *Fundamentals of Physics.* 9th ed. John Wiley & Sons, Inc. New York, ISBN:978-0-471-21643-8, 2011
[18] D. Jiang, B. Li, Novel electrode materials to enhance the bacterial adhesion and increase the power generation in microbial fuel cells (*MFC*s). Wat. Sci. Technol. 2009; 59.3: 557-563
[19] B. E. Logan, Simultaneous wastewater treatment and biological electricity generation. Water Sci. Technol. 2005; 52: 31-37

[20] H. M. Poggi-Varaldo, A. Vazquez-Larios, O. Solorza-Feria, Microbial fuel cells. In Rodríguez-Varela F.J., Solorza-Feria O., Hernández-Pacheco, E. (Eds). *Fuel cells.* Book Livres, Montréal, Canada, 2010, pp 124-161
[21] F. Li, Y. Sharma, Y. Lei, B. Li, Q. Zhou, Microbial fuel cells: The effects of configurations, electrolyte solutions, and electrode materials on power generation. Appl. Biochem. Biotechnol. 2011; 160: 168–181
[22] C. I. Torres, A. K. Marcus, H. S. Lee, P. Parameswaran, R. Krajmalnik-Brown, B. E. Rittmann, A kinetic perspective on extracellular electron transfer by anode-respiring bacteria. Bioresour. Technol. 2010; 102: 9335–9344
[23] K. Rabaey, G. Lissens, D. S. Steven, W. Verstraete, A microbial fuel cell capable of converting glucose to electricity at high rate and efficiency. Biotechnol. Lett. 2003; 25: 1531–1535
[24] H. Liu, B. E. Logan, Electricity generation using an air-cathode single chamber microbial fuel cell in the presence and absence of a proton exchange membrane. Environ. Sci. Technol. 2004; 38: 4040–4046
[25] B. Min, S. Cheng, B. E. Logan, Electricity generation using membrane and salt bridge microbial fuel cells. Water Res. 2005; 39: 1675–1686
[26] H. Liu, S. Cheng, B. E. Logan, Power generation in fed-batch microbial fuel cells as a function of ionic strength, temperature, and reactor configuration. Environ. Sci. Technol. 2005; 39: 5488–5493
[27] S. Cheng, H. Liu, B. E. Logan, Increased power generation in a continuous flow *MFC* with advective flow through the porous anode and reduced electrode spacing. Environ. Sci. Technol. 2006; 40: 2426–2432
[28] B. E. Logan. *Microbial fuel cells.* John Wiley-Interscience. New Jersey, USA, 2007
[29] D. Jiang, B. Li, Granular activated carbon single-chamber microbial fuel cells (GAC-SC*MFC*s): A design suitable for large-scale wastewater treatment processes. Biochem. Eng. J. 2009; 47: 31-37
[30] J. Wei, L. P., H. Xia, Recent progress in electrodes for microbial fuel cells. Bioresour. Technol. 2011; 102: 9335-9344
[31] S. Hays, F. Zhang, B. E. Logan, Performance of two different types of anodes in membrane electrode assembly microbial fuel cells for power generation from domestic wastewater. J. Power Sources 2011; 195: 8293-8300
[32] Y. Feng, Q. Yang, X. Wang, B. E. Logan, Treatment of carbon fiber brush anodes for improving power generation in air–cathode microbial fuel cells. J. Power Sources 2010; 195: 1841-1844
[33] A. Larrosa-Guerrero, K. Scott, K. P. Katuri, C. Godinez, I. M. Head, T. Curtis, Open circuit versus closed circuit enrichment of anodic biofilms in *MFC*: effect on performance and anodic communities**.** Appl. Microbiol. Biotechnol. 2010; 87: 1699-1713
[34] Y. Liu, F. Harnisch, K. Fricke, U. Schröder, V. Climent, J.M. Feliu, The study of electrochemically active microbial biofilms on different carbon- based anode materials in microbial fuel cells. Biosens. Bioelectron. 2010; 25: 2167-2171
[35] T. Jin, L. Zhou, J. Luo, J, Yang, Y. Zhao, M. Zhou, Hydrazine hydrate chemical reduction as an effective anode modification method to improve the performance of microbial fuel cells. J. Chem. Technol. Biotechnol. 2013; 88: 2075-2081
[36] L. Hsu, B. Chadwick, J. Kagan, R. Thacher, A. Wotawa-Bergen, K. Richter, Scale up considerations for sediment microbial fuel Cells. RSC Adv. 2013; 3: 15947–15954
[37] A. Dewan, H. Beyenal, Z. Lewandowski, Scaling up Microbial Fuel Cells. Environ. Sci. Technol. 2008; 42: 7643–7648
[38] M. Di Lorenzo, K. Scott, T. P. Curtis, I. M. Head, Effect of increasing anode surface area on the performance of a single chamber microbial fuel cell. Chem. Eng. J. 2010; 156: 40–48
[39] K. Rabaey, W. Verstraete, Microbial fuel cells: novel biotechnology for energy generation. Trends Biotechnol. 2005; 23: 291–298
[40] A. L. Vazquez-Larios, O. Solorza-Feria, J. Barrera Cortes, E. Ríos-Leal, M. T. Ponce-Noyola, F. Esparza-García, R. G. González-Huerta, N. Rinderknecht-Seijas, H. M. Poggi-Varaldo, Battelle 9th International Conference on Remediation of Chlorinated and Recalcitrant Compounds, May 19-22, 2014. Monterey, CA, USA. Platform Session H8 "Managing recalcitrant compounds in landfill leachate"
[41] G.W. Castellan, *Physical Chemistry*. 2nd Edition. Addison-Wesley, 1971
[42] I. Bronshtein, K. Semendaiev, *Manual de matemáticas para ingenieros y estudiantes (Handbook of mathematics for engineers and students).* Ediciones de Cultura Popular S.A., Mexico DF, Mexico, 1977
[43] R. Perry, Chemical Engineers Handbook, pp 5.50 & ff 4th ed., McGraw-Hill Co, New York, 1963
[44] G. Hernández-Flores, Interim Report. Sc D Thesis, CINVESTAV-IPN, México, D.F., 2013
[45] H.M. Poggi-Varaldo, L. Valdés, F.J. Esparza-García, G. Fernández-Villagómez, Solid susbtrate anaerobic co-digestion of paper mill sludge, bio-solids, and municipal solid waste. Water Sci. Technol. 1997; 35: 197-204
[46] H.M. Poggi-Varaldo, N. Rinderknecht-Seijas, A differential availability enhancement factor for the evaluation of pollutant availability in soil treatments. Acta Biotechnologica 2003; 23: 271-280
[47] H.M. Poggi-Varaldo, L.M. Alzate-Gaviria, A. Perez-Hernandez, V.G. Nevarez-Morillon, N. Rinderknecht-Seijas, A side-by-side comparison of two systems of sequencing coupled reactors for anaerobic digestion of the organic fraction of municipal solid waste. Waste Manage. Res. 2005; 23: 270-280
[48] APHA. *Standard methods for examination of water and wastewater*. 17th ed. APHA-AWWA-WEF, Washington DC, 1989
[49] D. Montgomery. *Design and analysis of experiments*. 3rd ed John Wiley & Sons, New York, 1991

Characteristics of a Single Chamber Microbial Fuel Cell Equipped with a low cost Membrane

G. Hernández-Flores[1], H. M. Poggi-Varaldo[1,*], O. Solorza-Feria[2], M. T. Ponce Noyola[3], T. Romero-Castañón[4], N. Rinderknecht-Seijas[5], J. Galíndez-Mayer[6],

[1]Environmental Biotechnology and Renewable Energies R&D Group, Dept. of Biotechnology and Bioengineering, Centro de Investigación y de Estudios Avanzados del Instituto Politécnico Nacional. Av. Instituto Politécnico Nacional 2508, Col. San Pedro Zacatenco, Delegación Gustavo A. Madero, México D.F., C. P. 07360 Apartado Postal: 14-740, 07000 México, D.F.
[2]Dept. of Chemistry, *ibídem.* Av. Instituto Politécnico Nacional 2508, Col. San Pedro Zacatenco, Delegación Gustavo A. Madero, México D.F., C. P. 07360 Apartado Postal: 14-740, 07000 México, D.F.
[3]Dept. Biotechnology and Bioengineering, *ibídem.* Av. Instituto Politécnico Nacional 2508, Col. San Pedro Zacatenco, Delegación Gustavo A. Madero, México D.F., C. P. 07360 Apartado Postal: 14-740, 07000 México, D.F.
[4]Electric Research Institute. Reforma 113, Col. Palmira, C. P. 62490 Cuernavaca, Morelos, México.
[5]ESIQIE del IPN, Division of Basic Sciences. Escuela Superior de Ingeniería Química e Industrias Extractivas, ESIQIE. Edificio N° 7, Unidad Profesional Adolfo López Mateos. Colonia Lindavista, Delegación Gustavo A. Madero, México D.F., C. P. 07738.
[6]ENCB del IPN, Division of Basic Sciences. Escuela Nacional de Ciencias Biológicas, ENCB. Unidad Profesional Lázaro Cárdenas, Prolongación de Carpio y Plan de Ayala s/n, Col. Santo Tomas C. P. 11340 Delegación Miguel Hidalgo México, D.F.
*Author for correspondence: Tel: +52 (55) 5747 3800 ext 4321 & 4324; r4cepe@yahoo.com

ABSTRACT

Currently, Nafion is the most common membrane used due its good transport properties; however its cost is very high and it determines about 40% of the *MFC* total cost. Thus, the aims of this research were: *(i)* to test a new organic membrane (*NOM*) in an air-cathode, single chamber *MFC*, and *(ii)* to compare its characteristics with those of an *MFC* equipped with a Nafion® 117 membrane (*NF*). The *MFC* consisted of a horizontal cylinder built in Plexiglas 80 mm long and 57 mm internal diameter. The anodic chamber was packed with graphite flakes as anodic material The *MFC* was seeded with a sulfate-reducing inoculum. The *MFC* performance was determined using the polarization curve method. The internal resistances (R_{int}) were 112.0 and 110.1 Ω using *NOM* and *NF*, respectively, whereas the maximum volumetric powers ($P_{V,max}$) were 2146 and 14246 mW/m^3 for *NOM* and *NF*, respectively. The relatively low value of R_{int} of the *MFC* equipped with *NOM* was encouraging. Furthermore, the value of the R_{int} *NF*-equipped *MFC* was in the same order. Yet, the power delivered with *NOM* was 15% of that with *NF*. However, the cost ratio *NOM*/*NF* was quite low, (\$14/m^2)/(\$1733/m^2) ~ 1/120 ~ 0.8%. These results point out to a trade-off between sacrificing some power output of the cell (85%) but achieving outstanding savings on membrane costs (99.2%).

Keywords: New Organic Membrane; Nafion 117 Membrane; Microbial Fuel Cell

1. Introduction

Petroleum oil is the main energy source in our modern societies. However, their adverse effects on the environment and its imminent depletion have arisen the interest in bioenergies as well as other renewable energy sources [1-3]. Microbial fuel cells

(*MFC*s) constitute an interesting technology for simultaneous wastewater treatment and energy recovery [4,5]. A *MFC* is a bioelectrochemical system that can generate electricity utilizing anaerobic microorganisms as the biocatalysts and effluents as substrate (or "fuel"); it converts chemical energy stored in organic and inorganic matter into electricity [6-8]. A *MFC* is a device with at least two electrodes (anode and cathode) commonly divided by a separator such as proton exchange membrane (*PEM*). In the anodic chamber, the microorganisms anaerobically oxidize the organic or inorganic matter and release electrons and protons. The electrons are transferred to the anode in order to flow to the cathode through an external connection under a load to be powered. On the other hand, the protons diffuse through the liquor of the *MFC* and the separator *PEM*, until they reach the cathode. Finally, at the cathode, the electrons react with protons and molecular oxygen from the air producing water in what is known as the oxygen reduction reaction (*ORR*).

A membrane is an important piece in the configuration of the *MFC*s. The main features and purpose of the membranes in *MFC*s are listed below [9-11]:

- to separate the anodic from the cathodic chamber (Fig 1.) in order to reduce the substrate flux from the anode to cathode, to avoid the back-diffusion of the electron acceptor, and to isolate the catalyst from the cathode in single-chamber *MFC*s
- to perform as a barrier to the transfer of other ions between the chambers
- to increase the Coulombic efficiency (*CE*) reducing the flux of the oxygen from the cathode chamber to the solution in the anode chamber
- to ensure an efficient and sustainable operation along time

However, there are disadvantages related to the *PEM* use. The main one is the high cost of standard membranes [9-11]. Logan (2008) reported that Nafion® can cost up to $1400/m^2 [10]. Currently the cost has increased to $1733/m^2 [12]. Furthermore, its use negatively affects the power generated by the *MFC* due to the increase of the internal resistance (R_{int}) [10,11,13]. Nafion® 117 (*NF*), a perfluorinated membrane, due to their good properties, is the most common used as *PEM* in *MFC*s, however is very expensive and their cost is reflected in the production cost of the *MFC* [8,10,14,15]

Nowadays, one of the challenges of the *MFC*s is the scaling up, but it depends of the performance *MFC* and cost materials [11,16]. In order to replace the Nafion® as *PEM*, in recent years, several polymeric membranes has been studied, such as ultrafiltration and microfiltration membranes, sulphonated polyether ether ketone membrane, anion and cation exchange membranes, bipolar membrane, forward osmosis membrane [1,6,8,10,11,15,16,17]. However, these polymeric membranes are also expensive. Recently, Sivasankaran and Sangeetha (2011) developed a sulphonated polyether ether ketone (SPEEK) to use in a *MFC* instead of *NF* [15]. The $P_{V,max}$ produced by their system, using dairy wastewater and domestic wastewater as influent were 5.7 ± 0.2 and 3.2 ± 0.2 W/m^3, respectively. The SPEEK was compared with *NF* and they report that the SPEEK membrane produced 55.2% higher power density than *NF*.

On the other hand, in order to reduce the costs there are some alternatives for instance:

- Membraneless *MFC*s
- New alternative materials

Membrane-less *MFC*s have been studied because of a membrane is not strictly necessary in a *MFC*. The water conducts the protons by itself, however, the most of the works operated without a membrane, the *CE* is low [6,8-11]. Liu and Logan (2004) explored the bioelectricity generation in a membrane-less *MFC*, in order to increase the energy output and reduce the cost. They reported a power density of 146 ± 8 mW/m^2 and 20% of *CE* for their membrane-less *MFC*. In contrast, their *MFC* equipped with *NF* membrane displayed a power density of 28 ± 3 mW/m^2 and 28% of *CE* [9].

Regarding new materials as *PEM*s, to reduce costs but to keep the *CE* and obtain an still attractive volumetric power (P_V), a few studies with glass fibers or glass wool, salt bridge, as well as other materials and configurations such as assemblies have been reported [10,11,18,19].

Yet, the efforts to find a low cost and effective separator or membrane to replace *NF* are still scarce. Thus, the aims of this research were *(i)* to test a new organic membrane (*NOM*) in an air-cathode, single chamber *MFC*, and *(ii)* to compare its characteristics with those of an *MFC* equipped with a Nafion® 117 membrane.

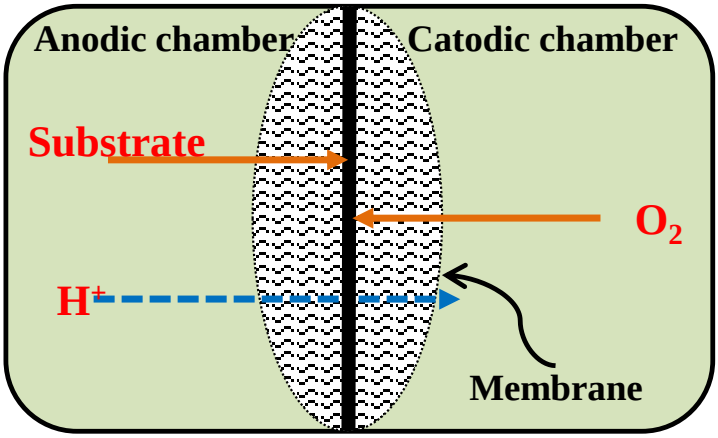

Fig 1. A *MFC* divided by a membrane

2. Experimental

2.1. Experimental design

The experiment consisted of the characterization of the *MFC*s packed with graphite flakes (*GF*) as anode and loaded with a sulfate-reducing inoculum (S*R-In*). The *PEM*s tested were a *NOM* and *NF* as reference. The experiment was carried out in two replicates. The main response variables were the maximum volumetric power ($P_{V,max}$) and the R_{int} of the *MFC*s. The *MFC*s were single compartment, air-cathode cells. They were operated at ambient temperature, with no mechanical mixing not heating.

2.2. Microbial fuel cell

The *MFC*s consisted of a horizontal cylinder built in Plexiglas 80 mm long and 57 mm internal diameter. The anodic chambers were packed with *GF* as anodic material with surface area of 0.28 m^2. For *GF*, we screened a large sample of material and collected the fraction between meshes 10 and 6 (diameters 2 mm and 3.55 mm, respectively). We took and weighed five 20 g subsamples of this fraction; the mass values were annotated. Afterwards, the number of particles in each subsample were determined and annotated. An average number of particles was estimated. With this number, we estimated the average weight of particle of each material. By using the equations shown below, it was possible to calculate the surface area of the mass of material loaded into the *MFC*. The shape factor of the material (also called sphericity factor in other textbooks) was taken into account as described in Perry [20]. For instance, we chose 0.43 for *GF*.

On the other hand, the net volume of the only chamber in our *MFC*s was calculated as the geometric volume of the chamber minus the physical volume of the anodic material. With the surface area of the anodic material and the net volume *V*, the specific surface area of the anode A'_s was finally calculated with Eq. 1 below

$$A'_s = \frac{\frac{M}{\Phi_s}\left(\frac{6^2 m_p{}^2 \pi^3}{m_p{}^3 \pi^2 \rho^2}\right)^{1/3}}{V} = \frac{\frac{M}{\Phi_s}\left(\frac{36\pi}{m_p \rho^2}\right)^{1/3}}{\left(V_{cell} - \frac{M}{\rho}\right)} \qquad (1)$$

where

$\bar{D}_p$ average particle diameter, defined as the diameter of a sphere of the same volume as the particle
Φ_s shape factor of the particle defined as the quotient of the area of a sphere equivalent to the volume of the particle divided by the actual surface of the particle
m_p average weight of a particle of the given size fraction
M total mass of anodic material loaded into the *MFC*
ρ actual density of the material

V_{cell} geometric volume of the cell chamber

The net volume of the *MFC* necessary for the denominator in the calculation of A'_s was estimated as described above in the denominator of Eq. 1.

The cathode of our *MFC* was a flexible carbon-cloth containing 0.5 mg/cm^2 platinum catalyst (Pt 10 wt%/C-ETEK). On the air side, the cathode was limited by a perforated plate of stainless steel 1 mm thickness. In the liquid side, the cathode was in contact with the *PEM* (*NF* or *NOM*) [12,21].

The *NF* was pretreated to activate and to remove impurities before to use in the *MFC*. We describe a modified technique from Oh and Logan (2006) [22]. The membrane was soaked first in H_2O_2 (3% v/v), followed by soaking in deionized water, in 2 M H_2SO_4 , and again in 1 h and deionized water, each stage for 1 h and at temperature of 80 °C. The *NOM* was fabricated and pretreated as reported elsewhere [12].

2.3. Sulfate-reducing inoculum SR-In

The *MFC*s were seeded with a *SR-In* sampled from a sulphate-reducing complete mix reactor. The biomass concentration in the inoculum was *ca*. 1280 mg VSS/L. The complete mix bioreactor was operated at 37°C in a constant temperature room. An influent containing sucrose as carbon source was fed at a flow rate of 120 mL/d to the complete mix sulphate-reducing bioreactor. Its composition was (in g/L): sucrose (5.0), acetic acid (1.5), $NaHCO_3$ (3.0), K_2HPO_4 (0.6), Na_2CO_3 (3.0), NH_4Cl (0.6), Na_2SO_4 (11.0).

2.4. Leachate

The *MFC* was loaded with 6 mL of a leachate similar to that produced in the hydrogen fermentation of the organic fraction of the municipal solid wastes [23]. The model leachate was concocted with a mixture of simple organic acids and solvents (in g/L): acetic, propionic and butyric acids (4 each) as well as acetone and ethanol (4 each) and mineral salts like $NaHCO_3$ and Na_2CO_3 (3 each) and K_2HPO_4 and NH_4Cl (0.6 each) [24,25].

2.5. Electrochemical characterization of the microbial fuel cells

The *MFC* characterization was performed by duplicate. The internal resistance of the cell was determined by using the polarization curve method, i.e., varying the external resistance and recording both the voltage and the current intensity [10, 21]. The *MFC*s were operated at open circuit for 1 h; afterwards different resistors were varied, 10 to 1 MΩ and viceversa, to determine the power generation an another response variables as a function of load. After this, the cell was set to open circuit conditions for 1 h in order to check the adequacy of the procedure (values of initial and final open circuit voltages should be close). The voltage was measured and recorded with a Multimeter ESCORT 3146A.

The current was calculated by the Ohm's law (Eq. 2) and the R_{int} was calculated as the slope of the linear section of the curve voltage versus the current intensity [8,21].

The volumetric power (P_V) was calculated according the Eq. 3:

$$I_{MFC} = \frac{E_{MFC}}{R_{ext}} \quad (2)$$

$$P_V = \frac{(E_{MFC})^2}{V_{cell} \times R_{ext}} \quad (3)$$

where I_{MFC} is the current intensity of the *MFC* in A, E_{MFC} is the voltage delivered by the cell in V, R_{ext} is the external resistance connected to the cell in Ω and V_{cell} is the net volume of the anodic chamber.

The initial chemical oxygen demand (*COD*) and biomass concentration in the cell liquor were *ca*. 3334 ± 106 mg O_2/L and 920 ± 71 VSS/L respectively. The pH and the electrical conductivity were 7.63 ± 0.03 and 16.75 ± 0.07 mS/cm respectively. The *COD* and VSS of the liquors of sulphate-reducing seed bioreactor and cells were determined according to the Standard Methods [26].

3. Results and discussion

3.1. *Assessment of the NOM as PEM in MFCs*

The *NOM* and *NF* were used as *PEM* in the corresponding *MFCs;* the *MFC*s were operated under the same conditions. Table 1 exhibits some properties of the anodic material (*GF*) used to pack the *MFC*s. The net working volume used to obtain the $P_{V,max}$ was 7.22×10^{-5} m^3.

Table 1. Selected physical characteristics of graphite flakes

Characteristics	Values
Working net volume (m^3)	$7.22\times10^{-5} \pm 5.05\times10^{-6}$
Anodic actual surface (m^2)	0.28 ± 0.08
A'_s [a] (m^2/m^3)	1302 ± 91
Conductance (S)[b]	0.13 ± 0.04

[a] Relationship between the anode surface area to cell volume, also known as specific surface area of the anode.
[b] Electrical conductance of the materials, expressed in Siemens.

Fig. 2 shows the electrochemical characterization of both *MFC*s. The R_{int} and $P_{V,max}$ for the *MFC* equipped with *NOM* were 112 Ω and 2146 mW/m^3, respectively (Fig. 2b). On the other hand for the *NF*-equipped *MFC* (Fig. 2a), the R_{int} and $P_{V,max}$ were 110 Ω and 14,246 mW/m^3 (Table 2). Regarding the R_{int} the values obtained were in the same order for both membranes in *MFC*. These results were very encouraging.

The power delivered with *NOM* was 15% of that with Nafion® 117 as *PEM*. However, the cost ratio *NOM*/Nafion was quite low, ($14/$m^2$)/($1733/m^2) ~ 1/120 ~ 0.8% (Table 3). These results point out to a trade-off between sacrificing some power output of the cell (85%) but achieving outstanding savings on membrane costs (99.2%).

Comparing our results with other works, Min *et al*. (2005), using a pure culture of *Geobacter metallireducens* and domestic wastewater, examined the power produced by their *MFC* equipped with a salt bridge as separator. The performance displayed by their *MFC* was 2.2 mW/m^2 with a high R_{int} of 19920 ± 50 Ω. Their maximum voltage recorded was 22 mV using a resistance of 1000 Ω, whereas in our system using the *NOM*, 124 mV was recorded with a resistance of 110 Ω [18]. Their *MFC* performance was too low compared with our system (61 mW/m^2 and R_{int} 112 Ω, Table 2).

On the other hand, Kargi and Eker (2007) used a *MFC* equipped with a salt-agar slab (salt bridge) to treat a synthetic wastewater composed of diluted molasses [19]. The electrodes were copper and gold-covered-copper wires as anode and cathode, respectively. The salt-agar slab used as separator depicted a low cost for their system, nevertheless, the electrodes cost is high.

The *MFC* performance reported was too poor, the maximum power density reached was only 2.9 mW/m^2, a maximum power density 20-fold lower than our results shown in Table 2.

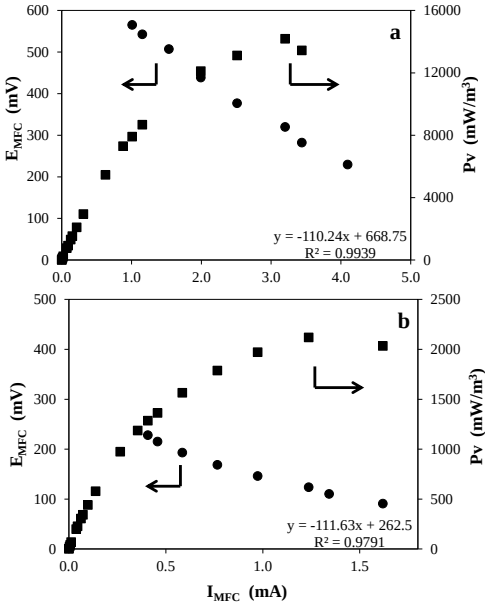

Fig 2. Characterization of the microbial fuel cell equipped either with (a) Nafion® 117 and (b) New organic membrane

Table 2. Results of characterization of the microbial fuel cells

Parameters	**Nafion® 117**	***NOM***
Inoculum	SR-In [a]	SR-In [a]
Anodic material	Graphite flakes	Graphite flakes
R_{int} (Ω)	110.1 ± 0.1	112.0 ± 5.0
$P_{s,max}$ (mW/m^2)[b]	403.0 ± 58.0	61.0 ± 14.0
$P_{V,max}$ (mW/m^3)[c]	14246.0 ± 2051.0	2146.0 ± 506.0
P_{max} (mW)	1.03 ± 0.15	0.15 ± 0.04
I_{max} (mA)[d]	3.20 ± 0.23	1.24 ± 0.15
$E_{MFC,max}$ (mV)[e]	320.0 ± 23.0	124 ± 15.0
$E_{MFC,OC}$ (mV)[f]	724.0 ± 23.0	363 ± 37.0

[a] Sulphate-reducing inoculum.
[b] Maximum power density based on surface area of electrode (cathode).
[c] Maximum volumetric power.
[d] Current intensity value at the maximum power.
[e] Potential value at the maximum power.
[f] Open circuit potential.

Table 3. Membrane cost analysis, costs in US dollars per square meter of membrane

Membrane	**Cost/m^2 ($)**
NF	1733
NOM	14

4. Summary and perspectives

The *NOM* tested in this work is a promising alternative to use as *PEM* in *MFC*s. It is the first report of *NOM* as *PEM*. The results obtained cost savings up to 99.2% in the cost of the membrane could be achieved compared to *NF*, although some power output by the *MF* had to be sacrificed (85%). The cost of *NOM* is the lowest reported in literature. Furthermore, it is worth highlighting that the *NOM* did not require any pretreatment; in contrast the *NF* typically had to be treated with hydrogen peroxide and sulfuric acid that in turn generated hazardous wastes, besides the increased costs of membrane fabrication and conditioning.

Finally, our work shows that it is possible to use our *NOM* as an alternative of *PEM* in *MFC*s.

Acknowledgements

The authors wish to thank CINVESTAV-IPN and SECITI-GDF (formerly ICYTDF), Mexico, for financial support to this research (PICCO-10-28). Giovanni Hernandez-Flores received a graduate scholarship from CONACYT, Mexico. Also the authors thank Mr. Rafael Hernández-Vera, and technicians of the Environmental of Biotechnology and Renewable Energy R&D Group, CINVESTAV-IPN for their excellent technical help.

References

[1] B. E. Logan, J. M. Regan, Microbial challenges and harnessing the metabolic activity of bacteria can provide energy for a variety of applications, once technical and cost obstacles are overcome. Environ. Sci. Technol. 2006; 5172–5180
[2] D. Das, T. N. Veziroglu, Hydrogen production by biological processes: a survey of literature. Int J. Hydrogen Energy 2001; 26: 13-28
[3] Y. Cheng-Dar, L. Chung-Ming, E. M. L. Liou, A transition toward a sustainable energy future: feasibility assessment and development strategies of wind power in Taiwan. Energy Policy 2001; 29: 951-963
[4] B.E. Logan, K. Rabaey, Conversion of wastes into bioelectricity and chemicals by using microbial electrochemical technologies. Science 2012; 337: 686-690
[5] J. Hou, Z. Liu, S. Yang, Y. Zhou, Three-dimensional macroporous anodes based on stainless steel fiber felt for high-performance microbial fuel cells. Journal of Power Sources 2014; 258: 204-209
[6] Y. Yang, G. Sun, M. Xu, Microbial fuel cells come of age. J. Chem. Technol. Biotechnol. 2010; 86: 625-632
[7] H. Wang, J. D. Park, Z. Ren, Active energy harvesting from microbial fuel cells at the maximum power point without using resistors. Environ. Sci. Technol. 2012; 46: 5247-5252
[8] B. E. Logan, B. Hamelers, R. Rozendal, U. Schröder, J. Keller, S. Freguia, P. Aelterman, W. Verstraete, K. Rabaey, Microbial fuel cells: Methodology and technology. Environ. Sci. Technol. 2006; 40: 5181-5192
[9] H. Liu, B. E. Logan, Electricity generation using an air-cathode single chamber microbial fuel cell in the presence and absence of a proton exchange membrane. Environ. Sci. Technol. 2004; 38: 4040–4046
[10] B. E. Logan. *Microbial fuel cells.* John Wiley-Interscience. New Jersey, USA, 2007
[11] W-W. Li, S. Guo-Ping, L. Xian-Wei, Y. Han-qing, Recent advances in the separators for microbial fuel cells. Bioresour Technol. 2011; 102: 244-252
[12] G. Hernández-Flores, Interim Report. Sc D Thesis, CINVESTAV-IPN, México, D.F., 2013
[13] X. Xia, J. C. Tokash, F. Zhang, P. Liang, X. Huang, B. E. Logan, Oxygen-Reducing Biocathodes Operating with Passive Oxygen Transfer in Microbial Fuel Cells. Environ. Sci. Technol**.** 2013**;** *47* (4): 2085–2091
[14] H. M. Poggi-Varaldo, A. Vazquez-Larios, O. Solorza-Feria, Microbial fuel cells. In Rodríguez-Varela F.J., Solorza-Feria O., Hernández-Pacheco, E. (Eds). *Fuel cells.* Book Livres, Montréal, Canada, 2010, pp 124-161
[15] A. Sivasankaran, D. Sangeetha, Development of *MFC* using sulphonated polyether ether ketone (SPEEK) membrane for electricity generation from waste water. Bioresour. Technol. 2011; 102(24): 11167-11171
[16] J. Wei, L. P., H. Xia, Recent progress in electrodes for microbial fuel cells. Bioresour. Technol. 2011; 102: 9335-9344
[17] F. Zhang, K. S. Brastad, Z. He, Integrating forward osmosis into microbial fuel cells for wastewater treatment, water extraction and bioelectricity generation. Environ. Sci. Technol. 2011; 45: 6690-6696
[18] B. Min, S. Cheng, B. E. Logan, Electricity generation using membranes and salt bridge microbial fuel cells. Water Research. 2005; 39: 1675-1686
[19] F. Kargi, S. Eker, Electricity generation with simultaneous wastewater treatment by a microbial fuel cell (*MFC*) with Cu and Cu-Au electrodes. J. Chem. Technol. Biotechnol. 2007; 82: 658-662
[20] R. Perry, Chemical Engineers Handbook, pp 5.50 & ff 4th ed., McGraw-Hill Co, New York, 1963
[21] A. L. Vazquez-Larios, O. Solorza-Feria, G. Vazquez-Huerta, F. J. Esparza-Garcia, E. Rios-Leal, N. Rinderknecht-Seijas, H. M. Poggi-Varaldo, A new design improves performance of a single chamber microbial fuel cell. J. New Mater. Electrochem. Syst. 2010; 13: 219-226
[22] S. E. Oh, B. E. Logan, Proton exchange membrane and electrode surface areas as factors that affect power generation in microbial fuel cells. Appl Microbiol Biotechnol 2006; 70: 162–169
[23] H.M. Poggi-Varaldo, L. Valdés, F.J. Esparza-García, G. Fernández-Villagómez, Solid susbtrate anaerobic co-digestion of paper mill sludge, bio-solids, and municipal solid waste. Water Sci. Technol. 1997; 35: 197-204
[24] H.M. Poggi-Varaldo, N. Rinderknecht-Seijas, A differential availability enhancement factor for the evaluation of pollutant availability in soil treatments. Acta Biotechnologica 2003; 23: 271-280
[25] H.M. Poggi-Varaldo, L.M. Alzate-Gaviria, A. Perez-Hernandez, V.G. Nevarez-Morillon, N. Rinderknecht-Seijas, A side-by-side comparison of two systems of sequencing coupled reactors for anaerobic digestion of the organic fraction of municipal solid waste. Waste Manage. Res. 2005; 23: 270-280
[26] APHA. *Standard methods for examination of water and wastewater*. 17th ed. APHA-AWWA-WEF, Washington DC, 1989

Alternative Proton Exchange Membrane Equipped in a Microbial Fuel Cell in Batch Operation

G. Hernández-Flores[1], H. M. Poggi-Varaldo[1,*], O. Solorza-Feria[2], T. Romero-Castañon[3], E. Ríos-Leal[4], J. Galíndez-Mayer[5], F. Esparza-García[6]

[1]Environmental Biotechnology and Renewable Energies R&D Group, Dept. of Biotechnology and Bioengineering, Centro de Investigación y de Estudios Avanzados del Instituto Politécnico Nacional. Av. Instituto Politécnico Nacional 2508, Col. San Pedro Zacatenco, Delegación Gustavo A. Madero, México D.F., C. P. 07360 Apartado Postal: 14-740, 07000 México, D.F.
[2]Dept. of Chemistry, *ibídem.* Av. Instituto Politécnico Nacional 2508, Col. San Pedro Zacatenco, Delegación Gustavo A. Madero, México D.F., C. P. 07360 Apartado Postal: 14-740, 07000 México, D.F.
[3]Electric Research Institute. Reforma 113, Col. Palmira, C. P. 62490 Cuernavaca, Morelos, México.
[4]Dept. Biotechnology and Bioengineering, *ibídem.* Av. Instituto Politécnico Nacional 2508, Col. San Pedro Zacatenco, Delegación Gustavo A. Madero, México D.F., C. P. 07360 Apartado Postal: 14-740, 07000 México, D.F.
[5]ENCB del IPN, Division of Basic Sciences. Escuela Nacional de Ciencias Biológicas, ENCB. Unidad Profesional Lázaro Cárdenas, Prolongación de Carpio y Plan de Ayala s/n, Col. Santo Tomas C. P. 11340 Delegación Miguel Hidalgo México, D.F.
[6]Dept. Biotechnology and Bioengineering, *ibídem.* Av. Instituto Politécnico Nacional 2508, Col. San Pedro Zacatenco, Delegación Gustavo A. Madero, México D.F., C. P. 07360 Apartado Postal: 14-740, 07000 México, D.F.
*Author for correspondence: Tel: +52 (55) 5747 3800 ext 4321 & 4324; r4cepe@yahoo.com

ABSTRACT

At present, Nafion is the most commonly used membrane in *MFC* due its good transport properties. Yet, its commercial price is up to $1470/m^2 and it determines *ca.* 40% of the *MFC* total cost. Therefore, the objective of this work was to compare the effect of membrane type on the performance of *MFC* operated in long batch process. The tested *PEMs* were Nafion 117 (*NF*) and a new organic membrane (*NOM*). The treated influent was a very recalcitrant, actual leachate from Mexico City sanitary landfill. The *MFC* was seeded with an inoculum previously enriched in electrochemically-active bacteria using a selective medium of Fe(III) salts and acetate. The batch lasted 15 days. *MFC* characteristics improved with time of operation; this suggested an in-cell enrichment process or acclimation of inoculum. During the batch operation, the cell equipped with *NOM* outperformed the one equipped with *NF*. In the first period, 0 to 8 d, average volumetric powers (P_V) were 9,000 and 4,000 mW/m^3 for the *MFC* equipped with *NOM* and *NF*, respectively. Considering the subperiod from 8 to 15 d when the external resistances were adjusted, the average P_V were 20,000 and 6,800 mW/m^3 for *NOM* and *NF*, respectively. At the end of the operational period, deposits of dry salts appeared on the external side of the cathode carbon cloth of the cell equipped with *NF*. This effect was not observed for the cell with *NOM*. Presumably, these deposits could be responsible for the decrease of power output during 11 to 15 d in the cell equipped with *NF*.

Keywords: Natural Organic Membrane; Batch Operation; Microbial Fuel Cell; Leachate

1. Introduction

Nowadays the humanity depends heavily on the use of petroleum oil and consequently faces two great risks: the inevitable depletion and the environmental pollution caused during exploration, transport, combustion of oil-based fuels. Thus, the investigation to develop new renewable energy sources as well as bioenergies has notably increased in the last years [1-3].

Microbial fuel cells (*MFCs*) are a promising technology that generates electrical power from a wide range of soluble substrates (organic or inorganic), wastes included. The *MFC*s constitute an interesting alternative to produce electrical energy and provide wastewater treatment simultaneously. [4-6].

In order to increase the *MFC* efficiency, several conditions of *MFC* operation and components have been the subject of intensive research such as the type of biocatalysts, membrane (electrolyte) or separators, temperature, pH, substrates, the type and materials of electrodes, electrode catalysts, cell configuration and architecture, among others [2,13-16].

The protonic exchange membrane (*PEM*) is an important part of *MFC*s. The main features and purposed of the membranes in *MFC*s are listed below [17-19]:

- to separate the anodic from the cathodic chamber in order to reduce the substrate flux from the anode to cathode, to avoid the back-diffusion of the electron acceptor, and to isolate the catalyst from the cathode in single-chamber *MFC*s
- to perform as a barrier to the transfer of other ions between the chambers
- to increase the Coulombic efficiency (*CE*) reducing the flux of the oxygen from the cathode chamber to the solution in the anode chamber
- to ensure an efficient and sustainable operation along time

Yet, there are disadvantages related to the *PEM* use, such as the high cost of standard membranes [17-19]. For instance, Nafion cost has increased up to \$1733/m^2 [20]. Furthermore, its use might affect negatively the power generated by the *MFC* due to the increase of the internal resistance (R_{int}) [18,19,21].

Nowadays, one of the challenges of the *MFC*s is the scaling up, but it depends of the performance *MFC* and cost materials [19,22]. So, in order to replace the *NF* as *PEM*, several polymeric membranes have been studied, such as ultrafiltration and microfiltration membranes, sulphonated polyether ether ketone membrane, anion and cation exchange membranes, bipolar membrane, forward osmosis membrane [2,13,18,19,22-25]. However, these polymeric membranes also are expensive.

Membrane-less *MFC*s have been studied because of a membrane is not strictly necessary in a *MFC*. The water conducts the protons by itself, however, the most of the works operated without a membrane, the *CE* is low [13,17-19,23]. Liu and Logan (2004) explored the bioelectricity generation in a membrane-less *MFC*, in order to increase the energy output and reduce the cost [17]. They reported a power density of 146 mW/m^2 and 20% of *CE* for their membrane-less *MFC*. In contrast, their *MFC* equipped with *NF* membrane displayed a power density of 28 mW/m^2 and 28% of *CE*.

Regarding new materials as *PEM*s, to reduce costs but to keep the *CE* and obtain an attractive volumetric power (P_V), there are few studies that have focused on glass fibers or glass wool, salt bridge, as well other materials and configurations such as assemblies [18,19,26,27].

Therefore, the objective of this work was to compare the effect of membrane type on the performance of *MFC* operated in long batch process, using actual leachates from Mexico City sanitary landfill and inoculum previously enriched (*E-in*) in electrochemically-active bacteria (*EAB*). The tested *PEMs* were a new organic membrane (*NOM*) and *NF* as reference.

2. Experimental

2.1 Experimental design

The experiment consisted of the operation in a long batch process of the *MFC*s equipped either with a *NOM* or *NF* (as control) as *PEM*s. The *MFC*s were packed with graphite flakes (*GF*) as anode and loaded with a mixture of inoculum previously enriched in *EAB* and a very recalcitrant, actual leachate from Mexico City sanitary landfill. The mix was in a proportion 80% inoculum and 20% actual leachate. The *MFC*s were operated along 15 d.

The long batch process was divided in two periods; first, from 0 to 8 d, and a second one, from 8 to 15 d. The first period was operated under the first external resistance (R_{ext}) defined by the first electrochemical characterization in time 0 d. The second electrochemical characterization was carried out at 8 d, then, the R_{ext} value was readjusted and the second period started.

The main response variables studied in the characterizations electrochemical were the maximum volumetric power ($P_{V,max}$) and the internal resistance (R_{int}) of the *MFC*s, whereas along the long batch process the average P_V, the chemical oxygen demand (*COD*) removal (η_{COD}), and the current (I_{MFC}) were the response variables analyzed.

The experiments were carried out at ambient temperature, with no mechanical mixing not heating and in a single compartment, air-cathode *MFC*s.

2.2. Microbial fuel cell

The *MFC*s were two horizontal cylinders built in Plexiglas 80 mm long and 57 mm internal diameter. The anodic chambers were packed with *GF* as anodic material with surface area of 0.28 m^2. Its anodic material was treated heating to 550 °C. The surface area was obtained as follow. A large sample of material was screened and the fraction collected was between meshes 10 and 6 (diameters 2 mm and 3.55 mm, respectively); of this fraction, five 20 g subsamples were taken and weighed. Afterwards, the number of particles in each subsample were determined and annotated. An average number of particles was estimated. With this number, the average weight of particle of each material was estimated and using the equations shown below, it was possible to calculate the surface area of the mass of material loaded into the *MFC*. The shape factor of the material (also called sphericity factor in other textbooks) was taken into account as described in Perry [28]. For instance, 0.43 was chosen for *GF*.

On the other hand, the net volume of the only anodic chamber in our *MFC*s was calculated as the geometric volume of the chamber minus the physical volume of the anodic material. With the surface area of the anodic material and the net volume, the specific surface area of the anode (A'_s) was finally calculated with Eq. 2 below

$$A'_s = \frac{\frac{M}{\Phi_s}\left(6^2 m_p{}^2 \pi^3\right)^{1/3}}{V} = \frac{\frac{M}{\Phi_s}\left(\frac{36\pi}{m_p \rho^2}\right)^{1/3}}{\left(V_{cell} - \frac{M}{\rho}\right)} \qquad (2)$$

where

$\overline{D}_p$ average particle diameter, defined as the diameter of a sphere of the same volume as the particle
Φ_s shape factor of the particle defined as the quotient of the area of a sphere equivalent to the volume of the particle divided by the actual surface of the particle
m_p average weight of a particle of the given size fraction
M total mass of anodic material loaded into the *MFC*
ρ actual density of the material
V_{cell} geometric volume of the cell chamber

The net volume of the *MFC* necessary for the denominator in the calculation of A'_s was estimated as described above in the denominator of Eq. 2. The cathode of the *MFC*s was a flexible carbon-cloth containing 0.5 mg/cm^2 platinum catalyst (Pt 10 wt%/C-ETEK). On the air side, the cathode was limited by a perforated plate of stainless steel 1 mm thickness. In the liquid side, the cathode was in contact with the *PEM* (*NF* or *NOM*) [9,20].

The *NF* was pretreated to activate and to remove impurities before to use in the *MFC*. We describe a modified technique from Oh and Logan (2006) [29]. The membrane was soaked first in H_2O_2 (3% v/v), followed by soaking in deionized water, in 2 M H_2SO_4 , and again in 1 h and deionized water, each stage for 1 h and at temperature of 80 °C. The *NOM* was fabricated and pretreated as reported elsewhere [20].

2.3. Enrichment of inocula

An enrichment procedure based on selective pressure using Fe (III) as an electron acceptor and sodium acetate as carbon source was implemented [20,30]. The departing inoculum consisted of soil sampled from an excavation made in the Centro de Investigación y de Estudios Avanzados del Instituto Politécnico Nacional (19°30´33"N, 99°07´46"O) at a depth of 2 m [31]. The soil was transferred to an anaerobic bottle, after this, 5 g of soil sample was suspended in anaerobic saline solution (50 mL); afterwards, 5 mL of sample was transferred to 50 mL metal-reduction medium with acetate as electron donor and Fe(III) oxide-hydroxide as electron acceptor. The enrichment of inocula was obtained with serial transfers [30,31].

Duplicate enrichments were incubated at 30 °C for 9 d in the dark condition. The enrichment procedure was repeated 3 times. The culture medium consisted of (g/L): 2.5 $NaHCO_3$, 0.25 NH_4Cl, 0.6 $NaH_2PO_4.H_2O$, 0.1 KCl, 10 mL vitamin solution and 10 mL mineral solution [32,33]. The Fe(III) oxide was synthesized as follows: a solution 0.4 M of $FeCl_3.6\ H_2O$ (pH adjusted to 7.0 with 10 M of NaOH) was added [33]. Finally, after the transferences, the *EAB* were transferred to a bioreactor of 1 L, it was incubated at 35°C in dark conditions. The inoculum was feeded every week and gassed with nitrogen to create anoxic environment [32].

2.4. Leachate

The leachates used as substrate were sampled from Mexico City sanitary landfill "Bordo Poniente". Two types of leachates highly recalcitrant were provided: samples from Section 1 (L-1) and samples from Section 4 (L-4), where the denomination 'section' is related to the chronological construction of the landfill cells. Organic matter contents of leachates were 4300 and 12 300 mg COD/L for L-1 and L-4, respectively. The *MFC* mas loaded with the sample from Section 4 (L-4) and their pH was slightly alkaline, *ca*. 8.0. The full characterization of the leachate is in Table 1 [31]. The relatively high organic matter content and high value of BOD_5/COD ratio indicated that the leachate is biodegradable and not quite aged [34]. Interestingly, we expected a lower pH consistent with fresh leachate. That was not the case. It is known that the "Bordo Poniente" landfill is emplaced in a site characterized by sodic-saline soil with pH of soil extract as high as 11. The local soil was likely used to cap the landfill cells during the daily operation of the landfill, possibly releasing sodium salts (carbonate, bicarbonate) as well as hydroxide that increased leachate pH. This explanation is supported by the high values of the electrolytic conductivity of the leachate (Table 1).

Table 1. Characteristics of municipal leachate.

Parameters	Value
pH	8.26 ± 0.02
Conductivity (mS/cm)	36.7 ± 0.1
Total Kjeldahl nitrogen (g/L)	2.9 ± 0.03
SO_4^{2-} (g/L)	0.281 ± 0.01
COD (g/L) [a]	12.3 ± 0.5
BOD_5 (g/L) [b]	10.6 ± 0.2
BOD_5/COD	0.86

Notes: [a] chemical oxygen demand; [b] biochemical oxygen demand

2.5. Electrochemical characterization of the microbial fuel cells

The *MFC* characterization was performed by duplicated. The internal resistance and power density curve of the *MFC* was determined by duplicate, using the polarization curve method by varying the external resistance and recording both the voltage and the current intensity [9,18,21,35].

The *MFC*s were operated at open circuit for 1 h; afterwards different resistors were varied, 10 to 1 MΩ and viceversa, to determine the power generation an another response variables as a function of load. After this, the cell was set to open circuit conditions for 1 h in order to check the adequacy of the procedure (values of initial and final open circuit voltages should be close). The voltage was measured and recorded with a Multimeter ESCORT 3146A.

The current was calculated by the Ohm's law (Eq. 3) and the R_{int} was calculated as the slope of the linear section of the curve voltage versus the current intensity [9,23]. The P_V was calculated according the Eq. 4 below.

$$I_{MFC} = \frac{E_{MFC}}{R_{ext}} \quad (3)$$

$$P_V = \frac{(E_{MFC})^2}{V_{cell} \times R_{ext}} \quad (4)$$

where I_{MFC} is the current intensity of the *MFC* in A, E_{MFC} is the voltage delivered by the cell in V, R_{ext} is the external resistance connected to the cell in Ω and V_{cell} is the net volume of the anodic chamber.

The initial *COD* and biomass concentration in the *MFC* liquor were *ca.* 2000 mg O_2/L and 1900 VSS/L respectively. The pH and the electrical conductivity were 9 and 39 mS/cm, respectively. The *COD* and VSS of the inoculum enriched in Fe (III)-reducing bacteria seed bioreactor and *MFC*s were determined according to the Standard Methods [36].

3. Results and discussion

3.1. Electrochemical characterizations

The physical characteristics of the anodic material *GF* are showed in the Table 2. This anodic material has a large surface area *c.a.* 0.3 m^2. The *MFC*s equipped with their respective *PEM*s were electrochemical characterized at 0 d, it leads to define the R_{ext} to start the power generation. The *MFC* equipped with *NOM* showed discouraging values (Fig. 1, Table 3,).

The R_{int} and $P_{v,max}$ were 650 Ω and 9 mW/m^3, whereas the *MFC* equipped with *NF* displayed a R_{int} and $P_{v,max}$ of 350 Ω and 1100 mW/m^3, respectively (Fig. 2, Table 3,). In this first test, the *NF* was far better than *NOM*. However, after 8 d, in the second electrochemical characterization the *MFC* equipped with *NOM* improve their performance, reaching a $P_{v,max}$ of 22,500 mW/m^3 (Fig. 1, Table 3,). The R_{int} decreased 94% (40 Ω) and the $P_{v,max}$ increased 4 magnitude orders, it was very encouraging.

Table 2. Selected physical characteristics of graphite flakes.

Characteristics	**Values**
Working net volume (m^3)	$7.22\times10^{-5} \pm 5.05\times10^{-6}$
Anodic actual surface (m^2)	0.28 ± 0.08
A'_s [a] (m^2/m^3)	1302 ± 91
Conductance (S)[b]	0.13 ± 0.04

Notes:
[a] Relationship between the anode surface area to cell volume, also known as specific surface area of the anode.
[b] Electrical conductance of the material, expressed in Siemens.

On the other hand, regarding the second characterization of the *MFC* equipped with *NF*, the R_{int} and $P_{v,max}$ observed were 80 Ω and 8,600 mW/m^3(Table 3, Fig. 2). The R_{int} only decreased 77%, whereas the $P_{v,max}$ increased 87% respect the initial value. The *MFC* performance equipped with *NOM* at 8 d, was better than the *MFC* equipped with *NF*.

Table 3. Electrochemical characterization of microbial fuel cells equipped with different membranes.

Parameter	**Time (d)**			
	0		**8**	
	Membranes			
	***NOM*[a]**	***NF*[b]**	***NOM***	***NF***
R_{int} (Ω)	649.3 ± 21.8	350.0 ± 218.1	40.8 ± 6.7	79.7 ± 1.3
$P_{v,max}$ (mW/m^3)[c]	9.31 ± 3.2	1142.7 ± 379.2	22560.0 ± 2727.0	8594.9 ± 1069.8
I_{MFC} (mA)[d]	0.026 ± 0.004	0.49 ± 0.08	8.59 ± 0.05	2.75 ± 0.17
P_{cath} (mW/m^2)[e]	0.26 ± 0.09	32.34 ± 10.73	638.40 ± 77.20	243.22 ± 30.30
$E_{MFC,max}$ (mV)[f]	25.6 ± 4.3	163.0 ± 27.7	189.0 ± 11.5	225.2 ± 14.02
$E_{MFC,OC}$ (mV)[g]	29.4 ± 19.4	380.0 ± 29.5	619.4 ± 47.7	549.7 ± 28.3

Notes:
[a] new organic membrane
[b] Nafion 117 membrane
[c] Maximum volumetric power.
[d] Current intensity value at the maximum power.
[e] Maximum power density based on surface area of electrode (cathode).
[f] Potential value at the maximum power.
[g] Open circuit potential.

3.2. Performance of the MFC equipped with NOM and NF in long batch operation

The influent characteristics are described in Table 4. In the first period, 0 to 8 d, the load resistances used were 470 and 680 Ω for the *MFC*s equipped with *NF* and *NOM*, respectively (defined by previous electrochemical characterizations). The average volumetric powers (P_Vs) recorded were 9,000 and 4,000 mW/m^3 for *MFC* equipped with *NOM* and *NF*, respectively (Fig. 3). The *MFC* equipped with *NOM* reached an average P_V higher than *MFC* equipped with *NF*, although the values in the first characterization. The second electrochemical characterizations were carried out due these results.

In the second period, 8 to 15 d, new load resistances were applied, 82 and 47 Ω in the systems using *NOM* and *NF*, respectively. In this period the *MFC* equipped with *NOM* reached and average P_V of 20,000 mW/m^3, almost the $P_{V,max}$ recording during the second electrochemical characterization. Furthermore, the P_V was stable along this period (Fig. 3).

On the other hand, the *MFC* equipped with *NF*, reached only an average P_V of 6,800 mW/m^3 during the day 8 to 11, after this time, the P_V began to fall down (Fig. 3). It behavior could be explained because of from the 11 d, in the *MFC* equipped with *NF*, deposits of dry salts appeared on the external side of the cathode carbon cloth of the *MFC* equipped with *NF* (Fig. 4). The influent loaded to the *MFC*s had a high salinity and high pH (Table 1) and the *NF* was affected by this parameters. However, this effect was not observed for the *MFC* equipped with *NOM*.

These deposits could be responsible for the decrease of power output during 11 to 15 d in the cell equipped with *NF*. Another issue was that the water level inside of the *MFC*s decreased by evaporation losses through the *PEM*s. In order to maintain the original level inside of the *MFC*s and guarantee a full hydration of the *PEM*s, sterile distilled water was supplied every time it was necessary.

Regarding the organic matter (*COD*, Table 4) of the effluent, both *MFC*s seemed to have enough "fuel" to convert in electrical energy. The η_{COD} at the end of the batch operation were 39.32 and 28.29% for the *MFC*s equipped with *NOM* and *NF*, respectively. Once more, in this parameter, the *MFC* equipped with the *NOM*, was higher than the device with *NF*. The deposits of dry salts on the external side of the cathode carbon cloth of the *MFC* equipped with *NF* affect the performance of the *MFC* equipped with *NF*. Furthermore, the influent color at the end of the batch operation becomes clear in both systems (Fig. 5). Overall, the performance of the *MFC* equipped with *NOM* was much better than *MFC* equipped with *NF*.

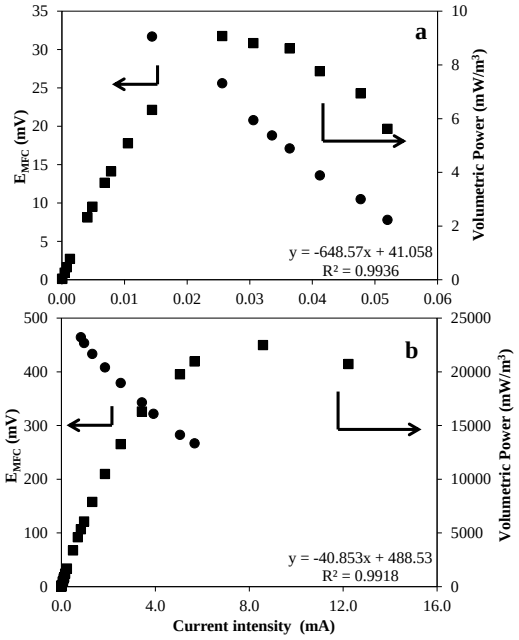

Fig 1. Electrochemical characterization of the *MFC* equipped with *NOM* at (a) 0 d and (b) 8 d.

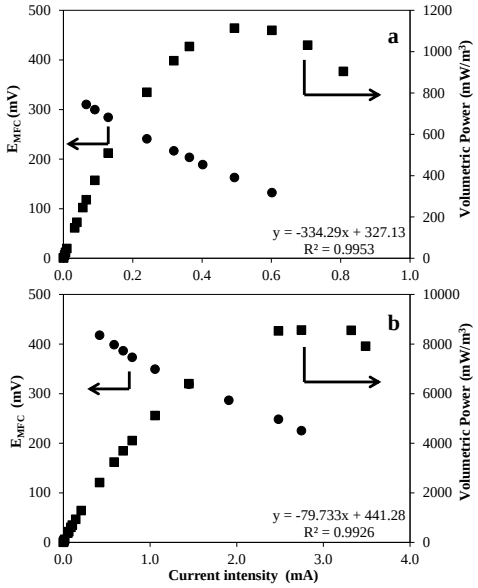

Fig 2. Electrochemical characterization of the *MFC* equipped with *NF* at (a) 0 d and (b) 8 d

Table 4. Influent and effluent characteristics of the *MFC*s equipped with both *PEM*s

Parameter	**Time (d)**		
	0	**15**	
	Membranes		
	NOM* and *NF	***NOM***	***NF***
pH	9.12 ± 0.03	8.87 ± 0.02	7.68 ± 0.05
Conductivity (mS/cm)	38.65 ± 0.07	29.5 ± 0.05	30.6 ± 0.06
COD (mg/L)	2022 ± 99	1227 ± 511	1450 ± 193
Temperature (°C)	28.50 ± 0.71	27 ± 0.66	26 ± 0.58

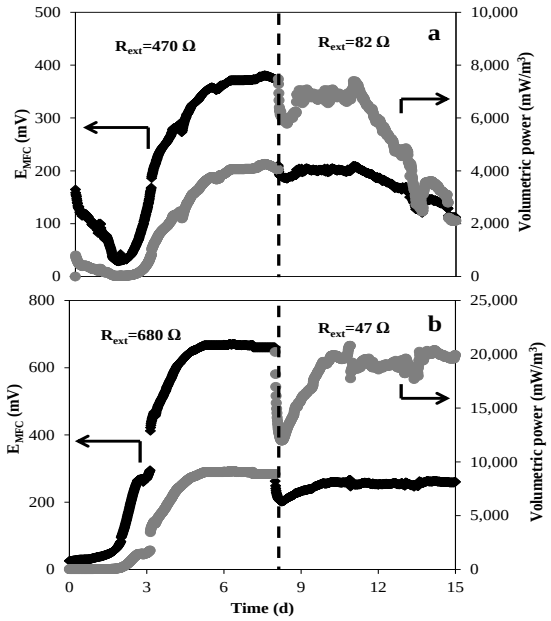

Fig 3. Time course of voltage and volumetric power outputs of *MFC*s using (a) *NF* and (b) *NOM*

Fig 4. Deposits of dry salts on the external side of the cathode carbon cloth of the *MFC* equipped with *NF* from the day 11th

In the open literature, there are reports on tests with organic membranes [26,27]. For instance, Min *et al*. (2005), using a pure culture of *Geobacter metallireducens* and domestic wastewater, examined the power produced by their *MFC* using a salt bridge as separator. The performance displayed by their *MFC* was 2.2 mW/m^2 with a high R_{int} 19,920 Ω [26]. Their system applied is very simple and attractive, however their *MFC* performance was poorer than that of our system (average powers 547 mW/m^2 and *ca*. 20,000 mW/m^3 in the batch operation of our *MFC* equipped with *NOM*, Fig. 3).

In another work, Kargi and Eker (2007) used a salt-agar slab (salt bridge) in order to separate the chambers in their *MFC* [27]. The electrodes were made of Cu and Au-covered copper wires as anode and cathode, respectively. Although the high cost of their electrodes, the performance of their *MFC* was also too poor, the maximum power density registered was 2.9 mW/m^2. On the other hand Liu and Logan (2004) studied the power generation in an air-cathode *MFC* with and without (membraneless) a *NF*. Using wastewater as substrate and with *NF* as *PEM*, the power density reached was 28 mW/m^2, whereas the power density increased up to 146 mW/m^2 in the membraneless cell [17].

Sivasankaran and Sangeetha (2011) developed a sulphonated polyether ether ketone (SPEEK) to use in a *MFC* instead of *NF* [24]. The $P_{V,max}$ produced by their system, using dairy wastewater and domestic wastewater as influent were 5,700 and 3,200 mW/m^3, respectively. Our average P_V obtained during the batch operation was *ca*. 20,000 mW/m^3. It means our membrane could

be considered a very good option for using as a *PEM* in a *MFC* system.

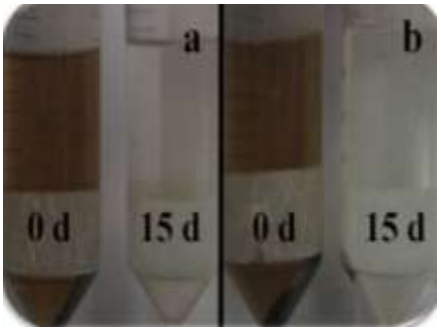

Fig 5. Visual evidence of leachate depuration after 15 d of batch operation in the *MFC* equipped with (a) *NOM* and (b) *NF*

4. Summary and perspectives

Our research was focused on the evaluation of a new membrane as *PEM* in order to replace the *NF*. The *NOM* tested in this work is a new alternative to use as *PEM* in *MFC*s. Along the batch operation, in a short time, the *MFC* performance using *NOM* delivered a volumetric power more than 2-fold the power of the *MFC* equipped with *NF*. Furthermore, the performance during the batch was more stable. Our new membrane is outstandingly more economic than *NF* and depicts good performance. Moreover, our *NOM* does not need any pretreatment; in contrast, the *NF* membrane requires a pretreatment with hydrogen peroxide and sulfuric acid that in turn generates hazardous wastes, besides the increased costs of membrane fabrication and conditioning.

Acknowledgements

The authors are grateful to CINVESTAV-IPN and SECITI-GDF (formerly ICYTDF), Mexico, for financial support to this research (PICCO-10-28). Giovanni Hernandez-Flores received a graduate scholarship from CONACYT, Mexico. Also the authors thank Mr. Rafael Hernández-Vera, and technicians of the Environmental of Biotechnology and Renewable Energy R&D Group, CINVESTAV-IPN for their excellent technical help.

References

[1] Y. Cheng-Dar, L. Chung-Ming, E. M. L. Liou, A transition toward a sustainable energy future: feasibility assessment and development strategies of wind power in Taiwan. Energy Policy 2001; 29: 951-963
[2] B. E. Logan, J. M. Regan, Microbial challenges and harnessing the metabolic activity of bacteria can provide energy for a variety of applications, once technical and cost obstacles are overcome. Environ. Sci. Technol. 2006; 5172–5180
[3] D. Das, T. N. Veziroglu, Hydrogen production by biological processes: a survey of literature. Int J. Hydrogen Energy 2001; 26: 13-28
[4] B. E. Logan, K. Rabaey, Conversion of wastes into bioelectricity and chemicals by using microbial electrochemical technologies. Science 2012; 337: 686-690
[5] J. Hou, Z. Liu, S. Yang, Y. Zhou, Three-dimensional macroporous anodes based on stainless steel fiber felt for high-performance microbial fuel cells. Journal of Power Sources 2014; 258: 204-209
[6] D. Pant, G. V. Bogaert, L. Diels, K. Vanbroekhoven, A review of the substrates used in microbial fuel cells (MFCs) for sustainable energy production. Bioresour. Technol. 2010; 101: 1533–1543
[7] O. Modin, D. J. Gustavsson, Opportunities for microbial electrochemistry in municipal wastewater treatment–an overview. Water Sci. Technol. 2014; 69(7): 1359-1372
[8] H. M. Poggi-Varaldo, A. Carmona-Martínez, A. L. Vázquez-Larios, O. Solorza-Feria, Effect of inoculum type on the performance of a microbial fuel cell fed with spent organic extracts from hydrogenogenic fermentation of organic solid wastes. J. New Mater. Electrochem. Syst. 2009; 12: 49-54
[9] A. L. Vazquez-Larios, O. Solorza-Feria, G. Vazquez-Huerta, F. J. Esparza-Garcia, E. Rios-Leal, N. Rinderknecht-Seijas, H. M. Poggi-Varaldo, A new design improves performance of a single chamber microbial fuel cell. J. New Mater. Electrochem. Syst. 2010; 13: 219-226
[10] Z. Du, H. Li, T. Gu, A state of the art review on microbial fuel cells: A promising technology for wastewater treatment and bioenergy Biotechnol. Adv. 2007; 25: 464–482

[11] O. Lefebvre, A. Al-Mamun, W. K. Ooi, H. Y. Ng, Z. Tang, D. H.C. Chua, An insight into cathode options for microbial fuel cells. Water Sci Technol. 2008; 57: 2031–2037
[12] S. Ouitrakul, M. Sriyudthsak, S. Charojrochkul, T. Kakizono. Impedance analysis of bio-fuel cell electrodes. Biosens. Bioelectron. 2007; 23: 721-727
[13] Y. Yang, G. Sun, M. Xu, Microbial fuel cells come of age. J. Chem. Technol. Biotechnol. 2010; 86: 625-632
[14] Y. Kim, S. H. Shin, I. S. Chang, S. H. Moon, Characterization of uncharged and sulfonated porous poly(vinylidene fluoride) membranes and their performance in microbial fuel cells. Journal of Membrane Science 2014; 463: 205–214
[15] P. Belleville, P. J. Strong, P. H. Dare, D. J. Gapes. Influence of nitrogen limitation on performance of a microbial fuel cell. Water Sci. Technol. 2011; 63: 1752-1757
[16] M. Zhou, M. Chi, J. Luo, H. He, T. Jin, An overview of electrode materials in microbial fuel cells. J. Power Sources 2011; 196: 4427-4435
[17] H. Liu, B. E. Logan, Electricity generation using an air-cathode single chamber microbial fuel cell in the presence and absence of a proton exchange membrane. Environ. Sci. Technol. 2004; 38: 4040–4046
[18] B. E. Logan. *Microbial fuel cells.* John Wiley-Interscience. New Jersey, USA, 2007
[19] W-W Li, S. Guo-Ping, L. Xian-Wei, Y. Han-qing, Recent advances in the separators for microbial fuel cells. Bioresour Technol. 2011; 102: 244-252
[20] G. Hernández-Flores, Interim Report. Sc D Thesis, CINVESTAV-IPN, México, D.F., 2013
[21] X. Xia, J. C. Tokash, F. Zhang, P. Liang, X. Huang, B. E. Logan, Oxygen-Reducing Biocathodes Operating with Passive Oxygen Transfer in Microbial Fuel Cells. *Environ. Sci. Technol*. 2013; *47* (4): 2085–2091
[22] J. Wei, L. P., H. Xia, Recent progress in electrodes for microbial fuel cells. Bioresour. Technol. 2011; 102: 9335-9344
[23] B. E. Logan, B. Hamelers, R. Rozendal, U. Schröder, J. Keller, S. Freguia, P. Aelterman, W. Verstraete, K. Rabaey, Microbial fuel cells: Methodology and technology. Environ. Sci. Technol. 2006; 40: 5181-5192
[24] A. Sivasankaran, D. Sangeetha, Development of *MFC* using sulphonated polyether ether ketone (SPEEK) membrane for electricity generation from waste water. Bioresour. Technol. 2011; 102(24): 11167-11171
[25] F. Zhang, K. S. Brastad, Z. He, Integrating forward osmosis into microbial fuel cells for wastewater treatment, water extraction and bioelectricity generation. Environ. Sci. Technol. 2011; 45: 6690-6696
[26] B. Min, S. Cheng, B. E. Logan, Electricity generation using membranes and salt bridge microbial fuel cells. Water Research. 2005; 39: 1675-1686
[27] F. Kargi, S. Eker, Electricity generation with simultaneous wastewater treatment by a microbial fuel cell (*MFC*) with Cu and Cu-Au electrodes. J. Chem. Technol. Biotechnol. 2007; 82: 658-662
[28] R. Perry, Chemical Engineers Handbook, pp 5.50 & ff 4th ed., McGraw-Hill Co, New York, 1963
[29] S. E. Oh, B. E. Logan, Proton exchange membrane and electrode surface areas as factors that affect power generation in microbial fuel cells. Appl Microbiol Biotechnol 2006; 70: 162–169
[30] D. R. Lovley, E. J. P. Phillips, Organic matter mineralization with reduction of ferric iron in anaerobic sediments. Appl. Environ. Microbiol. 1986; 51: 683-689
[31] A. L. Vazquez-Larios, O. Solorza-Feria, J. Barrera Cortes, E. Ríos-Leal, M. T. Ponce-Noyola, F. Esparza-García, R. G. González-Huerta, N. Rinderknecht-Seijas, H. M. Poggi-Varaldo, Battelle 9th International Conference on Remediation of Chlorinated and Recalcitrant Compounds, May 19-22, 2014. Monterey, CA, USA. Platform Session H8 "Managing recalcitrant compounds in landfill leachate"
[32] D. R. Lovley, E. J. P. Phillips, Rapid assay for microbially reducible ferric iron in aquatic sedimens. Appl. Environ. Microbiol. 1987; 53: 1536-1540
[33] D. R. Lovley, E. J. P. Phillips, Novel mode of microbial energy metabolism: organic carbon oxidation coupled to dissimilatory reduction of iron or manganese. Appl. Environ. Microbiol. 1988; 54: 1472-1480
[34] S. K. Singh, W. Z. Tang, Statistical analysis of optimum Fenton oxidation conditions for landfill leachate treatment. *Waste Manage.* 2013; 33(1): 81-88
[35] L. Damiano, J. R. Jambeck, D. B. Ringelberg, Municipal Solid Waste Landfill Leachate Treatment and Electricity Production Using Microbial Fuel Cells. Appl. Biochem. Biotechnol. 2014; 173: 472–485
[36] APHA. *Standard methods for examination of water and wastewater*. 17th ed. APHA-AWWA-WEF, Washington DC, 1989

Characterization of Cathode/Electrolyte Interphases for IT-SOFCs

L. Baqué[1,*], K. Padmasree[2], A. F. Fuentes[2], A. Serquis[1], A. Soldati[1]

[1]CONICET, CAB-CNEA, Av. Bustillo 9500, (8400) Bariloche, Argentina.
[2]Cinvestav Unidad Saltillo, Apartado Postal 663, Saltillo, México, 25000.
[*]Tel: +54294445100 Ext. 5383; e-mail: baquel@cab.cnea.gov.ar

ABSTRACT

Solid oxide fuel cells (SOFCs) represent an efficient and environmental friendly technology for obtaining electrical power and heat. In recent years, a considerable research effort has been done in order to decrease their operation temperature from 800-1000ºC to the 500-800ºC range. However, the main drawback of lowering SOFC operating temperature is the reduction of cell performance and, hence, each individual component and their interfaces must be optimized. In this work, we studied symmetrical cells composed by high performance nanostructured $La_{0.4}Sr_{0.6}Co_{0.8}Fe_{0.2}O_3$ (LSCFO) cathodes deposited by spin coating on $Ce_{0.8}Y_{0.2}O_2$ (CYO) substrates. CYO electrolytes were synthesized by mechanical milling using two different milling times. Longer milling time produces electrolytes with smaller grain sizes, narrow size distribution and higher density. Bulk conductivity values are similar for both electrolytes, while grain boundary conductivity was slightly higher for the electrolyte prepared with shorter milling time. All this indicates that longer milling time does not improve electrolyte conductivity but, instead, it can have a detrimental effect.

Keywords: Solid Oxide Fuel Cells; Electrolyte; Interphase

1. Introduction

Solid oxide fuel cells (SOFCs) represent an efficient and environmental friendly technology to convert directly hydrogen and fossil fuels into electrical power and heat [1]. These devices require high operation temperature to allow the transport of oxygen ions through the ceramic components of the cell, challenging the long term stability and inducing rapid degradation of the cell. In recent years, a considerable research effort has been done in order to decrease the operation temperature from 800-1000ºC to the 500-800ºC range in the so-called Intermediate Temperature (IT)-SOFCs [2]. One of the materials of choice for IT-SOFCs electrolytes is the ceria based oxides because they present higher oxygen ion conductivities at lower operation temperatures.

SOFC electrolytes must be completely dense in order to avoid the contact between the oxygen fed on the cathode side with the hydrogen supplied at the anode side [1]. Ceria based oxides require high temperatures (up to 1600ºC) for achieving appropriate density. The use of mechanical milling during the synthesis of electrolyte powders allows obtaining uniform ultrafine non-agglomerated particles with high surface area that can be easily compacted and sintered as dense pellets [1,3,4]. In general, the electrolyte performance is evaluated by measuring its electrical conductivity. The use of the Electrochemical Impedance Spectroscopy (EIS) technique is useful to separate the bulk and the grain boundary contributions to electrolyte conductivity. However, these phenomena occurs at an unworkable frequency range and, hence, the accurate evaluation of electrolyte performance must be done at low temperatures. The main drawback of using intermediate temperatures is the increase of the cathode overpotential [5]. Therefore, expensive Pt electrodes (not suitable for practical SOFC operation) are generally used to evaluate the electrolyte performance.

It is also important to note that the performance of the whole cell depends not only of each individual component but also of the interphase between them [6,7]. Therefore, the use of real SOFC cathodes is important when evaluating electrolyte performance. This issue can be overcome with the use of nanostructured mixed conducting oxide cathodes, since these cathodes present considerably low overpotential especially at low temperatures [8,9].

In this work, we have studied symmetrical cells composed of high performance nanostructured $La_{0.4}Sr_{0.6}Co_{0.8}Fe_{0.2}O_{3-d}$ (LSCFO) cathodes deposited by spin coating on $Ce_{0.85}Y_{0.15}O_{2-d}$ (CYO) electrolytes. LSCFO cathodes were synthetized by an acetic acid based method, while the CYO electrolytes were synthesized by mechanical milling. The microstructure of the electrolytes, the cathodes and the cathode/electrolyte interphases was investigated by Scanning Electron Microscopy (SEM). The electrochemical performance of these assemblies was studied by EIS within the 100-600ºC temperature range under pure oxygen.

2. Experimental

$Ce_{0.85}Y_{0.15}O_{2-d}$ (CYO) powders were prepared by mechanical milling [3,4]. Stoichiometric mixtures of high purity (Aldrich, >99+%) CeO_2 and Y_2O_3 oxides were placed in zirconia containers together with 20 mm diameter zirconia balls as grinding media (balls to powder mass ratio = 10:1). Dry mechanical milling was carried out in air in a planetary ball mill by using a rotating disc speed of 350 rpm. Two milling times were used: 1h and 18 h. The obtained powders were uniaxially pressed with a pressure of 5 MPa to form pellets with ~10 mm diameter and ~1.4 mm thickness, and then sintered at 1500ºC for 5 h.

$La_{0.4}Sr_{0.6}Co_{0.8}Fe_{0.2}O_{3-d}$ (LSCFO) powders were synthetized by an acetic acid-based method. Detailed preparation procedure and microstructural characterization of these cathodes were reported elsewhere [6,8,9]. These powders were dispersed in an ink and deposited onto both sides of CYO substrates by the spin coating technique. Cathode covered completely the electrolyte surface with a geometric area of ~0.95 cm^2. Afterwards, these assemblies were heat treated at 900ºC, resulting in a symmetrical cell configuration used for electrochemical measurements. Two LSCFO/CYO/LSCFO cells were obtained: one prepared with CYO powder milled for 1h (from now on called CYO1h) and another one prepared with CYO powder milled for 18 h (from now on denoted as CYO18h).

Impedance measurements were performed in the 100-600ºC temperature range under pure oxygen. Impedance spectra were recorded using a potentiotast/impedance analyzer Autolab (Eco Chemie BV) within 10^{-3}-10^{6} Hz frequency range. A stabilization time of at least 3 h elapsed before each EIS measurement. Gold grids, slightly pressed on electrodes, were used as current collectors. Electrolyte and cathode microstructure was characterized by SEM.

3. Results and discussion

3.1. Scanning electron microscopy

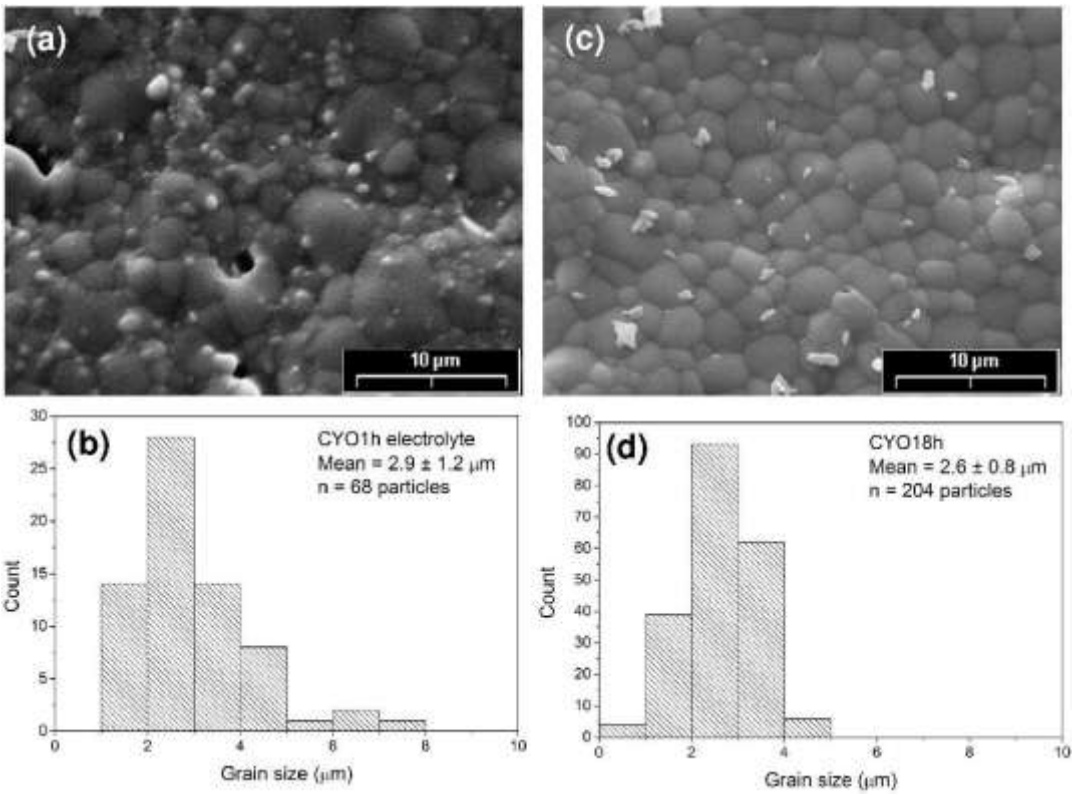

Fig 1. (a,c) SEM images and (b,d) grain size distributions of (a,b) CYO1h and (c,d) CYO18h electrolyte surfaces before cathode deposition.

SEM images from CYO1h and CYO18h electrolyte surfaces before cathode deposition are shown in Figures 1a and c, respectively. The corresponding grain size distribution is plotted in Figures 1b and d, respectively. Statistical analyses indicate that the CYO18h sample presents a smaller mean grain size with a narrow grain size distribution. All this is in agreement with the longer milling time used for preparing the starting powders of the CYO18h electrolyte.

Figure 2 displays SEM images from LSCFO/CYO1h/LSCFO and LSCFO/CYO18h/LSCFO cells after EIS measurements. Cathode surface is similar for both cells (see Figures 2a and b), showing some superficial cracks. It can be also observed that the cathode is composed of submicrometric particles. The thickness and porosity look also similar for both cathodes (see Figures 2c and d). Some closed pores of micrometric sizes can be observed in the CYO1h electrolyte cross-section (Figure 2c), while CYO18h appears fully dense Figure 2d). This suggests that the grain size distribution obtained by using 18 h milling time is more adequate for compacting the powders and sintering denser electrolyte pellets.

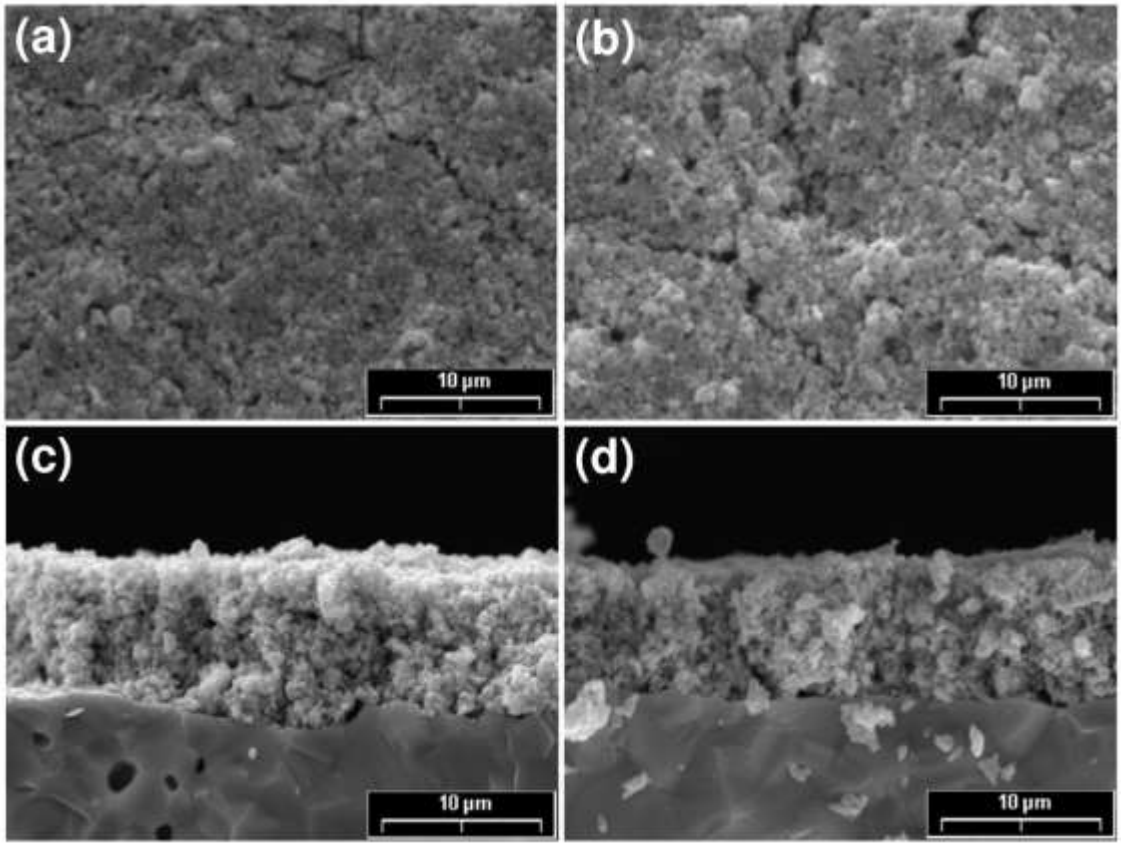

Fig 2. (a,b) Surface and (c,d) cross-section SEM images of (a,c) LSCFO/CYO1h/LSCFO and (b,d) LSCFO/CYO18h/LSCFO symmetrical cells after EIS measurements.

3.2. Electrochemical impedance spectroscopy

A typical impedance spectrum measured under pure oxygen at 250ºC corresponding to the LSCFO/CYO1h/LSCFO cell is shown in Figure 3. Part of an arc can be distinguished at the highest frequencies, a complete arc can be individualized at intermediate frequency, and a small part of a third arc can be observed at very low frequencies. These three contributions were observed for all the measured spectra and were fitted with the equivalent circuit displayed in the inset of Figure 3. The high frequency arc was fitted with a subcircuit composed of a resisitance (R_B) in parallel with a constant phase element (CPE_B), and represents the conduction through the electrolyte bulk. Similarly, the intermediate frequency contribution was fitted with the R_{GB}//CPE_{GB} parallel subcircuit and represents the grain boundary conduction in the electrolyte. The low frequency contribution is related to the oxygen reduction reaction (ORR) at the cathode, including the oxygen ion transfer through the cathode/electrolyte interface. The real part of this later contribution ($R_{cathode}$) was determined with the procedure described in [9].

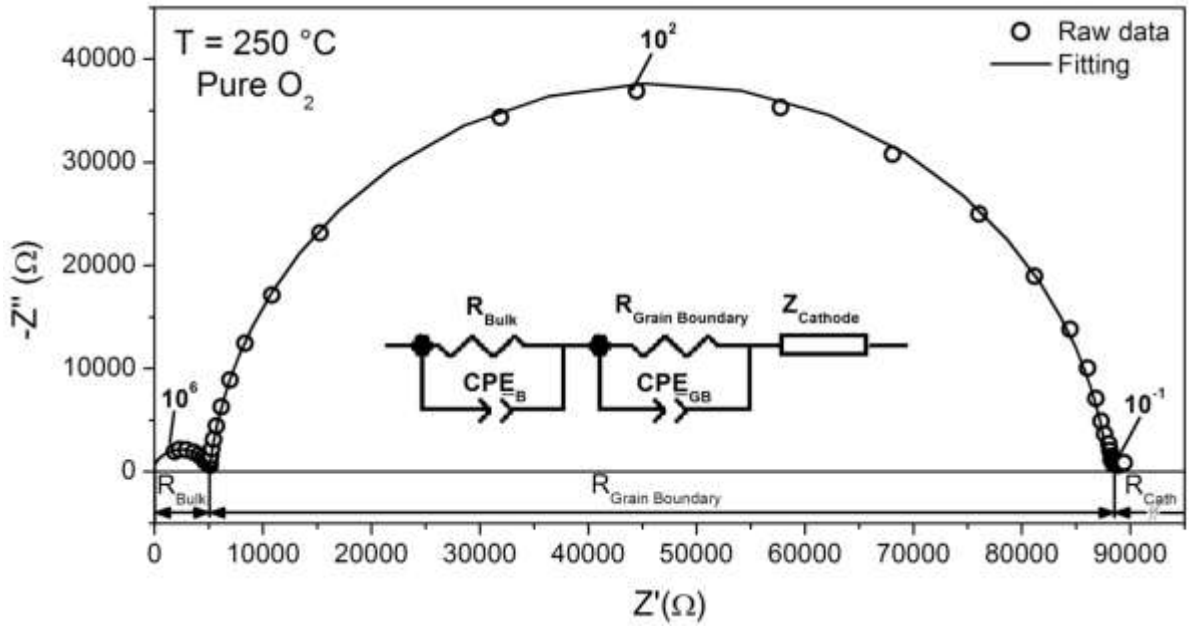

Fig 3. Nyquist plot of an EIS spectrum recorded under pure oxygen at 250°C for the LSCFO/CYO1h/LSCFO symmetrical cell. The numbers indicate the frequency in Hz. The inset shows the equivalent circuit used for fitting.

Electrolyte bulk and grain boundary conductivities can be estimated by using the equation:

$$\sigma_i = \frac{L}{R_i A} \qquad (1)$$

where σ_i is the conductivity (bulk or grain boundary), L is the electrolyte thickness, R_i is the corresponding resistance (estimated by fitting the EIS spectra as described above), and A is the geometric electrolyte area.

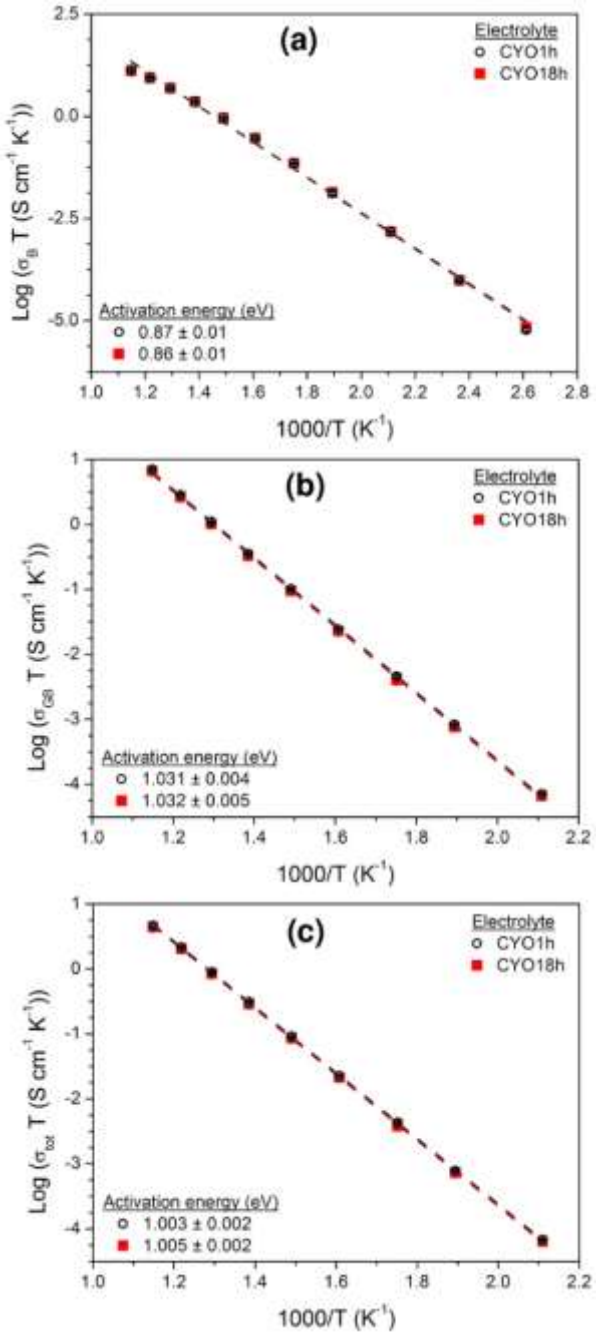

Fig 4. Arrhenius plots of (a) bulk, (b) grain boundary and (c) total conductivity values measured under pure oxygen corresponding to CYO1h and CYO18h electrolytes. The dotted lines represent the linear fitting of values.

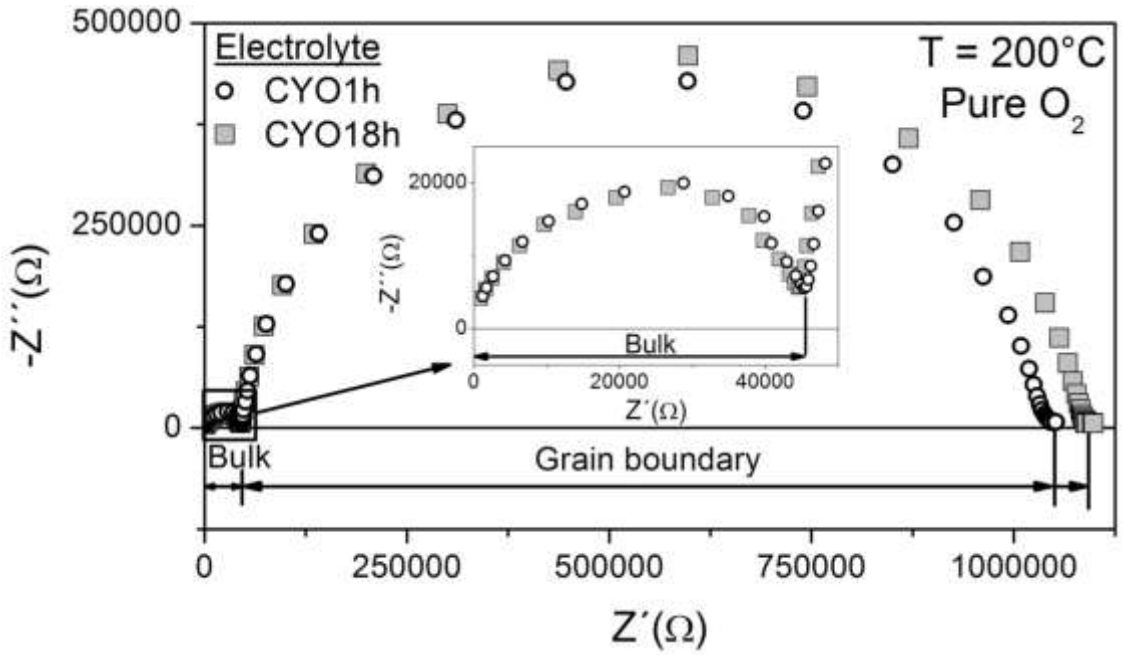

Fig 5. Nyquist plot comparing EIS spectra measured at 200°C under pure O_2 corresponding to CYO1h and CYO18h electrolytes. The inset shows a detail of the high frequency contribution.

Similarly, the total electrolyte conductivity can be estimated by using equation (1) with R_{total} defined as the sum of R_B and R_{GB}. Figure 4 shows the Arrhenius plots of the bulk, grain boundary and total conductivities of CYO electrolytes prepared with 1 h and 18 h milling time. Bulk conductivity values are practically the same for both electrolytes, while grain boundary conductivity is slightly higher (~ 5%) for the electrolyte prepared with 1 h milling time. Therefore, the conductivity values are also ~ 5% higher for the electrolyte prepared with 1 h milling time. This can be clearly observed in Figure 3, where two EIS spectra corresponding to CYO electrolytes prepared with 1h and 18 h milling time are compared. Spectra displayed in Figure 5 were measured at 200°C in pure oxygen but similar results were observed over the entire temperature range.

According to the SEM imaging analysis presented in the previous section, CYO18h electrolyte has slightly smaller grain sizes. It is a priori expected that electrolytes with smaller grain sizes exhibit higher grain boundary conduction. This is because they contain more grain boundaries and grain boundary conduction is, in principle, faster than in bulk [10]. Nonetheless, CYO18h electrolyte presents conductivity values that are 5% lower than those of the CYO1h electrolyte. Several factors can negatively influence grain boundary conduction. A typical example is the presence of impurities that tend to segregate at grain boundary hindering the conduction [11]. In order to elucidate this issue, a study of the composition in the electrolyte grain boundaries is planned in the near future.

Cathode area specific resistance ($ASR_{cathode}$) values were evaluated by using the following equation:

$$ASR_{cathode} = R_{cathode}A \quad (2)$$

$ASR_{cathode}$ values are plotted in Figure 6. LSCFO/CY1h/LSCFO cell shows $ASR_{cathode}$ values about 1.3-1.9 times higher than those corresponding to the LSCFO/CYO18h/LSCFO cell. However, some scatter within $ASR_{cathode}$ values corresponding to the same cathode can be observed. This scattering can be produced by two factors. The first one is the fact that there is some overlap between the electrolyte grain boundary contribution and the cathode contribution, especially at high temperature. In addition, the $R_{cathode}$ values are more than one order of magnitude lower than the total electrolyte resistance (R_{total}) values. Consequently, the estimation of $ASR_{cathode}$ is cumbersome yielding to some errors. The second factor is the apparent inherent scatter found in *ASR* values of cathodes deposited in the identical conditions by spin coating. Variations in *ASR* values up to a factor of 3 were previously reported [8]. All this indicate that the differences in $ASR_{cathode}$ values observed in Figure 6 are within the expected ones for these cathodes and they do not necessarily mean a difference between cathode microstructures and or cathode/electrolyte interphases.

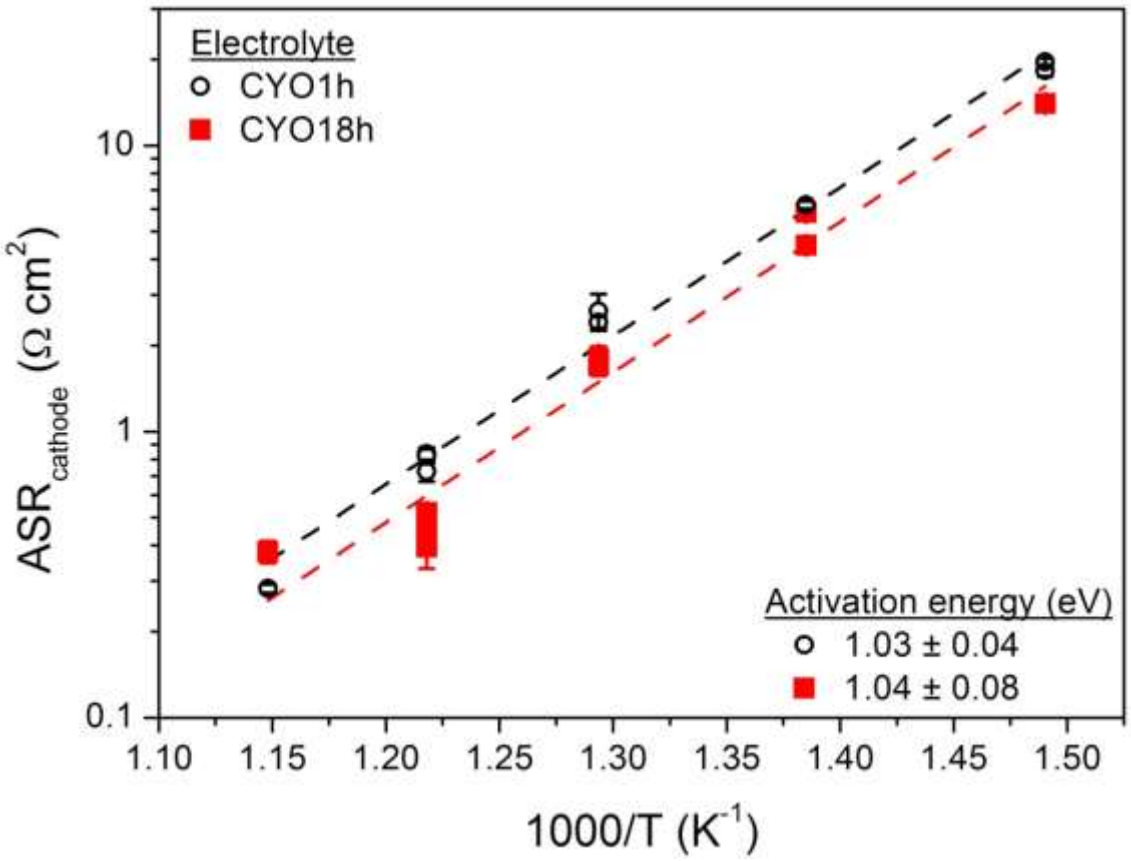

Fig 3. Nyquist plot comparing EIS spectra measured at 200°C under pure O_2 corresponding to CYO1h and CYO18h electrolytes. The dotted lines represent the linear fitting of values.

4. Summary and perspectives

The electrochemical and microstructural properties of LSCF/CYO/LSCFO symmetrical cells were evaluated. CYO electrolytes were prepared by mechanical milling using two different milling times: 1h and 18 h. CYO electrolyte prepared with longer milling time exhibits somewhat smaller grain sizes, a narrow size distribution, and a higher density. Bulk conductivity is similar for both electrolytes while grain boundary and total conductivities are ~5% higher for the electrolyte prepared with 1 h milling time. This indicates that increasing milling time does not improve electrolyte performance but, on the contrary, it can even have a detrimental effect on it.

Acknowledgements

This work is part of a bilateral collaboration project funded by CONICET-Argentina and CONACYT-Mexico (Funding D1765). This research effort was also funded by University of Cuyo, CNEA and ANPCyT-PICT (Argentina).

References

[1] N. Minh, Ceramic fuel cells. J. Am. Ceram. Soc. 1993; 76: 563-588.

[2] B. C. H. Steele, A. Heinzel, Materials for fuel-cell technologies. Nature 2001; 414:345-352.

[3] K. P. Padmasree, R. A. Montalvo-Lozano, S. M. Montemayor, A. F. Fuentes, Electrical conduction and electric relaxation process in $Ce_{0.8}Y_{0.2}O_{1.9}$ electrolyte system. J. Alloys Compd. 2011; 509: 8584–8589

[4] R. A. Montalvo-Lozano, S. M. Montemayor, K. P. Padmasree, A. F. Fuentes, Effect of Ca^{2+} and Mg^{2+} additions on the electrical properties of yttria doped ceria electrolyte system. J. Alloys Compd. 2012; 525: 184-190.

[5] E. Ivers-Tiffée, A. Weber, D. Herbstritt, Materials and technologies for SOFC components. J. Eur. Ceram. Soc. 2001; 21: 1805-1811.

[6] A. Soldati, L. Baqué, H. Troiani, C. Cotaro, A. Schreiber, A. Caneiro, A. Serquis, High resolution FIB-TEM and FIB-SEM characterization of electrode/electrolyte interfaces in solid oxide fuel cells materials. Int. J. Hydrogen Energy 2011; 36: 9180-9188.

[7] A. Montenegro-Hernández, A. Soldati, L. Mogni, H. Troiani, A. Schreiber, F. Soldera, A. Caneiro, Reactivity at the $Ln_2NiO_{4+\delta}$/electrolyte interphase (Ln = La,Nd) studied by electrochemical impedance spectroscopy and transmission electron microscopy. J. Power Sources 2014; 265: 6-13.

[8] L. Baqué, A. Caneiro, M. S. Moreno, A. Serquis, High performance nanostructured IT-SOFC cathodes prepared by novel chemical method. Electrochem. Commun. 2008; 10: 1905-1908.

[9] L. Baqué, E. Djurado, C. Rossignol, D. Marinha, A. Caneiro, A. Serquis, Electrochemical performance of nanostructured IT-SOFC cathodes with different morphologies. ECS Trans. 2009; 25: 2473-2480.

[10] P. Heitjans, S. Indris, Diffusion and ionic conduction in nanocrystalline ceramics. J. Phys.: Condens. Matter. 2003; 15: R1257.

[11] T. S: Zhang, J. Ma, H. Cheng, S. H. Chan, Ionic conductivity of high-purity Gd-doped ceria solid solutions. Mater. Res. Bull. 2006; 41: 563-568.

Mg-M-LiH Alloys Prepared by Mechanical Milling and their Hydrogen Storage Characteristics

K. Suárez-Alcántara[1*], A.F. Palacios-Lazcano[2], T. Funatsu[3]. J. G. Cabañas-Moreno[4]

[1] UNAM-IIM Morelia, Antigua carretera a Pátzcuaro 8710, Col. Ex-hacienda de San José de la Huerta, Morelia, Michoacán, 58190, México.
[2] ESIME Zacatenco, Av. Luis Enrique Erro S/N, Unidad Profesional Adolfo López Mateos, Zacatenco, Delegación Gustavo A. Madero, Distrito Federal, 07738, México.
[3] Techno System CO., LTD, Karasakinaka 3-1-1, Takatsuki-City, Osaka, Japan.
[4] Centro de Investigación y de Estudios Avanzados, IPN, Av. Instituto Politécnico Nacional 2508, México, D. F., 07360, México.

ABSTRACT

$Mg_{96}M_2(LiH)_2$ (M=Y, Zn, Al, Ag), $Mg_{98}(LiH)_2$ and $Mg_{96}(LiH)_4$ powder alloys were produced by ball milling and deliberately air-exposed by 12 hours in order to investigate their hydrogen storage properties. The addition of LiH at the level of 2 mol % had a beneficial effect on the kinetics of the hydriding and dehydriding processes at 300 and 350 °C compared to mechanically milled Mg powders. However, the additions of Al, Ag, Zn and Y had an opposite effect on the hydriding/ dehydriding kinetics. The addition of aluminum provided a small advantage in the capacity of hydrogen storage among the tested materials.

Keywords: Hydrogen storage, Mg-M-LiH alloys, magnesium hydride, mechanical alloying

1. Introduction

Magnesium is the archetypical material for hydrogen storage due to its high theoretical gravimetric hydrogen density of 7.6 wt.%. However, the main drawback of pure Mg/MgH_2 as a potential hydrogen storage material is the high temperature required for the dehydriding reaction, i.e., its high thermodynamic stability [1, 2]. This drawback severely limits the possibility of use in mobile applications; nevertheless, stationary applications for high temperature fuel cells or heat storage are still feasible [3]. Even more, $2LiH+Mg/\ 2Li+MgH_2$ (and the transition metal-doped system) have potential application as negative electrode in rechargeable batteries [4, 5]. A second challenge is to obtain adequate hydriding and dehydriding kinetics. The beneficial influence of ball milling of Mg or MgH_2 is well known in this respect [6, 7, 8]; but still, the dehydriding kinetics are not considered sufficiently adequate. Theoretical and experimental results support the use of different transition metals in order to improve the kinetics and thermodynamics of hydriding/ dehydriding reactions [9, 10, 11, 12, 13, 14, 15, 16, 17, 18, 19]. All together, these effects can be explained by the refinement of particle size and microstructure, increases in surface area, generation of crystalline defects on the surfaces and in the bulk, and the catalytic action of alloying metals or oxides, etc.

In a previous work it has been observed that addition of small quantities of Zn, Al or Ag to Mg during ball milling improves the hydriding kinetics [20]. In the present work, we report the results of synthesizing and testing $Mg_{98}M_2(LiH)_2$ (M = Y, Zn, Al, Ag) alloys, particularly in terms of the quantity of stored hydrogen and the kinetics of the hydriding/ dehydriding process. Also, we analyze the effects of air-exposed Mg alloys as a way to reduce the costs of production, storage and handling in high-purity Argon protective atmosphere. It must be considered that H_2 as fuel can be produced from different raw materials such as water, biomass, catalytic reforming of methane, etc. where the high purity and homogeneity cannot always be guarantee. Also accidental air-exposure of materials during handling or operation is possible. Thus fabrication, processing and testing of our "traditional" materials under more purity-relaxed oxygen conditions must be done if extensive use of hydrogen storage materials is intended.

2. Experimental

2.1 Production of the Powder Alloys

$Mg_{96}M_2(LiH)_2$ (M= Al, Ag, Zn, Y), $Mg_{98}(LiH)_2$ and $Mg_{96}(LiH)_4$ powder alloys were prepared by mechanical milling. The corresponding molar quantities of elemental powders of Mg, Al, Ag, Zn, Y (99.8 % purity, particle size < 45 µm) and LiH (99.9 % purity, particle size < 3 µm) were used as received from Aldrich. The addition of LiH, in lieu of metallic Li, was considered a better approach to ensure the retention of Li in the final, as-milled powder mixtures. The mixtures were prepared in a Fritsch Pulverisette, model 6, milling device, at 350 rpm. The total effective milling time was 60 hours in cycles of 1.5 hours of milling and 0.5 hours of pause. The ball-to-powder ratio was 11:1. The milling vial container (500 ml capacity) and the 50 balls of 1 cm diameter and 4 balls of 2 cm diameter were made of chromium steel. In total, 30 grams of the powders plus 3 ml of methanol (as milling control agent) were charged in the container and sealed under Argon atmosphere.

After milling, the container was cooled to room temperature and the powders were gradually exposed to air for 12 hours. Afterwards, these milled and passivated powders were kept in Ar-filled glass vials.

Subsequently, all handling for characterization was performed at open-air atmosphere. Pure Mg was given the same milling treatment, to be used as a reference and presented whenever needed below.

2.2 Hydriding and dehydriding reactions

Hydrogen storage properties were determined by means of a PCTM-6000 (Techno System Co., LTD) gravimetric equipment operating under chromatographically-pure hydrogen atmosphere. The equipment was carefully calibrated for pressure and temperature effects on the sample holder buoyancy. The alloys were subjected to hydriding and dehydriding activation cycles, before Pressure – Composition Isotherms (PCI) were determined. The activation cycles started with sample annealing at 350°C under dynamic vacuum for 30 minutes. Then, the samples were subject to consecutive hydriding and dehydriding cycles at 350°C. For the hydriding experiments, the hydrogen pressure was increased from 0.1 bar to 30 bar in steady pressure steps, the pressure increase ramp being performed in 25 minutes. The dehydriding process was carried out by reversing these conditions; the pressure decrease ramp was performed in 25 minutes. A single hydriding/dehydriding cycle took 6 hours.

In the PCI determination, the hydrogen pressure increase/decrease steps in PCI measurements were 0.1 bar in the 0.1-1 bar interval and 1 bar in the 1-30 bar interval. The PCI measurement was performed in a total time of 16 hours. After that, the temperature was fixed at 300°C and a hydriding/ dehydriding cycle was performed on the same sample. Finally, alloys were heated again at 350°C and exposed to hydrogen at 30 bar for 3 hours for further X-ray diffraction and scanning electron microscopy characterization of the hydrided powders.

2.3 Powder X-ray diffraction

X-ray diffraction (XRD) patterns were taken on a D-500 diffractometer (SIEMENS) using monochromatic CuKα1 (λ = 1.54056Å) radiation. A scanning range from 15° to 80° was used with steps of 0.03° and 5 s per step. XRD patterns were taken without any atmosphere-protective layer, the samples being flat pressed in the sample holder. The MUAD software was used for XRD data processing [21].

2.4 Scanning electron microscope

The as-milled and hydrided alloys were observed in a XL/SFEG/SIRION SEM microscope (FEI Company) at 5 and 15 kV. A few milligrams of sample were attached to a carbon tape and transferred to the microscope chamber. All handing was performed in open air.

3. Results

3.1 XRD and SEM Characterization of as-Milled Powders

XRD patterns of as milled powders are shown in Figure 1. The diffraction peaks corresponding to magnesium, the major component, were clearly defined. Minor Fe contamination from the milling operation produced a small peak at about 44.5° in 2θ; Rietveld refinements (and EDS analysis, see below) account for less than 2 wt. % of Fe. The slight shifts in Mg peaks positions indicate a small distortion in cell lattice compared to the values found for as-milled pure Mg (Table I, Mg ICSD-642651). These distortions can be attributed to alloying effects. The addition of LiH produced minor distortions in the Mg lattice in $Mg_{98}(LiH)_2$ and $Mg_{96}(LiH)_4$, as indicated in Table 1. A noticeable lattice contraction was observed in $Mg_{96}Al_2(LiH)_2$, probably due to the smaller atomic size and larger valency of Al compared to

Mg. The $Mg_{96}Al_2(LiH)_2$ mixture presented the larger contraction in the Mg lattice among the tested materials. Lattice contraction was also observed in $Mg_{96}Ag_2(LiH)_2$ and $Mg_{96}Zn_2(LiH)_2$, but to a lesser extent compared to $Mg_{96}Al_2(LiH)_2$. In the $Mg_{96}Y_2(LiH)_2$ powder mixture, the unit cell contraction was only detected in the "c" axis. Table I collects the refined Mg cell lattice parameters calculated for our materials.

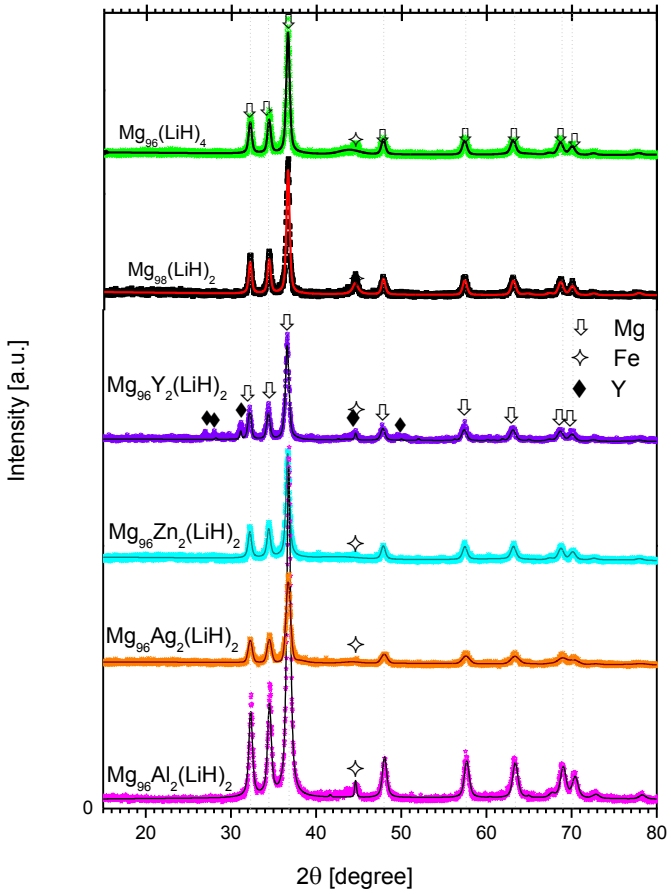

Figure 1. XRD patterns of as-milled and air-exposed powders. Dots: experimental patterns. Line: refined patterns.

Table I. Unit Cell parameters and crystallite size of as-milled materials estimated from XRD refinement.

As-Milled Material	Mg unit cell [Å] ICSD-642651 a=b=3.2094 Å c=5.2108 Å	Mg crystallite size [nm]

Mg	a=b=3.2096 ± 2 x 10^{-4} Å c=5.2129 ± 5 x 10^{-4} Å	36.4 ± 3.9
$Mg_{98}(LiH)_2$	a=b=3.2114 ± 4 x 10^{-4} Å c=5.2126 ± 8 x 10^{-4} Å	37.4 ± 1.0
$Mg_{96}(LiH)_4$	a=b=3.2090 ± 2 x 10^{-4} Å c=5.2084 ± 6 x 10^{-4} Å	40.2 ± 0.6
$Mg_{96}Al_2(LiH)_2$	a=b=3.1949 ± 2 x 10^{-4} Å c=5.1904 ± 5 x 10^{-4} Å	27.8 ± 0.3
$Mg_{96}Ag_2(LiH)_2$	a=b=3.2002 ± 5 x 10^{-4} Å c=5.1927 ± 9 x 10^{-4} Å	97.7 ± 14.3
$Mg_{96}Zn_2(LiH)_2$	a=b=3.2080 ± 5 x 10^{-4} Å c=5.2080 ± 9 x 10^{-4} Å	30.4 ± 0.3
$Mg_{96}Y_2(LiH)_2$	a=b=3.2097 ± 5 x 10^{-4} Å c=5.2093 ± 9 x 10^{-4} Å	33.3 ± 0.8

Mg crystallite sizes estimated by means of the Rietveld refinement of the X-ray patterns of the as-milled materials are also collected in Table I. The data reveal that ball milled $Mg_{96}Al_2(LiH)_2$, $Mg_{96}Zn_2(LiH)_2$ and $Mg_{96}Y_2(LiH)_2$ had crystallite sizes of about 30 nm; i.e., a slight reduction from the ~35-40 nm of pure Mg, $Mg_{98}(LiH)_2$ and $Mg_{96}(LiH)_4$ powders. The calculated value for $Mg_{96}Ag_2(LiH)_2$ was significantly different from all other samples, presenting a crystallite size of about 100 nm.

Despite the affinity of Mg for oxygen and the exposure of the as-milled powders to air at the time of removing them from the milling vial, no clear indication for the formation of crystalline MgO is found in the XRD patterns of Fig. 1. We will come back to this point in the Discussion section.

The as-milled powders were extensively agglomerated. The agglomerate size shows a wide dispersion, as illustrated on the SEM micrograph displayed in Fig. 2 (see supplementary file for more SEM pictures of all materials). Most agglomerates possess sizes in the interval of 1 - 10 μm. Nevertheless, individual particles can be observed with sizes clearly below 1 μm. In many instances, the SEM images provide evidence for the occurrence of cold-welding among small particles during milling, as the mechanism of formation of the agglomerates.

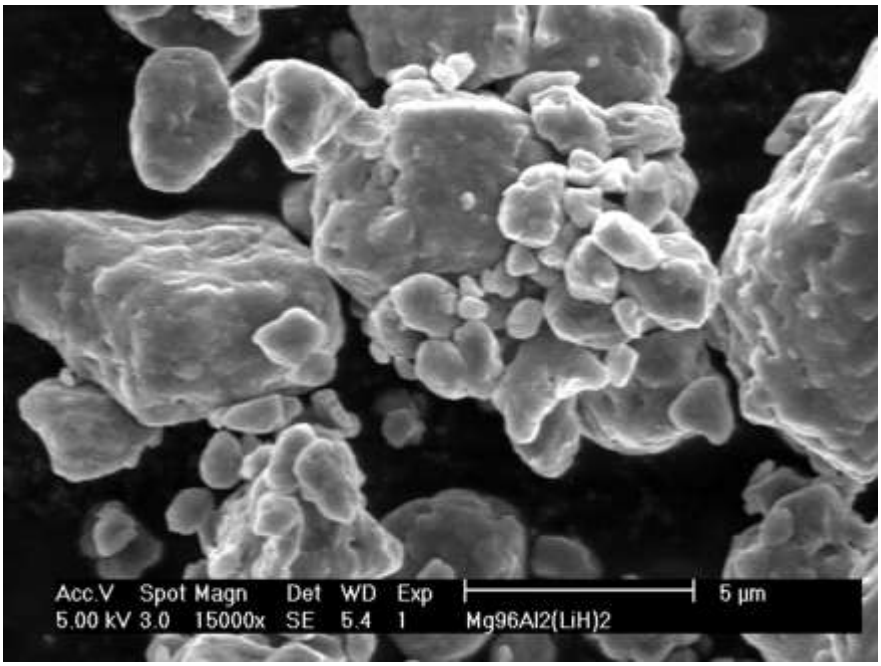

Figure 2. SEM micrograph of as-milled and air-exposed $Mg_{96}Al_2(LiH)_2$.

3.2 Hydriding and Dehydriding Experiments

Figure 3 presents the $Mg_{98}(LiH)_2$ cycling behavior at 350°C as representative of all our tested materials. The hydrogenation at the first cycle was slow and incomplete. As cycling proceeded the hydrogen uptake and hydriding/dehydriding kinetics were improved. Figure 4a presents the first 60 min of the absorption part of the third hydriding/ dehydriding treatment applied to all the mechanically milled powders at 350°C. The pressure increase up to 30 bar is also plotted (grey line). Results for as-milled Mg powders are included for comparison. Mg absorbed about 5.0 wt. % H_2 in 60 min and 5.1 wt. % at the end of experiment; i.e. the smaller value of hydrogen uptake of all the studied alloys. The $Mg_{98}(LiH)_2$ and $Mg_{96}(LiH)_4$ mixtures present the fastest kinetics, with a maximum hydrogen uptake of about 5.5 wt. %. In both materials the hydriding reaction is completed in 24 minutes. The $Mg_{96}Al_2(LiH)_2$ mixture also showed good hydriding kinetics and good hydrogen uptake. This mixture completed the hydrogen uptake in 36 minutes; it absorbed 6.3 wt.% H_2. Among the ternary alloys, the $Mg_{96}Ag_2(LiH)_2$ mixture presented the slowest hydriding kinetics, even slower than Mg. After 63 minutes, time to complete the hydrogen uptake, $Mg_{96}Ag_2(LiH)_2$ stored 5.8 wt.% of H_2. $Mg_{96}Zn_2(LiH)_2$ presented kinetics similar to Mg; after 45 minutes at the hydriding conditions it absorbed 5.2 wt.% as maximum amount of H_2. $Mg_{96}Y_2(LiH)_2$ powders presented good kinetics, the reaction is essentially completed in 27 minutes (5.3 wt.% H_2) and the maximum amount of 5.6 wt.% at the end of experiment. Table II condenses the hydriding characteristics of all the materials tested in the present work. These values are reported at the time of reaching 80% of the maximum hydrogen uptake (α=0.8, where α is the transformed fraction, i.e. the ratio between the current hydrogen uptake and the final hydrogen uptake) and at the end of experiment (140 minutes).

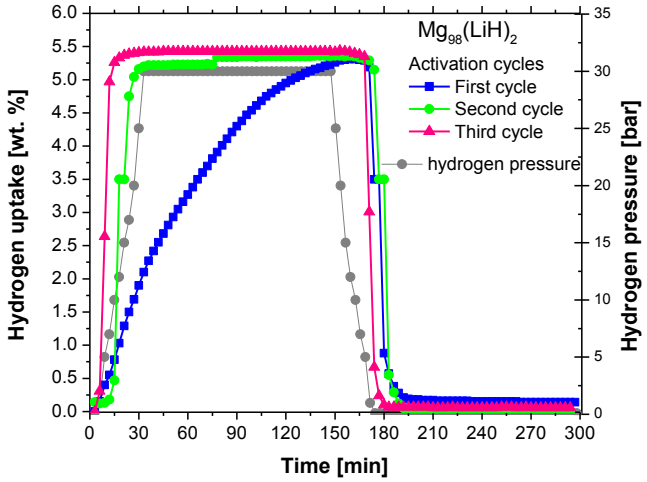

Figure 3. $Mg_{98}(LiH)_2$ cycling behavior at 350°C.

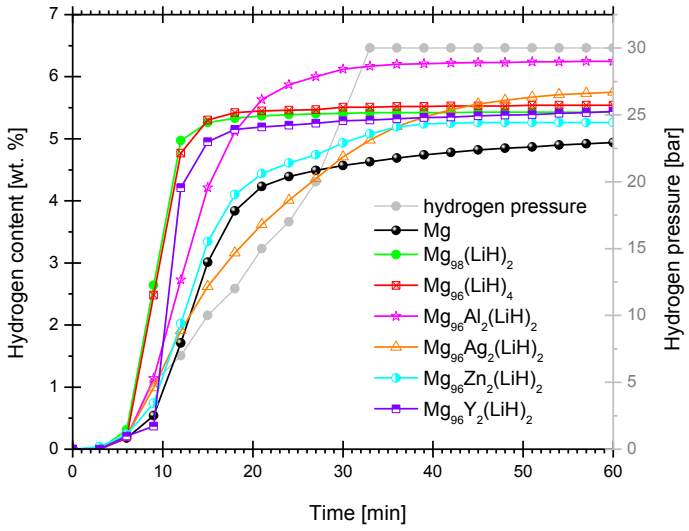

Figure 4a. Hydriding stage at 350°C in the mechanically alloyed powders and pure Mg.

Table II. Summary of hydriding characteristics at 350 and 300 °C. In parenthesis, values from the PCI curves.

Material	350°C / 30 bar		300°C / 30 bar	
	t_{sat} [min] *	Hydrogen content [wt.%] (theoretical; max‡; PCI)	t_{sat} [min]*	Hydrogen content [wt.%] (max‡; PCI)
$Mg_{98}(LiH)_2$	11	7.55; 5.4; 5.3	13	5.3; 5.3
$Mg_{96}(LiH)_4$	12	7.51; 5.6; 5.5	15	5.4; 5.3
$Mg_{96}Al_2(LiH)_2$	18	7.40; 6.3; 6.0	21	6.1; 6.0
$Mg_{96}Ag_2(LiH)_2$	30	6.96; 5.8; 5.5	28	5.2; 5.2
$Mg_{96}Zn_2(LiH)_2$	19	7.18; 5.3; 5.0	36	5.0; 4.9
$Mg_{96}Y_2(LiH)_2$	13	7.06; 5.6; 5.8	24	5.6; 4.8
Mg	20	7.60; 5.1; 4.9	23	5.1; 5.1

* α= 0.8 of reaction yield

‡ at 140 min.

The corresponding hydriding processes at 300°C and 30 bar are presented in Fig. 4b (first 60 minutes). At this temperature, $Mg_{98}(LiH)_2$ and $Mg_{96}(LiH)_4$ had the fastest kinetics, completing the reaction in 30 minutes. The $Mg_{96}Al_2(LiH)_2$ mixture showed again the highest hydrogen uptake (6.1 wt.%), completed in 39 minutes. $Mg_{98}Ag_2(LiH)_2$ and $Mg_{96}Zn_2(LiH)_2$ showed the slowest hydriding kinetics, even slower than Mg. The hydriding reactions in these materials were completed in 105 and 129 minutes, respectively. $Mg_{96}Y_2(LiH)_2$ and Mg presented similar slower kinetics and hydrogen uptake (about 57 minutes to

saturate; 5.3 wt.% and 5.0 wt.%, respectively). Table II summarizes the features of the hydriding processes displayed in Fig. 4b.

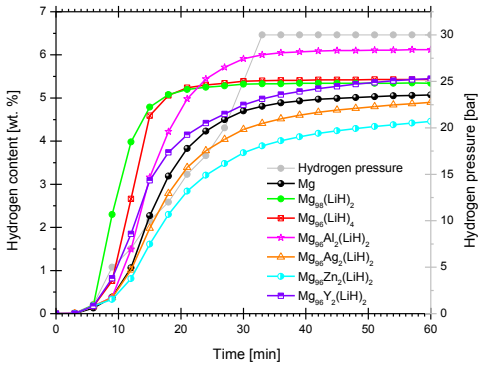

Figure 4b. Hydriding stage at 300°C in the mechanically alloyed powders and pure Mg.

Fig. 5a presents the results of the dehydriding experiments at 350°C. It should be noted that the thermogravimetric equipment used in our experiments was programmed with steps of small pressure changes; large changes in pressure could lead to disturbances. Therefore, the initial time for this stage was taken when the pressure was still 30 bar (grey line); actually, the dehydriding reaction started at about 5 bar for $Mg_{98}(LiH)_2$ and $Mg_{96}(LiH)_4$ (18 minutes) and at about 0.1 bar for the ternary alloys (24 minutes). The times for completion of the dehydriding stage at 350 °C are collected in Table III. The values are reported as "effective" values, by taking time zero as the minute 18 (5 bar) for the binary materials and 24 (0.1 bar) for the ternary materials, i.e., the actual pressures at which the dehydriding stage started. $Mg_{98}(LiH)_2$ and $Mg_{96}(LiH)_4$ presented a clear improvement on dehydriding kinetics compared with Mg. The reaction is completed in a few minutes for the binary alloys. With some minor differences, the dehydriding kinetics of the Al- and Ag-containing ternary alloys followed the same behavior than Mg. Some hydrogen content (< 0.4 wt.%) seem to remain in some of the alloys according to the curves in Fig. 5a, but this amount may be within the accuracy (zero level) of the testing procedure. The Zn- and Y-containing ternary alloys showed a slight kinetic improvement compared to Mg.

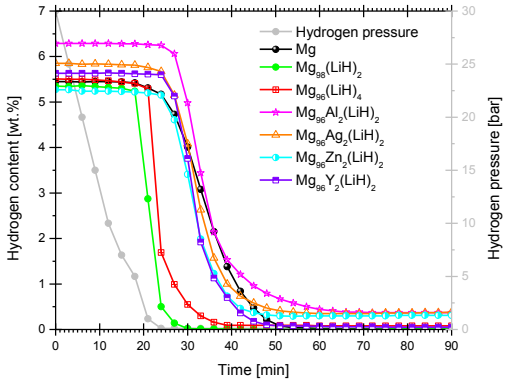

Figure 5a. De-hydriding stage at 350°C in the mechanically alloyed powders and pure Mg.

Table III. Summary of dehydriding characteristics at 350 and 300 °C.

Material	350°C / 0.1 bar		300°C / 0.1 bar	
	t_{end} [min]* ϟ	H remaining after 140 min [wt.%]	t_{end} [min]* ϟ	H remaining after 140 min [wt.%]
$Mg_{98}(LiH)_2$	5	0	20	0.2
$Mg_{96}(LiH)_4$	9	0	40	0.3
$Mg_{96}Al_2(LiH)_2$	18	0.4	116	3.0
$Mg_{96}Ag_2(LiH)_2$	16	0.4	>116	2.0
$Mg_{96}Zn_2(LiH)_2$	13	0.3	>116	2.4
$Mg_{96}Y_2(LiH)_2$	12	0	57	0.3
Mg	17	0	>116	4.3

* α= 0.8 of reaction yield

ϟ Effective time (registered time minus the beginning time of reaction); 18 minutes for Mg98(LiH)2 and Mg96(LiH)4; and 24 minutes for Mg and ternary alloys.

Finally, the kinetics of dehydriding at 300 °C are shown in Fig. 5b. The same correction for an "effective" time is considered in this case for the actual pressures at which the dehydriding reactions began. Here again, the process occurs faster in the $Mg_{98}(LiH)_2$ and $Mg_{96}(LiH)_4$ powders (36 and 60 min to completion, respectively; effective time), followed by the $Mg_{96}Y_2(LiH)_2$ powders (~ 87 min).The remaining alloys did not complete the dehydriding stage at this temperature within the 2.5 hours that the experiments were run. However, it can be seen from Fig. 5a and 5b that the dehydriding kinetics were rather similar in the $Mg_{96}Zn_2(LiH)_2$ and $Mg_{96}Ag_2(LiH)_2$ powders. In turn, the $Mg_{96}Al_2(LiH)_2$ and Mg samples exhibited the slowest kinetic behavior. Table III summarizes the features of the dehydriding processes displayed in Figs. 4b and 5b. Hydriding/ dehydriding and PCI details of $Mg_{98}(LiH)_2$ and $Mg_{98}(LiH)_2$ are available in the supplementary file.

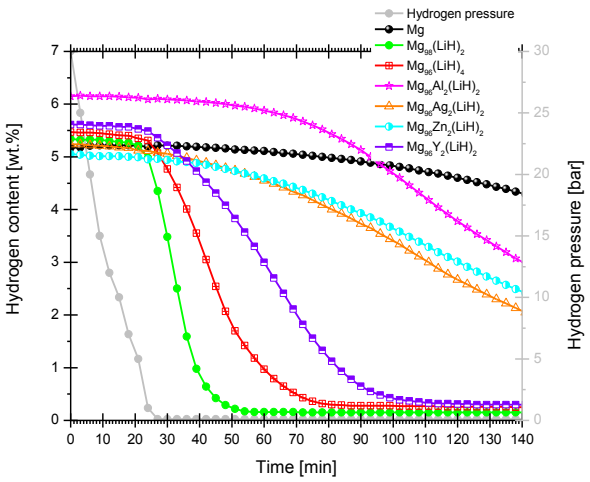

Figure 5b. De-hydriding stage at 300°C in the mechanically alloyed powders and pure Mg.

Due to time-constraining conditions, the PCI curves where not taken strictly at equilibrium conditions; hereafter, these curves are called quasi-PCI curves. The quasi-PCI curves determined at 350 °C are presented in Fig. 6. The upper frame of Fig. 6 displays the quasi-PCI curves of Mg, $Mg_{98}(LiH)_2$ and $Mg_{96}(LiH)_4$. The lower frame presents the ternary alloys quasi-PCI curves. The hydriding curves presented plateaus at similar pressures (~ 8 bar) for all the alloyed powders, whereas for Mg the plateau was not well defined; however, the middle point at the semi-plateau is located about 16 bar. The dehydriding quasi-PCI curves at 350° seem to be established under conditions close to equilibrium; in this case, the plateau pressures vary randomly with alloy composition in the range from approximately 2 bar to 4 bar, with the exception of Mg, for which the plateau pressure is about 0.7 bar. From Fig. 6 it can be observed that alloying with Li induced a reduction in the hydriding/ dehydriding hysteresis compared with Mg. In turn, Al, Ag Zn and Y alloying did not introduce further changes. The reduction of hydriding quasi-plateau pressure and the increase of the dehydriding quasi-plateau pressure upon alloying is a change in the correct direction to improve the hydriding/ dehydriding properties of these air-exposed materials.

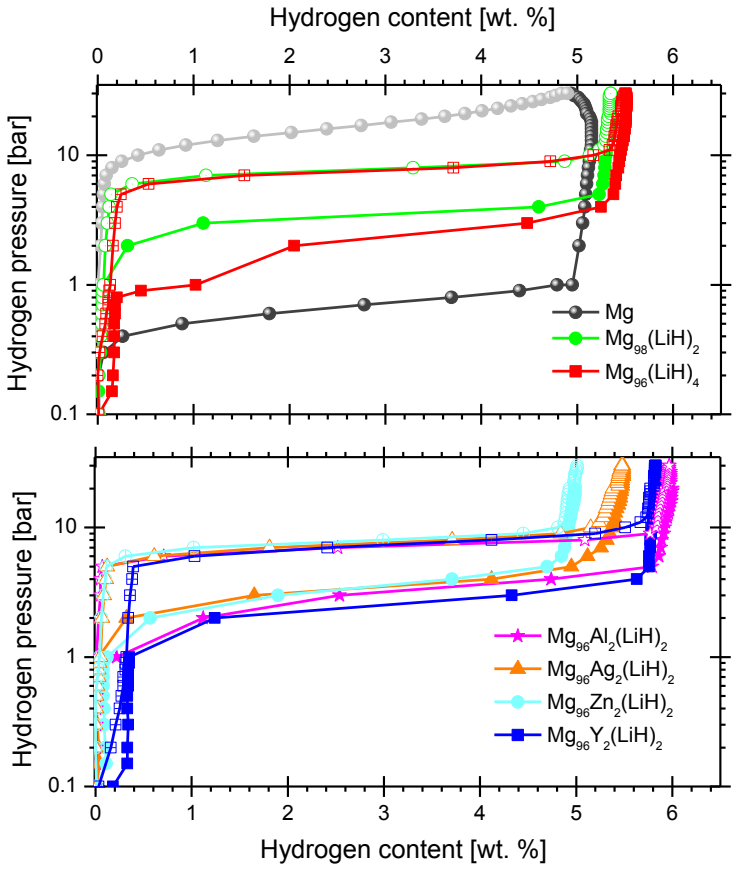

Figure 6. PCI curves determined at 350 °C. Open dots: hydriding. Closed dots: dehydriding.

3.3 XRD and SEM Characterization of Hydrided Powders

Figure 7 presents the XRD patterns from powder mixtures which underwent a final hydriding treatment at 350 °C and 30 bar after the determination of the corresponding quasi-PCI curves. As observed in a number of previous studies [22, 23], the XRD patterns presented a broad peak at the 2θ position expected for the main reflection from MgO. The Rietveld-estimated crystal size of MgO is about 4 - 7 nm. Table IV presents the composition estimated by Rietveld refinement. The main components are MgH_2 and MgO; the remaining components are elemental Mg, and Fe. Table IV also collects the MgH_2 unit cell parameters and crystallite size obtained from the Rietveld refinement of the XRD data. No correlation of the cell parameters with the alloy components was found. Still, the samples $Mg_{96}Al_2(LiH)_2$ and, unexpectedly, $Mg_{96}Zn_2(LiH)_2$ retain the smallest MgH_2 unit cell size. The MgH_2 phase presented a sensible increase of the crystallite size compared with the initial Mg crystallite size in all samples. The $Mg_{98}(LiH)_2$ and $Mg_{96}(LiH)_4$ samples have the smallest crystallite sizes. This corresponds also with the quickest de-hydriding kinetics.

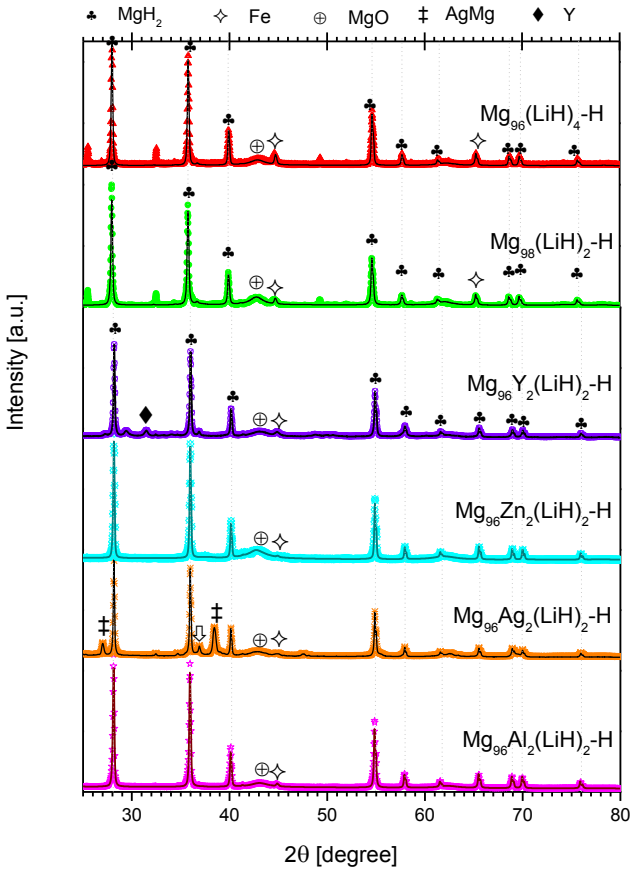

Figure 7. XRD patterns of hydrided powders at 350°C and 30 bar hydrogen pressure. Dots: experimental patterns. Line: refined patterns.

Table IV. Unit cell parameters and crystallite size of hydrided materials at 350°C and 30 bar H_2. Data estimated from XRD refinement.

Hydrided Material	Composition [wt. %]	MgH_2 unit cell [Å] ICSD-161962 a=b= 4.5140 c= 2.9920	MgH_2 crystallite size [nm]	MgO crystallite size [nm]
Mg	Mg: 21.0 ± 1.0 MgH_2: 60.1 ± 1.2 MgO: 18.9 ± 0.7	a=b= 4.5215 ± 4.2 x 10^{-4} c= 3.0233 ± 3.5 x 10^{-4}	57.3 ± 6.2	5.6 ± 0.2
$Mg_{98}(LiH)_2$	Mg: 0.8 ± 0.1 MgH_2: 61.4 ± 3.0 MgO: 36.7 ± 1.0 Fe: 1.0 ± 0.1	a=b= 4.5223 ± 4.6 x 10^{-4} c= 3.0244 ± 3.4 x 10^{-4}	131.7 ± 4.9	7.1 ± 0.2
$Mg_{96}(LiH)_4$	Mg: 0.8 ± 0.1 MgH_2: 67.9 ± 1.0 MgO: 29.2 ± 0.8 Fe: 2.0 ± 0.1	a=b= 4.5217 ± 2.9 x 10^{-4} c= 3.0241 ± 2.4 x 10^{-4}	129.3 ± 4.3	5.9 ± 0.2
$Mg_{96}Al_2(LiH)_2$	MgH_2: 72.9 ± 1.0 MgO: 26.4 ± 0.5 Fe: 0.6 ± 0.1	a=b=4.5182 ± 6.8 x 10^{-4} c= 3.0219 ± 4.8 x 10^{-4}	191.4 ± 17.9	5.1 ± 0.1
$Mg_{96}Ag_2(LiH)_2$	Mg: 5.0 ± 0.3 MgH_2: 54.9 ± 1.0 MgO: 34.8 ± 1.3 MgAg: 5.1 ± 0.1 Fe: 1.0 ± 0.1	a=b= 4.5221 ± 3.1x 10^{-4} c= 3.0241± 2.3 x 10^{-4}	217.9 ± 12.1	4.6 ± 0.2
$Mg_{96}Zn_2(LiH)_2$	MgH_2: 53.0 ± 1.0 MgO: 45.2 ± 0.9 Zn: 1.6 ± 0.1 Fe: 0.2 ± 0.05	a=b= 4.5178 ± 3.6 x 10^{-4} c= 3.0217 ± 2.5 x 10^{-4}	258.4 ± 16.9	4.1 ± 0.1
$Mg_{96}Y_2(LiH)_2$	MgH_2: 67.3 ± 1.0 MgO: 28.8 ± 0.9 Y: 1.7 ± 0.8 Fe: 2.1 ± 0.1	a=b= 4.5196 ± 2.9 x 10^{-4} c= 3.0228 ± 2.1 x 10^{-4}	196.8 ± 8.8	6.8 ± 0.3

A representative SEM picture of the hydrided materials is presented in Figure 8. More images are available as supporting info. The surface of the hydrided materials presented protuberances. This has been related with the nucleation and growing of MgH_2 over Mg particles [24].

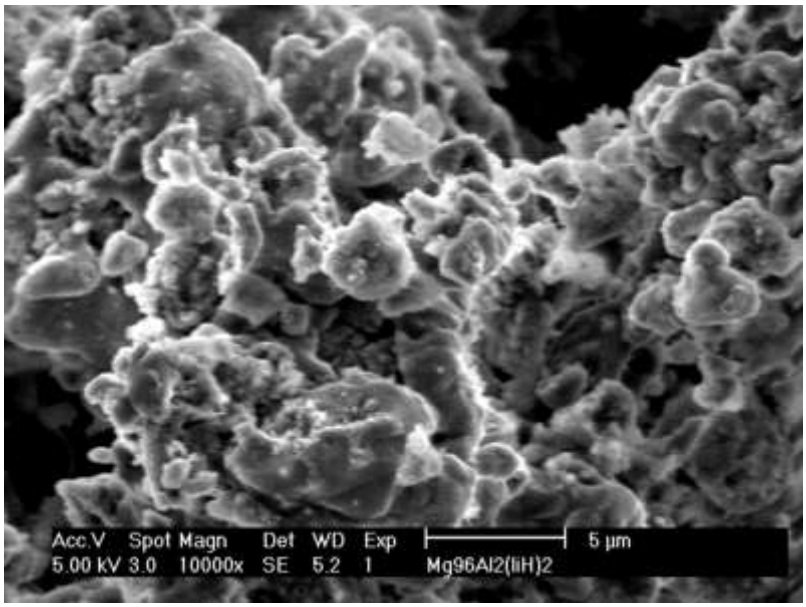

Figure 8. SEM micrograph of hydrided $Mg_{96}Al_2(LiH)_2$ at 350°C and 30 bar hydrogen pressure.

4. Discussion

4.1 LiH effect on Hydrogen Storage Properties

The results presented in this paper have indicated a significant accelerating effect of the kinetics of hydriding/ dehydriding reactions in oxide-covered Mg-base alloys by the addition of a small amount of LiH. Interestingly, the addition of 2 mole% LiH had a significantly higher accelerating effect than a larger addition of 4 mole%. In terms of the times to reach uptake saturation and complete dehydriding (Tables II and III); the kinetics in the $Mg_{98}(LiH)_2$ mixture improved by a factor of 2 in hydriding, and at least by 3 in dehydriding processes in comparison to as-milled Mg. Smith et al. [25] in a recent theoretical study on the substitution of Li^+ for Mg^{2+} in MgH_2 indicates that Li doping may enhance the hydrogen diffusion but only to a limited extent determined by an optimal dopant concentration. Liang et al. [26] and Huot et al. [27] previously reported some hydrogen storage properties of Mg-Li alloyed powders produced by mechanical alloying. In the work of Liang et al., the amount of Li was 10 at.%, but vanadium and graphite were also added in the amounts of 2.5 at.% and 2 wt.%, respectively [26]. Despite the expected catalytic activity of vanadium in this material, the reported kinetics of hydriding/ dehydriding processes at 350 °C are comparable to what is shown for our Mg-LiH alloys in Figs. 4a and 5a. On the other hand, the final materials prepared by Huot et al. [27] by lixiviation of Li from a mechanically alloyed Mg- 28 at.% Li

powder mixture, probably contained a small amount of Li (no final chemical analysis was given by the authors). In this case also the kinetics of hydriding/ dehydriding are close to those found in our work, at the same temperature of 350 °C. These authors suggested that the improved kinetics in their materials (as compared to Mg) was mainly the result of a much larger specific surface area in the lixiviated products. Taken together, the work of Liang et al. and Huot et al. seem to be consistent with the results of our own in that a small addition of Li induces considerably beneficial kinetics effects in the hydrogen storage properties of Mg powders.

The mechanisms by which Li influences the hydrogen storage characteristics of Mg powders may be complex and are open to debate. In a recent paper, Palacios et al. [28] had shown that a mixed hydride of the composition $Mg_{15}LiH_{32}$ has a lower thermodynamic stability than pure MgH_2 (ΔH_f = - 58.3 kJ·mol^{-1} and ΔH_f = - 71.7 kJ·mol^{-1} respectively); this, by itself, it is usually taken as a good indication of lower decomposition temperatures for the hydride phase [29], or conversely, faster reaction kinetics at a given temperature. A destabilizing effect had been observed in other Li-containing hydrogen storage materials such as $LiBH_4/MgH_2$ [30]. Nonetheless, the full explanation of the hydriding/dehydriding kinetics of our Mg-LiH powders is not solely based on the thermodynamic stability of the different hydrides, but also in structural factors.

4.2 Effect of M (M = Al, Ag, Zn and Y) Additions on Hydrogen Storage Properties

It is clear from the kinetics and PCI data (Figs. 4 to 6) that the addition of Ag, Zn and Y in the ternary powder mixtures did not represent any benefit to the hydrogen storage properties over those obtained by the addition of LiH alone. On the contrary, in these cases the ternary addition resulted in unfavorable properties compared to those shown by as-milled Mg, our reference material. Only the addition of Al seems to have improved the hydrogen uptake, but not the hydriding/dehydriding kinetics. Surprisingly, despite the large volume of literature dedicated to the hydrogen storage properties of Mg-based alloys, we have not found reports involving dilute, binary alloys of Al, Ag, Zn or Y in magnesium in which a consistent comparison of their hydriding/dehydriding properties with those of Mg was accomplished. A semi-quantitative comparison of mechanically milled Mg powders with mechanically alloyed Mg-M mixtures (M = Al, Ag, Zn and Y), having a nominal content of 2 at.% M, was presented recently by Palacios et al. [20]. According to their results, the additions of these elements had the effect of reducing the production of MgH_2 in basically all the alloyed powders and hydriding conditions

4.3 Effect of MgO on Hydrogen Storage Properties

An amorphous layer or islands of MgO could be formed during the air-exposure step after ball milling, which would become crystalline when being subjected to higher temperatures, as suggested by the XRD of as-milled and hydrided materials. Shih et al. [31] proposed the mechamisn of MgO formation over Mg as the following successive steps: oxygen chemisorption on the magnesium surface, formation and coalescence of oxide islands and oxide thickening. It was believed for a long time that the formation of oxide layers prevented at all further hydrogen uptake in Mg materials [32]. However, it was recently reported that the addition up to 10 wt.% of MgO to MgH_2 can reduce the dehydriding temperature to 262°C [33]. Barkhordarian et al demonstrated the potential use of metal oxides as suitable catalyst for hydrogen storage purposes [34]. In both reports, the metal oxides were milled together with the MgH_2. Borgschulte et al. [35] demonstrated that a surface layer of MgO is able to recombine atomic hydrogen. Friedrichs et al. performed a hydrogen desorption kinetics study of air- exposed Mg catalyzed with 2 mol % of Nb_2O_5 [36]. In that study; in the sample exposed to air for 24 hours, the hydrided Mg was able to

desorb about 3 wt.% hydrogen at 300°C and 0.001bar in 30 min. The 1 hour air-exposed sample was able to desorb about 4 wt. % under the same conditions. The present work demonstrates that 5.0 to 6.2 wt. % hydrogen storage is still feasible after deliberate air-exposure for 12 hours our Mg alloys. Meanwhile, the amount of MgO formed is apparently between 18.9 and 45.2 wt%. Similar MgO weight fractions had been frequently determined in a number of studies [20, 37]. Let us remark that this drop in storage capacity is a frequent observation in the literature on Mg-based alloys [38, 39, 40, 41]. A second common observation in such cases is the existence of a considerable amount of "disordered" magnesium oxide [39, 40, 42], evidently as a consequence of the high affinity of magnesium for oxygen and the large amount of "fresh" (reactive) surface area found in powders right after their production and/or after being subjected to a dehydriding treatment.

Two phenomenon have been proposed for explaining the observed dehydriding reactions at MgO covered MgH_2 [35]: (1) that the inactive MgO forms nano or micro-cracks, channels or pathways [31, 36], exposing fresh and active Mg/ MgH_2 surfaces; and (2) that the MgO formed on top of MgH_2 is indeed active by the formation of oxygen vacancies during hydrogen exposure and heating [36]. The SEM images (at the micrometer observation size range) do not reveal cracks or fissures on the surface of the powder particles, but the agglomerates look smaller in size. The cycling behavior presented in Figure 3 (common to all our samples), indicates the dificulty of performing the first hydriding reaction. This is consistent with the existence of an obstructive layer. Shih et al. [31] also proposed that the different thermal expansion coefficients of Mg and MgO could lead to cracks in the oxide film. This can explain in part the improvement in the hydriding/dehydriding kinetics after cycling.

5. Conclusions

$Mg_{98}(LiH)_2$, $Mg_{96}(LiH)_4$ and $Mg_{96}M_2(LiH)_2$ (M=Al, Ag, Zn and Y) alloys were produced by mechanical alloying and deliberately air-exposed after milling. Despite the formation of MgO, this alloy production technique is still suitable for hydrogen storage materials and has the potential to reduce the cost of using a high purity protective atmosphere during alloy fabrication and handling. The addition of Al, Ag, Zn or Y to $Mg_{96}(LiH)_4$ does not improve the kinetics of hydriding/ dehydriding. However, there is some improvement with respect to milled, nanocrystalline Mg. A special case is the $Mg_{96}Al_2(LiH)_2$ alloy in which the quantity of hydrogen stored increased as compared to $Mg_{96}(LiH)_4$ and Mg milled under the same conditions. The present results of the air-exposed Mg-based alloys would be useful in the design and practical production of new ternary and quaternary materials for hydrogen storage.

Acknowledgements

KSA and JGCM thank CINVESTAV for technical support. KSA thanks DGECI-UNAM for a mobility grant.

6. References

[1] R. Barbosa, J. Andaverde, B. Escobar, U. Cano, Stochastic reconstruction and a scaling method to determine effective transport coefficients of a PEMFC catalyst layer. J. Power Sources 2011; 196: 1248–1257

[2] A. J. Bard and L. R. Faulkner, Electrochemical Methods, Fundamentals and Applications, 2nd ed., John Wiley & Sons, Inc., N. Y., 2000.

[1] R. C. Jr Bowman, B. Fultz, Metallic Hydrides I: Hydrogen Storage and Other Gas-Phase Applications. MRS Bulletin 2002; 27: 688-693.

[2] L. Schlapbach, A. Züttel, Hydrogen-storage materials for mobile applications. Nature 2001; 414: 353-358.

[3] M. Felderhoff, B. Bogdanović, High Temperature Metal Hydrides as Heat Storage Materials for Solar and Related Applications. Int. J. Mol. Sci. 2009; 10: 325-344.

[4] Y. Oumellal, A. Rougier, G.A. Nazri, J.M. Tarascon, L. Aymard, Metal hydrides for lithium-ion batteries. Nature Materials 2008; 7: 916-921.

[5] M. Ramzan, S. Lebegue, R. Ahuja, Transition metal doped MgH_2: A material to potentially combine fuel-cell and battery technologies. Int. J. of Hydrogen Energy 2010; 35: 10373-10376.

[6] J. Huot, G. Liang, R. Schulz, Mechanically alloyed metal hydride systems. Appl. Phys. A. 2001; 72: 187–195.

[7] K. H. J. Buschow, P. C. P. Bouten, A. R. Miedema, Hydrides formed from intermetallic compounds of two transition metals: a special class of ternary alloys. Rep. Prog. Phys. 1982; 45: 937- 1039.

[8] N. Hanada, T. Ichikawa, S.I. Orimo, H. Fujii, Correlation between hydrogen storage properties and structural characteristics in mechanically milled magnesium hydride MgH_2. Journal of Alloys and Compounds 2004; 366: 269–273.

[9] S. Er, D. Tiwari, G. A. Wijs, G. Brocks, Tunable hydrogen storage in magnesium–transition metal compounds: First-principles calculations. Physical Review B. 2009; 79: 024105-8.

[10] F.P. Luo, H. Wang, L. Z. Ouyang, M. Q. Zeng, J. W. Liua, M. Zhua, Enhanced reversible hydrogen storage properties of a Mg-In-Y ternary solid solution. Int. J. of Hydrogen Energy 2013; 38: 10912-10918.

[11] H. Shao, M. Felderhoff, F. Schuth, C. Weidenthaler, Nanostructured Ti-catalyzed MgH_2 for hydrogen storage. Nanotechnology 2011; 22: 235401-7.

[12] L. Baum, M. Meyer, L. Mendoza-Zélis, Hydrogen storage properties of the Mg/Fe system. Physica B: Condensed Matter 2007; 389: 189-192.

[13] Y. Song, Z. X. Guo, R. Yang. Influence of selected alloying elements on the stability of magnesium dihydride for hydrogen storage applications: A first-principles investigation. Physical Review B 2004; 69: 094205-11.

[14] K. Miwa, A. Fukumo, First-principles study on 3d transition-metal dihydrides. Physical Review B. 2002; 65: 155114-7.

[15] K. Nakatsuka, M. Yoshino, H. Yukawa, M. Morinaga, Roles of the hydride forming and non-forming elements in hydrogen storage alloys. J. Alloys and Compounds. 1999; 293-295: 222–226.

[16] H. Yukawa, T. Matsumura, M. Morinaga, Chemical bond state and hydride stability of hydrogen storage alloys. J. Alloys and Compounds. 1999; 293–295: 227–230.

[17] H. Smithson, C.A. Marianetti, D. Morgan, A. Van der Ven, A. Predith, G. Ceder, First-principles study of the stability and electronic structure of metal hydrides. Physical Review B. 2002; 66: 144107-10.

[18] W. Grochala, P.P. Edwards, Chemical tuning of the thermal decomposition temperature of inorganic hydrides: Computational aspects. J. Alloys and Compounds. 2005; 404–406: 31–34.

[19] N. Hanada, T. Ichikawa, S. Hino, H. Fujii, Remarkable improvement of hydrogen sorption kinetics in magnesium catalyzed with Nb_2O_5. Journal of Alloys and Compounds 2006; 420: 46–49.

[20] A. F. Palacios-Lazcano, J. L. Luna-Sánchez, F. Cruz-Gandarilla, J. G. Cabañas-Moreno, Hydrogen storage in nanostructures Mg-Base alloys. J. Nano Research 2009; 5: 213-221.

[21] L. Lutterotti, Maud: a Rietveld analysis program designed for the internet and experiment integration. Acta Cryst. 2000; A56 (Supplement) s54.

[22] J. Huot, G. Liang, S. Boily, A. Van Neste, R. Schulz, Structural study and hydrogen sorption kinetics of ball-milled magnesium hydride. J. Alloys and Compounds 1999; 293–295: 495–500.

[23] R. A. Varin, S. Lia, A. Calka, Environmental degradation by hydrolysis of nanostructured -MgH_2 hydride synthesized by controlled reactive mechanical milling (CRMM) of Mg. J. Alloys and Compounds 2004; 376: 222–231.

[24] L. Mooij, B. Dam, Nucleation and growth mechanisms of nanomagnesium hydride from the hydrogen sorption kinetics. Phys. Chem. Chem. Phys. 2013; 15: 11501-11510.

[25] K. C. Smith, T. S. Fisher, U. V. Waghmare, R. Grau-Crespo, Dopant-vacancy binding effects in Li-doped magnesium hydride. Physical Review B 2010; 82: 134109-9.

[26] G. Liang, Synthesis and hydrogen strorage properties of Mg-based alloys. J. Alloys and Compounds 2004; 370: 123–128.

[27] J. Huot, S. Bouaricha, S. Boily, J. P. Dodelet, D. Guay, R. Schulz, Increase of specific surface area of metal hydrides by lixiviation. J. Alloys and Compounds, 1998; 266:307–310.

[28] A. F. Palacios-Lazcano, H. Yukawa, M. Morinaga, J. G. Cabañas-Moreno, Stability of mixed magnesium hydrides (Mg-M)H_2 (M = Al, Ag, Ga, Li, Sc, Y, Zn) estimated by density functional theory. (2014) Submitted to Transactions JIM.

[29] W. Grochala, P. Edwards, Thermal decomposition of the non-intersitial hydrides for the storage and production of hydrogen. Chem. Rev. 2004; 104:1283-1315.

[30] T. E. C. Price, D. M. Grant, D. Weston, T. Hansen, L. M. Arnbjerg, D. B. Ravnsbæk, T. R. Jensen, G. S .Walker, The effect of H2 partial pressure on the reaction progression and reversibility of Lithium-containing multicomponent destabilized hydrogen storage systems. J. Am. Chem. Soc. 2011; 133: 13534-13538.

[31] T. S. Shih, Y. B. Liu, P. S. Wei, Oxide films on magnesium alloys. Materials Chemistry and Physics 2007; 104: 497-504.

[32] C. W. Ostenfeld, M. Johansson, I. Chorkendorff, Hydrogenation properties of catalyzed and non-catalyzed magnesium films. Surf Sci. 2007; 601: 1862-1869.

[33] J. R. Ares-Fernández, K. F. Aguey-Zinsou, Superior MgH_2 kinetics with MgO addition: a tribological effect. Catalysts 2012; 2 :330-343.

[34] G. Barkhordarian, T. Klassen, R. Bormann, Fast hydrogen sorption kinetics of nanocrystalline Mg using Nb_2O_5 as catalyst. Scripta Materialia 2003; 49: 213–217.

[35] A. Borgschulte, M. Bielmann, A. Züttel, G. Barkhordarian, M. Dornheim, R. Bormann, Hydrogen dissociation on oxide covered MgH_2 by catalytically active vacancies. Appl. Surf. Sci. 2008; 254: 2377–2384.

[36] O. Friedrichs, J. C. Sánchez-López, C. López-Cartes, T. Klassen, R. Bormann, A. Fernández, Nb_2O_5 "Pathway Effect" on Hydrogen Sorption in Mg. J. Phys. Chem. B 2006; 110: 7845-7850.

[37] A. Montone, J. Grbovic, A. Bassetti, L. Mirenghi, P. Rotolo, E. Bonetti, L. Pasquini, M. Vittori Antisari, Microstructure, surface properties and hydrating behaviour of Mg–C composites prepared by ball milling with benzene. Int. J. Hydrogen Energy 2006; 31: 2088 – 2096.

[38] O. Gutfleisch, S. Dal Toe, M. Herrich, A. Handstein, A. Pratt, Hydrogen sorption properties of Mg–1 wt.% Ni–0.2 wt.% Pd prepared by reactive milling. J. Alloys and Compounds 2005; 404–406: 413–416.

[39] T. Czujko, R. A. Varin, Ch. Chiu, Z. Wronski, Investigation of the hydrogen desorption properties of Mg + 10 wt.% X (X =V, Y, Zr) submicrocrystalline composites. J. Alloys and Compounds 2006; 414: 240–247.

[40] G. Barkhordarian, T. Klassen, R. Bormann, Kinetic investigation of the effect of milling time on the hydrogen sorption reaction of magnesium catalyzed with different Nb_2O_5 contents. J. Alloys and Compounds 2006; 407: 249–255.

[41] G. Liang, J. Huot, S. Boily, A. Van Neste, R. Schulz, Catalytic effect of transition metals on hydrogen sorption in nanocrystalline ball milled MgH_2 –Tm (Tm=Ti, V, Mn, Fe and Ni) systems. J. Alloys and Compounds 1999; 292: 247–252.

[42] A. Révész, D. Fátay, T. Spassov, Hydriding kinetics of ball-milled nanocrystalline MgH_2 powders. J. Mater. Res. 2007, 22: 3144-3151.

Influence of the Synthesis Parameters in CNT Doped with Nitrogen Towards the Electroreduction of Oxygen

Isaías Zeferino González, Ivonne Alonso Lemus, Beatriz Escobar Morales, Ana María Valenzuela Muñiz, Ysmael Verde Gómez[a]

[a] *Instituto Tecnológico de Cancún, Av. Kabah Km. 3, Cancún, Q.R., México, 77500. yverde@yahoo.com*

ABSTRACT

One of challenges in the commercialization of fuel cells is the high cost and scarcity of platinum based catalysts. In addition, there is also the slow kinetics problem in the oxygen reduction reaction (ORR). Therefore, alternative electrocatalysts are needed. Systems based on doped carbon nanostructures (without the use of active metals) have been proposed as a good option to solve both of the drawbacks before mentioned. In the present study, nitrogen doped carbon nanotubes (N-CNTs) were synthesized by a modified chemical vapor deposition method. Pyridine was used as carbon and nitrogen precursor and ferrocene as a metal catalyst for the nanotubes growth. Different synthesis conditions such as temperature of the reactor, carrier gas flow, concentration of the reactants, and vaporizer temperature were studied. The purpose of this parameters variation was to figure out the optimal conditions in which the material achieves the best catalytic activity. The electrocatalytic performance was evaluated towards the ORR by linear sweep voltammetry measurements. A catalyst-coated rotating disk electrode at different rotation rates in 0.5 M H_2SO_4 solution was performed. The results show that the reactor temperature and gas flow had a significantly influence in the materials characteristics and hence the electrocatalytic activity for ORR. The factors that determine the high electrocatalytic activity for ORR of the N-CNTs are discussed.

Keywords: Nanotubes; Carbon; Synthesis.

1. Introduction

The fuel cell uses precious metals in the electrodes to carry out the reactions. Traditionally, Platinum is the best known electro-catalyst for the reaction of oxidation and reduction. However, scarcity, high price and degradation of platinum as a catalyst in the fuel cell represent a challenge to be overcome [1, 2]. In recent years,it has been efforts to reduce the platinum loading on the electrodes of the cell. However, the lack of this noble metal follows the trend of consumption. Therefore, it is necessary to develop new catalytic materials available, cheap and effective to replace Pt based electrocatalysts.

Carbon nanotubes doped with nitrogen have been considered as alternative catalysts for oxygen reduction reaction (ORR) in the cathode electrode of the fuel cell [3]. There are many studies concerning to the synthesis of carbon nanotubes doped with nitrogen atoms using different carbon-nitrogen precursor by chemical vapourdeposition (CVD) method. It has been shown that these materials have high electro-catalytic activity for ORR. Alexeyeva et al. [4] synthesized N-CNTs using acetonitrile as carbon and nitrogen source. They studied the ORRin acid media where analyzes reveal that the nitrogen content in the wall of the nanotubes shows significant activity than nanotubes without doping.Higgins et al. [5] synthesized carbon N-CNTs by CVD method using three different precursor solutions: Ethylenediamine (ED), 1,3-diaminopropane (DAP) and 1,4-diaminobutane (DAB). Their results showed that the precursor solutions which have a higher nitrogen atomic ratio in the N-CNTs yielded better oxygen reduction. The N-CNTs prepared with ED had a nitrogen content of 4.75 at. % and showed a superior activity of ORR than the DAP (2.48 at. %N) and the DAB (1.20 at.% N).Wong et al. [2] obtained N-CNTs through CVD using aniline, diethylamine (DEA) and ethylenediamine (EDA). Analysis revels that the N-CNTs obtained from EDA (6.58 at. % N) was the most active sample forORR in acidic media than aniline (5.99 at. % N) and DEA (4.33 at.% N).Xiong et al. [6] synthesized N-CNT via modified CVD using melamine and urea as different nitrogen precursors.The N-CNTs resulting from the malamine(4.55 at. % N) showed higher performance than urea (2.20 at. % N) forORR. These studies show the important role of nitrogen precursors on the structure of the N-CNTs.

Several N-CNTs studies have been carried out evaluating not only the effect of the nitrogen precursors but also the nitrogen concentration at different C/N ratio. Nevertheless, a few studieshave been made on effect of the different synthesis conditions of N-CNTs on the ORR.This work present the effect of various parameters such as reactor temperature, carrier gas flow rate, concentration of the reactants, and vaporizer temperature over the physical, chemical and electrochemical properties of N-CNTs synthesized with pyridine as nitrogen and carbon source.

2. Experimental

2.1 N-CNTs synthesis

N-CNTs synthesis was carried out by a simple and modified chemical vapour deposition process. Pyridine (99.5%, Merck) was used as carbon and nitrogensource and ferrocene (98%, Aldrich) as a metal catalyst for the nanotubes growth. Vycor tubes (0.7 cm internal diameter and 50 cm length) were utilized as substrate and it was placed into a tubular furnace (Lindberg/blue). Synthesis was carried out by heating

the tube and injecting the precursor solution under argon atmosphere. After the synthesis process the furnace was cooled down at room temperature under argon gas flow. The final products were obtained from Vycor tube subtrate. N-CNTs were treated with concentrated nitric acid (66.5%, J.T. Baker) for 12 h.Four factors were changed during the synthesis process, each one with two levels. The factors and the nomenclature used isshowed in Table 1. 16 experiments were carried out to study the effect of the factors on the electrocatalytic performance of the N-CNTs.

Table 1.Synthesis parameters of N-CNTs

FACTORS	LEVEL	
	Low	High
Solution concentration (g/L)	18 [Y]	36 [X]
Argon gas flow rate (L/min.)	0.5 [B]	1 [A]
Vaporizer temperature (°C)	180 [180]	200 [200]
Reactor temperature (°C)	800 [8]	900 [9]

2.2 Physical and chemical characterization

The Scanning electron microscope (SEM) Vega 3 Tescan was used to study the morphology and topology of the materials. The samples were placed on the copper strips, supported on the sample holder of the microscope. Images were acquired from different areas of the sample, in order to assess their average characteristics. The SEM was also used to determine the elemental composition of the sample by energy-dispersive X-ray spectroscopy (EDS). High Resolution Transmission Electron Microscopy (HRTEM) characterization was carried out on JEOL JEM-2200FS microscope to provide nanoscale images of the samples. For HRTEM analysis, the samples were dispersed in ethanol by sonication and then placed on copper grid support. X Ray diffraction was obtained using a D8 Advanced (Bruker), operated at 40kV and 40 mA. Cu-Kα radiation was used with a wave length λ =1.5418 Å. Raman spectroscopy (LabRAM He-Ne laser 632.8 nm with resolution of 1 cm^{-1}) was utilized in order to investigate the first order Raman scattering of the samples and determine the degree of structural defects present.

2.3 Oxygen reduction reaction activity evaluation

Electrochemical evaluation was carried out in a rotating disk electrode (RDE) using a BASi at different rotation speeds, connected to an Epsilon, whose response was analyzed on a computer with EpsilonEC-200-XP software. The electrochemical cell has three electrodes immersed in a 0.5 M H_2SO_4 solution. The electrodes that were used are: a glassy carbon as working electrode, with a geometric area of 0.07 cm^2, a reference electrode of Ag/AgCl in saturated 3 mol L^{-1}KCl and a platinum wire as counter electrode. Catalyst ink prepared with 5 mg N-CNT mixed with 0.5 mL of ethanol and 30 µL Nafion solution was set in ultrasound bath for 1 h. 20 µL of catalyst ink was deposited on the glassy carbon electrode surface and was subsequently slowly dried at room temperature. The working electrode potential was swept from -0.2 to 1 V vs. Ag/AgCl at a scan rate of 5 mV s^{-1}. Before the test, the electrolyte was saturated with argon gas and a potential sweep was performed in order to obtain a background reading. After the background scan, oxygen gas was introduced to saturate the solution. The experiments were performed at the same scan rate

with different working electrode rotation speeds. All potential values reported are referred to the standard hydrogen electrode (SHE).

3. Results and discussion

The estimated amount of N-CNT samples is reported in table 2. The weight average values of the samples indicate that larger amounts of samples were obtained at 900 °C than N-CNT at 800 °C. On the other hand, using SEM micrographs the N-CNTs morphology was studied. Figure 1 shows micrographs of the synthesized nanotubes a) at 800 °C and b) at 900 °C. Analysis indicates that N-CNTs are well-aligned and uniformly distributed on the support. The nanotubes obtained at 800°C have length between 12 and 24 µm, while the nanotubes at 900°C have some hundreds of µm (except sample 200NNBY9). Thus, when the length of nanotubes is higher also the amount of N-CNTs is increased. Therefore, the length of the nanotubes is a parameter that can be associated with quantity.

Table 2. Yield of N-CNTs synthesis.

N-CNT 800 °C		
Sample	**Length** (µm)	**Weight** (mg)
180NNBY8	24.60 ± 4.88	183.20
180NNAX8	12.77 ± 0.55	115.50
200NNBY8	13.97 ± 2.20	98.53
200NNAY8	21.84 ± 2.41	104.81
200NNAX8	20.50 ± 1.36	148.00

N-CNT 900 °C		
Sample	**Length** (µm)	**Weight** (mg)
180NNBY9	100.00 ± 7.91	526.33
180NNAX9	132.80 ± 11.08	811.29
200NNBY9	38.80 ± 3.96	615.48
200NNAY9	126.72 ± 5.06	765.35
200NNAX9	110.85 ± 5.31	630.89

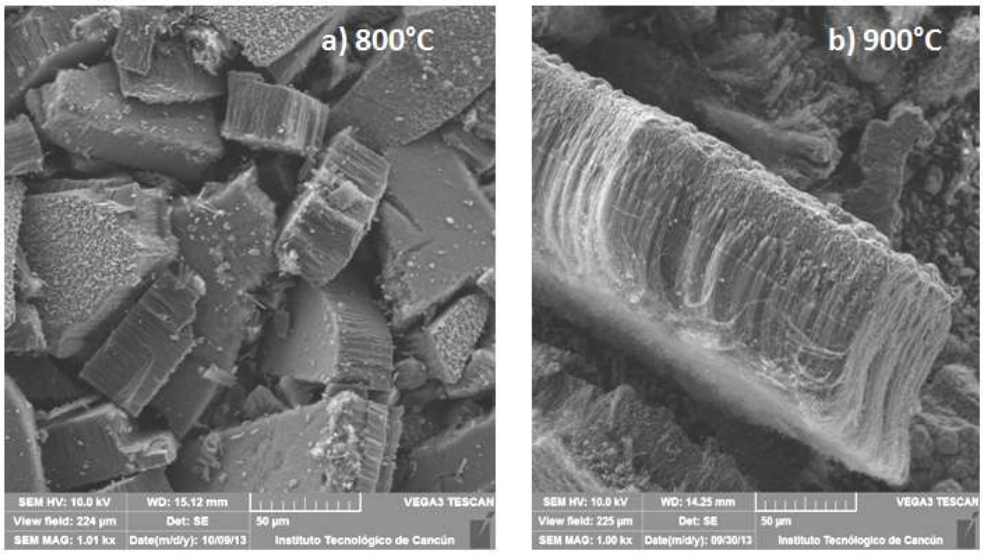

Figure 1. SEM micrographs of N-CNTs at a) 800 °C and b) 900 °C.

Morphology of the materials was also studied by HRTEM (Figure 2). As it can see multiwall carbon nanotubes were obtained with a typical bamboo-like structure; it is common feature observed after incorporation of the nitrogen into carbon lattice, which indicates that the nanotubes are doped with nitrogen [7]. The outer diameter of the carbon nanotubes was estimated, the average values are showed in table 3. The N-CNT at 900°C had higher average outer diameter (84±23 nm) than the N-CNT at 800°C (59±8 nm).

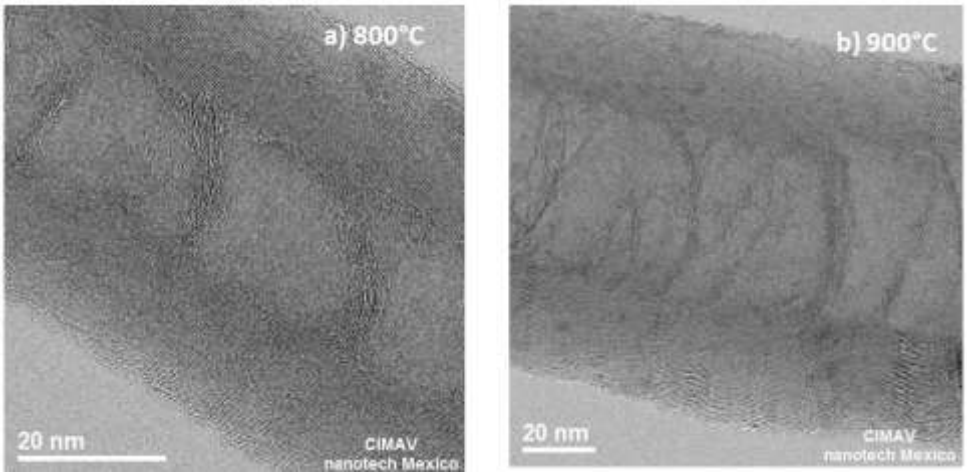

Figure 2. High Resolution Transmission Electron Microscope micrographs of N-CNTs at a) 800 °C and b) 900 °C.

Table 3. Evaluation of the external diameter of the N-CNTs.

N-CNTs at 900°C	
Sample	**Diameter (nm)**
180NNBY9	96.36 ± 11.81
200NNAY9L	80.00 ± 33.17
200NNAX9L	86.04 ± 38.52
180NNAX9L	75.45 ± 13.89
200NNBY9L	83.89 ± 20.43

N-CNTs at 800°C	
Sample	**Diameter (nm)**
180NNBY8	53.64 ± 21.11
200NNAY8L	64.00 ± 13.42
200NNAX8L	62.26 ± 3.60

Table 4. Elemental composition obtained by SEM-EDS.

Sample	**C**	**Fe**	**N**	**O**
	at. %	**at. %**	**at. %**	**at. %**
180NNBY8	79.14 ± 1.31	0.55 ± 0.14	4.95 ± 0.79	13.12 ± 1.69
180NNBX8	85.43 ± 0.59	0.3 ± 0.05	5.1 ± 0.71	7.83 ± 0.23
180NNAY8	82.7 ± 0.66	0.28 ± 0.04	4.62 ± 0.76	10.93 ± 0.35
180NNAX8	82.82 ± 0.41	0.23 ± 0.02	4.29 ± 0.48	11.75 ± 0.13
200NNBY8	80.48 ± 3.86	0.18 ± 0.06	5.43 ± 2.11	7.88 ± 1.27
200NNBX8	83.66 ± 0.74	0.16 ± 0.01	5.45 ± 0.54	9.45 ± 0.62
200NNAY8	87.97 ± 0.48	0.42 ± 0.02	4.29 ± 0.39	6.42 ± 0.72
200NNAX8	82.03 ± 0.5	0.3 ± 0.06	4.17 ± 0.47	12.48 ± 0.31
180NNBY9	86.31 ± 0.86	0.25 ± 0.02	4.86 ± 0.49	7.2 ± 0.27
180NNBX9	86.22 ± 0.56	0.34 ± 0.04	5.53 ± 0.41	6.9 ± 0.18
180NNAY9	84.63 ± 0.55	0.6 ± 0.13	5.25 ± 0.65	8.19 ± 0.48
180NNAX9	84.57 ± 0.59	0.87 ± 0.24	5.01 ± 0.58	8.13 ± 0.7
200NNBY9	87.49 ± 0.54	0.55 ± 0.09	4.91 ± 0.47	5.94 ± 0.27
200NNBX9	87.97 ± 0.35	0.3 ± 0.05	3.99 ± 0.18	7.16 ± 0.26
200NNAY9	84.55 ± 0.63	0.36 ± 0.04	5.6 ± 0.28	8.55 ± 0.25
200NNAX9	84.79 ± 0.72	0.48 ± 0.07	6.09 ± 0.7	7.15 ± 0.36

The elemental atomic composition analysis of carbon, iron, nitrogen and oxygen by SEM-EDS are showed in Table 4. Analysis demonstrates that nitrogen was successfully incorporated into the structure of the nanotube. SEM-EDS analyses revealed that the content of nitrogen in the nanotubes were slightly different between N-CNT at 900 °C (5.15±0.62 at. %) and N-CNT at 800 °C (4.78±0.51 at. %). On the

other hand, comparison of averages values of the N-CNTs at 900 °C indicate that the synthesized nanotubes with flow 1 L/min. nitrogen content (5.48±0.55 at. %) was higher than 0.5 flow L/min. (4.82±0.38 at. %)

Figure 3 shows of X-ray diffraction patterns obtained from the N-CNTs. It has also been included the pristine CNT for comparisons. Diffraction patterns exhibit intensity 2H graphite phase, which is associated with the formation of N-CNTs multiwall. The first peak located approximately at 26° corresponds to the carbon (002) which forms the hexagonal shape of the graphite. Other peaks located at 42.5°, 44.5° and 53.9 correspond also to the crystallographic planes of graphite at (100), (101) and (004) respectively [8]. The peaks marked with an asterisk (*) correspond to iron carbide (Fe_3C) [9]. In the diffraction pattern was also found Fe_2O_3 located 43.5° (+). The iron comes from residual catalytic agent, unreacted and oxidized during sample handling [10, 11].The peak around 18° (x) corresponds to SiO_2, which comes from the residual Vycor tube. The diffraction peaks of the N-CNTs are slightly displaced to the right with respect to the diffraction patterns of the CNT pristine, which could be attributed to the distortion in the crystal lattices and the vacancies caused by the introduction of nitrogen atoms into the carbon networks. Besides, the intensity of diffraction peaks of the N-CNTs in the plane (002) are obviously weaker than that of virgin CNT, because structural defects of carbon nanotubes [12].

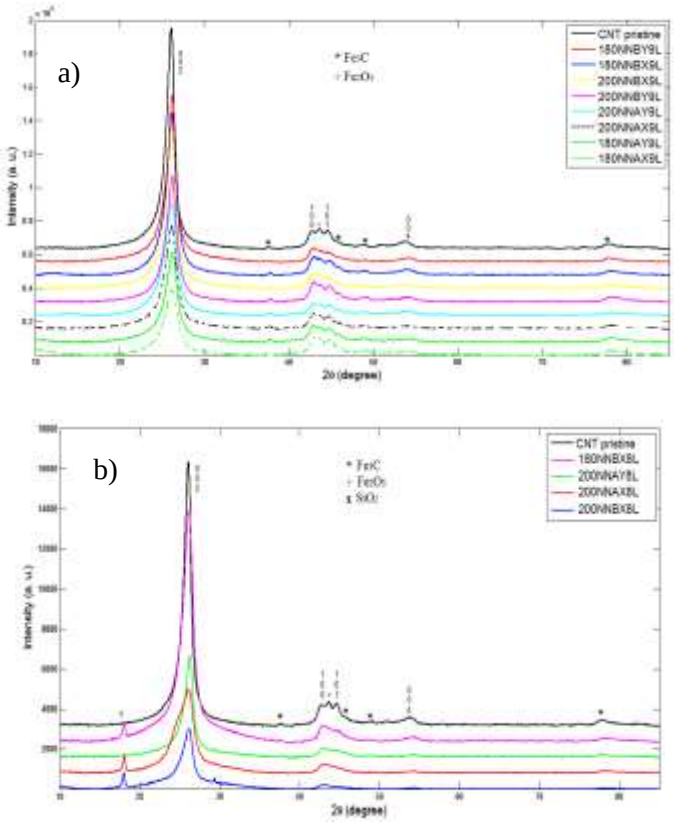

Figure 3. XRD patterns of CNT pristine and N-CNTs at a) 900 °Cand b) 800 °C.

Raman spectroscopy was performed in order to btain information about the crystallinity of the N-CNTs. Figure 4 show two main peaks around 1333 cm^{-1} and 1588 cm^{-1} corresponding to the D band and G band respectively. The D band is known as the band of disorder, which is caused by the atomic displacement and lattice defects. While the G band indicates the formation of nanotubes well graphitized [13]. The ratio I_D/I_G close to zero suggesting that carbon has a high ordered structured; while a high ratio indicates more defects present in the carbon nanotubes [14, 6]. Analysis of intensity ratio I_D/I_G show in Table 5 demonstrate that N-CNTs synthesized at 900 °C showed higher structural disorder than 800 °C; it can be attributed to the incorporation of nitrogen into the carbon lattice. Another important factor affecting the N-CNTs structure is the argon gas flow; N-CNTs synthesized with low flow (0.5 L/min.) have greater structural defects than carbon nanotubes with high flow (1 L/min).

The G' band (or 2D) around 2657 cm^{-1} is an overtone of the D band. The intensity ratio $I_{G'}/I_G$ measures the average degree of crystalline perfection [15, 16]. The intensity ratio $I_{G'}/I_G$ shows that the smoothing of N-CNTs decrease considerably with respect to CNT pristine, which it can be caused by the incorporation of nitrogen into the carbon.

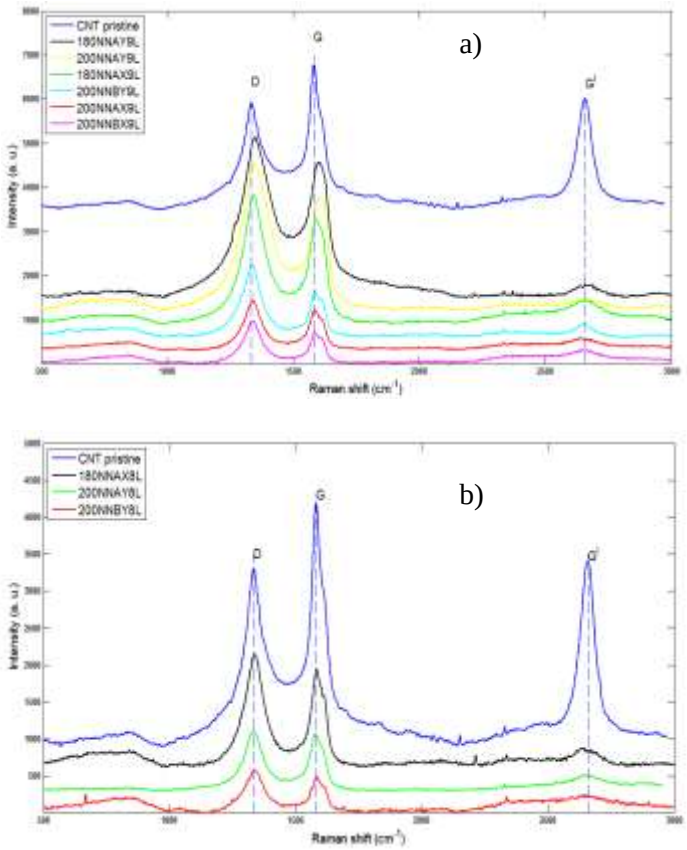

Figure 4. Raman spectra of CNT pristine and N-CNTs ata) 900 °C and b) 800 °C.

Table 5. I_D/I_G and $I_{G'}/I_G$ ratio from Raman spectra of N-CNTs.

Sample	I_D/I_G	$I_{G'}/I_G$
200NNBY9L	1.44 ± 0.11	0.45 ± 0.13
200NNBX9L	1.34 ± 0.01	0.51 ± 0.06
180NNAY9L	1.25 ± 0.06	0.18 ± 0.07
200NNAX9L	1.25 ± 0.04	0.37 ± 0.05
200NNAY9L	1.24 ± 0.05	0.14 ± 0.02
180NNAX9L	1.19 ± 0.03	0.21 ± 0.03
CNT pristine	0.7 ± 0.04	0.83 ± 0.07
200NNBY8L	1.29 ± 0.17	0.5 ± 0.13
200NNAY8L	1.07 ± 0.08	0.22 ± 0.02
180NNAX8L	1.15 ± 0.02	0.28 ± 0.09

Linear sweep voltammetry was used to evaluate the electrochemical performance of the N-CNTs. Figure 5 show the polarization curves for the electrochemical reduction of molecular oxygen. As expected, undoped CNT (CNT pristine) is not an active catalyst for ORR. The data show that the limiting current density is not formed in the range of potential studied as it has been know for unmodified carbon materials [4]. Moreover, the analysis of polarization curves was found that the initial potential of the most N-CNTs samples is about 1.15 V/SHE, which is a higher value of 1.11 V/SHE corresponding to commercial 20 wt. % Pt/C. It was noted that the initial potential shifted slightly with temperature variation. This indicates that N-CNTs possess good electrocatalytic activity for the ORR. On the other hand, the N-CNTs synthesized at 900 °C exhibited a limit current density higher than the N-CNTs at 800 °C. This is a clear indication that the N-CNTs (with higher nitrogen amount) at 900 °C showed better electrocatalytic activity. The effect of temperature on the catalytic activity of the N-CNTs has already been reported in the literature [12, 17, 18]. On the other hand, the results of ORR are consistent with the HRTEM micrographs where the nanostructure morphology allow the easy and higher contact with oxygen. Also the high temperature during the synthesis could cause higher nitrogen doping into the carbon nanotubes, having as result a higher ORR activity, which it is in agree with EDS analysis.

N-CNTs sample synthesized under the gas flow to 1 L/min at 900 °C showed higher electrocatalytic activity compare with samples at 0.5 L/min. This analysis revealed that argon gas flow significantly influenced the electrocatalytic properties of N-CNTs. Normally a CVD process, the carrier gas is used to feed precursor sources and catalyst in the reactor. As has been little research on the effect of the flow rate of the carrier gas in the nanotubes formation. Chaisitsak et al. synthesized carbon nanotubes pristine (doping free) and found that the variation of the gas flow changed the physical properties of nanotubes (length variation). They proposed that this is caused by the cooling rate of the substrate or the short time that the catalyst remain in the reactor [15].

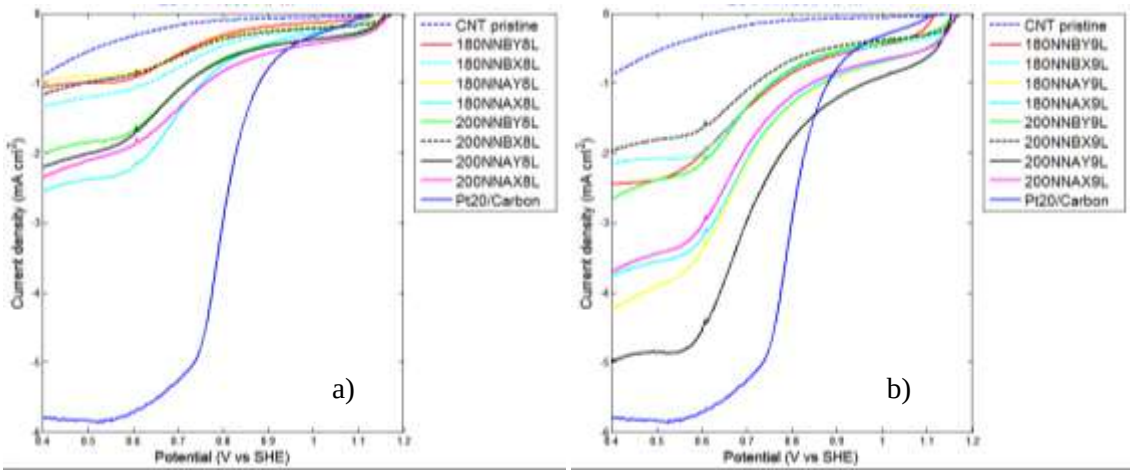

Figure 5. Oxygen reduction reaction curves a) N-CNTs at 800°C and b) N-CNTs at 900°C in O_2-saturated 0.5 M H_2SO_4 at 1600 rpm, $v = 5mV\ s^{-1}$.

The 200NNAY9L sample showed the highest current density limit in all the samples. Therefore, it was chosen to study the reaction kinetics for the ORR by RDE at different rotation speeds. As shown in Figure 6(a), the ORR current densities increase with increasing rotation speed. The kinetic parameter was analyzed using the Koutecky-Levich (K-L) equations.

$$\frac{1}{j} = \frac{1}{j_k} + \frac{1}{j_d} = \frac{1}{j_k} + \frac{1}{B\omega^{1/2}} \tag{1}$$

$$j_k = nFk_fC_O \tag{2}$$

$$j_d = 0.2nFD_o{}^{2/3}v^{-1/6}Co \tag{3}$$

where j is the measured current density, j_k and j_d are the kinetic and diffusion limited current density respectively, k_f is the electrochemical rate constant for O_2 reduction, D is the diffusion coefficient of oxygen ($1.8 \times 10^{-5} cm^2 s^{-1}$), C_o is its concentration in the bulk ($1.13 \times 10^{-6} molcm^{-3}$) and v is the kinematic viscosity of the solution ($0.01\ cm^2 s^{-1}$). The data are given for 0.5 M H_2SO_4[4].

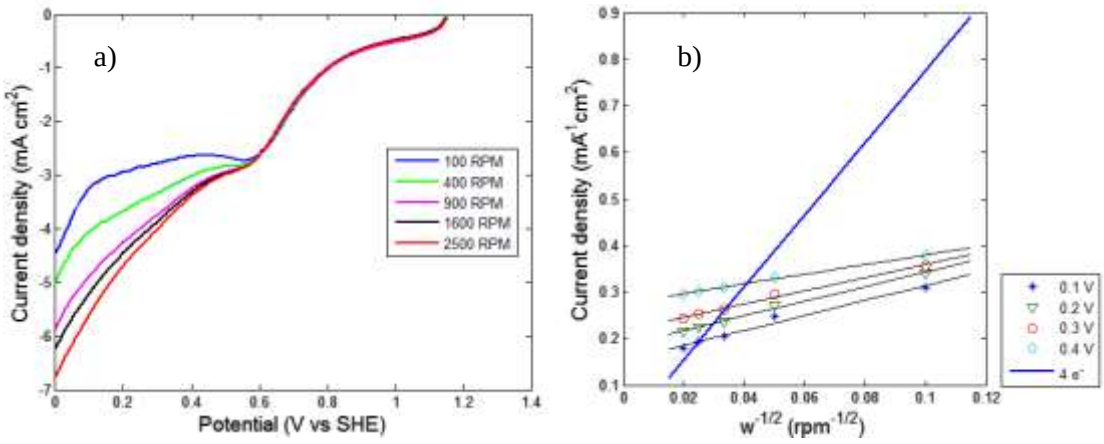

Figure 6. a) Polarization curves of oxygen reduction reaction (sample 200NNAY9L), O_2-satured 0.5 M H_2SO_4 with different rotation speed at potential rate of 5 mV s^{-1}. b) Koutecky-Levich plot for ORR at various potentials.

The K-L plots of oxygen reduction on the 200NNAY9L sample are presented in Figure 6(b). The K-L lines show the good linearity and parallelism, indicating that the ORR process over the N-CNT electrocatalyst follows first-order kinetics in the selected potential range. The number of electrons transferred per O_2 molecule (n) was calculated from the slope of the K-L lines. The slope of the line of 200NNAY9L is slightly shifted to the theoretical line of four electrons. This could be result of the deviation in number of electrons transferred or slight deviation from the proposed first order kinetic [5]. The obtained result indicates that the ORR of N-CNT may not proceed preferably by a 4-electron process [20].

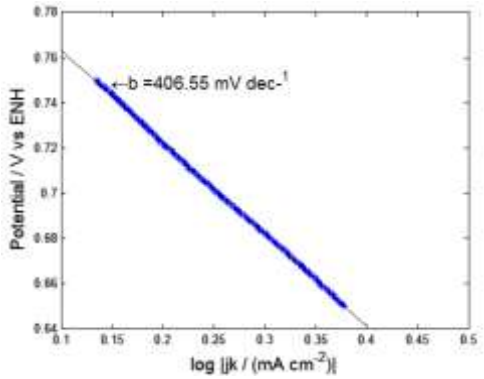

Figure 7. Tafel plot of ORR for 200NNAY9L (at 1600 rpm).

A more detailed comparison of the catalytic activity of the material can be obtained by the Tafel slope (Figure 7) which is obtained from the values of kinetic current density (j_k). The slope estimate for 200NNAY9L sample was 406 mV dec^{-1},which is four times higher than the 20 wt. % Pt/C (104 mV dec^{-1}).

This value indicates that the reaction rate is slow on the sample. High slope (greater than 130 mV dec^{-1}) can be attributed to the blocking of active sites by the peroxide formed as an intermediate in the reaction [20, 21]. Although the lower electrocatalytic activity, this is an interesting non platinum material to be used in fuel cells electrodes.

4. Summary and perspectives

In this work the influence of synthesis parameters in N-CNTs synthesized with pyridine on the ORR performance were studied. The higher ORR activity was founded in the N-CNTs synthesized at 900 °C and flow rate of 1 L/min. This activity could be attributed to higher content of nitrogen in the N-CNTs, which leads to increased disorder in structure. This proves that the nitrogen content plays an important role in the ORR activity. ORR kinetic analysis revealed that the N-CNTs has not yet reached the electrocatalytic properties of Pt/C, however shows a good electrochemical performance for a non-platinum catalysts. Finally, N-CNTs synthesized are suitable candidates for the ORR at the cathode of the fuel cell.

Acknowledgements

The authors acknowledge the financial support provided by FOMIX CONACYT - Estado de Quintana Roo, under project QR00-2011-001-174895. Also thanks to NANOTECH – CIMAV for technical support in HRTEM, Raman Spectroscopy and Thermogravimetric analysis.

References

[1] Chen Zhu, Drew Higgins, Haisheng Tao, Ryan S. Hsu, and Zhongwei Chen.Highly Active Nitrogen-Doped Carbon Nanotubes for Oxygen Reduction Reaction in Fuel Cell Applications.J. Phys. Chem. C 2009, 113, 21008–21013.

[2] Wong WY, Daud W.R.W., Mohamad A.B., Kadhum A.A.H. Influence of nitrogen doping on carbon nanotubes towards the structure, composition and oxygen reduction reaction. International Journal of Hydrogen Energy vol. 38 (2013) 9421-9430.

[3]Wang Yongxia, Xiangzhi Cui, Yongsheng Li, Lisong Chen, Hangrong Chen, Lingxia Zhang, Jianlin Shi. A co-pyrolysis route to synthesize nitrogen doped multiwall carbon nanotubes for oxygen reduction reaction. Carbon vol. 68 (2014) 232-239.

[4] Alexeyeva N., E. Shulga, V. Kisand, I. Kink, K. Tammeveski. Electroreduction of oxygen on nitrogen-doped carbon nanotube modified glassy carbon electrodes in acid and alkaline solutions. Journal of Electroanalytical Chemistry 648 (2010) 169–175.

[5] Higgins Drew, Zhu Chen, Zhongwei Chen. Nitrogen doped carbon nanotubes synthesized from aliphatic diamines for oxygen reduction reaction.ElectrochimicaActa56 (2011) 1570–1575.

[6] Xiong Chun, Zidong Wei, Baoshan Hu, Siguo Chen, Li Li, Lin Guo, Wei Ding, Xiao Liu, WeijiaJi, Xiaopei Wang. Nitrogen-doped carbon nanotubes as catalysts for oxygen reduction reaction. Journal of Power Sources 215 (2012) 216 - 220.

[7] MaubaneM. S., Messai A. Mamo, Edward N. Nxumalo, Willem A.L. Otterlo, Neil J. Coville. Tubular shaped composites made from polythiophene covalently linked to Prato functionalized N-doped carbon nanotubes. Synthetic Metals 162 (2012) 2307– 2315.

[8] Higgins Drew C., Jason Wu, Wenmu Li, Zhongwei Chen. Cyanamide derived thin film on carbon nanotubes as metal free oxygen reduction reaction electrocatalyst.ElectrochimicaActa59 (2012) 8-13.

[9] Choi Chang Hyuck, Seung Yong Lee, Sung Hyeon Park, SeongIhl Woo. Highly active N-doped-CNTs grafted on Fe/C prepared by pyrolysis of dicyandiamide on Fe_2O_3/C for electrochemical oxygen reduction reaction. AppliedCatalysis B: Environmental103 (2011) 362–368.

[10] Valenzuela Muñiz A.M., Y. Verde, M. MikiYoshida, G. Alonso Nuñez. Synthesis of Multi-walled carbon nanotubes by spray-pyrolysis using a new iron organometallic complex as catalytic agent.Journal of nanoscience and nanotechnology 8 (2008) 6456-6460.

[11] Alonso Nuñez G., A.M.ValenzuelaMuñiz, F. Paraguay Delgado, Y. Verde. New organometallic precursor catalysts applied to MWCNT synthesis by spray-pirolysis. Optical materials 29 (2006) 134-139.

[12] Zaiyong Mo, Shijun Liao, YuyingZheng, Zhiyong Fu. Preparation of nitrogen-doped carbon nanotube arrays and their catalysis towards cathodic oxygen reduction in acidic and alkaline media. Carbon vol. 50 (2012) 2620 - 2627.

[13] Liu Jian, Yong Zhang, MihneaIoanIonescu, Ruying Li, Xueliang Sun. Nitrogen-doped carbon nanotubes with tunable structure and high yield produced by ultrasonic spray pyrolysis. Applied Surface Science 257 (2011) 7837–7844.

[14] MhlangaSabelo D., Edward N. Nxumalo, Neil J. Coville, Vallabhapurapu V. Srinivasu. Nitrogen doping of CVD multiwalled carbon nanotubes: Observation of a large g-factor shift. Materials Chemistry and Physics 130 (2011) 1182– 1186.

[15] Chaisitsak S., J. Nukeaw, A. Tuantranont. Parametric study of atmospheric-pressure single-walled carbon nanotubes growth by ferrocene–ethanol mist CVD. Diamond & Related Materials 16 (2007) 1958 - 1966.

[16] B. Escobar, R. Barbosa, M. Miki Yoshida, Y. Verde Gomez. Carbon nanotubes as support of well dispersed platinum nanoparticles via colloidal synthesis. Journal of Power Sources 243 (2013) 88-94.

[17] VikkiskM., IvarKruusenberg, UrmasJoost, Eugene Shulga, KaidoTammeveski. Electrocatalysis of oxygen reduction on nitrogen-containing multi-walled carbon nanotube modified glassy carbon electrodes. ElectrochimicaActa.Vol. 87 (2013) 709– 716.

[18] DorjgotovAltansukh, Jinhee Ok, YuKwonJeon, Seong-Ho Yoon, Yong Gun Shul. Activity and active sites of nitrogen-doped carbon nanotubes or oxygen reduction reaction. Journal ApplElectrochem 43 (2013) 387 - 397.

[19] QiuYejun, Jing Yin, HuiwenHou, Jie Yu, XinbingZuo. Preparation of nitrogen-doped carbon submicrotubes by coaxial electrospinning and their electrocatalytic activity for oxygen reduction reaction in acid media.ElectrochimicaActa96 (2013) 225- 229.

[20] Zinola C.F. Castro A.M., Triaca W.E., Arvía A.J. Kinetics and mechanism of the electrochemical reduction of molecular oxygen on platinum in KOH. Journal Appl. Electrochem 24 (1994) 531-541.

[21] Yin Zhong-shu, Tian-hang Hu, Jian-long Wang, Cheng Wang, Zhi-xiang Liu, Jian-weiGuo.Preparation of highly active and stable polyaniline-cobalt-carbon nanotube electrocatalyst for oxygen reduction reaction in polymer electrolyte membrane fuel cell.ElectrochimicaActa119 (2014) 144– 154.

Electrochemical Studies of Poly(styrene-co-acrylic acid) PEM Membranes Synthesized by two Different Methods

J.C.O. Rodriguez[1], L. Melo[1], R. Benavides[1]*, M. M. S. Paula[2], L. da Silva[2]

[1] Centro de Investigación en QuímicaAplicada, Blvd. Enrique Reyna H. 140, Saltillo, Coahuila, México.
[2] Universidade do Extremo Sul Catarinense (UNESC), Av. Universitária, 1105 - Cx.P. 3167, Criciúma, SC. Brazil, 88.806-000
.*Corresponding author. Tel.: + 52 01 844 438 9830 ext. 1322
E-mail address: roberto.benavides@ciqa.edu.mx (Roberto Benavides)

ABSTRACT

The synthesis of two alternatives to Nafion random copolymers was carried out by radical copolymerization. Poly(styrene-co-acrylic acid) (PSAA) in a 94:6 styrene-acrylic acid molar relation, partially cross-linked with trimethylol propane trimethacrylate (TMPTMA) was synthesized by mass polymerization. The PSAA obtained was sulfonated (PSAAS-m) with sulphuric acid, considering the 100 % molar substitution of styrene benzene rings. Separately, same random PSAA was synthesized by solution polymerization, but cross-linked with Divinylbenzene (DVB) and sulfonated (PSAAS-s) with acetyl sulphate at a 20 % molar substitution with respect to benzene rings. Copolymers, including non sulfonated blanks, were dissolved in THF and used to coat a platinum (Pt) electrode by "deep coating" and studied electrochemically by the voltamperometric cycle technique in H_2SO_4 0.5 M. Both non-sulfonated PSAA copolymers showed only a baseline signal, indicating no proton conductivity through them. Similarly was observed for the PSAAS-s copolymer, suggesting no proton conductivity as well. On the other hand, the copolymer synthesized in mass and highly sulfonated (PSAAS-m) showed the corresponding signals of Pt reduction, as observed in the experiment carried out for the Pt electrode without any coating.

Keywords: *sulfonated PSAA, fuel cells, Pt electrode.*

1. Introduction

Fuel cells (FC) have the potential to become an important energy conversion technology. It is believed that FC are the next generation of solution for stationary energy supply systems, portable electronics and motor vehicles. With hydrogen as fuel, this technology is environmentally friendly, since power generation involves the reaction of hydrogen oxidation and oxygen reduction. Such reaction has water as the only one byproduct [1].

Among the different family types of FC´s, one of the most important is the Proton exchange membrane fuel cells (also named as "polymer electrolyte membrane"-PEM). The PEMFC are the most attractive candidates for applications in the automotive and portable electronics industry [2], [3], due to their advantages as reduced corrosion, mechanical simplicity, quick implementation, high efficiency, modularity and versatility.

The heart of a PEMFC is the polymeric membrane, which in turn must have some specific capabilities such as high proton conductivity, a suitable barrier to fuel mixture and reactant gases, as well as being chemically and mechanically stable in the demanding environment of the FC.

Commercial membranes of PEMFC are basically made of poly(perfluorosulfonic acid) (PFSA) and the most popular is the Nafion from DuPont. Nowadays some other makers have developed similar materials, as Flemion made from Asahi Glass or Aciplex from Asahi Chemical; all of them are highly expensive [4]. An alternative to this kind of membranes, are the hydrocarbonated copolymers. This materials are cheaper, commercially available comonomers, and their structure allow the introduction of polar sites, like hanging groups, with the intention of increasing the water absorption an ionic conductivity [5].

Electrolytic polymers and copolymers has been developed to replace PFSA membranes, as the poly(styrene-acrylic acid) (PSAA) sulfonated to enhance ion conductivity, and crosslinked with divinyl benzene (DVB) or trimethylol propane trimethacrylate (TMPTMA) [6], [7], [8].

In this work, two different random PSAA copolymers were synthesized and both cross-linked. One of them was synthesized via mass polimerization, sulfonated with sulfuric acid at 100 % molar substitution with respect to benzene rings and crosslinked with TMPTMA and the other was synthesized in solution, crosslinked with DVB and sulfonated with acetyl sulfonate at a 20 % molar substitution with respect to benzene rings. Electrochemical studies were carried out for both for inter-comparison.

2. Experimental

2.1 synthesis and sulfonation of mass copolymer (PSAAS-m)

The synthesis was carried out in a glass reactor with mechanical stirring at 250 rpm, 100 ºC and inert atmosphere of nitrogen during 2 hours. The molar ratio was 94:6 of styrene-acrylic acid. The amount of BPO (benzoyl peroxide) initiator was of 0.05 % molar and 0.01 % molar of the crosslinking agent TMPTMA. Acetone was added to finish the reaction and 5 minutes after methanol was added to precipitate the copolymer. The material was finally vacuum dried at 40 ºC.

The sulfonation procedure was carried out in the same glass reactor. 6 g of copolymer were dissolved in diclorometane (DCM) at 40 ºC and then the sulfonant agent (sulfuric acid 98 %) was added in a molar ratio of 100 % with respect to benzene rings. Atmosphere, time and stirring conditions were the same used during the copolymerization reaction.

2.2 Synthesis and sulfonation of solution copolymer (PSAAS-s)

This copolymer was synthesized using the same molar ratio of styrene-acrylic (94:6). The reaction was carried out via polymerization in solution of diethylbenzene, BPO 0.045 % molar as initiator and DVB (divinyl benzene) as crosslinking agent in a 0.25 % molar concentration. The reaction was carried out in a reactor at 200 rpm and 90 ºC during 2 hours in a nitrogen atmosphere. Methanol was added to finish the reaction after the 2 hours of polymerization time. The copolymer was dissolved in THF and precipitated again in methanol and finally dried at 65-70 ºC under vacuum during 48 h.

The sulfonation process was carried out by using acetyl sulphate in a 20 % molar ratio of the theoretical benzene rings in the copolymer. This reaction was carried out in the same reactor at 200 rpm dissolving the copolymer in DCM during 40 minutes at 40 ºC and then adding the sulfonation agent during a reaction time of 30 minutes.

2.3 FTIR characterization

Infrared spectroscopy was used to verify that synthesized copolymers contained the comonomers and sulfonic species in its chemical structure. A Nicolet 6700 spectrophotometer was used to analyze films, with 25 scans and a resolution of 4 cm^{-1}.

2.4 Electrochemical studies

With the general idea of investigating the capacity for proton conductivity of the materials, the unsulfonated and sulfonated materials were analyzed. A H_2SO_4 0.5 M electrolytic cell was used for measurements through the voltamperometric cyclic technique in the potentiostat at 100 mV/s. The copolymers were dissolved in THF and used to coat a Pt electrode by the "deep coating" technique. The uncoated Pt electrode was also analyzed in the same conditions. Figure 1 shows images of the Pt electrode before and after coating with PSAAS-m.

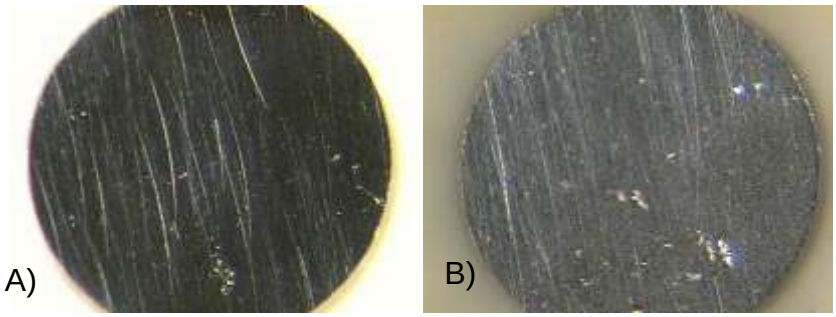

Figure 1. 40x image of Pt electrode: A) coated whit PSAAS-m; B) uncoated.

3. Results and discussion

The copolymers synthesized were analyzed by FTIR to corroborate their composition. Figures 2 and 3 show the corresponding spectra for the materials PSAA-s, PSAAS-s, PSAA-m and PSAAS-m. The characteristic C-H bands from benzene rings of styrene at 3000-3100 cm^{-1} are clear to see for both figures, as well as the characteristic aromatic overtone absorptions at the region of 1800- 1900 cm^{-1}. There is also a series of signals in 2925 cm^{-1} corresponding to the asymmetric and in 2852 the symmetric elongation of CH_2 signals corresponding to the presence of the vinyl part of styrene and to the acrylic acid. The latter is also seen in the 1740 cm^{-1} carbonyl signal. Spectra identify the copolymer of styrene/acrylic acid.

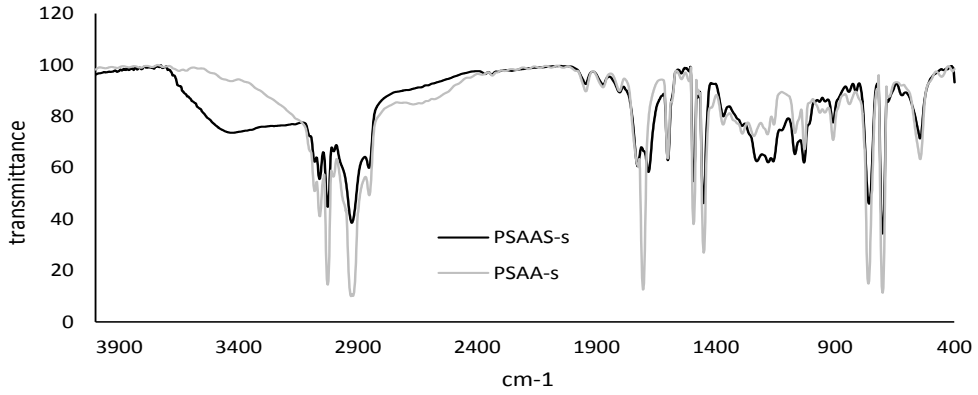

Figure 2. FTIR of PSAA-s and PSAAS-s

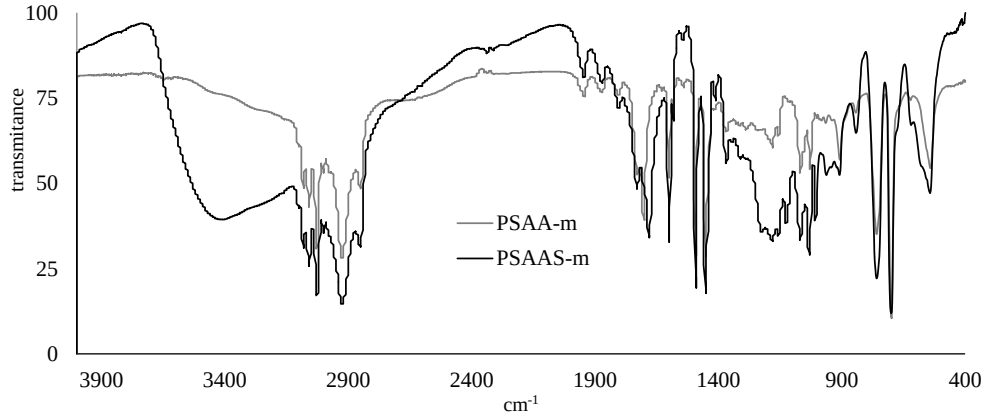

Figure 3. FTIR of PSAA-m and PSAAS-m

The main difference between the sulfonated and unsulfonated copolymers is a broad band in the region of 3100-3400 cm^{-1}, indicating the presence of the OH groups, which in turn confirms the incorporation of

the sulfonic groups (SO_3H). The absorptions between 1290-1390 cm^{-1} corresponding to the SO_2 group indicate sulfonation of the copolymers as well.

Figure 4 shows the corresponding voltamperogram for the uncoated Pt electrode. A typical sequence of Pt oxidation/reduction trace in a sulfuric acid media is seen; oxidation from 0-700 mV and reduction from 300 to -450 mV. Small signals at the region of -400 to -700 mV correspond to hydrogen adsorption [9].

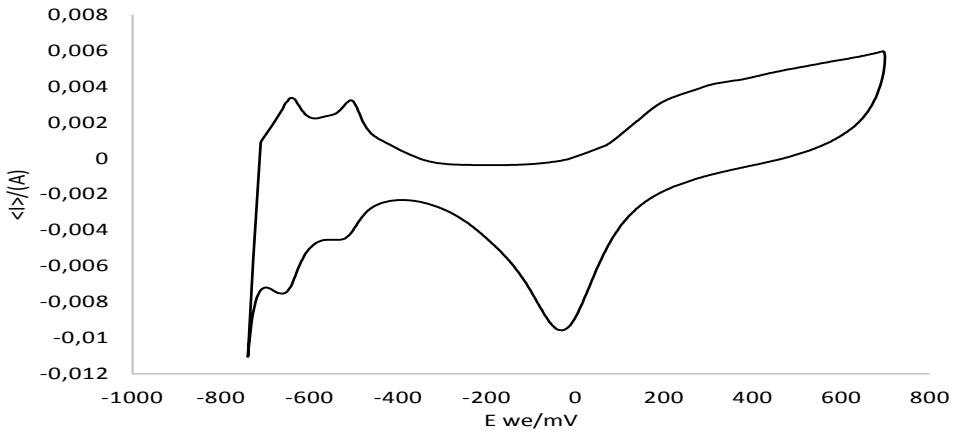

Figure 4. Voltamperogram of uncoated Pt electrode.

Figure 5 shows the same voltamperograms for the Pt electrode coated with the copolymer synthesized by mass copolymerization, before (PSAA-m) and after (PSAAS-m) sulfonation; the uncoated electrode trace is placed for comparison. It is very clear to see that unsolfonated material does not allow protons from the electrolytic cell go through for the redox reaction of the Pt electrode to take place. However, for the case of sulfonated copolymer (PSAAS-m), a very similar trace to the uncoated electrode is seen, indicating the ability of the material for proton transportation to reach the electrode [10].

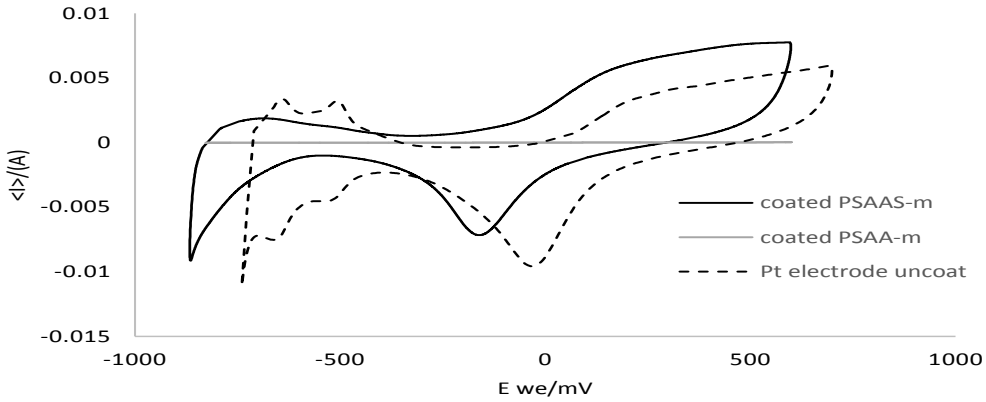

Figure 5. Volatmperograms of uncoated Pt electrode and coated with PSAA-m and PSAAS-m.

On the other hand, the results obtained for the copolymer synthesized by solution copolymerization are shown in Figure 6. The voltamperogram corresponding to the uncoated electrode is placed for comparison and the sulfonated copolymer (PSAAS-s) does not show any redox reaction for the Pt in the electrode. There seems to be a series of side reactions occurring during the copolymerization reaction in the solvent media, which in turn alter the sulfonation reaction and reduce its proton conductivity [11]. It has to be considered as well, that sulfonation was taken only to 20 % of theoretical benzene rings, while for mass copolymer it was taken to 100 %, and obviously the amount of sulfonic groups needed for proton conduction is considerable reduced in the copolymer structure.

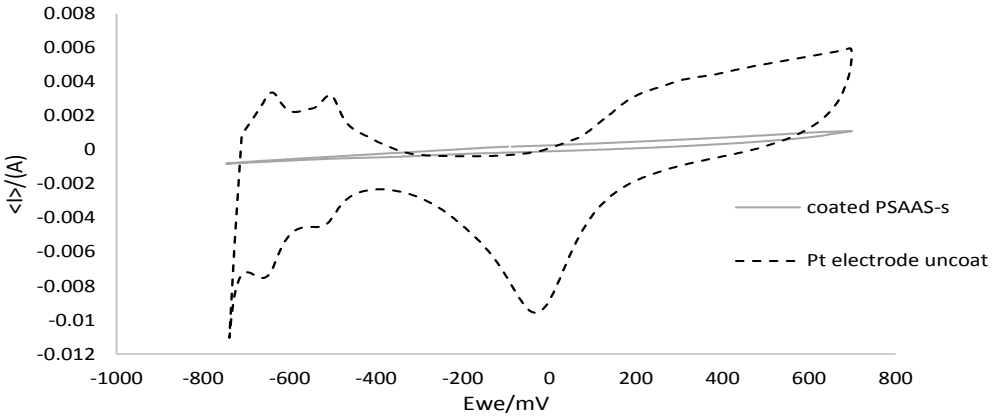

Figure 6. Voltamperograms of uncoated Pt electrode and coated with PSAAS-m.

4. Conclusions

Two styrene/acrylic acid copolymers were prepared by mass and solution copolymerizations reactions and then sulfonated for giving proton conductivity characteristics. Voltamperometric measurements with a Pt electrode coated with copolymers indicate that the material prepared by mass reaction has proton conductivity enough to allow redox reactions in the Pt electrode, while solution copolymer does not have enough proton conduction. The latter as a result of possible secondary reactions during copolymerization and to the low level of sulfonation in the material.

Acknowledgements

CONACYT is greatly acknowledged for the finance of this project.

References

[1] C. Wang, D. van der Vliet, K. L. More, N. J. Zaluzec, S. Peng, S. Sun, H. Daimon, G. Wang, J. Greeley, J. Pearson, A. P. Paulikas, G. Karapetrov, D. Strmcnik, N. M. Markovic, and V. R. Stamenkovic, "Multimetallic Au/FePt3 nanoparticles as highly durable electrocatalyst.," Nano Lett., vol. 11, no. 3, pp. 919–26, Mar. 2011.

[2] B. Du, Q. Guo, R. Pollard, D. Rodriguez, C. Smith, and J. Elter, "PEM fuel cells: status and challenges for commercial stationary power applications," Jom, vol. 58, no. 8, pp. 45–49, Aug. 2006.

[3] M. a Hickner, H. Ghassemi, Y. S. Kim, B. R. Einsla, and J. E. McGrath, "Alternative polymer systems for proton exchange membranes (PEMs).," Chem. Rev., vol. 104, no. 10, pp. 4587–611, Oct. 2004.

[4] M. K. Daletou, J. Kallitsis, and S. G. Neophytides, Interfacial Phenomena in Electrocatalysis, vol. 51. New York, NY: Springer New York, 2011.

[5] B. Smitha, S. Sridhar, and a. a. Khan, "Solid polymer electrolyte membranes for fuel cell applications—a review," J. Memb. Sci., vol. 259, no. 1–2, pp. 10–26, Aug. 2005.

[6] L. da Silva, F. E. da Silva, C. V. Franco, R. B. Nuernberg, T. Gomes, R. Miranda, and M. M. da Silva Paula, "Humidity and pH sensor based on sulfonated poly-{styrene–acrylic acid} polymer.," Mater. Sci. Eng. C, vol. 29, no. 2, pp. 599–601, Mar. 2009.

[7] L. W. Oenning, "Entrecruzamiento, sulfonación e incorporación de nanopartículas metálicas en membranas de poli (estireno-co-ácido acrílico) y su implicación en celdas de combustible," Centro de Investigación en Química Aplicada, 2012.

[8] R. Benavides, L. Oenning, M. Paula, and L. Da Silva, "Properties of Polystyrene/Acrylic Acid Membranes After Sulphonation Reactions," J. New Mater. Electrochem. Syst., Vol. 17, pp. 085–090, 2014.

[9] F. J. Rodriguez Varela, O. Solorza Feria, and E. Hernández Pacheco, Eds., Celdas de combustible. Canada, 2010.

[10] B.-R. Lim, J.-W. Kim, S.-J. Hwang, S.-J. Yoo, E.-A. Cho, T.-H. Lim, and S.-K. Kim, "Fabrication and Characterization of High-activity Pt/C Electrocatalysts for Oxygen Reduction," Bull. Korean Chem. Soc., vol. 31, no. 6, pp. 1577–1582, Jun. 2010.

[11] L. Melo, R. Benavides, G. Martínez, L. da Silva, M.M.S. Paula, "Degradation side reactions during sulphonation of poly(styrene-acrylic acid) used as membranes", Polym. Deg. Stab., in press, 2014

Novel Microbial Fuel Cell Design for raw High Organic Load Waste Water Treatment

Angel Rodrigo Montes Ochoa[1], O. Solarza-Feria[2], J. Tapia-Ramírez[3], K. Sathish-Kumar[1*]

[1]Universidad Politécnica de Aguascalientes, Ingeniería en Energía Calle Paseo San Gerardo No. 207. Fracc. San Gerardo. Aguascalientes, Ags. México, 20342.
[2]Centro de Investigación y de Estudios Avanzados del Instituto Politécnico Nacional, Departamento de Química, Av. Instituto Politécnico Nacional 2508, Col. San Pedro Zacatenco, Delegación Gustavo A. Madero, México D.F. 07360.
[3]Centro de Investigación y de Estudios Avanzados del Instituto Politécnico Nacional, Departamento de Genéticas y Biología Molecular
[*]Tel: +52 4491156589 ; e-mail: sathish.bot@gmail.com,sathishkumarkamaraj@hotmail.com

ABSTRACT

Microbial fuel cells (MFCs) provide new prospects for a sustainable production of energy from organic waste water. Most of the results obtained so far from the field of MFCs research can be exploited to design MFCs. From this context, we proposed the novel simplified softwood based MFC, using pencil was first reported. In pencil, the graphite rod could act as anode besides submerged with wooden portion into the raw high concentrated wastewater solution, and remained wooden portion bound with Pt/Carbon cloth (Cathode) exposed to air. Raw high concentrated waste waters was used both as inoculum to form electrochemically active bacteria on graphite based anode and also as the medium to be treated. Later we treated the softwood with sulphuric acid solution for overnight, tracheids cells lose its cell wall integrity and become swollen in nature. Further, FT-IR spectroscopy confirmed the presence of lignosulfonate on the sulphuric acid treated softwood in the 1032 cm^{-1} and 872 cm^{-1} regions. The conductivity (σ) followed the tendency as 6M sulphuric acid treated softwood < 3M sulphuric acid treated softwood < softwood, and increased almost with the increasing concentration of the sulphuric acid. The volumetric power densities of the novel softwood based MFCs were follows the propensity, 6M sulphuric acid treated softwood (956 mW/m^3) < 3M sulphuric acid treated softwood (212 mW/m^3) < softwood (3 mW/m^3). Thus, the presence of lignosulfonate on the sulphuric acid treated softwood, along with partially hydrolyzed tracheid cell surface bearing SO_3H group mediated proton exchange of both a surface bound proton and a covalently bonded proton between water and hydroxyl, could facilitate the proton exchange. In the case of 3M and 6M sulphuric acid treated softwood MFCs, anodic resistance exhibited higher than the cathode, due to the lower kinetics of the bacterial metabolisms on the anode. However, in softwood MFC showed high cathodic resistance, ascribable to lack of lignosulfonate. From the operation with raw high concentrated wastewater, 6M sulphuric acid treated MFC unveiled superior characteristics of volumetric power density of 1016 mW/m^3 with 19 % columbic efficiency. In addition, eliminating the commercial ion exchange membrane greatly decreases the cost and maintenance for MFC construction, since the costly ion exchange membranes (such as Nafion) contributes a significant portion of capital investment. Thus, this cost-effective feature increases the feasibility for practical application linked with wastewater treatment.

Keywords: microbial fuel cells,proton exchange, aircathode, wastewater treatement.

1. Introduction

Microbial fuel cells are a promising renewable energy production technology, especially in wastewater application, where bacteria act as bio-catalysts to oxidize complex organic or inorganic material to generate electricity, while at the same time the wastewater is treated [1-3]. The increase in MFC power output over the years by several orders of magnitude is a promising trend [4]. However, further increases in power densities are desirable to help improve the economic feasibility of MFC technologies for practical real-world applications [4]. Improved MFCs performance is likely to result from improvements made in optimizing component properties such as anode, cathode, electrolyte and separator (membrane) and reactor configurations. Biocatalysts are capable of directly transferring electrons without the addition of an external mediator to the anode were found in 1999 [5]. Since then, numerous studies of MFCs have been performed, including selection of electrochemically active bacteria, electron-transfer mechanisms, affecting the performance of electric power generation [6].

Many chemicals have been used as electron acceptors in MFCs, but oxygen is the most cost effective, sustainable and environmental friendly electron acceptor for wastewater treatment applications. Cathode design is challenging due to the relatively poor kinetics of oxygen reduction under neutral pH conditions in MFCs, compared to hydrogen fuel cells where cathodes work at much lower pH [7]. Improving cathode performance is therefore critical for increasing power production in MFCs by changes in system architecture that reduce internal resistance, such as by reducing electrode spacing and increasing solution conductivity [8].

Most MFCs require either a closed chamber or two chambers separated by an ion exchange membrane in order to prevent organics or oxidants crossing over to a counter chamber. However, chambered configurations having a membrane show limitations for scaling-up MFCs; for instance, the membrane requires regular cleaning when biofouling or contamination on membrane surface occurs [9]. In addition, closed two chambered MFCs should be designed to ensure that the membrane is not physically damaged by the high hydraulic pressure occurring in large-scale systems; even single-chambered MFCs using air cathodes or membrane electrode assemblies (MEAs) are not free from these challenges. Another concern for fabricating large-scale MFCs and their operation could be the availability of system optimization to minimize the internal resistance of the entire system. The use of one large electrode can cause MFCs to lose cell voltage (i.e., voltage drop) because of the internal resistance and mixed potential formation [10,11].

Among the MFCs components, MFCs reactor configurations is one of the major bottlenecks to high power density and improving its performance is critical to continued development of practical applications. For MFCs to be applied in the energy-recovering wastewater treatment process, both the entire configuration and unit cells should be scalable, moldable, and stackable in series, along with having a low operating cost and be easily serviceable.

We understand this is a first; we employed a softwood material of pencil exploited as integrated membrane via air cathode assembly for real time high concentrated wastewater application. Later we improved the performance of the system treated with sulfuric acid solutions. Moreover, this type of integrated system will have a possibility to scale up the MFCs for conventional wastewater treatment application.

2. Experimental

2.1. Collection of Inoculum

Wastewater was collected from a Universidad Politécnica de Aguascalientes (UPA) and stored in refrigerator at 4°C. The wastewater served as inoculum in anode and also as medium to be treated.

2.2 Construction of novel softwood microbial fuel cell and operation

We took the 5 pencils (4b, 6b, No2), generally protective layer of the graphite made up of softwood material. From that we select the Koh-i-Noor Hardtmuth pencil (Koh-i-Noor Hardtmuth a.s. is a Czech manufacturer and one of the world's largest producers and distributors of a full line of pencils, pens, and art supplies [12]) based on conductivity as well softwood material (Supplementary Table S1.).

Table S1. Electrical measurement of different pencils

No.	Pencils	Image	Resistance (Ω)	Conductivity* (S/m)
1	Conventional Pencil No.2		4.8 Ω	14.88 S/m
2	Pencil - Koh-i-Noor Hardtmuth		2.92 Ω	24.46 S/m
3	Pencil 4b		2.8 Ω	25.51 S/m
4	Pencil 6b		1.64 Ω	43.558 S/m
5	Graphite bar Pencil		1.18 Ω	60.53 S/m

* normalized with the surface area

Far ahead, we peal it off the protective layer (up to 4.2 cm) and remaining graphite could act as anode besides submerged wooden portion (4.2 cm) into the wastewater, remained wooden portion (4.2 cm) bound with Pt/Carbon cloth (0.5mg/cm^2) exposed to air, in order to reduction of oxygen in air to generate water as final by product (Figure 1.). Further, the softwood materials were treated with sulphuric acid

solution (3M and 6M) for overnight; then the samples were carefully rinsed with distilled water and left in distilled water for 12 hrs. Earlier, to construct the novel softwood microbial fuel cell using sulphuric acid treated softwood and raw high concentrated wastewater as source of inoculum in all the circumstances. Prominently, we didn´t utilize any external input energy (agitation, circulation, and air purging) in our system (Patent pending).

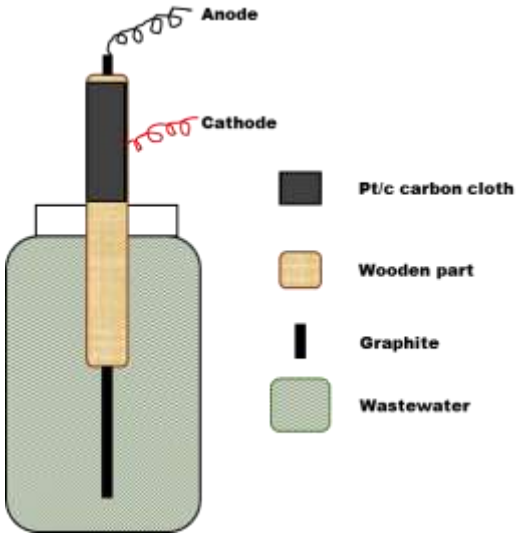

Fig 1. Schematic representation of novel softwood Microbial fuel cell

2.3 Optical microscopy analysis of softwood materials

For optical microscopy, part of the softwood materials was cut in to pieces and immersed in sulphuric acid solution (3M) for overnight. The samples were carefully rinsed with distilled water and left in distilled water for 12 hrs. They were then subjected to dry under ambient conditions. Future, microscopic structures of softwood and sulphuric acid treated softwood were analysed using a MEIJI Techno IM7100.

2.4 Fourier transform infrared (FTIR) spectral analysis of softwood materials

The softwood material and sulphuric acid treated softwood (3M) were characterized with FTIR spectroscopy. FTIR measurements were conducted on an infrared spectrophotometer (Bruker Co., Germany) equipped with an ATR accessory within a range of 4000 to 400 cm^{-1}.

2.5 Conductivity analysis of softwood materials

Proton conductivity of the samples were measured using an AC impedance method with Gamry reference600 Instruments, and the AC frequency ranged from 100 kHz to 10 mHz at a voltage amplitude of 10 mV. A four-electrode system was used to measure the softwood resistance with two outer current carrying electrodes and two inner potential sensing electrodes [13]. With this method the current passed

between the two outer electrodes and the resistance was calculated from the AC potential difference between the two inner electrodes. The conductivity was calculated with the following equation:

$$\sigma = \frac{l}{R \times S} \quad (1)$$

where σ, l, R and S are the proton conductivity, distance between the potential sensing electrodes, resistance of softwood and area and thickness of the membrane in contact with the blocking electrodes respectively. Conductivity measurements were carried out at an ambient temperature with the softwood under fully saturated conditions (100% humidity).

2.6 Electrochemical characterization of novel softwood microbial fuel cells

Novel softwood microbial fuel cell was characterized by linear sweep voltammetry (LSV) and electrochemical impedance spectroscopy (EIS). Liner sweep voltammetry (LSV) was performed in a Gamry Reference 600 Potentiostat/Galvanostat, run at a recommended scan rate of 0.1 mV s^{-1}, starting from the measured open circuit potential up to +50 mV [14,15]. Impedance spectra of microbial fuel cells were obtained at the open circuit potential (E_{ocp}). The amplitude of the signal perturbation was 10 mV, scanned in the frequency range from 100 kHz to 10 mHz. Data fitting was accomplished by Z-view software.

2.7 Analyses

Chemical oxygen demand of the feed and MFC liquor and pH were determined according to the Standard Methods [16]. COD removal efficiency η_{COD} and coulombic efficiency η_{coul} were calculated as reported elsewhere [17]. All the experiments were duplicated.

3. Results and discussion

In generally, pencil cores are made of graphite mixed with a clay binder which leaves grey or black marks, usually protective casing material permanently bonded to the core, which prevents the core from being broken. The protective case material could uses softwood. Softwoods are coniferous trees, such as pines or spruces. Cedar wood (*Calocedrus decurrens* (*syn. Libocedrus decurrens*)) is most commonly used in pencil production [18].

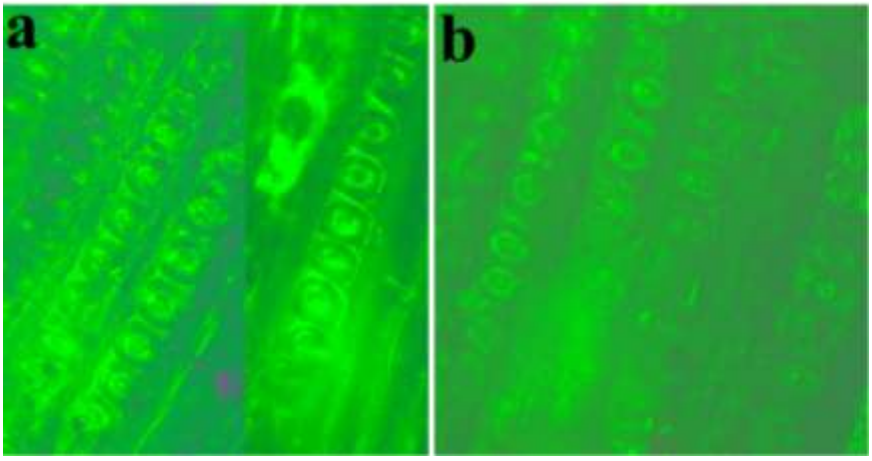

Fig 2. Optical microscopy images of softwood. a) Softwood b) Softwood treated with sulphuric acid

Softwood cellular structure is simple and 90-95 percent of the cells are longitudinal tracheids, longitudinal tracheids function in water conduction and support. The limited number of cell types makes softwoods more difficult to differentiate from one another [19]. Figure 2 shows the optical images of the longitudinal structure of the tracheids. Softwood exhibited the well-defined cell walls structure of the longitudinal tracheids cell (Fig 2.(a)), after the overnight treatment with sulphuric acid (3M) loses its cell wall integrity and become swollen (Fig 2.(b)).

The FT-IR spectra for the softwood and sulphuric acid tread softwood were explicit in Figure 3. The FTIR spectra of softwood (Fig 3.) showed a broadening to lower wavenumbers of the band at 3320 cm^{-1} corresponding to the O-H stretching vibration from alcohols (3600-3300 cm^{-1}) and carboxylic acid (3300-2500 cm^{-1}), present either in polysaccharides and lignin. In treated softwood exhibited slightly broader band at 3335 cm^{-1} and slightly increased sharpen band at 2925 cm^{-1} -2850 cm^{-1}. This could be speculated to the slight increase in carboxylic acids due to primary OH oxidation and/or hydrolysis of acetyl groups from hemicelluloses. Moreover the change of O-H stretching frequencies can also be due to the modification of cellulose crystallinity influenced by dehydration effects [20 ,21]. Even though O-H stretch due to polysaccharides could decrease, at the same time O-H from phenolic groups in lignin increases since it is a well fact that the lignin percentage increases due to carbohydrate degradation [22].

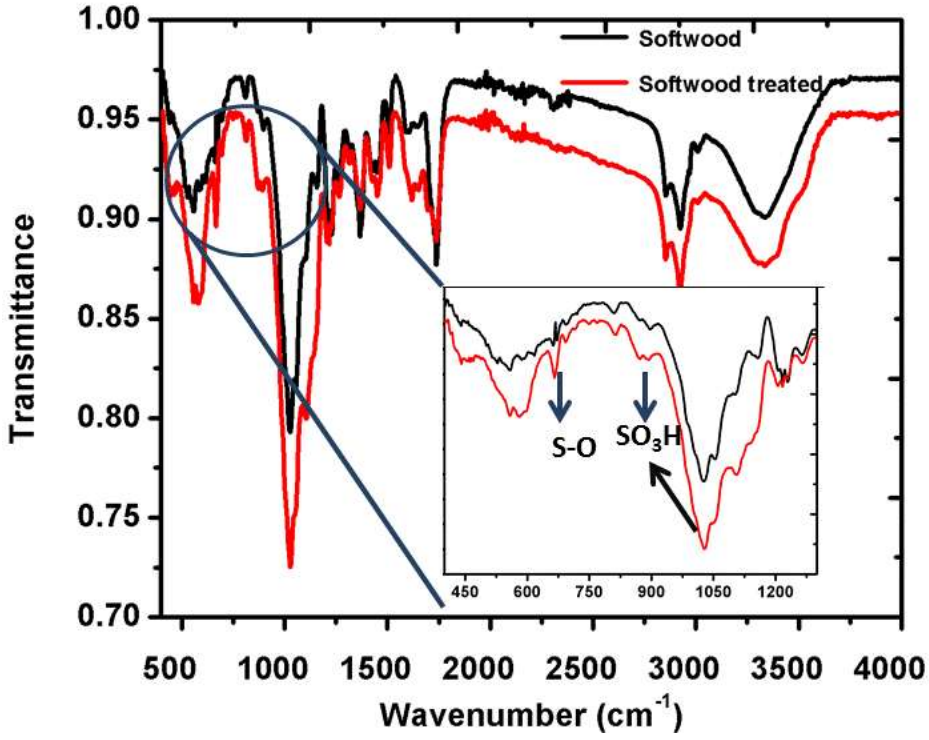

Fig 3. FTIR Spectrum of the softwood and sulphuric acid treated softwood, Inset- Footprint region of sulfonyl group

The two bands at 2900-2800 cm^{-1} are composed by the overlapping of the stretch asymmetric vibration of $–CH_2$ (2935-2915 cm^{-1}) and $–CH_3$ (2970-2950 cm^{-1}) and by the overlapping of stretch symmetric vibrations of $–CH_2$ (2865-2845 cm^{-1}) and $–CH_3$ (2880-2860 cm^{-1}). Untreated softwood showed the stretch asymmetric vibration of $–CH_2$ at 2925 cm^{-1} and $–CH_3$ at 2970 cm^{-1} and symmetric stretch at 2855 cm^{-1} of $–CH_2$. Normally the asymmetric band shows a higher absorptivity. The treated softwood shows evident disappear of frequency at 2970 cm^{-1} of $–CH_3$ and, slightly increase frequency at 2925 cm^{-1} of $–CH_3$ and 2852 cm^{-1} of $–CH_2$ bands are due to structural and relative composition changes, particularly at cellulose crystallinity level with influence of C-H and O-H stretch frequencies [20,21] and changes in the relative importance of lignin methoxyl groups for which the CH_3 stretching vibrations have lower CH stretching frequencies [23].

According to Mitchell and Higgins (2002) [24], the band around 1730 cm^{-1} is almost exclusively due to carbonyl group of acetoxy groups in xylan. In the spectra of untreated softwood shows sharp peak at 1735 cm^{-1} and treated softwood shows band decreases might be due to the breaking of hemicelluloses specifically acetyl or acetoxy groups in xylan. Similar results were obtained by Tjeersdsma and Militz (2005) [25].

The band at 1595 cm^{-1} corresponds to vibrations in the aromatic ring of lignin plus C=O stretching. The band at 1595 cm^{-1} broadens to about 1615 cm^{-1} for treated softwood but not for untreated softwood. This peak shifting suggests that there was an increase of structural diversity around the aromatic rings,

absorbing at a greater range of frequencies. The height of the band slightly increase only in the spectrum of treated softwood, might be an increase in the percentage of lignin in treated wood [26,27].

Aromatic rings exhibited band at 1510 cm^{-1} for softwood lignin (Guaiacyl- G) [28]. Fig 3. Shows the treated softwood exhibited the slightly increase peak at 1510 cm^{-1}, Also confirmed the increase the content of lignin after the acid treatment.

The band at 1460 cm^{-1} corresponds to the asymmetric deformation of C-H bond of xylan, while the band at 1420 cm^{-1} corresponds to the vibration of the aromatic ring of lignin [24]. Untreated softwood shows the peak at 1460 cm^{-1} corresponds to xylan. Interestingly, treated softwood exhibited two bands at 1460 $cm^{-1}$of $–CH_3$ and 1420 cm^{-1} of lignin. This could be speculated the effect of sulphuric acid on hemicellulose decrease and lignin peak arises.

The band at 1330 cm^{-1} represents the contributions of all structural components of wood because it corresponds to C-H bending of polysaccharides which joins the bands at 1327 cm^{-1} of S lignin condensed units [28]. There was a clear intense peak observed in treated softwood at 1330 cm^{-1} corresponding to an increase in lignin condensation. The report was corroborated by Windeisen et al., 2007 [29].

For treated softwood the band at 1240 cm^{-1} decreased in height, which once again confirms the existence of a more condensed structure [29,30]. This band has a shoulder at 1145 cm^{-1} with G lignin and 1105 cm^{-1} with GS lignin [28].

The peak at 897 cm^{-1} corresponding to the sugar ring tension, seemed to decrease with treated softwood treatment which is consistent with ring opening. Similar results were obtained by Kotilainen et al., 2000 [26], Gonzalez-Peña et al., 2009 [31]. The band appearing at 620-660 cm^{-1} is assigned to the sulfonic groups (S-O stretching vibration) formed from the reaction of sulphuric acid with the secondary OH of the aliphatic side chain of lignin's [32], formed on sulphuric acid treated softwood. The FT-IR spectrum of the SO_3H group-bearing sulphuric acid treated softwood is shown in the Figure 3. The peaks due to the SO_3H group are seen at 1032 cm^{-1} and at 872 cm^{-1}. Thus, confirmed the presence of lignosulfonate on the sulphuric acid treated softwood [33].

Figure 4. Illustrate the proton conductivity of the softwood, 3M sulphuric acid treated softwood and 6M sulphuric acid treated softwood. From the proton conductivity (σ) study, the value of the σ followed the tendency as 6M sulphuric acid treated softwood < 3M sulphuric acid treated softwood < softwood and increased almost with the increasing concentration of the sulphuric acid. It is well-known that SO_3H group bearing materials like Amberlyst-15 can be used as a cation exchanger [34-36]; therefore the sulfonated softwood materials also exhibited the high proton conductivity in 6M sulphuric acid treated softwood (10.8 mS/cm^2).

The polarization curve of the softwood, 3M sulphuric acid treated softwood and 6M sulphuric acid treated softwood based novel softwood MFCs were shown in figure 5. The volumetric power densities was follows the propensity, 6M sulphuric acid treated softwood (956 mW/m^3) < 3M sulphuric acid treated softwood (212 mW/m^3) < softwood (3 mW/m^3) (Table 1. Fig 5.). This behaviour could follow the conductivity results. Thus, the presence of lignosulfonate on the sulphuric acid treated softwood (Fig 3), along with partially hydrolysed tracheid cell surface bearing SO_3H group mediated proton exchange of both a surface bound proton and a covalently bonded proton between water and hydroxyl, could facilitate the proton exchange [37]. Further, the integrated membrane cathode enables a unidirectional flow, which improves proton transfer through convection. In addition, eliminating the commercial ion exchange membrane greatly decreases the cost and maintenance for MFC construction, since the costly ion exchange membranes (such as Nafion) contributes a significant portion of capital investment. Thus, this cost-effective feature increases the feasibility for practical application linked with wastewater treatment.

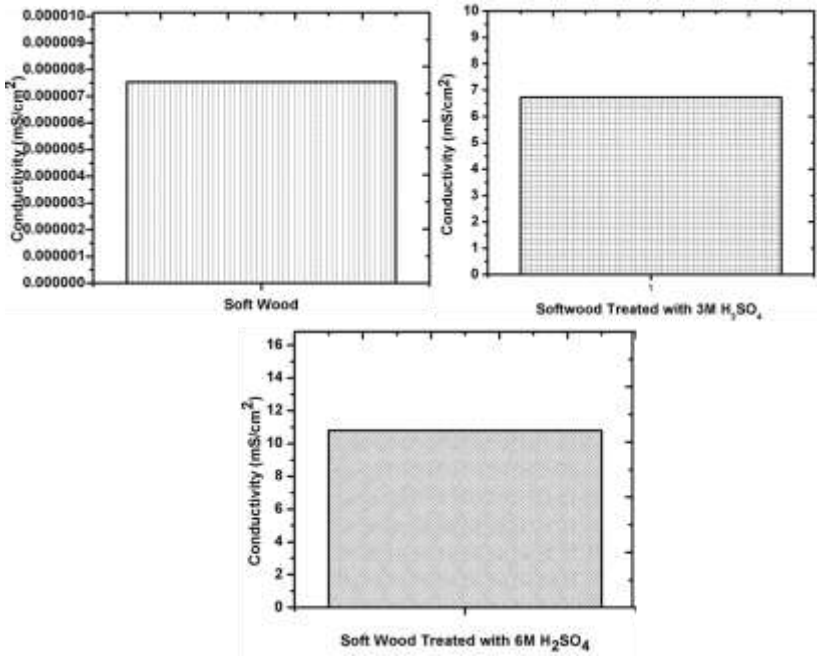

Fig 4. Conductivity of Softwood, Softwood treated with 3M and 6M of H_2SO_4

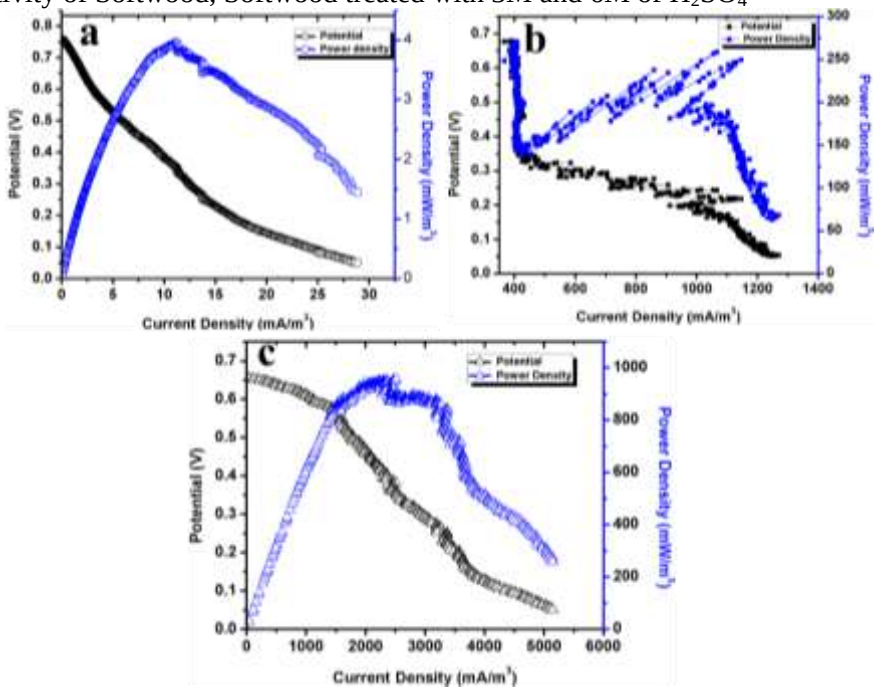

Fig 5. Polarization curve of Softwood (a), 3M treated H_2SO_4 (b) and 6M treated H_2SO_4 (c)

Table 1. Electrochemical characterization of novel softwood Microbial fuel cells

Types	I_{max} (mA)	P_{max} (mW)	$P_{v\text{-}max}$ [a] (mW/m^3)	$I_{s,max}$ [b] (mA/m^3)	E_{max} (V)	R_{anode} (Ω)	$R_{cathode}$ (Ω)	$R_{softwood}$ (Ω)	R_{int}(Ω)
Softwood	0.00099 ±4	0.00033 ±7	3±81	9±43	0.403 ±2	358±3	15175 ±42	26504±65	42037±52
3M H_2SO_4 treated Softwood	0.095 ±3	0.023 ±6	212± 63	863± 47	0.246 ±5	138±1	46±03	582±2	766±2
6M H_2SO_4 treated Softwood	0.276 ±2	0.105 ±2	956± 22	2511± 22	0.381 ±3	364±8	5±6	260±4	629±6

Note: [a] maximum volumetric power density; [b] maximum volumetric current density.

Electrochemical impedance spectroscopy of the novel softwood based MFCs are shown in Figure 6.the inset explicit the equivalent circuit fitted by Z-view. In the case of 3M and 6M sulphuric acid treated softwood MFCs, anodic resistance exhibited higher than the cathode, due to the lower kinetics of the bacterial metabolisms [38] on the anode. However, in softwood MFC showed high cathodic resistance, ascribable to lack of lignosulfonate (Table 1.).

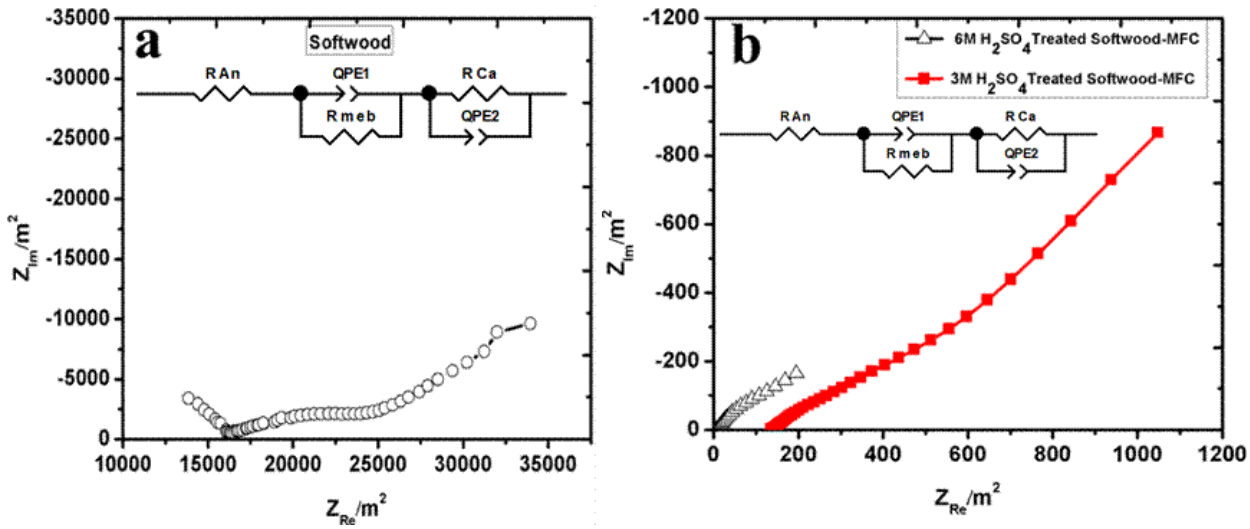

Fig 6. Electrochemical Impedance Spectroscopy of Softwood (a) and 3M H_2SO_4 [□], 6M H_2SO_4 [Δ] (b). Inset: Equivalent Circuit

Later, we operate the novel softwood based MFCs with high concentrated raw wastewater solution as sole carbon source and biocatalyst. Figure 7. Demonstrated the closed circuit operation of the novel

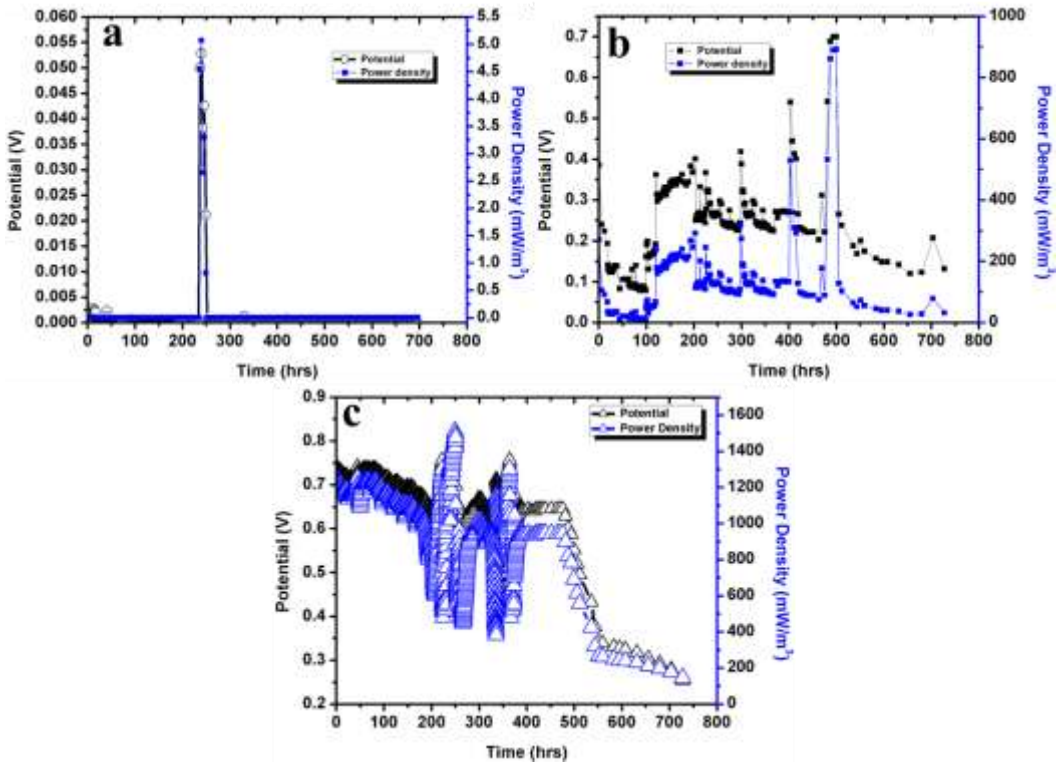

Fig 7. Closed circuit operation of Softwood (a), 3M H_2SO_4 (b) and 6M H_2SO_4 (c)

Table 2. Average values of parameters in operation of the novel softwood microbial fuel cell. Standard deviations were calculated with respect to time of operation.

Parameters	Softwood	3M H_2SO_4 treated Softwood	6M H_2SO_4 treated Softwood
P^a (mW/m^2)	0.0101±0.1	22.19±22	249.49±5
$P_V{}^b$ (mW/m^3)	0.0514±0.45	118.63±11	1016.11±202
P^c (mW)	0.0000056±4	0.0130±2	0.112±2
I (mA/m^2)	0.313±1	83.82±36	370.99±39
I (mA/m^3)	1.592±3	425.81±19	1510.95±162
I^d (mA)	0.000175±1	0.0468±1	0.166±2
E^e (V)	0.000876±0.005	0.234±0.1	0.665±0.8
$\eta_{COD}{}^f$ (%)	80.6	84.6	92.3
$\eta_{Coul}{}^g$ (%)	3	16	19

Notes: [a] surface area power density; [b] volumetric power density; [c] average power; [d] average current; [e] average potential; [f] chemical oxygen demand removal efficiency; [g] coulombic efficiency.

softwood based MFCs for 700 hrs. Their average parameters values were in Table 2. 6M sulphuric acid

treated MFC unveiled superior characteristics such as volumetric power density of 1016 mW/m^3 with 19 % columbic efficiency, among the other softwood based MFCs. Despite of the low columbic efficiency, especially during the treatment of real wastewater, had one of the following reasons: 1.entrapment and accumulation of organic particles from wastewater in the anodic biofilm [39]; 2. Production of methane [40]; 3. Losses in efficiency due to the energetic requirements to sustain fermentative and acetogenic communities in the anodic food web [41]; and 4. Diffusion of the terminal electron acceptor oxygen into the anode [42].

4. Summary and perspectives

The simplified novel softwood based microbial fuel cell using pencil was first reported. In pencil, the graphite rod could act as anode besides submerged with wooden portion into the raw high concentrated wastewater solution, and remained wooden portion bound with Pt/Carbon cloth (Cathode) exposed to air. Raw high concentrated waste waters was used both as inoculum to form electrochemically active bacteria on graphite based anode and also as the medium to be treated. Later we treated the softwood with sulphuric acid solution for overnight, lose its cell wall integrity and become swollen in nature. Further, FT-IR spectroscopy confirmed the presence of lignosulfonate on the sulphuric acid treated softwood in the 1032 cm^{-1} and 872 cm^{-1} regions. The proton conductivity (σ) followed the tendency as 6M sulphuric acid treated softwood < 3M sulphuric acid treated softwood < softwood, and increased almost with the increasing concentration of the sulphuric acid. The volumetric power densities of the novel softwood based MFCs were follows the propensity, 6M sulphuric acid treated softwood (956 mW/m^3) < 3M sulphuric acid treated softwood (212 mW/m^3) < softwood (3 mW/m^3). Thus, the presence of lignosulfonate on the sulphuric acid treated softwood, along with partially hydrolysed tracheid cell surface bearing SO_3H group mediated proton exchange of both a surface bound proton and a covalently bonded proton between water and hydroxyl, could facilitate the proton exchange. In the case of 3M and 6M sulphuric acid treated softwood MFCs, anodic resistance exhibited higher than the cathode, due to the lower kinetics of the bacterial metabolisms on the anode. However, in softwood MFC showed high cathodic resistance, ascribable to lack of lignosulfonate. From the operation with raw high concentrated wastewater for 700 hrs, 6M sulphuric acid treated MFC unveiled superior characteristics such as volumetric power density of 1016 mW/m^3 with 19 % columbic efficiency. In addition, eliminating the commercial ion exchange membrane greatly decreases the cost and maintenance for MFC construction, since the costly ion exchange membranes (such as Nafion) contributes a significant portion of capital investment. Thus, this cost-effective feature increases the feasibility for practical application linked with wastewater treatment.

Acknowledgements

The author KSK would like to acknowledge the Universidad Politécnica de Aguascalientes (UPA) and CINVESTAV-IPN, Zacatenco, D.F, for provided the necessary equipment for the characterisation. We thank the Programa de Apoyo al Desarrollo de la Educación Superior (PADES) of SECRETARíA DE EDUCACiÓN PÚBLICA (SEP), Mexico for funding this research work (Número de proyecto: 2014-01-01-002-039-Apoyo para adquisición de equipo e ins1rumentación para el desarrollo de celdas de combustible microbianas). We thank Dr. José Gerardo Cabañas Moreno for his technical assistance with

operation of FT-IR Spectroscopy. We are grateful to the excellent technical assistance from, Ing. Andrés Rodríguez-Castellanos, Ing. Sebastián Citalán Cigarroa, and Mr.Julio cesar magallon, Dept. of Chemistry, Mr. Victor Tapia, Dept. of Genetics and Molecular Biology, CINVESTAV-IPN, Zacatenco. Mexico,D.F. and Ing. Alejandro De la Torre, (data collection using Arduino) UPA. We also acknowledge the Dr. Andres Antonio Torres Acosta and SATELsa S.A de C.V (RENIECYT) for lending the Gamry Instruments Reference 600.

References

[1] A. L. Vazquez-Larios, O. Solorza-Feria, G. Vazquez-Huerta, F. Esparza-Garcia, E. Rios-Leal, N. Rinderknecht-Seijas, H. M. Poggi-Varaldo, A new design improves performance of a single chamber microbial fuel cell. J. New mater. Electrochem. Syste 2010; 13(3): 219-226.
[2]R. Navanietha Krishnaraj, S. Berchmans, P. Pal, Symbiosis of photosynthetic microorganisms with non-photosynthetic ones for the conversion of cellulosic mass into electrical energy and pigments. Cellulose 2014; 21:2349-2355.
[3] K. Sathish-Kumar, O. Solorza-Feria, J. Tapia-Ramı´rezc, N. Rinderkenecht-Seijas, H. M. Poggi-Varaldo, Electrochemical and chemical enrichment methods of a sodicesaline inoculum for microbial fuel cells. Inter. J. Hydrogen Energy 2013; 38:12600-12609.
[4]A. Rinaldi, B. Mecheri, V. Garavaglia, S. Licoccia, P. Di Nardo, E. Traversa, Engineering materials and biology to boost performance of microbial fuel cells: a critical review. Ener. Environ Sci 2008; 1:417-429.
[5] B.H. Kim, H.J. Kim, M.S. Hyun, D.H. Park, Challenges in microbial fuel cell development and operation. J. Microbiol. Biotechnol. 9 (1999) 127–131.
[6]K. Sathish-Kumar, O. Solorza-Feria, G. Vázquez-Huerta, J.P. Luna-Arias, and H.M. Poggi-Varaldo. Electrical Stress-Directed Evolution of Biocatalysts Community Sampled from a Sodic-Saline Soil for Microbial Fuel Cells. J. New Mater. Electrochem Syst. 2012;15: 181-86.
[7]J. Reyes-Rodríguez, F. Godínez-Salomón, M. Leyva, Solorza-Feria O. RRDE study on Co@ Pt/C core–shell nanocatalysts for the oxygen reduction reaction. International Journal of Hydrogen Energy 2013; 38:12634-12639.
[8]Z. Hu. Electricity generation by a baffle-chamber membraneless microbial fuel cell. Journal of Power Sources 2008;179:27-33.
[9]J. Xu, G.-P. Sheng, H.-W. Luo, W.-W Li, L.-F Wang, H.-Q. Fouling of proton exchange membrane (PEM) deteriorates the performance of microbial fuel cell. Water Research 2012;46:1817-1824.
[10]A. Dewan, H. Beyenal and Z. Lewandowski. Scaling up microbial fuel cells. Environ. Sci. Technol 2008;42(20): 7643-8.
[11]F. Harnisch, S. Wirth, U. Schroder. Effects of substrate and metabolite crossover on the cathodic oxygen reduction reaction in microbial fuel cells: platinum vs. iron(II) phthalocyanine based electrodes. Electrochem. Commun 2009;11: 2253–2256.
[12] http://www.koh-i-noor.cz/en/
[13]S. Slade, S.A. Campbell, T.R. Ralph, F.C. Walsh. Ionic Conductivity of an Extruded Nafion 1100 EW Series of Membranes. Journal of The Electrochemical Society 2002;149:A1556-A1564.
[14] S.B. Velasquez-Orta, T.P. Curtis, B.E. Logan. Energy from algae using microbial fuel cells. Biotechnol Bioeng 2009;103(6): 1068-76.
[15]V.J. Watson, B.E. Logan. Analysis of polarization methods for elimination of power overshoot in microbial fuel cells. Electrochem Commun 2011;13(1): 54-6.
[16]APHA. Standard methods for examination of water and wastewater. 17th ed. Washington DC: American Public Health Association; 1981.
[17]J.J. Fornero, M. Rosenbaum, L.T. Angenent. Electric Power Generation from Municipal, Food, and Animal Wastewaters Using Microbial Fuel Cells. Electroanalysis 2010;22:832-843.
[18] http://education.nationalgeographic.com/education/?ar_a=1
[19]R.B. Hoadley. Identifying Wood: Accurate Results with Simple Tools. Taunton Press, Inc. Newton, CT. 1990.
[20]M. Moharram, O. Mahmoud. FTIR Spectroscopic Study of the Effect of Microwave Heating on the Transformation of Cellulose I into Cellulose II during Mercerization. Journal of Applied Polymer Science 2008;107(1): 30-36.
[21]I. Spiridon, C. Teacă, R. Bodîrlău. Structural changes evidenced by FTIR spectroscopy in cellulosic materials after pre-treatment with ionic liquid and enzymatic hydrolysis. Bioresources 2011;6(1):400-413.
[22]B. Esteves, R. Videira, H. Pereira. Chemistry and ecotoxicity of heat treated pine wood extractives, Wood Sci Technol 2011;45 (6):661-676.
[23]J. Coates. Interpretation of Infrared Spectra, A Practical Approach in Encyclopedia of Analytical Chemistry. R.A. Meyers (Ed.). John Wiley & Sons Ltd. pp. 2000;10815-10837
[24]A. Michell, H. Higgins. Infrared Spectroscopy in Australian Forest Products research. CSIRO Forestry and Forest Products, Melbourne, Australia 60p. 2002.
[25]B. Tjeerdsma, H. Militz. Chemical changes in hydrothermal treated wood: FTIR analysis of combined hydrothermal and dry heat-treated wood. Holz als Roh- und Werkst 2005;63(2): 102-111.
[26]R. Kotilainen, T. Toivannen, R. Alén. FTIR monitoring of chemical changes in softwood during heating. Journal of Wood Chemistry and Technology 2000;20(3): 307-320.
[27]J. Li, B. Li, X. Zhang. Comparative studies of heat degradation between larch lignin and Manchurian ash lignin. Polymer Degradation and Stability 2002;78: 279-285.

[28]O. Faix. Classification of lignins from different botanical origins by FT-IR spectroscopy. Holzforschung 1991;45 (1): 21-27.
[29]E. Windeisen, C. Strobel, G. Wegener. Chemical changes during the production of thermotreated beech wood. Wood Sci Technol 2007;41(6): 523-536.
[30]D. Kocaefe, S. Poncsak, Y. Boluk. Effect of thermal treatment on the chemical compositionand mechanical properties of birch and aspen. Bioresources 2008;3(2): 517-537.
[31]M.M. González-Peña, S.F. Curling, M.D.C. Hale. On the effect of heat on the chemical composition and dimensions of thermally-modified wood. Polymer Degradation and Stability 2009;94(12): 2184-2193.
[32]P. Rodríguez-Lucena, J.J. Lucena, L. Hernández-Apaolaza. Relationship between the structure of Fe-Lignosulfonate complexes determined by FTIR spectroscopy and their reduction by the leaf Fe reductase. The Proceedings of the International Plant Nutrition Colloquium XVI. UC Davis: Department of Plant Sciences, UC Davis. 2009.
[33]D. Lee. Preparation of a Sulfonated Carbonaceous Material from Lignosulfonate and Its Usefulness as an Esterification Catalyst. Molecules 2013;18:8168-8180.
[34]C.B. Campbell, A. Onopchenko. Cation-exchange resin (Amberlyst-15) catalyzed alkylation of phenol with unhydrogenated PAO decene trimer. Rearrangement of tert-alkylphenols to sec-alkylphenols. Industrial & Engineering Chemistry Research 1992;31:2278-2281.
[35]X. Zang, Z. Zhang, F. Wang, Y. Wang, Q. Song, J. Xu. Lignosulfonate-based heterogeneous sulfonic acid catalyst for hydrolyzing glycosidic bonds of polysaccharides. J. Mol. Catal. A-Chem. 2013;377:102–107.
[36]F. Liu, J. Sun, Q. Sun, L. Zhu, L. Wang, X. Meng, C. Qi, F.S. Xiao. High-temperature synthesis of magnetically active and SO H-functionalized ordered mesoporous carbon with good catalytic performance. Catal. Today 2012;186:115–120.
[37]X.L. Hu, J. Klimes, A. Michaelides. Proton transfer in adsorbed water dimers. Physical Chemistry Chemical Physics 2010;12:3953-3956.
[38]K. Sathish-Kumar, O. Solorza-Feria, R. Hernández-Vera, G. Vazquez-Huerta, and H.M. Poggi-Varaldo, Comparison of Various Techniques to Characterize a Single Chamber Microbial Fuel Cell Loaded with Sulfate Reducing Biocatalysts Journal of New Materials for Electrochemical Systems 2012b; 15: 195-201.
[39]K. Rabaey, P. Clauwaert, P. Aelterman, W. Verstraete. (2005). Tubular microbial fuel cells for efficient electricity generation. Environ. Sci. Technol 2005; 39(20): 8077.
[40]Z. He, S.D. Minteer, L.T. Angenent. Electricity generation from artificial wastewater using an upflow microbial fuel cell.
Environ. Sci. Technol 2005; 39: 5262-5267.
[41]B. Min, B.E. Logan. Continuous Electricity Generation from Domestic Wastewater and Organic Substrates in a Flat Plate Microbial Fuel Cell. Environmental science & technology 2004;38:5809-5814.
[42]B. Min, J. Kim, S. Oh, J.M. Regan, B.E. Logan. Electricity generation from swine wastewater using microbial fuel cells. Water Research 2005;39:4961-4968.

Production of Electricity in an Electrobiochemical Slurry Reactor used for the Bioremediation of Pesticide Contaminated Soil

B. Camacho-Pérez [1], H.M. Poggi-Varaldo [1]*, J. Garcia-Mena [2], O. Solorza-Feria[3], E. Ríos-Leal [4], N. Rinderknecht-Seijas [5], Selvasankar Murugesan[2], Alberto Piña Escobedo[2]

[1]Environmental Biotechnology and Renewable Energies R&D Group, Dept. of Biotechnology and Bioengineering, CINVESTAV del IPN, México D.F., México, P.O. Box 14-740, 07000
[2]Dept. of Genetics and Molecular Biology, CINVESTAV del IPN, México D.F., México, P.O. Box 14-740, 07000
[3]Dept. of Chemistry, CINVESTAV del IPN, México D.F., México, P.O. Box 14-740, 07000
[4]Central Analítica, CINVESTAV del IPN, México D.F., México, P.O. Box 14-740, 07000
[5]ESIQIE del IPN, Mexico D.F., México.
*Author for all correspondence: r4cepe@yahoo.com

ABSTRACT

It is recognized that mass transfer of lindane from soil to liquid phase is the limiting process in biodegradation processes used for soil bioremediation. Surfactants are used due to their ability to increase water solubility and mass transfer. On the other hand, electrobiochemical slurry reactor (EBCR) constitutes a promising technology that could remove organic matter, phenol, petroleum hydrocarbons, and pesticides in contaminated soils with simultaneous electricity output. The aims of this research were *(i)* to evaluate the desorption of lindane from soil with Tween 80 at different concentrations; *(ii)* to determine the power output and removal of lindane in an electrobiochemical slurry reactor; and (*iii*) to characterize the dominant microorganisms in the electrobiochemical slurry reactor using 16S rRNA and denaturing gradient gel electrophoresis. The EBCR consisted of a Plexiglass cylinder approximately 6 cm in diameter and 8 cm in length, fitted with two anodes and two cathodes.

Addition of 2000 mg L^{-1} Tween 80 removed 9.61% of lindane in *in vitro* desorption experiments. The internal resistance of the EBCR determined by polarization curve was 820 Ω; a moderate volumetric power was recorded (374 mW m^{-3}) along with a potential of 600 mV when the two-electrode sets were connected in parallel. During the batch operation, the EBCR showed a 56% lindane removal whereas the reduction in the abiotic control was 3%. Unexpectedly the removal efficiency of lindane ($\eta_{lindane}$) in the EBCR was lower than that in an EBCR operated without surfactant in a previous experiment. This could be ascribed to the increased degradable organic matter supply related to Tween in our EBCR that possibly shifted microbial metabolism from lindane degradation to degradable matter uptake. An average volumetric power of 685 mW m^{-3} and average voltage of 420 mV were achieved. Results from the DGGE analysis and further sequencing, indicate the presence of *Trichococcus palustris* strain DSM 9172 (99% sequence identity). This bacterium has been reported in autotrophic biocathodes of other bioelectrochemical systems. Finally, the energy output obtained in our EBCR allows for the recovery of 20% of the power required for mixing, thus paving the way to sustainable bioremediation of soils

Keywords: Electrobiochemical slurry reactor; lindane; Tween 80

1. Introduction

Agriculture is an essential activity of modern societies. While agricultural products provide most of the food consumed by the world population, they also impose great pressures on global natural resources. Reliance on pesticides and fertilizers because of intense agricultural practices could also contribute to environmental degradation [1, 2]. Lindane (1, 2, 3, 4, 5, 6 - hexachlorocyclohexane, γ-HCH) is a moderately lipophilic, organochlorinated substance characterized by a high partition coefficient octanol-water $K_{ow} \approx 4*10^3$ with a low solubility in water, approx. 7 mg L^{-1} at 20ºC, and slight polarity due to the strong electronegative effects of chlorine atoms bound to the aliphatic ring [3, 4, 5]. The γ-HCH has been used in important agricultural applications as on fruits, vegetables crops, and forestry for control of leaf-eating insects, and it is used as a fungicidal seed treatment worldwide [6, 7, 8]. It is a Persistent Organic Pollutant (POP), potent carcinogen and teratogen and classified by the World Health Organization (WHO) as 'moderately hazardous' (human oral LDo: 840 mg kg^{-1}). Paknikar *et al*. [9], have been reported potential adverse health effects include neurological problems and immunosuppression in human and liver cancer in rats and mice [10]. The use of lindane has been restricted since the 1970s and banned later on because of their toxicity, but the problem of residues of lindane remains because of the high persistence and inter-conversion of lindane in soil [8, 10, 11]. Under natural conditions, the high adsorption of the hydrophobic compounds in the soil solid phase (mainly in the organic matter) and its restricted availability for the biological action of endogenous or exogenous microorganisms limits the extent and rate of degradation. The size of particles and aggregates, and soil structure, also contribute to making the desorption rate (mass transfer rate) the limiting stage in their degradation [12]. One possibility to favor the mobility of the pollutants is their transfer from the soil to the liquid phase; this possibility would enhance the pollutant bioavailability. Bioavailability is considered a dynamic process, determined by the rate of substrate-mass transfer to microbial cells relative to their intrinsic catabolic activity

One alternative to facilitate lindane desorption from the soil, and thus to increase lindane bioavailability in to use *ex-situ* technology such as soil slurry reactors. This technology consist of treating mixtures of contaminated soil and water in controlled stirred reactors [13].The advantages of the slurry reactor is the feasibility of controlling operating parameters such as mixing (facilitates aeration and enhances the rate of chemical exchange between soil particles), controlling pH, temperature, providing nutrients and other specialized amendments such as surfactants [14-16].

The addition of surfactants to increase the mass-transfer rate of PAHs in soils has received attention [17]. Surfactants consist of organic molecules with a hydrophobic and a hydrophilic part and can interact with polar as well as nonpolar surfaces. At low concentrations, surfactants exist solely as monomers; above a critical aqueous concentration, which is specific for each surfactant monomer, called critical micellar concentration (CMC), the surfactant monomers are aggregated in solution to form entities made up of a hydrophobic core and a hydrophilic shell [18]. These micelles result in increased pseudo-water-solubilities of pollutants, thereby increasing the concentration gradient and mass transfer rates [11, 17,18].

On the other hand, microbial fuel cells (MFC) constitute a promising technology for the biodegradation of several organic substrates such as glucose, acetate, xylose, cysteine, cellulose, leachates from solid substrate fermentation of municipal wastes and waterwastes, and other organic pollutants with simultaneous power generation [19- 31]. Recently, it has been proposed that soil microbial fuel cell (SMFC) technology could be applied to enhance the removal of organic matter, lindane, phenol, and petroleum hydrocarbons in contaminated soil, while at the same time allowing electric energy generation [32-34]. The aims of this research were *(i)* to evaluate the desorption of lindane from soil with Tween 80 at different concentrations; *(ii)* to determine the power output and removal of lindane in an

electrobiochemical slurry reactor; and (*iii*) to characterize the dominant microorganisms in the electrobiochemical slurry reactor using 16S rRNA and denaturing gradient gel electrophoresis; and (iv) to characterize the microorganisms in the electrobiochemical slurry reactor using the Ion Torrent Personal Genome Machine. We used a difficult to remediate soil. Since it had high contents of organic matter and clay.

2. Experimental

2.1 Desorption tests. Desorption assays were carried out in serum bottles at 100 rpm for 6 days in order to evaluate the effect of surfactant on lindane desorption. In each serum bottles was loaded with 5 g of sterilized soil polluted with lindane (100 mg kg^{-1} dry soil), 25 mL of a solution Tween 80 at different concentrations (0, 75, 500, 2000, 5000 mg L^{-1}). Sodium azide (300 mg L^{-1}), was added as a microbiological inhibitor, and $CaCl_2$ (0.01M). The supernatant solution was analysed for lindane concentration.

2.2 Electrobiochemical slurry reactor. EBCR consisted of a Plexiglass cylinder approximately 6 cm in diameter and 8 cm in height (308 mL capacity), fitted with two anodes and two cathodes. The anodes were graphite discs (5cm D x 0.5 cm) whereas the cathodes were of Toray carbon cloth, the cathodes were in contact with atmospheric air (Figure 1). The electrodes were separated by a cation exchange membrane (Nafion 117, coated with 0.5 mg cm^{-2} platinum catalyst, Pt 10wt%/C-ETEK) and was inoculated with a sulfate reducing inoculum acclimated to lindane [32].

The EBCR was batch-operated for 30 day at room temperature. The concentration of soil was 33% w/v and of Tween 80 was 2000 mg L^{-1}. The EBCR was fed a solution stock of sucrose: sodium acetate: lactate to give a final concentration of 2 g COD L^{-1} in the EBCR at 0 y 15 d. The contents of the EBCR were performed in an orbital shaker at 100 rpm. Measurements of the power output were performed using a Multimeter ESCORT 3146A. The process control was EBCR operated under open-circuit with live inoculum and soil.

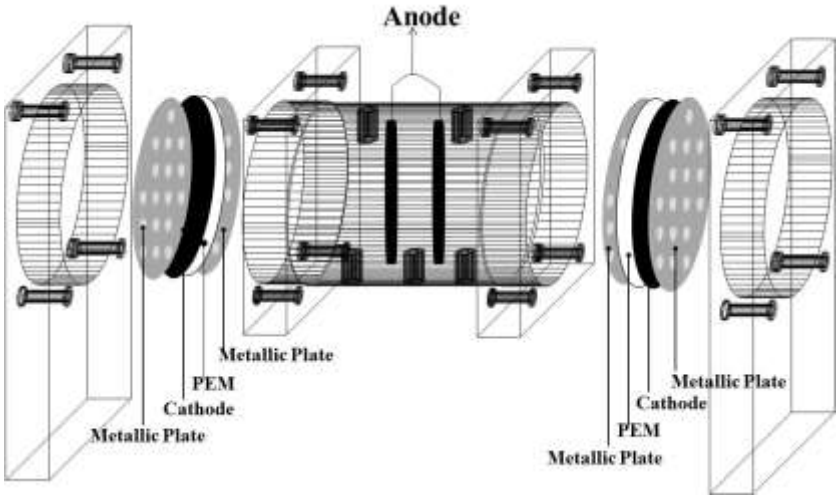

Fig 1. Schematic diagram of electrobiochemical slurry reactor.

2.3 Determination of internal resistence of the electrobiochemical slurry reactor. The internal resistance was determined using the polarization curve method, by varying the external resistance (100- 100 000 Ω) according to procedures outlined by elsewhere [23, 27, 29, 30], this was carried out 0 y 7 d of operation.

*2.4 Chemicals***.** The γ-HCH isomer (97% purity) was purchased from Sigma-Aldrich. Lindane is a moderately lipophilic, organo-chlorinated substance characterized by a high partition coefficient octanol-water Kow ≈ 4*103, with low solubility in water, approx. 7 mg L^{-1} at 20ºC, and slightly polar due to the strong electronegative effects of chlorine atoms bound to the aliphatic ring. Hexane and acetone were of analytical grade. Tween 80 was purchased from Sigma-Aldrich.

2.5 Soil. An agricultural soil with high contents of organic matter and clay, was sieved through a 20 mesh, and sterilized by tyndallisation. The soil was contaminated with 100 mg lindane kg^{-1}. Soil pH was determined in a slurry soil/deionized water 1:2 (w/w) [3], soil texture was measured by the hydrometer method, soluble BOD and soluble COD were determined in soil water extracts, according to the Standard Methods [35]. The main characteristics of the soil used in this work were: soil type, Cambisol; pH, 7.2; organic matter (%), 8.1 ± 0.1; soluble COD (mg COD kg^{-1}), 5100 ± 436; soluble BOD (mg BOD_5 kg^{-1}), 3725 ± 350; clay content (%), 42.3 ± 0.8; sand (%), 36.5 ± 2.7; silt (%), 21.2 ± 3.3. The texture was clayish and the hydraulic conductivity was low.

2.6 PCR-DGGE and Sequencing of 16S rDNA. A sample of 200 µl from the electrobiochemical slurry reactor (0, 15, 22, 30 days of treatment) were used to extract DNA using the PowerSoil® DNA Isolation kit (MoBio). Whole-community DNA from each sample was subjected to PCR amplification using of specific primers for the Eubacterial. The Eubacterial specific primers were CGO465F-GC (CTCCTACG GGAGGCAGCAGCGCCCGCCGCGCGCGGCGGGCGGGGCGGGGGCCCGGGGGG) and CGO465R (CTACCAGGGTATCTAATCCTG) targeting a region of 332-775 bp of *E. coli* 16S rRNA gen (gen 16S rDNA GenBank:J01859.1). The PCR mixture consisted of Buffer (1X), $MgCl_2$ (2 mM), dNTP´s (0.2 mM), Taq DNA polymerase (0.02U μL^{-1}), forward primer CGO465F-GC (0.2µM), reverse primer CGO465R (0.2µM), and template DNA (100 ng). Amplification was performed in a TECHNE (TC-312) thermocycler with cycling as follows: an initial denaturation step at 95°C for 5 min, followed by 25 cycles of 95°C for 45 s, 55 °C for 30 s, and 72°C for 30 s, and finally an extension step at 72°C for 10 min.
Denatured gradient gel electrophoresis (DGGE) was performed with a DCode™ universal mutation detection system (Bio-Rad®) according to the manufacturer's instruction. PCR amplicons were loaded onto 8% polyacrylamide gel with a denaturing gradient range from 25 to 70% consisting of urea and formamide. The gel was stained with SYBR® Green and DNA bands were observed by a Gel-Doc™ image analyzer (Bio-Rad) under UV illumination. After that denaturing gradient gel electrophoresis (DGGE), a representative band (when the EBCR exhibited the maximum voltage) was excised, cloned (Vector PCR® 2.1 TOPO®), sequenced (ABI PRISM 310, Applied Biosystems), sequence data were analyzed with BioEdit software and compared with sequences in GenBank (http://www.ncbi.nlm.nih.gov).

2.6.1 Richness estimation. Microbial richness variation between days of operation was estimated by the Jaccard similarity index IJ and Poggi's discrete divergence index Δ_{Poggi} [36, 37]:

$$IJ = \frac{n_{AB}}{(n_A + n_B - n_{AB})} \quad (1)$$

Where : IJ= Jaccard similarity index, n_{AB} = number of bands that are present both in lane A and lane B, nA = total number of bands in lane A, nB = total number of bands in lane B.

$$\Delta_{Poggi} = \frac{(n'_A + n'_B)}{n_A + n_B} \quad (2)$$

Where : Δ_{Poggi}= Poggi´s discrete divergence index , n'_A number of bands of lane A absent in lane B, n'_B = number of bands of lane B absent in lane A, nA = total number of bands in lane A, nB = total number of bands in lane B.

The IJ ranges from 0 to 1 where 1 occurs when the community profiles are completely similar and 0 when the profiles are completely different; the Δ_{Poggi} varies between 0 and 1, where 0 indicates similar communities and 1 indicates completely different profiles (the same bands and number of bands). Both indices can be used for comparing richness of two different communities, or comparing the richness of a community with respect to time. The divergence index Δ_{Poggi} allows for the calculation of the turnover ratio of richness of a community with respect to time $\dot{\Delta}_{Poggi}$ that gives more insight on the richness stability [35, 36]. In effect, $\dot{\Delta}_{Poggi}$ is defined by Equation (3) below as the derivative of Δ_{Poggi} with respect to time.

$$\dot{\Delta}_{Poggi} = {}^{d(\Delta_{Poggi})}/_{dt} \quad (3)$$

The units of $\dot{\Delta}_{Poggi}$ are (1/time), i.e., (1/day or day^{-1}).

Thus, a low value of $\dot{\Delta}_{Poggi}$ indicates that the microbial community is relatively stable with respect to time. For instance, analysis of a microbial community in attached-growth bioreactors with this tool has shown very low values of $\dot{\Delta}_{Poggi}$. On the other hand, higher values of $\dot{\Delta}_{Poggi}$ are related to significant dynamic changes on community composition.

2.7 Metagenome sequencing using the Ion Torrent (PGM) Platform. Total genomic DNA of the collected samples was extracted using PowerSoil® DNA Isolation kit (MoBio) according to the manufacturer's instructions. The extracted DNA was amplified with the primers targeting V3 region of the 16S rDNA**.** The forward primer was V3-341F containing a 12bp Golay barcode [38] and adapters for massive sequencing, and antisense V3-518R containing A and Truncated P1 adapters [39]. The PCR mixture consisted of Buffer (1X), $MgCl_2$ (2 mM), dNTP´s (0.2 mM), Taq DNA polymerase (0.025U μL^{-1}), forward primer V3-341F (0.2µM), reverse primer V3-518R (0.2µM), and template DNA (10 ng). Amplification was performed in a GeneAmp PCR System 2700 Thermocycler (Applied Biosystems). The PCR amplification was performed with an initial denaturation (95°C for 5 min) followed by 30 cycles of denaturation (94°C for 15 s), annealing (62°C for 15 s) and extension (72°C for 15 s) and final extension (72°C for 10 min). The PCR products were purified by electrophoretic separation on 2% agarose gel and using Wizard SV Gen PCR Clean-Up System (Promega). The concentration of PCR amplicons were

measured by NanoDrop spectrophotometer (ThermoScientific). After that the samples were sent out for the barcoded libraries preparation and sequencing on an Ion Torrent PGM with 316 chip using the Ion Sequencing 200 bp kit (Life Technologies) according to the standard protocol (Ion Xpress_ Plus gDNA and Amplicon Library Preparation, Life technologies).

After sequencing, sequence reads were filtered by the PGM software to remove low quality and polyclonal sequences. During this process sequences matching the 3'-adapter were automatically trimmed and filtered. Sequenced data-Microbiota analysis Ion torrent PGM software, Torrent_Suite v 4.0.2 was used to demultiplex the sequenced data based on their barcodes and poor quality reads were eliminated from the datasets, i.e. quality score <20, containing homopolymers >6, length <200 nt, and containing errors in primers and barcodes. Filtered datas were exported as Fastq files. Demultiplexed sequencing data were analized using QIIME version 1.8.0 software pipeline [40]. Fastq files were converted into Fasta files, and all the demultiplexed files were concatenated into a single fasta file. Closed reference Operational taxonomic units (OTU) were determined at 97% similarity level with UCLUST Algorithm [41].

Chimeras were detected and removed from the datasets using the Chimera Slayer [42]. Sequence alignments were done against the Greengenes core set [43]. Statistical analysis of the OTU table Microbial diversity had been assessed through both alpha and beta diversity. Using rarefied OTU tables, alpha diversities were calculated using various matrices like Shannon, PD whole tree, chao1, observed species. The beta diversity analysis was calculated using UniFrac analysis [44], by phylogenetic tree computed with FastTree and a rarefiled biom table as inputs. Abundance of the bacterial groups at different taxonomic levels (phylum, order, and genus) was separately explored with a Principal Component Analysis (PCA) and Unweighted Pair Group Method with Arithmetic mean (UPGMA) Clustering.

2.7.1 Calculations of ecological indices. Shannon-Weaver diversity index has been a popular index in the ecological literature [45-46]. Shannon-Weaver index is defined as:

$$H' = -\sum_{i=1}^{S}(p_i \log p_i) \qquad (4)$$

Where:

p_i= is the proportion of characters belonging to the i type of letter in the string of interest; yet, in ecology, p_i is often the proportion of individuals belonging to the i species in the dataset of interest, S is the total number of species.

Pielous evenness index is a measure of a biodiversity which quantifies how equal the community is numerically [46-47]. This index is defined as:

$$J' = \frac{H'}{\log S} \qquad (5)$$

where:

H´ = is the Shannon-Weaver index
S = is the total number of species
J´ = is constrained between 0 and 1, 1 indicates máximum evenness or the equitative distribution of species.

It is worth emphasizing that the log in Equations (4) and (5) should be on base 2, since the ShannoneWeaver index was originated on the grounds of the theory of information that uses binary system of numbers. Yet, in the literature there is a variety of bases. Most researchers have chosen base 10, others have selected base e (natural logarithms) for the calculation of H´. Because of this, we distinguish and report here the índices H´2, H´e, and H´10 to indicate that the base of the logarithm is 2, e, and 10, respectively. The base of log S in the denominator of the Pielou index should be consistent with base of the log used in the calculation ShannoneWeaver index. Furthermore and interestingly, Pielou index is invariant with respect to the base of the logarithm, as long as the base of logs in the numerator and denominator are the same [45].

2.8 Lindane and metabolite analysis. The procedure for the extraction and determination of HCH and intermediate metabolites in the electrobiochemical reactor were performed according by Quintero *et al.* [48]. The lindane was analyzed in a Perkin Elmer gas chromatograph equipped with an electron capture detector. The intermediate metabolites were analyzed in a Perkin Elmer GC/MS [32].

3. Results and discussion

3.1 Desorption tests. Figure 2 shows the lindane desorbed at different initial concentrations of Tween 80 in the water phase. The maximum desorption effect was observed at a dose of 2000 mg L^{-1} of Tween 80, 9 mg of lindane removed kg^{-1} of dry soil. Because of this, we applied an initial concentration of 2000 mg L^{-1} of Tween 80 in our EBCR.

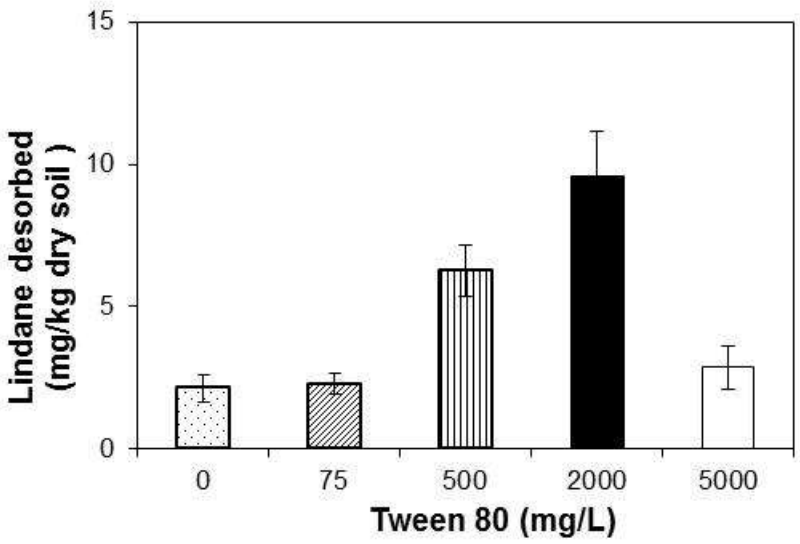

Fig 2. Lindane desorbed from the soil to the water phase. The initial concentration of lindane in soil was 100 mg kg^{-1} of dry soil.

3.2 Characterization of the electrobiochemical slurry reactor. The values obtained of internal resistance from the polarization curves method were, 5660, 6022, 12419 y 3845 Ω for face A, face B, connection in series and parallel, respectively, at time 0 day (Table 1). The maximum volumetric power was obtained when the connection was in parallel (60 mW m^{-3}) followed by connection in series, face A, and face B with 38, 12 and 11 mW m^{-3} respectively. After 7 days of operation another electrochemical characterization was carried out. The internal resistances decreased very much compared to those of the first characterization. Their values were approximately o 4652, 3867, 1041, 804 Ω for face A, face B, connection in series and connection in parallel, respectively (Table 1). The maximum volumetric power was obtained for parallel connection (373 mW m^{-3}, Table 1); it was sixfold the volumetric power obtained with characterization at 0 days.

Table 1. Values of several variables of electrobiochemical slurry reactor characterization at 0 and 7 day.

Parameter	Face A		Face B		Series		Parallel	
Time (days)	0	7	0	7	0	7	0	7
R_{int} (Ω)	5660	4652	6022	3687	12419	1041	3845	804
$P_{An\text{-}max}$ (mW m^{-2})	0.95	12.33	0.86	8.01	3.04	29.58	4.84	29.90
$P_{V\text{-}max}$ (mW m^{-3})	11.86	154	10.72	100	38.08	369	60.55	373
$I_{EBCR\text{-}max}$ (mA)	0.11	0.67	0.08	0.55	0.08	0.72	0.11	0.94
$E_{EBCR\text{-}max}$ (V)	0.31	0.57	0.32	0.58	0.50	0.60	0.54	0.59
$P_{EBCR\text{-}max}$ (mW)	0.003	0.05	0.001	0.03	0.01	0.11	0.02	0.12
$P_{An\text{-}ave}$ (mW m^{-2})	0.37	4.54	0.39	3.93	1.04	9.98	1.72	9.92
$P_{V\text{-}ave}$ (mW m^{-3})	4.57	56.82	4.86	49.20	13.01	124.79	21.46	123.96
$I_{EBCR\text{-}ave}$ (mA)	0.02	0.11	0.02	0.09	0.03	0.18	0.05	0.18
$E_{EBCR\text{-}ave}$ (V)	0.13	0.30	0.13	0.30	0.21	0.38	0.25	0.39
$P_{EBCR\text{-}ave}$ (mW)	0.001	0.02	0.001	0.02	0.004	0.04	0.007	0.04

Notes: R_{int}: internal resistance; P_{An}, surface area power density; P_V, volumetric power; E_{EBCR}, voltage; I_{EBQR}, current intensity; P_{EBCR}, power delivered. Subindices: max, maximum; ave, average.

The improved characteristics might be a consequence of the increased microbial activity resulting from enrichment of the biofilm on the anode [49].

Figure 3 shows the time course of the potential delivered by the device when the anodes and cathodes of the EBCR were connected in parallel; results of the average performance are exhibited in Table 2. The voltage with the EBCR in open circuit conditions (at the early 11 h) was approximately 666 mV (phase I). The voltage remained stable when the cell was operated with an external resistance of 3300 Ω, average 318 mV (first nineteen of phase II); however the voltage decreased to less than 160 mV afterwards. So, open circuit conditions were re-established in phase III where an expected increase of voltage occurred.

Subsequently, in phase IV, the cell was operated with an external resistance of 820 Ω, the voltage remained stable (341 mV). The EBCR at 16 d was supplemented with 2 g L^{-1} substrate (sucrose: sodium acetate: lactate) and Tween 80 (2 000 mg L^{-1}) that was used as the fuel. The electricity generation began to increase and reached a voltage output of approximately 488 mV (Figure 3).

The maximum voltage output of the EBCR (580 mV) and maximum power (108 mW m^{-2}) were higher than those reported by Wang *et al*. [34] (155 mV and maximum surface power 0.85 mW m^{-2}) for a cell loaded with soil polluted with total petroleum hydrocarbons. Our results also compared very favorably to

those observed by Yan *et al*. [50] who reported a voltage as low as 17 mV in the treatment of sediment contaminated with phenanthrene and pyrene. On the other hand, Huang *et al*. [33] registered a power density *ca.* 30 mW m^{-2} and a lower voltage (150 mV) in the treatment of a waterlogged soil polluted with phenol.

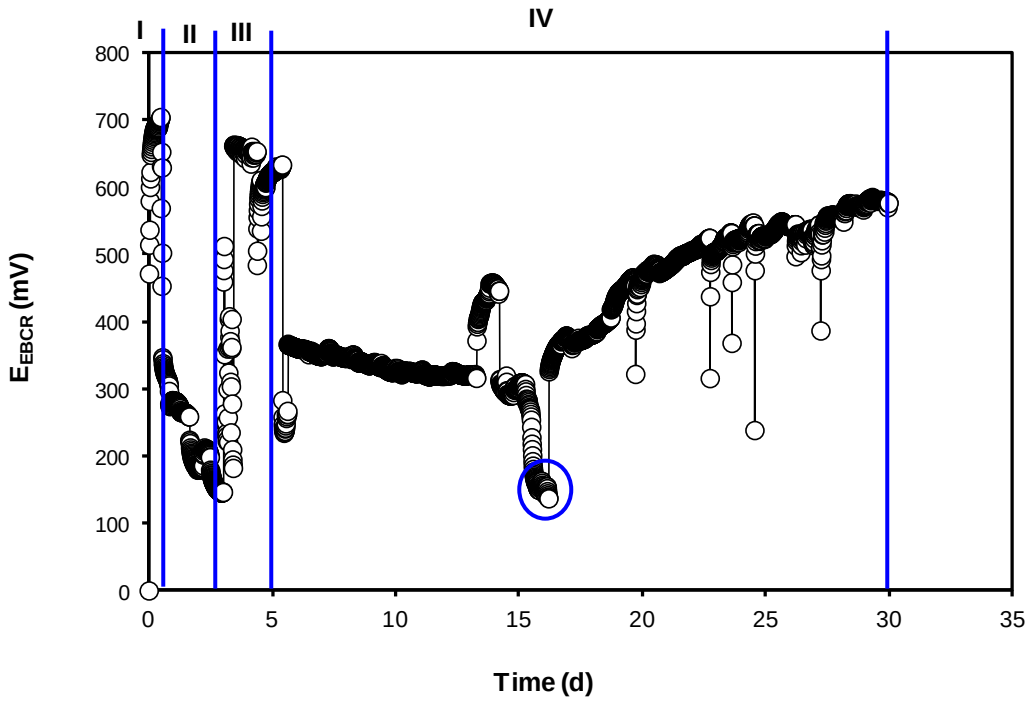

Fig 3. Electricity generation in electrobiochemical slurry reactor during batch operation for 30 d. The addition of substrate is indicated by the blue . Phase I, open circuit; phase II, closed circuit with external resistance 3300Ω; phase III, open circuit; phase IV, external resistance 820Ω.

Our EBCR exhibits a bonus besides soil remediation: the bioelectricity generation. The latter was estimated with Equation 1 below

$$\hat{E}_{harvested}\ (\text{MJ/tonne soil}) = P_{ave}\ (\text{W})*(30\ \text{d}*24\ \text{h/d}*3600\ \text{s/h})/(0.0001\ \text{tonne soil} * 1000000\ \text{J/MJ}) \quad (6)$$

where $\hat{E}_{harvested}$ is the energy produced in MJ tonne $soil^{-1}$, P_{ave} is the average power in 30 d of operation, 24 h d^{-1} and 3600 s h^{-1} are conversion factors for converting time from days to seconds; 0.0001 tonne soil is soil mass in the lab scale EBCR.

The $\hat{E}_{harvested}$ was estimated at 5.9 MJ $tonne^{-1}$ soil during 30 days of operation. This energy can partially offset the power required for mixing of both the EBCR and typical SBs. For instance, power requirements for mixing are determined empirically and can be estimated from manufacturer´s equipment specifications. Indeed, typical power requirements for complete mixing are in the range 20 to 50 kW/1000 m^3 for moderately thick suspensions [51]; a mid-point value of 35 kW/1000m^3 was chosen. Performing the

calculations with similar assumptions to those of Equation 6, the energy required for mixing during the 30 d batch would be given by Equation 7 below

$\hat{E}_{mixing}$ = 35 (W/m^3)*(0.33 tonne soil/m^3)*(30 d*24 h/d*3600 s/h) = 29.9 MJ/tonne soil (7)

That is, the EBCR allows for a bioelectricity harvest that could represent *ca.* 20 % of the energy required for mixing.

Table 2. Average performance of electrobiochemical slurry reactor

Parameter	
$P_{An\text{-}max}$ (mW m^{-2})	108
$P_{V\text{-}max}$ (mW m^{-3})	1357
$_{EBCR\text{-}max}$ (V)	0.58
$I_{EBCR\text{-}max}$ (mA)	0.71
$P_{EBCR\text{-}max}$ (mW)	0.42
$P_{An\text{-}ave}$ (mW m^{-2})	54 ± 30
$P_{V\text{-}ave}$ (mW m^{-3})	685± 377
$E_{EBCR\text{-}ave}$ (V)	0.42± 0.12
$I_{EBCR\text{-}ave}$ (mA)	0.47 ± 0.17
$P_{EBCR\text{-}ave}$ (mW)	0.19 ± 0.02

Notes: P_{An}, surface area power density; P_V, volumetric power; E_{EBCR}, voltage; I_{EBCR}, current intensity; P_{EBCR}, power delivered. Subindices: max, máximum; ave, average. Standard desviation is with respect to time

3.3 Lindane removal and intermediate metabolites. Lindane removal achieved in the EBCR was 56 %, whereas the removals of the biotic (live) control and abiotic control EBCRs were 72 and 3%, respectively. Main metabolites due to lindane degradation in the EBCR were detected by analysis by GC/MS in the EBCR: 1,2,3-trichlorobenzene (1,2,3 TCB), 1,4 dichlorobenzene (1,4-DCB), 1,2-dichlorobenzene (1,2-DCB), and chlorobenzene (CB) (Figure 4). Lindane removals observed in our EBCR compared similarly with lindane removals reported for standard slurry bioreactors in the literature. Okeke *et al*. [52] carried out experiments with SB inoculated with *Pandorea* sp., with a presumably anaerobic operation of 9 weeks duration. Initial lindane concentration was 100 mg kg^{-1}; they found removals of 59.6% γ-HCH.

Unexpectedly the $\eta_{lindane}$ in EBCR was lower than that in EBCR operated without surfactant, 78% [32]. This could be ascribed to the influence of increased degradable organic matter supply in the experiment. Quintero *et al*. [12] treated a sandy soil polluted with a mixture of isomers α, β, γ and δ-HCH (100 mg kg^{-1} each) in anaerobic SB. Starch was supplemented at 2 g L^{-1} every 3 days. High removals of nearly 100% for α and γ isomers of HCH and 65 to 70% for β and δ HCH were found. On other hand, Robles-Gonzalez *et al*. [3] studied the bioremediation of a heavy soil polluted with 100 mg lindane kg^{-1} in full sulfate reducing SB. Removal was 88% whereas the detected metabolites after 30 d operation were PCCH; 1,2,4-TCB; 1,2,3-TCB; CB, and benzene; they also demonstrated that in methanogenic SBs the removal of lindane was between 41-47%. The SB was operated with similar soil operational conditions. In other studies of our Group, Varo-Arguello *et al*. [4] carried out experiments with SB in sulphate-reducing conditions; they reported removals of 78% γ-HCH in 30 days.

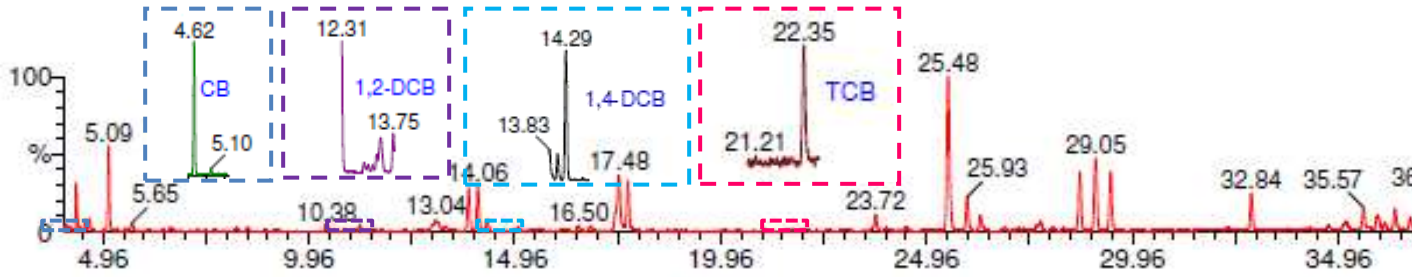

Fig 4. GC-MS detection of intermediate metabolites in electrobiochemical slurry reactor at the end of operation (30 d)

3.4. Microbial consortia characterization

3.4.1. Resuls of DGGE analysis

Results from the DGGE analysis (Figure 5) and further sequencing, indicate the presence of *Trichococcus palustris* (99% sequence identity, Band 11). This bacterium has been reported in autotrophic biocathodes of other bioelectrochemical systems [53]. *Trichococcus* (Firmicutes) also has been isolated of Arctic tundra soil and was identified as facultatively anaerobic bacterium [54].

On the other hand Freeman *et al*. [55] found *Trichococcus flocculiformis* as the dominant clone in the microflora of a sulfidogenic lab scale expanded granular sludge blanket bioreactor (mesophilic conditions, V = 2.9 l) fed with a simulated semiconductor manufacturing wastewater containing 425 mg L^{-1} isopropanol, 1,370 mg L^{-1} citric acid, and 615 mg L^{-1} polyethylene glicol, and divalent copper (Cu(II) . They further characterized this microbe as a fermentative organism in the low G-C Gram positive bacteria, originally isolated from anoxic digestor sludge [56]. *T. flocculiformis* could grow on citrate [57] and might have contributed to the effective removal of this substrate in the bioreactor.

In the case of DGGE analysis (Figure 5); twenty-four initial bands were found at the beginning of the experiment; this bands were constants at the 15 and 22 days of operation, at the end of experiment (30 days of operation) 9 bands dissappeared. On the other hand, at 22 days of operation the band 1 and 11 were more intense, when the EBCR exhibited the maximum voltage. The richness of eubacterial community was relatively stable during the 15 and 22 days of operation time, as reflected by high IJ values (0.71 and 0.77 at15d and 22d, respectively, Table 3) or alternatively, by low divergence index values (0.16 and 0.12 at15d and 22d, respectively). On the other hand, $\dot{\Delta}_{Poggi}$ (0.005) at 22 days of operation shown that the microbial community is relatively stable with respect to time.

Table 3. Summary of variation of richness of eubacterial communities in the bioreactor. The left number is the Jaccard index of similarity, the medium number is the divergence index, the right number is the $\dot{\Delta}_{Poggi}$

Operation time	15d	22d	30d
	Jaccard index/divergence index/$\dot{\Delta}_{Poggi}$	Jaccard index/divergence index/$\dot{\Delta}_{Poggi}$	Jaccard index/divergence index/$\dot{\Delta}_{Poggi}$

0d	0.71/0.16/0.01	0.77/0.12/0.005	0.39/0.43/0.01
15d		0.71/0.16/0.02	0.50/0.33/0.02
22d			0.44/0.38/0.04

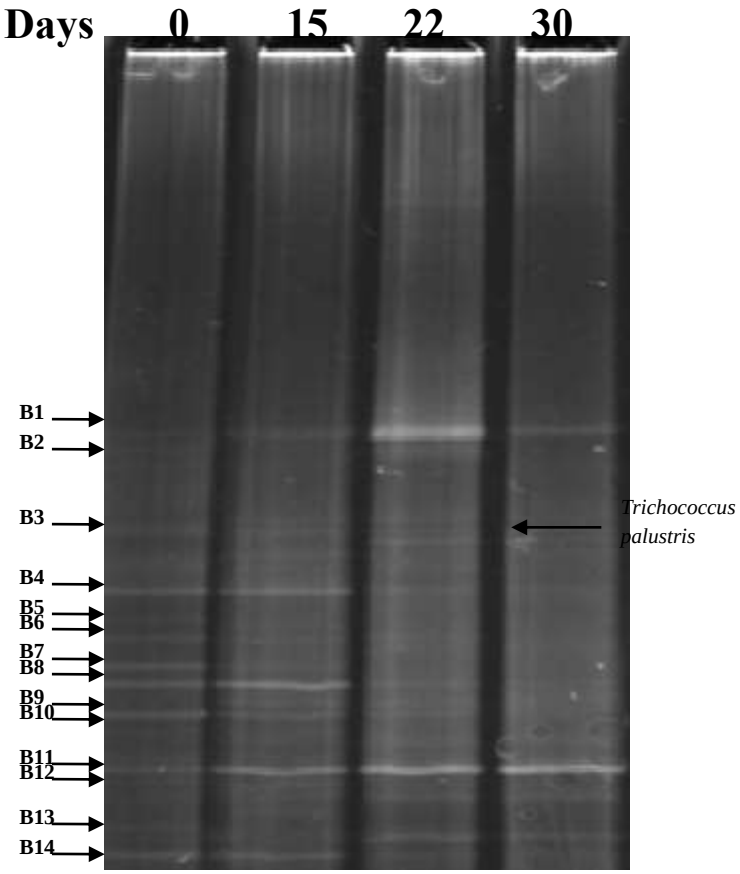

Fig 5. DGGE gels for microbial community monitoring for DGGE gels. eubacterial community. Bj: eubacterial bands

3.4.2. Results from massive semiconductor sequencing

Figure 6. shows the composition of bacterial population obtained from sulphate inoculum and EBCR at different days of operation. The more representative phylum were actinobacteria, bacteroidetes, firmicutes, proteobacteria and synergistetes.

Kim *et al*. [58] performed a phylogenetic analysis of microbial samples that revealed a diverse bacterial community consisting of Proteobacteria, Firmicutes, Bacteroidetes and Spirochaetes. The authors worked with a single MFC with air cathode membrane electrode assembly combined into duplicate two-module longitudinal tubular reactors. The reactor was inoculated with anaerobic digester sludge.

In our work, the most dominant genera belonged to *Arcobacter*, 40.8%, and *trichococcus* (41.6%) at 22 days of operation (Table 6), when the EBCR exhibited the maximum voltage. *Arcobacter* was reported to

harbor in electrodes of MFC, and rapidly generates a strong electronegative potential as a pure culture when it is supplied with acetate [59]. *Thrichococcus* has been reported in autotrophic biocathodes of other bioelectrochemical systems [53]. *Trichococcus* was identified as facultatively anaerobic bacteria by Kim *et al*. [54].

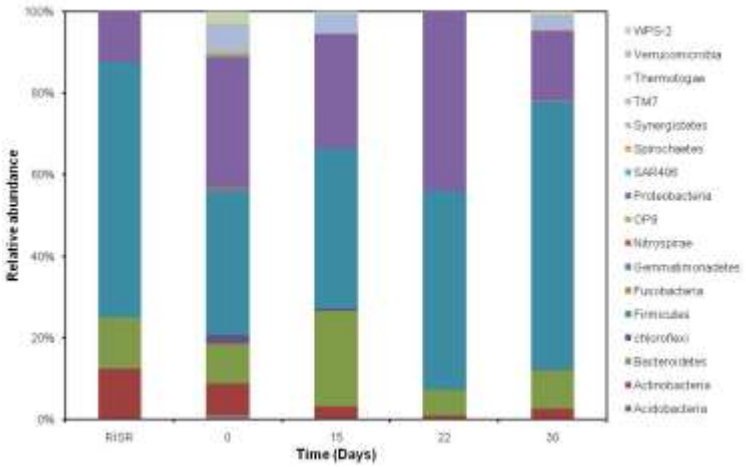

Fig 6. Phylum level identification by massive semiconductor sequencing of microbial community in our electrobiochemical slurry reactor.

3.4.3. Analysis of ecological indices

Shannon-Weaver index and Pielou´s indices for the sulphate reducing inoculum were 1.54 and 0.38 respectively (Table 5). Ortega-Martínez *et al.*[46] characterized a sulphate reducing inoculum, they reported 1.84 and 0.66 for Shannon-Weaver index and Pielou´s index respectively. In the case of the electrobiochemical slurry reactor , Shannon-Weaver index was 2.42, 2.00, 1.33, and 1.39 (Table 5) for 0, 15 , 22, and 30 days of operation respectively. The Pielou´s index for electrobiochemical slurry reactor was 0.59, 0.49, 0.32, and 0.39 (Table 5) for 0, 15, 22, and 30 days of operation respectively. The above results concluded that the different distributions of species were identified in the electrobiochemical slurry reactor at diferents days of operation.

Table 5. Ecological indices of the electrobiochemical slurry reactor based on phylum

Sample	**Shannon-Weaver index based on phylum**			**Pielou´s index based on phylum**
	H'_e [a]	**H'_{10} [b]**	**H'_2 [c]**	**J´**
SR-In[d]	1.07	0.46	1.54	0.38
0d[e]	1.68	0.73	2.42	0.59
15d[e]	1.39	0.60	2.00	0.49
22d[e]	0.92	0.40	1.33	0.32
30d[e]	1.10	0.48	1.59	0.39

Notes: [a], calculated with logarithm base $_e$; [b], calculated with logarithm base $_{10}$; [c], calculated with logarithm base $_2$; [d], sulphate reducing inoculum; [e]. operation time

Table 6. Genus level identification of all the sequences (Only relative abundances of identified Genus higher than 1 % are listed and all the other sequences are included in "others")

Genus/Time (Days)	SR In	0	15	22	30
Actinobacteria Acidimicrobiia Acidimicrobiales	0	1.3	0.6	0.2	0.3
Actinobacteria Actinobacteria Actinomycetales Actinomycetaceae __N09	0	1.2	0.6	0.2	0.9
Actinobacteria Actinobacteria Actinomycetales Nocardioidaceae Propionicimonas	6.2	0	0.1	0	0.1
Actinobacteria Actinobacteria Actinomycetales Propionibacteriaceae	6.2	0.2	0	0	0.2
Bacteroidetes Bacteroidia Bacteroidales	0	4.2	17.6	0.3	1.7
Bacteroidetes Bacteroidia Bacteroidales Porphyromonadaceae	0	0.9	3.5	5.4	4.9
Bacteroidetes Bacteroidia Bacteroidales Prevotellaceae Prevotella	6.2	2.1	0.4	0	0.8
Bacteroidetes Bacteroidia Bacteroidales Rikenellaceae Blvii28	6.2	0.1	0.5	0	0
Firmicutes Bacilli Bacillales Bacillaceae Bacillus	6.2	2	1.9	0.6	0.8
Firmicutes Bacilli Lactobacillales Carnobacteriaceae Trichococcus	6.2	1.9	7.4	41.6	45
Firmicutes Bacilli Lactobacillales Lactobacillaceae Lactobacillus	0	1.6	0	0	0.5
Firmicutes Bacilli Lactobacillales Streptococcaceae Lactococcus	6.2	0.2	0	0	0.1
Firmicutes Clostridia Clostridiales	12.5	0.8	3.2	0.3	1.4
Firmicutes Clostridia Clostridiales Clostridiaceae	0	1.3	0.6	0.6	1
Firmicutes Clostridia Clostridiales Clostridiaceae Clostridium	0	8.8	3.9	1.1	3.9
Firmicutes Clostridia Clostridiales Lachnospiraceae	6.2	1.9	6.9	0.1	0.7
Firmicutes Clostridia Clostridiales Lachnospiraceae Anaerostipes	6.2	0	0	0	0
Firmicutes Clostridia Clostridiales Ruminococcaceae	0	1.8	2.9	0.6	1.6
Firmicutes Clostridia Clostridiales Ruminococcaceae Ethanoligenens	0	1.8	0	0	0.3
Firmicutes Clostridia Clostridiales Ruminococcaceae Faecalibacterium	12.5	1.5	0.5	0	0.6
Firmicutes Clostridia Clostridiales Ruminococcaceae Oscillospira	6.2	0.4	0.2	0.2	0.4
Firmicutes Clostridia Clostridiales [Mogibacteriaceae] Anaerovorax	0	0.2	1.6	0.3	0.8
Firmicutes Clostridia Clostridiales [Tissierellaceae] Sedimentibacter	0	0.1	3.5	1	1.2
Proteobacteria Alphaproteobacteria Sphingomonadales Sphingomonadaceae	0	0.2	1.1	0	0
Proteobacteria Alphaproteobacteria Sphingomonadales Sphingomonadaceae Sphingomonas	0	0.1	1.8	0	0
Proteobacteria Deltaproteobacteria Desulfovibrionales Desulfovibrionaceae Desulfovibrio	0	2	0.6	0.1	0.7
Proteobacteria Deltaproteobacteria Desulfuromonadales Pelobacteraceae	0	0.1	1.3	0.1	0.2
Proteobacteria Epsilonproteobacteria Campylobacterales Campylobacteraceae Arcobacter	0	0.2	1	40.8	9.7
Proteobacteria Epsilonproteobacteria Campylobacterales Helicobacteraceae	0	2.3	6.2	0.8	0.5
Proteobacteria Gammaproteobacteria Enterobacteriales Enterobacteriaceae	6.2	6.1	3.6	0.1	0.8
Proteobacteria Gammaproteobacteria Enterobacteriales Enterobacteriaceae Enterobacter	0	1.5	2.1	0	0.2
Proteobacteria Gammaproteobacteria Pasteurellales Pasteurellaceae Haemophilus	6.2	0	0	0	0
Proteobacteria Gammaproteobacteria Thiotrichales Piscirickettsiaceae Thioalkalimicrobium	0	2.1	0	0	0.1
Synergistetes Synergistia Synergistales Dethiosulfovibrionaceae HA73	0	1.7	1.9	0	1.8
Synergistetes Synergistia Synergistales Thermovirgaceae	0	4.7	2.4	0	0.1
Thermotogae Thermotogae Thermotogales Thermotogaceae Kosmotoga	0	2.8	0.5	0	0.7
Others	0.6	41.9	21.6	5.6	18

CONCLUSION

- A dose of 2000 mg L^{-1} Tween 80 exhibited the best desorption of lindane from soil to water phase, although its absolute value was low-to-moderate
- The bioremediation of lindane in soil could be achieved in an EBCR with similar removals to those reported in anaerobic slurry bioreactors loaded with lindane-acclimated, methanogenic inoculum, as well as other conventional slurry bioreactors.
- The EBCR not only provided bioremediation of a toxic, recalcitrant organo-chlorinated pesticide, but also supplied (as bioelectricity) *ca.* 20 % of the energy required for mixing the device.
- The results of bacterial community analysis of the electrobiochemical slurry reactor, the phylum more representative were actinobaceria, bacteroidetes, firmicutes, proteobacteria, and synergistetes.

Thus, the EBCR is a significant step towards the green/sustainable remediation of contaminated soils.

Acknowledgements

The authors wish to thank Mr. Rafael Hernández-Vera (GBAER, DBB CINVESTAV del IPN), Mr. A. Rodríguez-Castellanos (Dept Chemistry), Mr. A. Barbosa-Fernández (Mechanical Shop), Mr. J. Barrera Rojas (Dept. of Biochemistry), and Mr. Gustavo Medina (chromatographic analyses), for their excellent technical help. CONACYT granted a graduate scholarship to BC-P. SECITI-GDF (formerly ICYTDF) supported the research with grant PICCO 10-28.

REFERENCES

[1] F. Macary, S. Morin, J.L. Jean-Luc Probst, F. Saudubray, A multi-scale method to assess pesticide contamination risks in agricultural watersheds. Ecological Indicators. 2014; 36: 624– 639.

[2] C. Sattler, H. Kächele, G. Gernot Verch, Assessing the intensity of pesticide use in agriculture. Agriculture Ecosystems and Environment. 2007;119: 299–304.

[3] I.V. Robles-González, E. Ríos-Leal, I. Sastre-Conde, F. Fava, N. Rinderknecht-Seijas, H.M. Poggi-Varaldo, Slurry bioreactors with simultaneous electron acceptors for bioremediation of an agricultural soil polluted with lindane. Process Biochemistry. 2012; 47(11):1640-1648.

[4] W.E. Varo-Arguello, B. Camacho-Pérez, E. Ríos-Leal, P.A. Vázquez-Landaverde, M.T. Ponce-Noyola, J. Barrera-Cortés, I. Sastre-Conde, N.F. Rindernknecht-Seijas, H.M. Poggi-Varaldo, Triphasic slurry bioreactors for the bioremediation of lindane-impacted soil under aerobic and anaerobic conditions. Environmental Engineering and Management Journal. 2012;11(10):1811-1823.

[5] B. Camacho –Pérez, E. Ríos-Leal, N. Rinderknecht-Seija, H.M.Poggi-Varaldo, Enzymes involved in the biodegradation of hexachlorocyclohexane: A mini review. Journal of Environmental Management, 2012;95:S306-S318.

[6] Y.F. Li, D.J. Cai, A. Singh, Technical hexachlorocyclohexane use trends in china and their impact on the environment. Archives of Environmental Contamination and Toxicology. 1998; 35:688–697.

[7] Y.F. Li, Y.F, Global technical hexachlorocyclohexane usage and its contamination consequences in environment: from 1948 to 1997. The Science of the Total Environment. 1999; 232:123–160.

[8] O. Prakash, M. Suar, V. Raina, C. Dogra, R. Pal, R. Lal, Residue of hexachlorocyclohexane isomers in soil and water samples from Delhi and adjoining areas. Current Science. 2004, 87 (1):73–78.

[9] K.M. Paknikar, V. Nagpal, A.V. Pethkar, J.M. Rajwade, Degradation of lindane from aqueous solutions using iron sulfide nanoparticles stabilized by biopolymers. Science and Technology of Advanced Materials, 2005; 6:370–374.

[10] K.L. Willett, E.M. Ulrich, R.A. Hites, Differential toxicity and environmental fates of hexachlorocyclohexane isomers. Environmental Science and Technolog. 1998; 32:2197–2207.

[11] J.C. Quintero, M.T. Moreira, G. Feijoo, J.M. Lema, Effect of surfactants on the soil desorption of hexachlorocyclohexane (HCH) isomers and their anaerobic biodegradation. Journal of Chemical Technology and Biotechnology. 2005; 80:1005–1015.

[12] J.C. Quintero, M.T. Moreira, G. Feijoo, J.M. Lema, Anaerobic degradation of hexachlorocyclohexane isomers in liquid and soil slurry systems. Chemosphere. 2005;61:528-536.

[13] J.T. Cookson, Bioremediation engineering: design and application New York, USA: McGraw-Hill Publishing Co.; 1995.

[14] I.V. Robles-González, F. Fava, H.M. Poggi-Varaldo, A review on slurry bioreactors for bioremediation of soils and sediments. Microbial Cell Factories. 2008;7: 5. doi:10.1186/1475-2859-7-5

[15] S. Venkata-Mohan, K. Sirisha, R. Sreenivasa-Rao, P.N. Sarma, Bioslurry phase remediation of chlorpyrifos contaminated soil: process evaluation and optimization by taguchi design of experimental (DOE) methodology. Ecotoxicology and Environmental Safety. 2007;68:252–262.

[16] I. Robles-González, E. Ríos-Leal, R. Ferrera-Cerrato, F. Esparza-García, N. Rinderkenecht-Seijas, H.M. Poggi-Varaldo, Bioremediation of a mineral soil with high contents of clay and organic matter contaminated with herbicide 2,4-dichorophenoxyacetic acid using slurry bioreactors: Effect of electron acceptor and supplementation with an organic carbon source. Procces Biochemistry. 2006; 41:1951-1960.

[17] P. Di Gennaro, A. Franzetti, G. Bestetti, M. Lasagni, D. Pitea, E. Collina, Slurry phase bioremediation of PAHS in industrial landfill samples at laboratory scale. Waste Management. 2008; 28:1338–1345.

[18] C.N. Mulligan, R.N. Yong, B.F. Gibss, Surfactant-enhanced Remediation of Contaminated Soil: a Review". Engineering Geology. 2001; 60:371-380.

[19] I. Valdez-Vázquez, E. Ríos-Leal, K.M. Muñoz-Páez, A. Carmona-Martínez, H.M. Poggi-Varaldo, Effect of inhibition treatment, type of inocula, and incubation temperature on batch H_2 production from organic solid waste. Biotechnology and Bioengineering. 2006;95:342-349.

[20] H.M. Poggi-Varaldo, J. Trejo-Espino, G. Fernandez-Villagomez, F. Esparza-Garcia, S. Caffarel-Méndez, N. Rinderknecht-Seijas, Quality of anaerobic compost from paper mill and municipal solid wastes for soil amendment. Water Science Technology. 1999; 40(11-12):179-186.

[21] Z. Du, H. Li, T. Gu, A state of the art review on microbial fuel cells: apromising technology for wastewater treatment and bioenergy. Biotechnology Advances, 2007; 25:464–482.

[22] H. Liu, R. Ramnarayanan, B. E. Logan, Production of electricity during wastewater treatment using a single chamber microbial fuel cell Environmental Science & Technology. 2004;38(7):2281–2285.

[23] B.E. Logan, B. Hamelers, R. Rozendal, U. Schroder, J. Keller, S. Freguia, P. Aelterman, W. Verstraete, K. Rabaey, Microbial fuel cells: methodology and technology. Environmental Science & Technology. 2006; 40(17): 5181-5192.

[24] J.M. Morris, S. Jin, Feasibility of using microbial fuel cell technology in bioremediation of hydrocarbons in groundwater. Journal of Environmental Science and Health Part A. 2008;43:18-23.

[25] A. Ortega-Martínez, K. Juárez-López, O. Solorza-Feria, M.T. Ponce-Noyola, E. Ríos-Leal, N.F. Rinderknecht-Seijas, H.M. Poggi-Varaldo, Parallel connection and sandwich electrodes lower the internal resistance in a microbial fuel cell. Journal of New Materials for Electrochemical Systems. 2012; 15(3):187-194.

[26] D. Pant, G. Van Bogaert, L. Diels, K. Vanbroekhoven, A review of the substrates used in microbial fuel cells (MFCS) for sustainable energy production. Bioresource Technology. 2010; 101(6): 1533–1543.

[27] H.M. Poggi-Varaldo, A. Carmona Martínez, A.L.Vázquez-Larios , O. Solorza-Feria, Effect of inoculum type on the performance of a microbial fuel cell fed with spent organic extracts from hydrogenogenic fermentation of organic solid wastes. Journal of New Materials for Electrochemical Systems. 2009;12:49-54.

[28] F. Rezaei, T.L. Richard, B.E. Logan, Analysis of chitin particle size on maximum power generation, power longevity, and coulombic efficiency in solid-substrate microbial fuel cells. Journal of Power Sources, 2009; 192:304–309.

[29] K. Sathish-Kumar, O. Solorza-Feria, G. Vázquez-Huerta, J.P. Luna-Arias, H.M. Poggi-Varaldo, Electrical stress-directed evolution of biocatalysts community sampled from a sodic-saline soil for microbial fuel cells. Journal of New Materials for Electrochemical *Systems*. 2012;15 (3):181-186.

[30] A.L. Vázquez-Larios, O. Solorza-Feria, G. Vázquez-Huerta, F. Esparza-García, E. Ríos-Leal, N. Rinderknecht-Seijas, H.M. Poggi-Varaldo, A New design improves performance of a single chamber microbial fuel cell. Journal of New Materials for Electrochemical Systems. 2010; 13: 219-226.

[31] A.L. Vázquez–Larios, O. Solorza-Feria, G. Vázquez-Huerta, F. Esparza-García, N. Rinderknecht-Seijas, H.M. Poggi-Varaldo, Effects of architectural changes and inoculum type on internal resistance of a microbial fuel cell designed for the treatment of Leachates from the dark hydrogenogenic fermentation of organic solid wastes. International Journal of Hydrogen Energy. 2011;36:6199-6209.

[32] B. Camacho-Pérez, E. Ríos-Leal, O. Solorza-Feria, P.A. Vazquez-Landaverde, J. Barrera-Cortés, M.T. Ponce-Noyola, J. García-Mena, N. Rinderknecht-Seijas, H.M. Poggi-Varaldo, Performance of an electrobiochemical slurry reactor for the treatment of a soil contaminated with lindane. Journal of New Materials for Electrochemical Systems 2013; 217-228.

[33] D.Y. Huang, S.G. Zhou, Q. Chen, B. Zhao, Y. Yuan, L. Zhuang, Enhanced anaerobic degradation of organic pollutants in a soil microbial fuel cell. Chemical Engineering Journal. 2011;172: 647– 653.

[34] X. Wang, Z. Cai, Q. Zhou, Z. Zhang, C. Chen, Bioelectrochemical stimulation of petroleum hydrocarbon degradation in saline soil using u-tube microbial fuel cells. Biotechnology and Bioengineering. 2011;109(2):426-433.

[35] APHA (1992) *Standard Methods for the Examination of Water and Wastewater*. 18th ed. American Public Health Association (APHA), American Water Works Association (AWWA), Water Environment Federation (WEF). Washington DC, EEUU. 1085 pp.

[36] H.M. Poggi-Varaldo, J.D. Bárcenas-Torres, C.U. Moreno-Medina, J. García-Mena, C. Garibay-Orijel, C., Ríos-Leal, E., Rinderknecht-Seijas, N. Influence of discontinuing feeding degradable cosubstrate on the performance of a fluidized bed bioreactor treating a mixture of trichlorophenol and phenol Journal of Environmental Management 2012; 113:527-537.

[37] P. Zárate-Segura, J. García-Mena, H.M. Poggi-Varaldo, Effect of biomass type and PCE on archaea communities of anaerobic reactors. In: Alleman, B.C., Kelley, M.E. (Eds.), In Situ and On-Site Bioremediation-2005. Battelle Press, Columbus, OH, ISBN 1-57477-152-3. Book in CD-ROM.

[38] N. Fierer, M. Hamadyc, C. L. Lauberb, R.Knight, The influence of sex, handedness, and washing on the diversity of hand surface bacteria. Proceedings of the National Academy of Sciences, 2008;105 (46):17994-17999.

[39] A.S. Whiteley, S. Jenkins , I. Waite, N. Kresoje, H. Payne, B. Mullan, R. Allcock, A. O'Donnell, Microbial 16S rRNA Ion Tag and community metagenome sequencing using the Ion Torrent (PGM) Platform. J Microbiol Methods 2012; 91: 80–88.

[40] J.G. Caporaso, J. Kuczynski, J. Stombaugh, K. Bittinger, F. D. Bushman, E. K. Costello, N. Fierer, A. Gonzalez-Peña, J.K . Goodrich, J.I. Gordon, G.A. Huttley, S.T. Kelley, D. Knights, J.E. Koenig, R.E. Ley, C.A. Lozupone, D. McDonald, B.D. Muegge, M. Pirrung, J. Reeder, J. R Sevinsky, P. J. Turnbaugh, W. A. Walters, J. Widmann, T. Yatsunenko, J. Zaneveld, R. Knigh. QIIME allows analysis of high-throughput community sequencing data. Nature Methods 2010;**7**, 335–336.

[41] R. C. Edgar, Search and clustering orders of magnitude faster than BLAST. Bioinformatics, 2010;26 (19): 2460-2461.

[42] T.Z. DeSantis, P. Hugenholtz , N. Larsen , M. Rojas, E.L. Brodie, K. Keller, T. Huber, D. Dalevi , P. Hu , G.L. Andersen. Greengenes, a chimera-checked 16S rRNA gene database and workbench compatible with ARB. Appl Environ Microbiol, 2006; 72: 5069–5072.

[43] B. J. Haas, D. Gevers, A.M. Earl, M. Feldgarden, D.V. Ward, G. Giannoukos, D. Ciulla, D. Tabbaa, S. K. Highlander, E. Sodergren, B. Methe´, T.Z. DeSantis, J.F. Petrosino, R. Knight, B. W. Birren, Chimeric 16S rRNA sequence formation and detection in Sanger and 454-pyrosequenced PCR amplicons. *Genome Res.* 2011; 21: 494-504.

[44] Y. Vázquez-Baeza, M. Pirrung, A. Gonzalez, R. Knight, EMPeror: a tool for visualizing high-throughput microbial community data. Gigascience. 2013;2(1):16

[45] C.E. Shanon, A mathematical theory of communication. Bell System Technical Journal 1948; 27:379-423.

[46] A.C. Ortega-Martínez, K. Juárez-López, O. Solorza-Feria, M.T. Ponce-Noyola, J. Galindez-Mayer, N. Rinderknecht-Seijas, H.M. Poggi-Varaldo, Analysis of microbial diversity of inocula used in a five-face parallelepiped and standard microbial fuel cells. International journal of hydrogen energy 2013; 38:12589-12599.

[47] C.P.H. Mulder, E. Bazeley-White, P.G. Dimitrakopoulos, A.H.M. Scherer-Lorenzen, B. Schmid, Species evenness and productivity in experimental plant communities, Oikos, 2004;107:50-63.

[48] J.C. Quintero, M.T. Moreira, J.M. Lema, G. Feijoo, An anaerobic bioreactor allows the efficient degradation of HCH isomers in soil slurry, Chemosphere, 2006; 63: 1005–1013

[49] N. Lu, S.G. Zhou, L. Zhuang, J.T. Zhnag, J.R. Ni, Electricity generation from starch processing wastewater using microbial fuel cell technology. Biochemical Engineering Journal. 2009;43: 246-251.

[50] Z. Yan, N. Song, H. Cai, J.H. Tay, H. Jiang, Enhanced degradation of phenanthrene and pyrene in freshwater sediments by combined employment of sediment microbial fuel cell and amorphous ferric hydroxide. Journal of Hazardous Materials, 2012;199–200: 217– 225.

[51] J.B. Eweis, S.J Ergas, D.P.Y. Chang, E.D. Schroeder Bioremediation Principles McGraw-Hill. USA; 1998

[52] B.C. Okeke, T. Siddique, M.C. Arbestain, W.T. Frankenberger, Biodegradation of γ-hexachlorocyclohexane (lindane) and α-hexachlorocyclohexane in water and a soil slurry by a *pandoraea species*, Journal of Agricultural and Food Chemistry. 2002; 50:2548-2555.

[53] Z. Zaybak, J.M. Pisciotta, J.C. Tokash, B.E. Logan, Enhanced start-up of anaerobic facultatively autotrophic biocathodes in bioelectrochemical systems. Journal of Biotechnology 2013;168: 478– 485.

[54] H.M. Kim, N. Chae, J.Y. Jung, Y.K. Lee, Isolation of facultatively anaerobic soil bacteria from Ny-A° lesund, Svalbard. Polar Biol 2013; 36:787–796.

[55] S.A. Freeman, R. Sierra-Alvarez, M. Altinbas, J. Hollingsworth, A.J.M. Stams, H. Smidt, Molecular characterization of mesophilic and thermophilic sulfate reducing microbial communities in expanded granular sludge bed (EGSB) reactors. Biodegradation 2008; 19:161–177.

[56] G. Scheff, O. Salcher , F. Lingens, *Trichococcus flocculiformis* gen nov. sp. nov. a new Gram-positive filamentous bacterium isolated from bulking sludge. Appl Microbiol Biotechnol 1984;19:114–119.

[57] J.R. Liu, R.S. Tanner, P. Schumann, N. Weiss, C.A. McKenzie, P.H. Janssen, E.M. Seviour, P.A. Lawson, T.D. Allen, R.J. Seviour, Emended description of the genus *Trichococcus*, description of *Trichococcus collinsii* sp nov., and reclassification of *Lactosphaera pasteurii* as *Trichococcus pasteurii* comb. nov and of *Ruminococcus palustris* as *Trichococcus palustris* comb. nov in the low-G+C Gram-positive bacteria. Int J Syst Evol Microbiol 2002; 52:1113–1126.

[58] J.R. Kim, N.J. Beecroft, J.R. Varcoe, R.M. Dinsdale, A.J. Guwy, R.C.T. Slade, A. Thumser, C.A. Rossa, G.C. Premier, Spatiotemporal development of the bacterial community in a tubular longitudinal microbial fuel cell. Appl Microbiol Biotechnol 2011; 90:1179–1191.

[59] V. Fedorovich, M.C. Knighton, E. Pagaling, F.B. Ward, A. Free, I. Goryanin, Novel electrochemically active bacterium phylogenetically related to *arcobacter butzleri*, isolated from a microbial fuel cell. Applied And Environmental Microbiology, 2009; 7326–733.

Abbreviations and Acronyms

sCOD	soluble Chemical oxygen demand
EBCR	Electrobiochemical slurry reactor
E_{EBCR}	Voltage
$\hat{E}_{harvested}$	Energy per tonne of soil associated to 30 days of treatment in an EBCR
$\hat{E}_{mixing}$	Energy per tonne of soil required for mixing during 30 days of treatment
HCH	Hexachlorocyclohexane
I_{EBQR}	Current intensity
Max	Maximum
MFC	Microbial Fuel Cell
NOM	Natural organic matter
P_{An}	Surface area power density
P_{ave}	average power
P_{EBCR}	Power delivered
P_V	Volumetric power
R_{int}	Internal resistance
SMFC	Soil microbial fuel cell technology
SB	Slurry reactors
SR	Sulphate reducing

Greek characters

η_{coul}	Coulombic efficiency
η_{COD}	Removal efficiency of organic matter as chemical oxygen demand
$\eta_{Lindane}$	Removal efficiency of lindane

Biohydrogen Production from Organic Solid Waste in a Discontinuous Process

I. Moreno-Andrade[1,*], M.C. Bujanos-Adame[1]

[1]Universidad Nacional Autónoma de México, Instituto de Ingeniería, Academic Unit Juriquilla, Laboratory for Research on Advanced Processes for Water Treatment, Blvd. Juriquilla 3001, Juriquilla, C.P. 76230, Querétaro, Mexico
[*]Tel: +524421926171; e-mail: imorenoa@ii.unam.mx

ABSTRACT

The organic solid waste (OSW) represents more than 60% of total urban waste and include 75% of easy-to-degrade matter. Using a fermentative process, the organic matter is transformed into H_2, CO_2 and organic acids and alcohols, this make feasible the biological production of H_2. There exist several parameters that affect the H_2 production as the hydraulic residence time (HRT). In order to optimize the process is necessary to determine the HRT where the H_2 production is maximized. The objective of this study was to evaluate the effect of HRT on H_2 production form OSW in a Sequencing Batch Reactor (SBR). Different HRT (72, 24, 12 and 6 h) were evaluated in an SBR of 1.25L (with a head space of 250 mL and an exchange volume of 50%). Each HRT was maintained in the reactor at least 10 degradation cycles. OSW at 5gVS/L was filled as substrate at each degradation cycle. The reactor was inoculated with fermentative H_2 producers selected by a thermal shock pre-treatment (103-105 °C during 1 h). H_2, CO_2, methane and Volatile Fatty acids (VFA) were determined by gas chromatography. Kinetics of H_2 production was adjusted to the Gompertz model. The results showed that the values for H_2 in biogas varied from 22 to 48% depending the HRT. The highest H_2 production was obtained applying an HRT of 24 followed by the HRT of 12 h. The maximum H_2 percentage in gas (48 ± 6 %), maximum volumetric H_2 production (757 ± 391 mL H_2) and the maximum H_2 production rate (328 ±144 mL H_2/h) were obtained at HRT of 24 h. Acetic acid was the main VFA obtained. Higher propionic acid production was observed at HRT of 6h, reducing the maximal H_2 generation to 282 ± 24.

Keywords: Bio-hydrogen; HRT;organic solid waste.

1. Introduction

Hydrogen (H_2) is considered an energy vector that has a high heat capacity (33.3 - 39.4 kWh / kg) compared to other fuels [1]. It is possible to produce H_2 from organic waste, biomass and/or waste water through a dark fermentation using microorganisms, which has proven to be a relatively simple and inexpensive process [2]. One kind of waste that can be used in the hydrogen production is the organic solid waste (OSW). The OSW represents an environmental problem, particularly in large cities where the typical methods of disposal are landfills or open dumps. The OSW is mainly composed of carbohydrates (rich components cellulose and starch), lipids and proteins, all of these complex polymers are useful for fermentation. Therefore, it is possible to degrade the OSW and obtain H_2 as a value-added product [3].

The application of the hydrolytic-acidogenic stage of the anaerobic digestion process is an appropriate alternative to produce hydrogen and to obtain an effluent rich in dissolved organic matter, composed by volatile fatty acids, (VFA), mainly acetic, propionic and butyric acid, lactate and solvents (acetone and ethanol). The H_2 production yields are closely related to the fermentation pathway and end-products [1,4].

One of the main factors affecting the production of H_2 is the hydraulic residence time (HRT). Different HRT has been reported depending the OSW origin and reactor operation mode for H_2 producing reactors, these time ranging from 5 to 144 h [2,5]. This parameter affects the fermentation metabolism, microbial composition and activity. It has been reported that short HRT promoted the H_2 production, and can be used for washing of methanogenic microorganisms in the fermentative reactor. Because of this, it is necessary to determine the optimal HRT for the highest production of H_2. For this reason, the aim of this study focuses on evaluating different HRT in a sequencing batch reactor (SBR) to produce H_2 using OSW as substrate.

2. Experimental

The OSW was obtained from the main cafeteria at the UNAM campus Juriquilla, in Queretaro, Mexico. The collected residues was characterized by NMX-AA-015-1985 standard [6]. Some non-fermentative residues were discarded including inert material (paper and plastic) and bones, with this only the fermentable material was preserved. Sampling was performed during three weeks and the OSW were refrigerated at 4 °C for preservation. In each collection, bones and inert material (paper and plastic) were discarded; only the fermentable matter was preserved. The collected residue was triturated with the help of a blender to homogenize the particle size (<0.5 mm), then frozen at -20 °C until use.

An SBR reactor constructed of acrylic material with a working volume of 1L and an exchange volume of 50% was used. The biogas collection and measurement was performed by the brine displacement method, with an inverted cylinder and characterization of biogas by gas chromatography (Varian 8610 SRI C). The reactor remained constant agitation and constant temperature (35-37 °C).

Anaerobic granular sludge from a UASB reactor of a brewery industry was used as inoculum. The reactor was inoculated with 16 g/L of thermally pretreated sludge (103 - 105 °C for 24 h) equivalent to 26.7 gTS/L. The reactor was operated under four different HRT: 72, 24, 12 and 6 h. Due to the low alkalinity of the OSW a mineral solution and citrate buffer (1M) was added to avoid acidification of the medium due to the presence of VFA according to [3]. The initial pH was adjusted at the beginning of each feeding cycle to a value of 7. The COD_{total}, Total and volatile solids (TS and VS) and NH_3 were determined according to the Standard methods [7].

The calculations for the kinetic analysis was performed based on the cumulative hydrogen production production obtained. The modified Gompertz equation (Eq. 1) was used for data analysis [3].

$$H(t) = H_{max} * \exp\left[-\exp\left(\frac{2.71828 * R_{max}(\lambda - t)}{H_{max}} + 1\right)\right] \quad (1)$$

Where, H(t) (mL/$L_{reactor}$) is the total amount of hydrogen produced at culture time t (h); H_{max} (mL/$L_{reactor}$) is the maximal amount of hydrogen produced. Rmax (mL/$L_{reactor}$/h) is the maximum hydrogen production rate; λ (h) is the lag time before the exponential hydrogen production.

Microbial characterization of the reactor at HRT of 24 and 12 h was obtained by a pyrosequencing analysis was performed using a Roche Genome Sequencer FLX Titanium system. The 16S rRNA genes were amplified with primer set 515 forward and 806 reverse Sequences were analyzed using the Quantitative Insights into Microbial Ecology (QIIME) software [8]. OTUs were defined using the UClust algorithm on the basis of 97% sequence identity. Reads were classified using the Classifier tool from the Ribosomal Database Project, setting the bootstrap cutoff at 50%.

3. Results and discussion

The characterization of the OSW of the university cafeteria showed that there is great variation in the fractions depending the menu, in this sense, the values of different fractions is presented: Fruits and Vegetables 62.7±16.1 %, Meat 8.2±7.2 %, flour (including pasta, tortillas and bread) 13.9 ± 8.0%, and others (mixed residues difficult to separate in the other groups e.g. eggshell, etc.) 15.17±16.0%. After performing grinding and homogenization of the various samples days, a homogenous mash was used as reactor feed. The feed for the SBR showed the following values: moisture 82%, TS 203 g/L, Fixed solids 48 g/L, VS 155 g/L, density 1115 kg/m^3, COD_{total} 336 g/L, 400 mg NH_3/L and alkalinity 8 g/L of $CaCO_3$. Due to the low alkalinity, it was necessary to add a buffer solution to prevent and mineral acidification reactor.

The reactor was operated for 60 cycles. The initial HRT was 72 h (cycles 1 through 9) and was subsequently decreased to 24h (cycles 10 to 20), 12 h (cycles 21-43) and 6h (cycles 44-59). Figure 1 shows the percentages of H_2, CO_2 and methane in the biogas during operation of the bioreactor. It is observed that after 72 h the highest percentage of H_2 was 44.1±12.0% at 24, 12 and 6 h the percentage reported is 52.6 ±6.0, 44.2±13.03 and 42.1±14.1%, respectively.

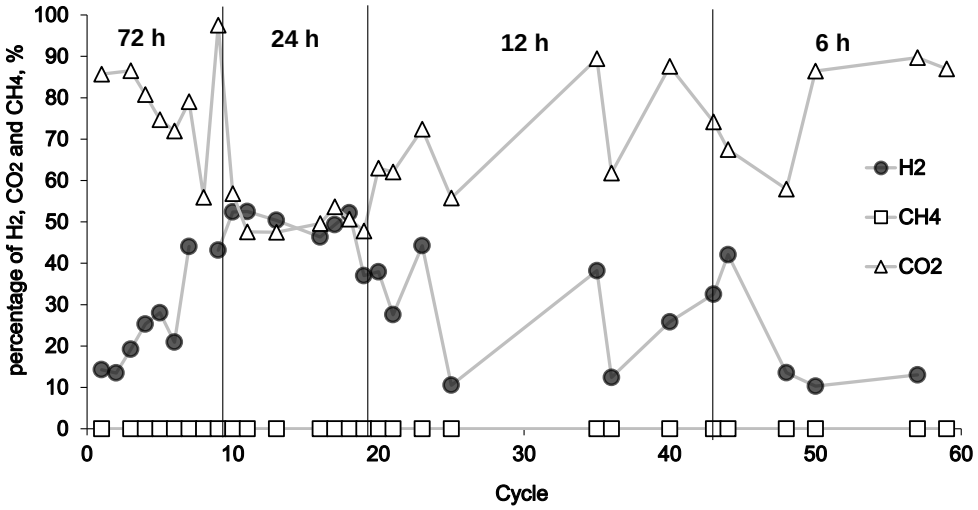

Fig 1. Percentage of hydrogen, CO_2 and methane in biogas at different HRT.

The general behavior observed in the hydrogen production kinetics at different HRT evaluated is shown in Figure 2. It is possible to observe that there higher H_2 production was produced during HRT of 24 h and 12 h (24.6 and 22.3mmolH_2/ h), while than for cycles 72 and 6 h the maximum production was 8.5 and 7.6 mmolH_2/h, respectively.

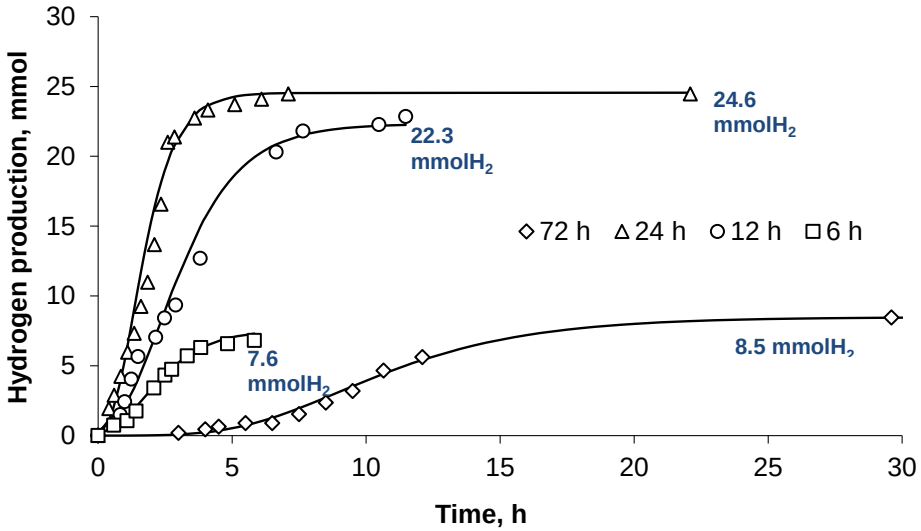

Fig 2. Hydrogen production kinetics at different HRT

The higher hydrogen production per gram of VS was obtained applying an HRT of 24 h (15.2 mmolH_2/g$VS_{removed}$). The maximum production in the case of HRT of 72, 12 and 6 h was 2.5, 4.4 and 1.6 mmolH_2/g$VS_{removed}$, respectively. The specific hydrogen production rate of (SHPR) for different HRT in

this study is shown in Figure 3. I was observed that higher SHPR was obtained at 24 h. The average values for SHPR were 0.53±0.19, 8.5±4.1, 5.6±4.0, 5.1±1.4 mmolH_2/gVS/d for HRT of 72, 24, 12 and 6 h, respectively.

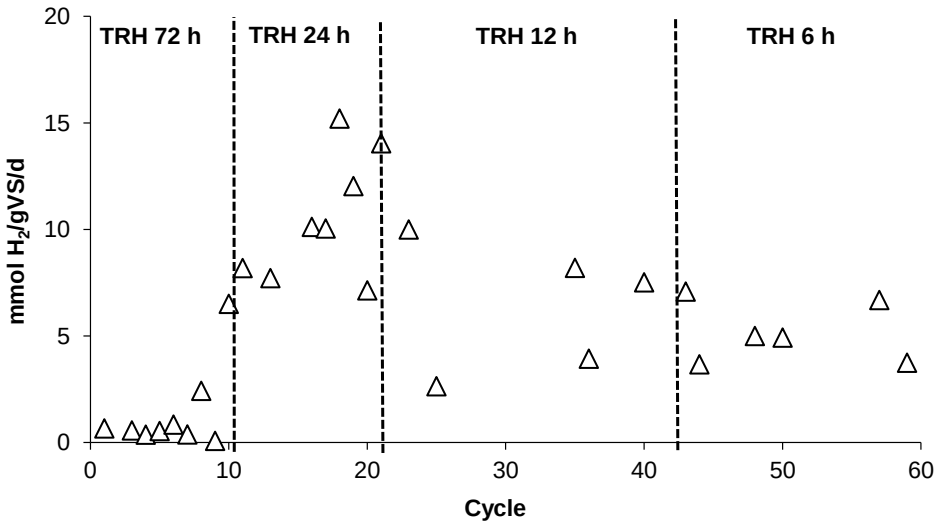

Fig 3. The specific hydrogen production rate for different HRT.

The principal VFA produced was the acetic acid. The higher acetic, butyric, isovaleric, acetone and ethanol production was obtained at 24 h and is related with the high hydrogen production. For the case of the propionic acid, the higher production was obtained in a HRT of 6h. This increase in the propionic acid is correlated with the decrease in the hydrogen production since this VFA consume H_2 to be produced. It has been reported that if the process is mainly oriented to acetic and butyric acid production pathway, the H_2 production can be maximized [4].

Table 1. Volatile fatty acids, acetone and ethanol production for the different HRT evaluated.

HRT	Concentration (*g/L*)						
(*h*)	Acetic	Propionic	Butyric	Isobutyric	Isovaleric	Acetone	Ethanol
72	4.30 ± 1.70	0.72 ± 0.37	2.46 ± 1.89	0.45 ± 0.26	0.34 ± 0.08	0.27 ± 0.13	0.85 ± 0.45
24	5.77 ± 4.06	0.46 ± 0.16	4.13 ± 3.86	0.82 ± 0.35	0.46 ± 0.07	0.80 ± 0.41	1.51 ± 1.17
12	2.37 ± 2.80	0.90 ± 0.18	0.90 ± 0.13	0.015 ± 0.0	0.03 ± 0.01	0.03 ± 0.01	0.02 ± 0.01
6	2.97 ± 0.17	1.29 ± 0.14	1.05 ± 0.01	0.07 ± 0.05	0.07 ± 0.01	0.02 ± 0.01	0.02 ± 0.02

The microbial characterization demonstrate the phylum Firmicutes represent more than the 99% of the OTUs found in the sample of the reactor. The family Veillonellaceae represent 99% of the OTUs of the Firmicutes. The Veillonellaceae are a family of the Fimicutes and Clostridia class. Members of this family are all obligate anaerobes and occur in habitats such as rivers, lakes, and the intestines of vertebrates. it has been reported that this family could contribute to greater hydrogen production at low OLRs using easy-to-

degrade substrate (as glucose) and lactate [9]. The genus Megasphaera represent 88% of all the OTUs obtained in the analysis, i.e., the dominant genus in the microbial community. Megasphaera sp. was reported to be present in hydrogen production in reactors and also reported in fermentation including Ethanol + butyrate and ethanol type fermentation [10,11].

4. Summary and perspectives

The results showed that the values for H_2 in biogas varied from 22 to 48% depending the HRT. The highest H_2 production was obtained applying an HRT of 24 followed by the HRT of 12 h. The maximum H_2 percentage in gas (48 ± 6 %), maximum volumetric H_2 production (757 ± 391 mL H_2) and the maximum H_2 production rate (328 ±144 mL H_2/h) were obtained at HRT of 24 h. Acetic acid was the main VFA obtained. Higher propionic acid production was observed at HRT of 6h, reducing the maximal H_2 generation to 282 ± 24 mL. The genus Megasphaera showed to be the dominant genus in the microbial community.

Acknowledgements

The authors gratefully acknowledge the financial support of DGAPA-UNAM trough project RR180612 and CONACYT project 100298. Jaime Pérez Trevilla is acknowledged for his technical assistance.

References

[1] P. P. Edwards, V.L. Kuznetsov, W. I. F. David, N.P. Brandon, Hydrogen and fuel cells: towards a sustainable energy future. Energy Policy 2008; 36:4356-4362.

[2] I. Valdez-Vazquez, E. Ríos-Leal, F. Esparza-García, F. Cecchi, H.M. Poggi-Varaldo, Semi-continuous solid substrate anaerobic reactors for H2 production from organic waste: mesophilic versus thermophilic regime. Int. J. Hydrogen Energ 2005; 30:1383–1391.

[3] C. Ramos, G. Buitrón, I. Moreno-Andrade, R. Chamy, Effect of the initial total solids concentration and initial pH on the bio-hydrogen production from cafeteria food waste. Int. J. Hydrogen Energ 2012; 37:13288-13295.

[4] Zhu, H., Parker, W., Conidi, D., Basnar, R., & Seto, P., Eliminating methanogenic activity in hydrogen reactor to improve biogas production in a two-stage anaerobic digestion process co-digesting municipal food waste and sewage sludge. Bioresour Technol, 2011; 102, 7086-7092.

[5] H. S. Shin, J. H. Youn, Conversion of food waste into hydrogen by thermophilic acidogenesis. Biodegradation 2005; 16: 33–44.

[6] NMX-AA-15-1985. Norma Mexicana. Protección al ambiente - contaminación del suelo – residuos sólidos municipales - muestreo - método de cuarteo.

[7] APHA. Standard Methods for the Examination of Water and Wastewater (21th ed.), APHA/AWWA/WEF, Port city press. Baltimore, 2005.

[8] Caporaso JG, Kuczynski J, Stombaugh J, Bittinger K, Bushman F, Costello EK, Fierer N, Peña AG, Goodrich J, Gordon JI, Huttley GA, Kelley ST, Knights D, Koenig JE, Ley RE, Lozupone CA, McDonald D, Muegge BD, Pirrung M, Reeder J, Sevinsky JR, Turnbaugh PJ, Walters WA, Widmann J, Yatsunenko T, Zaneveld J, Knight R. QIIME allows analysis of high-throughput community sequencing data. Nat Methods. 2010; 7:335–336.

[9] G.M. Shida, L.T. Sader, C.L.C. de Amorim, I.K. Sakamoto, S.I. Maintinguer, N.K. Saavedra, M.B.A Varesche, E.L Silva. Performance and composition of bacterial communities in anaerobic fluidized bed reactors for hydrogen production: Effects of organic loading rate and alkalinity .Int. J. Hydrogen Energ 2012; 37:16925-16934.

[10] C-H. Hung, Y-T Chang, Y.J. Chang, Roles of microorganisms other than Clostridium and Enterobacter in anaerobic fermentative biohydrogen production systems – A review. Bioresour. Technol. 2012; 102, 8437–8444.

[11] N. Ren, D. Xing, B.E. Rittmann, L. Zhao, T. Xie, X.Zhao, Microbial community structure of ethanol type fermentation in bio-hydrogen production. Environ. Microbiol, 2007; 9, 1112–1125.

Metallic Nanoparticles for the Treatment of Effluents Contaminated with Chlorinated Organic Compounds: a Review

L. Bretón-Deval[1], H.M. Poggi-Varaldo[1*] F. Godinez[2], O. Solorza-Feria[2],

[1] CINVESTAV-IPN, México, Environmental Biotechnology and Renewable Energies Group, Dept. of Biotechnology and Bioengineering, México D.F., México. [2] CINVESTAV-IPN, Dept. of Chemistry. México D.F., México.
[*]Tel: +525557473800 ext4321,4324; e-mail: r4cepe@yahoo.com

ABSTRACT

Nanomaterials are the core of a promising technology that can be used to accelerate and improve the transformation and detoxification of chlorinated organic compounds (COCs). Hence this review will cover topics such as efficient nanomaterials for COCs treatment, supports and stabilizers that improve the process, interactions of nanomaterials with the microorganisms involved, and emerging fields. The most common material used for treatment of waters polluted with COCs has been zero-valent iron (ZVI) because of its efficiency and low cost. However, there are concerns on the stability and long term durability of ZVI *NP* (NP). For this reason there are some works with other materials such as Pd, Zn or Ni and with combination of materials in the fabrication of NP. The bimetallic NPs allow for a lower cost of production, since one of the materials could be the most economic but not the most efficient whereas the second metal, the most expensive, provides a higher degradation capability. Alloyed and core-and-shell types of bimetallic NP have been tested. The process with NP can be made more efficient by using a support that prevents the aggregation of NP during reaction and in some cases can facilitate the recovery of the NP afterwards. Currently, the application of NP in bioreactors and *in situ* treatments is gaining momentum. Another significant issue especially for hybrid treatments is the interaction between NP and the microbial community harbored in bioreactors and devices, ranging from toxicity issues to biosynthesis of NP. There has been an attempt to incorporate metal NP onto the microbial cells for COC treatment, although more research is needed. Furthermore, there is increased interest on biosynthesis of NP with microorganisms in order to have true "nanoparticle-ized biomass" with increased degradation capability of pollutants. Among important emerging fields we can highlight the environmental impact assessment as well as life cycle analysis of the NP fabrication and use.

Keywords: nanoparticles, water treatment, chlorinated compounds

1. Introduction

The organochlorines compounds are part of persistent organic compounds, due of their physical chemical properties, degradation is slow and tends to accumulate in fatty tissues of various animals throughout the food chain. The use of these compounds in industrial processes start to mid twentieth century, such as plastics manufacture (vinyl chloride), aerosols, cleaning and degreasing metals (perchlorethylene, trichloroethylene), chemical manufacturing (dichloromethane, chloroform), additives paints and adhesives (dichloromethane, trichloroethane), pulp and paper industry (dioxins, furans), manufacture of pesticides (hexachlorobenzene and others), *etc*.

The organochlorine compounds also are used and are heavily used in agriculture, especially as pesticides for controlling pests. The main exponent of this group is DDT, manufactured in 1943 and used for decades until several investigations showed that its highly toxic [1], hormonal disruptor [2], carcinogenic [3] and exposure affects the nervous, respiratory and immune system [4],[5]. Other COCs belonging to this group are aldrin, chlordane, dieldrin, lindane, tozafeno, heptachlor, hexachlorocyclohexane, etc. Although the use of some of these compounds has been banned some years ago, the effect persists in the environment due their recalcitrance. For that reason is necessary to find technologies with efficient removal capability of COCs.

The metal particles and *NP*, particularly Fe particles, have been used for treating organochlorine compounds due to the ability of these metals to reduce chlorine compounds. The main chlorinated compound that has been removed using this technology is perchloroethylene (PCE) and its metabolites TCE, DCE, and VC. However because of the principle governing this removal, it's feasible to apply over other chlorinated compounds.

2. Nanoparticle as a technology for COCs treatment

One way to enhance the removal of chlorinated compounds is using nano-materials. The latter are characterized by their low size, ranging from 1 to 100 nanometers. Because of their small size, their properties are different compared to their millimeters counterparts, such as more surface contact and increased reactivity. Indeed, the changes in the crystal structure and chemical reactivity increase the catalytic activity.

The removal capacity of COCs by NP (*NP*) is often dependent on their size; some research suggests that with the use of smaller particles the removal is greater, as reported by Lin et al. [6] who used *NP* of 500 and 100 nm for the treatment of the dye acid black 24, and found that the decrease in particle size increased the removal by 90-fold. Nanoparticles are very efficient technology but expensive, the cost of 1 kg of supported *NP* is around 90 USD. The *NP* cost is variable depending of purity, size, support and the presence and concentration of catalyst (www.us-nano.com).

The reuse of *NP* can reduce the cost of the treatment. However the feasibility depends on solubility and stability of the compounds [7]. Regeneration of ZVI is difficult to achieve because of its reductive property is rarely recovered. Researches by Sun et al. [8] have tried to use acid wash to disrupt the iron oxide layer that passivated the removal of the contaminant. Wang et al. [9] regenerated *NP* of Fe/Pd by washing the *NP* in 0.4M of KBH_4 for 30 min. The wash caused the formation of active ZVI again. Another way to reduce the treatment cost is to reuse *NP*. Li et al. [10] used nZVI several times to remove a black dye BDE209: in the first five cycles the removal was high but in the sixth cycle the removal dropped to 23%. Another research with similar results of Li et al. [10] was performed by Velimirovic et al., [11]; they applied nZVI for the CACs removal and during the first five removal cycles the pollutant removal was 92% but in the sixth cycle the removal was under 22%.

3. Zero valent iron, a common nanoparticle used in COCs treatments

The ZVI is the material most used in the treatment of COCs compounds due to its low cost, abundance, ease handling and reactivity [7]. The nZVI technology has been tested in *in situ* remediation projects in US and Europe [12]. In most of these direct injection of nZVI, permeable barriers and small reactors were used [13, 14, 15, 16, 12]. The removal of COCs compounds by nZVI can be carried out mainly by abiotic reductive dechlorination that is a chemical reduction of the contaminant that requires direct contact between nZVI and the pollutant. The nZVI electrons are transferred to the chlorinated compound, generating lesser chlorinated compounds, oxides of iron on the surface of the ZVI NP, and release of chloride anion. A schematic chemical process is depicted below [15].

$$Fe^0 \rightarrow Fe^{2+} + 2e^- \quad (1)$$

$$RCl + 2e^- + H^+ \rightarrow RH + Cl^- \quad (2)$$

$$Fe^0 + RCl + H^+ \rightarrow Fe^{2+}RH + Cl^- \quad (3)$$

Under aerobic conditions

$$2Fe^0 + O_2 + 2H_2O \rightarrow 2Fe^{2+} + 4OH^- \quad (4)$$

Under anoxic conditions

$$Fe^0 + 2H_2O \rightarrow Fe^{2+} + H_2 + 2OH^- \quad (5)$$

In both conditions (aerobic and anaerobic) there is a rise in the pH solution and release of reductants such as Fe_2^+ and H_2 that continues the dechlorination.

The application of nZVI directly to *in situ* remediation still faces challenges, like the longevity of *NP* activity and transport through aquifer. Nanoparticles tend to agglomerate and forms aggregates, resulting in decrease in the activity and mobility of nNZVI [17, 8]. Recent research carried out using nZVI has focused on using various stabilizers, surfactants and membranes for the *NP* (Table 1). Several studies have been used carboxy methyl cellulose (CMC) as stabilizing agent [18, 19, 20]. The stabilizing agents enhance steric or electrostatic repulsions between particles in order to inhibit nZVI aggregation and increase solution stability. The CMC it's a low cost material, very soluble and highly biocompatibility [21]. Bennett et al. [22] used CMC to stabilize nZVI in the treatment of sludge contaminated with PCE and its metabolites; they found that CMC was attached on the nZVI particles that adsorbed onto the sand of the aquifer. This effect of *NP* enhanced organic matter adsorption could improve the *in situ* bioremediation and the CMC provides additional carbon source to bacteria. Kaifas et al. [23] obtained nZVI *NP* with CMC. The CMC protected the surface of the nanoparticle and blocked their active sites. The authors discussed that this prolonged the life of *NP*s. Sunkara et al. [20] besides utilized CMC as stabilizer, also employed activated carbon granules of 1-3 mm size to prevent nZVI aggregation and to increase their adsorptive capacity. The final *NP* nZVI plus carbon were around 500 nm. They found that this relatively larger size facilitated the particle transport in groundwater. Roman et al. [24] compared a set of stabilizers of *NP*s: CMC, polyacrylic acid (PAA) and PAP. The results showed that the PAA-stabilized *NP* were more reactive and removed greater amounts of lindane in less time than those with PAP, followed by the *NP* stabilized with CMC. During the first 12 hours there was a difference of 25% between removals of PAA and PAP-treated NP, however, after 50 hours of contact, both types of *NP* removed all lindane. The decision of which stabilizer use will depend of other factors such as cost and easy handling.

While it is true that over the years researchers have tried various stabilizers, carriers and surfactants as dodecilsulfato sodico (SDS), tetrabutylammonium (TBA), poly-aspartate, methacrylic acid, methyl methacrylate, styrenesulfonate [8, 17, 25] and supports such as silica and activated carbon [26, 27], in order to prepare smaller, more reactive, more stable *NPs*, the research on these issues is still very active. As results of these investigations, commercial products are emerging, as reported by Chen et al. [28]. They evaluated Na-acrylic copolymer designed for the remediation of contaminated subsurface water. This product has the combination of a biodegradable organic and inorganic stabilizer. The results show that TCE degradation with Na-acrylic copolymer plus nZVI was faster than that with NP made of CMC plus nZVI. It was reported that some anions like NO_3-, Cl-, HCO_3- and SO_4^{-2} inhibited slightly the TCE degradation.

4. Bimetallic Nanoparticles

Iron is an efficient metal in the chlorinated compounds removal but the addition of an extra metal like Pd, Pt, Cu, Ni or Ag usually enhances the stability of Fe due the second metal is a catalyst that avoids the iron oxidation and the formation of iron oxide coatings on the surface of the nanoparticle [29, 25, 30]. The incorporation of a second metal may increase the surface area and the number of potential reactive sites for interacting with the contaminant. Some authors suggest that catalysts like Pd and Ni could absorb the H_2 produced by iron corrosion into its lattice to form a transitional compound that can accelerate the reductive dechlorination of the COC [9, 31]. Other authors suggest that the removal mechanism by bimetallic *NP* is based on the attack of the hydrogen product of ZVI corrosion to the contaminant that is absorbed into the surface of the metal acting as a catalyst, resulting in the dechlorination of the COC (both the mother compound and its chlorinated degradation compounds) [32, 33, 30].

However the studies to elucidate the mechanism of bimetallic *NP* operation are still scarce or plainly lacking. Some researchers have used various combinations of bimetallic *NP* like ZVI/Ni, ZVI/Cu, ZVI/Mg and ZVI/Pt, ZVI/Zn [34, 35]. Also there have been efforts to use other metals besides iron. For instance, Lin et al. [36] synthesized *NP* of Pd/Sn (400 mg) of 50 a 100 nm with a BET de 5.9 m^2g^{-1} for TCE treatment (7 mg L-1). The results reported were encouraging; a removal of 2 and 1.56 h-1 was obtained. In turn, these results were higher than the removals obtained with more conventional bimetallic particles of Pd/ZVI [37]. Another example is the research by Li et al. [29] who synthesized *NPs* of Pd/Au y Pd/Al_2O_3 of 4 nm with a BET of 200 m^2/g to remove 8.5 mg/L of TCE. Their results show that these *NPs* were 10^5 x more reactive that commercial products NANOFER 25 y NANOFER25S.

The bimetallic *NP* commonly used in the treatment of chlorinated compounds is ZVI/Pd [38, 39, 40, 9, 41]. These bimetallic *NPs were* so efficient that they could treat aromatic compounds, as Yang et al. [42] reported. Indeed, they used *NPs* < 100 nm with a BET of 9.21 m2/g for monochlorobenzeno treatment and achieved 97% removal of the pollutant. Furthermore they examined the effect of different concentrations of Pd in order to abate costs of NP fabrication (0.2%, 0.4%, 0.6%, 1%, 2% Pd on mass basis). The results indicate that 0.6% is the best concentration to stabilize iron and reach a removal similar to Pd 1%. When used a 2% proportion of Pd was used, the removal of pollutant was surprisingly lower.

Table 1. Recent research carried out using nZVI

Nanoparticle	Contaminant	Remotion	Size(nm)/BET(m^2g)	Supported	Ref.
nZVI	TCE	75%	50/25	Na-acrylic copolymer	[28]
Core/nZVI	TCE	ND	ND	Polyacrylic acid c.	[43]
nZVI	Chlorophenol	ND	80-120 nm	CMC	[18]
nZVI	TCE	100%	50 nm	CMC	[23]
nZVI	PBDEs	92%	50-80/35	Silica/microspheres	[26]
nZVI/Fenton	chloronitrobenzenes	ND	10-50 nm	ND	[44]
nZVI	Lindane	100%	ND	PAA/CMC	[24]
nZVI	Vinyl chloride	ND	80-120/55	surfactant	[45]
nZVI	PCE	99%	ND/15	ND	[46]
nZVI	TCE	80%	100-800 nm	carbon	[47]
nZVI	TCE	ND	500/320	CMC	[20]
nZVI	TCE	99%	5	alginate	[48]
nZVI	PCE, TCE,DCE	100%	15-40 nm	CMC	[22]

The authors suggestd that a high Pd concentration such as Pd 2% could block some Fe active sites and inhibit the Fe acitivy and further corrosion. Other authors that used bimetallic nanopartices for the removal of COCs also added various cations (Cu+, Ni+) hoping to find a stimulating effect on the removal of pollutant and also emulating the possible aquifers conditions. Shi & Chen, [38] used 12.5 g/L of Fe/Pd *NP* of 20-80 nm with 37 m^2g^{-1} and some cations (Fe^+, Na^+, Mg^+, Cu^+, Ni^+) in order to remove pentachlorophenol (PCP).

They observed a removal of 98% of the pollutant. Addition of Na+ did not influence the pollutant removal, whereas addition of Mg^{2+} and Cu^{2+} cations were associated to an impaired removal of the pollutant. On the other hand the cations Fe^{3+} y Ni^{2+} enhanced the removal of the pollutant. Shih et al. [49] use *NP* Fe/Pd of 60-90 nm and cations in sulfate form, Na_2SO_4, $CuSO_4$, $NiSO_4$ and $Fe_2(SO_4)_3$ for the pentachlorophenol removal. The SO_4^{-2} inhibited the removal process but the Cu, Ni, and Fe cations enhanced the rate of contaminant removal. The Cu^{2+} and Ni^{2+} cations were added to the surface of the Fe/Pd *NP*.

The bimetallic *NP* can also be immobilized on carriers [9, 39, 50, 40, 51, 42]. In fact in recent years the majority of synthesized *NP* used some kind of medium support. Wang et al. [9] use a poly-vinylidene fluoride support with Fe/Pd *NP* of 50 nm for the remotion of 5 mg/L of Trichloroacetic acid; it was possible to remove 96% in 30 min. because the use of the support increased the removal 6.8 times. Other authors have chosen to use organic compounds that may be able to be incorporated into the system. Kustov et al. [39] used chitosan with Fe/Pd *NP* to remove uo to 276 mgl^{-1} of PCE. The use of a support allowed for a smaller size of the *NP* as well as increased reactivity; the NPs were able to remove 99% of the pollutant in 5 hr. The *NP* were attached to chitosan surface via

-OH and $-NH_2$ groups. Cho & Choi [51] used CMC with Fe/Pd *NP* of 99 nm for removal of 13 mg/L of PCE, TCE and TCA. It was possible to remove 85% of the pollutant mixture; the use of CMC increased the removal 6-fold.

The use of polymers and membranes in bimetallic *NP* preparation and conditioning have improved NP properties such as dcreased agglomeration, longer activity and increased pollutant removals.

5. In situ treatment with NP

The application of *NP* in organochlorine *in situ* treatments began in 2001 with the experiments of Elliott & Zhang. The first experiments focused on the application of filings of millimeter ZVI in the treatment of COCs (PCE, TCE, DCE, VC, CT). This generated knowledge and experience at laboratory and in situ levels, and paved the way to start using *NP*. Elliott & Zhang made bimetallic *NP* Fe/Pd, to prevent the rapid oxidation of Fe. Batch experiments tested various combinations of bimetallic *NP* Fe/(Pd, Ag, Cu, Co, Ni). The most efficient *NP* was Fe/Pd, this alloy enhanced the dechlorination of COCs by hydrogenation. The *NP* exhibited a size in the range 100 to 200 nm with a specific surface area of 33.5 m^2/g. Removals of 99% of initial 4.6 mg/L pollutant (a mixture of chlorinated aliphatic compounds, i.e., PCE, TCE, DCE, VC, CT and CF were observed.

Another well documented case study in which NP were used in the treatments of COCs was carried out by Quinn et al. [52] in the NASA's Launch Complex 34 (LC34). They applied a particular type of NP called EZVI because an oil-liquid membrane of Span 89 surfactant and corn oil surrounded the zero valent iron particle. The EZVI *NP* removed concentrations higher than 80% of TCE after 90 days of EZVI injection. The research on the action mechanism developed in the LC34 was continued by O'Hara et al. [53]. The results show that the EZVI technology can be an effective treatment for DNAPL zones, capable of treating dissolved phase besides even if the amount of ZVI is not enough to degrade all TCE, because then the vegetable oil and Span 89 surfactant can act as a slow release electron donor for improve the biodegradation processes. A removal of 86% of the whole DNAPL was reported, the mass flux decreased from 1826 to 810 mmoles/day. They found an increase in the

DCE and VC concentration indicating that there was an incomplete microbial degradation. One of the problems they faced during the research was the method of injecting the NP. The direct injection did not allow a homogenous distribution of the EZVI, so they tested different methods: pneumatic fracturing, hydraulic fracturing, and pressure pulsing and direct push injection. The best methods were pneumatic fracturing and direct push.

O'Hara et al. [53] also carried out batch experiments in order to show that pollutant degradation due to EZVI was mainly abiotic whereas the fast decrease in TCE concentration was due to a combination of sequestration of pollutant in the oily phase (solubilization) and abiotic degradation. He et al. [21]. used ZVI *NP* with Pd stabilized with carboxymethyl cellulose (CMC) for the removal of PCE (1.2-12 mg/L), TCE (1.6-23.8 mg/L), DCE (8.5-20 mg/L), VC (1.1-2.2 mg/L) and PCBs (6.9-97.7 mg/L) in the South of USA. The CMC avoided the nanoparticle aggregation, *NP* without a stabilizer could aggregate rapidly in water and form larger particles that could not travel through the soil matrix and become unavailable for further reduction of contaminants. Besides, CMC could be used as electron donor for microorganisms [54]. During treatment, two injections were performed separated by 596 days. After the first injection there was a 87% reduction of the DNAPL and a gradual reduction of DCE and VC by-products started, which were presumably generated by biological dehalogenation. At the end of the treatment, up to 70% of all injected iron was found in some wells.

Su et al. [55] also applied EZVI for CVOCs treatment in the site 45 MGRD, Parris Island, California. The site was monitored for two years and half. At the end a reduction of 86% of the whole CVOCs mass and a removal of 93% in the DNAPLs of PCE were achieved. The groundwater flow rate was from 0.046 to 0.055 m day-1. After the first injection of EZVI there was an increase in the DCE and VC concentration, due that PCE and TCE degradation was carried out by the microorganism. Also they observed an increase in the concentrations of methane, ethene, ethane and acetylene. The increase in the DCE and VC concentrations started to decrease 220 days after the injection. The propionic, acetic and butyric acid concentrations increased from 1 mg/L-1 to 1700, 1300 y 420 mg/L-1 respectively. This release of VFA may have served as electron donor to microorganisms and stimulated the biological dehalogenation.

The information about the EZVI distance travel and the transformations to other minerals was discussed by Su et al. [56]. The travel distance from injection points was up to 0.89 m. for the direct injection and 2.1. m with pneumatic injection. The X-ray diffraction and scanning electron microscopy analysis showed that the EZVI nano was transformed to magnetite in the first 9 months; afterwards lepidocrocite started to appear, whereas after 2.5 years goethite and ferrihydrite appeared at the top of the aquifer.

Thus, NP began to be increasingly released into the environment in *in situ* treatments. Yet, there are some questions to be answered, such as the development of stronger NP that ideally will have very active sites, the study of some factors that inhibit the proper function of NP in uncontrolled conditions, etc..

6. Nanopartículas and Microorganism

The release of NP used in *in situ* treatments may have some effects on the indigenous microorganism. Although most of the NP are made of materials previously used in the removal of chlorinated compounds, due to their characteristics influenced by their small size, it is necessary to understand the interaction between NP – microorganism. Indigenous microorganisms also contribute to the removal of the compound besides to the ecological importance of them in the ecosystem they habit. For that reason it is necessary to know whether the NP – microorganism could affect positively or negatively the process of removing pollutants and the possible effect on the indigenous microorganism. Papers relating to elucidate these interactions and possible effects are scarce and clearly there is a need to foster research in this area.

Ma & Wu [57] treated PCE with 1 g/L of NP with the following treatments: ZVI, Zn, and both types of NP combined with microorganisms (MO). The best results corresponded to NP ZVI+MO. They reported that the combination of abiotic-biotic tools did not negatively affect the pollutant removal rate but changed the dechorination process; however they did not report on how this change took place. They suggested that perhaps the MO promoted the dissolution of the iron oxides, promoting a lasting activity of the NP. Xiu et al. [58] investigated the effect of 1 g/L of nZVI on dechlorinating microorganisms that participate in bioremediation of 20 mg/L of TCE. The methanogenic MO were stimulated by the presence of nZVI and by the hydrogen released from the iron oxidation whereas dehalogenatinn MO were inhibited and presented a lag period of 300 hours. Afterwards, the dehalogenating MO began to recover. The authors suggested that it is necessary to carried out batch studies before the direct injections to know if the indigenous MO will be able to recover from possible inhibition episodes.

On the other hand Kirschling et al. [59] investigated the effects of 1.5 g/L of nZVI mixed with biopolyaspartate. The studies were carried out in batch operation, with material of three different aquifers polluted with 100 mg/L of TCE plus microbial population of these aquifers. The NP addition was also associated to some environmental changes such as reduced redox potential, which decreased from 400 to 100 mV after 68 days. The pH increased from 7.8 to 8.5 and the concentration of sulfate and methane increased. Such geochemical changes would be capable of modifying the indigenous microbial populations. The DNA increased in the treatment nZVI plus polyaspartate likely because this polymer is biodegradable and may have been used by

the MO as carbon and nitrogen source or maybe the use of that polymer decreases the *NP* toxicity as suggests the research of Li et al. [10]. The polymer could have prevented the *NP* adhesion to the MO surface. After 250 days there was a positive change in the microbial populations as a result of the changes generated in the environment and the release of H+ product of nZVI corrosion.

Barnes et al. [60] focused on knowing whether the exposure of indigenous MO for 36 days to 100 mg/L of nZVI and pollutant TCE was able to modify the diversity and structure of the microbial community. A decrease in the abundance of microorganism was found. The 100 mg/L of nZVI were not toxic to MO because after 36 days the latter showed a recovery. In another study of Barnes et al. [60] the biological TCE degradation decreased as the nZVI concentration increased from 10 to 100 mg/L; the microbial activity ceased when the NP concentration increased to 300 mg/L. That concentration also inhibited the dehalogenating MO activity and the viable number of bacteria. They suggested that the best option is to apply combined abiotic and biotic treatments in two steps: first, to stimulate the MO with a carbon source, and second, to use high concentrations of *NP* to remove the metabolites generated for the MO as DCE and VC.

Cullen et al. [61] investigated the effect of 10 mg g-1 of nZVI on soil MO. They observed that addition of nZVI enhanced dehydrogenase activity and had minimal influence on hydrolase activity probably. These enzymes measured the activity of either the transfer of electrons or hydrogen from substrates via electron carrier proteins and oxidorreductases to the terminal electron acceptor in respiration. This increase in the enzymatic activity might have been due to H^+ released in the nZVI corrosion. While Fajardo et al. [62] applied molecular and optical tools to determine whether the addition of 34 mg g-1 of nZVI had some impact on the activity of soil MO or not. They carried out a transcriptomic analysis of three genes, narG, nirS and gyrA. The first genes encode the denitrification enzymes nitrate reductase, the second encoded the cytochrome cd1 that containins the nitrite reductase, and the quantification of the third gene made a good approach of the overall DNA replication capacity. The results did not show any changes in gene expression after the nZVI addition. Yet, other NP that penetrated the membrane bacteria caused damage and in the worst case, they caused cellular lysis. Changes were also found in the structure and composition of the bacterial community.

Tilston et al. [63] investigated the addition of 10 g nZVI kg^{-1} with a polyacrylic acid coating on a soil contaminated with Aroclor 1242. The treatment lasted 28 days in a two phase soil operation. First, using nZVI and then using aerobic biodegradation, the nZVI removed low concentrations of Aroclor 1242. Physico-chemical changes associated to the *NP* (pH, oxide potential reduction) disrupted the bacterial community and decreased the rate of removal and mineralizztion of the contaminant. Other research such as Li et al. [10], Chen et al. [28] and Zhou at al. [18] suggested that nZVI coated with polyelectrolytes, natural organic matter or CMC reduced the toxicity and availability of *NP* to MO because the physical contact between NP and microrganism was impaired, via electrosteric repulsive force.

Therefore, the research presented so far suggests that the NP applied *in situ* treatments can have a variety of negative impacts on the indigenous MO. Yet, some researchers showed that some impacted microbial populations could recover over time. The negative impacts of the NP have been decreased using stabilizers and emulsifying agents that cover the *NP* and prevent some attached between *NP* and MO membrane; in addition these covers could be used as carbon source for the MO. In the treatment of COCs, MO are not the only potentially exposed to *NP*: for instance, the exposure of subsurface water that is used as a source of drinking water to NP is of concern. In this regard, there are recommendations regarding the of *NP* in *ex situ* treatments, or to develop some technology that allows for the capture and recovery of the NP at the end of the treatment.

7. Health and environmental issues related to nanoparticles use in environmental remediation and treatment

Nanoparticles can be released into the wastewater and finally end in a treatment plant or be released after a nanoaprticle treatment. However there is a broad range of environmental and human health impacts can arise from different exposure routes of *NP*. Due this is necessary understanding the environmental benefits and disadvantage of nanomaterials compared with conventional products. In order to investigate the possible effect of NP on human health have been used some animal models that will predict the possible effects of NP exposicion. Fako & Furgeson [64] have suggested the Zebrafish as an efficient model for predicting nanoparticle toxicity in humans due to the homology of it is genome with the human genome. Choi et al. [65] investigated the liver toxicity of Ag *NP* in Zebrafish. There were cellular alterations like disruption of hepatic cell cords and apoptotic changes. DNA damage and alterations in catalase and glutathione peroxidase enzymes were found. Other animals like oysters have been good models because these animals are filtering and are in direct contact with wasterwater for many industries. Ringwood et al. [66] observed that oyster in direct contact with *NP* increased the expression of a metallothionein levels and damage the embryonic development. Other animals that have been used as models in nanotoxicology are *Drosophila melanogaster*, *Caenorhabditis elegans* [67, 68, 69, 70].

There are some reports that *NP* can entry living organism through some routes like gut, lung and skin and attack target organs such as lung, liver heart and brain [71]. The *NP* can disturb the cells by chemical or physical mechanisms. The chemical mechanisms are: *(i)* the production of reactive oxygen species (ROS), that can cause cell damage because they are involved in

inflammatory processes and the free radical formation can impact the cell integrity and damage the DNA [72, 43, 73] *(ii)* Dissolution and release of toxic ions, *(iii)* Lipid peroxidation [74], and *(iv)* disturbance of the cell membrane transport activity [75]. The physical mechanisms of NP disturbance are related with size and surface properties of *NP* and affect *(i)* transport processes, *(ii)* protein folding/aggregation, *(iii)* membrane, and *(iv)* lysosomes [76, 77, 78, 79].

Due the high risk in the use of nanoparticle technologies it is necessary to evaluate the products that use *NP* in terms of the environmental and health impacts of all the processes involved. One way to evaluate the environmental impact could be using the life cicle assesment (LCA) methodology, defined in standardized guidelines under the International Organization for Standardization (ISO 14040 and ISO 14044). The LCA is a widely accepted methodology for the evaluation of the potential environmental impacts. However it is necessary some adaptations when the impact is about water treatment. The traditionally approach focus on the volume of effluent treated or water produced and the others compare the treatment alternatives. [80, 81]. Actually the application of LCA to NP studies is very scarce. The LCA includes some steps: scope and definition of system boundaries, inventory of material, energy requirements and environmental impact) analysis and improvement analysis. The LCA studies will provide the necessary information to develop regulations and legislation for themes like occupational health and safety, environmental protection and consumer protection also develop information for comparative purposes about designs, processes and materials for the use of NP technologies.

8. Summary and perspectives

Nanomaterials are the core of a promising technology that can be used to accelerate and improve the transformation and detoxification of chlorinated organic compounds (COCs). We have reviewed significant subjects such as efficient nanomaterials for COCs treatment, use of supports and stabilizers that improve the process, interactions of nanomaterials with the microorganisms involved, and emerging fields. The most common material used for treatment of waters polluted with COCs has been zero-valent iron (ZVI) because of its efficiency and low cost. However, there are concerns on the stability and long term durability of ZVI *NP*. For this reason there are some works with other materials such as Pd, Zn or Ni and with combination of materials in the fabrication of NP. The bimetallic NPs allow for a lower cost of production, since one of the materials could be the most economic but not the most efficient whereas the second metal, the most expensive, provides a higher degradation capability. Alloyed and core-and-shell types of bimetallic NP have been tested. The process with NP can be made more efficient by using a support that prevents the aggregation of NP during reaction and in some cases can facilitate the recovery of the NP afterwards. Currently, the application of NP in bioreactors and *in situ* treatments is gaining momentum. Another significant issue especially for hybrid treatments is the interaction between NP and the microbial community harbored in bioreactors and devices, ranging from toxicity issues to biosynthesis of NP. There has been an attempt to incorporate metal NP onto the microbial cells for COC treatment, although more research is needed because some adverse effect has been detected. Furthermore, there is increased interest on biosynthesis of NP with microorganisms in order to have true “nanoparticleized biomass” with increased degradation capability of pollutants. Among important emerging fields we can highlight the studies on health and environmental impact as well as life cycle analysis of the NP fabrication and application. We have found that in spite of its importance the research on this area is scarce and has to be increased to avoid future, unpleasant surprises in the use of NP.

References

[1]Beard J. (2006). DDT and human health. Science of the Total Environment. 355 pp 78-89.

[2]Naidoo V., Katsu Y., Iguchi T. (2008). The influence of non toxic concentrations of DDT and DDE on the old world vulture estrogen receptor alpha. General and Comparative Endocrinology. 159 p. 188-195.

[3]Ingber S., Buser M., Pohl H., Abadin H., Murray E., Scinicariello F. (2013). DDT/DDE and breast cancer: Ameta analysis. Regulatory Toxicology and Pharmacology. 67 p. 421-433.

[4]Cupul-Uicab L.A., Terrazas-Medina E.A., Hernandez-Avila M., Longnecker M.P. (2014). Prenatal exposure to pp-DDE and ppDDT in relation to lower respiratory tract infections in boys from a highly exposed área of Mexico. Environmental Research. 132 pp. 19-23.

[5]Nuñez G. M.A., Estrada I., Calderon-Aranda E.S. (2002). DDT inhibits the functional activation of murine macrophages and decreases resistance to infection by Mycobacterium microti. Toxicology. 174 pp. 201-210.

[6]Lin Y., Weng CH., Chen FY. (2008). Effective removal of AB24 dye by nano/micro size zero valent iron. Separation and Purification Technology 64, pp.26-30.

[7]Cross K.M., Lu Y., Zheng T., Zhan J., McPherson G.L., John V.T. (2014). Water Decontamination Using Iron and Iron Oxide Nanoparticles. Street, Sustich, Duncan and Savage. Nanotechnology Applications for Clean Water, 2nd Edition. Elsevier Inc.

[8] Su Y.P., Li XQ., Zhang WX., Wang HP. (2007). A method for the preparation of stable dispersion of zero valent iron *NP*. Colloids and Surfaces A: Physicochemical and Engineering Aspects. 308 pp. 60-66.

[9]Wang X., Yang J., Zhu M., Li F. (2013). Characterization and regeneration of Pd/Fe *NP* immobilized in modified PVDF membrane. Journal of the Taiwan Institute of Chemical Engineers. 44 pp.386-392.

[10] Li Z., Greden K., Alvarez P.J.J., Gregory K.B., Lowry G.V. (2011). Adsorbed polymer and NOM limits adhesion and toxicity of nano-scale zerovalent iron to E. coli. Environmental Science Technology 44 pp. 3462 – 3467.

[11]Velimirovic M., Simons Q., Bastiaens L. 2014. Guar gum microscale ZVI for in situ treatment of CAHs: Continuous-Flow column study. Journal of Hazardous Materials 265 pp. 20-29.

[12]Velimirovic M., Tosco T., Uyttebroek M., Luna M., Gastone F., De Boer C., Klaas N., Sapion H., Eisenmann H., Larsson P., Braun J., Sethi R., Bastiaens L. (2014). Field assessment of guar gum stabilized microscale zerovalent iron particles for in situ remediation of 1,1,1-trichloroethane. Journal of Contaminant Hydrology.

[13]Wilkin R.T., Acree S.D., Ross R.R., Puls R.W., Lee T.L. Woods L.L. (2014). Fifteen year assessment of a permeable reactive barrier for treatment of chromate and trichloroethylene in gronundwater. Science of the total environment pp 186-194.

[14]Muchitsch N., VanNooten T., Bastiaens L., Kjeldsen P. (2011). Integrated evaluation of the performance of a more than seven year old permeable reactive barrier at a site contaminated with chlorinated aliphatic hydrocarbons (CAHs). Journal of Contaminant Hydrology. 126 pp 258-270.

[15] Ruhl A.S., Franz G., Gernert U., Jekel M. 2014. Corrosion product and precipitate distribution in two component Fe permeable reactive barriers. Chemical Engineering Journal 239 pp 26-32.

[16]Shin-Shian C. Yi-Chu H., Tzu-Yen K. The remediation of perchloroethylene contaminated groundwater by nanoscale iron reactive barrier integrated with surfactant and electrokinetics. Ground Water Monitoring & Remediation. 30 pp 90-98.

[17]Phenrat, T., Saleh N., Sirk K., Tilton RD., Lowry GV. (2007). Aggregation and sedimentation of aqueous nanoscale zerovalent iron dispersions. Enviromental Science and Technology. 41 pp. 284-290.

[18]Zhou L., Thanh TL., Gong J., Kim JH., Kim EJ., Chang YS. (2014). Carboxymethyl cellulose coating decreases toxicity and oxidizing capacity of nanoscale zerovalent iron. Chemosphere 104 pp. 155-161

[20]Sunkara B., Zhan J., He J., McPherson GL., Piringer G., John VT. (2010). Nanoscale zerovalent iron supported on uniform carbon microspheres for the In situ remediation of chlorinated hydrocarbons. ACS Applied Materials and Interfaces. 10 pp. 2854-62.

[21]He F., Zhao D., Paul C. (2010). Field assessment of carboxymethyl cellulose stabilized iron nanoparticles for in situ destruction of chlorinated solvents in source zones. Water Research 44 pp. 2360 – 2370

[22]Bennett P., He F., Zhao D., Aiken B., Feldman L. (2010). In situ testing of metallic iron nanoparticle mobility and reactivity in a shallow granular aquifer. Journal of Contaminant Hydrology. 116 pp. 35-46.

[23] Kaifas D., Malleret L., Kumar N., Fetimi W., Claeys-Bruno M., Sergent M., Doumenq P. (2014). Assessment of potential positive effects of nZVI surface modification and concentration levels on TCE dechlorination in the presence of competing strong oxidants using and experimental design. Science of the total Environment. 481 pp. 335-342.

[24] Roman IS., Alonso ML., Bartolome L., Galdames A., Goiti E., Ocejo M., Moragues M., Alonso R.M., Vilas J.L. (2013). Relevance study of bare and coated zero valent iron nanoparticles for lindane degradation from its by product monitorization. Chemosphere. 93 pp. 1324-32.

[25]Kim EJ., Kim JH., Azad AM., Chang YS. (2011). Facile Synthesis and Characterization of Fe/FeS Nanoparticles for Environmental Applications. ACS Applied Materials and Interfaces. 3 pp. 1457-62.

[26]Xie Y., Fang Z., Qiu X., Tsang E.P., Liang B. (2014). Comparisons of the reactivity, reusability and stability of four different zero valent iron based nanoparticles. Chemosphere. 108 pp. 433-436.

[27]Zheng, T.G., Zhan J.J., He J.B., Day C., Lu FY., Mcpherson G., Piringer G., John V. (2008). Reactivity characteristics of nanoscale zerovalent iron silica composites for trichloroethylene remediation. Environmental Science Technology. 42 pp. 4494-4499.

[28]Chen MY., Su YF., Shih YH. (2014). Effect of geochemical properties on degradation of trichloroethylene by stabilized zerovalent iron nanoparticle with Na-Acrylic copolymer. Journal of Envriomental Management. 144 pp. 88-92.

[29]Li S., Fang YL., Romanczuk C.D., Jin Z.J., Li T., Wong M.S. (2012). Establishing the trichloroethene dechlorination rates of palladium based catalysts and iron based reductants. Applied Catalysis B: Environmental. 125 pp. 95-102.

[30]Cwiertny DM., Bransfield SJ., Roberts AL. (2007). Influence of the oxidizing species on the reactivity of iron based bimetallic reductants. Environmental Science and Technology. 41 pp.3734-40.

[31]Xu J., Dozier A., Bhattacharyya D. (2005). Synthesis of nanoscale bimetallic particles in polyelectrolyte membrane matrix for reductive transformation of halogenated organic compounds. Journal of Nanoparticle Research. 7 pp. 449-467.

[32]Schrick B., Blough J.L., Jones A.D., Mallouk T.E. (2002). Hydrodechlorination of trichloroethylene to hydrocarbons using bimetallic nickel-iron *NP*. Chem.Mater. 14 pp.5140-47.

[33]Lin C.J., Lo SL., Liu YH. (2004). Dechlorination of trichloroethylene in aqueous solution by noble metal modified iron. Journal of Hazardous Materials. 116 pp.219-28

[34]Fu F., Dionysiou DD., Liu H. (2014). The use of zero valent iron for groundwater remediation and wastewater treatment. Journal of Hazardous Materials. 267 pp.194-205.

[35]Tosco T., Papini MP., Viggi CC., Sethi R. (2014). Nanoscale zerovalent iron particles for groundwater remediation: a review. Journal of Cleaner Production. 77 pp. 10-21.

[36]Lin CJ., Liou YH., Lo SL. (2009). Supported Pd/Sn bimetallic *NP* for reductive dechlorination of aqueous trichloroethylene. Chemosphere. 74 pp.314-319.
[37]Xu X.H., Zhou H.Y., He P., Wang D.H. (2005). Catalytic dechlorination kinetics of p-dichlorobenzene over Pd/Fe catalysts. Chemosphere, 58 pp. 1135-40
[38]Shih Y.H and Chen M.Y. (2010). Effect of cations on degradation of pentachlorophenol by nanoscale Pd/Fe bimetallic particles. Sustainable Enviromental Research. 5 pp.333-339.
[39]Kustov L.M., Finashina E.D., Shuvalova E.V., Tkachenko O.P., Kirichenko O.A. (2011). Pd-Fe nanoparticles stabilized by chitosan derivatives for perchloroethene dechlorination. Environment International 37 pp. 1044-1052
[40]Ma H., Huang Y., Shen M., Guo R., Cao X., Shi X. (2012). Enhanced dechlorination of trichloroethylene using electrospun polymer nanofibrous mats immobilized with iron/palladium bimetallic nanoparticles. Journal of Hazardous Materials pp. 349-356
[41]Yu X., Tian X., Wang S. (2014). Adsorption of Ni, Pd, Pt, Cu, Ag and Au on the Fe3O4 (111) surface. Surface Science. 628 pp. 141-47.
[42]Yang L., Lv L., Zhang S., Pan B., Zhang W. (2011). Catalytic dechlorination of monochlorobenzene by Pd/Fe nanoparticles immobilized within a polymeric anion exchanger. Chemical Engineering Journal. 178 pp. 161-167.
[43]Kim JS., Jo SD., Seah GL., Kim I., Nam YS. (2014). ROS-induced biodegradable polythioketal *NP* for intracellular delivery of anti-cancer therapeutics. Journal of Industrial and Engineering Chemistry.
[44]Li B., Zhu J., Zhan F. (2014). Removal of p-chloronitrobenzene from groundwater: Effectiveness and degradation mechanism of a heterogeneous nanoparticulate zero valent iron induced fenton process. Chemical Engineering Journal.
[45]Wei YT., Wu SC., Yang SW., Che CH., Lien HL., Huang DH. (2012). Biodegradable surfactant stabilized nanoscale zero valent iron for in situ treatment of vinyl chloride and 1,2 dichloroethane. Journal of Hazardous Materials. 211-212 pp. 373-80.
[46]Fagerlund F., Illangasekare TH., Phenrat T., Kim HJ., Lowry GV. (2012). PCE dissolution and simultaneous dechlorination by nanoscale zero valent iron particles in a DNAPL source zone. Journal of Contaminant Hydrology. 131 pp. 9-28
[47]Zhan J., Kolesnichenko I., Sunkara B., He J., McPherson GL., Piringer G., John VT. (2011). Multifunctional Iron Carbon Nanocomposites through an aerosol based process for the insitu remediation of chlorinated hydrocarbons. Environmental Science and Technology. 45 pp.1949-54
[48]Kim H., Hong HJ., Jung J., Kim SH., Yang JW. (2010). Degradation of trichloroethylene (TCE) by nanoscale zero valent iron (nZVI) immobilized in alginated bed. Journal of Hazardous Materials 176 pp. 1038-1043.
[49]Shih Y.H., Chen M.Y., Su Y.F. (2011). Pentachlorophenol reduction by Pd/Fe bimetallic nanoparticles: Effects of copper nickel and ferric cations. Applied Catalysis B: Environmental 105 pp. 24-29
[50]Smuleac V., Varma R., Sikdar S., Bhattacharyya D. (2011). Green synthesis of Fe and Fe/Pd bimetallic nanoparticles in membranes for reductive Degradation of chlorinated organics. Journal of Membrane Science. 379 pp. 131-137.
[51]Cho and Choi. (2010). Degradation of PCE, TCE and 1,1,1-TCA by nanosized FePd bimetallic particles under various experimental conditions. Chemosphere. 81 pp. 940-945.
[52]Quinn J., Geiger C., Clausen C., Brooks K., Coon C., O'Hara S., Krug T., Major D., Yoon M.S., Gavaskar A., Holdsworth T. (2005). Field demonstration of DNAPL Dehalogenation using emulsified zero valent iron. Environmental Science and Technology. 39 pp 1309-1318
[53]O'Hara S., Krug T., Quinn J., Clausen C., Geiger C. (2006). Field and Laboratory Evaluation of the treatment of DNAPL source zones using emulsified zero valent iron. Wiley Periodicals.
[54]Mahendra S., Li Q., Lyon D.Y., Brunet L., Alvarez P.J.J. (2014). Nanotechnology-Enabled water disinfection and microbial control: merits and limitations. Street, Sustich, Duncan and Savage. Nanotechnology Applications for Clean Water, 2nd Edition Elsevier Inc.

[55]Su C., Puls R.W., Krug T.A., Watling M.T., O'Hara S.K., Quinn J.W., Ruiz N.E. (2012). A two and half year performance evaluation of a field test on treatment of source zone tetrachloroethene and its chlorinated daughter products using emulsified zero valent iron nanoparticles. Water Research 46 pp 5071-5084.
[56]Su C., Puls R.W., Krug T.A., Watling M.T., O'Hara S.K., Quinn J.W., Ruiz N.E. 2013. Travel distance and transformation of injected emulsified zerovalent iron nanoparticles in the subsurface during two and half years. Water Research 47 p 4095-4106
[57]Ma C., Wu Y. (2008). Dechlorination of prechloroethylene using zero valent metal and microbial community. Dechlorination of perchloroethylene using zero valent metal and microbial community. Enviromental Geol. 55 pp.47-54.
[58]Xiu Z.M., Jin Z.H., Li T.L., Mahendra S., Lowry G.V., Alvarez P.JJ. (2010). Effects of nano scale zero valent iron particles on a mixed culture dechlorinating trichloroethylene. Bioresource Technology. 101 pp. 1141-1146.
[59]Kirschling T.L., Gregory K.B., Minkley E.G., Lowry G.V., Tilton R.D. (2010). Impact of Nanoscale zero valent iron on geochemistry and microbial populations in trichloroethylene contaminated aquifer materials. Environmental Science Technology. 44 pp. 3474-3480.
[60]Barnes R.J., Van der Gast C.J., Riba O., Lehtovirta L.E., Prosser J.I., Dobson P.J., Thompson I.P. (2010). The impact of zero valent iron *NP* on a river water bacterial community. Journal of Hazardous Materials. 184 pp. 73-80.
[61]Cullen L.G., Tilston E.L., Mitchell G.R., Collins C.D., Shaw L.J. (2011). Assessing the impact of nano and micro scale zerovalent iron particles on soil microbial activities: Particle reactivity interferes with assay conditions and interpretation of genuine microbial effects. Chemosphere. 82 pp. 1675-1682.
[62]Fajardo C., Ortiz L.T., Rodriguez-Membibre M.L., Nande M., Lobo M.C., Martin M. (2012). Assessing the impact of zero-valent iron (ZVI) nanotechnology on soil microbial structure and functionality: A molecular approach. Chemosphere. 86 pp. 802-808.

[63]Tilston E.L., Collins C.D., Mitchell G.R., Princivalle J., Shaw L.J. (2013). Nanoscale zerovalent iron alters soil bacterial community structure and inhibits chloroaromatic biodegradation potential in Aroclor 1242-contaminated soil. Environmental Pollution. 173 pp 38-46.

[64]Fako VE, Furgeson DY. (2009). Zebrafish as a correlative and predictive model for assessing biomaterial nanotoxicity. Advanced Drug Delivery Review. 61 pp. 478-86.

[65]Choi JE., Kim S., Ahn JH. (2010). Induction of oxidative stress and apoptosis by silver *NP* in the liver of adult zebrafish. Aquatic Toxicology. 100 pp. 151-9.

[66]Ringwood AH., McCarthy M., Bates TC., Carroll DL. (2009). The effects of silver *NP* on oyster embryos. Marine Environmental Research.

[67]Khare P., Sonane M., Pandey R., Ali S., Gupta K., Satish A. (2011). Adverse effects of TiO_2 and ZnO *NP* in soil nematode, *Caenorhabditis elegans.* Journal of Biomedical Nanotechnology. 7 pp.116-117

[68]Ahamed M., Posgai R., Gorey TJ., Nielsen M., Hussain S., Rowe J. (2010). Silver *NP* induced heat shock protein 70, oxidative stress and apoptosis *in Drosophila melanogaster.* Toxicology Applied Pharmacology. 242 pp. 263-9.

[69]Roh JY., Sim SJ., Yi J. (2009). Ecotoxicity of silver *NP* on the soil nematode Caenorhabditis elegans using functional ecotoxicogenomics. Environmental Science Technology 43 pp. 3933-40.

[70]Posgai R., Ahamed M., Hussain SM., Rowe J., Nielsen M. (2009). Inhalation method for delivery of *NP* to the Drosophila respiratory system for toxicity testing. Science Total Environmental. 408 pp.439-43.

[71]Handy RD., Von der Kammer F., Lead JR., Hassellov M., Owen R., Crane R. (2008). The ecotoxicology and chemistry of manufactured *NP*. Ecotoxicology 17 pp. 287-314.

[72]Ma H., Wallis LK., Diamond S., Li S., Canas-Carrell J., Parra A. (2014). Impact of solar UV radiation on toxicity of ZnO *NP* through photocatalytic reactive oxygen species (ROS) generation and photo induced dissolution. Environmental Pollution. 193 pp.165-172.

[73]Chairuangkitti P., Lawanprasert S., Roytrakul S., Aueviriyavit S., Phummiratch D., Kulthong K., Chanvorachote P., Maniratanachote R. (2013). Silver *NP* induce toxicity in A549 cells via ROS dependent and ROS independent pathways. Toxicology in vitro, 27 pp. 330-338.

[74]Kamat J.P., Devasagayam T.P., Priyadarsini K.I., Mohan H. (2000). Reactive oxygen species mediated membrane damage induced by fullerene derivatives and its possible biological implications. Toxicology 155 pp. 55-61.

[75]Mahmoudi M., Meng J., Xue X., Liang XJ., Rahman M., Pfeiffer C., Hartmann R., Gil PR., Pelaz B., Parak WJ., Pino P., Carregal-Romero S., Kanaras AG., Selvan ST. (2014). Interaction of stable colloidal *NP* with cellular membranes. Biotechnology Advances. 32 pp. 679-692

[76]Grudzinski IP., Bystrzejewski M., Cywinska MA., Kosmider A., Poplawska M., Cieszanowski A., Fijalek Z., Ostrowska A. (2014). Comparative cytotoxity studies of carbon-encapsulated iron *NP* in murine glioma cells. Colloids and Surfaces B: Biointerfaces. 117 pp.135-143.

[77]Makumire S., Chakravadhanula V., Kollisch G., Redel E., Shonhai A. (2014). Immunomodulatory activity of zinc peroxide (ZnO_2) and titanium dioxide (TiO_2) *NP* and their effects on DNA and protein integrity. Toxicology Letters. 227 pp 56-64.

[78]Karlsson HL., Cronholm P., Hedberg Y., Tornberg M., De Battice L., Svedhem S., Wallinder IO. (2013). Cell membrane damage and protein interaction induced by copper containing *NP* Importance of the metal release process. Toxicology. 313 pp.59-69.

[79]Wang F., Yu L., Monopoli MP., Sandin P., Mahon E., Salvati A., Dawson KA. (2013). The biomolecular corona is retained during nanoparticle uptake and protects the cells from the damage induced by cationic *NP* until degraded in the lysosomes. Nanomedicine: Nanotechnology, Biology and Medicine. 9 pp. 1159-1168.

[80]O'Connor M., Garnier G., Batchelor W. (2014). Life cycle assessment comparison of industrial effluent management strategies. Journal of Cleaner Production.

[81]Igos E., Dalle A., Turita-Barna L., Benetto E., Baudin I., Mery Y. (2014). Life cycle assessment of wáter treatment: what is the contribution of infrastructure and operation at unit process level. Journal of Cleaner Production 65 pp. 424-431.

Saccharification of Fermented Solids for a Hydrogen Producing Biorefinery

C. Escamilla-Alvarado[1], H.M. Poggi-Varaldo[1], T. Ponce-Noyola[2,*], K.M. Munoz-Paez[1], E. Ríos-Leal[3], F. Esparza-García[4], J. Barrera-Cortez[5], J. García-Mena[6], I. Robles-Gonzalez[7], N. Rinderknecht-Seijas[8]

[1]Environmental Biotechnology and Renewable Energies R&D Group, Dept. of Biotechnology and Bioengineering, Centro de Investigación y de Estudios Avanzados del IPN, P.O. Box 14-740, 07000 México D.F., México.
[2]Microbial Genetics Group, ibidem.
[3]Central Analítica, ibidem.
[4]Biochemical Ecology, ibidem.
[5]Intelligent Control, ibidem.
[6]Dept. of Genetics and Molecular Biology, ibidem.
[7]Nova Universitas
[8]Escuela Superior de Ingeniería Química e Industrias Extractivas del IPN, Mexico D.F., México.

*Author for all correspondence: tponce@cinvestav.mx.

ABSTRACT

Biorefineries may be used to decrease dependence on fossil fuels by producing biofuels, or to produce new bioproducts and commodities. The production of hydrogen has been successfully coupled to a biorefinery model coined H-M-Z, providing advantages such as the generation the environmental friendly clean fuel hydrogen, and surprisingly an intermediate organic by-product coined as fermented solids (FS) that showed interesting properties for more biofuel and enzymes production. The objective in this work was to add a new stage for the saccharification of lignocellulosic substrates in a hydrogen producing biorefinery model.

Two saccharification experiments were performed. In the first one (SS-1) two factors were evaluated: type of substrate and type of holocellulolytic enzymes according to a 2x3 factorial design. The substrates were OFMSW, FS, and filter paper Whatman No. 1 (FP). The holocellulolytic enzymes used were the enzyme extract from Z-stage (*Trichoderma reesei* extract) of the biorefinery and the commercial enzyme Celluclast (Sigma-Aldrich, USA). In the second experiment (SS-2), the FS were subjected to evaluation at four different levels of enzyme:substrate ratio [40, 60 80, 100 and 120 FP units (g volatile solids)$^{-1}$].

In SS-1 all substrates were best saccharified with the *T. reesei* extract, whereas the most saccharified substrate, independently of the enzyme used, was the FP [up to 18 g of glucose and xylose (L)$^{-1}$]. The FS had up to 34 % higher saccharification than OFMSW, with up to 13.09 g of glucose and xylose (L)$^{-1}$. The highest saccharification efficiency for FS was 75 % on holocellulose basis. In the SS-2, we found that contrary to expected, the highest enzyme:substrate ratio had no significant positive effect on saccharification yields. Indeed, the ratio 40 FP units (g volatile solids)$^{-1}$ had the highest saccharification yield [11 mg sugars (filter paper unit)$^{-1}$].

In conclusion, the hydrogen production in a biorefinery is transcendental because on the one hand, it provides a renewable clean fuel, and on the other hand, it provides a pre-degraded substrate (saccharified liquors) easily convertible into valuable bioproducts, or even into more biofuels.

Keywords: biohydrogen; cellulases; municipal organic solid wastes; saccharification.

1. Introduction

Biorefineries may contribute to decrease dependence on fossil fuels and to produce new bioproducts. One of the most acknowledged advantages of biorefineries is its flexibility and wide spectrum of possible products. There is not only one possible configuration for biorefineries; this depends on feedstock, aim and bioproducts or biofuels orientation [1]. The most common biofuels produced in expected biorefineries are ethanol, methane and vegetable or microbial oils [2, 3]; whereas the bioproducts include enzymes, proteins, resins, biomolecules, carbohydrates, fertilizers, among others [1, 4, 5].

Due to the thermodynamic and ecological characteristics of hydrogen, it is considered to be a promising bioproduct in biorefineries [2, 6]. Hydrogen may be produced via biological processes such as dark fermentation or photo fermentation, with axenic cultures or consortia [7]. The consortia have metabolic interactions that can degrade more exhaustively a complex substrate and may use unsterilized substrate. In contrast, axenic cultures have a reduced metabolic capability and often need microbial-contamination free substrate. When biomass is hard to assimilate by microorganisms of interest, a common approach is to hydrolyze its polymeric chains using enzymes. For instance, the efficient hydrogen producing *Clostridium pasteurianum* is unable to assimilate starch directly [8]. However if starch is hydrolyzed either by physical-chemical or biological methods, *C. pasteurianum* effectively evolves hydrogen from this hydrolyzate.

Holocellulases are an important group of enzymes for hydrolyzing cellulose and hemicellulose [9]. Cellulose is the most abundant natural polymer on earth and it has been identified as a robust feedstock for biofuels and bioproducts [10]. However, the forms in which cellulose is found in nature are as diverse as the number of plant species. Residual biomass from agriculture and from the organic fraction of municipal solid wastes (OFMSW) is regarded as a renewable and non-food competing substrate.

The saccharification is the depolimerization of the carbohydrates that constitute the vegetable biomass cell walls into simple sugars [11]. One of the most common applications of the hydrolyzates from saccharification, is its fermentation into compounds such as ethanol, butanol, lactic acid, and even hydrogen [12]. When converting lignocellulosic biomass to hydrogen, glucose and xylose are the conducive reducing sugars [13].

In the initial step of the biorefinery model coined as H-M-Z [14, 15], the dark fermentation of OFMSW produced hydrogen and an organic by-product termed as fermented solids (FS) that showed good biodegradability properties in contrast to the OFMSW. Consequently, methane and holocellulases were produced in parallel from the FS. The objective in this work was to add a new stage for the saccharification of lignocellulosic substrates in a hydrogen producing biorefinery model.

2. Materials and methods

2.1. Biorefinery H-M-Z set up

This biorefinery H-M-Z was comprised by an in-series process for hydrogen and methane production and by the parallel process for holocellulases production (Fig. 1).

The hydrogen-producing process (H-stage) was fed with the organic fraction of municipal solid wastes (OFMSW). The hydrogenogenesis was performed at 55 °C and semi-continuous feeding at 21 d MRT, with a maximum productivity of 202 NmL $H_2/kg_r/d$ [15]. The fermented solids (FS) were the purges from

the H-stage, which were fed as they were to the methanogenic stage, and washed and then fed to the enzyme producing stage.

The methanogenic stage (M-stage) was operated at 55 °C and semi-continuous operation at 28 d MRT. The productivity was 2 023 NmL $CH_4/kg_r/d$ [15].

The enzymes production (Z-stage) was performed using *Trichoderma reesei* MCG 80 in 450 mL working volume fed with FS at 1.5 %VS. The operation was fed batch at 30 °C, 450 rpm, 9 d. The enzyme titers were 2.06 FPU/mL and 1.23 IU_{CMC}/mL [14].

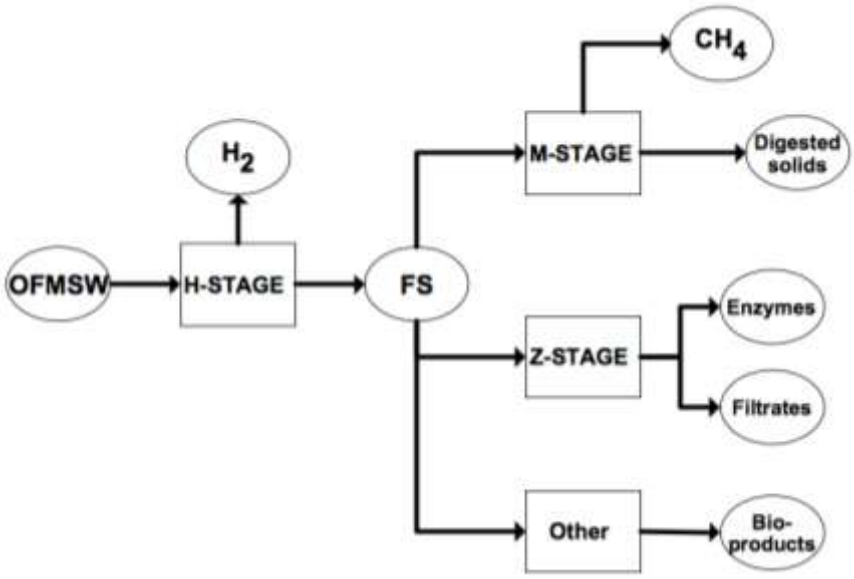

Fig. 1. Biorefinery model H-M-Z

2.2. Saccharification experiments evaluating types of enzyme and substrate

Two factors were evaluated: type of substrate and type of holocellulolytic enzymes according to a 3x2 factorial design. The substrates were OFMSW, FS, and filter paper Whatman No. 1. As holocellulolytic enzymes, we used the enzyme extract from Z-stage from biorefinery model (*Trichoderma reesei* extract) and the commercial enzyme Celluclast (Sigma-Aldrich, USA).

Saccharification was carried out in 125 mL Erlenmeyer flasks with 25 mL working volume at 50 °C, 150 rpm. The substrates concentration was 2 %VS in 0.05 M citrate buffer (pH 5.0). The enzyme loading was 60 FPU/g VS. The enzymes had the composition described in Table 1.

Table 1. Enzyme activities of Celluclast and *Trichoderma reesei* enzyme extract.

Parameter	Celluclast [a]		
	Volumetric	Specific	Specific normalized[b]
Filter paper activity	98.5 ± 2.7 FPU/mL	0.80 ± FPU/mg	1 FPU/FPU
Carboximethylcellulase activity	65.1 ± IU/mL	0.53 ± IU/mg	0.66 IU/FPU
Xylanase activity	156.3 ± U/mL	1.26± U/mg	1.58 U/FPU
β-glucosidase activity	14.0 ± µmol/min/mL	0.11 ± µmol/min/mg	0.14 µmol/min/FPU
Protein	123.6 ± mg/mL	-	-
Parameter	*Trichoderma reesei* enzyme extract [c]		
	Volumetric	Specific	Specific normalized[b]
Filter paper activity	37.01 ± 3.0 FPU/mL	0.87 ± 0.07 FPU/mg	1 FPU/FPU
Carboximethylcellulase activity	35.25 ± 0.01 IU/mL	0.83 ± 2.3E-4 IU/mg	0.95 IU/FPU
Xylanase activity	87.6 ± 0.42 U/mg	2.07 ± 0.01 U/mg	2.4 U/FPU
β-glucosidase activity	1.63 ± µmol/min/mL	0.04 ± µmol/min/mg	0.04 µmol/min/FPU
Protein	42.3 ± 1.2 mg/mL	-	-

Notes: [a] commercial enzyme Celluclast (Sigma-Aldrich); [b] specific enzyme normalized at 1 FPU/mL; [c] enzyme extract from *T. reesei* MCG 80 in Z-stage.

2.3. Saccharification experiments evaluating enzyme:substrate ratio

The FS were subjected to evaluation at four different levels of enzyme:substrate ratio: 40, 60 80, 100 and 120 FPU/g VS. The experiments were performed in 10 mL working volume assay tubes at 50 °C and 150 rpm, with enzyme extract from *T. reesei* at corresponding loadings. The substrate were the FS at 2 %VS.

2.4. Residual enzyme analysis

Supernatant from the saccharification experiments of the enzyme:substrate ratio evaluation was recovered, centrifuged at 5 000 g and assayed for filter paper activity, in order to determine the potential of reusing the enzymes after 72 h saccharification.

2.5. Analysis

Samples were first centrifuged at 5 000 g, 10 min and 4 ºC. Glucose and xylose analysis were performed by triplicate using a biochemical analyzer YSI 2700 Select (YSI Inc, OH, EUA). The response variables used are listed in Table 2.

Determination of enzyme titers as paper filter activity was performed as previously described [14] by the dinitrosalicylic acid method [16] according to Mandels et al. [17]. Filter paper activity units (FPU) expressed the amount of glucose released per min under proper assay conditions. All determinations were made by triplicate along with respective enzyme and substrate blanks.

Table 2. Response variables

Response variables	Units	Equation	
Sugar concentration	g/L	$[GX] = [glucose] + [xylose]$	(1)
Xylose/glucose ratio	-	$X/G = \frac{[xylose]}{[glucose]}$	(2)
Saccharification efficiency in volatile solids basis	$\%_{VSb}$	$h_{s,VS} = \frac{[GX]}{[VS]_{substrate}[substrate]} * 100$	(3)
Saccharification efficiency in holocellulose basis	$\%_{holocel}$	$h_{s,h} = \frac{[GX]}{[Holocellulose]_{substrate}[substrate]} * 100$	(4)
Saccharification yield	g sugars/FPU	$Y_s = \frac{[GX] * Vr}{EL * m_{VS}} * 100$	(5)

Notes: [glucose], glucose concentration (g/L); [xylose], xylose concentration (g/L); $[VS]_{substrate}$, concentration of volatile solids in substrate (%); [substrate], substrate concentration (g/L); $[Holocellulose]_{substrate}$, concentration of holocellulose in substrate (%); Vr, reaction volume (L); EL, enzyme loading (FPU/g VS); m_{VS}, amount of VS (g VS).

3. Results and discussion

3.1 Saccharification experiments evaluating types of enzyme and substrate

The OFMSW, paper filter and FS were used as substrates for saccharification using enzyme extract and the commercial enzyme Celluclast on a 3x2 experimental design.

Both enzyme preparations were load in the same proportion: 1.2 FPU/mL or 60 FPU/g VS. The profile of all the saccharification curves was asymptotic (Fig. 2). When using the enzyme extract, all the saccharifications were higher than those obtained with Celluclast in all the substrates, whereas the best saccharifications were obtained with filter paper, independently of the enzyme used (Table 3).

Better saccharification results were obtained with FS than with the OFMSW. Similarly, the FS had given better results than OFMSW in the methane and enzyme production stages. Several explanations may be formulated such as an effective pre-hydrolysis of cellulose resulting in more accessible and readily digestible polysaccharide chains.

Saccharification efficiencies (η_s) were near 50 % for OFMSW, and up to 65 % for FS. The higher η_s was obtained with filter paper, a result almost expectable being this refined cellulose with no presence of inhibitors [18, 19].

It was found that both the substrates and the enzymes had significant effect on saccharification, yet no interaction was found amidst the factors (Table 4). Moreover, Fig. 4 shows that the substrates where best saccharified in the order filter paper > FS > OFMSW, whereas the enzyme extract was statistically superior to Celluclast.

Compared to literature our results fell in the superior range (Table 5). Most of the saccharification studies used chemical, thermal or mechanical pretreatments, being the most common the diluted acid hydrolysis, steam pressure explosion, ball milling and ozonation. For instance, Ballesteros et al. [20] applied thermal pretreatment (160 ºC, 30 min) to municipal solid waste (MSW) 20 %TS, obtaining 35 g glucose/L after saccharification with a cellulose mix of Celluclast 1.5L and ß-glucosidase Novozyme 188. Clanet et al. [21] used enzyme extract from *T. reesei* CL847 achieving 48 $\%_{VSb}$ of saccharification from MSW at 6 %TS. After applying sequential diluted acid (1% v/v H_2SO_4, 3 h, 60 ºC) and thermal (120 ºC, 15 min) pretreatments to MSW, Li et al. [22] obtained a higher saccharification of 72.8 % with an enzymatic load of 60 FPU/ g from *T. viride* applied to 1 %TS MSW.

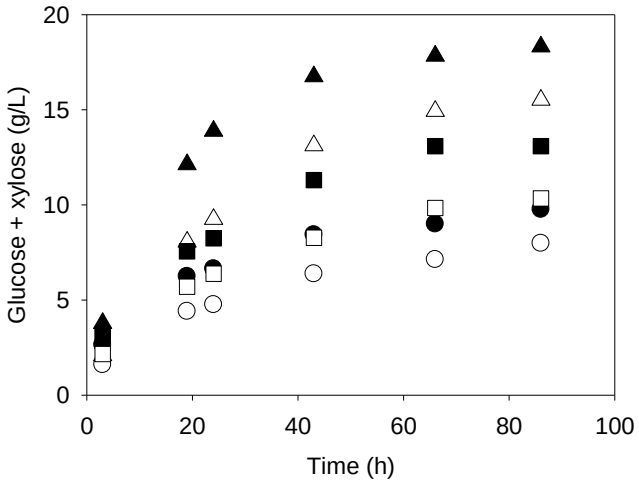

Fig. 2. Saccharification profiles. Solid symbols, *T. reesei* enzyme extracts; open symbols, Celluclast; Triangles, filter paper; Squares, FS; Circles, OFMSW.

Table 3. Maximum saccharifications at 60 FPU/g VS

Substrate	[GX] (g/L)	X/G (-)	$\eta_{s,VS}$ ($\%_{VSb}$)	$\eta_{s,h}$ ($\%_{holocel}$)
OFMSW + *T. reesei* enzyme extract	9.77 ± 0.63	0.30 ± 0.011	48.9 ± 3.2	54.3 ± 3.5
OFMSW + Celluclast	7.99 ± 0.52	0.28 ± 0.010	39.9 ± 2.6	44.4 ± 2.9
Filter paper + *T. reesei* enzyme extract	18.32 ± 0.56	0.13 ± 0.002	91.6 ± 2.1	96.4 ± 2.4
Filter paper + Celluclast	15.51 ± 0.22	0.09 ± 0.025	77.6 ± 2.6	83.3 ± 2.9
FS + *T. reesei* enzyme extract	13.09 ± 0.79	0.18 ± 0.009	65.4 ± 3.8	72.7 ± 4.2
FS + Celluclast	10.34 ± 2.61	0.24 ± 0.029	51.7 ± 12.6	57.4 ± 14.1

Table 4. Analysis of variance of the effects on saccharification

Source	Sum of squares	Degrees of freedom	Mean square	F value	p-value (prob > F)	Effect
Model	151.7	5	30.34	11.42	0.005	Significant
Substrate	132.95	2	66.47	25.03	0.0012	Significant
Enzyme	18.08	1	18.08	6.81	0.0402	Significant
Substrate x Enzyme	0.67	2	0.34	0.13	0.8832	Not significant
Pure error	15.94	6	2.66			

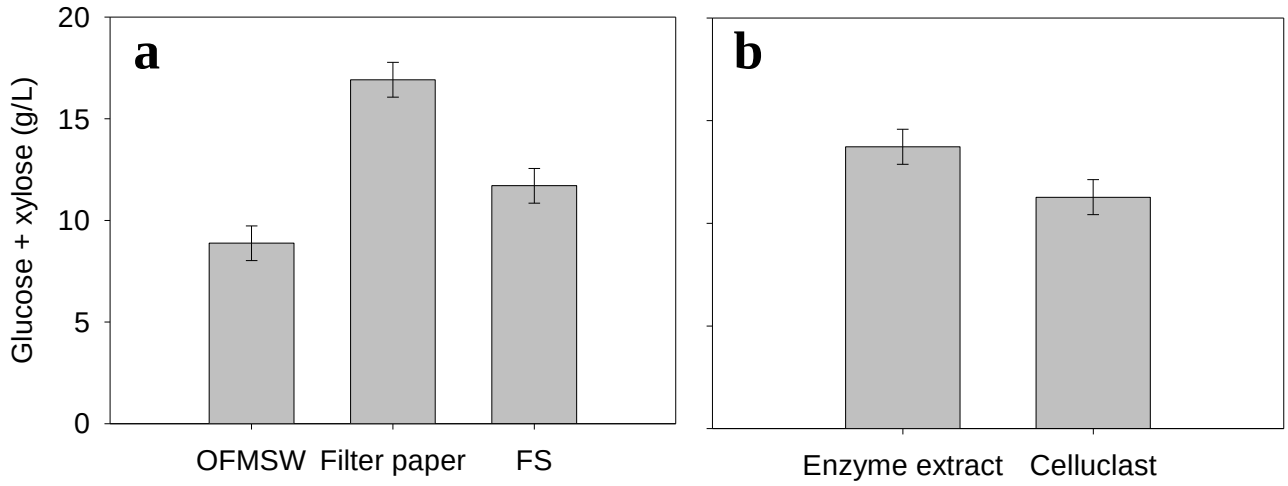

Fig. 3. Effects on saccharification. a) substrates, b) enzymes

Most pretreatments increase the saccharification of lignocellulosic substrates, however it must be considered their impact on environment and their costs. Diluted acid is regarded to have lower costs than short duration thermal pretreatments and a higher effect on saccharification [22]. Some pretreatments produce inhibitors to enzymes, mainly furaldehydes, organic acids, and phenolic compounds derived from the hydrolysis of lignin [19].

Recalling Table 1 (Materials and methods), it is observed that probably the reason for the better results with the enzyme extracts was due to its higher content of hemicellulases and endocellulases, despite of the lower content of glucosidases compared to the Celluclast.

Table 5. Saccharification of organic residuals

Substrate	Pretreatment	Enzymes	Results	Ref
OFMSW 20 %TS	Thermal (160 ºC, 30 min)	Cellulase (NS50013) and ß-glucosidase (NS50010)	$\eta_{s,VS}$ [b] = 41.6 % 35 g glucose/L	[20]
Kitchen waste 1 %TS	Thermochemical (1.5 % HCl, 120 ºC, 120 min)	NU	$\eta_{s,VS}$ = 57.3 %	[23]
OFMSW 6 %TS	NU [a]	Extract from *Trichoderma reesei* CL847 at 9 FPU/g substrate	$\eta_{s,VS}$ = 48 %	[21]
Sugarcane bagasse 5 %TS	Ball milling	*Trichoderma reesei* QM9414	$\eta_{s,VS}$ = 50.4 %	[17]
MSW 1 %TS	Acid (H_2SO_4 1 %v/v, 3 h, 60 ºC)+ thermal (120 ºC, 15 min)	*Trichoderma viride* at 60 FPU/g	$\eta_{s,cel}$ [c] = 72.8 %	[22]
Mixed solid waste 2.7 %TS	Acid (H_2SO_4 0.4 %v/v, 3 h, 60 ºC)+ steam pressure explosion (210 ºC, 3 min)	Cellulase at 66 FPU/g cellulose	$\eta_{s,cel}$ = 80 %	[24]
Milled cotton stalks 10 %TS	Ozone (45 mg O_3/L at 0.37 L/min, 150 min)	Cellulase at 20 FPU/g, ß-glucosidase at 45 IU/g and pectinase at 15 IU/g	$\eta_{s,VS}$ = 43.1 %	[25]
Fermented organic waste (FS) 2 %VS	Dark fermentation (55 ºC, 21 d mass retention time)	*Trichoderma reesei* MCG 80 60 FPU/g	$\eta_{s,VS}$ = 65.4 % $\eta_{s,h}$ = 72.7 %	This work

Notes: [a] not used, [b] saccharification efficiency VS basis, [c] saccharification efficiency cellulose basis

3.2. Saccharification experiments evaluating enzyme:substrate ratio

Increasing the enzyme:substrate ratio gave higher saccharifications (Table 6). The maximum saccharification was 11.59 g/L at 120 FPU/g VS. However the highest yield 11.06 mg sugar/FPU was observed at 40 FPU/g VS. This means that the saccharification did not increase proportionally to the enzyme:substrate ratio. Ballesteros *et al*. [20] also assayed the effect of different enzyme loads on 20 %TS MSW, observing a higher but no proportional saccharification when increasing enzyme loads from 20 to 60 FPU/g cellulose. In fact, the 3-fold higher enzyme load of 60 FPU/g cellulose only increased 16 % the saccharification of the 20 FPU/g cellulose enzyme load. In our case the doubling of the enzyme load increased 20 % the saccharification. Considering the high cost of enzymes, it would be better to find a enzyme:substrate ratio that sets a compromise solution between efficiency, yield and costs of the enzyme and substrate.

The unsaccharified organic matter may be used as substrate for other processes. For instance, Singh et al. [18] used the saccharified potato pulp to induce enzyme production from *T. reesei* Rut C30, with slightly better results than the enzyme induction from fresh potato pulp.

Table 6. Enzyme:substrate ratio saccharification results

Enzyme:substrate (FPU/g SV)	[GX] (g/L)	$\eta_{s,VS}$ ($\%_{VSb}$)	$\eta_{s,h}$ ($\%_{holocel}$)	Y_s (mg sugars/FPU)
40	10.02 ± 0.26	50.1 ± 1.0	55.7 ± 1.33	11.06
60	9.60 ± 0.29	48.0 ± 1.9	53.3 ± 2.2	6.80
80	9.65 ± 0.40	48.2 ± 3.6	53.6 ± 3.9	5.43
100	10.49 ± 0.29	52.5 ± 3.4	58.3 ± 3.7	4.59
120	11.59 ± 0.13	58.0 ± 1.5	64.4 ± 1.9	4.31
Control Celluclast 60 FPU/g VS	7.13 ± 0.23	35.6 ± 1.4	39.6 ± 1.8	5.34

Confirmatory assays showed that enzyme loads of 40 and 60 FPU/g VS did not show significant differences in saccharification results (data not shown), leading to infer that 40 FPU/g VS is an adequate load for saccharifying FS with satisfactory results.

Saccharification time could be reduced to less than 72 h in order to decrease energy expenses, just down to the necessary time to reach an acceptable result, which could be 80 % of the maximum experimental saccharification at 72 h. For instance, when using OFMSW after 29 h of reaction the saccharification reached 80 % of the maximum experimental saccharification, whereas for filter paper the same percentage was achieved at 40 h. Ballesteros *et al*. [20] using enzyme loads of 40 and 60 FPU/g VS, reported that maximum saccharification was reached at 48 h. Kaur et al. [25] also reported that for alkali or ozone pretreated cotton stalks, their respective maximum saccharification was reached at 48 h.

The saccharification results from the assays of the FS and the enzyme extract from *T. reesei*, show that it is technically feasible to include this process in the biorefinery H-M-Z, thus becoming the biorefinery H-M-Z-S. Table 7 shows the compositional characteristics of the lignocellulosic materials produced/used in this proposed biorefinery H-M-Z-S. The main consumed component of the holocellulose was the hemicellulose, which constituted 40 % of the holocellulose in the OFMSW, and ended up constituting 7 and 12 % of the FS and of the digested solids, respectively. Moreover, in the re-fermented solids of the Z-stage and in the hydrolyzed solids from the saccharification process, the hemicellulose content was as low as 1 % of the total holocellulose. Due to the recalcitrance of the lignin, its concentration in the TS augmented as the holocellulose was degraded. The re-fermented solids had a cellulose concentration as low as that of the digested solids from the methane producing stage. In the case of the hydrolyzed solids, the cellulose concentration was found in a higher proportion, presumably in the form of crystalline cellulose [26].

To achieve an integral use of the hydrolyzates from a saccharification process, it is important that these are not inhibitory to other microbiological processes. The hydrolyzates obtained by Clanet et al. [21] were used successfully as substrate for bacteria, yeast and fungus, with growth comparable to those obtained from glucose as carbon source. On their behalf, Ballesteros et al. [20] also used hydrolyzates from MSW for the ethanol production (30 g/L) by simultaneous saccharification-fermentation in fed-batch. In the case reported by Nguyen et al. [24], who obtained hydrolyzates from a mixture of different solid residues, it was necessary an acclimatization of their *Saccharomyces cerevisiae* strain to this substrate. This was mainly because of a slight generation of toxic compounds during the pretreatment of acid hydrolysis and steam pressure explosion (0.4 % H_2SO_4, 210 ºC, 3 min). When the concentration of toxic compounds (e.g.

furaldehydes, phenolic compounds) is high, one of the strategies for their removal is by biological methods, as the addition of laccases or the use of microorganisms with affinity to those toxics [19].

Table 7. Compositional characteristics of lignocellulosic materials of H-M-Z-S biorefinery

Parameter	OFMSW	Fermented solids (FS) from H-stage	Digested solids from M-stage	Re-fermented solids from Z-stage	Hydrolyzed solids from S-stage
Volatile solids ($\%_{db}$)	85.8 ± 0.24	81.6 ± 0.33	30.3 ± 0.20	67.5 ± 0.06	80.7 ± 1.78
Ashes ($\%_{db}$)	14.2 ± 0.35	18.4 ± 0.24	69.7 ± 0.54	32.2 ± 0.50	19.3 ± 0.95
Cellulose ($\%_{db}$)	46.6 ± 1.40	66.2 ± 0.75	14.8 ± 0.35	19.7 ± 0.81	52.8 ± 0.44
Cellulose ($\%_{VSb}$)	54.3 ± 1.54	81.1 ± 0.88	48.8 ± 1.31	29.2 ± 1.20	65.4 ± 0.74
Holocellulose ($\%_{db}$)	77.7 ± 1.80	71.6 ± 0.83	16.9 ± 0.21	20.3 ± 0.45	53.0 ± 1.01
Lignin ($\%_{db}$)	8.1 ± 0.98	9.9 ± 0.54	13.5 ± 0.68	21.0 ± 0.02	28.7 ± 0.40

Regarding hydrogen production from hydrolyzates, Lo et al. [12] hydrolyzed starch with *Caldimonas taiwanensis* On1 to feed *Clostridium butyricum* CGS2 thus producing 0.22 L H_2/h/L. Moreover, they fed the metabolites from dark fermentation to a photo fermentation process using *Rhodopseudomonas palustris* WP3-5 for more hydrogen production. Ren et al. [13] assayed different mixtures of glucose and xylose with *Thermoanaerobacterium thermosaccharolyticum* W16. They found that both pure glucose and xylose, and their mixtures were effectively used to produce hydrogen, yet the preferred substrate was glucose (2.42 mol H_2/mol glucose). Consequently, they used corn stover hydrolyzates containing 5.8 g glucose/L, 4.2 g xylose/L and 0.6 g/L arabinose, which was successfully converted into hydrogen (120 mmol H_2/L, 2.3 mmol H_2/mol substrate) at similar yields than a synthetic medium containing glucose and xylose at the same proportion than the hydrolyzates. They also pointed out that apparently, the components in hydrolyzate of corn stover did not inhibit the growth of the microorganism used.

3.3. Residual enzyme analysis

The potential reuse of the enzymes after 72 h saccharification of the FS was evaluated (Table 8). At the end of saccharification, the residual enzyme activity in the hydrolyzates was assayed. When dividing this residual activity by the initial enzyme activity, the enzyme recovery was obtained. In general good enzyme recoveries were attained (> 70 %) It could be appreciated that the enzyme recovery was higher at lower enzyme loads (Table 8). In the saccharification with 40 FPU/g VS the highest enzyme recovery of 86 % was obtained. The enzyme adsorption may have been the cause of this phenomenon. In deed, it has been reported that the proportion of the enzyme adsorbed to the residual substrate is depending of the enzyme:substrate ratio, of the hydrolysis efficiency and of the lignin content in the substrate [26]. The adsorption and desorption phenomena are very important for the hydrolysis and enzyme recovery, as there is a strong relation amidst enzyme adsorption and substrate hydrolysis. It is considered that a stronger adsorption leads to a higher hydrolysis [26]. Consequently when there is a strong adsorption in the endo and exoglucanases to the cellulosic substrate, the desorption is not realized unless the substrate has been degraded [27]. The exoglucanases may be bound to the insoluble substrate by means of two elements, the catalytic dominion and the cellulose-binding domain. The adsorption only by the cellulose binding domain

does not allows the hydrolysis of the substrate; to achieve this it is necessary the binding of the catalytic domain.

The observed enzyme recoveries of 70 – 86 % open up the possibility to recover and recycle the enzyme extract for new saccharification. The enzyme recycle is observed as an alternative to reduce the costs associated to the enzyme hydrolysis, as it is considered that the cost of the enzymes is nearly 60 % of the total cost of the process [18, 24]. Some enzyme recycling or reuse techniques are its immobilization, recovery by ultrafiltration of the hydrolyzate or by desorption from the residual substrate using fresh phosphate buffer, or reuse by contact of the adsorbed enzymes in the hydrolyzed substrate with fresh substrate [18, 24].

Table 8. Residual enzyme activity analysis

Enzyme load (FPU/g SV)	FPx,i [a] t = 0 h	FPx,f [b] t = 72 h	FPx,r [c] (%)
40	1.00	0.86	86
60	1.31	1.08	82
80	1.68	1.28	76
100	2.03	1.57	77
120	2.45	1.77	72
Control Celluclast 60 FPU/g SV	1.34	1.00	75

Notes: [a] FPx initial at 0 h, [b] FPx final at 72 h, [c] Amount of enzyme activity recovery (FPx,r = FPx,f/FPx,i *100). The filter paper activity of the *T. reesei* extract and of Celluclast were 17.55 and 111.2 FPU/mL respectively.

The hydrolyzed solids from FS may even have further application in other biotechnological processes. One of such could be its reuse in combination with fresh substrate to increase the enzyme production as proposed by Hogan and Mes-Hartree [26], who combined hydrolyzed residual poplar with steam pressure explosion pretreated fresh poplar. They reported higher enzyme activities (0.72 – 0.85 FPU/mL) when compared to fresh substrate (0.55 0.67 FPU/mL).

4. Conclusions

- The substrates were best saccharified in the order filter paper > FS > OFMSW.
- The enzyme extract from *Trichoderma reesei* MCG 80 was statistically superior to Celluclast.
- Saccharification efficiencies were near 50 % for OFMSW, and up to 65 % for FS.
- Increasing the enzyme:substrate ratio gave higher saccharification.
- The highest saccharification yield was obtained with enzyme load at 40 FPU/g VS.
- The enzyme loads of 40 and 60 FPU/g VS did not show significant differences in saccharification results (data not shown), leading to infer that 40 FPU/g VS could be an adequate load for saccharifying FS with satisfactory results.

- Results show that it is technically feasible to add a saccharification stage to the H-M-Z biorefinery model, thus achieving an integral use of the enzyme produced in Z-stage and the FS from H-stage.
- Hydrolyzates from FS need to be assayed to confirm its potential use to hydrogen production.

Acknowledgements
This work received partial funding from SECITI- ICYTDF (Project PICCO 10-27), CONACYT (Project 104333) and CINVESTAV del IPN.

References

[1] M. Wellisch, G. Jungmeier, A. Karbowski, M. K. Patel, and M. Rogulska, Biofuels, Bioprod Bioref, 4, 275 (2010).
[2] L. T. Angenent, K. Karim, M. H. Al-Dahhan, B. A. Wrenn, and R. Dominguez-Espinosa, Trends Biotechnol, 22, 477 (2004).
[3] V. Menon and M. Rao, Progress in Energy and Combustion Science, 38, 522 (2012).
[4] Y.-H. P. Zhang, J Ind Microbiol Biotechnol, 35, 367 (2008).
[5] J. J. Bozell and G. R. Petersen, Green Chem, 12, 525 (2010).
[6] H. M. Poggi-Varaldo, K. M. Munoz-Paez, C. Escamilla-Alvarado, P. N. Robledo-Narváez, M. T. Ponce-Noyola, G. Calva-Calva, E. Ríos-Leal, J. Galíndez-Mayer, C. Estrada-Vázquez, A. Ortega-Clemente, and N. F. Rinderknecht-Seijas, Waste Manage Res, 32, 353 (2014).
[7] I. K. Kapdan and F. Kargi, Enzyme and Microbiol Technol 38, 569 (2006).
[8] S. Chen, K. Lee, Y. Lo, W. Chen, J. Wu, and C. Lin, Int J Hydrogen Energy, 33:, 1803 (2008).
[9] L. R. Lynd, P. J. Weimer, W. H. van Zyl, and I. S. Pretorius, Microbiol Mol Biol Rev, 66, 506 (2002).
[10] R. Navia and A. K. Mohanty, Waste Manage Res, 30, 215 (2012).
[11] A. K. Chandel, G. Chandrasekhar, M. Borges-Silva, and S. S. da Silva, Crit Rev Biotechnol, 32, 187 (2012).
[12] Y.-C. Lo, S.-D. Chen, C.-Y. Chen, T.-I. Huang, C.-Y. Lin, and J.-S. Chang, 33, 5224 (2008).
[13] N. Ren, G. Cao, A. Wang, D.-j. Lee, W. Guo, and Y. Zhu, Molecular Biology and Evolution, 33, 6124 (2008).
[14] C. Escamilla-Alvarado, H. M. Poggi-Varaldo, and M. T. Ponce-Noyola, Waste Manage Res, 31, 849 (2013).
[15] C. Escamilla-Alvarado, M. T. Ponce-Noyola, E. Ríos-Leal, J. García-Mena, N. Rinderknecht-Seijas, and H. M. Poggi-Varaldo, Int J Hydrogen Energy, Accepted for publication, (2014).
[16] G. L. Miller, Anal Chem, 31, 426 (1959).
[17] M. Mandels, L. Hontz, and J. Nystrom, Biotechnol Bioeng 16, 1471 (1974).
[18] A. Singh, P. K. R. Kumar, and K. Schügerl, J Biotechnol, 18, 205 (1991).
[19] W. Parawira and M. Tekere, Crit Rev Biotechnol, 31, 20 (2011).
[20] M. Ballesteros, F. Sáez, I. Ballesteros, P. Manzanares, M. J. Negro, J. M. Martínez, R. Castañeda, and J. M. O. Dominguez, Appl Biochem Biotechnol, 161, 423 (2010).
[21] M. Clanet, H. Durand, and G. Tiraby, Biotechnol Bioeng, 32, 930 (1988).
[22] A. Li, B. Antizar-Ladislao, and M. Khraisheh, Bioprocess and Biosystems Engineering, 30, 189 (2007).
[23] A. I. Vavouraki, E. M. Angelis, and M. Kornaros, Waste Manage, 33, 740 (2013).
[24] Q. A. Nguyen, F. A. Keller, M. P. Tucker, C. K. Lombard, B. M. Jenkins, D. E. Yomogida, and V. M. Tiangco, Appl Biochem Biotechnol, 77-79, 455 (1999).
[25] U. Kaur, H. S. Oberoi, V. K. Bhargav, R. Sharma-Shivappa, and S. S. Dhaliwal, Industrial Crops and Products, 37, 219 (2012).
[26] C. M. Hogan and M. Mes-Hartree, J Ind Microbiol, 6, 253 (1990).
[27] S. J. B. Duff and W. D. Murray, Bioresour Technol, 55, 1 (1996).

Notation

GX	glucose plus xylose concentration
H-M-Z	three-stages biorefinery model for the production of hydrogen, methane and holocellulases.
FPU	filter paper unit
FS	fermented solids
IU	international enzyme activity unit
MSW	municipal solid waste
NmL	volume in millilitres, normalised at 273 K and 101.325 kPa

OFMSW	organic fraction of municipal solid waste
TS	total solids
VS	volatile solids
X/G	xylose to glucose ratio
Ys	saccharification yield

Greek characters

η_s	saccharification efficiency

Subindices

db	dry basis
h	holocellulose basis

The effect of physicochemical Pretreatment of Supported Pt Nanoparticles for the ORR. A Novel Carbon from Natural Source.

J.L. Reyes-Rodríguez[1], K. Sathish-Kumar[2], O. Solorza-Feria[1,*]

[1] Departamento de Química, Centro de Investigación y Estudios Avanzados del IPN, Av. IPN 2508, Col. San Pedro Zacatenco, A. Postal 14-740, 07360 México D.F., México.
[*] Tel: 011 +52 +55 5747-3715 ; osolorza@cinvestav.mx

[2] Academia de Ingeniería en Energía, Universidad Politécnica de Aguascalientes, Calle Paseo San Gerardo No. 207, Fracc. San Gerardo, C.P. 20342 Aguascalientes, Aguascalientes, México.

ABSTRACT

Materials used as nanoparticles supports play an important role in the performance, efficiency and stability of catalysts applied in polymer fuel cells. Carbon supports have been employed for their excellent properties like good electronic conduction, high surface area, relative crystallinity and resistance to acids and alkalis moderate. The surface modification of carbon by physical-chemical treatment (functionalization) has a favorable effect on the performance and stability of the catalyst to improve the metal-support interaction through anchoring sites which in turn favor the distribution of the metal particles on the carbon matrix. The shape and particle size are influenced by the properties of the support and these characteristics are directly related (together with the diffusion of gases and ionomer interaction conductor) with the catalytic activity towards the reactions of interest. Pre-treated Carbon Vulcan with nitric acid is the most used support for nanoparticles in polymer fuel cell. However its origin derived from the combustion of waste oil (non-renewable energy source) makes it unattractive for future applications by issues of environmental pollution, furthermore the sulfur content and other impurities can degrade and decrease the lifetime of the metal catalysts. In this study we present the research for a new type of carbon obtained by a simple process from natural sources. This carbon was treated by different physicochemical methods and then Pt nanoparticles were synthesized and supported by chemical reduction with $NaBH_4$ on the different pre-treated carbons. This work plan is performed with the main target to evaluate the potential use of natural carbon as a novel support material and to analyze the effect of different treatments on the catalytic activity of nanoparticles towards the ORR. The study is complemented by physical characterization techniques like XRD, FTIR, Raman, SEM, EDAX, HRTEM and electrochemical techniques by RDE in acid medium. All the results are compared with Pt/Vulcan Carbon XC-72R pre-treated.

Keywords: Novel natural carbon; Oxygen reduction reaction; Physicochemical pretreatment to carbon.

1. Introduction

Catalytic processes play an important role in the development of new chemicals, many of them of great value added worldwide. Catalysis involves accelerating the reaction rate and favor selectivity of the chemical reactions of interest. [1] In our particular case, the oxygen reduction reaction (ORR) is of

relevant importance in the performance of a proton exchange membrane fuel cell (PEMFC) because the cathodic region (place wherein said reaction is carried out) limiting the efficiency of system given that the kinetics reaction is very slow compared to the hydrogen oxidation reaction at the anodic region [2]. Platinum is, until today, the best catalyst to the ORR. To increase its catalytic activity is necessary to form Pt nanoparticles on the order of 2 to 3 nm. With decreasing size of the nanoparticles is achieved to increase the number of active sites on which the reaction is carried out, this results in an increase of the Platinum Electrochemical Surface Area (ECSA) and improved the catalytic activity [3,4]. Generally nanoparticles are dispersed on a conductive support material of high surface area such as carbonaceous matrices [5]. Supports have the aim to be a matrix which promotes a good homogeneous distribution by reducing the effects of agglomeration of the metal particles (this results in an improvement of the catalytic activity), also have a great influence on the stability of the catalyst itself and allow to reduce costs by not using full loads of catalytic metal [5]. The materials used as supports have highly porosity and they must have preferably the following characteristics [1]:

- High surface area to promote a good dispersion of the catalyst.
- Suitable size and distribution of pores for the successful diffusion of the reactant gases and byproducts.
- Good electrical conductivity to transfer electrons between the electrodes.
- Chemical and electrochemical corrosion stability.
- Suitable surface chemistry (functionalization) to facilitate the interaction with the catalytic material during the synthesis process.
- Hydrophilicity (affinity to water).
- Low level of surface impurities.
- Ease recovery of catalytic metal at the end of their life cycle.
- Abundant and affordable.

In this sense many materials have been investigated in order to obtain a better support for metal catalysts. Some like graphite and the significant improvement of its activity by chemical treatments for use in microbial fuel cells [6]; metal oxide nanowires as WO_3 (tungsten trioxide) which has had a significant interest in recent years as supported of Pt nanoparticles showing a higher catalytic activity than Pt/C and excellent tolerance to CO [7]; carbon nanotubes used as a 3D structural network which confers high stability and high catalytic properties of materials [8,9]; graphene sheets whose high number of edges and small pores allows to the formation of the catalyst active sites [10]; mesoporous carbons, aerogels and xerogels whose pore sizes ranging between 2 and 50 nm [8,11-13] give a greater surface area as Ketjen Black EC 300J carbon with 829 m^2 g [14]; among other materials supports.

Among all the supports mentioned above, Vulcan Carbon XC-72R is the most widely material used as catalyst supports for PEM fuel cell applications [8,11]. It is obtained from the pyrolysis of hydrocarbons from the oil fractionation and natural gas sources that are fed to a furnace at 1400 °C with flowing air. This process maintains a low ash content of about 1% by weight [8]. Vulcan carbon has 254 m^2g^{-1} of surface area and maintains a certain degree of crystallinity and good electronic conductivity; however belongs to the category of microporous carbon because their pores are below 2 nm in diameter in spite of maintaining a mean particle size of 30 nm; this is a disadvantage because the pores are too small to accommodate Pt nanoparticles with similar sizes (2-3 nm) and therefore metal particles reside primarily on the carbon surface making them prone to agglomeration effects or detachment of the support [11]. Nevertheless Vulcan Carbon XC-72R continues to hold as the ideal support and his substitute has not been discovered yet, thus opening a wide research around the world whose objective is the search for new materials that

allow replace it, and as far as possible implement process more friendly with environmental to carbon generation such as obtaining carbon from natural sources [15,16].

When carbon is used as nanocatalyst support without performing a surface modification does not have binding sites suitable for anchoring the metal ion precursors or the metal nanoparticle directly during the synthesis process [5]; which leads to a low dispersion of nanoparticles and a high probability of agglomeration which has a direct negative effect on the catalytic activity, especially working in conditions where it has a high metal loading and even when working with magnetic metals. To avoid such problems is carried out a process known as functionalization or modification of the carbon surface conducted through chemical agents or heat treatments. Derbyshire et al. [17] found that the surface chemistry of carbon associated with the surface functional groups which are formed during chemical pre-treatments given to the carbon plays an important role in the distribution of metal catalysts, and consequently there is an improvement in its catalytic properties. Many functional groups can be incorporated into carbon and which are based on elements such as oxygen, nitrogen, hydrogen, carbon, sulfur, phosphorus and some halogens [18], the most investigated are those groups containing C-O. It is difficult to establish the precise nature of surface oxygen groups on the carbonaceous material; however, the most common types of such groups are carboxylic, phenolic, lactones, ethers, quinones, carbonyl, anhydrides and others groups which are the result of oxidative processes given to carbon mainly with HNO_3, H_2SO_4, KOH, H_2O_2 or with O_2 and O_3 in gas phase [8, 18 - 20]. The presence of such groups reduces the hydrophobic character of the carbon material, thereby making the surface more accessible to the metal precursors during the impregnation process with aqueous solutions and serve as anchoring sites for fixing metal nanoparticles and preventing agglomeration during the reduction process [1, 8, 19, 20].

The objective of this study is primarily focused on presenting a new type of carbon obtained from natural sources such as camphor by a simple process (which is patent pending). Secondly it is desired to elucidate the effect of the functionalization treatment given to the new carbon support on the catalytic activity of Pt nanoparticles toward the oxygen reduction reaction. This materials was both physically evaluated by HRTEM, SEM, XRD, Raman spectroscopy and FTIR and electrochemically by Rotating Disk Electrode (EDR) techniques.

2. Experimental

2.1 Preparation of a new carbon from natural source

The new type of carbon was obtained from a natural source such as the camphor (Camphor Carbon = CC) by a simple procedure which we cannot give specifics details because the methodology is patent pending. Amounts of 160 mg from powder carbon obtained (CC) were subjected to different methods: 1) Camphor carbon without any treatment (CC). 2) Thermal treatment under inert conditions at 400 ° C for four hours (CC-TT). 3) Chemical treatment with 160 ml of 1M HNO_3 under reflux conditions for four hours with magnetic stirring (CC-HNO_3). 4) Chemical treatment with 160 ml of 0.5M KOH under reflux conditions for four hours with magnetic stirring (CC-KOH). In methods 2 and 3 it was observed that the initial carbon without functionalization had hydrophobic characteristics and precipitates after a few minutes. However, with the heating and the first drops of refluxing, a more homogeneous mixture was observed, this is evidence of a more hydrophilic carbon. Once reflux time finish, carbons were filtered and

washed under vacuum conditions with deionized water until the filtrate had a pH near neutrality. The final product was dried in a furnace at 120 °C for 2 hours under N_2.

2.2 Preparation Vulcan Carbon XC-72R for comparison

Vulcan Carbon XC-72R (Cabot) was used in order to compare the properties of new carbon. Vulcan Carbon was subjected to chemical treatment following a modified procedure reported by Senthil-Kumar et al. [20]. Vulcan Carbon powder (2 g) was dispersed in 500 ml of 5% v/v HNO_3. The mixture was brought to reflux conditions and magnetic stirring at 120 °C for 16 hours. The material was recovered by vacuum filtration and washed with deionized water until the filtrate reached a pH near neutrality. The final product was dried in a furnace at 120 °C for two hours under N_2. This material was identified simply as Vulcan.

2.3 Preparation of Platinum nanoparticles catalysts supported on carbon

Supported catalysts of platinum nanoparticles were prepared with reference to the method reported by Zeng et al. [21] which was modified and adapted to our laboratory conditions. In a typical procedure: In a 250 ml three necked flask 48 mg of any of the previously treated carbons were dispersed in 50 ml of deionized water. Subsequently 91 mg of Sodium Citrate Di-hydrate and 31 mg of K_2PtCl_6 (Citrate:K_2PtCl_6 = 5:1) were dissolved in 20 ml of deionized water and then were added to the first mixture. The mixture was dispersed under ultrasonic bath for 15 minutes and then was kept under magnetic stirring for two hours under N_2 flow to deoxygenate the solution. The mixture was heated by oil bath while maintaining the inert atmosphere and upon reaching 80 °C an excess reducing solution (14 mg of $NaBH_4$/5 ml of deionized water) was added via syringe. The mixture was maintained at reflux for one hour. The final product was recovered by centrifugation and several washes were performed with water-acetone mixture. Finally the material was dried in a furnace at 120 °C for 2 hours under N_2. The yields in all cases were above 95%. Thus, five carbon supported catalysts with metal loading estimated at 20% weight were obtained with the following identifications: Pt/Vulcan, Pt/CC, Pt/CC-TT, Pt/CC-HNO_3 and Pt/CC-KOH.

2.4 Physical characterization

2.4.1 UV-Vis spectroscopy

With the purpose to observe the reduction reaction evolution of $[PtCl_6]^{2-}$ species, a UV-Vis spectra was obtained from a control synthesis which not contained carbon. The experiment was carried out on a Perkin-Elmer Lambda 12 UV-Vis spectrometer. Aliquots from the solution were extracted at different times and rapidly they measured to obtain their UV-Vis spectra.

2.4.2 Fourier Transform Infrared and Raman Spectroscopy

Raman spectra were recorded for all the carbon supports on a HORIBA Jobin Yvon LabRAM HR800 confocal microscope Raman spectrometer used a red laser with an excitation wavelength λ=632.81 nm to characterize the degree of graphitization of the carbon support materials. FT-IR was performed with a IR2 module FTIR spectrometer coupled to the confocal microscope Raman using an attenuated total reflection (ATR) accessory.

2.4.3 X-Ray Diffraction

Powder X-Ray Diffraction (XRD) analyses were carried out on a Rigaku Miniflex 600 diffractometer using a Cu Kα: λ=1.5406 Å radiation operated at 40 kV and 15 mA. Scans were measured in the range of 15-90° with a scan speed of 3 degrees/min and step width of 0.0100 deg. XRD patterns of all carbon supports and Pt catalyst supports were recorded.

2.4.4 Scanning Electron Microscopy

Scanning Electron Micrographs for all materials were obtained from a Zeiss HRSEM Auriga 3916 microscope equipped with a Schottky field emission GENIMI column working at 2 keV to examine the particle morphology. Elemental composition and mapping of the catalyst were measured by an Energy Dispersive X-Ray (EDX) detector attached to the microscope.

2.4.5 High Resolution Transmission Electron Microscopy

High Resolution Transmission Electron Micrographs for Pt supported catalyst were obtained from a Jeol JEM-ARM 200F microscope equipped with a Schottky field emission gun working at 200 keV to examine the particle morphology and the size distribution.

2.5 Electrochemical characterization

Electrochemical measures were carried out using a PARSTAT 2273 potenciostat/galvanostat coupled with a Rotating Disk Electrode system and using a three-electrode electrochemical cell. A Pt catalyst ink for each materials was prepared taking as reference the methodology reported by Garsany et al. [22] using a mixture of 2-Butanol, 2-Propanol and 5%w Nafion as dispersant media. 10 µl of the catalyst ink were deposited on the surface of a glassy carbon electrode, using as working electrode, with a geometric area of 0.196 cm^2 previously polished, rinsed and boiled with deionized water and dried in oven. The thin catalyst film formed had a Pt loading of 22.96 $\mu g/cm^2$. A fresh Hydrogen bubble electrode was used as reference electrode and a Pt mesh as counter electrode. 0.1M $HClO_4$ solution was employed as electrolyte. Firstly Cyclic Voltammetry was performed to activate the materials on a potential window of 0.05-1.2 V with a scan rate of 100 mV/s under a bubbling of N_2 flow. CO-stripping technique was performed on a potential windows of 0.05-1.2V with a scan rate of 20 mV/s with the purpose to determine the electrochemical surface area (ECSA). ORR sweep profiles were performed using the rotating electrode mode at 400, 900, 1600 and 2500 rpm under bubbling of O_2 flow. For this last measure, the potential window was 0.05-1.0V with a scan rate of 20 mV/s. A background profile was measure at the same conditions of the potential window for ORR measurement, but without electrode rotation and under N_2 flow. This was made with the purpose of subtract the background to the experimental ORR current and to eliminate any contribution of capacitive current [22]. The electrochemical characterization allows to determine the catalytic properties of the materials toward the oxygen reduction reaction.

3. Results and discussion

It knows experimentally that Sodium Citrate reduces the $[PtCl_6]^{2-}$ species to Pt metallic (see eq. 1, 2) at elevated temperature [21], however with the purpose of accelerate the reaction it was added $NaBH_4$ as reducing agent. With this methodology the reduction process occurs very fast. Fig. 1 shows the UV-Vis spectra, with time dependence, for the absorption of the aqueous $[PtCl_6]^{2-}$ species (Carbon free-contained) before and after to add the reducing solution. During the process it was evident the decrease of the

absorption band of the $[PtCl_6]^{2-}$ species at 264 nm, after 120 s the band practically disappears, this is result of the decrease of the precursor concentration to form Pt nanoparticles. Experimentally it observed a change of colour from pale yellow to a dark brown solution. The UV-Vis results are consistent with the found in the literature [23-25].

$$[PtCl_6]^{2-} + 2e^- \longrightarrow [PtCl_4]^{2-} + 2Cl^- \quad (1)$$

$$[PtCl_4]^{2-} + 2e^- \longrightarrow Pt^0 + 4Cl^- \quad (2)$$

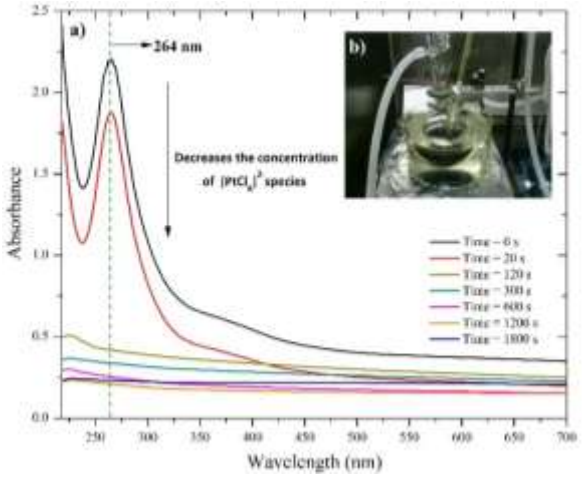

Fig. 1. a) Time dependent UV-Vis spectra for the reduction of $[PtCl_6]^{2-}$ species. b) Final dark brown colour obtained after one hour of reflux.

Raman spectroscopy is a powerful tool extensively used to distinguish the degree of ordering and disordering of carbonaceous materials [26]. Fig. 2a show the Raman spectra for all the carbon supports. The characteristic G band is appear at 1596 cm^{-1} and it is associated to all graphitic sp^2 carbon forms. Meanwhile the D band around at 1336 cm^{-1} is associated to the sp^3 hybridization of carbon atoms which indicates defects and disorder on a lightly graphitized material [27, 28]. The I_D/I_G (intensities) ratio is a qualitative measure of the disorder degree and number of the sp^2 domains [26]. In our case it appreciates that all the materials presents an amorphous behaviour because the 2D band practically is absent and the D and G bands are wide. Fig. 2a contains the values of the I_D/I_G ratio. Vulcan carbon has the higher value and is observed as the D band is higher than the G band, this suggests a possible dominance of a weak crystalline phase within the same amorphous carbon. It is necessary to take in count that this type of carbons in study belong to a class of materials called Carbon Blacks and they have a different form respect to diamond, graphite, charcoal, coke, among others. Carbon Blacks have a spherical or ellipsoidal form (which is possible see with HRSEM) and in their microstructure present both crystalline and amorphous substructures similar to a graphite layer with oriented planes [5]. For CC material the I_D/I_G ratio decreases compared with Vulcan carbon, this suggests the dominance of a more amorphous phase in this type of carbon. The subsequent treatments given to the CC slightly decrease the value but no results are relevant

for purposes of establishing a trend. In general, it can be suggested that the Vulcan carbon maintains a higher density of functionalized surface as evidenced by an increase in a high degree of defects in graphitic layers of the material compared to camphor carbons as suggested by changes in relationships I_D/I_G [27].

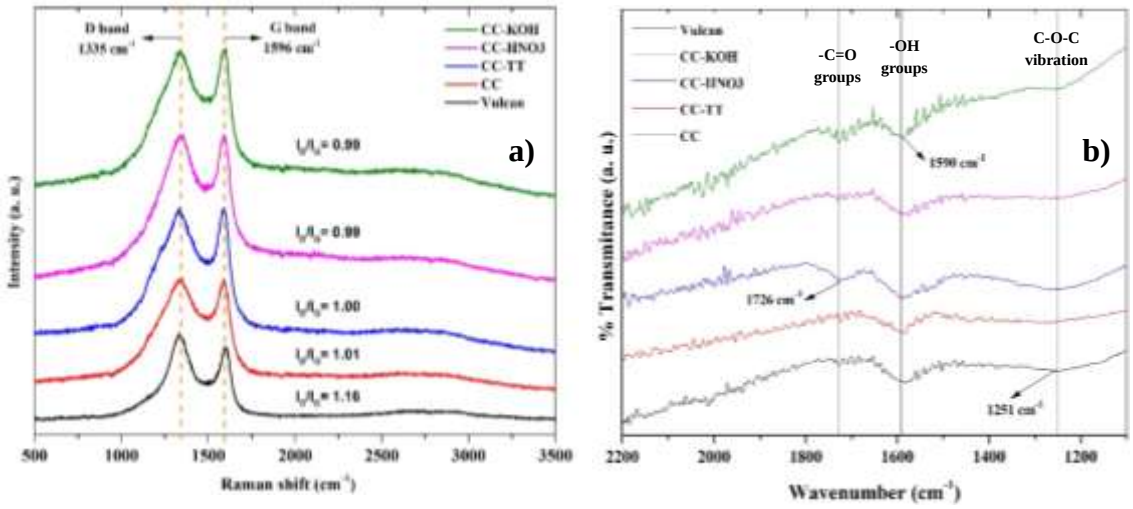

Fig. 2. a) Raman spectra and b) FT-IR spectra for carbon supports.

FT-IR spectra for carbon supports are showed in Fig. 2b. Three small characteristic bands were found in accordance to the literature [27, 29, 30]. The band at ~1726 cm^{-1} found slightly more pronounced for Vulcan and CC-HNO3 and less pronounced for CC, and CC-KOH is associated to stretching mode of carbonyl groups. These groups were included on the surface of material after to the oxidative treatments with nitric acid given to Vulcan and CC-HNO3 carbons in accordance to the literature [8, 17, 27]. CC-TT material does not present this band possibly because the thermal treatment at 400°C eliminates this functional groups at this temperature interval. The wide band at ~1590 cm^{-1} is assigned to bending vibration of the O–H group, evidence of the incorporation of -OH and -COOH groups which make more hydrophilic to the carbon. While CC material has this band originally, a slight increase in intensity after oxidative treatments is observed. This does not happen with the CC-TT in which the intensity decreases; so this is consistent with what previously said for the band at ~1726 cm^{-1} due to the thermal treatment. The last less intense and wide band at ~1251 cm^{-1} pronounced for all the materials, except CC-TT, can be assigned to the C–O–C vibration in ethers groups [27, 29, 30].

The X-Ray powder diffraction patterns for carbon supports and Pt/C are show in Fig. 3a and 3b respectively. For all the carbon supports (Fig. 3a) is evident a similar pattern which corresponds to an amorphous carbon with two diffraction maxima well defined according to the literature [28, 29], one broad (002) peak around at 24.47° and other less intense around at 43.33° which corresponds with the (100) reflection. It possible to appreciate a third peak around 80°, however this is much less intense and has not been found reported in the literature. If it takes the (002) diffraction maximum as comparative

reference for all carbons it is evident that CC-TT presents the most broad peak, which suggest a smaller crystallite size. When carbon are submitted to an oxidative chemical treatment it is possible that the microstructures may collapse and form a more amorphous carbon. Sharper (002) diffraction maximum around 26.38° corresponds to graphite phase, a shift of the (002) reflection to lower values below 26° is evidence, how occurs in our case, of the presence of an amorphous carbon [28].

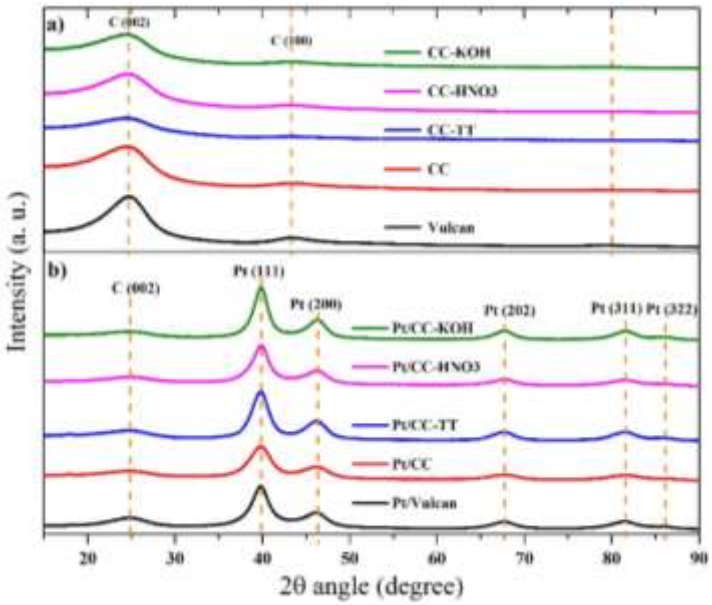

Fig 3. XRD patterns. a) Carbon supports. b) Pt/C catalysts.

Figure 3b shows the X-Ray powder diffraction maxima for Pt supported nanocatalyst. All patterns show clearly the characteristics reflections: (111) around at 40°, (200) around at 46°, (202) around at 67°, (311) around at 81° and (322) around at 85° correspond to a fcc lattice for pure bulk Pt metal [20]. Platinum crystallite size was calculated for (111) reflection using the Debye-Scherrer equation (eq. 3):

$$d = \frac{0.9\ \lambda_{k\alpha 1}}{B_{2\theta}\ cos\theta_{max}} \qquad (3)$$

where $\lambda_{k\alpha 1}$ is the wavelength of X-ray (1.5406 Å), $B_{2\theta}$ is the width half height (in rad) of the peak, and θ_{max} is the angle at the peak maximum [20, 28, 31]. Table 1 show the crystallite size for Pt/C catalysts, note that it exists a dependence of the Pt crystallite size respect the nature of each treated carbon. Pt-CC has the smaller crystallite size (2.9 nm) and all the treated carbons conducive an increase in the crystallite size. The chemical compositions were similar for all materials in accordance with theoretical expectations.

Scanning electron micrographs for Vulcan and CC supports are showed in Fig. 4a and 4b respectively. The morphology found for camphor carbon corresponds to particles like spheres and irregular ellipses

with an average size of 54 nm as shown in Table 2. Similar morphology was observed for Vulcan carbon with particle size of 53 nm, but there is a larger number of defects and smaller particles, possibly due to chemical attack with HNO_3. This feature was also seen in the CC-HNO3 material (micrograph not shown); however the damage is less compared with Vulcan. This might suggest that camphor carbon is more resistant to oxidative acid media; however keep in mind that the treatment given to Vulcan carbon was almost similar in concentration of HNO_3 but lasted four times higher (16 hours) compared with the treatment given to camphor carbon. Future studies BET surface area could clarify what hitherto found. The thermal treatment appear not to affect the morphology of carbon as is evidenced in the micrographs obtained (not shown); however the particle size decreased to 47 nm. Alkaline treatment apparently produces better rounded particles and increases the particle size (~60 nm).

Table 1. Properties for Pt/C catalysts obtained by XRD, EDAX-SEM and HRTEM.

Material	XRD crystallite size Pt(111) (nm)	XRD Semiquantitative Analysis		EDAX-SEM Quantitative Analysis		HRTEM Pt Particle size (nm)
		%C	%Pt	C (wt. %)	Pt (wt. %)	
Pt/Vulcan	3.5	80.0	20.0	83.5	16.6	2.51
Pt/CC	2.9	82.1	17.9	83.8	16.2	3.45
Pt/CC-TT	3.7	77.3	22.7	85.0	15.0	3.88
Pt/CC-HNO3	3.8	76.2	23.8	86.9	13.0	2.74
Pt/CC-KOH	4.4	78.5	21.5	88.9	10.9	3.58

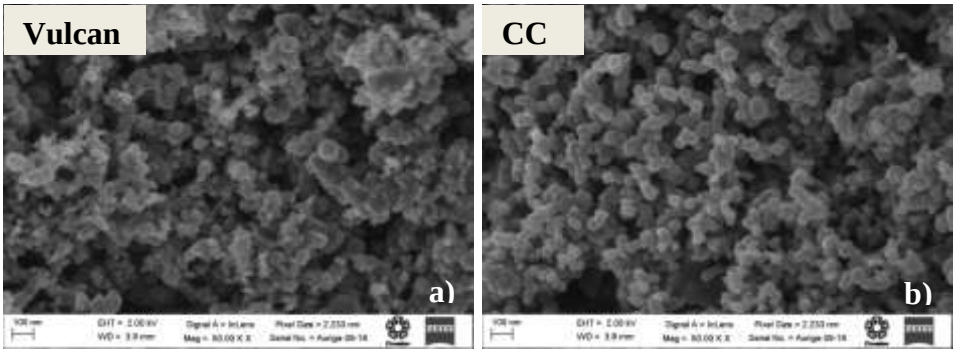

Fig. 4. SEM micrographs for: a) Vulcan carbon and b) Camphor carbon (CC).

Chemical composition for carbon supports are shown in Table 2. It can be seen that carbon with higher oxygen content is the CC-HNO3 suggesting that oxidative treatment in effect incorporates new surface atoms and that the thermal and alkali treatment reduces the oxygen present. A prominent feature is that the camphor carbon do not contain sulphur.

The particle size of the catalysts of Pt supported was determined from the particle count of the HRTEM micrographs (Fig. 5a-d) as shown in Table 1. Is clearly observed that the treatment given to each carbon support influences in the Pt particle size. HNO_3 treatment allows a smaller particle size and thus a higher

surface area which have a positive effect on the catalytic activity for Pt/Vulcan. However the treatment with HNO3 and KOH given to camphor carbon promotes agglomeration of particles of Pt, which is detrimental to the catalytic activity towards ORR and could explain the reduction of the elemental composition of Pt observed by EDAX (Table 1).

Table 2. Particle size and chemical composition for carbon supports.

Material	SEM Carbon particle size (nm)	C (atom %)	O (atom %)	N (atom %)	S (atom %)
Vulcan	53.0	94.58	2.71	2.57	0.14
CC	54.2	93.74	3.72	2.54	0 .0
CC-TT	44.7	94.60	3.34	2.06	0.0
CC-HNO3	65.3	90.64	6.84	2.50	0.0
CC-KOH	59.6	94.65	3.10	2.25	0.0

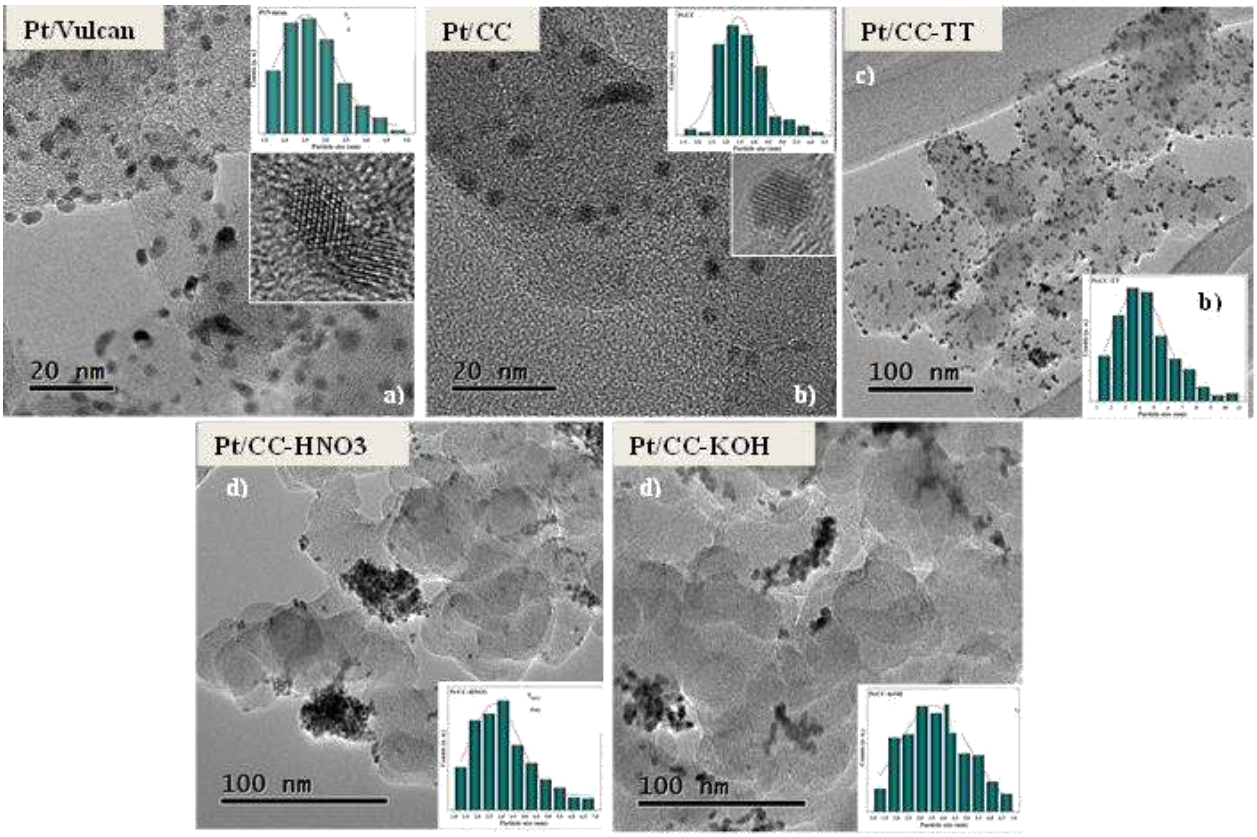

Fig. 5. HRTEM micrograph with size distribution for Pt/C catalysts.

Fig. 6 shows the cyclic voltammetries for the Pt/C catalysts. It has essentially the characteristic response for Pt nanoparticle where the capacitance region is more pronounced for the Pt /Vulcan and Pt/CC-HNO3

materials, which were treated with nitric acid. This feature suggests the presence of impurities in form of surface functional groups on the carbon which carried out oxidation-reduction process as a typical response of the quinone-hydroquinone equilibrium [32]. It is relevant to note that the Pt/CC-HNO3 material exhibits a marked widening of voltammetric profile suggesting particle agglomeration problems which is indicated by HRTEM. Fig. 7a shows reduction curves for Pt/C catalysts with Tafel slopes corrected for mass transport (Fig. 7b). It is clear that materials with enhanced catalytic activity toward the ORR are in decreasing order: Pt/CC-KOH > Pt/CC-TT > Pt/CC > Pt/Vulcan > Pt/CC-HNO3. This paradoxical behavior again is attributed to negative agglomeration effects seen in the micrographs despite having smaller Pt particles and contradicts the theory that a properly functionalized carbon promotes a better distribution of the metal nanoparticles on the surface. A better distribution leads to a more efficient use of the catalytic surface of the particles and if these are smaller, the material will have a greater active surface toward the ORR. In our study materials the best distribution was obtained for the Pt / CC-TT material even with the largest particle size obtained by HRTEM. Finally, Table 3 shows the numerical values for the specific activity and mass activity.

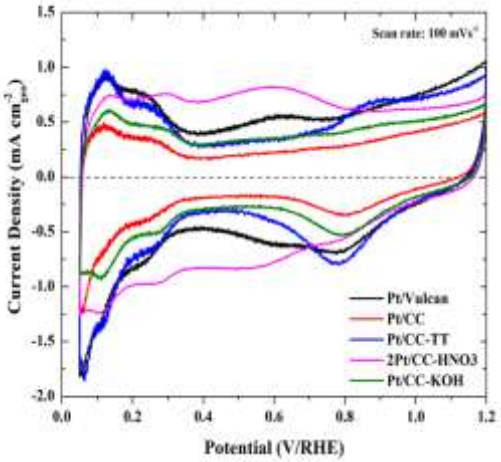

Fig. 6. Cyclic voltammetries for Pt/C catalysts

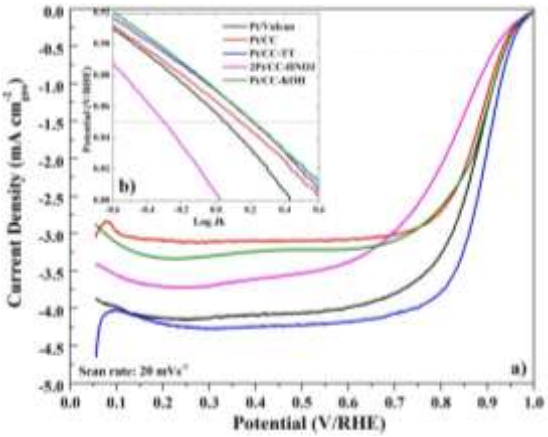

Fig. 7. a) ORR polarization curves. b) Tafel's slopes for Pt/C catalysts.

Table 3. Catalytic properties for Pt/C catalysts.

Material	Specify Activity ($\mu A/cm^2_{Pt}$) @ 0.85 V	Mass Activity (mA/mg_{Pt}) @ 0.85 V	ECSA (m^2/g)	Tafel Slope ($mV\ dec^{-1}$)	BC_u [$mA\ cm^{-2}\ rpm^{1/2}$]
Pt/Vulcan	1290 ± 59	423 ± 21	26	97	0.1130
Pt/CC	1346 ± 62	315 ± 11	19	97	0.0831
Pt/CC-TT	1448 ± 95	465 ± 43	32	98	0.1097
Pt/CC-HNO3	883 ± 23	149 ± 9	17	136	0.1077
Pt/CC-KOH	1537 ± 129	303 ± 17	17	108	0.0823

4. Summary and perspectives

A new kind of carbon obtained from natural sources such as camphor can be used as support for nanoparticles catalysts toward the oxygen reduction reaction. The appropriate functionalization of the carbon surface has a significant effect on catalyst performance, and formation of metal nanoparticles. Oxidative treatments with acid chemical agents seem to promote agglomeration of particles with a considerable negative effect on catalytic activity. For this new type of carbon apparently it is enough just to carry out a thermal treatment to achieve satisfactory results.

Acknowledgements

We gratefully acknowledge to Luis Moreno M.Sc., Jose Andraca Ph.D., Josue Romero M.Sc. and Alvaro Angeles M.Sc. for their invaluable assistance in the obtaining of FT-IR/Raman, XRD, SEM-EDAX and HRTEM measurements.

The authors acknowledge the support of the National Council of Science and Technology, Conacyt (grant FOINS 75/2012) and the University of Texas TAMU (TAMU-Conacyt Alloy nanocatalysts for fuel cell electrodes project).

References

[1] F. Rodríguez-Fragoso, Carbon, 36, 159-175 (1998).
[2] K.J.J. Mayrhofer, D. Strmcnik, B.B. Blizanac, V. Stamenkovic, M. Arenz, N.M. Markovic, Electrochimica Acta, 53, 3181–3188 (2008).
[3] K. Kinoshita, Journal of Electrochemical Society, 137, 845-848 (1990).
[4] M.L. Sattler, P.N. Ross, Ultramicroscopy, 20, 21-28 (1986).
[5] Mei-xian Wang, Fan Xu, Qi Liu, Hong-fang Sun, Rui-hua Cheng, Hao He, Eric A. Stach, Jian Xie, Carbon, 49, 256-265 (2011).
[6] B. Erable, N. Duteanua, S.M. Senthil Kumar, Y. Feng, M. M. Ghangrekar, K. Scott, Electrochemistry Communications , 11, 1547–1549 (2009).
[7] M.S. Saha, Y. Zhang, M. Cai, X. Sun, International Journal of Hydrogen Energy, 37, 4633 - 4638 (2012).
[8] E. Antolini, Applied Catalysis B: Environmental, 88, 1-24 (2009).
[9] D.Z. Mezalira, M. Bron, Journal of Power Sources, 231, 113-121 (2013).
[10] C. Arbizzani, S. Righi, F. Soavi, M. Mastragostino, International Journal of Hydrogen Energy, 36, 5036 - 5046 (2011).
[11] D. Banham, F. Feng, T. Fürstenhaupt, K. Pei, S. Ye, V. Birss, Journal of Power Sources, 196, 5438–5445 (2011).
[12] S. Shrestha, S. Asheghi, J. Timbro, W. E. Mustain, Carbon, 60, 28-40 (2013).

[13] C. Alegre, M.E. Gálvez, E. Baquedano, E. Pastor, R. Moliner, M.J. Lázaro, International Journal of Hydrogen Energy, 37, 7180-7191 (2012).
[14] G. Wang, G. Sun, Q. Wang, S. Wang, J. Guo, Y. Gao, Q. Xin, Journal of Power Sources, 180, 176–180 (2008).
[15] K. Mukhopadhay, M. Sharon, Materials Chemistry and Physics, 49, 105-109 (1997).
[16] M. Kumar, Y. Ando, Journal of Physics: Conference Series, 61, 643-646 (2007).
[17] F.J. Derbyshire, V.H.J. de Beer, G.M.K. Abotsi, A.W. Scaroni, J.M. Solar, D.J. Skrovanek, Applied. Catalysis, 27, 117 (1986).
[18] D.S. Cameron, S.J. Cooper, I.L. Dodgson, B. Harrison, J.W. Jenkins, Catal. Today, 7, 113 (1990).
[19] P. Serp, J.L. Figueiredo, Carbon materials for catalysis, John Wiley & Sons Inc., p. 47-51, USA, (2009).
[20] S.M. Senthil Kumar, N. Hidyatai, J. Soler Herrero, S. Irusta, K. Scott, International Journal of Hydrogen Energy, 36, 5453 - 5465 (2011).
[21] J. Zeng, J. Yang Lee, W. Zhou, Applied Catalysis A: General, 308 99–104, (2006).
[22] Y. Garsany, O.A. Baturina, K.E. Swider-Lyons, S.S. Kocha, Analytical Chemistry, 82, 6321-6328 (2010).
[23] R.A. Caruso, M. Ashokkumar, F. Grieser, Colloids and Surfaces A: Physicochemical and Engineering Aspects, 169, 219-225 (2000).
[24] Z. Tang, D. Geng, G. Lu, Materials Letters, 59, 1567-1570 (2005).
[25] M. Luty-Błocho, M. Wojnicki, K. Pacławski, K. Fitzner, Chemical Engineering Journal, 226, 46-51 (2013).
[26] P. Shi, R. Su, S. Zhu, M. Zhu, D. Li, S. Xu, Journal of Hazardous Materials, 229-230, 331-339 (2012).
[27] P. Dubey, K. M. Tripathib, S. K. Sonkar, RSC Advances, 4, 5838 (2014).
[28] H. Liu, J. Li, X. Xu, F. Wang, J. Liu, Z. Li, Jing Ji, State, Electrochimica Acta, 93, 25-31 (2013).
[29] J.R.C. Salgado, R.G. Duarte, L.M. Ilharco, A.M. Botelho do Rego, A.M. Ferraria, M.G.S. Ferreira, Applied Catalysis B: Environmental, 102, 496-504 (2011).
[30] S. Hu, J. Hou, L. Xiong, K. Weng, T. Yang, Y. Luo, Separation and Purification Technology, 77, 214-219 (2011).
[31] W. Chen, Q. Xin, G. Sun, Q. Wang, Q. Mao, H Su, Journal of Power Sources, 180, 199-204 (2008).
[32] O. Martinez-Alvarez, M. Miranda-Hernandez, Carbon-Science and Technology, 1, 30-38, 2008.

Evaluation of Biohydrogen Production from Cheese whey and Assessment of the Associated Microbial Community

K. M. Muñoz- Páez [1], H. M. Poggi-Varaldo[1]*, J. García-Mena [2], Selva Sankar[3]; Alberto Piña-Escobedo [2]

[1]Environmental Biotechnology and Renewable Energies R&D Group, Dept. Biotechnology and Bioengineering. CINVESTAV-IPN. P.O. Box 14-740, México D.F.

[2] Dept. Genetic and Molecular Biology, ibidem;

[3] Dept. Pharmacology, CINVESTAV- IPN, México DF, México;

*Author for all correspondence .

*Tel: +52 (55) 5747 3800; e-mail: r4cepe@yahoo.com

ABSTRACT

The use of cheese whey as substrate for biological H_2 production could help to the waste management problem. The H_2 production at ambient temperature showed the advantage of energy savings. The study of the microbial community may help to determine it links with the performance of the biological process. The aims of this work were: (*i*) to evaluate the H_2 production in anaerobic fluidized bed reactor at ambient temperature using CW as substrate and (*ii*) to determine the changes in the microbial community. There were 4 stages of operation (with H_2 production), 3 with an organic volumetric load (B_v) of 10 g/(L.day) using: (*i*) sucrose, (*ii*) CW, and (*iii*) CW with 1 g/L of NaCl and one using a B_v of 5 g/(L.day) with 0.5 g/l of NaCl . The main response variables were: H_2 productivity (NmL H_2/L_{bed}.day), H_2 pseudoyield (mmol $H_2/gCOD_{fed}$) , Jaccard similarity index), Poggi's discrete divergence index, and Shannon-Weaver index. In sucrose stage the H_2 productivity was 1 011 NmL H_2/L_{bed}.day. In the CW stage, H_2 productivity was 101 NmL $H_2/(L_{bed}$.day), 10 fold lower than the H_2 productivity observed in the sucrose operation. In the CW-NaCl-1 stage we observed H_2 productivity increased 3 times (316 NmL $H_2/(L_{bed}$. day) compared to the value with only CW. We could conclude that the addition of NaCl had positively effect on H_2 productivity. The IJcw-CWNaCl was 0.2 and the ΔP was 0.02, this indicates that the community profiles are almost completely different. The main phyla detected were *Firmicutes, Bacteroidetes, Proteobacteria* and *Actinobacteria* and the abundance of the phyla change with the change of substrate and the heat shock treatments. There was detected *Lactobacillus* and was related with low H_2 productivity..In the stage with cheese whey and NaCl, the main genus detected were *Clostridium* and *Bifidobacterium.*

Keywords: bioH_2 production, cheese whey, fluidized bed bioreactor

1. Introduction

Hydrogen has been considered as very attractive biofuel because is versatile, safe and has high energy content per unit mass (122 kJ/g; Das & Veziroglu, 2008). There are several biological processes to H_2 generation, but one important goal is to achieve the sustainability of bioH_2 production. The sustainability depends on several factors; two very relevant factors are (*i*) availability of cheap, renewable substrate and (*ii*) the establishment of fermentation conditions that augment the yield of H_2 production [1].

The feasibility of H_2 production from organic waste has been demonstrated [2-4] and has the advantage that organic wastes are cheap and renewable substrate [4]. Therefore, the use of organic wastes can be used as adjutant of both waste treatment and energy recovery. Cheese whey (CW) is considering a dairy industry residue that needs to be

treated before its discharge in order to avoid pollution. The CW is the liquid that separates from the cheese manufacture, containing a high content of organic matter (mainly lactose) and low bicarbonate alkalinity [5, 6]

One meaningful parameter on bioH_2 producing processes is the operating temperature. The selection of the temperature is very important due to could influence the (*i*) substrate degradation, (*ii*) distribution of aqueous products, (*iii*) the growth rate and (*iv*) the metabolic activity of microorganisms [7,8]. And the heat energy used to maintain higher operational temperatures could diminish the net energy gain of biofuels production [9]. Therefore, the H_2 production at ambient temperature attractive due to the save on processes energy expenses such as heating. Currently, little is known on dark fermentation of CW in the psychrophilic range. Furthermore, H_2 production in anaerobic fluidized bed reactors (AFBR) is still scarce, since other bioreactor configurations have been studied

The knowledge of the microbial community is essential in order to understand the bioreactor processes [10]. The PCR combined with the Denaturing Gradient Gel Electrophoresis (DGGE) provide analytical methods of microbial population's research without prior separation of each type of microorganism [11]. These techniques had been successfully used to analyze the microbial communities of bioH_2 fermentations [10, 12, 13]. The Massive semiconductor sequencing of 16S rDNA library is one of the next-generation sequencing technologies that could monitor millions, and potentially billions, of simultaneous sequencing reactions [14].

Thus, the main goals of this work were *(i)* to evaluate the H_2 production in a lab scale AFBRs at ambient temperature using CW as substrate and (*ii*) to determine the change of the microbial community.

2. Experimental

Experimental design

The experimental design evaluated the H_2 production at ambient temperature in AFBR using cheese whey as substrate. The stages of operation (with H_2 production) are distinguished according to the type of substrate used; three of them were with a volumetric loading rate (B_v) of 10 g/L_{bed}.day: (*i*) sucrose (S), for bioreactors start-up and hydrogenesis development; (*ii*) cheese whey (CW); and (*iii*) CW with 1 g/L of NaCl (CW-NaCl-1); the fourth was CW with 0.5 g/L of NaCl but with a B_v of 5 g/L_{bed}.day (CW-NaCl-2). The main response variables were: H_2 productivity (NmL H_2/L_{bed}.day) and H_2 pseudoyield Y' (mmol H_2/gCOD_{fed}), Jaccard similarity index (IJ), Poggi's discrete divergence index ($\dot{\Delta}_P$) and Shannon-Weaver index (H'_{10}; H'_2; H'_e).

Inocula and substrate

The inoculum of the AFBR was digestates from methanogenic anaerobic digesters degrading sucrose. Those digesters were operated at mesophilic temperature. Before loading into the reactor, the digestates were pre-treated by heat-shock (90ºC, 1h) in order to select for H_2-producing bacteria.

The start up of the AFBR was with sucrose and a synthetic wastewater: (mg/L; [15, 16]: CH_4N_2O (125); $CaCl_2$*$6H_2O$ (47); $NiSO_4$*$6H_2O$ (1); $FeSO_4$*$7H_20$ (5); $FeCl_3$*$6H_2O$ (0.5); $CoCl_2$*$2H_2O$ (0.08); $NaHCO_3$ (1 g/L); SeO_2 (0.07); KH_2PO_4 (85); K_2HPO_4 (21.7); Na_2HPO_4*$2H_2O$ (33.4).

The cheese was in powder and had the following characteristics: 0.85% fat, pH 6.3, 12.6 % protein and 5 .58% of ash. In the three and four stages NaCl were added in order to reduce the bacteriocin effect to the H_2 producers.

Experimental setup

The AFBR consisted of a glass column of 4.5 cm internal diameter, 185 cm length and 3 L capacity. Granular activated carbon (1 L; 1-2 mm diameter) was used as bed. The hydraulic residence time (HRT) was1 day (fluidized bed volume basis; [17].

Analyses

The H_2 and CH_4 concentration were determined in a Gow-Mac chromatograph (model 350) with a thermal conductivity detector and Molecular Sieve 5A packed column: injector, detector and column temperatures were 25, 100 and 25 ºC, respectively. Argon was the carrier gas [18, 19]. The acids and solvents concentration were

determined in the effluent after filtration through a glass-membrane filter. An aliquot of the filtrate was injected in a gas chromatography Varian Star 3400 equipped with FID. The injector and detector temperatures were set at 250ºC with N_2 as a carrier gas with a 20 mL/min flow rate. The oven temperature was programmed as follows: 60 ºC for 2 min, increasing to 140 ºC at 5ºC/min, and then kept constant at 140ºC for another 6 min. A 50 m 0.32 mm internal diameter fused silica capillary column coated with 0.2 mm CP-Wax 57 CB was used.

A/B ratio and specific energetic potential due to H_2

The ratio of acetic-to-butyric acid (A/B) is a parameter that could indicate the metabolic pathway favored in the fermentative process [17]. The energy evaluation of the process was performed with the analysis of the specific energetic potential ($\hat{E}_H$; [20]).

DNA preparation and PCR- DGGE analysis

Genomic DNA was extracted from bioparticles of the AFBR using the PowerSoil® DNA Isolation Kit of MO BIO Laboratories, Inc. Then, a PCR amplification was made using specific primers for Eubacterial: CGO465 with GC clamp (5'-CTC CTA CGG GAG GCA GCA GCG CCC GCC GCG CGC GGC GGG CGG GGC GGG GGC CCG GGG GG-3') and CGO465R (5´-CTA CCA GGG TAT CTA ATC CTG-3´) ; targeting a region of 332-775 bp of E. coli 16S rRDNA gen. The PCR mixture (25 µL) consisted of: (*i*) 1x buffer 4.0 mM $MgCl_2$, 0.2 mM of each deoxynucleoside triphosphate, 0.2 µM of forward and reverse primers, 0.025 U/µL of AmpliTaq DNA Polymerase (Fermentas), and 5-7 ng of DNA template. Amplification was performed in an TC-3000 Termocycler (Techne) with cycling as follows: an initial denaturation step at 94ºC for 5 min, followed by 30 cycles of 94 ºC for 30 s, 55.3 ºC for 30 s, and 72 ºC for 30 s, and finally an extension step at 72 ºC for 7 min.

The PCR products (18 µg) were loaded into an 8% polyacrylamide gel with a denaturing gradient of 25%-70%. Bands of the DGGE gels were visualized by staining them with SYBR Green I (Molecular Probes, Eugene, OR). Gels were digitized and analyzed with the UV transilluminator of electrophoresis documentation and Analysis, Model System 120 (Kodak).

Massive semiconductor sequencing of 16S rDNA library

The sequencing was performed at Ion Torrent PGM. The primers used for the amplification targeted the V3 region of the 6S rDNA. The forward primer was V3-341F with 12bp Golay barcode [21] and adapters for massive sequencing; the antisense primer V3-518R containing A and Truncated P1 adapters [22].

The PCR mixture consisted of: (*i*) 1X Buffer, (*ii*) 2 mM $MgCl_2$, (*iii)* 0.2 mM dNTP´s, (*iv*) 0.025U/µL Taq DNA, (*v*) 0.2µM of each primer, and (*iv*) 10 ng of DNA template. Amplification was performed in a GeneAmp PCR System 2700 Thermocycler (Applied Biosystems) with an initial denaturation (95°C for 5 min) followed by 30 cycles of denaturation (94°C for 15 s), annealing (62°C for 15 s) and extension (72°C for 15 s) and final extension (72°C for 10 min).

The PCR products were purified by electrophoretic separation on 2% agarose gel and using Wizard SV Gen PCR Clean-Up System (Promega). The concentration of PCR amplicons was measured by NanoDrop spectrophotometer (ThermoScientific).After purification, the samples were sent out for the barcoded library preparation and sequencing on an Ion Torrent PGM with 316 chip using the Ion Sequencing 200 bp kit (Life Technologies) according to the standard protocol (Ion Xpress_ Plus gDNA and Amplicon Library Preparation, Life Technologies). The sequence reads were filtered by the PGM software to remove low quality and polyclonal sequences; and sequences matching the 3'-adapter were automatically trimmed and filtered.

The demultiplex of the sequenced data was performed using a Sequenced data-Microbiota analysis Ion torrent PGM software, Torrent_Suite v 4.0.2. It was based on their barcodes and poor quality reads were eliminated from the datasets, i.e. quality score <20, containing homopolymers >6, length <200 nt, and containing errors in primers and barcodes. The analysis of the demultiplexed sequencing data was made with the program QIIME version 1.8.0 software pipeline. Closed reference Operational taxonomic units (OTU) were determined at 97% similarity level with UCLUST Algorithm [23].

It was used the Chimera Slayer in order to detect and removed chimeras from the datasets [24]. Sequence alignments were done against the Greengenes core set [25]. Statistical analysis of the OTU table Microbial diversity had been assessed through both alpha and beta diversity. Using rarefied OTU tables, alpha diversities were calculated using various matrixes like Shannon, PD whole tree, chao1, observed species.

The beta diversity analysis was calculated using UniFrac analysis [26], by a phylogenetic tree computed with FastTree and a rarefiled biom table as inputs. Abundance of the bacterial groups at different taxonomic levels (phylum, order, and genus) was separately explored with a Principal Component Analysis (PCA) and Unweighted Pair Group Method with Arithmetic mean (UPGMA) Clustering.

Richness and diversity estimation

The Jaccard similarity index (IJ) was used for estimation of the microbial richness variation intra-stage and between stages, in the DGGE. The IJ ranges from 0 to 1 when the community profiles are completely similar and 0 when the profiles are completely different [27]:

$$IJ = \frac{n_{AB}}{(n_A + n_B - n_{AB})} \qquad (1)$$

Where:
n_{AB}= number of bands that are present both in lane A and lane B
n_A= total number of bands of lane A
n_B= total number of bands of lane B

To compare the richness of a community with respect to time it was used the Poggi's divergence index ($\dot{\Delta}_P$; [28]):

$$\dot{\Delta}_P = \frac{d\Delta P}{dt} \qquad (2)$$

$$\Delta_P = \frac{(\dot{n\prime}_A + n\prime_B)}{(n_A - n_B)} \qquad (3)$$

Where:
n'_A= number of bands of lane A absent in lane B
n'_B= number of bands of lane B absent in lane A
n_A= total number of bands of lane A
n_B= total number of bands of lane B

The $\dot{\Delta}_P$ index indicates that the microbial community is relatively stable with respect to time. For instance, analysis of a microbial community in attached-growth bioreactors with this tool has shown very low values of $\dot{\Delta}_P$. On the other hand, higher values of $\dot{\Delta}_P$ are related to dynamic changes in community composition such as those that occur in suspended-growth bioreactors.

The results of the massive semiconductor sequencing of 16S rDNA library were analyzed using the Shannon-Weaver diversity index [29], defined as:

$$H' = \sum_{i:1}^{S} \dot{(p_i log p_i)} \qquad (4)$$

where:

p_i : is often the proportion of individuals belonging to the i species in the dataset of interest,
S: is the total number of species.

3. Results and discussion

3.1. Operation with sucrose

The fluidized bed reactor was operated for 30 days with a B_v of 10 g sucrose/L_{bed}.day. The average H_2 productivity obtained was 1011 NmL H_2/L_{bed}.day with a H_2 pseudoyield of 4.51 mmol H_2/$gCOD_{fed}$ (Table 1) that is 1.13 times lower than the obtained in the same system using 8 g sucrose/L_{bed}.day [17]. This could be due to the high concentration of solvents in the effluent with ratio φ (defined as the sum of volatile organic acid divided the sum of solvent products) 5.8 times lower than the ratio with Bv=8 g/L_{bed}.day (3.3. and 19, respectively). The low value of φ in our work may indicate that the fermentation was being diverted to a solvent production. Indeed, ethanol was the main solvent in the effluent (Table 1) and it is known that the ethanolic fermentation is related to low production of H_2 [30].

Table 1. Average performance of anaerobic fluidized bed reactor at ambient temperature using cheese whey as substrate

Parameter	Sucrose	Cheese whey		
	(S) 10 g/L_{bed}.day	**Without NaCl (CW) 10 g/L_{bed}.day**	**With NaCl (CW-NaCl-1) 10 g/L_{bed}.day**	**With NaCl (CW-NaCl-2) 5 g/L_{bed}.day**
pH	4.27 ± 0.12	4.31 ± 0.07	4.1 ± 0.2	4.3 ± 0.2
H_2 concentration (%)	39.4 ± 8.5	11.8 ± 1.6	32.1 ± 6.9	14.5 ± 3.1
H_2 productivity				
(NmL H_2/L_{bed} day)	1 011 ± 339	101 ± 25	316 ± 67	92.12 ± 20
(mmol H_2/gCOD day)	4.2	0.4	1.4	0.8
Soluble microbial products (mg COD/L)				

Acetic acid	885 ± 362	289 ± 149	720 ± 259	682 ± ---
Propionic acid	282 ± 140	14.2 ± 13.7	273 ± 4	106 ± ---
Butiric acid	4 392 ± 1 570	299 ± 28	942 ± 194	1864 ± 1580
Lactic acid	ND	0.07 ± 0.02	0.012 ± 0.07	ND
Acetone	ND	ND	ND	ND
Methanol	ND	ND	ND	ND
Ethanol	1193 ± 822	117 ± 67	ND	263 ± 79
Butanol	477 ± 98	77 ± 12	ND	76.7 ± ---
EtOH/SMP (%)	17.1 ± 10.8	14.0 ± 4.6	0 ± 0	15.7 ± 14.9
BuOH/SMP (%)	6.9 ± 1.8	9.8 ± 1.1	0 ± 0	6.1 ± ---
HAc/SMP (%)	12.0 ± 2.5	35.1 ± 9.3	36.6 ± 4.9	8.6 ± ---
HPr/SMP (%)	3.9 ± 1.7	1.6 ± 1.3	14.5 ± 3.6	1.3 ± ---
HBu/SMP (%)	60.1 ± 6.4	39.4 ± 14.1	48.8 ± 1.3	68.2 ± 9.4
A/B	0.20 ± 0.02	1.0 ± 0.6	0.8 ± 0.1	0.11 ± ---
TVOA (mg COD/L)	5 559± 2027	602 ± 135	1 935 ± 449	2258 ± 2139
SMP (mg COD/L)	7 229 ± 2 320	796. ± 215	1 935 ± 449	2598 ± 1959
ρ, TVOA/SOLV	3.9 ± 2.6	3.2 ± 0.6	---	9.65 ± ---

Notes: Average results were obtained under steady-state conditions: S: day 8 to 22; CW: and CW-NaCl: day 15 to 22. A/B: acetic to butyric acid ratio. EtOH: ethanol; BuOH: butanol; HAc: acetate; HPr: propionate; HBu: butyrate; TVOA: total volatile organic acids= HAc+HPr+HBu; SMP: soluble microbial products=TVOA+EtOH+BuOH. Based in COD/L.

3.2. Operation with cheese whey

Afterwards, CW was used as substrate (stage two) and the productivity decreased to 101 ca. NmL H_2/L_{bed}.day (Figure 1 a), that was almost 10 times lower than the H_2 productivity observed in the operation with sucrose (Table 1). The Figure 1b shows the pH in the effluent of the AFBR, the values were between 4-5, that low values of pH could be related to a high accumulation of organic acids. However, in this case, the organic acid accumulation diminished in the same way as pH.

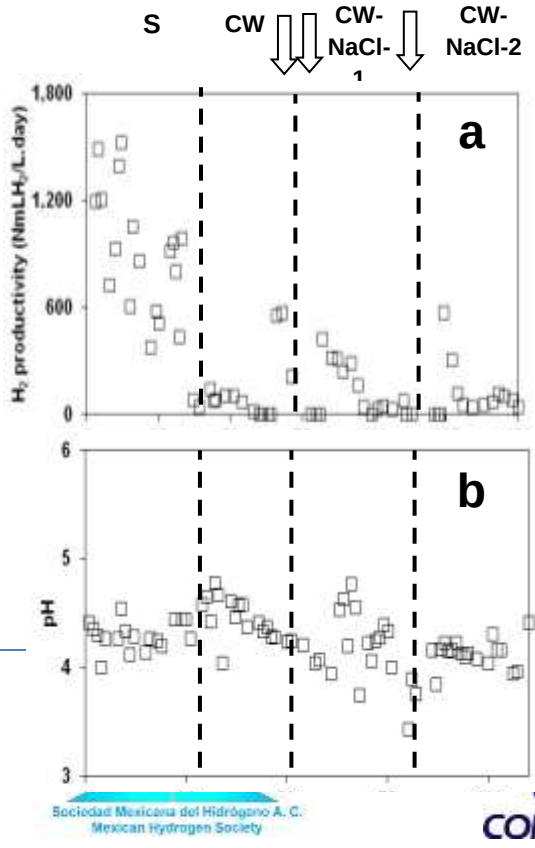

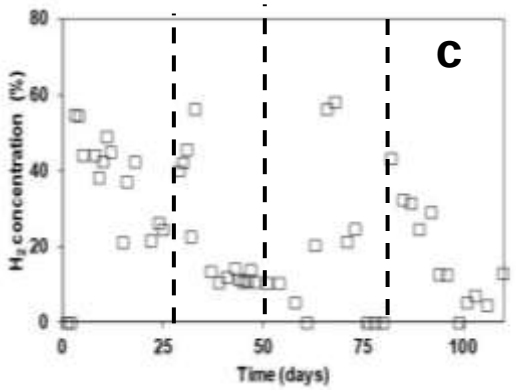

FIGURE 1. Time courses of: (a) H_2 productivity.; (b) pH and (c) H_2 concentration. Arrows indicate a heat shock treatment.

We detected lactic acid in the effluent, and its presence could indicate the presence of lactic acid bacteria (LAB, [31]. This type of bacteria is related to low H_2 production [31, 32] as a combination of H_2 sink when hexoses are fermented to lactic acid as well as inhibitory effects of LAB on H_2-producing bacteria.

There are three known mechanisms that can explain the antimicrobial activities of LAB: (*i*) increased amount of organic acids that can cause rapid acidification of the medium [33], (*ii*) nutrient competition [31], and (*iii*) generation of antimicrobial compounds [31, 34, 35] investigated the effect of LAB on H_2 fermentation of organic waste and suggested that the inhibitory effect on H_2 production could be explained by the excretion of bacteriocins. Bacteriocins are proteins that have activity towards gram-positive bacteria, frequently include organisms capable of sporulation such as *Clostridium* and/ or food pathogens [35-38].

In this work, the inocula had a shock treatment in order to eliminate the microorganisms that are the main competitors of the H_2-producers, such as methanogenic archeae and LAB's that cannot sporulate [31,39]. It seems that the shock treatment was not sufficient to eradicate these microorganisms; the detection of methane during the operation with sucrose [18] could support that affirmation. Therefore, the first strategy implemented was to repeat the heat shock treatment, but now for more hours (arrows in Figure 1) and after that the AFBR-A was operated with CW but no H_2 production was detected (data no shown). We realized another shock treatment and start up with sucrose but no H_2 production was produced (data not shown).

Table 2. Hydrogen production using cheese whey as substrate.

Inoculum	Bioreactor, fermentations conditions, and volumetric organic load (gCOD/(L.day))	Y', Hydrogen pseudoyield * ($mmolH_2/gCOD_{fed}$)	$\hat{E}_{H2}$ (J/gCOD)	Ref.
Sludge Heat shock treatment	CSTR ; HRT: 1, 2 y 3.5 d T = 55ºC ; pH = 5.5 ; 47	0.91	257.5	[39]
Digestates of acidogenic reactor	UASB ; HRT=12 h T=30°C; pH=5 ; 20	0.18	50.9	[40]
Microorganisms in wastewater	CSTR ; HRT: 24 h T = 35°C; pH = 5.2; 30	1.5	424.5	[41]
Anaerobic mixed microflora Heat shock treatment	CSTR ; HRT:24 h T = 55ºC; pH=5.5; 30	3.5	990.5	[42]
Methanogenic sludge Heat shock treatment	AFBR ; HRT:24 h T = 25ºC; pH=4.1; 10	1.4	396.2	This study

Notes: HRT, hydraulic retention time; CSTR, continuously stirred tank reactor; UASB, upflow anaerobic sludge blanket reactor; AFBR, anaerobic fluidized bed reactor.

A sample of bioparticles of the reactor was cultivated in MRS agar (agar formulation designed to make evident the growth *Lactobacilli* and other LAB's) and growth of colonies was observed. We concluded that the heat treatment did not eliminate the LAB. This could be due to the microorganisms present in the biofilm protected from environmental conditions by the particle. Hence, it is possible that the temperature of the inner biofilm layers (where it seems to be the place where anaerobic microorganisms concentrate, [43, 44] is lower than that at the surface of the biofilm. Regarding the effect of LAB on hydrogen producer microorganisms, we look for other alternative besides the heat treatment. There are reports that supplementation of cultures with salts, such as NaCl, could reduce the

bacteriocin effect. So, we tested a second strategy that consisted of new heat shock treatment and the addition of 1 g/L of NaCl to the influent to the AFBR.

3.3. Operation with cheese whey and NaCl

The AFBR was operated with sucrose (B_v=5 g/(L_{bed}.day) and at day 75 we changed to CW (B_v=10 g/(L.day)). Afterwards, no H_2 was detected in 7 days and the highest concentration of lactic acid was observed the highest concentration of lactic acid. After this, the supplementation of CW with NaCl started; almost immediately the H_2 production resumed, with an H_2 concentration of almost 20% and a noticeable increase in the pH (Figure 1 b).

BioH_2 productivity increased to up to 316 NmL H_2/(L_{bed}. day), i.e., 3 times compared to the value obtained without the presence of NaCl. A reduction in the concentration of lactic acid was also observed. The effect of the NaCl is unclear but some works suggested that there exists a decrease in bacteriocin production in the presence of salt because of the interference of NaCl binding to bacteriocin induction factor, which is essential for bacteriocin production. Other authors indicated that in the case of the bacteriocin of *L. sakei CTC 494*, however, it appears that the water binding effect of salt is the major factor responsible for the decrease in specific bacteriocin production [45].

The Y' with CW-NaCl-1 was 1.4 mmol H_2/gCOD_{fed} and the specific energetic potential was ca. 400 J/g COD; these values are in the middle of the range of reported H_2 productions from CW in others works where the bioreactors were operated at higher temperatures than our AFBR (0.18-3.5 mmol H_2/g COD_{fed} ; Table 2) .

3.4. Operation with cheese whey and NaCl with Bv= 5 g/L_{bed}.day

The H_2 production last one month, after that, almost no H_2 was detected. The third strategy was to repeat the shock treatment and the feed with CW-NaCl but now start with a low Bv (5 g/L_{bed}.day) and increase slowly until reach the 10 g/L_{bed}.day. The average H_2 productivity achieved was 0.8 mmol H_2/g COD_{fed} that is almost 2 fold to that obtained with 10 gS/L_{bed}.day. The H_2 production decreased after 30 days and no more H_2 was detected.

4. PCR- DGGE analysis of microbial communities harbored in the bioreactors

Figure 2 shows the DGGE of bioparticles samples of the different stages of operation. Regarding the meaning of the Jaccard Index, a value near to 1 indicates that the profiles are similar and when the value is near to 0 the profiles are completely different. It can observe (Table 3) that the profiles with sucrose operation and the CW are moderately different (IJ=0.4), that could be due to the change of a more complex substrate (cheese whey), this could restrict the growing of some microorganisms.

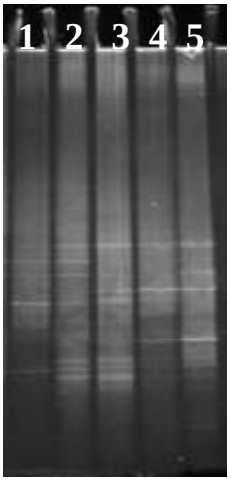

Table 3. Jaccard similarity index (IJ) and Poggi's divergence index ($\dot{\Delta}_P$)

Lane	Stage	IJ					$\dot{\Delta}_P$				
		1	**2**	**3**	**4**	**5**	**1**	**2**	**3**	**4**	**5**
1	Sucrose	1	0.4	0.2	0.1	0.1	1	0.01	0.02	0.02	0.01
2	CW		1	0.5	0.2	0.2		1	0.01	0.02	0.01
3	CW-1hst			1	0.2	0.2			1	0.02	0.01
4	CW -2hst				1	0.4				1	---
5	CW-NaCl-1					1					1

FIGURE 2. DGGE of different stages of operation in a fluidized bed bioreactor.

The profiles with the sucrose to the operation with CW-NaCl-1 are very different (IJ=0.1: Table 3), it is important to remember that the stage with cheese whey and NaCl was after two shock heat treatment, this could explain the change to the profiles. Huang *et al*. [46] observed that the heat shock treatment could result in the elimination of non-spore-forming bacteria with the consequence reducing to the consume oxygen system and the decreased conversion of the substrate into H_2. The values of Poggi's divergence index(ΔP) are low and could be related with attached-growth bioreactors.

3.6. Massive semiconductor sequencing of 16srDNA library

The phyla of the sequences detected with the massive semiconductor sequencing are displayed in Figure 3. The main phyla observed in all stages are *Firmicute*, *Proteobacteria*, *Bacteroidetes* and *Actinobacteria.* In the sucrose stage, the abundance of the phyla was: 70% *Firmicute*, 6%, *Proteobacteria*, 21% *Bacteroidetes* and 3% *Actinobacteria.* These percentages vary with the change of substrate, there were and increment in *Firmicutes* (91%) and *Actinobacteria* (5%) and a substantial decrease of *Proteobacteria* (2%) and *Bacteroidetes* (2%).

It is important to recall that the H_2 productivity decreased 10 fold with the change to CW. This tendency continued after the first heat shock treatment and no H_2 production was detected. With the second heat shock treatment, *Bacteroidetes*, *Proteobacteria* and *Actinobacteria* incremented to 14%, 61% and 15%, respectively. The *Firmicutes* reduced to 11%; but still no H_2 was observed. With a third heat shock treatment and the addition of NaCl (CW, 5 g/L) *Firmicutes* and *Actinobacteria* incremented to 26 and 54%, respectively, the *Proteobacteria* reduced to 6% and the *Bacteroidetes* remained to 13%. In this last stage the H_2 productivity incremented 2 fold with respect to that obtained with only CW.

Table 4 shows the genus of some microorganisms (> 1%) obtained at the different stages of operation. The *Clostridium* is known as H_2 producer and its abundance increased 2 fold (20.9%) when the substrate to bioreactors was changed to CW but less H_2 was detected. Possibly there were present a few non-clostridia bacteria, that despite there are not H_2 producers, might have contributed to the degradation of carbon substrates [47]. Furthermore, not all *Clostridia* species in the dark fermentation system are capable or responsible for H_2 production [48,49].

In the two stages with shock heat treatment, the abundance of *Clostridium* diminished to 11.2 and 0.6 %, respectively; no H_2 was observed. In the stage CW-NaCl-2 the H_2 productivity was 2 fold of the obtained with only CW, whereas the abundance of *Clostridium* was 7.7%.

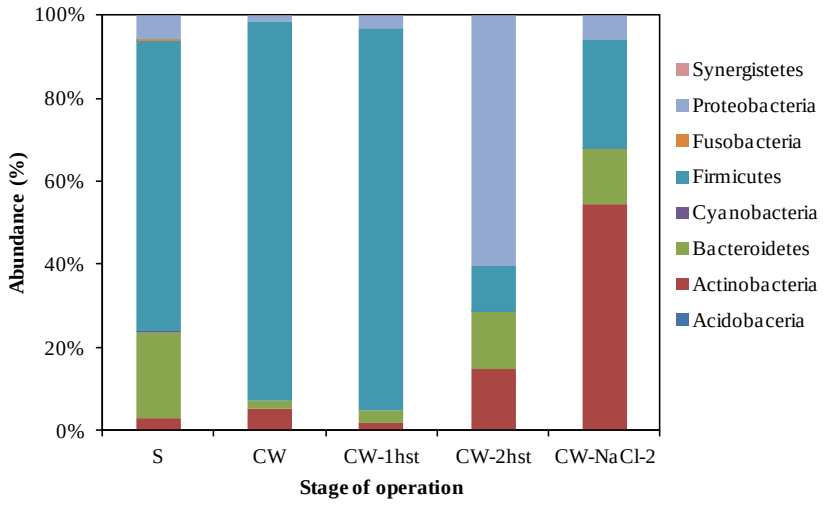

FIGURE 3. Phylum level identification of all sequences.

Table 4. Microorganisms profiles (phylum, class, order and genus) at different stages of operation

Phylum	Class	Order	Genus	Abundance (%)				
				S	CW	CW-1hst	CW-2hst	CW-NaCl-2
Actinobacteria	*Actinobacteria*	*Actinomycetales*	*Lentzea*	0.0	0.0	0.0	5.0	0.2
			Rhodococcus	0.0	0.0	0.0	2.6	0.3
			Propionibacteriaceae (family)*	1.3	0.4	0.1	2.0	5.5
			Streptomyces	0.1	0.0	0.0	1.0	1.2
		Bifidobacteriales	*Bifidobacterium*	0.5	0.0	0.7	2.0	44.3
Bacteroidetes	*Bacteroidia*	*Bacteroidales*	*Bacteroides*	6.9	0.1	0.1	0.7	1.0
			Prevotella	11.1	1.6	2.8	7.0	11.4
	Flavobacteriia	*Flavobacteriales*	*Flavobacterium*	0.0	0.0	0.0	4.8	0.1
Firmicutes	*Bacilli*	*Bacillales*	*Sporolactobacillus*	19.9	1.4	0.2	0.0	0.2
		Lactobacillales	*Lactobacillus*	1.0	6.0	65	0.0	0.0
			Lactococcus	1.2	0.0	0.0	0.0	0.0
	Clostridia	*Clostridiales*	*Clostridiales* (order)*	2.8	0.3	0.3	0.7	1.1
			Clostridiaceae (familiy)*	1.7	10.1	2.6	1.6	0.6
			Clostridium	11.6	20.9	11.2	0.6	7.7
			Lachnospiraceae (family)*	7.2	0.5	0.7	2.1	3.6
			Coprococcus	1.6	0.1	0.1	0.5	0.6
			Lachnospira	1.0	0.1	0.1	0.4	0.6
			Ruminococcaceae (family)*	3.5	9.3	0.7	1.1	1.8
			Anaerofilum	0.1	2.2	0.0	0.0	0.0
			Ethanoligenens	1.2	30.4	3.9	0.0	0.3
			Faecalibacterium	7.0	0.4	0.6	1.9	3.7
			Oscillospira	1.5	0.6	0.1	0.4	1.1
			Ruminococcus	1.6	7.3	4.5	1.2	1.2
Proteobacteria	*Alphaproteobacteria*	*Rhizobiales*	*Rhizobiales* (order)*	0.0	0.0	0.0	1.1	0
			Xanthobacter	0.0	0.0	0.0	5.0	0.1
	Betaproteobacteria	*Burkholderiales*	*Curvibacter*	0.0	0.0	0.0	18.8	0.1
			Oxalobacteraceae (family)*	0.1	0.0	0.0	18.0	0.2

	Gammaproteobacteria	*Aeromonadales*	*Succinivibrio*	1.3	2.1	1.2	0.4	0.6
		Enterobacteriales	*Enterobacteriaceae* (family)*	2.4	0.7	1.6	1.2	0.6
		Pseudomonadales	*Pseudomonas*	0.1	0.0	0.1	1.3	0.1
		Xanthomonadales	*Xanthomonadaceae* (family)*	0.0	0.0	0.0	0.1	1.2

Note: * the genus are not identified yet

As we mentioned before, *Lactobacillus* are microorganisms related to low H_2 production [50]. We have found this type of microorganism in the stage with sucrose and there was and increment of *Lactobacillus* with the change to the CW substrate (1.0 to 6.0), it is important to mention that H_2 productivity decreased 10 folds in this stage.

After the first heat shock treatment, the feed was only CW and the *Lactobacillus* increased to almost 66%. After performing a second heat shock treatment we fed sucrose during a first short subperiod and afterwards, the substrate was changed to CW. In this process, *Lactobacillus* diminished to 0.1% but still no H_2 was detected. In this stage *Clostridium* decreased its abundance (10%).

It is important to remark that in the stage with CW-NaCl-2 the percentage of *Bifidobacterium* was almost 10 fold higher than in the stage with only CW. *Bifidobacterium sp.* is a microorganism that has been found in H_2 fermentation of starch and xylose [47, 51]. In the H_2 production using starch [51], the highest H_2 yield was observed at the HRT of 0.5 h and with *Clostridium sp.* and *Bifidobacterium sp.* as the main microorganisms detected (a cell counts of 40 and 40-60%, respectively).

Table 5. Shannon-Weaver Index of the different stages of operation

Shannon-Weaver Index	**S**	**CW**	**CW-1hst**	**CW-2hst**	**CW-NaCl-2**
H_{10}	0.38	0.16	0.15	0.48	0.49
H_2	1.27	0.54	0.51	1.61	1.62
H_e	0.88	0.38	0.35	1.11	1.12

Table 5 shows the Shannon-Weaver index of the operation stages, it can observe that they decreased to the CW-1hst stage, after that, the index increase in the CW-2hst and remains in the CW-NaCl-2 stage.

4. Summary and perspectives

- The H_2 productivity using CW as substrate was almost 10 fold lower than the obtained using sucrose.
- The use of CW-NaCl allowed the increase of H_2 productivity (almost 3 times) compared to the value obtained without the supplementation of the salt.
- The H_2 pseudoyield was in the middle of the range of H_2 production using CW reported in other works that performed the dark fermentation of CW at higher temperatures.
- The main phyla detected were *Firmicutes, Bacteroidetes, Proteobacteria* and *Actinobacteria*. The abundance of the phyla changed with the change of substrate
- Presence of *Lactobacillus* was related with low H_2 productivity; we found *Clostridium* in all the stages of operation
- In the stage with CW and NaCl, the main microbial orders detected were *Clostridium* and *Bifidobacterium*

Acknowledgements

The authors wish to thank SECITI-GDF for support with projects PICCO 10-27 and PICCO 10-28 and CINVESTAV del IPN for financial support to this research, and CONACYT for a graduate scholarship to KMM-P. The excellent help of Professor Elvira Ríos Leas, Mr Cirino Chávez-Rojas and Mr Gustavo Medina as well as Mr Rafael Hernández-Vera from the GBAER-EBRE Group, CINVESTAV del IPN, is gratefully acknowledged.

References

[1] M. Ferchichi, E. Crabbe, G.H. Gil, W. Hintz, A. Almadidy, Influence of initial pH on hydrogen production from cheese whey. J Biotechnol 2005; 120:402–09.
[2] P. Yang, R. H Zhang,. J. MeGarvey, J. R Benernann. Biohydrogen production from cheese processing wastewater by anaerobic fermentation using mixed microbial communities. Int J Hydrogen Energy 2007; 32:4761–71
[3] R.S. Prakasham, T. Sathisha, P. Brahmaiah, C.H. Subba Rao, R. Sreenivas Rao, P. J. Hobbs, Biohydrogen production from renewable agri-waste blend: Optimization using mixer design. Int J Hydrogen Energy 2009; 6143- 6148.
[4] P.T Sekoai, E.B. Gueguim Kana, Semi-pilot scale production of hydrogen from Organic Fraction of Solid Municipal Waste and electricity generation from process effluents. Biomass Bioenerg 2014; 60: 156-163.
[5] F. Malaspina, C.M. Cellamare, L. Stante, A. Tilche, Anaerobic treatment of cheese whey with a downflow upflow hybrid reactor. Bioresource Technol 1996. 55:131–139.
[6] E. Valencia-Denicia, M.L. Ramírez- Castillo, La industria de la leche y la contaminación del agua. Elementos: Ciencia y cultura.16 (73)enero-marzo 2009; 27-31
[7] K. Lee, P. Lin, J. Chang, Temperature effects on biohydrogen production in a granular sludge bed induced by activated carbon carriers. Int J Hydrogen Energy 2006; 31(4):465-72.
[8] Y. Mu, X. Zheng, H. Yu, R. Zhu, logical hydrogen production by anaerobic sludge at various temperatures. Int J Hydrogen Energy 2006; 31(6): 780-785.
[9] K.R.J. Perera, B. Ketheesan, Y. Arudchelvam, N. Nirmalakhandan, Fermentative biohydrogen production II: Net energy gain from organic wastes. Int J Hydrogen Energy 2012; 37(1):167-78.
[10] Y. Miura, M.N Hiraiwa, T. Ito, T. Itonaga, Y. Watanabe, S. Okabe, Bacterial community structures in MBRs treating municipal wastewater: relationship between community stability and reactor performance. Water Res 2007; 41, 627–637
[11] G. Muyzer, K. Smalla, Application of denaturing gradient electrophoresis (DGGE) and temperature gradient gel electrophoresis (TGGE) in microbial ecology. Antonie van Leeuwenhoek 1998; 73, 127–141.
[12] H.H.P.Fang, C.L. Li, T. Zhang, Acidophilic biohydrogen production from rice slurry. Int J Hydrogen Energy 2006; 31: 683–92.
[13] Y. Ueno, S. Haruta, M. Ishii, Y. Igarashi, Microbial community in anaerobic hydrogen producing microflora enriched from sludge compost. Appl Microbiol Biotechol 2001; 57:555–62.
[14] B. Merriman, Ion Torrent R&D Team; J.M. Rothberg, Progress in Ion Torrent semiconductor chip based sequencing. Electrophoresis 2012; 33: 3397–3417.
[15] J.A.C. Leite, B.S. Fernandes, E. Pozzia, M. Barboza, M. Zaiata, M., Application of an anaerobic packed-bed bioreactor. for the production of hydrogen and organic acids. Int J Hydrogen Energy 2008; 33:579-86
[16] Z.P. Zhang, J.H. Tay, K.Y. Show, R. Yan, D.T. Liang, D.J. Lee, W.J. Jiang, Biohydrogen production in a granular activated carbon anaerobic fluidized bed reactor. Int J Hydrogen Energy 2007; 32:185–191.
[17] K.M. Muñoz-Páez, N. Ruiz-Ordáz, J. García-Mena, M.T. Ponce-Noyola, A.C. Ramos-Valdivia, I.V. Robles- González, L. Villa- Tanaca, N. Rinderknecht-Seijas, H.P. Poggi-Varaldo, Comparison of biohydrogen production in fluidized bed bioreactors at room temperature and 35°C. Int J. Hydrogen energy 2013; 38: 12570-12579.
[18] K.M. Muñoz-Páez, E. Ríos-Leal, I.Valdez-Vazquez, N. Rinderknecht-Seijas, H.M. Poggi-Varaldo. Re-fermentation of washed spent solids from batch hydrogenogenic fermentation for additional production of biohydrogen from the organic fraction of municipal solid waste. J Environ Manage 2013; 95:S355–S359.
[19] I. Valdez-Vazquez, H.M. Poggi-Varaldo, Alkalinity and high total solids affecting H_2 production from organic solid waste by anaerobic consortia. Int J Hydrogen Energy 2009; 34:3639 – 3646
[20] C. Escamilla-Alvarado, E. Ríos-Leal, M.T. Ponce-Noyola, H.M. Poggi-Varaldo, Gas biofuels from solid substrate hydrogenogenic–methanogenic fermentation of the organic fraction of municipal solid waste. Process Biochem 2012; 47(11): 1572–1587
[21] N. Fierer, M. Hamady, C.L. Lauber, R. Knight, R. The influence of sex, handedness, and washing on the diversity of hand surface bacteria. Proc Natl Acad Sci U S A 2008; 105(46): 17994–17999.
[22] P. Whiteley, D. Haracopos, A.M. Knivsberg, K.L. Reichelt, S. Parlar, J. Jacobsen, A. Seim, L. Pedersen, M. Schondel, P. Shattock, The ScanBrit randomised, controlled, single-blind study of a gluten- and casein-free dietary intervention for children with autism spectrum disorders. Nutr Neurosci 2012; 13(2):87-100.
[23] R.C. Edgar, Search and clustering orders of magnitude faster than BLAST. Bioinformatics 2010; 26(19): 2460-2461.
[24] T.Z. DeSantis, P. Hugenholtz, N. Larsen, M. Rojas; E.L. Brodie, K. Keller, T. Huber, D. Dalevi, P. Hu, G.L. Andersen, Greengenes, a chimera-checked 16S rRNA gene database and workbench compatible with ARB. Appl Environ Microbiol 2006; 72:5069–5072.
[25] B.J. Haas, D. Gevers, A.M. Earl, M. Feldgarden, D.V. Ward, G. Giannoukos, D. Ciulla, D. Tabbaa, S.K. Highlander, E. Sodergren, B. Methé, B. T.D. DeSantis, T.D, The Human Microbiome Consortium, J.F. Petrosino, R. Knight, B.W. Birren, Chimeric 16S rRNA sequence formation and detection in Sanger and 454-pyrosequenced PCR amplicons. Genome Res 2011; 21:494-504.

[26] Y. Vázquez-Baeza, M. Pirrung, A. Gonzalez, R. Knight, EMPeror: a tool for visualizing high-throughput microbial community data. Gigascience 2013; 2(1):16.
[27] P. Zárate-Segura, J. García-Mena, H.M. Poggi-Varaldo, Effect of biomass type and PCE on *archaea* communities of anaerobic reactors. In: Alleman, B.C., Kelley, M.E. (Eds.), In Situ and On-Site Bioremediation-2005. Proceedings of the Eighth International in Situ and On-Site Bioremediation Symposium(Baltimore,Maryland; June 6e9, 2005). Battelle Press, Columbus, OH, ISBN 1-57477-152-3. Book in CD-ROM.
[28] H.M. Poggi-Varaldo, J.D. Bárcenas-Torres, C.U. Moreno-Medina, J. García-Mena, C. Garibay-Orijel, E. Ríos-Leal, N. Rinderknecht-Seijas. Influence of discontinuing feeding degradable cosubstrate on the performance of a fluidized bed bioreactor treating a mixture of trichlorophenol and phenol. J. Environmental Management 2012; 113: 527-537.
[29] C.E. Shanon, A mathematical theory of communication. Bell System Technical Journal 1948; 27:379-423.
[30] P.E Koskinen, A.H. Kaksonen, J.A. Puhakka, The relationship between instability of hydrogen production and compositions of bacterial communities within a dark fermentation fluidized-bed bioreactor. Biotechnol Bioeng 2007; 97:742–58.
[31] T. Noike, H. Takabatake, O. Mizuno, M. Ohba, Inhibition of hydrogen fermentation of organic wastes by lactic acid bacteria. Int J Hydrogen Energy 2002; 27(11-12): 1367-71.
[32] C. Escamilla-Alvarado, E. Ríos-Leal, M.T. Ponce-Noyola, H.M. Poggi-Varaldo, Gas biofuels from solid substrate hydrogenogenicemethanogenic fermentation of the organic fraction of municipal solid waste. Process Biochemistry 2012, 47(11):1572-1587.
[33] M. A. Daeschel. Antimicrobial substances from lactic acid bacteria for use as food preservatives. Food Technol 1989. 43: 164–167.
[34] J. M. Jay, Antimicrobial properties of diacetyl. App Environ Microbio 1982; 44: 525–32.
[35] T.R. Klaenhammer, Bacteriocins of lactic acid bacteria. Biochimie 1988; 70: 337–349.
[36] C.G. Nettles, S.F. Barefoot, Biochemical and genetic characteristics of bacteriocins of food-associated lactic acid bacteria. J Food Prot 1993. 56: 338–356.
[37] L. De Vuyst, E.J. Vandamme, Antimicrobial potential of lactic acid bacteria, p. 91–142. In L. De Vuyst and E. J. Vandamme (ed.), Bacteriocins of lactic acid bacteria: microbiology, genetics and applications 1994. Blackie Academic & Professional, London, United Kingdom.
[38] P.D. Cotter, C. Hill, R.P Ross, Bacteriocins: developing innate immunity for food. Nature Rev Microbiol 2005; 3: 777–788.
[39] N. Azbar, F.T.C Dokgoz, F. Tuba, T. Keskin, K.S. Korkmaz, H.M. Syed, Continuous fermentative hydrogen production from cheese whey wastewater under thermophilic anaerobic conditions. Int J Hydrogen Energy 2009; 34. 7441–7447.
[40] E. Castello, C. García y Santos, T. Iglesias, G. Paolino. J. Wenzel, L. Borzacconi, C. Etchebehere, C. Feasibility of biohydrogen production from cheese whey using a UASB reactor: Links between microbial community and reactor performance. Int J Hydrogen Energy 2009; 34(14): 5674-5682
[41] N. Venetsaneas, G. Antonopoulu, K. Stamatelatou, M. Kornaros, G. Lyberatos, Using cheese whey for hydrogen and methane generation in a two-stage continuous process with alternative pH controlling approaches. *Bioresource Technology 2009*; 100 (15): 3713-3717.
[42] N. Azbar, F.T.C. Dokgoz, The effect of dilution and L-malic acid addition on bio-hydrogen production with *Rhodopseudomonas palustris* from effluent of an acidogenic anaerobic reactor. Int J Hydrogen Energy 2010. 35: 5674-5682.
[43] F.A. McLeod, S.R. Guiot, J.W. Costerton, Layered structure of bacterial aggregates produced in an upflow anaerobic sludge and filter reactor. Appl. Environ. Microbiol 1990; 56(6):1598-1607.
[44] G.M Shida, A.R. Barros, C.M. dos Reis, E.L.C de Amorim, M.H.R.Z Damianovic, E.L. Silva, Long term stability of hydrogen and organic acids production in an anaerobic fluidized-bed reactor using heat treated anaerobic sludge inoculum. *Int J Hydrogen Energy 2009*. 34:3679–3688.
[45] F. Leroy, L. De Vuyst, The Presence of Salt and a Curing Agent Reduces Bacteriocin Production by Lactobacillus sakei CTC 494, a Potential Starter Culture for Sausage Fermentation. Appl Environ Microb 1999. 5350–5356.
[46] Y. Huang, W. Zong, X. Yan, R. Wang, C.L. Hemme, J. Zhou, Z. Zhou, Z., Succession of the bacterial community and dynamics of hydrogen producers in a hydrogen-producing bioreactor. Appl. Environ. Microbiol 2010; 76: 3387–3390
[47] Y.-C. Lo, W.-M. Chen, C.-H. Hung, S.-D. Chen, J.-S. Chang, Dark hydrogen fermentation from sucrose and xylose using hydrogen-producing indigenous bacteria: feasibility and kinetic studies. Water Res 2008. 42, 827–842.
[48] C.-H. Hung, Y.-T. Chang, Y.-J.Chang, Roles of microorganisms other than *Clostridium* and *Enterobacter* in anaerobic fermentative biohydrogen production systems – A review. Bioresource Technology 2011; 102: 8437–8444
[49] M.E. Nissilä, H.P. Tähti, J.A. Rintala, J.A. Puhakka, Effects of heat treatment on hydrogen production potential and microbial community of thermophilic compost enrichment cultures. Bioresource Technol 2011. 102: 4501-4506.
[50] P. Saraphirom, A. Reungsang, Biological hydrogen production from sweet sorghum syrup by mixed cultures using an anaerobic sequencing batch reactor (ASBR). Int. J. Hydrogen Energy 2011; 36(14): 8765–8773.
[51] C.-H. Cheng, C.-H. Hung, K.-S Lee, P.-Y. Liau, C.-M. Liang, L.-H. Yang, P.-J. Lin, C.-Y. Lin, Microbial community structure of a starch-feeding fermentative hydrogen production reactor operated under different incubation conditions. Int. J. Hydrogen Energy 2008;33: 5242–5249.

Y@Pt/C Core-Shell Electro-Catalyst for Oxygen Reduction Reaction

M.M. Tellez-Cruz[1], J.F. Godínez-Salomón[1], O. Solorza-Feria[1].*

[1]Departamento de Química, Centro de Investigación y Estudios Avanzados del IPN, Av. IPN 2508, Col. San Pedro Zacatenco, A. Postal 14-740, 07360 México D.F., México.
*Tel: 011 +52 +55 5747-3715 ; e-mail: osolorza@cinvestav.mx

ABSTRACT

The synthesis of yttrium decorated platinum core-shell nanocatalyst for the oxygen reduction reaction (ORR) in acid media is presented. The core of the nanocatalysts was prepared through colloidal reduction of YCl_3 with $NaBH_4$ while the shell was deposited by galvanic displacement on the surface of Y nanoparticles. The presence of Pt in the core was proved by XRD. TEM micrographs have showed highly dispersed nanoparticles with an average 2 nm. The presence of Y and Pt on 81 and 19 wt. % respectively was confirmed by EDAX. The electrochemical performance of Y@Pt/C is evaluated by cyclic voltammetry, CO stripping and using rotating disk electrode setup, was carried out for the ORR in HClO4 electrolyte; indicated that have more catalytic activity than that of commercial 20% Pt / C-Etek® catalyst, used as reference.

Keywords: Y@Pt / C; ORR; core-shell.

1. Introduction

Fuel cells offer a potentially cleaner and more efficient source of energy due to their high efficiency and low emissions compared with internal combustion engines and other energy-conversion devices. However, two major technical gaps limit their commercialization: cost and reliability. Currently, platinum (Pt)-based catalysts and their corresponding cathode catalyst layers are among the major causes of limited performance and high cost for proton exchange membrane fuel cells (PEMFC), although these are the most promising and practical fuel cell catalysts [1].

In a PEM fuel cell, the major limit on performance is the cathodic oxygen reduction reaction (ORR). The cathode of the fuel cell is the electrode where oxygen is reduced to water by the following reaction, known as the oxygen reduction reaction (ORR):

$$O_2 + 4H^+ + 4e^- \rightarrow 2H_2O \text{ (1.23 V vs. NHE [2])} \quad (1)$$

This reaction is slow, for that reason Pt is used as a catalyst, and requires a large overpotential before reaction kinetics increase. Consequently, developing alternative catalysts to Pt for the ORR in PEMFC is a major goal for researchers and a necessity for the commercialization of fuel cells.

Numerous efforts have been devoted to the optimization of the existing platinum nanoparticle catalysts and to the design of new catalysts with less Pt. In addition to nanoparticles morphology control, recent research has also focused on fabrication of multicomponent metal catalysts to modify the Pt electronic structure affected by the second transition metal with the improvement in the catalytic activity for the ORR [3]. Some studies have shown good catalytic activity for the ORR in metals and alloys in compared with Pt [4] [5] [6] [7]. For this reason in this work was decided to synthesize a core-shell Y@Pt catalyst in 80:20 wt. % Y: Pt for the ORR.

2. Experimental

2.1 Catalyst synthesis

Vulcan carbon was heat treated at 500 ° C for 2h under N_2. Subsequently 300 mg of it is heat treated carbon added 50 mL of 50% HNO_3 and sonicated for 1 h, over this were refluxed for 1h. It was dried at 120° C for 1 h in N_2 atmosphere. The acid treated carbon was dispersed in 50 mL of water and added ethanolamine in 1:1 molar ratio was allowed 1h to reflux. It was dried at 120 ° C for 1 h in N_2 atmosphere.

Yttrium nanoparticles were synthesized by the borohydride reduction method in ethanol. 200 mg of treated carbon were mixed with YCl_3 (nominal weight C:Y ratio 70:30), and in 1:1 molar ratio TBAB:YCl_3 in 70 mL of ethanol. The mixture was sonicated 10 min and magnetically stirred during 20 min in a N_2 atmosphere.

Then, $NaBH_4$ (in the molar ratio 3.3:1 $NaBH_4$:Y) dissolved in 20 mL of ethanol was added drop by drop to promote the reduction, and was left 1 hour, then are added 10 mL of H_2O.

2 mL of K_2PtCl_6 (nominal weight Y:Pt ratio 80:20) dissolved in 30 mL of water was added, and subsequently the temperature is increased to boiling. Once at reflux is added drop by drop the remaining solution. He left in 4h reaction. Was separated by centrifugation and washings were performed with water. Finally dried at 150 ° C for 2 hours in CO atm.

2.2 Electrochemical measurement

The electrochemical measurements were conducted at 25°C in a typical three electrodes cell filled with 0.1 M $HClO_4$ electrolyte solution. Disk potential was controlled with a potenciostato /galvanostat (PARSTAT model 2273). A Pt mesh was used as counter-electrode and the potentials were determined using a freshly prepared reversible hydrogen electrode (RHE).

Catalyst inks were prepared as follows: 12 mg of the corresponding Y@Pt/C catalyst (2 nm) and 2mL of solution of 20% isopropanol and 0.02% Nafion ionomer (5 % wt.) were dispersed ultrasonically. 10 µL of the catalyst ink was added onto a polished glassy carbon electrode and the film was dried by air flow at 45°C leading to a Pt loading of 18 $\mu g_{Pt}\ cm^{-2}$. The CV curves of these catalysts were recorded in deaerated electrolyte solution at a sweep rate of 50 mV s^{-1} between 0.05 V and 1.2 V until a stable voltammogram was recorded (around 30 cycles).

The ORR polarization curves for the RDE in an O_2-saturated 0.1 M $HClO_4$ solution at 25°C were obtained at a sweep rate of 20 mV s^{-1} through a positive sweep at rotation rates of 400, 900, 1600 and 2500 rpm. Additionally, the CO-stripping charge was used to determine the electrochemical surface area (ECSA). For CO stripping measurements, the catalyst surface was previously saturated with CO by bubbling CO through the electrolyte solution polarizing the electrode at 0.1 V/RHE for 5 min. Then the remaining CO was purged by flowing N_2 for 10 min before measurements which were performed at scan rate of $20mVs^{-1}$.

2.3 X-ray diffraction (XDR)

Crystal structure identification was performed by X-ray diffraction (XRD) using a diffractometer (PAN-analytical R&D Empyrean) whit monochromatic Cu-Kα radiation (λ= 1.5405 Å) in a 2θ range from 5° to 90°.

2.4 High resolution transmission electron microscopy (HRTEM)

Particle size, morphology and distribution of the Y@Pt nanomaterial were assessed from high resolution transmission electron microscopy (HRTEM) from JEM ARM200F instrument operated at an accelerated voltage of 300 kV. Y@Pt nanoparticle size distribution was calculated based on random counting of particles from TEM with image J software.

2.5 Scanning electron microscopy (SEM) and energy dispersive X-ray analysis (EDX)

Secondary electron images and the elemental mapping of the Y@Pt catalysts were determined by the EDX technique coupled to a scanning electron microscopy by AURIGA-39-16 applying 10 kV.

3. Results and discussion

3.1 X-ray diffraction (XDR)

The Fig. 1 shows XRD pattern for Y@Pt after removing the background. The results reveal that there are defined peaks characteristic diffraction inorganic sample plus they are wide, which allows qualitatively interpret that is materials of small crystallite sizes. This pattern show metallic Pt phase, besides Pt_3Y phase which has a positive displacement of the diffraction angles which is qualitatively rationalize with a tension process caused by the compression of the lattice crystal of Pt in Pt_3Y phase because platinum attempts to adopt the Y structure during the galvanic replacement [8]. A compact Pt surface layer with moderate lattice contraction seemingly is a common structural feature that enhances the ORR activity [9]. Additionally the phase of pure yttrium is not shown because it is at the center of the particle, which is covered with platinum.

The presence of a maximum width at low diffraction angles (24-26 °) associated with the carbon used as support was observed. Finally the quantitative phase analysis reveals the presence of Pt and C in the relative weight fraction of 2.3 and 97.7 wt. %

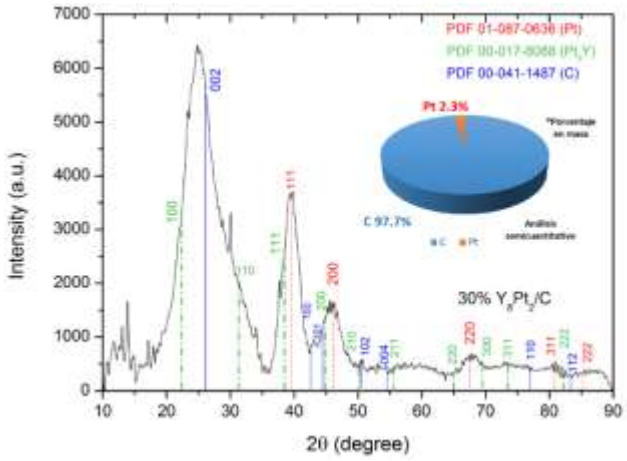

Fig. 1 XRD two theta scan after background subtractions for samples Y@Pt/C

3.2 High resolution transmission electron microscopy (HRTEM)

Fig. 2 shows representative images of low and high magnification transmission micrographs for Y@Pt/C, showed nanoparticles with cubeoctahedron like shape, well distributed and rather uniform on carbon. The histogram for particle size distribution, includes analysis of several different regions of the catalysts, revealed that the average particle size is ca. 2 nm with a very small size distribution with particles from 1-5 nm. Additionally you can see the lattice of particle in uniform form.

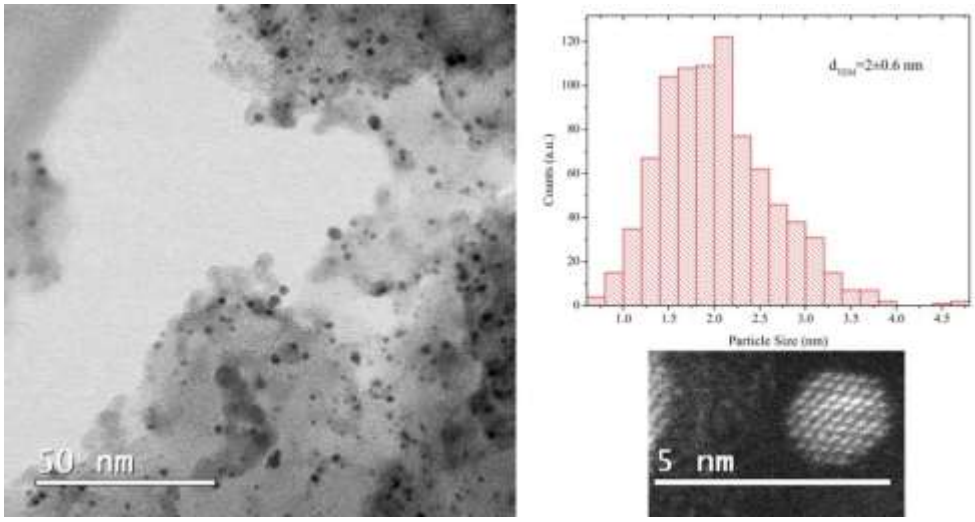

Fig. 2 High resolution TEM image of Y@Pt/C nanocatalyst.

3.3 Scanning electron microscopy (SEM) and energy dispersive X-ray analysis (EDX)

Fig. 3 shows images of the elemental EDX mapping on the sample, the results suggested a uniform Y and Pt elemental phase distribution. Note that these percentages are close to the theoretically estimated during synthesis of materials.

3.4 Electrochemical measurement

The catalysts were electrochemically characterized by cyclic voltammetry (CV). Figure 4A shows the cyclic voltammograms of Y@Pt/C. The curves showed three different potential regions. The hydrogen underpotential deposition domain (Hupd) were well defined, between 0.05 and 0.35 V. The voltammetry curves for the Y@Pt catalyst did not revealed anodic current associated to oxidation/dissolution of Y, demonstrating that the core of Y is completely covered by the Pt Shell.

The potential range between 0.4 V and ~ 0.75 V correspond to "double layer" region. The presented width peak here observed was attributed to the quinone/hydro-quinone equilibrium owing to the carbon support [10]. Above 0.8 V corresponding to OH adsorption area, during the positive sweep and then subsequent reduction in back sweep took place.

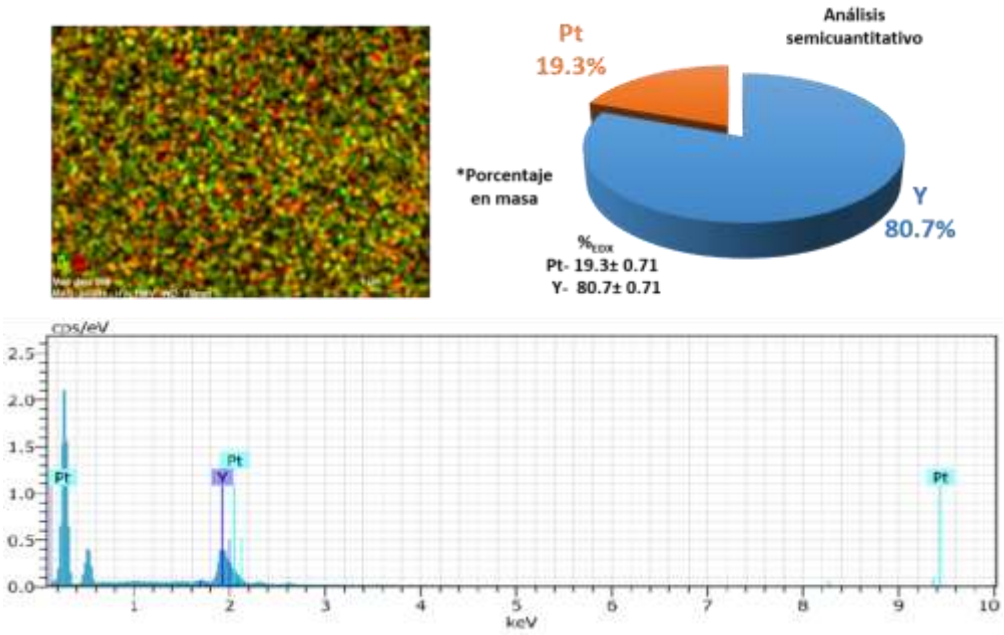

Fig. 3 Images of the elemental phase distribution of Y and Pt obtained by EDX mapping

Fig. 4B, shows the corresponding CO_{ad} stripping curves, after second scan subtraction previously cycled

30 times between 0.5 V and 1.2 V. CO electro-oxidation was used to determine the specific surface area from the normalized curves, considering the charge takes to oxidized the pre-adsorbed monolayer of CO, The charge of full coverage for clean polycrystalline Pt is Q_{CO}= 420 μC cm^{-2} and is used as the conversion

factor. The Pt electrochemical surface area ($ECSA_{Pt,cat}$) is reported in $m^2\ g_{Pt}^{-1}$; L_{Pt} is the working electrode Pt loading ($mg_{Pt}\ cm^{-2}$) and A_g (cm^2) is the geometric surface area of the glassy carbon electrode (i.e., 0.196 cm^2). According to the equation (2) given the ECSA for Y@Pt of 66.41 $m^2\ g_{Pt}^{-1}$, higher than reported for platinum [11]

$$ECSA_{Pt,Cat}\ (m^2 g_{Pt}^{-1}) = \left[\frac{Q_{CO}\ (C)}{420\mu C cm^{-2} L_{Pt}(mg_{Pt}\,cm^{-2}) A_g(cm^2)}\right] 10^5 \quad (2)$$

After CV characterization, the catalysts were evaluated using RDE technique for assessing their electrocatalytic activity and stability for ORR. The Fig. 5A shows a typical set of polarization curves for the ORR on Y@Pt. By starting at 1.05 V and scanning the electrode potential negatively, a mixed kinetic-diffusion control region between $0.85 \leq E \geq 0.95$ V is followed by a defined diffusion-limiting current bellow 0.85 V. The Y@Pt sample showed half-wave potential of $\Delta E_{1/2} = 0.90$ V with a small positive shift compared with platinum $\Delta E_{1/2} = 0.89$ V [11]. In addition to be close to values previously reported in Y-Pt alloys [12][13][14].

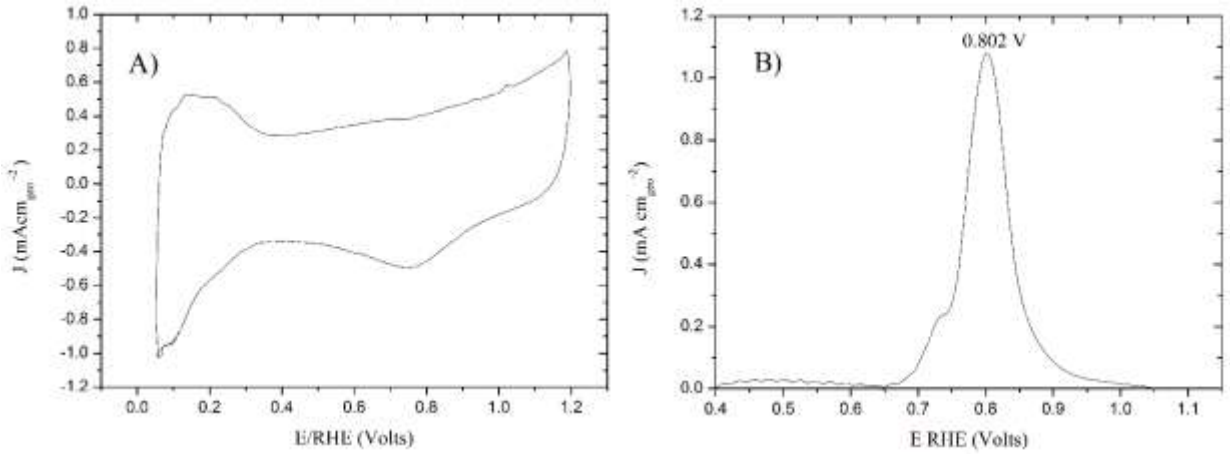

Fig. 4 (A) Base voltammograms on N_2-purged (B) CO_{ad} stripping voltammograms on Y@Pt nanoparticles. The voltammograms were carried out in 0.1 M $HClO_4$ at room temperature and scan rate of 20 mV s^{-1}.

The Fig. 5B, shows the Tafel plots for the mass transport corrected surface specific current density, obtained from the negative sweep direction at 1600 rpm using Eq (3) in potentials between $0.85 \leq E \geq 0.95$ V.

$$J_k = \frac{J_L J}{J_L - J} \quad (3)$$

Tafel slope is shifted positively with respect to Pt (not shown), showing a noticeably activity increase.

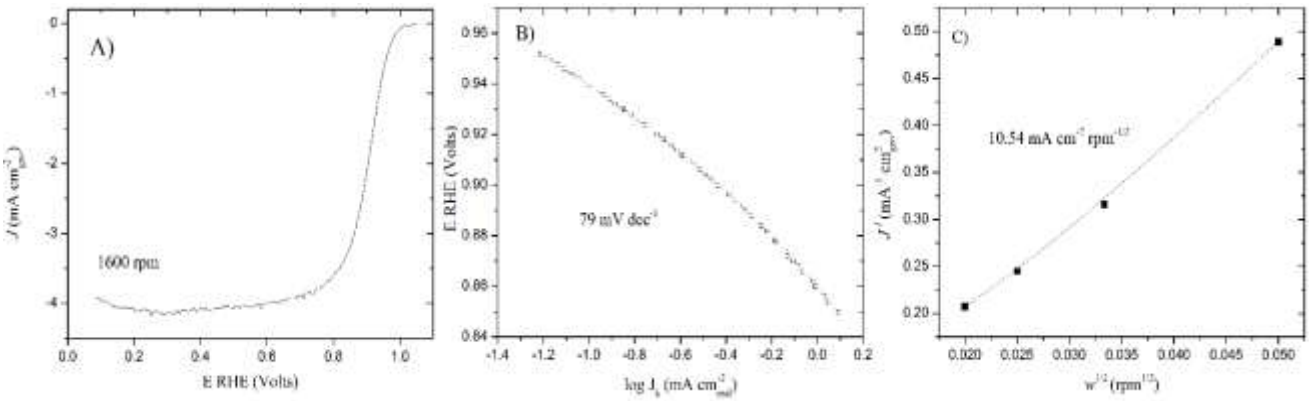

Fig. 5 (A) Steady-state polarization curves for the ORR, and (B) mass-transfer corrected Tafel plot (C) Kouteckye-Levich plots in O_2 saturated 0.1 M $HClO_4$.

Fig. 5C shows the inverse of the overall limiting current density (J^{-1}), as a function of the inverse square root of the rotation rate ($w^{-1/2}$), known as Kouteckye-Levich plot Ec (4).

$$\frac{1}{J} = \frac{1}{J_k} + \frac{1}{J_L} + \frac{1}{J_f} = \frac{1}{J_k} + \frac{1}{Bw^{1/2}} \qquad (4)$$

The linear relation between J^{-1} vs $w^{-1/2}$, in the plot indicated a first order kinetic and in agreement with the theoretical slope value, i.e. $B_0 = 12.63 \times 10^{-2}$ mA cm^{-2} rpm$^{-1/2}$, calculated considering a four-electron transfer process leading to water formation, i.e., $O_2 + 4H^+ + 4e^- \rightarrow 2H_2O$.

The most relevant results are summarized in Table 1.

Table 1. Values of kinetic parameters for the ORR on Pt and Y@Pt at 20 mV^{s-1}.

Electrode	$E_{1/2}$ (mV)	ECSA $m^2\ g_{Pt}$	$B_0 \times 10^{-2}$ (mA/cm^2 rpm$^{1/2}$)	Tafel slope (mV/dec)[a]	$J_{k0.9}$ (mA/cm$^2_{Pt}$)	$J_{m0.9}$ (mA/mg$_{Pt}$)
Pt	0.89 [c]	61	13.7 [b]	88.7[b]	0.347 [c]	210 [c]
Y@Pt [d]	0.90	66	10.54	78.6	0.365	229

[a] Tafel slope were obtained between 0.9 - 0.8V for Pt and .95-.85V for Y@Pt. [b] Data taken from [15] in 0.5 M H_2SO_4 [c] Data taken from [11] [d] Datas in 0.1 $HClO_4$.

4. Summary and perspectives

Well defined carbon supported Y@Pt core-shell nanocatalysts with around 2 nm size were synthesized through chemical reduction and galvanic replacement.

X-ray diffraction for the catalyst sample showed phases of Pt3Y, Pt and Carbon with composition relative of two phases assigned to metallic Pt and C in the relative weight fraction of 2.3 wt% and 97.3 wt. %, respectively. The change in the reflection profile suggests a strong interaction between Pt and Y which resulted in a Pt lattice contraction and a possible lattice expansion for Y. The CV in the O_2 free electrolyte resembled that of pure Pt and confirms a complete Pt shell covering Y-core. The Y@Pt shows an ECSA of 66 m^2 g_{Pt}. The RRDE measurement shows a catalytic activity enhancement with respect to pure platinum.

Acknowledgements

This work was supported by CONACYT (grant FOINS/75/2012). The authors gratefully acknowledge to University of Texas TAMU for the TAMU-CONACYT project (Alloy nanocatalysts for fuel cell electrodes). The authors gratefully acknowledge also to Josue E. Romero Ibarra and Daniel Bahena Uribe for the support in the SEM and TEM. Techniques and José Luis Reyes-Rodríguez for their support in the development of this work.

References

[1] C.W.B. Bezerra, L. Zhang, K. Lee, H. Liu, A.L.B. Marques, E.P.Marques, H. Wang and J. Zhang, A review of Fe–N/C and Co–N/C catalysts for the oxygen reduction reaction. Electrochimica Acta 2008; 53:4937-4951.

[2] P.H. Matter, L. Zhang and U.S. Ozkan, The role of nanostructure in nitrogen-containing carbon catalysts for the oxygen reduction reaction. Journal of Catalysis 2006; 239: 83-96.

[3] V. Mazumder, M. Chi, K.L. More and S. Sun. Core/Shell Pd/FePt Nanoparticles as an Active and Durable Catalyst for the Oxygen Reduction Reaction. J. Am. Chem. Soc. 2010; 132:7848-7849.

[4] V.R. Stamenkovic , B. Fowler, B.S. Mun, G. Wang, P.N. Ross, C.A. Lucas, N.M. Markovic, Improved oxygen reduction activity on Pt3Ni(111) via increased surface site availability. Science 2007; 315:493-497.

[5] J.K. Nørskov, J.Rossmeisl, A. Logadottir, L. Lindqvist, J.R. Kitchin, T. Bligaard, et al. Origin of the overpotential for oxygen reduction at a fuel-cell cathode. J. Phys Chem B 2004; 108: 17886-17892.

[6] J. Zhang, M.B. Vukmirovic, K. Sasaki, A.U. Nilekar , M. Mavrikakis and R.R. Adzic, Mixed-metal Pt monolayer electrocatalysts forenhanced oxygen reduction kinetics. J Am Chem Soc 2005; 127:12480-12481.

[7] V.R. Stamenkovic, B.S. Mun , M. Arenz, K.J.J. Mayrhofer, C.A. Lucas, G. Wang, et al. Trends in electrocatalysis on extended and nanoscale Pt-bimetallic alloy surfaces. Nat Mater 2007; 6:

241-247.

[8] J.L. Reyes-Rodríguez, F. Godínez-Salom+on, M.A. Leyva and O. Solorza-Feria, RRDE study on Co@Pt/C coreeshell nanocatalysts for the oxygen reduction reaction, International journal of hydrogen energy 2013; 38: 12634-12639.

[9] J.X. Wang, H. Inada, L. Wu, Y. Zhu, Y. Choi, P. Liu, W.P. Zhou and R.R. Adzic,Oxygen Reduction on Well-Defined Core-Shell Nanocatalysts: Particle Size, Facet, and Pt Shell Thickness Effects, J. Am. Chem. Soc. 2009; 131: 17298-17302.

[10] J. Maruyama, I. Abe, Influence of anodic oxidation of glassy carbon surface on voltammetric behavior of Nafion®-coated glassy carbon electrodes, Electrochimica Acta 2001;46: 3381–3386.

[11] Y. Garsany, O.A. Baturina, K. E. Swinder-Lyons and S.S. Kocha Experimental Methods for Quantifying the Activity of Platinum Electrocatalysts for the OxygenReduction Reaction Anal. Chem. 2010; 82: 6321–6328.

[12] S.J. Yoo, K.S. Lee, S.J. Hwang, Y.H Cho, S.K. Kim, J.W. Yun, Y.E. Sung and T.H. Lim Pt3Y electrocatalyst for oxygen reduction reaction in proton exchange membrane fuel cells, International journal of hydrogen energy 2012; 37: 9758-9765.

[13] S.J. Hwang, S.K. Kim, J.G. Lee, S.C. Lee, J.H. Jang, P. Kim, et. al. Role of Electronic Perturbation in Stability and Activity of Pt-Based Alloy Nanocatalysts for Oxygen Reduction, Journal of the American Chemical Society 2012; 134:19508-19511.

[14] J. Greely, I.E.L. Stephens, A.S. Bondarenko, T.P. Johansson, H.A. Hansen, T.F, Jaramillo, J. Rossmeisl, I. Chorkendorff and J.K. Norskov Alloys of platinum and early transition metals as oxygen reduction electrocatalysts Nature Chemistry; 1:552-556.

[15] F.Godínez-Salomón, M.Hallen-López and O. Solorza-Feria,Enhanced electroactivity for the oxygen reduction on Ni@Pt core-shell nanocatalysts, International journal of hydrogen energy 2012; 37: 14902-14910.

NiO@Pt/C Core-Shell Nanocatalyst for Oxygen Reduction Reaction

D. Vega-Villalobos[1], F. Godínez-Salomón[1], J. L. Reyes-Rodríguez[1], L. Lartundo-Rojas[2], O. Solorza-Feria[1*].

[1]Departamento de Química, Centro de Investigación y Estudios Avanzados del IPN, Av. IPN 2508, Col. San Pedro Zacatenco, A. Postal 14-740, 07360 México D.F., México.[2]Centro de Nanociencias y Micro y Nanotecnologías-IPN, UPALM, Col. San Pedro Zacatenco; A. Postal 07738 México D.F., México.
[*]Tel: 011 +52 +55 5747-3715 ; e-mail: osolorza@cinvestav.mx

ABSTRACT

In this work, we present the synthesis, as well physical and electrochemical characterization of the nickel oxide supported in Ketjenblack carbon decorated platinum core-shell nanocatalyst for the oxygen reduction reaction (ORR) in acid media. The core was synthesized by chemical reduction with $NaBH_4$ of $Ni(NO_3)_2.6H_2O$, while the shell was deposited by galvanic displacement on the surface of Ni nanoparticles. The presence of Pt in the core was proved by XRD. On the other hand, TEM micrographs have showed highly dispersed nanoparticles with an average between 2-20nm. The presence of Ni and Pt on 71 and 29 wt. % respectively was confirmed by EDAX while XPS and Raman spectroscopy confirms the presence of NiO. The electrochemical performance of NiO@Pt/C is evaluated by cyclic voltammetry, CO stripping and using rotating disk electrode setup, was carried out for the ORR in HClO4 electrolyte; indicated that have more catalytic activity than that of commercial 20% Pt / C-Etek® catalyst, used as reference.

Keywords: NiO:Pt core-shell nanoparticles; oxygen reduction reaction, electrochemical analysis.

1. Introduction

Increasing energy demands have stimulated intense research on alternative energy conversion and storage systems with high efficiency, low cost and environmental benignity. That's why has generated substantial interest in electrochemical energy conversion, particularly in fuel cells and therefore has generated vigorous investigation of the oxygen reduction reaction (ORR) on a wide range of materials Pt-based [1-2].

One important part of the fuel cells is the catalysts, but Pt is expensive and increases the price of this. The proposed is reducing the amount of the noble metal, therefore Pt-alloyed with various transition metals are employed to further improve the electrocatalytic activity of ORR and reduce the cost of electrocatalyst. So the responsible for the surface catalytic reactivity might be at on reduced Pt-Pt distance near the particle surface stabilized by the lattice contracted alloy core, i.e. the presence of transition metal located within the core due to the structure and electronic effects caused by the partial alloying and vacant d-orbital from the transition metal, and the dissolution of the transition metal is expectably reduced due to the protection by Pt on the shell [3-6].

An ideal electrocatalysts for ORR would be capable of activating molecular O_2 while at the same time not binding oxygen intermediates, O*, OH* and OOH*, so strongly as to inhibit their reduction to water[7]. The ORR on Pt and Pt-family metals occurs by the parallel mechanism following predominantly a direct four-electron reduction (see Fig. 1); little hydrogen peroxide is generated, particularly when some adventitious impurities contaminated the electrode surface [6-8].

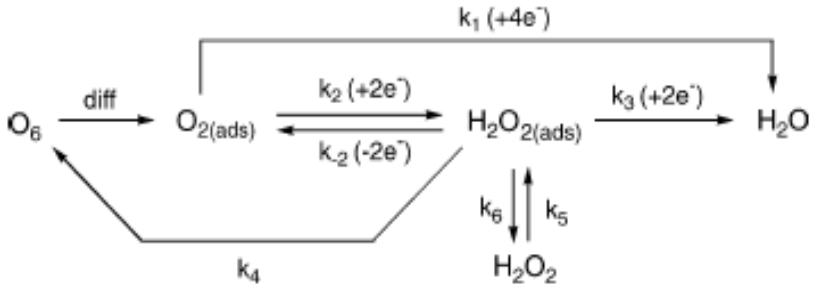

Fig.1 Reaction Mechanism of the ORR, taken from the reference [8].

There were many reports on the fabrication of core–shell particles, such as electrochemical method, electroless plating, layer-by-layer deposition, laser pulses, self-assembly, chemical reduction, microwave synthesis, sonochemical method, decomposition of organometallic precursors and photoreduction [9].

2. Experimental

2.1. Material synthesis.

The electrocatalytic material was synthesized by modified Bönnemann procedure [10]. First the precursor salt $Ni(NO_3)_2$* $6H_2O$ and the capping agent Tetrabutyl ammonium hydroxide (TBAOH) in

molar ratio 1:1, were dissolved in 60 ml of ethanol and magnetically stirred during 19 h at room temperature. Then the agent reduction $NaBH_4$ in molar ratio 1:6 with respect at precursor; dissolved in 40 ml of ethanol was added drop by drop, using a ultrasonic lance, with the potency of 20kHz ±50 Hz and with a period of 30 seconds ON and 10 seconds OFF for 90 minutes. The core was supported on carbon Ketjenblack, estimating a 50% metal loading expressed as a weight. The NiO@Pt/C core-shell catalyst was prepared by galvanic replacement, mixing Ni:Pt ratio of 85:15. [11-12]

2.2. Electrochemical characterization

The electrochemical measurements were conducted at room temperature in a typical three electrodes cell filled with 0.1M $HClO_4$ electrolyte solution; using a rotating disk electrode (RDE) setup with a potenciostat /galvanostat (PARSTAT model 2273). The electrochemical cell and the working electrode were prepared according to Garsany et al. [13] Nominal Pt loading around 23 µg cm^2_{geo} were used. In the cyclic voltammetry the potential was cycled between 0.05 V and 1.2 V to obtain a stable voltammogram in a nitrogen-saturated 0.1M $HClO_4$. Electrochemical surface area was determinate by Co stripping techniques according to Markovic et al. [14]. Using the thin.-film disk electrode method [11-12,15], were determined of the parameters kinetic for the ORR. For this, the solution electrolyte was saturated with oxygen; the measurement was performed in a backward manner from 1.05 V to 0.05 V at 20 mV s^{-1}, maintaining the starting potential during 50 seconds before scanning.

2.3 X-ray diffraction

Crystal structure identification was performed by X-ray diffraction (XRD) using a diffractometer (PAN-analytical R&D Empyrean) whit monochromatic Cu-Kα radiation (λ= 1.5405 Å) in a 2θ range from 5° to 100°. Was analyzed the diffractogram using the Match 2 software.

2.4 Transmission electron microscopy (TEM)

Particle size, morphology and distribution were evaluated through transmission electron microscopy (TEM) using a JEM ARM200F instrument operated at an accelerated voltage of 300 kV. Nanoparticles size distribution was calculated based on a random counting of particles using the Image J software.

2.5 Energy dispersive X-ray analysis (EDAX)

The elemental mapping of the NiO@Pt catalysts were determined by the EDAX technique coupled to a scanning electron microscopy by AURIGA-39-16 applying 10 kV.

2.6 Raman spectroscopy

Raman spectra were recording using a Lap Ram HR800, Horiba Join Yvon, with a beam aperture of Pinhole of 400µm and 150 µm of Slit. The spectra are measurement from 0 to 4500 cm^{-1}.

2.7 X-ray photoelectron spectroscopy (XPS)

The XPS analyses were carried out with a Kratos Axis Ultra spectrometer using a monochromatic Al Kα source (*hv* = 1486.6 eV). The signal C1s was used with reference for the analyses. For the deconvolution of the spectra, was used the free program XPS Peak Fit 4.1.

3. Results and discussion

3.1 Physical characterization

3.1.1 X-ray diffraction (XRD)

Fig. 2 displays the XRD-pattern for the NiO/C, the core-shell NiO@Pt and PtC-Etek® catalysts, the last used as reference. The samples exhibited high background intensity indicating a portion of highly disordered material by the presence of amorphous carbon and small particle size. The wide peak at 25.12 ° observed in all samples, was ascribed to the hexagonal carbon plane (003) (PDF-01-075-0444-red). The PtC-Etek® shows peaks related to reflection of Face Cubic Center (FCC) crystal structure from metallic Pt (light-green). For the NiO/C sample, were characterized at least two phases: metallic nickel in FCC structure (black) and α-$Ni(OH)_2$ (Blue). We assume that the presence of α-$Ni(OH)_2$ is related to the reaction of Ni with ethanol during the synthesis. On the other hand, the core-shell sample (NiO@Pt), showed well separate diffraction peaks related to those phases from the core and Pt. This feature suggests a strongly phase segregation, which is consistent with that expected for a core-shell structure. The last, agree with that obtained by electrochemistry (see below), where the presence of Ni species on the surface of nanoparticles, characterized by an oxidation peak around 0.4 V was not observed, instead, only a profile related to Pt was observed. This condition together with XRD observation, make us suppose that nanoparticles with high Pt surface segregation were obtained.

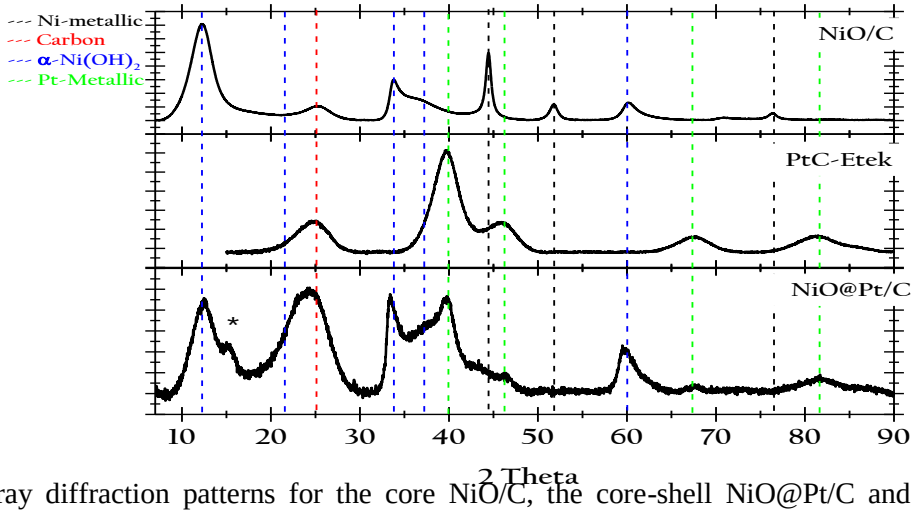

Fig. 2 X-ray diffraction patterns for the core NiO/C, the core-shell NiO@Pt/C and commercial PtC-Etek®. Dashed lines were depicted to clarify the interpretation of different patterns.

3.1.2 Transmission electron microscopy (TEM)

Fig. 3 shows representative low-magnification micrographs and the histograms with the mean particle size distribution determined after evaluation on several regions of the grid. The Fig. 3a depicts dark field scanning transmission electron micrograph (ADF-STEM) for PtC-Etek® catalysts. The Fig. 3b shows a common transmission electron image for NiO@Pt/C. The analysis for both catalysts exhibited spherical morphology with very narrow size distribution for PtC-Etek® 2.45 ± 0.5 nm, however even when the image for NiO@Pt/C shows well distribution 1.73±0.52 nm, they were also found some agglomeration which were not considered during particle size determination, owing to difficulty it implies.

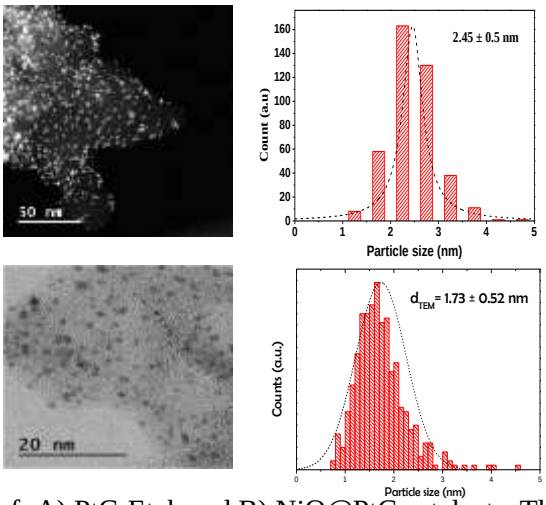

Fig. 3 TEM micrograph of: A) PtC-Etek and B) NiO@PtC catalysts. The histograms show the particle size distribution from several different regions.

3.1.3 Energy dispersive X-ray analysis (EDAX)

Fig. 4a shows images of elemental EDAX mapping on NiO@Pt/C sample. Results suggested a uniform Ni and Pt elemental phase distribution. The amount of Pt obtained was approximately double respect to initially proposed, this to due to impurities of catalysts such as oxides in the core. The oxygen and nickel present in the core have a uniform elemental phase distribution (see Fig. 4b). In the Table 1 are summarized of results real and theoretical of the elemental phase Ni and Pt for the core-shell, and for the core, elemental phase Ni and O_2.

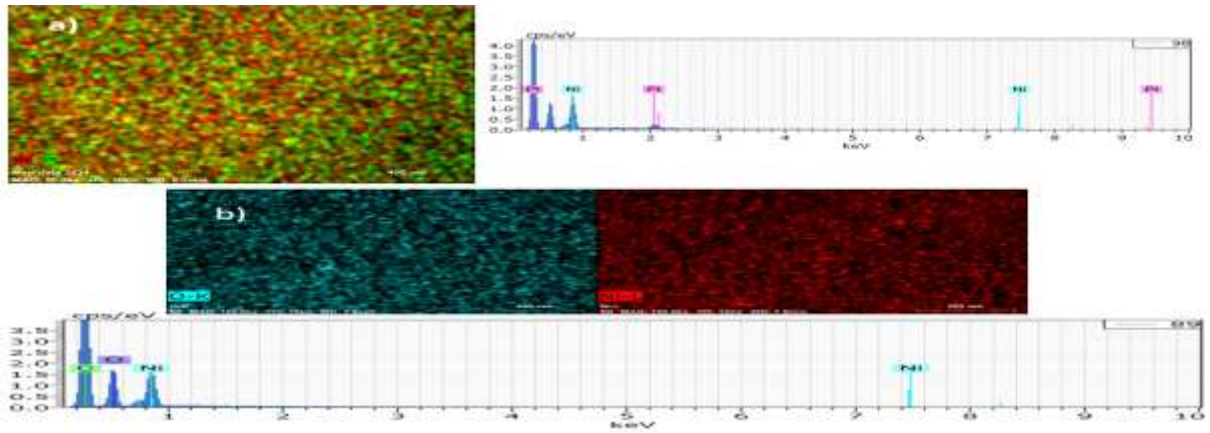

Fig. 4 EDAX mappings of NiO@Pt/C and NiO/C samples: a) Ni and Pt elemental phase distribution, b) Ni and O_2 elemental phase distribution respectively

Table 1 EDAX results real and theoretical of the elemental phase Ni and Pt for the core-shell, and for the core, elemental phase Ni and O2

Sample	EDAX		Theoretical	
NiO@Pt/C	Ni	Pt	Ni	Pt
	70.72±4.4%	29.28±4.4%	85%	15%
NiO/C	Ni	O_2	Ni	O_2
	47.53±2.4%	52.46±2.4%	90%	10%

3.1.4 Raman spectroscopy

Fig. 5 shows the Raman spectra of NiO@Pt/C, was observed that bands of 433 cm^{-1}, 518 cm^{-1} and 1065 cm^{-1} are associated with NiO [16-17]; for the great content support (carbon) the band 1065 cm^{-1} is overlapped. For the carbon, the principal bands are the D, G and 2D at 1330 cm^{-1}, 1595cm^{-1} and 2678-2886 cm^{-1} respectively. The D band represents the amorphous carbon part, the G band is the crystalline part, and the 2D band is the doublet was explained by the 3D graphitic ordering of the crystallites. [18]

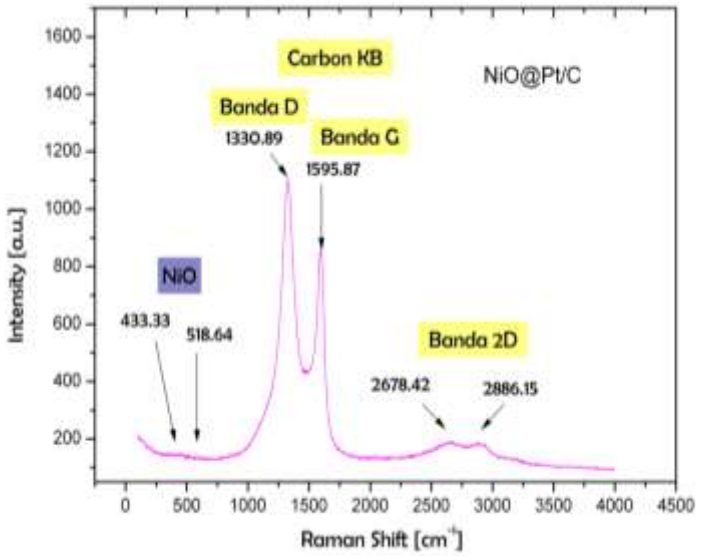

Fig. 5 Raman spectra of NiO@Pt/C

3.1.5 X-ray photoelectron spectroscopy (XPS)

NiO@Pt/C XPS general spectral revealed that the chemical species involucrate (Ni, Pt, C and O_2) as shown in Fig. 6; for this were realized the high resolutions spectra of the Ni 2p, Pt4f, C1s and O1s (Fig. 7). The Shirley method was used for deconvolution of spectra; in the Ni2p XPS spectra was obtained 6 species: the Ni metal, NiO, NiOH (located at 852.3±0.2eV, 853.69±0.2eV and 855.5±0.2eV) and the satellites respectively (located at 858.1±0.2eV, 860.83±0.2eV and 864±0.2eV), the major Ni specie for this case is oxide state; indicating that the core has a thick overlying the nickel metal [19-21]. The Pt4f XPS spectra has a overlapped Ni3p signal therefore the name of this spectra is Pt4f-Ni3p, was obtained 6 species: the Ni metal, NiO, Pt metal, $Pt(OH)_2$ (located at 67.75±0.2eV, 69.2±0.2eV, 71.19±0.2eV and 72.02±0.2eV respectively) and the satellites for the Ni metal and NiO (located at 72.75±0.2eV and 77.8±0.2eV). The Ni specie indicating an interaction with the Pt, the ratio between Ni and Pt is according at so mentioned EDAX. The $Pt(OH)_2$ is referent at hydration of the ambient, this specie overlying the nanoparticles has in minor proportion[22]. For the C1s XPS spectra was obtained 5 contributions: three functional groups (C-O, COH at 286.17±0.2eV and COOH at 288.34±0.2eV), two carbon atoms in different hybridized states (sp2 at 284.44±0.2eV and sp3 at 285.03±0.2eV) and one transition state (π-π^* at 290.7±0.2eV), if has a hybridized state sp2 the transition π-π^* is present, the presence of sp3 indicates the presence of defects in the graphitic structure and finally the presence of functional groups is due to chemical and physical activation [23]. The results proposed in O1s XPS spectra may be oxide species (530.27±0.2eV), hydroxide species (531.89±0.2eV) and absorbed water along with C-O bond (534.39±0.2eV).[19,21]

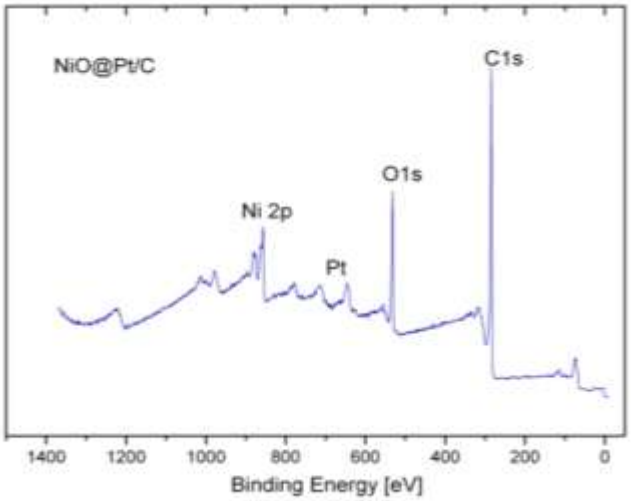

Fig. 6 XPS general spectra of NiO@Pt/C

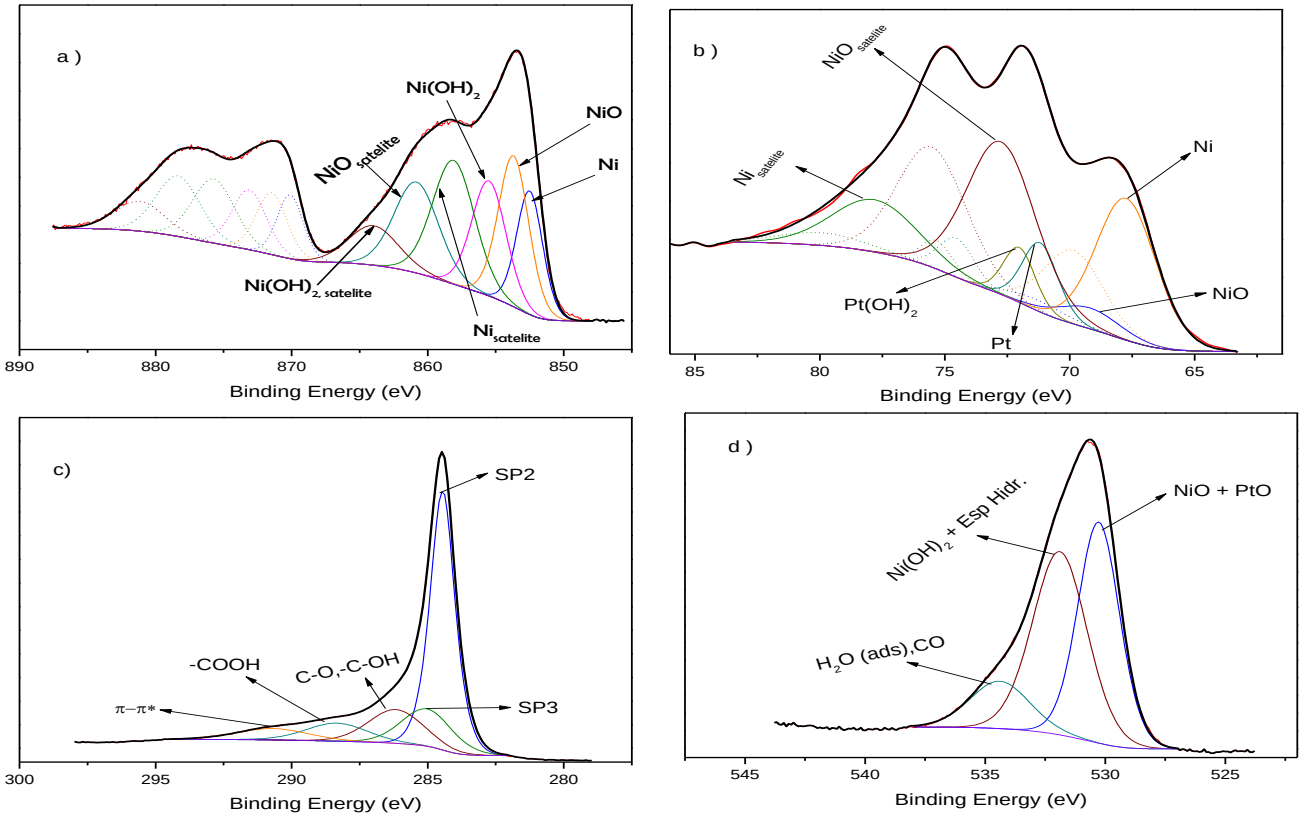

Fig. 7XPS high resolution spectra of NiO@Pt/C sample: a) Ni 2p spectra, b)Pt 4f-Ni 3p spectra, c) C1s spectra, d) O1s spectra

3.2 Electrochemical characterization

The catalysts were electrochemically characterized by cyclic voltammetry (CV) (Fig. 8a). As a systematic procedure, the potential immersion of the working electrode was controlled at 0.1V to avoid possible Ni oxidation during the sample immersion, and then cycled several times between 0.05V and 1.2V until a stable curve was attained. During the first scan was not observed processes assigned to the Ni oxidation, this indicates that the Pt shell completely encapsulate the Ni core. The resolution of the hydrogen adsorption/ desorption region (0.05-0.4V) were not also so well defined and therefore is lower at the Pt features, but this confirms little differences on crystalline surface domain on both catalysts [4,6,11]. In the voltammogram, in the area of the capacitance (localized in the double layer) were observed two peaks associated at process quinine/hydroquinone of the carbon, this process was rationed with the reduction and oxidation of some intrinsic superficial oxide of the carbon black [24-26].

The CO stripping technique was used to determine the specific surface area of the NiO@Pt/C catalysts; considering the charge takes to oxidize the pre-absorbed monolayer of CO is 420μCcm^{-2}[11-12,14]. For CO stripping curves (see Fig. 8b), were recorded in CO-free solution after completely surface saturation by absorbing CO at 0.1V; and cycled several times between 0.5V and 1.2V; the determination of the area was obtained by subtraction of the second sweep. The particle size was calculated by CO stripping as previously reported [27], considering a spherical shape for the catalysts, therefore the particle size estimate was 15.22±2.2 nm. Exist one inconsistency in the particle size determination for this form respect at the other techniques (TEM), because is no takes in consideration the particles agglomeration and/or incomplete stripping of the capping agent during the washing step; by this, exist decreasing the CO adsorption sites in the surface area. Apart the surface analyzed is different for the two cases.

Assessing their electrocatalytic activity for ORR (Fig. 9a) was realized through TF-RDE technique for the catalyst according previously reported Fernando-Godínez et.al [11]. By starting at 1.05 V and scanning the electrode potential negatively, a mixed kinetic-diffusion control region between $0.8 \leq E \leq 0.95$ V is followed by a well defined diffusion-limiting current bellow 0.8 V [11,13,15]. Catalyst electrocatalytic activity towards the ORR is quantified at E= 0.90 V because interferences from mass-transport losses cannot be completely excluded at the higher current densities observed below E= 0.90 V. The electrocatalytic activity of catalysts is best compared by their mass- and area-specific activities using the mass-transport correction for thin-film RDE (equation 1):

$$J_K = \frac{J_L * J}{J_L - J} \qquad (1)$$

The mass-specific activities are estimated via calculation of J_K and normalization to the Pt loading of the disk electrode, and results are summarized in Table 2. The Tafel slopes (Fig. 9b) were fitted the same potential region, and it's important to mention that catalyst was evaluated at least three times even with different electrode Pt loadings to corroborate reproducibility. The values of Tafel slopes were very similar between NiO@Pt/C and Pt-Etek, 81.3mV/dec and 77.71mV/dec respectively. the slight displacement of the Tafel slopes to the right from NiO@Pt/C sample with respect to Pt/C-Etek represents a slight kinetic gain. The inverse of the overall current density (J^{-1}), as a function of the inverse square root of the rotation rate ($\omega^{-1/2}$), known as Koutecky-Levich (equation 2), exist a linear relation between J^{-1} vs. $\omega^{-1/2}$, indicating a first order kinetic of the sample respect to the ORR.

$$\frac{1}{J} = \frac{1}{J_K} + \frac{1}{J_L} + \frac{1}{j_f} = \frac{1}{J_K} + \frac{1}{B\omega^{1/2}} \qquad (2)$$

In agreement with the theoretical Koutecky-Levich slope value, i.e. $B_{th} = 12.63 \times 10^{-2}$ mAcm^{-2} rpm$^{-1/2}$, calculated considering a four-electron transfer process leading to water formation, i.e., $O_2 + 4H^+ + 4e^- \rightarrow 2H_2O$ [11-12-15].

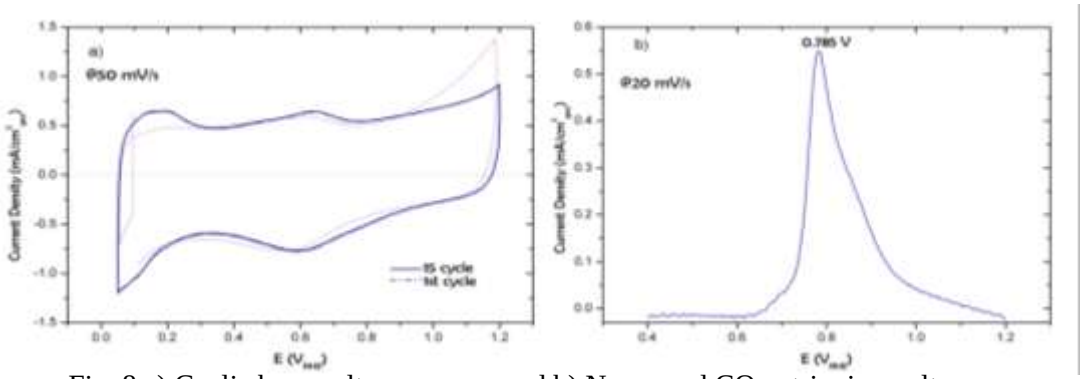

Fig. 8 a) Cyclic base voltammogram and b) N_2-purged CO_{ad} stripping voltammogram of NiO@Pt/C. CV and CO-stripping were carried out in 0.1 M $HClO_4$ at room temperature.

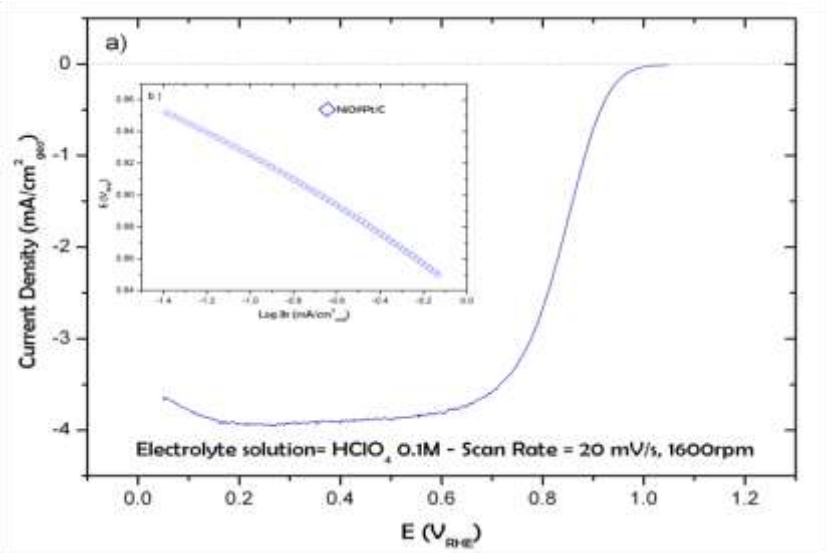

Fig. 9 a) Steady-state polarization curve for the ORR on NiO@Pt/C in O_2 saturated 0.1 M HClO4, b) mass-transfer corrected Tafel plot.

Table 2 Values of kinetic parameters for the ORR on Pt, NiO@Pt/C determined from 1.05 to 0.05 V in negative going sweep at 20 mV s^{-1}. Some data taken from literature are used as reference.

Electrode	$E_{1/2}$ (V)	BC_0 [$mAcm^{-2}{}_{geo}rpm^{-1/2}$]	Tafel slope (mV/dec)	$J_{k0.9V}$ ($mA/cm^2{}_{Pt}$)	$J_{m0.9V}$ (mA/mg_{Pt})	ECSA (m^2/g_{Pt})
Pt	0.89±0.01	0.12±0.004	77.71±9.21	0.21±0.04	180±0.04	77.43±9.59
NiO@Pt/C	0.83±0.01	0.11±0.005	81.43±3.21	0.23±0.04	43.45±2.04	17.63±2.48

4. Summary and perspectives

In summary, well defined and highly disperse NiO@Pt core-shell nanoparticles with size 1.7-15 nm were synthesized by modified Bönnemann procedure using TBAOH as capping agent. XPS, Raman and EDAX showed that the phase present in the core is NiO, but the elemental phase of Ni is present in minor proportion, this indicated that the catalyst is in layers therefore it has form core-shell. The layer or elemental phase that interacts with the Pt is actually the NiO, i.e. Pt-NiO. On the other hand XRD indicate that the NiO, Ni and Pt phases are present, the shifting of Pt reflections to positive diffraction angles indicate that reduced Pt-Pt inter atomic distance on the surface of nanoparticles.

The CV in the O_2 free electrolyte proves that the Pt shell completely encapsulated the Ni core. The electrocatalytic activity of the catalyst has slight kinetic gain for the ORR compared to Pt-Etek under the same measurement conditions; probably this increase is due to the changes in electronic properties of the platinum caused by higher amount of non-noble metal. While the mass activity of ORR is reduced because the particle size that used on the calculations is the obtained by CO stripping. These results reveal that core-shell structure of NiO@Pt could be a good candidate for proton exchange membrane fuel cells.

Acknowledgements

We gratefully acknowledge Ph. D Josue E. Romero, Daniel Bahena and Luis Moreno, for their invaluable assistance in carrying TEM, SEM-EDAX and Raman measurements. The authors acknowledge the support of the National Council of Science and Technology (CONACYT grant FOINS 75/2012) and the University of Texas TAMU-CONACYT project (Alloy nanocatalysts for fuel cell electrodes).

References

[1]Y. Liang, Y. Li, H. Wang, J. Zhou, J. Wang, T. Regier,H. Dai, Co_3O_4 nanocrystals on graphene as a synergistic catalyst for oxygen reduction reaction, ,NATURE MATERIALS, 2011, 10, 780-786

[2] N. M. Markovic´, H. A. Gasteiger, P. N. Ross (Jr.),Oxygen Reduction on Platinum Low-Index Single-Crystal Surfaces in Alkaline Solution:Rotating Ring DiskPt(hkl) Studies, J. Phys. Chem. 1996, 100, 6715-6721

[3]Y. Bing, H. Liu, L. Zhang, D. Ghosh, J. Zhang, Nanostructured Pt-alloy electrocatalysts for PEM fuel cell oxygen reduction reaction, Chem. Soc. Rev., 2010, 39, 2184–2202

[4]G. Wang, H. Wu, D. Wexler, H. Liu, O. Savadogo, Ni@Pt core–shell nanoparticles with enhanced catalytic activity for oxygen reduction reaction, Journal of Alloys and Compounds (2010), 503, L1–L4

[5]D. Jing-Shan,C. Ya-Ting,L. Mei-Hua,Effect of thermal annealing on the properties of Co rich core–Pt rich shell/C oxygen reduction electrocatalyst, Journal of Power Sources (2007), 172, 623–632

[6]L.G.R.A. Santos, C.H.F. Oliveira, I.R. Moraes, E.A. Ticianelli, Oxygen reduction reaction in acid medium on Pt–Ni/C prepared by a microemulsion method,Journal of Electroanalytical Chemistry (2006), 596,141–148

[7]A. Jackson,V. Viswanathan, A.J. Forman,A. H. Larsen,J.K. Nørskov,T. F. Jaramillo ,Climbing the Activity Volcano: Core–Shell Ru@Pt Electrocatalysts for Oxygen Reduction, Chem Electro Chem 2014, 1, 67–71

[8]B. Wang,Review Recent development of non-platinum catalysts for oxygen reduction reaction,Journal of Power Sources 152 (2005) 1–15

[9]H.X. Shen, M.M. Xu, X. Yan, J.L. Yao, S.Y. Han, R.A. Gu, Synthesis and surface enhanced optical properties of multibranched spindle particles and core–shell structures, Colloids and Surfaces A: Physicochem. Eng. Aspects (2010),353 , 204–209

[10]H. Bönnemann,R. M. Richards,Nanoscopic Metal Particles 2 Synthetic Methods and Potential Applications,Eur. J. Inorg. Chem. 2001, 2455-2480

[11]F. Godínez-Salomón, M. Hallen-López, O. Solorza-Feria,Enhanced electroactivity for the oxygen reduction on Ni@Pt core-shell nanocatalysts, international journal of hydrogen energy (2012),37, 14902-14910

[12]J.L. Reyes-Rodríguez, F. Godínez-Salomón, M.A. Leyva, O. Solorza-Feria,RRDE study on Co@Pt/C coreeshell nanocatalysts for the oxygen reduction reaction, international journal of hydrogen energy (2013),38, 12634-12639

[13]Y. Garsany,O.A. Baturina, K.E. Swider-Lyons, S.S. Kocha, Experimental Methods for Quantifying the Activity of Platinum Electrocatalysts for the Oxygen Reduction Reaction Anal. Chem. 2010, 82, 6321–6328

[14]M. Arenz,K. J. J. Mayrhofer,V. Stamenkovic,B. B. Blizanac,T. Tomoyuki,P. N. Ross,N. M. Markovic,The Effect of the Particle Size on the Kinetics of CO Electrooxidation on High Surface Area Pt Catalysts,J. AM. CHEM. SOC. 2005, 127, 6819-6829

[15]U.A. Paulus, T.J. Schmidt, H.A. Gasteiger, R.J. Behm, Oxygen reduction on a high-surface area Pt:Vulcan carbon catalyst: a thin-film rotating ring-disk electrode study,Journal of Electroanalytical Chemistry (2001),495, 134–145

[16]J. Nan, Y. Yang, Z. Lin, In situ photoelectrochemistry and Raman spectroscopic characterization on the surface oxide film of nickel electrode in 30 wt.% KOH solution,Electrochimica Acta (2006), 51, 4873–4879

[17]S.S. Chan, I.E. Wachs,In Situ Laser Raman Spectroscopy of Nickel Oxide supported on y-Al2O3, Journal of Catalysis, 1987, 103, 224-227

[18]N. Larouche, B. L. Stansfield, Classifying nanostructured carbons using graphitic indices derived from Raman spectra, Carbon, 2010, 48, 620-629

[19]M. C. Biesinger, B. P. Payne,L. W. M. Lau,A. Gersonb, R. St. C. Smart, X-ray photoelectron spectroscopic chemical state quantification of mixed nickel metal, oxide and hydroxide systems, Surf. Interface Anal. 2009, 41, 324–332

[20]S.G. Zhang, Y. Hara, S. Suda, T. Morikawa, H. Inoue, C. Iwakura, Physicochemical and electrochemical hydriding-dehydriding characteristics of amorphous $MgNi_x$ (x=1.0, 1.5, 2.0) alloys prepared by mechanical alloying, J Solid Sate Electrochem (2001),5, 23-28

[21]M. C. Biesinger, B. P. Paynec, A. P. Grosvenord, Leo W.M. Laua,c, Andrea R. Gersonb, R. St .C. Smart, Resolving surface chemical states in XPS analysis of first row transition metals, oxides and hydroxides: Cr, Mn, Fe, Co and Ni, Applied Surface Science (2011),257, 2717–2730

[22]C. Battistoni, A. M. Giuliani, E. Paparazzo, F. Tarli, Platinum Complexes of the Methyl Esters of Dithiocarbazic Acid and 3-Phenyld it hiocarbazic Acid, J. CHEM. SOC. DALTON TRANS. 1984, 1293-1299

[23]H. Inoue, K. Hosoya, N. Kannari, J. Ozaki, Influence of heat-treatment of Ketjen Black on the oxygen reduction reaction of Pt/C catalysts, Journal of Power Sources (2012), 220, 173-179

[24]O. Martinez-Alvarez, M. Miranda-Hernández, Characterization of carbon pastes as matrices in composite electrodes for use in electrochemical capacitors, Carbon – Sci. Tech. (2008),1 , 30 - 38

[25]F. Godínez-Salomón, E. Arce-Estrada,M. Hallen-López, Electrochemical Study of the Pt Nanoparticles Size Effect in the Formic Acid Oxidation, Int. J. Electrochem. Sci., (2012), 7, 2566 - 2576

[26]P. S. Guin,S. Das,P. C. Mandal, Electrochemical Reduction of Quinones in Different Media: A Review, International Journal of Electrochemistry, 2011, 1-22

[27]S.A. Grigoriev, P. Millet, V.N. Fateev, Evaluation of carbon-supported Pt and Pd nanoparticles for the hydrogen evolution reaction in PEM water electrolysers, Journal of Power Sources, (2008), 177, 281–285

Catalytic Layer Location in MEA and Air Supply Influence on The Performance of an Open-Cathode Direct Ethanol Fuel Cell

D. A. Moreno J, Daniella E. Pacheco C., L. C. Ordóñez*

Centro de Investigación Científica de Yucatán, A.C Unidad de Energía Renovable, Centro de Investigación Científica de Yucatán, C. 43 No. 130 Col. Chuburná de Hidalgo, Mérida, Yucatán, 97200. México. Tel +52-999-9428330, e-mail: lcol@cicy.mx

ABSTRACT

The influence of the catalytic layer location on the performance of an open-cathode Direct Ethanol Fuel Cell (DEFC) was investigated using three different methods of preparation of the membrane electrode assembly (MEA). A catalytic load of 1 $mgPtcm^{-2}$ of a commercial catalysts of PtRu/C was used in both anode and cathode electrodes. In MEA 1, catalyst layers (CL) were deposited directly onto the Nafion® membrane surface. MEA 2 consisted of two CL´s: an inner, placed on the member surface and an outer CL located onto the carbon cloth diffuser layer (DL). MEA 3 was prepared using Pt-Black as the inner CL and PtRu/C or PtSn/C as the outer CL. Additionally we report two approaches for the operation of the open-cathode DEFC: air-self breathing (ASB) and forced-air convection (FAC). The combination of the inner and outer CL improved cell performance. The best activity was recorded with the outer CL prepared with PtSn/C catalyst. There is a strongly dependence between air supply to the cathode and cell performance. Our Open-Cathode DEFC design showed a decrease of 24.6 % of the power density in air-self breathing operation with respect to forced-air convection at RT.

Keywords: DEFC, Open-Cathode design, MEA preparation

1. Introduction

Direct ethanol fuel cells (DEFCs) are attractive power source devices since alcohols can be easily handled, transported and stored using the existing infrastructure. On the other hand, ethanol is available from biomass fermentation, it is not as toxic as methanol, it presents lower permeation rates through Nafion® membranes probably by its larger molecular size [1] and, it has a higher energy density than methanol [2]. One of the most important challenges to achieve the DEFC portability is avoiding the oxygen feeding from heavy tanks or air pumps. . An alternative is to consider open-cathodes designs that allow the operation with oxygen from air. There are two operational approaches for DEFC usage with open cathodes [3]:

- Air-self breathing (ASB): it takes oxygen from the air by natural convection [4].
- Forced-air convection (FAC): It uses fans at the cathode edge to force the air convection into the cathode [3].

The air-self breathing approach is very attractive since parasitic loads by external devices are minimized. But this type of operation reduces the overall performance of the fuel cell since the oxygen diffusion by natural convection is slow[4]. On the other hand the forced-air convection approach gives a higher cell performance [5]. However this type of architecture requires tight control of the air flow since its excess could reduce the average temperature of the stack causing a decrease in the electrochemical reaction rate [6]. A good performance of an open-cathode design requires an optimal architecture in the field of the flow channels and the Membrane electrode assembly (MEA) design. and: The improvement of MEA performance depends on its components and the assembly process [7]. In all cases, the MEA manufacture must consider the optimal interaction between the reactants (liquid or gas), the catalytic site and the electrolyte.
There are two basic methods for the assembly process,: a) the deposition of the catalyst layer on the DL followed by the addition or hot pressing to the membrane and b) deposition of catalyst layer directly onto the membrane surface followed by the addition or hot pressing of the DL [8], this process is called catalyst-coated membrane (CCM).
Due to the importance of the MEA manufacture on the global efficiency of the open-cathode ethanol fuel cell, we constructed an open-cathode DEFC and studied the influence of the catalytic layer location on its performance. Three different methods for MEA preparation were investigated: a) Depositing catalyst layers (CL) directly on the membrane surface, b) using two CLs, an inner layer placed on the member surface and an outer CL located onto the carbon cloth diffuser (DL) and c) using Pt-Black as the inner CL and PtRu/C or PtSn/C as the outer CL, which presented best performance. Results also showed that the air supply to the cathode plays an important role in the performance of the Open-Cathode DEFC design

2. Experimental

2.1. Materials

In all experiments Nafion® 117 membranes (DuPont) were used as a polymer electrolyte. We followed a three steps procedure to remove organic materials and activate the membranes consisting on: boiling in 3% H_2O_2 solution for 45 min; boiling in 1 M H_2SO_4 for 45 minutes and washing in de-ionized water.
The catalytic materials used were $Pt_{0.2}Ru_{0.1}$/C HiSPEC™ 5000 (Alfa Aesar), Pt-Black (Alfa Aesar) and PtSn/C (Pt:Sn, 1:1) 50 wt % prepared in our laboratory. Carbon cloth EC-CC1 (ElectroChem Inc) was used as DL. Graphite-polymer compose was used as anode and cathode plates for the single cell (table 1).

Table 1. Graphite-polymer compose properties

Density	1.82 gcm^{-3}
Tensile modulus at 25 °C	17000 MPa
Electrical conductivity	50 ± 10 S/cm
Thermal conductivity at 25 °C	15.8 $W\ m^{-1}K^{-1}$

2.2. Synthesis of PtSn/C

The carbon-supported PtSn electrocatalyst 50 wt % (Pt:Sn, 1:1, atomic ratio) was synthesized using sodium borohydride reduction method. Pt salt (H_2PtCl_6, Aldrich) and Sn salt (SnC_3, Aldrich) were used as precursors for the catalyst. Carbon Vulcan XC-72 was ultrasonically dispersed by 30 minutes in a three neck volumetric flask with 50/50 % v/v 2-propanol/de-ionized water solution. Then, appropriate amounts of Pt salt and Sn salt were added to the dispersed carbon. The mixture was stirred in a reflux system for 3 hours at room temperature, then appropriate amount of $NaBH_4$ solution was added drop by drop to the mixture and stirred for 6 h. The obtained slurry was filtered, washed and dried in a vacuum oven at 80 °C overnight. Finally, the catalyst was thermal treated at 200 °C for 2 h in a nitrogen atmosphere.

2.3. MEA preparation

The catalytic ink was composed of the catalyst (Pt-black, PtRu/C or PtSn/C) with ionomer solution (5 % w/w, Alfa Aesar) and 2-propanol. This dispersion was sonicated for 30 minutes to get a homogeneous ink. The deposition of the catalytic ink was carried out by brush painting method at different locations in the MEA. For the comparison, all MEAs have 9 cm^2 of active area with a catalyst load of 1 $mgPtcm^{-2}$ in anode and cathode electrodes.

2.3.1. MEA-1

Commercial PtRu/C catalyst was used in anode and cathode electrodes. The catalytic load was $1mgPtcm^{-2}$. Catalytic ink was deposited directly on both sites of the membrane surface at 60 °C. After that, a 9 cm^2 piece of carbon cloth was placed over each catalytic layer and finally the MEA was assembled into the cell.

2.3.2. MEA-2

Two CL´s of PtRu/C were deposited on anode and cathode electrodes: an inner CL with a catalytic load of 0.5 $mgPtcm^{-2}$ was painted directly onto membrane surface like in MEA-1. Next, an outer CL with total catalytic load of 0.5 $mgPtcm^{-2}$ was coated onto the carbon cloth diffuser (DL). Finally the electrodes were assembly by hot-pressing at 201 $kgcm^{-2}$ for 9 minutes at 120 °C.Total catalytic load was $1mgPtcm^{-2}$ in anode and cathode.

2.3.3. MEA-3

Two CL´s were deposited in anode and cathode electrodes similar to MEA-2. But in this case, in the anode side two different CL´s with $0.5mgPtcm^{-2}$ were tested. The first one was composed by PtRu/C (MEA-3a) and the latter was composed by PtSn/C (MEA-3b). Finally, the electrodes were assembled by hot-pressing at 50 $kgcm^{-2}$ for 1 minute at 130 °C.

2.4. Open-cathode fuel cell design

All experiments were performed in an Open-Cathode DEFC designed at our laboratory figure 1a and 1b show the anode and cathode designs respectively. The anode flow field is a single-serpentine pattern. The cathode design is a rhomboid array that facilitates water removal and suitable air convection into the cell. The cathode side has an electrical surface contact area of 61 %. In both electrodes the active area is 9 cm^2.

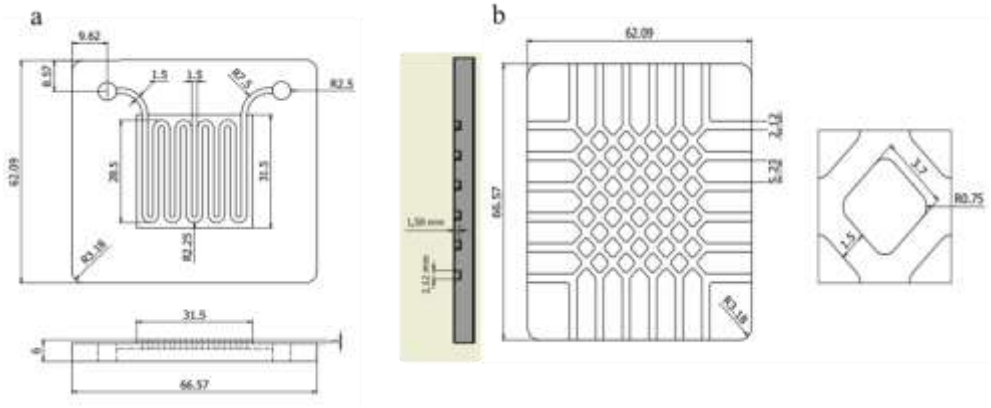

Fig 1. Open-Cathode DEFC design: a) anode mono-polar plate, b) cathode mono-polar plate

2.5. Cell performance test

The electrochemical measurements were performed in a potentiostat/galvanostat AutoLab PGSTAT302. Before testing the cell, all MEAs were activated by heating the cell at 60 °C and passing de-ionized water through the anode side for 3 hours at 1.5 mL/min to ensure suitable humidification of the membrane. Next, 1M ethanol solution was fed to the anode at 1.5 mL/min. A chronoamperometry measurement was carried out at 0.1 V for 1800 seconds. At this step, the current was recorded to find a point very close to the limiting current of the cell. Then, a chronopotentiometry measurement was performed to hold the current, at the point recorded before, during 1800 seconds. This procedure was performed until the fuel cell presented a stable signal. After activation, polarization curves were registered using scan rates of 5 and 10 mVs^{-1} at 25 °C and 60 °C. In both temperatures, the cell was tested in air-self breathing (ASB) and forced-air convection (FAC) mode to measure the air supply influence on the cell performance. Electrochemical impedance spectroscopy (EIS) analysis was carried out to understand the mass transport process, ohmic and charge transfer resistance. The galvanostatic impedance spectra were obtained at a frequency range between 3 kHz and 0.1 Hz at a constant current, very close to the limiting current in the mass transport zone of polarization curve. We tested 50 points, and sinusoidal current amplitude of signal around 6 % of the constant current setting. The potentiostatic impedance spectra were obtained at a frequency range of 250 kHz-0.01 Hz and 25 kHz-0.1 Hz according to the response of each MEA. We used 50 points and sinusoidal voltage amplitude of 0.005 V, in all cases at open circuit potential (OCP).

3. Results and discussion

3.1. MEA-1, MEA-2 and MEA-3a

Three MEAs with different catalytic layer location were tested under the same conditions. Figure 2 shows the comparison of the polarization curves registered for the three MEAs at 60 °C. It can be observed that the OCP is very similar in MEA-1 and MEA-2 (0.34 V and 0.36 V respectively). However, the current and power densities increase with the utilization of two catalytic layers. This could be attributed to the lower ohmic resistance in the assembly as can be seen in the table 2. MEA-1 has 11.7 Ωcm^2 and MEA-2 has 2.61 Ωcm^2. This decrease in ohmic resistance of the assembly implies a better contact between the diffusion layer, catalytic layer and membrane.

Hot-pressing helps to reduce the resistance in the assembly in comparison with not hot-pressing electrodes as observed in MEA-2.

As observed in figure 2, the best performance was recorded with MEA-3a which has an inner unsupported Pt catalyst layer. In this case, OCP and current density is higher (0.46 V and 11 $mAcm^{-2}$ respectively) than in MEA-1 and MEA-2.

According with Chien-Hao *et al*. [9] the inner catalyst layer helps to reduce the ethanol crossover since catalysts particles deposited onto membrane acts as ethanol barrier. Probably the MEA-3a behavior could be related to a reduction of ethanol crossover. However, the ethanol crossover measurement is technically difficult to perform with the open-cathode design because a nitrogen inert atmosphere at cathode is needed. Nevertheless it is clear that there is an improvement in the MEA performance by using two catalyst layers.

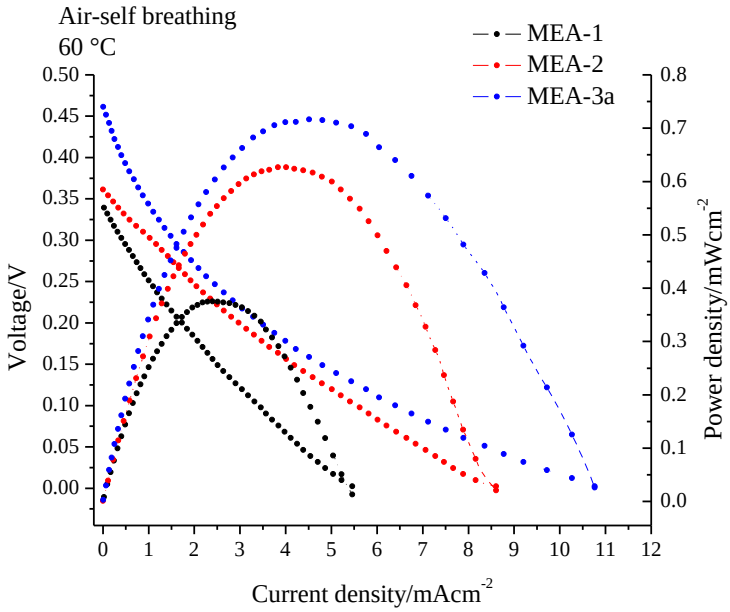

Fig 2. Polarization curves and density power for MEA-1, MEA-2, MEA-3a: ASB mode, scan rate of 10 mVs-1. Fuel: 1 M ethanol solution. Operation temperature of 60 °C

Table 2. Ohmic resistances determinated by Potentiostatic EIS.

MEA	Ohmic resistance/ Ωcm^2
MEA-1	11.7
MEA-2	2.61
MEA-3a	1.5

3.2. MEA-3a and MEA-3b: catalyst performance and air supply influence

PtSn/C and PtRu/C catalysts were deposited in the outer layer in order to test their influence in the MEA performance. The PtSn/C presented the best activity for ethanol oxidation reaction (EOR) [9, 10]. Figure 3 and figure 4 show the polarization curves and power density of the MEA-3a and MEA-3b at 25 °C and 60 °C respectively. In both cases, air-self breathing (ASB) and Forced-air convection (FAC) mode were tested using a scan rate of 5 mVs^{-1} and 1M ethanol solution. It can be seen that the OCP at 25 °C is higher with PtSn/C synthesized in our laboratory in comparison with the commercial PtRu/C material. At 25 and 60 °C the limiting current density and power density are higher using PtSn/C than with PtRu/C. This increase on the power density is 68.8% in ASB mode and 74.6% in FAC at 25 °C. These results are important since they could imply higher efficiency in portable applications. On the other hand we observed dependence between air supply and performance of the cell.

MEA-3b, which showed the best performance, presented a reduction in the peak of power density between the operation in FAC *vs* ABS mode, being 23.8% at 25°C and 34.5% at 60°C as observed in figure 4. Considering the several advantages related to parasitic losses by external devices at ASB operation, our open-cathode fuel cell has relative low decrease and it could be operated with suitable performance in ASB mode in comparison with FAC.

Table 3 presents the different power densities of the MEAs in ASB and FAC mode at 25 °C and 60 °C. The highest peak of power density is 3.21 $mWcm^{-2}$ recorded at 60 °C with the MEA-3b in FAC mode. The increment on the performance with forced air supply is mostly related to a charge transfer effect than to the ohmic resistance affect, since the potentiostatic EIS spectra (table 4) shows no significant variations on the ohmic resistance between the two operation approaches, especially at 25 °C. Instead, at 60 °C, the ohmic resistance slightly increased, probably due to membrane dehydration caused by airflow. However, the forced-air convection mode helps to improve the oxygen diffusion and it has the strongest influence on the charge transfer resistance and performance of the cell. From galvanostatic EIS espectra at 60 °C (Fig. 5) it can be seen that the charge transfer resistance goes down with the increment on the air supply flux in MEA-3a and MEA-3b.The lowest charge transfer resistances was recorded in the MEA-3b, this agrees with the best performance in terms of power and current densities. Table 5, shows the values of ohmic and resistance to the charge transfer (RCT) obtained by galvanostatic EIS at 60 °C. as well as the influence of air supply on the RCT that cause a reduction from 37 Ωcm^2 to 26 Ωcm^2 in MEA-3a and from 23 Ωcm^2 to 17 Ωcm^2 in MEA-3b . The improved activity of MEA containing the PtSn/C catalyst could be explained by a reduction in the RCT. The impedance values were obtained using “electrochemical circle fit” in NOVA 1.9 considering the follow equivalent circuit: (R1+ CPE/R2) where R1 is related with the ohmic resistance, CPE is a constant phase element related with the capacitance of the double layer and R2 is the resistance to the charge transfer.

Table 3. Power density of MEA-3a and MEA-3b at 25 °C and 60 °C.

MEAs	Power density in ASB/ $mWcm^{-2}$	Power density in FAC/ $mWcm^{-2}$	Temperature °C
MEA-3a	0.3	0.32	25
MEA-3b	0.96	1.26	25
MEA-3a	0.72	1.13	60
MEA-3b	2.1	3.21	60

Table 4. Potentiostatic EIS: ohmic resistance for MEA-3a and MEA-3b.

MEAs	Constant potential (V) ASB/FAC	Ohmic resistance Ωcm^2/ ASB	Ohmic resistance Ωcm^2/ AFC	Temperature/°C
MEA-3a	0.46/0.52	1.6	1.6	25
MEA-3b	0.63	1.3	1.3	25
MEA-3a	0.46/0.57	1.5	1.9	60
MEA-3b	0.63	1.08	1.5	60

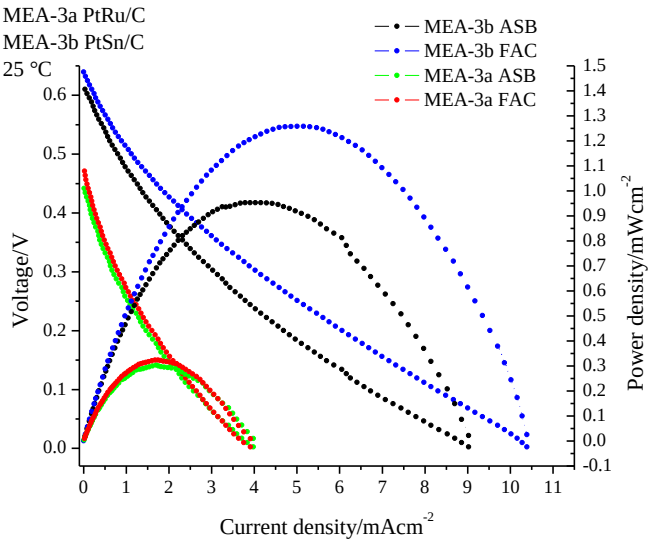

Fig 3. Polarization curves and density power for MEA-1, MEA-2, MEA-3a: ASB mode, scan rate of 10 mVs^{-1}. Fuel: 1M ethanol solution. Operating temperature of 60 °C.

Table 5. Galvanostatic EIS: ohmic and charge transfer resistance (RCT) for MEA-3a and MEA-3b.

MEAs	R ohmic (Ωcm^2) ASB/FAC	RCT (Ωcm^2) ASB	RCT (Ωcm^2) FAC	Constant Current(A) ASB/FAC	Temperature °C
MEA-3a	1.62/1.71	-	161	0.03/0.03	25
MEA-3b	1.2/1.4	-	38.7	0.07/0.07	25
MEA-3a	1.57/1.9	37	26	0.07/0.11	60
MEA-3b	1.1/1.6	23	17	0.19/0.27	60

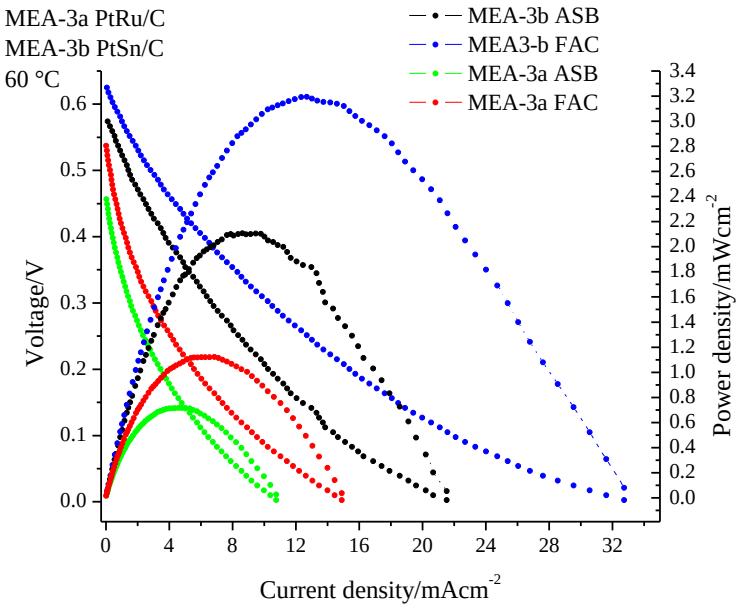

Fig 4. Polarization curves and density power for MEA-3a and MEA-3b: ASB mode, scan rate of 10 mVs^{-1}. Fuel: 1M ethanol solution. Operating temperature of 60 °C.

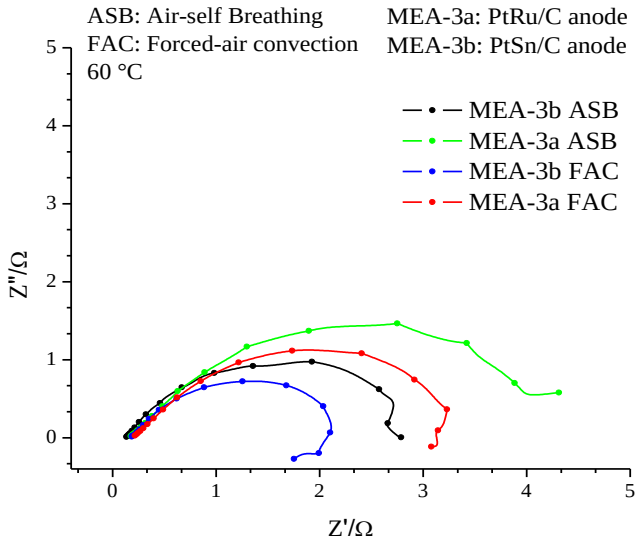

Fig 5. Galvanostatic EIS spectra for MEA-3a and MEA-3b in ASB and FAC mode at 60 °C, frequency range of 3 kHz to 0.1 Hz in mass transfer zone of polarization curve.

4. Summary and perspectives

The influence of the catalytic layer location and air supply on the performance was determined by testing three different MEA-preparation methods and two operational open-cathode approaches. It was observed that the ohmic resistance is affected by the assembly method, in MEA-1 and MEA-2, since a better contact between DL, CL and membrane gives lower ohmic resistances. In this case, the utilization of two catalytic layers, an inner directly deposited onto the Nafion membrane surface and an outer catalyst layer deposited onto the DL, helps to improve the contact resistance generating higher power and current densities. Additionally, the use of unsupported Pt inner catalyst layer shows a significant increment on the OCP, probably by decreasing the rate of ethanol crossover due to the Pt particles acting as a reactive ethanol filter. The use of PtSn/C on the catalyst layer presented better performance than PtRn/C. This is explained by an important increment on the OCP, current and power density mostly related to a lower resistance to the charge transfer. The air supply to the cathode also has an important impact on the cell performance. The FAC helps to improve the oxygen diffusion and increases the power and current densities. According to the test with MEA-3b, the difference in the power density between the operation in ASB and FAC is 23.8 % at 25 °C and 34.5 % at 60 °C. Considering that ASB operation does not have parasitic losses by external devices, our open-cathode fuel cell has a relatively low power density decrease and it could be considered as a promising portable power supply.

Acknowledgements

The authors express their gratitude to M. C. Enrique Escobedo Hernández and Ing. Romeo Moreno for his collaboration in DEFC tests, Ing. Gustavo Martinez and Dra. Ana Valenzuela for technical support. The authors acknowledge the financial support for this work from FOMIX-Quintana Roo with the project 175119. D. A. Moreno thank to CONACYT for grant No. 280971.

References

1. Song, S. and P. Tsiakaras, Recent progress in direct ethanol proton exchange membrane fuel cells (DE-PEMFCs). Applied Catalysis B-Environmental, 2006, 63(3): p. 187-193.
2. Ekdharmasuit, P., A. Therdthianwong, and S. Therdthianwong, Anode structure design for generating high stable power output for direct ethanol fuel cells. Fuel, 2013, 113(0): p. 69-76.
3. Liu, W., et al., Experimental study of proton exchange membrane fuel cells using Nafion 212 and Nafion 211 for portable application at ambient pressure and temperature conditions. International Journal of Hydrogen Energy, 37(5): p. 4673-4677.2012
4. Bussayajarn, N., et al., Planar air breathing PEMFC with self-humidifying MEA and open cathode geometry design for portable applications. International Journal of Hydrogen Energy, 34(18): p. 7761-7767.2009
5. Dhathathreyan, K.S., et al., Forced Air-Breathing PEMFC Stacks. International Journal of Electrochemistry, 2012: p. 7.2012
6. Barreras, F., et al., Experimental study of the pressure drop in the cathode side of air-forced Open-cathode proton exchange membrane fuel cells. International Journal of Hydrogen Energy, 36(13): p. 7612-7620.2011
7. Wu, B., et al., The performance improvement of membrane and electrode assembly in open-cathode proton exchange membrane fuel cell. International Journal of Hydrogen Energy, 2013, 38(25): p. 10978-10984.
8. Mehta, V. and J.S. Cooper, Review and analysis of PEM fuel cell design and manufacturing. Journal of Power Sources, 114(1): p. 32-53.2003
9. Wan, C.-H. and C.-L. Chen, Mitigating ethanol crossover in DEFC: A composite anode with a thin layer of Pt50–Sn50 nanoparticles directly deposited into Nafion® membrane surface. International Journal of Hydrogen Energy, 34(23): p. 9515-9522.2009
10. Song, S.Q., et al., Direct ethanol PEM fuel cells: The case of platinum based anodes. International Journal of Hydrogen Energy, 30(9): p. 995-1001.2005

Bi-Directional Flyback DC-DC Converter for Supercapacitor Stack for Hybrid Renewable Energy System

J. M. Sandoval Cancino[1], I. Domínguez Ibarvo[2], D. E. Pacheco Catalán[1*], Y. Verde-Goméz[3], J. L. Durán Gómez[2]

[1] Centro de Investigación Científica de Yucatán, A.C. Calle 43 No. 130, Colonia Chuburná de Hidalgo, Mérida, Yucatán, México; 97200.
[2] Instituto Tecnológico de Chihuahua, Av. Tecnológico #2909, Chihuahua, Chih., México, 31310
[3]Instituto Tecnológico de Cancún, Av. Kabah, Km.3 Cancún, Quintana Roo México 77515,
*Tel : +52 999 942 83 30-Fax :+52999 981 39 00;
email: dpacheco@cicy.mx; jlduran@ieee.org

ABSTRACT

Energy Storage Systems (ESS) is quite necessary for renewable energy; they give them more autonomy and better power quality solving intermittency issues by supplying power when sources are unavailable. This work proposes an integrated bi-directional flyback converter (IBFBC) topology to interconnect a supercapacitor (SC) module to a hybrid renewable energy system. The proposed topology uses the symmetric nature of flyback converter topology to simplifying the bi-directional needs with minor components than half and full bridge topologies. Also, this topology features a magnetic isolating transformer which serves as an additional protection to the SC module and DC bus. The IBFBC, has been designed to store energy by charging up a Maxwell Technologies™ +48Vdc 165F SC module from a +24Vdc source, and once it was fully charged, supply power to the +24Vdc source via a single device. The IBFBC is controlled by means of increments of fixed duty-cycle steps in order to charge-up the SC module, and using the state-space average control technique to discharging stored energy.

Keywords: Flyback, bi-directional converter, supercapacitor.

1. Introduction

Renewable energy technologies have taken great importance in the present and future of energy supply for humanity development. However, many renewable energy technologies are already mature enough to be exploited such as wind, photovoltaic, and hydraulics, etc. It is well known that these technologies central issues are intermittency and energy storage [1], for that purpose traditional is used Pb and Ion-Li batteries. Nevertheless, their high energy density but low power density may cause stress at high power demands and may cause further damage [2]. On the other side, supercapacitors have a high power density and low energy density, causing no damage at high power, but reducing the autonomy of the device [3–5].

Hybrid Energy Storage Systems (HESS) attempt to enhance the energy storage using two or more storage technologies, in this case, supercapacitors and batteries are considered. The combination of SC and batteries offer high power density (from SC) and high energy density (from Batteries), reducing the stress in the system caused by high power demand and, at the same time, giving more autonomy to the HESS. Many forms of interconnect SC and batteries are reported in the literature [6–11], but in this case, it is proposed a bi-directional converter (IBFBC) because offers the possibility to charge and discharge the storage device, saving components and space, which is sometimes a relevant design factor. Also, due to its high power density, the SC can damage the converter, or failure on the energy bus can damage the converter and the SC as well. The flyback topology was chosen due to its simplicity, isolating transformer, and symmetric nature; also requires minor replacements of the components and adjustments such transformer secondary windings number, transformer turns ratio and components or circuit add-ons [12, 13].

In this work, the interconnection of a SC module to a mobile Hybrid Renewable Energy System (HRES) via an integrated bi-directional flyback converter (IBFBC) is shown in figure 1. Two renewable energy sources (wind turbine and photovoltaic panels) to supply +24Vdc bus, and then an IBFBC is used to interconnect with a SC module.

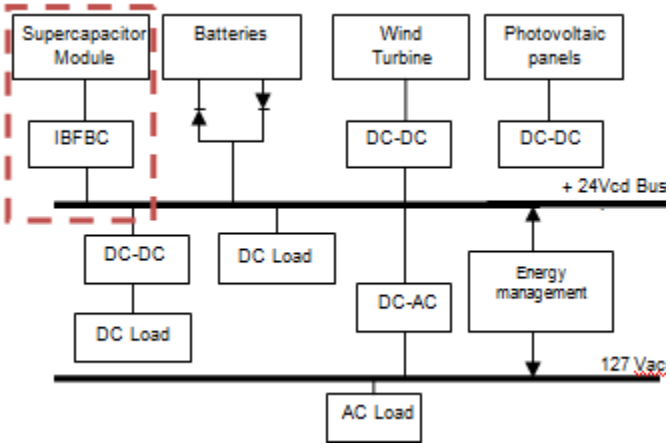

Fig. 1. Hybrid Renewable Energy System scheme and SC module interconnection via the IBFBC (red rectangle).

2. Proposed IBFBC Approach

In figure 2 the topology of an IBFBC proposed in J.L. Durán work [14] work is shown, which contains: a high-frequency single-phase transformer, a main switch (S_1) a filter capacitor C_i in the primary side, and the addition of the IGBT switch (S_2) to the D_2 diode, and then, grounded to the SC module cathode. As well, it uses the SC module itself as a secondary side filter capacitor, and the leakage inductance L_{l1} and L_{l2} for both sides of the transformer, respectively; and finally, the magnetization inductance L_m. This topology charges up the SC module and can discharge its full energy to the +24Vdc bus as well.

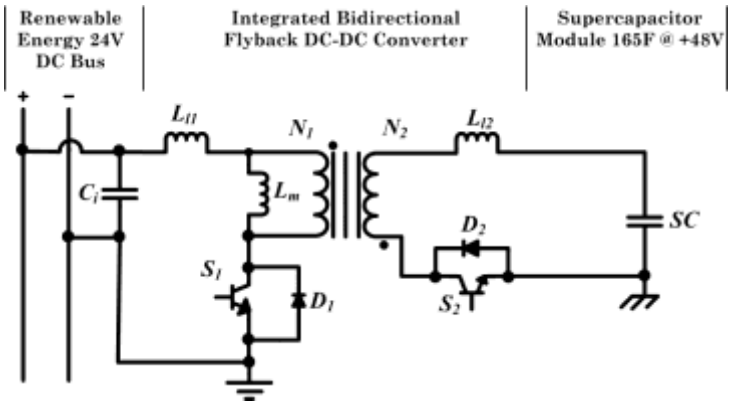

Fig. 2. Proposed topology of an Integrated Bidirectional Fly-Back Converter (IBFBC).

2.1 Bi-directional DC-DC Converter Design

2.1.1. Power Stage Design

The design parameters chosen for this topology that are obtained from, DC bus nominal voltage, the SC module datasheet and form the high frequency transformer previously designed, are described as follows:

V_{SC} = +48.6Vdc [=] Supercapacitor rated voltage.
C_{SC} = 80 F [=] Capacitance.
E_{max} = 2.48 Wh/kg. [=] Maximum supercapacitor energy.
$V_{o,dc}$ = +24Vdc [=] DC-bus output voltage.
fs = 20 kHz [=] Switching frequency.
$N_2/N_1 = n$=1 [=] IBFB transformer turns ratio.
d_1 and d_2 [=] Duty cycles for S_1 and S_2 power switches respectively.

This proposed topology has two main functions, to charge and discharge an SC module. So the design could be separated in two conditions; however, the methodology of the analysis of the conditions is practically the same. For the first condition of charge, is used the +24Vdc bus to charge the SC module, and during this process the regulation does not have to be rigorous due to the use of the supercapacitor module as a filter capacitor. However, the control must be set to not have an over-voltage condition above the nominal +48Vdc and protect internally the SC cells. The second condition corresponds to the discharge, and this will be triggered by the overall energy management. When this condition operates, the main IGBT switch (S_1), will be in off the state, but an internal fast & soft inverse diode (D_1) will be conducting under discharge condition, and supply power from de SC module to the DC bus. In this case, the regulation of the output power becomes important, so an adequate control must be properly designed. Some important parameters are the duty cycle and the voltage in the diodes and switches. The following expression defines the duty cycle for the main IGBT (S_1):

$$d_1 = \frac{1}{\left[\left(\frac{V_d}{V_0}\right)\cdot\left(\frac{N_2}{N_1}\right)+1\right]} \quad (1)$$

where, d_1 is the charge operation duty-cycle in S_1; V_d the input voltage; V_o the output voltage; and N_1 and N_2, the inductor primary and secondary turn number, respectively. Considering the topology symmetry, the duty cycle for the discharge operation, is done by:

$$d_2 = \frac{1}{\left[\left(\frac{V_o}{V_d}\right)\cdot\left(\frac{N_1}{N_2}\right)+1\right]} \quad (2)$$

Now, the voltage in the switch and the diode can be useful to select the parts avoid damage and validate the simulation and design with the experimental results. The IGBT switches *S1* and *S2* voltages are obtained by next expressions.

$$V_{sw} = \left[\frac{1}{(1-d)}\right]\cdot V_d \quad (3)$$

$$V_{sw2} = \left[\frac{1}{(1-d)}\right]\cdot V_o \quad (4)$$

Where: *d* is the duty cycle for the corresponding operation (charge or discharge). Moreover, the voltage of the diode is given by:

$$V_{diodo} = \left(\frac{N_2}{N_1}\right)\cdot V_d + V_0 \quad (5)$$

2.1.2. Control Stage Design

The control of the IBFBC was separated in two stages, one for charge and another for discharge. Both control strategies were written in separated PIC18F2680 microcontrollers in micro C programming language. The control strategy for the charge is the next:

For the supercapacitor charging operation, a simple step control was designed. The program code was set for to start with a low duty cycle (50%) until a 25V potential is reached. Then, is increased in steps of 5% duty cycle, every 5V until the 70% is reached, and finally, is shutdown the pulse when the charge process is complete. This control strategy was selected for its simplicity and knowing that the +24Vdc source is constant, so it is just matter to set manually the duty cycle and shut it down in the end**.** On the other hand, for the discharge operation an average state space control was designed. For this topology, the matrices corresponding *to* ON state, A_1 and B_1 based on input and SC X_1 and X_2 currents are:

$$\begin{bmatrix} \boldsymbol{X_1} \\ \boldsymbol{X_2} \end{bmatrix} = \underbrace{\begin{bmatrix} \boldsymbol{0} & \boldsymbol{0} \\ \boldsymbol{0} & \boldsymbol{0} \end{bmatrix}}_{\boldsymbol{A_1}} + \underbrace{\begin{bmatrix} \frac{\boldsymbol{1}}{\boldsymbol{L_m}} & \boldsymbol{0} \\ \boldsymbol{0} & -\frac{\boldsymbol{1}}{\boldsymbol{C}} \end{bmatrix}}_{\boldsymbol{B_1}} \begin{bmatrix} \boldsymbol{U_1} \\ \boldsymbol{U_2} \end{bmatrix} \tag{6}$$

where, L_m is the magnetizing inductance, and U_1 and U_2 are input and output voltage, respectively; and the matrices C_1 and E_1 based on the output voltage are done by the follow expression,

$$\boldsymbol{V_o} = \underbrace{[\boldsymbol{0} \quad \boldsymbol{1}]}_{\boldsymbol{C_1}} \begin{bmatrix} \boldsymbol{X_1} \\ \boldsymbol{X_2} \end{bmatrix} + \underbrace{[\boldsymbol{0} \quad \boldsymbol{1}]}_{\mathbf{E_1}} \begin{bmatrix} \boldsymbol{U_1} \\ \boldsymbol{U_2} \end{bmatrix} \tag{7}$$

Now, once are have the matrices during "ON" state, the matrices on the "OFF" operation based on L_m and SC currents A_2 and B_2 are,

$$\begin{bmatrix} \dot{\boldsymbol{X}}_1 \\ \dot{\boldsymbol{X}}_2 \end{bmatrix} = \underbrace{\begin{bmatrix} \frac{\boldsymbol{re}}{\boldsymbol{L_m}}\left(\frac{\boldsymbol{N_1}}{\boldsymbol{N_2}}\right)^{\boldsymbol{2}} & \frac{\boldsymbol{1}}{\boldsymbol{L_m}} \cdot \frac{\boldsymbol{N_1}}{\boldsymbol{N_2}} \\ \frac{\boldsymbol{N_1}}{\boldsymbol{C} \cdot \boldsymbol{N_2}} & \boldsymbol{0} \end{bmatrix}}_{\boldsymbol{A_2}} \begin{bmatrix} \boldsymbol{X_1} \\ \boldsymbol{X_2} \end{bmatrix} + \underbrace{\begin{bmatrix} \boldsymbol{0} & -\frac{\boldsymbol{re}}{\boldsymbol{L_m}} \cdot \frac{\boldsymbol{N_1}}{\boldsymbol{N_2}} \\ \boldsymbol{0} & -\frac{\boldsymbol{1}}{\boldsymbol{C}} \end{bmatrix}}_{\boldsymbol{B_2}} \begin{bmatrix} \boldsymbol{U_1} \\ \boldsymbol{U_2} \end{bmatrix} \tag{8}$$

Finally, the matrix C_2 and E_2 are obtained based on the output voltage in the OFF state,

$$\boldsymbol{V_o} = \underbrace{\left[\boldsymbol{re}\frac{\boldsymbol{N_1}}{\boldsymbol{N_2}} \quad \boldsymbol{1}\right]}_{\boldsymbol{C_2}} \begin{bmatrix} \boldsymbol{X_1} \\ \boldsymbol{X_2} \end{bmatrix} + \underbrace{[\boldsymbol{0} \quad -\boldsymbol{re}]}_{\mathbf{E_2}} \tag{9}$$

Once the matrices of the topology are obtained, the transfer function can be determined by the following expression:

$$\boldsymbol{TF(s)} = \boldsymbol{C} \cdot [\boldsymbol{sI} - \boldsymbol{A}]^{-\boldsymbol{1}} \left[(\boldsymbol{A_1} - \boldsymbol{A_2}) \cdot \begin{bmatrix} \boldsymbol{X_1} \\ \boldsymbol{X_2} \end{bmatrix} \right] \tag{10}$$

This transfer function is computed with the Matlab™ software to obtain the bode plot, and from that plot adjust the desired cross frequency, which has to be at least the 20% of the switching frequency.

2.2.3. Charge and Discharge Logistic

Due to the topology employed, the charge and discharge operation of the converter will be done by an external energy management system. To protect the converter, and avoid enabling the charge and discharge operation at the same time, the control board has been limited by relays as shown in figure 3.

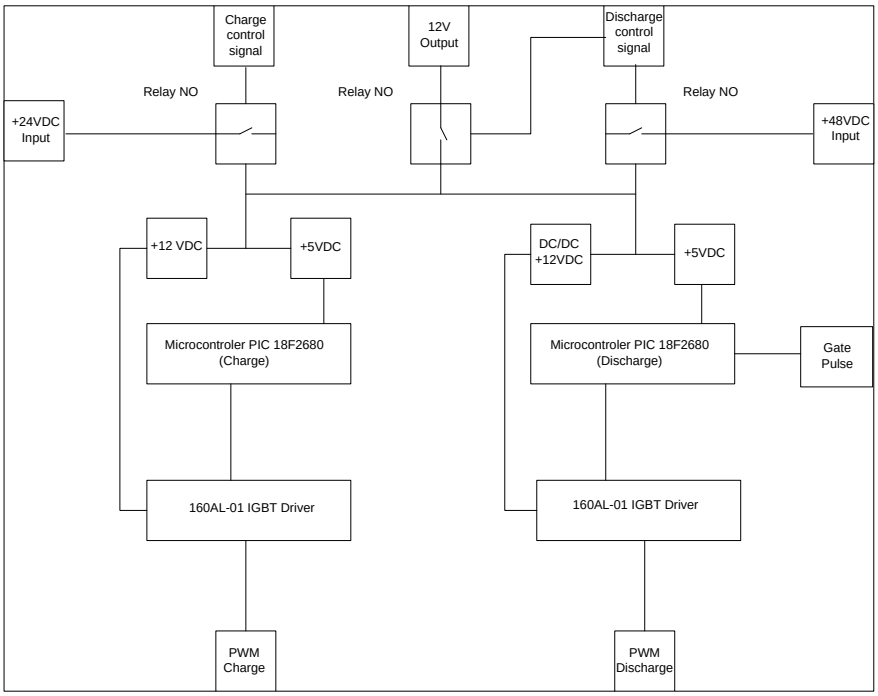

Fig. 3. Integrated Bi-directional FlyBack Converter Control Board distribution

The inputs of the board, both +24Vdc and +48Vdc (for the DC bus and the SC module), are limited by relays in both sides. An external energy management sends a control signal that activates the normally open relays to charge or discharge the SC module when needed. Once activated, the power will flow to a +12Vdc voltage regulator (for a charge) and a +12Vdc DC-DC converter for discharge. Those regulators will supply power to an insulated gate bipolar transistor (IGBT) driver and a +5Vdc voltage regulator to energize the corresponding microcontroller. The microcontrollers will generate the chosen pulse, either charge or discharge, and will be sent to the IGBT driver to get the output pulse with modulation (PWM). In addition to the PWM pulse output for charge and discharge, an additional gate was implemented, this for put in or out the load during the discharge operation.

3. Simulation and Experimental Results

The simulation and experimental results of the IBFBC design are discussed in this section. So, the duty cycles are 67% for the charging operation and 33% for the discharge operation. Based on these parameters, and the ones exposed in section 2, simulation results of charge and discharge have been done using PSIM™ Software. In figure 4, the voltages and currents in diode, D_2, as well as in power switch S_1 are shown for the charge operation.

3.1. Simulation Results

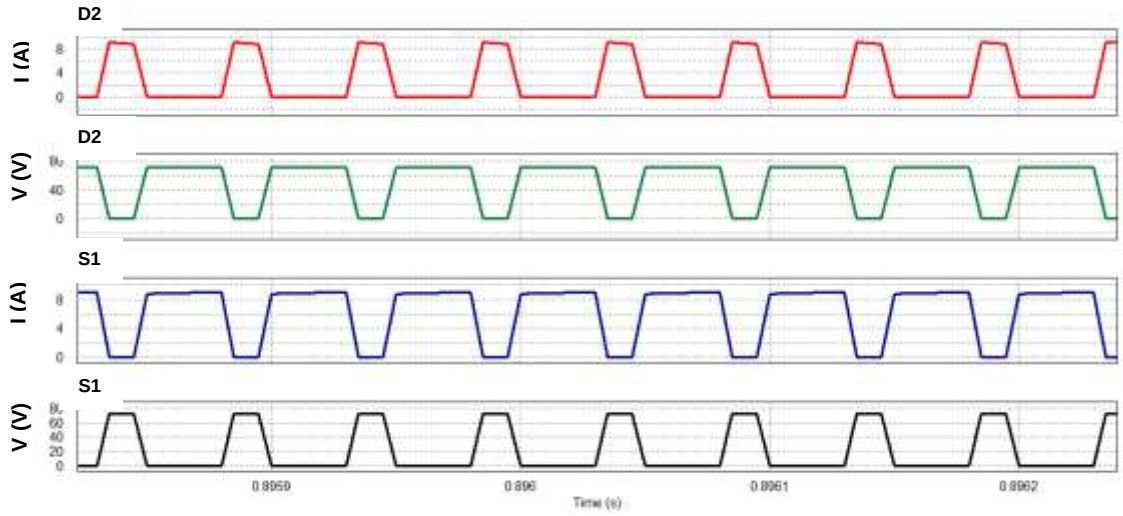

Fig. 4. Integrated Bi-directional Flyback Converter charge operation (24V-48V) D_2 and S_1 waveforms simulation used PSIM™.

The simulation results show that the values obtained from ec. 1 to 5 during the design of the converter are accurate by giving the same values. The waveforms show that voltages and currents between diode D_2 and switch S_1 are complementary forming the voltage and current in the transformer, suggesting a correct and stable operation [12, 13]. The discharge simulation results (figure 5), shows the voltage and current waveforms generated by the diode D_1 and switch S_2.

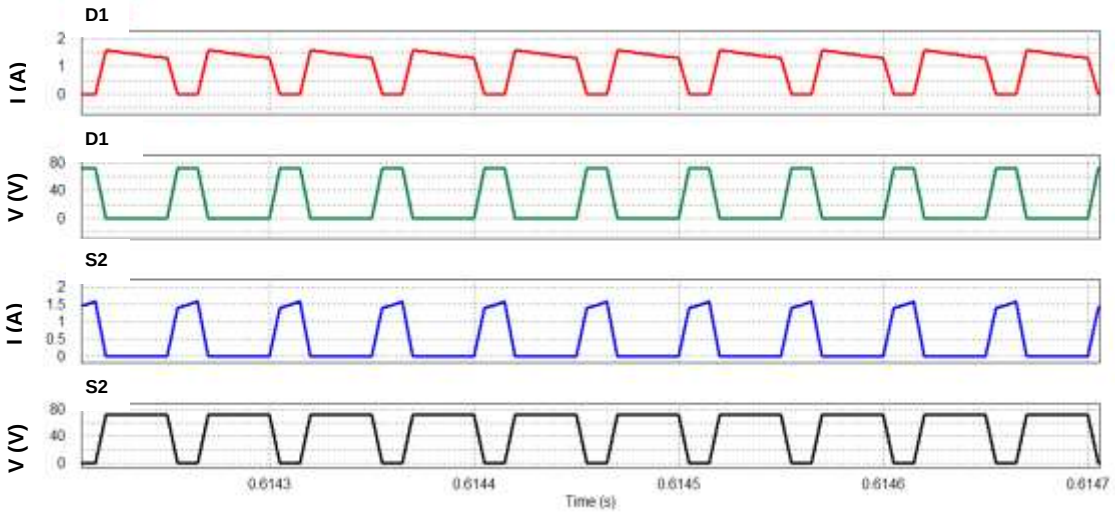

Fig. 5. Integrated Bi-directional Flyback Converter discharge operation (48V-24V) D_1 and S_2 waveforms simulation in PSIM™.

3.2. Experimental Results

Like in the charge operation waveforms, it can be appreciated that values are close to the ones obtained during the converter design. Also, voltage and current waveforms through diode D_1 are complementary to the switch power device, S_2, waveforms forming the voltage and current on the inductor suggesting stability and correct operation as well. On following paragraphs, the waveforms during experimental operation will be presented. Figure 6 shows the 33% PWM signal, D_1 current, and the S_2 voltage and current waveforms. It can be seen that wave-forms values obtained in experimental tests are similar to the ones obtained during design and simulation, confirming the design. The switch voltage, V_{SW}, presents a peak due to leakage inductance losses due to the manual high-frequency transformer construction therefore; a snubber RCD circuit was added to reduce the voltage peaks on the IGBT S_2. The S_2 voltage V_{sw} can be seen to be anti-proportional to the S_2 current and proportional to D_1 current which suggest the correct operation of the proposed topology. Moreover, it can be seen that current wave-forms shows a capacitive effect, probably due to the high transformer inductance L_m and the leakage inductance L_l in the circuit and transformer conductors.

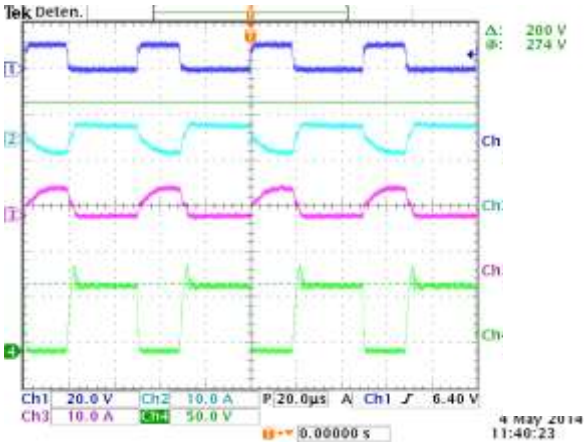

Fig. 6. Experimental results of the converter waveforms at 33% PWM signal (dark blue), D_1 current in A (cyan), S_2 current in A (pink) and S_2 voltage in V (green) during discharge operation.

For the charge operation (figure 7), the waveforms, it can be seen that are complementary to the discharge waveforms, suggesting the change of the output power and, therefore, the correct operation of the converter. Because of the voltage peak present in S_1 voltage, a RCD snubber was also added to the IGBT switch S_1. And, as seen in figure 6, leakage inductance in the circuit makes a deformation in S_1 and D_2 current wave-forms.

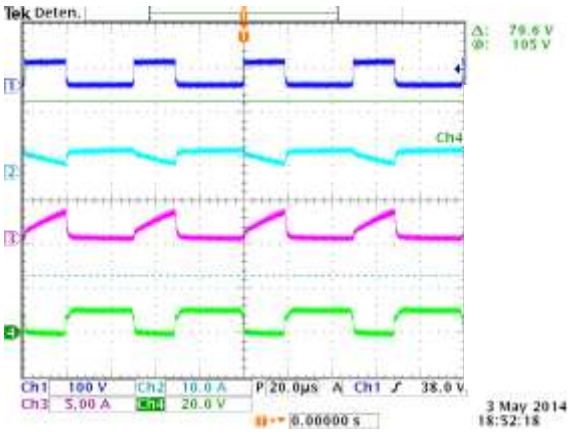

Fig. 7. Experimental results of the converter waveforms S_1 voltage in V (dark blue), S_1 current in A (cyan), D_2 current in A (pink) and 63% PWM signal (green) during charge operation.

Now that the correct converter bidirectional operation has been set, the SC module charge performance is shown in figure 8. It can be seen that the converter can charge the SC module from a +24Vdc source in an approximate time of one and a half hours. The charge curve shows a fast initial increase to +25Vdc in the SC voltage and then the charging rate starts to drop with the increasing voltage in the SC terminals regardless of the increasing duty cycle.

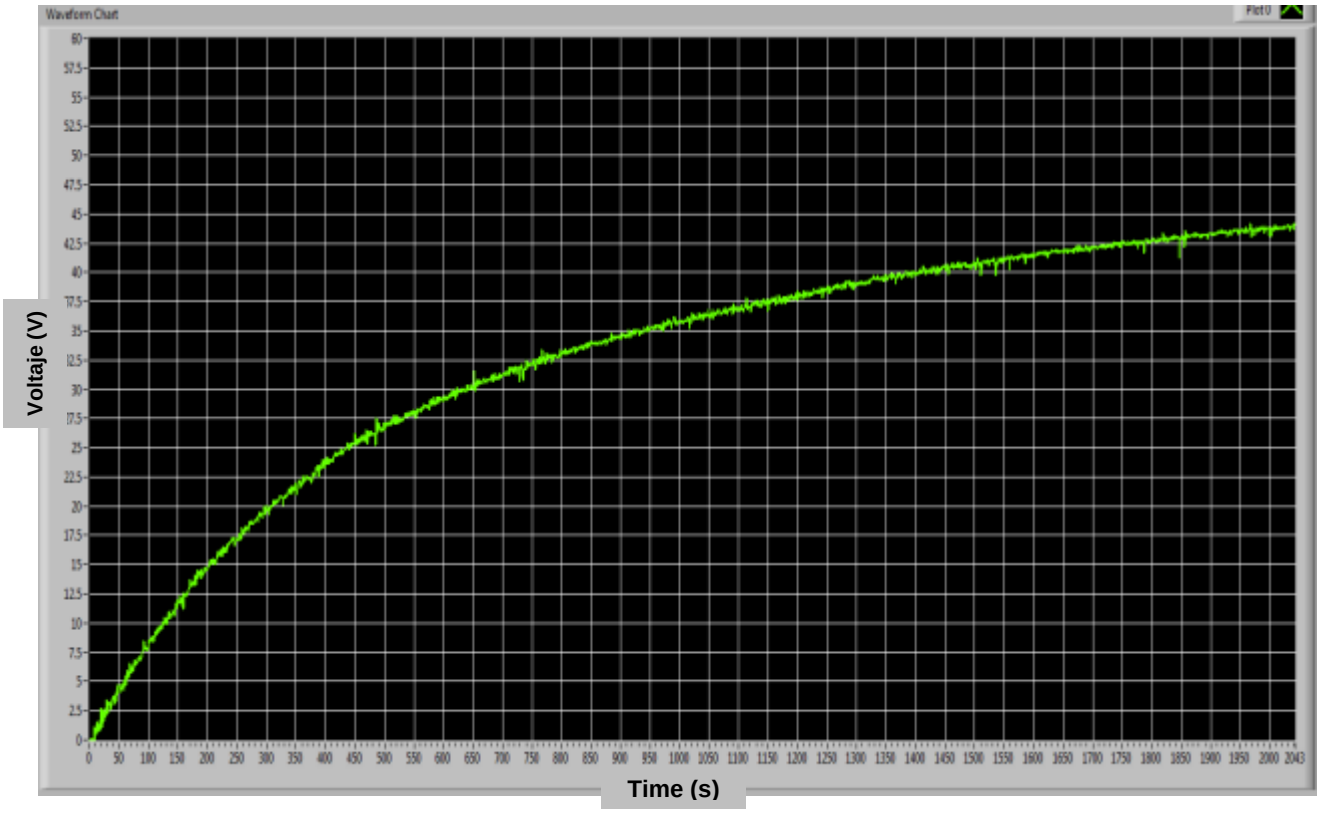

Fig. 8. Supercapacitor module from 0 to +48Vdc charge via IBFBC

4. Summary and perspectives

In this paper, a topology of an integrated bi-directional flyback converter (IBFBC) has been proposed to operate as an interconnection power device for supercapacitors in hybrid renewable energy systems. Simulation and experimental results were presented, giving a fully operating converter; the topology has been presented with a simple design that can save space, and economic resources, due to the utilization of a high-frequency single-phase transformer and the use of an IGBT switches with antiparallel diodes employed for the bi-directional operation. The IBFBC is able to charge a +48Vdc, 165F SC module in an average charging time of an hour and a half, and allows a 20% discharge used a +24Vdc Bus.

Acknowledgements

This research work was supported in part by CONACYT FOMIX QRoo-2011-001-174895, under Grant BS123CONACYT No. 280955.

The authors gratefully acknowledge the contribution of Manuel Israel Flota Bañuelos, Enrique Escobedo Hernandez, Carlos Alberto Muñoz Baca, Kevin Basto Perez, for their technical support for the realization of this project.

References

[1] P. F. Ribeiro, B. K. Johnson, M. L. Crow, A. Arsoy, and Y. Liu, Energy storage systems for advanced power applications, Proceedings of the IEEE 2001; 89: 12; 1744–1756.

[2] A. Lahyani, P. Venet, A. Guermazi, and A. Troudi, Utilization of supercapacitors to reduce lead acid battery stresses in UPS , First Int. Conf. Renew. Energies Veh. Technol. 2012; 90–100.

[3] X. Andrieu and J. F. Fauvarque, Supercapacitors for telecommunication applications, Telecommunications Energy Conference, INTELEC '93. 15th International 1993:1; 79–82

[4] S. C. Smith and P. K. Sen, Ultracapacitors and Energy Storage: Applications in Electrical Power System, Power Symposium. NAPS '08. 40th North American. 2008; 1–6.

[5] A. Rufer, D. Hotellier, P Barrade,. A supercapacitor-based energy-storage substation for voltage-compensation in weak transportation networks. Power Delivery, IEEE Transactions on 2004: 19, 2; 629 - 636

[6] A. F. Burke, Batteries and Ultracapacitors for Electric, Hybrid, and Fuel Cell Vehicles, Proc. IEEE 2007; 95: 4; 806–820.

[7] S. Park, Y. Kim, and N. Chang, Hybrid energy storage systems and battery management for electric vehicles, Design Automation Conference (DAC), 50th ACM / EDAC / IEEE 2013; 1–6.

[8] F. Ongaro, S. Saggini, and P. Mattavelli, Li-Ion Battery-Supercapacitor Hybrid Storage System for a Long Lifetime, Photovoltaic-Based Wireless Sensor Network, Power Electronics, IEEE Transactions on 2012, 27: 9; 3944–3952.

[9] S. D. G. Jayasinghe, D. M. Vilathgamuwa, and U. K. Madawala, A direct integration scheme for battery-supercapacitor hybrid energy storage systems with the use of grid side inverter, Applied Power Electronics Conference and Exposition (APEC) Twenty-Sixth Annual IEEE 2011; 1388–1393.

[10] M. E. Glavin, P. K. W. Chan, S. Armstrong, and W. G. Hurley, A stand-alone photovoltaic supercapacitor battery hybrid energy storage system, Power Electronics and Motion Control Conference EPE-PEMC 2008, 13; 1688–1695.

[11] A. M. Gee, F. V. P. Robinson, and R. W. Dunn, Analysis of Battery Lifetime Extension in a Small-Scale Wind-Energy System Using Supercapacitors, Energy Conversion, IEEE Transactions on 2012, 28:1; 24–33.

[12] D. W. Hart, Power Electronics, first edition, Tata McGraw-Hill, 2011.

[13] N. Mohan and T. M. Undeland, Power Electronics: Converters, Applications, and Design. Wiley India, 2007.

[14] J.L. Duran, Power Conditioning structures and schemes for alternative renewable resources technologies, Power Electronics Congress 2008; 19-27.

Performance study of Membranes on an Electrochemical Hydrogen Compressor

J. L. Pineda[a].,M. P. Gurrola[a], S. Rivas[b]., B. Bahar[c].,J. Ledesma-García[b]., L.G. Arriaga[a]., A. U. Chávez-Ramírez[a]

[a]Centro de Investigación y Desarrollo Tecnológico en Electroquímica S. C., Parque Tecnológico Querétaro s/n, Sanfandila, Pedro Escobedo, C.P. 76703. Querétaro, México.
[b]Universidad Autónoma de Querétaro, División de Investigación y Posgrado, Facultad de Ingeniería. 76010. Querétaro, México.
[C]Xergy Incorporated. 310 North race Street. Georgetown. DE 19947, USA.

ABSTRACT

The electrochemical hydrogen compression (EHC) is a scarcely explored alternative to conventional hydrogen compression methods. The EHC uses the transport phenomena presented in the operation of Proton Exchange Membrane (PEM) technologies, provides important advantages such as low energy demand to reach high compression rates, it is noiseless, low maintenance is required, and unpolluted hydrogen can be obtained. Like in a PEM fuel cell or PEM electrolyzer, the core of the compressor is a Membrane-Electrode Assembly (MEA). One of the main challenges is to find a membrane with a high ionic conductivity and capable of withstand a high pressure between anode and cathode. This work shows the evaluation of four different membranes Nafion, S-PEEK, F>N1, F>S in an EHC system based on an Electrochem PEMFC (5 cm^2). Potential pulses from 100 to 800 mV were applied to the EHC while the pressure increase in the compression chamber was monitored.

Keywords: **Hydrogen; Electrochemical Hydrogen Compressor; Fuel Cell;**

1. Introduction

The use of hydrogen as an energy carrier depends on the development of efficient technologies for production and storage. Water electrolysis in a solid polymer electrolyzer (SPE) is the most efficient method in terms of purity, its operation is exactly opposite to a Proton Exchange Membrane Fuel Cell, PEMFC , in which the oxygen reduction occurs at the cathode and hydrogen oxidation at the anode, resulting in the generation of energy available to do electric work, plus water and heat as the only byproducts, making it the ideal device for the utilization of the hydrogen energy (1 kg of hydrogen contains the same energy as 2.5 kg of gasoline). Regarding to the storage systems, the methods available to date require a high energy investment for either, compressing, liquefying and storing it as metal hydride. The level of the technology of hydrogen storage is not sufficient to satisfy the projected demand for infrastructure because it has many limitations [1]. Some of the limitations of the existing compressors are that they are inefficient and have many moving parts, resulting in the deterioration of the components and therefore excessive maintenance. Besides, using oils or lubricants to migrate wear into the compressor causes hydrogen contamination. An alternative unexplored is the electrochemical compression that has a close operating principle of the PEM fuel cell in terms of transport phenomena [2]. The energy investment in these devices is very low, since it is sufficient to apply a potential of 0.3 V or less to promote oxidation of hydrogen at the side of the compressor and reducing gas in the compression chamber. Like in a PEM fuel cell and solid polymer electrolyzer, the heart of the electrochemical compressor is a membrane electrode assembly (MEA), however; new challenges arise in materials and design, since the MEA's are not designed to operate under high pressure difference between anode and cathode (the maximum pressure difference the manufacturer indicates for ionic conductive membrane, is commonly lower than 10 psi). Besides requiring higher strength materials, it is stated that cell design should allow compressing hydrogen without increasing electrical contact resistance between flow diffuser plates [3].

The working principle of the electrochemical hydrogen compressor is shown in Fig. 1. Because of an applied potential difference, hydrogen at pressure (Pa) is oxidized at the anode to H+, transported through the PEM and reduced at the cathode to hydrogen at pressure (Pc). If the cathode compartment is hermetically sealed, the formation of hydrogen at the cathode results in the increase of the pressure Pc [4].

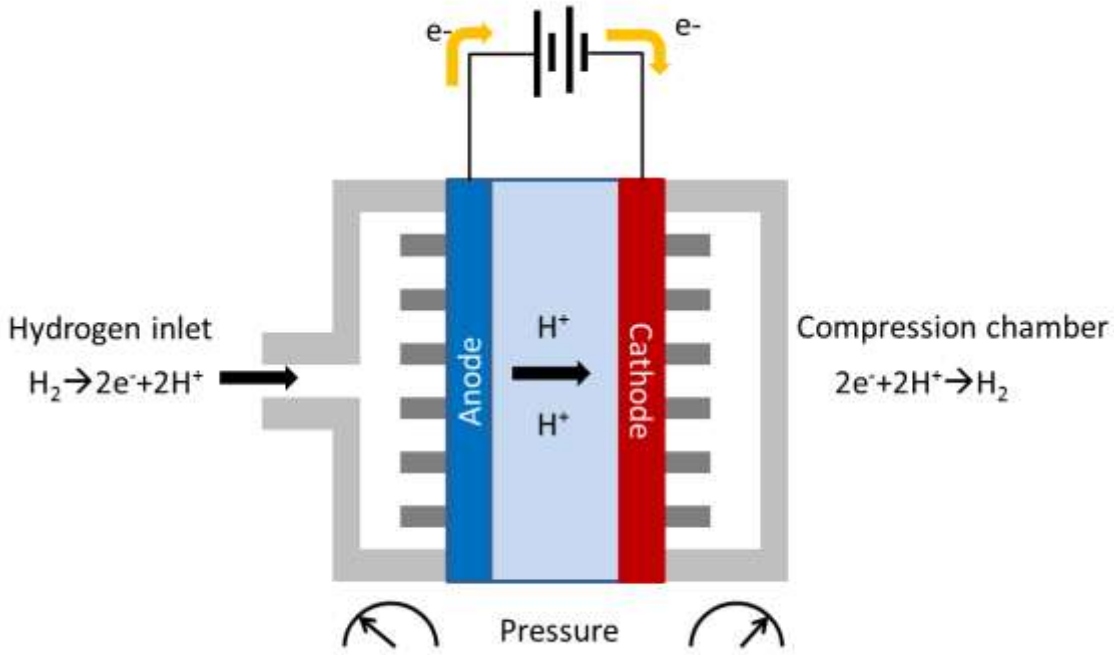

Fig. 1. Electrochemical Hydrogen Compressor

2. Experimental

The experimental section used for this work is schematized in Fig. 2. A regular Proton Exchange Fuel Cell by ElectroChem® was used as a platform for the hydrogen compressor. The Membrane Electrode Assembly for this Fuel Cell has an electrode area of 5cm^2, platinum was used as electrocatalysts (20 % wt., supported on Vulcan carbon XC-72) and Sigracet 35 BC gas diffusers were employed. The hydrogen flux is fixed at 120 ml/min, 100% humidified by ElectroChem® Fuel Cell Test Station. The catalytic ink was spray deposited on the Sigracet 35 BC. The membranes utilized were Nafion 115 (Dupont) 127 µm, S-PEEK (Sulfonated Polyeter-eter-ketone) 73µm, F>N1 (Xergy Incorporated) 26 µm and F>S (Xergy Incorporated) 15µm. A potentiostat/galvanostat Autolab PGSTAT 302 coupled to a Booster 20 A was used for the evaluation tests.

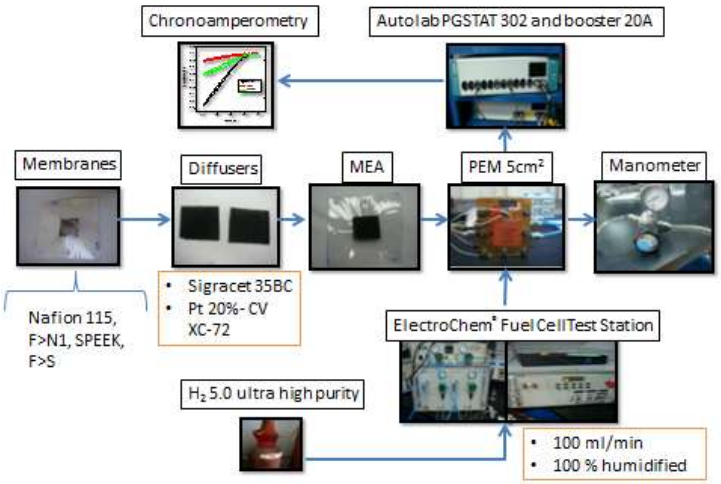

Fig.2 Experimental set-up for the electrochemical hydrogen compressor.

3. Results and discussion

Each membrane performance was observed during a period of 10 min, which is the time at which the highest pressure is reached and stabilized when a potential from 100 to 700 mV is applied. Analysis of the pressure behavior was observed for each membrane.

Nafion 115

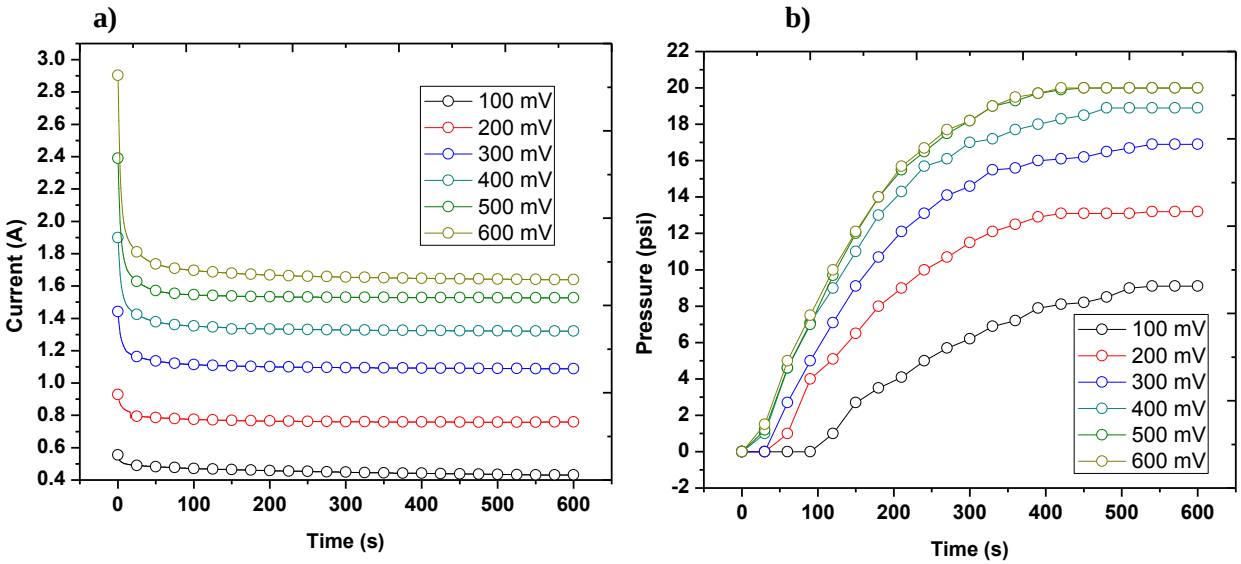

Fig.3 a) Chronoamperogram of Nafion 115 at different potentials on the HEC. b) Pressure vs time graphs obtained from the Nafion 115 assembly in the HEC through a period of 600 s at different potentials.

F>N1

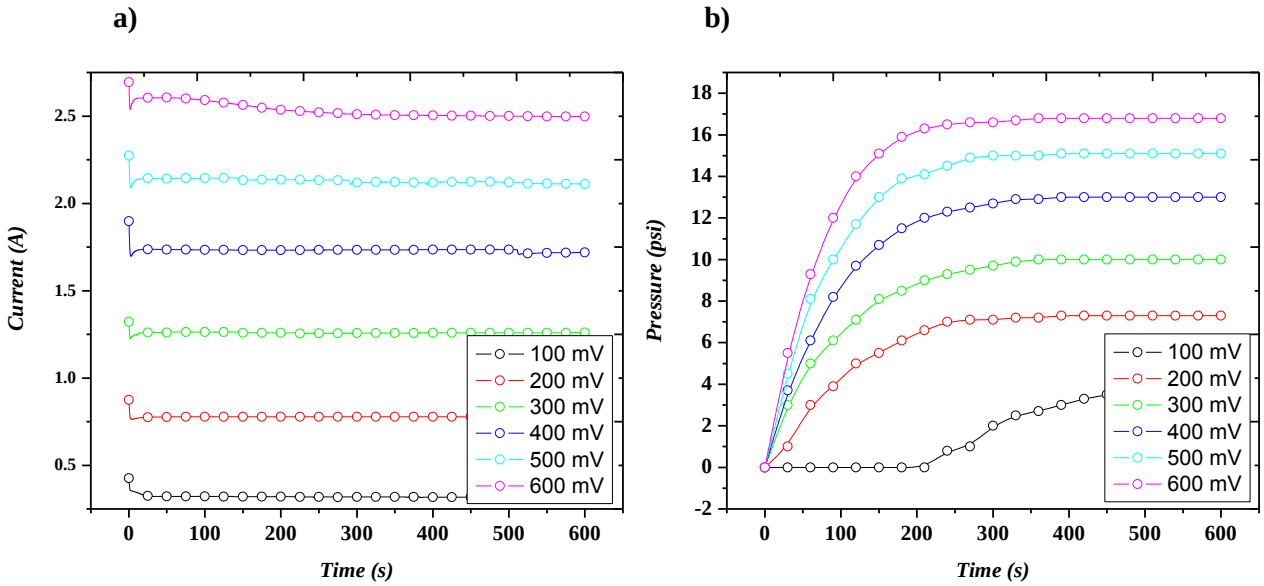

Fig.4 a) Chronoamperogram of F>N1 at different potentials on the HEC. b) Pressure vs time graphs obtained from the F>N1 assembly in the HEC through a period of 600 s at different potentials.

F>S

a) **b)**

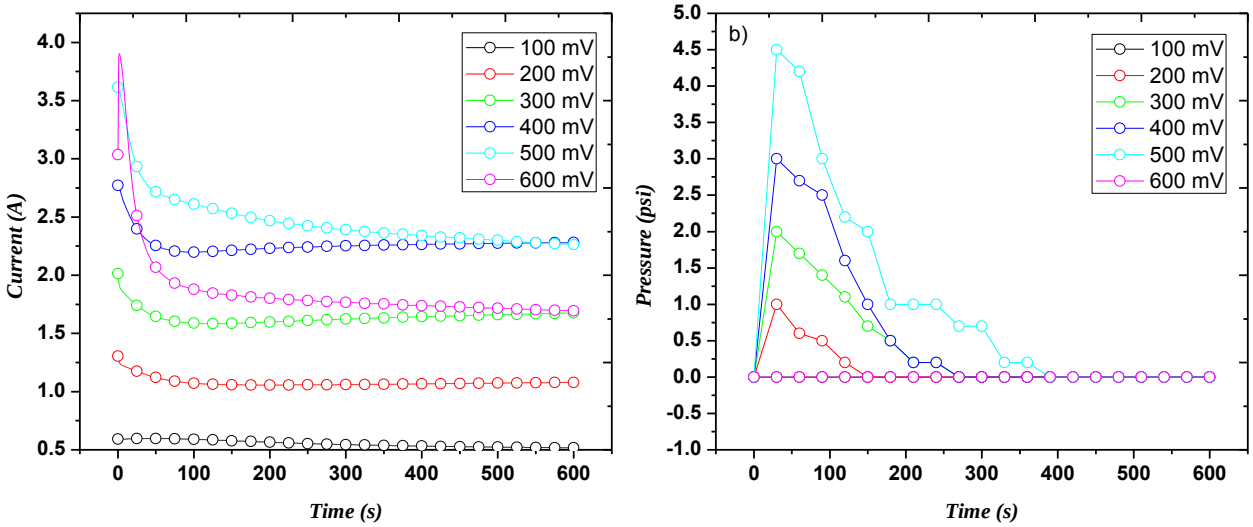

Fig.5 a) Chronoamperogram of F>S at different potentials on the HEC. b) Pressure vs time graphs obtained from the F>S assembly in the HEC through a period of 600 s at different potentials.

S-PEEK

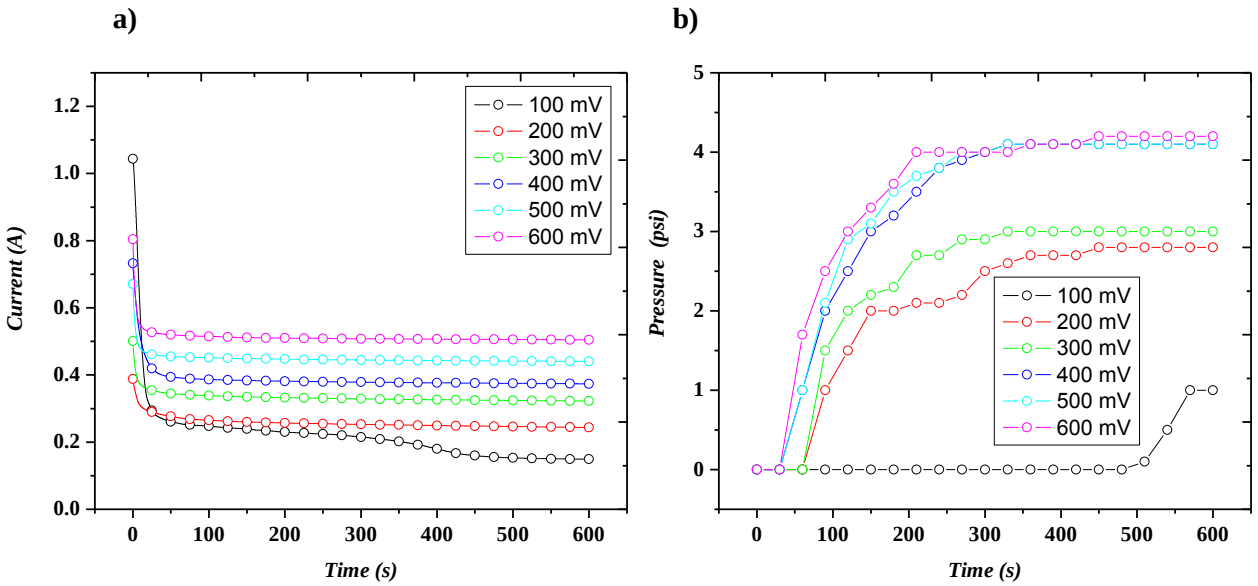

Fig.6 a) Chronoamperogram of S-PEEK at different potentials on the HEC. b) Pressure vs time graphs obtained from the S-PEEK 115 assembly in the HEC through a period of 600 s at different potentials.

Membranes F> N1 and F> S provided by Xergy Inc. shown the highest values of current when were used in MEAs in the compression system, besides they also present the quickest stabilization (around 300 s) however they failed at high pressure due their low mechanical resistance. In contrast the S-PEEK membrane, presents high mechanical resistance, but low conductivity not achieving high pressures. Nevertheless, the high conductivity and mechanical resistance of Nafion allowed to reach an elevated pressure but with a stabilization time of 500 s.

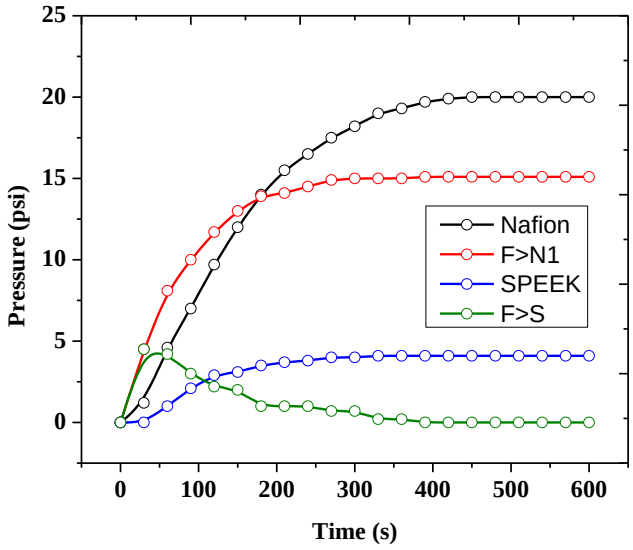

Fig. 7 shows the EHC performance on every membrane at 500mV (the most efficient potential observed).

4. Summary and perspectives

According to tests performed in the membrane evaluation, it was demonstrated that the Nafion ® 115 is the polymer with better efficiency for fuel cell and hydrogen compression applications, however, this research is focusing on find other alternatives for the electrochemical compression system with high mechanical strength, humidity retention and high proton conductivity that could substitute Nafion®.

Acknowledgements

The authors gratefully acknowledge the financial support from the Mexican Council of Science and Technology through Fomix-Querétaro (grant 193148) and Fomix-Zacatecas (grant 203095).

References

[1] L. Zhou, "Progress and problems in hydrogen storage methods," Renewable & Sustainable Energy Reviews 9, 395 (2005)

[2] L. Lipp, “Electrochemical Hydrogen Compressor”, 2012 DOE Hydrogen Program Merit Review and Peer Evaluation Meeting, Arlington, VA, May 14–18, 2012.

[4] M. Winter and R. J. Brodd, "What are batteries, fuel cells, and supercapacitors?," Chem. Rev. 104, 4245 (2004)

[6] James Larminie, Andrew Dicks. Fuel Cell Systems Explained. 2nd Edition.John Wiley & Sons Ltd. England. 2003.

Preparation of Nickel Catalysts Deposited on Gamma Alumina to Process Hydrodeoxygenation First Generation Biodiesel

E. Mora, J. Medina[2], J. Rodriguez[3], D. González[3], M. Sanchez[1]

[1]Universidad Politécnica de Aguascalientes, Calle Paseo, San Gerardo, 207, 20342, Aguascalientes, Ags., México, 20342.
[2] Instituto Tecnológico de Aguascalientes, Av. Adolfo López Mateos #1801 Ote.
Fracc. Bona Gens, Aguascalientes, Ags., México, 20256.
[3] Cinvestav Unidad Saltillo, Av. Industria Metalúrgica 1062, Zona Industrial, Ramos Arizpe, Coahuila de Zaragoza, México, 25900.
[1]Tel: +524494490720; e-mail: up110014@alumnos.upa.edu.mx

ABSTRACT

Due to the current problems in the consumption of fossil fuels nowadays; by the wet impregnation method incipient, a nickel catalyst supported on gamma alumina was prepared using as precursor salt Nickel acetate tetrahydrate, because the precursor salt is not soluble in water, a variant of the method, consisting of a grinding and physical blending of boehmite precursor to nickel salt, once the homogeneous physical mixture drops of a solution of nitric acid dissolved 1:16 in water was added, was applied in this possible to modify the pH of the boehmite surface and achieve the impregnation of the salt. They were anchored nickel particles by a controlled, to obtain nickel oxide, calcination method finally the metal oxide catalysts were reduced by exposure to a flow of hydrogen at 400 ° C, obtaining as a product catalyst Ni/γ -Al_2O_3 can accelerate and direct the hydrodeoxygenation reaction of oxygenated organic compounds for converting a first generation biodiesel second generation biodiesel.

Keywords: Ni/ γ-Al_2O_3; second generation biodiesel, oxygenated organic compounds.

1. Introduction

At present about 80% of world energy demand is obtained by burning fossil fuels. This leads to a depletion of fossil energy resources, which are limited, which has led to the use of fossil fuels is identified as the main cause of global climate change due to emission of pollutants as a result of combustion.

One option to reduce the consumption of fossil fuels and their impact on the environment is the use of renewable energy based on biomass processing, because they have a huge energy potential, and can contribute to the reduction of emissions of greenhouse emissions. Such is the case of Biodiesel.

The method of application of biodiesel and its blends with diesel fuel based oil can be used in diesel engines without any significant engine modification [1].

The disadvantages encountered in the application of first generation biodiesel have attracted interest for the development of catalytic hydrogenation processes of methyl esters from vegetable oils and animal fats, so that they can transform a condition of polyunsaturated to monounsaturated. This new biodiesel is what is known as second generation biodiesel.

In recent years, strategies have been developed for the catalytic production of second generation biodiesel from oils and fats. These processes reacted oils, fats and first generation biodiesel at elevated temperatures in the presence of a heterogeneous catalyst and hydrogen injection, which is achieved with oxygen can be separated through the formation of oxygenated functionalities groups, among which we mention H_2O, CO_2 and CO, such reactions are known as hydrodeoxygenation reactions (HDO) [2].

With the results of performance characterization of catalysts and reaction conditions most suitable catalysts preparation, and the conditions of temperature and hydrogen pressure submit higher reaction yield (HDO).

2. Experimental

- The necessary amounts of boehmite and acetate tetrahydrate Ni $(C_2H_3O_2)_2 \cdot 4H_2O$, in order to obtain the percentages of active metal phase sought (3%, 5% and 7%) are weighed.
- A physical mixing of the catalyst support and the precursor salt is performed by applying a fine grinding process, mixed quantities of boehmite and acetate tetrahydrate Ni $(C_2H_3O_2)_2 \cdot 4H_2O$.
- A solution volume ratio of 1:16 (water:acid) Nitric acid is prepared.
- Once you have the powder catalyst support precursor salt and thoroughly mixed, begin to incorporate drip solution of nitric acid, until a smooth paste.
- The paste was allowed to dry at room temperature for 48 hours.
- Once dry the paste extrusion process is performed to obtain pellets cut to the same size, making sure not pulverized, because if so, the catalyst could be recovered after hydrodeoxygenation process.

- Subsequently all mixtures into pellets were calcined at 510 ° C in the presence of oxygen. The purpose of the catalyst is to calcine the removal of water from the boehmite and obtain γ-Al_2O_3, and moreover, burn acetylacetonate and nitric acid to obtain the end oxides of Nickel on γ-Al_2O_3 deposited.

3. Results and discussion

Characterization of catalysts Ni/γ-Al_2O_3 with 3%, 5% and 7% by weight of active phase was performed by Raman spectroscopy, X-ray diffraction, scanning electron microscopy and EDS. Then the results of the characterization and the interpretation and discussion of the results obtained by each technique is.

Figure 1 shows Raman spectra which were used to monitor the preparation process of the catalysts of Nickel γ-Al_2O_3, in the blue spectrum of the precursor salt of Nickel (Nickel acetate tetrahydrate Ni $(C_2H_3O_2)_2 \cdot 4H_2O$, NIAC4H2O) occurs are shown. Can also be observed in the Raman spectrum green mix in coordination (NIAC4H2O + Boehmite = PTACABO5), where you can observe the characteristic Raman shift of the prepared mixture to obtain a 5 wt% Nickel on gamma alumina, which is apparent that the process of deposition of the precursor salt by the wet impregnation method was incipient adequate, and pH modification helped the impregnation of salt, with a new mix in coordination was obtained with very different peaks which presents the single precursor salt. It also shows clearly that the catalyst of Nickel oxide on gamma alumina ONIGA5 (preparation to obtain 5% by weight of Ni) no characteristic peaks in Raman shift, this is because it is very small amount of Nickel oxide deposited on bracket. But it was also demonstrated that the process of calcination at 510 ° C is suitable because the characteristic peaks disappeared from the organic components of the mixture in coordination. Finally, the spectrum of the catalyst over 5% by weight of Nickel on gamma alumina (ONIGA5) which was reduced to 400 ° C and a pressure of 20 bar of hydrogen, which is observed that there are no peaks characteristic Raman occurs, this is because Raman metals detected at baseline, regardless of the percentage of metal containing the substance.

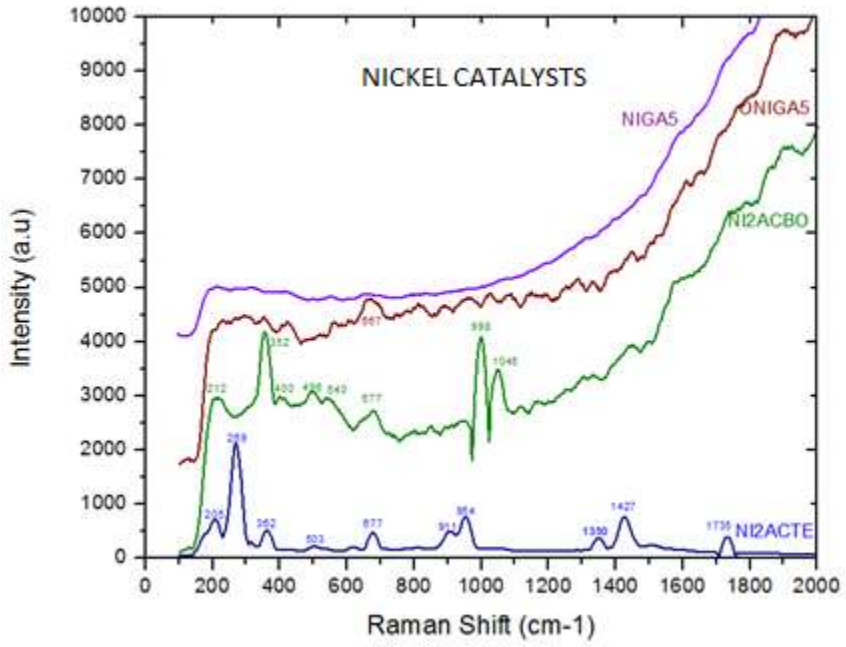

Figure. 1. Monitoring process of preparing Nickel catalysts on γ-Al2O3 by Raman spectroscopy.

In Figure 2, the patterns of X-ray diffraction of the catalysts of Nickel deposited on gamma alumina with 3% by weight (ONIGA3 display), reflection in 2 θ of 32.6 ° is observed, 37.2 °, 39.8 °, 46.25 ° and 67.1 ° which are characteristic of the gamma phase alumina (GA). But an indication of the presence of metal particles of Ni was reflected in the sharp reflections at 2 θ of 39.8 ° and 46.25 ° and increasing the intensity of the reflections of the gamma alumina phase.

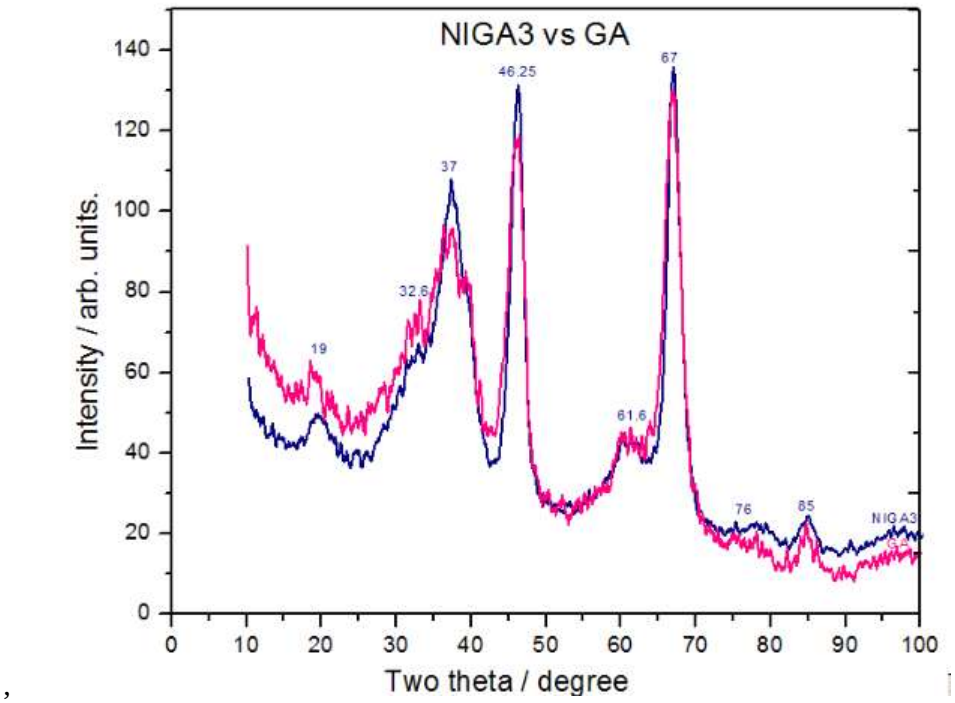

,

Figure 2. Patterns XRD Nickel catalyst on γ-Al_2O_3 with 3 wt% (ONIGA3) and γ-Al_2O3 catalyst support (GA).

In figure 3 the image of scanning electron microscopy of Nickel catalysts deposited on gamma alumina with 3% by weight is shown, are achieved see crystals or clusters ranging in size from nanoscale to 7 μm.

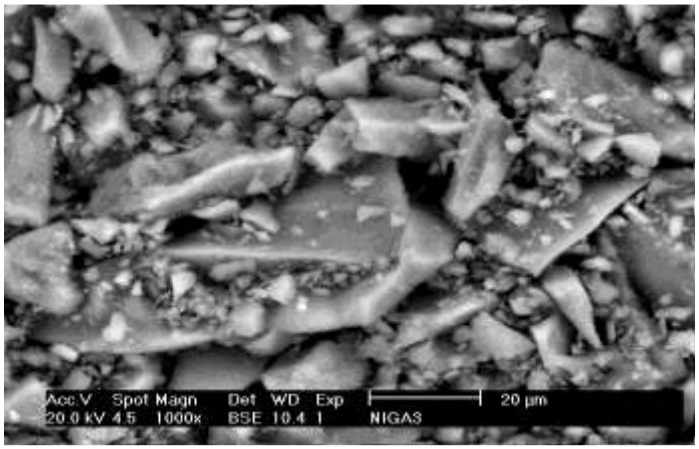

Figure 3. Image of scanning electron microscopy of Nickel catalysts deposited on gamma alumina with 3% by weight of active phase.

Table 1 shows the percentages by weight and the catalyst atomic percentage of platinum deposited on gamma alumina with 3% by weight of active phase, the data show that the amounts of reactants mixed and the preparation process of the catalysts was appropriate.

Table. 1. Average chemical composition by EDS for the nickel catalyst deposited on gamma alumina with 3% and 5% by weight of active phase.

CHEMICAL COMPOSITION OF NICKEL CATALYSTS						
Catalyst	O		Al		Ni	
	Wt %	At %	Wt %	At %	Wt %	At %
NIGA3	36.24	49.765	59.425	48.6	4.345	1.63
NIGA5	38.045	52.625	54.135	44.42	7.82	2.955

4. Summary and perspectives

With Raman spectroscopy it was found that the deposition process of the precursor salt of Nickel by the incipient wetness impregnation method was adequate, as the calcination process. By interpreting patterns of X-ray diffraction showed the presence of metal particles of Ni, and the results of chemical composition by EDS showed that the amounts of reactants mixed and the preparation process of the catalysts were suitable. With the results of characterization ensures that the catalysts will direct and accelerate the reaction hydrodeoxygenation oxygenate conversion to biodiesel and second-generation. The next stage of the project is to apply the catalysts in a reactor containing first generation biodiesel, a temperature and pressure controlled hydrogen, and evaluate the conditions under which the highest yield hydrodeoxygenation reaction occurs.

5. Acknowledgements

Thanks to Dr. Javier Rodríguez Varela CINVESTAV Saltillo Unit for their support in the characterization of materials.

6. References

[1] Agency for toxic substances and disease registry. (Agosto, 2005). *atsdr*. Retrieved from Agency for toxic substances and disease registry: http://www.atsdr.cdc.gov/es/toxfaqs/es_tfacts15.pdf

[2] H. Barzengar-Bafrooei, T. E. (2011). Synthesis of nanocomposite powders of gamma-alumina-carbon nanotube by sol-gel. 22.

Electrochemical Impedance Studies of Co-Based Nanomaterials for Hydrogen Evolution Reaction

J.V. Medina, E. M. Arce, J. G. López

Instituto Politécnico Nacional. ESIQIE. Departamento de Ingeniería en Metalurgia y Materiales, México, D.F.

ABSTRACT

The electrocatalytic activity for hydrogen evolution reaction (HER) of cobalt based nanomaterials synthesized by high energy mechanical milling was studied to use in PEM electrolyzers. X-ray diffraction, scanning electron microscopy and transmission electron microscopy were used to characterize the synthesized powders. Their composition was established by means of energy dispersive spectroscopy, showing the presence of iron which was caused by the wear of grinding medium. Analysis SEM and TEM showed the formation of agglomerates of 1-5 microns, constituted by particles close to 20 nanometers. The electrocatalytic activity of the materials $Co_{80}Ru_{20}$ and $Co_{80}Ru0_{15}Pt_5$ in acid medium was evaluated in 0.5 M H_2SO_4 at 25 °C using linear polarization technique and electrochemical impedance spectroscopy (EIS). From polarization curves was possible to determinate the mechanism of HER. Nyquist diagrams were obtained in a frequency range from 100 kHz to 10 mHz at selected overpotentials in order to avoid the formation of bubbles on the surface of electrode. These diagrams showed the presence of two semicircles, the diameter of the first one, at high frequency, remained constant at all overpotentials, while the diameter of the second one, at low frequency, decreased when overpotential increased. Electrical equivalent circuit 2-CPE was used for the purpose of explaining the electrochemical response. The kinetic parameters for HER obtained from analysis of polarization and impedance data showed that both materials exhibit good performance as electrocatalysts toward to HER. The material with the best performance was $Co_{80}Ru0_{15}Pt_{5.}$

Keywords: Impedance; linear polarization; hydrogen evolution reaction

1. Introduction

The carbon dioxide emissions from human activities and the expected depletion of oil reserves are the subject of a global debate about energetic sustainability and climatic stability, accelerating global initiatives to develop new renewable energy systems [1]. In spite of the energy sources of the future there will always be a need for convenient, clean, safe, efficient and versatile energy carriers or forms of energy that can be delivered to the end user. One of these energy carriers is electricity, already being used worldwide. Electricity is a convenient form of energy, produced from various sources and transported over large distances. It is clean, although its production from fossil fuels is not. Hydrogen is another clean, efficient and versatile energy carrier, supplemented electricity very well. Together these two carriers may satisfy all the energy needs and form an energy system that is permanent and independent of energy sources [3-4]. However, hydrogen is not a primary energy source, in nature cannot be found it in elemental or molecular form, only taking part of different compounds, water being the most abundant source. H_2 can be produced from a wide range of material, including fossil fuels, biomass and water electrolysis [5].

Water electrolysis is relatively efficient (>70%), but because it needs electricity, hydrogen produced by water-electrolysis is expensive, and this is due to the laws of thermodynamics, inasmuch the energy required to separate the H_2 and O_2 from water is higher than the energy which can be released by hydrogen utilization [6]. Hydrogen can be produced efficiently using electricity from renewable energy sources such as solar and wind [7]. In conventional PEM water electrolyzers, precious metals are used as electrocatalysts, implying one of the most important issues about the choice of the electrodes materials for hydrogen and oxygen evolution. The ability of a given metal to catalyze the HER is usually measured by the exchange current density. Three properties play an important role in selecting catalytically active materials for hydrogen evolution: (a) an actual intrinsic electrocatalytic effect of the material, (b) a large active surface area per unit volume ratio, both of which are directly related to the overpotential used to operate the electrolyzer at significant current densities, and (c) catalyst stability [8]. Platinum was found to be an electrode material on the top of which hydrogen evolves with the minimum overpotential [9]. Unfortunately, due to the high price and limited resources, the application of Pt in the future will be limited [10]. One of the main challenges in PEM technologies is to reduce noble metals contents or completely replace them and to maintain the same level of efficiency [11]. Alternatively non-precious metals, such as Ni, Co and their allows have been studied for HER, but the activity of these systems in electrolyzers PEM was poor due to instability en acid medium [12].

In this work, cobalt based nanostructured materials were prepared by mechanical alloying and were characterized by scanning electron microscopy; crystallite size was obtained by means X-ray diffraction using Sherrer and Williamson-Hall methodologies. The catalytic properties toward HER were described by Tafel linear and Electrochemical Impedance Spectroscopy (EIS).

2. Experimental

2.1. Electrode preparation

Preparation of the catalytic powders was performed by the mechanical alloying technique, two different systems were tested $Co_{80}Ru_{20}$ and $Co_{80}Ru_{15}Pt_5$, Co (Sigma-Aldrich 325 mesh powder), Ru (Sigma-Aldrich 200 mesh powder) and Pt (Sigma-Aldrich 1 µm) were introduced in a high energy ball mill Spex 8000 during 40 h using a stainless steel vial and balls with a ball to powder ratio of 4:1. Their chemical composition, in *wt.%*, was tested by Energy Dispersive Spectroscopy. The carbon paste used as working electrode was prepared as follows: 0.1 g of metallic phase and 0.4 g of graphite were mixed with 0.25 mL of silicone oil. The carbon paste obtained was packed into a polypropylene holder to control the exposed surface. Electrical contact to the paste was established via a thin copper rod passed through the polypropylene holder.

2.2. Electrochemical setup

A conventional glass cell was used with a separated compartment for the reference electrode. The reference electrode was a mercury-potassium sulfate electrode Hg/K_2SO_4 (E = 0.64 V/NHE). All potentials are referred to NHE. A graphite bar was used as counter electrode. All electrochemical measurements: the *dc* polarization and the electrochemical impedance spectroscopy (EIS) were carried out in aqueous acid 0.5 M H_2SO_4, bubbled with ultra-high purity nitrogen to remove the present oxygen. The flux of nitrogen was maintained above the electrolyte surface during the measurements. The temperature at which the measurements were performed was at 25 °C, controlled by means an isothermal bath. Polarization measurements of hydrogen evolution were carried out by first stabilization at open-circuit potential (OCP), then a linear polarization measurement was conducted starting from OCP to negative direction, at a scan rate of 5 mV s^{-1}. Electrochemical impedance spectroscopy measurements were performed at selected overpotentials of 0 V, -0.010 V, -0.025 V y -0.035 V.

2.3. Apparatus and methods

A D5000 SIEMENS X-ray diffractometer using Mo Kα radiation and operating at 35 kV and 25 mA was utilized for the structural and phase analysis of the obtained powders. The XRD patterns were recorded in a 2θ range from 10 to 70° at a step time of 0.5° min^{-1}. The particles and their surface morphologies were examined using Transmission Electron Microscope JEOL 2000-FXII and a field emission scanning electron microscope JEOL JSM-6701F equipped with an energy dispersive spectrometer. Electrochemical measurements were performed using a Potentiostat/Galvanostat Autolab-30 system connected to a personal computer.

3. Results and discussion

3.1. XRD analysis

The present phases in the studied powders were identified by using XRD analysis. XRD spectra are shown in fig. 1.

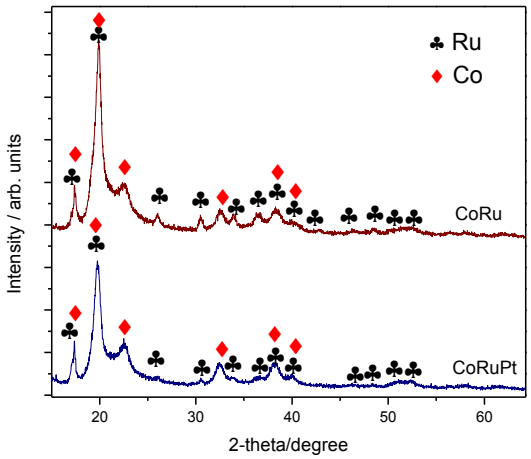

Fig. 1. XRD patterns of $Co_{80}Ru_{20}$ and $Co_{80}Ru0_{15}Pt_5$ powders after 40h milling time.

Co and Ru both presented a HCP crystalline structure before they were submitted to milling, but the characteristic peaks for Co after milling do not correspond to this structure, so there was a change phase, corresponding to FCC structure, in the other hand, the characteristic peaks for Ru were the same, XRD spectra do not show evidence of

formation of intermetallic compounds, because new peaks do not appear, although there are overlapping in certain characteristic peaks. The presence of platinum was not detected; this could be attributed to its low percentage or its small crystallite size.

It was estimated crystallite size by means Sherrer [13] and Williamson-Hall [14] methodologies, table 1 lists the values obtained. Sherrer methodology assume that microdeformations in the crystal lattice are negligible, unfortunately in the preparation of electrocatalysts by mechanical milling technique the presence of microdeformations in the crystal lattices of the materials are inevitable, leading the crystallite size estimated using Sherrer to an erroneous result. Considering this situation, other methodologies are needed to estimate the crystallite size, where the broadening of the peak due to microstrains is considered. Williamson-Hall methodology considers this situation and it is possible to employ the different kind of profile of diffraction peaks (Gaussian, Lorentzian and Pseudo-Voigth). The calculated values from these methodologies are displayed in the table 1, the values from Scherrer methodology are completely different to values from Williamson-Hall methodology this is due to the mentioned above, on the other hand, values from Gaussian profile are different from other profiles, results from Lorentzian profile are so similar to Pseudo-Voigth results, inasmuch as Pseudo-Voigth profile let combine Gaussian and Lorentzian profiles it can be taken this value like the most reliable.

Table 1. Crystallite sizes calculated from XDR data.

	Cristallyte size (nm)			
Sample	**Williamson-Hall**			**Sherrer**
	Profile			
	Gaussian	Lorentzian	Pseudo-Voigth	
$Co_{80}Ru_{20}$	15.71	21.42	21.74	14.7
$Co_{80}Ru_{15}Pt_5$	18.78	24.99	24.68	17.55

3.2. SEM and TEM analysis

SEM and TEM analysis was performed to observe the particle size and the morphology of the prepared electrocatalyst, fig. 2. In both electrocatalysts agglomerates from 1 to 5 microns in size were formed, conformed by particles lower close to 20 nm, this confirms the results obtained from XDR analysis. From fig. 2 a, corresponding to the micrograph of $Co_{80}Ru_{20}$ system, it can be seen that the particles are slightly smaller than particles of system $Co_{80}Ru_{15}Pt_5$, fig. 2b.

The composition and content of CoRu and CoRuPt were established by means EDS analysis. Fig. 2 also shows EDS spectra of a) $Co_{80}Ru_{20}$ and b) $Co_{80}Ru_{15}Pt_5$ and it can be observed the presence of the characteristic lines of iron, stemming from the grinding media wear, iron modifies the nominal composition, so the weight ratio of Co, Ru and Fe is 73:20:7 for Co-Ru, and for Co-Ru-Pt the weight ratio of Co, Ru, Pt and Fe is 78:15:5:2.

a)

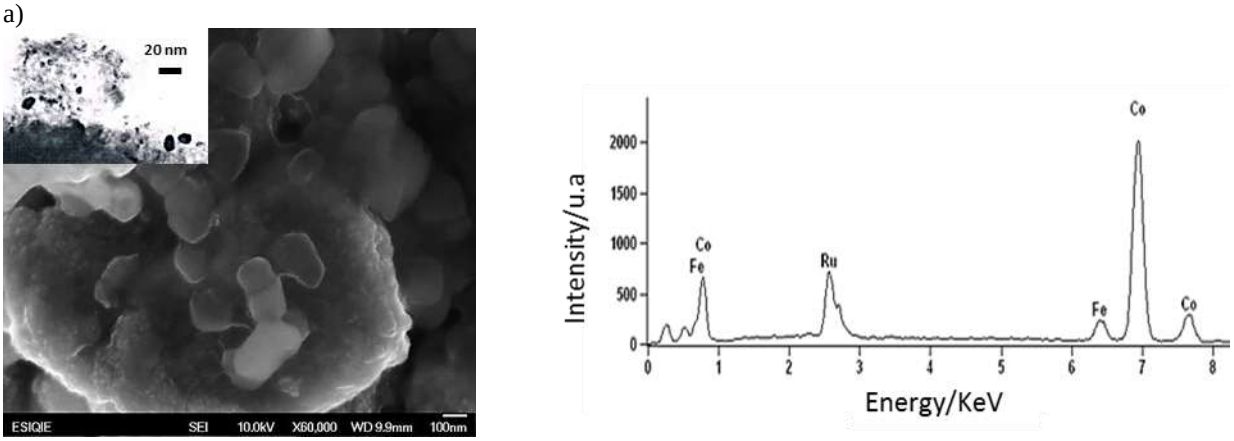

b)

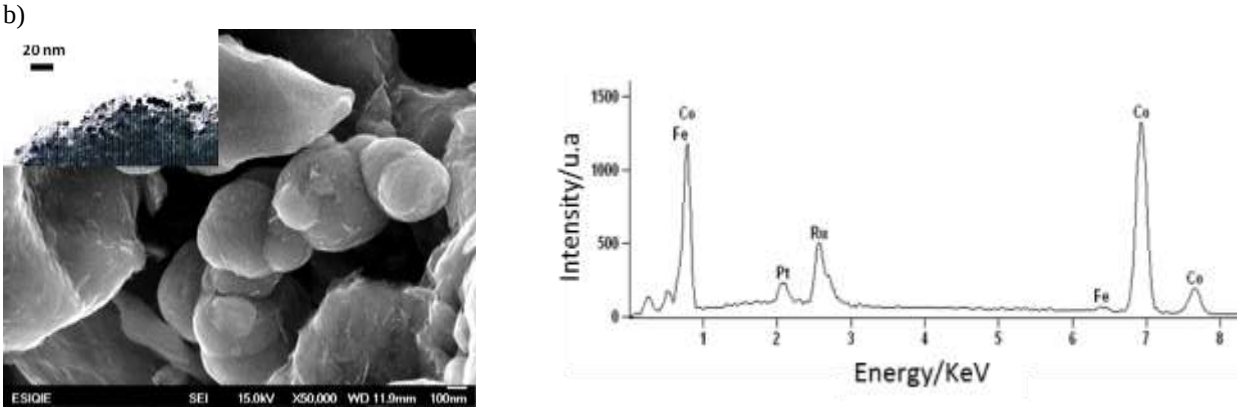

Fig. 2 TEM and SEM images: a) material $Co_{80}Ru_{20}$ and b) material $Co_{80}Ru_{15}Pt_5$ and their respective EDS spectra.

3.3. Electrocatalytic activity toward HER

Polarization curves for the hydrogen evolution reaction (HER) of the synthesized electrocatalytic materials were obtained by potentiodynamic method in a solution 0.5 M H_2SO_4 at a sweep rate of 5 mV s^{-1} and 25 ° C. The polarization was started at open circuit potential and toward negative direction in all cases, Tafel linear polarization measurements were performed to obtain the corresponding electrochemical parameters, fig. 3, such as Tafel slope, exchange current density and transfer coefficient, listed in table 2.

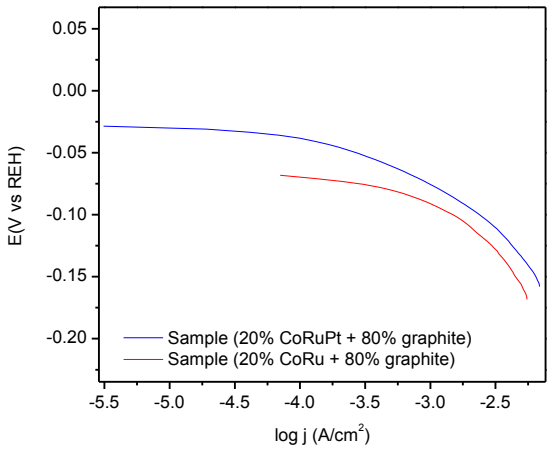

Fig. 3 Linear Tafel polarization curves for the HER of the studied materials, in 0.5 M H_2SO_4 at 5 mV s^{-1}.

Table 2 Kinetic parameters obtained from Tafel curves.

Sample	b_c **(mVdec^{-1})**	α	j_0 **(A cm^{-2})**	η **(mV)** $j = 4\ mA\ cm^{-2}$
Co-Ru	42.8	0.3456	$3.09\ x\ 10^{-4}$	93.1
Co-Ru-Pt	30.4	0.4866	$3.16\ x\ 10^{-4}$	73.1

The absolute value of the Tafel slope, which is an intensive quantity and does not depend on the true surface area of the electrode, is a diagnosis to establish the mechanism and the determining step of the reaction. Slope values close to 40 mV dec^{-1} suggest that the possible mechanism is a classic sequence Volmer-Heyrovsky [15], where the first step is the discharge of the proton by electrosorption:

$$M + H + e^- \leftrightarrow MH_{ads} \qquad Volmer\ reaction \tag{1}$$

The second step in this sequence is the electrochemical desorption:

$$MH_{ads} + H^+ + e^- \leftrightarrow M + H_2 \qquad \text{Heyrovsky reaction} \tag{2}$$

Values close to 29 mV dec^{-1} suggest that the possible mechanism is a Volmer-Tafel sequence [16], where the first step is again discharge electrosorption proton followed by chemical recombination:

$$2MH_{ads} \leftrightarrow 2M + H_2 \qquad Tafel\ reaction \tag{3}$$

Tafel slopes for HER in the studied materials are 30.4 and 42.8 mVdec^{-1} for $Co_{80}Ru_{20}$ and $Co_{80}Ru_{15}Pt_5$, respectively, indicating that the possible reaction mechanism is the classical sequence Volmer -Heyrovsky for

$Co_{80}Ru_{20}$, being the determining step reaction Heyrovsky reaction, whereas for $Co_{80}Ru_{15}Pt_5$ the possible reaction mechanism is the sequence Volmer-Tafel, where the determining step is the reaction of Tafel.

A value of exchange current density is frequently used for the characterization of electrocatalytic activity, so the catalyst $Co_{80}Ru_{15}Pt_5$ showed a better performed because of its value of exchange current density,3.16 x 10^{-4}, although the value of exchange current density for $Co_{80}Ru_{20}$ is close to the last one, 3.04 x 10^{-4}, considering this it was necessary to regard other way to evaluate the performing, it has been reported that values of Tafel slope in the low overpotential region (Tafel region) are as or even more important than a favorable exchange current density value [17]. This is due to the fact that the HER does not occur at a reversible potential, although a certain overpotential is required for the reaction to proceed at a measurable rate. Therefore, in order to compare the electrocatalytic activity of the prepared catalysts, it was fixed a current density and the resulting overpotentials required to reach the given current density value were compared. This has to give an indication of the amount of energy which must be provided to produce a specified amount of hydrogen. Overpotential values for each catalyst, measured at current density of 4 mA cm^{-2} are listed in table 2, $Co_{80}Ru_{15}Pt_5$ required the lowest overpotential to get the current density given, -73.1 mV, on the other hand, $Co_{80}Ru_{20}$ required a larger energy, -93.1 mV. According to the parameters obtained from the studied materials with general composition 80 % graphite + 20% metallic phase, determined by Tafel linear polarization, the material that showed the best performing was $Co_{80}Ru_{15}Pt_5$.

3.4. Electrochemical impedance spectroscopy

To accomplish a better characterization of the interface electrode/electrolyte and the corresponding processes toward the HER in the prepared materials, electrochemical impedance spectroscopy measurements were performed, obtained in a frequency range from 100 kHz to 10 mHz in 0.5 M H_2SO_4 at imposed overpotentials of 0, -10,-25 y -35 mV, other more negative potentials were discarded to avoid possible formation of bubbles over the electrode surface, all measurements were carried at 25 °C.

Fig. 4 presents the complex plane plots (-Z" vs. Z') of both systems, $Co_{80}Ru_{20}$ and $Co_{80}Ru_{20}Pt_5$, obtained at different overpotentials.

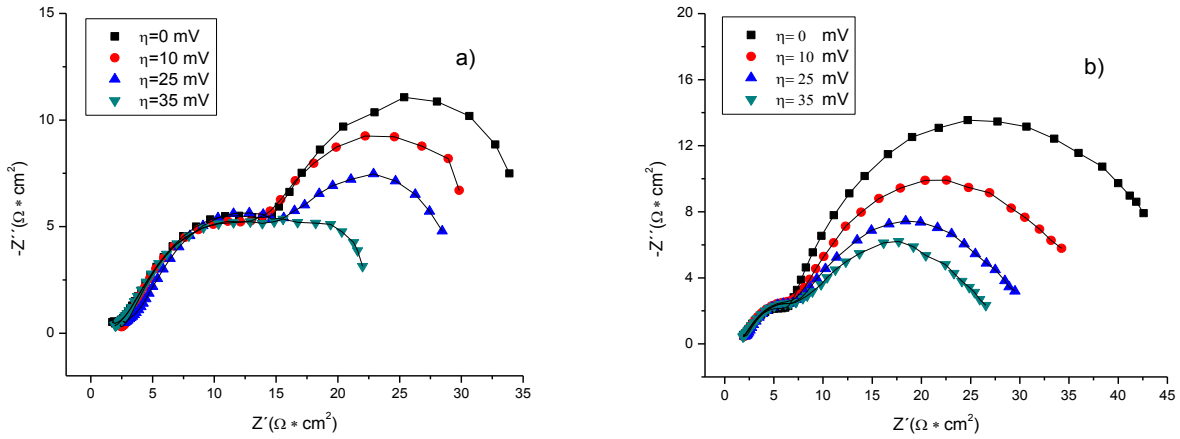

Fig. 4 Nyquist diagrams obtained on a) $Co_{80}Ru_{20}$ and b) $Co_{80}Ru_{20}Pt_5$ in 0.5 M H_2SO_4 at selected overpotentials. The solid lines represent the fitted data using equivalent electrical circuit 2-CPE (⟶).

It can be observed on Nyquist diagrams the presence of two semicircles: the first at high frequency, where its diameter varies slightly with the overpotential imposed, while the diameter at low frequency decreases considerably as the potential is more negative. From these graphs, there is no a significant difference in the characterization of these materials, inasmuch as both materials are characterized by two time constants. However, qualitatively the detected high frequency semicircle has a diameter smaller for the system $Co_{80}Ru_{15}Pt_5$ than for the system $Co_{80}Ru_{20}$. Preliminarily it could be considered that Pt favors the phenomenon commonly associated with a process electrosorption and/or reduction of protons to the electrode. Generally, the impedance spectra revealed the presence of two time constants, which agrees with the EIS spectra obtained in other electrocatalysts for HER previously studied [18,19].

To describe the electrochemical response and the corresponding processes, experimental EIS data were modeled using NOVA 1.8 software, employing a non-linear fix and an electrical equivalent circuit. Until now three equivalent models have been used to explain the behavior of this kind of electrodes toward HER [20-23]: (i) 1-CPE, (ii) two-CPE and (iii) porous model, the 1-CPE model can produce one or two semicircles on the complex plane plots both of them potential dependent. The second model is the 2-CPE model, introduced by Chen and Lasia [24], this one is commonly used to describe the electrochemical response of two semicircles, the first one, considered potential independent, is associated with the surface porosity and the second one, because of its behavior, is considered potential dependent and can be related to the process of the HER. The third model, introduced by Levie [25], predicts a straight line at 45° at high frequencies, followed by one or two deformed semicircles.

The experimental data for Co- based electrode were simulated using the 2-CPE, fig. 5, consisting of a solution associated resistance, *Rs* in series with two parallel connection of CPE with a resistance, due to the semicircles at high-frequency kept almost constant it was thought to simulate the experimental data using this model. It was tried to use the electrical equivalent model 1-CPE but this model could not be used to describe the experimental *ac* impedance data because the produced circles have to be potential dependent and it did not occur.

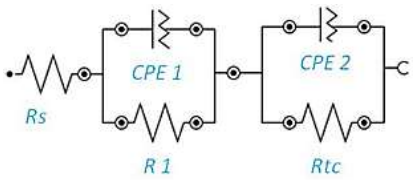

Fig. 5 Electrical equivalent circuit 2-CPE.

From the semicircles at high frequency of Nyquist diagrams it was possible to obtain the parameters *Rs*, A_1, T_1 and ϕ_1, associated with the porosity of the material and therefore they were not affected by the change of overpotential. From the semicircles at low frequency could be found parameters A_2, T_2 *and* ϕ_2, related to the faradic process. Detailed information about the meaning of these parameters is given in Ref. [20-22]. Briefly, the parameter A_2 represents the inverse of the charge transfer resistance R_{TC}:

$$A = \frac{1}{R_{ct}} \tag{4}$$

It was possible determinate parameter T_2 from the impedance given by a CPE, introduced when there is a distribution of the time constants causing a rotation of the semicircle on complex plane:

$$Z_{CPE} = \frac{1}{T(j\omega)^{\phi}} \tag{5}$$

Where ϕ is a constant, taking values from -1 to 1, T is a capacity parameter associated with the double layer capacitance, C_{dl}. When ϕ is equal to 1, T has units of a capacitance, F cm^{-2}. When ϕ is different from 1, T has units expressed in F cm^{-2} s$^{\phi-1}$. To estimate double-layer capacitance, Brug [26] presented a method where faradic process can be expressed by a single equivalent resistance, R_{ct}, as:

$$T = {C_{dl}}^{\phi}\left[{R_s}^{-1} + {R_{ct}}^{-1}\right]^{1-\phi} \quad (6)$$

and finally the capacitances calculated from 6 have units of F cm^{-2}.

Table 3 shows the parameters obtained from EIS analysis. *Rs* is almost constant for each material at different imposed overpotentials, being slightly higher for $Co_{80}Ru_{20}$ system, and this may be due to the variations during the experimentation, such as the distance of the electrodes, the inert atmosphere and/or temperature variation. The behavior is the same for the parameters at high frequency, there is not a noticeable change on CPE_1, ϕ_1 and R_1, taken from high frequency semicircles. On the other hand, parameters taken from low frequency semicircles, it was observed that R_{tc} values for both materials decreased when the applied overpotential was increased, although clearly R_{tc} values for Pt-containing system are lower at more negative overpotentials. It is evident a considerable decrease in value of CPE_2 at values higher of overpotencial to both systems being smaller values for $Co_{80}Ru_{20}Pt_5$.

Table 3 Parameters obtained from electrical circuit equivalent 2-CPE for the studied materials.

System	η (mV)	Rs (Ω cm^2)	CPE_1 (μF cm^{-2})	ϕ_1	R_1 (Ω cm^2)	CPE_2 (μF cm^{-2})	ϕ_2	R_{CT} (Ω cm^2)
$Co_{80}Ru_{20}$	0	2.43	118.43	0.63	15.16	18798.89	0.90	41.73
	10	2.45	81.62	0.56	19.72	18648.30	0.94	37.75
	25	3.02	114.44	0.60	18.18	17234.30	0.94	29.70
	35	2.21	75.71	0.59	19.76	3960.13	0.92	22.78
$Co_{80}Ru_{15}Pt_5$	**0**	1.70	13.27	0.68	4.55	801.49	0.68	42.51
	10	1.76	14.95	0.67	5.51	612.75	0.70	31.00
	25	2.03	14.03	0.72	5.19	404.24	0.71	23.46
	35	1.63	7.10	0.62	4.92	325.15	0.71	18.90

Analyzing Nyquist plots (Z '- Z"), it can observe that for $Co_{80}Ru_{20}$ when a overpotential higher is imposed the semicircle at low frequencies tends to disappear, this can be attributed to rate determining step, as it was discussed above, the reaction mechanism for non-platinum system was the classic sequence Volmer-Heyrovsky at low overpotentials, this behavior is according to H_2 evolution over Ni [27,28], where the Tafel slope must be close to 40 mV dec^{-1}, but after a certain threshold potential, the Tafel slope may increase until it gets a limiting value of 120 mV dec^{-1} [29], so the second stage tends to do not proceed, leading to reduction and/or disappearance of the semicircle. Accordingly, the mechanism for HER in $Co_{80}Ru_{20}$ is Volmer-Heyrovsky.

For $Co_{80}Ru_{20}Pt_5$ is observed the presence of both semicircles at high and low frequencies all imposed overpotentials, establishing the kinetics of the first step is greater than either the kinetics of the reactions desorption or recombination. Considering this, it would be carrying out both reaction adsorption and desorption of protons, both dependent on the potential, as well as the recombination process. From the study of the Tafel slopes was established the reaction mechanism for HER in $Co_{80}Ru_{20}Pt_5$ is Volmer-Tafel. However, EIS study showed that also electrodesorption stage was carried out therefore both stages, after electrosorption, are competing to remove adsorbed species on the surface of the material.

4. Summary and perspectives

XRD analysis showed that there is no the intermetallic formation, analysis of scanning and transmission electron microscopy showed that the synthesized materials formed agglomerates with a size between 1-5 microns, composed by particles smaller than 20 nm, the composition and content of CoRu and CoRuPt were established by means EDS analysis, it could be observed the presence of the characteristic lines of iron, stemming from the grinding media wear, iron modifies the nominal composition, so the weight ratio of Co, Ru and Fe is 73:20:7 for the Co-Ru and for the Co-Ru-Pt the weight ratio of Co, Ru, Pt and Fe is 78:15:5:2. The addition of Pt increases electrocatalytic activity and stability of the material at high potentials. Both materials exhibited good performance toward HER. Tafel slopes for CoRu and CoRuPt were 42.8 and 30.4 mVdec-1, respectively, indicating that the reaction mechanism for this process is Volmer-Heyrovsky for CoRu and Volmer-Tafel for CoRuPt. Tafel analysis showed the material with better electrocatalytic performance is CoRuPt because it is the material with the lowest overpotential value to get at current density of 4 mA cm^{-2}. EIS analysis determined that the kinetics of the material containing Pt was the fastest due to its transfer resistances, extracted from semicircle at low frequency.

Acknowledgements

The authors gratefully acknowledge the financial support provided by Consejo Nacional de Ciencia y Tecnología CONACYT-CNPq 174247, *Instituto de Ciencia y Tecnología del Distrito Federal* ICyTDF 325/2011, Secretaria de Investigación y Posgrado SIP-IPN 20130138 project and Programa Institucional de Formación de Investigadores PIFI-IPN, Sistema Nacional de Investigadores SNI and CONACYT scholarships.

References

[1] A. Miltner, W. Wukoviks, T. Pröll, A. Fried, Renewable hydrogen production: a thechnical evaluation based on process simulation, www.elsevier.com/locate/jclepro, 2010; 551-562.

[2] J.O'M. Bockris, Energy: The Solar-hydrogen Alternative. Halsted Press, New York, 1975.

[3] J.O'M. Bockris, T.N. Veziroglu, A solar-hydrogen energy system for environmental compatibility. Environ. Conserv., 1985; 12: 105-118.

[4] J.O'M. Bockris, T.N. Veziroglu, D. Smith, Solar Hydrogen Energy: The Power to Save the Earth. Optima, London 1991.

[5] T.N. Veziroglu, F. Barbir, Hydrogen: The wonder fuel. Int. J. Hydrogen Energy, 1992; 17: 391-404.

[6] T.N. Veziroglu, F. Barbir, Solar-hydrogen energy system: the choice of the future. Environ. Conser., 1991; 18: 304-312.

[7] M Ni, MKH Leung, DYC Leung. Energy and exergy analysis of hydrogen production by a proton exchange membrane (PEM) electrolyzer plant. Energy Convers Manage, 2008; 49: 2748-56.

[8] N.K. Labhsetwar, V. Balek, E. Večerníková, P. Bezdička, J. Subrt, T. Mitsuhashi, S. Kagne, S. Rayalu, H. Haneda, J. Colloid Interface Sci., 2006; 30: 232-236.

[9] H. Kita, in Electrochemistyr: The Past Thirty and the Next Thirty Years, H. Bloom and F. Gootman, Eds., Plenum Press, New York, 1977: 117.

[10] K. Lee, J. Zhang, H. Wang, DP Wilinson, Progress in the synthesis of carbon nanotube- and nanofiber-supported Pt electrocatalysts for PEM fuel cell catalysis. J. Appl. Electrochem., 2006; 36: 507-22.

[11] S.A. Grigoriev, M.S. Mamat, K.A. Dzhus, G.S. Walker, P. Millet, Platinum and palladium nano-particles supported by graphitic nano-fibers as catalysts for PEM water electrolysis, Int. J. Hydrogen Energy 2011:36 4143-4147.

[12] P. Paunović, O. Popovski, AT. Dimitrov, D. Slavkov, E. Lefterova, S. Hadži Jordanov, Study of structural and electrochemical characteristics of Co-based hypo-hyper d-electrocatalysts for hydrogen evolution, Electrochim. Acta, 2007; 52: 4640.

[13] C. Barret, Estructure of Metals, McGraw-HillBook Company, Inc. New York, 1957.

[14] G.K. Williamson, W.H. Hall, X-Ray Line Broadening From Filed Aluminium and Wolfram, Acta Metallurgica, 1953; 1: 22.

[15] E. Fachinotti, E. Guerrini, A.C. Tavares, S. Trasatti, Electrocatalysis of H2 evolution by thermally prepared ruthenium oxide, J. Electroanal. Chem., 2007; 600: 103.

[16] J. Chenga, H. Zhanga, H. Ma, H. Zhonga, Y. Zoua, Study of carbon-supported IrO2 and RuO2 for use in the hydrogen evolution reaction in a solid polymer electrolyte electrolyzer, Electrochim. Acta 2010; 55: 1855-1861.

[17] R. Šimpraga, G. Tremiliosi-Filho, S.Y. Qian, B. E. Conway, In situ determination of the "real area factor" in H_2 evolution electrocatalysis at porous Ni-Fe composite electrodes, J. Electroanal. Chem., 1997; 424: 141-151.

[18] E. Ndzebet, O. Savadogo, Study of the hydrogen evolution reaction in a basic-medium on palladium highly dispersed in graphite-electrodes electro-activated with SiW12O404- (STA), Int. J. Hydrogen Energy, 1995; 20: 635-640.

[19] E. Navarro-Flores, Z. Chong, S. Omanovic, Characterization of Ni, NiMo, NiW and NiFe electroactive coatings as electrocatalysts for hydrogen evolution in an acidic medium, J. Mol. Catal. A: Chem., 2005; 226: 179-197.

[20] A. Lasia, Applications of the electrochemical impedance spectroscopy to hydrogen adsorption, Evolution and absorption into metals, In: B. E. Conway and R.E. White, editors Modern Aspects of Electrochemistry, New York: Kluwer/Plenum, 2002; 35: 1-49.

[21] A. Lasia, Electrochemical Impedance Spectroscopy and Its Applications, In: B. E. Conway, J. Bockris and R.E. White, editors Modern Aspects of Electrochemistry, New York: Kluwer/Plenum, 1999, Vol. 32, p. 143-248.

[22] A. Lasia, L. Birry, Studies of the hydrogen evolution reaction on Raney nickel–molybdenum electrodes, J. Appl. Electrochem. 2004; 34: 735-749.

[23] B. Łosiewicz, A. Budniok , E. Rówiński , E. Łągiewka, A. Lasia , The structure, morphology and electrochemical impedance study of the hydrogen evolution reaction on the modified nickel electrodes, Int. J. Hydrogen Energy, 2004; 29: 145-157.

[24] L. Chen, A. Lasia, Study of the Kinetics of Hydrogen Evolution Reaction on Nickel-Zinc Powder Electrodes, J. Electrochem. Soc., 1992; 139: 3214.

[25] R. De Levie, in P. Delahay and C.W. Tobias (eds.), Advances in Electrochemistry and Electrochemical Engineering, Wiley, 1967; 6: 239.

[26] G.J. Brug, A.L.G. Van Den Eeden, M. Sluyters-Rehbach, J.H. Sluyters, The Analysis of Electrode Impedances Complicated by the Presence of a Constant Phase Element, J. Electroanal. Chem., 1984; 176: 275-295.

[27] J.O'M. Bockris, A.K.N. Reddy, Modern Electrochemistry, Plenum, 1970; 2: 1248.

[28] A.J. Appleby, H. Kita, M. Chemla, G. Bronoel, in: A.J. Bard (Ed.), Encyclopedia of Electrochemistry of the Elements, New York, 1982; 9: 383.

[29] J.G. Highfield, E. Claude, K. Oguro, Electrocatalytic synergism in Ni/Mo cathodes for hydrogen evolution in acid medium: a new model, Electrochim. Acta, 1999; 44: 2805-2814.

Novel $(Ir_xSn_ySb_z)O_w$ Material as Catalyst for The Oxygen Evolution Reaction

N. J. Pérez-Viramontes[1], C. Guzmán-Martínez[1], M. Galván-Valencia[1,] S. M. Durón-Torres[1*]

[1]Universidad Autónoma de Zacatecas, Programa de Maestría en Ciencias de la Ingenieria, Campus Siglo XXI, Carretera Zacatecas-Guadalajara Km. 6.0, Ejido la Escondida, Zacatecas, Zacatecas, México, 98160.
[*]Tel: +524929256690 Ext. 4655; e-mail: duronsm@prodigy.net.mx

ABSTRACT

The synthesis of a novel material of general composition $(Ir_xSn_ySb_z)O_w$ for use in solid polymer electrolyte water electrolysers (SPEWE) was accomplished from the simultaneous synthesis of the electrocatalyst and the support by means of thermal decomposition of chlorides precursors H_2IrCl_6 , $SnCl_2{\cdot}2H_2O$ and $SbCl_5$ in ethanol . Different H_2IrCl_6 proportions in the reaction mixture were tested to observe their effect on the amount and electrocatalytic activity of the material obtained. The electrochemical properties of the different syntheses were measured by using: cyclic voltammetry (CV), linear scan voltammetry (LSV) and electrochemical impedance spectroscopy (EIS). Electrochemical tests were conducted using as support electrolyte H_2SO_4 0.5 M in a conventional three-electrode cell. A mechanical mixture of IrO_2 with Vulcan carbon and iridium oxide with antimony doped tin oxide were also tested respect to the oxygen evolution reaction to compare the properties of catalyst/support obtained. The results indicate that synthesized materials could represent a suitable candidate to be used use as anode in SPWE to catalyze the oxygen evolution reaction (OER).

Keywords: Water Electrolysis; Electrocatalyst; Oxygen Evolution Reaction.

1. Introduction

Hydrogen has been considered as the most promising fuel for clean energy obtaining carbon free energy to meet growing global energy demand. The capacity to generate clean and pure hydrogen as its storage and distribution is one limitation for its use. A promising method for hydrogen production is water electrolysis, which is less efficient than a direct chemical route but produces virtually no pollution or toxic byproduct when electrical energy is produced by renewable energy [1–3]. Water electrolyzers electrical energy used to divide the liquid water into oxygen and protons (anode reaction). Solvated protons migrate toward the cathode, which are reduced to molecular hydrogen (cathodic reaction). The anode and cathode are separated by an electrolyte, in the case of the polymeric electrolyte membrane water electrolyzer (PEMWE), the electrolyte is solid. PEMWEs have received special interest due to the high current densities that reached, the energy efficiency and the purity of the hydrogen produced, in comparison with the alkali electrolysis.[4,5]

Oxygen evolution reaction (OER) is the limiting step in the development and requiring electrolyzers, suitable catalysts for performing a suitable reaction rates. Electrocatalysis plays an important role in the development of materials for electrolyzers. In conventional PEMWE type oxides are used with rutile structure,[6] such as iridium oxide (IrO_2) or ruthenium (RuO_2) as catalysts to promote the OER.[7–9] The use of these metals has been necessary due to the highly acidic environment found in the polymeric membrane, which may cause corrosion of other materials. Great efforts are being to improve the catalytic activity of such catalysts, due to their nature of precious metals. A method of dispersing metal nanoparticles on a support in order to maximize the specific surface area and hence the specific activity of the catalyst.

Therefore, another aspect to consider is the catalyst support on which will disperse the catalyst, it must have a good performance to high operation potentials electrolyzers (E> 1.6 V vs NHE),[4] since, for example, the Vulcan carbon (which in general is a good catalyst support due to their large surface area) suffer phenomena of corrosion under these operating conditions, which can cause degradation and loss of electrical contact with the electroactive material, i.e. the material is not reliable for use as the anode catalyst support to get it carry out efficiently the OER alternative. The stability and durability of the catalyst support in the OER is the main challenge in the development of electrocatalysis.

The materials used as supports for catalysts should possess several important features: i) a highly superficial surface to provide better dispersion of the catalyst nanoparticles, ii) high electrical conductivity to allow high efficiency for transporting electrons to the ions involved in the electrochemical reactions, iii) mechanical and chemical stability, iv) good metal support interaction to improve the intrinsic catalytic activity of the catalyst phase.[10,11] Studied materials are based in oxides and other ceramic, which include Ti_nO_{2n-1},[11] TiC, SiC-Si, SnO_2 [12,13] and $SbSnO_2$ [5]. SnO_2-IrO_2 mixtures have been extensively investigated for the oxygen evolution reaction in acid environment. Such mixtures have been obtained by thermal decomposition of the corresponding metal salts onto plates of titanium, reported a significant increase in surface area remarkable iridium oxide together with an increase in the surface charge of the mixed oxide in comparison with the pure oxides, reducing the load of the noble metals [3,8,14,15]. The object of present study is the synthesis of a mixed oxide powder with ($Ir_xSn_ySb_z$) O_w composition for its use in PEMWE.

2. Experimental

2.1 Mixed oxide preparation.

A 50 *mL* of a solution 0.25 M was prepared adding metal precursors (H_2IrCl_6, $SnCl_2{\cdot}2H_2O$ and $SbCl_5$) in absolute ethanol. This solution was heated at 50 *°C* in nitrogen atmosphere for 2 *h*. After this time the solution was calcined at 450 *°C*, the powder obtained was washed tree time whit deionized water and dry for 5 *h* at 80 *°C*[8],[16–18].

2.2 Electrochemical characterization

The electrochemical probes was conducted in 0.5 *M* H_2SO_4 in a typical tree electrodes cell, employing a sulphate electrode (0.63 V vs NHE) as a reference electrode, a platinum mesh as a counter electrode and glassy carbon with a thin layer of ink as a work electrode. The ink consist in powder 95 *wt.%* and 5 *wt.%* Nafion (Aldrich) mixture, these were prepared by mechanically mixing vulcan carbon (VC) and IrO_2 and a mechanical mixture of IrO_2 and $SbSnO_2$(ATO), both of 50:50 weight of catalyst and support, inks of mixed oxides synthesized by thermal decomposition were prepared with the same proportions of powder and Nafion. Measurements were performed using a potentiostat / galvanostat (EG&G, PAR Versastat 3) and a precision rotor (PINE MSRX) for controlling the rotation speed. Cyclic voltammetry (CV) was used to meet the electrochemical profile of synthetic materials, performing sweeps potential of -0.600 *V* to 0.800 *V* vs reference electrode at a scan rate 50 $mV\ s^{-1}$, where the electrolytic cell was saturated with nitrogen. To evaluate the oxygen evolution reaction was employed linear can voltammetry (LSV) rate of 5 $mV\ s^{-1}$, a potential range of 0.500 *V* to 1.000 *V* vs reference electrode with 1000 rpm rotation rate. Electrochemical impedance spectroscopy were carried out in potensiostatic mode at 1.47 *V* of potential with an alternate signal amplitude of 10 *mV* and a frequency limits of 100 *kHz* and 10 *mHz*. The shown data are referenced versus normal hydrogen electrode (NHE).

3. Results and discussion

3.1 Cyclic voltammetry

The cyclic voltammograms obtained for the supported iridium oxide in the ATO, IrO_2 supported on vulcan carbon and the synthesized composite oxide $Ir_xSb_{0.05(1-x)}Sn_{0.95(1-x)}O_2$ (x=0.1,0.4), in N_2 saturated 0.5 M H_2SO_4 are shown in Fig. 1. The oxide electrodes have the normal iridium oxide shape. The current density (j/ $mAcm^{-2}$) is greater for IrO_2 supported on vulvan carbon, the mixed oxides have similar shape. The off-peak potential for oxygen appears to a potential of 1.40 V for iridium oxide supported on vulcan carbon, 1.42 *V* form mixed oxide and 1.45 *V* for IrO2 supported on antimony doped tin oxide, consistent with that reported[8]. The results show that the synthesis of the mixed oxide by the thermal decomposition promotes rate reaction.

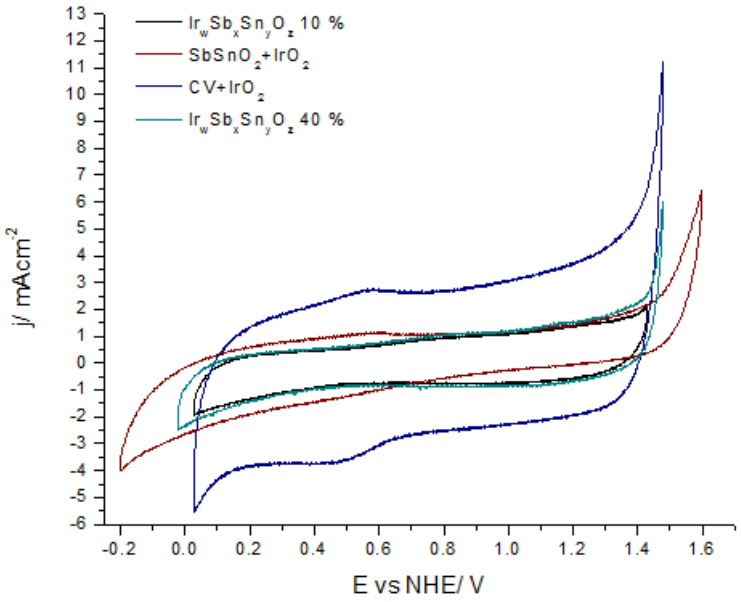

Fig 1. Cyclic voltammogram $CV+IrO_2$, $Ir_xSb_{0.05(1-x)}Sn_{0.95(1-x)}O_2$ (x=0.1, 0.4) and $SbSnO_2+IrO_2$ at 50 $mV\,s^{-1}$.

3.2 Linear voltammetry

Linear scan voltammetry was performed for OER for IrO_2 supported in vulcan carbon and ATO, in N_2 saturated 0.5 *M* H_2SO_4 at a scan rate of 5 $mVcm^{-1}$. Same probes was conducted for mixed oxide $Ir_xSb_{0.05(1-x)}Sn_{0.95(1-x)}O_2$, (x= 0.1, 0.4). These test are show in Fig. 2. Its observed that the OER starts at 1.43 *V* in both mixed oxides, 1.40 *V* $CV+IrO_2$ and 1.48 *V* for $SbSnO_2$. Mixed oxide linear voltammogram slope changes with respect to VL of the mechanical mixture of iridium oxide and vulcan carbon, suggesting a change in reaction mechanism. This suggests that the OER is favored when the mixed oxide obtained by thermal decomposition is used as anode. Comparison between the mixed oxide electrodes indicate that, although the oxygen evolution reaction start at similar potential in both electrodes, the current density is higher for the electrode with the highest percentage by weight of iridium.

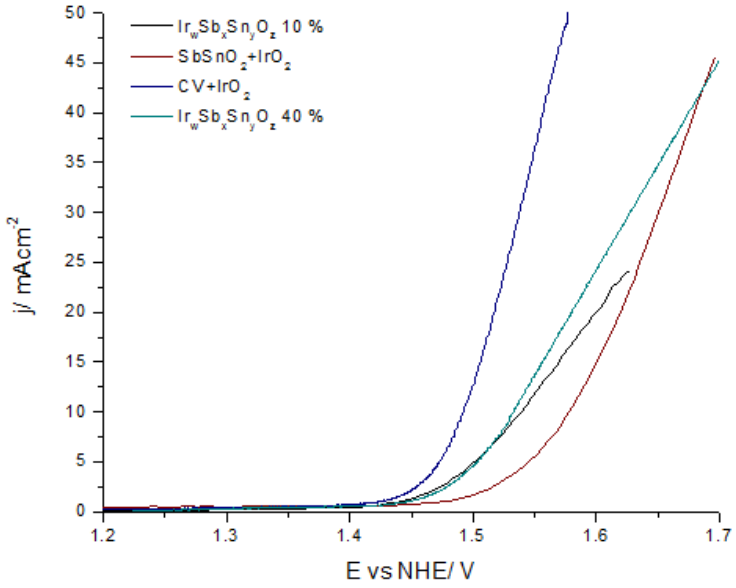

Fig 2. Linear scan voltammogram of $CV+IrO_2$, $Ir_xSb_{0.05(1-x)}Sn_{0.95(1-x)}O_2$ (x=0.1, 0.4) and $SbSnO_2+IrO_2$ at 5 $mV\ s^{-1}$.

In addition above, Tafel plots were drawn from LSV curves for OER after ohmic drop (IRs) correction due to the electrolyte resistance (Rs). This correction was done by subtracting the IR to the applied potential. The Rs values were obtained by electrochemical impedance spectroscopy (EIS) for each electrode. Rs values were in the 3 Ω – 7.5 Ω interval which are mainly attributed to the solution resistance.

In addition to the above, polarization curves were developed from LSV curves for OER, for it, first was made the ohmic drop correction (IRs) due to the electrolyte resistance (Rs). Rs values were obtained by electrochemical impedance spectroscopy (EIS) for each electrode, the values ranged from 0.91 Ω – 4.28 Ω range which is mainly attributed to the resistance of the solution. Fig. 3 shows the Tafel plots for OER for all the electrodes in study, the value of Tafel slope are show for each material. For the mixed oxides, the Tafel slope (b) are 79 $mVdec^{-1}$ for x=0.1 and for x=0.4, the Tafel slope has a value of 78 $mVdec^{-1}$, was found that the Tafel slope on Ir–Sn oxide DSA electrodes was 70 mV dec−1 for iridium contents of 50–100 mol% Ir, and 100–170 for lower iridium contents, [8],[19]. There are several proposed mechanisms which can describe the oxygen evolution reaction in acidic media. According to the above, the following reaction mechanism is proposed[20]:

$$S + H_2O \rightarrow S - OH + H^+ + e^- \quad (1)$$
$$S - OH \rightarrow S - O^- + H^+ \quad (2)$$
$$S - O^- \rightarrow S - O + e^- \quad (3)$$
$$2S - O \rightarrow 2S + O_2 \quad (4)$$

where S stands for active sites on oxides surface, and S– OH, S–O are two adsorption intermediates. The different Tafel slopes predict which is the rate determining step of reaction (rds). This mechanism predicts the following Tafel slope: 120 $mV\ dec^{-1}$ if (1) rds, 60 $mV\ dec^{-1}$ for (2), 40 $mV\ dec^{-1}$ for (3) and 15 $mV\ dec^{-1}$. The Tafel slopes close to 60 $mVdec^{-1}$ obtained for this materials suggests the dissociation of the surface complex[18][21].

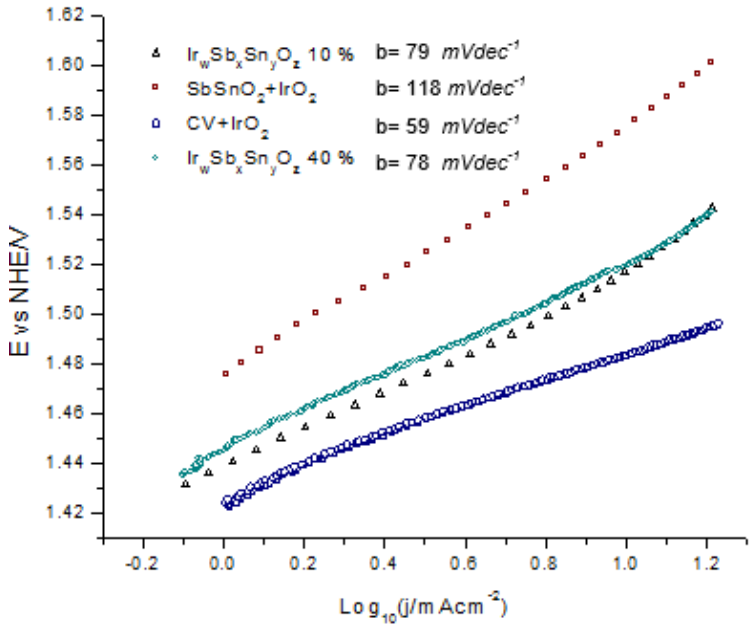

Fig 3. Tafel plots for OER of $CV+IrO_2$, $Ir_xSb_{0.05\,(1-x)}Sn_{0.95(1-x)}O_2$ (x=0.1, 0.4) and $SbSnO_2+IrO_2$ after IR_s correction.

3.3 Electrochemical impedance spectroscopy

EIS measurements for oxygen evolution was carried out on mixed oxides (x=0.1,0.4) electrodes, in electrochemical cell, N_2 saturated 0.5 *M* H_2SO_4 solution, at potensiostatic mode with an anodic potential of 1.47 *V*. Nyquist plots for mixed oxides are shown in Fig 4. The depressed semicircles presented in that figure were adjusted by EIS Spectrum Analyser to the equivalent circuit presented in Fig 5[22][23].

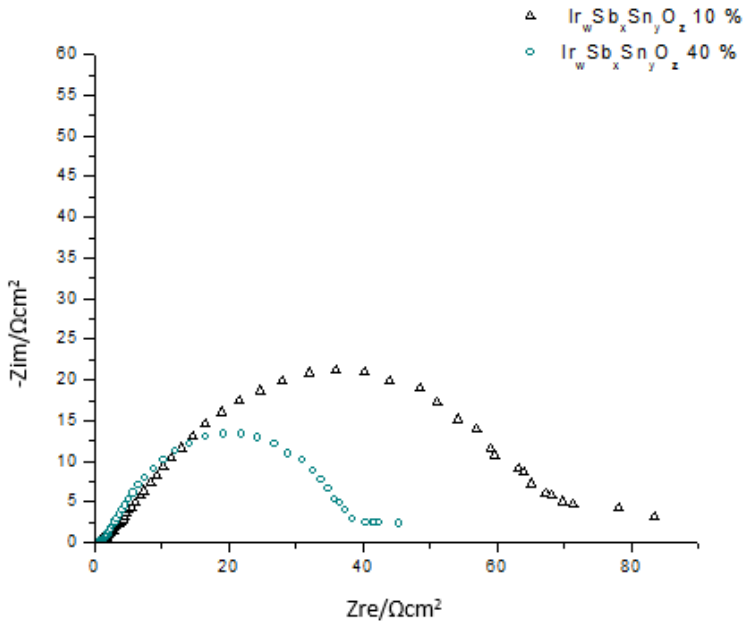

Fig 4. Nyquist plots of $Ir_xSb_{0.05(1-x)}Sn_{0.95(1-x)}O_2$ (x=0.1, 0.4) at anodic potential value of 1.47 V, in N_2 saturated 0.5 M H_2SO_4 solution.

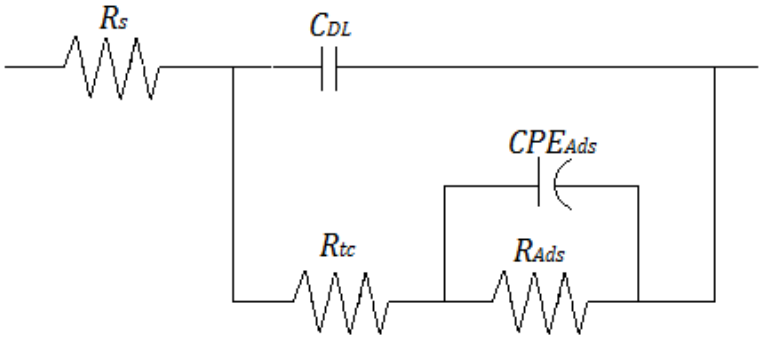

Fig 5. Equivalent circuit used to fit the EIS data for OER on mixed oxide, $Ir_xSb_{0.05(1-x)}Sn_{0.95(1-x)}O_2$ (x=0.1, 0.4) electrodes [22].

Where R_S is the electrolytic solution resistance, R_{tc}, is the resistance of charge transfer, associated with OER in parallel with the capacitance of double layer (C_{DL}), R_{Ads} and CPE_{Ads} are the elements associated to adsorption process in OER. The values of R_S and R_{tc} calculated for the mixed oxides electrodes are resumed in Table 1 along with other OER kinetic parameter values.

Table 1. Summary of polarisation measurements, EIS probes for OER on mixed oxides $Ir_xSb_{0.05(1-x)}Sn_{0.95(1-x)}O_2$ (x=0.1, 0.4) electrodes.

	E_{REO}(vsNHE)/V	j/$mAcm^{-2}$ *1.47 V	$R_S/\Omega cm^2$	$R_{tc}/\Omega cm^2$	b/$mVdec^{-1}$
$Ir_{0.1}Sb_{0.45}Sn_{0.855}O_2$	1.45	2.11	0.22	4.9	79
$Ir_{0.4}Sb_{0.03}Sn_{0.570}O_2$	1.45	5.06	0.19	2	78

The results obtained by EIS are consistent with the results obtained by LSV, where is observed that OER for both mixed oxides are similar, nonetheless current density is greater for the electrode with the highest percentage weight of iridium oxide, which is reflected in the resistance to charge transfer.

4. Summary and perspectives

Electrochemical studies were performed for the OER on mixed oxides electrodes, $Ir_xSb_{0.05(1-x)}Sn_{0.95(1-x)}O_2$ (x=0.1, 0.4), which were obtained from thermal decomposition of metal precursors. Cyclic voltammetry show that oxide electrodes have the normal iridium oxide shape. Linear scan voltammetry show that the mixed oxide is synthesized by thermal decomposition a promising material for use in solid electrolyte electrolyzer, due it has potential for the reaction of oxygen evolution close to that obtained with the use of vulcan carbon as support and iridium oxide as catalyst. Tafel slopes obtained for the electrodes prepared from mechanical mixtures of catalyst and supports give an indication of the reaction mechanism for the oxygen evolution reaction, and its limiting step. The results obtained by EIS are consistent with results obtained using LSV, here the values of the resistance to charge transfer of electrodes were obtained, being higher for electrodes with a lower percentage by weight of iridium.

Subsequently arises perform physicochemical characterization of materials with which will be analyzed the composition, the particle size and the phases present in the mixed oxide is obtained by thermal decomposition.

References

[1] J.A. Turner, A Realizable Renewable Energy Future, Science. 285 (1999) 687–689. doi:10.1126/science.285.5428.687.
[2] J.A. Turner, Sustainable hydrogen production, Science. 305 (2004) 972–974. doi:10.1126/science.1103197.
[3] K. Kadakia, M.K. Datta, O.I. Velikokhatnyi, P. Jampani, S.K. Park, P. Saha, et al., Novel (Ir,Sn,Nb)O2 anode electrocatalysts with reduced noble metal content for PEM based water electrolysis, Int. J. Hydrog. Energy. 37 (2012) 3001–3013. doi:10.1016/j.ijhydene.2011.11.055.
[4] S.A. Grigoriev, V.I. Porembsky, V.N. Fateev, Pure hydrogen production by PEM electrolysis for hydrogen energy, Int. J. Hydrog. Energy. 31 (2006) 171–175. doi:10.1016/j.ijhydene.2005.04.038.
[5] J. Xu, Q. Li, M.K. Hansen, E. Christensen, A.L. Tomás García, G. Liu, et al., Antimony doped tin oxides and their composites with tin pyrophosphates as catalyst supports for oxygen evolution reaction in proton exchange membrane water electrolysis, Int. J. Hydrog. Energy. 37 (2012) 18629–18640. doi:10.1016/j.ijhydene.2012.09.156.
[6] S. Sunde, I.A. Lervik, M. Tsypkin, L.-E. Owe, Impedance analysis of nanostructured iridium oxide electrocatalysts, Electrochimica Acta. 55 (2010) 7751–7760. doi:10.1016/j.electacta.2009.11.009.
[7] S. Ardizzone, C.L. Bianchi, G. Cappelletti, M. Ionita, A. Minguzzi, S. Rondinini, et al., Composite ternary SnO2–IrO2–Ta2O5 oxide electrocatalysts, J. Electroanal. Chem. 589 (2006) 160–166. doi:10.1016/j.jelechem.2006.02.004.
[8] A. Marshall, B. Børresen, G. Hagen, M. Tsypkin, R. Tunold, Electrochemical characterisation of IrxSn1−xO2 powders as oxygen evolution electrocatalysts, Electrochimica Acta. 51 (2006) 3161–3167. doi:10.1016/j.electacta.2005.09.004.

[9] A. Marshall, B. Børresen, G. Hagen, M. Tsypkin, R. Tunold, Hydrogen production by advanced proton exchange membrane (PEM) water electrolysers—Reduced energy consumption by improved electrocatalysis, Energy. 32 (2007) 431–436. doi:10.1016/j.energy.2006.07.014.
[10] X.-M. Wang, Y.-Y. Xia, The influence of the crystal structure of TiO2 support material on Pd catalysts for formic acid electrooxidation, Electrochimica Acta. 55 (2010) 851–856. doi:10.1016/j.electacta.2009.09.037.
[11] P. Paunović, O. Popovski, E. Fidančevska, B. Ranguelov, D. Stoevska Gogovska, A.T. Dimitrov, et al., Co-Magneli phases electrocatalysts for hydrogen/oxygen evolution, Int. J. Hydrog. Energy. 35 (2010) 10073–10080. doi:10.1016/j.ijhydene.2010.07.143.
[12] C. Du, M. Chen, X. Cao, G. Yin, P. Shi, A novel CNT@SnO2 core–sheath nanocomposite as a stabilizing support for catalysts of proton exchange membrane fuel cells, Electrochem. Commun. 11 (2009) 496–498. doi:10.1016/j.elecom.2008.12.034.
[13] H. Chhina, S. Campbell, O. Kesler, An oxidation-resistant indium tin oxide catalyst support for proton exchange membrane fuel cells, J. Power Sources. 161 (2006) 893–900. doi:10.1016/j.jpowsour.2006.05.014.
[14] M. Rubel, R. Haasch, P. Mrozek, A. Wieckowski, C. De Pauli, S. Trasatti, Characterization of IrO2□SnO2 thin layers by electron and ion spectroscopies, Vacuum. 45 (1994) 423–427. doi:10.1016/0042-207X(94)90314-X.
[15] C.P. De Pauli, S. Trasatti, Composite materials for electrocatalysis of O2 evolution: IrO2+SnO2 in acid solution, J. Electroanal. Chem. 538–539 (2002) 145–151. doi:10.1016/S0022-0728(02)01055-0.
[16] S. Fierro, A. Kapałka, C. Comninellis, Electrochemical comparison between IrO2 prepared by thermal treatment of iridium metal and IrO2 prepared by thermal decomposition of H2IrCl6 solution, Electrochem. Commun. 12 (2010) 172–174. doi:10.1016/j.elecom.2009.11.018.
[17] L. Ouattara, S. Fierro, O. Frey, M. Koudelka, C. Comninellis, Electrochemical comparison of IrO2 prepared by anodic oxidation of pure iridium and IrO2 prepared by thermal decomposition of H 2IrCl6 precursor solution, J. Appl. Electrochem. 39 (2009) 1361–1367. doi:10.1007/s10800-009-9809-2.
[18] J.-M. Hu, J.-Q. Zhang, C.-N. Cao, Oxygen evolution reaction on IrO2-based DSA® type electrodes: kinetics analysis of Tafel lines and EIS, Int. J. Hydrog. Energy. 29 (2004) 791–797. doi:10.1016/j.ijhydene.2003.09.007.
[19] E.N. Balko, P.H. Nguyen, Iridium-tin mixed oxide anode coatings, J. Appl. Electrochem. 21 (1991) 678–682. doi:10.1007/BF01034045.
[20] Y. Matsumoto, E. Sato, Electrocatalytic properties of transition metal oxides for oxygen evolution reaction, Mater. Chem. Phys. 14 (1986) 397–426. doi:10.1016/0254-0584(86)90045-3.
[21] L.M. Da Silva, J.F.C. Boodts, L.A. De Faria, Oxygen evolution at RuO2(x)+Co3O4(1−x) electrodes from acid solution, Electrochimica Acta. 46 (2001) 1369–1375. doi:10.1016/S0013-4686(00)00716-7.
[22] E. Barsoukov, J.R. Macdonald, Impedance Spectroscopy: Theory, Experiment, and Applications, 2 edition, Wiley-Interscience, Hoboken, N.J, 2005.
[23] V. Ávila-Vázquez, J.C. Cruz, M. GalvÁn-Valencia, J. Ledesma-García, L.G. Arriaga, C. GuzmÁn, et al., Electrochemical study of sb-doped SnO2 supports on the oxygen evolution reaction: Effect of synthesis annealing time, Int. J. Electrochem. Sci. 8 (2013) 10586–10600.

Multi-Objective Optimization of a Hybrid Generating System

M. Hernan[1], M. Lopez, Victor Sanchez[1], R. Barbosa[1], J. Hernandez[1], Juan M. Ramirez[2]

[1]Universidad de Quintana Roo, Boulevard Bahía s/n, Chetumal, Q. Roo, México, 77019.
Tel: +5298350300; e-mail: vsanchez@uqroo.edu.mx
[2]CINVESTAV Guadalajara, Av. del Bosque 1145, Zapopan, Jalisco, México, 45019.
[*]Tel: +523337773600; e-mail: jramirez@gdl.cinvestav.mx

ABSTRACT

Renewable generating systems are a sustainable solution for the electrical energy production; however the costs associated with the initial investment and due to that usually these kind of electrical generating systems are over-sized with the aim of satisfying the electrical load connected to them, implies an increase in the costs of investment, maintenance and operation as well as a reduction of their overall efficiency. Therefore, optimal sizing is an important issue in the design of renewable generation systems, in order to reach an efficient relationship between cost and benefit. Likewise, the random nature of the renewable sources increases the complexity for sizing a renewable generating system with regard to a conventional system. This paper is aimed to estimate the cost/sizing relationship of a hybrid energy solar-wind-diesel generator system using solar irradiation and wind data. The hybrid energy system uses the hydrogen as storage vector, so that it employs a fuel cell and electrolyzer for such task. The formulation is made up as a multi-objective optimization problem, solved by a genetic algorithm. The optimizer calculates the best system configuration to meet the commitment between the energy supply reliability and cost. Moreover, the optimizer allows an easy way for optimal sizing without depth knowledge of the relationship between the hybrid system costs and the generated power. Results are presented for a domestic installation load located in the south-east region of Mexico (Chetumal city).

Keywords: fuel cells; genetic algorithm, multi-objective optimization.

1. Introduction

At the present time, daily activities in the society are mostly dependent on non-renewable fossil fuels that have been and will continue to be an important factor of pollution and climate change. Because of these problems and our dwindling supply of petroleum, finding sustainable alternatives is becoming increasingly urgent. Perhaps the greatest challenge in realizing a sustainable future is to develop technology for integration and control of renewable energy sources in smart grids distributed generation (Strzelecki, 2008; Keyhani, 2010).

The interest in distributed generation systems (DGs) is rapidly increasing, particularly for on-site generation. This interest is because larger power plants are economically unfeasible in many regions due to increasing system, fuel costs, and more rigorous environmental regulations. In addition, recent technological advances in small generators, power electronics, and energy storage devices have provided a new opportunity for distributed energy resources at the distribution level; in particular, the incentive laws to utilize renewable energies have also encouraged a more decentralized approach to power delivery (Keyhani, 2010).

There exist various generation sources for DGs: conventional technologies (diesel or natural gas engines), emerging technologies (micro-turbines or fuel cells or energy storage devices), and renewable technologies (small wind turbines or solar/photovoltaics or small hydro-turbines). These DGs are used for applications to a standalone, a standby, a grid-interconnected, a cogeneration, and peak shavings (Keyhani, 2010).

Many distributed generation sources such as photovoltaic cells, fuel cells, and advanced energy storage systems (batteries, flywheels, and ultracapacitors) produce energy in the form of DC power. Other devices can also be suited to DC output, such as micro turbines and wind turbines.

The energy losses entailed in converting DC to AC power for distribution could be eliminated with DC power delivery, enhancing efficiency and reliability and system cost-effectiveness. For instance, the total life cycle cost of photovoltaic energy (PV) for certain DC applications could be reduced by more than 25% compared to using a conventional DC to AC approach—assuming that the specific end-use applications are carefully selected. The costs of new distributed generation such as PV arrays are still high, so optimization of designs with DC power delivery may help spur adoption and efficient operation (Gellings, 2009). Meanwhile, DC/AC conversion is utilized yet, and this consideration will be taken into account here.

Since it is expected that, in the short term, the use of new technologies will be quotidian, it is quite important to be prepared with tools able to take into account such elements.

This paper formulates the problem of an optimal sizing of a hybrid energy system (wind-photovoltaic-fuel cell-electrolyzer), solved by the NSGA-II software (Srinivas, 1994). In the formulation, the concepts of loss power supply probability (LPSP) and annual costs are taken into account. The optimization process evaluates the best configuration of the hybrid energy system that satisfies the commitment between energy supply and cost.

2 HYBRID GENERATING SYSTEM

In this paper the hybrid generation system is constituted by different power sources such as the wind turbine generator (WTG), photovoltaic panels (PVs), fuel cell generator and diesel generator, figure 1.

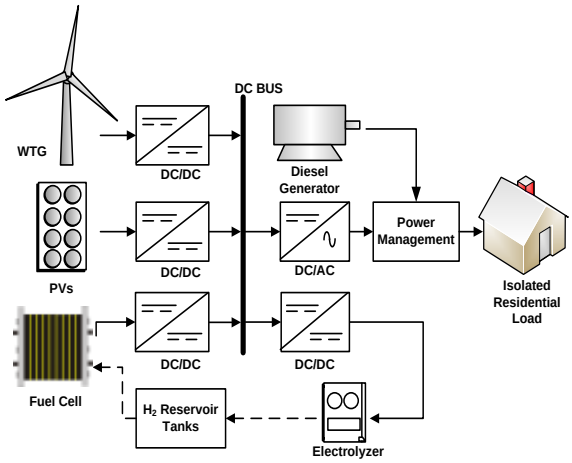

Figure 1. Hybrid generation system.

Likewise, if these renewable sources are not enough, then the non-supplied energy is taken from a fossil fuel generator.

2.1 Wind turbine generator (WTG)

The output power $P_W(t)$ from WTG subject to wind speed ($v(t)$) can be calculated by (1).

$$\begin{cases} P_W(t) = P_{nom}, & V_{nom} < v \quad (t) < V_{co} \\ P_W(t) = \frac{1}{2} \cdot \rho \cdot A_{eol} \cdot C_p \cdot v \quad (t)^3, & V_{ci} < v \quad (t) < V_{nom} \\ P_W(t) = 0, & v \quad (t) < V_{ci}, v \quad (t) > V_{co} \end{cases} \tag{1}$$

Where V_{ci}, V_{nom}, V_{co} are the cut-in, rated, and cut-out wind speed, respectively. ρ is the air density, A_{eol} is the rotor's swept area (m^2), and C_p is the wind turbine efficiency.

Likewise, if these renewable sources are not enough, then the non-supplied energy is taken from a fossil fuel generator.

2.2 Photovoltaic panels

Sunlight is converted into electric energy by PV panels. The output energy from PVs ($P_s(t)$) can be calculated by (2),

$$P_s(t) = G(t) A_s \eta_s \tag{2}$$

where $G(t)$ is the insolation level (kW/m^2), A_s and η_s are the area and efficiency of the PVs, respectively.

2.3 Fuel cells (FC)

A simplified fuel cell model is used in this paper. We assume that the fuel cell works on a fixed operation point, so that its output power ($P_{FC}(t)$) can be evaluated from (3) (Nelson, 2005),

$$P_{FC}(t) = \eta_{FC}\left[P_{load}(t)/\eta_{inv} - P_{gen}(t)\right] \tag{3}$$

where η_{FC} and η_{inv} are the FC and inverter's efficiency, respectively. $P_{load}(t)$ is the demand, and $P_{gen}(t)$ is the total wind and PV generated power every hour, computed as (4).

$$P_{gen}(t) = P_v(t) + P_s(t) \tag{4}$$

One hour time step is employed. Thus, generated and demanded powers are equivalent to generated and demanded energies at a particular hour.

2.3.1 Electrolizer (elec)

We assume that the electrolyzer operates at a constant operating point, so that the hydrogen produced by the electrolyzer is proportional to its efficiency. The Hydrogen's equivalent energy drawn from the electrolyzer and stored in the reservoir tanks (*tk*) is described by equation (Dufo-Lopez, 2007),

$$E_{tk}(t) = \eta_{elec} \cdot (E_{gen}(t) - E_{load}(t)/\eta_{inv}) \tag{5}$$

where η_{elec} is the electrolyzer's efficiency.

2.4 Diesel generator

The Diesel generator model used in this paper calculates the fuel consumption, F_{cons} (l/h), as a function of the supplied power, P_G (kW), during an hour (5),

$$F_{cons} = B_G * P_{NG} + A_G * P_G(t) \quad (6)$$

where P_{NG} is the generator's rating power (kW), A_G and B_G are the consumption's power curve coefficients, (l/kWh). In (Skarstein, 1989) A_G = 0.2416 l/kWh and B_G = 0.08145 l/kWh are proposed.

3 SIZING METHODOLOGY

In this paper, the sizing of the stand-alone generating system is formulated as a multi-objective optimization problem,

min f = [f_1 f_2 f_3]

f_1: investment + operating and maintenance (O&M) costs + hydrogen's tank size

f_2 : LPSP + recovering stored energy in fuel cell each cycle (24 hours).

f_3: CO_2 emission

Thus, one of the main objectives of the hybrid system sizing is to minimize the total cost, which includes investment, operation and maintenance (O&M) cost. In this paper, the method of annualized costs is employed. The annualized investment cost for each element is calculated by,

$$C_{AC} = C_{INV} \cdot FRC(i_r, N_p) = \frac{i_r(1+i_r)^{N_p}}{(1+i_r)^{N_p} - 1} \quad (7)$$

where C_{INV} is the investment cost, i_r and N_p are the annual interest rate and the lifetime of the element, respectively. *FRC* is the capital recovery factor, and

$$i_r = \frac{(i-f)}{(i+f)} \quad (8)$$

where *i* is the annual interest rate and *f* is the annual inflation rate.
In this paper, the components' O&M costs are calculated using (9)

$$OMC = \sum_{k=PV,WTG,\ldots} O\&M_k * (1+f)^{N_p} \quad (9)$$

The fuel cells and electrolyzer have a shorter lifetime than the project one, thus the replacement cost of these components must be taken into account by,

$$C_{REMP} = C_R \cdot \frac{i_r}{(1+i_r)^{N_H} - 1} \tag{10}$$

where C_R is the replacement cost and N_H the replaced component's lifetime.
Thus, the objective function f_1 is described by (11), which includes investment, O&M, and replacement cost of the system's components,

$$f_1 = min\{\sum_{m=WTG,PV,elec,FC,tk}(C_{AC_m} + C_{OM_m}) + \sum_{n=elec,FC}(C_{rep_n})\} \tag{11}$$

The second objective function is related to the loss of power supply. When the renewable sources do not satisfy the demand, then there is an index to account for the loss of power supply (*LPS(t)*) during the current time *t*. This factor is calculated as follows,

$$LPS(t) = E_{load}(t) - (E_{gen}(t) + E_t(t-1) \cdot \eta_{FC}) \tag{12}$$

where $E_{load}(t)$ is the load at time *t*, $E_{gen}(t)$ is the available renewable energy at time *t*, $E_t(t-1)$ is the stored energy in the electrolyzer at time *(t-1)*, η_{FC} is the fuel cell efficiency.

The probability of the non-served power supply is described by,

$$LPSP = \frac{\sum_{t=1}^{T} LPS(t)}{\sum_{t=1}^{T} E_{load}(t)} \tag{13}$$

where *T* is the time period evaluated and *LPSP* is the Loss of Power Supply Probability. *LPSP* represents the number of days that the supply is lost over a given time period. For instance, LPSP = 0.0003 means to have a loss of power supply of roughly one day in ten years (Borowy, 1996; Abouzahr, 1991).

$$f_2 = \min\left\{LPSP + k_2[Et(1) - Et(24)]^2\right\} \tag{14}$$

where $Et(1)$ and $Et(24)$ are the stored energy in the electrolyzer during the first and the 24-*th* hour of a day. k_1 and k_2 are penalizing factors.

$$f_3 = \min \text{ (emissions of } CO_2) \tag{15}$$

The CO_2 produced per litre of consumed fuel depends upon the characteristics of the diesel generator and the type of fuel. The CO_2 produced by the fuel usually falls within 2.4 – 2.8 kg/l (Sonntag, 2002). In this paper this value is taken as 2.6 kg of CO_2 per litre.

3.1 Operating considerations

When the energy drawn from the WTG and PVs (E_{gen}) are greater than the demand (E_{load}), the excess energy is sent to the electrolyzer to be converted and stored into the hydrogen tank. Equivalent energy stored in the reservoir tanks is accounted for by,

$$E_t(t) = E_t(t-1) + (E_{gen}(t) - E_{load}(t)) \cdot \eta_{elec} \quad (16)$$

On the other hand, when the demand is greater than the available energy stemming from the WTG and PVs, the difference must be supplied by the fuel cell. The fuel cell recovers the equivalent energy stored as hydrogen in the reservoir tanks, causing a reduction in the stored energy as described by,

$$E_t(t) = E_{load}(t) - (E_{gen}(t) + E_t(t-1)) / \eta_{FC} \quad (17)$$

Likewise, one constraint is related to the maximum energy that can be stored in the reservoir tank,

$$0 \le E_t(t) \le E_{tk\max} \quad (18)$$

where E_{tkmax} is the hydrogen-tank's maximum capacity.

3.2 Optimization strategy

Figure 2 depicts the flowchart of the proposed strategy.

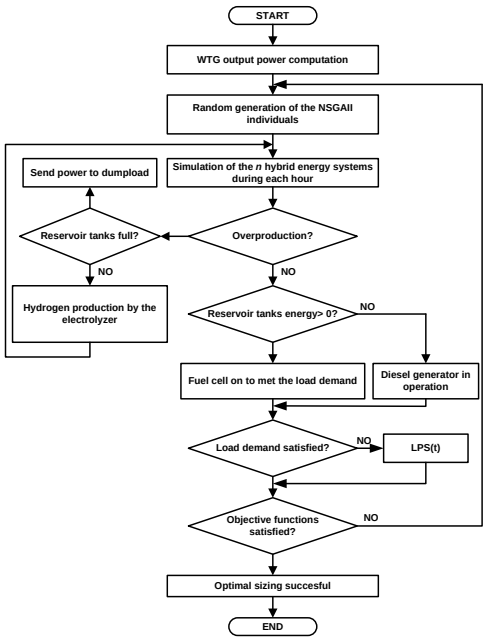

Figure 2. Flowchart of the strategy

The input data to optimize the hybrid energy system are the investment and O&M cost of each component. Likewise, efficiency and lifetime, energy demand in each hour for a period of 24 hours, as well as solar and wind resources available at the site. The optimizer determines the number of photovoltaic panels, as well as the hydrogen's initial energy storage, required to meet the energy demand and the required LPSP. In this paper the NSGA-II software is used to solve the problem. This one is selected due to its well known performance (Srinivas, 1994). The corresponding information required for simulations is shown in the appendix.
In this paper, the problem is formulated with three objective functions and two variables: (*i*) the area extended for the photovoltaic panels; (*ii*) the hydrogen-tank capacity. It is assumed that one wind-turbine generator is installed, which generated energy is subject to the available wind (Table A2 in appendix). A population of 25 individuals and 30 generation was used in the NSGA-II optimization algorithm.

4 SIMULATION RESULTS

The optimal sizing is estimated for three cases using the load in figure 3. The three cases are: (*i*) the use of renewable energy only; (*ii*) the use of renewable-diesel generator configuration; (*iii*) diesel only. The best results with respect to the total costs obtained by the multi-objective optimizer are shown in Table 1.

Table 1: Results obtained by NSGA-II

Item	Renewable System	Renewable-Diesel System	Diesel-only System
WTGs	1	1	-
PV modules	143	141	-
Energy stored in tanks	21.46 kW	21.33kW	-
Fuel (l)	-	234.7	7055.45
CO_2 emitted (tons)	-	0.62	18.34
Energy supplied	46.8 kWh	46.8 kWh	46.8 kWh
Annual total costs	$7147	$7933	$21893

As figure 3 illustrates, these stand-alone generating systems correctly satisfies the demand.

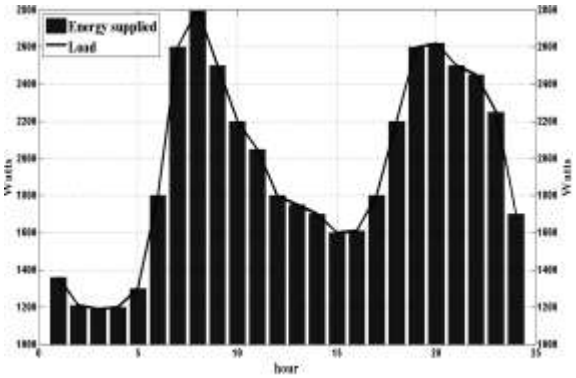

Figure 3. Load profile and supplied power.

It is noteworthy that the cost of using renewable sources is higher than the use of the diesel generator. However, it is important to limit the use of the latter one due to the emissions of CO_2 and other pollutants. Thus, in order to establish a commitment between the cost and an ecological solution to the energy supply, monetary penalization is applied for the use of the fossil fuel. In this paper, this penalization is $1.55 per fuel litre.

For the case of the renewable-diesel combination, this energy system employs during an hour the diesel generator along the year. If the economical penalization is taken into account due to the use of the fossil fuel, the total cost of this system is bigger than the renewable stand-alone system. Under this consideration, the cost of the diesel use is quite expensive. Figure 4 shows the energy stored in the hydrogen tanks when there is a residual renewable energy after to satisfy the demand.

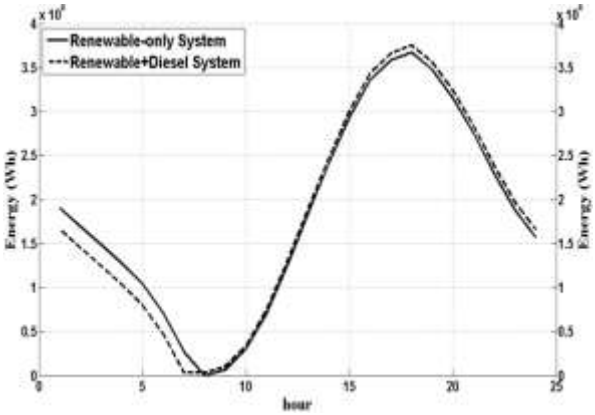

Figure 4. Equivalent energy stored in the hydrogen tanks.

CONCLUSIONS

This paper has estimated the optimal sizing of a renewable energy system using the algorithm NSGA-II. Simulation results show that the prices of the storage system elements are expensive yet, so that the total cost of the energy system using renewable sources and hydrogen storage is high. However, pollution is eliminated. Hence, in order to reduce the green energies' prices, economical penalization must be applied for the use of fossil fuels.

NSGA-II has found the optimal systems configuration to meet the commitment between the energy supply reliability and cost. The optimizer allows an easy way to attain an optimal sizing without deep knowledge about the relationship between the renewable generation system costs and the power generated by the accounted for sources.

The optimal configurations were selected and tested by the LPSP analysis. Simulations indicate the necessity of a high quantity of stored energy in the hydrogen tanks, which implies an increase in the total system cost and a voluminous solution. However, the use of hydrogen as energy storage has an important positive environmental impact.

REFERENCES

R. Strzelecki, G. Benysek. *Power Electronics in Smart Electrical Energy Networks*. Editorial Springer London. 2008.

A. Keyhani, M. N. Marwali, M. Dai, *Integration of green and renewable energy in electric power systems*. John Wiley and Sons, Inc., 2010.

C. W. Gellings, *The smart grid. Enabling energy efficiency and demand response*. The Fairmont Press Inc., 2009.

N. Srinivas, K. Deb, 1994. *Multiple Objective Optimization Using Nondominated Sorting in Genetic Algorithms*. Evolutionary Computation.

D.B. Nelson, M.H. Nehrir, V. Gerez, Economic evaluation of Grid-connected Fuel-Cell Systems, *IEEE T. Energy Conver*, 2005.

R. Dufo-Lopez, J.L. Bernal-Agustin, J. Contreras, Optimization of control strategies for stand-alone renewable energy systems with hydrogen storage, *Renew. Energ.*, 2007.

O. Skarstein, K. Ulhen. Design considerations with respect to long-term diesel saving in wind/diesel plants. Wind Eng 1989.

B.S. Borowy and Z.M. Salameh, Methodology for optimally sizing the combination of a battery bank and PV array in a Wind/PV hybrid system, *IEEE T Energy Conver*, 1996.

I. Abouzahr and R. Ramakumar, Loss of power supply probability of stand-alone photovoltaic systems: a closed form solution approach, *IEEE T. Energy Conver.*, 1991.

R. Sonntag, C Borgnakke, GJV Wylen. Fundamentals of thermodynamics. 6th ed. New York:Wiley:2002.

APPENDIX

Table A1: Parameters

System Parameters	
Nominal WTG Power (P_W)	4 kW
Nominal FC power	3 kW
Nominal electrolyzer power	3 kW
Nominal diesel generator power(P_{NG})	4 kW
Cut-in wind speed (V_{ci})	2.5 m/s
Nominal wind speed (V_{nom})	12.5 m/s
Cut-out wind speed (V_{co})	20 m/s
WTG efficiency (C_p)	0.5
PV efficiency (η_s)	0.12
FC efficiency (η_{FC})	0.5
Inverter efficiency (η_{inv})	0.95
Electrolyzer efficiency (η_{elec})	0.74
WTG price	$3000
PV panel price per module	$450
FC price	$10000
Electrolyzer price	$10000
Diesel generator price	$2100
Diesel litre price	$2
Inverter price	$2500
Reservoir tanks price	$2000
O&M costs of WTG	$72/year
O&M costs of PVs	$10/mod/year
O&M costs of FC	$800/year
O&M costs of electrolyzer	$70/year
O&M costs of diesel gen.	$900/year
Annual interest rate (i)	3.75%
Annual inflation rate (f)	1.5%
Life span of Project (N_P)	20 years
Life span of electrolyzer and FC (N_H)	5 years
Life span of diesel generator (N_{GDI})	2.5 years

Table A2: load and energy availability

hour	Load (kW)	Irradiance (W/m^2)	wind (m/s)
1	1.36	0	4.4
2	1.21	0	4.3
3	1.19	0	4.25
4	1.20	0	4.35
5	1.30	0	4.25
6	1.80	0	4.4
7	2.60	0.02	4.25
8	2.80	0.08	4.2
9	2.50	0.19	4.5
10	2.20	0.3	4.75
11	2.05	0.42	5.3
12	1.80	0.51	5.7
13	1.75	0.54	6
14	1.70	0.51	6.3
15	1.60	0.46	6.8
16	1.61	0.38	6.82
17	1.80	0.25	6.2
18	2.20	0.17	6.1
19	2.60	0.07	5.85
20	2.62	0.04	5.5
21	2.50	0.02	4.8
22	2.45	0	4.78
23	1.36	0	4.78
24	1.21	0	4.78

Nanoparticles of Pt and Ag-Pt Synthesized by Ultrasonic for Oxygen Reduction Reaction

M.E.Beltrán-Perez[1], F.M. Hernández-Mendoza[1], P.A. López-Peréz[2], B. Ruiz-Camacho[1,*]

[1]Ingeniería en Energía, Universidad Politécnica de Guanajuato, Av. Universidad Norte s/n, Juan Alonso Cortázar Guanajuato, 38438

[2]Universidad Politécnica Metropolitana de Hidalgo, Bld. acceso a Tolcayuca # 1009 Ex Hacienda de San Javier, Tolcayuca, Hidalgo, 43860

[*]Tel: +524624414307; e-mail: beatrizr@upgto.edu.mx

ABSTRACT

This paper presents the synthesis of nanoparticles of Pt, Ag and Pt-Ag using ultrasonic irradiation at room temperature. The metal nanoparticles were supported on carbon substrates. A concentration study of alcohol was carried out to determine the kinetics of reduction metallic using UV-vis spectroscopy. The materials synthesized (Pt/C, Ag/C and Pt-Ag/ C) were evaluated on the oxygen reduction reaction (ORR) for be applied as cathodes in a Proton Exchange Membrane Fuel Cell (PEMFC). The electrochemical evaluation of the materials synthesized was performed using a cyclic and linear voltammetry technique in acidic medium and room temperature conditions. The kinetic reaction study indicates that the higher alcohol concentration favors the reduction of the metal precursor. Preliminary results demonstrate that the bimetallic electrocatalyst exhibits greater catalytic activity for the ORR compared to the monometallic sample. Pt-Ag/C electrocatalyst can be used as a cathode in a fuel cell.

*Keywords:*Ag-Pt electrocatalyst, ultrasonic, oxygen reduction reaction, fuel cells

1. Introduction

Fuel cells are promising technologies due to their high energy density and low pollutant emission compared to conventional power sources [1]. Recent advances in polymer anion exchange membranes have led to increasing studies of alkaline fuel cells (AFCs). AFCs have advantages over traditional proton exchange membrane fuel cell (PEMFCs) due to improved kinetics in the alkaline media where transitions metals that are cheaper than Pt can be used without a significant penalty in activity [2]. One of the best advantages of this technology is the low or cero emission pollution. However, the high cost related with the use of electrocatalysts as Pt nanoparticles is one of the first problems. In the past decade, a number of studies have been carried out to Pt alloys with enhanced electrocatalytic performance toward oxygen reduction reaction (ORR) with respect to pure Pt [3-4]. Two kinds of effects, ie ligand and geometric effects are identified for improved the electrocatalytic activity of Pt alloys.

Recently, a series of nanostructured Pt-Ag catalyst with different load of Pt and Ag are been investigated in order to improve the electrocatalytic activity, especially in AFCs due to the alkaline medium. Also, is interesting to prove the Pt-Ag alloys in acid medium. The synthesis of Pt and Ag mono and bimetallic nanoparticles has been reported in several works previously with different methodologies asimpregnation [5], chemical reduction [1,6], mechanical mixed [2], thermal method[7], photochemical method [8], etc. However, is most of them, either organic solvents, toxic reducing agents and stabilizers, which had potential environmental and biological risks, or more than one reactive step is required. Sonochemical method, since discovered, has been studied for yielding kinds of materials, especially noble metal nanoparticles. In the present work we present the preliminary results of the synthesis of Pt and Pt-Ag alloy via ultrasonic irradiation without adding any surfactant to be used as electrocatalysts in fuel cells. During the process, high temperature and pressure resulting from the broken of cavitation bubbles caused by ultrasonic irradiation is an important role. The metallic and bimetallic nanoparticles were supported on carbon Vulcan. We have mainly focused in this study on the effect of concentration of alcohols in the kinetic of the synthesis method and the effect on the activity of Pt-Ag electrocatalysts. The results show significant enhancement of electrochemical activity due to use of Ag in the conventional Pt/C catalysts compared to the commercial catalyst Pt/C.

2. Experimental

2.1 Synthesis of Pt and Pt-Ag nanoparticles

Carbon Vulcan was used as support of Pt nanoparticles and Pt-Ag alloys synthesized by ultrasonic technique. 20 mL H_2PtCl_6 (Aldrich) solution ($1x10^{-3}$ M) and ethanolwas mixed in ultrasonic bath at room temperature for 5 h in N_2 atmosphere.Nitrogen was used to purge the solution before and during the irradiation.After, carbon Vulcan was added to solution and continued the sonication during 30 min. The reduction of Pt^{4+} to Pt^0 was followed by UV-Vis absorption spectra recorded using a spectrophotometer (ThermoSicentific) and quartz 3 mL cell before to added the carbon. 1:1 y 2:1 ratios of alcohol : solution were investigated for kinetic reaction rate.The band a 260 nm was sampling by UV-vis every 1 h during the process (0-6h). The solvent was removed by evaporation, then, it was dried in an oven at 100°C for 2 h. Two catalysts of Pt/C, Pt-Ag/C were synthesized using the method described before.

2.2 Electrochemical Characterization

The electrocatalytic properties of Pt and Pt-Ag catalysts supported on Vulcan carbon were examined at room temperature in a standard three-electrode cell. A platinum mesh was used as the counter electrode, and a standard saturated calomel electrode (SCE = 0.24 V) as the reference electrode. The potentials in this paper were related to the normal hydrogen electrode (NHE). Glassy carbon disk with a cross-sectional area of 0.19 cm^2 was used as a support for the thin films and used as an ink-type working electrode. The catalytic ink was prepared with 1 mg of catalyst, 25 μLof 5 wt% solution Nafion® (Du Pont, 1100 EW) and 125 μL of ultrapurewater. For Rotating Disk Electrode experiments, 10μL of this sonicated mixture were deposited on glassy carbon electrode (0.06 mg cat).Cyclic voltammetry (CV), in a nitrogen-saturated H_2SO_4 0.5 Melectrolyte was performed to clean the electrode surface from 0.05to 1.2 V/NHE at 50 mV s−1. 20 cycles were necessary to stabilize thesystem. Hydrodynamic experiments were recorded at oxygen atmospherein the rotation range of 200, 400, 900, 1600 and 2500 rpm at 5 mVs^{-1} from 1.0 to 0.2 V/NHE. All the electrochemical results of the materials synthesized were test and compared with the commercial sample of Pt/C (10 wt. Pt)

3. Results

Figure 1 shows the UV-Vis spectrum of H_2PtCl_6 as a function of ultrasonic time using (a) 1:1 and (b) 2:1 ratios of alcohol: solution. Both plot exhibit an absorption band located at 262 nm thatcan be attributed to ligand-to-metal charge transfer of $PtCl_6^{2-}$ complex [9]. After sonicated for 6 h the platinum precursor solution with alcoholic concentration of 1:1 as show the Fig. 1-a. The same observation was found in the platinum solution with an alcoholic concentration of 2:1, Fig. 1-b. A higher concentration of alcohol helps to the kinetic of metal reduction by ultrasonic method. These results indicate that the ultrasonic reduction of H_2PtCl_6 in water-alcohol solutions leads to the reduction of Pt^{4+} to Pt^0 metal particles via Pt^{2+}[10]. The coloration of solution change from yellow to brown and no other color change was observed; therefore we assume that reduction to Pt^0 was obtained.

Fig. 2-a show the UV-Vis spectrum of silver after sonicated for 7 h. The alcoholic concentration of solution was 2:1. An absorption band appears at a wavelength that varies between approximately 420-430 nm which is related to the Plasmon resonance of silver nanoparticles spherical and nearly spherical shape, respectively [11]. During the ultrasonic process, the alcohol acts as reducing agent and the water molecules decompose to hydrogen radicals (H◦) and hydroxyl radicals (◦OH) under ultrasonic condition, and then H◦ supply electron for the reduction of Ag^+:

$$H_2O \xrightarrow{sonicated} H\circ + \circ OH, \quad H\circ + Ag^+ \rightarrow H^+ + Ag^0 \qquad (1)$$

During the reaction, an increase of pressure is caused by the slight formation of oxygen produced by the following way:

$$HO\circ + \circ OH \rightarrow H_2O_2, \quad H_2O_2 \rightarrow H_2O + 1/2O_2 \qquad (2)$$

That means, that the overall reaction can be written as:

$$2Ag^{+} + H_2O \xrightarrow{Sonicate} 2Ag^{0} + 1/2O_2 + 2H^{+} \quad (3)$$

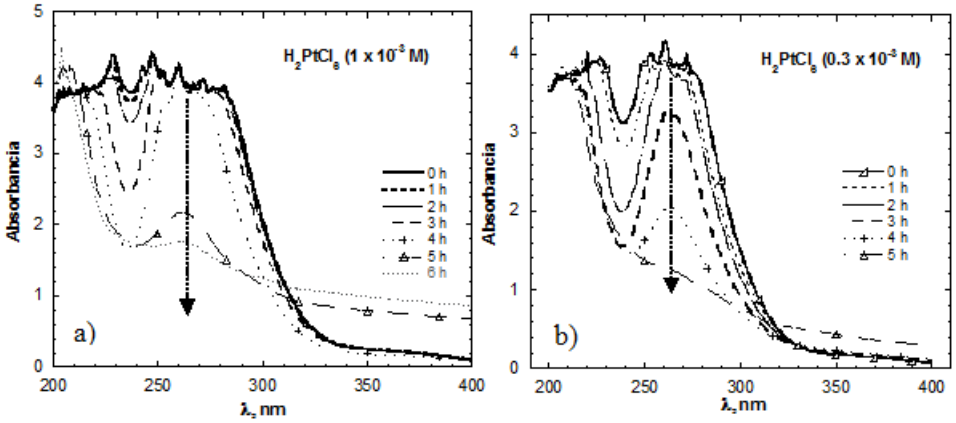

Fig. 1 UV–VIS spectra of absorption of H_2PtCl_6 ($Pt^{4+} \rightarrow Pt^{2+} \rightarrow Pt^{0}$) after sonication using a platinum precursor solution with a concentration of alcohol of a) 1:1 and b) 2:1.

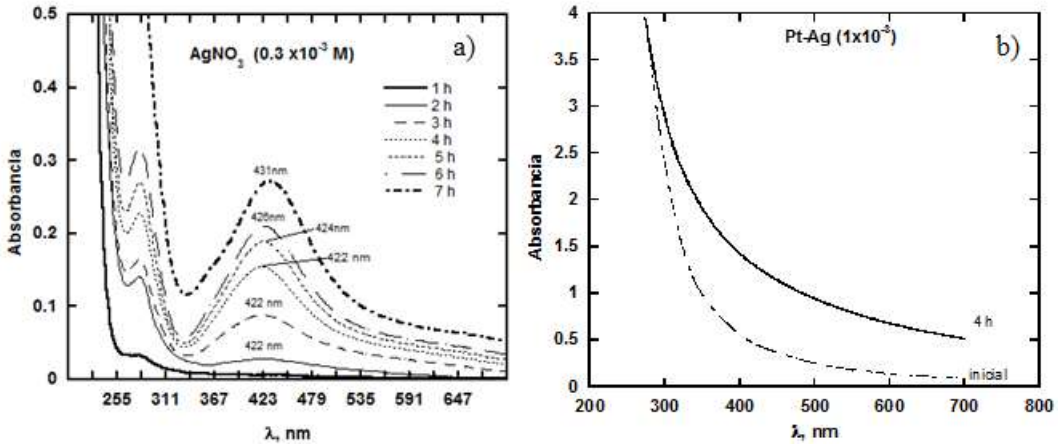

Fig. 2 UV–VIS spectra ofabsorption obtained as a function time during the ultrasonic of different alcohol:solutionof a) $AgNO_3$ ($Ag^{+} \rightarrow Ag^{0}$) and b) H_2PtCl_6-$AgNO_3$

The UV-Vis absorption spectrum of the bimetallic catalysts Pt-Ag obtained using a $AgNO_3$ and H_2PtCl_6alcoholic solution (2:1) before and after 4 h of sonicated is presented in Figure 2-b. The absorption band of Ag-Pt corresponding to the plasmon resonance around 200-400 nm does not appear. However, the absorption band increases after irradiation with ultrasound. According to those reported in the literature [11] this is related to the size of the nanoparticles because nanoparticles are less than 4 nm, which is reduced to a change of their electronic properties by which the spectrum is observed absorption. This

hypothesis would be confirmed by microscopy characterization studies to confirm the size of the nanoparticles.

CV curves measurements were recorded in the range of potential from 0.05 to 1.2 V/NHE. The results of Pt/C and Pt-Ag/C synthesized by sonication are presented in Fig. 3. The CV curve of commercial Pt/C Etek is also show of Fig 3 for comparison purposes. All shapes of the voltammograms are very similar and correspond to the typical voltammograms of Pt nanoparticles in acid medium [12].

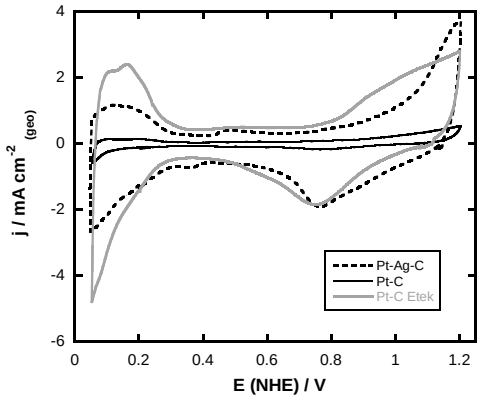

Fig. 3 Cyclic voltammetry of (─)Pt/C, (---)Pt-Ag/C and (—)Pt/C-Etekin 0.5 M H_2SO_4saturated with nitrogen at a scan rate of 50 mV s^{-1}at RT with 20 cycles.

A rotating disk electrode (RDE) study of Pt/C, Pt-Ag/C and Pt/C Etek electrocatalysts to carry out the ORR are presented in Fig. 4. The typical curves on Pt nanoparticles en acid medium exhibit the three distinct regions characteristic: (I) the kinetic region, where the current, i_k, is independent of the rotation velocity; (II) the mixed control region, where the behavior is determined by kinetic as well as diffusion processes; and (III) the mass-transfer region, where the diffusion current, i_d, is a function of the rotation velocity [12]. One of the most important results in this study is that the polarization curves of Pt-Ag/C exhibit higher electrochemical activity than Pt/C and Pt/C Etek.

Fig.5 represents the inverse current density (i^{-1}) as a function of the inverse of the square root of the rotation rate ($\omega^{-1/2}$), corresponding to a Koutecky-Levich (K-L) plot for (a) Pt/C, (b) Pt-Ag/C and c)Pt/C Etek samples at various electrode potentials. The linearity of the K-L plots indicates first-order kinetics with respect to molecular oxygen [3, 4]. For all of the samples, a similar K-L slope of 105-116 mA^{-1} $rpm^{1/2}$ was obtained. The theoretical slope of 100.7 mA^{-1} $rpm^{1/2}$ was calculated for the four-electron process, indicating that the ORR on Pt nanoparticles catalyst at different potentials follows the four-electron pathway leading to water [14].

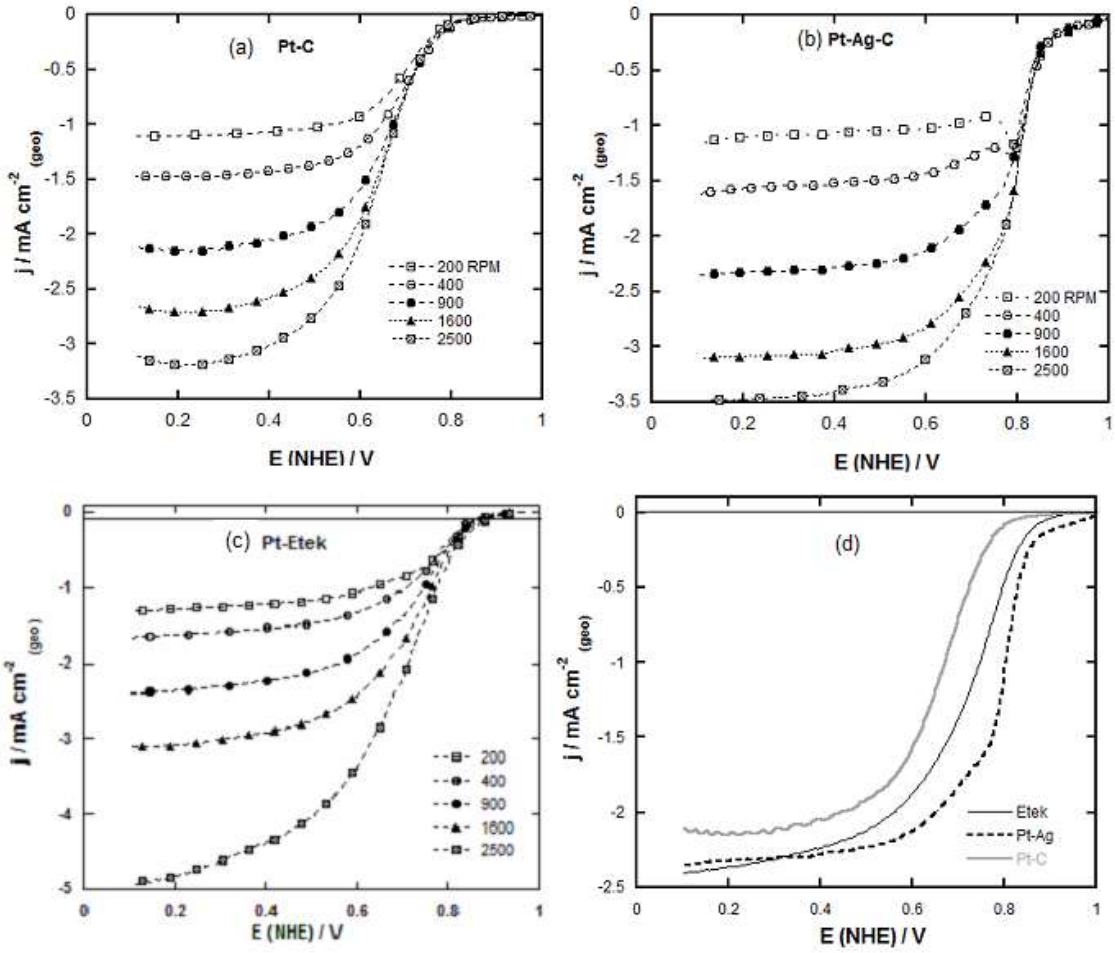

Figure 4. Oxygen reduction reaction (ORR) curves of a) Pt/C, b) Pt-Ag/C prepared by ultrasound compared to c) Pt/C Etek in 0.5 M H_2SO_4 at different rotating speed. Scan rate of 5 mV s^{-1} at RT.

Fig. 6 shows the mass transfer–corrected Tafel plots deduced for the RDE analysis on (a) Pt/C and (b) Pt-Ag/C electrocatalysts prepared by ultrasonic compared with those of (c) Pt/C Etek commercial catalyst. The Tafel slope at a high current density has a value of 60 mV $decade^{-1}$, as expected for a first electron transfer rate-determining step. Table 1 summarizes the kinetics parameters deduced for the ORR on the Pt/C and Pt-Ag/C electrocatalysts. The interaction of the Pt with Ag shows that at 0.9 V/ENH, the cathode over-potential increases by 83 mA/cm^2 in relation to the Pt/C samples. These results indicated that Pt alloyed to the Ag exhibits high catalytic activity compared with traditional Pt/C for the oxygen reduction reaction in a sulfuric acid solution. The different values depended on the adsorption energy of the oxygen and mean that the transfer of the first electron to the adsorbed oxygen is the rate-determining step of the ORR kinetic reaction.

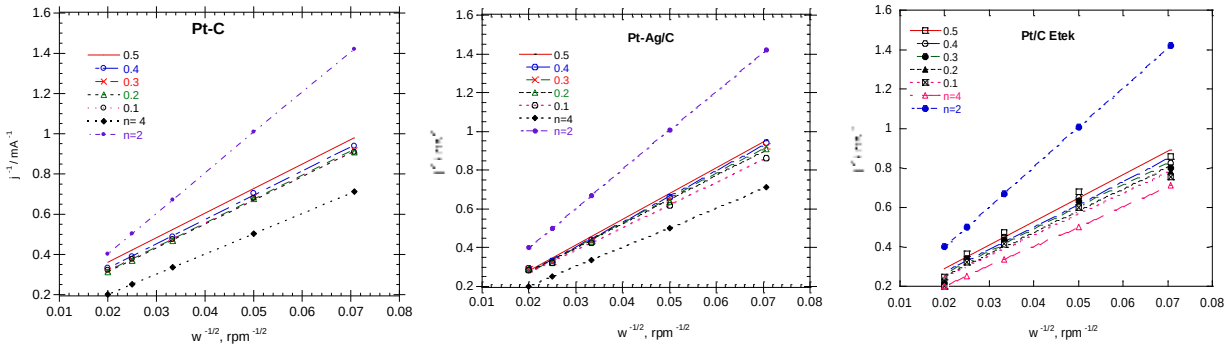

Figure 5.Koutecky-Levich (K-L) plot of a) Pt/C, b) Pt-Ag/C prepared by ultrasound compared to c) Pt/C Etek obtained of the data experiments of Fig. 4.

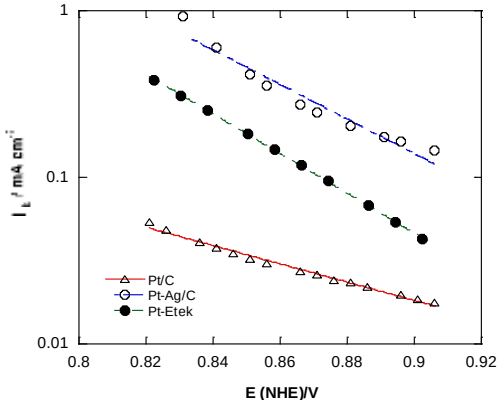

Figure 6. Mass-transfer–corrected Tafel plot deduced for the RDE analysis on a) Pt/C, b) Pt-Ag/C prepared by ultrasound compared to c) Pt/C Etek

Table 1.a) Pt/C and b) Pt-Ag/C electrocatalysts synthesized prepared by ultrasound compared

Catalyst	Koutecky-Levich slope (mA^{-1} $rpm^{1/2}$)	α	b ($mV\ dec^{-1}$)	j_k a 0.9 V/NHE (mA/cm^2_{Pt})
Pt/C	116.3	0.62	95	0.009
Pt-Ag/C	115.1	0.56	105	0.151
Pt/C Etek	106.9	0.53	110	0.068

4. Summary and perspectives

Pt/C and Pt-Ag/C electrocatalysts were successfully synthesized by ultrasonic technique on friendly environmental conditions. According to the electrochemical results the activity of the bimetallic Pt-Ag catalyst synthesized has better electrocatalytic propertiesfor to be used as fuel cell cathodes than Pt/C

synthesized at the same conditions as well as the commercial catalyst. The presence of Ag on the Pt structure modifies the electronic properties of Pt favorably to carry out the ORR. However, is important support this investigation with help of the physical characterization of the samples synthesized with electron microscopy andX-ray diffraction. Also, is necessary analysis the electrochemical behavior in basic medium for to be used as cathodes on an AFC.

Acknowledgements

The authors are grateful to the Universidad Politécnica de Guanajuato (UPG) for the financial support of this work under the project PROMEP No.103.5/12/3400

References

[1] F. Yuan-Yuan, Z. Gui-Rong, M. Jun-Hong, L. Gang, X. Bo-Qing. Carbon-support Pt-Ag nanostructures as cathode catalysts for oxygen reduction reaction. Phys. Chem. Chem. Phys. 2011; 13: 3863-3872.

[2] R.C. Sekol, X. Li, P. Cohen, G. Doubek, M. Carmo. Silver palladium core-shell electrocatalyst supported on MWNTs for ORR in alkaline media. Appl. Catal. B 2013; 138-139: 285-293.

[3] A.J. Bard, L. Faulkner, Electrochemical Methods: Fundamentals and Applications, Wiley, New York, 2001, pp. 340-344.

[4] K. Kinoshita, Electrochemical Oxygen Technology, Wiley, California, 1992.

[5] C.-T. Hsiech, C. Pan, W.-Y. Chen, Synthesis of silver nanoparticles on carbon papers for electrochemical catalysts. J. Power Sources 2011; 196: 6055-6061.

[6] X. Song, D. Zhang. Bimetallic Ag-Ni/C particles as cathode catalyst in AFCs (alkaline fuel cells).Eenergy 2014; 70: 223-230.

[7] Q Wu, L. Jiang, L. Qi, L. Yuan, E. Wang, G. Sun. Electrocatalytic activity and stability of Ag-MnOx/C coposites toward oxygen reduction reaction in alkaline solution. Electrochim. Acta 2014; 123: 167-175.

[8] B. Ruiz-Camacho, M.A. Valenzuela, J.A. Perez-Galindo, F. Pola, M. Miki-Yoshida, N. Alonso-Vante, R.G. González Huerta. J. New Mat. Electrochem. Syst. 2010; 13: 183-189.

[9] B. Ruiz Camacho, R.G. González-Huerta, M.A. Valenzuela, N. Alonso-Vante. Preparation and characterization of Pt/C and Pt/TiO2 electrocatalysts by liquid phase photodeposition. Top Catal 2011; 54: 512-518.

[10] M. Harada, K. Okamoto, M. Terazima. Diffusion of platinum nanoparticles during photoreduction process using the transsient grating method. Langmuir 2006; 22: 9142-9149.

[11] C. He,L.Liu, Z. Fang; J. Li; J. Guo; J. Wei.Formation and characterization of silver nanoparticles in aqueous solution via ultrasonic irradiation.Ultrasonics Sonochemistry 2014; 21: 542 - 548.

[12] b. Ruiz-Camacho, O. Martínez-Álvarez, H.H. Rodríguez-Santoy, V. Granados-Alejo, Pt/C and Pt/TiO2-C electrocatalysts prepared by chemical vapor deposition with high tolerance to alcohols in oxygen reduction reaction. J. Electroanal. Chem. 2014; 725: 19-24.

[13] L. Timperman, Y.J. Feng, W. Vogel, N. Alonso-Vante, Electro-chim. Acta, 55, 7558 (2010).

Development and Application of Hybrid Membranes by The sol-gel Process for The Enrichment of Hydrogen and Methane Gases

P. Quechulpa-Pérez[1], JF. Pérez Robles[1], AF Pérez-de Brito[2], LM. Avilés-Arellano[1], J. Pineda-Piñón[3]

[1]Centro de Investigación y de Estudios Avanzados del Instituto Politécnico Nacional Unidad Querétaro, Libramiento Norponiente No.2000. Frac. Real de Juriquilla Querétaro, Qro. C.P. 76230, Tel: +52 (442) 2 11 99 00. E-mail: martin.pompeyo@hotmail.com

[2]Grupo de tribología y superficies. Facultad de minas. Universidad Nacional de Colombia Sede Medellin,

[3]Centro de Investigación en ciencia Aplicada y Tecnología Avanzada del IPN, Unidad Querétaro, C.P. 76090, Cerro Blanco No. 141. Colinas del Cimatario, Querétaro, Qro., México.

Abstract

The production of renewable energies is an important topic in our present-day society. Many researchers are currently working in processes for the production of biofuels and also the use of them. Among biofuels the production of hydrogen and methane from different wastes play an important role today. Normally biohydrogen and methane biogas are produced in anaerobic biodigesters using different organic wastes. Nevertheless the produced gas in both cases has undesirable gases like carbon dioxide and sulphur compounds among others. Then it is necessary to decrease the concentration of undesirable gases and at the same time to increase the quantity of hydrogen and methane gas.

Taking into account the aforementioned, our research group has made an extensive work for the development of some hybrid membranes to separate the hydrogen and methane from carbon dioxide and in general from undesirable gases. The hybrid membranes were prepared using colloidal silica by the sol-gel process and polyvinyl acetate, PVac. The membranes were characterized by Thermogravimetric Analysis, Optical Microscopy, Scanning Electron Microscopy and Raman Spectroscopy. Also mechanical tests like tensile strength, penetration and superficial hardness were performed on the hybrid material used for the production of the membranes.

A homemade device was fabricated for testing the diffusion of gases through the membranes. It was demonstrated that that the best performance of the membranes was attained using a ratio silica/PVAc of 35/65 %w/w, methanol as solvent and annealed at temperature 40°C. From the results it was fabricated a device of three columns of 6" for using it in a biodigester prototype of 7.0 tons that will be used for the production of hydrogen and methane.

Keywords: **Biohydrogen, membranes, sol-gel.**

Introduction

Biogas (colorless and flammable gas) is produced from different organic wastes (domestic, agricultural and agro-industrial) [1, 2, 3], and it is an alternative kind of energy with high ecological impact. The biogas production is usually made using bio-digesters and the produced gas is composed by approximately 20 - 50 % v/v of CO_2, 1% - 4% de N_2, small amounts of other gases like Hydrogen, H_2, Hydrogen Sulfide (H_2S) and 50 - 80 % v/v of methane as main component of the biogas [2, 3, 4]. Because of this fact, the biogas can be enriched to increase the obtained CH_4 using hybrid membranes [5]. A membrane can be defined as a selective barrier used to separate two different phases and blocks the free transport for one o more components if a mixture is treated. Also it may be defined as a region between two fluids that hinders or favors the movement through it of some gases [6, 7, 8, 9]. It is necessary to consider that the size and the shape of the gas molecule affect positively or negatively its movement through the membrane [9]. As it is described, the biogas from biodigesters is a mixture of gases and for this reason to increase the % of hydrogen or methane in it [6] (to enrich the biogas) the use of polymeric membranes has a high potential, due to their low cost investment [7, 8].

In the bibliography is mentioned the use of polymeric membranes for the elimination of CO_2 from a gas mixture of H_2, N_2, CH_4 and O_2 [10 - 16] and hybrid membranes (normally an inorganic material with some kind of resins) membranes for a gas separation process [17 - 43]. Among the means used for gas separation, polymeric membranes have importance due to their advantages such as low cost, high efficiency and low ecological footprint [43, 44]. Also some authors discuss how the transport through polymeric membranes follows the solution–diffusion transport mechanism; that is, dissolution of penetrant molecules in the polymer and their diffusion through the membrane [45]. The selection of a suitable polymeric material is crucial in determining the gas separation performance of the membrane. The chemical structure, crystallinity and morphology of the polymer play an important role in determining the transport properties of the membrane [46].

An article by Thomas Graham was published in 1866, where the author established the basic principles for the diffusion-dissolution model, which governs the transport and gas separation through porous polymeric membranes [47]. On the other hand, the market of gas separation membranes has increased significantly since 1970. In this way some articles and reviews describe the advancement in materials, specifically in polymers, for the production of gas separation membranes [13, 48].

In this our current research, we prepared, by the sol-gel process, a hybrid membrane made of polyvinyl acetate and silica for gas separation. This is both a very simple material and easy to prepare and additionally so different from that presented for other researchers. We do not discuss the mechanism for gas separation because this was not the objective of this work. This will be discussed later in other paper. The point is that when we use the material for the preparation of membranes, we have obtained excellent results and it is possible to enrich the hydrogen and methane gases to acceptable levels for being used in motor vehicles or the generation of electricity using motogenerators [5].

Methodology for preparing the membranes

Hybrid SiO_2-PVAc (PVAc known commercially as B-18) solutions were prepared by the sol-gel process [49] in concentrations of 50, 65 and 75 % w/w of PVAc resin and using four different solvents (methanol, ethanol, propanol and butanol in different ratios for controlling the porosity. Figure 1 is an schematic representation of the used methodology for preparing the solutions.

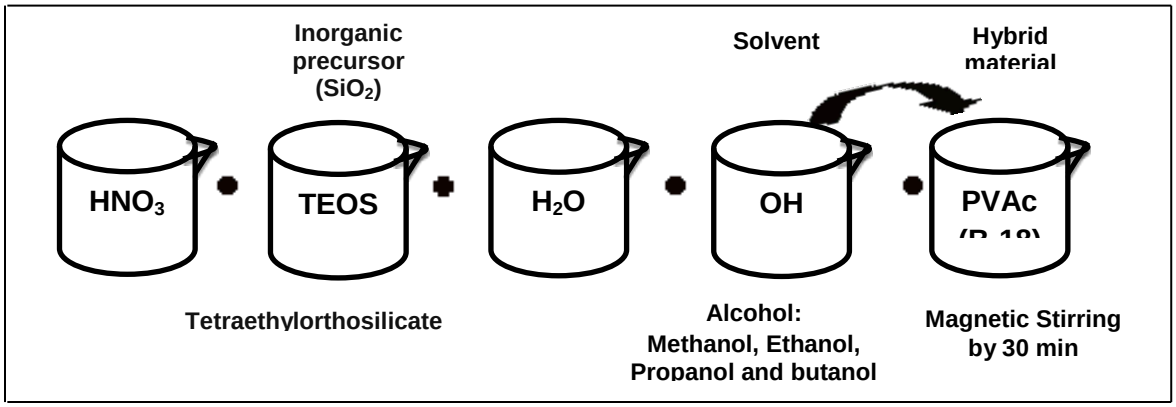

Figure1. Methodology for preparing the hybrid SiO_2-PVAc solutions by the sol-gel process

Once the hybrid solutions were ready the membranes were made by dip coating, introducing a small piece of stainless steel mesh as a support (275 and 325 mesh) of 1 in x 3 in, and withdrawing it at a constant rate of 3.33 mm/sec. The membranes prepared as described above were heat treated at 25, 40 and 100°C for 15 hours. For a second coating the aforementioned steps were repeated, but in this case the time for the heat treatment was only 20 min.

The obtained membranes were characterized by Termogravimetric Analysis (TGA), Optical Microscopy (OM), Scanning Electronic Microscopy (SEM) and Raman Spectroscopy (RS). Also mechanical tests like tensile strength, penetration and superficial hardness were performed on the hybrid material used for the production of the membranes. In addition, CH_4, H_2, N_2 and CO_2 pure gases were diffused through the membranes to test their efficiency for the enrichment of methane. Below only the best results using methanol are presented. Sometimes ethanol is mentioned only for comparison.

Membranes without the mesh were prepared to determine the mechanical properties of tension, according to the standard NMX-E-082-SCFI-2002 [50]. Those membranes were prepared by casting [13, 51], in a mould of 12.5 cm x 2.5 cm x 2 mm (length, width, thickness). In that way dried membranes of 0.5 mm of thickness was obtained. Tension tests were run in a Texturometer Texture Analyzer, model TA-TX2. For knowing the response of them when they are under an extreme load like that of the pressure of the gas during the diffusing process. This parameter can be related to the pressure during the diffusion process [52]. The deformation under load allows us to evaluate and quantify the most outstanding properties of the membranes like the elastic and plastic behavior. Those properties are so important because let us know the elastic limit where the original dimensions of the material are re-established and the point where the membranes break.

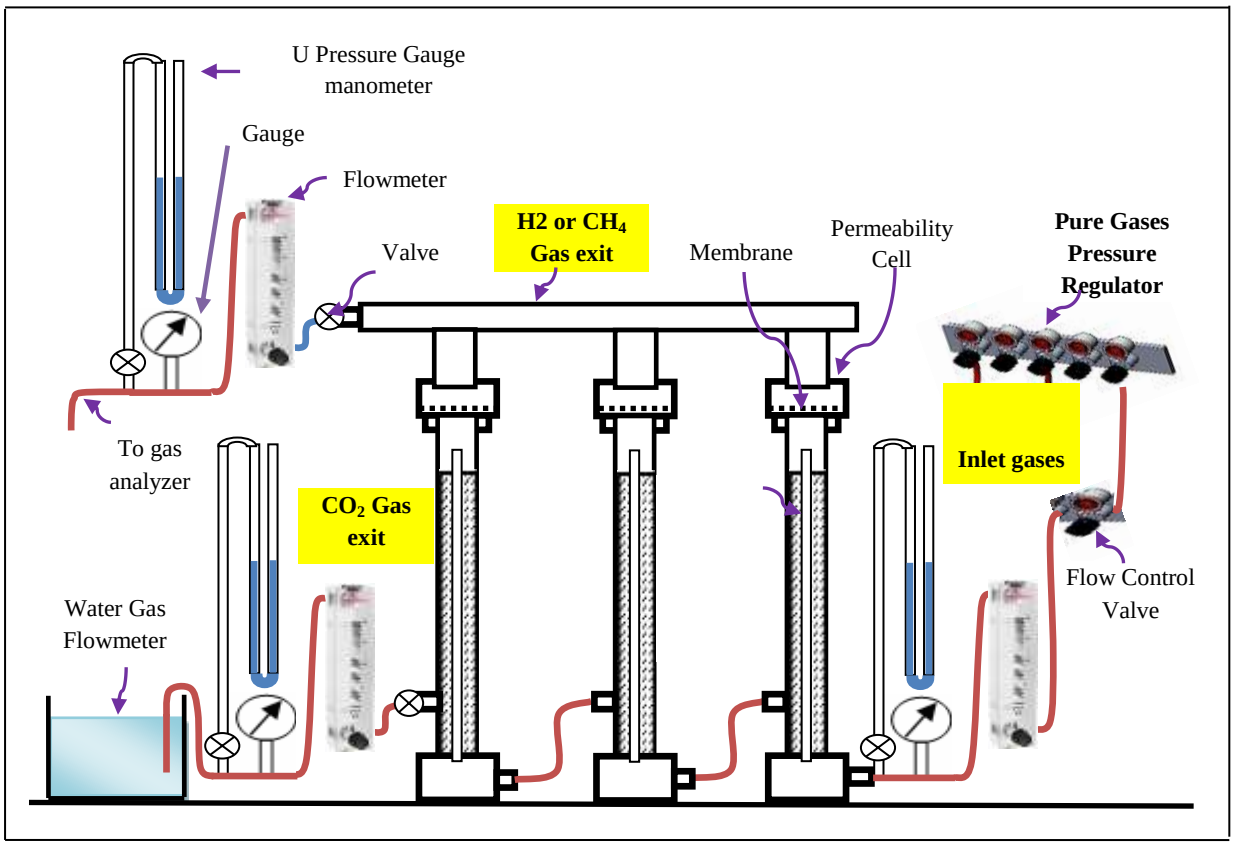

Figure 2. Schematic diagram of the device for testing the selectivity of membranes

For carrying out the diffusion tests, a device was designed and constructed, according to the schematic diagram, shown in Figure 2. The purpose of these tests was to determine the conditions for the best selectivity in the separation of methane, from nitrogen, N_2 and carbon dioxide, CO_2.

The device for measuring the diffusion of gases through the membranes is in reality bench test equipment which is made up of a system for feeding the gases and three gas separation columns. The permeability cell is the main part of the equipment, which contains the prepared hybrid membranes whose properties are going to be determined. The gas fed through the system diffuses slowly through the membranes and it is transferred to a manifold set in the upper part of the system. The gas molecules that do not diffuse through the membrane are diffused through a sand bed (-200 +325 Mesh Tyler) for delaying the flow of the remaining gases. Both streams of gases can be analyzed using an Orsat gas analyzer or any other equipment when a mixture of gases is fed.

Each test was carried out at constant gauge pressure, increasing it from 2.5 to 30 psig at increments of 2.5 psig. The tests were run taking note of the gas flow and pressure at the input and at the exit of the system, besides the average temperature at the time of the day. This procedure was followed for each one of the prepared membranes, using different silica/polymer ratio and annealed at different temperatures.

Results and discussion

1. Analysis Termogravimetric

In Figure 3 it is shown the obtained thermogravimetric analysis, TGA, for the hybrid precursor suspension of 35/65 % w/w of SiO_2/PVAc solutions obtained with different solvents, methanol, ethanol, propanol and butanol From the thermogram it is possible to observe that the material loses the larger part of the solvent about 100 ^oC, which it is the limit temperature for annealing the produced membranes. It was determined in some tests, that it is better to anneal the membranes at temperatures no more than 50 °C. Higher temperatures to that decrease the adherence of the material to the mesh used as support, giving raise also to the appearing of microcracks and consequently the selectivity of the membrane is low. From the thermogram it is observed also that the used material for the preparation of the membranes is stable about 300 ^oC, beyond that temperature the material suffers degradation. For those reasons it was decided to anneal the membranes at temperatures no longer than 100 ^oC and times of 15 hours for assuring the decreasing of the solvent inside the membrane at acceptable levels and at the same time to obtain the proper porosity

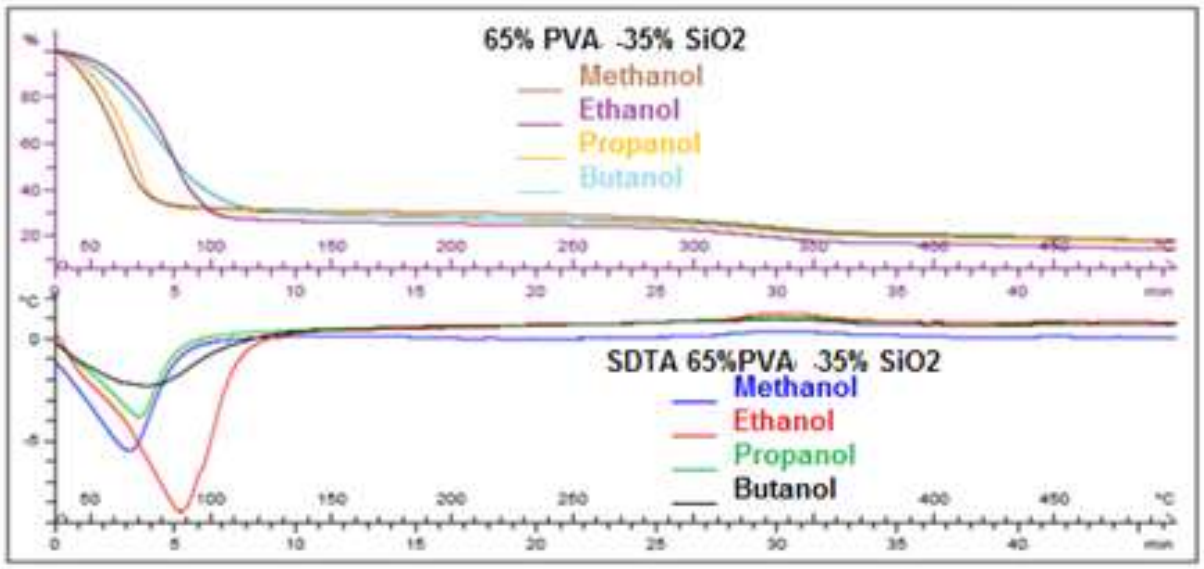

Figure 3. Hybrid materials TGA analysis prepared with two different solvents

2. Characterization by Optical Microscopy

The inspection of the 35/65 w/w SiO_2/PVac membranes under the optical microscopy, using methanol as solvent and annealed at 100 ^oC is presented in Figure 3. Optical microscopy results in Figure 4 shows that membranes are of homogeneous porosity and have small microcracks. When a second coating was deposited over the first one, that microcracks almost disappeared, as it is observed in Figure 3b. When ethanol, propanol and butanol were used as solvents, the obtained membranes were of bad quality, showing abundant microcracks, visible to the eye, and for this reason they were rejected and not tested for the gas separation process.

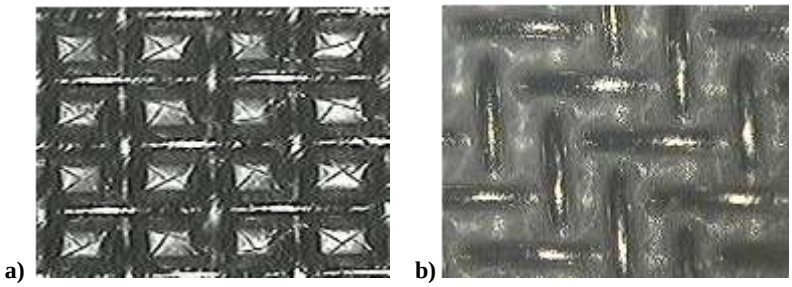

Figure 4. Optical microphotographs of membranes prepared using methanol as solvent, annealed at 100 ^oC, with a ratio of 35/65 w/w SiO_2/PVAc at 10X. a) coated with one layer and b) with two layers respectively

3. Characterization by Scanning Electron Microscopy (SEM)

These results were corroborated by means of SEM microphotographs. In Figure 5 it is shown a micrograph of a membrane annealed at 25 °C. In Figures 5a and 5b it is noticeable the good adherence of the hybrid material to the 325 mesh. Notice that fractures due to the annealing are not observed. In Figure 5c it is appreciated both that the polymeric resin is covering the silica particles and micro cavities where gases that will be separated from a stream will be diffused.

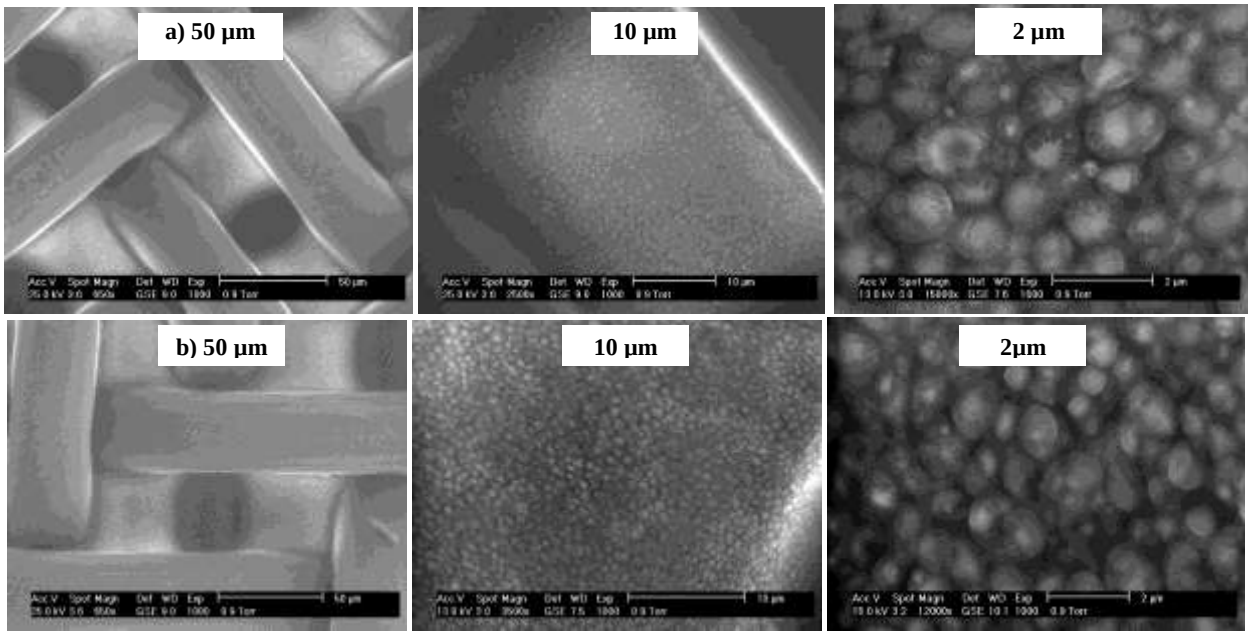

Figure 5. SEM micrographs of membranes with 65 % w/w PVAc annealed at a). 25 °C and b). 40 °C.

In Figure 6a, b and c shows a good coating when 325 mesh is used. The uniformity of the membrane is attributed to the methanol, which has the smallest size, volatilizes both easily and gradually, properties that help to obtain a proper porosity, with a minimum microcracks for the gas separation process.

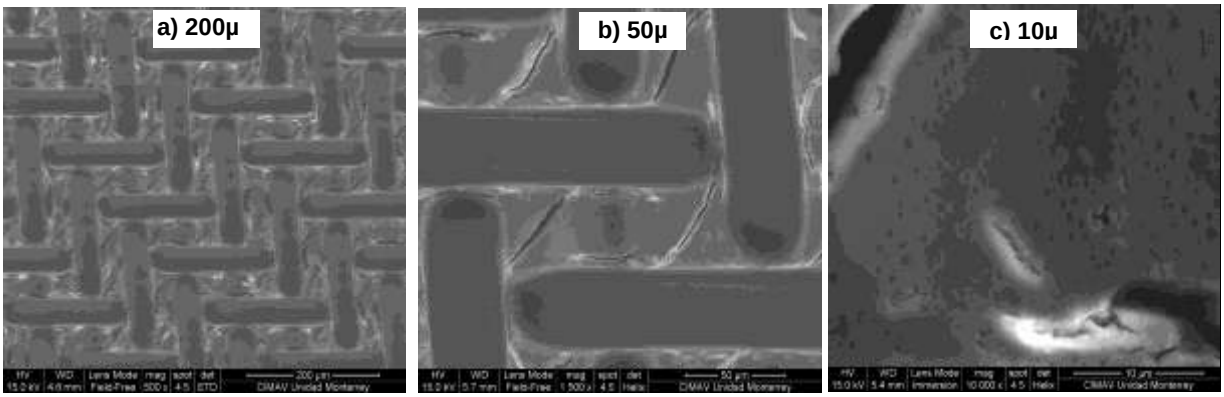

Figure 6. SEM microphotographs of membranes prepared with 35/65 w/w SiO_2/PVAc, annealed at 100 ^{o}C and using methanol as solvent in the silica preparation.

4. Testing of gas diffusion

For determining the ability of the prepared membranes toward the gas separation, some tests were accomplished diffusing pure gases through the membrane and measuring the flow of the exit gases, at an inlet gas pressure of 110 cm in water column. From Figure 7, the diffusion of gases follows the next order: H_2 diffuses first, starting with a flow of 8 mL/sec, increasing in an approximately exponential way in the next 5 min and after this the flow keeps constant at 10.5 mL/sec. Later CH_4 and N_2 gases were diffused through the membrane with a flow between 4 and 5 mL/sec for methane and between 2 and 3 mL/sec for nitrogen. Finally carbon dioxide diffuses through the membrane, starting with a flow of 2 mL/sec and after 10 min the flow decays to zero.

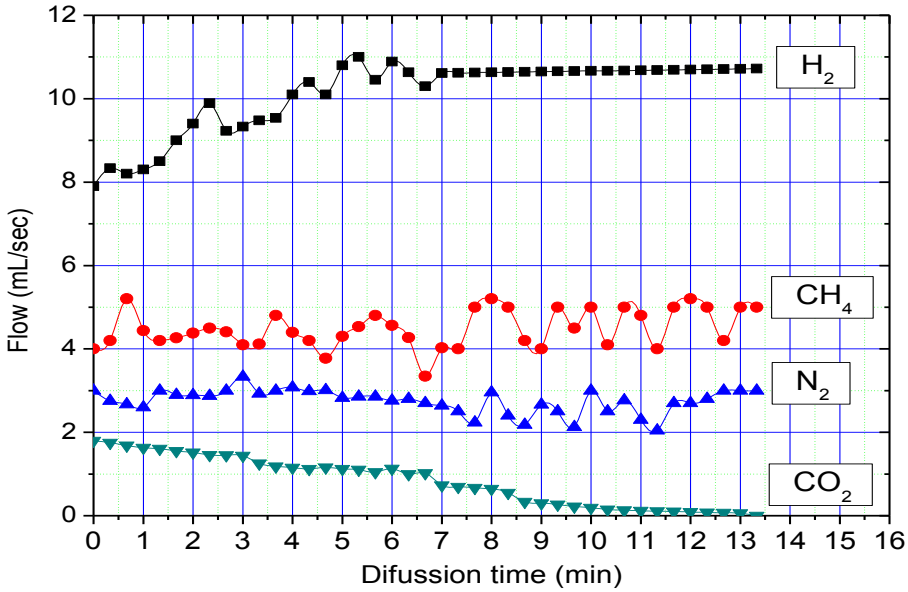

Figure 7. Gas diffusion test through a membrane 35/65 w/w SiO_2/PVAc, annealed at 40 ^oC.

5. Characterized by Raman Spectroscopy

For establishing why this behavior of the membrane toward the gases, after being prepared the membrane was characterized by Raman Spectroscopy at zero time, after 2 min and then after 13 min of diffusion of CO_2 gas. The results of this characterization are presented in Figure 8. At 2 min, it is clearly demonstrated that during the diffusion of CO_2 some kind of bond between the carbon of the polymer and that of the CO_2 is formed. In this way, the entrapped CO_2 hinders the diffusion of the remaining gases, promoting the selective separation of them.

Accroding to our Raman observations, in the literature has been reported the presence of a very strong band around 2976 cm^{-1} for the stretching of OH groups and also a band between 641 and 684 wavenumber assigned to δ(COO) groups [49]. Mitterdorfer et. al [53] mention that some di and polycarboxilicc acids show the existence of some small Raman bands in the region between 1607 and 1782 cm^{-1}, corresponding to the assimetric stretching of the C=O group; as a consequence of the connection of the OH group to the carboxylic group or directly to a carbon atom. This can be observed for both the alfa form (1630 cm^{-1}) and the beta form (1608 cm^{-1}). This suggests that the CO_2 was entrapped on the surface and also inside the pores of the membrane or probably it can exist the formation of carbonic acid in those sites. In that way the entrapped CO_2 occupies the existent active sites and consequently hinders the formation of new bonds on the surface of the membrane or inside the pores. The result is an effect of repulsion against the new molecules which try to pass through the membrane. This can explain the selectivity of the membrane to CH_4 gas as it was observed in our experiments.

6. Tensile mechanical strength tests

In Table 1 the strength-deformation curves are obtained for the membranes without the mesh and for 50, 65 and 75 % w/w of PVAc. According to the results, the elastic limit for the membranes with 50 % w/w of PVAc is located at 7 MPa, with an elastic deformation of 5 mm and a breakdown limit at 8.5 MPa, with a limit deformation of 9.5 mm. For the membranes with 65 % w/w of PVAc, the limit deformation is presented at 1 MPa with a deformation of 40 mm and elastic limit at 1.25 MPa with a deformation of 150 mm. Finally, the membranes with 75 % w/w of PVAc present an elastic limit at 1.5 MPa with a deformation of 5 mm and a breakdown limit deformation at 2 MPa and a deformation of 95 mm.

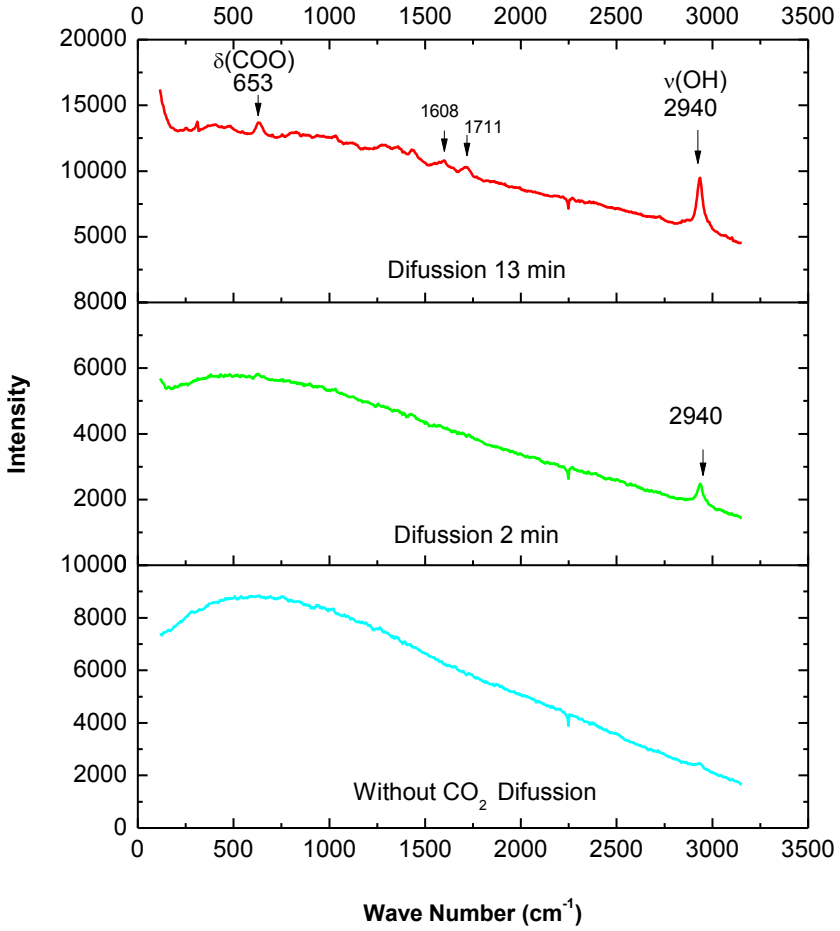

Figure 8. Raman analysis of the preceding membrane at 2 and 13 min of CO_2 gas diffusion

Table 1. Elastic strength and deformation of membranes

Membrane	Elastic strength (MPa)	Elastic deformation (mm)	Ultimate strength (MPa)	Fracture deformation (mm)	Young's modulus (MPa)
50% PVAc	7.0	5	8.50	9.5	1400
65% PVAc	1.0	40	1.25	150.0	25
75% PVAc	1.5	5	2.00	95.0	300

According to Figure 9, a membrane with an optimum both elastic deformation and strength must be prepared with 65 % w/w PVAc. This could be probably due to a better interaction of the surface groups of the resin with the silanol groups of the nanometric particles of silica. There will be a balance among the surface groups of the resin and those of the silica for having a material with excellent properties that can be used for the preparation of the membranes. When the percentage of the resin is higher than certain value, the interaction among the bonds of the resin itself will prevail. On the other side, when silanol groups of the silica prevail the bonds among them will determine the properties of the whole material. This establishes the difference among the membranes prepared with different ratios of resin and silica. A membrane prepared with a high content of resin will be very elastic but with a low porosity and this makes so difficult the flow of gas molecules through it. Therefore it is posible to have a membrane with a good interaction between the fillers and the polyme; which was confirmed by menans of the charactertization that was carried out using SEM [22].

On the contrary, membranes prepared with a high content of silica will be a little elastic and will be affected in a larger degree by the gas pressure, and in this way they will be susceptible of suffering fractures and therefore to decrease their efficiency for the gas permeation. It is preferred a membrane with intermediate content of silica and resin and of course, with intermediate properties of the resin and those of the silica. The membranes obtained with 65 % w/w of resin fulfill the aforementioned requirement, as it is shown in Figure 9.

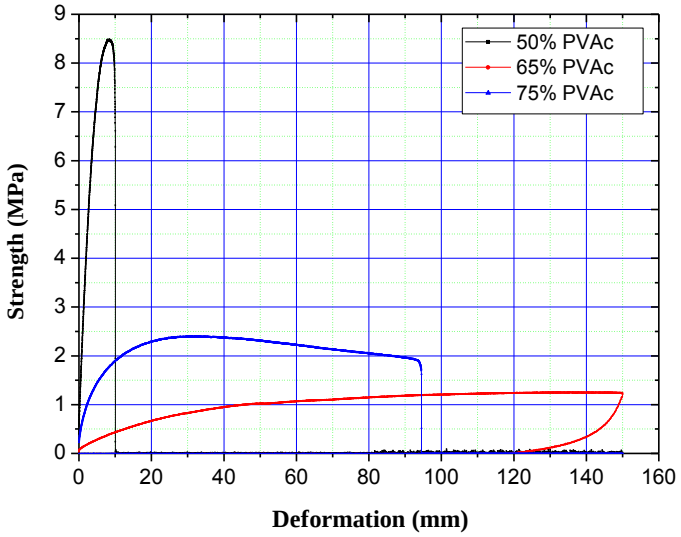

Figure 9. Deformation versus strength of membranes with 50, 65 y 75 % w/w of PVAc

7. Resistence to penetration tests

In Figure 10 it is shown the resistance to penetration test of the membrane prepared with 65 % w/w of PVac resin at temperatures of 25 and 40 ^{o}C.

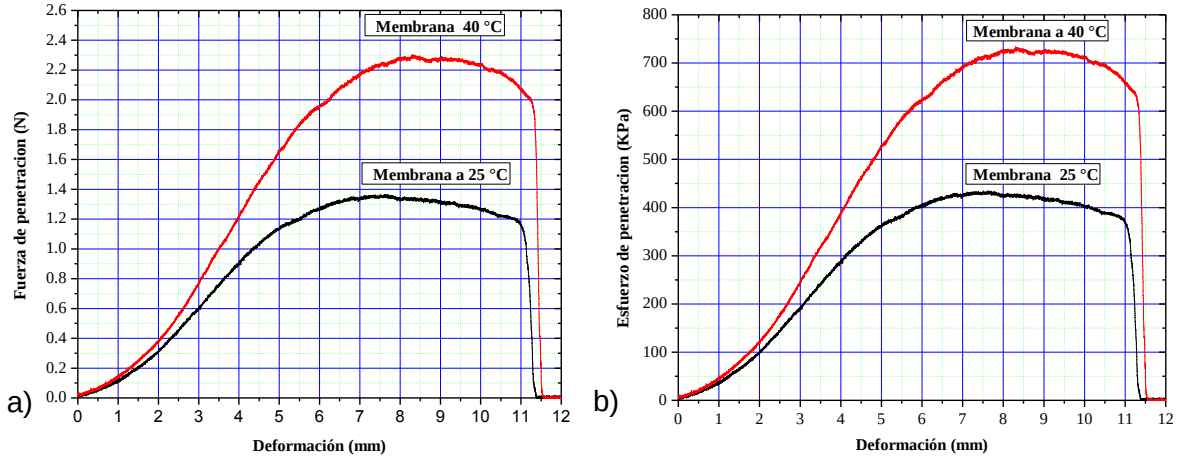

Figura 10. Deformation vs penetration of membrane without support prepared with 65 % w/w of PVac acontra. a) deformation vs penetration strength and at 25 ^{o}C and b) deformation vs penetration strength at 40 ^{o}C

From Figure 10 it was prepared Table 2, which indicates the penetration and the hardness of the film prepared with 65 % w/w of PVAc resin and annealed at 25 and 40 °C, where it is appreciated that the memebrane annealed at 40 °C is more resistant to penetration.

Table 2. Penetration and hardness for the memebrane with 65 % w/w de PVAc.

Variable		Annealed at 25 °C	Annealed at 40 °C
Strength to the elsatic limit	(kPa)	362.235	460.275
Deformation to the elastic limit	(mm)	5	4.5
Strength to the creep limit	(kPa)	400.433	621.021
Deformation to the creep limit	(mm)	5.8	6
Breaking strength limit	(kPa)	426.215	733.703
Deformation to the penetration limit	(mm)	8.615	8.305
Hardness to penetration	(N)	1.339	2.305

8. Hardness test of the membrane

The results of hardness test pencil of membranes are presented in Table 3. The data show that the membrane annealed at 40 °C is compsoed of a material hard and resistant to the scratch.

Table 3. Hardness test pencil of membranes

Membranes	Dureza a lápiz	
	Temperature 25 °C	Temperature 40 °C
50 % w/w PVAc	8 H	9 H
65 % w/w PVAc	6 H	7 H
75 % w/w PVAc	3 H	4 H

9. Gas separation tests

Additional tests were carried out using the membrane for the separation of methane from a synthetic mixture of methane and carbon dioxide and analyzing the exit gases with an Orsat Analyzer. The tests were run in the same way like that of Figure 7, saturating first the membrane with pure CO_2 gas and then continuing to diffuse a synthetic gas composed of 80.1 % of CH_4 and 19.9 % of CO_2 under different inlet gauge gas pressures. The results of the elimination of CO_2 are presented in Figure 11. It can be seen from the figure, that 75 % v/v of CO_2 was eliminated at 0.17 Bar (2.5 psi) and 60 % v/v at 2.07 Bar (30 psi).

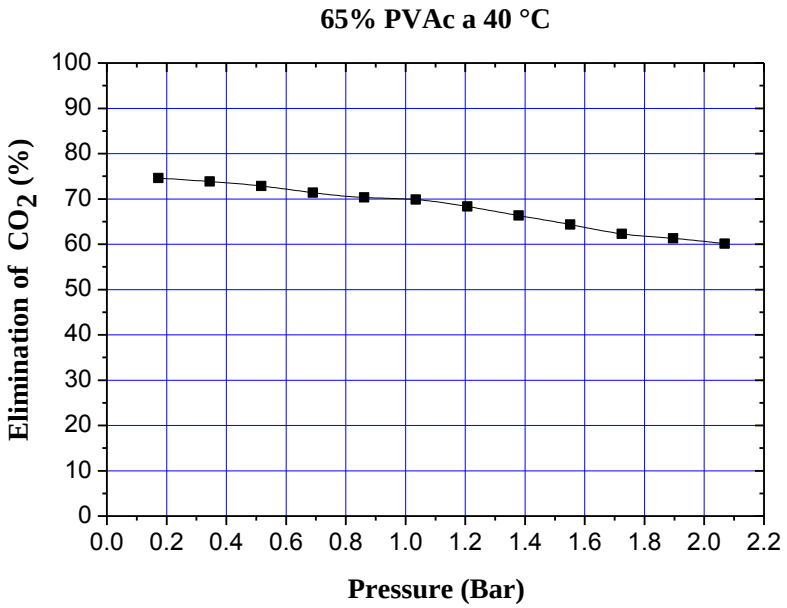

Figure 11. Tests for the separation of CO_2 from CH_4 using a membranes prepared with a ratio of 35/65 w/w SiO_2/PVAc and methanol as solvent

From the results it is concluded that it is

possible to use these membranes for enriching the hydrogen and methane produced in a biodigester. These results are being implemented in a biodigester prototype of 340 liters of materials Figure 12, putting the membranes in a specially designed device to separate the CO_2 from H_2 and CH_4.

Figure 12. Continuous digester 340 liters

There were carried out tests for the separation of methane from a synthetic mixture of methane and carbon dioxide and analyzing the exit gases with and Orsat Analyzer. The tests were carried out using a membrane prepared with 65 % w/w of PVAc resin annealed at 25 and 40 ^{o}C. The initial composition of the gas was 20,0 % v/v of CO_2. The results are shown in Table 4. From the table it is concluded that the best results are for a pressure of 20 psig and for the membrane annealed at 40 ^{o}C, decreasing the percentage of CO_2 in the exit gas to 6.7 % v/v, which iti is equivalent to 65 % V/V of the total volume. These results agree with that obtained from the experimental characterization of the membranes

Table 4. Percentage of CO_2 in the exit gas stream using the separation device above described.

Annealing Temperature	% CO_2 in the exit gas stream	
	20 psig	30 psig
25 °C	11.3 %	11.5 %
40 °C	6.7 %	7.9 %

Conclusions

Hybrid membranes were prepared for the separation of gases produced in the anaerobius biodigestion process. The membranes were manufactured in a simple way from hybrid suspensions of silica-PVAc prepared by the sol-gel process. It was possible to generate proper porosity for gas separation using both the proper resin composition of the hybrid as well as the proper annealing conditions of the material.

Membranes produced using propanol and butanol were of bad quality, with abundant microcracks generated during the drying time, and for that reason were not tested for the gas separation process.

From the mechanical test results it was concluded that membranes with 65 % w/w of resin and annealed at 40°C present both the best porosity and of course selectivity with regard to H_2 and CH_4

The results were illustrated in a separation of the gases of a mixture of a hypothetical and synthetic gas, showing that it is possible to use these membranes for methane enrichment of a biogas.

Acknoledgments

We thank CONACYT by the economic support (FOMIX QRO-2010-01-146489). To Eng. Ma. Carmen Delgado for her support in TGA and DSC, to M. Sc. Adair Jiménez, to Eng. Francisco Rodríguez to M. T. J. Juan Velez for SEM, Raman and Tension properties of materials respectively.

References

[1] Biogas forum – India (BiGFIN), A Registered Society for Promotion of Biogas. Technology in India, E - Newsletter, Volume III, No. 3. 2012.
[2] Prajapati S. K; Kaushik P; Malik A; Vijay V. K. Phycoremediation and biogas potential of native algal isolates from soil and wastewater. BioresourTechnol 2013:135:232–8.
[3] J. Läntelä, S. Rasi, J. Lehtinen, J. Rintala. Landfill gas upgrading with pilot-scale water scrubber: Performance assessment with absorption water recycling. Applied Energy 92, 2012: 307–314.
[4] EPA Technology Market Summit. Case Study Primer for Participant. Discussion: Biodigesters and Biogas, U. S. Environmental Protection Agency, 2012, p. 30, 5 – 6.
[5] Hans Oonk, Oonkay. Review: Methane from landfills, methods to quantify generation, oxidation and emission. Innovations in Environmental Technology. Netherlands, 2010, p 75, 8 – 11.
[6] Asim Laeeq Khan, et - al. Mixed gas CO_2/CH_4 and CO_2/N_2 separation with sulfonated PEEK membranes. Elsevier B. V. All rights reserved. Journal of Membrane Science, 2011: 372, 87 - 96. www.elsevier.com/locate/memsci.
[7] Fiore Pasquale N., Daniela Cupelli, et – al; Light Responsive Polymer Membranes: A Review, Membranes, 2012: 2, 134 - 197. Doi:10.3390/membranes2010134.
[8] Reza Abedini, Amir Nezhadmoghadam. Application of membrane in gas separation processes: its suitability and mechanisms, Petroleum & Coal. 2010; 52(2), 69 – 80.
[9] Richard W. Baker. Membrane Technology and Applications. 2nd Ed., John Wiley and Sons, Ltd. McGraw-Hill, California, 2004, p 545.
[10] Yuan Zhanga, JakaSunarso, Shaomin Liu, Rong Wang. Current status and development of membranes for CO_2/CH_4 separation: A review. International Journal of Greenhouse Gas Control 12, 2013: 84–107.
[11] Lv YX, Yu XH, Jia JJ, Tu ST, Yan JY, Dahlquist E. Fabrication and characterization of superhydrophobic polypropylene hollow fiber membranes for carbon dioxide absorption. Appl Energy 2012;90:167–74.
[12] YuexiaLv, Xinhai Yu, Shan-Tung Tu, Jinyue Yan, Erik Dahlquist; Experimental studies on simultaneous removal of CO_2 and SO_2 in a polypropylene hollow fiber membrane contactor. Applied Energy. Sci: 97, 2012: 283-288.
[13] David F. Sanders, Zachary P. Smith, Ruilan Guo, Lloyd M. Robeson, James E. McGrath, Donald R. Paul, Benny D. Freeman. Energy-efficient polymeric gas separation membranes for asustainable future: A review, Polymer 54 2013: 4729 – 4761.
[14] P. Bernardo, E. Drioli, G. Golemme. Membrane Gas Separation: A Review/State of the Art. Ind. Eng. Chem. Res. 2009: 48, 4638–4663.
[15] Pei Li, Hang Zheng Chen, Tai-Shung Chung. The effects of substrate characteristics and pre-wetting agents on PAN–PDMS composite hollow fiber membranes for CO_2/N_2 and O_2/N_2 separation.
[16] Xuezhong He, May-Britt Hägg. Membranes for Environmentally Friendly Energy Processes. Membranes 2012: 2, 706-726; doi:10.3390/membranes2040706.
[17] Jamil Ahmad, May-Britt Hägg; Preparation and characterization of polyvinyl acetate/zeolite 4A mixed matrix membrane for gas separation. Journal of Membrane Science. Sci: 427,2013: 73-84.
[18] Ryan T. Adams, Jong Suk Lee, Tae-Hyun Bae, Jason K. Ward, J.R. Johnson, Christopher W. Jones, Sankar Nair, William J. Koros. CO_2–CH_4 permeation in high zeolite 4A loading mixed matrix membranes. Journal of Membrane Science 367, 2011: 197–203.
[19] Nathan W. Ockwig, Tina M. Nenoff. Membranes for Hydrogen Separation. Chem. Rev. 2007: 107, 4078-4110.

[20] José M. Bermúdez, Pablo Haro Dominguez, Ana Arenillas, Jaume Cot, Jens Weber and Rafael Luque. CO_2 Separation and Capture Properties of Porous Carbonaceous Materials from Leather Residues. Materials 2013: 6, 4641-4653; doi: 10.3390/ma6104641.
[21] Dong, G., Li, H., Chen, V. Challenges and opportunities for mixed-matrix membranes for gas separation. J. Mater. Chem. A1, 2013: 4610.
[22] Philipp Burmann, Beatriz Zornoza, Carlos Téllez, Joaquín Coronas. Mixed matrix membranes comprising MOFs and porous silicate fillers prepared via spin coating for gas separation. Chemical Engineering Science Elsevier. Sci. 107, 2014; 66-75.
[23] Harold B. TanhJeazet, Claudia Staudt and Christoph Janiak. Metal–organic frameworks in mixed-matrix membranes for gas separation. Dalton Trans., 2012: 41, 14003. DOI: 10.1039/c2dt31550e.
[24] Kenji Sumida, David L. Rogow, Jarad A. Mason, Thomas M. McDonald, Eric D. Bloch, Zoey R. Herm, Tae-Hyun Bae, and Jeffrey R. Long. Carbon Dioxide Capture in Metal Organic Frameworks. Chemical Reviews. 2012, 112, 724–781. dx.doi.org/10.1021/cr2003272.
[25] SedaKeskin, Timothy M. van Heest, and David S. Sholl. Can Metal–Organic Framework Materials Play a Useful Role in Large-Scale Carbon Dioxide Separations.ChemSusChem 2010, 3, 879 – 891. DOI: 10.1002/cssc.201000114.
[26] Jian - Rong Li; Yuguang Ma; et – al; Carbon dioxide capture - related gas adsorption and separation in metal - organic frameworks Elsevier – Coordination Chemistry Reviews, 2011; 255, 1791 – 1823.
[27] Stuenkel, S; Drescher, A. Wind, J; Brinkmann, T; Repke, J.-U; Wozny, G. Carbon dioxide capture for the oxidative coupling of methane process – A case study in mini-plant scale. Elsevier Chemical Engineering Research and Design 2013. DOI: 10.1016/j.cherd.2011.02.024.
[28] Zhang, Yuan; Wang, Rong. Novel method for incorporating hydrophobic silica nanoparticles on polyetherimide hollow fiber membranes for CO_2 absorption in gas-liquid membrane contactor. (Main article). Elsevier B.V. doi.org/10.1016/j.memsci.2013.10.011.
[29] Asim Mushtaq, Hilmi Bin Mukhtar, Azmi Mohd Shariff, Hafiz Abdul Mannan. A Review: Development of Polymeric Blend Membrane for Removal of CO_2 from Natural Gas. International Journal of Engineering & Technology IJET-IJENS, 2013: Vol:13 No:02. 135902-7272-IJET.
[30] A. Car, C. Stropnik, W. Yave, K. Peinemann, Pebax/polyethylene glycol blend thin film composite membranes for CO_2 separation: performance with mixed gases, Sep. Purif. Technol. 2008; 62, 110–117.
[31] Eric Favre, Roda Bounaceur, Denis Roizard. Biogas, membranes and carbon dioxide capture. Journal of Membrane Science 328. 2009: 11–14.
[32] J. Läntelä, S. Rasi, J. Lehtinen, J. Rintala. Landfill gas upgrading with pilot-scale water scrubber: Performance. assessment with absorption water recycling. Applied Energy 92. 2012: 307–314.
[33] Katharina Hunger, Nadine Schmeling, Harold B. TanhJeazet, ChristophJaniak, Claudia Staudt and Karl Kleinermanns. Investigation of Cross-Linked and Additive Containing Polymer Materials for Membranes with Improved Performance in Pervaporation and Gas Separation. Membranes 2012: 2, 727-763; doi:10.3390/membranes2040727.
[34] V.I. Bondar, B.D. Freeman, I. Pinnau, Gas sorption and characterization of poly(ether-b-amide) segmented block copolymers, J. Polym. Sci. Part B: Polym. Phys. 1999; 37, 2463–2475.
[35] V.I. Bondar, B.D. Freeman, I. Pinnau, Gas transport properties of poly(etherb-amide) segmented block copolymers, J. Polym. Sci. Part B: Polym. Phys. 2000; 38, 2051–2062.
[36] Colin A.Scholes, Kathryn H. Smith, Sandra E. Kentish, Geoff W. Stevens. CO2 capture from pre-combustion processes—Strategies formembrane gas separation. International Journal of Greenhouse Gas Control 4, 2010: 739–755.
[37] Zhao G Y, Aziz B, Hedin N. Carbon dioxide adsorption on mesoporous silicasurfaces containing amine-like motifs. Appl Energy 2010;87:2907–13.
[38] Bingbing Jiang, Xianfeng Wang, Mc Mahan L. Gray, YuhuaDuan, David Luebke, Bingyun Li; Development of amino acid and amino acid-complex based solid sorbents for CO_2 capture. Applied Energy; 109, 2013: 112–118.
[39] Asim Mushtaq, Hilmi Bin Mukhtar, AzmiMohdShariff, Hafiz Abdul Mannan. A Review: Fabrication of Enhanced Polymeric Blend Membrane with Amines for Removal of CO_2 from Natural Gas. ISSN 2250-2459, ISO 9001:2008 Certified Journal, Volume 3, Issue 6, 2013.
[40] Bingbing Jiang, Xianfeng Wang, McMahan L. Gray, YuhuaDuan, David Luebke, Bingyun Li. Development of amino acid and amino acid-complex based solid sorbents for CO_2 capture. Applied Energy 109, 2013: 112–118.
[41] Sanjeev Kumar Prajapati, PrachiKaushik, Anushree Malik, Virendra Kumar Vijay., Phycoremediation coupled production of algal biomass, harvesting and anaerobic digestion: Possibilities and challenges. Biotechnology Advances. ELSEVIER. Sci: 31. 2013; 1408 – 1425.
[42] Prajapati SK, Kaushik P, Malik A, Vijay VK. Phycoremediation and biogas potential ofnative algal isolates from soil and wastewater. BioresourTechnol 2013;135:232–8.

[43] S. Basu, A.L. Khan, A. Cano-Odena, C. Liu, I.F.J. Vankelecom, Chem. Soc. Rev. 2010; 39, 750–768.
[44] S. A. Stern, Polymers for gas separation: the next decade, J. Membr. Sci. 1994; 94, 1–65.
[45] Du N, Park HB, Dal-Cin MM, Guiver MD. Energy & Environmental Science 2012;5:7306e22.
[46] L. M. Robeson, Polymer membranes for gas separation, Curr. Opin. Solid State Mater. Sci. 1999; 4, 549–552.
[47] Graham T. Journal of Membrane Science 1995;100:27e3.
[48] Du N, Park HB, Dal-Cin MM, Guiver MD. Energy & Environmental Science 2012;5:7306e22.
[49] Dolish F.R., Fateley W.G., Bentley F.F., Characteristic Raman Frecuencies of Organic Compounds, Wiley; New York, 1974, pp 105.
[50] NMX-E-082-SCFI-2002. Resistencia a la tensión de materiales plásticos. Industria del plástico - Tubos y conexiones.
[51] Wijmans J. G, Baker R. W. Journal of Membrane Science 1995;107(1e2):1e21.
[52] Chung, T. S.; Jiang, L. Y.; Li, Y.; Kulprathipanja, S., "Mixed matrix membranes (MMMs) comprising organic polymers with dispersed inorganic fillers for gas separation" Prog. Polym. Sci. 2007; 32, 483-507.
[53] Mitterdorfer C., Bernard J., Klauser F., Winkel K., Kohl I., Liedl K.R., Grothe H., Mayer E., and Loerting T., Local Structural Order in carbonic Polymorphs: Raman and FT-IR Spectroscopy. Journal of Raman Spectroscopy, 2012, 43, 10 -115.
[54] Frank Rindfleisch, Todd P. DiNoia, and Mark A. McHugh; Solubility of Polymers and Copolymers in Supercritical CO_2. J. Phys. Chem. 1996, 100, 15581-15587.
[55] Kazarian, S. G.; Vincent, M. F.; Bright, F. V.; Liotta, C. L.; Eckert, C. A. J. Am. Chem. Soc. 1996, 118, 1729.
[56] YuexiaLv, Xinhai Yu, Shan-Tung Tu, Jinyue Yan, Erik Dahlquist; Experimental studies on simultaneous removal of CO_2 and SO_2 in a polypropylene hollow fiber membrane contactor. Applied Energy. Sci: 97, 2012: 283-288.
[57] C. J. Brinker y G. W. Scherer. Sol - gel Science, Academic Press Inc. 1990.
[58] Zornoza, B., Tellez, C., Coronas, J. Mixed matrix membranes comprising glassy polymers and dispersed mesoporous silica spheres for gas separation. J. Membr. Sci. 2011a; 368,100.
[59] Jeazet, H. B. T., Staudt, C., Janiak, C. A method for increasing permeability in O_2/N_2 separation with mixed matrix membranes made of water stable MIL-101 and polysulfone. Chem. Commun. 2012; 48, 2140.
[60] Robeson, L. M., "The upper bound revisited" J. Membr. Sci. 2008; 320, 390 – 400.
[61] Bertelle S, Gupta T, Roizard D, Vallières C, Favre E. Study of polymer-carbon mixed matrix membranes for CO2 separation from flue gas. Laboratories des Sciences du GénieChimique, France, 2006, 401-402.
[62] Jansen J, M Acchione M, Raharjo R, Freeman B, Drioli E. "Pure and mixed gas transport properties of novel asymmetric poly(ether ether ketone) membranes with diferents morphologies", Research Institute on Membrane Technology, Italy, 2006; 462-463.
[63] Matteucci ST, Yampolskii YP, Freeman BD, Pinnau I. Transport of gases and vapors in glassy and rubbery polymers. In: Yampolskii Y, Pinnau I, Freeman BD, editors. Materials science of membranes for gas and vaporseparation. Chichester: John Wiley & Sons; 2006. p. 1e47.
[64] Md. Nurul Islam, Weilang Zhou Honda, Kazuhiro Tanaka, Hidetoshi Kita, Ken-ichi Okamoto. "Preparation and gas separation performance of flexible pyrolytic membrane by low-temperature pyrolysis of sulfonated polyimides", Yamaguchi University, Japón. 2005; 18-25.
[65] Sen, D.; Kalipcilar, H.; Yilmaz, L., "Development of polycarbonate based zeolite 4A filled mixed matrix gas separation membranes" J.Membr. Sci. 2007; 303, 194-203.
[66] Vu, D. Q.; Koros, W. J.; Miller, S. J., "Mixed matrix membranes using carbon molecular sieves - II. Modeling permeation behavior", J.Membr. Sci. 2003; 211, 335-348.
[67] Jian - Rong Li; Yuguang Ma; et – al; Carbon dioxide capture - related gas adsorption and separation in metal - organic frameworks" Elsevier – Coordination Chemistry Reviews, 2011; 255, 1791 – 1823.
[68] Zhanat Umarova, Sharipzhan Eskendirov "Mathematical and Technical Model Biogas Plant with a Membrane Separator". International Conference on System Engineering and Modeling (ICSEM 2012). IPCSIT vol. 34, IACSIT Press, Singapore. 2012.
[69] Faiz R, Al-Marzouqi M. Insights on natural gas purification: simultaneous absorption of CO_2 and H2S using membrane contactors. Sep Purif Technol 2011; 76:351–61.
[70] C. K. Yeom, S. H. Lee, J. M. Lee, Study of transport of pure and mixed CO2/N2 gases through polymeric membranes, J. Appl. Polym. Sci.78, 2000: 179–189.

High H_2 Production From The Reforming of CH_4 by Hydrogen Sulphide Using Mo-Cr Supported on Heterogeneous Catalysts

A. L. Martínez-Salazar[1,*], J. A. Melo-Banda[1], J. M. Domínguez- Esquivel[2], V. H. Martínez-Sifuentes[1], Y. Salazar-Cerda[1], M. A. Coronel-García[1], A. I. Reyes de la Torre[1]

[1]Instituto Tecnológico de Ciudad Madero, 1° de mayo s/n col. Los Mangos, Cd. Madero, Tamaulipas, México, 89440.
[2]Instituto Mexicano del Petróleo, Eje Central Lázaro Cárdenas 152, San Bartolo Atepehuacan, Gustavo A. Madero, Ciudad de México, Distrito Federal, México, 07730.

[*]Tel: +528332111039; e-mail: analidiams@gmail.com

ABSTRACT

Catalytic steam reforming has been for a long time the principal method for the production of hydrogen. According to this method, hydrogen is generated by the reaction of steam with methane (CH_4) at quite high temperatures from 923 to 1223 K requiring the removal of hydrogen sulphide (H_2S) present in natural gas streams or light hydrocarbons.

Alternative processes for hydrogen production have been studied. A proposed method is the reforming of CH_4 by H_2S. With this process, the removal of H_2S in natural gas streams is no longer necessary and sulfur, usually considered as a strong pollutant on liquid fuels in refineries, is used as a reagent in H_2S form of hydrodesulphurization processes.

This research involved the synthesis of modified SBA-15 support with zirconia dioxide; achieving the mechanical resistance, chemical stability and redox properties of zirconia improving the textural characteristics. Furthermore, lanthanum oxide incorporation in zirconia was carried out allowing increase of its surface area with enhanced thermal stability. The supports were impregnated with molybdenum as active phase and chromium as promoter.

The materials were evaluated in a quartz reactor at range temperatures of 873 – 1123 K, feed molar ratio CH_4:H_2S of 1:12. Synthesized materials were characterized before and after reaction by X-Ray diffraction, nitrogen physisorption, thermogravimetry techniques and Diffuse Reflectance Infrared Fourier Transform Spectroscopy (DRIFTS). All techniques confirm the mechanical and thermal stability of the supports and their textural properties.

Molybdenum supported on zirconia-lanthanum catalyst showed better catalytic performance, achieving high selectivity to hydrogen (64%).

Keywords: reforming, hydrogen, modified supports

1. Introduction

Currently, 80-85% of the hydrogen produced in the world is obtained from the reforming of methane with steam (SMR) of natural gas streams [1]:

$$CH_4 + H_2O \longrightarrow CO + 3H_2 \quad (1)$$

Hydrogen production by this route requires great energy consumption. It also requires the removal of sulfur compounds present in natural gas streams. This extra cleaning step in the process, with its additional cost is necessary because the catalysts are quickly poisoned by sulfur compounds. In the petrochemical and refining industry, the removal of hydrogen sulfide from natural gas and refinery gas streams has increased its importance due to the environmental and economic damage caused by the processes used today impact. The gas sweetening process is to remove contaminants, H_2S and carbon dioxide (CO_2), received the sour wet gas producing wells. This process involves the selective absorption of contaminants, using an aqueous, a base formulation amine solution which circulates in a closed circuit where it is regenerated for continued use. The acid gas ($H_2S + CO_2$), from sweetening process goes through a thermal reactor (combustor), and then passes two catalytic reactors , where finally the conversion of H_2S to elemental sulfur (S) is achieved, this process known as Claus [2] :

$$H_2S + 3/2\ O_2 \longrightarrow SO_2 + H_2O \quad (2)$$
$$2\ H_2S + SO_2 \longrightarrow 3/x\ Sx + 2H_2O \quad (3)$$

Sulfur is recovered at the end of the processes in liquid phase and is to be sent "hot" boat market, thus the sum of costs associated with the extraction, transport heating operation and risks make unprofitable marketing especially with prices ranging around $ 40 per ton [3]. In México, National Industry of Petroleum announced that the daily production of sulfur subsidiary in Gas and Basic Petrochemicals and Refining amounts to about three thousand 500 ton/day, which makes this element becomes a problem logistics due to its high production , low capacity of some gainful sale and export , because sulfur should be kept in liquid phase at a temperature of 403 K in special pools and if it takes the sale, then the process train is saturated, so you would have to reduce or stop the production of gas and fuel.

Additionally, a thermodynamic study by Sitja and Bravo in relation to the conditions of non-stoichiometric operation of a sulfur recovery plant, it is concluded that it cannot comply with the provisions of the EPA (Environmental Protection Agency), as it have atmospheric emissions of 440 and 705 lbs of sulfur dioxide (SO_2) / ton of sulfur produced as the Claus process does not allow full exploitation of the hydrogen sulfide to convert sulfur and hydrogen [4]. This problem requires solving by developing new processes that remove sulfur from gas streams, avoiding the Claus process. He has been investigating the reaction of hydrogen sulfide content in the acid gas with methane for direct hydrogen production (considered as the fuel of the future) [5] and carbon disulfide, which has a market price four times higher the sulfur. Methane and hydrogen sulfide react in a temperature range of 743-960 K at atmospheric pressure, to produce hydrogen and carbon disulfide, according to the following reaction [6].

$$CH_4 + 2H_2S \longleftrightarrow 4H_2 + CS_2 \quad (4)$$

Catalytic reforming of CH_4 and H_2S to produce H_2 and CS_2 is proven by experimental evidence scant research done over the years. However, these investigations are based on tests with extreme operating conditions (high temperature and vacuum pressure), which generate extra economic cost, to achieve good conversions. Moderate operating conditions (optimum reaction system) have achieved only low conversions of the desired products; it is believed that this deficiency is due to the use of bulk catalysts or simple supports that, given their catalytic properties do not meet the needs of activation, selectivity and / or stability required for this reaction [7]. Therefore, it is a

priority need to extend the search for catalysts that possess characteristics that generate high conversion potential at moderate operating conditions.

In this work, the mesoporous support SBA-15 was synthesized by modifying its micellar dioxide zirconia (ZrO_2) structure, this combination can seize the mechanical strength, chemical stability and redox properties posé zirconia increasing their low surface area and porosity [8]. Further, the zirconia is synthesized changing its micelle structure with lanthanum oxide (La_2O_3) with this increasing their surface area and forming a mesoporous solid with enhanced thermal stability [9]. The supports were impregnated with molybdenum (Mo) as the active phase and chromium (Cr) as promoter [11, 10, 6, 4, 3, 7].

2. Experimental

2.1 Synthesis of materials

The synthesis of mesoporous material SBA-15 was carried out in acidic medium from clear solutions (TEOS/H_2O) and Pluronic-123 ($[OE]_{20}$ - $[OP]_{70}$ - $[OE]_{20}$ PM 5838 g/gmol, where EO: ethylene oxide PO: polyethylene oxide). In a typical synthesis 4 g of Pluronic P123 was weighed and dissolved in 140 ml of water (H_2O). Subsequently 7.5 ml of hydrochloric acid (HCl) is added. The solution is transferred into a cell at 318 K and stirred for 2 to 3 h. 9.6 ml of TEOS was added dropwise with constant stirring is added and let stand with stirring for a period of 24 hours. It is placed in the oven at 363 K for 24 hours. Following this, the solid formed is filtered and washed, placed in the oven to complete drying for 12 hr. Subsequently, calcined at 393 K for 1 hr and then at 823 K for 6 h in air flow. The modification of the support SBA-15 was made via metallic chemical grafting, as the source of zirconium is zirconium propoxide used IV, Zr (Npro) 4, 70% in 1-propanol.

The composite oxide, ZrO_2 - La_2O_3 was prepared by co- precipitation of a solution of zirconium oxychloride ($ZrOCl_2$) and lanthanum nitrate hexa- hydrate ($La(NO_3)$ $3.6H_2O$), with ammonia solution. The pH during the precipitation was controlled. The precipitate was collected by filtration and washed with deionized water until no Cl - detecting anions. The gel was dried at 378 K for 24 hours and then calcined in flowing air for three hours at 823K [9].

Impregnation of active stages and the synthesized media promoters was conducted by the incipient wetness method. The substrate is heated to dry the pores and then soak it in enough solution of ammonium molybdate ((NH_4) $6Mo_7O_{24}$) [12] and nano hydrated chromium nitrate ($Cr(NO_3)$ $3.9H_2O$), to fill the pores with the desired amount of active component , stirring for one hour at 343 K. The pores are filled with the correct amount of salt solution. The solvent is removed by evaporation and the resulting samples are dried for 23 hours at 393 K. Catalytic materials are calcined in air flow at 673 K for 2 hours.

Mesoporous supports were modified under a 1:1 ratio, while the load of Mo and Cr was 15% and 5% by weight respectively.

2.2. Physicochemical Characterization

The textural properties of the catalyst were characterized by a surface area analyzer ASAP-2405, Micromeritics brand, with a liquid nitrogen temperature of 77K, and a degassing temperature of 573 K. Measuring patterns XRD for phase identification was performed using a Siemens D-500 diffractometer, Cu wavelength Kα1, 2 = 1518 Angstroms.

2.3. Catalytic tests

The catalytic evaluation of materials was carried out in a micro plant where they were subjected to the conversion reactions of CH_4 and H_2S to H_2. The system is mainly constituted by three sections, 1st feed section consists of a gas supply control, H_2S, CH_4.

The second section reaction system, consisting of a vertical reactor, equipped with an oven termolyne 11000 with internal temperature controller. 3rd Section of identifying reaction products, has a gas chromatograph Varian Star 3400 equipped with a capillary column Pora-Q bond with a length of 25.0m, 0.32mm, 5µm, #CP7361.

Catalyst at 393 K were dried for 2 hours under nitrogen (N_2) using a flow of 6,838 L/h. Continuing with the same gas flow N_2-H_2S gas (5.95 L/h) was added raising the temperature to 723 K at a rate of 353 K/h keeping it under these conditions for 4 hours in order to ensure the formation of the sulfur materials molybdenum disulfide (MoS_2) and chromium sulphide III (Cr_3S_2). Then, the flow of N_2 gas was changed through the gas flow helium (He) at a rate of 6.84 L/h starting increased from 723 to 873 K at a rate of 353 K/h.

With the ratio CH_4:H_2S 1:12 proceeded to change the flow of He gas and CH_4 gas was fed from the top side of setting a flow 0.189 L/h, and the H_2S gas from the top of a flow 2.47 L/h. The temperature reaction began to 873 K and it was increased at 973, 1073 and 1123 K each 2 h, maintaining the reaction state work for 2h, 3h and 5h respectively assaying gas chromatograph the product at time zero and every 0.5 h. Before releasing the product gases into the atmosphere, the gases are sent through a scrubber 2 liter containing a solution of sodium hydroxide (NaOH, 6M) and hydrogen peroxide (H_2O_2), that to remove them, effectively, the H_2S and other sulfur gases.

3. Results and discussion

3.1 Structural properties

Figure 1 was obtained on diffraction angle in order to provide evidence of the presence of the SBA-15 in Mo/ZrO_2-SBA15 and CrMo/ZrO_2-SBA15 phases. The SBA-15 is characterized by three main peaks corresponding to the planes (100, 110, 200). The materials studied showed the characteristic intense reflection in the plane (100) of the hexagonal mesoporous structures of high symmetry. The absence of the plane (110), indicative of the order of 2-D pores, and the level (200), which shows the regularity of pore arrangement, is due to the addition of ZrO_2 in its structure micelles.

Figure 2 evidence the characteristic peaks of the elements comprising the materials Mo/ZrO_2-SBA15 and CrMo/ZrO_2-SBA15 respectively to high angle and calcinations temperatures in the range of 873 to 1073 K. The results confirm the assumption of the impregnation of molybdenum oxide species and chromium oxides were appropriate. Thus, the diffraction peaks corresponding to the reflection of the ortho- rhombic Mo_4O_{11} phase, being the characteristic peaks of monoclinic phase $Cr_2(MoO_4)_3$ in the diffractogram of the catalyst CrMo/ZrO_2-SBA15. Zirconia (ZrO_2) pure cubic phase transforms tetragonal is stable up to ~1240 °C, and finally, at lower temperatures, down to room temperature, the monoclinic phase is stable [13]. It is known to stabilize the stable tetragonal ZrO_2 phase within a glassy matrix containing silicon oxide IV (SiO_2). In this composite, the presence of SiO_2 in the matrix has a double effect: first inhibits the formation of cubic phase in favor of the tetragonal phase and moreover inhibits transformation tetragonal ZrO_2 to monoclinic ZrO_2. The diffractograms show the stabilization of the tetragonal ZrO_2 to calcination temperatures of 823 K as a result of the addition of SBA-15 by modifying its micelle structure giving higher thermal stability and mechanical. As temperature increases, the characteristic peaks of SBA-15 at low angles disappear and SiO_2 structure changes to monoclinic zirconium silicate ($ZrSiO_4$). Upon reaching the temperature of 1073 K peak intensity and appear $ZrSiO_4$ near it monoclinic phases of ZrO_2, breaking the stability achieved. Similarly, Figure 3, shows the peaks characteristic of the elements CrMo/La_2O_3-ZrO_2 and the Mo/La_2O_3-ZrO_2 materials. Unlike ZrO_2-SBA15 mesoporous support, it is seen in that even under the presence of monoclinic ZrO_2, no phase changes occur that modify the structure of the support by increasing the temperature, showing no formation of

new elements and/or collapsing structures. This confirms that the addition of La_2O_3 support provides the constant thermal and mechanical stability to temperature deltas [13].

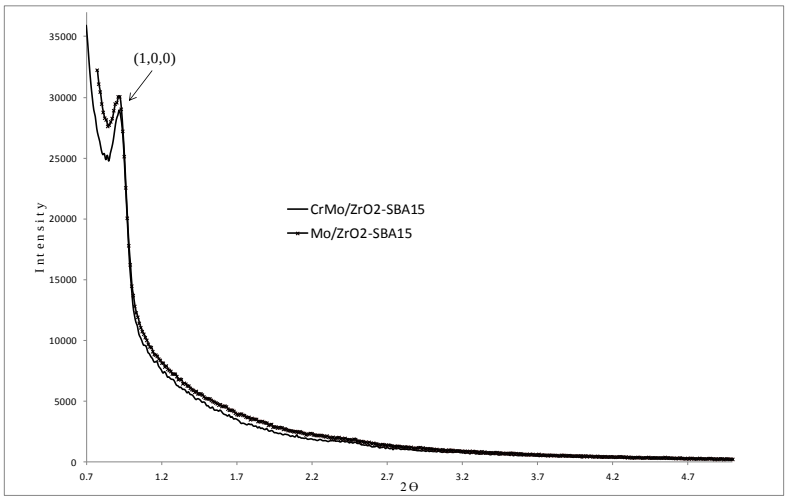

Figure 1. X-Ray Diffraction patterns (small angle) of $CrMo/ZrO_2$-SBA15 and Mo/ZrO_2-SBA15 catalysts.

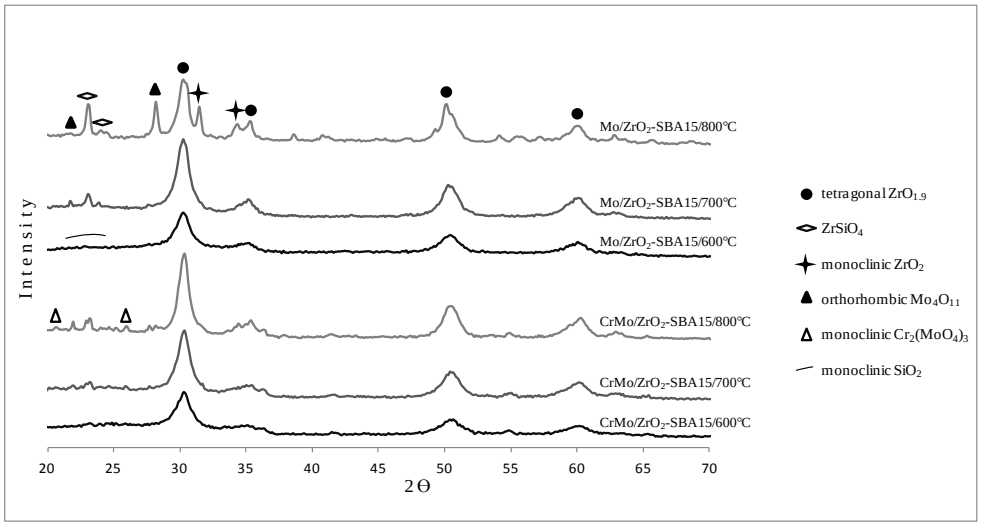

Figure 2. X-Ray Diffraction patterns (wide angle) of $CrMo/ZrO_2$-SBA15 and Mo/ZrO_2-SBA15 catalysts.

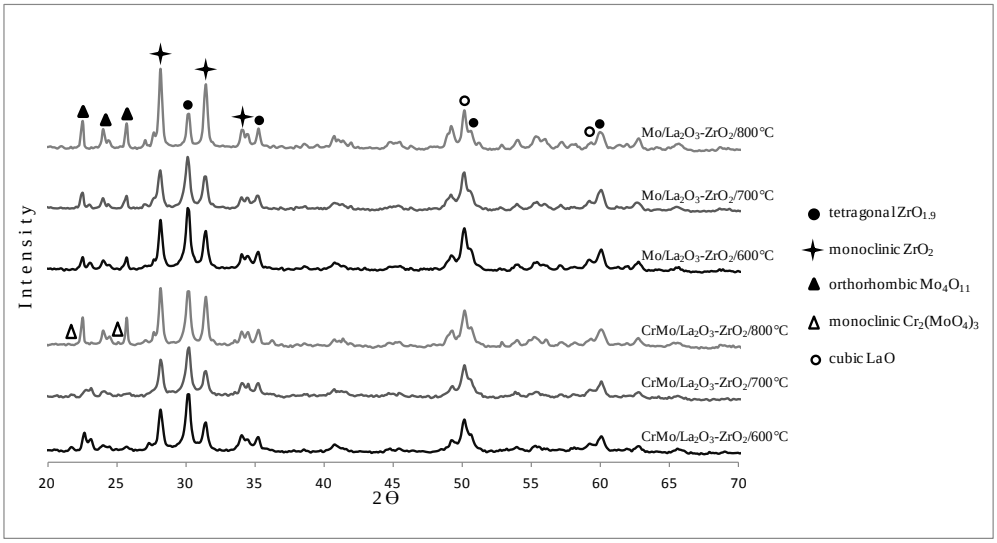

Figure 3. X-Ray Diffraction patterns of Mo/La_2O_3-ZrO_2 y $CrMo/La_2O_3$-ZrO_2 catalysts at different temperatures of synthesis.

3.2 Textural properties

The analysis by nitrogen physisorption generated the results shown in Table 1 on the textural properties of the sintered materials, they are classified as mesoporous at the discretion of the IUPAC because the pore diameters are in the range of 20-500 Å calculated according to the method Barrett- Joyner- Halenda of (BJH) [14]. Surface areas obtained for Mo/La_2O_3-ZrO_2 and $CrMo/La_2O_3$-ZrO_2 are characteristic of these types of catalysts. Won Kim et al. mentioned that the incorporation of transition metals, particularly noble metals, it provides the ZrO_2 increased catalyst activity and stability, further confirmed by experimental results that the impregnation of the second metal in the ZrO_2 support encourages sintering considerably modified to low temperature [9-15]. The remaining catalysts make structural advantage provided by the natural properties of SBA -15 in the modification of ZrO_2 support, thus increasing its low surface area.

Table 1. Textural properties of source catalysts.

Materials	Surface area (m^2/g)	Pore volume (cc/g)	Pore diameter (Å)
$CrMo/La_2O_3$-ZrO_2	13,68	0,042	122,87
$CrMo/ZrO_2$-SBA15	197,78	0,263	53,22
Mo/La_2O_3-ZrO_2	9,67	0,032	133,49
Mo/ZrO_2-SBA15	239,61	0,297	49,53

The adsorption isotherms Mo/La_2O_3-ZrO_2 and $CrMo/La_2O_3$-ZrO_2 (Fig. 4a), are type II according to the IUPAC classification, feature a macro porous solid type H3 hysteresis behavior that is related to solid aggregates particle with recesses in which no pores of uniform size and shape, as is verified in the pore diameter (Fig. 4b).

Furthermore, the adsorption isotherm Mo/ZrO_2-SBA15 and CrMo/ZrO_2-SBA15 catalysts (Fig. 5a) are type IV according to the classification of the IUPAC, typical of mesoporous solids with a hysteresis type behavior H1 that is related to the presence of pores of uniform size and shape to form cylindrical channels open, as corroborated by the graphs of the pore diameter (Fig. 5b), which show a narrow distribution of pores with a character and a behavior monomodal uniform. Importantly, the trend of behavior obtained is attributed to the textural properties provided by the SBA-15 present in the materials.

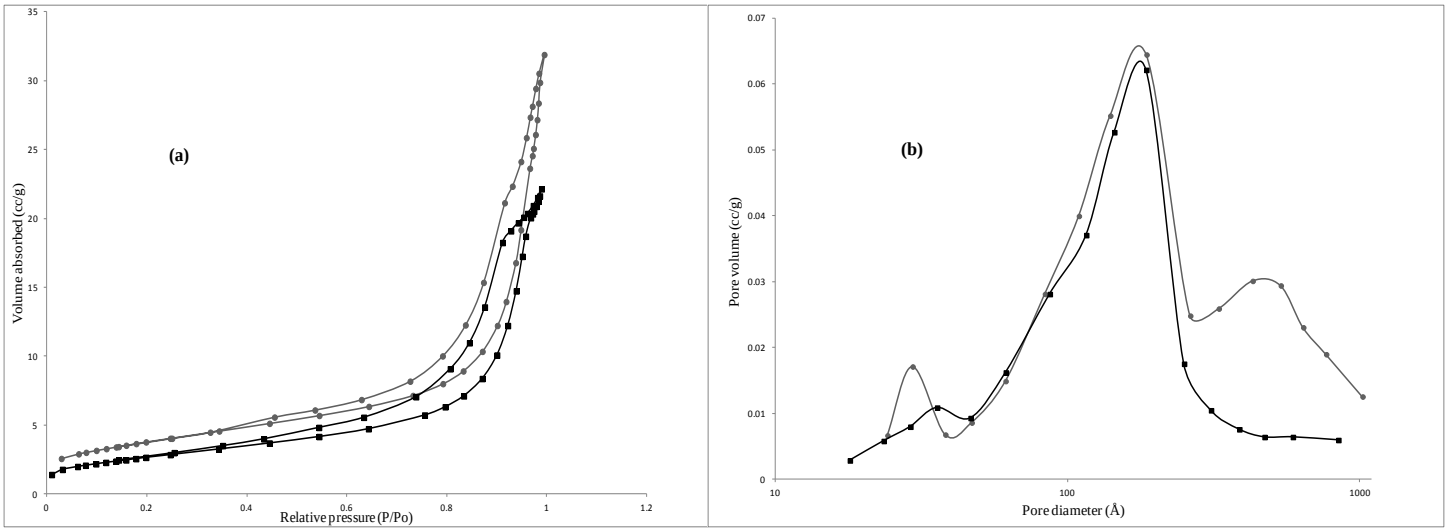

Figure 4. Adsorption-desorption isotherm of N_2 (a) and Pore size distribution of (b) Mo/La_2O_3-ZrO_2 ■ and CrMo/La_2O_3-ZrO_2 ●

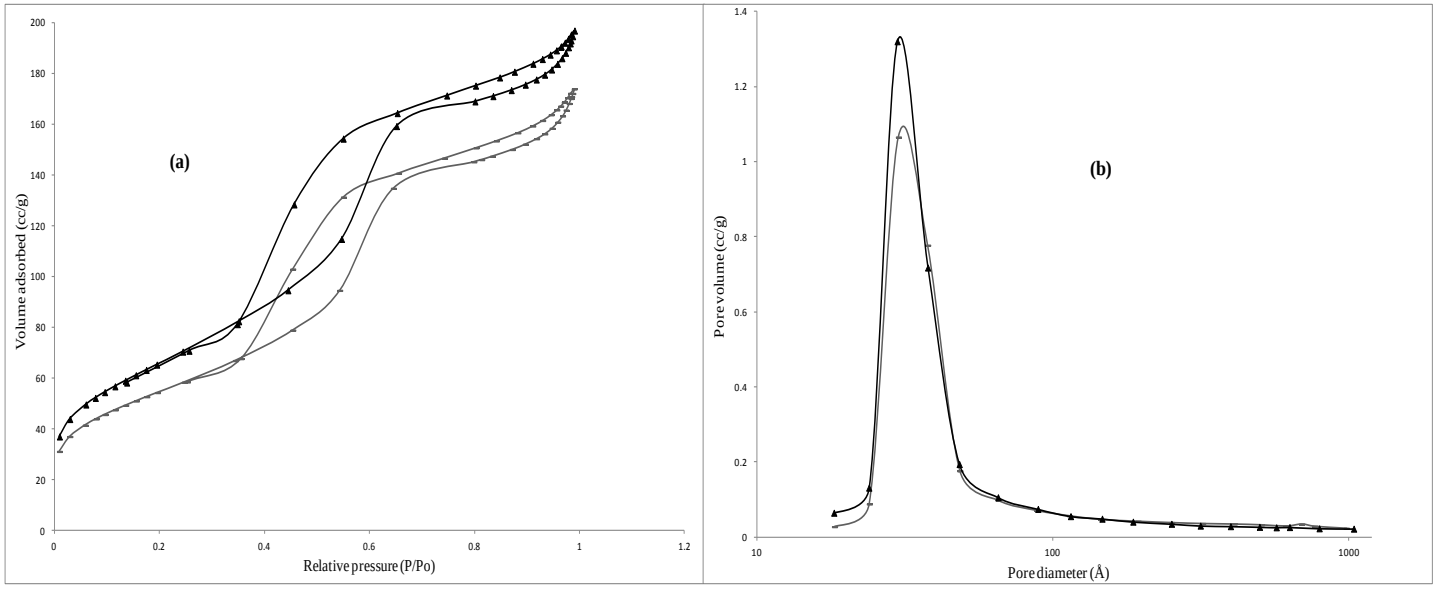

Figure 5. (a) Adsorption-desorption isotherm and (b) Pore size distribution of Mo/ZrO_2-SBA15 ▲ and CrMo/ZrO_2-SBA15 +

3.3 Catalytic Activity

The reforming of methane with hydrogen sulfide (R1) proceeds via H_2S thermal decomposition of H_2S (R2) and methane pyrolysis (R3):

$$CH_4 + 2H_2S \longleftrightarrow 4H_2 + CS_2 \quad (R1)$$
$$2H_2S \longleftrightarrow S_2 + 2H_2 \quad (R2)$$
$$CH_4 \longleftrightarrow C + 2H_2 \quad (R3)$$

The results of evaluating the catalysts in the reforming process of methane with hydrogen sulfide in the pilot plant shown in Figure 6 to Figure 9.

The synthesized catalysts are classified as bifunctional both, the support and the supported phase activate different elementary steps of the chemical reaction, following different catalytic schemes.

In the case of the supported metals, the reaction takes place initially in the metal, resulting in an intermediate which is subsequently converted by the action of the support. Molybdenum disulfide (MoS_2), obtained from the sulfurization step in the tubular reactor before the reaction stage, has proven to be a highly effective catalyst for the decomposition of hydrogen sulfide reaching conversions higher than 95% at temperatures above 600 °C [10].

High conversion (92 to 99%) of H_2S in R2 is observed in Figure 7, the lower magnitude correspond to the materials $CrMo/La_2O_3$-ZrO_2 and $CrMo/ZrO_2$-SBA15 as a consequence that the Cr_2S_3 is only effective for the catalytic decomposition of hydrogen sulfide at temperatures below 600°C. The performance of these metal salts is based on the presence of incompletely coordinated atoms containing *d* orbitals available.

The ZrO_2-SBA15 and La_2O_3-ZrO_2 support, lacking of free electrons, produce an ionic intermediary during the catalytic process (carbonium ion type), necessary for carry out the disintegration of hydrocarbons.

The mesoporous silicates are inert materials. They do not possess acid-base or redox properties. Figures 6 and 7 confirm this fact by obtaining lower average CH_4 conversions in R1 and R3 and of H_2S in R1 at 600°C for $CrMo/ZrO_2$-SBA15 and Mo/ZrO_2-SBA15 materials. It is necessary to note that as temperature increases reflected a significant increase in conversions R1 and R3 for those materials, the cause relates to the disappearance of the characteristic peaks of SBA-15 and the consequent transformation of SiO_2 monoclinic structure on zirconium silicate thereby increasing the acidity of the supports.

On average, maximum conversions are achieved at short reaction times (~ 10h), in general, the stability is reached at 800°C. Maximum conversions in reaction R3 (in the order of 95-100%) are achieved at reaction time upper than 15h and a temperature of 850°C, under these operating conditions the selectivity to carbon (C) decreases significantly (Figure 9), therefore, a higher amount of H_2 is produced. Thermodynamic calculations have shown that with a greater amount of H_2S than stoichiometric at temperatures of 950-1000°C, carbon formation is avoided.

The material efficiency distinction confirms the characteristic of La_2O_3, which, it being a transition metal provides a higher activity and stability to ZrO_2.

In Figure 8, the percentage of selectivity to CS_2 (16%) and the hydrogen production (64%) are detected, these values increase as the reaction time and temperatures enhance. Molybdenum supported on zirconia-lanthanum catalyst showed better catalytic performance, achieving high selectivity to hydrogen, corresponding to the effectiveness of MoS_2 in the decomposition of hydrogen sulfide. Furthermore, Mo/ZrO_2-SBA15 reached maximum selectivities to CS_2 at lower reaction time and temperature.

As shown in Figure 9, high selectivity to carbon occurs in the first hours of reaction at a temperature of 600°C, conditions in which the pyrolysis of methane is taking place without the reforming reaction; as the reaction time and temperature are increased selectivity to C decreases significantly to 82% as the lower limit. High selectivity of H_2S to S_2 is achieved, an intermediary to the reforming process of methane with hydrogen sulfide.

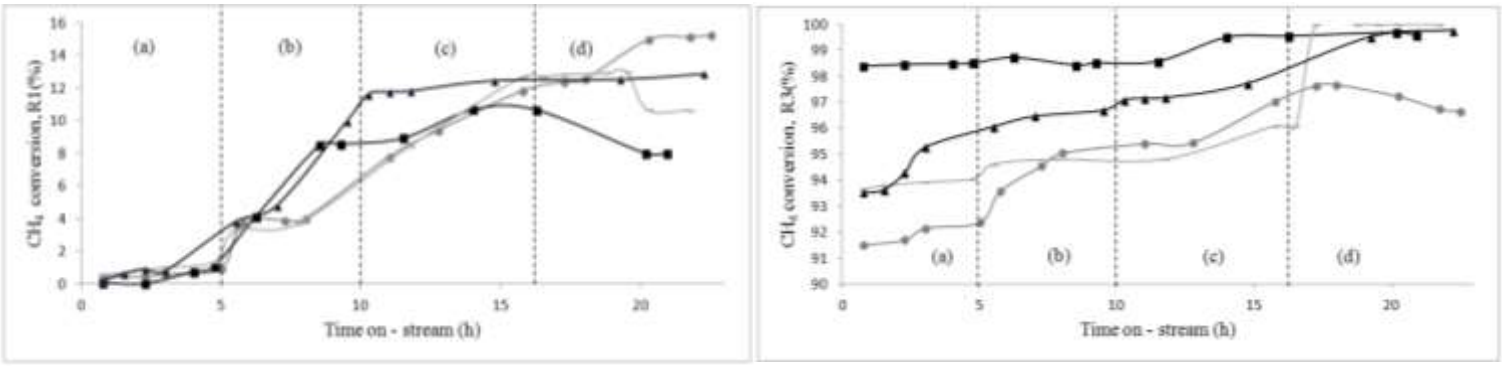

Figure 6. Conversion of CH_4 in R1 and R3 at (a) 873 K, (b) 973 K, (c) 1073 K and (d) 1123K using the catalysts: Mo/La_2O_3-ZrO_2, $CrMo/La_2O_3$-ZrO_2, Mo/ZrO_2-SBA15 and $CrMo/ZrO_2$-SBA15.

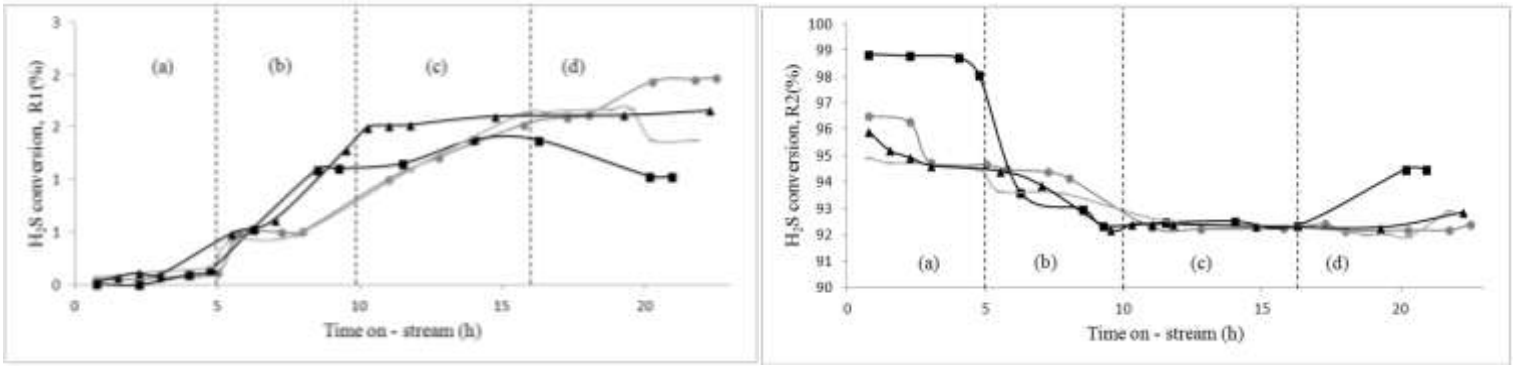

Figure 7. Conversion of H_2S in R1 and R2 at (a) 873 K, (b) 973 K, (c) 1073 K and (d) 1123K using the catalysts: Mo/La_2O_3-ZrO_2, $CrMo/La_2O_3$-ZrO_2, Mo/ZrO_2-SBA15 and $CrMo/ZrO_2$-SBA15

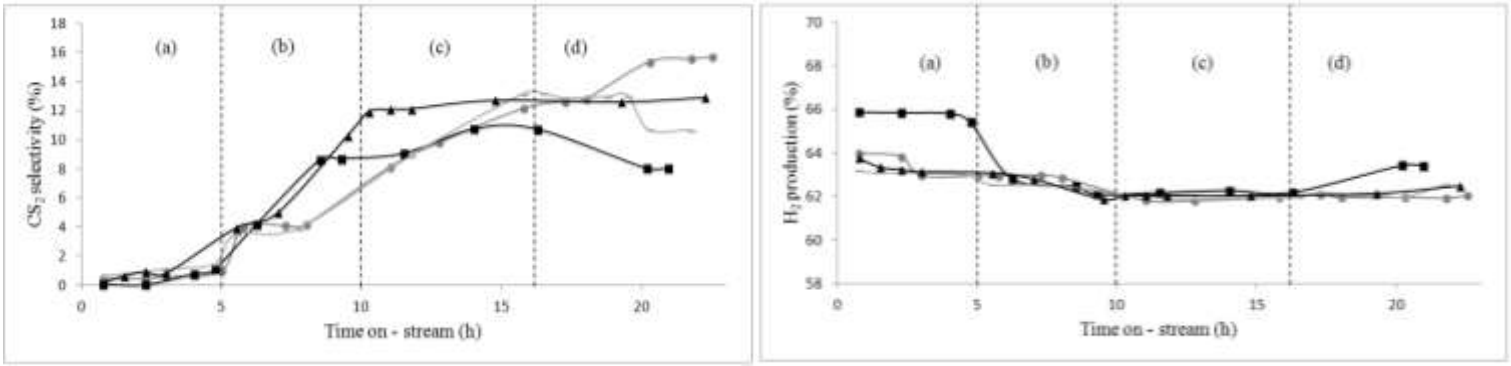

Figure 8. Selectivity of CS_2 and production of H_2 at (a)873K, (b) 973K, (c) 1073K and (d) 1123K using the catalysts: Mo/La_2O_3-ZrO_2, $CrMo/La_2O_3$-ZrO_2, Mo/ZrO_2-SBA15 and $CrMo/ZrO_2$-SBA15

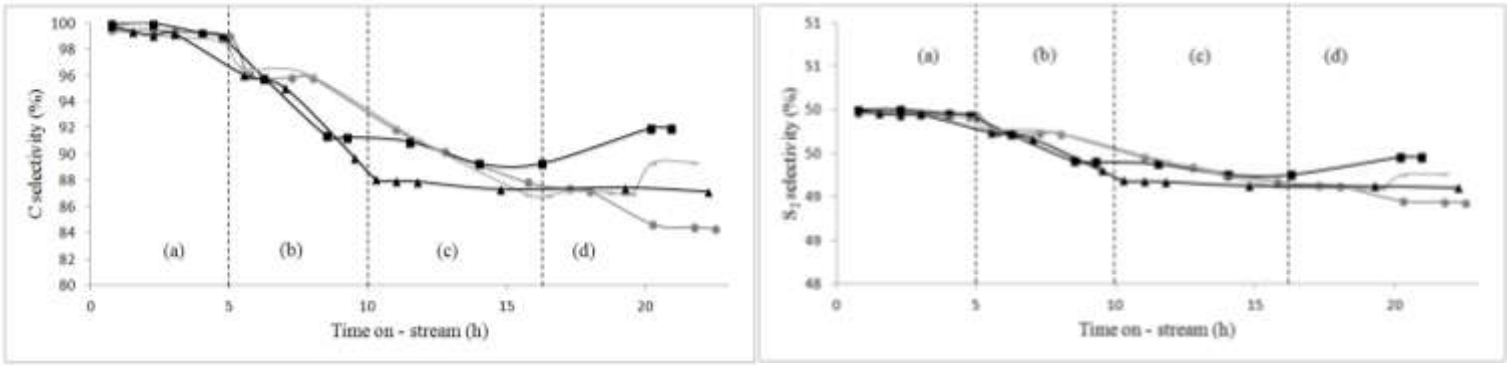

Figure 9. Selectivity of C and S_2 at (a)873K, (b) 973K, (c) 1073K and (d) 1123K using the catalysts: ■ Mo/La_2O_3-ZrO_2, ● $CrMo/La_2O_3$-ZrO_2, ▲ Mo/ZrO_2-SBA15 and + $CrMo/ZrO_2$-SBA15

Fig 10 show the comparison of diffractograms obtained before reaction (BR) and after reaction (AR) of $CrMo/ZrO_2$-SBA15 and $CrMo/La_2O_3$-ZrO_2 materials. The appearance of new elements is observed due to the thermal decomposition of H_2S and the methane conversion on transition metal sulfides and carbides generated respectively. Some characteristic peaks of ZrO_2 remained present after reaction with a visible decrease in intensity. In Section 3.1 of this document, it was mentioned that the impregnation of a second metal on the support of ZrO_2 modified greatly encouraged to low sintering temperature [9, 15], providing strength and resistance to catalyst. This is explained by the observed peaks with increased intensity and frequency in the diffraction patterns after reaction of those catalysts impregnated with chromium, however the greater the presence of carbides thus decreasing the catalytic activity, but the presence of coal was found.

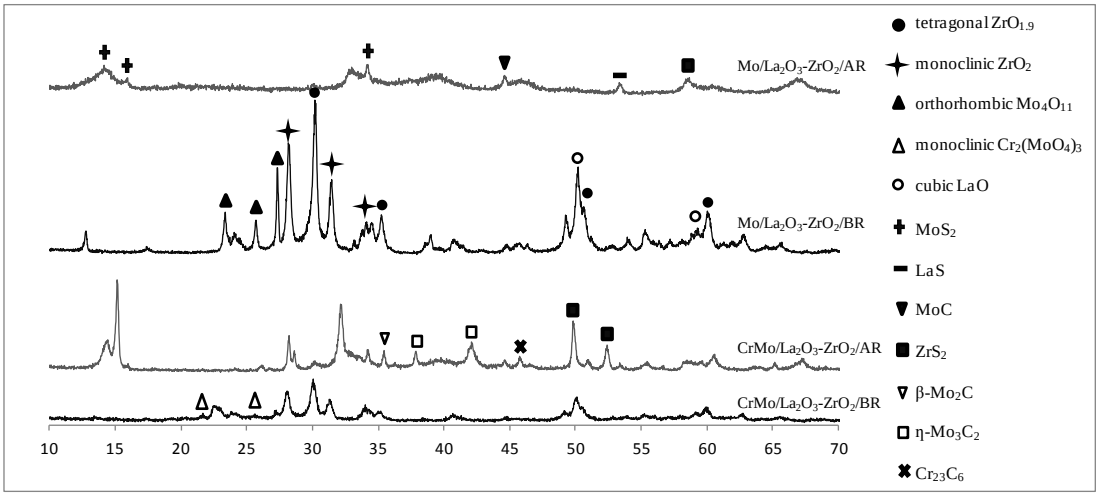

Figure 10. X-Ray Diffraction patterns of Mo/La_2O_3-ZrO_2 and $CrMo/La_2O_3$-ZrO_2 materials: before reaction (BR) and after reaction (AR).

Figure 11 confirms the presence of carbon deposits on the catalyst; flow of dry air and the presence of high temperatures during the diffuse reflectance infrared Fourier Transform spectroscopy generates the formation of characteristic spectra of CO_2 (2349.3, 720.5, 667.3 cm^{-1}). SO_2 bands (1308-1340 and 1135-1160 cm^{-1}) suggest the molecular oxidation of S_2 on the catalyst, decrease in intensity with increasing temperature.

The resulting spectra using the KBr pellet technique for handling solid samples spectrometry often present, bands at 3,450 and 1,640 cm^{-1} due to the absorbed moisture.

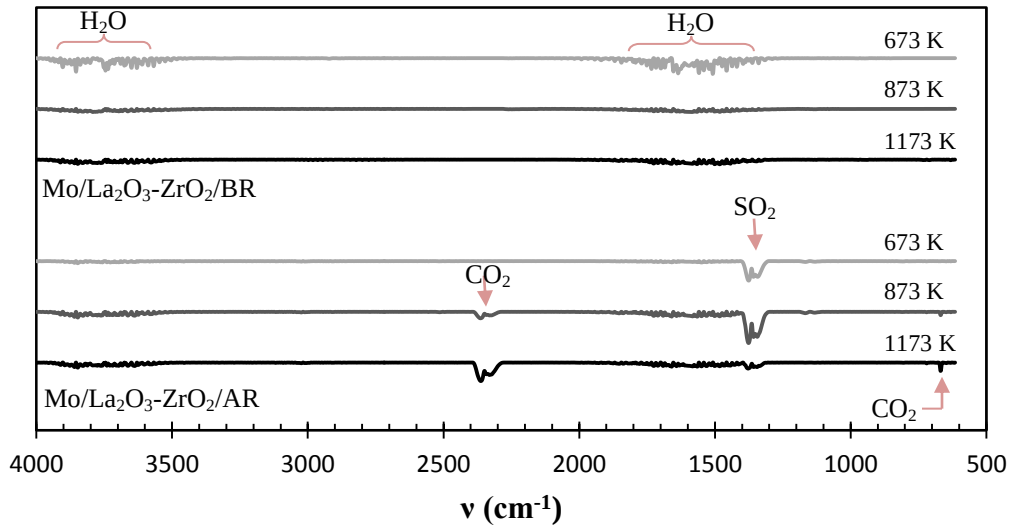

Figure 11. Infrared spectrograms of Mo/La_2O_3-ZrO_2 material: before reaction (BR) and after reaction (AR).

4. Summary and perspectives

Catalysts were synthesized with defined characteristics to achieve high conversions of H_2 by reforming of CH_4 with hydrogen sulfide addition to low energy, lowering costs.

The ZrO_2 support with high chemical resistance but poor mechanical stability and surface area, porosity and thermal stability, was modified SBA-15 (1:1) and La_2O_3 (1:1) respectively in order to counteract these deficiencies. In addition to this, metals were impregnated to provide greater activation reaction (15 % Mo and Cr 5 wt% respectively).

The graphs resulting from the catalytic activity of the materials in the pilot plant confirmed providing these characteristics to achieve high yields of H_2 (64%) at temperatures from 973 K with great stability. The catalyst showed better performance was Mo/La_2O_3-ZrO_2, because they managed to times and lower temperatures, high conversions and yields to the desired products.

However, in the low range of temperatures studied, the conversion of methane in the reaction R1 and CS_2 selectivity in this reaction are low. There is also a notable selectivity to carbon; negative consequences on the catalyst.

References

[1] D. R. Simbeck, Hydrogen costs with CO_2 capture, 7th international conference on greenhouse gas control technologies (GHGT-7), Vancouver, Canada, 2004.
[2] B. W. Gomson, R. H. Elkins, Sulfur from Hydrogen Sulfide, Chemical Engineering Progress 49 (1953) 203-217.
[3] E. J. Erekson, Gasoline from Natural Gas by Sulfur Processing, Institute of Gas Techonology (1996).
[4] F. J. Sandoval, L. L. Jaimes, R. Marroquin, Proceso para eliminar azufre del gas natural con producción de hidrógeno, Journal of the Mexican Chemical Society 41 (1997) 21-29.
[5] C. Huang, A. T-Raissi, Liquid hydrogen production via hydrogen sulfide methane reformation, Journal of Power Sources 175 (2008) 464-472.
[6] S. K. Megalofonos, N. G. Papayannakos, Hydrogen Production From Natural Gas and Hydrogen Sulfide, Int. J. Hydrogen Energy 15 (1991) 319-327.
[7] A. I. Reyes de la Torre, J. M. Domínguez Esquivel, B. Portales Martínez, J.A. Melo Banda, Carburos y Sulfuros de metales de transición evaluados en reacciones de conversión de H_2S + CH_4 a CS_2, XXI SICAT, Simposio Iberoamericano de Catálisis, Malaga, España (2008) I885-I891.
[8] T. Yamaguchi, Application of ZrO_2 as a catalyst and a catalyst support, Catal. Today 20 (1994) 199–218.
[9] R. S. Jong, C. S. Dong, W. K. Hae, NiO Supported on La_2O_3-ZrO_2 Modified with WO_3 for Ethylene Dimerization, I. Ind. Eng. Chem. 13 (2007) 47-56.
[10] K. Fukuda, M. Dokiya, T. Kameyama, Y. Kotera, Catalytic Decomposition of Hydrogen Sulfide, Ind. Eng. Chem. Fundam. 17 (1978).
[11] Q. Zhu, S. L. Wegener, C. Xie, O. Uche, M. Neurock and T. J. Marks, Sulfur as a selective 'soft' oxidant for catalytic methane conversion probed by experiment and theory, Nature Chemistry 5 (2013) 104-109.
[12] J. R. Sohn, M. Y. Park, Preparation and Characterization of Tungsten Oxide-Zirconia Catalyst, Journal of Industrial and Engineering Chemistry 4 (1998) 84-93.
[13] V. V. Srdic, Ceramics with partially stabilized zirconia for cutting tools, Mater. Res. Bull. 43 (2008) 2727–2735.
[14] P. J. Aguayo, Catálisis Heterogénea, Preparación y Caracterización de Catalizadores (1992) 87-103.
[15] S. J. Rack, C. H. Dong, S. D. Cheol, NiO/La_2O_3-ZrO_2/WO_3 Catalyst Prepared by Doping ZrO_2 with La_2O_3 and Modifying with WO_3 for Acid Catalysis, Bull. Korean Chem. Soc. 27 (2006).

Kinetics and Modelling Study of The Catalytic Reaction of Methane and Hydrogen Sulphide Over Mo/La_2O_3-ZrO_2 Catalyst

A. L. Martínez-Salazar[1,*], J. A. Melo-Banda[1], J. M. Domínguez- Esquivel[2], V. H. Martínez-Sifuentes[1], Y. Salazar-Cerda[1], M. A. Coronel-García[1], M. A. Meraz-Melo[3]

[1]Instituto Tecnológico de Ciudad Madero, 1° de mayo s/n col. Los Mangos, Cd. Madero, Tamaulipas, México, 89440.
[2]Instituto Mexicano del Petróleo, Eje Central Lázaro Cárdenas 152, San Bartolo Atepehuacan, Gustavo A. Madero, Ciudad de México, Distrito Federal, México, 07730, [3]Instituto Tecnológico de Iztapalapa, Av. Telecomunicaciones s/n Col. Chinampac de Juárez, Del. Iztapalapa, Ciudad de México, Distrito Federal, Mexico, 09208.

[*]Tel: +528332111039; e-mail: analidiams@gmail.com

ABSTRACT

Catalytic steam reforming is a widely used method today either to produce hydrogen or to give syngas as the first step for the conversion of methane into liquid fuels through the Fischer-Tropsch synthesis.

The reforming of CH_4 by H_2S can be considered as an alternative route to produce hydrogen from methane. With this process, the removal of H_2S in natural gas streams is no longer necessary and sulfur, usually considered as a strong pollutant on liquid fuels in refineries, is used as a reagent in H_2S form of hydrodesulphurization processes. This alternative produces hydrogen, a valuable chemical and clean energy source, as the principal product and carbon disulphide as a secondary petrochemical.

The open literature concerning the kinetic study of the methane-hydrogen sulphide reaction is very poor. In this research the reaction of CH_4 and H_2S over zirconia catalyst modified with lanthanum oxide impregnated with molybdenum has been studied in a fixed bed tubular reactor varying the inlet CH_4 flow rate over a temperatures range of 1023 – 1323 K and feed molar ratio CH_4:H_2S of 1:12. The Langmuir-Hinshelwood theory has been used to analyze kinetic models. Model discrimination has been performed and the kinetic parameters and adsorption constants calculated.

Finally, the simulation process of reforming CH_4 by H_2S has been developed in which separation of the produced hydrogen and no reacted H_2S involves absorption through diethanolamine. A tubular reactor from kinetic parameters was dimensioned. Aspen Plus ® 11.1and Hysys V.8 simulation software was used. Preliminary results showed a high purity H_2 can be produced by this route.

Keywords: reforming, hydrogen, kinetics

1. Introduction

Hydrogen, in addition to be used as essential in the industry of petroleum for obtaining improved fuels, is considered an attractive energy supply because it can be burned like gasoline and natural gas, or converted to electricity without any carbon emissions at the point of use [1]. Its main advantage is that its combustion produces only water, which means that does not emit greenhouse gases, such as fossil fuels and biomass. This makes it particularly appropriate to replace the petroleum-based products.

Catalytic reforming of CH_4 and H_2S to produce H_2 and CS_2 has experimental evidence recorded by little research over the years. Mass catalysts or simple supports that have been used, given their catalytic properties, do not meet the needs of activation, selectivity or stability required for this reaction.

Recently, research has been focusing on the structure of catalysts that have characteristics that generate high potential for conversion on moderate conditions of operation and that could be the basis of an interesting option of process in the production of hydrogen. One of these catalysts is zirconia catalyst modified with lanthanum oxide impregnated with molybdenum, Mo/La_2O_3-ZrO_2, which has shown some advantages in the improvement of the properties of the catalyst [1].

In this work, kinetics of the reactive system reforming of CH_4 by H_2S using Mo/La_2O_3-ZrO_2 catalyst, based on the methodology of Langmuir-Hinshelwood-Hougen-Watson was studied. Pilot plant experimental data of conversion for a range of temperatures and residence times were obtained and, by means of them, it was determined which kinetic model among several possible gave the best fit to the experimental data. The kinetic parameters and adsorption constants of the model of the best fit were obtained.

In order to observe an engineering application of the results of the project, two simulation models were created: one to propose a process flowsheet that, based on the conditions of the reaction studied, allows obtain and separate from the reaction system products with commercially acceptable purity. The other is for calculating the sizing of a tubular reactor for a given production, based on the kinetic parameters and adsorption constants calculated.

2. Experimental

2.1 Proposed kinetic mechanism and models

Catalytic reactions involved in this research work, for the kinetic study of the reforming of methane with hydrogen sulfide are as follows:

$$2H_2S + CH_4 \longrightarrow CS_2 + 4H_2$$
$$2H_2S \longrightarrow S_2 + 2H_2$$

In the temperature range in which we worked, the reaction of pyrolysis of methane can be ignored [2].

The reactions of table 1 represent the mechanism proposed for this study. Writing rate expressions every step is considered as an elementary reaction; the only difference is that the concentration of the species in gas phase is replaced by its respective partial pressures.

Table 1. Steps of a Langmuir-Hinshelwood kinetics mechanism

$CH_4 + (s) \longleftrightarrow CH_2(s) + H_2$	Adsorption
$4H_2S + 4(s) \longleftrightarrow 4S(s) + 4H_2$	
$CH_2(s) + 2S(s) \longleftrightarrow CS_2(s) + H_2 + 2(s)$	Surface reaction
$S(s) + S(s) \longleftrightarrow S_2(s) + (s)$	
$CS_2(s) \longleftrightarrow CS_2 + (s)$	Desorption
$S_2(s) \longleftrightarrow S_2 + (s)$	

The expressions of rate for adsorption of methane and hydrogen sulfide are:

$$r_{AD1} = k_{A1}\left(P_{CH_4}\cdot C_V - \frac{C_{CH_2(s)}}{K_{CH_4}}\cdot P_{H_2}\right) \quad (1)$$

$$r_{AD2} = k_{A2}\left(P_{H_2S}^4\cdot C_V^4 - \frac{C_{S(s)}^4}{K_{H_2S}}\cdot P_{H_2}^4\right) \quad (2)$$

The expressions of rate for the step of surface reactions that produce adsorbed carbon disulfide and sulfur and hydrogen in gaseous phase are:

$$r_{s1} = k_{rs1}\left[C_{CH_2(s)}.C_{S(s)}^2 - \frac{C_{CS_2(s)}\cdot P_{H_2}\cdot C_V^2}{K_{rs1}}\right] \quad (3)$$

$$r_{s2} = k_{rs2}\left[C_{S(s)}\cdot C_{S(s)} - \frac{C_{S_2(s)}\cdot C_V}{K_{rs2}}\right] \quad (4)$$

The expressions of rate for desorption of the carbon disulfide and sulfur are:

$$r_{D1} = k_{D1}\left(C_{CS_2(s)} - \frac{P_{CS_2}\cdot C_V}{K_{DCS_2}}\right) \quad (5)$$

$$r_{D2} = k_{D2}\left(C_{S_2(s)} - \frac{P_{S_2}\cdot C_V}{K_{DS_2}}\right) \quad (6)$$

For the mechanism postulated in the sequence given by table 1, we want to determine the limiting step of the speed. First it is supposed that one of the steps limits speed (controls rate) and then rate expressions are formulated in terms of partial pressures of the present species.

a) Assuming surface reactions is the rate controlling step.

$$r_{S1} = k_1\left[\frac{P_{CH_4}P_{H_2S}^2}{P_{H_2}^3} - \frac{P_{CS_2}\cdot P_{H_2}}{K_{e_1}}\right]\frac{1}{Q_r^3} \quad (7)$$

$$r_{s2} = k_2\left[\frac{P_{H_2S}^2}{P_{H_2}^2} - \frac{P_{S_2}}{K_{e_2}}\right]\frac{1}{Q_r{}^2} \quad (8)$$

where

$$\left[1 + \frac{K_{CH_4}\cdot P_{CH_4}}{P_{H_2}} + \frac{K_{H_2S}\cdot P_{H_2S}}{P_{H_2}} + K_{CS_2}\cdot P_{CS_2} + K_{S_2}\cdot P_{S_2}\right] = Q_r \quad (9)$$

b) Assuming adsorption of methane and hydrogen sulfide over the surface is the rate controlling step.

$$r_{AD1} = k_1\left[P_{CH_4} - \frac{P_{CS_2}\cdot P_{H_2}^2}{K_{e_1}}\right]\frac{1}{Q_r} \quad (10)$$

$$r_{AD2} = k_2\left[P_{H_2S} - \frac{P_{S_2}^{0.5}\cdot P_{H_2}}{K_{e_2}}\right]\frac{1}{Q_r} \quad (11)$$

where

$$\left[1+\frac{K_{CS_2}\cdot P_{CS_2}\cdot P_{H_2}\cdot K_{rs2}}{K_{rs1}\cdot K_{S_2}\cdot P_{S_2}}+\frac{K_{S_2}^{0.5}\cdot P_{S_2}^{0.5}}{K_{rs2}^{0.5}}+K_{CS_2}\cdot P_{CS_2}+K_{S_2}\cdot P_{S_2}\right]=Q_r \quad (12)$$

c) Assuming desorption of the carbon disulfide and sulfur from the surface is the rate controlling step.

$$r_{D1}=k_1\left[\frac{P_{CH_4}\cdot P_{H_2S}^2}{P_{H_2}^4}-\frac{P_{CS_2}}{K_{e_1}}\right]\frac{1}{Q_r} \quad (13)$$

$$r_{D2}=k_2\left[\frac{P_{H_2S}^2}{P_{H_2}^2}-\frac{P_{S_2}}{K_{e_2}}\right]\frac{1}{Q_r} \quad (14)$$

where

$$\left[1+\frac{K_{CH_4}\cdot P_{CH_4}}{P_{H_2}}+\frac{K_{H_2S}\cdot P_{H_2S}}{P_{H_2}}+\frac{K_{CH_4}\cdot P_{CH_4}\cdot K_{H_2S}^2\cdot P_{H_2S}^2\cdot K_{rs1}}{P_{H_2}^4}+\frac{K_{H_2S}^2\cdot P_{H_2S}^2\cdot K_{rs2}}{P_{H_2}^2}\right]=Q_r \quad (15)$$

2.2 Procedure for the analysis of the models and estimation of the kinetics parameters

A number of experimental sets were carried out in a tubular reactor varying molar feed flows with Mo/La_2O_3-ZrO_2 catalyst and operating in the temperature range: 750 - 1050 ° C. The mass of the catalyst was fixed as 3 g and the rest of operating parameters remained constant. Volumetric feed flows used are shown in table 2.

Table 2. Variation of feed flows

Volumetric feed flows		
Experimental run	CH_4 (L/h)	H_2S (L/h)
1	0.189	2.268
2	0.236	2.83
3	0.315	3.78
4	0.4725	5.67
5	0.945	11.34

The experiments were conducted in the CGA-VI microplanta located in the "Laboratorio de evaluación en microplanta y escalamiento de catalizadores" of the Instituto Mexicano del Petróleo in Mexico D. F. The system mainly consists of three sections:

1st Feed section; consists of a control of supply of gas with mass controllers.

2ª Reaction section; consists of a vertical fixed bed tubular reactor of quartz, equipped with an oven Thermolyne 11000 with internal temperature controller.

3ª Identification of reaction products section; has a gas chromatograph mark Varian Star 3400 CX equipped with a capillary column HP plot - Q phase of polymer divinylbenzene with a length of 30 mm and inner diameter 530µm.

Measurement of the compositions of inlet and outlet of the reactor allowed to calculate variables to graph results. These are: the total conversion of methane (x_{CH_4}) and the conversion of H_2S to S_2 (x_{S_2}) versus residence time, τ.

$$x_{CH_4}=\frac{mole\ of\ inlet\ CH_4-mole\ of\ outlet\ CH_4}{mole\ de\ inlet\ CH_4} \quad (16)$$

$$x_{S_2}=\frac{mole\ of\ outlet\ S_2}{moles\ of\ inlet\ H_2S} \quad (17)$$

$$\tau = m_{cat}/F^{E}_{CH_4} \quad (18)$$

$m_{cat} = mass\ of\ catalyst$
$F^{E}_{CH_4} = molar\ feed\ plow\ of\ methane$

a) Conversions were calculated: total conversion of methane and conversion of H_2S to S_2, as a function of inlet and outlet moles of species. Moles were calculated by means of the experimental data of composition obtained for the different values of temperature in the range of 750°C a 1050°C and at the different values of residence times in the range of 0.5 a 1.5 kgcat.h/mole.
b) For a given temperature, through Excel, constants were calculated fitting polynomial function to the experimental data curves conversion versus residence time (τ),

$$x_{CH_4} = a_0 + a_1\tau + a_2\tau^2 + a_3\tau^3 \quad (19)$$

and

$$x_{S_2} = b_0 + b_1\tau + b_2\tau^2 + b_3\tau^3 \quad (20)$$

c) By means of the equations

$$r_{CH_4} = \frac{\partial x_{CH_4}}{\partial \tau} = a_1 + 2a_2\tau + 3a_3\tau^2 \quad (21)$$

and

$$r_{S_2} = \frac{\partial x_{S_2}}{\partial \tau} = b_1 + 2b_2\tau + 3b_3\tau^2 \quad (22)$$

A table of values of reaction rate versus residence time was obtained for each temperature.
d) Since

$$r_{CH_4} = r_{s1}$$

and

$$r_{S_2} = r_{s2}$$

We have now the information needed to calculate the values of the kinetic rate constants k_1 and k_2, as well as the values of the constants of adsorption equilibrium K_{CH_4}, K_{H_2S}, K_{CS_2} and K_{S_2}, through an iterative calculation procedure, assuming that they depend only on the temperature. Computer program Polymath was used; this program lets you know so well is the fitting that makes the model to the experimental data and, as a consequence, compare models.
e) Based on the results obtained in the last step for the best model, pre-exponential factors of reaction rate, A_j, where j = 1,2 and pre-exponential factors of adsorption, A_{ad_i}, where i = CH_4, H_2S, CS_2, S_2, are calculated. Also activation energies, E_j, and adsorption enthalpies, ΔH_i are obtained in the same calculation. For these calculations, values of k_j vs T and K_{ad_i} vs T, obtained in the last step are used, as well as the well-known equations

$$\ln k_j = \ln A_j - \frac{E_j}{R}\left(\frac{1}{T}\right) \quad (23)$$

$$\ln K_{ad_i} = \ln A_{ad_i} - \frac{\Delta H_i}{R}\left(\frac{1}{T}\right) \quad (24)$$

A graph $ln\ k_j$ o $ln\ K_{adi}$ as a function of (1/T) is built, according to we are calculating [3].


2.3 Process flowsheet

The proposed process flowsheet was created with the support of process Simulator Aspen plus and has as basic initial part a stoichiometric reactor, *Rstoic*, in which occur the following reactions:

$$CH_4 + 2H_2S \longleftrightarrow 4H_2 + CS_2$$
$$2H_2S \longleftrightarrow S_2 + 2H_2$$

at 950° C, 1 atmosphere of pressure and with a feed molar relationship of $H_2S/CH_4 = 12$. Fractional conversions of 0.99 and 0.28 were given as data, respectively.

2.4 Sizing of a tubular reactor

The size of a reactor for the rates of reactants used in process flowsheet of the last section was calculated for a catalytic reactor using, process simulator Hysys V8.4 and *Plug flow reactor model*.

3. Results and discussion

3.1 Kinetic study of the reactive system
Plots of conversion versus residence time are shown as figure 1 y 2.

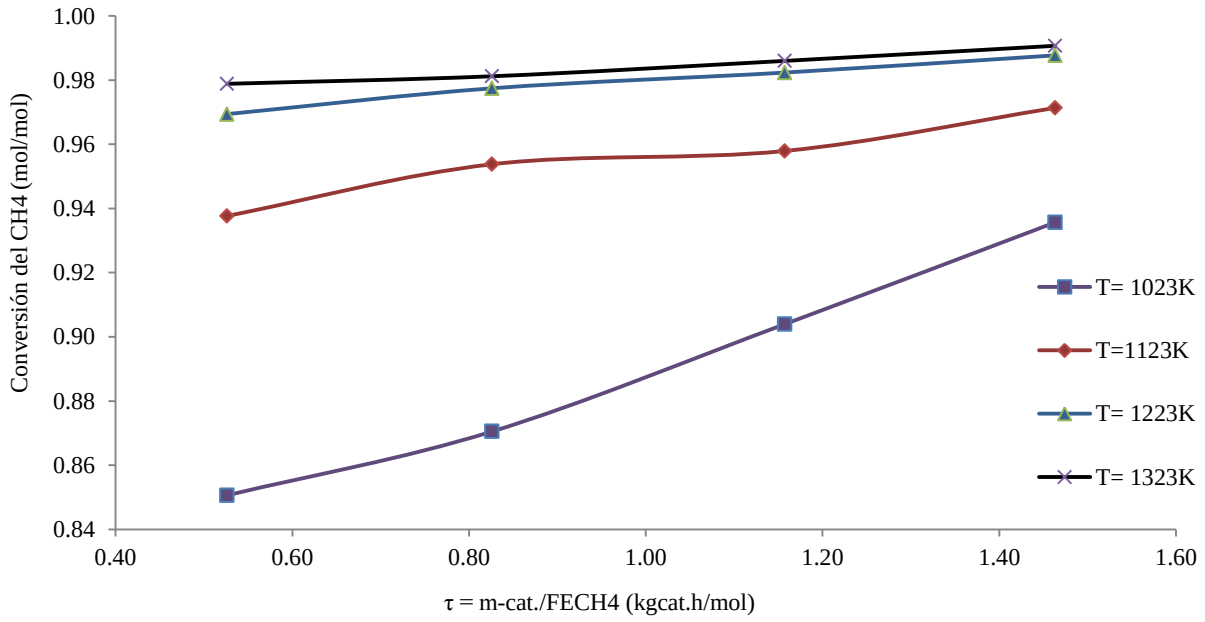

Figure 1 Total conversion of CH_4 vs residence time at different temperatures, with a feed relation of CH_4:H_2S (1:12) and Mo/La_2O_3-ZrO_2 as catalyst.

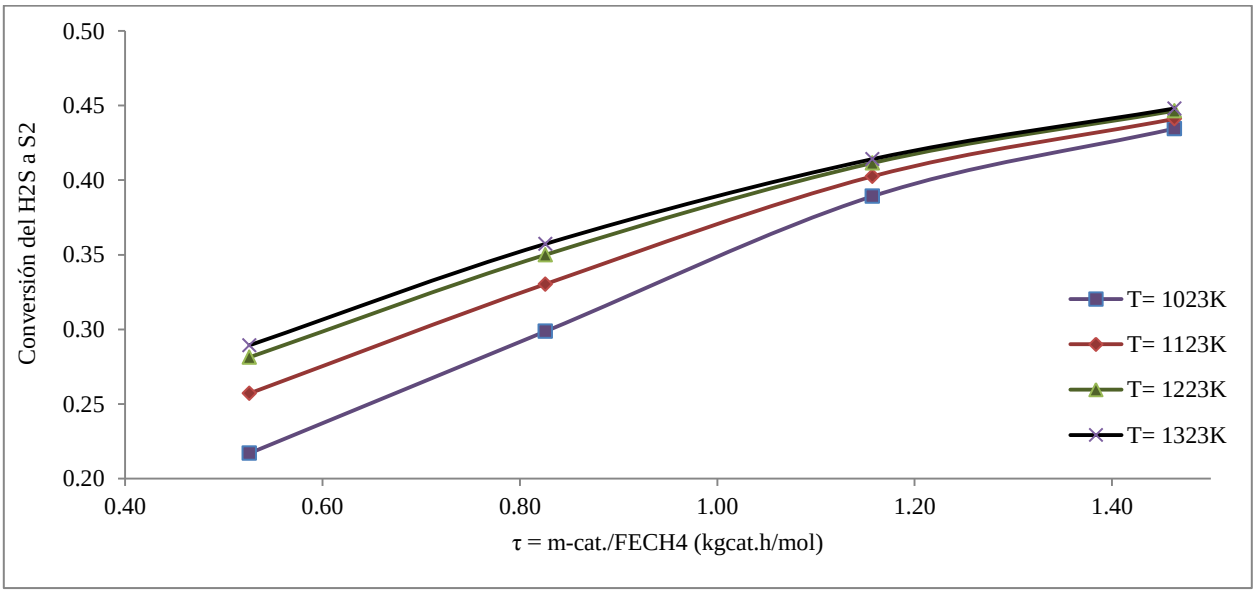

Figure 2 Total conversion of H_2S a S_2 vs residence time at different temperatures, with a feed relation of CH_4:H_2S (1:12) and Mo/La_2O_3-ZrO_2 as catalyst.

For each temperature, at a given value of τ the reaction rates r_{CH_4} y r_{S_2} were calculated with the corresponding quadratic equations. Partial pressures of the species at the given τ value were calculated with the equation $P_i = (n_i / n_T)P$ were n_i are moles of specie i y n_T are total moles. Both, n_i y n_T, were calculated as a function of the fractional conversions x_{CH_4} y x_{S_2} at the given value of τ.

The next step was proving the proposed kinetic models because we already had a table of reaction rate versus residence time and versus Pi, for each temperature.

The values of kinetic constants k_1 y k_2 as well as the values of the adsorption constants K_{CH4}, K_{H2S}, K_{CS2} y K_{S2}, were solved for each proposed kinetic model, by means of the software Polymath using the Levenberg-Marquardt (LM) algorithm for non-linear regression. Values of the results of variance and Rmsd (Root mean square deviation) are shown in table 3. These indicators were used for comparison of various models representing the same dependent variable and thus be able to make a discrimination among them. The model with the smaller variance and Rmsd represents data with more accuracy.

For the present study, the surface reaction model generates smaller values of indicators. There is a good concordance, which implies that the proposed mechanism could be correct and the controlling step of the speed is the surface reaction.

Table 3 Variances and Rmsd of solved models, using the Levenberg-Marquardt algorithm

	Surface reaction		**Adsorption**		**Desorption**	
Temperature K	**Variance**	**Rmsd**	**Variance**	**Rmsd**	**Variance**	**Rmsd**
1023	0.5141	0.1179	0.2160	0.0765	**0.0290**	**0.0281**
1123	**0.0426**	**0.0340**	12.010	0.5762	0.0885	0.0489
1223	**0.1588**	**0.0650**	0.5994	0.1273	0.1634	0.0665
1323	**0.0055**	**0.0122**	0.0170	0.0215	0.2147	0.0762

Once it was concluded which was the kinetic model that better fit the experimental data, we have the kinetic constants and equilibrium adsorption constants. In table 4 can be observed the values of the kinetic constants k_1 y k_2 and equilibrium adsorption constants K_{CS2} y $K_{S2,}$ K_{CH4}, K_{H2S} obtained, taking the surface reactions as the rate controlling step.

Table 4 Values of the kinetic constants and equilibrium adsorption constants as a function of temperature.

	Temperature (K)			
Constants	**1023**	**1123**	**1223**	**1323**
k_1	139.66	244.56	550.27	581.42
k_2	267.40	329.53	586.82	588.82
K_{CS2}	71.27	33.29	7.88	6.90
K_{S2}	6.05	11.00	4.05	3.50
K_{CH4}	102.00	102.00	102.00	102.00
K_{H2S}	2.83	3.73	1.62	1.50

Finally, pre-exponential factors, activation energies and adsorption enthalpies were calculated. Results are shown in table 5.

Table 5 Kinetic parameters and adsorption constants.

Reaction	**A(mol/kgcat.h)**	**E(J/mol)**
R1	129,832.44	57,910.73
R2	13,164.78	33,326.42

Specie	**Aad (bar^{-1})**	**ΔH (J/mol)**
CS_2	0.00095	-95,656.41
S_2	0.3063	-27,968.97
CH_4	101.99 bar	-0.5285
H_2S	0.1012 bar	-29,961.71

3.2 Process flowsheet

Results of variables in the important currents of input and output of the proposed flowsheet are observed in table 6:

Table 6 Results of the main streams of the flowsheet.

Component	CH_4	H_2S	H_2	CS_2	S_2
Molar flow (kmol/h)	100.0	690.0	890.9	94.5	485.3
Molar fraction	1.0	1.0	0.996	0.993	0.992
Temperature (°C)	25.0	25.0	26.3	46.4	150.0
Pressure (at.)	1.0	1.0	10.0	1.0	1.0
Vapor fraction	1.0	1.0	1.0	0.0	0.0

It can be observed high purity in all products and significant production of hydrogen, since it is produced in both reactions.

3.3 Sizing of a tubular reactor

Figure 3 shows the variation of the flows of the components versus length of the reactor calculated with the hysys simulator. It can be observed that all flows reach stabilization on three meters of length.
The size of the tubular reactor is:
Diameter: 30 cm
Length: 3 meters

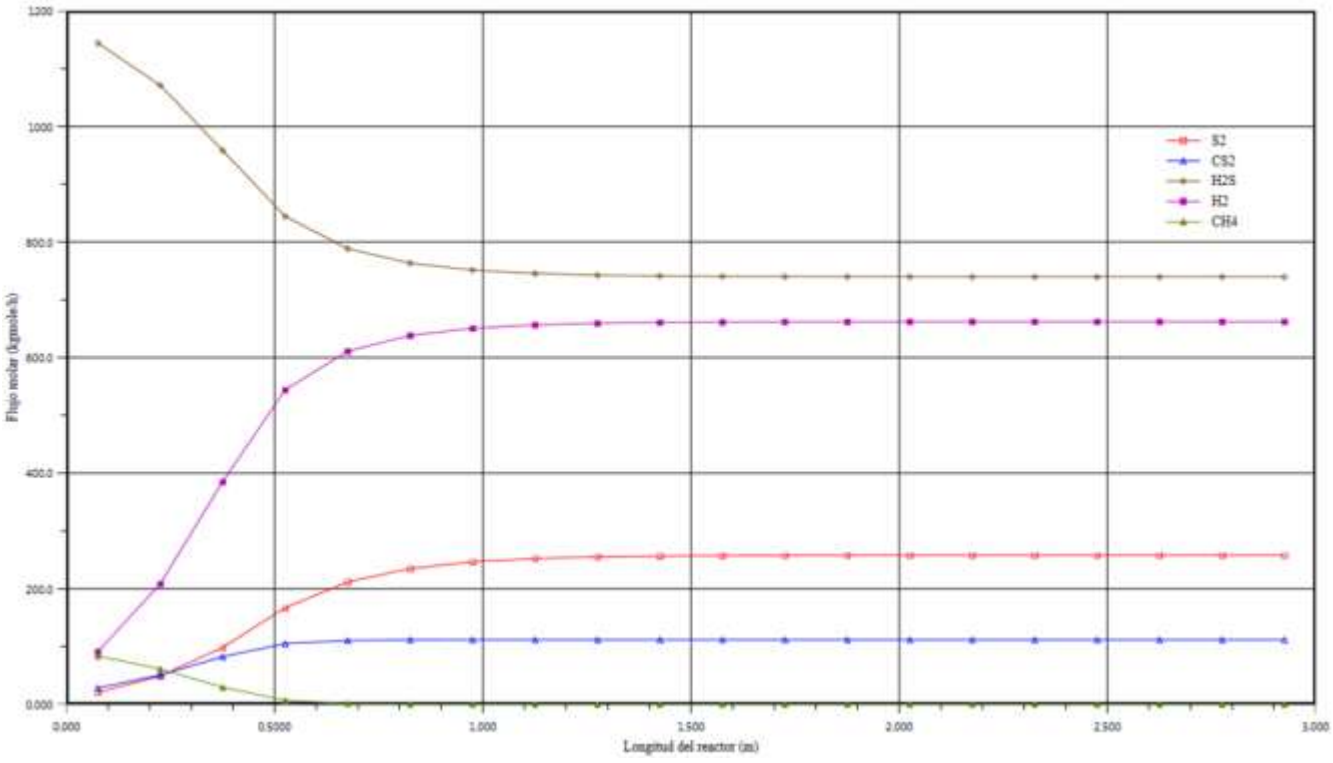

Figure 3 Variation of the flows of the components of the reforming of CH_4 with H_2S as a function on the length of the reactor.

4. Summary and perspectives

One could conclude that the best of the proposed models is that considered surface reaction as controlling rate step. Values of the kinetic parameters and the adsorption constants were obtained as a result of the regression analysis.

Build the process flowsheet with the Aspen Plus Simulator, it was observed that it is possible to get and separate the three products of the reactive system with high purities and controlling the purity of the main product based on a separation of hydrogen sulfide by absorption in diethanolamine.

The size of the basic equipment of the process, which is the tubular reactor, is reasonable: three meters in length and 30 centimeters in diameter.

Acknowledgements

We gratefully acknowledge the financial support of this work by Instituto Mexicano del Petróleo.

References

[1]. A. P. Simpson and A. E. Lutz. Exergy analysis of hydrogen production via steam methane reforming. *International Journal of Hydrogen Energy, 32*, 4811-4820 (2007).
[2]. C. Huang and A. T-Raissi. Liquid hydrogen production via hydrogen sulfide methane reformation. *Journal of Power Sources, 175*, 464-472 (2008).
[3]. S. H. Fogler. *Elementos de ingeniería de las reacciones químicas*. Pearson Prentice Hall. Fourth Edition (2006).

Hydrogen Production from NO and CH_4 Treatment with non Thermal Plasma

E Alva[b], M Pacheco[a], J Pacheco[a], R Valdivia[a], H. Frías[a], G. Soria[a,c], S. Darío[a,c],F. Ramos[a], M. Duran[a], M. Hidalgo[a], A Colín[b], V Sánchez[b].

[a]Instituto Nacional de Investigaciones Nucleares, Carretera México-Toluca s/n, La Marquesa, Ocoyoacac, México, C.P.52750
[b]Universidad Autónoma del Estado de México, Instituto Literario # 100. Col. Centro Toluca, México, C.P.50000
[c]Instituto Tecnológico de Toluca, Av. Instituto Tecnológico s/n, Metepec, México, C.P.52140
E-mail: marquidia.pacheco@inin.gob.mx

ABSTRACT

In this project a chemical kinetics model and its experimental demonstration to produce hydrogen from nitrogen oxide (NO) and methane (CH_4) treatment is proposed. A reactor with dielectric pellets as discharge barrier is used to perform the experiments to enhance the electric field strength and create a channel across the discharge region.

The research was carried out in 2 phases: The first one was the analysis of the simulation degradation of NO and CH_4. The second step was the experimental methodology to treat the mixture (NO and CH_4).

To produce the non-thermal plasma, an AC power source was also developed. This energy source works with a high frequency series resonant inverter in the range of 20 kHz to 180 kHz, able to generate a voltage of 15 kV. The discharge can be sustained at atmospheric pressure. The experimental conditions of this special case were: 30V, 1-2 A and 27 kHz.

Chemical model elucidates the degradation of NO and CH_4, theoretical results concerning hydrogen production are overestimated when compared to experimental results; therefore a set of additional equations are then proposed.

Results obtained from the model, illustrate that in a mixture of NO in humid air, the main path for the NO removal is the oxidation to nitrogen dioxide (NO_2) and, soon after, to nitric acid (HNO_3). Concerning the diminution of CH_4, the electron impact reactions are crucial.

Keywords: Hydrogen, non-thermal plasma, toxic gases treatment

1. Introduction

The air quality is elementary to the human welfare and wildlife. Some natural disasters like volcanoes eruptions and fire on forestry areas have impact on it and might alter such balance. Air quality is poorer on the major populated cities with intensive automotive parking lot, especially on the daily rush hour. For this reason the impact coming from the human activities are greater than nature.

The air pollution has no boundaries and has adversely impacts on everybody, altering the ozone concentration on atmosphere producing the greenhouse effect. This production has a direct impact on earth; for this reason many environment agreements to prevent reduce and gradually control the green house effect emissions like the methane gas and nitrogen oxides (NOx) have to be signed.

In Mexico as in other countries, the automobile is the main source of air pollution, especially emissions of carbon monoxide (CO), nitrogen oxides(NOx), hydrocarbons (HC) and particle matter (PM) coming from Otto diesel engines [1].

In Mexico, the daily amount of vehicles moving along roads is around 15 millions. The transportation sector used up to 56% of the total energy in Mexico, which is equivalent to 95 millions of gasoline liters daily used [2]. The main fuel used in Mexico is the Magna gasoline, followed by Diesel fuel (mainly used in heavy trucks) and, finally, the Premium gasoline.

From the uncompleted burning of hydrocarbons, slights portions of CO, CH_4, and volatile organic compounds (VOC's) are formed, besides the formation of nitrous oxide (N_2O) and nitrogen oxides (NOx).

Higher methane concentrations from automobiles are part of an uncompleted combustion process. They are highly depending of temperature operation, especially in an automotive car with no maintenance program (tuned-up) the levels of methane pollution are greater.

In the case of nitrogen oxides (NO_x), they produce photochemical pollution that contributes to the formation of acid rain and leads to rivers acidification, lakes and other water bodies; this contaminant also damages vegetation and buildings. Furthermore NO_x are related to several adverse effects on human health, mainly in eyes, heart and lungs [3, 4].

Emissions of greenhouse gases like methane (CH_4) and nitrogen oxides (NOx) are one of the major problems to solve; additionally methane conversion could offer a promising route to produce higher value-added products (i.e. hydrogen). For this reason, the development of research projects to create sustainable alternative technologies is imperative.

Kinetic model

The kinetic model used to symbolize the treatment of toxic gases with a dielectric barrier discharge reactor is described and developed elsewhere [5, 6].The model defines the micro discharge development in two phases: the first step concerns the formation of the streamer head at 1ns with high values of electric field (600Td) [7]; and the second one is the formation of a streamer channel, connected to the streamer head. When micro discharge is established, the electric field decreases by maintaining itself almost constant until the dielectric wall is reached [7].The energetic electrons transfer their energy toward neutral molecules resulting in quenching, attachment, dissociation or ionization process; other species like free radicals, meta stables, atoms and ions will be also formed.

The formation of active species is maintained during this phase and the removal of NOx and CH_4 is realized when they react with active species. The model takes into account the following chemical species:(e^-, N_2, O_2, H_2O, O_3, NO_2, NO_3, N_2O_5, N_2O, HNO_3, HNO_2, C, $^-CH_3$, CH_3, CH_2, $CH_3O^\bullet$,CH_2O, $O^\bullet$, $N^\bullet$, $OH^\bullet$, $H^\bullet$, $O_2(a^1\Delta g)$, $O(^1D)$, $N_2(A)$, O^-_2 , O^-, O^+_2 and H^-) [5,6,8,9].

Consequently, the chemical model for NOx and CH_4 removal, proposes the simulation of the formation of active species in the streamer head with an initial electron density of 1 cm^{-3} and at 1×10^{-8} s. Rate coefficients were used at an electric field of 600Td for 2DBD [5, 10]. The reaction rate coefficients involving electrons were taken from [11, 15, 16, 17, 18, 19, 20] and the rate coefficients between neutral species from [9, 11, 12 14]. The model, here applied, considers a balance of the chemical species mentioned above. Radicals produced are supposed to be well mixed with the reactants and uniformly distributed within the whole volume. For the development of the kinetic model Matlab® simulation software was used, specifically an equation differential solver called ODE1s based on the Runge-Kutta method for solving differential equations differential equations [19].

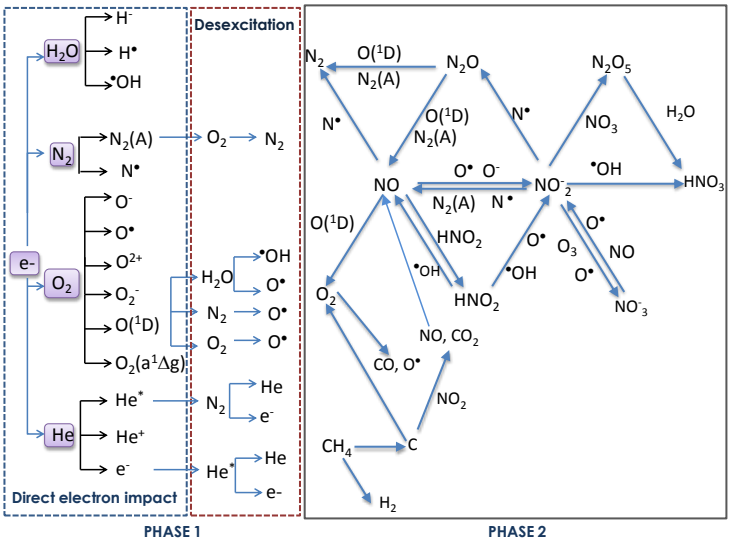

Figure 1. Chemical Model

2. Experimental setup

To produce the non-thermal plasma, an AC power source was developed. This energy source works with a high frequency series resonant inverter in the range of 20 kHz to 180 kHz, able to generate a voltage of 15 kV [6]. The discharge can be sustained at atmospheric pressure using nitrogen or air, as plasma gas. The experimental conditions of this special case were: 21V, 0.7-1A and 30kHz.

For optical emission diagnosis (OES) a digital spectrometer Jaz Ocean Optics was used, this enables an optical resolution of 0.3 nm (FWHM) covering from 200 nm to 1100 nm.

Inlet and outlet gases were analyzed with a PG-250 Horiba able to identify and quantify CO, CO_2, NO_x, SO_2 and O_2. A mass spectrometer (Cirrus MKS Spectra products) and a gas chromatographer (Thermo Scientific Trace GC Ultra) were also used to identify compounds formed. The experimental system used in the degradation of NO-CH_4 mixture is shown in Figure 2.

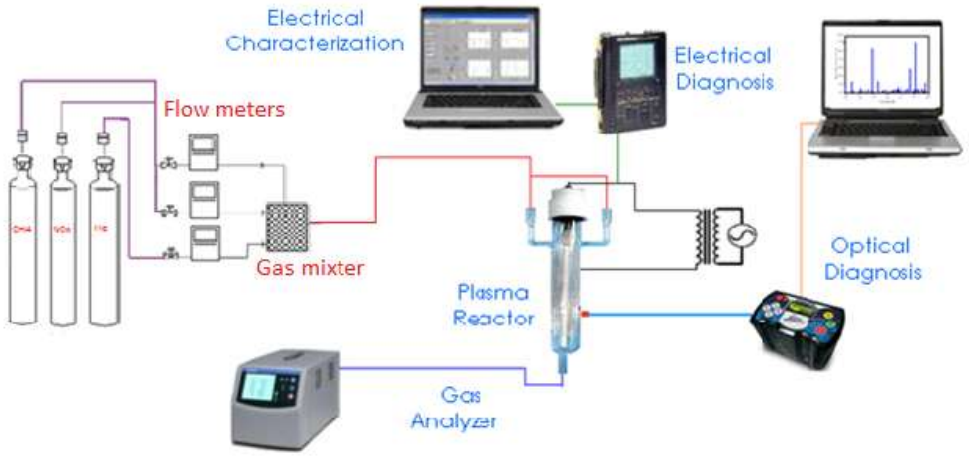

Figure 2. Experimental set up

The schematic of the reactor is shown in Fig. 3, it consists of a tube of quartz with an internal radius of 12.3 mm, a length of 212 mm and a thickness of 1.2 mm. Two copper concentric central electrode of radius of 2 mm is set inside the quartz tube. A metallic mesh covering the quartz tube plays the role of the external electrode.

Into the quartz tube, several glass pellets uniformly distribute the plasma. Spherical pellets were chosen because the electric field is concentrated and numerous filamentary discharge channels are formed along the pellet surface, enabling better interaction between plasma and the gas to be treated [20].

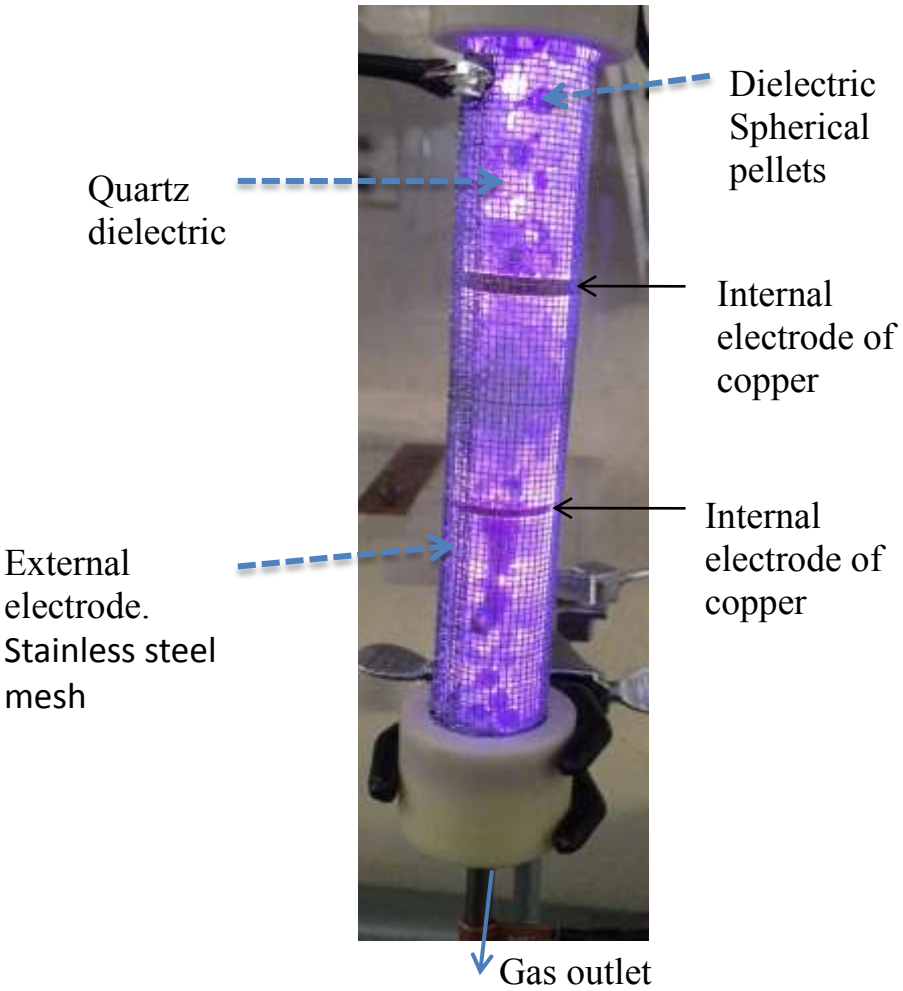

Figure 3.Plasma reactor

To obtain electronic temperature (T), Boltzmann plot method is applied to data obtained from OES study. The spectroscopic data were obtained from [27].

For every spectral line, this method plots $\ln\left(\frac{\varepsilon_{hb}\lambda}{g_h A_{hb}}\right)$ versus E_h. The negative slope obtained from the line represents $1/kT$.

Where:

ε_{hb}: Line emissivity

λ : Wavelength (nm)

g_h: statistical weight (upper level)

A_{hb}: Spontaneous emission probability
E_h: Excitation energy (upper level) in eV
k: Boltzmann constant (8.6173324×10^{-5} eV K^{-1}).

3. Results and discussion

3.1 Chemical model

During first nanoseconds, the energetic electrons collide with neutral molecules appearing primary radicals ($^{\bullet}OH$, $O^{\bullet}$ and $N^{\bullet}$). Ions and excited molecules, like excited oxygen, $O^1(D)$, forms radicals by rapid quenching. Soon after, the electron–ion and ion–ion reactions create secondary radicals. NO and CH_4removal is mainly controlled by oxidation reactions. The role of $O^{\bullet}$ radical is the oxidation of NO to $NO_2$and N_2.

NO and NO_2 could be removed by the $^{\bullet}OH$ radical to form HNO_2 and HNO_3, respectively, but also NO can be reduced by $N^{\bullet}$ radical [8, 22]. The evolution of species formed in the plasma reactor can be appreciated in Figure 4a.

The diminution of methane concentration is around 30% as can be saw more detailed in figure 4b. An interesting product of methane decomposition is the hydrogen; in figure 4c a concentration of approximately 400ppm is observed. The formation of CO is also formed from the decomposition of methane.

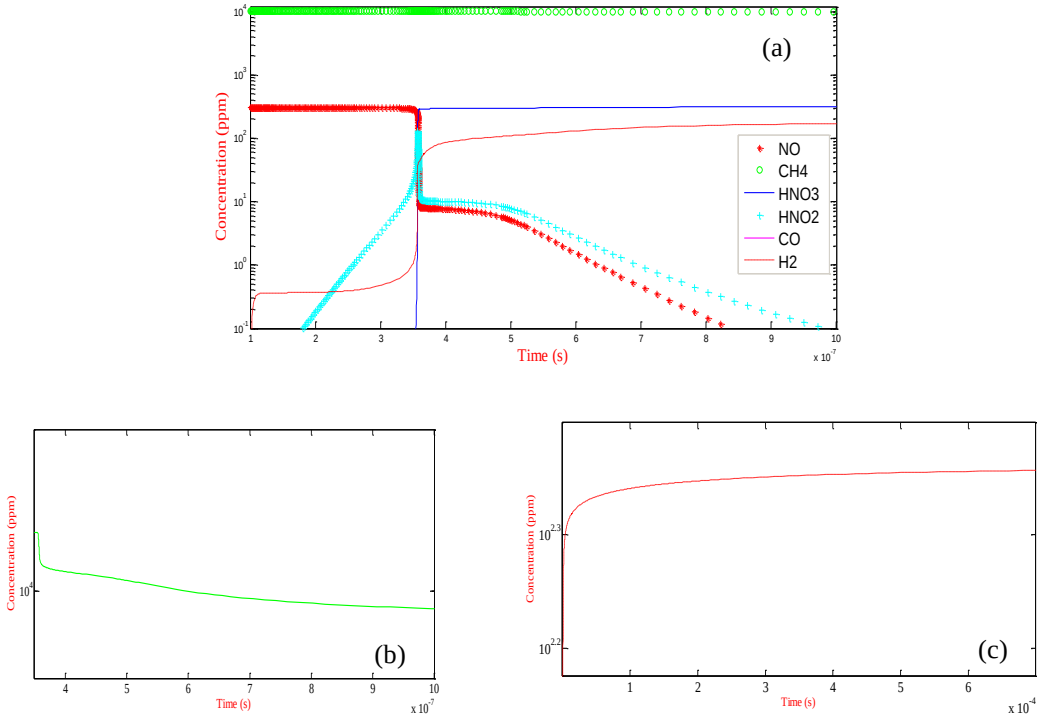

Figure 4.NO-CH_4 plasma treatment. **(a)** Degradation NO-CH_4. **(b)** Degradation CH_4. **(c)** Hydrogen production

Based on simulation results (Fig. 4a, 4b and 4c), a rapid diminution of NO is obtained, being notice able the increase of N_2, HNO_2 and HNO_3. The degradation of methane is lower, but significant, leading to the formation of atomic carbon and an added value: the hydrogen production at low power consumption (24 to 27W).

3.2 Experimental Model

3.2.1 Chromatography and mass spectroscopy results

Several experimental tests were done; gaseous products were analyzed with different methods. For the methane analysis a first approach was obtained with gas chromatography. In figure 5, two chromatograms, with and without plasma treatment, were plotted. The methane peak at time retention of 4.10min considerably diminishes when plasma is applied and intensities of oxygen and nitrogen lines increase, it could probably explain the dissociation of NO into N_2 and O_2.

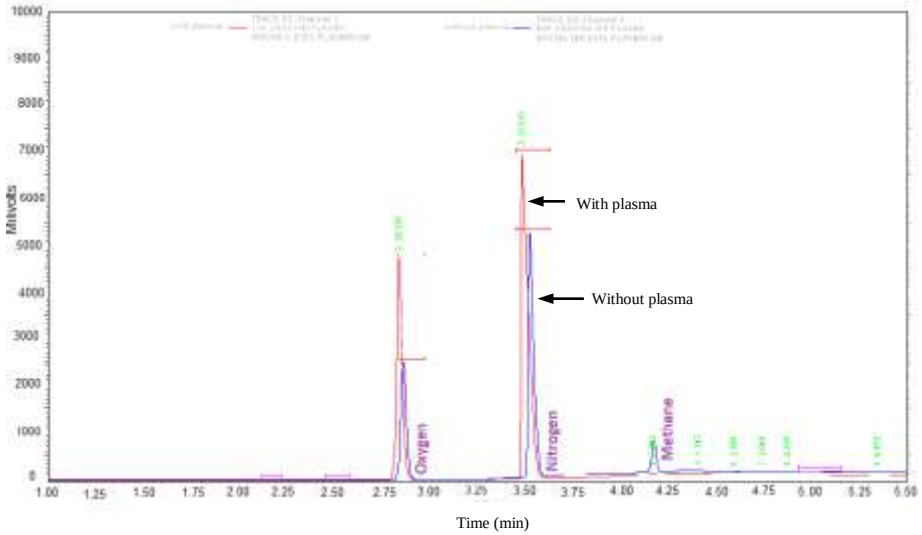

Figure 5: Gas chromatography with and without plasma treatment

Additional results from a qualitative analysis are showed in figure 6 (a and b). A reduction of NO and CH_4 is visible and any acids (i.e. HCO,) cannot be observed. After the plasma treatment a formation of HCO^+, CO, C can be observed (figure 6b).The formation of H_2 is also reported in Figure 6b.

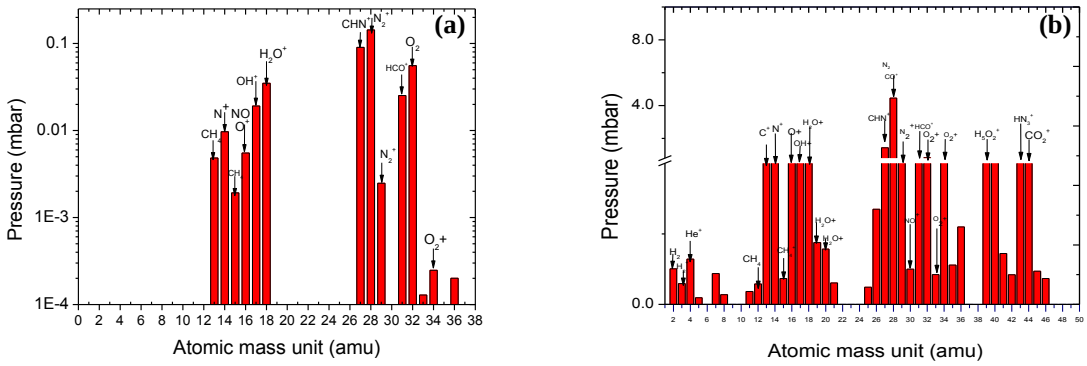

Figure 6. Mass spectra of CH_4 and NO (a) without plasma treatment (b) with plasma treatment.

From chromatographic and mass spectra results the dissociation of NO by non thermal plasma could be explained with the following reactions:

$$N_2 + e^- \rightarrow N^\bullet + N^\bullet + e^- \quad \text{.....(1)}$$

$$N^\bullet + NO \rightarrow N_2 + 1/2\,O_2 \quad \text{.....(2)}$$

OES analysis was achieved under three specific experimental conditions, plasmas with mixtures of CH_4+He (figure 7a), NO + He (figure 7b) and CH_4+NO + He (figure 7c).

In figure 7a is possible to appreciate few lines of C, H and He atoms. Any C_2 band can be appreciated between 513nm and 517nm. This band, normally knew as Swan band, is precursor of carbon nanostructures in electric arc [23]. The absence of the C_2 band is consistent with the no formation of carbon soot in the plasma reactor.

In figure 7b the spectral lines are characteristic of He plasma with NO. Atomic He and O are founded. N_2 positive band is observed between 350and 370nm.

From Boltzmann plot method the electronic temperatures calculated at 14W and 17 respectively were 2.71eV and 2.78eV. The calculation was obtaining from data of OII lines situated at 274.73nm and 340.72nm. When a mixture of NO_x and CH_4 is introduced into the He plasma, atomic lines of C almost disappear, He and N become more intense and ionized nitrogen appears. In order to maintain the stability in the plasma discharge the input power has to be increased, this could explain a better ionization of nitrogen.

In this case the electronic temperature diminishes until approximately 2eV, and it could be explained by an energy loss of electron kinetic energy by collisions to form ions. Results obtained from OES analysis illustrate the influence of power input; even if the variation in power is not significant (from 14W to 18W) the line emission considerably increases with power input, in this case the species population in excited and ionized levels growth (see figures 7a to7c).

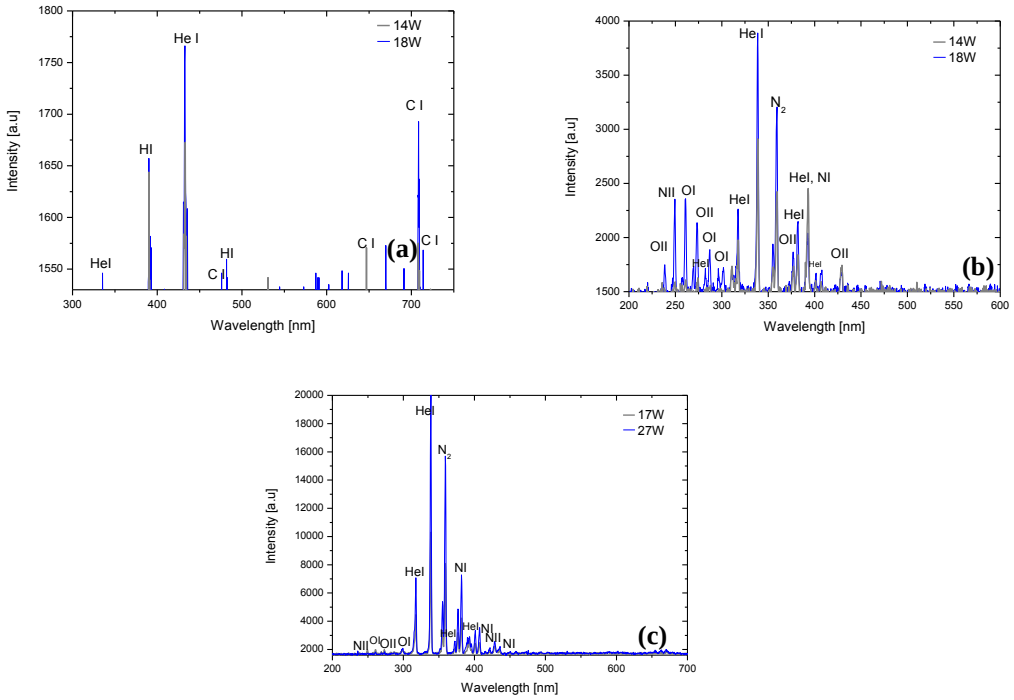

Figure 7.OES analysis. (a) He+CH_4 plasma, (b) He + NO plasma (c) He+CH_4+NO plasma

3.2.2. Removal efficiencies.

From Table 1 it can be observed that best removal efficiencies of CH_4 and NO respectively are 29% and 99% at approximately 5-6KJ/l.

At these conditions the production of H_2 and CO are relatively higher; this gas mixture has an energetic capacity of 2265kcal/m^3.Okumoto et al [22] have obtained CH_4 conversions from 5% to around 30% at SIE under 5kJ/Lin pulsed discharge plasma.

Table 1. Experimental conditions and removal efficiencies and production of CO, and H_2 (Treatment of NO-CH_4 mixture)

Voltage [V]	**I [A]**	**Pa [W]**	**NO removal (%)**	**CH_4removal (%)**	**H_2 [ppm]**	**CO [ppm]**
30	0.8	24	99.99	20	400	200
33	0.78	25.9	99.99	25	364	280
31	0.87	27	99.99	21	492	149
32	0.85	27.2	99.99	29	500	285

Additional experiments were done with an "individually" treatment of NO and CH_4. The NO removal slightly diminishes certainly due to a catalytic effect of the CH_4. The catalytic effect of hydrocarbons can be seen in [24].

The analysis was done with NO gas analyzer Horiba PG-250, using the chemiluminescence method. Methane was evaluated with the gas analyzer Gasboard 3200L method using non-dispersive infrared (NDIR). Hydrogen was quantified through the analyzer iBrid MX6, which uses the electrochemical analysis method.

Table 2: Treatment of NO and CH_4

Contaminants	Voltage [V]	I [A]	Pa [W]	Removal (%)
NO	**25**	**0.75**	**18.75**	**98**
CH_4	**21**	**0.84**	**17.64**	**23**

From the comparison between the chemical model and experiences, the prediction of NO diminution is properly explained with the mechanism proposed (figure 1). However the generation of H_2 is overestimated in the model, so at our experimental conditions the following equations [25, 26, 27] must be studied with more precision:

$$e + CH_4 \rightarrow CH_2 + H_2 + e \quad (3)$$
$$e + CH_4 \rightarrow CH + H_2 + H + e \quad (4)$$
$$CH_3 + H \rightarrow CH_2 + H_2 \quad (5)$$
$$H + H \rightarrow H_2 \quad (6)$$
$$O(´D) + CH_4 \rightarrow HO + CH_3 \quad (7)$$
$$CH_3 + O \rightarrow CO + H_2 + H \quad (8)$$
$$CH_3 + CH_3 \rightarrow C_2H_5 + H \quad (9)$$
$$C_2H_5 + H \rightarrow C_2H_4 + H_2 \quad (3)$$

4. Conclusions.

$O^{\bullet}$ and $^{\bullet}OH$ radicals mostly generated by O_2 and H_2O molecules play an important role in NOx removal. Results obtained from the model, illustrate that the main path for the NO removal is the oxidation to NO_2 and, soon after, to N_2 and HNO_3.

Results of the numerical simulation showed good agreement with experimental data of the removal process, achieving more than 99% removal of NO and 29-30% CH_4. The efficiency of removal of contaminants with non-thermal plasma is demonstrated. Concerning the diminution of CH_4 the electron impact and $^{\bullet}CH_3$ are crucial.
The removal efficiency results for the NO-CH_4 mixture depicts the feasibility to use this technology for the treatment of automotive toxic gas pollutants; whit the added value of obtaining products with a high energetic value (formation of CO and H_2)

Acknowledgements. The presentation of this work was financially supported by COMECYT– Gobierno del Estado de México 2009 CO2-131982, SENER CONACyT127499 and ININ EA-002 2013. Thanks to CONACyT for the scholarship 71674.

References

[1] Norma oficial mexicana nom-020-SSA1-1993. "Salud ambiental. criterio para evaluar la calidad del aire ambiente, con respecto al ozono (O_3). valor normado para la concentración de ozono (O_3) en el aire ambiente, como medida de protección a la salud de la población".
[2] Secretaria del medio ambiente, Inventario de emisiones de contaminantes tóxicos en la ZMVM, 2006,67–92.
[3] Programa para mejorar la calidad del aire de la zona metropolitana del valle de México 2002–2010, Informe Ejecutivo de Avances, Secretaria del Media Ambiente y Recursos Naturales, 2004, 5–20.
[4] I. Ferris, J. Tortajada, I Garcia, J Castell, A López, Diseases associated to the atmospheric contamination by fossil fuels, Journal Specialist Pediatric, No. 2006, 12, Vol. 57, 213–225
[5] Lee, H.S., W.F.J. Vermaas B.E. Rittmann, "Biological Hydrogen production: prospects and challenges", Trends Biotechnology, 2010, 28, pp.262-271.
[6] S. Woo, J Park, Y Kim, S Hong, Numerical study on influence of barrier arrangements on dielectric barrier discharge characteristics, IEEE Transactions on Plasma Science, 2003,No. 4, Vol. 31, 504 – 510
[7] H Moreno, M Pacheco, J. O Pacheco, C. E Torres, J. A Díaz, Modeling and Experimental Study on Nitric Oxide Treatment Using Dielectric Barrier Discharge, IEEE Transactions on Plasma Science, 2007,No. 5, Vol. 35, 1533–1540
[8] M Pacheco, J Pacheco, H Moreno, A Santana, Application of non-thermal plasma on gas cleansing, Physical Script a, 2008,No.23 ,Vol. 131, 114–117
[9] Y Kim, S Woo, S Hong, H Young, Comparative study of pulsed corona and dielectric barrier discharges using single-streamer modeling and NO decomposition experiment, IEEE Transactions on Plasma Science, 2000,No. 5, Vol. 22, 305–309
[10] M Pacheco, J Pacheco, H Moreno, A Mercado, R Valdivia, A Santana, OES Analysis in a Nonthermal Plasma Used for Toxic Gas Removal: Rotational and Excitation Temperature Estimation, Laser Physics, 2008,No. 3, Vol. 18, 303–307
[11] M Pacheco, J Pacheco, H Moreno, J Diaz, A Mercado, M Yousfi, DBD-Corona Discharge for Degradation of Toxic Gases, Plasma Science and Technology, 2007,No. 6, Vol. 9, 682 –685
[12] R Valdivia, Efecto de la frecuencia de excitación en la conductividad eléctrica de gases ionizados: Estudio y desarrollo electrotécnico, Tesis de Doctorado, Instituto Tecnológico de Toluca, México, 2008, 69-75.
[13] J Lowke, R Morrow, Theoretical analysis of removal of oxides of sulfur and nitrogen in pulsed operation of electrostatic precipitators, IEEE Transactions on Plasma Science, 1995,No. 4, Vol. 23, 661–671
[14] H Moreno, M Pacheco, J Pacheco, C Torres, J Diaz, Modeling and experimental study on nitric oxide treatment is using dielectric barrier discharge, IEEE Transactions on Plasma Science, 2007,No. 5, Vol. 35, 1533–1540.
[15] S. Rauf and M.J. Kushner, "Dynamics of a coplanar-electrode plasma display panel cell", J. Appl. Phys., 1999,Vol. 85, pp.3460-3469.
[16] J. W. Shon and M.J: Kushner, "Excitation mechanism and gain modeling of the high-pressure atomic Ar laser in He/Ar mixtures", J. Appl. Phys. 1994, Vol. 75, pp. 1883-1890.
[17] T.J. Sommerer and M.J.Kushner; "Numerical investigation of the Kinetics and Chemistry of RF glow discharge plasmas sustained in He, N2, O_2, He/N_2/O2, He/CF_4/O_2 and SiH_4/NH3 using a monte carlo fluid hybrid model"; J. Appl. Phys., 1992,Vol. 71, pp. 1654-1673.
[18] Xiaohui Yuan and Laxminavayan L. Raja, "Computational study of capacitive coupled high-pressure glow discharges in Helium", IEEE, Transactions on plasma science, 2003, Vol. 31, No.4, pp. 495-503.
[19] Indarto Antonius, Choi Jae-Wook, Lee Hwaung & Song Hyung Keun, "The kinetic studies of direct methane oxidation to methanol in the plasma process; Chinese Science Bulletin, September 2008, Vo. 53, No. 18, pp 2783-2792.
[20] Tomohiro Nozaki, Ken Okazaki, Non-thermal plasma catalysis of methane: Principles, energy efficiency, and applications. Catalysis Today 211, 2013, 29– 38
[21] R. Atkinson, "Evaluated kinectic and photochemical data for atmospheric chemistry. Atmos. Chem. Phys.,2006 Vol. 6, pp 3625-4055.
[22] R Valdivia Barrientos, J Pacheco Sotelo, M Pacheco Pacheco, J S Benítez Read, R López Callejas, Analysis and electrical modelling of a cylindrical DBD configuration at different operating frequencies, Plasma sources science & technology, 2006, No. 2, Vol. 15, 237–245
[23] Pacheco, PhDThesis, Synthèse des nanotubes de carbone par arc électrique. Paul Sabatier. France, 2003, 45-58
[24] A.Khacef, P. Da Costa, GDjéga-Mariadassou, Plasma assisted catalyst for NOx remediation from lean gas exhaust, Journal of Engineering And Technology Research, 2013, 1 (1):112-122
[25] Okumoto, M. Hyun Ha Kim ; Takashima, K. ; Katsura, S. ; Mizuno, A. Reactivity of methane in nonthermal plasma in the presence of oxygen and inert gases at atmospheric pressure Industry Applications, IEEE Transactions., 2002,Volume:37 , Issue: 6 1618 – 1624.
[26] M. Garduño, M. Pacheco, J.Pacheco, R. Valdivia, A. Santana, B. Lefort, N. Estrada,C. Rivera, Hydrogen production from methane conversion in a gliding arc, Journal Of Renewable And Sustainable Energy ISSN:,2012, 1941-7012 4, 021202.
[27] Antonius Indarto, Nowarat Coowanitwong, Jae-Wook Choi, Hwaung Lee, Hyung Keun Song, "Kinetctic modeling of plasma methane conversion in a dielectric barrier discharge", Fuel Processing Technology, 2008,Vol. 89, pp-214-219.
[28] Kramida, A., Ralchenko, Yu., Reader, J., and NIST ASD Team (2013). *NIST Atomic Spectra Database* (ver. 5.1), [Online]. Available: http://physics.nist.gov/asd [2014, July 8]. NationalInstitute of Standards and Technology, Gaithersburg, MD.

Synthesis and Characterization of Chitosan-Starch as Electrolyte with MWNTs Reinforced for Lithium Batteries

Y. Estévez-Martínez[1,2], C. Guzmán-Martínez[2], D. Alaníz-Lumbreras[3], M. Mendoza-Duarte[4], V.M. Castaño[5], S.M. Durón-Torres[2],*.

[1]Nano Coating Technologies SA de CV, Paseo de las Palmas 555, Miguel Hidalgo, Distrito Federal, México, 11000.
[2]U. A. Cs. Químicas, Universidad Autónoma de Zacatecas, CU Siglo XXI Edificio 6, Km 6 Carr. Zac-Gdl, Zacatecas, Zac., México, 96160.
[3]Fac. de Ing. Eléctrica, Universidad Autónoma de Zacatecas, Avenida Ramón López Velarde No. 801, Zacatecas, Zac., México, 98000.
[4]Centro de Investigación en Materiales Avanzados CIMAV, Ave. Miguel de Cervantes 120, Chihuahua, Chih., México, 31109.
[5]Centro de Física Alicada y Tecnología Avanzada, Universidad Nacional Autónoma de México, Blvd. Juriquilla 3001, Querétaro, Qro., México, 76230.
*Tel.: +524929256690 ext 4655, duronsm@prodigy.net.mx

ABSTRACT

In recent years it has been reported that solid electrolytes may be considered promising materials for storing energy, due to their unique properties, such as high ionic conductivity, physical flexibility and their ability to provide good electrode / electrolyte contact. Compared to the liquid state, the production of leak and gas formation during the decomposition of the solvent is avoided, in addition to being compact, lightweight and safe.

In this work is reported the synthesis and the physical and electrochemical characterization of chitosan-starch polymers modified with carbon nanotubes and lithium. The structural and physicochemical properties of the polymers were characterized by Dynamical Mechanical Analysis, FTIR and Raman spectroscopy. The electrical and electrochemical properties were then determined by using Electrochemical Impedance Spectroscopy and Conductivity Measurements. The results obtained indicate that the polymeric material is a viable candidate to be used as electrolyte for lithium batteries.

Keywords: Nanocomposite-Biopolymer; Electrolyte; Lithium Batteries.

1. Introduction.

A polymer electrolyte can be defined as a membrane having transport properties comparable with those of common ionic liquids solutions [1]. The electrolyte is the heart of a cell which separates the electrodes upon the occurrence of an electrochemical reaction through the conduct of an ion in specific from one electrode to another at high operating speeds in the cell, where transport should be fast and highly selective, but these properties are often in conflict with each other. Proton conductive materials are used as electrolyte fuel cells of low and medium temperature and are attracting great interest [2]. That is, the high ionic conductivity requires an electrolyte, but is often inversely proportional to its mechanical strength. This represents a challenging paradigm for the design of new multifunctional materials focused on engineering [3]. Complexes between lithium salt form classic examples used as electrolyte membranes, LiX, $LiClO_4$ or $LiN(CF_3SO_2)_2$ and a high molecular weight polymer containing groups coordinated with Li^+. Examples of these polymers are: poly (ethylene oxide), poly (propylene oxide) poly (bis (methoxy ethoxyethoxide)-phosphazene), poly (dimethyl siloxane), poly (acrylonitrile), poly (methyl methacrylate), poly (vinyl chloride) and poly (vinylidene fluoride) [1,4]. All polymers referred above relate to monomeric chains that are difficult to degrade, causing a big problem of pollution to environment. For these reason it has been great interest to perform research on natural polymers (carbohydrates) that by their nature are naturally degraded to a certain time. Such polymers are commonly called biopolymers.

These biopolymers, according to a review on the use of these polymers as electrolytes a like to cellulose, starch, chitosan, agar, pectin and gelatin were used [5]. However, the use of chitosan an starch were studied for different authors [6–15], where the properties and characteristics are explained in detail, but only some papers have published their use as matrix in the carbon nanotube reinforcement[9,16–18], but the most important is know the use of the biopolymer like to electrolyte, where its use is currently very fertile field of research forward [5,19–22].

2. Experimental.

Multiwalled carbon nanotubes (MWNTs) were obtained from Sun Nanotech Co., which produced them by chemical vapor deposition, with a diameter from 10 to 30 nm and 1 to 10 μm long, with a purity >90% and surface area of 90 to 350 m^2/g[23]. The other reactive were purchased from Sigma-Aldrich Co. LLC., and used without further purification.

Based on previous reports [24–29], the purification/oxidation of the MWNTs was achieved in liquid phase with a 3:1 mix of NHO_3 (95%) and H_2SO_4 (98%) at 85º C for 3 h in a reflow process. The resulting material was vacuum-washed to a neutral pH with deionized water. For the lithiated-nanotubes, according to a report by The Naval Academy, Annapolis [30], the following method is proposed: 25 ml at 6:1 w/w MWOHs to LiOH were mixed and reacted at reflux to 75º C by 2h (RLi) and sonicated by 2 h (SLi), respectively. On the other hand, according to previous research [7,10,22,31–34], experimental methodology suggested for the synthesis of starch-chitosan film (ChSt) to 1:1 at 2% m/v: the chitosan solution (2% m / v) was prepared by dispersing 2 g of chitosan in 100 ml of acetic acid solution (1% v / v), then stirred mechanically at 100 rpm. After the chitosan is completely dispersed, sonicated for 15 minutes to break any air bubbles present, then allowed stand until homogenous solution. The aqueous starch solution (2% m/v) was prepared by heating above its gelatinization temperature[35], of 90 ± 2° C

by 20 min with mechanical stirring. During this time, the glycerin (1% v/v) was added to final cooling to room temperature with mechanical stirring. The films were dried chitosan-starch deposited on a polystyrene mold at room temperature in an extraction hood for 24 h. After this time, the corresponding characterizations were made. To reinforce the electrolyte: MWNTs (ChStMW), MWOHs (ChStOH), lithiated-nanotubes by reflux (ChStRLi) and sonicated (ChStSLi) were used with a 0.025% w/v with at biopolymer respect.

Infrared (FTIR) spectra were recorded in a Vector 33 Bruker spectrophotometer at 32 scans, with a resolution of 4 cm^{-1}. Solid samples were embedded in KBr disks. Raman spectra were recorded in a Micro-Raman Dilor with a resolution of 515 cm^{-1}, with a 514.5 nm laser with 15 s of integration time. The analyses X-ray Photoelectron Spectrometer (XPS) were performed with a JPS-9200 Photoelectron Spectrometer (ESCA). Dynamic mechanical analysis (DMA) were recorded in a TA instruments, RSA III model, were run using tweezers to tension in a temperature range from 30 ° C to 350 ° C. In all the samples using a frequency of 1.0 Hz. The electrical conductivity of the membranes was measured by a standard four-probe method on a milliohm-meter (Agilent 4338B Milliohm Meter 1kHz) at room temperature, where the equipment was calibrated with platinum and gold pure that knowing the theoretical resistivity of the two materials ($10.6x10^{-8}$ Ωm and $2.44x10^{-8}$ Ωm respectively [36]), a geometric factor was obtained (1.063 a.u.).

. The electrochemical measurements were performed using an EG&G PAR VersaSTAT 3 Potentiostat/Galvanostat, where electrochemical impedance spectroscopy (EIS) experiments were carried out in the potentiostatic mode in the 1 MHz to 1Hz frequency range. The impedance spectra were registered with a logarithmic data collection scheme at 10 steps per decade at the open-circuit potential (0.22 V) with alternate signal amplitude of 10 mV.

3. Results and discussion.

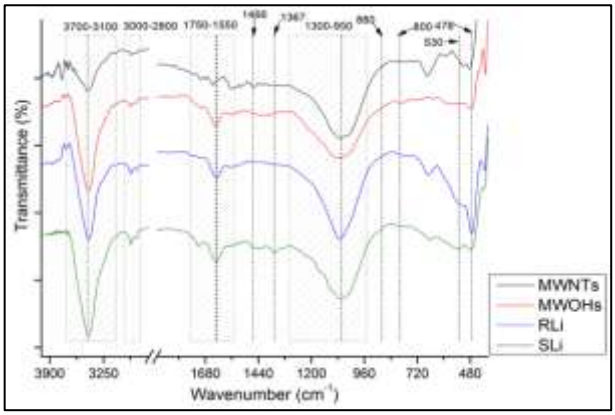

Figure 01. FTIR of nanotubes oxidized and lithiated.

Regardless of the characteristic FTIR peaks of the carbon nanotubes, that describe at normal modes of vibration at ~1632 cm^{-1} for E_{1u} and ~800 cm^{-1} for A_{2u} in multiwall carbon nanotubes (MWNTs), confirmed by different authors[37–41] and increases in other bands that identify in the oxidation of

multiwall oxidized carbon nanotubes (MWOHs) as between 1750—1550 cm^{-1} for ν(C=O), 1466 cm^{-1} for δ(O-H) and between 1300—950 cm^{-1} for ν(C-O) due to vibrations of the carboxyl groups, 3443 cm^{-1} for isolated surfaces of ν_s(OH)[41–44], the presence of lithium in the samples, was measured according to the interaction with the oxygen and carbon to generate electrostatic bonds with the metal, thus, according with some authors[45–50], The molecular vibration bands, suggest the presence of $ROCO_2Li$, Li_2O, Li_2CO_3, ROLi and LiOH are appreciated. For lithium hydroxide, is visible the O-H band at 3700-3100 cm^{-1}, these bands are broader than MWOHs for the same range of wave number. For st(C-H) at 3000-2800 cm^{-1} and st(C-O) at 1064 cm^{-1}, corresponding to $ROCO_2Li$ and ROLi respectively, where st(Li-O) of the Li_2O is visible at 530 and 476 cm^{-1} too. In addition, the C-O band at 880 cm^{-1} of the Li_2CO_3, is caused by the intensity strong of the band like an arm weak. Finally, the bending vibrations CH_2 at 1466 cm^{-1} and C=O like a symmetric at 1628 cm^{-1} and asymmetric at 1367 cm^{-1} vibrations, indicate the presence of $ROCO_2Li$. In the Figure 01 shows the comparative, where all the vibrations of the nanotubes with lithium are present.

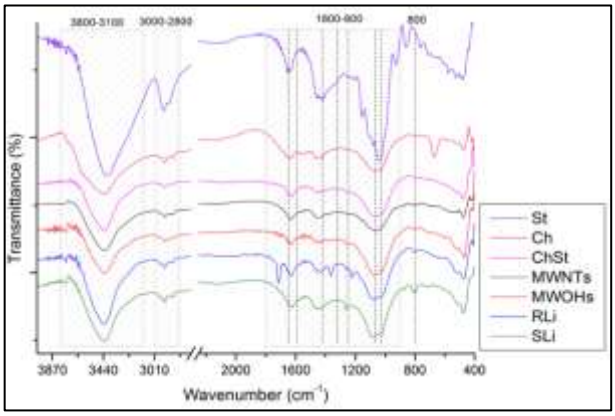

Figure 02. FTIR of starch (St), chitosan (Ch) and chitosan-starch (ChSt). ChSt are reinforced with nanotubes oxidized and lithiated.

For the nanocomposites Chitosan-Starch as matrix and with different reinforcements (Carbon nanotubes with lithium), the FTIR spectrum is presented in Figure 02. For starch at 3274 cm^{-1} the st(O-H) of the glycosidic chains, are present. Addition to this band, at 2921 y 2926 cm^{-1} is because the st(CH) are associated with the ring methine hydrogen atoms [14,51–53]. For chitosan, at 3496 cm^{-1} is due to OH group (ν_{OH}), at 3345 cm^{-1} is due to NH group-stretching vibration (ν_{NH}), at 2926, 2873, 1421, 1322 and 1249 cm^{-1} is due to symmetric or asymmetric CH_2 stretching vibration attributed to pyranose ring (ν_{CH}), at 1646 cm^{-1} is due to C=O in amide groups (amide I band), at 1593 cm^{-1} is due to NH_2 bending vibration in amino group (δ_{NH2}), at 1421 and 1322 cm^{-1} is due to vibrations of OH, CH in the ring, at 1381 cm^{-1} is due to CH_3 in amide group, at 1249 cm^{-1} is due to C—O group, 1156 cm^{-1} is due to —C—O—C— in glycosidic linkage, 1096 and 1030 cm^{-1} is due to C—O group ($\nu_{C—O}$) in amide group and, 897 cm^{-1} is due to CH_3COH group, are presents [54–56]. When mixing both polymers (Chitosan-Starch), there is a widening with respect to chitosan in the OH band due to the presence of starch, in addition to amide and amines groups, which characterize the chitosan [14,34,52,53]. Due to the very low concentration reinforcement in the matrix, the characteristics bands of carbon nanotubes with lithium are very weak,

however, come to appreciate some of them, like those that have been described to be characterized and discussed by this technique.

The Raman spectroscopy was used to characterize MWNTs, MWOHs and lithiated-nanotubes (RLi and SLi), where the graphic shows in the Figure 03 and tabulated in the same Figure. For many authors, Raman spectroscopy is considered as the fingerprint of carbon nanotubes[57–63], that's why is very important make a deep analysis on the oxidation, purification and modification in the structure of the outer walls of carbon nanotubes. In Raman spectroscopy, the peaks to ~1570 cm^{-1} (G band), ~1340 cm^{-1} (D band) and ~2684 cm^{-1} (G' band) were studied and have been analyzed by different authors [43,61,63–72]. To verify the oxidation/purification of the multiwall carbon nanotubes (from MWNTs to MWOHs), some publications [73,74] consider the G band (≈1590 cm^{-1}) as an indicator of purity due to the excellent graphitic orientation that this represents in the carbonaceous materials by its sp^2 hybridization, free of broken links or other hybridizations present including sp^3, however, other papers[75,76], they evaluate the purity of carbon nanotubes with the D band (≈1350 cm^{-1}), because it is sensitive to the carbonaceous impurities and structural defects in the graphitic sp^2 networks samples (this contrary to the G band), therefore, we can conclude that the relationship between the intensities of these two bands is related to the purity of carbon nanotubes, but with the disadvantage, according to Anne C. Dillon[76], that only not the intensity is important, the full-width-at-half-maximum (FWHM) of the D band is much broader than that of the nanotube D-band, from 86 cm^{-1} a 57 cm^{-1} of graphite to 42cm^{-1} a 17 cm^{-1} of carbon nanotubes. The G' band, according to Roberta A. DiLeo[77], its intensity is proportional to the purity of the multiwall carbon nanotubes due to the absence of nano-carbons (disordered phase) in the samples. For all the reasons described above, in this work, we related the areas of the G'/G, G'/D and D/G bands to find a relationship purity of carbonaceous material and presence of intercalated lithium. The dimensionless values areas of G, D and G' bands and the relationship of them, suggest the carbonaceous purification of MWNTs at the oxidation with acids MWOHs due to the decrease in the ratio D/G and the increase in the ratio G'/D and low difference G'/G by the removal of carbonaceous material.

Sample	D	G	G'	G'/G	G'/D	D/G
MWNTs	72,068	79,955	81,314	1.02	1.13	0.90
MWOHS	40,546	52,738	51,791	0.98	1.28	0.77
RLi	64,666	80,951	77,683	0.96	1.20	0.80
SLi	98,968	117,520	108,288	0.92	1.09	0.84

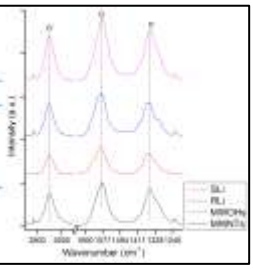

Figure 03. Raman spectroscopy of nanotubes oxidized and lithiated with the relationship of the characteristic area bands of nanotubes oxidized and lithiated in Raman.

For the samples intercalated with lithium show a drop in G'/D regarding oxidized nanotubes due to the increased area of the G' band because of the exfoliating action through basic lithium hydroxide which degrades carbonaceous materials[78,79], making more active nanotubes walls[80] but that also increases the band D for the lithium intercalated in the walls that in the center of the tube that is less favorable because of the strong core repulse between Li ions and carbon inner walls[81]. Furthermore, the

most important is the significant increase of the G, band that could be assigned to the lithiated carbon nanotubes, according to various publications [81–88].

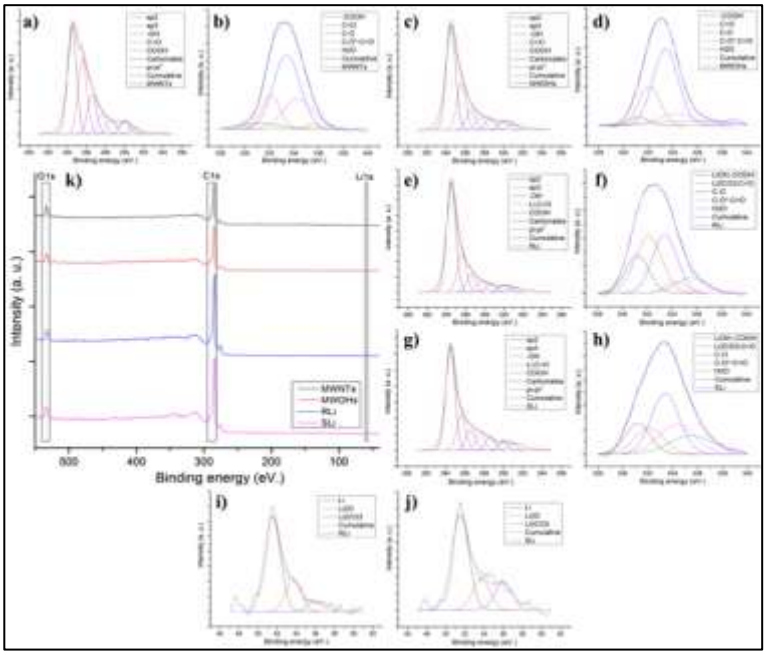

Figure 04. XPS of MWNTs, MWOH, RLi and SLi samples of C_{1s} (a), c), e) and g) respectively), O_{1s} (b), d), f) and h) respectively) and Li_{1s} in i) and j) of RLi and SLi, respectively.

X-ray photoelectron spectroscopy was used for quantify the lithium on multiwall oxidized carbon nanotubes with respect to carbon and oxygen. Binding energy ranges for carbon (C1s) at 295-281 eV, oxygen (O1s) at 540-528 eV and lithium (Li1s) at 61-57 eV were evaluated. For C1s and O1s there are different focus to determine the energy levels in which the molecules related to these two elements can occur. The deconvolution of C1s, O1s and Li1s peaks [48,89–92]. C1s peak at 284.5 eV shows sp2 hybridization for CH_3OLi, at 285.6 eV shows sp3 hybridization for CH_3CH_2OLi, at 286.6 eV shows the hydroxyl groups of oxidized carbon nanotubes with not relation with lithium, at 287.6 eV for carbonyl C=O in CH_3OCO_2Li, at 288.6 eV shows the carboxyl groups —COOH of oxidized carbon nanotubes with not relation with lithium, at 290 eV shows lithium carbonate and finally, at 290.9 eV shows electronic transitions π-π* with not relation with lithium but is a characteristic special in the walls of carbon nanotubes. O1s peak at 531.2, 532.1, 533.4, 534.3 and 535.5 eV correspond to LiOH, O=C of Li_2CO_3, O—C of $ROCO_2Li$, C—O*-C=O and H_2O respectively. Li1s peak at 51.5 eV and 53.7 eV for Li_2O and at 56 eV for lithium carbonate (Li_2CO_3). The Figure 04 shows the percent of deconvolution in each band. In C1s, the hydroxyl (—OH at 286.6 eV) and carboxyl (—COOH at 288.6 eV) band of lithiated nanotubes are higher than oxidized nanotubes, thus as the carbonate band (290.0 eV) probably to lithium carbonate on nanotube walls. The increase of the electronic transitions (π-π* at 290.9 eV) in oxidized carbon nanotubes suggests that there is to exfoliation walls due to acids[41], however, there is a decrease in the lithiated nanotubes suggests a non covalent interaction among them. Removing carbonaceous material is reflected in the hybridization of the carbon atoms of the nanotubes (sp^2 at 284.5 eV and sp^3 at 285.6 eV),

reflecting the same behavior as G and D bands Raman. In O1s, according is oxidized and lithium intercalates in the walls of carbon nanotubes, carboxyl, carbonyl and carbonate bands (—COOH at 531.2 eV, O=C at 532.1 eV and C—O*—C=O at 534.3 eV) increases. The carbonate is confirmed in Li1s (Li2CO3 at 56 eV), however, the greater amount of lithium is manifested as a strong electrostatic interaction of lithium ions due to a decrease in the peak transitions in C1s (π-π* at 290.9 eV) and the increase in lithium ions band (51.5 eV)[89].

Scanning electronic microscopy (SEM) and dynamic mechanical analysis (DMA), were used to characterize at the electrolyte with MWNTs and MWOHs as reinforcement, since the purpose of these characterizations, it is to know the ability of carbon nanotubes in the polymeric matrix for scattering, regardless of the lithiation of the carbon nanotubes. DMA can be categorized as a thermo-mechanical test because data are obtained corresponding to the viscoelastic nature of the material at different temperatures. Some of the general purpose DMA are determine the storage modulus and heat dissipation of viscoelastic materials over time spectrum (frequency) by temperature and strain, detecting transitions and change variables associated with each other in the viscoelastic properties to relate structure—property [93,94].

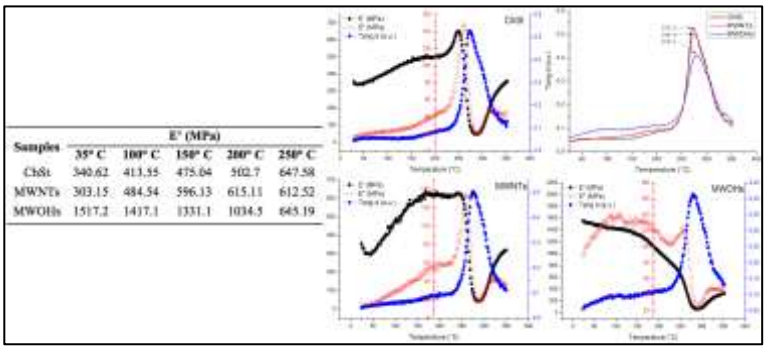

Samples	E' (MPa)				
	35° C	100° C	150° C	200° C	250° C
ChSt	340.62	413.55	475.04	502.7	647.58
MWNTs	303.15	484.54	596.13	615.11	612.52
MWOHs	1517.2	1417.1	1331.1	1034.5	645.19

Figure 05. DMA of ChSt and nanocomposites reinforced with MWNTs and MWOHs. Also, the elastic modulus at different temperatures tabulated.

The graph of the elastic modulus E', the material ability to store energy was evaluated at five different temperatures (35°, 100°, 150°, 200°, and 250° C) where the samples have a viscoelastic behavior to its degradation. The results are tabulated and showed in Figure 05, where is visible the ability of the MWOHs for increase the elastic modulus up to 445.4% to 35ºC, where still 200º C the elastic module up to 205.8% grater than with respect to the original matrix of chitosan-starch. With MWNTs, the elastic modulus of material is practically the same.

The loss modulus (E") related to the liquid-like, reflecting the viscous behavior of the nanocomposite and the glass transition temperature of the material (tg), where in the same Figure 05 is evident the increase of the chitosan-starch film with multiwall oxidized carbon nanotubes reinforcement. Here is possible to view a null activity of MWNTs in the biopolymer matrix.

In the nanocomposite, the energy dissipation is manifested as an internal friction of the material, where a friction between the reinforcement and the matrix is developed. The internal friction can be

determined by the relationship between the loss and stored energy, known as tangent delta. The amount of internal energy dissipated in the interface depends on the degree of adhesion between the phases, where an adhesion charge/weak matrix promotes high internal friction which is reflected in higher values of delta tangent (Tang δ).

With Tang δ, suggest that the nanocomposite with MWNTs as reinforcement does not show a significant difference in the coefficient of dispersion, however, to oxidize (MWOHs) have a lower coefficient of dispersion. This infers that has a good interface between the materials, since the internal friction between polymer chains has greatly decreased due to the hydrogen bonds generated between the functional groups of the carbon nanotubes with the amino and hydroxyl groups of the chitosan matrix-starch, which limits its mobility and, therefore, reduces its friction. Thus, not only nanotubes oxidized carbon help in the mechanical properties of the polymer, but also on its thermal properties, since the glass transition temperature is significantly increased from 272º C to 279º C, are 7° C improvement.

The electrical and ionic conductivity values are tabulated in the Figure 07. Is possible see that the electrical conductivity is affected by the reinforcement of the MWNTs and MWOHs, however, with the lithiated carbon nanotubes, the increase is insignificant, considering that there is a relationship 6:1 w/w of MWOHs with respect to LiOH and only there is a reinforcement of 0.025% m/v with respect to biopolymer. Perhaps electrical conductivity could be considered low, however, when compared with similar results, for example the use of reinforced polyaniline (semiconducting polymer) with amidized multiwall carbon nanotubes, one can see values of 0.73 S/m with relationship 1:120 of multiwall carbon nanotubes with respect to monomer[95]. For Starch–NH_4NO_3 electrolyte, was reported a conductivity of 0.00283 S/m at room temperature[96].

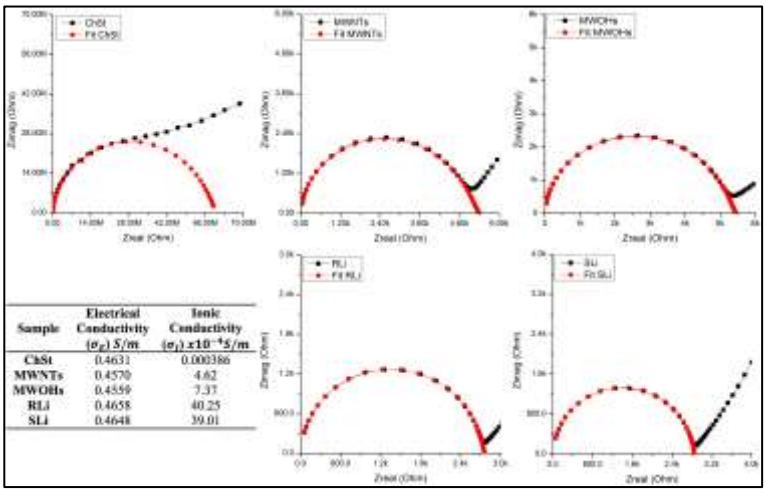

Sample	Electrical Conductivity (σ_e) S/m	Ionic Conductivity (σ_i) x10^{-4}S/m
ChSt	0.4631	0.000386
MWNTs	0.4570	4.62
MWOHs	0.4559	7.37
RLi	0.4658	40.25
SLi	0.4648	39.01

Figure 07. Nyquist plot of the membrane samples with fitted by trial and error, where is obtained R_b. Also, the electrical and ionic conductivity of the samples are showed in the same figure.

For the calculation of the ionic conductivity, the impedance spectroscopy has been widely used to characterize the nature of lithium-ion electrode processes and interfacial properties, as well as for

distinguishing individual contributions to overall cell impedance and resistivity[97,98]. From the impedance plot in the Nyquist format, the bulk resistance, R_b can be obtained at minimum Z_{im} obtained by trial and error until the experimental plot is fitted and the ionic conductivity can be calculated by substituting R_b into the equation below: $\sigma = l/(R_b A)$ where σ is the ionic conductivity, R_b is the bulk resistance, l is the thickness of the pellet and A is the cross sectional area. The bulk resistance was calculated from the high frequency intercept on the real impedance axis of the Nyquist plot[22] demonstrated in the Figure 07.

Is visible the decreasing the semicircle to be reinforced with carbon nanotubes MWNTs and MWOHs, however, with carbon lithiated nanotubes, RLi and SLi, the bulk resistance value is less. When the resistance value decreases accordingly, thus the conductivity increases when considering the cross-sectional area and thickness of the samples are considered. The prolongation of the semicircles of Nyquist plot is plotted in Figure 07. At know the ionic conductivity values of the samples, is easy to distinguish the increase of its conductivity at reinforced with carbon nanotubes, but mainly carbon lithiated nanotubes, ranging from 0.000386 to 40.25 x 10^{-4} S/m.

4. Summary and perspectives.

Conjunction with the different XPS, FTIR and Raman spectroscopies, the carbon lithiated and oxidized nanotubes were confirmed, where the interaction of the OH of LiOH are bonded with the different groups of hydroxyls and carbonyls of oxidized nanotubes is satisfactory. For scanning electros microscopy and dynamic-mechanical analysis, the MWNTs and MWOHs behavior was studied on the biopolymer ChSt matrix, where is visible the capacity of this nanostructured of improve their mechanical properties, but are the carbon lithiated nanotubes (RLi and SLi) where the electrical and ionic conductivity are enhanced, mainly its high ionic conductivity that helps propose it as an electrolyte battery.

Acknowledgments.

The authors are indebted to Dr. Genoveva Hernández-Padrón, Mrs. Carmen Vazquez, and Mrs. Alejandra Núñez Pineda of Universidad Nacional Autonoma de Mexico and Dr. Erick Cuevas Yañez and Gustavo López Téllez of Universidad Autonoma del Estado de Mexico for their technical support with the synthesis, FTIR, Raman and XPS studies. They thank the National Council of Science and Technology of Mexico (CONACyT) and FOMIX-CONACYT (ZAC-2010-C04-149908) for their financial support.

References.

[1] F. Croce, R. Curini, A. Martinelli, L. Persi, F. Ronci, B. Scrosati, et al., Physical and chemical properties of nanocomposite polymer electrolytes, J. Phys. Chem. B. 103 (1999) 10632–10638.

[2] E.L. Chávez, R. Oviedo-Roa, G. Contreras-Pérez, J.M. Martínez-Magadán, F.L. Castillo-Alvarado, Theoretical studies of ionic conductivity of crosslinked chitosan membranes, Int. J. Hydrog. Energy. 35 (2010) 12141–12146.

[3] P. Liu, E. Sherman, A. Jacobsen, Design and fabrication of multifunctional structural batteries, J. Power Sources. 189 (2009) 646–650.

[4] J.Y. Song, Y.Y. Wang, C.C. Wan, Review of gel-type polymer electrolytes for lithium-ion batteries, J. Power Sources. 77 (1999) 183–197.

[5] P.K. Varshney, S. Gupta, Natural polymer-based electrolytes for electrochemical devices: a review, Ionics. 17 (2011) 479–483.

[6] M.B. Vásconez, S.K. Flores, C.A. Campos, J. Alvarado, L.N. Gerschenson, Antimicrobial activity and physical properties of chitosan–tapioca starch based edible films and coatings, Food Res. Int. 42 (2009) 762–769.

[7] F.M. Pelissari, M.V. Grossmann, F. Yamashita, E.A.G. Pineda, Antimicrobial, mechanical, and barrier properties of cassava starch–

chitosan films incorporated with oregano essential oil, J. Agric. Food Chem. 57 (2009) 7499–7504.
[8] Y.X. Xu, K.M. Kim, M.A. Hanna, D. Nag, Chitosan–starch composite film: preparation and characterization, Ind. Crops Prod. 21 (2005) 185–192.
[9] K.Y. Castrejón-Parga, H. Camacho-Montes, C.A. Rodríguez-González, C. Velasco-Santos, A.L. Martínez-Hernández, D. Bueno-Jaquez, et al., Chitosan–starch film reinforced with magnetite-decorated carbon nanotubes, J. Alloys Compd. (2014).
[10] S. Chillo, S. Flores, M. Mastromatteo, A. Conte, L. Gerschenson, M.A. Del Nobile, Influence of glycerol and chitosan on tapioca starch-based edible film properties, J. Food Eng. 88 (2008) 159–168.
[11] M.A. Garcia, A. Pinotti, N.E. Zaritzky, Physicochemical, water vapor barrier and mechanical properties of corn starch and chitosan composite films, Starch- Stärke. 58 (2006) 453–463.
[12] H. Liu, R. Adhikari, Q. Guo, B. Adhikari, Preparation and characterization of glycerol plasticized (high-amylose) starch–chitosan films, J. Food Eng. 116 (2013) 588–597.
[13] C. Bangyekan, D. Aht-Ong, K. Srikulkit, Preparation and properties evaluation of chitosan-coated cassava starch films, Carbohydr. Polym. 63 (2006) 61–71.
[14] T. Bourtoom, M.S. Chinnan, Preparation and properties of rice starch-chitosan blend biodegradable film, LWT - Food Sci. Technol. 41 (2008) 1633–1641.
[15] A. Lazaridou, C.G. Biliaderis, Thermophysical properties of chitosan, chitosan–starch and chitosan–pullulan films near the glass transition, Carbohydr. Polym. 48 (2002) 179–190.
[16] L. Yan, P.R. Chang, P. Zheng, Preparation and characterization of starch-grafted multiwall carbon nanotube composites, Carbohydr. Polym. 84 (2011) 1378–1383.
[17] M.V. Deepthi, G.S. Ananthapadmanabha, P. Sampathkumaran, S. Seetharamu, V.V. Pattenshetti, S. Ganga, et al., Preparation of bio-nanocomposites of chitosan/thermoplastic starch reinforced with multiwalled carbon nanotubes, in: Prop. Appl. Dielectr. Mater. ICPADM 2012 IEEE 10th Int. Conf. On, IEEE, 2012: pp. 1–4.
[18] F. Xie, E. Pollet, P.J. Halley, L. Averous, Starch-based nano-biocomposites, Prog. Polym. Sci. 38 (2013) 1590–1628.
[19] Y.M. Yusof, M.F. Shukur, H.A. Illias, M.F.Z. Kadir, Conductivity and electrical properties of corn starch–chitosan blend biopolymer electrolyte incorporated with ammonium iodide, Phys. Scr. 89 (2014) 035701.
[20] M.F. Shukur, N.A. Majid, R. Ithnin, M.F.Z. Kadir, Effect of plasticization on the conductivity and dielectric properties of starch–chitosan blend biopolymer electrolytes infused with NH4Br, Phys. Scr. 2013 (2013) 014051.
[21] M.F. Shukur, R. Ithnin, M.F.Z. Kadir, Electrical properties of proton conducting solid biopolymer electrolytes based on starch–chitosan blend, Ionics. (2013) 1–23.
[22] Y.N. Sudhakar, M. Selvakumar, Lithium perchlorate doped plasticized chitosan and starch blend as biodegradable polymer electrolyte for supercapacitors, Electrochimica Acta. 78 (2012) 398–405.
[23] Sun, X., Zeng, X., Cheng, G., Sun Nanotech Company, Sun Nanotech Co Ltd. (2013). http://www.sunnano.com/.
[24] Z. Spitalsky, D. Tasis, K. Papagelis, C. Galiotis, Carbon nanotube–polymer composites: chemistry, processing, mechanical and electrical properties, Prog. Polym. Sci. 35 (2010) 357–401.
[25] S. Osswald, M. Havel, Y. Gogotsi, Monitoring oxidation of multiwalled carbon nanotubes by Raman spectroscopy, J. Raman Spectrosc. 38 (2007) 728–736.
[26] C.-E. Hong, J.-H. Lee, P. Kalappa, S.G. Advani, Effects of oxidative conditions on properties of multi-walled carbon nanotubes in polymer nanocomposites, Compos. Sci. Technol. 67 (2007) 1027–1034.
[27] H. Yu, Y. Jin, F. Peng, H. Wang, J. Yang, Kinetically controlled side-wall functionalization of carbon nanotubes by nitric acid oxidation, J. Phys. Chem. C. 112 (2008) 6758–6763.
[28] J. Zhang, H. Zou, Q. Qing, Y. Yang, Q. Li, Z. Liu, et al., Effect of chemical oxidation on the structure of single-walled carbon nanotubes, J. Phys. Chem. B. 107 (2003) 3712–3718.
[29] T.-C. Hung, C.-F. Chen, M. Chen, C.-C. Chen, Quantitative limitation of active site and characteristics of chemical oxidized well-aligned carbon nanotubes, Thin Solid Films. 516 (2008) 5236–5240.
[30] J.R. Jaunsen, The Behavior and Capabilities of Lithium Hydroxide Carbon Dioxide Scrubbers in a Deep Sea Environment., Naval Academy Annapolis MD, 1989.
[31] J. Ai, M. Rezaei-Tavirani, E. Biazar, K.S. Heidari, R. Jahandideh, Mechanical properties of chitosan-starch composite filled hydroxyapatite micro-and nanopowders, J. Nanomater. 2011 (2011) 16.
[32] M.O. Tuhin, N. Rahman, M.E. Haque, R.A. Khan, N.C. Dafader, R. Islam, et al., Modification of mechanical and thermal property of chitosan–starch blend films, Radiat. Phys. Chem. 81 (2012) 1659–1668.
[33] L. You, F. Lu, D. Li, Z. Qiao, Y. Yin, Preparation and flocculation properties of cationic starch/chitosan crosslinking-copolymer, J. Hazard. Mater. 172 (2009) 38–45.
[34] A. Espíndola-González, A.L. Martínez-Hernández, F. Fernández-Escobar, V.M. Castaño, W. Brostow, T. Datashvili, et al., Natural-Synthetic hybrid polymers developed via electrospinning: The effect of PET in chitosan/starch system, Int. J. Mol. Sci. 12 (2011) 1908–1920.
[35] H. Liu, L. Yu, K. Dean, G. Simon, E. Petinakis, L. Chen, Starch gelatinization under pressure studied by high pressure DSC, Carbohydr. Polym. 75 (2009) 395–400.
[36] Sigma-Aldrich Co. LLC., Sigma-Aldrich Co. LLC., MSDS Search Prod. Saf. Cent. (2014). http://www.sigmaaldrich.com/safety-center.html.
[37] T. Belin, F. Epron, Characterization methods of carbon nanotubes: a review, Mater. Sci. Eng. B. 119 (2005) 105–118.
[38] U. Kuhlmann, H. Jantoljak, N. Pfänder, P. Bernier, C. Journet, C. Thomsen, Infrared active phonons in single-walled carbon nanotubes,

Chem. Phys. Lett. 294 (1998) 237–240.
[39] A. Aqel, K.M. El-Nour, R.A. Ammar, A. Al-Warthan, Carbon nanotubes, science and technology part (I) structure, synthesis and characterisation, Arab. J. Chem. 5 (2012) 1–23.
[40] R.L. McCreery, Advanced carbon electrode materials for molecular electrochemistry, Chem Rev. 108 (2008) 2646–2687.
[41] Y. Estévez-Martínez, C. Velasco-Santos, A.-L. Martínez-Hernández, G. Delgado, E. Cuevas-Yáñez, D. Alaníz-Lumbreras, et al., Grafting of multiwalled carbon nanotubes with chicken feather keratin, J. Nanomater. 2013 (2013).
[42] L. Stobinski, B. Lesiak, L. Kövér, J. Tóth, S. Biniak, G. Trykowski, et al., Multiwall carbon nanotubes purification and oxidation by nitric acid studied by the FTIR and electron spectroscopy methods, J. Alloys Compd. 501 (2010) 77–84.
[43] J.H. Lehman, M. Terrones, E. Mansfield, K.E. Hurst, V. Meunier, Evaluating the characteristics of multiwall carbon nanotubes, Carbon. 49 (2011) 2581–2602.
[44] U. Kuhlmann, H. Jantoljak, N. Pfänder, P. Bernier, C. Journet, C. Thomsen, Infrared active phonons in single-walled carbon nanotubes, Chem. Phys. Lett. 294 (1998) 237–240.
[45] P. Verma, P. Maire, P. Novák, A review of the features and analyses of the solid electrolyte interphase in Li-ion batteries, Electrochimica Acta. 55 (2010) 6332–6341.
[46] C. Naudin, J.L. Bruneel, M. Chami, B. Desbat, J. Grondin, J.C. Lassègues, et al., Characterization of the lithium surface by infrared and Raman spectroscopies, J. Power Sources. 124 (2003) 518–525.
[47] M.A. Karakassides, D. Gournis, D. Petridis, An infrared reflectance study of Si-O vibrations in thermally treated alkalisaturated montmorillonites, Clay Miner. 34 (1999) 429–438.
[48] K.-I. Morigaki, A. Ohta, Analysis of the surface of lithium in organic electrolyte by atomic force microscopy, Fourier transform infrared spectroscopy and scanning auger electron microscopy, J. Power Sources. 76 (1998) 159–166.
[49] D. Aurbach, B. Markovsky, I. Weissman, E. Levi, Y. Ein-Eli, On the correlation between surface chemistry and performance of graphite negative electrodes for Li ion batteries, Electrochimica Acta. 45 (1999) 67–86.
[50] L.J. Radziemski, R. Engleman Jr., J.W. Brault, Fourier-transform-spectroscopy measurements in the spectra of neutral lithium, I6 and I7 (Li I), Phys. Rev. A. 52 (1995) 4462–4470.
[51] S. Brouillet-Fourmann, C. Carrot, N. Mignard, Gelatinization and gelation of corn starch followed by dynamic mechanical spectroscopy analysis, Rheol. Acta. 42 (2003) 110–117.
[52] S. Mathew, M. Brahmakumar, T.E. Abraham, Microstructural imaging and characterization of the mechanical, chemical, thermal, and swelling properties of starch-chitosan blend films, Biopolymers. 82 (2006) 176–187.
[53] F. Liu, B. Qin, L. He, R. Song, Novel starch/chitosan blending membrane: Antibacterial, permeable and mechanical properties, Carbohydr. Polym. 78 (2009) 146–150.
[54] F.A. López, A.L.R. Mercê, F.J. Alguacil, A. López-Delgado, A kinetic study on the thermal behaviour of chitosan, J. Therm. Anal. Calorim. 91 (2008) 633–639.
[55] N.L.G.D. Souza, H.M. Brandão, L.F.C. De Oliveira, Spectroscopic and thermogravimetric study of chitosan after incubation in bovine rumen, J. Mol. Struct. 1005 (2011) 186–191.
[56] M. Sugimoto, M. Morimoto, H. Sashiwa, H. Saimoto, Y. Shigemasa, Preparation and characterization of water-soluble chitin and chitosan derivatives, Carbohydr. Polym. 36 (1998) 49–59.
[57] J.R. Ferraro, Introductory raman spectroscopy, Academic press, 2003.
[58] H. Jantoljak, J.-P. Salvetat, L. Forró, C. Thomsen, Low-energy Raman-active phonons of multiwalled carbon nanotubes, Appl. Phys. Mater. Sci. Process. 67 (1998) 113–116.
[59] E.V. Efremov, F. Ariese, C. Gooijer, Achievements in resonance Raman spectroscopy. Review of a technique with a distinct analytical chemistry potential, Anal. Chim. Acta. 606 (2008) 119–134.
[60] X. Wang, C. Wang, L. Cheng, S.-T. Lee, Z. Liu, Noble metal coated single-walled carbon nanotubes for applications in surface enhanced raman scattering imaging and photothermal therapy, J. Am. Chem. Soc. 134 (2012) 7414–7422.
[61] R.Y. Sato-Berrú, E.V. Basiuk, J.M. Saniger, Application of principal component analysis to discriminate the Raman spectra of functionalized multiwalled carbon nanotubes, J. Raman Spectrosc. 37 (2006) 1302–1306.
[62] C. Thomsen, S. Reich, Raman scattering in carbon nanotubes, 2006.
[63] H. Kataura, Y. Achiba, X. Zhao, Y. Ando, Resonance Raman scattering of multi-walled carbon nanotubes, in: 2000: pp. 113–118.
[64] H. Athalin, S. Lefrant, A correlated method for quantifying mixed and dispersed carbon nanotubes: Analysis of the Raman band intensities and evidence of wavenumber shift, J. Raman Spectrosc. 36 (2005) 400–408.
[65] M.S. Dresselhaus, G. Dresselhaus, M. Hofmann, The big picture of Raman scattering in carbon nanotubes, Vib. Spectrosc. 45 (2007) 71–81.
[66] S. Gupta, R.J. Patel, Changes in the vibrational modes of carbon nanotubes induced by electron-beam irradiation: Resonance Raman spectroscopy, J. Raman Spectrosc. 38 (2007) 188–199.
[67] A. Jorio, R. Saito, G. Dresselhaus, M.S. Dresselhaus, Determination of nanotubes properties by Raman spectroscopy, Philos. Trans. R. Soc. Math. Phys. Eng. Sci. 362 (2004) 2311–2336.
[68] P. Delhaes, M. Couzi, M. Trinquecoste, J. Dentzer, H. Hamidou, C. Vix-Guterl, A comparison between Raman spectroscopy and surface characterizations of multiwall carbon nanotubes, Carbon. 44 (2006) 3005–3013.
[69] H.M. Heise, R. Kuckuk, A.K. Ojha, A. Srivastava, V. Srivastava, B.P. Asthana, Characterisation of carbonaceous materials using Raman spectroscopy: A comparison of carbon nanotube filters, single- And multi-walled nanotubes, graphitised porous carbon and graphite, J. Raman Spectrosc. 40 (2009) 344–353.

[70] M. Zdrojek, W. Gebicki, C. Jastrzebski, T. Melin, A. Huczko, Studies of multiwall carbon nanotubes using raman spectroscopy and atomic force microscopy, 2004.
[71] M.S. Dresselhaus, G. Dresselhaus, R. Saito, A. Jorio, Raman spectroscopy of carbon nanotubes, Phys. Rep. 409 (2005) 47–99.
[72] M.S. Dresselhaus, A. Jorio, A.G. Souza Filho, R. Saito, Defect characterization in graphene and carbon nanotubes using Raman spectroscopy, Philos. Trans. R. Soc. Math. Phys. Eng. Sci. 368 (2010) 5355–5377.
[73] D. Nishide, Y. Miyata, K. Yanagi, T. Tanaka, H. Kataura, PERIPUTOS: Purity evaluated by Raman intensity of pristine and ultracentrifuged topping of single-wall carbon nanotubes, Phys. Status Solidi B Basic Res. 246 (2009) 2728–2731.
[74] V.M. Irurzun, M.P. Ruiz, D.E. Resasco, Raman intensity measurements of single-walled carbon nanotube suspensions as a quantitative technique to assess purity, Carbon. 48 (2010) 2873–2881.
[75] H. Kataura, Y. Miyata, K. Mizuno, Purity and defect characterization of single-wall carbon nanotubes using raman spectroscopy, J. Nanomater. 2011 (2011).
[76] A.C. Dillon, M. Yudasaka, M.S. Dresselhaus, Employing Raman spectroscopy to qualitatively evaluate the purity of carbon single-wall nanotube materials, J. Nanosci. Nanotechnol. 4 (2004) 691–703.
[77] R.A. DiLeo, B.J. Landi, R.P. Raffaelle, Purity assessment of multiwalled carbon nanotubes by Raman spectroscopy, J. Appl. Phys. 101 (2007).
[78] R.P. Rocha, J.P.S. Sousa, A.M.T. Silva, M.F.R. Pereira, J.L. Figueiredo, Catalytic activity and stability of multiwalled carbon nanotubes in catalytic wet air oxidation of oxalic acid: The role of the basic nature induced by the surface chemistry, Appl. Catal. B Environ. 104 (2011) 330–336.
[79] X. Liu, R. Wang, L. Song, H. He, G. Zhang, X. Zi, et al., The oxidation of carbon monoxide over the palladium nanocube catalysts: Effect of the basic-property of the support, Catal. Commun. 46 (2014) 213–218.
[80] C. Ingrosso, G.V. Bianco, P. Lopalco, M. Tamborra, M.L. Curri, A. Corcelli, et al., Surface chemical functionalization of single walled carbon nanotubes with a bacteriorhodopsin mutant, Nanoscale. 4 (2012) 6434–6441.
[81] J. Zhao, A. Buldum, J. Han, J.P. Lu, First-principles study of Li-intercalated carbon nanotube ropes, Phys. Rev. Lett. 85 (2000) 1706–1709.
[82] G. Maurin, C. Bousquet, F. Henn, P. Bernier, R. Almairac, B. Simon, Electrochemical lithium intercalation into multiwall carbon nanotubes: A micro-Raman study, Solid State Ion. 136-137 (2000) 1295–1299.
[83] Y.A. Kim, M. Kojima, H. Muramatsu, S. Umemoto, T. Watanabe, K. Yoshida, et al., In situ Raman study on single- and double-walled carbon nanotubes as a function of lithium insertion, Small. 2 (2006) 667–676.
[84] G. Maurin, F. Henn, B. Simon, J.-F. Colomer, J.B. Nagy, Lithium Doping of Multiwalled Carbon Nanotubes Produced by Catalytic Decomposition, Nano Lett. 1 (2001) 75–79.
[85] J. Li, C. Wu, L. Guan, Lithium insertion/extraction properties of nanocarbon materials, J. Phys. Chem. C. 113 (2009) 18431–18435.
[86] J.T. Ye, Z.M. Li, Z.K. Tang, R. Saito, Raman spectra of lithium doped single-walled 0.4 nm carbon nanotubes, Phys. Rev. B - Condens. Matter Mater. Phys. 67 (2003) 1134041–1134044.
[87] A.K. Yoong, M. Kojima, H. Muramatsu, D. Shimamoto, T. Hayashi, M. Endo, et al., Raman study on electrochemical lithium insertion into multiwalled carbon nanotubes, J. Raman Spectrosc. 39 (2008) 1183–1188.
[88] M. Müller, R. Meinke, J. Maultzsch, B. Gebhardt, F. Hauke, A. Hirsch, et al., Resonant Raman scattering on carbon nanotubes covalently functionalized with lithium decyne, Phys. Status Solidi B Basic Res. 247 (2010) 2863–2866.
[89] A. Schechter, D. Aurbach, H. Cohen, X-ray photoelectron spectroscopy study of surface films formed on Li electrodes freshly prepared in alkyl carbonate solutions, Langmuir. 15 (1999) 3334–3342.
[90] K. Kanamura, S. Shiraishi, H. Takezawa, Z. Takehara, XPS analysis of the surface of a carbon electrode intercalated by lithium ions, Chem. Mater. 9 (1997) 1797–1804.
[91] D. Aurbach, I. Weissman, A. Schechter, H. Cohen, X-ray photoelectron spectroscopy studies of lithium surfaces prepared in several important electrolyte solutions. A comparison with previous studies by Fourier transform infrared spectroscopy, Langmuir. 12 (1996) 3991–4007.
[92] I. Ismail, A. Noda, A. Nishimoto, M. Watanabe, XPS study of lithium surface after contact with lithium-salt doped polymer electrolytes, Electrochimica Acta. 46 (2001) 1595–1603.
[93] M.E. Brown, P.K. Gallagher, Handbook of thermal analysis and calorimetry: Recent advances, techniques and applications, Elsevier, 2011.
[94] D.A. Skoog, F.J. Holler, T.A. Nieman, M. del C.M. Gómez, Principios de análisis instrumental, McGraw-Hill Madrid, 2001.
[95] Y.-J. Wu, L. Chao, K.-S. Ho, Y.-J. Huang, Y.-L. Huang, C.-S. Yang, et al., Characterizations on the amidized multiwalled carbon nanotubes grafted with polyaniline via in situ polymerization, J. Appl. Polym. Sci. 124 (2012) 5270–5278.
[96] A.A. Khiar, A.K. Arof, Conductivity studies of starch-based polymer electrolytes, Ionics. 16 (2010) 123–129.
[97] A.K. Arof, S. Amirudin, S.Z. Yusof, I.M. Noor, A method based on impedance spectroscopy to determine transport properties of polymer electrolytes, Phys. Chem. Chem. Phys. 16 (2014) 1856–1867.
[98] M.R. Johan, S. Ibrahim, Neural networks for Nyquist plots prediction in a nanocomposite polymer electrolyte (PEO–LiPF6–EC–CNT), Ionics. 17 (2011) 683–696.

XIV International Congress of the Mexican Hydrogen Society
Cancun, Mexico, 2014

A Microbial Fuel Cell Equipped with a Denitrifying Biocathode Effectively Degrades the Toxic Carbon Tetrachloride

A.C. Ortega-Martínez[1]; H. M. Poggi-Varaldo[1*]; O. Solorza-Feria[2]; G. Hernández-Flores[1]; E. Ríos-Leal[3]; M. T. Ponce-Noyola[4]; K. Juárez-López[5]; J. Galíndez-Mayer[6]; N. F. Rinderknecht-Seijas[7]

[1]Environmental Biotechnology and Renewable Energies R&D Group, Dept. Biotechnology & Bioengineering, Centro de Investigación y de Estudios Avanzados del I.P.N., P.O. Box 14-740, C.P. 07000 México, D.F., México
[2]Dept. of Chemistry, Centro de Investigación y Estudios Avanzados del I.P.N., México
[3]Central Analítica Dept. of Biotechnology & Bioingineering, Centro de Investigación y Estudios Avanzados del I.P.N., México
[4]Microbial Genetic Group, Dept. of Biotechnology & Bioingineering, Centro de Investigación y Estudios Avanzados del I.P.N., México
[5]Depto. Ingeniería Celular y Biocatálisis, Instituto de Biotecnología, Universidad Nacional Autónoma de México, Cuernavaca, Mor., México
[6]Escuela Nacional de Ciencias Biológicas, Depto. De Ingeniería Bioquímica, Instituto Politécnico Nacional, México, D.F., México
[7]Escuela Superior de Ingeniería Química e Industrias Extractivas, Instituto Politécnico Nacional, México, D.F., México
*Author for correspondence: H. M. Poggi-Varaldo, E-mail: r4cepe@yahoo.com

ABSTRACT

The aim of this work was to design and operate a MFC equipped with a denitrifying biocathode (MFC-BIO-DN) in the perspective of carbon tetrachloride reduction from polluted effluents.
The MFC-BIO-DN consisted of two plexiglass cubic chambers of 3 cm filled with small graphite cubes (3 mm side length). The anode and cathode compartments were separated by a proton exchange membrane (Nafion 117). The anode chamber was loaded with 12 mL of enriched inoculum, E-In that was cultured in an acetate-ferric citrate medium. The cathode chamber was seeded with a mixed culture of denitrifying bacteria. A synthetic wastewater containing potassium buffer salts, Na_2CO_3, and KNO_3 was fed to the cathode chamber. The CT concentration within the cathode of the MFC-DN was 10 mg/L.
In the characterization experiment, the internal resistance R_{int} of MFC –DN was 1450 Ω with a maximum cell voltage of 230 mV. The values of P_v and P_S of the MFC were 772 mW/m^3 and 24 mW/m^2, respectively, where P_S is the power density expressed on the basis of projected surface area of membrane. During the batch operation the average voltage of the MFC-DN was 132 mV, whereas average P_v and P_S were 11 620 mW/m^3 and 35 mW/m^2. A nearly 100% CT depletion in the cathodic liquor was observed in the first 12 h of operation, which was equivalent to a removal rate higher than 20 mg CT/(L.d). Abiotic removal of CT by sorption to the electrode graphite cubes (anodic and cahtodic) was negligible as determined by headspace GC-FID. We can conclude that a MFC-DN shows promise for the bioelectrochemical remediation of waters polluted with CT.

Keywords: Biocathode, Carbon Tetrachloride, Microbial Fuel Cell

1. Introduction

Chlorinated hydrocarbons such as carbon tetrachloride and chloroform have been widely used in large quantities for different industrial and domestic purpose [1]. Carbon tetrachloride (CT) is a volatile chlorinated solvent, which has been used widely over decades as an industrial degreasing agent, as a pesticide, for dry cleaning and in fire extinguishers [2]. It is toxic and predicted to be carcinogenic, with deleterious effects on stratospheric ozone. As a consequence, commercial production and use of has been progressively restricted. Its use as pesticide and grain fumigant was banned in 1986 [3]. Currently, CT is still produced, but only as a intermediate in the production of other chemical compounds. With an estimated half-life for abiotic hydrolysis of 7000 years in water at 20°, CT is highly persistent in the environment compared with other halogenated aliphatic compounds [4]. The low water solubility of CT leads to its accumulation in subsurface aquifers as a poorly bioavailable, dense non-aqueous-phase liquid, which only dissolves very slowly into groundwater [5]. Degradation or transformation of CT, is the other major source of toxicity of the compound, as some dechlorination pathways generate toxic intermediates and products. This mainly seems to be due to

intracellular CT transformation of reactive radicals that, by promoting nonspecific oxidation, can detrimentally affect and inactivate key cellular components [6].

CT has been shown susceptible to degradation in anaerobic environments by both biotic and abiotic mechanisms. Much of the research on the microbial transformation of CT has focused on the roles of methanogenic, sulphate-reducing, and nitrate-reducing bacteria [7]. Denitrifying conditions do not produce any secondary pollutant, and denitrifying bacteria grow much faster and can a wider range of substrate, including some reductive dechlorination products [8]. There is a need to remove low-level CT concentrations from contaminated drinking water supplies, as well as a high-level CT concentration from superfund sites and industrial wastewaters, because of the risks posed by CT to human health and the environment [9]. While a number of bioreactors have been developed for CT reduction [10], reduction using a biologically active cathode (biocathode) within a microbial fuel cell (MFC) is a novel and potentially cost-effective approach. Biocathodes harness the capacity of specific microorganims to accept electrons from a solid surface (cathode) [11]. High-rate oxygen reduction without a platinum catalyst and denitrification have been accomplished using biocathodes [12-13], as well as reduction of chlorinated groundwater pollutants [11,14]. An advantage of this process is the opportunity for electrical energy recovery from the treatment process [15].

Therefore, the objective of this work was to design and operated a MFC equipped with a denitrifying biocathode (MFC-BIO-DN) in the perspective of carbon tetrachloride reduction from polluted effluents.

2. Materials and methods

2.1 Microbial fuel cell equipped with a denitrifying biocathode.

The MFC fitted with a denitrifying biocathode consisted of two plexiglass cubic chambers of 3 cm (Fig. 1). Each electrode compartment was filled with small graphite cubes (3 mm x 3mm) and they had a 27 mL geometric volume, net volume of 15 mL discounting the volume of the electrode material. External contact to the electrodes was made via graphite rods inserted into the anode and cathode chambers.

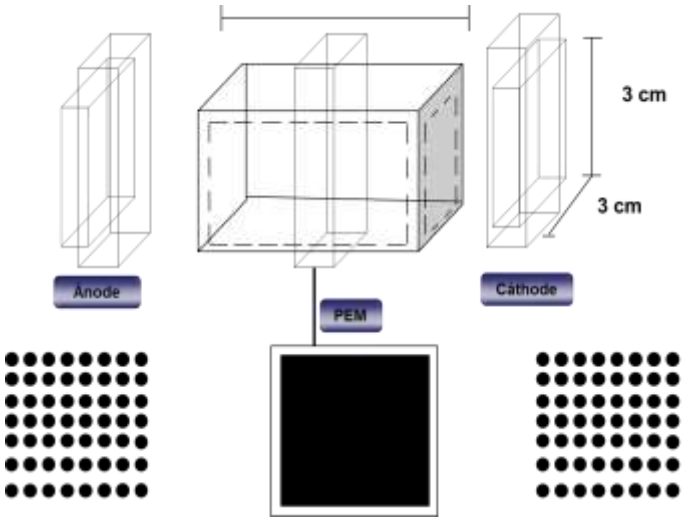

Fig. 1. Isometric view of the lab scale microbial fuel cell equipped with biocathode MFC-BIO.

The anode and cathode compartments were separated by a proton exchange membrane (Nafion 117). The anode chamber was loaded with 12 mL of biocatalyst (E-In), whereas the cathodic chamber received a denitrifying inoculum previously acclimated to carbon tetrachloride. Initial COD and biomass concentrations in the anode liquor of the cell were *ca.* 950 mg O_2/L and 800 mg VSS/L, respectively. The cathode chamber was seeded with a mixed culture of denitrifying bacteria sampled from a denitrifying lab-scale reactor acclimated to 6 mg/L CT. The synthetic wastewater fed to the cathodic chamber contained (in g/L) 6.8 of K_2HPO_4. 8.7 of KH_2PO_4, 2.0 of Na_2CO_3, finally 6.0 of KNO_3. The initial CT concentration within the cathode of the MFC-BIO-DN was 10 mg/L.

2.2 Enriched inocula

The E-In for the anodic chamber of the MFC-BIO-DN was obtained with serial transfers. A sediment sample was suspended in nitrogen filled pressure tubes containing media with ferric citrate (55 mM) as electron acceptor and sodium acetate (2 M) as electron donor. The tubes were incubated at 30°C for 7 days in the dark. The enrichment procedure was repeated 3 times [16].

The bioreactor with E-In had an operation volume of 1.5 L was operated at 35°C in a constant temperature room. The bioreactor was fed at a flow rate of 75 mL/d an influent whose composition was (in g/L): Sodium acetate (2.0), $NaHCO_3$ (1.8), Na_2CO_3 (0.5), Na_2SeO_4 (0.1).

The biocatalyst used in the cathodic chamber was sampled from a denitrifying complete mix bioreactor that was acclimated to 6 mg/L carbon tetrachloride in the influent [17].

2.3 Analyses

Polarization curves. The main conditions in both chambers of the MFC-BIO used in the characterization studies are shown in Table 1. The internal resistance of cells was determined using the polarization curve method, by varying the external resistance (R_{ext}) and monitoring both the voltage and the current intensity, according to procedures suggested by [14,18]. MFC was batch-operated for 8 h at room temperature. The circuit of the MFCs were fitted with an external variable resistance. In this regard, we carried out the polarization curve of the MFC, relating mathematically the cell voltage (E_{MFC}) and current intensity (I_{MFC}) against the R_{ext} value, forwards and backwards regarding the R_{ext} values. *Ab initio*, the MFCs were operated at open circuit for 1 h. Afterwards, the R_{ext} was varied from 100 Ω to 100 KΩ and backwards. After this, the cell was set to open circuit conditions for 1 h in order to check the adequacy of the procedure (values of initial and final open circuit voltages should be close). The voltage was measured and recorded with a multimeter. The current was calculated by the Ohm's law [19].

Analytical methods and calculations. The COD and VSS of the liquor of iron-reducing seed bioreactor and cell were determined according to the Standard Methods [20]. The current intensity (I_{MFC}), the power (P_{MFC}) and the power density (P_S) were determined according to the [19].

The power per unit volume or volumetric power (P_V) was calculated as follows:

$$P_V = \frac{E^2_{MFC}}{V_{MFC} \cdot R_{ext}} \quad (1)$$

where: R_{ext} = the external resistance, E_{MFC} = the voltage, and V_{MFC} = the cell volume.

Table 1. Conditions for the characterization experiments by polarization curve method

	Anode	Cathode
Biocatalyst	Enriched inoculum (iron-reducing bacteria)	Denitrifying inoculum
Substrate	2 M sodium acetate	None
Toxic compound	None	CCl_4 (10 mg/L)
Electron acceptor	None	Nitrate

2.4 Determination of Fe(III) reduction

It is known that the ferric ion (Fe^{3+}) can serve as an exogenous electron acceptor during microbial respiration (dissimilatory Fe(III) reduction) [21-24]. Ferric ion-respiring microorganisms are diverse and some of them have a biotechnological interest because of their potential role in electricity production in microbial fuel cells (MFCs) where the terminal acceptor of the electrons during anaerobic respiration is not a ferric ion or different metal but the anode [22]. We used ferric citrate in order to enrich the metal-reducers from the initial consortium. Fe(III) reduction activity was determined using a previous method [25]. A half mL of culture was aseptically sampled with a syringe and mixed with 1 mL HCl solution (0.5 N). This mixture was reacted for 15 min. at room temperature, and then centrifuged for 5 min. The mixture of supernatant (0.1 mL) and ferrozine solution (1mL, 1 g/L in 50 mM HEPES buffer) was reacted for 15 min before measurement of optical density at 562 nm using a spectrophotometer. The fresh medium was used as a control sample instead of culture. Ferrous ethylenediammonium sulfate tetrahydrate ($C_2H_{10}N_2O_4SFeSO_44H_2O$) was used to make a standard Fe(II) solution [23].

An enrichment factor ε was defined as follows:

$$\varepsilon \text{ (mM/d)} = ([Fe^{+2}]_{final} - [Fe^{+2}]_{initial})/t_{lag} \quad (2)$$

where $[Fe^{+2}]_{final}$ is the final concentration of Fe (II) in a given transfer, $[Fe^{+2}]_{initial}$ is the initial concentration of Fe (II) in the

transfer (both concentrations in mM), and t_{lag} is the lag time (in d) of Fe(II) appearance in the transfer. Please note that in spite that ε seems to have units of concentration rate mM/d, it is not a true rate because the denominator is the lag time of the given culture [26].

2.4 Determination of carbon tetrachloride

Carbon tetrachloride concentration in the influent and liquors was determined by gas chromatography in /(GC-FID Perkin Elmer 9000)/ flame ionization analysis of a 0.5 mL sample taken from the 60 mL headspace of the serum bottles, as previous described [27-28].

3. Results and discussion

3.1 Cell characterization

In the characterization experiment, the R_{int} of MFC-BIO was 1450 Ω. The values of R_{int} was calculated as the slopes of the sets of aligned points of the corresponding polarization curve. The maximum cell voltage was of 230 mV (Table 2, Fig. 2). This relatively high value of R_{int} is typical of two-chamber MFCs (Lefebvre *et al.* 2008). The maximum values of P_v and P_S of the MFC were 772 mW/m^3 and 24 mW/m^2, respectively, where P_S is the power density expressed on the basis of projected surface area of membrane.

Our results seem to be in agreement with other works that report high values of R_{int}. For instance Lefebvre *et al.*, 2008 [17] designed a type of two-chambered microbial fuel cell wherein an autotrophic denitrifying biofilm. This two-chambered MFC consisted of two acrylic cubic chambers separated with a PEM made of Nafion. On each side of the PEM, two electrodes consisting of non-wet-proof carbon paper. The volume of each chamber was 125 cm^3. Two-chambered MFC equipped with a biocathode generated a R_{int} of 5000 Ω. The maximum values of P_v and P_S of the two-chambered MFC were 190 mW/m^3 and 9.7 mW/m^2, respectively.

In our work the characteristics parameters of MFC-BIO were higher than two-chambered MFC, this could be related to the electrodes materials. MFC-BIO electrodes were small graphite cubes, this cubes filled each compartment of MFC. On the other hand, the two-chambered MFC was equipped with non-wet-proof carbon paper.

3.2 Enrichment of inoculum.

Fig. 3 shows the results of the serial transfers procedure for inoculum enrichment. A concentration of 12 mM Fe^{+2} was achieved on day 4 in the first stage inoculation, whereas this concentration in the other stages is achieved on the second day or shorter.

Table 2 shows Fe^{+2} initial and final concentration in serial transfers procedure. We could achieve a 43.7 mM Fe^{+2} final concentration in the last transfer, this value is more than twice what was obtained in the final inoculation stage. Increase of the enrichment factor in subsequent transfers (Table 3) was an evidence that the enrichment procedure was successful.

Our results were similar to those reported by Hyun *et al*. (1999) [16] who isolated a Fe(III)-reducer from the natural environment. Soil samples were collected from various paddy fields and enriched with ferric citrate as a source of Fe(III) under anaerobic conditions. The final enriched culture showed the highest Fe(III)-reduction activity. Bacterial growth was coupled with oxidation of lactate and pyruvate to Fe(III)-reduction, final concentration Fe^{+2} was 19.23 mM and 23.19, respectively, their results were obtained after 4 days of incubation.

Table 2. Values of selected parameters in the characterization studies of the MFC-BIO[a].

Parameter	MFC-BIO
R_{int}[b] (Ω)	1453 ± 250
P_s[c] (mW/m^2)	24 ± 2
$P_{V\text{-}max}$[d] (mW/m^2)	772 ± 120
$E_{MFC\text{-}max}$[e] (V)	0.230 ± 0.08
$I_{MFC.max}$[f] (mA)	0.141 ± 0.05
$P_{MFC.max}$[g] (mW)	0.013 ± 0.003

Notes: [a]Microbial fuel cell equipped with a biocathode, [b]Internal resistance; [c]Maximun power density expressed on the basis of projected surface area of membrane; [d]Maximum volumetric power; [e]Maximum voltage; [f]Maximum current intensity, [g]Maximum power output.

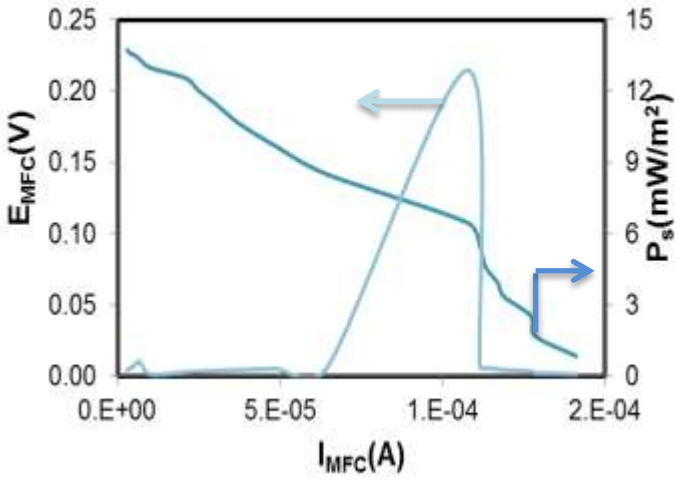

Fig. 2. Electric potential variation in the variable resistance procedure for cell characterization and power with respect to cell current intensity.

Table 3. Results of the enrichment procedure in the serial transfers: Concentration of Fe^{+2} during serial transfer procedure

Stage	Initial Fe^{+2} (mM)	Final Fe^{+2} (mM)	ε (mM/d)
Inoculation	2.4 ± 0.01	19.0 ± 0.8	5.5
First transfer	4.3 ± 1.61	35.4 ± 3.6	31.1
Second transfer	4.3 ± 0.16	36.3 ± 3.1	45.7
Third transfer	4.3 ± 0.10	43.7 ± 2.3	56.3

3.3 Batch operation of the cell with denitrifying biocathode and 10 mg/L carbon tetrachloride in the cathodic chamber.

For the batch operation, the MFC-BIO was connected to an external resistance of 100 Ω because when connected to 1500 Ω the cell potential drastically decreased to 32 mV. During the batch operation the average voltage was 132 mV, whereas average P_v and P_S were 11 620 mW/m^3 and 35 mW/m^2 (Fig. 4, Table 3).

A 92% CT depletion in the cathodic liquor was observed in the first 12 h of the run. This corresponded to a volumetric removal rate higher than 18 mg CT/(L.d). Abiotic removal of CT by sorption to the electrode graphite cubes in the cathodic chamber was negligible as determined by headspace GC-FID. We can conclude that a MFC fitted with a denitrifying biocathode holds promise for the bioelectrochemical remediation of effluents contaminated with CT.

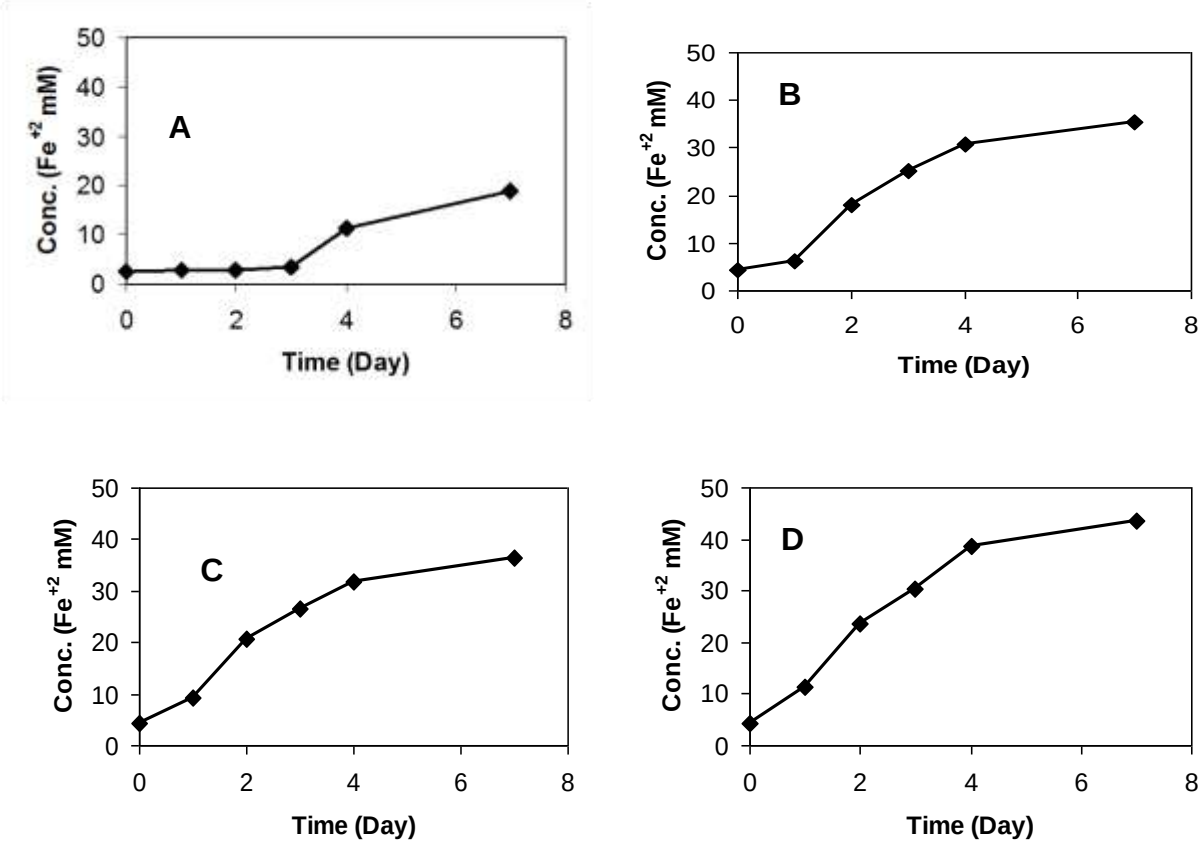

Fig. 3. Serial transfers procedure. (A) Inoculation, (B) First Transfer, (C) Second Transfer, and (D) Third Transfer.

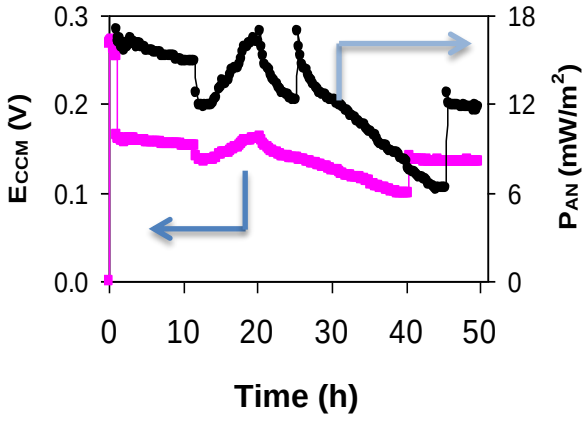

Fig. 4. Time course of cell potential and power density during the batch operation of the MFC-BIO-DN with carbon tetrachloride in the cathodic chamber. An external resistance of 100 ohms was used.

Table 3. Average results from the batch run of the MFC-BIO-DN with carbon tetrachloride in the cathodic chamber.

Parameter	MFC-BIO[a]
R_{ext} [b] (Ω)	100
P_s [c] (mW/m^2)	35 ± 1.4
$P_{V\text{-}max}$ [d] (mW/m^2)	11620 ± 136.5
$E_{MFC\text{-}max}$ [e] (V)	0.132 ± 0.0008
$I_{MFC.max}$ [f] (mA)	1.32 ± 0.008
η_{CCl4} [g] (%)	92
$\eta_{NO3.}$ [h] (%)	90
$\eta_{COD.}$ [i] (%)	87
η_{Coul} [j] (%)	24

Notes: [a]Microbial fuel cell equipped with a biocathode, [b]External resistance; [c]Maximun power density expressed on the basis of projected surface area of membrane; [d]Maximum volumetric power; [e]Maximum voltage; [f]Maximum current intensity, [g]Removal efficiency of CCl_4, [h]Removal efficiency of NO_3^-, [i]Chemical oxygen demand removal efficiency; [j] Coulombic efficiency .

4. Conclusion

In the characterization studies performed with the variable resistance method, the R_{int} of MFC-BIO was 1450 Ω with a maximum cell voltage of 230 mV. The values of P_v and P_S of the MFC-BIO were 772 mW/m^3 and 24 mW/m^2, respectively.

During the batch operation the average voltage was 132 mV, whereas average P_v and P_S were 11 620 mW/m^3 and 35 mW/m^2. A 92% CT removal (from an initial 10 mg CT/L) in the cathodic liquor was observed in the first 12 h of the run, which was equivalent to a removal rate higher than 18 mg CT/(L.d). Also, a high removal of nitrate was achieved in the cathodic chamber, as high as 90%.

We can conclude that a MFC fitted with a denitrifying biocathode holds promise for the bioelectrochemical bioremediation of effluents contaminated with CT.

ACKNOWLEDGEMENTS

The authors also wish to thank ICYTDF (now SECITI-GDF) and CINVESTAV-IPN and Mexico, for financial support to this research. Areli del C. Ortega-Martinez received a graduate scholarship from CONACYT, Mexico. The excellent technical help of Mr. Rafael Hernández-Vera and personnel of the Environmental of Biotechnology and Renewable Energy R&D Group CINVESTAV-IPN, Mr. Cirino Rojas and Mr. Gustavo Medina of Central Analítica, is greatly appreciated.

REFERENCES

[1] R.A. Maithreepala, R. Doong, Transformation of carbon tetrachloride by biogenic iron species in the presence of *Geobacter sulfurreducens* and electron shuttles. J. Hazard Mater 2008; 26:511-516

[2] R.E Doherty, A history of the production and use of carbon tetrachloride, tetrachloroethylene, trichloroethylene and 1,1,1-trichloroethane in the United States: part 1 – historical background; carbon tetrachloride and tetrachloroethylene. Environ Forensics 2000; 1:69-81

[3] C. Penny, S. Vuilleumier, F. Bringel, Microbial degradation of tetrachloromethane: mechanisms and perspectives for bioremediation. Microbiology Ecology 2010; 74:257-275.

[4] T.M. Vogel, C.S. Criddle, P.L. McCarty, Transformations of halogenated aliphatic compounds. Environmental Science Technology 1987; 21:722-736.

[5] ITRC in Situ Bioremediation Team, A systematic approach to *in-situ* bioremediation of carbon tetrachloride in groundwater. Proceeding of the 2002 Conference of Application of Waste Remediation Technologies to Agricultural Contamination of Water Resources, Kansas City, MO.

[6] D. McGregor, M. Lang, Carbon tetrachloride genetic effects and others modes of action. Mutat Res 1996;366:181-195.

[7] M.L. McCormick, E.J. Bouwer, P. Adriaens, Carbon tetrachloride transformation in a model iron-reducing culture: relative kinetics of biotic and abiotic reactions. Environmental Science Technology 2002; 36:403-410.

[8] Z. Yu, G.B. Smith, Dechlorination of polychlorinated methanes by a sequential methanogenic-denitrifying bioreactor system. Applied Microbiology Biotechnology 2000; 53:484-489.
[9] P.B. Hatzinger, Perchlorate biodegradation for water treatment. Environmental Science Technology 2005; 39:239A-247A.
[10] B.E. Logan, Treatment of perchlorated – and nitrate – contaminated water in an autotrophic, gas phase, packed bed bioreactor. Water Research 2002; 36:3647-3653.
[11] K.B. Gregory, D.R. Bond, D.R. Lovley, Graphite electrodes as electron donors for anaerobic respiration. Environmental Microbiology 2004; 6:596-604.
[12] C. Shea, P. Clauwaert, W. Verstraete, R. Nerenberg, Adapting a denitrifying biocathode for perchlorate reduction. Water Science Technology 2008; 58:1941-1946.
[13] J.C. Thrash, J.I. Van Trump, K.A. Weber, E Miller, L.A. Achenbach, J.D. Coates, Electrochemical simulation of microbial perchlorate-reduction. Environmental Science Technology 2007; 41:1740-1746.
[14] P. Clauwaert, D. Van Der Ha, N. Boon, K. Verbeken, M. Verhaege, K, Rabaey, W. Verstraete, Open air biocathode enable effective electricity generation with microbial fuel cell. Environmental Science Technology 2007; 41:7564-7569.
[15] C.S. Butler, P. Clauwaert, S.J. Green, W. Verstraete, R. Nerenberg, Bioielectrochemical perchlorate reduction in a microbial fuel cell. Environmental Science Technology 2010; 44:4685-4691.
[16] M.S. Hyun, B.H. Kim, I.S. Chang, H.S. Park, H.J. Kim, G.T. Kim, Isolation and identification of an anaerobic dissimilatory Fe(III)-reducing bacterium, *Shewanella putrefaciens* IR-1. Journal of Microbiology 1999; 37: 206-212.
[17] O. Lefebvre, A. Al-Mamun, H.Y. Ng, A microbial fuel cell equipped with a biocathode for organic removal and denitrification. Water Science Technology 2008; 58:881-885.
[18] B.E. Logan, B. Hamelers, R. Rozendal, U. Schröder, J. Keller, S. Fregia, Microbial fuel cells: methodology and technology. Environmental Science and Technology 2006; 40:5182-5192.
[19] H.M. Poggi-Varaldo, A. Carmona-Martinez, A.L. Vazquez-Larios, O. Solorza-Feria. Effect of inoculum type on the performance of a microbial fuel cell fed with spend organic extracts from hydrogenic fermentation of organic solid wastes. Journal of New Materials and Electrochemical Systems 2009; 12:49-54.
[20] APHA. Standard methods for the examination of water and wastewater. 17th ed. Washington, DC, USA: American Public Association; 1989.
[21] A. Wang, D. Sun, N. Ren, C. Liu, W. Liu, B.E. Logan, A rapid strategies for an anodophilic consortium for microbial fuel cells. Biosource Technology 2010; 101:6449-6454.
[22] D.E. Holmes, D.R. Bond, D.R. Lovley, Electron transfer to Fe(III) and graphite electrodes by *Desulfobulbus propionicus*. Applied and Environmental Microbiology 2004; 70:1234-1237.
[23] D.R. Lovley, E.J.P. Phillips, Novel mode of microbial energy metabolism: organic carbon oxidation coupled to dissimilatory reduction of iron or manganese. Applied and Environmental Microbiology 1988; 54:1472-1480.
[24] D.R. Lovley, E.J.P. Phillips, Rapid assay for microbial reducible ferric iron in aquatic sediments. Applied and Environmental Microbiology 1987; 53:1536-1540.
[25] D.R. Lovley, E.J.P. Phillips, Organic matter mineralization with reduction of ferric in anaerobic sediment. Applied and Environmental Microbiology 1986; 51:683-689.
[26] A.C. Ortega-Martinez, K. Juarez-Lopez, O. Solorza-Feria, M.T. Ponce-Noyola, J. Galindez-Mayer, N. Rinderknecht-Seijas, H.M. Poggi-Varaldo, Analysis of microbial diversity of inocula used in a five-face parallelepiped and standard microbial fuel cell. International Journal of Hydrogen Energy 2013; 38:12589-12599.
[27] D.L. Freedman, J.M. Gossett, Biological reductive dechlorination of tetrachloroethylene and trichloroethylene to ethylene under methanogenic conditions. Applied Environmental Microbiology 1989; 55:2144-2151.
[28] D.L. Freedman, J.M. Gossett, Biodegradation of dichloromethane and its utilization and growth substrate under methanogenic conditions. Applied Environmental Microbiology 1991; 57:2847-2857.

Notation

CT	carbon tetrachloride
E-In	enriched inoculum
MFC	microbial fuel cell
MFC-BIO-DN	microbial fuel cell equipped with a denitrifying biocathode
P_S	power density per unit area of electrode
P_v	volumetric power
R_{ext}	external resistance
R_{int}	internal resistance

Greek characters

ε	enrichment factor
η_{CCl4}	carbon tetrachloride removal efficiency

η_{coul}	coulombic efficiency
η_{NO3}	nitrate removal efficiency; η_{COD}, organic matter removal efficiency, as COD;

Subindices

ave	average
CCM	microbial fuel cell
max	maximum
MFC	microbial fuel cell

Hybrid Electric Vehicle (NAYAA II)

Batteries – Fuel Cell

A. Rodríguez-Castellanos, J. C. Magallón Martínez, S. Citalán-Cigarroa, C. Castro-Morales, O. Solorza-Feria.

Centro de investigación y de Estudios Avanzados del I.P.N., Av. IPN 2508, D.F., México, 07360.
Tel: 57473800; e-mail: acastella@cinvestav.mx

ABSTRACT

Worldwide, the trucking sector emits about 25% of all CO2 emissions and is projected to increase to 50% by 2030 and more than 80% by 2050, according to the International Energy Agency (IEA, info. 2009).

The use of hybrid vehicles can significantly reduce the amount of emission of polluting gases into the atmosphere. A hybrid electric vehicle (HEV) could have two or more power sources on board and depending on system configuration; two or more sources of energy are used to drive the vehicle. The interest in reducing the emission of pollutants in automobiles has created the need to develop and build a wide variety of systems and devices for this purpose.

This experimental work presents the design, construction and performance evaluation of a hybrid electric vehicle (Nayaa), powered by a generator with PEM fuel cell and / or rechargeable batteries. The generator design was done using AutoCAD software, construction of fuel cells using a CNC router and CNC laser cutter.

The characterization of the cell was performed by potentiostatic polarization tests.
The operation conditions of generator with fuel cell was: feeding the fuel (H2) and oxidant (air) at room temperature and a pressure of 0.1 atm (1.5psi), operating temperature of 20 º C at 70 º C.

Keywords: Design; Stack Fuel Cell; Electric Vehicle.

1. Introduction.

The use of fossil fuels in automobiles, produce large amounts of emissions, it affects climate change and leads to global warming and deteriorating health of living beings. In worldwide many laboratories and institutions have been developing prototypes and marketing, based on different technologies, such as hybrid vehicles (ie., different motor carriers), this will help to reduce energy dependence on fossil fuels and significantly reduce the amount of greenhouse gas emissions to the atmosphere.

PEM fuel cells are devices that produces direct current when fed with hydrogen (fuel) and oxygen (oxidant) through an electrochemical reaction. The end product of this reaction is water and heat, therefore, it does not produce any green house gases [1].

A hybrid electric vehicle can have two or more power sources, used to drive the vehicle depending on system configuration. For the first time in Mexican renewable energy scenario our group of researchers developed an improved prototype vehicle called as NAYAA. It utilizes the primary source of energy in reachable batteries as secondary source.

2. Experimental conditions.

2.1. Generator of electricity by PEM-FC.

The power generator consists of the PEM fuel cell stack with fuel system supply and power electronics. The generator provides electrical energy through the unregulated D.C. The weight of the generator is 13.5 kg.

The design of the fuel cell stack were carried out by AutoCAD software, taking into account of different designs proposed in the literature [2-3-4-5]. The construction of the monopolar, bipolar and end plates were used milling machine through CNC controller. Gaskets, membranes and acrylic pieces were cut by a laser cutter.

Fuel cells is constituted by plates of high density carbon with a thickness of 5mm, 150mm wide and 150mm long. The field design flow of gas to the anode and cathode is shaped cross straight channels.

Brass sheet act as current collector, acrylic plates channel input and output for hydrogen and air. Aluminum end plates, silicone gaskets and stainless steel studs were used. Between each current collector plate there is a membrane-electrode assembly (MEA), which is formed by membrane Nafion ® NRE-212, carbon cloth diffusers with catalyst loading of 20 wt% Pt / C loading of 0.5 mg / cm^2 in both the anode and cathode. The performance of fuel cells was determined by potentiostatic polarization in a test module.

Figure 1 shows a photo of the generator, contains the PEM-FC, and peripheral system.

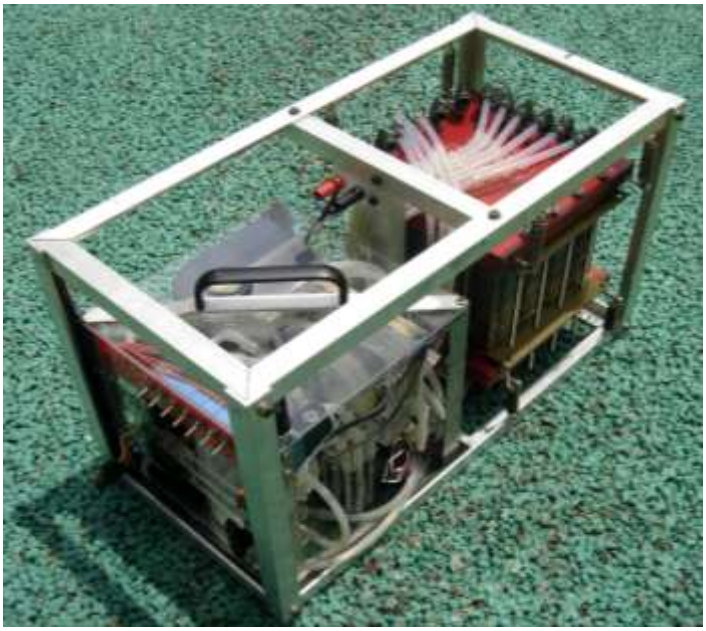

Fig 1. Power generator.

2.2. Rechargeable batteries.

Two rechargeable lead-acid batteries with an electrical capacity of 12V, 24 Ah (VISION CP12240) were used. They are connected in series to obtain a total voltage of 24 V.

The following table describes the specifications of the battery and the figure shows the component parts.

Table 1.General Specifications.

Component	Positive plate	Negative plate	Container	Cover	Safety valve	Terminal	Separator	Electrolyte
Raw material	Lead dioxide	Lead	ABS	ABS	Rubber	Copper	Fiberglass	Sulfuric acid

Fig 2. VISION CP12240 Battery.

2.3. Power electronics.

2.3.1. Power Electronics generator.

The 360W load control was use to be regulated electricity and take advantage of gaining the full power of the cell. The load control operates with input voltages from 12.7V to 14.4V and produces an output voltage of 12.7V with a variation of ± 1.5%. A 400W inverter was coupled to load control, which operates with an input voltage of 12.8V at 25A and produces an output voltage of 115V AC, 60Hz. Figure 3 shows a picture of the power electronics, DC / DC converter - DC / AC 100W.

Fig 3. Power Electronics, DC / DC converter and inverter DC / AC.

2.3.2. Power Electronics for rechargeable Vehicle batteries.

A 500W power converter was designed and built for conditioning the electrical energy and voltage boost from the PEM-FC. The DC-DC converter uses a digital control to adjust the output voltage. The Spain of the input voltage is 9 to 18 volts. The output voltage varies between 28 and 29 volts. A 480W load control was coupled to boost converter for recharge the batteries of the vehicle. The load control operates with input voltages from 26.2V to 29V and produces an output voltage of 26.2V with a variation of ± 1.5%.

Fig 4. Power Electronics DC / DC converter-load control

2.4. Diagrams of energy systems.

2.4.1. Diagram of the fuel cell generator.

Figure 5 shows the diagram of the components that make up the autonomous system: pressurized tank with hydrogen at 136 atm, auxiliary systems recirculation of hydrogen pressurized to 0.1 atm with humidification [6], feeding of the oxidant (atmospheric oxygen), fuel cells, DC / DC load control and inverter DC / AC. The lines show the flow of the different states of electricity and fuel.

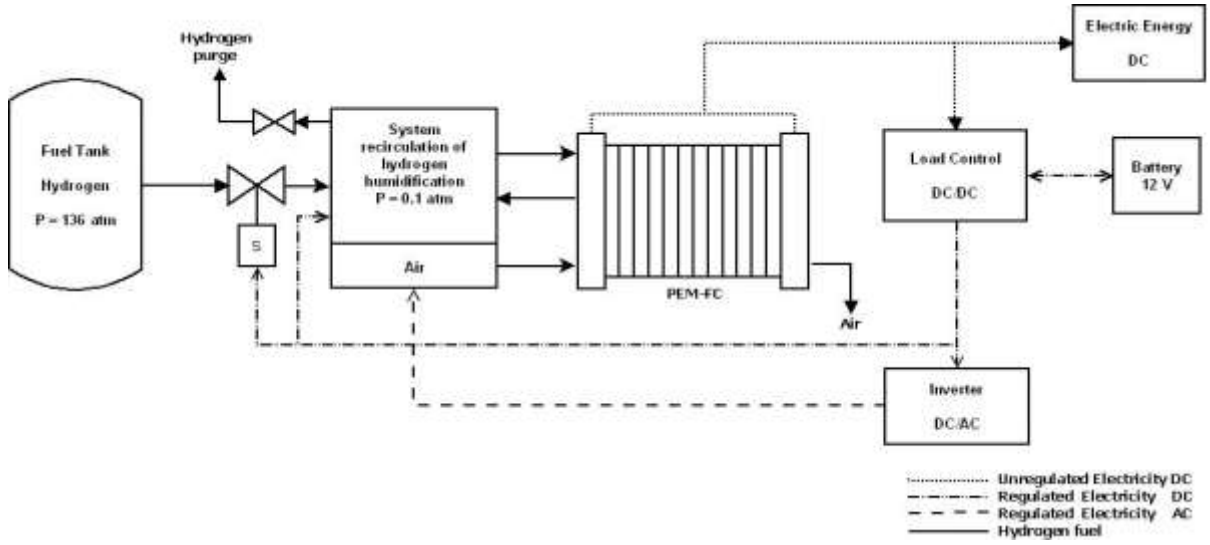

Fig 5. Diagram of the autonomous system based on fuel cells.

2.4.2. Diagram of the installation of energy sources.

Figure 6 shows the two power sources that are on board the vehicle and also the main components that make up for its operation.

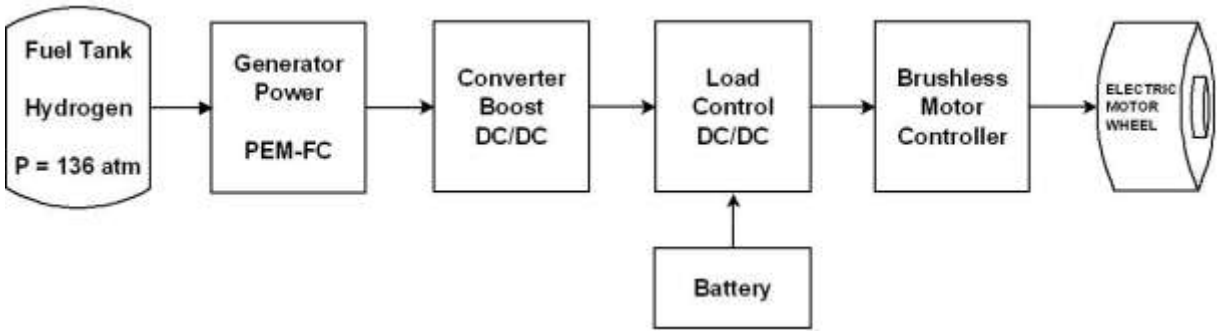

Fig 6. Diagram of energy sources (Battery, PEM-FC).

2.5. Hybrid Electric Vehicle.

The hybrid electric vehicle (HEV) has two power sources (PEM and rechargeable battery) board for propulsion [6].

It consists of four wheels, two rear-wheel drive for progress and two front for steering, were used aluminum for the chassis and bodywork fiberglass, which has a total weight of 180kg.

The displacement front is provided by two electric motors with maximum power of 500W each one, the brake system of the vehicle is made up of magnetic brake motors and mechanical disc brakes on the front wheels.

Figure 7 shows a photo of the HEV (Nayaa II), powered by rechargeable batteries and PEM-FC and all peripheral systems.

Fig 7. Hybrid electric vehicle (Nayaa II).

3. Results and discussion.

3.1. Performance of PEM-FC power generator.

The pressurized hydrogen in tanks 136atm is fed to the cell by auxiliary recirculation system and humidification of hydrogen at 0.1atm, using 5 diaphragm pumps.

The hydrogen consumption is variable to times, depend on the load demand will range cells, whereas the cell operating at its maximum power consumption of total hydrogen is approximately 6 l / min.

Figure 8 shows the voltage-current response of the power fuel cell.

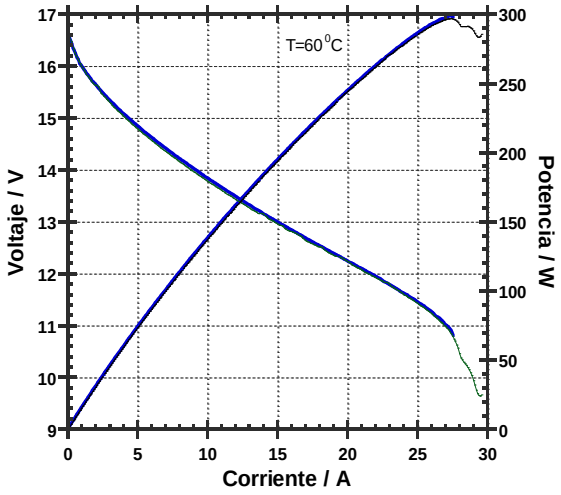

Fig 8. PEM-FC Performance.

3.2. Performance of Rechargeable Lead-Acid battery.

This battery is typically used for UPS that provides constant power. Figure 9 shows the typical behavior of discharge to the ambient temperature of 25 ° C.

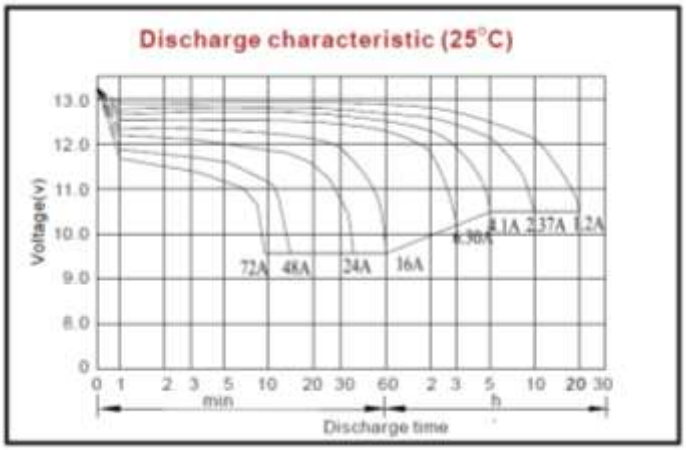

Fig 9. Discharge curve.

3.3. Strategy and distribution of energy to the vehicle.

The vehicle progress is achieved by two brushless electric motors that are powered by two speed controllers, the speed controllers operate by electricity (DC) regulated from battery load control, the batteries are recharged by the fuel cell and the boost converter (DC / DC)

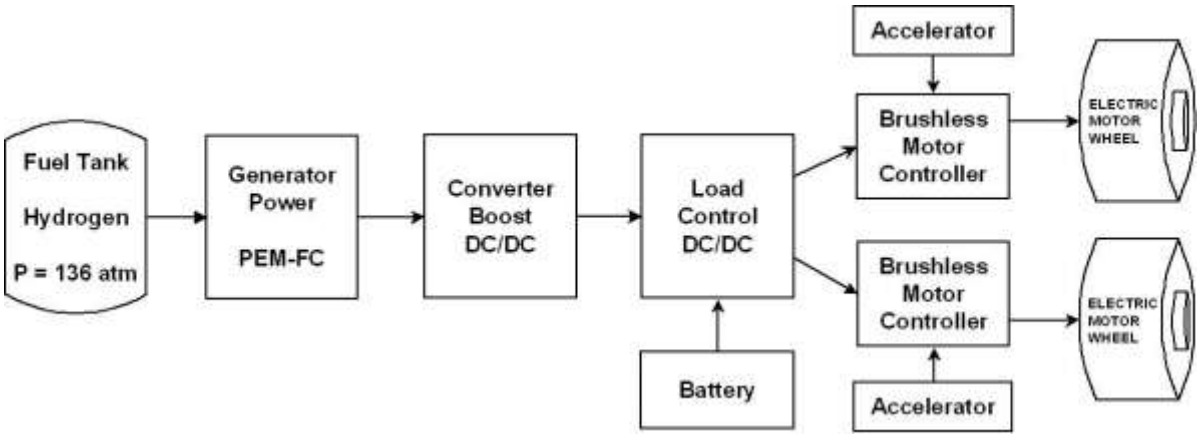

Fig 10. Strategy and distribution of energy.

Figure 11 shows a photo of the different electrical systems, generator and batteries of the vehicle.

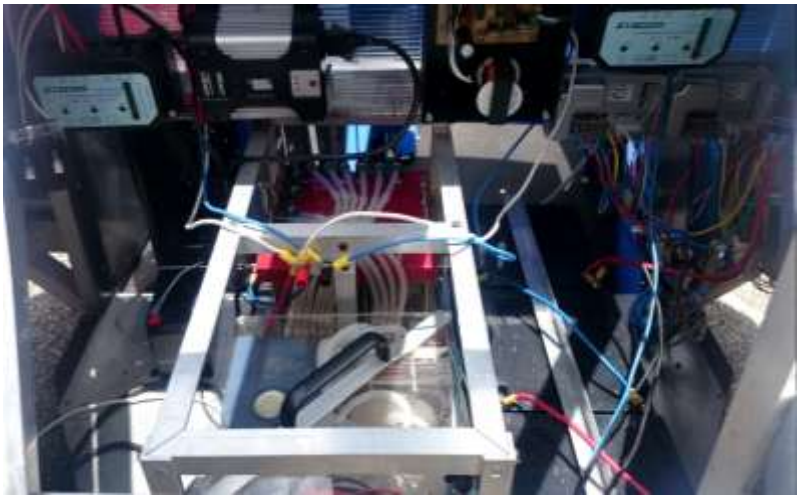

Fig 11.PEM-FC Generator and power electronics.

4. Conclusions.

This hybrid solution (battery, fuel cell) for vehicle could be profitable and eco friendly.

Power generator PEM-FC provides maximum power of 300 W @ 11 V and 27 A with a maximum consumption of 6 l / min of hydrogen.

In our laboratory for the first time in Mexican renewable energy scenario, we achieved to build a hybrid electric vehicle and to analyze the possibility to wards the automobiles application.

Acknowledgements.

The authors thank CINVESTAV the facilities.

The financial support provided by the project ICyTDF OCF-OSF.

The company INFRA SA de CV by hydrogen provided for this project.

References.

[1] Barriers, and R&D Needs, *The Hydrogen Economy: Opportunities, Cost*, The National Academies Press, Washington DC, 2004.

[2] A. Rodríguez Castellanos, E. López Torres, O. Solorza Feria, *J. Mex. Chem. Soc.*, 50(4), 97, (2007).

[3] F. Urbani, G. Squadrito, O. Barbera, G. Giacoppo, E. Passalacqua, O. Zerbinati, *Journal of Power Sources*, 169, 334, (2007).

[4] Xianguo Li, Imran Sabir, *International Journal of Hydrogen Energy*, 30, 359, (2005).

[5] Frano Barbir, *PEM Fuel Cells: Theory and Practice*, 147, Ed. Elsevier Academic Press, USA, (2005).

[6] Frano Barbir, Haluk Görgün, *Journal of Applied Electrochemistry*, 360, (2007).

[7] Ali Emadi, *Handbook of Automotive Power Electronics and Motor Drives*, Ed. CRC Press, USA, (2005).

ATO Nanoparticles as Support for Reduction and Evolution Oxygen Reactions in PEM Electrolysers

V. Ávila -Vázquez[1], C. Guzmán-Martínez[1], M. Galván-Valencia[1], V. H. Collins-Martínez[2], S. M. Durón-Torres[1].

[1]Universidad Autónoma de Zacatecas, U. A. Ciencias Químicas, Km 6 Carr. Zac-Guad, Ejido la Escondida, C.P. 98160, Zacatecas, Zac. México.
[2] Centro de Investigación en Materiales Avanzados, S.C. Dpto. de Materiales Nanoestructurados, Miguel de Cervantes 120, Complejo Industrial Chihuahua, Chihuahua, C.P. 31190
*Tel: 4929256690 ext. 4655, mail:duronsm@prodigy.net.mx

ABSTRACT

Sb was used as dopant of SnO_2 to prepare a powder of conductive nanoparticles with the aim to be used as a support for PEM electrolysers and fuel cells, the support were prepared by a chemical coprecipitation method. In this work it is reported the physicochemical characterization and the evaluation of the electrochemical response of antimony doped tin oxide as catalytic supports for ORR and OER. Pt and IrO_2 were used as catalysts in the electrochemical oxygen reactions. The ATO was characterized by X-ray Diffraction (XRD), High Resolution Transmission Electron Microscopy (HRTEM) and Energy Dispersive Spectrometry (EDS) techniques. The resistivity of SnO_2 Sb doped conductive nanoparticles was measured by using a Milliohmeter,The electrochemical properties respect to the oxygen reactions were obtained by using CV, LV, RDE, EIS and chronoamperometry techniques. The material obtained presented nanoparticles sizes of 6-8 nm and the electrochemical results indicate that ATO nanoparticles synthesized could be used as support in electrolysers and fuel cells.

*Keywords:*ATO, OER, Coprecipitation

1. INTRODUCTION

The direct chemical-electrical energy conversion processes in fuel cells (FC) with high efficiency and low pollutant emission is a well known fact and different FC systems are currently under study. Platinum or platinum-based catalysts highly dispersed on a conductive support are commonly used as cathodic electrode materials in low temperature FC. By the other side, water electrolysers (WE) are recognized as electrochemical devices for hydrogen production that require materials (catalysts and supports) with good features to carry out the reactions. In this case, supported oxide catalyst as IrO_2 or RuO_2 are used for the oxygen reaction. An ideal support should offer the following properties: (i) good electrical conductivity, (ii) good catalyst–support interaction, (iii) large surface area, (iv) mesoporous structure enabling the ionomer and polymer electrolyte to bring the catalyst nanoparticles close to the reactants and maximize the triple-phase boundary (TPB), (v) good water handling capability to avoid flooding, (vi) good corrosion resistance, and (vii) easy recovery of the catalyst[1, 2]. A good interaction between the catalyst and the support not only improves catalyst efficiency and decreases catalyst loss but also governs charge transfer. The support can also assist in sufficiently enhancing the catalyst performance and durability by reducing catalyst poisoning (e.g. CO, S, etc.); and in some cases it affects the catalyst particle size. Among non-carbonaceous based materials, titania, indium oxide, alumina, silica, tungsten oxide nanostructures and conducting polymers have been widely investigated with the aim to improve the issue of carbon corrosion, which is suffered by all carbon supports [1-3].

Tin dioxide, SnO_2, belongs to the family of transition-metal dioxide compounds with rutile structures. The mineral form of SnO_2 is called cassiterite, and this is the main ore of tin. SnO_2 is usually regarded as an oxygen-deficient n-type semiconductor. Hydrous forms of SnO_2 have been described in the past as stannic acids, although such materials appear to be hydrated particles of SnO_2 [4, 5]. This oxide has been proposed as a support material for fuel cell and electroyser electrocatalysts because of its chemical properties For its use as an electrocatalytic catalyst support, however, the electrical conductance of SnO_2 has to be improved. Tin dioxide has a wide bandgap semiconductor (Eg~3.6 eV) with electrical resistivity varying from 10 to 10^6 Ω cm, depending on the temperature and the stoichiometry of the oxide[6, 7] and doping is needed to increase its intrinsic conductivity. Antimony is one of the most common n-type dopant for SnO_2 used to modify the oxide band structure[8-12]. The SnO_2 modified with Sb (ATO) presents high resistance to corrosion in acid media and because is doped withconductivespeciesasSb^{5+} or Sb^{3+},its electrical conductivity reaches values of 10^2or $10^3\Omega^{-1}$ cm^{-1}[13-15].Several studies indicate that ATO could be used as catalyst support for OER and ORR in water electrolizer (WE) and FCs, being reported an improvement in the stability of the support as compared with a nundoped oxide, at the conditions of oxygen evolution[12, 13, 16-22].

According to previous reports, ATO powders have been mainly synthesized by different procedures: sol–gel, hydrothermal preparation, coprecipitation , thermal evaporation , polymer pyrolysis and solid-state reaction. Compared to other methods, coprecipitation from homogeneous solutions containing metallic sources is a cost-efficient method of ATO synthesis, which presents many advantages like high purity, small crystalline size, short preparation time, low cost and large scale production. Thus, it is recognized as the best method for commercial production of ATO powders [8, 9, 23-28].

This paper presents the results of the study of the OER and ORR kinetics of IrO_2 an Pt catalyst supported on ATO synthesized by co-precipitation with a heat treatment time of 1h. X-ray Diffraction (XRD), High Resolution Transmission Electron Microscopy (HRTEM) and Energy Dispersive Spectrometry (EDS) techniques were employed to characterize the microstructure of ATO. The electrochemical properties respect to the oxygen reactions were obtained by using CV, LV, RDE, EIS and chronoamperometry techniques. The resistivity of SnO_2 Sb doped conductive nanoparticles was measured by using a Milliohmeter system. The ATO support obtained suitable candidate to be used in the reactions of oxygen.

2. EXPERIMENTAL SECTION

2.1 Synthesis of materials.

The IrO_2catalyst for OER was synthesized using a coloidal system that consist in mixing a 0.02M $H_2IrCl_6 \cdot nH_2O$ solution with 1M KOH for 50 min at a temperature near to 100 °C. The dark iridium hidroxide precursor obtained was then annealed at 400°C for 1 h [29-34]. ATO supports were obtained by a co-precipitation method from the reaction between $SnCl_4.5H_2O$ and $SbCl_3$ (StremChem) precursors in hidrochloric acid medium at moderate temperature (50 °C) for 1 h, the precipitate was dried at 90°C for 24 h, followed by an annealing procedure at 500 °C and heat treatment time of 1h[35-38].

2.2 Electrodes preparation

The electrodes were prepared from a catalytic ink comprising of 90µL of Nafion® (5wt. %, Aldrich), 540 µL of ethanol spectroscopic grade, 6mg of IrO_2 or Pt as catalyst and 6 mg of ATO or vulcan as support. The ink was obtained using a FRITSCH/PULVERISETTE 23 mini-mill for a period of 0.5h in order to homogenize the mixture and promote dispersion of the ink. Later, the resulting suspensions were hold in an ultrasonic bath for 0.5 h with the aim of gain additional dispersion of the mixture. Subsequently, a volume of each ink was deposited on a clean polished glassy carbon disk electrode (GCE) (A = 0.07068 cm^2). The coated GCEs were dried in a furnace at 80°C for 10 min. IrO_2 and Pt films supported on ATO or vulcan were used as working electrodes for the OER and ORR kinetic studies. All the current values reported in this paper are normalized to the electrode geometric area.

2.3 Electrochemical characterization of electrodes

All the experiments were performed in a double-compartment electrochemical glass cell. An Hg/Hg_2SO_4/0.5 M H_2SO_4 (ESM = 0.69V vs. NHE) electrode was used as reference which was positioned as close to the working electrode as possible by means of a Luggin capillary. A Pt-mesh was used as counter-electrode and the aqueous electrolytic medium was 0.5 M H_2SO_4 at room temperature. The electrochemical measurements were performed using an EG&G PAR VersaSTAT 3 Potentiostat/Galvanostat. In this study, all measured values of potential are reported respect to the normal hydrogen electrode (NHE).

Cyclic voltammetry (CV) was carried out to evaluate the effect of different ATO in the IrO_2 or Pt electrodes by scanning the potential at a rate of 50 mV s^{-1} between -0.16 V and 1.54 V under a N_2 atmosphere. Oxygen evolution experiments were performed by linear scan voltammetry (LSV) at a scan rate of 5 mV s^{-1} in the anodic direction from 0.59 V to 1.69 V in O_2-free electrolyte solution at a constant electrode rotation frequency of 1000 rpm. The rotation rate was controlled by a PINE MSRX precision rotating system.

In addition, electrochemical impedance spectroscopy (EIS) experiments were carried out in the potentiostatic mode in the 100 kHz to 10 mHz frequency range. The impedance spectra were registered with a logarithmic data collection scheme at 10 steps per decade at 1.67 V of potential with an alternate signal amplitude of 10 mV.

3. **RESULTS AND DISCUSSION**

3.1 **Physicochemical Characterization**

The XRD diffraction patterns of ATO are shown in Figure 1, here the characteristic peaks of SnO_2 with a cassiterite tetragonal stucture and a rutile phase can be observed. Due to the minimal dopant quantity used, any diffraction peak related with Sb could be identified. The two diffractograms shown correspond to samples obtained from annealing times of 1h (black) and 3h (red) respectively. A SnO signal peak has been identified at 29 degrees in the red diffractogram.

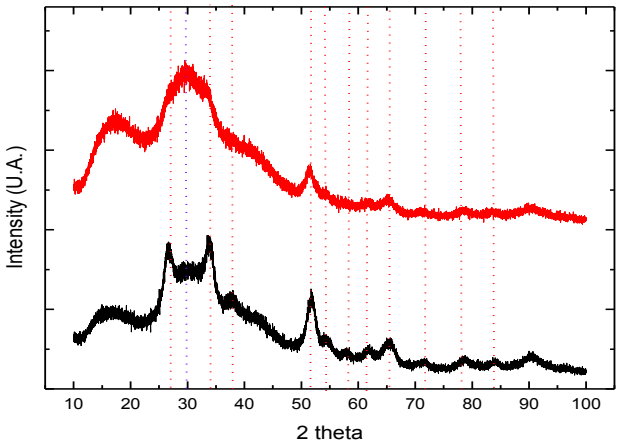

Figure 1. X-ray diffraction patterns of ATO obtained at 500 °C.

Figure 2 a) shows the SEM micrograph of 4 wt% antimony-doped tin oxide nanoparticle of ATO. The surface morphology of ATO powder showed the presence of spherical-shaped particles of 60-70nm composed by the

agglomeration of smaller crystallites. An ATO TEM micrograph is shown in Figure 2 b), homogeneous particles with sizes ranging from 5 to 7 nm can be clearly observed. The particles were nanocrystalline in nature with an estimated average size of 6 nm such as shown in histogram of Figure 2 c), which indicates that the nanoparticles should be monocrystalline. [37, 39-41]. These sizes are smaller than the average value of 20 to 7 nm reported for commercial ATO [15, 42].

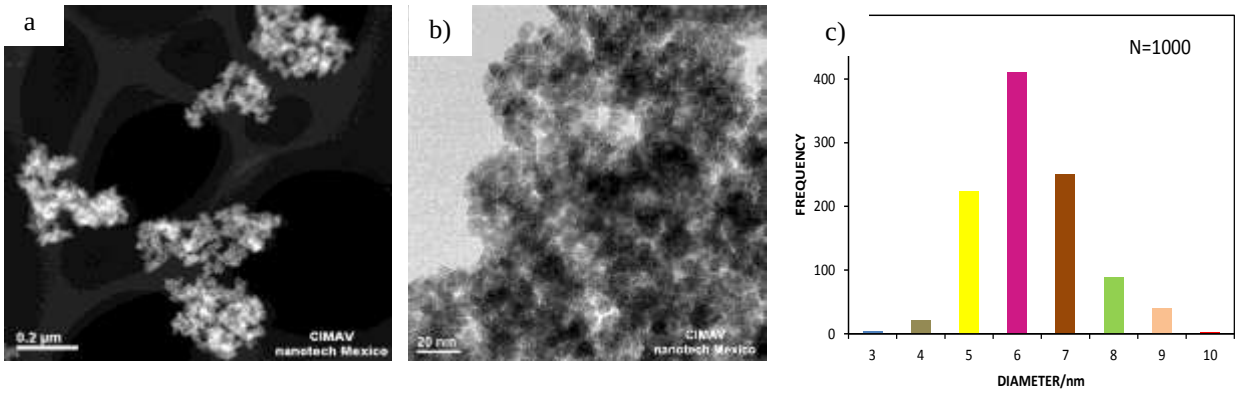

Figure 2. SEM micrograph of ATO powder a), TEM micrograph b), histogram of the particle size average of ATO.

Figure 3 shows HR-TEM and a typical electron diffraction pattern of ATO 1h nanocrystalline grain. The electron diffraction (ED) rings can be indexed to the pattern of ATO with cassiterite structure. The small size ATO particles is responsible for the somewhat thicker diffraction circles in Figure 3 b). The typical lattice parameters of SnO_2 are changed when Sn ions were replaced by Sb ions. The ionic radius of Sn^{4+}, Sb^{5+} and Sb^{3+} is 0.72, 0.62 and 0.90 Å respectively. When Sb^{5+} enters the SnO_2 lattice, the lattice parameters became therefore smaller, contrarily if Sb^{3+} ions increase the lattice parameters [9,10, 23, 43].

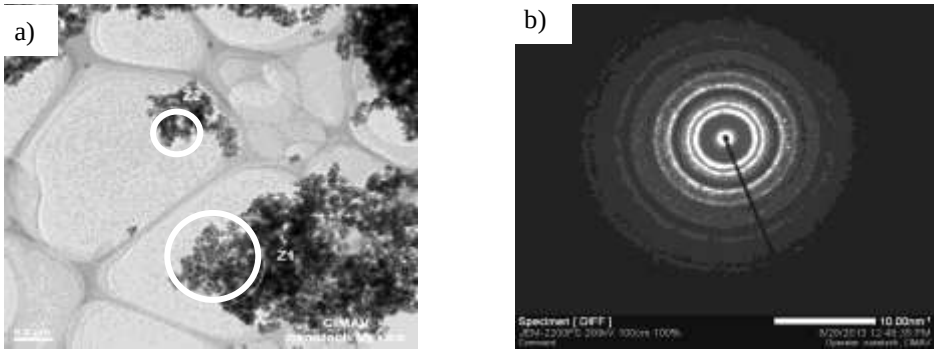

Figure. 3 HR- TEM micrographs of ATO a) and the corresponding electron diffraction patterns (right) b).

As obtained from the high-resolution fringes of synthesized ATO (Figure 4), the particles were composed of regularly ordered crystallites with a lattice distance of 3.34 $\dot{A}$ corresponding to the (d 110) inter- planar spacing, this value was slightly smaller that 3.458 $\dot{A}$, wich correspond to the standard lattice spacing of SnO_2 sample (JCPDS PDF# 41-1445).This result confirms the formation of tetragonal crystal structure of Sb-doped SnO_2[43, 44].

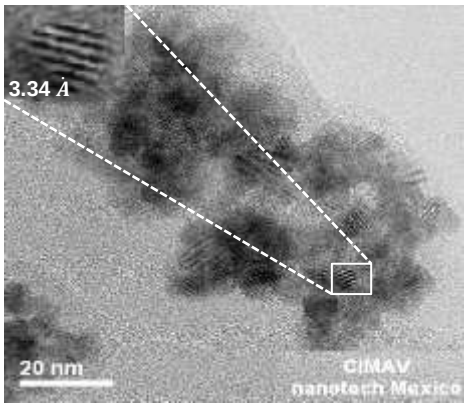

Figure 4. HR-TEM image of ATO.

Figures 5 b) and c) show the Sn and Sb abundance histograms obtained from EDS spectrum of ATO in a particular area correspondig to the linear scanning of sample showed in micrograph 5 a). The metallic element contents in the EDS spectra of different sample regions are shown in Table 1.Theoretically for synthesis was placed a 16% weight of dopant corresponding to a theoretical atomic ratio of Sn: Sb of 6:1, however, the EDS analysis indicates that only between 2% and 4% in weight of dopant is present in the final material.

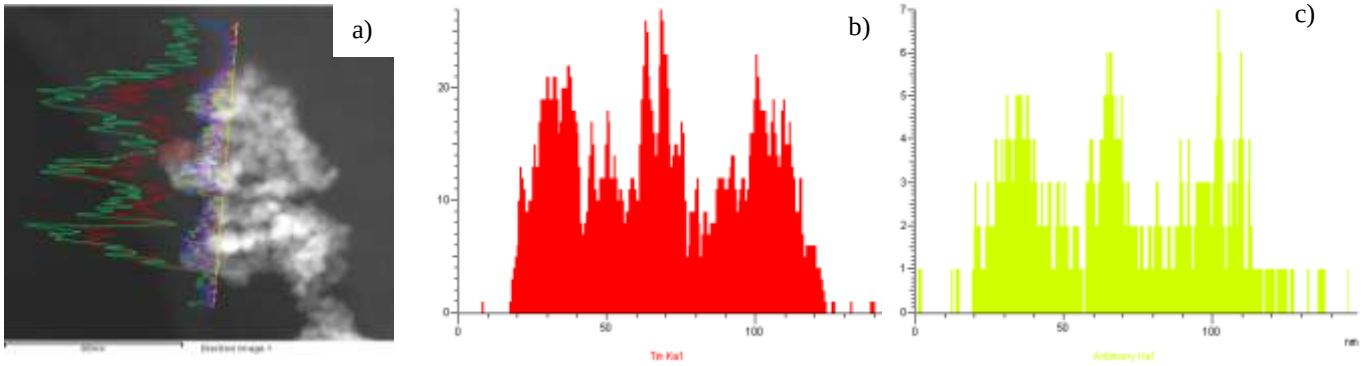

Figure. 5 EDS elements abundance histograms of ATO, Sn (red), Sb (green).

Table 1 EDS concentration of Sn and Sb for ATO synthesized.

	ATO			
Spectrum	Sn % weight	Sb % weight	% Sn atomic	% Sb atomic
Spectrum 1	82.16	4.56	70.44	3.81
Spectrum 2	78.26	2.39	62.4	1.86
Spectrum 3	76.63	6.92	63.3	5.58
Max.	82.16	6.92	72.36	5.94
Min.	76.63	2.39	59.87	1.82

3.2 Electrochemical characterization

3.2.1 Evaluation of the supports by cyclic voltammetry

Previous studies on the relationship between annealing time and the electrochemical performance ATO shown that less time heat treatment presented best performance[16, 45]. The Figure 6 shows typical cyclic voltammograms a) and linear scan voltammograms b), obtained for IrO_2 supported on ATO 1h and 3h in N_2 saturated 0.5 M H_2SO_4 solution. The CV diagrams reveal that the electrochemical response for IrO_2 is practically unchanged with the use of different ATO supports, the current density (j) attributed to IrO_2 supported on ATOs may be considered an evidence that the dispersion of IrO_2 is improved with the use of this supports. The off-peak potential for oxygen evolution on all the IrO_2/ATO electrodes appears near to 1.5 V, this response is more clearly defined in the linear voltammograms showed in Figure 6 b).

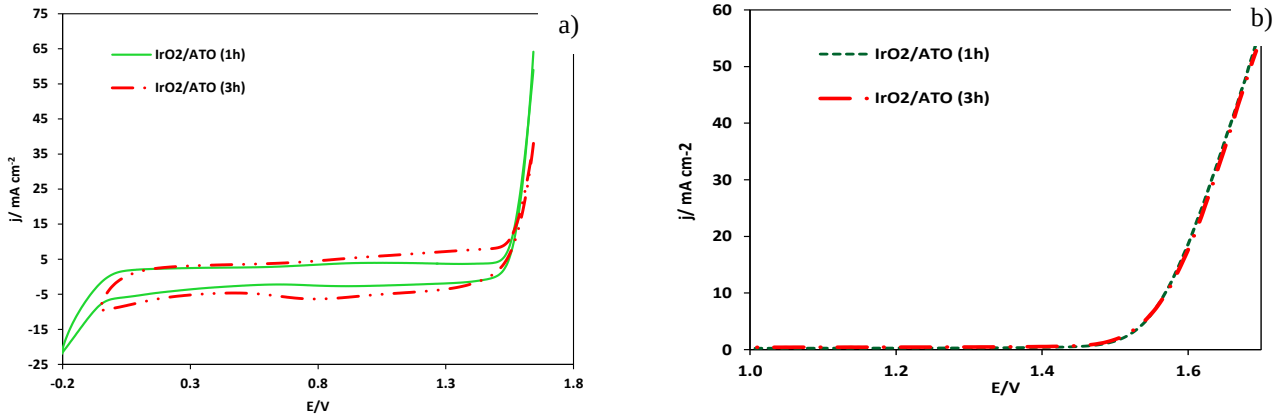

Figure 6. Cyclic voltammogram a) and linear scan voltammetry b) of GCEs coated with IrO_2/ATO in N2 saturated 0.5 M H_2SO_4 at 50 mV s^{-1}. 50 wt % IrO_2/ATO: and room temperature.

The suitable electrochemical behavior of ATO as support for OER is already known [12, 15, 35, 38, 45, 46]. The trends in the development of supports and catalysts is to optimize the synthesis for the preparation of such materials, in this context, it is intended that these materials can be used interchangeably in the OER and ORR, where main application may be in the development of URFC, for this reason in this work also was developed a study with the aim to probe the electrochemical activity of mixtures of ATO based supports and catalysts in the both reactions of oxygen.

For this study was utilized Vulcan and ATO for the mixtures as support and Pt and IrO_2 as catalysts. The proportions used are described in Table 2.

Table 2. Proportion used by inks in mixed support study.

Item	Catalysts		Support	
	% weight Pt	% weight IrO_2	% weight Vulcan	% weight ATO
1	-	100	75	25
2	-	100	25	75
3	100	-	75	25
4	100	-	25	75
5	100	-	50	50
6	-	100	50	50
7	50	50	50	50

The Figure 7 compares the cyclic voltammograms obtainedfor Pt a) and IrO_2 b) supported on vulcan and ATO in N_2 saturated 0.5 M H_2SO_4 solution. The voltammograms of Pt a) supported on mixture support shows that the reactions associated with the surface of Pt in an acid medium are limited by the support especially when the vulcan was in a smaller proportion avoiding identify the characteristic peaks of Pt on a clearly way, nevertheless the general electrochemical behavior in acid medium of platinum is still outlined in the voltammogram. The voltammograms corresponding to IrO_2 catalyst, Figure b), show broad waves corresponding to the redox reactions over the Ir surface, these waves are more evident when Vulcan is in a higher proportion in the support. In the voltammograms of Figure. 7 a) also can also be observed that the potential onset for oxygen evolution in the Pt/ATO electrode appears near to 1.7 V, while the corresponding oxygen evolution peaks of IrO_2/mixed supports electrodes (Figure. 7 b)) appear about 300 mV less positive potential values.

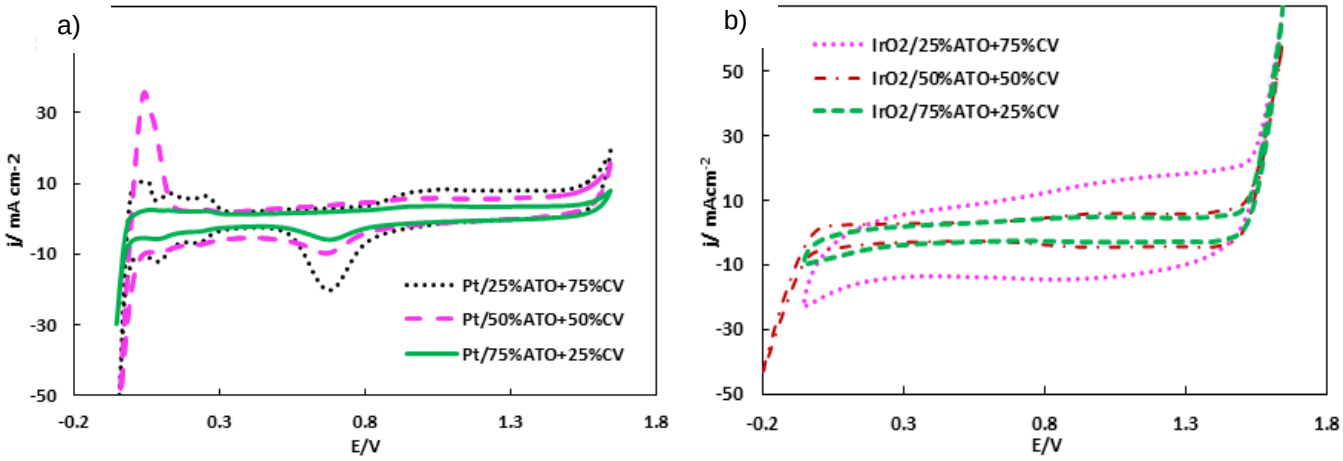

Figure 7. Cyclic voltammograms of Pt a) and IrO_2b) supports on mixtures of vulcan and ATOin N_2satured0.5 M H_2SO_4 at 50 mV s^{-1}.

The Figure 8 shows the RDE diagram a) with typical diagram j–V for ORR at a constant rotating speed of RDE, the difference in the limiting currents for different mixed supports may be attributed to the surface coverage of the catalyst and the physical properties such as the porosity of the catalyst and nature the supports deposited on the glassy carbon electrode. The ORR curves show the classical mixed, kinetic and diffusion control zones, although these regions are better defined when the vulcan is in a greater proportion. On the other hand the Figure 8 b) shows the linear scan voltammograms for OER with IrO_2 t on different mixtured supports, the voltammograms practically

remain unchanged with the use of mixtues, the OER begins in a potential near to 1.54 V, although can observe a higher current densities are obtained when higer ATO proportions are used in the mixed support.

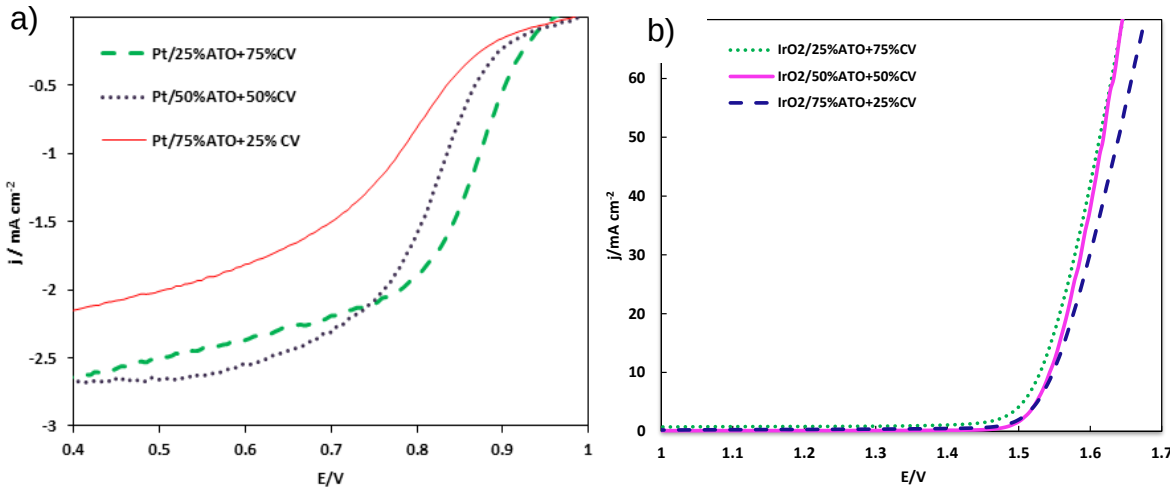

Figure 8. RDE for ORR of Pt support on mixture support in O_2 satured a) and linear scan voltammograms for OER of IrO2in N_2 saturedb), in solution 0.5 M H_2SO_4, at v=5 mVs^{-1}.

EIS measurements for both oxygen reactions was carried out on Pt and IrO_2 on mixed supports in 0.5 M H_2SO_4 solution, in the potensiostatic mode at an anodic potential of 1.67V for OER and 0.8V for ORR. Figure 9 a) shows the Nyquist plots for ORR, it can be observed that the reaction is faster when the Pt is supported on a mixed support with 50:50 % weight ratio, followed by the support of proportion 25% weight of ATO. A similar behavior occurs for the OER, in this case the suport of proportion 75% weight in vulcan is better for OER as can be seen by the smaller semicircle in the complex impedance plane, however the lesser stability and the corrosion problems that carbon presents at the OER potentials, means an opportunity of use of 50:50 % weight support mixture in this reaction. The R_{ct} and R_S values obtained from Non-Linear Square Adjustment of EIS data for the oxygen reactions are shown in Table 2.

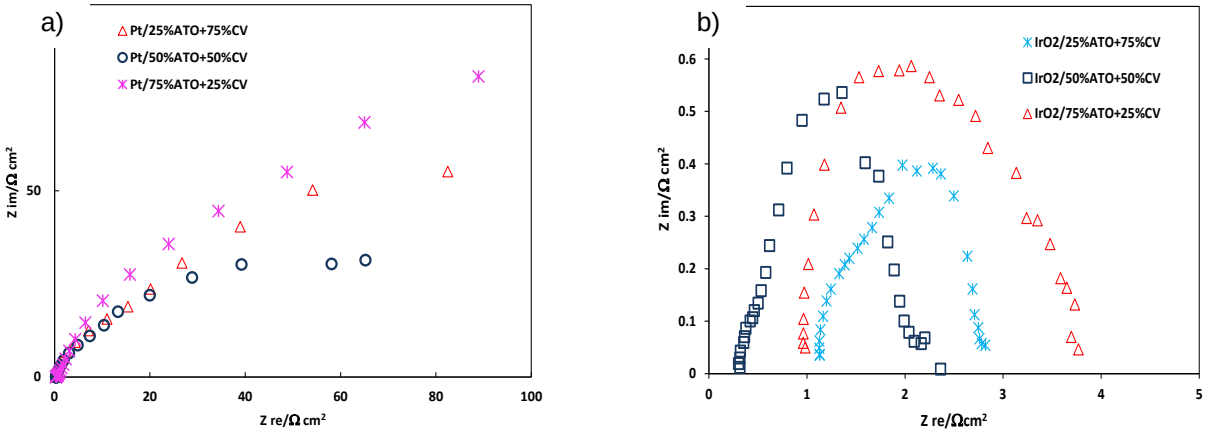

Figure 9. Nyquist plots for ORR and OER on Pt and IrO_2 support on mixtures at anodic potential value of 0.8 and 1.57 V respectively, in O_2-free 0.5 M H_2SO_4 solutions.

Table 2. R_{ct} and R_S values obtained of EIS for OER and ORR with mixtures support.

	Proportion of catalyst/support	Rs / Ω cm^2	Rct / Ω cm^2
RRO (0.8V)	Pt/75%ATO+25%CV	6.6	151.8
	Pt/50%ATO+50%CV	1.32	110.5
	Pt/25%ATO+75%CV	5.3	506.2
REO (1.67 V)	IrO_2/75%ATO+25%CV	1.1	2.6
	IrO_2/50%ATO+50%CV	0.5	2.4
	IrO_2/25%ATO+75%CV	1.3	1.5

Figure 10 shown the electrochemical stability for the OER, The chronoamperograms shown, were obtained at a potential of 1.63V vs. ENH for 8 h. Can be observed that the IrO_2 support on proportion 50:50 % weight of Vulcan and ATO presents more stability for OER since virtually no significant current loss is obtained during the test period, while in the rest of the proportions a slight loss of the current density can be observed, this results suggests that the proportion of 50:50 % weight may be a promising option of support to perform the OER.

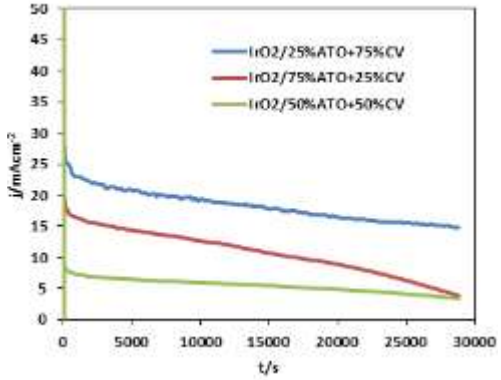

Figure 10.Chronoamperograms of IrO_2 on mixtures of supports for OER in 0.5 M H_2SO_4 at 1.63 V and room temperature.

Finally, the consecutive cyclic performance respect to the EOR and ORR was evaluated using the mixed Pt and IrO2 catalysts and mixed ATO and CV supports proportions described in the item 7 of Table 1. The Figure 11 shows the RDE and LSV plots obtained from 100 sequential experiments between ORR and OER. The Figure 11 a) shows the RDE plots for ORR obtained with rotation and b) without rotation from the first to the 100th measurement (in aim of simplicity only four curves of the series are presented). It can be observed in Figure 11 b) that the absence of rotation does not allow a clear formation of kinetic, diffusional and mixed control zones in the voltammograms. However in the case the LSV was observed that the rotation could be causing physical perfidious of the film deposited on the electrode Figure 11 c), and a loss of lower current density when not rotation Figure 11 d).

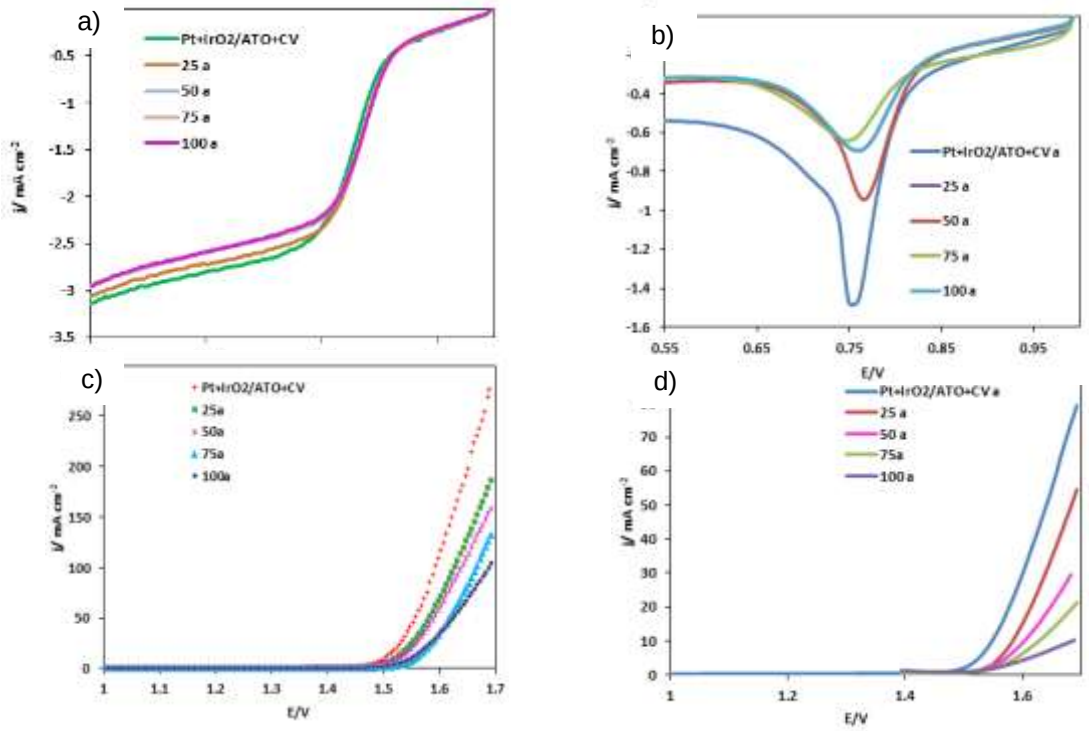

Figure 11. RDE for ORR with rotation a) no rotation b) and LSV with rotation c) no rotation d) of catalyst and support mixture electrodes in O_2 satured (for RDE), in N_2 satured (for LSV)0.5 M H_2SO_4, at v=5 mVs^{-1}.

4. CONCLUSIONS

ATO was obtained with characteristics of a suitable support for IrO_2 used as catalyst the present sufficient catalytic activity for OER, the parameters that have the greatest impact on performance Electrochemical bracket are pH and the time of calcining, being neutral pH calcined short times (1 and 3 h) the most suitable conditions for the synthesis.

The ATO calcined for 1 h showed particle sizes between 5-7 nm , quasi-spherical shape and a homogeneous distribution into small 60-70 nm agglomerates. Furthermore ATO presented calcined for 3 h similar particles with sizes between 7 and 10 nm, grouped in small agglomerates of 200 to 300 nm. The comparison of ATO + vulcan mixture was determined that mixtures ATO 25 +75%vulcan weight and 50 % ATO +50% vulcan are those that can be used indistinctly in the ORR and OER. Studies to the mixture of Pt + IrO_2/ATO+ vulcan with and no rotation showed promising results for OER give greater electrochemical stability when the experiments were carried no rotation. The ORR is not significantly altered with various catalyst / support mixtures

.

5. ACKNOWLEDGMENTS

The authors wish to thank the mexican CONACyT (Project 167012) for financial support of this work.

6. REFERENCES

1. Antolini, E., Composite materials: An emerging class of fuel cell catalyst supports. Applied Catalysis B: Environmental, 2010. 100(3–4): p. 413-426.
2. Sharma, S. and B.G. Pollet, Support materials for PEMFC and DMFC electrocatalysts—A review. Journal of Power Sources, 2012. 208(0): p. 96-119.
3. Long, N.V., et al., The development of mixture, alloy, and core-shell nanocatalysts with nanomaterial supports for energy conversion in low-temperature fuel cells. Nano Energy, 2013. 2(5): p. 636-676.
4. Oviedo, J. and M.J. Gillan, Energetics and structure of stoichiometric SnO2 surfaces studied by first-principles calculations. Surface Science, 2000. 463(2): p. 93-101.
5. Rajendran, V. and K. Anandan, Size, morphology and optical properties of SnO2 nanoparticles synthesized by facile surfactant-assisted solvothermal processing. Materials Science in Semiconductor Processing, 2012. 15(4): p. 393-400.
6. Antolini, E. and E.R. Gonzalez, Ceramic materials as supports for low-temperature fuel cell catalysts. Solid State Ionics, 2009. 180(9–10): p. 746-763.
7. Zhang, D., et al., Surface morphologies and properties of pure and antimony-doped tin oxide films derived by sol–gel dip-coating processing. Materials Chemistry and Physics, 2006. 100(2–3): p. 275-280.
8. Lu, H.F., et al., Preparation of ATO nanorods and electrical resistivity analysis. Materials Letters, 2012. 68(0): p. 237-239.
9. Krishnakumar, T., et al., Structural, optical and electrical characterization of antimony-substituted tin oxide nanoparticles. Journal of Physics and Chemistry of Solids, 2009. 70(6): p. 993-999.
10. Hu, P., H. Yang, and J. Ouyang, Synthesis and characterization of Sb–SnO2/kaolinites nanoparticles. Applied Clay Science, 2012. 55(0): p. 151-157.
11. Hu, Y., H. Zhang, and H. Yang, Synthesis and electrical property of antimony-doped tin oxide powders with barite matrix. Journal of Alloys and Compounds, 2008. 453(1–2): p. 292-297.
12. Xu, J., et al., Antimony doped tin oxides and their composites with tin pyrophosphates as catalyst supports for oxygen evolution reaction in proton exchange membrane water electrolysis. International Journal of Hydrogen Energy, 2012. 37(24): p. 18629-18640.
13. Wang, L.S., et al., Synthesis and electrical resistivity analysis of ATO-coated talc. Powder Technology, 2012. 224(0): p. 124-128.
14. Zhukova, A.A., et al., Influence of antimony doping on structure and conductivity of tin oxide whiskers. Thin Solid Films, 2009. 518(4): p. 1359-1362.
15. Marshall, A.T. and R.G. Haverkamp, Electrocatalytic activity of IrO2–RuO2 supported on Sb-doped SnO2 nanoparticles. Electrochimica Acta, 2010. 55(6): p. 1978-1984.
16. Cruz, J.C., et al., Synthesis and evaluation of ATO as a support for Pt–IrO2 in a unitized regenerative fuel cell. International Journal of Hydrogen Energy, 2012. 37(18): p. 13522-13528.
17. Jung, D.-W. and D.-W. Park, Synthesis of nano-sized antimony-doped tin oxide (ATO) particles using a DC arc plasma jet. Applied Surface Science, 2009. 255(10): p. 5409-5413.
18. Kim, D.-W., et al., Preparation of hard agglomerates free and weakly agglomerated antimony doped tin oxide (ATO) nanoparticles by coprecipitation reaction in methanol reaction medium. Materials Chemistry and Physics, 2006. 97(2–3): p. 452-457.
19. Wu, X. and K. Scott, RuO2 supported on Sb-doped SnO2 nanoparticles for polymer electrolyte membrane water electrolysers. International Journal of Hydrogen Energy, 2011. 36(10): p. 5806-5810.
20. Gurrola, M.P., et al., High surface electrochemical support based on Sb-doped SnO2. Journal of Power Sources, 2013. 243(0): p. 826-830.
21. Pan, C., et al., Platinum–antimony doped tin oxide nanoparticles supported on carbon black as anode catalysts for direct methanol fuel cells. Journal of Power Sources, 2011. 196(15): p. 6228-6231.
22. You, D.J., et al., Platinum–antimony tin oxide nanoparticle as cathode catalyst for direct methanol fuel cell. Catalysis Today, 2009. 146(1–2): p. 15-19.
23. Sladkevich, S., et al., Antimony doped tin oxide coating of muscovite clays by the Pechini route. Thin Solid Films, 2011. 520(1): p. 152-158.
24. Liu, T.J., et al., Conducting antimony-doped tin oxide films derived from stannous oxalate by aqueous sol–gel method. Applied Surface Science, 2008. 254(20): p. 6547-6553.
25. Zhang, D., et al., Microstructure and electrical properties of antimony-doped tin oxide thin film deposited by sol–gel process. Materials Chemistry and Physics, 2006. 98(2–3): p. 353-357.
26. Benrabah, B., et al., Impedance studies of Sb doped SnO2 thin film prepared by sol gel process. Superlattices and Microstructures, 2011. 50(6): p. 591-600.
27. Yang, F., et al., Preparation of Highly Dispersed Antimony-doped Tin Oxide Nano-powder via Ion-exchange Hydrolysis of SnCl4 and SbCl3 and Azeotropic Drying. Chinese Journal of Aeronautics, 2007. 20(2): p. 181-186.

28. Yang, F., et al., Preparation of highly dispersed antimony-doped tin oxide nanopowders by azeotropic drying with isoamyl acetate. Transactions of Nonferrous Metals Society of China, 2007. 17(3): p. 626-632.
29. Cruz, J.C., et al., Nanosized Pt/IrO2 electrocatalyst prepared by modified polyol method for application as dual function oxygen electrode in unitized regenerative fuel cells. International Journal of Hydrogen Energy, 2012. 37(7): p. 5508-5517.
30. Siracusano, S., et al., Electrochemical characterization of single cell and short stack PEM electrolyzers based on a nanosized IrO2 anode electrocatalyst. International Journal of Hydrogen Energy, 2010. 35(11): p. 5558-5568.
31. Vazquez-Gomez, L., S. Ferro, and A. De Battisti, Preparation and characterization of RuO2–IrO2–SnO2 ternary mixtures for advanced electrochemical technology. Applied Catalysis B: Environmental, 2006. 67(1–2): p. 34-40.
32. Zhang, Y., et al., Deposited RuO2–IrO2/Pt electrocatalyst for the regenerative fuel cell. International Journal of Hydrogen Energy, 2007. 32(3): p. 400-404.
33. Mayousse, E., et al., Synthesis and characterization of electrocatalysts for the oxygen evolution in PEM water electrolysis. International Journal of Hydrogen Energy, 2011. 36(17): p. 10474-10481.
34. Papazisi, K.M., et al., Preparation and characterization of IrxPt1−xO2 anode electrocatalysts for the oxygen evolution reaction. International Journal of Hydrogen Energy, 2012. 37(21): p. 16642-16648.
35. Huaming, Y.P.H., Controlled coating of antimony-doped tin oxide nanoparticles on kaolinite particles. Applied Clay Science, 2010. 48(3): p. 368-374.
36. Yang, H., Y. Hu, and G. Qiu, Preparation of antimony-doped SnO2 nanocrystallites. Materials Research Bulletin, 2002. 37(15): p. 2453-2458.
37. Zheng, M. and B. Wang, One-step synthesis of antimony-doped tin dioxide nanocrystallites and their property. Transactions of Nonferrous Metals Society of China, 2009. 19(2): p. 404-409.
38. Xiaozhen, L., et al., Complexation-Coprecipitation Synthesis and Characterization of Erbium and Antimony Doped SnO2 Conductive Nanoparticles. Journal of Rare Earths, 2007. 25, Supplement 1(0): p. 72-76.
39. Bai, F., et al., One-step synthesis of monodispersed antimony-doped tin oxide suspension. Materials Letters, 2006. 60(25–26): p. 3126-3129.
40. Liu, G., et al., Nanosphere-structured composites consisting of Cs-substituted phosphotungstates and antimony doped tin oxides as catalyst supports for proton exchange membrane liquid water electrolysis. International Journal of Hydrogen Energy, 2014. 39(5): p. 1914-1923.
41. Zhang, J. and L. Gao, Synthesis and characterization of antimony-doped tin oxide (ATO) nanoparticles by a new hydrothermal method. Materials Chemistry and Physics, 2004. 87(1): p. 10-13.
42. Gurrola, M.P., et al., Evaluation of the corrosion of Sb-doped SnO2 supports for electrolysis systems. International Journal of Hydrogen Energy, (0).
43. Du, Y., et al., Fabrication and excellent conductive performance of antimony-doped tin oxide-coated diatomite with porous structure. Materials Chemistry and Physics, 2012. 133(2–3): p. 907-912.
44. Chen, X., Synthesis and characterization of ATO/SiO2 nanocomposite coating obtained by sol–gel method. Materials Letters, 2005. 59(10): p. 1239-1242.
45. Manesse, M., et al., Preparation and characterization of antimony-doped SnO2 thin films on gold and silver substrates for electrochemical and surface plasmon resonance studies. Electrochemistry Communications, 2008. 10(7): p. 1041-1043.
46. Yin, M., et al., Highly active and stable Pt electrocatalysts promoted by antimony-doped SnO2 supports for oxygen reduction reactions. Applied Catalysis B: Environmental, 2014. 144(0): p. 112-120.

Synthesis and Characterization of Pt/NTC Electrocatalysts for Oxygen Reduction Reaction

Edwin R. Oseguera[1*], C. A. Cortés[1] and Rosa de G. González[2]

1 Laboratorio de Energías alternas CIITEC IPN, Cda. Cecati s/n, Azcapotzalco, Mexico D.F.
2 Laboratorio de Foto-Electrocatálisis, ESIQIE- IPN UPALM, México, DF.
*E-mail: eosegueraiqi@hotmail.com Tel.: 57296000 ext 54246

ABSTRACT

Recent research has found that the decomposition of the support and particularly in the cathode side is compromising the useful life of the fuel cells, since the carbon vulcan is oxidized to CO_2 in the operating conditions of the cell. In order to improve operation, carbon support has been modified with an exfoliation treatment to increase capacitance of carbon nanotubes (CNTs). The enhanced capacitance can be attributed to improved effective surface area and increased defect density of the tubular structure. The results declared that the exfoliated CNTs are promising electrode materials for high capacitance supercapacitors.

Results on cathode electrocatalyst synthesized by the polyol method are shown. This method was chosen in order to obtain nanometric particle sizes, because according to the literature, smaller particle size produce enhanced catalytic activity by increasing contact area. A solution of diethylene glycol (DEG) with platinum chloride and multiwalled carbon nanotubes was refluxed for 4 hours at 214 ° C. Resulting solution after reflux process was filtered and washed with ethanol to remove DEG excess. Nanotubes underwent an exfoliation treatment to increase the surface area and get a higher dispersion of the active phase, which allow oxygen diffusion and improvement of reaction kinetics.

The results are shown by means of linear sweep voltammetry (LSV), scanning electronic microscopy (SEM), transmission electronic microscopy (TEM) and X-ray diffraction (XRD) and compared with the performance of catalyst 10% Pt/90% NTC.

Keywords: Electrocatalyst, PEM fuel cell, polyol mediated synthesis.

1. Introduction

For a long time it was believed that oil supplies would be safe and almost unlimited, but the oil shocks transformed the secure supply of cheap oil in an unsafe and expensive delivery. In view of the available reserves and so pessimistic projections, it is clear that in the near future will require alternative energy sources, taking into account the huge energy needs of the industrialized world. Clean, available and efficient: a new energy regime, which must comply with the following characteristics is required. Has recently been paid much attention to fuel cells, electrochemical devices that are intended or being one of the preferred sources of energy in the future medium.

Interest in fuel cell proton exchange membrane (PEMFC) is its cleanliness, versatility and high efficiencies obtained from the conversion of chemical energy to electrical energy, especially for portable applications such as cell phones, laptops and cars, because its low operating temperature.

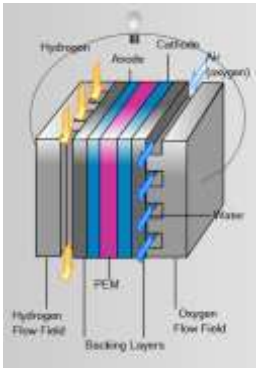

Figure 1. Inputs and outputs of a fuel cell

The chemical reactions taking place in a fuel cell are the follows:

Anode (ROH): $2H_2 \rightarrow 4H^+ + 4e^-$

Cathode (RRO): $O_2 + 4H^+ + 4e^- \rightarrow 2H_2O$

Global reaction: $2H_2 + O_2 \rightarrow 2H_2O + electricity + heat$

Of the two half-reactions that occur in the cell, the RRO is the limiting reaction in a fuel cell, for presenting a slow kinetics that is crucial to the overall performance of the fuel cell (CC) that is why it is considered very important to study and develop catalysts that offer good performance at the lowest possible cost RRO. When RRO occurs in the fuel cell a high overpotential is neddes, associated with the fact that the O-O bond requires high energy to be dissociated which causes reduction occurs three orders of magnitude slower than the reaction requires hydrogen oxidation (ROH). Although studies have been performed for the reaction mechanism of the RRO is not fully understood, however the most acceptable model is the simple and Damjanovic numbered individually and consecutively in square brackets (figure 2) [1-4].

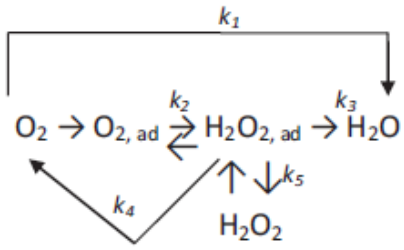

Figure 2. Pathways proposed by Damjanovic reaction [4].

k1. Route without intermediaries known as "direct" or 4 e-.
k2. Adsorbed hydrogen peroxide is formed.
k3. The adsorbed peroxide formed with K2 can be reduced to water.
k4. Adsorbed hydrogen peroxide can be chemically broken by the electrode surface.
k5. Desorbing and can be diluted in the solution.

Catalysts based platinum, carbon supported high surface are widely used in fuel cells to low temperature (CC), however, the corrosion of the materials of carbon support for the catalyst as the vulcan carbon, has been recognized as a causes of performance degradation of the CC, particularly under repeated start-stop cycles or conditions of high potential. To improve the stability of the carbon support, materials with higher graphitic character as nanotubes or carbon nanofibers have been tested in terms of the CC. These nanostructured carbons show lower corrosion rate, however, does not prevent oxidation of the carbon, simply reduce its velocity. With lower Pt loadings, the average distance between the metal particles is larger, therefore, the conduction of electrons involving filtration or electron hopping mechanism is unlikely [5].

Carbon nanotubes (CNTs) are emerging as new electrode materials for oxygen reduction reaction (ORR), due to their high conductivity, high surface area and good corrosion resistance. The effective surface of a supercapacitor material is referred to the active layer that is accessible by electrolyte ions; however it is energetically unfavorable for solvated ions to diffuse into the inner tube of CNT, in particularly for multi-walled carbon nanotubes (MWCNTs). In this regard, the specific capacitance of MWCNTs, especially at high current operation, can be limited by the slow diffusion of ions. Considerable efforts have been placed to improve the specific capacitance of MWCNTs. For example, the CNTs treated with sulfuric acid or nitric acid showed several times enhanced capacitance due to the increased surface detected density, which facilitated the diffusion of ions into the inner tube. In this work was used a simple way to enhance the capacitance of MWCNTs by increasing the active surface area and defect density trough exfoliation.

2. Experimental

2.1 Synthesis of catalysts

For the synthesis and characterization of catalysts Pt/C multi walled carbon nanotubes (MWCNTs) were used as support. As platinum precursor salt, platinum dichloride was used (PtCl2 Sigma Aldrich®) and diethylene glycol (DEG) as solvent (Alfa Aesar®). First and to obtain a homogeneous distribution of nanotubes were dispersed in DEG for 30 minutes using a disperser IKA Ultra-Turrax ® T 18 DIGITAL, then salt of platinum was added to obtain a correct homogenization. This solution was heating up to the boiling point of DEG, held at boiling for 3 hours to ensure complete reduction of the platinum salt. A three-necked flask of 250ml PYREX ® was used and rotary agitation to maintain the solution in stir during the reaction time. Subsequently the catalyst was filtered and washed with ethanol to remove excess of DEG. Finally the sample was treated thermally (TT) at 500 ° C for one hour in a tube furnace.

Figure 3. Equipment used for the synthesis by the polyol method

2.2 Exfoliation treatment of carbon nanotubes

Exfoliated carbon nanotubes (ex-CNT) were prepared by dispersing 0.25g in 15 mL of concentrated H_2SO_4, the solution was kept stirred for 1 hr and brought to 50 ° C. Then carefully added 1.5 g of $KMnO_4$ and are allowed to react. When all the $KMnO_4$ was consumed 30 mL of deionized water and 3 mL of 30% H_2O_2 were added. The NTC-former were extracted by means of a centrifuge, which was operated at 2500 rpm for 20 min to separate the nanotubes from the liquid, to remove excess of oxidizing solvent washes were performed with deionized water.

2.3 Electrochemical study

For electrochemical analysis of the samples a Pyrex three electrode double-walled cell was used the working electrode RDE0008 commercial glassy carbon electrode with a 0.196 cm^2 area with teflon support was used using the reference electrode as sulfates Hg / Hg_2SO_4 (ES), whose standard potential is E = 0.680 V with respect to the normal hydrogen electrode (NHE) as the counter electrode and platinum titanium mesh was used with a geometric area greater than 10 cm^2. The potentials are reported with respect to the standard hydrogen electrode, NHE and 0.5M H_2SO_4 solution is used as electrolyte, the currents are referenced with respect to the geometric area of the working electrode.

For preparation of the working electrode, a glassy carbon surface exposed with a sandpaper # 600, until a flat surface together with Teflon to support the thin film of ink to adhere to the glassy carbon is then cleaned ethyl the surface to remove impurities on the surface are alcohol. The catalyst inks were prepared in a vial weighing 1 mg of catalyst were added 60 µL of ethyl alcohol as a diluent and 8µL of Nafion ® liquid (5% weight of ethanol) as adhesion to the electrode, the mixture was homogenized in a bath ultrasound for 15 minutes to form a homogeneous suspension called "catalyst ink." Of the catalyst ink 8 µL taken with a micropipette and deposited in the center of the electrode covering the entire geometric area of the glassy carbon. Allowed to dry the ink at room temperature for 15 minutes to observe a thin and homogeneous film on the surface. The working electrode was attached to a rotor Pine, controlled for different speeds of rotation, connected to a Potentiostat/Galvanostat Autolab whose response was analyzed with the software Autolab NOVA.

Before linear voltammetry studies cyclic voltammetry technique, which aims to enable the working electrode to remove surface oxides and adsorbed oxygen during the preparation of the electrode is used. The reduction-oxidation process of the surface increases the electrocatalytic properties of the materials analyzed, besides that there is restructuring of the surface at atomic catalytic stabilizing compounds. This technique in addition to activating the surface of the catalysts can also be used to analyze the signals redox characteristics that are carried out in certain metals, such as platinum which is being studied in this work. Argon was bubbled to deoxygenate the electrolyte for 15 min. Was conducted 10 cyclic sweeps over a range of potential of 0 V to 1.2 V (NHE) at a scan rate of 100 mV s^{-1} for cleaning the electrode and 2 swept at a speed of 50 mV s^{-1}, in the same range of potential to analyze the distribution of active sites and the redox processes occurring at the electrode surface.

Once activated the linear electrode are made voltammetries different rotation speeds for the study of the RRO. The electrolyte solution was bubbled with oxygen for 15 minutes to saturate the electrolyte solution, reaching a open circuit potential, Eca, in this technique this is a very important parameter, you must monitor and verify each experimental run linear voltammetry at different rotational speeds of the electrode is analyzed if it is stable and the time it takes to reach the expected value, you should also take care to always reach the same value, if the voltage between each run of the first run is not reached is an indicator of catalyst instability. The sweep rate was 5 mV s^{-1}. The potential range was used to open circuit voltage (OCV). The speeds used for runs of different catalysts were: 100, 200, 400, 900, 1600 and 2500 rpm, starting from maximum to minimum. Between each scan the system is allowed to reach the initial OCV bubbling oxygen for 5 min, after reaching the potential flow of oxygen is removed from the electrolyte to prevent noise in the electrochemical response, but is left on the surface of the solution to ensure saturation of the solution.

3. Results and discussion

Figure 4 shows the last 2 cycles performed at a speed of 50 mV s^{-1} from 0 to 1.23 V/NHE of the media used for the synthesis of electrocatalyst Pt/C, can also exhibit the curves generated by the vulcan carbon because it serves as commercial support for this type of catalysts and included for comparison, further behavior of CNTs is shown with 10 wt% of WO_X to know if could have a role as co-support.

Carbon nanotubes with exfoliation treatment exhibit greater capacitance regarding carbon nanotubes without exfoliate, in this case the surface area corresponding to the capacitance as it has no faradaic process, indicating that the NTC-former have better properties due its top surface area.

It is noted that treatment of exfoliation in carbon nanotubes produced an increase in the interfacial activity of the NTC-ex. These signals, in both the anodic and cathodic sweep, appear at the same potential, so that these processes are attributed to the phenomena of adsorption/desorption of species of functional groups, thus exfoliation treatment has given functional groups on the "open" pipes surfaces.

The increase in capacitance is attributed to exfoliation treatment product functional groups, these functional groups also favour the nucleation of particles of platinum on the surface of carbon nanotubes.

Table 1. Carbon supports capacitance

Support	Capacitance
MWCNT	278.37
e-MWCNT	11762.00
Carbon Vulcan	1048.50
Mass Pt	40

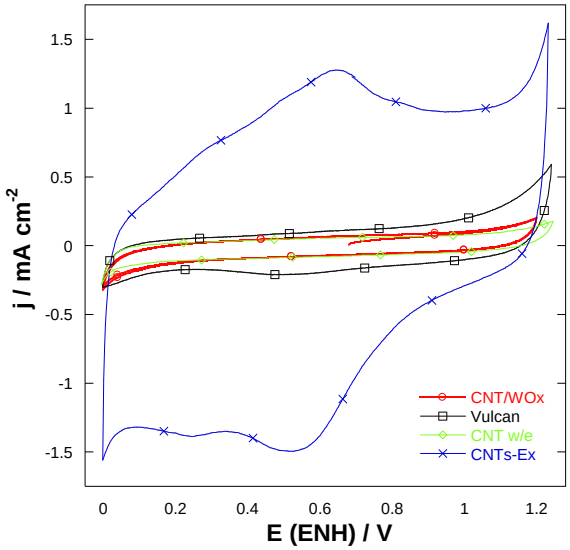

Figure 4. Comparison of Cyclic voltammery at 50 mV s-1 catalyst supports Pt/C

Figure 5 shows the cyclic voltammetries catalysts synthesized by the polyol method. The area of adsorption and desorption of protons, lies between 0 and 0.3 V/ENH, continuing the anodic oxide formation sweep begins at 0.5 V/ENH and ends at 1.2 V / ENH. In the cathodic scan signal is reduced at a potential of 0.75 V/NHE and the double layer area between 0.3 and 0.5 V/ENH. Platinum response characteristic only in the sample with ex NTC and treated thermally (TT) is observed. Similar current density in the catalyst 10% Pt/90% NTC-former with TT and the Pt-Etek wide potential range is observed, this indicates a similar distribution of active sites on these samples as opposed to the other without or thermal exfoliation treatment, this indicates a greater distribution of active sites and larger surface area due to oxidation treatment.

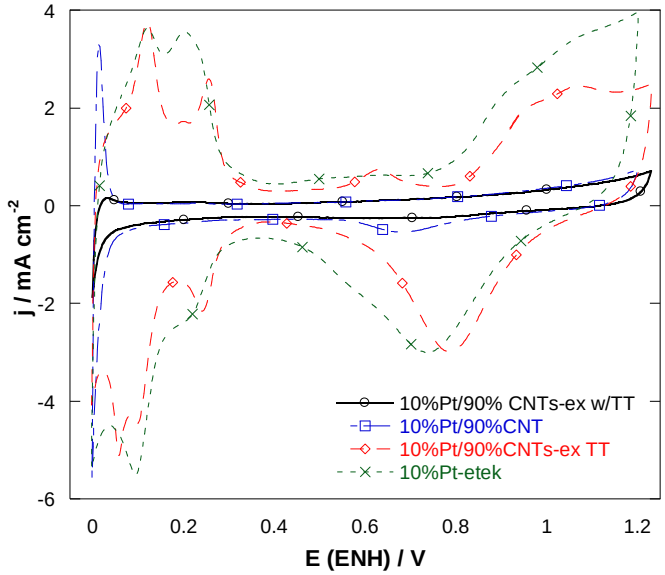

Figure 5. Cyclic voltammetries at 50 mV s^{-1} of 10% Pt/90%CNT catalysts.

Figure 6 shows the polarization curves of the samples tested at 900 rpm of electrocatalysts with Pt/CNTC. Three zones of the response characteristics of rotating disk electrode, a low overpotential one between 0.95 and 0.85 V/NHE, where electron transfer is the rate determining step of the reaction is observed as the current density, j, is clearly independent of the rotational speed of the electrode, ω and low current densities are observed. Control diffusional area of 0.7 V is observed up to 0.2 V, the current depends on the rotation speed of the electrode was observed almost horizontal plateau, indicating that the reaction is carried out at sufficient speed that allows a diffusion controlling at more cathodic potentials. Finally the mixed zone where the two phenomena are present, the first one is the transfer of electrons (contributes to increasing current) and the mass transport (transport of oxygen to the electrode surface via diffusion). Both processes influence the reaction rate.

Higher catalytic activity in the catalyst with carbon nanotubes cleaved and heat treated gender as higher current density (-3.2 mA cm^{-2}) is observed at 500 ° C and present a better definition in the control region that diffusional is in the range of 0.5 to 0.2V/ENH, of treating the catalyst without exfoliation good response is observed in the reduction of oxygen but higher potential applied to start the reduction in the range of plus potential is primarily required is a phenomenon of charge transfer, it has slow kinetics for this catalyst.

For determining step of the reaction speed is necessary to determine the Tafel slope, transfer coefficient and the exchange current. In Figure 7, the Tafel slope represented as a semi-logarithmic relationship of current density against the potential for different catalysts Pt/C is observed They are obtained outstanding polarization curves of Figure 6, eliminating the contribution to the total current density of mass transport, showing only the kinetic contribution. It is observed that the catalyst with heat treatment at current density of 0.1 mA cm^{-2} generates a potential difference greater than the catalyst with carbon nanotubes exfoliate and even Pt-etek.

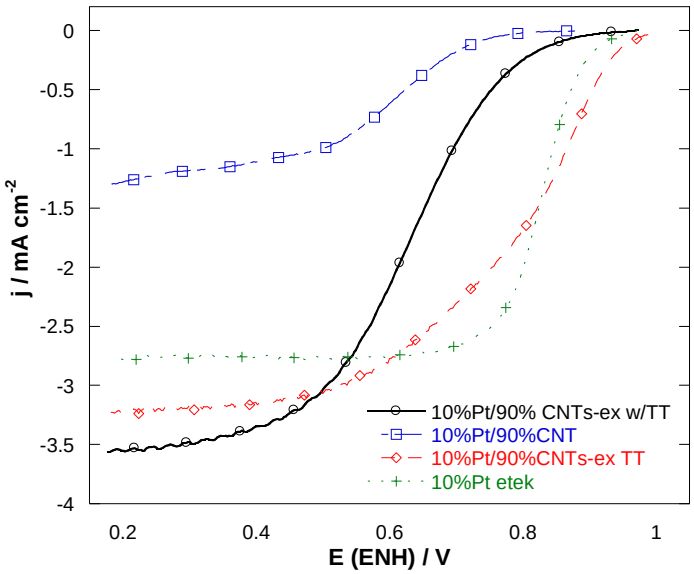

Figura 6. Comparison of linear voltammetries at 900 rpm of 10%Pt/90%NTC catalyst.

The kinetic parameters that were deduced from Tafel slopes of Figure 6 are shown in Table 2. The kinetic Tafel slope information provides an electrochemical reaction of a Tafel slope of about 60 mV dec^{-1} to 120 mV dec^{-1} corresponds to a first-order kinetics, with the transfer of the first electron electrocatalyst for oxygen chemisorbed molecule on the electrode surface.

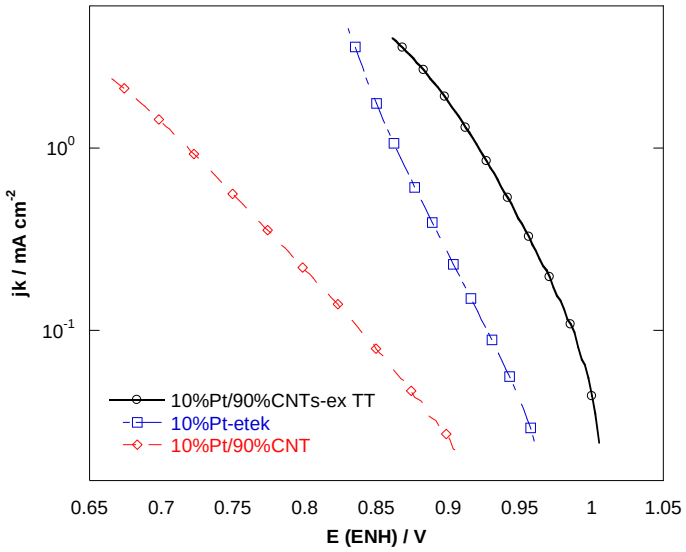

Figure 7. Tafel slope of 10%Pt/90%CNT catalysts

Table 2. Kinetic parameters obtained from the RRO

Catalyst	E_{ca} V / ENH	-b mV dec^{-1}	α	Jo mA cm^{-2}	Potential / j J=0.1 mA cm^{-2}
10%Pt/90%CNT	0.9	120.6	0.4832	6.4906 x10^{-5}	0.84
10%Pt/90%CNTs-ex TT	1.01	59.74	0.991	8.2578 x10^{-6}	0.99
10%Pt/C (E-tek)	0.98	62.95	0.9866	9.6858 x10^{-7}	0.93

From the results in the table shows that catalyst with NTC-former has higher open circuit potential, smaller slope of Tafel and higher transfer coefficient, this can be attributed to that the catalyst has greater capacity to absorb oxygen because of its greater surface area.

4. Summary and perspectives

When performing the exfoliation treatment CNTs higher capacitance is obtained on support, which in no faradaic processes results in surface area and beneficiary distribution of active sites to obtain higher catalytic activity. Additionally it was observed that heat treatment is necessary to obtain higher catalytic activity, apparently because heat treatment induces a more uniform distribution over the support, which is checked by scanning electron microscopy but can also be observed in cyclic voltammetry.

Acknowledgements

Thanks to the Consejo Nacional de Ciencia y Tecnología and COFAA for the financial support.

References

[1] R. J. M. J. L. Blomen and M. N Mugerwa, Fuel Cell Systems, Plenum Press, New York and London, (1993). Barbosa, J. Andaverde, B. Escobar, U. Cano, Stochastic reconstruction and a scaling method to determine effective transport coefficients of a PEMFC catalyst layer. J. Power Sources 2011; 196: 1248–1257

[2] A. J. Bard and L. R. Faulkner, Electrochemical Methods, Fundamentals and Applications, 2nd ed., John Wiley & Sons, Inc., N. Y., 2000.

[3]Kinoshita Kim Electrochemical Oxygen Technology, John Wiley and Sons Inc., first edition, United States of America (1992).

[4] M. K. Ravikumar and K. Shukla, J. Electrochem. Soc., 143, 2601 (1996).

[5]A. J. Bard and L. R. Faulkner, Electrochemical Methods, Fundamentals and Applications, 2nd ed., John Wiley & Sons, Inc., N. Y., (2000). K. B. Prater, J. Power Sources, 51, 139 (1994).

[6] Gongming Wang et al, Enchanced capacitance in partially exfoliated multi-walled carbon nanotubes, Journal of Power Sources, (2011).

Influence of Exfoliation on Multi-walled Carbon Nanotubes in Their Performance as Electrode Support Material

C.A. Campos-Roldán[1,2*], R.G. González-Huerta[1], J.R. Vargas-García[2]

[1] Lab of Electrochemistry, National Polytechnic Institute, Mexico 07300 D.F.
[2] Dept of Materials and Metallurgical Eng., National Polytechnic Institute, Mexico 07300 D.F.
[*] e-mail: charly1909@hotmail.com

ABSTRACT

In this work physical and electrochemical characterization of modified carbon nanotubes are reported. Modification consisted in two different functionalization processes and an exfoliation process. After functionalization, carbon nanotubes (CNT) obtained a better crystalline quality and purity, however, exfoliation granted a high defects density on CNT`s surface. After treatment, IR and XPS analysis reveled that exfoliated CNT (*e*-CNT) granted functional groups onto their surface, mainly carbonyl and carboxyl groups. Finally, cyclic voltammetry measurements confirmed that exfoliated CNT have the biggest electrochemical active surface, which together with carbonyl and carboxyl groups, can provide a greater density of nucleation sites to metal nanoparticles than the commercial support material: carbon Vulcan.

Keywords: Carbon nanotubes (CNT), Capacitance, Electrochemical surface area

Introduction

Electrode material based on carbonaceous compounds has been widely applied in electrochemistry since their special properties, remaking their surface chemistry, which make them a proper choice to determine a wide range of substances in electrocatalytic area.

By the other hand, since their discover, carbon nanotubes (CNT) has been intensively studied due to their excellent properties, such as high specific surface area, high electronic conductivity, outstanding chemical and electrochemical stability and so on [1-5].

Recently, CNT have received considerable attention as the supports of noble metal catalysts in heterogeneous catalysis, such as PEM fuel cells. The interaction between noble metal nanoparticles and CNT in nanohybrids induces a peculiar microstructure or modification of the electron density of the noble metal clusters, and enhances the catalytic activity [1].

It is well known that for CNT without surface modification, there are insufficient binding sites for anchoring the precursor of metal ions or metal nanoparticles, which usually leads to poor dispersion and large metal nanoparticles, specially under high loadings conditions. To introduce more binding sites and surface anchoring groups, surface functionalization of CNT is generally carried out [1].

Because of the pore and surface structures of CNT play an important role in electrochemical activity, the understanding of the surface chemistry and the pore structure of CNT are integral for their optimal use.

In this work, the data obtained from Raman spectroscopy, Electron Microscopy and X-Ray diffraction are related with the enhance electrochemical performance of modified CNT.

Experimental

1.1. Functionalization of CNT

Pristine carbon nanotubes (M1) were synthetized by Chemical Vapor Deposition (CVD) technique by research group. Functionalization consisted in two different processes. At the first one, 100mg of M1 were weighed and suspended into a HNO_3 solution (37mL of concentrated HNO_3/450mL of distilled water at room temperature). They were called M2. At the second treatment, the same quantity of M1 was suspended into a mix of acids (27mL of concentrated H_2SO_4 + 10mL of concentrated HNO_3/450mL of distilled water at room temperature). They were called M3. Both samples were sonicated at 42kHz at room temperature for 20min. Then samples were washed out with distilled water many times and finally filtrated at vacuum.

1.2. Exfoliation of CNT

250mg of NTC were weighed and dispersed into 15mL of concentrated H_2SO_4 and stirred for 1hr. Then 1.5g of $KMnO_4$ was added at 50ªC. When all $KMnO_4$ were consume, the solution was

quenched by adding 40mL of deionized water and 30% H_2O_2. Exfoliated NTC (M4) were extracted by centrifugation and vacuum filter, washed out them with distilled water.

1.3. Raman spectroscopy

The Raman spectra were obtained using a Horiba Jobin Yvon Spectrometer HR 800 with a laser of 532 nm in the range of 100-3100 cm^{-1}.

1.4. X-Ray Diffraction

X–ray diffraction (XRD) analyses were carried out with a Bruker D8/Focous X–ray diffractometer with Cu–Kα radiation.

1.5. Field Emission Scanning Electron Microscopy

A Field Emission Scanning Electron Microscope (FESEM) JEOL JSM-6701F, coupled with a detector for microanalysis Energy Dispersive Spectroscopy (EDS) was used for morphology study.

1.6. Cyclic Voltammetry

Cyclic voltammetry measurements were carried out in a typical three-electrode electrochemical cell, with $Hg/HgSO_4$ as reference electrode (E=0.680 NHE) and a Pt mesh as the counter electrode. For working electrode, a catalytic ink was prepared by weighing 1 mg of each material under study, which was subsequently mixed with 8µL of Nafion® and 60µL of absolute ethanol. This mixture was stirred for 15 minutes in an ultrasonic bath to generate a homogeneous suspension. Finally, 8µL of said suspension were carefully impregnated on a glassy carbon electrode (geometric area of 0.196 cm^2) to form a thin film. A 0.5M H_2SO_4 aqueous solution was used as electrolyte. Finally, the electrochemical cell was bubbled with Ar gas to displace the dissolved oxygen. Corresponding measurements were carried out in a potentiostat-galvanostat GPES AutoLab connected to a PC, evaluating a potential range of 0 to 1.23 V vs. NHE, with scanning speeds from 10 to 100 mV s^{-1}. Note that the potentials obtained were reported compared to NHE. For this technique, commercial carbon Vulcan XC76 (M5) was used as a reference material, because of it is the material support to commercial electrocatalyst.

Results and discussion

3.1 Crystalline quality and purity

Raman Spectra is shown in Fig. 1. All samples presents the characteristic signals of CNT: D (present at about 1300 cm^{-1}), G (1600 cm^{-1}) and G' (near 2650 cm^{-1}) bands [6-14]. By the other hand, in the low frequency range of 140-350 cm^{-1}, there is a signal corresponding to the respiratory mode in the radial direction (RBM), which is characteristic of single-walled CNT [6], suggesting the presence of this type of CNT in all samples.

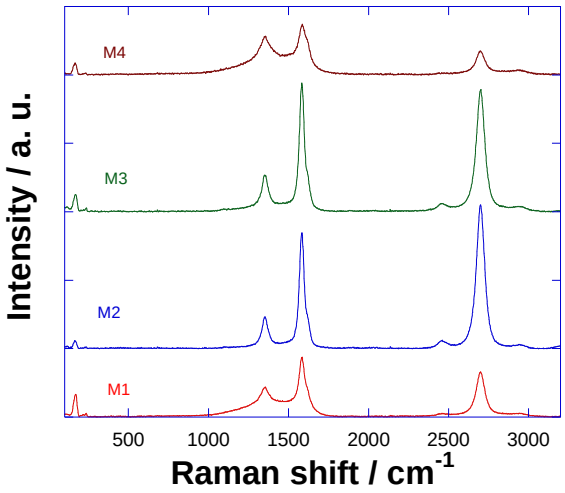

***Fig. 1**. Raman spectra of M1, M2, M3 and M4*

From Fig. 1, the corresponding spectra M1 exposes the existence of impurities such as amorphous carbon and catalyst particles (area under the bands D and G), showing a crystallinity index (I_D/I_G) of 0.50. Subsequently, it is evident that M2 and M3 have increased the crystalline quality significantly, since I_D/I_G has decreased in both cases (0.27 and 0.28, respectively) and the intensity of G' has increased considerably, suggesting a long-range order on CNT´s walls [6-8]. Simultaneously, these chemical treatments have removed impurities observed in M1. However, M4 reveled a reduced crystalline quality (I_D/I_G=0.77). This decrease could be attributed to a high defects density on the walls of the CNT [6-14] due to the treatment damage strongly the carbon lattice. By the other hand, there is a very high degree of disorder, because the intensity of the band G' has decreased substantially. X-Ray diffraction patterns are reported in Fig.2.

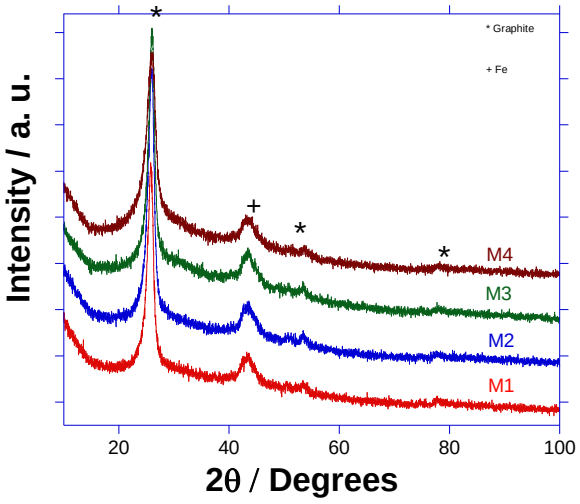

***Fig. 2**. X-Ray diffraction patterns of M1, M2, M3 and M4*

At 26.6º, it is possible to observe the strongest reflection signal of hexagonal graphite, which is associated directly with CNT. Another reflections attributed to graphite from CNT are visible at 54º and 77.5º. In addition, at 43.5º was detected a reflection related with cubic Fe, which its presence was suggested by Raman spectra.

Analysis of the peak detected at 44º is shown in Fig. 3. It is well known that Fe characteristic reflection signal appears at 44.6º, therefore, this shift suggests the formation of a solid solution C/Fe or the presence of a semi-stoichiometric iron carbide, since carbon is introducing at iron cubic lattice.

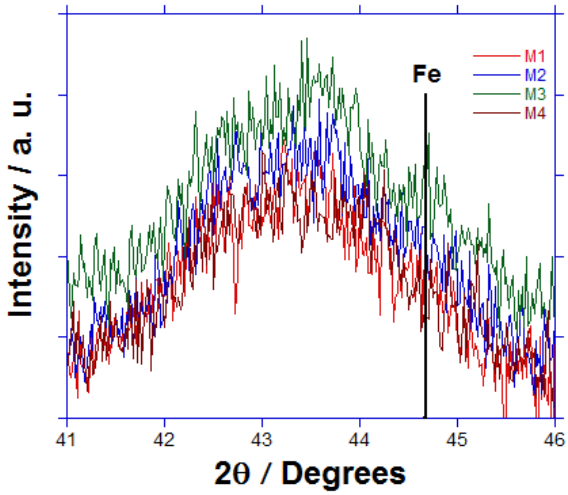

Fig. 3*. Fe peak analysis of M1, M2, M3 and M4*

3.2 Morphology

Fig. 4 shows the FESEM micrographs of the samples under study. In M1 exists the characteristic tubular morphology, observing a preferential orientation growth, however, it is evident the presence of several defects onto surface, being consistent with Raman measurement. CNT´s size is relatively long, because of their average length is on micrometers order. The M2 micrographs show a tubular structure with pronounced curvatures, respecting the oriented growth. Removal of defects onto surface is remarkable, following up with the I_D/I_G increment and elimination of area under D and G bands of Raman spectra. The length in this sample is very similar to that observed in M1. Analyzing the M3 micrographs, the tubular structure is very similar to that seen in M1, with the small difference that the density of defects was reduced significantly, which was predicted from the Raman spectra. Concerning the length, it can be seen that some tubes have a few micrometers because exit broken tubes. Finally, M4 micrographs reveal conservation of aligned tubular structure and defects have mostly disappeared, however, CNT´s walls are irregular because of the damage that exfoliation caused.

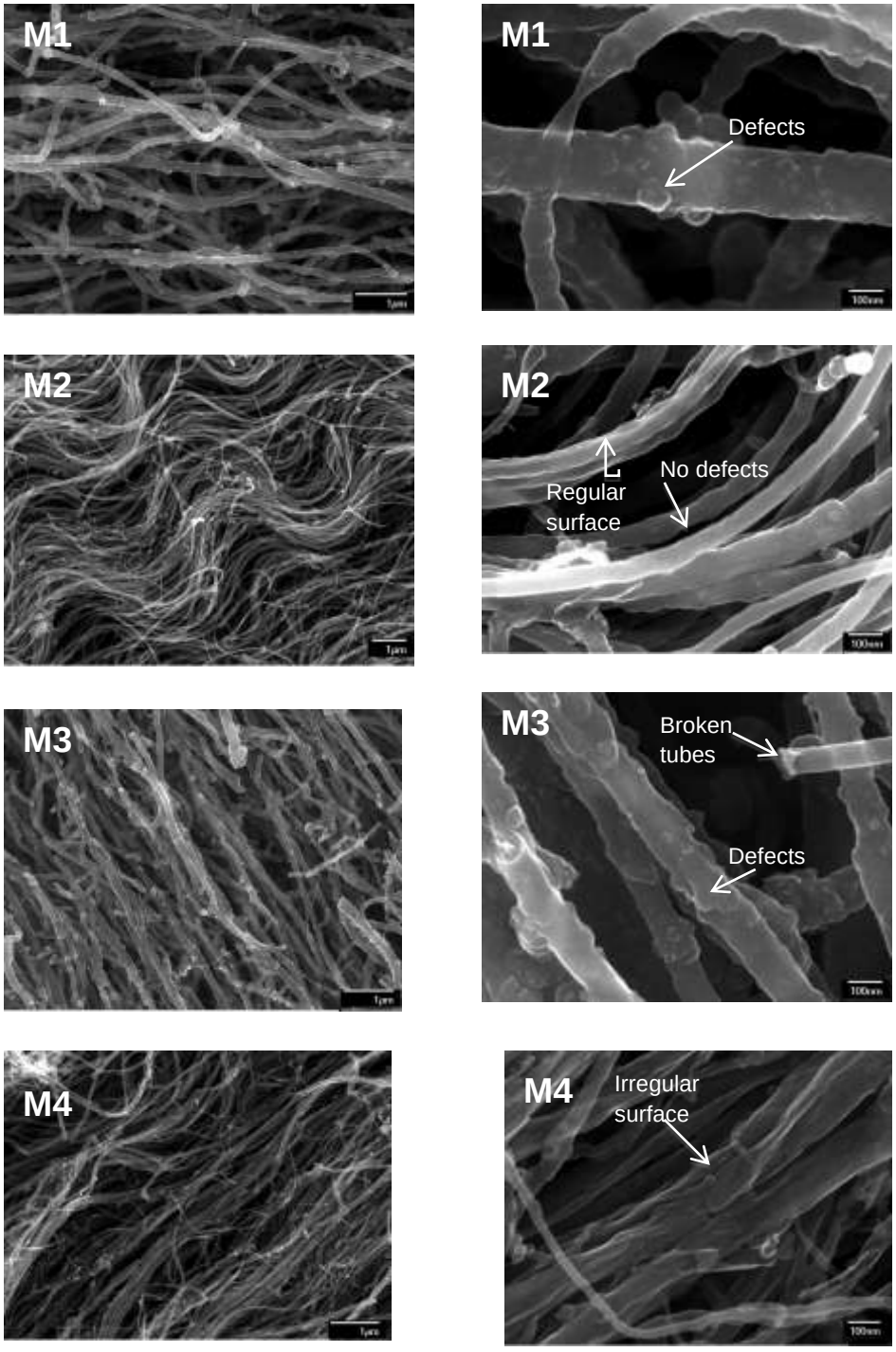

Fig. 4. *FESEM micrographs of M1, M2, M3 and M4*

This observation has a relationship with Raman results. Despite carbon defects have mostly disappeared, exist a higher amorphous carbon quantity, therefore, area under D and G bands in Raman spectra of M4 rose considerably, and I_D/I_G increased substantially. Since G´ band intensity results from a two-phonon process it is plausible that its intensity should decrease as the sample becomes less ordered (i.e., more impurities present) not allowing for the coupling effect which is necessary for the two-phonon process [7]. Then, microanalysis by EDS (see Table 1) revealed the composition of samples, demonstrating existence of Fe, catalyst used to CNT growth, and predicted by XRD measurements. As may be evident, M2 is the one who has fewer quantity of Fe and lower crystallinity index, concluding that treatment with HNO_3, which is allowed to have the best crystalline quality in CNT, however, there is considerable quantity of oxygen in M4, as there is a small amount of sulfur. These two elements were not found in the other samples using this technique.

Table 1. EDS results (%w)

	C	O	Fe	S
M1	97.56	--	2.44	--
M2	98.21	--	1.79	--
M3	97.60	--	2.40	--
M4	87.62	11.05	0.38	0.95

3.3 Electrochemical characterization

Fig. 5 presents cyclic voltammograms of all samples. These graphics were obtained at 100mV s^{-1}, by reporting the last one of 10 applied cyclics, noting minimum waste current density. By observing M1, its evident the presence of an electroactive specie, because of there is an reversible redox process between 0.2 and 0.4 V, where current density intensities, in both directions, are similar (approximately 0.2 mA cm^{-2}). According to X-Ray diffraction patterns and EDS results, these signals can be attributed to agglomerated Fe particles. By analyzing the rest of the profile, exists an electrochemical stability, since there is no considerable increases in current density and the whole signal possess an almost rectangular shape, as expected for a carbon electrode material showing a capacitance characteristic of a steady state behavior [12-18].

Regarding M2, the signals corresponding to Fe disappeared, showing a steady-state in both directions. It is noteworthy that the current density from 0.6 to 1.23 V increases discretely. Finally, it can be seen that M3 signals related to contamination by Fe disappeared, despite EDS results revel almost the same quantity of Fe than M1. This phenomenon could be attributed to the leaching of Fe onto CNT´s surface. According to XRD patterns, there is a solid solution C/Fe, probably the treatment which was used for M3 was not enough strong to eliminate such contamination, as well as current density across the profile moderately increased compared to the previous ones. However,

the most important thing to mention here is the presence of two shoulders near 0.8 V. These signals can be associated with pseudo-capacitive contributions of oxygenated functional groups present in the walls of the CNT [13-17].

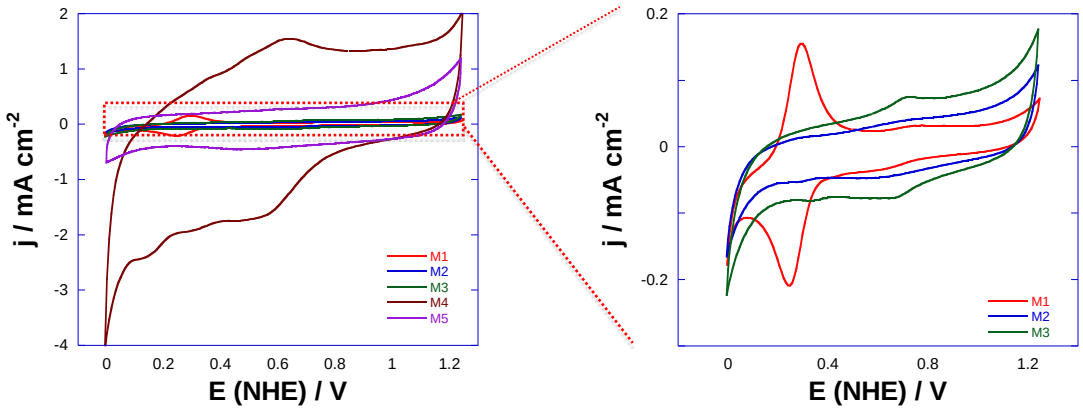

Fig. 5. *Cyclic voltammograms of M1, M2, M3, M4 & M5*

The increase in the current density in j vs. E profiles is an indicator that the available electrochemical area has increased [12-18]. Finally, the "shoulders" observed in M3 have a pseudo-capacitive contribution, as the oxygen-containing functional groups may react faradaic manner, increasing the current density [14-16].

By observing carefully Fig. 5, signals obtained by the three samples analyzed above practically disappear, because the registered current densities of M4 and M5 increases by one order of magnitude. For M5 it is visible the stability that comes in the range of applied potential, showing a steady state, however, about 0.5 V a very light signal related to irreversible pseudo-capacitive contributions were markedly reduced, as suggesting that this material has small amounts of oxygen-containing functional groups at their surface, in which there is an irreversible reduction. The maximum current density for this material is slightly larger 1 mA cm^{-2} in the anodic direction, while the maximum cathodic direction is greater than -1 mA cm^{-2}. Finally, the registered signals by M4 represent a very marked increase of current density respect to its precursors, having a maximum in the anodic direction of 2 mA cm^{-2} and a maximum in cathodic direction slightly lower than -4 mA cm^{-2}. The signals observed at about 0.6 V represent pseudo-capacitive contributions from the oxygen-containing functional groups on the nanotubes´ walls. The current density profile suggests that the electrochemically available area of this material far exceeds the materials discussed above, by adding the oxygen-containing functional groups present on the surface of nanotube. This analysis corresponds to the detected by EDS, since the amount of oxygen detected in M1 was zero,

while the quantity of the same element to M4 is substantially increased, peaking at 11.05 %w. Qualitatively, the capacitance of the electric double layer (DLC, area under the curve j vs. E profiles, excluding pseudo-capacitive contributions) is directly proportional to the surface area and the area of the material available electrochemically [12-18]. Fig. 6 shows DLC determination for all samples.

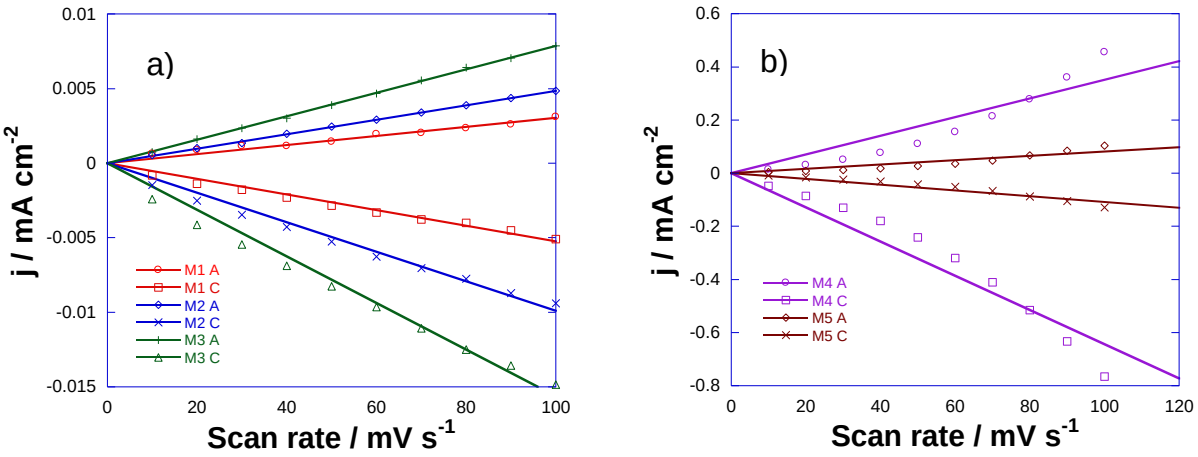

Fig. 6. *DLC determination, in both directions, of: a) M1, M2 & M3; and b) M4 & M5*

DLC was determined at a potential of 0.66V, reporting the response obtained in the anodic and cathodic direction. According to Fig. 6 it is evident that the value of DLC increased after chemical treatments. The increase in value of DLC from chemical treatments can be attributed to the presence of oxygenated functional groups, placing greater emphasis to the carbonyl group (C=O) [13]. In addition, for the particular case of M4, DLC can also be attributed to the substantial increase in the effective surface area by the increased defect density of the tubular structure exfoliated [16] having detected tracking with SEM micrographs and Raman spectra. Table 2 reports DLC values for all samples.

Table 2. DLC values ($\mu F\ cm^{-2}$)

	Anodic direction	Cathodic direction
M1	$2.632x10^{-5}$	$4.323\ x10^{-5}$
M2	$4.825\ x10^{-5}$	$8.825\ x10^{-5}$
M3	$7.919\ x10^{-5}$	$1.376\ x10^{-4}$
M4	$4.770x10^{-3}$	$7.865x10^{-3}$
M5	$1.099\ x10^{-3}$	$1.299\ x10^{-3}$

Conclusion

After functionalization treatments, CNT obtained better crystallinity, that means, less density of agglomerates and amorphous carbon onto their surface, however, exfoliation treatment granted a higher defects density onto CNT walls. By XRD measurements emerged a hypothesis that agglomerates could be a (Fe,C) solid solution. EDS results reveled the presence of Fe particles, which were almost eradicated by exfoliation treatment, however, functionalization couldn´t be efficient to remove Fe particles. In addition, a high quantity of oxygen was found onto exfoliated CNT´s walls, suggesting the formation of oxygenated functional groups on this sample.

Electrochemical measurements confirmed the capacitance´s development while chemical treatments were applied. Moreover, exfoliated CNT showed the highest capacitance, therefore, they have the highest electrochemical surface area (beating carbon Vulcan), where there are pseudo-capacitive contributions that belongs to oxygenated functional groups onto their surface. This result suggest a possible application of this material as support material electrode for PEM fuel cells and electrolizers.

Acknowledgements

Campos Roldán wants to thank to SMH for the economical support.

References

[1] Wu, B., Kuang, Y., Zhang, X., Chen, J., *Noble metal nanoparticles/carbon nanotubes nanohybrids: Synthesis and applications,* Nano Today (2011) 6, 75-90

[2] Hirsch, A., Vostrowsky, O., *Functionalization of carbon nanotubes,* Top Curr Chem (2005) 245:193-237

[3] Wang, S., *Optimum degree of functionalization for carbon nanotubes,* Current Applied Physics 9 (2009), 1146-1150

[4] Goo-Hwan, J., *Surface functionalization of single-walled carbon nanotubes using metal nanoparticles,* Trans. Nonferrous Met. Soc. China 19 (2009), 1009-1012

[5] Tasis, D., Tagmatarchis, N., Blanco, A., Prato, M., Chem. Rev. 106 (2006), 1105-1136

[6] C. Domingo, G. Santoro, *Raman spectroscopy of carbon nanotubes,* Opt. Pura Apl. 40 (2007), 175-186

[7] R. Raffaelle et. al., *Purity assessment of multiwalled CNT by Raman spectroscopy,* Journal of Applied physics 101, (2007), 064307

[8] U. Ritter et. al., *Radiation damage to multi-walled carbon nanotubes and their Raman vibrational modes* Carbon 44 (2006) 2694-2700

[9] B. Rosario-Castro et. al., *Combined electron microscopy and spectroscopy characterization of as-received, acid purified, and oxidized HiPCO single-wall carbon nanotubes,* Materials Characterization 60 (2009) 1442-1453

[10] A. Jorio et. al., *Advances in single nanotube spectroscopy: Raman spectra from cross-polarized light and chirality dependence of Raman frequencies* Carbon 42 (2004) 1067-1069

[11] X. Zhao et. al., *Characteristic Raman spectra of multiwalled carbon nanotubes,* Physica B 323 (2002) 265-266

[12] Pognon, G., Brousse, T., Bélanger, D., *Effect of molecular grafting on the pore size distribution and the double layer capacitance of activated carbon for electrochemical double layer capacitors,* Carbon 49 (2011) 1340-1348

[13] Li-xiang, L., Feng, L., *The effect of carbonyl, carboxyl and hydroxyl groups on the capacitance of carbon nanotubes,* New Carbon Materials, 2011, 26(3): 224-228

[14] Microporous and Mesoporous Materials 96 (2006) 357-362

[15] Pajootan, E., Arami, M., *Structural and electrochemical characterization of carbon electrode modified by multi-walled carbon nanotubes and surfactant,* Electrochemica Acta 112 (2013) 505-514

[16] Wang, G., Ling, Y., Qian, F., Yang, X., Liu, X. Li, Y., *Enhance capacitance in partially exfoliated multi-walled carbon nanotubes,* Journal of Power Sources 196 (2011) 5209-5214

[17] Electrochemistry Communications 9 (2007) 569-573

[18] Portale, B., et. al., *Enhance capacitance of microwave-assisted functionalized ordered mesopourous carbon for supercapacitors,* J. New Mat. Electrochem. Systems 15 (2012) 203-209

Greenhouse Gas Treatment and H_2 Production, by Warm Plasma Reforming

J. Pacheco[1], G. Soria[2], R. Valdivia[1], M. Pacheco[1], F. Ramos[1], S. Darío[2], H. Frías[1], M.Durán[1], M. Hidalgo[1].

[1] Instituto Nacional de Investigaciones Nucleares. Km 36.5 Carretera México-Toluca, La Marquesa Ocoyoacac, México CP 52750
[2]Instituto Tecnológico de Toluca, Av. Instituto Tecnológico, S/N, Ex- Rancho la Virgen, Metepec, México

E-mail: joel.pacheco@inin.gob.mx
Tel 53297200 ext. 12646

ABSTRACT

Carbon dioxide (CO_2) and methane (CH_4) have been identified as the most significant greenhouse gas (GHG) arising from anthropogenic activities affecting the climatic global change. It is of great importance to reduce GHG emissions in order to counteract global warming.
This paper considers dry GHG reforming, involving synthesis gas generation followed by the production of some other solid by-products. CO_2 and CH_4 are both relatively stable compounds with low potential energies. The dry reforming reaction is highly endothermic and external energy must to be provided in order to drive it in the forward direction. More recently, applications of plasma gas reforming are highlighted as promising technique for energy saving and environment safe purposes with increasing demand of hydrogen and synthesis gas. In the case of plasma reforming, high energy electron must provide not only radical species, but also enthalpy required for endothermic reaction. The conversion of hydrocarbon in by-products with high added value, is mainly contributed by dissociation and ionization, when a plasma discharge processes is used; therefore, the more energy consumed by these two kinds of reactions, the more energy-effective for hydrocarbon reforming. Although the low pressure plasma, such as radiofrequency or microwave plasma could achieve high hydrocarbon conversion and good H_2 selectivity, the low H_2 production rate and extra energy requirement for vacuum device restrict its practical use, therefore, the plasma reactor here proposed must fulfill two principal characteristics: Environment-friendly and Auto-sustainable. Warm plasma is a transitional discharge which has low specific energy requirement (1-3eV) but still maintaining enough high temperature (1000-3000K) to produce excited species supporting subsequent chemical reactions. Such plasma discharges have significant advantages: Do not require extra cooling systems, since they work with reduced electric current flows and high voltages, this avoid electrodes erosion and stainless steel walls in the reactor designs can be used.

Keywords: Plasma Reforming, Greenhouse gas, Synthetic gas

1. Introduction

Environmental and energetic problems have enforced researchers into finding and developing alternative and renewable methods for substitute energy production. Most of the chemical energy derived from hydrocarbons today is by a well-known process called combustion. Fuel combustion is an exothermic reaction whereby a fuel is oxidized leading to energy conversion of the chemical species usually present in the GHG, and delivering exhaust gases normally composed by NOx, CO and CO_2 considered as GHG. Over the latest decades, different laboratories around the world, have investigated the reforming capability in fuel conversion by using all types of plasma, from thermal to non-thermal ones [1-8]. Plasma researchers have utilized various reforming processes, such as Partial Oxidation Reforming (POR), Dry Reforming (DR), Steam Reforming (SR), and Steam-Oxidative Reforming (SOR) to test plasma reactors capabilities in order to replace traditional combustion process or metal catalysis-based systems. The catalytic process has the disadvantages of restricted operating conditions and problems associated with catalytic converters such as cost, sulfur poisoning and extended start up time [9-11].
In warm plasma discharge, the ionization process induced by the electric field, dominates the thermal effect and gives relatively high-energy electrons as well as excited ions, atoms or molecules leading in selective chemical transitions in a very effective manner. The average residence time of the reagents in the reaction zone is about 10^{-3} s, and then very high specific throughputs in the reaction zone are achieved. Because of its high power density, this plasma reactors can be designed for small and large -scale applications, these types of reactors can also work in portable or on-board processes [12].

Warm plasma is a transitional discharge, which lies between conventional thermal plasma and nonequilibrium plasma conditions, working under moderate power density; but still maintaining enough high gas temperature (1000–3000 K) to produce excited species supporting subsequent chemical reactions. Such plasma discharges have significant advantages: they do not require extra cooling systems, since they work with reduced electric currents and high voltages, thus avoiding electrode erosion, and the reactor has simple construction [13]. Warm plasmas are also characterized by high chemical selectivity, and has found applications in fuel conversion for syngas production, hydrogen sulfide dissociation, carbon dioxide dissociation among others Examples of warm plasma discharges include gliding arc plasma discharge or Jet Atmospheric Pressure Plasmas.

The focus of this work consists in research the warm plasma discharge, applied for GHG reforming optimizing the electrical energy cost to produce higher syngas GHG conversion and obtaining a high yield and selectivity rates of H_2. However, hydrogen as a fuel, has significant drawbacks, especially those related with its storage. Despite hydrogen's high mass heating value (120 kJ/g), it has a very low volumetric heating value (11kJ/l), compared to 16000 kJ/l for methanol for instance.

There are many methods to generate syngas having the desired H_2/CO ratio [14]. These methods include steam reforming, dry reforming (also called CO2 reforming), and partial oxidation, as shown in the following (1)– (3):

Steam reforming:	$CH_4 + H_2O \rightarrow 3H_2 + CO$	(ΔH = 229 kJ/mol)	(1)
Dry reforming:	$CH_4 + CO_2 \rightarrow 2H_2 + 2CO$	(ΔH = 247 kJ/mol)	(2)
Partial oxidation:	$CH_4 + \frac{1}{2}O \rightarrow 2H_2 + CO$	(ΔH = −38 kJ/mol)	(3)

The merits of dry reforming (2), compared with these other processes, include the use of carbon dioxide, which is an important contributor to global greenhouse gas inventories, as well as a theoretical product yield ratio of H_2/CO = 1. Reforming reactions (1 - 3) are not only a process of substance conversion, but a process of energy conversion, it is important that the novel technology for CH_4-CO_2 reforming should be with high conversions, large treatment capacity and easy to enlarge. To discuss the convenience of specific energy and energy conversion efficiency these concepts will be treated in section 2.1.
The real energy needed for such process cannot solely be deduced from thermodynamic calculations, since a significant amount of extra energy will be needed to overcome the energy barrier of the reaction. This amount of extra energy is not reflected in the thermodynamic enthalpy values. Moreover, these enthalpy values are defined only for a specific reaction, whereas in a plasma conversion reactor not all energy can be directed selectively into a specific reaction in a specific place; then a lot of energy is lost due to heat loss, competing chemical reactions; therefore, there will always be a large difference between the thermodynamic ideally required energy and the required energy for a real process. Besides, the rotationally and vibrationally excited species are generally considered useless for hydrocarbon reforming because of the short lifetimes (several ns) and low threshold energy (<2 eV). It is noted that the bonding energy for most hydrocarbons are generally between 3 and 6 eV. As a result, the decomposition of hydrocarbons mainly attributes to electron-impact dissociation and

ionization. As expected, a higher electric field leads to higher electron energy, which is more favorable for the electron-impact reactions responsible for hydrocarbon reforming. In other words, the energy consumed by the electron-impact reactions would be reduced while the electric field is increased. That is why; we have researched and developed warm plasma reactors for this application in GHG reforming.

1.2.- Dry reforming or Dry CO2 reforming (DR)

Gasification is the thermochemical conversion of organic matter (i.e. hydrocarbons) into a gaseous product, which could be used directly for combustion or synthesized into fuel or chemicals. The main exhaust gas is the syngas composed by H_2 and CO in majority, including lower concentrations of CO_2, H_2O, CH_4, higher hydrocarbons and N_2.

Dry CO2 reforming can be described as a reforming technique whereby the reaction between carbon dioxide and a hydrocarbon yields a combination of hydrogen and carbon monoxide as in eq. (2). As an alternative, several authors [6,12] have proposed to use the CO_2 produced by various industrial facilities: cement plants, blast furnaces and to conduct studies on the Dry CO_2 reforming of hydrocarbons into synthesis gas. The dry reforming produces synthesis gas with H_2/CO ratio equal to 1.

The ideal scenarios where dry reforming might be considered is where the supply of methane is contaminated with carbon dioxide and there are no ready facilities for separation, or where a product syngas with a H_2/CO ratio of unity is desired when a second process i. e. Fischer-Tropsch is required to transform syngas into synthetic oils [15].

DR is an endothermic reaction that requires a significant amount of energy in order for the reforming reaction to progress. This energy must be delivered by the warm plasma reactor.

1.3.- On Board Reforming or Partial Oxide Reforming:

A disadvantage of reforming is the thermodynamic cost of extracting hydrogen from hydrocarbon fuels; therefore the partial oxidation is an alternative to produce hydrogen at high yield rates with low spent of energy, for instance, in research scale a rate up to 30 standard LPM, is sufficient for a fuel cell to generate 3kW of electrical power. The general idea behind partial oxidation consists in using air to balance the energy required by oxidizing some of the fuel (CH_4). The N_2 participates as an inert gas in the 800-2000K temperature range; that's why the warm plasma reactor was selected because the operating temperature is not bigger than 3000K (as in thermal plasmas torch) neither lower than 500K (as in cold plasmas reactor).

If only one half of air mole is present and considering N_2 as inert gas, then chemical equilibrium predicts that the exhaust gas mixture is mostly composed by CO and H_2 with some traces of CO_2 and H_2O vapor. For a general hydrocarbon fuel, that's means that

$$C_nH_m + \frac{1}{2}O_2 \rightarrow nCO + \frac{m}{2}H_2 \qquad (4)$$

Partial oxidation reactions proceed in two distinct phases; a rapid, highly exothermic combustion phase where all free oxygen is consumed to form heat and the products of CO_2 and H_2O; and a much slower endothermic reforming phase where residual unconverted fuel reacts with the CO_2 and H_2O plus the reaction heat to form syngas products H_2 and CO

In addition, hydrogen selectivity is an important parameter in partial oxidation processes, since the selectivity is directly related with process efficiency. In methane reforming using the partial oxidation process, hydrogen selectivity is defined as below

$$H_2\ selectivity(\%) = 0.5 * \frac{mole\ produced\ H_2}{mole\ converted\ CH_4} * 100\% \qquad (5)$$

100% of hydrogen selectivity means that all hydrogen atoms of the methane molecules are converted into hydrogen molecules.

2. Experimental

The flux rate of GHG (CH_4 + CO_2) and the plasma gas (N_2) are previously measured and mixed, ant then introduced to the reactor (See Fig. 1), which is constructed in double wall stainless steel, the gas mixture enter by the bottom side and ascend between the space formed by a double wall; having a dual purpose: to maintain the reactor wall at low temperature and to preheat the gas mixture before to be treated. The plasma discharge is generated between an external electrode, in this case the reactor wall and a central conical electrode; then it moves down to the end of conical electrode and does not detach from it, formerly, the arc column length increases slowly, just rotating by the flow, during a time represented by ($1/\omega_c$). The arc discharge continues the spiral motion descending along the chamber reactor increasing the column length (during time $1/\omega d$) and a new cycle is recommenced each 25 ms. The plasma jet is expelled out the reactor chamber and can flow in a free space or in a container. In our case, the post-chamber elongates the plasma jet and has a shield effect, keeping away the atmospheric air surrounding the jet, therefore, the plasma jet is spread out with a very long volume, as it was reported in [13]. Contrary, when the plasma jet blows directly in air, it has a smaller volume.

The residence time *tr* of the gas inside the reactor could be calculated by the following relation:

$$t_r = [\pi(R_1\text{-}r)^2(\ell_1) + (\pi(R_2)^2(\ell_2)\ ]\ (\text{ml})/\text{flow rate (ml/s)} \qquad (6)$$

where, R_1 the radius of the discharge chamber, R_2 the radius of the post-discharge chamber, r the radius of the internal electrode, and ℓ_1 and ℓ_2 the discharge and post discharge length respectively. As the arc length expands, the heat dissipation increases. This results in a lowered temperature, and the plasma tends to be in nonthermal plasma discharge.

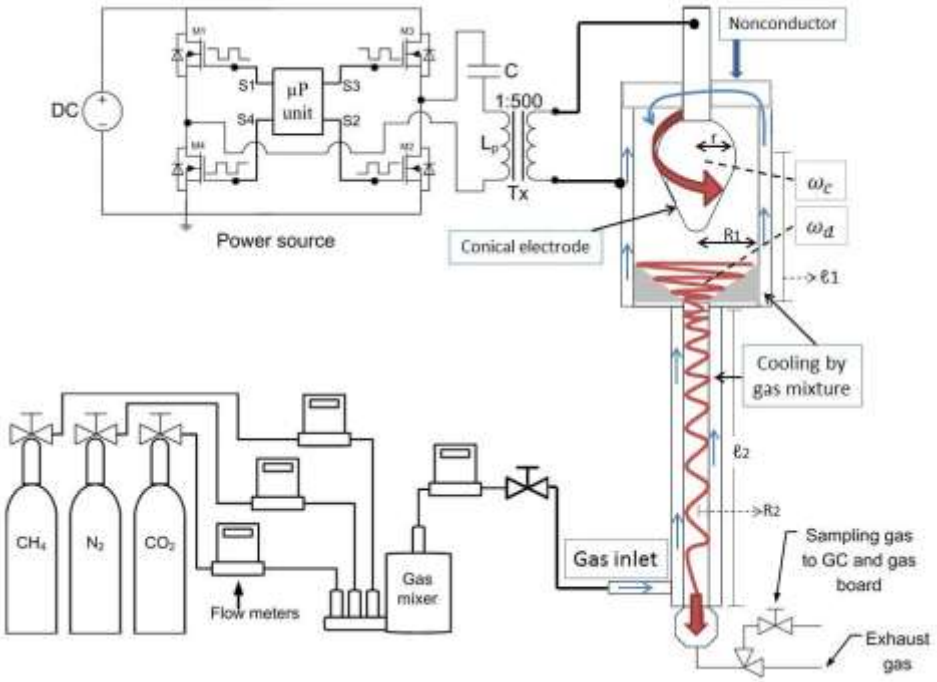

Fig 1.- Warm Plasma Reactor with power source and GHG system.

The power source consists on a high-frequency series resonant inverter [16] constituted by one setup ferrite core transformer, capable to provide 15 kV at high frequencies in the secondary winding. Four sequential control pulses (S_1 – S_4) generated by a simple logic circuit active the high-power MOS transistor (M_1 - M_4) in order to command the transformer primary side. The power supply handles a wide frequency range (5–200 kHz). The duty cycle in each phase is adjusted to 50% providing a soft start in the MOS and with the intention of avoiding unnecessary power consumption in the plasma discharge. The high frequency transformer was assembled to attain the maximum energy transfer towards the plasma discharge; besides, it also

functions as a stabilizer, because a natural negative feedback allows the plasma discharge ignition, and when the impedance charge descends, then the voltage is automatically adjusted to sustain a stable plasma discharge, and consequently an electrical field of about 3 kV/mm is applied in air between electrodes, as a result, a low-current discharge streaks between the closest points of the electrodes, preionizes the gas gap, provoking the formation of a stronger current to sustain the warm plasma discharge at atmospheric pressure, using nitrogen or the GHG as plasma gas; the gliding discharge on the central electrode is reflected in the electrical signals [13]. The gliding period (*Tg)* can be determined from the electrical signals, in this case, a *Tg* of 25 ms is obtained, so the gliding frequency corresponds to 40 Hz. The arc column length is a function of power applied to the discharge, reactor geometry, and nature of the gas to be treated.

2.1.-. Energy Consumption Analysis

By using the same procedure indicated in [17], based in the instantaneous values intensity of voltage and current waveforms; the root medium square power P_{RMS} can be deduced, and finally the energy consumption during operational experiences can be obtained. The operational condition in the power supply was 450W of power and a frequency of 140 kHz, and flow rates were 2LPM for CH_4 and 1LPM for CO_2. According these operating conditions, the specific energy (SE) required generating CO and H_2 (syngas) can be calculated with the following expression [14, 17]:

$$SE = \frac{P}{[CO+H_2]_{produced}} \tag{7}$$

where, P refers to the input power of plasma in kW (kJ/s); $[CO + H_2]_{produced}$ refers to moles of (CO + H_2) produced per second (mol/s). Equation (7) is referred as the energy consumption needed to produce a mole of CO and H_2 (a syngas mole). This calculation includes the energy input as electrical power from the plasma discharge. The SE is optimal when the energy consumption of the reforming process is lower. According (7) a value of 310.79 kJ/mol of syngas is obtained; not so far from the thermodynamically value (2).

In addition, to determine the energy conversion efficiency (ECE) applied to the gas mixture entering to the plasma reactor; the expression (8) is used:

$$ECE = \frac{nH_2 * LHV\ H_2 + nCO * LHV\ CO}{P + nCH_4 * LHV\ CH_4} \tag{8}$$

From [18] and [19], next values can be obtained: 1) LHV H_2 = 242.056 kJ.mol^{-1}; 2) LHV CO = 283.179 kJ.mol^{-1}; and 3) LHV CH_4 = 802.933 kJ.mol^{-1} @ 298.16 K. By making the pertinent calculations, the ECE obtained is 22.05%. It's worthy to note, that the maximal ECE for these operations conditions will be 34%, therefore the warm plasma reactor is a profitable alternative method to confirm the destruction efficiency.
In [14], a comparison for ECE and SE in syngas production is reported for different plasma configurations. Taking this into consideration, the SE, and ECE results obtained in this paper for syngas generation, places the Warm Plasma discharge as one of the most efficient methods for the syngas production.

The conversion percentage for CH_4 and CO_2 can be calculated by

$$Conversion\ percentage = \frac{X_0 - X}{X_0} \times 100\% \tag{9}$$

where X_0 is their initial concentration and X is the final concentration.

A chemical mechanism of hydrogen and carbon monoxide generation was studied in [20]. In general, the H_2 production can be explained by the interaction of CH_4 with O*· and H*· radicals. CO formation could be mostly explained by the collision of CO_2 with electrons and a three-body reaction with N_2; consequently, the selectivity coefficient can be obtained with the subsequent equations [20]:

$$S_{CO} = \left\{\frac{[CO_{produced}]}{CO_{2\ consumed}}\right\} \times 100\% \tag{10}$$

$$S_{H_2} = \left\{\frac{[H_{2\ produced}]}{CH_{4\ consumed}}\right\} \times 100\% \tag{11}$$

Based on the operating conditions already described, and using (9) - (11), the CO and H_2 selectivity respectively was 63% and 99.44%. The conversion capacity of CO_2 and CH_4 correspondingly was 29.41% and 98.44%.

3. Results and discussion

For the case of Partial Oxidation the CH_4 and Air mixture has a flow rate of 2:1 LPM respectively. This mixture is introduced into the bottom reactor and immediately at the reactor exit, a gas analyzer is connected (Gas Analyzer Board®) to measure real-time concentration of up to 6 different gases: CO_2, CH_4, CO, O_2,C_2H_6 and H_2.
The plasma is applied (Zone 1, in Fig 2); the power source supplies a sinusoidal voltage at a frequency of 140 kHz and a power of 250W. Fig. 2, shows the results obtained from the reforming gas analyzer expressed in % volume versus time, two zones are clearly revealed: Zone 1 presents conditions under plasma action, and zone 2 represents the period of time when the plasma discharge is turned off, a change of gas concentration is rapidly exposed; the gas mixture (GHG) increase to the initial conditions, whereas the syngas concentration descends to the lower level.

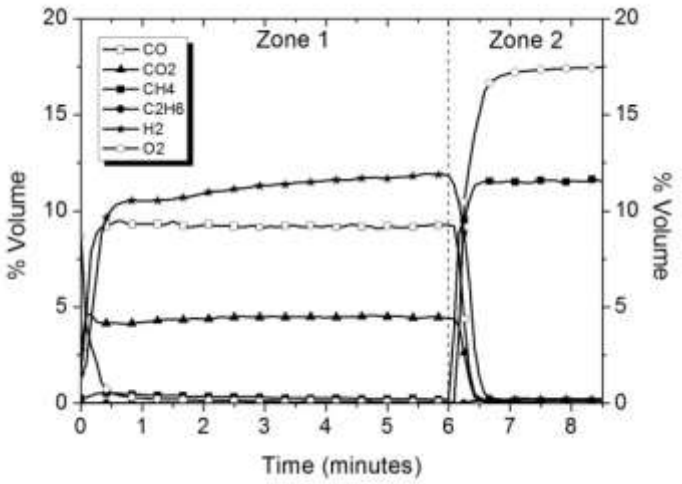

Fig. 2.- GHG and Syngas Concentration Evolution (%Vol).

The experimental results are shown in Table I indicating the initial and resultant concentration in % volume for the GHG and syngas components.

Table I.- GHG and Syngas compounds after and before plasma treatment

Compound	Before treatment (%vol)	After treatment (%vol)
Oxygen	17.5	3.4
Nitrogen	71	71
Methane	11.5	0.2
Carbon monoxide	0	9.2
Carbon dioxide	0	4.4
Hydrogen	0	11.8

Once the plasma discharge is ON, instantly an increase in H_2 concentration around 12% volume occurs, at the same time, the carbon monoxide reach 9.2% and carbon dioxide touch 4.4%; getting, according (9), a conversion of CH_4 of 98.6%. These values were also confirmed by Gas Chromatography (TRACE GC ULTRA®). In Fig. 3a), three significant peaks were previously identified with sample gas standards to confirm the presence of O_2 (first peak at 2.8m), N_2 (at 3.5m) and CH_4 (at 4.3m) of time retention. In the case of output components (Fig 3b) the CG results shows the presence of H_2 at 2.4m, O_2 at 2.8m, N_2 at 3.5m, and CO at 5.0m, the occurrence of CH_4 no longer arises.

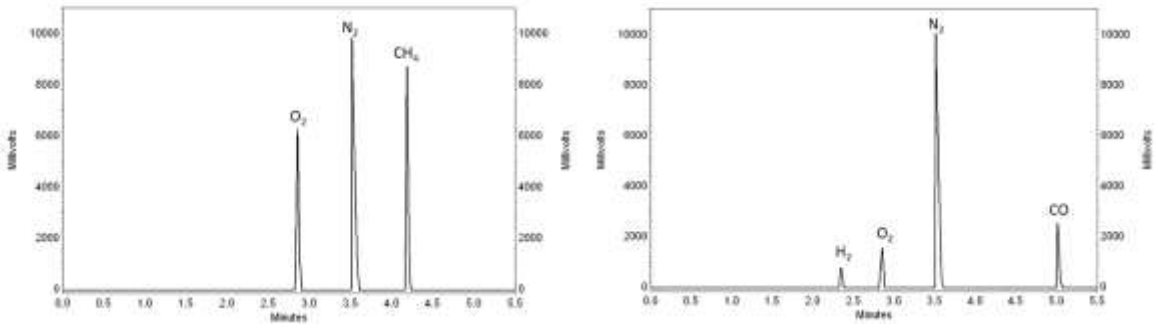

Fig. 3.- Chromatogram of the sample before (a) and after (b) warm plasma treatment.

Figure 4, displays a bar graph derived from the GC analysis and indicates the concentration of the mixture before and after treatment; the black bars indicate the mixture composition before treatment (O_2, N_2 and CH_4.). The gray bars correspond to the exhaust gas components which are CO_2, H_2, O_2, N_2 and CO. In the case of N_2 the peak intensity is fairly similar before and after treatment, this confirms that it functions like a plasma gas and does not react with other compounds; hence any NOx formation is produced during GHG reforming. It is noteworthy that methane concentration during the reformation process, descends to 0%, therefore a high CH_4 conversion and a high production of hydrogen is obtained. Additionally, a second reliable result is related with nitrogen behavior, it's clearly shown that it does not react with other gas, because its intensity level is quite the same before and after treatment.

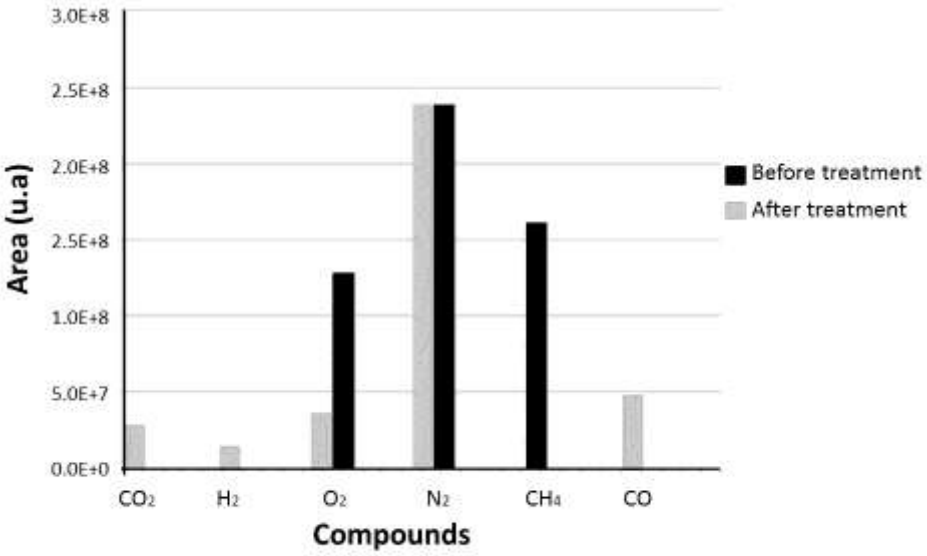

Fig. 4.- Concentration of input and output gas in warm plasma reactor

4. Summary and perspectives

Warm plasma fuel reforming technology has several advantages over traditional catalytic or thermal processes including fast start time, high productivity with a relatively low electrical energy costs operation.
The results show that warm plasma reactor is capable of reforming heavy hydrocarbon fuels with high conversion efficiency and is an important piece of technology for on-board vehicular reforming systems that should be further developed and optimized.
In plasma reforming process, considering electricity coming from methane combustion (combustion value of 890 kJ/mol), only 42% of combustion energy is converted to electricity, and only 67% of electric energy is utilized by the reforming reaction, therefore, to get 1 mol CO, it would burnt 0.5 mol of methane and 0.5 mol CO_2 released in the power plant. However, these CO_2 would be balanced by that removed during the reforming process.
In one word, to obtain 1 mol CO in CH_4 + CO_2 reforming by plasma process, it expends 1 mol of methane without CO_2 exhaust; in steam reforming of CH_4, it expends 1.33 mol of methane and 0.33 mol of CO_2 released.
The growing demand for chemicals derived from syngas has led to the development of several technologies (e.g. Fischer–Tropsch synthesis, NH_3 or oxygenate production). These processes are of strategic importance for any country.
In this paper, a Resonant Electronic Converter has been developed and applied assuring the energy consumption with high transfer efficiency.
The system presented here is able to provide enough energy required to break GHG gas chemical bonds, under atmospheric pressure without using supplementary inert gases.
Electric analysis was performed to determine the current, voltage, power and energy required for the GHG treatment.
Reforming conversion of GHG by warm plasmas offers a promising route to generate higher value products such as syngas at low energetic cost.

Acknowledgements

The authors would like to thank for the invaluable support of the LAP laboratory of the ININ. This work was supported under EAOO2 project from ININ

References

[1] WH Lai, MP Lai, RF Horng. Study on hydrogen-rich syngas production by dry autothermal reforming from biomass derived gas. *Int J Hydrogen Energy* (2012); vol. 37; 9619-9629.

[2] Yuichiro Takemura, Yuusuke Kubota, Naohiro Yamaguchi, and Tamio Hara, "Development of Atmospheric Plasma Jet With Long Flame", IEEE Transactions on Plasma Science, Vol 37, No. 8, pp 1604-1606, (2009).

[3] D. H. Lee, K.T. Kim, M. Suk, Y. Soong; "Plasma-controlled chemistry in plasma reforming of methane"; International Journal of Hydrogen Energy 35 (2010) 10967 – 10976.

[4] A. Indarto, C. J. Wok, L. Hwaung, and S. H. Keun, "Effect of additive gases on methane conversion using gliding arc discharge," *Energy*, vol. 31, no. 14, pp. 2986–2995, Nov. 2006.

[5] F. Ouni, A. Khacef, and J. M. Comier, "Syngas production from propane using atmospheric non-thermal plasma," *Plasma Chem. Plasma Process.*, vol. 29, no. 2, pp. 119–130, 2009.

[6] X. Li, X. Liao, X. Ren "Carbon Dioxide Reforming of Methane to Syngas by Warm Plasma: Low Energy Consumption" Power and Energy Engineering Conference (APPEEC), pp 1-5 Asia-Pacific, 28-31 March 2010.

[7] TV Choudhary, VR Choudhary. Energy-efficient syngas production through catalytic oxy-methane reforming reactions. *Angew Chem Int Ed* (2008); vol.47:1828-1847.

[8] A. York, T Xiao, MLH Green, JB. Claridge; Methane oxyforming for synthesis gas production. *Catal Rev* (2007);vol 49:511-560.

[9] X. Zhu , K. Li, JL Liu, XS Li, AM Zhu; Effect of CO2/CH4 ratio on biogas reforming with added O2 through an unique spark-shade plasma. *Int J Hydrogen Energy* (2014); (Article in Press); 1-7.

[10] S Ozkara, AE. Aksoylu. CO2 reforming of methane over Pt-Ni/Al2O3 catalysts: effects of catalyst composition, and water and oxygen addition to the feed. *Int J Hydrogen Energy* (2011); vol. 36:2950-2959.

[11] AJ. Zhang, AM. Zhu, J. Guo, Y. Xu, C. Shi. Conversion of greenhouse gases into syngas via combined effects of discharge activation and catalysis. *Chem Eng J* (2010); vol. 156:601-606.

[12] M. J. Gallagher, R. Geiger, A. Polevich, A. Rabinovich, A. Gutsol b, A. Fridman; On-board plasma-assisted conversion of heavy hydrocarbons into synthesis gas; *Fuel* 89 (2010) 1187–1192

[13] J. Pacheco, G. Soria, R. Valdivia, M. Pacheco, F. Ramos, H. Frías, M. Durán, M. Hidalgo, J. Salazar, J. Silva, M. Ibañez. Warm Plasma Reactor with Vortex Effect Enhanced Used for CH_4-CO_2 Reforming. *IEEE Transactions on Plasma Science*, Articlein Press (2014).

[14] X. Tao, M. Bai, X. Li, H. Long, S. Shang, Y. Yin, et al., "CH4-CO2 reforming by plasma—Challenges and opportunities," Progr. Energy Combustion Sci., vol. 37, no. 2, pp. 113–124, Apr. 2011.

[15] Fischer F, Tropsch H. The composition of products obtained by the petroleum synthesis. Brennst Chemistry 1928;39(3).

[16] J. Pacheco-Sotelo, R. Valdivia, M. Pacheco-Pacheco, J. Ramos, M. Durán, J. Benitez, R. Peña, and R. López; "A Universal Resonant Converter for Equilibrium and Nonequilibrium Plasma Discharges", *IEEE Trans. on Plasma Science*, Vol 32, No. 5, pp 2105-2112, (2004).

[17] J. Pacheco, J, A. Salazar, R. Valdivia, M. Pacheco, M. Ibañez, G. Soria, J. Silva ; An Environmental Application in Acid Gas. Cracking With a High-Frequency Pulsed Gliding Arc; *IEEE Transactions on Plasma Science*, Vol 22, No. 3, pp 767-773, (2014).

[18] L. Waldheim and T. Nilsson, "Heating value of gases from biomass gasification," IEA Bioenergy Agreement, Nyköping, China, Tech. Rep. TPS-01/16, May 2001.

[19] U. Bossel "Well to wheel studies, heating values and energy conservation principle", in Proc. Eur. Fuel Cell Forum, vol 22, Oct. 2003, pp 572-577

[20] J. S. Torres, "Recuperación energética de la eliminación de H_2S y CO_2 con tecnología de plasma híbrido"; PhD Dissertation, Dept. Electron. Eng., Inst. Tecnol., Toluca, México 2014.

Design, Construction and Performance Evaluation of a Solid Polymeric Electrolyzer

S. Citalán-Cigarroa, A. Rodríguez-Castellanos, C. Castro-Morales, O. Solorza-Feria.

Centro de investigación y de Estudios Avanzados del I.P.N., Av. IPN 2508, D.F., México, 07360.
Tel: 57473800 ext. 4473, e-mail: scitalan@cinvestav.mx

ABSTRACT

In this paper the design, construction and characterization of a Solid Polymer Electrolyte (SPE) as water electrolyzer is presented. As anode, titanium grade 2 with geometric surface area of 12 cm^2 impregnated with a mixture of oxides of RuO-IrO2/Ti was used. This material offer advantages in terms of stability, resistance to extreme corrosion and good electrical conductivity, determined by chronoamperometry experiments. Commercial carbon black supported Pt (Pt/C 20wt%) was used as a cathode electrode. The electrolyzer uses DC power which was supplied by a 30W solar panel. The hydrogen produced was fed to a 5W PEM fuel cell.

Keywords: Design; Electrolyzer; Stack Fuel Cell;

1. Introduction.

Hydrogen has been considered as an ideal energy carrier to support sustainable energy development, which can be effectively produced through fossil-fuel-based process. However, the development of renewable hydrogen production technologies to replace fossil fuel-based hydrogen production methods is an important step towards a sustainable hydrogen economy [1,2].

Up to now, most of the research and development on water electrolysis related to renewable hydrogen production projects have focused on alkaline electrolysis systems and PEM electrolysers. The PEM electrolyzers are more advantageous due to their ecological cleanness, easy maintenance, compactness. Recently, most studies on PEM electrolysis emphasize on the development of new catalysts. However, the development of technologies for renewable hydrogen production methods to replace hydrogen production based on fossil fuels is an important step towards sustainable hydrogen [3-5].

2. Experimental conditions.

2.1 *Preparation of surface titanium.*

The current collectors are made of titanium foil grade 2. These were polished using mechanical and electrochemical methods for removal of oxides. The RuO_2 ink was prepared with Hexane (Aldrich), it was painted with brushed over a titanium foil and was heating in an oven at 250 ºC for 15 minutes and repeating 10 times until catalysts loading was reached of about 0.5 mg cm^{-2}.

2.1 *Preparation of membrane electrode*

The Nafion 117 (SPE electrolyzer) and 112 (fuel cell) membranes were treated before being used in order to clean and improve ions transfer. The membrane was first preheated in pure water at 80 ºC and then transferred to a solution of 3% H_2O_2 at 80 ºC for 1 h to remove organic impurities. After these step, the membrane was vigorous washed by deionized water. The membrane was boiled at 80 ºC for 1 h using 2M H_2SO_4 solution, for ion exchange the membrane completely with protons and removes the inorganic impurities. After these steps, the membrane was washed by deionized water and stored in deionized water, the membrane became active and ready to be used [6-8].

2.3 *Preparation of membrane electrode assemblies for the electrolyzer.*

The catalytic inks were prepared by mixing the corresponding catalysts, $70RuO_2$-$30IrO_2$ (Aldrich 99.99%) and PtC 40 wt%, as anode and cathode respectively, with 2-propanol (Aldrich) and 5% Nafion solution (Aldrich). The corresponding ink was then brushed over a stainless steel mesh with geometrical surface area of 12 cm^2, which was used as gas diffusion medium. The anode and cathode were then hot-pressed using Nafion 117 as solid electrolyte at 120 °C during 90 seconds at 16 kg cm^2. The electrolizer was feed with deionized water and the performance evaluated trough galvanostatic polarization in a PARSTAT 2273 and 2273 Power Booster system (KEPCO BOP 20-10M). A schematic representation of the SPE electrolyzer and their components are shown in Figure 1. The cell was made of acrylic pieces with flow fields machined using a computer numerical control (CNC) milling and CNC laser cutter. Titanium sheet acted as current collector in both cases (i.e., anode-Ti/RuO2, and cathode –Ti/Pt/C).

Figure 2. Stainless steel mesh / RuO2 and IrO2.

Figure 3 shows the components of an experimental electrolyzer cell. The MEA was inserted into the electrolyzer cell for testing. An electrolyzer cell is shown in Figure 4. The performance of electrolyzer was determined by galvanostatic polarization in a PARSTAT 2273 and 2273 Power Booster system (KEPCO BOP 20-10M). The electrolyzer was fed with deionized water.

Figure 3. SPE electrolyzer Components

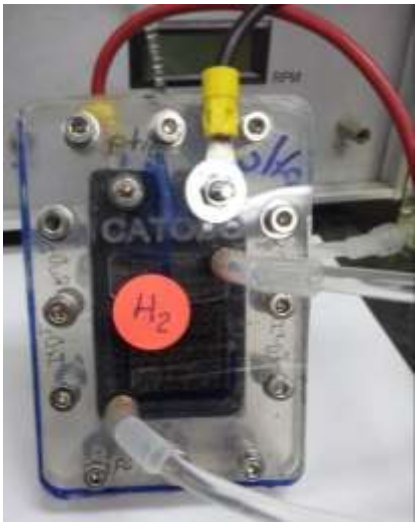

Figure 4. Electrolyzer cell

2.2 *Preparation of membrane electrode assemblies for the fuel cell stack*

The MEAs of fuel cell stack were prepared using a commercial carbon cloth as gas diffusion catalysts (GDC) with geometrical surface of 9 cm^2. Previously to assembled, the GDC was covered with a thin layer of Nafion 5 % solution (Aldrich). Each single MEA was prepared by hot-pressing of the catalysts GDC, in order to prevent ohmic resistance and to form good contact between the electrodes and the polymer membrane. The MEAs were inserted into the fuel cell testing system. A fuel cell stack is shown in Figure 5. The performance of fuel cell was determined by potentiostatic polarization in a fuel cell stack test system (electrochem 890e). The anode was feed with H_2 and air at the cathode side, without pressure.

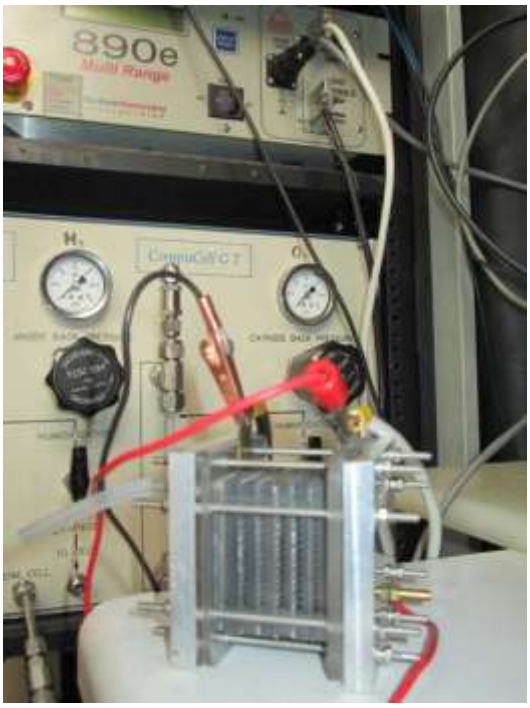

Figure 5. A fuel cell Stack

3. Results and discussion

Figure 6 shows chronopotentiometric curves obtained when current pulses are applied during 180 sec. The constant voltages are suggesting the reproducibility of electrochemical processes occurring on its surface. Carbon supported platinum nanoparticles was used at the cathode of PEM electrolyzer for the hydrogen evolution reaction. At the anode mixed oxides RuO_2 and IrO2 was used for the Oxygen evolution reaction. Current-voltage polarization curve measured at 30 °C on PEM water electrolysis cell is illustrated in Figure 7.

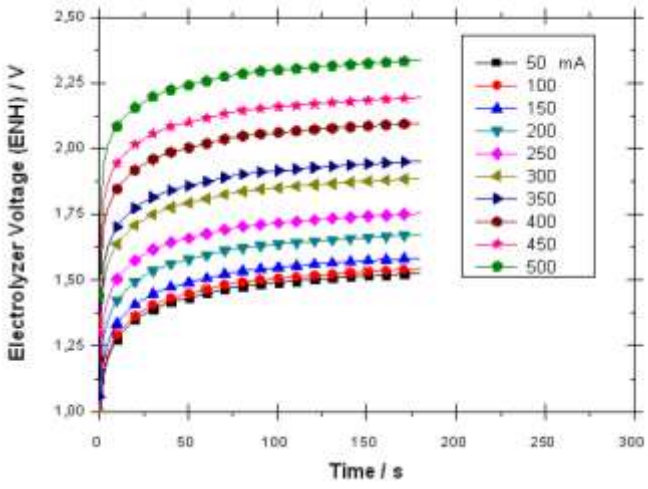

Figure 6. Electrode potential response during the application of pulses of different current at 25°C.

The hydrogen produced during the electrolysis operation is collected in glasses containers. The theoretical yield of hydrogen is calculated using Faraday laws equation given by [9].

$$W_{H2} = \frac{ItM}{FM_e}$$

Where w is the weight of the hydrogen produced at the cathode, I the applied current intensity (A), t the time (s), M the molecular weight of hydrogen (g mol^{-1}), F the Faraday's constant (96485 C mol-1) and N_e the number of electrons involved in the reaction.

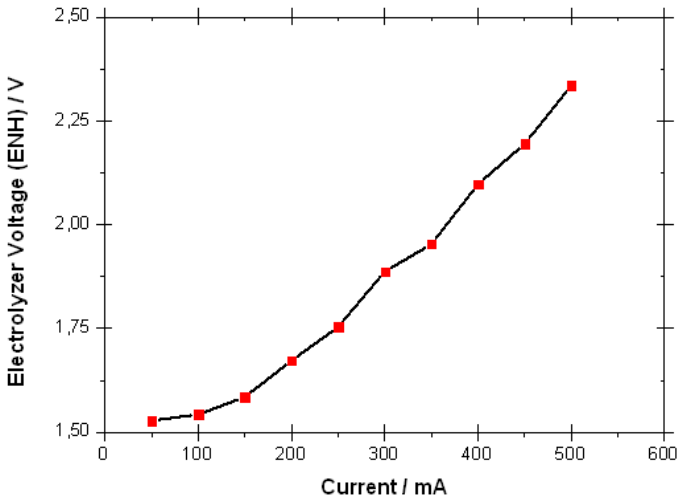

Figure 7. Polarization curve measured using 117 Nafion membrane at 30 °C.

The experiments were performed for 180 s at currents of 50, 100, 150, 200, 250, 300, 350, 400, 450, 500 mA at temperature 30 °C, and the produced hydrogen and oxygen gases were collected in separate containers. The yield of the hydrogen was calculated for a production of 25.8 ml h^{-1} at 50 mA.

3.1 Fuel cell Performance.

The polarization and power density curves for a PEMFC stack using a Nafion 112 membrane are presented in Figure 8. A power output closed to 3.42 W was determined.

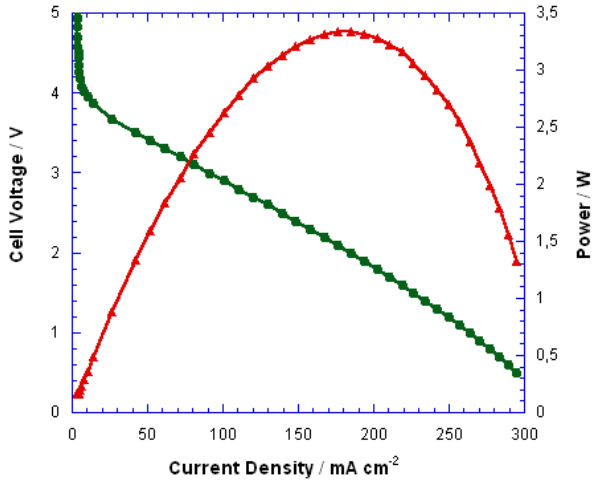

Figure 8. PEMFC performance polarization curves and power density evaluated at 30°C.

4. Conclusions

In this work, we have tested various electrocatalysts materials that were integrated in the membrane-electrode assemblies as part of an electrolyzer which allow us to build a demonstrative and efficient solar-hydrogen prototype.

5. Acknowledgements

The authors acknowledge the financial supports from the National Council of Science and Technology of Mexico, Conacyt (FOINS/75/2012). Also acknowledges The University of Texas TAMU-Conacyt for providing help and support in the design and development (Alloy nanocatalysts for fuel cell electrodes).

6. Referentes

[1] O. Fakuk Selemet, Fatih Becerikli, Mahmut d. Mat, Yuksel Kaplan, *Int.J. Hydrogen Energy*, 36, 11480, (2011).

[2] Luis M. Gandia, Gurutze Arzamendi and Pedro M. Dieguez. *Renewable Hydrogen and Technologies, Production, Purification, Storage, Application and Safety*,Elsevier, pp. 6-10, ISBN:978-0-444-56352-1(2013)

[3] H. Zhang, Shanhe Su, Guoxing Lin, Jincan Chen, *Int. J. Electrochem. Sci*., 7, 4143, (2012).

[4] D. Webb, S. Mùller-Hols, *Journal of Power Sources* 103, 54,(2001)

[5] M. Carmo. David l. Fritz, Jurgen Mergel and Detlef Stolen, *I. J. Hydrogen Energy* 38, 4901, (2013).

[6] J. B. Benzinger, M. B. Satterfield, W. H.J. Hogarth, J. P. Nehlsen, I. g. Kevrekidis, *J. Power Sources*, 155, 272, (2006).

[7] N. Monoranjan, K. Chandra-Sarma and N. Gopil-Singh., *I. J. Computer Application*, 48, 975, (2012).

[8] L.G. Arriagaa, W. Martínez, U. Cano, H. Bluda, *Int. J. Hydrogen Energy*, 32, 2247, (2007).

[9] K. Mazloomi1,*, Nasri b. Sulaiman1, H.Moayedi2, *Int. J. Electrochem. Sci.*, 7, 3314, (2012).

[9] Andrés Rodríguez Castellanos, Ernesto López Torres, Omar Solorza Feria, *J. Mex. Chem. Soc*., 51, 55, (2007).

Electrical Properties of $Gd_2Hf_{2-x}Zr_xO_7$ Solid Electrolytes Synthesized by Mechanical Milling

N.M. Cepeda-Sánchez[1], A.F. Fuentes[1], F.A. López-Cota[2], M. Rodríguez-Reyes[2] and J.A. Díaz-Guillén[2,*]

[1]Cinvestav Saltillo, Apartado Postal 663, 25000-Saltillo, Coahuila, México.
[2]División de Estudios de Posgrado e Investigación, Instituto Tecnológico de Saltillo, 25280-Saltillo, Coahuila México.
*Tel: +528444389539; e-mail: j.a.diazguillen@gmail.com

ABSTRACT

Gadolinium hafnates $Gd_2Hf_2O_7$ belong to a family of complex oxides with general formula $A_2B_2O_7$ which can show two different structural arrays, pyrochlore and non stoichiometric fluorite. These materials are known by their interesting electrical and thermal properties; thus, some of them are good oxygen ion conductors at high temperatures and can be used as solid electrolytes in SOFC's (Solid oxide Fuel Cells). Some others show low thermal conductivity and high thermal stability which make them attractive materials for TBCs (Thermal Barrier Coatings) to protect metal components of gas turbines and diesel engines.

The properties of these materials are significantly affected by the presence of defects such as vacancies and structural disorder. Therefore, their electrical and thermal properties can be modified by single or multiple chemical substitutions or by processing.

The ceramic method to obtain lanthanides hafnates usually involves thermal treatments at temperatures higher than 1500°C by long periods of time. This work deals with the mechanochemical synthesis and characterization of advanced ceramics of general formulae $Gd_2Hf_{2-x}Zr_xO_7$ (x = 0, 0.4, 0.8, 1.2, 1.6 and 2). This powder processing method allows obtaining metastable phases at room temperature that include a large number of structural defects, which will have an interesting effect on their electrical properties for their use as solid electrolytes. We also analyze the effect of substitution of Hf by Zr on the crystal structure and electrical properties of the gadolinium hafnate.

Results show that solid solutions $Gd_2Hf_{2-x}Zr_xO_7$ can be obtained by mechanical milling, by using a planetary mill and Yttria Stabilized Zirconia vials and balls. Their electrical properties, analyzed by impedance spectroscopy, reveal that these oxides are potential candidates to be used as solid electrolytes in SOFC's.

Keywords:SOFC's, pyrochlores, hafnates

1. Introduction

Solid Oxide Fuel Cells (SOFC´s) represent a highly efficient and environmentally friendly technology with a large variety of potential applications. Its operation is based on the combination of oxygen and hydrogen to produce electric energy and water. This technology is currently based on a combination of three active elements, a Sr-doped $LaMnO_3$ (LSM) cathode, 8YSZ solid electrolyte (yttria-stabilized zirconia with 8 mol% Y_2O_3) and a Ni-YSZ cermet anode. Unfortunately, cell performance is significantly affected by solid state reactions between components, which have been frequently observed during co-sintering or even during long-term operation at temperatures as low as 1000ºC. These reactions result in insulating phases, such as La_2Zr_2O7 and $SrZrO_3$, both having a detrimental effect on cell performance [1, 2]. Different possibilities to overcome this problem have been examined, such as using deficient La-site LSM perovskites for cathodes [3] or replacing La by some other lanthanides in LSM [4]. Alternative ceramic oxide-ion conductors have been also proposed to replace 8YSZ as solid electrolyte, among them $A_2B_2O_7$ oxides, such as $Gd_2Zr_2O_7$ and $Ln_2Hf_2O_7$ (Ln = Lanthanides), with the pyochlore-type structure [5,6]. These complex oxides represent an interesting group of solid ionic conductors because of their intrinsic concentration of oxygen vacancies (one vacancy by unit cell), their capacity to incorporate lanthanides and actinides in solid solution, their different degrees of structural order/disorder and stability at high temperatures [7].

Electroneutrality in these materials can be achieved by a large combination of cation species A and B (in $A_2B_2O_7$), with different oxidation states, and that is why their electrical behavior in pyrochlores varies widely. Thus, some pyrochlores such as $Gd_2Zr_2O_7$ represent the best pyrochlore-type oxygen ion conductors known, with σ_{dc} values similar to those of 8YSZ. On the other hand, pyrochlores as $Gd_2Mo_2O_7$ show at room temperature a metallic conducting behavior [7]. Different methods to obtain pyrochlores have been reported, such as solid state reaction at temperatures up to 1600ºC during long periods of time [8], co-precipitation [9], sol-gel [10], among others. Each method provides particular properties to the obtained powder.

Partial substitution of A and B ions for others in these materials can also have an effect on their properties. Some previous works reported the effect of partial substitution of Gd ion by different Lanthanides in the electrical properties of $Gd_2Zr_2O_7$ ([5, 11] and some other analyzed the properties of $Gd_2Ti_{2-x}Zr_xO7$ solid solutions [12]. In all cases results showed that solid solution can result in a increasing of ionic conductivity, one relevant property for solid electrolytes application, when the appropriate dopant elements are used.

In this context, and considering the importance of pyrochlores as solid electrolytes, this work studies the viability to obtain solid solutions of general formulae $Gd_2Hf_{2-x}Zr_xO7$ by mechanical milling, a powder processing method which has been successfully used by our group to prepare similar materials and that allows to obtain powders with high degree structural disorder.

Mechanical milling is a well known method to mechanically activate materials and to promote chemical reactions and alloying. This method has become a powerful powder processing method for the room temperature synthesis of a number of important multicomponent oxides (pyrochlores, fluorites and perovskites, to mention some). The obtained phases are frequently metastable, showing a large number of structural defects that are difficult to obtain by any other powder processing method. Contamination from the milling tools can be considered as a serious problem when hard and abrasive oxides are milled at high intensity for a prolonged time, but this problem can be substantially reduced by the appropriate selection of milling parameters [13].

We also evaluate, by impedance spectroscopy, the electrical properties of these ionically conducting materials. The changes of *dc* conductivity σ_{dc} and activation energy for ionic conduction E_{dc} are analyzed as a function of dopant content (x) in $Gd_2Hf_{2-x}Zr_xO_7$ series.
Considering the absence of reports on electrical properties of $Gd_2Hf_{2-x}Zr_xO_7$ system synthesized by mechanical milling, the results obtained in this study might be an important contribution to the scientific community.

2. Experimental

Five compositions of general formula $Gd_2Hf_{2-x}Zr_xO_7$ (x = 0-2) were prepared by mechanical milling starting from high purity (99.99%) Gd_2O_3, ZrO_2 and HfO_2. Starting chemicals were weighed out as required by stoichiometry, mixed and milled together in a planetary ball mill by using 125-ml zirconia containers with 20 mm diameter zirconia balls as to keep a ball-to-powder mass ratio of 10:1.
Mechanical milling was performed in air at room temperature by using a rotating disc speed of 350 rpm. Phase evolution on milling was analyzed by X-ray diffraction (XRD) in a Philips X'Pert diffractometer using Ni-filtered CuKα radiation (λ = 1.5418 Å). All reactions were considered complete when no traces of starting powders were identified by XRD. Electrical properties were measured from 280 to 750°C, on sintered pellets (10 mm diameter and ~1mm thickness) obtained by uniaxial pressing of the powders prepared by mechanical milling. In order to increase their mechanical strength and obtain dense samples, pellets were sintered at 1500°C for 12 hours (heating and cooling rate = 2°C/min). Analysis of electrical properties was carried out in air by Impedance Spectroscopy using a Solartron 1260 Frequency Response Analyzer over the 100 Hz-1MHz frequency range. Electrodes were made by coating both sides of the pellets with conductive platinum paint and firing them at 600°C to eliminate organic components and harden the Pt coating.

3. Results and discussion

Fig 1(a) shows an XRD study of the evolution, as a function of milling time, of the $Gd_2O_3 + ZrO_2 + HfO_2$ mixture, weighted in the appropriate proportion to obtain the composition $Gd_2Hf_{0.4}Zr_{1.6}O_7$, considered as representative of all five samples. XRD patterns correspond to the starting mixture and samples milled during 1, 3, 6, 9, 20 and 30 hours. As a reference, Fig 1(b) shows the XRD pattern reported in the International Centre for Diffraction Data, ICDD (PDF 80-0471) for the fluorite structure of $Gd_2Zr_2O_7$.
An important decrease in intensity and broadening of the characteristic reflections of starting oxides are observed after the first hour of milling, as a consequence of a considerable decrease in particle size and the introduction of a large number of structural defects. After 6 hours of milling, XRD patterns do not show appreciable changes, only a light decreasing of intensity of the main peaks.
After 9 hours, the powder mixture shows a pattern where the main reflections of the cubic anion deficient fluorite (e.g. (100), (200), (220) and (311)) can be appreciated. As the patterns of samples milled during 20 and 30 hours shows, further milling produces a significant increase in their intensities. Growth of the crystallites initially formed of this phase or the increment in their number with milling time, could be responsible for this effect. No additional phases seem to be present in the powder so reactions were considered completed after 30 hours of milling.
This behaviour is presented by all five studied compositions of the $Gd_2Hf_{2-x}Zr_xO_7$ system, such as Fig 2 shows.

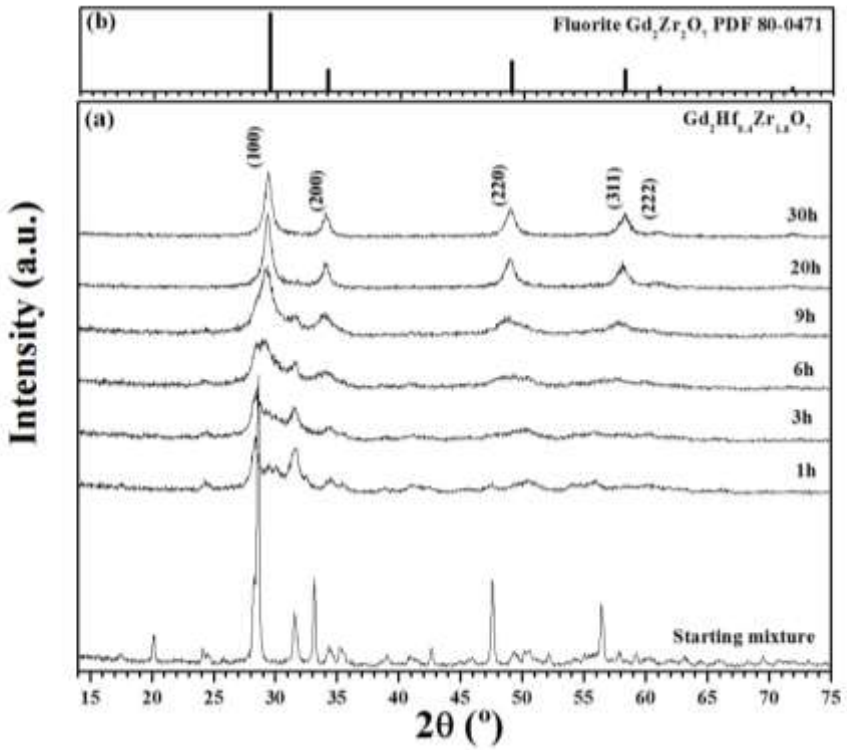

Fig 1. X-ray powder diffraction patterns showing the evolution of the composition $Gd_2Hf_{0.4}Zr_{1.6}O_7$ as a function of milling time (a). X-ray pattern of the fluorite-type $Gd_2Zr_2O_7$ reported in the ICDD (PDF 80-0471) (b).

Most of $A_2B_2O_7$ are known to exist in two crystal forms, as a highly disordered pyrochlores and as anion deficient fluorites [14]. The fully ordered ideal pyrochlore crystal structure exhibits cubic symmetry (S.G.: Fd3m) and can be regarded as an ordered anion deficient fluorite (cubic, S.G.: Fm3m) with twice the cell constant (see reference [7] for a complete description of the pyrochlore structure). The pyrochlore stability field at room temperature and atmospheric pressure in zirconates and titanates is limited to the $1.46 \leq R_A/R_B \leq 1.78$ range [15], corresponding values for $Gd_2Zr_2O_7$ (R_A/R_B for $Gd_2Zr_2O_7$ = R_{Gd}/R_{Zr} = 1.053 Å/0.72 Å = 1.46) [16], and $Sm_2Ti_2O_7$, respectively, and for anion-deficient fluorites R_A/R_B value should be less than 1.46). For the $Gd_2Hf_{2-x}Zr_xO_7$ system studied in this work, R_A/R_B ratio is in the range of 1.48 (for $Gd_2Hf_2O_7$) to 1.46 (for $Gd_2Zr_2O_7$), considering a R_{Hf} of 0.71 Å [16]. According to this ratio, all compositions analyzed in this work should present a pyrochlore type structure and degree of structural disorder will increase lightly with increasing of Zr (x) content (decreasing R_A/R_B).

Fig 2(a) shows a comparison between XRD patterns obtained for all studied compositions after milling for 30 hours as described above. As a reference, Fig 1(b) and (c) show the XRD patterns reported in the ICDD for the fluorite structure of $Gd_2Zr_2O_7$ (PDF 80-0471) and $Hf_2Zr_2O_7$ (PDF 24-0425) respectively. As Fig 2(a) shows, irrespective of their Zr-content and the R_A/R_B value, milled powders present simple and very

similar XRD patterns which resemble the characteristic of a fluorite-type compound, with no evidence of the reflections characterizing the long range atomic ordering of the pyrochlore crystal structure.
These results reveal that, as a far-from-equilibrium processing method, mechanical milling allows the preparation of metastable phases and defect structures existing at equilibrium only at high temperature and/or high pressure. Defect fluorites showing significant stability at elevated temperatures have been also prepared by mechanical milling in the $Gd_2(Ti_{1-y}Zr_y)_2O_7$ and $GdLaZr_2O_7$ system, for compositions with R_A/R_B values well above 1.46 [11,12] and that seems to be also the case in the $Gd_2Hf_{2-x}Zr_xO_7$ system where R_A/R_B changes from 1.46 to 1.48.

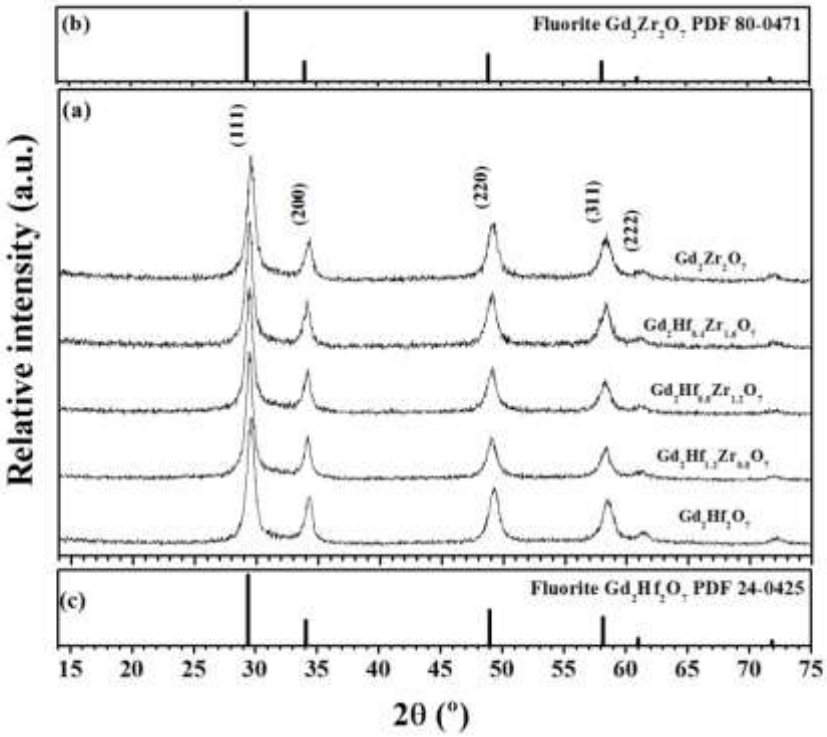

Fig 2. XRD patterns of five compositions of the $Gd_2Hf_{2-x}Zr_xO_7$ system after milling 30 hours (a). XRD patterns reported in the ICDD for the fluorite structure of $Gd_2Zr_2O_7$ (PDF 80-0471) (b) and $Hf_2Zr_2O_7$ (PDF 24-0425) (c).

Postmilling thermal treatments of these metastable powders, facilitates the rearrangement of the cation and anion substructures and the partial relaxation of mechanochemically induced defects in these materials.
This behaviour is showed in Fig 3 (a), which present the XRD patterns of all studied samples milled during 30 hours and fired at 1500°C for 12 hours. All samples fired present the superstructure reflections characterizing the pyrochlore crystal structure (i.e. the (111), (311) and (331) peaks at 2θ ≈15, 28 and 37° respectively). No additional reflections belonging to other phases are observed. The absence of reflections shift towards low or high angles (2θ) is not evident since Zr (0.72 Å) and Hf (0.71 Å) are very similar in size and then the change in the cell size with increasing of Zr content in $Gd_2Hf_{2-x}Zr_xO_7$ might be small to be identified by XRD.

Fig 3(b) and (c) show the XRD patterns reported in the ICDD for the pyrochlore structure of $Gd_2Zr_2O_7$ (PDF 80-0469) and the fluorite structure of $Hf_2Zr_2O_7$ (PDF 24-0425) respectively. Fig 3 (d) show an insert with an enlargement of an area of the XRD patterns and exhibits clearly the presence of the (311) peak corresponding to pyrochlore superstructure.

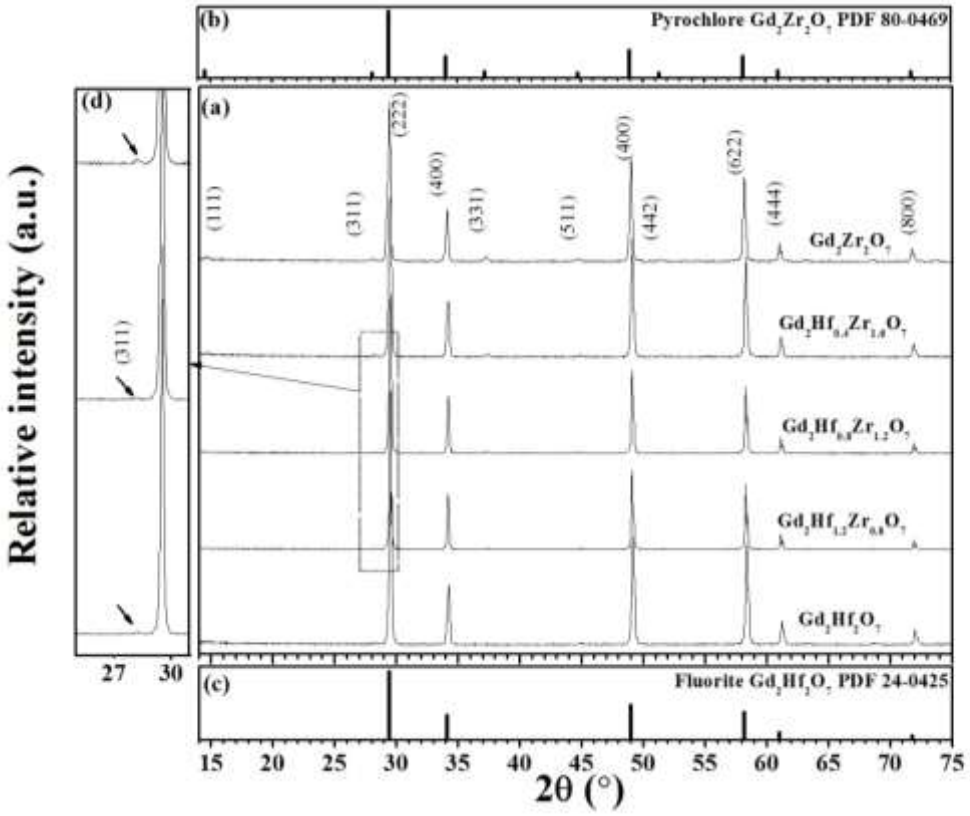

Fig 3. XRD patterns of $Gd_2Hf_{2-x}Zr_xO_7$ samples milled during 30 hours and fired at 1500°C for 12 hours (a). XRD patterns reported in the ICDD for the pyrochlore structure of $Gd_2Zr_2O_7$ (PDF 80-0469) (b) and fluorite structure of $Hf_2Zr_2O_7$ (PDF 24-0425) (c). Enlargement of XRD patterns showing the presence of the (311) peak of the pyrochlore superstructure (d).

The typical morphology of the unpolished $Gd_2Hf_{0.4}Zr_{1.6}O_7$ sample, milled during 30 hours and sinterized during 12 hours at 1500ºC is presented in Fig 4. It is clearly seen a microstructure with grains inhomogeneous and a grain size for less than 1 micrometer. Grain boundaries seem clean and no other phases are found at interfaces. Remanent porosity indicates that higher temperatures are necessaries to obtain totally dense samples. Similar behaviour was showed by all studied compositions.

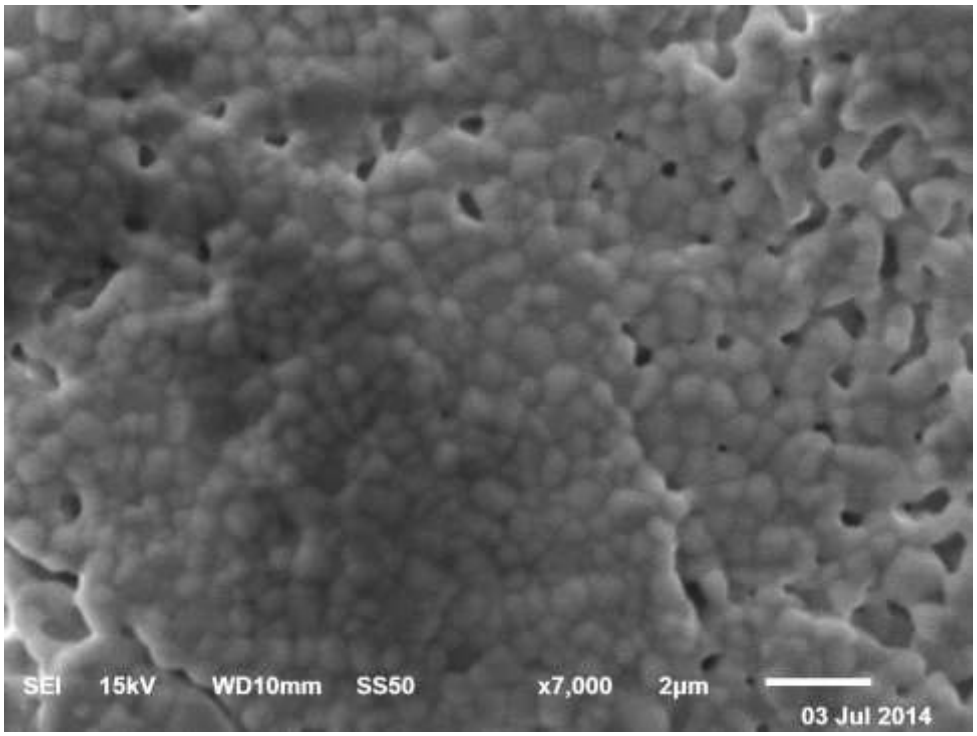

Fig 4. Morphology of the unpolished $Gd_2Hf_{0.4}Zr_{1.6}O_7$ sample, milled during 30 hours and sinterized 12 hours at 1500ºC, obtained by SEM (JEOL JSM 6610).

Fig 5 shows the frequency and temperature dependence of the real part of the electrical conductivity, σ'(ω), for the pyrochlore-type $Gd_2Hf_{0.4}Zr_{1.6}O_7$ sample selected as representative of the series. Similar conductivity plots were obtained for all samples analyzed in this work. As this Fig 5 shows, the frequency (ω) dependence of conductivity at low temperatures may be well described by the so-called Jonscher empirical expression , $\sigma'(\omega) \propto \omega^n$, consistent with a power law-type dependence at high frequencies followed by a frequency-independent conductivity plateau associated to the *dc* conductivity regime, σ_{dc}. This behavior constitutes the main feature of the so-called "Universal Dielectric Response" and has been linked with the existence of cooperative effects in the dynamics of hopping ions [17]. The value of the fractional exponent n ($0 \leq n < 1$) is determined by the strength of the ion-ion interactions in the ionic hopping process; i.e. in the absence of interactions among mobile ions (completely independent and random ion hopping), the exponent n would be 0. The decrease in conductivity clearly visible at low frequencies between 280 and 400°C is caused by blocking effects at grain boundaries whereas that observed at 750°C is due to blocking at the electrodes.
Fig 6 shows the real part of the electrical permittivity as a function of frequency and temperature for the same composition in a log-log representation. Blocking effects at grain boundaries and electrodes, which are characteristic of a charge transport dominated by the contribution of hopping ions, are evident in this graph and also points to the ionic nature of the electrical conductivity in these materials.

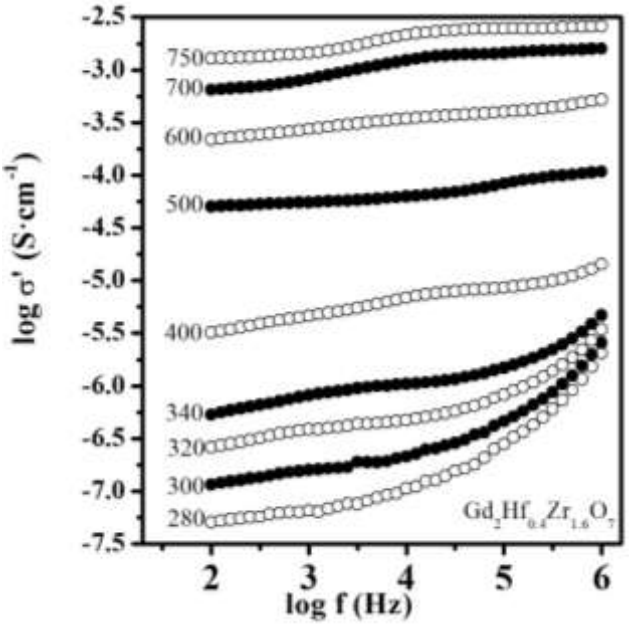

Fig 5. Real part of the conductivity vs frequency at several temperatures (°C) for the $Gd_2Hf_{0.4}Zr_{1.6}O_7$ composition showing a power-law behavior at high frequencies and low temperatures.

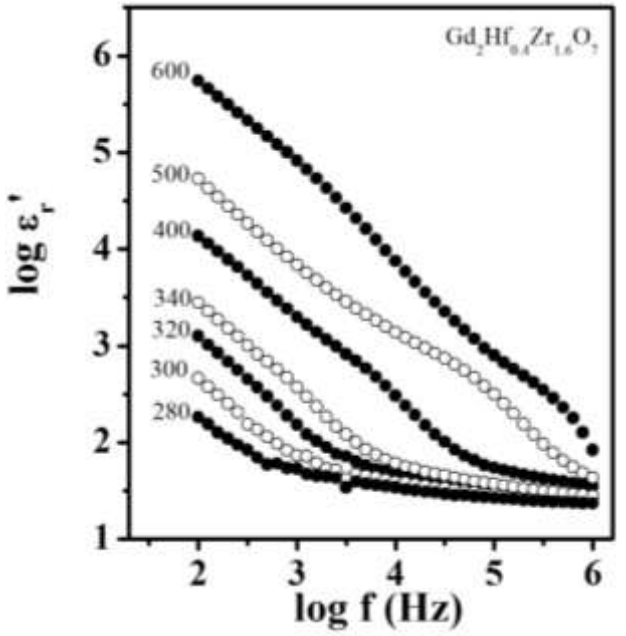

Fig 6. Frequency dependence of the real part of permittivity of $Gd_2Hf_{0.4}Zr_{1.6}O_7$, at selected temperatures (°C).

The temperature dependence of the *dc* conductivity for the samples under study was analyzed by using an Arrhenius-type law of the form:

$$\sigma_{dc} T = (\sigma_0) \exp(-E_{dc}/k_B T) \quad (1)$$

where σ_0 is the pre-exponential factor which is related to the effective number of mobile oxygen ions and E_{dc} denotes the activation energy for the ion conduction process. Fig 7 shows such representation for a selected sample, where the line is the least squares best fit to an Arrhenius law confirming that ionic diffusion in the series is thermally activated. Activation energies E_{dc} for the whole series were calculated from the slope of these linear fits.

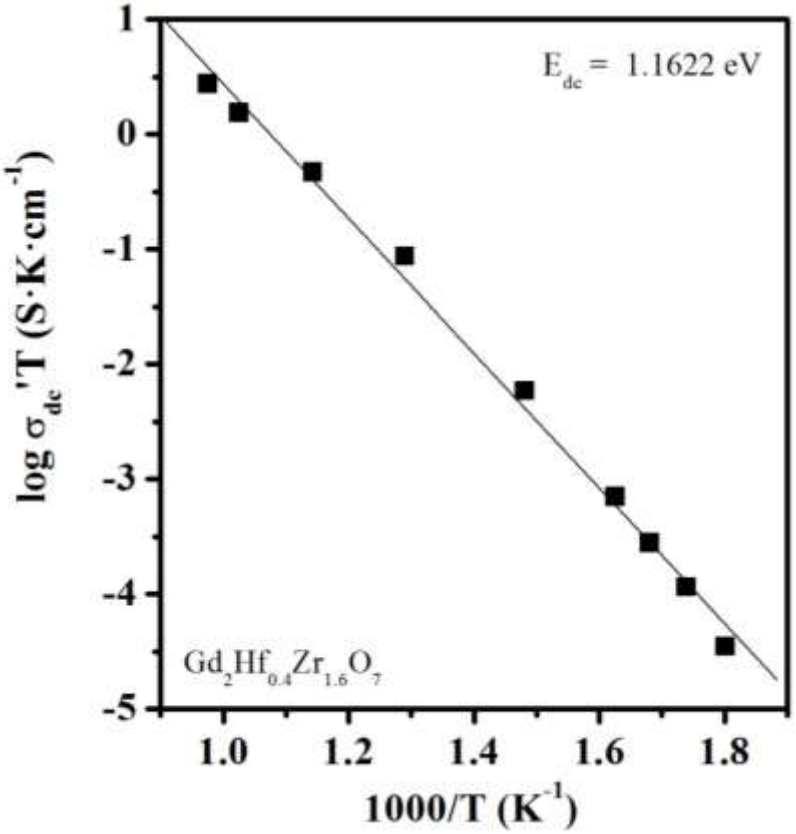

Fig 7. Arrhenius plot of the dc conductivity for the $Gd_2Hf_{0.4}Zr_{1.6}O_7$ composition. Solid line is the best fits to the experimental data.

Finally, Fig 8. shows *dc* conductivity activation energy E_{dc} and the *dc* conductivity σ_{dc} at 750ºC on Zr as a function of Zr content (x) for all the compositions of the system $Gd_2Hf_{2-x}Zr_xO_7$. An increasing of E_{dc} is evident with increasing of Zr content, in the interval of 0.87 to 1.17 eV. This behaviour suggests that incorporation of Zr (decreasing R_A/R_B) in the lattice of $Gd_2Hf_2O_7$ generates an increasing of structural

disorder and therefore an increment of the number of charge-carrier ions, which will contribute to the ionic conductivity. This will generate a higher correlation or interaction between mobile ions and will result in an increasing of the activation energy for *dc* conductivity.
However, the resulting *dc* conductivity shows an increment with increasing of Zr content, reaching a maximum for x = 1.6 and then decreases. Results show that σ_{dc} is a compromise between the increase in the number of carriers (higher disorder) and the activation energy E_{dc}, so that there is an optimum degree of disorder for which the highest *dc* conductivity is obtained.
These results showed that the most disordered material not always has the highest conductivity and the maximum is obtained for the 1.6 would represent precisely the optimal degree of disorder in the system $Gd_2Hf_{2-x}Zr_xO_7$.

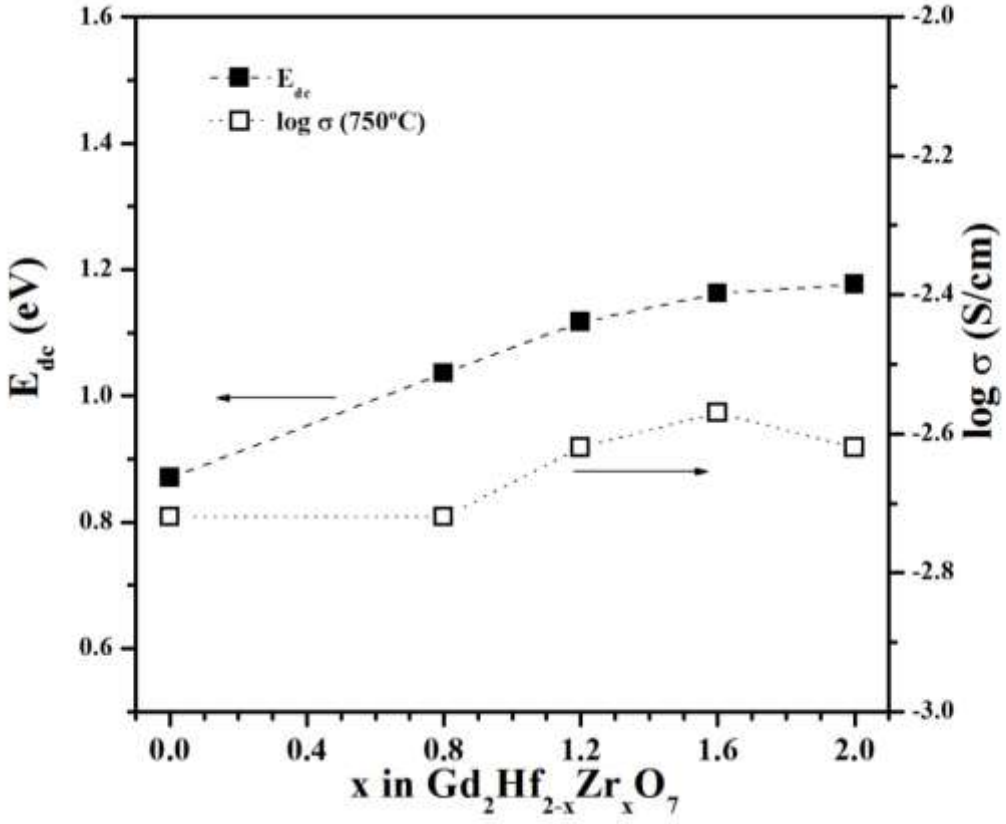

Fig 7. Dependence of the *dc* conductivity activation energy E_{dc} and the *dc* conductivity σ_{dc} at 750ºC on Zr content (x) for the system $Gd_2Hf_{2-x}Zr_xO_7$.

4. Summary and perspectives

We have shown that compositions in the $Gd_2Hf_{2-x}Zr_xO_7$ system having different Hf/Zr ratios can be easily prepared at room temperature by mechanically milling stoichiometric mixtures of the corresponding elemental oxides. As-prepared powder samples show XRD patterns similar to those characteristic of highly disordered anion-deficient fluorites, while postmilling thermal treatments at 1500ºC give rise to a partial redistribution of cations and oxygen vacancies and the appearance of the long-range atomic ordering characteristic of pyrochlores for all studied samples. Activation energy for migration increases as disordering increases (Zr content) and *dc* conductivity in the series reaches a maximum for x = 1.6 at 750ºC. This degree of doping would represent precisely the optimal degree of disorder in the system $Gd_2Hf_{2-x}Zr_xO_7$ to obtain the higher ionic conductivity.
Complex oxides of the general formula $Gd_2Hf_{2-x}Zr_xO_7$ represent an interesting group of ionic conductors that can be used as solid electrolytes in SOFC's technology.

Acknowledgements

This work has been carried out with the financial support of Mexican DGEST and CONACYT.

References

[1] J.A. Labrincha, J.R. Frade, F.M. Marques, $La_2Zr_2O_7$ formed at ceramic electrode / YSZ contacts. Journalof Materials Science 1993; 28: 3809-3815.
[2] A. Mitterdorfer, L.J. Gauckler, $La_2Zr_2O_7$ formation between yttria stabilized zirconia and $La_{0.85}Sr_{0.15}MnO_3$ at 1773 K. Journal of Solid State Chemistry of Inorganic Materials 1997; 453: 425-430.
[3] H. Yokokawa, N. Sakai, T. Kawada and M. Dokiya, Thermodynamic analysis of reaction profiles between $LaMO_3$ (M = Ni , Co , Mn) and ZrO_2. J. Electrochem. Soc 1991; 138: 2719-2727.
[4] Y. Takeda, Y. Sakaki, H-Y Tu, M. B. Phillipps, N. Imanishi and O. Yamamoto, Perovskite oxides for the cathode in solid oxide fuel cells. Electrochemistry 2000; 68: 764-770.
[5] J.A. Díaz-Guillén, A.F. Fuentes, M.R. Díaz-Guillén, J.M. Almanza, J. Santamaría, C. León, The effect of homovalent A-site substitutions on the ionic conductivity of pyrochlore-type $Gd_2Zr_2O_7$. Journal of Power Sources 2009: 186: 349–352.
[6] A.V. Shlyakhtina, L.G. Shcherbakova, Polymorphism and high-temperature conductivity of $Ln_2M_2O_7$ (Ln=Sm─Lu; M=Ti, Zr, Hf) pyrochlores. Solid State Ionics 2011; 192: 200–204.
[7] M.A. Subramanian, G. Aravamudan, G.V. Subba Rao, Oxide pyrochlore, A review. Progress in Solid State Chemistry 1985; 15: 55-143.
[8] B.P. Mandal, Nandini Garg1, Surinder M. Sharma1, A.K. Tyagi, Preparation, XRD and raman spectroscopic studies on new compounds $RE_2Hf_2O_7$ (RE = Dy, Ho, Er, Tm, Lu, Y): Pyrochlores or defect-fluorite. Journal of Solid State Chemistry 2006; 179: 1990–1994.
[9] Z.G. Liu, J.H. Ouyang, Y. Zhou, X.L. Xia, Coprecipitation synthesis and sintering property of $(Yb_xSm_{1-x})_2Zr_2O_7$ ceramic powders. Advances in Applied Ceramics 2010; 109: 12-17.
[10] B. Vijaya Kumara, Radha Velchuria, G. Prasadb, B. Sreedharc, K. Ravikumard, M. Vithala, Preparation, characterization, photoactivity and XPS studies of Ln_2ZrTiO_7 (Ln = Sm and Nd). Ceramics International 2010; 36, 4: 1347–1355.
[11] J.A. Díaz-Guillén, M.R. Díaz-Guillén, J.M. Almanza, A.F. Fuentes, J. Santamaría, C. León, Effect of La substitution for Gd in the ionic conductivity and oxygen dynamics of fluorite-type $Gd_2Zr_2O_7$. Journal of Physics: Condensed Matter 2007; 19: 356212.
[12] K.J. Moreno, G. Mendoza, A.F. Fuentes, J. García-Barriocanal, C. León, J. Santamaría, Cooperative oxygen dynamics in fuel cell materials $Gd_2Ti_{2-y}Zr_yO_7$. Physical Review B 2005; 71: 132301.
[13] A.F. Fuentes; L. Takacs , Preparation of multicomponent oxides by mechanochemical methods. Journal of Materials Science 2013; 48, 2: 598-611.
[14] M.P. van Dijk, A.J. Burggraaf, A.N. Cormack, C.R.A. Catlow, Defect structures and migration mechanisms in oxide pyrochlores. Solid State Ionics 1985; 17: 159-167.
[15] P.K. Moon, H.L. Tuller, Fast ion conduction in the $Gd_2(Zr_xTi_{1-x})_2O_7$ pyrochlore system. Mater. Res. Soc. Proc. 1989;135: 149-155.
[16] R.D. Shannon, Revised effective ionic radii and systematic studies of interatomic distances in halides and chalcogenides. Acta Crystalografica A32 1976; 751-767.
[17] A.K. Jonscher, Dielectric relaxation in solids, Chelsea Dielectric London 1983.

Numerical Study of Fluid Dynamics and Heat Transfer in a PEM Fuel Cell Stack

J. M. Sierra[1,*], S. J. Figueroa-Ramírez[1], C. Patiño-Carachure[1], S. Díaz[1], O. Meza[1], M. A. Meza[1]

[1] Facultad de Ingeniería, Universidad Autónoma del Carmen, Cd. del Carmen, Campeche, México, 24115.
[*]Tel: +52(777)1843585; e-mail: juanmsg@live.com.mx

ABSTRACT

In this work, a numerical study of fluid dynamics and heat transfer in the flow distributor of a PEM fuel cell is presented. The aim of this work is focused on studying the pressure drops and temperature variations presented by stacks with serpentine channels. Different fuel cells with flow fields of 1, 2 and 3 parallel channels; active areas of 5 and 25 cm^2; and stacks with 3 and 5 assemblies were evaluated. From simulation results, it was found that the use of channels in parallel improves the gas distribution inside the fuel cell, increasing of this way the utilization of fuel and oxidant. Also, it was observed that the relationship between the channel width and the active area of the fuel cell is considered as an important factor in the design of the flow field. If this relationship is not taken into account, the pressure drops that occur in the flow channels will impact the overall performance of the stack. Moreover, based on the heat transfer study were identified the spots with more temperature variation in fuel cell and it could be demonstrated that heat convection is the mechanism by which the fuel cell dissipates its heat.

*Keywords:*Flow field; Stack; CFD.

1. Introduction

One of the most promising technologies at the new hydrogen economy are the fuel cells. These are characterized by their high conversion efficiency, modularity and zero pollution. Their advantages have made them a leading technology that can replace the internal combustion engines in transportation and batteries in portable applications [1]. Currently there are different types of fuel cells, which are distinguished by the operating temperature and the electrolyte. However, the proton exchange membrane (PEM) fuel cell has gained more attention by their low operating temperature and high efficiency. The operation of a fuel cell is simple, hydrogen and oxygen are supplied separately to the cell and they react electrochemically to generate electricity, the only products obtained are water and heat. The reactions that take place at the anode and the cathode of the fuel cell are described below:

$$2H_2 \rightarrow 4H^+ + 4e^- \quad (1)$$

$$O_2 + 4H^+ + 4e^- \rightarrow 2H_2O \quad (2)$$

A fuel cell is composed of a membrane, catalyst layers, gas diffusion layers and bipolar plates. The membrane (electrolyte) is a perfluorosulfonic acid commonly called Nafion, which allows the transport of H^+ ions from the anode to the cathode, next there are the catalyst layers or electrodes (anode and cathode), the zones were oxidation and reduction reactions take place. The catalyst layers are composed essentially of Vulcan carbon and platinum particles. The electrodes and electrolyte together form the membrane-electrode assembly (MEA), the main component of the fuel cell. Next to the catalyst layers are the gas diffusion layers, which are made of carbon paper or carbon cloth, these are porous zones that allow the uniform distribution of reactant gases over the catalyst layers. Finally, there are the bipolar plates, which are made from graphite and give mechanical support and electrical contact to the fuel cell besides containing channels that supply the reactant gases into the electrochemical device.

In spite of the PEM fuel cell operation can be described in a simple form, its performance is considerably affected by the operating conditions of pressure, temperature and gas composition, as well as the material properties that compose it. These factors influence considerably on the cell potential, the magnitude of the activation overpotential, the ohmic resistance and the mass transport losses that characterize the fuel cell [2].

In recent years there have been many efforts to minimize these losses, through the development of new catalytic materials and different types of novel electrolytes [3, 4]; however few studies have been reported on the flow field designs and the bipolar plates [5]. It is important to take into account that the performance of a stack depends on the sum of the performance of all its components and this correlation has not been achieved in a practical way so far. One of the main troubles that arise in the stack is the poor distribution of reactant gases into the cell, which is reflected in a non-uniform distribution of current density, dead zones in the membrane, hot spots, degradation of the membrane-electrode assembly and in general a poor performance of the cell [6]. Although this issue has been given enough attention by using numerical simulation and experimental analysis, there are still too many design alternatives to improve the fuel cell performance.

Recent reports about flow field designs indicate that each channel configuration has advantages and disadvantages, which depend on the operating conditions for which they were designed. The most common designs are classified into serpentine, straight channels, interdigitated, columns, mesh, and cascade designs [6, 7].

The flow field with the simplest configuration is the straight channel version, this design works efficiently and causes low pressure drops although requires ideal conditions for good performance, for example, when the flows are not supplied with enough pressure a non-uniform distribution of gases on the catalyst layer is developed. Likewise, any water droplet formed in the flow field blocks the channels. Probably, the most common design used in commercial fuel cells is the serpentine flow field, either with single or multiple channels. In this design the gas flows through the channels circulating throughout the active area of the fuel cell. This configuration increases both, the flow speed and the pressure drop; furthermore it improves the water and heat management by transporting liquid and vapor water through the channels [6, 7]. The interdigitated flow field was designed on a dead-end channel concept, which forces the gases to flow through the gas diffusion layers before they leave the plate. This structure induces forced water removal from the open structure of the gas diffusion layer but it also induces higher pressure drops between the inlet and the outlet than those of the through-flow options [5].Their advantages and drawbacks were reported in other works. [8, 9].

Although in the literature have been reported several studies of CFD in the flow fields, most of them are focused on single cell and are very few studies aimed at stacks. In this regard, the aim of this work is focused on studying the pressure drops and temperature variations presented by stacks with serpentine channels. Different fuel cells with flow fields of 1, 2 and 3 parallel channels; active areas of 5 and 25 cm^2; and stacks with 3 and 5 assemblies are evaluated in this work.

2. Description of the computational model

The computational models evaluated in this work consist of two types of fuel cells: (1) Conventional fuel cells with 5 and 25 cm^2 of active area (Fig. 1), that include gas diffusion layers (GDL), catalyst layers (CL), membrane (MEM) and monopolar plates (MP), and (2) Half-cells in stack with 5 and 25 cm^2 of active area (Fig. 2), that include a gas diffusion layer (GDL), a porous media (PM), and cathode plate (CP). The cathode compartment was simulated as stack because the oxygen reduction reaction has the lowest performance in the fuel cell. The dimensions of the components are specified in Table 1.

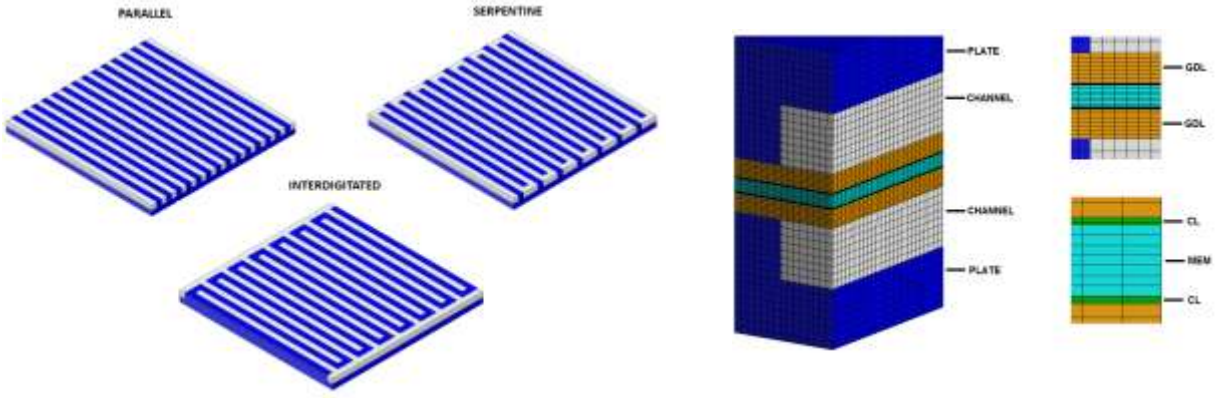

Fig. 1. Computational models of single fuel cells with 5 cm^2 of active area, conventional flow-fields (left), mesh visualization and components (right).

In order to establish the accuracy of the results and to ensure that they were independent of the grid, previous simulations were performed. The reference parameter used to do the analysis in stacks was the average pressure, and

for single fuel cells was the average current density. The final mesh used in the models had the following intervals: channels and plates (0.1), GDL's (0035), MEM (0025), and CL's (0004). The mesh elements obtained in the stacks with only one assembly was around 7.8 million and for single fuel cells was 3.5 million.

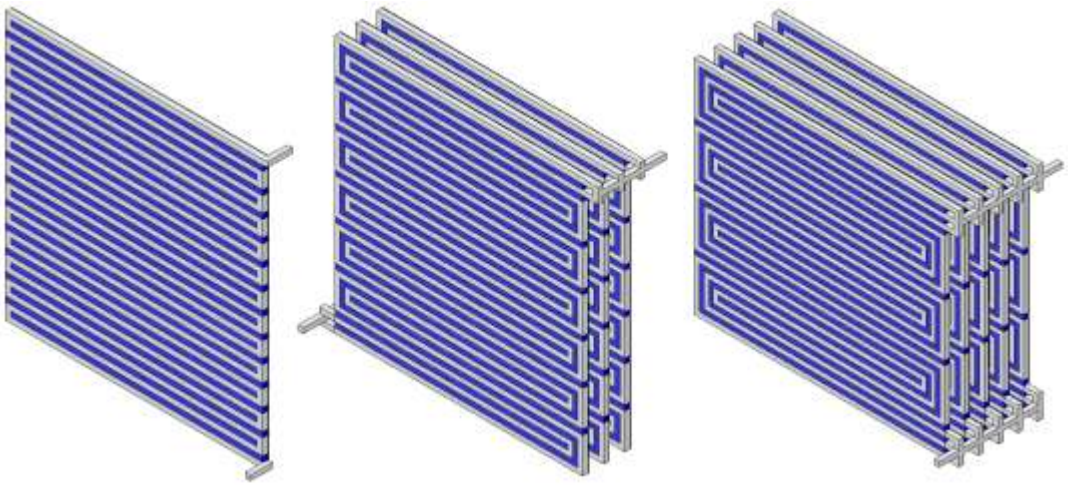

Fig. 2. Stacks of 25 cm^2 of active area, (a) single serpentine of 1 assembly, (b) double serpentine of 3 assemblies, and (c) triple serpentine of 5 assemblies.

The assumptions to carry out the numerical simulation of the computational models were the following: (a) steady state conditions, (b) laminar flow in channels, (c) isotropic porous zones, (d) the electrochemical reactions take place on the catalyst layer surface, (e) transport of species in the gas phase, and (f) the transport of liquid water in the membrane is controlled by diffusion mechanisms and electro-osmotic drag.

Table 1. Dimensions of the PEM fuel cell components.

	unit	value
Channel width	mm	0.8
Channel height	mm	0.8
Plate thickness	mm	1.6
Active area	mm^2	549
GDL thickness	mm	0.25
CL thickness	mm	0.02
MEM thickness	mm	0.178

2.1 Mathematical Model

Transport phenomena occurring inside a PEM fuel cell are represented by the governing equations of mass conservation, momentum, energy, species and charge transport. These equations are described below.

2.1.1 Continuity equation

The continuity equation represents the mass conservation for all transport processes that take place in the fuel cell, such as fluid flow, mass diffusion, phase change and electrochemical reactions. This equation is written in a simplified form (steady state) as:

$$\nabla \cdot (\rho \vec{v}) = S_m \tag{3}$$

where ρ is the fluid density, $\vec{\boldsymbol{v}}$ is the vector velocity and S_m is the source term for the species balance.

2.1.2 Momentum transport

The momentum transport equation in a steady state is described by:

$$\boldsymbol{\nabla \cdot (\rho \vec{v} \vec{v}) = -\nabla p + \nabla \cdot \left(\mu^{eff} \nabla \vec{v}\right) + S_p} \tag{4}$$

where p is the static pressure, μ^{eff} is the average viscosity of the mixture and S_p is a source term that contains the physical characteristics of porous media and it is defined as:

$$\boldsymbol{S_p = -(\mu/k)\vec{v}} \tag{5}$$

where μ is the gas viscosity (kg/m·s), k is the permeability (gas diffusion layers and catalyst layers), and $\vec{\boldsymbol{v}}$ is the superficial vector velocity at the porous media (m/s) [11].

2.1.3 Species transport

The species transport equation represents the mass conservation for each individual species of a gas. To determine the local mass fraction of each species y_i, the following equation is used:

$$\boldsymbol{\nabla \cdot (\rho \vec{v} y_i) = -\nabla \cdot \vec{J}_i + S_i} \tag{6}$$

where S_i is the source term for each phase, $\vec{\boldsymbol{J}}_{\boldsymbol{i}}$ is the flux diffusion for the species i, which is calculated for a laminar flow as:

$$\boldsymbol{\vec{J}_i = -\rho D_i \nabla \cdot y_i} \tag{7}$$

where D_i is the diffusion coefficient for the species i.

2.1.4 Energy

The energy equation for steady state is expressed by:

$$\nabla \cdot [\vec{v}(\rho E + p)] = \nabla \cdot \left(k_{eff} \nabla T - \sum_i h_i \vec{J}_i\right) \quad (8)$$

where E is the total energy, k_{eff} is the effective conductivity and $\vec{J}_i$ is the flux diffusion for the species i.

2.1.5 Electrochemical model

The fluid dynamics equations preceding this section were coupled to the electrochemical model using a commercial fuel cell module implemented in Ansys-Fluent®. This set of equations allows to solve the transport phenomena and electrochemical processes occurring in the fuel cell. This model consists of two equations for solving the two potential fields: equation (9) associated with the transport of electrons in the catalyst layers, the gas diffusion layers and the plates and, equation (10) associated to proton transport through the membrane and the catalyst layers.

$$\nabla \cdot (\sigma_{sol} \nabla \varphi_{sol}) + R_{sol} = 0 \quad (9)$$

$$\nabla \cdot (\sigma_{mem} \nabla \varphi_{mem}) + R_{mem} = 0 \quad (10)$$

where σ is the electric or ionic conductivity, φ is the cell potential and R is the transfer current; the subscripts *sol* and *mem* correspond to the solid and the electrolyte phases, respectively.

The transfer current or source terms in equations 9 and 10 are determined from the general Butler-Volmer formulation, which is used to calculate the local current density on the catalyst layers by the following equations:

$$R_{an} = j_{an}^{ref} \left(H_2 / H_{2,ref}\right)^{\gamma_{an}} \left(e^{\alpha_{an} F \eta_{an}/RT} - e^{\alpha_{ca} F \eta_{an}/RT}\right) \quad (11)$$

$$R_{ca} = j_{ca}^{ref} \left(O_2 / O_{2,ref}\right)^{\gamma_{ca}} \left(-e^{\alpha_{an} F \eta_{ca}/RT} + e^{-\alpha_{ca} F \eta_{ca}/RT}\right) \quad (12)$$

where j^{ref} is the exchange current density, H_2 y $H_{2,ref}$, are the local and reference species concentrations, γ is the concentration coefficient, α is the transfer coefficient, η is the activation losses defined in equations 13 and 14, and F is the Faraday constant (9.65×10^7 C. kg^{-1} mol^{-1}).

The reaction kinetics is controlled by the local surface overpotential, η, known as activation losses, which is associated with the difference of surface potentials between the electrode and the electrolyte φ_{sol} and φ_{mem}. This overpotential is calculated for both the anode and the cathode, including as last term the open circuit voltage (V_{OC}) and thus establishing the potential difference between both electrodes.

$$\eta_{an} = \varphi_{sol} - \varphi_{mem} \quad (13)$$

$$\eta_{ca} = \varphi_{sol} - \varphi_{mem} - V_{oc} \quad (14)$$

The membrane is modeled as a porous zone and its properties such as ionic conductivity σ_{mem} and the electro-osmotic drag coefficient are evaluated as a function of the water content λ. These properties are represented by the correlations reported by T. E. Springer et. al [12] (equations 15-17):

$$\sigma_{mem} = (0.00514\lambda - 0.00326)e^{1268\left(\frac{1}{303}-\frac{1}{T}\right)} \quad (15)$$

$$\lambda = 0.043 + 17.81a - 39.84a^2 + 36a^3 (a < 1) \quad (16)$$

where *a* is the water activity. The saturation model reported by T. Nguyen [13] and J. H. Nam et. al. [14] is used to model the formation and transport of liquid water in the membrane-electrode assembly. From these equations (9-16) both potential fields are solved, also the electrochemical process that causes the three potential losses in a fuel cell are included, which are known as: activation overpotential, ohmic overpotential and concentration overpotential.The operating conditions and the electrochemical parameters used in the simulation were taken from experimental data and literature data [15-18].

2.1.6 Boundary conditions

The boundary conditions applied to the computational domain of single fuel cell were (1) mass flow inlet, (2) pressure outlet, (3) constant potential at anode and, (4) variable potential at cathode, which were set to calculate the current density in the cell. The flows of hydrogen and oxygen were fed in the same direction in order to obtain uniform current density distributions as well as reported by J. M. Sierra et. al [19]. The mass flow rates were calculated for an active area of 5 cm^2 with a stoichiometry of 1.25 and 2 for the anode and the cathode, respectively. Likewise, the concentrations of hydrogen and oxygen flows were determined, they were supplied at 1 atm of pressure and 300 K of temperature, with 25% and 25% of relative humidity for the anode and the cathode, respectively.

From these boundary conditions, the fluid dynamics equations and the electrochemical model of Ansys-Fluent®, the computational model of PEM fuel cell was solved. A segregated method, the first order scheme and SIMPLE algorithm were used to solve the equations [11].The model was evaluated in different operating potentials and thereby the current density was calculated. Using these data, polarization curves were generated to evaluate the performance of each flow field. The boundary conditions applied to the computational domain of stacks were (1) mass flow inlet, (2) pressure outlet, (3) gas diffusion layers and porous media were considered as porous jump without reactions. The flow supplied to the stacks was air.

3. Results and discussion

In this section the numerical results for different models of PEM fuel cell are presented. First, numerical results of pressure drop in stacks of 5 and 25 cm^2 are presented. These are shown by distribution contours of pressure at the interfaces: channel - gas diffusion layer (CHN / GDL) and gas diffusion layer - catalyst layer (GDL / CL), both of them at the cathode compartment. Then, numerical results of heat transfer analysis are presented by temperature contours, ohmic heating, reaction heat and enthalpy, at the cathode interface (CHN / GDL).

3.1 Pressure distributions in the stack of 5 cm^2 with single channel.

The results for serpentine design of 5 cm^2 with single channel are shown in Figure 3. In Fig. (left) it can be observed that gas pressure decreases gradually throughout the channel, from input to output channel with a maximum pressure gradient of 274 Pa. This happens due to channel length and the pressure losses generated by elbows of 90°, which are located at the end of each channel of the flow field. In Fig. (right) the maximum pressure reached was 129 Pa, which

is caused by the properties of the porous media. This pressure distribution adopted a similar pattern to the channel distribution presented previously. The average pressure at this interface was 33.7 Pa.

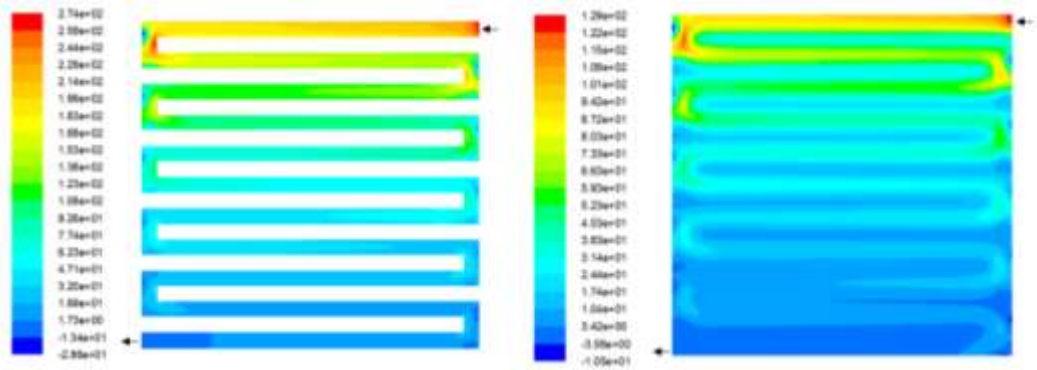

Fig. 3. Pressure distributions (Pa) for serpentine design with single channel and 5 cm^2 of active area, (left) interface (CHN/GDL) and, (right) interface (GDL/CL).

Figure 4 shows the simulation results for stacks of 2, 3 and 5 assemblies, where the gas inlet is at the top of the first assembly (right) and outlet at the bottom of the last assembly (left). For the stack with 2 assemblies, it can be observed that the pressure distribution for the first field of flow is similar to a single cell (Fig. 3a); however, for the second flow field pressure drop occurs in the region next to the gas outlet with the same magnitude as the atmospheric pressure, which affect the performance of the fuel cell. For the stack with 3 assemblies (Fig. 4b) a similar pattern distribution to the previous case is observed; however, unlike the stack with 2 assemblies, the pressure drop on the last assembly is corrected, the same goes for the stack with 5 assemblies (Fig. 4c). From these results we can deduce that flow fields with stacks of 5 cm^2 and a single channel must be at least 3 assemblies.

(a) (b) (c)

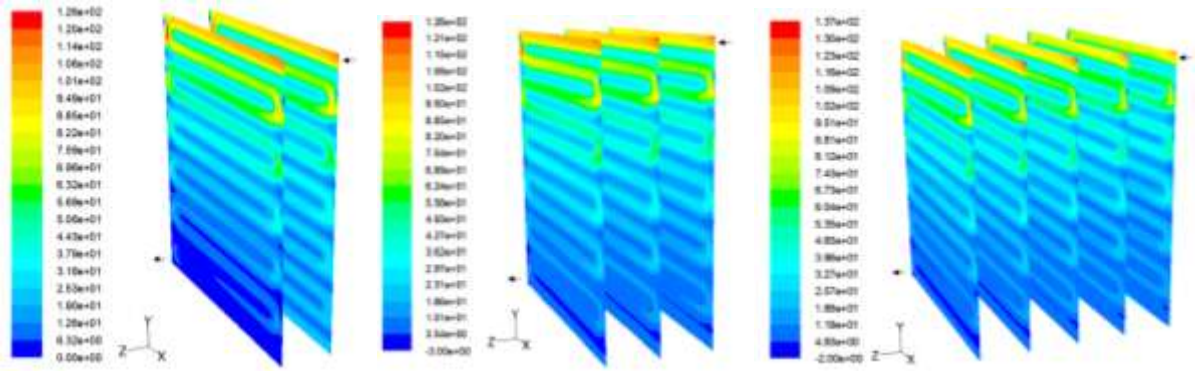

Fig. 4 Pressure distributions (Pa) in stacks with single channel configuration and active area of 5cm^2, (a) 2 assemblies, (b) 3 assemblies and, (c) 5 assemblies.

3.2 Pressure distributions in the stack of 25 cm^2 with triple channel.

The simulation results for serpentine design with three parallel channels are presented in Figure 5. Figure (left) shows that pressure distribution is significantly improved compared to the flow field with single and dual channels, this configuration provided a pressure gradient of 430 Pa, from the inlet to the outlet channels. In Figure (right) it can be observed a similar pattern of distribution, but the pressure drop was 198 Pa. This indicates that the use of parallel channels is useful for reducing pressure drop of serpentine flow fields. The average value of pressure at this interface was 19.29 Pa.

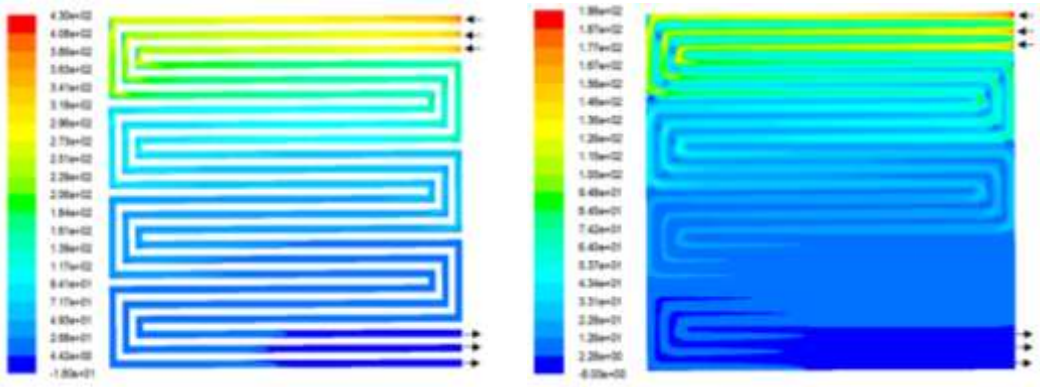

Fig. 5 Pressure distributions (Pa) for serpentine design with triple channel and 25 cm^2 of active area, (left) interface (CHN/GDL) and, (right) interface (GDL/CL).

Figure 6 shows the simulation results for stacks with 3 and 5 assemblies and three parallel channels. In Fig (left) a better pressure distribution on the three assemblies is observed, compared with two previous designs, but in the same way the first assembly has the lowest pressure values, which is not useful to use efficiently the fuel / oxidant. For the stack with 5 assemblies Fig. (right) the same distribution pattern is observed, with very low values of pressure at the first 4 assemblies.

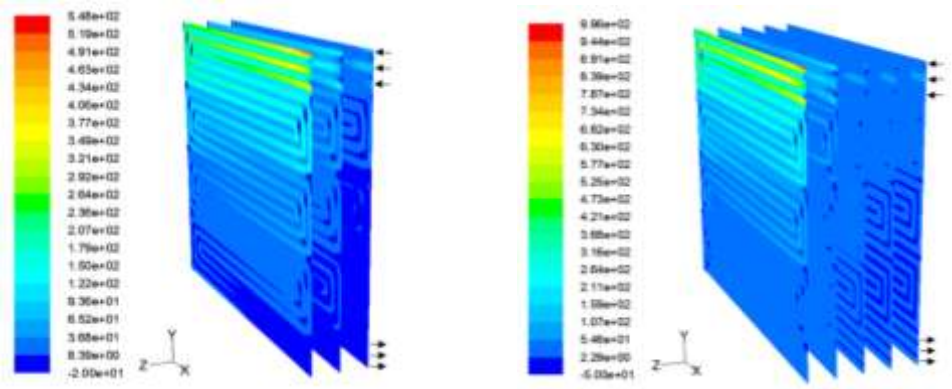

Fig. 6 Pressure distributions (Pa) in stacks with triple channel configuration and active area of 5cm^2, (left) 3 assemblies and, (right) 5 assemblies.

From this analysis it can be deduced that use of parallel channels benefits the gas distribution inside the cell, but the relationship between the width of the channel and the active area must be taken into account for the design of fuel cell stacks. Also, the location of the feed channel and its diameter must be considered, because it contributes to the first pressure drop across the stack.

3.3 Heat transfer analysis in a PEM fuel cell.

The numerical results for the fuel cell model with 5 cm^2 of active area are presented in this section. The analysis consisted on studying the temperature variation of fuel cell at different potentials operating. The analysis was done under atmospheric conditions with the aim to identify areas where there is greater heat generation in the cell. Results are presented at the GDL/CL interface for cathode side by means of temperature distributions, contours of heat reaction, ohmic heating and current density.

3.3.1 Parameters related to the heat transfer in the fuel cell.

In Fig. 7 different distribution contours for the cathode side are presented. From these results it can be seen that areas with the highest temperatures are found at the interfaces of the flow channels, where the gas reacts with the catalytic layer. Likewise, it can be seen that heat generation occurs due to processes which occur within the cell, most notably: exothermic reactions, ohmic heating, enthalpy of the reactants, the phase change of products, among others. Convection is the mechanism by which the flow dissipates more heat generated in the cell.

3.3.2 Temperature distributions in a single PEM fuel cell model.

Figure 8 shows the temperature distributions at the GDL / CL interface cathode of the fuel cell. These results were simulated at different operating voltages and under atmospheric conditions. In the figures it can be observed that as the potential of the cell is decreased the temperature increases from 300 K to 305 K. This occurs due to the generation of current in the cell and the various phenomena described above.

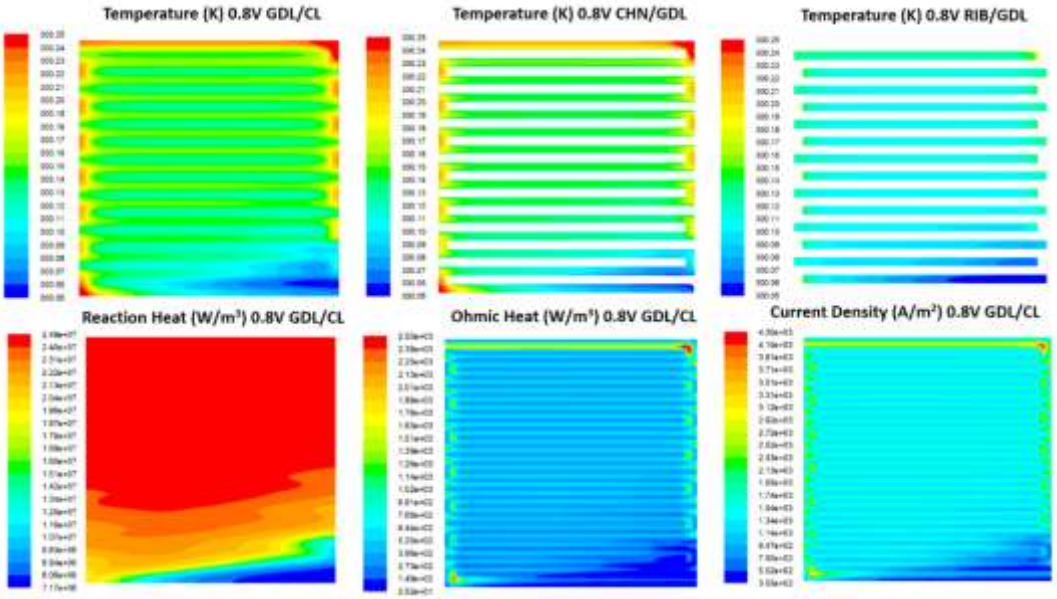

Fig. 7 Contours of distribution for different variables at the cathode compartment of the fuel cell.

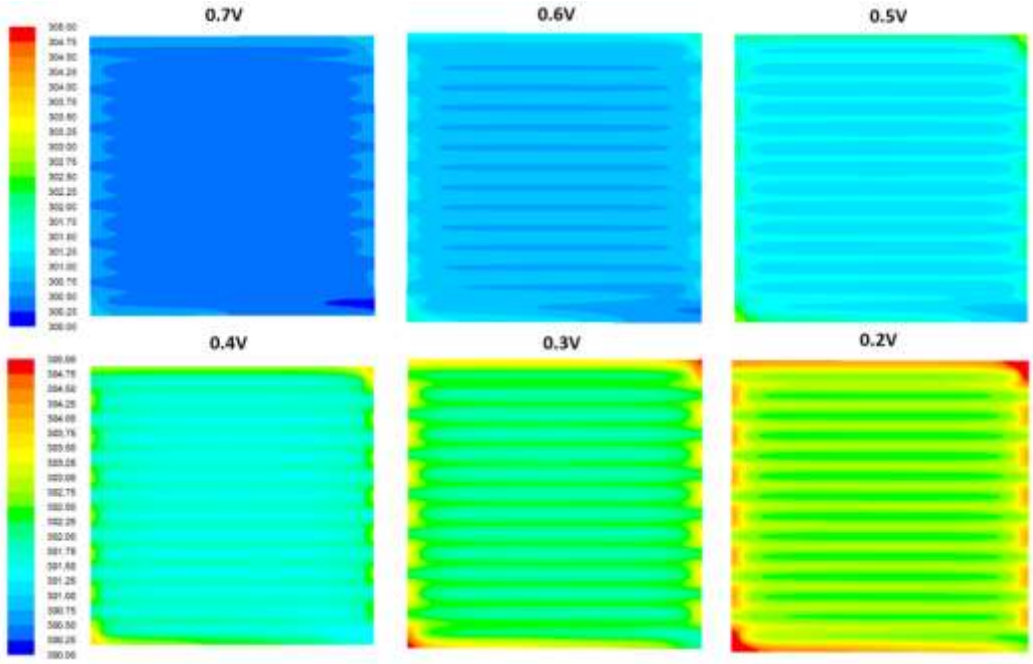

Fig. 8 Temperature distributions (K) at the cathode interface (GDL/CL) for different operating voltages.

4. Conclusions

A CFD study of flow fields in a PEM fuel cell was carried out in this work. Pressure drops that occur with serpentine designs were studied. From the numerical results, the conclusions are the following:

The pressure drops in a serpentine flow field can be reduced when the number of channels in parallel increases; this favors an even distribution of gas at GDL / CL interface, as well as the use of fuel / oxidant in the fuel cell.

The channel dimensions of 1 x 1 mm in the flow fields with 25 cm^2, are not suitable to efficiently distribute the gas on the GDL / CL interface. The channel width should be increased, otherwise the gas pressure will not be enough to cover the entire flow field due to the channel length and the elbows.

The supply system in the stacks must be modified. The design is not suitable for simultaneously supplying multiple flow fields connected in parallel form. Both the diameter, shape and location of the main supply channel should be modified to improve the gas distribution inside the fuel cell stack.

From the analysis of heat transfer could be inferred that the highest values of temperature are presented in the flow channels and the heat convection is the mechanism by which the fuel cell dissipates its heat.

Acknowledgements

The authors gratefully acknowledges to Engineering Faculty of Autonomous University of Carmen for the granted support to perform the numerical simulations in their computing equipment and the use of Ansys-Fluent® software license.

References

[1] Jeremy Rifkin, The Hydrogen Economy, Penguin Putman Inc., New York (2000).

[2] J. Larminie, A. Dicks, Fuel Cells Systems Explained, 2nd ed., Wiley, (2003).

[3] A. A. Santiago, J. Vargas, J. Cruz-Gómez, M. A. Tlenkopatchev, R. Gaviño, M. López-González, E. Riande, Synthesis and ionic transport of sulfonated ring-opened polynorbornene based copolymers. Polymer, 2011; 52: 4208-20.

[4] A. A. Santiago, J. Vargas, M. A. Tlenkopatchev, M. López-González, E. Riande, Electrochemical performance of membranes based on hydrogenated polynorbornenes functionalized with imide side groups containing sulfonated fluorinated moieties, Journal of Membrane Science 2012; 403-404: 121-8.

[5] G. Hoogers, Fuel Cell Technology Handbook, Ed. CRC Press, New York (2002).

[6] A. P. Manso, F.F. Marzo, J. Barranco, X. Garikano, M. Garmendia Mujika, Influence of geometric parameters of the flow fields on the performance of a PEM fuel cell. A review. Int. Journal of Hydrogen Energy, 2012; 37:15256-87.

[7] F. Barbir, PEM Fuel Cells – Theory and Practice, Academic Press, Elsevier, 2005.

[8] Nam Jin Hyun, Lee Kyu-Jin, Sohn Sangho, Kim Charn-Jung. Multi-pass serpentine flow-fields to enhance under-rib convection in polymer electrolyte membrane fuel cells: design and geometrical characterization. Journal of Power Sources 2009;188:14-23.

[9] Xianguo Li. Imran Sabir, Review of bipolar plates in PEMFCs: Flow-field designs. Int. Journal of Hydrogen Energy, 2005; 30: 359-71.

[10] Bladimir Ramos-Alvarado, Abel Hernandez-Guerrero, Daniel Juarez-Robles, Peiwen Li., Numerical investigation of the performance of symmetric flow distributors as flow channels for PEM fuel cells. Int. Journal of Hydrogen Energy, 2012; 37: 436-48.

[11] Fluent 6.3 – Fuel Cells Module Manual (2007).

[12] T. E. Springer, T.A. Zawodzinski, and S. Gottesfeld, Polymer Electrolyte Fuel Cell Model. J. Electrochemical Soc., 1991;138:2334-42.

[13] Jung Seok Yi, Trung Van Nguyen, Multicomponent Transport in Porous Electrodes of Proton Exchange Membrane Fuel Cells Using the Interdigitated Gas Distributors. J. Electrochemical. Society, 1999; 146: 38-45.

[14] J. H. Nam, M. Kaviany, Effective diffusivity and water-saturation distribution in single- and two-layer PEMFC diffusion medium. Int. J. Heat and Mass Transfer 2003; 46: 4595-4611.

[15] S. Shimpalee, and J.W. Van Zee, The impact of channel path length on PEMFC flow-field design. J. Power Sources, 2006; 160: 398-406.

[16] N. Djilali, and T. Berning, Computational model of a PEMFC with serpentine gas flow channels. J. Power Sources, 2004; 130: 149-157.

[17] T. Berning and N. Djilali, Three-dimensional computational analysis of transport phenomena in a PEM fuel cell, a parametric study. J. Power Sources, 2003; 124: 440-452.

[18] Um S, Wang CY. Three-dimensional analysis of transport and electrochemical reactions in polymer electrolyte fuel cells. J Power Sources 2004;125:40-51.

[19] J.M. Sierra, J. Moreira, P.J. Sebastian, Numerical analysis of the effect of different gas feeding modes in a proton exchange membrane fuel cell with serpentine flow-field. J. Power Sources, 2011; 196: 5070-5076.

[20] J. M. Sierra, P. J. Sebastian, S.A. Gamboa, Study of activation losses and ohmic resistance in a PEM fuel cell using computational fluid dynamics. ECS Transactions, 2009; 20 (1): 395-405.

[21] Fang-Bor Weng, Ay su, Guo-Bin Jung, Yen-Chiao Chiu, Shih-Hung Chan, Numerical prediction of concentration and current distributions in PEMFC. J. Power Sources, 2005; 145: 546-554.

[22] J. A. Alanís Navarro, Diseño, fabricación y caracterización de celdas de combustible de intercambio protónico utilizando tecnología MEMS, Tesis de Doctorado, Instituto de Energías Renovables, Universidad Nacional Autónoma de México (2014).

Start-up of Continuous Stirred-Tank Reactor for Biohydrogen Production from Restaurant Organic Waste

A. Castillo-Hernández[1], I. Mar-Alvarez[1], I. Moreno-Andrade[1*],

[1]Universidad Nacional Autónoma de México, Instituto de Ingeniería, Academic Unit Juriquilla, Laboratory for Research on Advanced Processes for Water Treatment, Blvd. Juriquilla 3001, Juriquilla, C.P. 76230, Querétaro, Mexico
[*]Tel: +524423393782; e-mail: acastilloh@ii.unam.mx

ABSTRACT

Recently, continuous stirred-tank reactor (CSTR) has been applied to degrade organic solid waste (OSW) in anaerobic digestion. If the anaerobic process is separated in two phases (hydrolytic-acidogenic and methane production steps), it is possible to increase the energy production due to the hydrogen (H_2) generation in the first step. The objective of this study was to star up and operation of a CSTR to generate H_2 from food waste of a restaurant in order to determine the operational conditions for increase the H_2 production. The start-up was obtained in three phases: 1) Inoculum activation with glucose, 2) Acclimation of inoculum to H_2 production in a discontinuous process and 3) CSTR operation. The reactor was constructed by acrylic with a total useful volume of 2 L with a headspace of 0.3 L. The hydraulic residence time (HRT) was fixed in 24 h and the organic loading rate (OLR) was of 22 g TS/$L_{reactor}$/d. The reactor was inoculated with anaerobic sludge from a brewery. Fermentative H_2 producers selected by a thermal shock pre-treatment (103-105 °C during 24 h). H_2, carbon dioxide (CO_2), methane (CH_4) and Volatile Fatty acids (VFA) were determined by gas chromatography (GC). H_2 production was 365mL H_2/$L_{reactor}$/d and H_2 yield was 19 ml H_2/g SV. CH_4 was not detected. The total solid (TS), volatile solid (VS), and chemical oxygen demand (COD) removal was 42.8±6.3 and 50.9±6.4 and 24.1±10.7 respectively. The removal carbohydrate (80%) was bigger than proteins (24%).

Keywords: CSTR; bio-hydrogen; organic solid waste, organic loading rate, hydraulic residence time

1. Introduction

The H_2 has been widely recognized as an alternative energy source to substitute fossils fuels. This is a clean fuel, it can be used in fuel cells to produce electrical energy where only water is produced as a byproduct, and because H_2 has high specific energy content (33- 39.4 kWh/kg) compared and other fuels [1-4]. Among the H_2 production methods, the most promoting and friendly method is dark fermentation from organic solid waste, especially food waste [2].

Dark fermentation is a biological process where a microbial consortium degrades the organic matter at anaerobic condition to produce biogas composed with the H_2 and CO_2 and a digestate rich in volatile fatty acids that can be used in other biological processes as photofermentation. However, dark fermentation is a step intermediate in anaerobic digestion. Anaerobic digestion is performed in four stages; hydrolysis, fermentation, acetogenesis and methanogenesis [1]. Thus, H_2 is a key intermediate consumed mainly in methanogenesis by archeas methanogenic. Therefore, for producing H_2 would inhibit methanogens. Methanogen inhibition is possible by means of a biokinetic control and heat-shock treatment. Biokinetic controls refers to the control of pH during operation, usual used pH between 5-6, the use of low HRT in continuous reactor to eliminate microorganism growth rates below the rate of dilution as the archeas methanogenic [8]. The theory of the method of treatment by thermal shock is based on the thermal shock that can inactivate methanogenic archaea and cultivate fermentative spore-forming bacteria such as *Clostridium* sp. [7].

It has been reported the H_2 production from biological fermentation of organic fraction of solid waste especially food waste. Food waste is a carbohydrates rich waste; this can be used in the dark fermentation to produce H_2. This available waste has high organic matter content and they are low cost [4,7-9].

In 2006 was reported the study of H_2 production in continuous stirred-tank reactor (CSTR) from food waste the production of H_2 from organic solid wastes from home in a CSTR. The operating conditions were organic loading rate of 37.5 g VS / $L_{reactor}$ / d, HRT 2 d, pH 5.2 and mesophilic conditions at 35 ° C. The H_2 production rate was 1.6 L $H_2/L_{reactor}$/d and H_2 yield 43 ml H_2/g SV [4].On other hand, in 2009 was reported the study of H_2 production in a semi-CSTR. The operating conditions were organic loading rate of 22.5 g VS / $L_{reactor}$ / d, HRT 6.7 d, pH 5.5 and mesophilic conditions at 40 ° C. The H_2 production rate was 1.4 L $H_2/L_{reactor}$/d and H_2 yield 65 ml H_2/g SV [9].

The objective of this study was to evaluate the start-up and operation of a CSTR for bio H_2 production from the organic fraction of restaurant food waste at mesophilic conditions and at low concentration of initial total solids in order to determine the operational conditions for increase the H_2 production.

2. Experimental

2.1. Inoculum

Anaerobic granular sludge from an anaerobic sludge blanket reactor treating brewery wastewater was used as inoculum. The sludge was pretreatment whit thermal shock at 105°C during 24 h in order to inhibit the activity of methanogen archeas and to select hydrolytic and fermentative bacteria (mainly related to microorganisms of genus *Clostridium*) [7].

2.2. Food waste

Food waste was obtained from a restaurant in the city of Querétaro, Mexico. Waste was collected during 7 days, physically characterized and store a 4°C. In each collection, the citrus waste, bones and inert material (paper and plastic) were discarded; only the fermentable matter was preserved. The physics compositions of the food waste was fluor waste 30±8%, citrus waste 22±4%,fruits and vegetable waste17±4% and meat waste 10±3.

After selecting the food waste, it was crushed and homogenized in a grinder JR MJ22 ® of 1HP. After, the particle size less than 5mm was obtained in a sieve. Finally food waste was frozen at -20°C until it was used. The physics and chemical characteristic of the food waste used in this study are showed in table 1.

Table 1. Characteristic of raw food waste

Parameters	Food Waste
Moisture (%)	75.7±4.6
TS (%)	24.3±4.6
VS (%)	20.8±2.3
COD (g/kg)	344.7±35.3
Carbohydrates (g/kg)	59.6±2.7
Proteins (g/kg)	108.1±8.3
Density (kg/m^3)	1097.6±29.7
pH	4.4±0.01

2.3. Set-up and operation

The start-up of CSTR for H_2 production was obtained in three phases: 1) Inoculum activation with glucose, 2) Acclimation of inoculum to H_2 production in a discontinuous process and 3) continuous operation. The inoculum was activated for 48 h whit glucose in aqueous prepared with 10 g/l of inoculum, 5 g/L of glucose, 0.3 g/L of K_2HPO_3, 0.4 g /L of NH_4Cl, 20 ml/L of solution mineral A and B prepared as show in [7], in a sequential batch reactor (SBR) at mesophilic conditions 37°C and agitation of 70 rpm.

The inoculum activated was acclimatized to the food waste in discontinuous mode for two cycles of 24 h. The reactor was operated with the following operating conditions temperature 35°C, pH 5.5, ST 22 g/L and agitation of 70 rpm. After the end of the second cycle of the SBR operation, the operation mode was switched to continuous operation until steady state was reached. The operating conditions were the following: hydraulic residence time (HRT) 24 h, organic loading rate (OLR) 22 g of TS/$L_{reactor}$/d, at 35 °C, pH of 5.5, reaction volume of 1.7 L and feed and discharge flow of 1.7 L / d.

The experimental set-up is show in figure 1. It consisted of one 2L reactor whit 1.7 L working volume. Food waste whit a concentration of 2.2 % of TS was added at CSTR with a peristaltic pump Cole Parmer System 7553-12 ®. The substrate was added from a storage tank at 4°C with a peristaltic pump Cole Parmer System NO-7553-12 ®.

The pH in the reactor was maintained at 5.5 ±3 by a controller pH Black Stone BL931700®. It was coupled to a peristaltic pump Marlow Watson 120U®. Peristaltic pump added Sodium hydroxide (NaOH)

2 N when the pH dropped until 5.4 and stopped when the pH achieved 5.5.The temperature in the reactor was maintained at 37°C via water bath through water jacket surrounding the reactor.

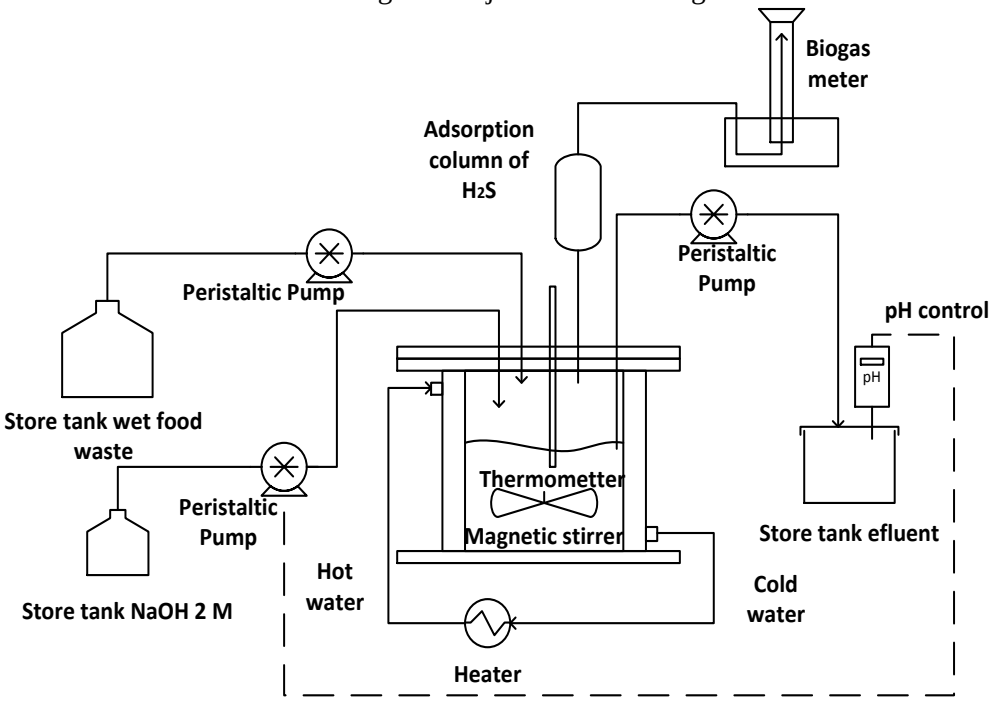

Fig 1. Schematic diagram of H_2 production process

H_2S was removed from biogas with an adsorption column. The adsorption column packed with ferric oxide (Fe_2O_3). The measurement of biogas production was done by liquid displacement method. This method consisted of measure fluid volume displace in an interval time.

2.4. Analytical techniques

TS, VS, COD, protein and carbohydrates were determined according to the procedures described in Standard Methods [11]. The percentages of H_2 and CO_2 in the gas phase were determined using a gas chromatograph (GC) SRI8610C® equipped whit a thermal conductivity and column packet. The operation temperatures of the injector port, the column and detector were 156, 41, and 156°C, respectively. Nitrogen was used the carrier gas at the flow rate of 30ml/min. VFAs (acetic, propionic, isobutyric, butyric and isovaleric), solvents (ethanol and acetone) were determined by GG with flame ionization detectors (FID) and column packet. The operation for the injection port, the oven, and the FID were 190, 70, 210 respectively. Nitrogen flow rate was 2.5 ml/min

3. Results and discussion

The activation with glucose was obtained in 3 d, H_2 accumulative production was 858 ml. In this phase only fermentative bacteria which use glucose as substrate were selected and hydrolytic bacteria were not

activated. The reactor was operated in mode SBR during two cycles of 24h. In the first cycle was produced 157 ml $H_2/L_{reactor}/d$ and the second cycle was produced 137 ml $H_2/L_{reactor}/d$.

The CSTR of H_2 production was operated in the laboratory forty days. The profile of H_2 production rate and volatile fats acids production shown in the figure 2. H_2 was produced immediately from the first day; however, H_2 production rate declined drastically from day 1 to 3 of 530 to 4 $ml/L_{reactor}/d$. This drop is due to the change of substrate and type of operation.

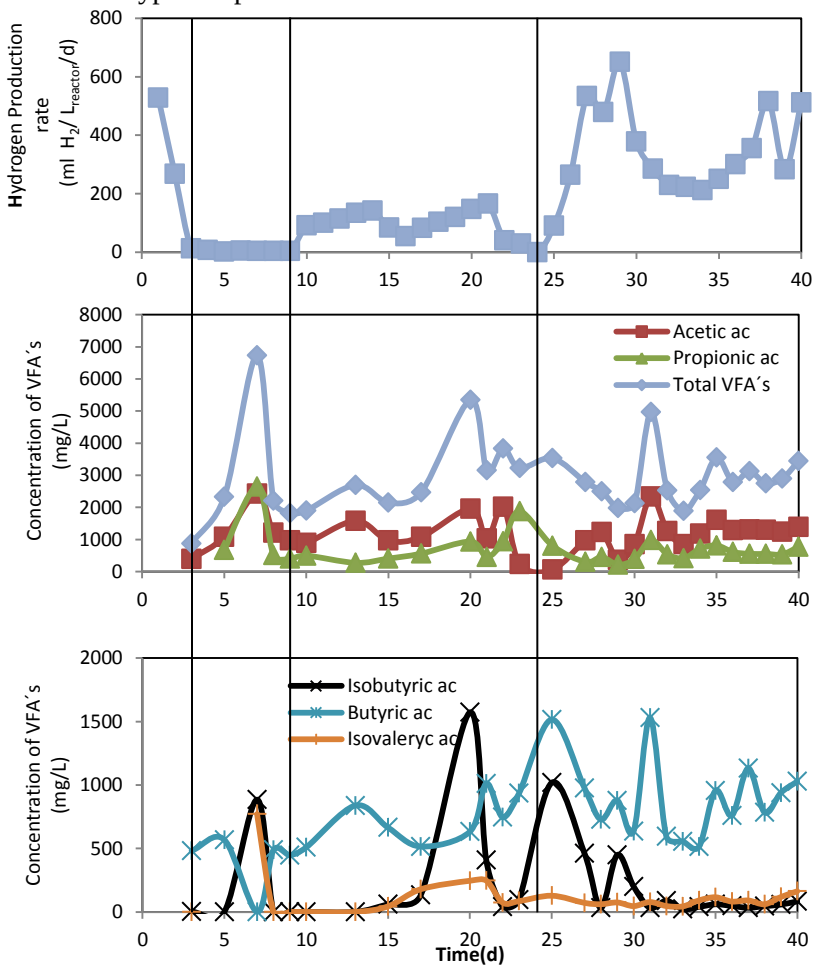

Fig 2. Profile of H_2 production rate and volatile fats acids concentration(ac: acids)

Between the day 3 and 9 the H_2 production was very low and fluctuated between 4-12 $ml/L_{reactor}/d$. This time was an adaptation phase hydrolytic and fermentative bacteria. In this phase the VFA´s concentration was 2794±144 mg/L. The acetic and propionic acids concentration were the highest concentration presented 1217±1062 and 1060±395 respectively. Isobutyric, butyric and isovaleric acids showed a lower concentration 178±395, 397±226 and 193±386 mg/L respectively.

For the 10 day and 21, H_2 production rate increase to 100±40 $ml/L_{reactor}/d$. In this period of time, a large amount of lipids was accumulated inside the CSTR (in the top part of the surface, between the

fermentation phase and the headspace). This caused a decrease in the mass transferer between the reaction and the headspace producing a decrease in H_2 production between days 21 to 24. During this period the concentration the total VFA´s was 3267±2274 mg/L. In this period of time, acetic, propionic and butyric acids concentration were the highest concentration presented 1269±632, 780±547 and 763±17 mg/L respectively. Isobutyric and isovaleric acids showed a lower concentration 330±564 125±99 mg/L respectively.

In the day 24, the lipids were removed inside CSTR, and then H_2 production rate increase between days 25 to 40. During this period, the H_2 production rate was approximately 338±151 ml/$L_{reactor}$/d. In this time acetic and propionic acids was produced in higher concentration (1230±441 and 858±270 ml/$L_{reactor}$/d respectively) than propionic, isobutyric and isovaleric. The concentration the total VFA´s was 2850±780 mg/L.

The profiles of H_2 yield and organic load removal are shown in the figure 3. The profile of H_2 yield presented a similar behavior compared with the profile of H_2 production rate. H_2 yield dropped between days 1 and 3, during the day 3 to 9 the average H_2 yield was 0.2±0.19ml H2/g SVadd. Between days 10 and 23 H_2 yield was 4.8±2.6 ml H_2/gVS_{added}. The maximum H_2 yield 19.2±16 ml H_2/g SV_{add} was presented between days 25 and 40.

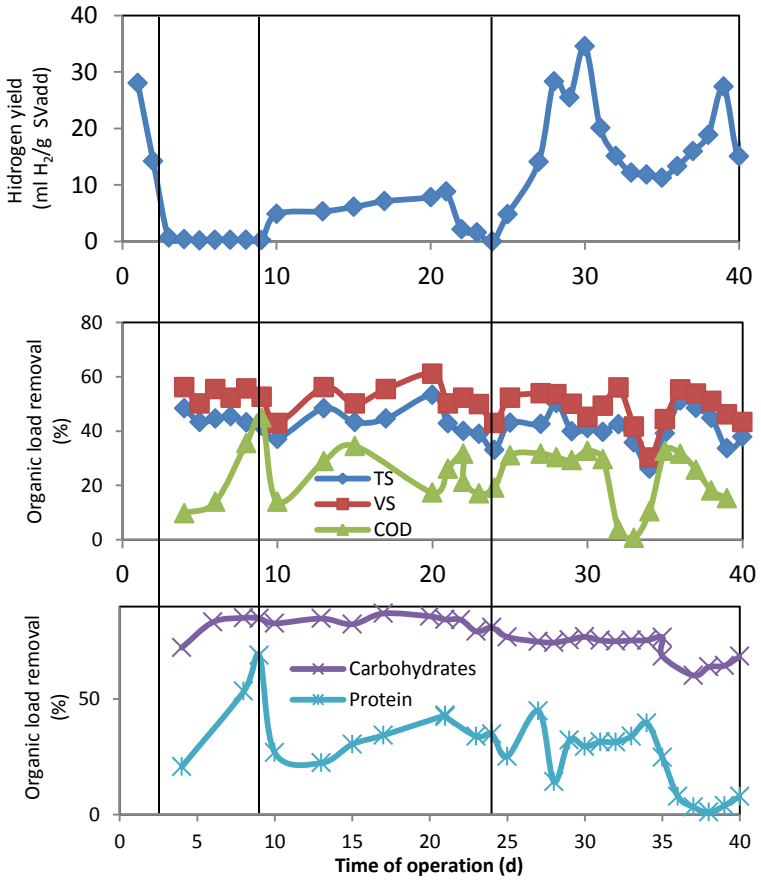

Fig 3. Profile of H_2 yield and organic load removal

However, removal of TS and VS varied in a range of 26% to 54% and 40% to 60 %, respectively. Average removal of ST and VS was 42.8±6.3 and 50.9±6.4 percent respectively. Removal carbohydrates 77.1±7% were bigger than removal proteins 26.7±17. Removal carbohydrates varied in a range slightly constant 60 to 84% compared whit protein.

In this present study, maximum H_2 yield and production was less than similar study with food waste (table 2). This difference can be related to the differences on operation condition. The H_2 production rate was 36% that is similar to other reports [4,9]. It is important to note that the inoculum, OLR and HRT applied are different in each study.

Table 2. Examples of maximum H_2 yield and production from food waste in CSTR

Source	[4]	[9]	This study
Type reactor	CSTR	Semi-CSTR	CSTR
Substrate	Food waste	Food waste	Food waste
Inoculum	Anaerobic sludge	Microbial cultures contained in food waste	Anaerobic granular sludge
T (°C)	37	40	35
pH	5.2	5.5	5.5
HRT (d)	2	6.7	1
OLR (g VS/L/d)	37.5	22.5	18.7
H_2 (ml $H_2/L_{reactor}/d$)	1600	1462	533
Yield (ml $H_2/g\ VS_{added}$)	43	65	28

4. Conclusions

The start-up of the reactor for H_2 production from food waste demonstrated working successfully reaching a H2 production of 365mL $H_2/L_{reactor}/d$ and H_2 yield was 19 ml H_2/g SV. Stoichiometric relationships between H_2, acetate and butyrate in the really dynamic fermentation are observed in this study. The accumulation of lipids inside CSTR produced a negative effect on the production of H_2. The total solid (TS), volatile solid (VS), and chemical oxygen demand (COD) removal was 42.8±6.3 and 50.9±6.4 and 24.1±10.7 respectively. The removal carbohydrate (80%) was bigger than proteins (24%)

Acknowledgements

Financial support from Fondo de Investigación del Instituto de Ingeniería, UNAM. A. Castillo-Hernández and I. Mar-Alvarez thanks to CONACYT for the scholarship.

References

[1]. A. Almeida, E. Nafarrete, A. Alvarado, A. Cervantes, M.P.E Luevanos, R. Oropeza and N. Balagurusamy, Expresión genética en la digestión anaerobia: un paso adelante en la comprensión de las interacciones tróficas de esta biotecnología. Revista Científica de la Universidad Autónoma de Coahuila 2011. 3: 14-34.

[2] J. Benemann. Hydrogen biotechnology: progress and prospects. Nature Biotechnol 1996. 14: 1101–1103.

[3] PP. Edwards, V.L. Kuznetsov, W.I.F. David, and N.P. Brandon. Hydrogen and fuel cells: Towards a sustainable energy future. Energy Policy 2008. 36: 4356–4362.

[4] D. Liu, D. Liu, R. J. Zeng and I. Angelidaki. Hydrogen and methane production from household solid waste in the two-stage fermentation process. Water Research 2006. 13: 1000 – 1013.

[5] A. Pandey, J. S. Chang, P. Hallenbec, and C. Larroche. Biohydrogem. Primera ed.: Elsevier. San Diego CA. (2013).

[6] O. Pakarinen , P. Kaparaju, J. Rintala. The effect of organic loading rate and retention time on hydrogen productionfrom a methanogenic CSTR. Bioresource Technology 2011. 102: 8952–8957.

[7] C. Ramos, G. Buitron, I. Moreno and R. Chamy. Effect of the initial total solids concentration and initial pH on the bio-hydrogen production from cafeteria food waste. i nternat i onal jou r n a l o f hydrogen energy 2012 . 37: 13288-132 95.

[8] I. Valdez and H. M. Poggi, Hydrogen production by fermentative consortia. Renewable and Sustainable Energy Reviews 2009, 13: 1000-1013.

[9] X. Wang and Y. Zhao. A bench scale study of fermentative hydrogen and methane production from food waste in integrated two-stage process. international journal of hydrogen energy 2009. 34: 245– 254.

[10] APHA. Standard Methods for the Examination of Water and Wastewater (21th ed.), APHA/AWWA/WEF, 2005; Baltimore, Port city press.

Modeling and Optimization of Hybrid Nafion Membranes Modified With Oxides Based on Artificial Neural Networks and Genetic Algorithms

J.C. Jaime-Domínguez[1], C. K. Gutiérrez Beltrán[2], S. Martínez Montemayor[2], S.M. Durón-Torres[1], A.U. Chávez-Ramírez[3]

[1] Universidad Autónoma de Zacatecas, Programa de Maestría en Ciencias de la Ingenieria, Campus Siglo XXI, Carretera Zacatecas-Guadalajara Km. 6.0, Ejido la Escondida, Zacatecas, Zacatecas, México, 98160. *Tel: +524929256690 Ext. 4655; e-mail: duronsm@prodigy.net.mx
[2] Universidad Autónoma de Coahuila, Facultad de Ciencias Químicas, Blvd. Venustiano Carranza s/n, Colonia República, C.P. 25280, Saltillo, Coahuila.
[3] Centro de Investigación y Desarrollo Tecnológico en Electroquímica S. C., Parque Tecnológico Querétaro s/n Sanfandila, Pedro Escobedo, C. P. 76703, Querétaro, México.

ABSTRACT

Recent studies have demonstrated the successful application of artificial intelligence tools in modeling, optimization and design of new materials. This paper describes the application of a Backpropagation Multilayer Perceptron (MLP-BP) neural network based on Levenberg-Marquardt learning algorithm in combination with evolutionary models based on genetic algorithms (GA) to find the optimal operation conditions to provide the highest proton conductivity from a set of hybrid membranes in fuel cell applications. A total of six membranes were analyzed, each one fabricated from a polymer matrix of Nafion and then modified with several oxides (N-HfO2, N-ZrO2, N-La2O3, N-(HfO2, ZrO2), N-(HfO2-La2O3) and N-(ZrO3-La2O3)). The experimental conditions considered for optimization were: temperature of the humidifier (Th) [30-100] ° C, the cell temperature (Tc) [30-120] ° C, voltage [0.05-0.8] (V), relative humidity (RH) [50% -100%] and the membrane thickness (σ). Four-electrode method was employed in fuel cell mode and pulse voltammetry were obtained. The pressure was kept at 15 psi and the nitrogen flow at 500ml/min.

The MLP-BP -GA combination throws the following optimal condition for the Hf-La membrane 1% wt: with 100% of relative humidity and temperatures around 80 ° C in the humidifier and cell (fig. 1). This model also provides the best conditions where the highest conductivity is achieved for every membrane, this estimations were compared against experimental tests obtaining a variation of less than 10%.

Keywords: Artificial Neural Network, Genetic Algorithm, hybrid membranes.

Introduction

One of the main obstacles for mass production of proton exchange membranes fuel cell (PEMFC) is the cost and durability balance [1-2]. It is affected by the performance of proton exchange membrane (PEM) design and performance in different environments [3-4]. Investigations in the field of PEMFCs were focused on improving the efficiency of proton-conducting materials. Polymer electrolyte membrane fuel cells (PEMFCs) are electrochemical devices operating at temperatures below 130^{o}C characterized by a high energy conversion efficiency, high energy density and a good compatibility with the environment [5]. PEMFCs are promising energy devices for residential, portable, and automotive applications [6].

The properties that must be considered for polymer electrolyte membrane are: (a) chemical and electrochemical stability in the operating system; (b) mechanical strength and stability under operating condition; (c) chemical properties of compounds that are compatible with the bonding requirements of the membrane electrode assembly (MEA); (d) high proton conductivity to sustain large current densities with a minimal resistive loss and no electronic conductivity; and (e) low production cost compatible with application. Nafion®, whose primary structure consists of acid-tipped side chains dangling from a perfluorinated backbone, is currently the reference among proton-conducting materials. Nevertheless, Nafion is not exempt from drawbacks, which include: the decrease of conductivity due to dehydration at high temperature and high cost [7].

the use of specialized software in the design and simulation of electrochemical systems been increasing, this due to the high cost of materials used for this purpose, one of the most used system for this task is artificial intelligence (AI). This techniques have emerged in system simulation for more than two decades as effective tool for model, design and solve complex systems [8-9].Artificial neural network (ANN) is a class of neural network represented by a mathematical model that is inspired by the biological nervous system; The main advantages of utilizing NNs are [10]: (1)it handles stochastic variations of the scheduled operating points via the increase of data,(2)it significantly accelerates both online processing and classifications, and (3) it contains implicit nonlinear modeling and a built in function for system data filtration.

Studies about the modeling fuel cell parameter through ANN models are numerous. Lee et al.[11] have used a feed forward back propagation network in which the cell potential was modeled as a function of four input variables (i.e., current density, reactant pressures and cell temperature). It was shown that the ANN can predict well the fuel cell power system. Wu et al. [12] have applied the ANN to simulate an experimental data set with six input independent variables (i.e., operating temperature and pressure, anode and cathode humidification temperature, anode and cathode stoichiometric flow ratio) with respect to electrical power.

Utilizes tools to find the maximum point are numerous but its use in non-linear systems is limited. Genetic algorithm is a special technique for function approximation that can be considered as a set of computational techniques more closely linked in their concepts to biological processes than traditional computational techniques. They are quite different from other more conventional optimization methods that are mainly stochastic in nature. The basic process of genetic algorithm is as follows. First, a population of chromosomes is created. Second, the chromosomes are evaluated by a defined fitness function. Third, some of the chromosomes are selected for performing genetic operations. Fourth, genetic operations of crossover and mutation are performed. The produced good offspring replace their parents in the initial population. This process repeats until a user-defined criterion is reached.

This study attempts to show how the union of different computational techniques can model and optimize hybrid Nafion membranes modified with oxides based. This work aims to demonstrate that the proposed model can find the maximum point of proton conductivity for each of the different membranes.

Experimental

To find the best operational condition must know the membrane proton conductivity obtained based on experiments previously made, this was determined by the four electrode method. A Bekktech® conductivity cell coupled to a PS-CompuCell® Test Station and an AUTOLAB PGSTAT302. Linear voltammetry was used as characterization technique; each membrane was evaluated in four different tests (fig.1).
ANN model consist of a training algorithm based on data base established. This data base contain different values of temperature of the humidifier (Th) [30-100] ° C, the cell temperature (Tc) [30-120] ° C, voltage [0.05-0.8] (V), relative humidity (RH) [50% -100%], the membrane thickness (σ) and gas pressure [15](psi). a typical ANN is show in fig 2. It is seen that an ANN consists of a network with three main elements, input vector, hidden layer(s), and output layer. As show in the fig. 3, each neuron receives an input signal P. each input is multiplied by synaptic weight W and then each input is summed an then added by a bias b. this product is used as input to the network and is taken as an argument of a transfer function f, which determines an output of a neuron. A typical transfer function is log-sigmoid f, which is also used in this study and has the following form;

$$a = f(WP + b) = \frac{1}{1 + \exp(-(WP + b))} \quad (1)$$

The database was randomly partitioned into training data, testing data and validation data, so that the training and testing data set was changed in every loop, then the data set has been normalized. The normalizing function is calculated by:

$$X_n = \frac{X}{X_{max}} \quad (2)$$

Where Xn is the normalized value of X, Xmax is the maximum value of the properties.

This transfer function takes any value and outputs a value between 0 and 1. In this work were used the multi layer perceptron (MLP) model. The MLP is the most commonly used ANN, characterized by interconnections that do not from any loop[]. The neural network are organized to form a feed-forward network. The ANN simulation consist of two main phases; training and testin, the training phase is used to minimize the difference between input and output, the training algorithm used was the levenber-Marquard algorithm (LMA) also known as the damped least-squares (DLS) that is one of the most commonly used training algorithm for MLP models.

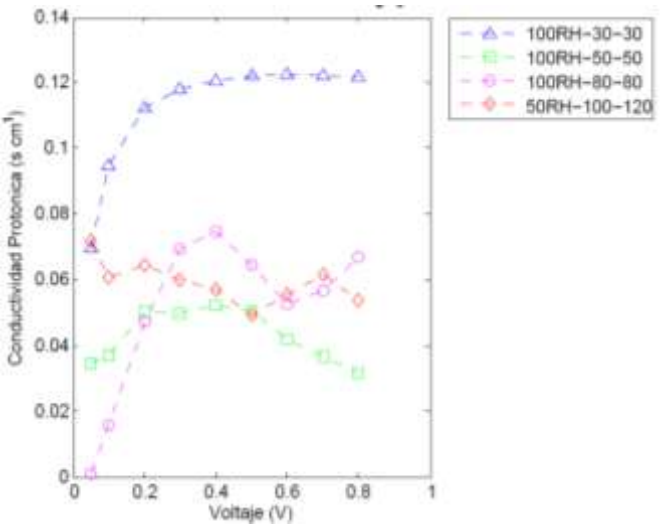

Figure 1. PC of N-La_2O_3 at different temperature and RH.

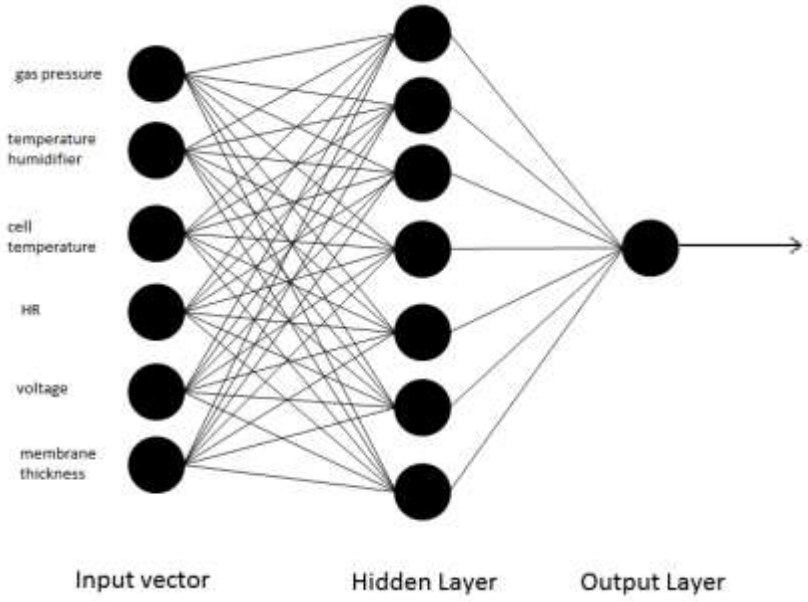

Fig. 2 Schematic diagram of a typical artificial neural network (ANN)

The obtained traininig ANN model is consequently used in GA to optimize a system and find best performance and maximum point of proton conductivity (PC) in the PEM for a given experimental parameters. GA works by generating a large set of possible solutions to a given problem. It then evaluates each of these solutions. In order to optimize the PEM a Matlab code was developed. The code stars with generating solution by randomly selecting

values for the all parameter involve in the ANN model. The parameters values of genetic algorithms used are given in table1. Table 3 gives the upper and lower limits of the optimized parameters.

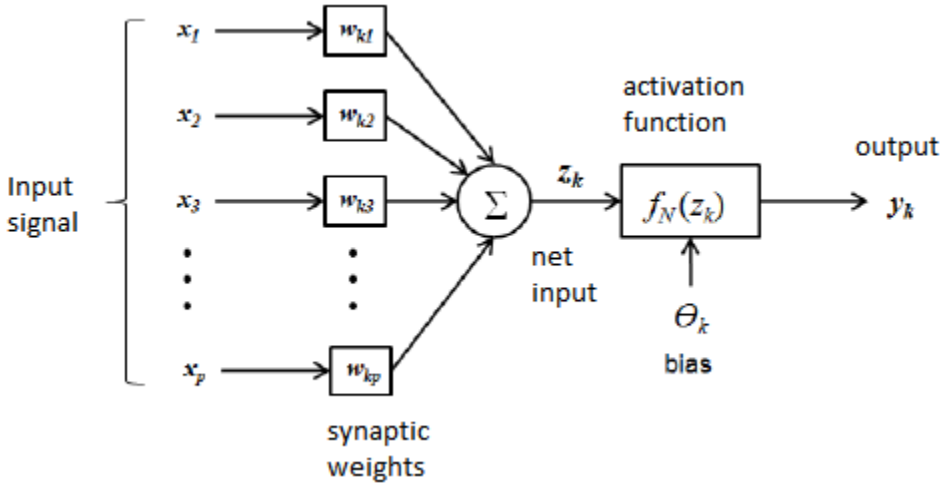

Fig. 3 Mathematical model of a neuron

Table 1. Values of genetic algorithm parameters

Parameter	Value
Number of generations	100
Population size	20
Number of parameters	5
Crossover rate	90%
Mutation rate	10%

Membrane simulation result

To complete the simulation of any system using artificial neural networks, we first need to identify its experimental behavior of any system. The simulation model based on the MATLAB/SIMULINK software of the PEM to obtain the best proton conductivity of each membrane, the total number of experimental data set was 36. After the training the optimized ANN model the network performance parameter described was very similar in all tests. The mean

square error (MSE) and sum of square errors (SSE) of training and testing data sets for the membranes simulate are shown in table 3.

Table 2. Upper and lower values of the parameters to be optimized (search space)

Parameter	Lower limit	Upper limit
Gas pressure	15	30
Temperature humidifier	30	100
Cell temperature	30	120
HR	50%	100%
Voltage	.05	.8

Table 3. Upper and lower values of the parameters to be optimized (search space).

Membrane	MSE	SSE
N-HfO_2	7.6044	0.00027376
N-ZrO_2	4.3648	0.000157
N-La_2O_3	5.1832	0.00018659
N-(HfO_2, ZrO_2)	4.6256	0.0017
N-(HfO_2-La_2O_3)	2.251	0.00081035
N-(ZrO_3-La_2O_3)	1.5849	0.00057055

Proton conductivity of N-La2O3 and its simulation are shown in the following diagram (fig 4). The highest proton conductivity reached experimentally of N-La2O3 occurs at 100°C and 50%RH with values of 0.1225 S cm-1, the conductivity reached in ANN model is 0.1242 S cm-1.
All model reached values close to the experimental proton conductivity. GA technique was used to find the optimum configuration of inputs to reach the maximal PC, in the table 4 the maximum proton conductivities were achieved using genetic algorithm.

Table 4. best point reached for genetic algorithm.

Membrane	PC
N-HfO_2	0.135
N-ZrO_2	0.072
N-La_2O_3	.127
N-(HfO_2, ZrO_2)	0.22
N-(HfO_2-La_2O_3)	0.05
N-(ZrO_3-La_2O_3)	0.065

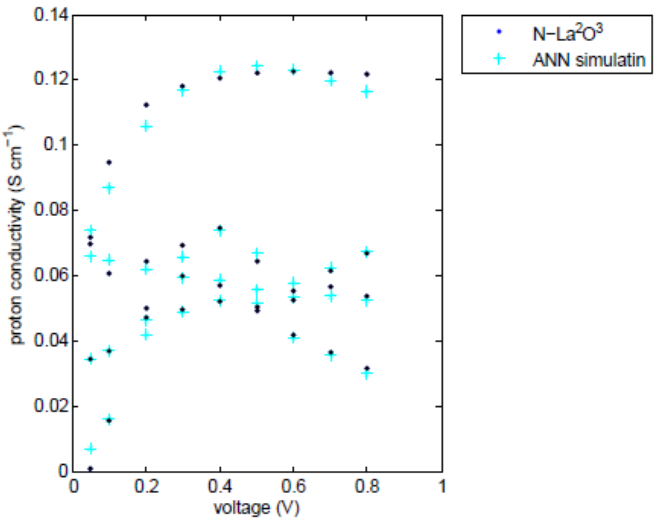

Fig 4. PC of N-La_2O_3 Vs ANN simulated

Summary and perspectives

In this research work, a feed-forward back propagation neural network model and genetic algorithm was used for simulate Six membranes, each one fabricate from polymer matrix of nafion. The aim of the model was to specify the optimal conditions with wich is reached the best proton conductivity that could be acquired by linear voltammetry and know the conditions in which is reached.

The next work will simulate fuel cells with different membranes, and knowing the conditions under which each operates better, this in order to improve the PEMFC performance to various working conditions.

Acknowledgements

CONACYT for the scholarship, UAdeC and CIDETEQ the opportunity afforded by the use of facilities and equipment

References

[1] Madaeni, S. S., N. T. Hasankiadeh,. "Modeling and optimization of membrane fabrication using artificial neural network and genetic algorithm." Separation and Purification Technology, (2010) 76(1): 33-43.

[2]Sahoo, G. B. and C. Ray. "Predicting flux decline in crossflow membranes using artificial neural networks and genetic algorithms." Journal of Membrane Science,(2006) 283(1–2): 147-157.

[3] Misra Rakesh K, Singh Shiv P. "Efficient ANN method for post-contingency status evaluation". Journal Electric Power Energy Sys 2010;32(1):54–62.

[4] Alanis Alma Y, Sanchez Edgar N, Loukianov Alexander G, Perez Marco A. Realtime recurrent neural state estimation. IEEE Trans Neural Netw 2011;22(3).

[5] V. Di Noto, M. Bettiol, F. Bassetto, N. Boaretto, E. Negro, S. Lavina and F. Bertasi," Hybrid inorganic-organic nanocomposite polymer electrolytes based on Nafion and fluorinated TiO2 for PEMFCs" International Journal of Hydrogen Energy,2012, 37,6169-6181.

[6] Rohland B, Eberle K, Ströbel R, Scholta, Garche, J. Electrochemical hydrogen compressor, Electrochim Acta,1998, Vol. 43, No. 24, pp. 3841-3846.

[7] Ströbel R, Oszcipok M, Fasil M. The compression of hydrogen in an electrochemical based on a PE fuel cell design. J. Power Sources, (2002),115, 208-215

[8] Kuei-Hsiang Chao, Chia-Lung Chiu, Li Ching-Ju, Yu-Choung Chang." A novel neural network with simple learning algorithm for islanding phenomenon detection of photovoltaic systems". Expert Syst Appl 2011;38:12107–15.

[9] Mohamad H ."A review on islanding operation and control for distribution network connected with small hydropower plant". Renewable Sustainable Energy Rev 2011;15:3952–62.

[10] Tarafdar Haque M, Kashtiban AM. "Application of neural networks in power systems; a review." In: Proceedings of world academy of science, engineering and technology, 53–70.

autores, nombre, journal, ano, edicion, paginas

[11] W.Y. Lee, G.G. Park, T.H. Yang, Y.G. Yoon, C.S. Kim, Int. J. Hydrogen Energy, " Effect of pore structure of catalyst layer in a PEMFC on its performance ",(2004),29, 961–966.

[12] S.J. Wu, S.W. Shiah, W.L. Yu, Renew. Energy,, (2009),34, 134–144.

Analysis of microbial communities associated with hydrogen production obtained from wastewater

Chacón-Carrera, R.A.[1], Zavala-Díaz de la Serna, F.J.[1], Ramos-Sánchez, V.H.[1], Camacho-Dávila, A.[1], Robles-Venzor, J.C.[1].

(1)Universidad Autónoma de Chihuahua, Facultad de Ciencias Químicas, Nuevo Campus Universitario s/n, Chihuahua, Chih. C.P.31125,
México. Tel: 6142366000 Ext.4298 email: vramos@uach.mx

ABSTRACT

Microbial Fuel Cells (MFCs) are devices capable to supply energy from organic substrates. Although MFCs offer low current densities, they have proven to be a feasible option for wastewater treatment. When a suitable overpotential is applied to MFCs, hydrogen is produced, these devices are known as Microbial Electrolysis Cells (MECs). México has a huge potential for solar energy, particularly Chihuahua exhibits a solar irradiance of 18kJ/m2. Bearing this in mind, this project aims to feed the overpotential for a MEC through a solar cell, in order to assess the potential to produce hydrogen through wastewater effluents in public universities. The microorganisms responsible of hydrogen production in these devices have not been fully characterized, as a matter of fact; the occurrence of microbial consortia able to optimize the operation of MECs is still under study. Therefore, at this stage of research, a wastewater sample was growth in differential cultures; and communities were compared by molecular techniques using a Polymerase Chain Reaction - Denaturing Gradient Gel Electrophoresis (PCR-DGGE) in order to compare their electrochemical performance and hydrogen yield within a MEC.

Keywords: wastewater, MEC, PCR-DGGE

1. Introduction

The use of fossil fuels in recent years has accelerated the depletion of non-renewable resources. Furthermore, the unprecedented increase in greenhouse gas emissions due to combustion of fossil fuels is greatly contributing to the climate change.[1] Hydrogen is recognized as an impermanent renewable energy carrier of the future with many advantages such as the high-energy yield of 122 kJ/g. Although hydrogen is produced from natural gas, oil or coal, these methods are not sustainable due to CO2-emissions and exploitation of fossil fuels.[2] Among the technologies currently available for hydrogen production, biological methods are generally preferred over chemical and thermal methods, since organic wastes can be used as substrates. As a result, potential pollutants such as wastewater (WW) are now being regarded as potential commodities for bioenergy and biochemical production rather than useless residues.[3] A new alternative process for biohydrogen production is electrohydrogenesis, which uses exoelectrogenic bacteria in a microbial electrolysis cell (MEC).[4] MECs have attracted considerable attention over the last years as a promising technology for the production of biohydrogen on account of its great hydrogen yield compared to conventional hydrogen producing-dark fermentation.[5] In a MEC, microorganisms oxidize organic compounds at the anode to CO2, protons and electrons. At the cathode, protons conducted by an ion selective membrane, and electrons derived from the anode, together with those externally supplied, are combined to produce H2.[6] Within this cell, electrochemically active bacteria transfer electrons to the anode and protons are released to the aqueous media. In order to produce hydrogen at the cathode, a potential of at least -0.414 V is required under standard biological conditions.[7]

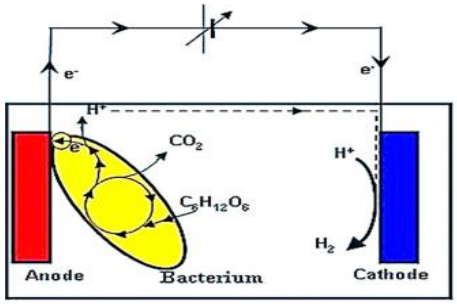

Figure 1. Schematic of typical single chamber MEC construction and operation [7]

It has been demonstrated that cathodic biofilms inoculated with microorganisms originated from wastewater treatment plants exhibit good electron transfer. Indeed the ability of some bacteria to transfer electrons as part of their bacterial respiration process has been exploited; such bacteria are known as exoelectrogens. To date, reported exoelectrogens include members from diverse bacteria genre, such as *Geobacter*, *Shewanella*, *Pseudomonas*, *Clostridium*, *Desulforomonas*, *Escherichia* and *Klebsiella*.[9] With the fast progress of molecular biological technologies in the last decade, some powerful tools, such as denaturing gradient gel electrophoresis of polymerase chain reaction (PCR-DGGE) and fluorescent *in situ* hybridization (FISH) etc., have been developed, and now it is possible to look into bacterial community structures without relying on time-consuming bias-bearing cultivation methods. To date, most studies of MECs and MFCs have investigated the microbial composition, using methods such as 16S rDNA sequencing and denaturing gradient gel electrophoresis [10].

México has a high level of solar radiation. It receives, for example, twice as much solar radiation as Germany. Across México, daily radiation varies between 4.4 kWh/m2 and 6.3 kWh/m2 of solar energy. Mexico's six northern Border States cover nearly half of the country's total surface. These states have a predominantly arid desert climate with high level of solar irradiation. Chihuahua is recognized as having one of the highest solar irradiation levels (18kJ/m2), which exhibits the potential to supply the abovementioned voltage required for operation of a MEC using photovoltaic panels.[8] Based on this geographical context, in the first stage of this research, wastewater was taken from a public university and then enriched culture media were prepared with salts in order to promote the growth of exoelectrogens microorganisms and to compare the communities using PCR-DGGE. In a second and final stage, not yet reported, the performance of a MEC inoculated with the culture media richest in exoelectrogens will be assessed to prove the feasibility to promote this sustainable wastewater treatment in Chihuahua's public sector.

2. Experimental

2.1 Sampling

Samples were collected from a septic tank in the Universidad Autonoma de Chihuahua. The samples contained water and also soil, pH (Table 1) was recorded to observe initial conditions.

Table 1.pH of wastewater samples

	Sample 1	*Sample 2*	*Sample 3*	*Sample 4*	*Sample 5*	*Sample 6*
pH	6.388	6.287	6.601	6.912	5.862	5.767

2.2 Preparation of enriched culture media.

To make enrichment culture, samples were cultured in a Winogradsky's column, which is a plastic container with one-third of the solid sample (sediment) and two-thirds of liquid sample (water). Two cultures were prepared with 3 g of $CuSO_4$ and the two remaining with 3 g of Na_2SO_4. The columns were kept under normal conditions of temperature and pressure during two months for further observation (Figure 2).

Figure 2: Enriched culture media.

2.3 DNA Extraction and PCR

Wastewater samples were filtered in order to collect as many organisms as possible. The filter was placed in a phosphate buffer solution pH 8. The DNA extraction was developed by the DNAzol protocol with previous modifications, while 16S rDNA was amplified using PCR technique with the 3R and 3F oligonucleotides. The mix used for PCR is described in Table 2.

The conditions in the thermocycler were a) denaturalization 5 min 94° C; b) amplification: 35 cycles, each one with a denaturalization step 94° C for 1 min, alignment step 55° C for 1 min and synthesis step 72° C for 1 min; d) the final extension step 72° C for 5 min.

Table 2. PCR Components for 18 samples with no dilution.

Component	Final Conditions
Reaction Buffer 10X	1X
$MgCl_2$ 50 mM	2 mM
Dntps 10 mM	0.4 mM
Primer F 10X	0.8 mM
Primer R 10X	0.8 mM
Taq pol	1.5 µL
DNA	5 µL
Water	12 µL

2.4 Denaturing gradient gel electrophoresis

In this case two solutions were prepared, one of a gradient of 100 % and other with a 0 % gradient. In Table 3, the components of each solution are shown.

Table 3. Components of the solutions for DGGE for 50 mL

	Solution A (100 %)	*Solution B (0 %)*
Urea	22.16 g	-
Formamide	20.00 mL	-
Polyacrilamide	26.65 mL	26.65 mL
TAE 50X	1.00 mL	1.00 mL

3. Results and discussion

3.1 Media Analysis

Table 4 shows the pH data of the enriched media culture. Data suggest that there is a significant difference between wastewater and wastewater in the culture enriched media. pH measurements show that the media rich in sodium are the most suitable for a MEC, according to Ya-Peng *et al* [11] that found an optimal pH of 9 for hydrogen production in MEC, which suggests that exoelectrogenic activity is favored at this pH.

Table 4. pH of enriched media culture

	Media Na_2SO_4 *(1)*	*Media* $NasSO_4$ *(Bis)*	*Media* $CuSO_4$ *(1)*	*Media* $CuSO_4$ *(Bis)*
pH	8.831	8.861	7.356	7.683

3.2 DNA Extraction

Extraction was successfully accomplished in an agarose gel 1%. DNA was obtained of good size and quality, as shown in Figure 3.

Figure 3. DNA Extraction: In lane 1(L1) the molecular weight marker was placed; whereas samples were set in lanes 2 to 6 (L2-L6).

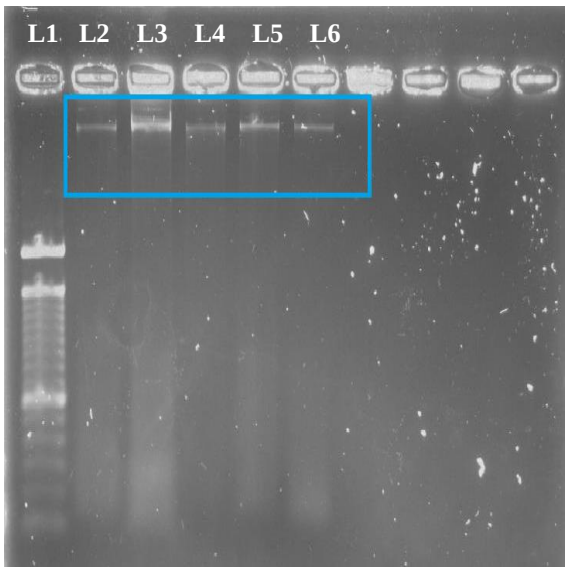

3.3 Polymerase Chain Reaction.

The amplification by PCR showed fragments of an approximate size of 300 pbs, which correspond to expected sizes. Figure 4 shows samples amplified before enriched media culture and those obtained from the enriched culture

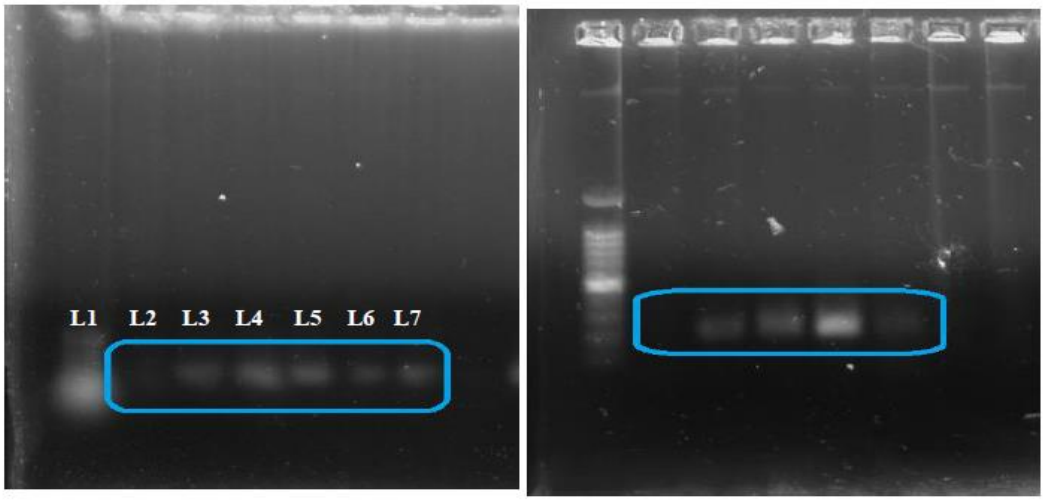

Figure 4. Amplification with sample distribution as in Figure 3, except lane 2 (L2) contains a negative control: *Left*: samples before enrichment; *Right*: samples after enrichment.

Summary and perspectives

The enrichment culture media showed that the most suitable media to use in a MEC is the one with sodium, also the conditions provided for the media are those reported as optimal for hydrogen production, which is an advantage for the following stage of this research.

The DNA extraction and amplifying by PCR is the first phase to make a comparison between microbial communities in wastewater and those communities favored in the enrichment culture media. This comparison is in process and will be developed by DGGE. Such analysis might indicate whether a variation among individuals is occurring or if there is a diverse population. The latter would favor isolation to achieve a suitable microbial consortium; whereas the former condition would require maintaining a suitable culture media to promote growth of exoelectrogenic species.

References

[1]Zhang, Y., Angelidaki, I. Microbial electrolysis cells turning to be versatile technology: recent advances and future challenges. J. Water Research 2014; 56: 11-25

[2]Ruiz, V., Esra, Z., Kang, D.,Krajmalnik, R., Buitrón,G.

[3]Escapa, A., Gil-Carrera, L., García, V., Morán, A. Performance of continuous flow microbial electrolysis cell (MEC) fed with domestic wastewater. Biosource technology 2012; 117: 55-62

[4]Chae, K., Choi, M., Kim, K., Ajayi, F. Chag, I., Kim, I. Selective inhibition of methanogens for the improvement of biohydrogen production in microbial electrolysis cell. International Journal of Hydrogen Energy 2010; 35: 13379-13386

[5]Croese, E., Jeremiasse, A., Marshall, Ian., Spormann, A., Euverink, G., Geelhoed, J., Stams, A., Plugge, C. Influence of setup and carbon source on the bacterial community of biocathodes in microbial electrolysis cells. Enzyme and Microbial techonology 2014; 61-62: 67-75

[6]Varroné, C., Van, J., Liu, W., Zhou, B., Wang, Z., Liu, W., He, Z., Wu, L., Zhou, J., Wang, A. Metagenomic-based analysis of biofilm communities for electrohydrogensis: from wastewater to hydrogen. International Journal of Hydrogen Energy 2014: 39; 4222-4233.

[7]Kadier, A., Simayi, Y., Sahaid, M., Abdeshanian, P., Abdul, A. A review of the substrates used in microbial electrolysis cells (MECs) for producing sustainable and clean hydrogen gas. Renewable Energy 2014: 71; 466-472.

[8]Romero-Hernández, S., Rodriguez-Granada, B., Romero-Hernández, O., Wood, D. Re-energizing the border: renewable energy, green Jobs and border infrastructure Project; solar energy potential in Mexico's northern border states. 2012. Mexico Institute. 1-2 pp.

[9]Croese, E., Jeremiasse, A., Marshall, I., Spormann, A., Euverink, G., Geelhoed, J., Stams, A., Plugge, C. Influence of setup and carbon source on the bacterial community of biocathodes in microbial electrolysis cell. Enzyme and Microbial Techonology

[10]Liu, X., Zhang, Y., Yang, M, Wang, Z., Wen, L. Analysis of bacterial community structures in two sewage treatment plants with different sludge properties and treatment performance by nested PCR-DGGE method. Journal of Environmental Sciences 2007: 19; 60-66

[11]Ya-Peng, L., Yung-Hai, W., Bai-Shi, W., Qing-Yung, Chen. Effect of anolyte pH and cathode Pt loading on electricity and hydrogen co- production performance of the bio-electrochemical system. International Journal of Hydrogen Energy 2014; 1-5

Control and Automation System of Power Generation Hhrough Photovoltaic-Hydrogen Technology to Lighting

J. Olmedo-González[1], R.G. González-Huerta[1], M. Tufiño-Velázquez[2], L.A.Loera-Cervantes[3]

[1] ESIQIE-IPN, Laboratorio de Electroquímica y Corrosión, UPALM, CP 07738, México, D.F.
[2]ESFM-IPN, Laboratorio de Física Avanzada, UPALM, CP 07738, México, D.F.
[3]CECyT 3-IPN, Laboratorio de Maquinas Eléctricas, CP 55119, México, Edo.Mex
Tel: 5527092864; e-mail: jolmedog0900@alumno.ipn.mx

ABSTRACT

At present, it is very important study new power generation systems, like a photovoltaic-hydrogen. This is a hybrid system where the photovoltaic modules are used to provide power to the electrolyzer for producing hydrogen and oxygen through the water electrolysis. Gases produced are stored to be supplied when they are required into a fuel cell to generate electrical power.

The prototype is integrated by solar photovoltaic modules to generate 8964KJ every day (2.49 KWh/day), a PEM electrolyzer is used to produce hydrogen from $1x10^{-6}$ m^3/s to $5x10^{-6}$ m^3/s at 7KPa to 827KPa. The prototype has a variable volume storage system at atmospherically conditions (295.15 K and 77.99KPa) and a fuel cell stack can be operated in a range of 50 W to 150 W.

The system is able to operate with different fuel cells in a range of $1.67x10^{-7}$ m^3/s to $1.67x10^{-5}$ m^3/s hydrogen flow. In order to be a safe system and make easier the regulation flow, it is really important to develop a control and automation system. In this project, it is proposed a closed loop system where the hydrogen and oxygen required is selected in a control panel. Gasses flow is controlled by pumps and proportional electro-valves that use a recirculation system which is monitored by flow sensors. Algorithm main aspect is the flow regulation, because the gases are storage in a variable volume system where the flow is not constant. Also, the project includes a monitoring system where power energy behavior can be reviewed.

Keywords: Fuell Cells; Automation; Renewable Energy

1. Introduction

We live in a world where technology grew up very fast and it almost requires electrical energy, society depends more and more of it, this is the reason it is really important to innovate in power sources as we do in electronic devices. At present, the main power source is fossil fuels, however it generate pollution and it is a nonrenewable source. In spite of different renewable power sources have been developed like solar, wind and geothermal energy. The society still depending on fossil fuels, this is mainly in oil countries like Mexico where sustainable power sources are not sufficiently supported. It is really important to develop new power sources that do not pollute the environment and that are able to satisfy the requirements of the society, it must be understand that we have to be more ecological.

The aim of this paper is exposing the advances of the photovoltaic-hydrogen system design and the development of the control and automation system to produce electricity in a safe and controlled way. In this project solar energy is used as primary power source and hydrogen as secondary power source. Therefore, solar energy can be used in an efficient way during the day that is when it can be converted as electrical energy, at nights hydrogen is used as the secondary power source to produce electrical energy.

The process consist in generate hydrogen and oxygen from the water using an electrolyzer that requires electrical energy produced by the solar panels in the day, the gases are stored in a tank and at night these are used by the PEM fuel cell that is an electrochemical energy converter to produce direct current (DC) electricity from hydrogen and oxygen, required for the charge (LED lamps).

The system is integrated by a solar photovoltaic modules to generate 8964 KJ every day (2.49 KWh /day), a PEM electrolyzer where the hydrogen is produced at 55KPa in a flow of $1x10^{-6}$ m^3/s, a pressure regulator where the hydrogen is delivered at 55KPa in a flow of $1.67x10^{-6}$ m^3/s, a variable volume storage system at atmospherically conditions in Mexico City (295.15 K and 77.99KPa) which capacity is 0.03 m^3 of hydrogen and 0.015 m^3 of oxygen , a control system where the hydrogen and oxygen are regulated automatically in a range of $1.67x10^{-7}$ m^3/s to $1.67x10^{-5}$ m^3/s , creating a flexible system that it is able to operate with different PEM fuel cells and a fuel cell stack that is operated at 50 W using $1.33x10^{-5}$ m^3/s of hydrogen and $6.67x10^{-6}$ m^3/s of oxygen. The charge consist in two LED lamps that requires 12V and consumes 2A each one.

Implementing an automatic control system that controls the gases delivery in to de PEM fuel cell it is really important because the PEM fuel cell requires a continual gases flows for a better performance, the control system monitors in a real time the flow rates hydrogen and oxygen and as consequence adjust it in relation with the wanted flow, selected by an operator.

2. Experimental

Photovoltaic system dimension and design was made by studying the electrical requirements of electrolyzer and the sunlight in Mexico City, where the average of peak sunlight is 18000s (5 hours). This information was taken from Geophysics Institute of Universidad Autónoma de México (UNAM), figure 1. [1]

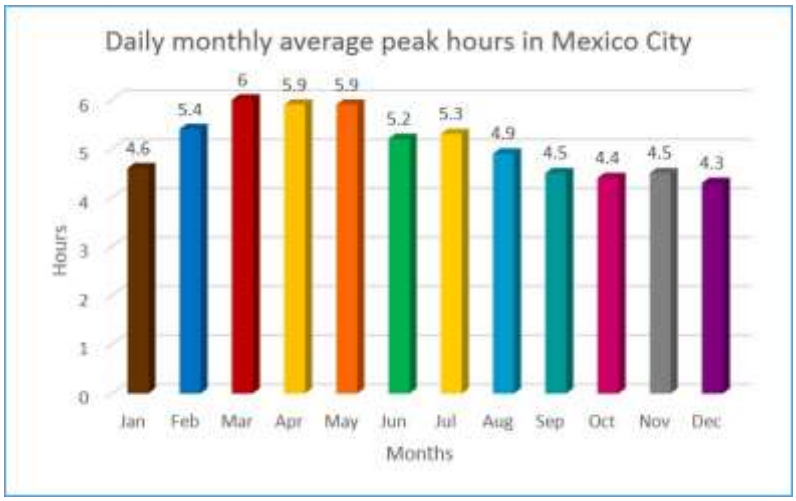

Fig 1. Daily monthly average peak hours in Mexico City

México City has an excellent position to get sun light, one of these reasons is that it is located near of equator where the hours of sun light are relative continual in the all seasons and months, in consequence the peak hours are also continual, allowing to have a stable photovoltaic system. [1]

The photovoltaic system is composed for 6 polycrystalline silicon modules of 85 W each one, this modules were connected in a series-parallel arrangement to producing 510 W in the peak sunlight and during the day is achieved 8956.8KJ (2.488KWh). This is enough to use the electrolyzer that requires 340W or 1224KJ (0.34KWh). [2, 3]

It was designed a photovoltaic system type island, which needs a DC/DC regulator and an inverter, these devices were purchased according with the electrical characteristics of solar panels and the electrolyzer. The performance of solar panels in Mexico City was studied according to the electrical behavior with the electrolyzer. The electrical specifications of the solar panels, the DC/DC regulator and inverter are presented in the table 1. [2, 4]

Table 1. Electrical specifications of photovoltaic system

Electrical Performance under Standard Test Conditions each panel		DC/DC Regulator	
Maximum Power	87W (+10%/ -5%)	Nominal Voltage	12/24V
Maximum Power Voltage	17.4V	Maximum Current	20A
Maximum Power Current	5.02A	Inverter	
Open Circuit Voltage	21.7	Output Voltage	120VAC
Short Circuit Current	5.34A	Output Frequency	60Hz
*STC: Irradiance 1000W/m^2 AM1.5 Spectrum, module temperature 25°C			

It was used a commercial PEM electrolyzer manufactured by Peak Scientific company, model PH300 which capacity production is $1x10^{-6}$ m^3/s to $5x10^{-6}$ m^3/s at different pressures 7KPa to 827KPa. This device uses alternate current, 110V at 60Hz, 340W. [3]

Production process of hydrogen and oxygen was analyzed in the commercial electrolyzer, where it was understood the internal structure. Schematic diagram was developed presented in the figure and table 2, where it can be appreciated the different components of it. [3]

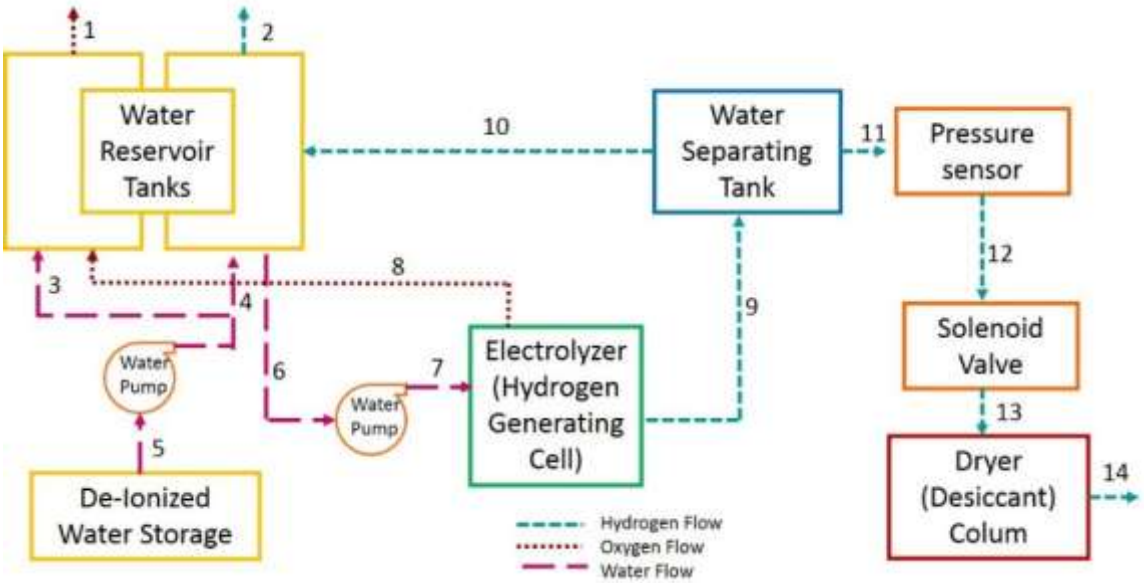

Fig 2. PEM Electrolyzer PEAK Scientific PH300 System

Table 2. PEM electrolyzer PEAK Scientific PH300 System

Flow	Typology	Flow	Typology	Flow	Typology
1	O_2 Delivery	6	H_2O	11	H_2
2	H_2 Vent	7	H_2O	12	H_2
3	H_2O	8	$O_2 + H_2O$	13	H_2
4	H_2O	9	$H_2 + H_2O$	14	H_2 Delivery
5	H_2O	10	$H_2 + H_2O$		

Electrochemical and electrical performance of electrolyzer was also analyzed, the following parameters were measuring: current and voltage directly in the cell and the hydrogen and oxygen flow delivery, it was made at different pressures at atmospherically conditions in Mexico City.

Storage system was designed to satisfy the demand for the fuel cell, it is important to mention hydrogen has the highest energy content per unit weight but not per unit volume. It is relatively low volumetric energy content is a significant challenge for storage. Stationary hydrogen storage systems have less stringent requirements, it can occupy a relatively large volume, operate at lower temperatures and pressures and time to refueling can be large, in the appropriate conditions. Also, the storage was designed in order to save energy, storage systems like pressured tanks need a compressor to store gases and that requires more energy, hydrides systems to store hydrogen are really efficient, however this systems are expensive and requires significant careless, for those reasons it was designed a variable volume system at atmospherically Mexico City conditions.[5, 6]

Hydrogen and oxygen storage system consists in a principal container manufactured in acrylic which contains water, into this big container there are two floating capsules or containers, where hydrogen and oxygen are stored. These were also made of acrylic with joints coated aluminum anodized layer. The connections were designed anti-spark for handling hydrogen gas. The gas

storage capacity is 0.015 m^3 of oxygen and 0.03 m^3 of hydrogen. The storage system is feasible because the water avoids that gases get way for the bottom of the containers.

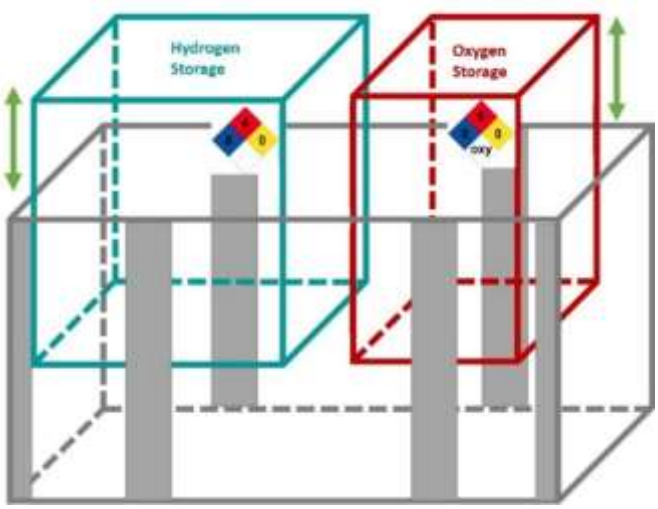

Fig 3. Hydrogen and oxygen storage system

Different connections were designed so the storage system requires to operate adequately from the electrolyzer and the fuel cell, increasing the efficiency and security of the process. [7, 8]

PEM fuel cell was designed at CINVESTAV by a research group. The proton exchange membrane fuel cell (PEMFC) is composed of bipolar plates, end plates, membrane electrode assemblies (MEAs) and gas diffusion layers (GDLs). Among the constituents of PEMFCs, the bipolar plate is a key component that collects and conducts the current from cell to cell. Bipolar plates and endplate were made of low porosity graphite. The fuel cell stack designed in this project contains 20 individual cells, each having a 0.0035m^2 active area. The cells are stacked in a series configuration with current collectors placed on the anode and cathode sides. The components considered in the volume size restriction are: endplates, current collectors, bipolar plates, all sealing materials, and MEAs. The dimensions of stack are 0.13m x 0.140 m x 0.075m when the stack is fully assembled and compressed and its weigh is 1.6 Kg. [9, 10]

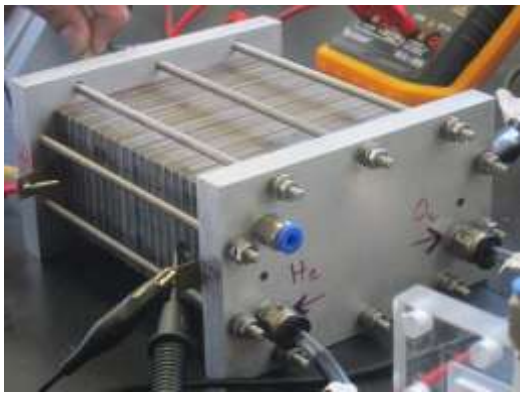

Fig 4. PEM Fuel Cell Stack

PEM fuel cell at $1.33x10^{-5}$ m^3/s of hydrogen and $6.65x10^{-6}$ m^3/s of oxygen is expected to generate 18V at opened circuit. It was designed an automatic system of gases regulation to the fuel cell, allowing to use different PEM fuel cells for future experiments, and a continual supplement, generating experiments with more precision. [9]

The aim of the photovoltaic-hydrogen system is to energize two LED lamps in a time frame, according with the PEM fuel cell electrical characteristics. In the design of the LED lamps, it was studied the congruence of electrical conditions and the high LEDs efficiency. [10]

3. Results and discussion

According with the statistical information about the sun light in México City, it can be determinate that the photovoltaic system is able to satisfy the electrical demand of PEM electrolyzer. Time of hydrogen production was studied based in the storage system. Considering losses in the photovoltaic system up to 20% by temperature, cables, inverter controller, among others, having available 7164KJ every day (1.99 KWhr/ day). [1]

It was analyzed the electrical behavior of the PEM electrolyzer at different pressures and a continual flow, $1x10^{-6}$ m^3/s as we can see in the figure 5.

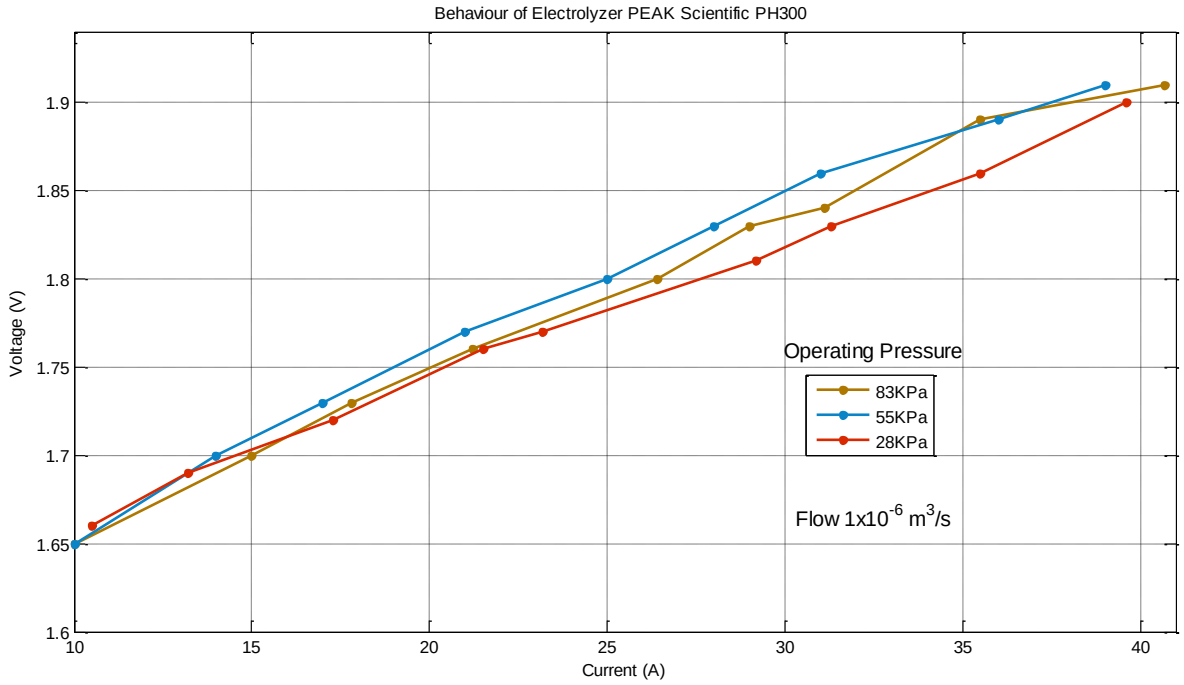

Fig 5. Electrolyzer PEAK scientific PH300 electrical behavior

We can appreciate in the graphic the PEM electrolyzer electrical behavior that is too similar at different pressures in a continual flow. It is able to understand that the operating pressure does not depend of the gases production. Analyzing the electrolyzer system and the gases production it was possible to determinate that the electrolyzer only controls the hydrogen production, where it works at maximum capacity $5x10^{-6}$ m^3/s until getting the selected pressure, thus the pressure is not relevant before obtained the selected pressure. It was found that it is really important that the equipment operate at 20% of hydrogen production, $1x10^{-6}$ m^3/s, for security and durability conditions.

For a correct operation of PEM electrolyzer, it was implemented a pressure regulator for the hydrogen delivery, it was made of resistant plastic, the regulator have an emergency valve, and a manometer. This regulator was implemented to control the electrolyzer system, avoiding algorithm mistakes in this. [7]

Understanding the electrical behavior in relation to the pressure it was studied the best operating pressure between 28KPa to 83KPa presented in the figure 6.

It was studied the delivery behavior at different pressures, the hydrogen deliver measure was made after the pressure regulator, changing considerably the behavior of it, compared with the oxygen delivery. As we can see the best delivery pressure is at 48KPa, however it was decided to work at 55KPa in relation to the stoichiometric oxygen production, getting a proportional gases delivery, reducing the time of recharge the storage system, considering that the minimum pressure to store is 3.6KPa.

According with the hydrogen and oxygen production and the storage system capacity, PEM electrolyzer operating at conditions before mentioned, it has to work for 16822 s (4.7hours) every day in relation to the photovoltaic system analysis, the system is able to provide enough electrical energy to perform this process part.

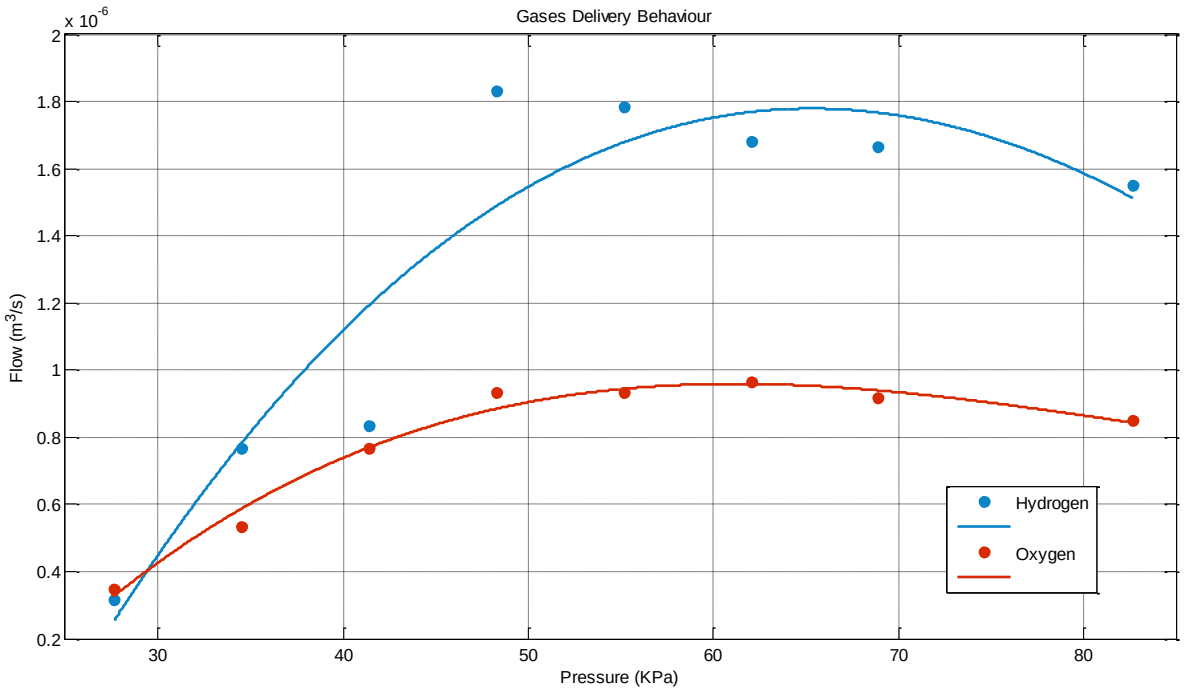

Fig 6. Gases delivery behavior

Mass quantity was analyzed from the hydrogen and oxygen storage, finding that the system is able to store only 9.5145×10^{-4} Kg of hydrogen and 7.5499×10^{-3} Kg of oxygen, proving the arduousness of store gases, principally hydrogen. In relation with these results and considering the intake gases, the quantity stored of it is sufficient only for 2400s (40minutes) of PEM fuel cell operation, for this reason this system is considering demonstrative and as an emergency lighting system. [5]

This was obtained using the ideal gases equation, taking in consideration that is a feasible equation because the gases are a low operating pressure and in relation with it their dew point is an extremely low temperature, far away from the operating temperature (295.15 K and 77.99KPa).[11]

$$PV = nRT \quad (1)$$

Schematic diagram was developed as we can see in the figure 7 where different connections and lines have been detailed that de global system requires for a correct and safe operation, in the table 3 they are explained. [7,12,13]

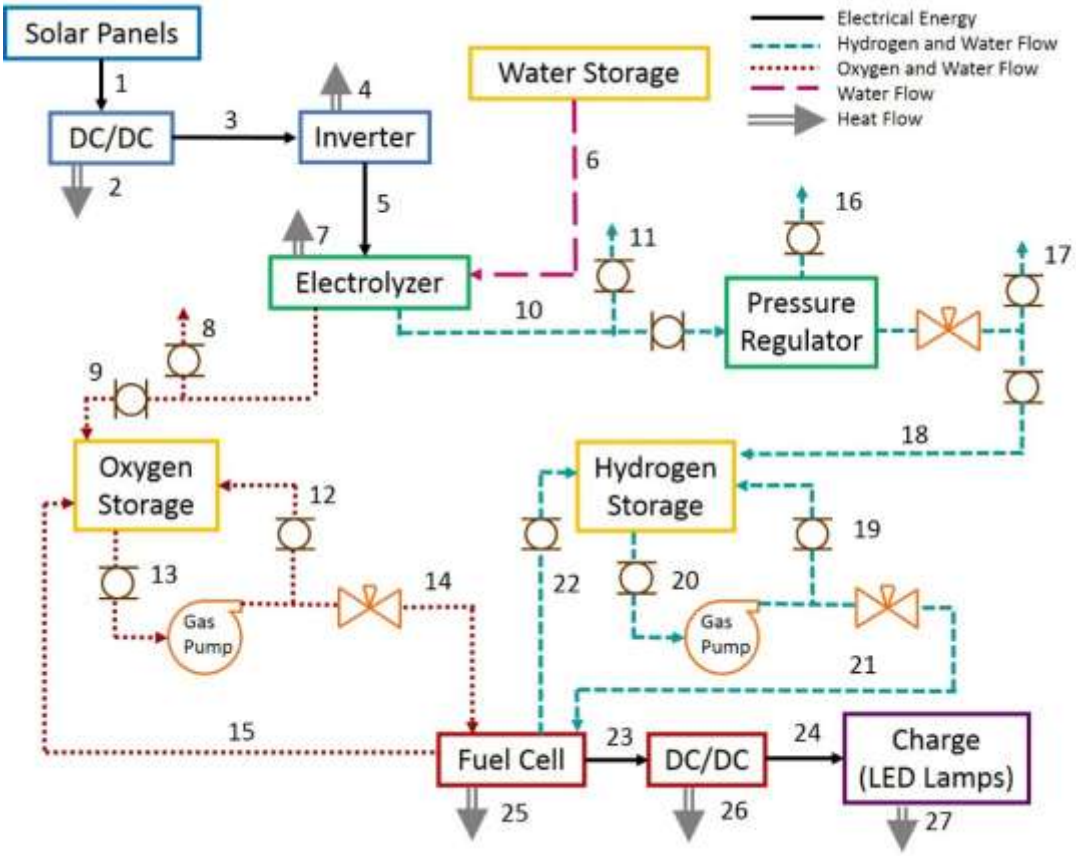

Fig 7. Photovoltaic-hydrogen system schematic diagram

Table 3. Information of photovoltaic-hydrogen system schematic diagram

Flow	Typology	Flow	Typology	Flow	Typology
1	Electrical Energy	10	H_2	19	H_2 Recirculation
2	Heat Flow	11	Purge	20	H_2
3	Electrical Energy	12	O_2 Recirculation	21	H_2 Regulated
4	Heat Flow	13	O_2	22	$H_2 + H_2O$ Recirculation
5	Electrical Energy	14	O_2 Regulated	23	Electrical Energy
6	H_2O	15	$O_2 + H_2O$ Recirculation	24	Electrical Energy
7	Heat Flow	16	Purge	25	Heat Flow
8	Purge	17	Purge	26	Heat Flow
9	O_2	18	H_2	27	Heat Flow

The de-ionized water line appears in colour pink, the hydrogen lines appears in blue and oxygen lines in colour red, in the diagram we can also see the heat flows, this flows are really important because they show the areas where the global system has a considerable energy loses. [7]

One of the important lines are the purge lines, these are really important because the operating gases have to be really pure to have a better electrochemical reaction mainly for hydrogen, it is really dangerous to have a combination of air and hydrogen, thus the system reduce the explosion risk. [7, 6]

For the global system was planned two recirculation lines for the hydrogen storage and two for the oxygen system, the first recirculations come to the pumps, this lines are important because they care the an excessive effort when the valves are not totally open. The second recirculations come to the fuel cell where there are the non-reaction gases with water. These lines save hydrogen and oxygen and increase fuel cell operation period. The diagram makes easier the operation of the system, and it allows to analyse the electrical process generation in the right way. [6]

We can see needle valves and pumps in colour orange, these system parts will be controlled by an automatic system, presented in the figure 8. It will be developed for gases regulation and it will allow to have a controlled system, therefore it will increase the precision of the fuel cell system. [12]

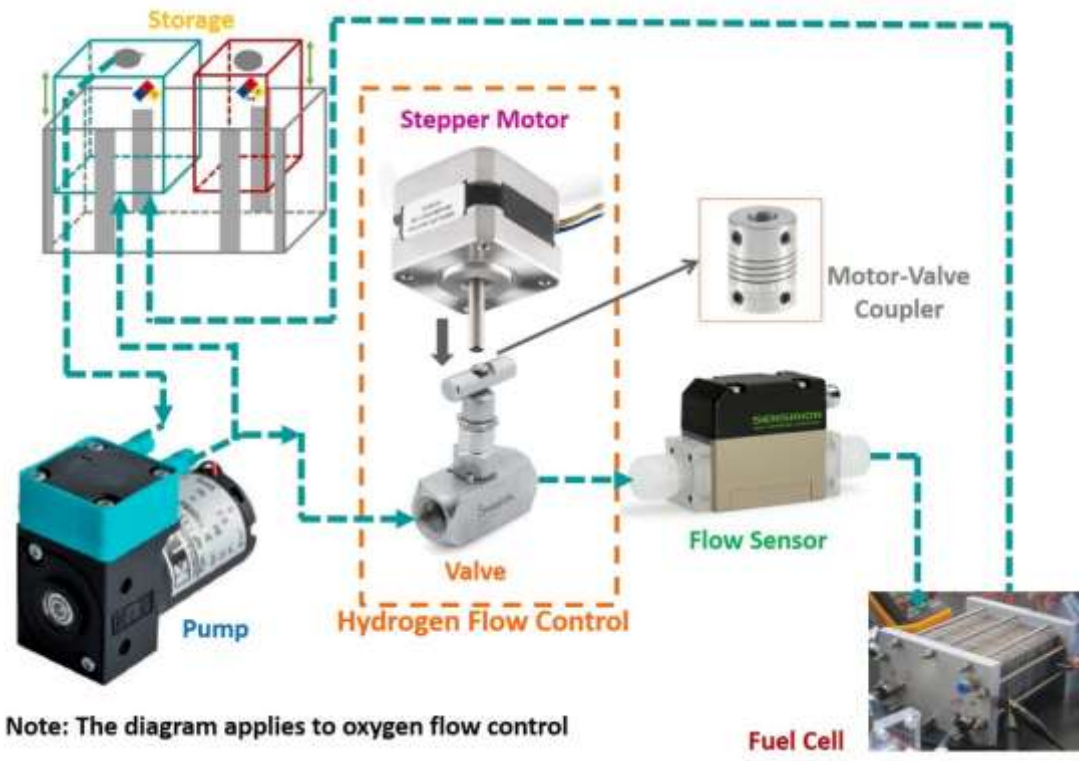

Fig 8. Gases regulation automatic control system

In the diagram we can see the different devices that the hydrogen line requires to be controlled in an automatically way, with the aim of supply a regulated and continual flow in the period time of fuel cell operation, the diagram applies to oxygen flow control. [12, 13, 14]

The automatic control system is a closed loop control or feedback control system, this type of control consists in a system that maintains a prescribed relationship between the output and the reference input by comparing them and using the difference as a means of control. In a closed-loop control system the actuating error signal, which is the difference between the input signal and the output signal, is fed to the controller so as to reduce the error and bring the output. [15]

The control regulation system is formed by a pump, it operates in a rage voltage from 5 to 12V, it will used when the storage system is not able to satisfy the selected flow, the system has a valve, this have a stepper motor which function will be regulate the gases flow to the PEM fuel cell, it is really important because it will allow that the system can be automatic. The system will have a flow sensor, this device is very important because it will measure the gases flow and the obtained information will be compared with the selected flow, thus the system will know if it is needed to increase the flow or reduce it. The sensor converts a physical variable, in this case the flow rate into an electrical signal which will be received for an integrated circuit. [6, 10, 15]

The mentioned system will allow to regulate the gases flow in a range of $1.67x10^{-7}$ m^3/s to $1.67x10^{-5}$ m^3/s, making possible work with different PEM fuel cells, the system will also control the gases flow in a relation with the operating time because where gases are stored it is a variable volume storage. When the gases are used, the flow rate supplied presents a decrement in relation with the time, and the automatic control system will right the gases flow rate. [7, 11]

It was obtained that PEM fuel cell at open circuit voltages is around 18 V with a capacity for 50W when is used $1.33x10^{-5}$ m^3/s of hydrogen flow and the measured maximum power density, W_{max}, is 150 W (14 A and 10.5 V) when is operated with $5x10^{-5}$ m^3/s of hydrogen flow. [9]

The PEM fuel cell was implemented to supply electrical energy for two LED lamps, each one consumes 25 W and operating optimal conditions are 12.5 V and 2 A. LED lamps was designed in order to be efficient, the high luminous efficiency was determined using LED's of 1 W with an efficiency of 100 lm/W. It was used special regulator for LED´s arrangement. [5, 10]

4. Conclusions

In this paper, it was demonstrated how a photovoltaic-hydrogen system can be integrated with different devices that this requires for a correct performance with the aim to satisfy the electric power demand of low-power devices such as LED lamps. It was proposed a control and automation system with the aim of regulate the gases flow rate, allowing to used different PEM fuel cells and they can be regulated a constant flow rate.

Solar-hydrogen-fuel cell technology has an impact on the global energy international scenery. Note further that since the development of hydrogen system is a continuous effort, demonstrative hydrogen system may contribute to improving the role of hydrogen in society. Ignoring the existence of public support and acceptance would definitely lead to a misleading policy towards "green" solar hydrogen planning and its infrastructure management. Then, experience indicates that greater knowledge about renewables energies and hydrogen system can imply higher political, social and research support. Therefore, with better understanding, imply greater attitude to support a sustainable environment and hydrogen technology, which can consistently involve greater support for the applications of hydrogen and hybrid systems.

Acknowledgements

The authors wish to thank the IPN and SECITI DF, this work was partially supported by IPN multidisciplinary project SIP-1540/2014 and by Secretaria de Ciencia, Tecnología, e Innovación del DF, SECITI DF.

References

[1]Geophysics Institute, Radiación Solar Promedio Disponible en la Ciudad de México, UNAM., Mexico., 2005
[2] JM.Fernández, Compendio de Energía Solar, Fotovoltaica,Térmica y Termoeléctrica; 1st ed; Mundi-Prensa AMV Ediciones; Madrid;2010
[3] PH User Manual, PEAK Scientific, Scotland., 2011
[4] P.Mompin, Energía Solar Fotovoltaica; 2nd ed; Marcocombo; Barcelona; 1985
[5] M.Aguer,A.Miranda, El Hidrógeno, Fundamento de un futuro equilibrado, 1st ed; Ediciones Díaz de Santos; España; 2005
[6] JR.Couper, W.Penney,J.Fair, S.Walas, Chemical Process Equipment, Selection and Design, 2nd ed; Elsevier, Inc; USA; 2010
[7] R.Sinnot,G.Towler, Diseño en Ingeniería Química, 5th ed; Revarte, Barcelona; 2012
[8] P.Ollero, E.Fernández, Instrumentación y Control de Plantas Químicas, 1st ed; Sítesis, S.A, Madrid
[9] G.Hoogers, Fuell Cell Techonology, Handbook, 1st ed; CRC Press LLC; 2003; USA
[10] F.Barbir, PEM Fuel Cells, Theory and Practice, 2nd ed; Elsevier, Inc; USA; 2013
[11] J.M.Smith, H.C. Van Ness, M.M. Abbott, Introducción a la termodinámica en Ingeniería Química, 7th ed.,Mc Graw Hill, Mexico, 2007
[12] A.Creus, Instrumentation Industrial, 8th ed ., Alfaomega; Mexico, 2011
[13] C.Smith, A.Corripio, Principes and Practice of Automatic Process Control, 2nd ed., John Wiley & Sons, Inc., USA., 1997
[14] DOJ. Desá, Instrumentation Fundamentals for Process Control, 10th ed; Taylor and Francis; USA; 2001
[15] K.Ogata, Ingeniería de Control Moderna, 5th ed; Pearson Education; Madrid; 2010

Ni and Ru Loading on $Sr_2Ta_2O_7$ by Electroless to Enhance Its Photocatalytic Hydrogen Evolution from Water

C.L Compean-González[1], V. M. Arredondo-Torres[2], M.E Zarazúa-Morin[1], M.Z Figueroa-Torres[1*]

[1]Departamento de Ecomateriales y Energía, Facultad de Ingeniería Civil, Universidad Autónoma de Nuevo León, Av. Universidad s/n Ciudad Universitaria San Nicolás de los Garza Nuevo León, México. CP. 66451.
[2]Facultad de Químico Farmacobiología, Universidad Michoacana de San Nicolás de Hidalgo, Tzintzuntzan #173, Col. Matamoros, Morelia, Michoacán, México. C.P. 58240
*Tel: +5214424400 ext. 5106; e-mail: m_zyzlila@yahoo.com.mx

ABSTRACT

Water splitting using a photocatalyst is one of the most attractive alternatives for hydrogen production. However, most semiconductors cannot give high H_2 evolution activities without a cocatalyst even in the presence of sacrificial electron donors. This work evaluates the effect of the surface modification with nickel and ruthenium on the hydrogen evolution of strontium tantalate. X-ray powder diffraction results shows that the single phase of $Sr_2Ta_2O_7$ was obtained at 900 ℃. The optical energy band gab was calculated from UV-vis absorption sprectrum and Kubelka-Muck formula giving a Eg value of 4.6 eV. Specific surface areas was estimated by nitrogen adsorption at -196 °C and the BET equation, the material exhibited a surface area of 3.58 m^2/g. Nickel and ruthenium loading on $Sr_2Ta_2O_7$ surface was done by using electroless deposition technique at 40 and 70 ºC respectively. By scanning electron microscopy it was observed that the particle size of $Sr_2Ta_2O_7$ was around 0.5 μm and the Ni and Ru nanoparticles were highly dispersed onto its surface with a narrow size range between 5-15 nm. It was found that hydrogen evolution under UV irradiation was increased when a suitable amount of nanoparticles is dispersed. Moreover, the higher hydrogen evolution was achieved when Ni was used as cocatalysts, increasing 1.4 times the hydrogen production compared with the pure $Sr_2Ta_2O_7$.

Keywords: electroless; UV-light, cocatalyst

1. Introduction

Hydrogen has been recognized as an important energy carrier, especially for use it in fuel cells, environmentally friendly vehicles, domestic heating, and stationary power generation. Clean and sustainable hydrogen production is still a challenge for scientists to solve energy and environmental problems. Photocatalytic water splitting using a semiconductor material is one of the most promising technologies for producing hydrogen; this is because H_2 can be obtained directly from water and solar light radiation, both of which are abundant and renewable resources [1,2].

Since Fujishima and Honda first demonstrated the photocatalytic water splitting on TiO_2 electrode, extensive efforts have been made to improve the reaction efficiency using metal oxide semiconductors [3,4]. Many metal oxides, such as titanates ($SrTiO_3$, BaTiO), niobates ($K_4Nb_6O_{17}$, $Ba_5Nb_4O_{15}$) and tantalates ($NaTaO_3$, $LaLnTa_2O_7$) have been developed as photocatalysts material for water splitting. Among these material, the oxides with layered crystal structures exhibited attractive photocatalytic activity for water splitting due to their interlayer acts as reaction sites [5–7]. Several research groups have proposed that metals ions with electronic d^{10} configuration improve charge separation and transport which enhance photocatalytic water splitting [4,8]. However, most semiconductors cannot give high H_2 evolution activities without a cocatalyst even in the presence of sacrificial electron donor. As it is known, loading a cocatalyst on the surface of semiconductor is often indispensable for achieving efficient hydrogen evolution [9,10]. The Sr_2TaO_7 with a perovskite-layered structure showed photocatalytic activity for hydrogen evolution from water [11]. In the literature, it is stated that water splitting is enhanced by the addition of nickel oxide onto its surface. They prove that hydrogen gas is formed on the nickel oxide surface and the oxygen is released from the photocatalyst surface [12]. On the other hand, the actuals methods for loading cocatalysts on a semiconductor surface are not efficient enough because of the dispersion of nanoparticles is low and it is hard to control the particle size and shape. In this sense, the search of alternative low-cost and short preparation time techniques to highly disperse nanoparticles are desirable. The electroless plating method is an attractive alternative and suitable choice for nanoparticles deposition because it has been proved to control the loading amount, particle size and dispersion [13]. In the present study $Sr_2Ta_2O_7$ were synthesized by solid-state reaction method and the influence Ni and Ru cocatalysts loading by using electroless deposition on the photocatalytic activity of Sr_2TaO_7 for hydrogen evolution were investigated.

2. Experimental

2.1. Preparation of $Sr_2Ta_2O_7$

The $Sr_2Ta_2O_7$ compound was prepared by a conventional solid-state reaction method. $SrCO_3$ (Sigma-Aldrich 99.9%) and Ta_2O_5 (Sigma-Aldrich 99.9%) were used as raw materials. The powders were dried at 200 ºC for 4 h before the synthesis. Then, stoichiometric amounts of each reactant were mixed with acetone in an agate mortar until the acetone completely evaporated. The solid mixture was placed into a platinum crucible and calcined between 800 and 1000 °C under an air atmosphere using a heating rate of 5 °C min^{-1} for 24 h with intermediate regrinding to complete the reaction.

2.2. Nickel and Ruthenium loading on $Sr_2Ta_2O_7$ surface

Fist, the $Sr_2Ta_2O_7$ surface was activated by the conventional two-step $SnCl_2/PdCl_2$ procedure [14]. The conditions of the nickel electroless deposition (ED) were taken from the work of Figueroa-Torres et. al. [15] and for ruthenium deposition from the work of Cheng-Hong et al. [16]. The ED deposition was carried out by adding the $Sr_2Ta_2O_7$ on a baker with electroless solution. Then the solution was placed on a hot plate at the desired temperature with a magnetic stirrer. Deposition temperatures were from 30 to 80 °C. The amount of nickel and ruthenium loading were controlled by deposition time. After electroless treatment, the Ni/ $Sr_2Ta_2O_7$ and Ru/ $Sr_2Ta_2O_7$ samples were separated from the solution by filtration, rinsed several times with distilled water and dried at 80 °C.

2.3. Characterization

$Sr_2Ta_2O_7$ samples were characterized by X-ray powder diffraction (XRD) using Cu Kα radiation as the incident X-ray source. XRD data were collected at room temperature from 10° to 70° with a step interval of 0.01° and a counting time of 1 s $step^{-1}$. Morphologies of samples were observed by scanning electron microscope (SEM) adapted with energy dispersive spectrometry system (EDS) which was used to determine the amount of Ni and Ru deposited. To evaluate the surface area of the samples, physical adsorption of N_2 at – 196 °C was carried out. Before measurements, samples were outgassed at 300 °C for 3 h. Surface area (A_{BET}) was obtained using the multipoint BET method. Optical absorption properties of the samples were analyzed in the range of 200–900 nm at room temperature with a UV–vis spectrophotometer with an integrating sphere attachment. Optical Energy band gap (Eg) values were obtained using the Kubelka–Munk function based on the diffuse reflection (DR UV–vis) spectra data.

2.4. Photocatalytic Hydrogen Production Evaluation

The photocatalytic water splitting reaction was carried out at low pressure in a reactor with inner quartz cell and a 400 W high pressure mercury lamp as the irradiation source. Firstly, 0.3 g of the materials was dispersed into 300 mL of pure water under vigorous stirred. Prior to the reaction, argon was bubbled to deaerate the solution. Pressure was set at 100 Torr and temperature was kept at 20 °C using a cooling system. The evolved gases were analyzed using a chromatograph equipped with a TCD detector and column Hayesep D 100/120 using argon as carrier gas. Reaction evolution was analysed each 30 min during 4 h.

3. Results and discussion

Figure 1 shows the XRD diffractograms of $Sr_2Ta_2O_7$ synthesized by solid-state reaction method at different temperatures. The diffractograms of the raw materials indicated that they are pure because only Sr_2CO_3 and Ta_2O_7 phases were presented. According to XRD analysis results, at 800 °C, $Sr_2Ta_2O_7$ phase begins to crystallize, it is observed a diffractogram with wide diffraction peaks that can be identified like a mixture of phases of the corresponding raw oxides and the first diffraction peaks of $Sr_2Ta_2O_7$. As temperature increased to 900 °C, the $Sr_2Ta_2O_7$ phase was only identified. As can be seen, the diffraction

peaks were intensive and narrow, suggesting a good crystallization degree. The further increase in the temperature do not generate significant changes in the diffractograms.

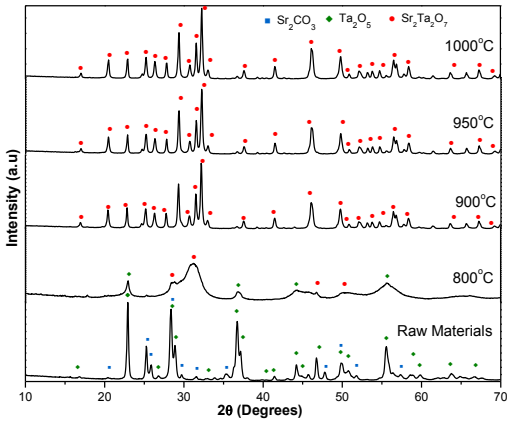

Fig 1. XRD patterns of $Sr_2Ta_2O_7$ prepared by solid-state reaction at different temperatures.

Figure 2 shows SEM images of $Sr_2Ta_2O_7$. In figure 2a, it can be observed big agglomerates of particles with sizes of more than 15 μm. This can be attributed that solid state reaction occurs at 900 °C favoring the partial sintering of particles. At higher magnifications (Fig 2b) it is possible to observe that the agglomerates are formed by $Sr_2Ta_2O_7$ particles of semispherical shape with a smooth surface. The average particle size is round 300 nm.

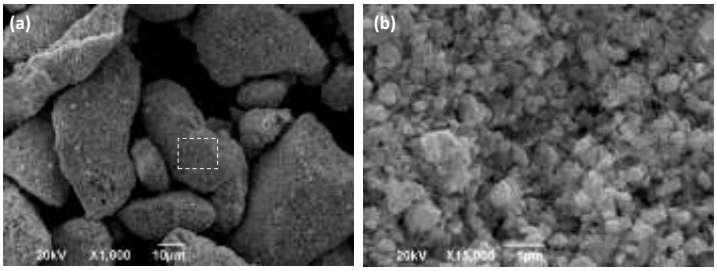

Fig 2. SEM images of $Sr_2Ta_2O_7$ prepared by solid-state reaction.

In order to find convenient deposition parameters to disperse Ni or Ru on $Sr_2Ta_2O_7$ surface, different temperature and deposition time were tested. Figure 3 shows weight percent of Ni or Ru deposited at different temperatures as function of deposition time. From the figure 3, it can be appreciated that temperature was an important factor that influences Ni and Ru deposition process. Particularly, the Ni deposition can be done from ambient temperature (30°C) or higher temperatures. At 30 and 40 °C, the

reaction rate allows a good control of the deposited Ni nanoparticles amount as function of time. However, an increase from 40 to 50 °C the deposition rate was highly increased; in a few minutes, the Ni deposited amount is twice. On the other hand, it was found that for Ru deposition required higher temperatures to deposition reaction started. Below 70 °C the reaction did not initiate even at long deposition time. Between 70 and 80 °C the reaction rate is appropriate to control the Ru loading amount.

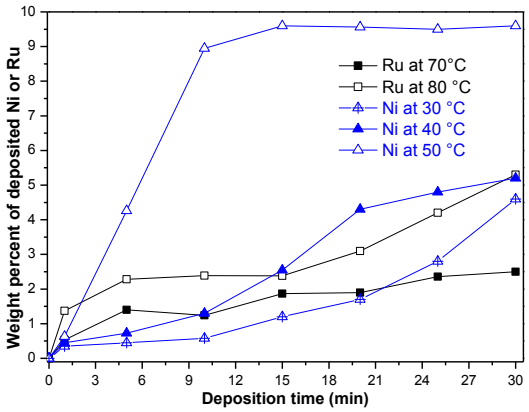

Fig 3. Weight percent of Ni or Ru as function of deposition time at different temperatures on $Sr_2Ta_2O_7$.

The morphology of the Ni and Ru on the $Sr_2Ta_2O_7$ surface is illustrated in figure 4. The image reveals that Ni and Ru nanoparticles are uniformly dispersed through the $Sr_2Ta_2O_7$ surface. Moreover, presented a semispherical shape with a narrow size range between 5 to 15 nm. The EDS spectrum confirms the presence of Ni and Ru nanoparticles.

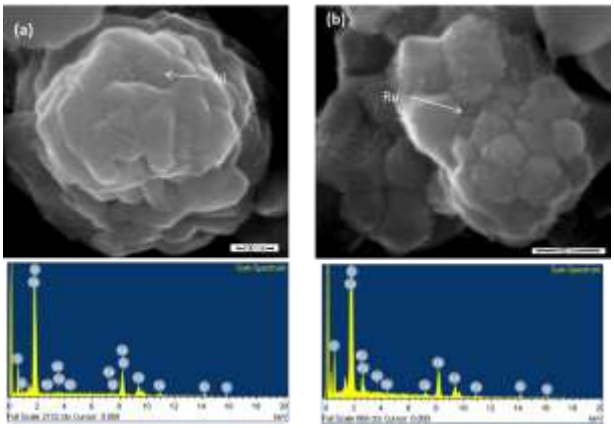

Fig 4. SEM images and EDS spectrum of Ni and Ru nanoparticles on $Sr_2Ta_2O_7$.

The optical absorption properties of $Sr_2Ta_2O_7$ and 1 %wt. $Ni/Sr_2Ta_2O_7$ and 1%wt. $Ru/ Sr_2Ta_2O_7$ were measured by UV-Vis spectroscopy, and the results are shown in figure 5. As can be seen from the figure, the $Sr_2Ta_2O_7$ shows a very weak absorption at the visible range region. It is evident that the loading on Ni and Ru nanoparticles promotes the absorption of light in the visible region. The optical band gap values obtained by using the Kubelka–Munk function and extrapolating the linear portion against photoenergy are reported in table 1.

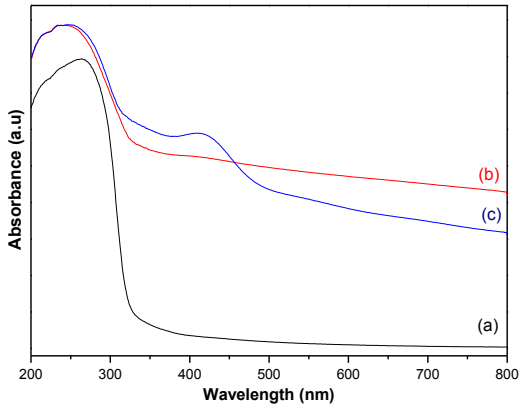

Fig. 5. UV–vis absorbance spectra of (a) $Sr_2Ta_2O_7$; (b) $1\%Ni/ Sr_2Ta_2O_7$ and (c) $1\%Ru/ Sr_2Ta_2O_7$.

The Eg values were 4.6 eV. This property is not modified by the loading of nanoparticles because of they are on the oxide surface. Table 1 also reports the specific surface area values. The $Sr_2Ta_2O_7$ exhibit a surface area of 3.58 m^2/g. After electroless deposition, the surface area was increased more than twice; this is mainly due to $Sr_2Ta_2O_7$ particles deagglomerated during electroless deposition; this is and additional benefic that can have a favorable influence in the photocatalytic activity of the material. It is also appreciated that the increase in surface area was independent of the metal type and metal amount.

Table 1. Optical band-gap and surface area values

Sample	**Eg (eV)**	**A_{BET} (m^2/g)**	
		Before ED	**After ED**
$Sr_2Ta_2O_7$			N/A
$Ni/Sr_2Ta_2O_7$	4.6	3.58	9.9
$Ru/Sr_2Ta_2O_7$			9.5

Prior to the photocatalytic reaction test, blank controls were performed with the same reaction system in dark or in the absence of photocatalyst. No hydrogen was generated under these conditions, thus the hydrogen production is due to the presence of the photocatalyst material. Figure 6a illustrate the photocatalytic hydrogen evolution as a function of irradiation time from pure water of Ni/$Sr_2Ta_2O_7$ samples and the hydrogen evolution of Ru/$Sr_2Ta_2O_7$ are presented in figure 6b. According to the results showed in Figure 6, it was observed that $Sr_2Ta_2O_7$ is able to produce hydrogen without loading a cocatalyst. However, the loading metals provide efficient active sites for H_2 evolution. It can be seen that during the 30 first minutes, samples presented a similar behavior after that time; differences were found in the hydrogen evolution as function of the metal type and metal loading amount. It can be seen that exits a better synergism when Ni is used as cocatalysts than Ru. It was found that for nickel between 0.15 and 1 wt % is an appropriate amount to enhance hydrogen evolution. At higher contents, hydrogen evolution decreased and it is even less than $Sr_2Ta_2O_7$ alone. For the ruthenium samples, the enhance in hydrogen production is not significant and higher amounts of Ru are required compared to Ni-samples. The better H_2 production was achieved with the sample with 2 wt% of Ru.

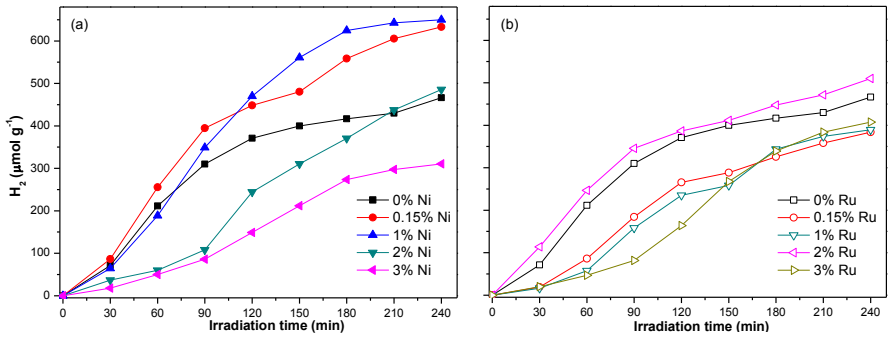

Fig. 6. Photocatalytic hydrogen production a) Ni/$Sr_2Ta_2O_7$ and b) Ru/$Sr_2Ta_2O_7$ samples

The H_2 evolution rate of the samples is reported in table 2. The H_2 evolution of 0.15 wt.%Ni/ $Sr_2Ta_2O_7$ was 158 μm/h g, which is approximately 1.4 times higher that of $Sr_2Ta_2O_7$. Whilst for the 2wt.%Ru/ $Sr_2Ta_2O_7$ sample was 128 μm/h g, which is 1.1μm/h g times higher than $Sr_2Ta_2O_7$. When and overload of metal was used, the decrease in H_2 evolution can be associated with a limited light absorption by $Sr_2Ta_2O_7$, which reduces the generation of electron-hole pairs and they also can acts as recombination centers.

Table 2. Hydrogen evolution rates

	H_2 evolution rate ($\mu m\ h^{-1}\ g^{-1}$)	
Metal wt.%	**Ni**	**Ru**
0	116	116
0.15	158	95
1	162	98
2	121	128
3	77	102

4. Summary and perspectives

This work demonstrates that electroless deposition technique is an attractive alternative route to highly dispersed Ni and Ru nanoparticles of approximately 5 to 15 nm in a few minutes on $Sr_2Ta_2O_7$ surface. Ni and Ru nanoparticles are effective cocatalysts to enhance hydrogen evolution reaction. However, exist a better synergism when Ni is used in an appropriated amount. The highest hydrogen evolution was presented by 1wt% Ni/ $Sr_2Ta_2O_7$ sample. At this Ni content, hydrogen amount was 1.4 times higher than $Sr_2Ta_2O_7$.

Acknowledgements

Presented work was supported by the CONACYT thought the project CB-2012-177079 and PROMEP/103.5/13/6644 projects and in part by projects PAICYT-UANL-IT881-11 and FOTOSÍNTESIS ARTIFICIAL 75/2012.

References

[1] K. Maeda, Photocatalytic water splitting using semiconductor particles: History and recent developments. J. Photochem. Photobiol. C Photochem. Rev. 2011; 12: 237–268.
[2] D. Jing, L. Guo, L. Zhao, X. Zhang, H. Liu, M. Li, S. Shen, G. Liu, X. Hu, and X. Zhang, Efficient solar hydrogen production by photocatalytic water splitting: From fundamental study to pilot demonstration. Int. J. Hydrogen Energy. 2010; 35: 7087–7097.
[3] A. Ibhadon and P. Fitzpatrick, Heterogeneous Photocatalysis: Recent Advances and Applications. Catalysts, 2013; 3: 189–218.
[4] H. Kisch, Semiconductor photocatalysis: mechanistic and synthetic aspects, Angew. Chem. Int. Ed. Engl. 2013; 52: 812–847.
[5] Y. Inoue, Photocatalysts with tunnel structures for decomposition of water, J. Chem. Soc. Faraday Trans. 2010; 90: 797–802.
[6] Y. Miseki and A. Kudo, Water splitting over new niobate photocatalysts with tungsten-bronze-type structure and effect of transition metal-doping, ChemSusChem 2011; 4: 245–251.
[7] H. Xu, R. Q. Zhang, A. M. C. Ng, A. B. Djuri, H. T. Chan, W. K. Chan, and S. Y. Tong, Splitting Water on Metal Oxide Surfaces, 2011; 115: 19710–19715.
[8] Y. Inoue, Photocatalytic water splitting by RuO_2 loaded metal oxides and nitrides with d^0 and d^{10} related electronic configurations, 2009; 2: 364–386.
[9] J. Yang, D. Wang, H. Han, and C. A. N. Li, Roles of Cocatalysts in Photocatalysis and Photoelectrocatalysis, 2013; 46: 1900-1909.

[10] M. Tian, W. Shangguan, J. Yuan, S. Wang, and Z. Ouyang, Promotion effect of nanosized Pt , RuO_2 and NiO_x loading on visible light-driven photocatalysts $K_4Ce_2M_{10}O_{30}$ (M = Ta , Nb) for hydrogen evolution from water decomposition, Sci. Tech. Adv. Mat. 2007: 8: 82-88.

[11] C. Zhou, G. Chen, Y. Li, H. Zhang, and J. Pei, Photocatalytic activities of $Sr_2Ta_2O_7$ nanosheets synthesized by a hydrothermal method, 2009; 34: 2113–2120.

[12] A. Kudo, Photocatalyst materials for water splitting, 2003; 7:1–3.

[13] Z. Wu, S. Ge, M. Zhang, W. Li, and K. Tao, Journal of Colloid and Interface Science Synthesis of nickel nanoparticles supported on metal oxides using electroless plating: Controlling the dispersion and size of nickel nanoparticles, J. Colloid Interface Sci. 2009; 330: 359–366.

[14] T. N. Khoperia, Electroless deposition in nanotechnology and ULSI, 2003; 69: 384–390.

[15] M. Z. Figueroa-Torres, C. Domínguez-Ríos, J. G. Cabañas-Moreno, O. Vega-Becerra, and a. Aguilar-Elguézabal, The synthesis of Ni-activated carbon nanocomposites via electroless deposition without a surface pretreatment as potential hydrogen storage materials, Int. J. Hydrogen Energy 2012; 37: 10743–10749.

[16] C.-H. Liu, B.-H. Chen, C.-L. Hsueh, J.-R. Ku, M.-S. Jeng, and F. Tsau, Hydrogen generation from hydrolysis of sodium borohydride using Ni–Ru nanocomposite as catalysts, Int. J. Hydrogen Energy. 2009; 34: 2153–2163.

$Ni_xMo_{1-x}O_3$ ($x \leq 0.4$) as Electrocatalysts for Electrochemical Hydrogen Production from Acid Water

K. K. Aruna [psg institute of advanced studies], R. Manoharan* [psg institute of advanced studies]

Electrochemical Energy Materials Laboratories
Nanotech Research Facility, PSG Institute of Advanced Studies, Coimbatore, India 641 004
Phone: 0422- 4344000 x 4322
*email: krsmano@gmail.com

Abstract:

In this work, nickel has been doped into α-MoO_3 and the resulting $Ni_xMo_{1-x}O_3$ nano structured materials have been examined as electrocatalysts for the cathodic hydrogen evolution reaction (HER). X- ray diffraction (XRD) analysis of our synthesized materials indicated that Ni enters into the orthorhombic structure of α – MoO_3 up to x = 0.2. Above x = 0.2, $NiMoO_4$ (monoclinic) phase is formed along with the formation of trace quantities of MoO_3. Nanobelt morphologies have been observed for oxides with $x \leq 0.2$ in Transmission Electron Microscope (TEM) analysis and with the increase in the Ni concentration above 0.2, presence of broken belts along with few spherical particles has been observed. The HER evolving rates as inferred from the linear sweep voltammograms recorded at the 500th cycle for x = 0, 0.1, 0.2, 0.3 and 0.4 are compared.

Key words: Hydrogen Evolution Reaction, Ni_xMoO_{1-x}, catalytic studies

Introduction:

The increasing global demand and the after effects of liberation of harmful by products from burning hydrocarbon fuel have triggered the research world in implementing and exploring renewable clean carbon free alternatives. Pure hydrogen is one important alternative fuel. Although water electrolysis for hydrogen production is one of the oldest and easiest well-known methods, its usage was demarked often to small scale and specialized situations where an access to large scale hydrogen production plants was not commercialized mainly because hydrogen has been, until recent time, produced more affordably and economically from fossil fuel reforming. However, the recent, excessive rise in fuel price and the global environmental regulations make the water electrolysis an attractive field [1, 2]. High pure hydrogen gas can be obtained only by water electrolysis and especially the proton exchange membrane water electrolyzer (PEMWE) result in least crossover of the product gas compared to alkaline electrolyzer, hence yielding ultra high pure of product gas. Integrated with solar cell systems or wind power systems, hydrogen produced with water electrolysis can lead for sustainable pathways for energy production [3]. The main hindrance for the commercialization of H_2 generation electrolytic system is the incorporation of platinum group elements as electrocatalysts. Recent advances have revealed that nano structured oxides, sulfides, nitrides, carbides and phosphates would be promising alternatives to Pt for the electrochemical generation of hydrogen from water [4-11]. Recently, we have been focusing on oxide based electrocatalysts in our laboratory.

Normally, oxide materials tend to get corroded under electrochemical conditions in acidic environments. However some oxide materials such as $Sr_{1-x}NbO_{3-\delta}$, $SrPdO_3$, $Cu_{1-x}Ni_xWO_4$ WO_3/C and $SrMoO_4$ have been found to be stable in acids and several reports have indicated that these oxide materials would be interesting as alternatives to Pt for catalyzing the HER in acidic electrolytes [6, 12-15]. MoO_3 has already been tested as the HER catalyst in acid medium by Phuruangrat et al in 2009 [4] where the materials stability was not reported. In this work, we have prepared $Ni_xMo_{1-x}O_3$ ($x \leq 0.4$) nanostructured materials and tested their abilities to catalyze HER over a few hundreds of continuous scan cycles. The variation in morphologies of $Ni_xMo_{1-x}O_3$ and the variation of their catalytic properties with the variation in Ni doping have been studied. To our knowledge, a HER catalytic study on $Ni_xMo_{1-x}O_3$ nanomaterials is not covered in the literature. The HER study was carried out in 2.5 M H_2SO_4 solution since its pH is equivalent to that of nafion membrane used for membrane electrode assembly (MEA) in PEMWE.

2. Experimental Section:

2.1 Synthesis and characterization of MoO_3 and $Ni_xMo_{1-x}O_3$

MoO_3 and $Ni_xMo_{1-x}O_3$ nanostructured materials have been prepared by hydrothermal method. The synthetic procedure for MoO_3 is as reported by Phuruangrat and group [4]. For synthesizing $Ni_xMo_{1-x}O_3$ nanostructured materials, 0.1 M $Ni(CH_3COO)_2$. $4H_2O$ was used as Ni source along with stoichiometrically calculated amount of ammonium hepta molybdate (AHM) $(NH_4)_6Mo_7O_{24}$. 4 H_2O and 3 M HNO_3. Cetyl trimethyl ammonium bromide (CTAB) was used as a surfactant. Weighed amount of CTAB was dissolved in double distilled (DD) water, stirred continuously for couple of minutes, AHM was added and the stirring was continued for half an hour. Then calculated amount of nickel acetate was summed into the solution and left stirred. The entire mixture was then transferred to a 300 ml teflon lined digestion bomb. The bomb was sealed and kept at a temperature of 180^0C for 20 hours. After completion of the reaction, the resulting precipitate was filtered, washed with DD water several times and finally with ethanol. The precipitate thus obtained was dried at 100^0C for couple of hours. The phase formations of the synthesized samples were confirmed using Shimadzu XRD-600 and JEOL JEM 2100 (manufactured in Japan) has been used for recording the TEM and HRTEM images.

2.2 Electrochemical characterization:

A three electrode cell consisting of a working electrode, Pt as a counter electrode and Ag/AgCl (in saturated KCl) as a reference electrode has been employed. 2.5 M H_2SO_4 solution has been used as electrolyte. All the electrochemical measurements have been performed using an M/S Biologic Science electrochemical work station (VSP multichannel model) at room temperature.

The catalysts inks have been fabricated by ultrasonication of a turbid solution containing few milligram catalysts powder, 100 µl ethanol and 20 µl of 5 wt% Nafion for half an hour. A known amount of homogeneously dispersed catalysts ink has been taken and placed on a glassy carbon electrode (GCE) having an active surface area of $0.071cm^2$ which is acting as the working electrode (W.E) in the three electrode cell system. Before coating, the GC was cleaned mechanically with alumina and diamond polishing liquid and washed thoroughly with DD water. The linear sweep voltammetry (LSV) and Tafel polarization measurements were performed to evaluate the HER activity of the synthesized samples. LSV and Tafel polarization were carried at a scan rate of 50 mV s^{-1} and 20 mV s^{-1}, respectively.

3. Results and Discussions

3.1 Structural Characteristics

Fig. 1 shows the diffraction patterns for MoO_3 and $Ni_xMo_{1-x}O_3$ materials. The diffraction patterns are in good accordance with the standard diffraction pattern of orthorhombic MoO_3 (JCPDS file no: 05-0508) for samples up to x = 0.2. Ni doping in orthorhombic MoO_3 structure does not take place beyond this Ni^{2+} concentration and above this value, formation of monoclinic $NiMoO_4$ (JCPDS file no: 450-142) phase takes pace. Patterns corresponding to $NiMoO_4$ phases are observed for x ≥

0.3. Some peaks corresponding to α – MoO_3 are also observed in the $NiMoO_4$ XRD pattern suggesting that trace quantities of MoO_3 are present along with $NiMoO_4$ phase.

For x = 0.1 and x = 0.2, diffraction angles are shifted towards high degree from 25.73^0, 27.28^0 and 39.02^0 to 25.80^0, 27.39^0 and 39.12^0 respectively. Also peak broadening was observed for these compositions.

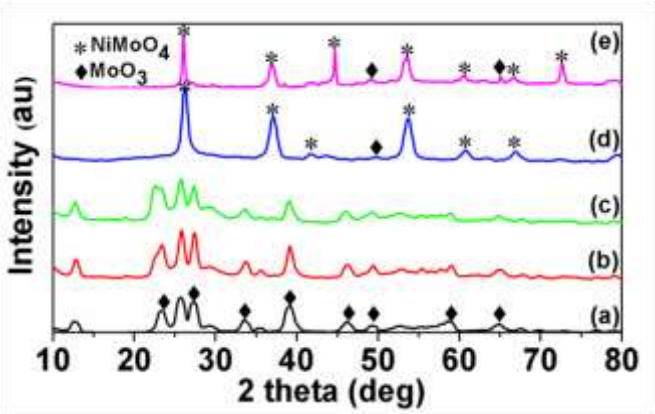

Fig. 1 XRD pattern of (a) MoO_3 and $Ni_xMo_{1-x}O_3$ with (b) x = 0.1 (c) x = 0.2 (d) x = 0.3 and (e) x = 0.4

The morphologies of the MoO_3 and $Ni_xMo_{1-x}O_3$ materials were examined by TEM and HRTEM images. The TEM images in Fig 2 show the presence of nanobelt morphology for $Ni_xMo_{1-x}O_3$ with x = 0.1 and 0.2. For x = 0.3 and x = 0.4, broken nanobelts along few irregular shaped particles were observed. While nanobelt particles are attributed to the presence of orthorhombic MoO_3 phase materials, the irregular shaped particles are attributed to the presence of monoclinic phase $NiMoO_4$ materials. We have previously noticed the formation of nanobelt morphology for orthorhombic α-MoO_3 phase materials [6] which were prepared under same hydrothermal conditions. Thus nanobelt morphology observed for $Ni_xMo_{1-x}O_3$ materials with x = 0.1 and x = 0.2 also support our XRD data that these materials are formed in orthorhombic phase. The present TEM morphology data also support the information inferred from the XRD analysis, that x = 0.3 and x = 0.4 materials contain mixtures of $NiMoO_4$ phase and orthorhombic $Ni_xMo_{1-x}O_3$ phase.

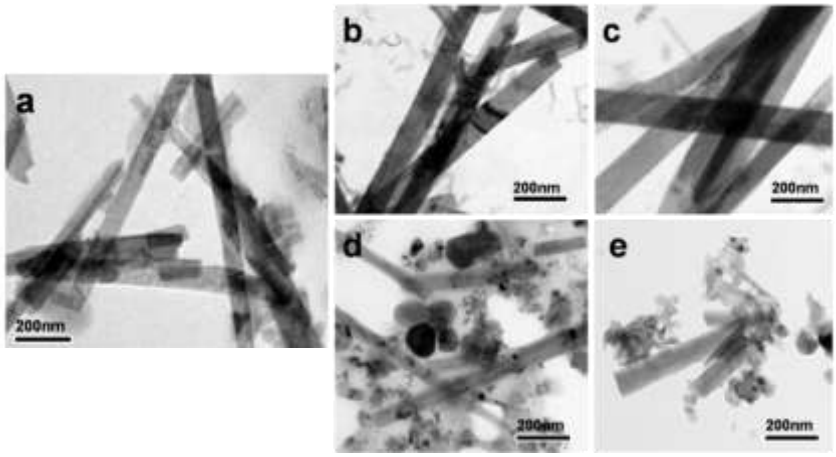

3.2 Electrocatalysis for the HER in acid medium:

Fig. 2 TEM images of (a) MoO_3 and $Ni_xMo_{1-x}O_3$ with (b) x = 0.1 (c) x = 0.2 (d) x = 0.3 and (e) x = 0.4

It is observed that the over potential decreased and the current density increased when all the materials were subjected to continuous scan cycling in the acid electrolyte. Fig. 3 show the LSVs recorded at a scan rate of 50 mVs^{-1} on MoO_3 and Ni_xMo_{1-}

$_xO_3$ with (b) x = 0.1 (c) x = 0.2 (d) x = 0.3 and (e) x = 0.4. The materials were found to be quite stable within the potential window -0.2 V to -1.00 V. Tafel plots were obtained at a scan rate of 20 mVs^{-1} and are shown in the insets of Fig. 3.

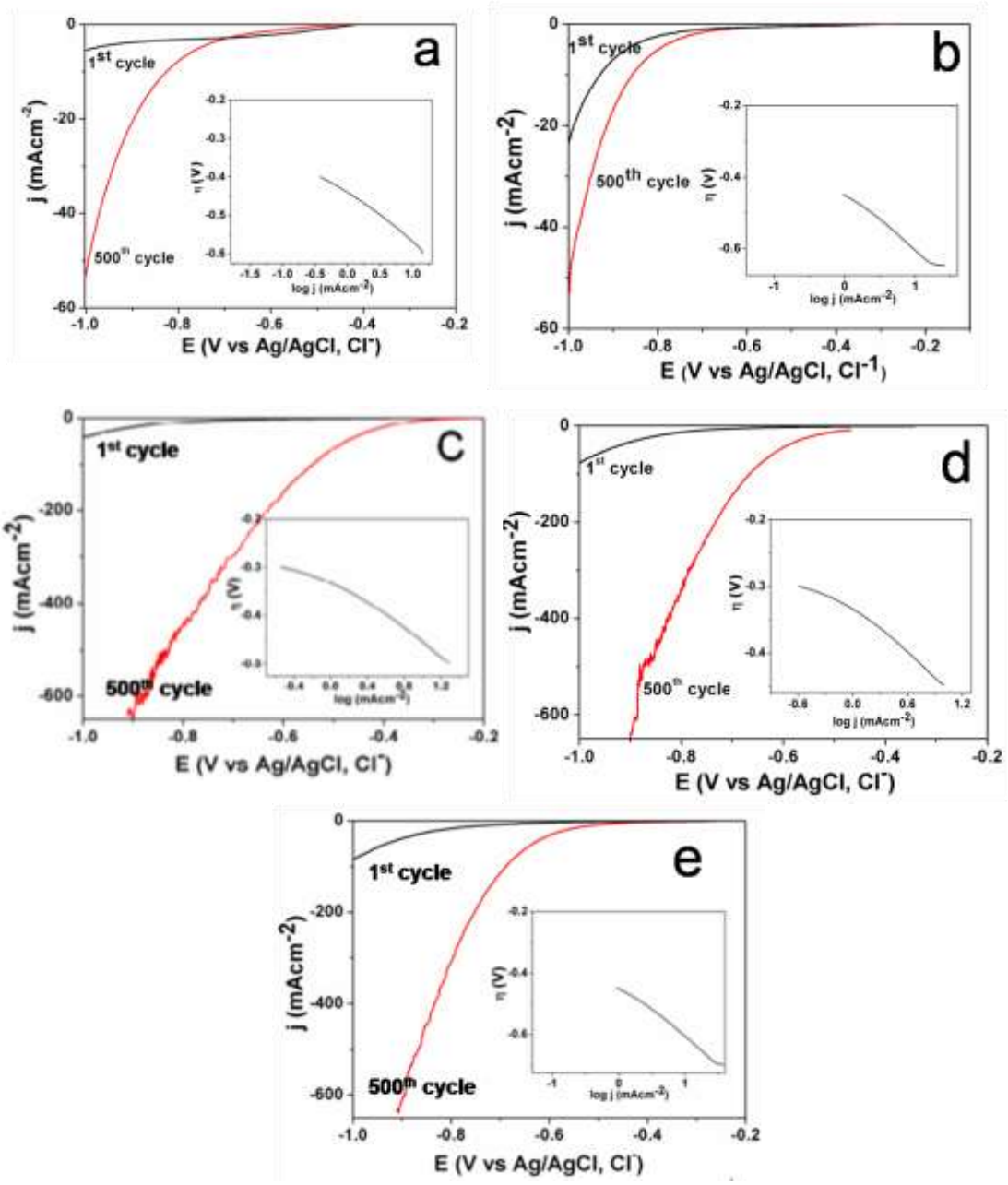

Fig. 3 LSVs for the HER on (a) MoO_3 and $Ni_xMo_{1-x}O_3$ with (b) x = 0.1 (c) x = 0.2 (d) x = 0.3 and (e) x = 0.4 in 2.5 M H_2SO_4 solution with Tafel plot as inset.

The electrochemical parameters for the HER deduced from Fig. 3 are shown in Table. 1.

Table 1. Electrochemical parameters for the HER on the synthesized samples.

Sample $Ni_xMo_{1-x}O_3$	$j_{E=0.8V}$ [$mAcm^{-2}$][a]	Tafel slope, b ($mVdec^{-1}$)
x = 0	-8.16	126
x = 0.1	-40.13	153
x = 0.2	-442.92	122
x = 0.3	-302.26	114
x = 0.4	-300.13	157

[a] cathodic current densities at observed potential E = -0.8 V

The order of the HER activity performances of $Ni_xMo_{1-x}O_3$ is as follows: x = 0.2 > x = 0.1 > x = 0.3 > x = 0.4 > x = 0. This suggests that the HER activity enhances with the increase in Ni^{2+} in MoO_3 structure up to x = 0.2, and on forming $NiMoO_4$ phase beyond x ≥ 0.2, the HER catalytic activity decreases. It is discernable that encapsulation of Ni^{2+} into the crystalline lattice of MoO_3 helps to catalyze the HER activity better than the Ni^{2+} present in the $NiMoO_4$ lattice although Mo^{6+} is present in octahedral environment in both cases. A high HER current density, j = 600 $mAcm^{-2}$ has been observed on $Ni_{0.2}Mo_{0.8}O_3$ at η = -700 mV. This is a much better performance than what has been observed for $SrMoO_4$ which was examined by us previously [6].

According to classical theory of mechanism for the HER, the overall reaction occurring at a catalyst modified electrode surface in acid solution starts with a proton discharge Volmer reaction (Equation 1) followed by either an ion and atom Heyrovsky reaction (Equation 2) or combination Tafel reaction (Equation 3)

$$H_3O^+ + M + e^- \rightarrow H_2O + M-H \quad (1)$$

$$M-H + H_3O^+ + e^- \rightarrow H_2 + M + H_2O \quad (2)$$

$$2M-H \rightarrow 2M + H_2 \quad (3)$$

where M is active reactive site of the catalyst and $M-H$ denotes the hydrogen atom adsorbed on the active site. The first step is considered to be a fast reaction and either of the following reactions is regarded as the rate determining step (rds) [16, 17].

The O^{2-} species which are differently bonded to different cations under different coordinates in oxide materials have been identified as the active sites for the HER and they can absorb H with a small free energy [6, 12, 18 and 19]. In our previous report [6], we had explained the following three possible reaction steps that can take place on molybdenum oxide catalyst using a HER study on $SrMoO_4$ material.

$$Mo^{6+}OH^- + H_3O^+ + e^- \rightarrow Mo^{5+}OH_2 \quad (4)$$

$$Mo^{5+}OH_2 + H_3O^+ + e^- \rightarrow Mo^{6+}OH^- + H_2O + H_2\uparrow \quad (5)$$

$$2Mo^{5+}OH_2 \rightarrow 2Mo^{6+}OH^- + H_2\uparrow \quad (6)$$

The observed Tafel slope values for all the $Ni_xMo_{1-x}O_3$ materials in 2.5 M H_2SO_4 solution are around 120 mV dec^{-1} and it appears that proton discharge Volmer reaction is the rate determining for the occurrence of the HER on $Ni_xMo_{1-x}O_3$ (x ≤ 0.4) materials.

The strength of Mo-O bonds present in the octahedral environment of the compounds $Ni_{0.1}Mo_{0.9}O_3$ and $Ni_{0.2}Mo_{0.8}O_3$ seems to be appropriate for adsorbing protons from the electrolyte and convert them efficiently into H_2 molecules via the Volmer reaction pathways and hence high HER activities are noticed for the two materials.

Conclusion:

The effect of doping Ni in MoO_3 nanobelts were investigated for the HER activites in 2.5 M H_2SO_4 solution. Our studies showed that incorporation of Ni in MoO_3 crystal structure leads to the formation of orthorhombic $Ni_xMo_{1-x}O_3$, phase for x ≥ 0.2. For x ≥ 0.2, monoclinic $NiMoO_4$ phase is formed along with the formation of trace quantities of MoO_3. The HER catalytic studies have been performed on these particles using 2.5 M H_2SO_4 solution as the electrolyte in a three electrodes cell assembly. The data suggest that the highest HER current densities are observed for $Ni_{0.2}Mo_{0.8}O_3$ and with further increase in the doping concentration beyond x = 0.2, the HER activities decrease. When compared with the HER performances of $SrMoO_4$ nanomaterials which were examined by us recently, all the $Ni_xMo_{1-x}O_3$ nanostructured materials have shown higher current densities. This give the confidence that there is a lot of scope for further tailoring and engineering molybdenum based oxides appropriately to reduce the HER over potential at higher current densities.

Acknowledgement:

This study was supported PSG Management. We gratefully acknowledge DST Nano mission, India for the financial support. K. K. A. thanks PSG Sons and Charities for the award of Research Fellowship.

References:

[1] R. F. de Souza, J.C. Padilha, R.S. Goncalves and J. Rault-Berthelot, Electrochem. Commun, 8, 211 (2006).
[2] M. G. Walter, E. L. Warren, J. R. McKone, S.W. Boettcher, Q. Mi, E. A. Santori and N. S. Lewis, Chem. Rev, 110, 6446 (2010).
[3] J. A. Turner, Science, 305, 972 (2004).
[4] A. Phuruangrat, D. J. Ham, S. Thongtem and J. S. Lee, Electrochem. Commun, 11, 1740 (2009).
[5] Z. Chen, D. Cummins, B. N. Reinecke, E. Clark, M. K. Sunkara, and T. F. Jaramillo, Nano Lett, 11, 4168 (2011).
[6] K. K. Aruna and R. Manoharan, Int. J. Hydrogen Energy, 38, 12695 (2013).
[7] L. Liao, J. Zhu, X. Bia, L. Zhu, M. D. Scanlon, H. H. Girault, and B. Liu, Adv. Funct. Mater, 23, 5326 (2013).
[8] D. Voiry, H. Yamaguchi, J. Li, R. Silva, D. C. B. Alves, T. Fujita, M. Chen, T. Asefa, V. B. Shenoy, G. Eda, and M. Chhowalla, Nature Materials, 12, 850 (2013).
[9] H. Vrubel and X. Hu, Angew. Chem. Int. Ed, 51, 12703 (2012).
[10] W. F. Chen, K. Sasaki, C. Ma, A. I. Frenkel, N. Marinkovic, J. T. Muckerman, Y. Zhu, and R. R. Adzic, Angew. Chem. Int. Ed, 51, 6131 (2012).
[11] E. J. Popczun, J. R. McKone, C. G. Read, A. J. Biacchi, A. M. Wiltrout, N. S. Lewis and R. E. Schaak, *J. Am. Chem. Soc*, 135 , 9267 (2013).
[12] R. Manoharan and J. B. Goodenough, J. Electrochem.Soc, 137, 910 (1990).
[13] A. Galal, N. F. Nada, S. A. Darwish, A. A. Fatah and S. M. Ali, J. Power Source, 195, 3806 (2010).
[14] R. Kalaiselvan and A. Gedanken, Nanotechnology, 20, 105602 (2009).
[15] H. Zheng and M. Mathe, Int. J. Hydrogen Energy, 36, 1960 (2011).
[16] J. O'M. Bockris and E.C. Potter, J. Electrocchem. Soc, 99, 169 (1952).
[17] Southampton Electrochemistry Group, Instrumental Methods in Electrochemistry, Wiley, New York, 1985.
[18] J. B. Goodgenough, R. Manoharan and M. Paranthaman, J. Am. Chem. Soc, 112, 2076 (1990).
[19] R. Manoharan, Proc. Indian Acad. Sci. (Chem Sci), 109, 1 (1997).

Ecological Structure Comparison Between Hydrogen Producing and Anaerobic Digestion Prokaryotic Consortia

Marcelo Navarro Díaz[1], Idania Valdez-Vazquez[2], Ana E. Escalante[1*]
[1]Laboratorio Nacional de Ciencias de la Sostenibilidad (LANCIS), Instituto de Ecología, Universidad Nacional Autónoma de México
[2]Instituto de Ingeniería, Unidad Juriquilla, Universidad Nacional Autónoma de México.
* anaelena.escalante@gmail.com

ABSTRACT

To date, high hydrogen yields by dark fermentation has been challenging because tight control of methanogenic microbial assemblies used as inocula, is needed and rarely achieved. This control is commonly seek through aggressive pretreatment of such inocula (e.g. activated sludge, agricultural disposal) which has been somewhat successful despite little knowledge on the effects on the microbial composition and dynamics that we believe is key to overcome challenges like long-term stability and up-scaling of production. Specifically, we propose that ecological analyses with a systemic view of microbial communities composition coupled with modeling of their dynamics and interactions among members is a key step towards a sustainable biohydrogen production. In this work, we reviewed scientific publications corresponding to 104 hydrogen producing (dark fermentation) and 99 methanogenic (anaerobic digestion) experimental settings and constructed databases including microbial composition and environmental conditions for each experiment (e.g. maximum H_2 yield, temperature, pH). With the hydrogen-producing database we performed multivariate (PCA and CCA) and indicator species analyses to investigate correlation of performance (hydrogen production) and culture conditions with key species in these communities. Comparison between hydrogen producing and methanogenic consortia was based on the inferred ecological (co-occurrence) networks derived from the databases. Networks were compared in terms of their robustness, modularity and other topological aspects in order to unravel important interactions between populations of these communities and unknown roles of some groups. From the multivariate analyses we found that richness of the microbial consortia can explain 20% of the variance among experiments, and that richer consortia present higher H_2 yields. We also found that Ruminococcaceae and Oxalobacteraceae families were associated to high hydrogen yields and represent important nodes in the reconstructed networks. In addition, topological features of the anaerobic digestion network suggest that these communities are more robust (i.e. less centrality, higher diameter, density and connectance) than hydrogen producing networks. Overall, multivariate and network analyses showed that more diverse communities (number of different microbial groups) have systemic properties that make them more robust in terms of long term stability.

Keywords: dark fermentation; ecological networks; biohydrogen production.

1. Introduction

The urgent necessity of finding alternatives to fossil fuels has driven the development of sustainable forms of producing less polluting forms of energy. Hydrogen is a high-energy fuel that can be used for generating electricity, in transport vehicles and as a domestic or industrial fuel while its combustion results mainly in water and NO_x traces[1]. Nowadays, hydrogen is mainly produced by high-energy demand processes like water electrolysis and methane reforming [2] so recent research has focused on less costly and more sustainable hydrogen production.

Dark fermentation is a very promising process to produce hydrogen at large scale. It involves the heterofermentation of carbohydrate-rich substrates by prokaryotic consortia and is derived from a more general process of anaerobic digestion that consists of four phases (hydrolysis, acidogenesis, acetogenesis and methanogenesis). In dark fermentation, inocula are pretreated in order to eliminate methanogenic populations and, as a consequence, the process stops at the acidogenesis phase where, along

with volatile fatty acids (VFA's) and alcohols, hydrogen is produced. Following the pretreatment, overall diversity is reduced mainly to Firmicutes species (specially *Clostridium* and *Bacillus* species due to their ability to form spores and resist pretreatment conditions [3]). Yet, pretreatment of inocula has little understood ecological consequences to the process stability (i.e. process collapsing or metabolic changes) and performance.

Dark fermentation allows the coupling of fuel production with sustainable waste management. In addition to hydrogen, VFA´s can be used in hydrogen production by photo-fermentation or for producing biopolymers [4] and the solid residues can be used as compost for agricultural fields. However, dark fermentation faces important obstacles that preclude large-scale implementation, namely, stability issues and low yields that make the process unprofitable.

To overcome many of the obstacles in biohydrogen production it is important to investigate the microbial component of bioreactors from an ecological and systemic perspective. Ecological interactions are important in the sense that they drive communities dynamics and impact organisms evolution [5], potentially leading to variations in reactors performance.

Current knowledge about microbial interactions in hydrogen-producing reactors is mainly focused in granules formation (e.g. *Streptococcus* species[6]), anoxic conditions maintenance (e.g. *Klebsiella* species[6]) and substrate hydrolysis (e.g. *Pseudomonas* and *Bifidobacterium* species[7]). Beyond this processes very little is known or has been investigated. For example, there is very little information on other types of interactions among microbial consortia of the hydrogen-producing bioreactors and we neither know which members or interactions are lost with pretreatments of anaerobic digestion consortia, nor how this impacts ecological processes. Moreover, there are not reviews that explore microbial composition beyond lists of members to evaluate potential interactions or correlations among bioreactor performance, microbial composition and culture conditions to better understand community dynamics.

Multivariate and networks analyses can be the first step into modelling and understanding complex biological systems like microbial communities. On the one hand, multivariate analysis are a classic approach to relate culture conditions and species composition that is underused in microbial ecology [8]. On the other hand, topological network analyses can help to understand the systems functioning [9] and graphically they help to make inferences about important relations between biological entities. A step further can be taken and mathematical models (i.e. Boolean or differential equations) can be designed to study the dynamic properties of such systems [10].

In this work we reviewed scientific publications corresponding to 104 hydrogen producing (dark fermentation) and 99 methanogenic (anaerobic digestion) experimental settings, with which information we constructed databases with composition and environmental conditions, and analyzed it quantitatively. The goals of this review were: (i) to investigate the statistical relationship between microbial compositions in hydrogen producing experiments and culture conditions; (ii) to reconstruct the co-occurrence networks of hydrogen and anaerobic digestion consortia and (iii) to compare both networks in order to find significant changes in their structure.

2. Materials and methods

2.1 Literature search

We conducted a key word search in SCOPUS using "dark fermentation" and "microbial" for hydrogen producing experiments and "anaerobic digestion" and "microbial" for methane producing experiments. We did not restrict the search in terms of publication dates but experiments consisting of two or more digestion phases were excluded from the analyses.

2.2 Data extracted from the literature

Attributes registered for the experiments of hydrogen producing reactors were: hydrogen yield, temperature, pH and microbial composition. For the experiments of anaerobic digestion reactors we only recorded microbial composition. For all cases, we only registered information at the time of maximum production (either hydrogen or methane) based on the assumption of equivalent

ecological status thus potential coexistence of the recorded members of the communities. When possible (43 out of 104 hydrogen producing experiments), the hydrogen yield data was transformed to mol H_2/mol hexose $_{consumed}$.

2.3 Microbial composition data

Microbial composition was analyzed in terms of presence/absence data based on 16S rDNA gene sequence differences as the standard for species identity in prokaryotes [11]. For experiments where no 16S rDNA gene sequences were available, we recorded the reported species identities without any further analysis. For these cases, we assigned a Genbank's accession number only if the closest relative (at least 97% 16S rDNA sequence identity) was also reported. If the similarity between the sequences was between 95 and 97% we recorded the genera identity and if it was between 90 and 95% we recorded the family identity. Then, we downloaded the sequences using the accession numbers and grouped them according to species identities using UCLUST[12] and QIIME[13] (95% similarity cut). The multivariate analyses and network inferences were performed at the species, genera, family and phyla levels, although we only could find and report ecological patterns at the family level.

2.4 Multivariate and statistical analyses

To visualize and identify patterns of environmental variables (ecological parameters of the reactors) and evaluate their correspondence with microbial composition, we followed multivariate and ordination approaches [8].We first standardized parameters of culture conditions and hydrogen yield via z-score transformations [8]. We then performed Principal Component Analysis (PCA) to visualize environmental variance of the different experiments, and Canonical Correspondence Analysis (CCA) was performed to model OTU (family level) response to selected environmental parameters. All these analyses were performed using vegan package[14] implemented in R software [15].

An indicator species analysis was carried out using community composition and hydrogen yield. In order to classify each experiment we categorized the hydrogen yield information using 3 quantiles: low, medium and high yield. We used R[15] and indicspecies package [16]for this analysis.

2.5 Network analysis

To investigate the network properties of the studied microbial communities we reconstructed co-occurrence networks using the complex networks reconstruction algorithm implemented in Sets2Networks [17]. For these analyses we used only experiments where two or more families were reported. In addition we considered as statically significant those correlations which probability value was 0.70 or higher. The average number of neighbors, clustering coefficient, network density, centralization and diameter were measured from the resulting networks using *networks analyzer* function implemented in Cytoscape software [18]. Other topological analyses such as modularity and average path length were measured performed using Gephi software [19]. Finally, we measured connectance as an important topological parameter for ecological networks [20] using the following formula:

$$Connectance = \frac{L}{S^2} \quad (3)$$

Where L is the number of links and S the number of nodes.

3. Results and Discussion

3.1 Multivariate and statistical analyses of microbial composition

Ordination and multivariate analyses showed some important correlations between bioreactor H_2 yield, culture conditions and microbial composition of biohydrogen reactors. On the other hand, PCA results (Figure 1) showed that although there is not a clear clustering of the different sites with respect to culture conditions, features like species richness and H_2 yield explained most of the variance observed among the bioreactors analysed. We identified three components that accounted for most of the variance observed among the analyzed experiment. The first component accounted for 35.08% of the total variation, mainly involving temperature and pH; the second component of the PCA accounted for 27.40% of the total variation, mainly involving H_2 yield;

and the third component accounted for 20.09% of the total variation mainly involving richness. It is worth to mention that reactors that were maintained at high temperature (maximum temperature: 70°C) tend to have a medium to high H_2 yields (Med: 1.6-2.16 mol H_2/ mol $hexose_{consumed}$; High: 2.16-3.2 mol H_2/ mol $hexose_{consumed}$). On the other hand, the CCA (Figure 2) showed that families present at high temperatures tend to be associated with some of the highest H_2 yields. CCA also showed that some families where associated with high hydrogen yields (Ruminococcaceae and Oxalobactereceae). These families were also linked to high hydrogen yield sites in the indicator species analysis (although this result was not statistically significant; p value= 0.405 and 0.31). Streptococcaceae, Bacillaceae and Pseudomonaceae were not associated with the highest yields of hydrogen. This is surprising since these families have members associated with granules formation and anoxic conditions maintenance that promote Clostridiaceae species growth [3]. It is worth mentioning that Streptococcaceae and Pseudomonadaceae were located at the same point on the graph meaning that they tend to co-occur in most experiments with different culture conditions.

Clostridiaceae family was not associated with any of the two CCA axes implicating first, that Clostridiaceae species can grow under a wide variety of environmental conditions, and second, that not all of its members produce hydrogen. These results are in accordance with some studies where high hydrogen yield is achieved even without inoculum pretreatment which reduces the diversity to mainly Clostridiaceae species[21]. Thermoanaerobacteraceae family correlated with low hydrogen yields, although it is known that its presence (in high temperature experiments) is associated with high hydrogen production [6][22]. Enterobacterecae family was related to high hydrogen yield which was expected since some species like *Klesiella pneumoniae* are associated with granules formation which may promote hydrogen producers growth [6]. Finally some other families like Flavobacteraceae where associated with high H_2 yield although little is known about their role in hydrogen production. It has to be noted here that the number of studies that were reviewed may not be numerically representative of all the taxonomical groups present in hydrogen producing bioreactors, thus caution should be taken regarding major generalizations.

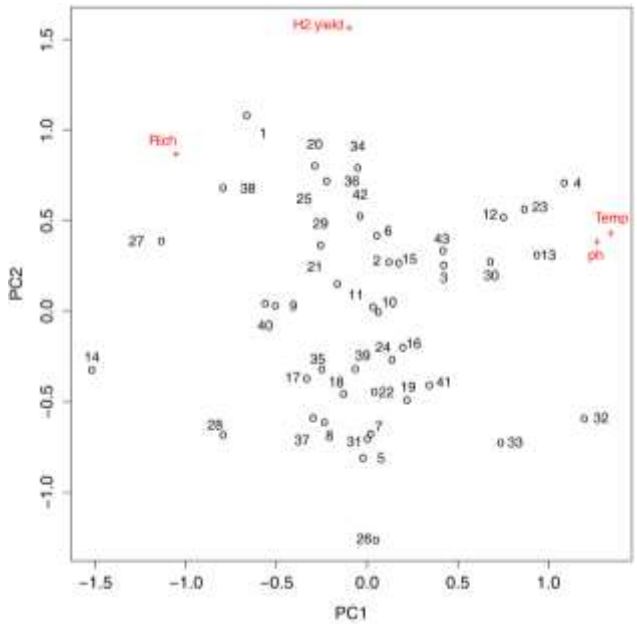

Figure 1. Biplot generated from a principal component analysis (PCA) of the standardized environmental variables (pH; Temperature, Temp; Maximum hydrogen yield, H_2 yield) and species richness (Rich). The different consortia (experiments) are shown in the graph as open circles (1-43). Vectors show scaled environmental variables. The first component of the PCA analysis accounted for 35.08% of the total variation, mainly involving temperature and pH. The second component of the PCA accounted for 27.40% of the total variation, mainly involving H_2 yield. The third component accounted for 20.09% of the total variation mainly involving richness.

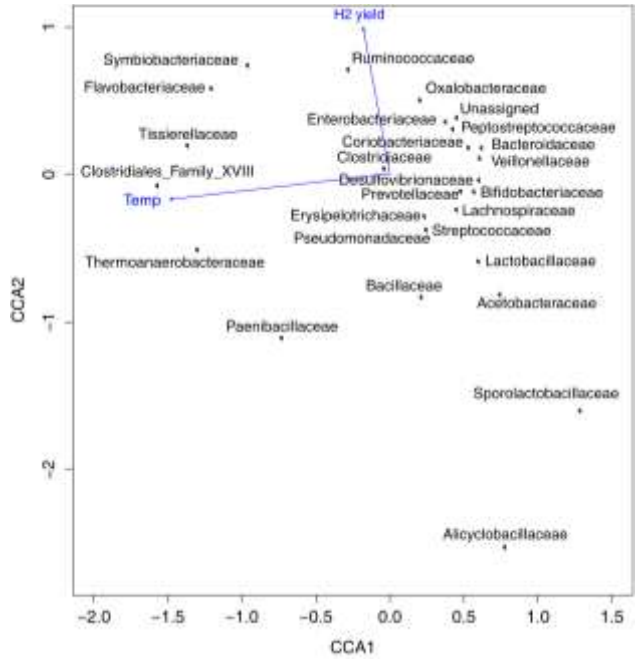

Figure 2. Canonical correspondence analysis (CCA) modeling OTUs (family level) response to environmental parameters of hydrogen producing bioreactors. Text corresponds to family names for the prokaryotes found in the experiments included in the analysis (n=43), and vectors show scaled environmental variables. Two explanatory variables are shown (Temp=temperature, H_2 yield=maximum hydrogen production). The first axis accounted for 4.4% of the total variation, mainly involving temperature. The second axis accounted for 7.34% of the total variation, mainly involving H_2 yield.

3.2 Network analysis

At the family level, the hydrogen producing consortia network (Figure 3) showed great centrality (centrality ranges from 0 to 1) being the Clostridiaceae node the most important of the network (given by its betweenness centrality values). Other important nodes in the network are Bacillacaeae and Thermonaerobacteraceae, the latter being especially important at high temperature cultures. The anaerobic digestion network (Figure 4) showed a very central node (Clostridiaceae) but in addition, other nodes are also significantly central (Methanosarcinaceae, Methanomicrobiaceae and Methanosaetaceae).

The topological attributes of both networks (Table 2) are similar, but anaerobic digestion network tends to be bigger, more connected, less modular and much less central. Both networks are almost of the same size (number of nodes and network diameter) which can be due to the lack of statically significant co-occurrence interactions that results from the sample size. Since anaerobic digestion consortia are more diverse (in terms of number of different microbial species) than the hydrogen consortia, more sets of experiments (samples) may be required to establish significance to certain co-occurrences. Connectance of the anaerobic digestion network is greater but both networks have low connectance, even when compared with macroorganisms networks [20]. This is not surprising since the data used in this review is not from high-throughput sequencing and the nodes where defined at a family level, both conditions greatly reduce the recovered diversity and can prevent the detection of co-occurrence patterns that might occur at lower taxonomic levels.

The intersection network (Figure 5) showed the 12 shared nodes and co-ocurrences between both networks. It is worth noting that in both networks the co-occurrence between Clostridiaceae, Bacillaceae and Thermoanaerobacteriaceae members was significant. This might indicate and important interaction between these three families. The presence of Lactobacillaceae members is expected due to the origins of many of the inocula and substrates (i.e. wastewater treatment plants, animal feces and food

waste). Also the presence of Ruminococcaceace members (gen: *Ruminococcus, Ethanoligenens*) in both networks in addition to its probable importance in hydrogen producing consortia requires further research. Oxalobacteraceae (gen: *Janthinobacterium*) along with Ruminococcaceae, are somewhat important nodes in the hydrogen network (given their degree=3 for both; the average degree for all the nodes in the network is 2.7 excluding Clostridiaceae). Although members of both families are commonly found in hydrogen producing experiments little is known about their ecological role in these communities.

Table 2. Topological attributes of the resulting networks at a family level.

Attribute	Hydrogen Network	Anaerobic digestion Network
Avg. number of neighbors	3.548	4.343
Avg. path length	2.043	2.112
Clustering coefficient	0.453	0.536
Connectance	0.057	0.05864
Modularity	0.312	0.210
Network density	0.118	0.128
Network centralization	0.836	0.676
Network diameter	4	4
Nodes	31	35
Unique nodes	19	23
Shared nodes	12	

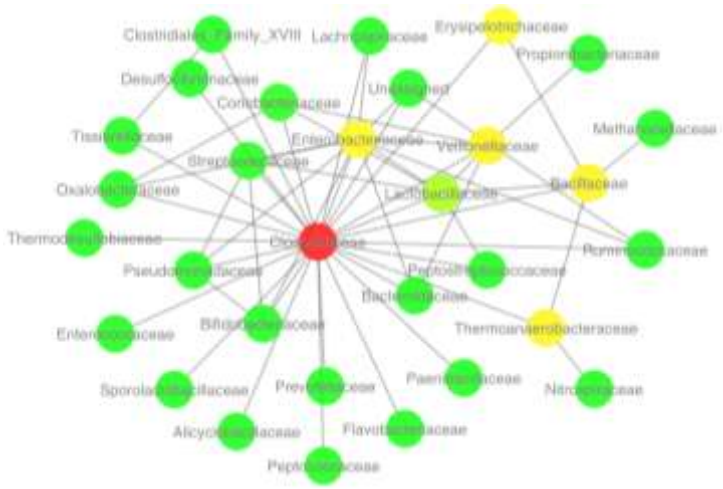

Figure 3. Co-occurence network of the hydrogen producing consortia at a family level. Color accounts to betweeness centrality of the nodes from low (green) to high values (red).

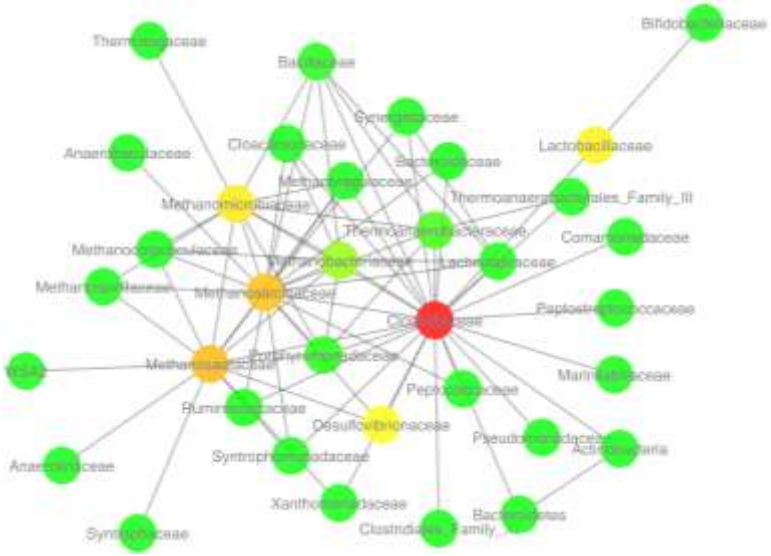

Figure 4. Co-occurrence network of the anaerobic digestion consortia at a family level. Color accounts to betweenness centrality of the nodes from low (green) to high values (red).

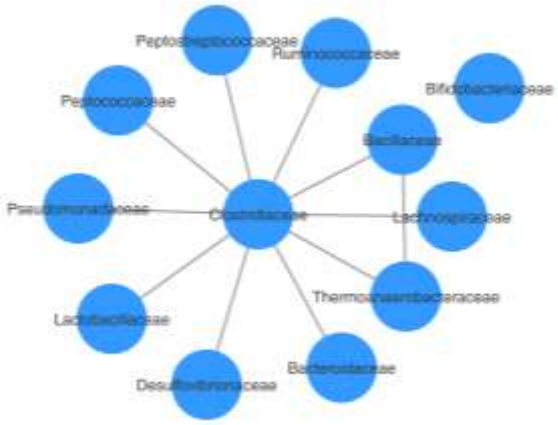

Figure 5. Intersection network between hydrogen producing and anaerobic digestion consortia.

4. Summary and perspectives

Overall, multivariate and network analyses showed that more diverse communities in hydrogen producing bioreactors have systemic properties that make them more robust in terms of long term stability.

- Multivariate and statistical analyses of hydrogen producing bioreactors showed correspondence of richness with high hydrogen yield. Although caution should be taken given relatively small sample size and methodological biases in species identification (mainly DGGE profiling), the reason behind this richness-high H_2 yield correspondence might be that, as more *Clostridium* species are present more chances that hydrogen is produced from a more wide variety of substrates [23].
- Multivariate Canonical Correspondence Analysis (CCA) identified Ruminococcaceae and Oxalobacteraceae families as associated to high hydrogen yields, and also conformed important nodes in the reconstructed networks. Further research has to be conducted to determine the role these groups have in hydrogen consortia since little is known at this respect. Also, it remained unclear the role in hydrogen production of some families that are associated with improving conditions in the bioreactors. Apparently, these families have a positive impact not only in hydrogen producing microorganisms but also on "cheaters" that take advantage from these conditions.
- Network analysis did not show major topological differences between hydrogen-producing and methanogenic consortia. However, the anaerobic digestion (methanogenic) network had topological features that suggest that these communities are more robust (i.e. less centrality, higher diameter, density and connectance) [20]. This is concordant with the hypothesis that more rich communities tend to be more robust in terms of resilience and resistance (although in microbial communities the evidence for this is mixed) [24].

Finally, it is important to remark that although big efforts have been made in the research community in order to explore hydrogen-producing microbial consortia, it is evident that to gain a deeper understanding a different approach should be followed. Specifically, high-throughput sequencing should be considered when investigating these consortia because in that way we can capture, with more detail and deeper sampling, information about its composition and the abundance of the members of these communities. With this information we can discover patterns at a finer scale and we could be able to model mathematically these communities, which is important since we can use models to predict changes in reactors performance given some information about culture conditions. Also, we can use this information in the construction of engineered synthetic microbial consortia that could significantly improve this process performance and profitableness.

5. Acknowledgements

This work was funded by Consejo Nacional de Ciencia y Tecnología (CONACyT grant 16891) as a scholarship to MN (No. 21236).

6. References

[1] Momirlan M, Veziroglu T. The properties of hydrogen as fuel tomorrow in sustainable energy system for a cleaner planet. Int J Hydrogen Energy 2005;30:795–802.

[2] Salvi BL, Subramanian K a., Panwar NL. Alternative fuels for transportation vehicles: A technical review. Renew Sustain Energy Rev 2013;25:404–19.

[3] Show KY, Lee DJ, Tay JH, Lin CY, Chang JS. Biohydrogen production: Current perspectives and the way forward. Int J Hydrogen Energy 2012;37:15616–31.

[4] Lee WS, Chua ASM, Yeoh HK, Ngoh GC. A review of the production and applications of waste-derived volatile fatty acids. Chem Eng J 2014;235:83–99.

[5] Freilich S, Kreimer A, Meilijson I, Gophna U, Sharan R, Ruppin E. The large-scale organization of the bacterial network of ecological co-occurrence interactions. Nucleic Acids Res 2010;38:3857–68.

[6] Hung C-H, Chang Y-T, Chang Y-J. Roles of microorganisms other than Clostridium and Enterobacter in anaerobic fermentative biohydrogen production systems--a review. Bioresour Technol 2011;102:8437–44.

[7] Weiland P. Biogas production: current state and perspectives. Appl Microbiol Biotechnol 2010;85:849–60.

[8] Ramette A. Multivariate analyses in microbial ecology. FEMS Microbiol Ecol 2007;62:142–60.
[9] Newman M. The structure and function of complex networks. SIAM Rev 2003;45:167–256.
[10] Faust K, Raes J. Microbial interactions: from networks to models. Nat Rev Microbiol 2012;10:538–50.
[11] Stackebrandt E, Goebel BM. Taxonomic Note: A Place for DNA-DNA Reassociation and 16S rRNA Sequence Analysis in the Present Species Definition in Bacteriology. Int J Syst Bacteriol 1994;44:846–9.
[12] Edgar RC. Search and clustering orders of magnitude faster than BLAST. Bioinformatics 2010;26:2460–1.
[13] Caporaso J, Kuczynski J, Stombaugh J. QIIME allows analysis of high-throughput community sequencing data. Nat Methods 2010;7:335–6.
[14] Oksanen J, Blanchet G, Kindt R, Legendre P, Minchin PR, O'Hara RB, et al. vegan: Community Ecology Package 2013.
[15] R Core Team. R: A Language and Environment for Statistical Computing 2013.
[16] De Cáceres M, Legendre P. Associations between species and groups of sites: indices and statistical inference. Ecology 2009;90:3566–74.
[17] Clark NR, Dannenfelser R, Tan CM, Komosinski ME, Ma'ayan A. Sets2Networks: network inference from repeated observations of sets. BMC Syst Biol 2012;6:89.
[18] Shannon P, Markiel A, Ozier O, Baliga NS, Wang JT, Ramage D, et al. Cytoscape: a software environment for integrated models of biomolecular interaction networks. Genome Res 2003;13:2498–504.
[19] Bastian M, Heymann S, Jacomy M. Gephi: an open source software for exploring and manipulating networks. ICWSM 2009:361–2.
[20] Dunne J a, Williams RJ, Martinez ND. Food-web structure and network theory: The role of connectance and size. Proc Natl Acad Sci U S A 2002;99:12917–22.
[21] Kim D-H, Wu J, Jeong K-W, Kim M-S, Shin H-S. Natural inducement of hydrogen from food waste by temperature control. Int J Hydrogen Energy 2011;36:10666–73.
[22] Rittmann S, Herwig C. A comprehensive and quantitative review of dark fermentative biohydrogen production. Microb Cell Fact 2012;11:115.
[23] Tracy BP, Jones SW, Fast AG, Indurthi DC, Papoutsakis ET. Clostridia: the importance of their exceptional substrate and metabolite diversity for biofuel and biorefinery applications. Curr Opin Biotechnol 2012;23:364–81.
[24] Shade A, Peter H, Allison SD, Baho DL, Berga M, Bürgmann H, et al. Fundamentals of microbial community resistance and resilience. Front Microbiol 2012;3:417.

Composite sPEEK-TPyP Membranes Development for Portable Applications

A Carbone[1*], A. Saccà[1], R. Pedicini[1], I. Gatto[1], M.A. Castriciano[2], L. Monsù Scolaro[3]

[1] Istituto di Tecnologie Avanzate per l'Energia "Nicola Giordano", via S. Lucia sopra Contesse 5, 98126 Messina , Italy.
[2]Istituto per lo Studio dei Materiali Nanostrutturati, c/o Dipartimento di Scienze Chimiche Viale Ferdinando Stagno D'Alcontres n.31, 98166 Villaggio S. Agata, Messina, Italy
[3]Dipartimento di Scienze Chimiche, University of Messina Viale Ferdinando Stagno D'Alcontres n.31, 98166 Villaggio S. Agata, Messina, Italy.
[*]Tel: +39090624273; e-mail: alessandra.carbone@itae.cnr.it

ABSTRACT

Composite membranes based on sulphonated Polyetheretherketone (sPEEK) and 5,10,15,20-tetra(4-pyridyl)porphyrin (TPyP) were developed for portable applications. A sulphonation degree of 65% and different weight percentages (0-5%) of TPyP porphyrin were used. The membranes were realized with a standardized doctor-blade method, thermally and chemically treated. Physical-chemical characterizations were carried out in terms of spectroscopic studies (UV-Vis and Fluorescence), ionic exchange capacity, water uptake, dimensional variations and swelling, structural and morphological analyses. Moreover, proton conductivity measurements at a temperature useful for portable applications, were performed. SEM analyses of composite membranes highlight a similar morphology to the pristine sPEEK membrane. XRD profiles of composite membranes correspond to the amorphous pattern of sulphonated polymer, while the fundamental peaks of TPyP were completely suppressed. This effect indicates that a good interaction occurs between the filler and the polymer matrix. This interaction, in particular between nitrogenous groups of porphyrin and sulphonic groups of polymer, leads to slight changes in physico-chemical properties and a proton conductivity respect to the sPEEK membrane, used as a reference. In particular, the membrane with the lowest loading (~1 wt%) of TPyP, shows slightly lower water uptake and unaltered λ values than the reference membrane, resulting in quite unaltered proton conductivity. This behavior could be attributed to the interaction of porphyrin groups and polymer matrix able to contribute to the proton conduction mechanism. In addition, the developed membranes were characterized in a PEFC 25cm^2 single cell to verify their applicability in portable devices. Also in this case the sample with the lowest loading of TPyP is the best compromise for a real application.

Keywords: Sulphonated PEEK; TPyP; PEFC.

Introduction

Fuel cells are clean and highly efficient electrochemical systems for energy conversion, that are fed by hydrogen in advanced systems with the highest performance, or by alternative fuels (e.g. methanol or ethanol) with significant reduction in performance [1]. Among the existing typologies of fuel cells, the system that has attracted most interest is the Proton Exchange Membrane Fuel Cell (PEMFC) due to its wide range of power density ($1x10^{-3}$-100 kW), simplicity of components and its friendly user operating conditions.

A polymer electrolyte membrane fuel cell (PEMFC) is composed of a membrane able to conduct protons, between the anodic and cathodic compartments, separating two catalytic electrodes where the fuel oxidation and the comburent reduction take place.

Due to the high energy density with respect to the traditional batteries, fuel cells are particularly suitable for the fabrication of portable systems, more efficient and less bulky than currently available systems.

The Portable Fuel Cell systems tend to use either DMFC (direct methanol fuel cells) or PEFC (polymer electrolyte fuel cells fed by hydrogen) technology, even if the DMFC are nowadays the most diffused.

However, several problems to be solved, such as catalyst poisoning during methanol oxidation reaction and methanol crossover through solid-polymer-electrolyte membrane, limit their commercialization [2]. The most used polymer electrolyte membrane is Nafion®, that has high proton conductivity, chemical and mechanical stability, but suffers a high methanol permeability, that drastically reduces the performance. To solve this problem, associated to a high production cost of this polymer, the research aims at developing low-cost and highly efficient proton conducting membranes to be used as polymer electrolytes for portable fuel cells fed with hydrogen and air under air-breathing conditions.

The development of poly-aromatic based membranes plays a key role as an alternative to Nafion® membranes [3-7]. A wide literature exists on this class of polyelectrolyte but some problems should be overcome such as a low proton conductivity at reduced relative humidity, the mechanical stability and lifetime. One of the most used polymer membrane is based on sulphonated polyetheretherketone (s-PEEK) with a sulphonation degree in the range 40-70%. Compared to the membranes reported in the state-of-the-art, the alternative membranes exhibit reduced cost (by a factor of about 40); better mechanical properties; improved stability to radical species; reduced hydrogen crossover; similar unit area resistance.

In addition to the above mentioned characteristics, nowadays, the research is moving on the development of membranes containing nitrogenous groups that promotes specific acid-base interactions between functional amino-sulphonic groups, by improving the proton conductivity [8-10]. In fact, the sulphonic acid groups interact with the nitrogenous base by forming hydrogen bridges, protonation of the nitrogen sites and polysalts formation. Particular attention is addressed to a class of modified membranes containing porphyrins as nitrogenous sources, in which porphyrin protons are bonded to the ion channel of the SPEEK membrane to form a hydrogen ion sieve structure, resulting in a higher proton transmissibility.[11-15]. This class of porphyrin is able to aggregate in different form and creates a network as a function of the used solvent, the aim of the work is to exploit this ability in a polymetric matrix containing polar functional groups to create specific interactions that stabilize the polymer maintaining a proton path for the conduction mechanism. In this work composite membranes based on sulphonated Polyetheretherketone (sPEEK) and 5,10,15,20-tetra(4-pyridyl)porphyrin (TPyP) were developed and tested for their use in portable applications.

Experimental

2.1 Polymer sulphonation

A Polyetheretherketone (Victrex PF450) was functionalized in concentrated sulphuric acid according to a standardized procedure, reported elsewhere [16], in order to obtain a a sulphonation degrees (SD) of 65%.

2.2 Membrane Preparation

Membranes were prepared with a doctor-blade standardized procedure [16] Composite membranes were further prepared using the sulphonated polymer. The 5,10,15,20-tetrakis(4-pyridyl)-21H,23H-porphine (TPyP) was purchased from Aldrich Chemical Co. and used without further purification. The porphyrin was added to the polymer in different weight percentages 0.77, 1.5 and 5wt% in DMAc solution. This latter, used for membrane recasting procedure, ensures the presence in solution of the porphyrin in monomeric form and avoid the formation of aggregates. In order to better solubilize the porphyrin, the resulting mixture was stirred for 1 hr before to be added to the polymeric solution. All the membranes were dried at 80°C for 3 hours then detached from the glass by impregnation with H_2O. A thermal treatment was carried out at 120°C for 16 hrs, followed by an acid treatment (1M H_2SO_4) at 60°C to purify them of any residual solvent and activate groups for proton ion exchange for the coordination of water molecules. Membranes with a thickness ranging from 50 to 70 □m were obtained.

2.3 Polymers and membranes X-ray analyses (XRD)

The X-ray powder diffraction (XRD) analyses were performed by using a Philips X-ray automated diffractometer (model PW3710) with Cu K□ radiation source. The 2θ Bragg angles were scanned between 5°and 100° 2□□

2.4 UV-Vis and Fluorescence

UV/Vis spectra were obtained on a Hewlett-Packard mod. 8453 diode array spectrophotometer directly on the membranes. Fluorescence measurements were carried out on a Jasco mod.FP-750 spectrofluorimeter.

2.5 SEM–EDX analyses

A field emission Scanning Electron Microscope (Philips mod. XL30 S FEG) was used to investigate the cross-section morphology of the membranes. A gold coating was used to avoid sample charging and to permit electronic conduction. Samples for cross-section were prepared dipping the membrane in liquid Nitrogen and breaking the samples to have a perfect fracture.

2.6 Ion Exchange Capacity (IEC)

An acid-base titration was carried out to determine the membrane IEC_m (meqSO_3H/mg) and is based on the neutralization of H^+ ions, belonging to the acid group -SO_3H. The experimental procedure is described elsewhere [6] The IEC is calculated using the following formula:

$$IECm = \frac{Vtit \bullet [M]}{mdry} \qquad (1)$$

where:
Vtit = titrant volume (ml);

[M] = titrant molarity;
m_{dry} = dry mass of the sample (g);
To determine the interaction between SPEEK and TPyP, IEC of SPEEK polymer (IEC_p) within the composite membrane was determined considering the Polymer Fraction (PF) calculated from Eq. (2):

$$IECp = \frac{IECm}{PF} \quad (2)$$

where IEC_m is the experimental IEC of the membrane

2.7 Water uptake and lambda

The ability to retain the water of the membrane (Wup,%) is usually calculated from the difference in weight between the dried and the wet sample. The wet weight (m_{wet}) is determined after immersion of the sample in distilled water at room temperature for 24 hours, while for the dry weight (m_{dry}), the sample is dried in a vacuum oven at 80°C for 2 hrs. The percentage of water absorbed is given by the following expression:

$$wu = \frac{mwet - mdry}{mdry} 100 \quad (3)$$

The λ value (expressed as moles H_2O/moles-SO_3H) was calculated through the water uptake and IEC values ratio, both expressed in moles:

$$\lambda = \frac{mol\ H2O}{mol\ SO3H} \quad (4)$$

Through this parameter is possible to evaluate the capability of the SO_3H groups in the composite membranes to coordinate water molecules.

2.8 Proton conductivity

The conductivity was measured at 30°C and full humidification (100% RH) using a commercial cell (Bekktech). The measure is carried out in the longitudinal direction of the sample with a four-probe technique and calculated using the formula:

$$\sigma = \frac{L}{RWT} \quad (5)$$

Where:
L = 0.425 cm , constant distance between the two Pt electrodes;
R = resistance in Ω;
W = sample width in cm;
T = sample thickness in cm.

2.9 Fuel cell tests

Home-made electrodes were prepared by a spray technique described in the referenced paper [17] and coupled to the membranes to obtain MEAs. The same Pt loading (0.5mg/cm^2) in the catalytic layer was used for both anodes and

cathodes and a 50% Pt/C (Alfa Aesar) was used as an electrocatalyst. A Sigracet-24BC (SGL group) was used as a gas diffusion layer. Membranes and electrodes were assembled by cold-pressing.
Fuel cell tests, in terms of polarisation curves, were carried out in a commercial 25cm^2 single cell at 30°C, with fully humidified H_2/air and dry H_2/humidified air at 1 absolute Bar. The gas fluxes were fixed at 1.5 and 2 times the stoichiometry at the current work for hydrogen and air, respectively.
Electrochemical impedance spectroscopy (EIS) was performed by using a potentiostat/galvanostat (AUTOLAB PGSTAT30) equipped with a frequencies response analyzer (FRA module) and a 20A BOOSTER. All impedance measurements were performed in the potentiostatic mode of fuel cell operation at a constant potential of 850mV. The impedance spectra were obtained varying the frequency of the voltage perturbation signal from 0.1 Hz to 100 kHz, by using amplitude of 10mV for the perturbing signal.

Results and discussion

The membranes were first characterized in terms of XRD profile, to understand the good dispersion of porphyrin in the polymeric matrix. In Fig.1 is reported the comparison among the XRD patterns of pristine SPEEK membrane, composite membranes with different amount of of tetra(4-pyridyl)porphine (TpyP, hereafter) and TPyP powder. It is visible the typical amorphous profile of the sulphonated polymer centred at about 18° 2θ, that remains quite unaltered after the TPyP introduction. Moreover, no peak of the TPyP is visible in composite membranes, due to their preparation procedure. In fact the TPyP is solubilized within the confined membranes environment and it is present or in monomeric form or in small oligomers/aggregates without a crystalline structure.

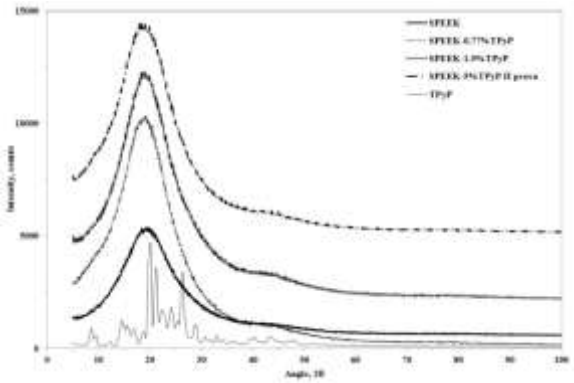

Fig.1 XRD patterns of developed membranes compared to TPyP

Due to their structural features, i.e. the extended planarity, the porphyrins favour the formation of van der Waals, π - stacking and hydrophobic interactions, that allow, in appropriate experimental conditions, the formation of dimers, trimers small oligomers or larger aggregates. The aggregation phenomena for this class of molecules are accompanied by characteristic changes in their spectroscopic properties, i.e. bathochromic or ipsochromic shifts of the absorption and emission bands, Beer law's deviation, quenching of the luminescence. In this framework, in order to exclude the presence in the membranes of porphyrin aggregates or small oligomers spectroscopic investigation on the composites were performed.

The photophysical properties of this porphyrin in its monomeric form have been reported in organic solvents. [18,19] while a report on its aggregation behaviour in mixed organic-aqueous media pointed out the elusive nature of the aggregates [20]. The TPyP is insoluble in aqueous solution where it is readily soluble under acidic conditions. The X-ray structure of its fully protonated form has been reported.[21]. The TPyP porphyrin solubilized in organic solvent show in the UV/Vis spectra a B-band centred at 417 nm and 4 Q bands in the absorption region 500-700 nm. The fluorescence emission spectra evidence two typical emission bands centred at 653 and 713 nm [18]. In Figs. 2 and 3 the UV-Vis and fluorescence emission spectra of SPEEK-5% TPyP are shown. This profile remains unchanged for all the investigated samples.

Due to high porphyrin concentrations it was not possible to detect the B-band typical for this porphyrin. The extinction spectra of the membranes, obtained by using DMAc as a casting solvent, show the presence of 4 Q-bands centred at 523-564-597 and 648 nm. The fluorescence emission spectrum show two typical emission bands for this porphyrin centred at 662 and 718 nm, respectively.

This spectroscopic behaviour, especially the presence of 4 Q bands, points out the presence of an unprotonated porphyrin core, typical of the free base porphyrin (D2h, symmetry). [22] The red shift of Q-bands in extinction spectrum as well as fluorescence emission bands with respect porphyrin in solution may be ascribed to the different polarity of the environment or to the confined micro-enviroments in which the TPyP is located [23].

Independently, from the membrane thickness and from the porphyrin loads, this chromophore embedded in the membranes exhibits good stability and chemical resistance to thermal annealing and acidic treatment. In fact, the spectroscopic features before and after the treatments remain unchanged for all investigated samples. The reported spectra are related to treated membrane having the highest amount of TPyP (5wt%) and are perfectly overlapped to the other samples.

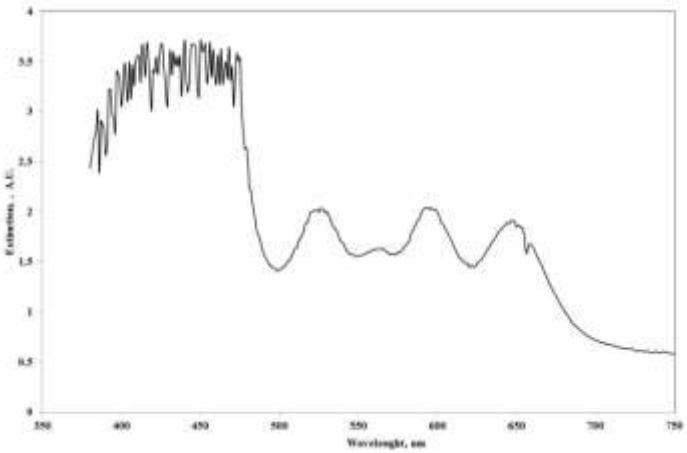

Fig.2 UV-VIS spectrum of SPEEK-5% TPyP

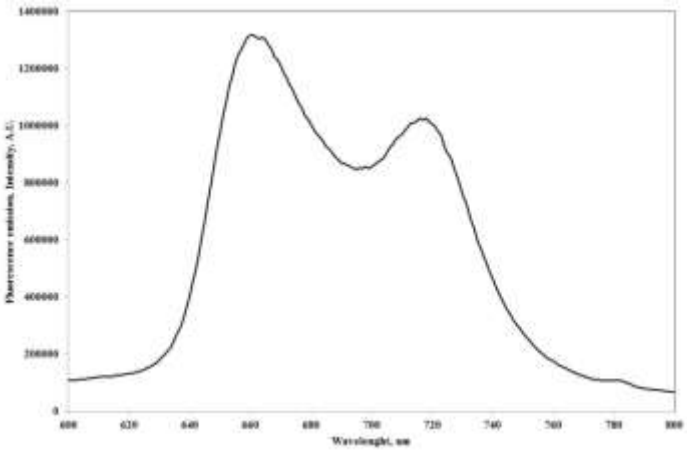

Fig.3 Fluorescence emission spectrum of SPEEK-5% TPyP

SEM analyses were performed to check the morphology of composite membrane compared to pristine SPEEK one (Fig.4). In both cases a dense and homogeneous structure was highlighted, meaning that no agglomeration of TPyP occurred, even for membrane with the highest TPyP content (reported in Fig.4b).

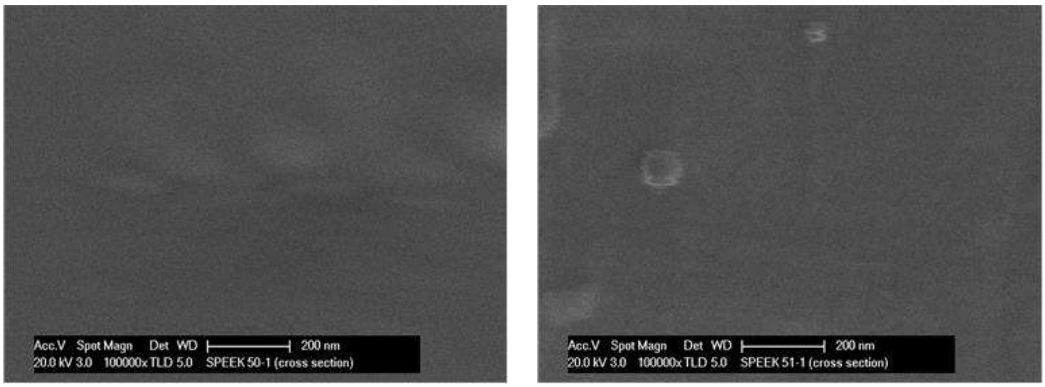

Fig.4 SEM analysis of a) SPEEK membrane b) SPEEK-5%TPyP membrane

To verify the influence of TPyP on the proton exchange properties of SPEEK, the experimental (IEC_m) and the calculated IEC_p were compared and reported in Fig.5.

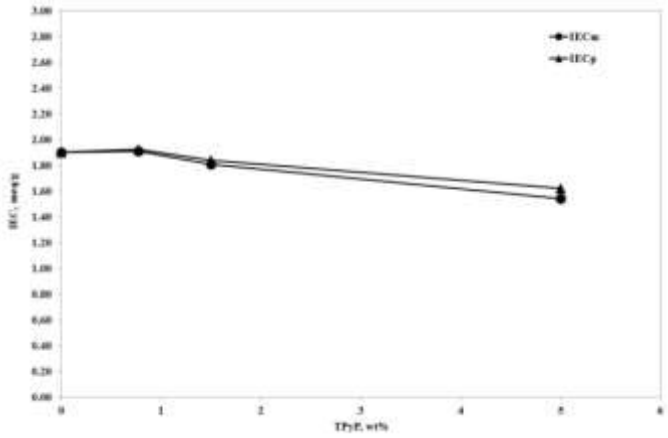

Fig.5 IEC behaviour as a function of TPyP loading

The IEC_m decreases with the increase of porphyrin amount, because the TPyP has not own exchangeable protons. In addition, the ability of SPEEK polymer to form interactions with nitrogenous groups is known and elsewhere reported [16]. Also with the TPyP introduction, specific interactions between sulphonic and nitrogenous groups are present, as highlighted from IEC_p data. This values were calculated by considering the theoretical amount of TPyP introduced in the membranes and the obtained values are related to the SPEEK polymer in the composite membranes. As reported in Fig. 5, the IEC_p is still lower than pristine SPEEK membrane, indicating that interactions occurred that limit the proton exchange capacity.

The behaviour of water uptake (w.u.) and dimensional variation (area %) is shown in Fig.6, as a function of the TPyP content.

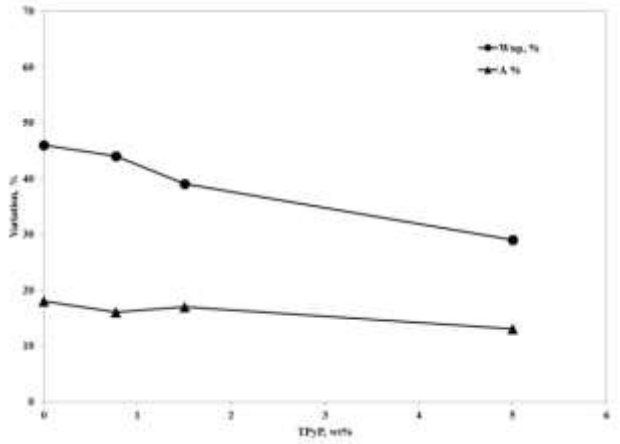

Fig.6 Water uptake and area variation as a function of TPyP amount

In accordance to IEC behaviour, both w.u. and A% decrease by increasing filler loading, meaning that the TPyP interaction with the sulphonic groups of the PEEK reduces the swelling of the polymeric matrix. An interesting trend is highlighted in Fig.7, where is reported the proton conductivity as a function of the lambda values. Because of the lambda values is generally related to the hydration of sulphonic groups of the polymer, the capability to maintain unaltered the properties to coordinate water in composite membranes is an important feature to be considered. As expected, the proton conductivity increases with the increase of water content but sample SPEEK-0.77% TPyP maintains its proton conductivity quite similar to pristine recast SPEEK (values at λ=13), even if a slight reduction of w.u. and A% is found. Moreover, if compared to the other investigated samples, it has the ability to retain water in drastic conditions (dry gas) and consequently to maintain a proton conduction, as reported in Tab.1.

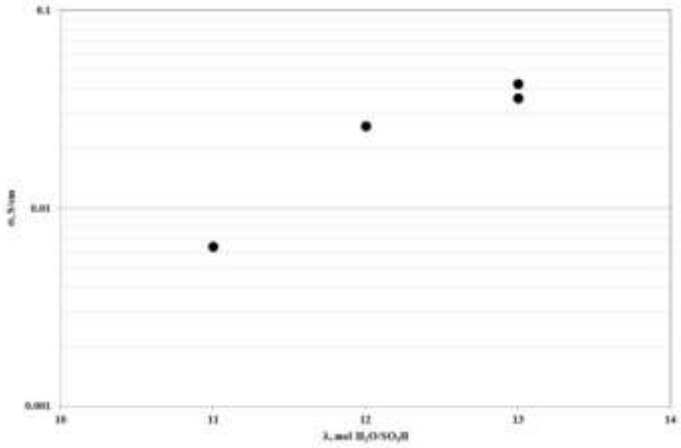

Fig.7 Proton conductivity as a function of lambda values

In fact, in Tab.1 the proton conductivity data measured at 30°C, 100%RH and dry hydrogen are compared. Because the setup of the measurement is different from fuel cell, in which the membrane is constrained in the MEA, in this kind of measurement the sample is more available to hydration changes and can prompt respond to these changes. The SPEEK-0.77 TPyP sample is the only that maintains a suitable hydration to reach a proton conduction,

due to its intrinsic properties. The other samples showed a drop in the proton conduction with a reported value <0.01 mS/cm, under the instrument sensitivity limit, due to a rapid de-hydration.

Tab.1 Proton conductivity values at different operative conditions

		Proton Conductivity at 30°C, mS/cm	
Membrane	λ, mol H_2O/SO_3H	100%RH	Dry
SPEEK	13	42	<0.01
SPEEK-0.77%TPyP	13	36	10
SPEEK-1.5%TPyP	12	26	<0.01
SPEEK-5%TPyP	11	7	<0.01

To verify the single cell performance useful for portable applications, the composite membranes, were tested in the operative conditions of low temperature and pressure and compared to recast SPEEK. In Fig.8, the polarisation curves at 30°C, 1 abs. bar and full hydrated gases are shown. Since the useful voltage range, for a real application, is between 0.6-0.7 V, the I-V curves are cut off at 200mA/cm^2. The performance of composite membranes are in accordance to the previous chemical-physical and ex-situ electrochemical data, in fact the performance decreases with the increase of TPyP amount. The SPEEK-0.77% TPyP shows slight higher performance than SPEEK recast membrane.

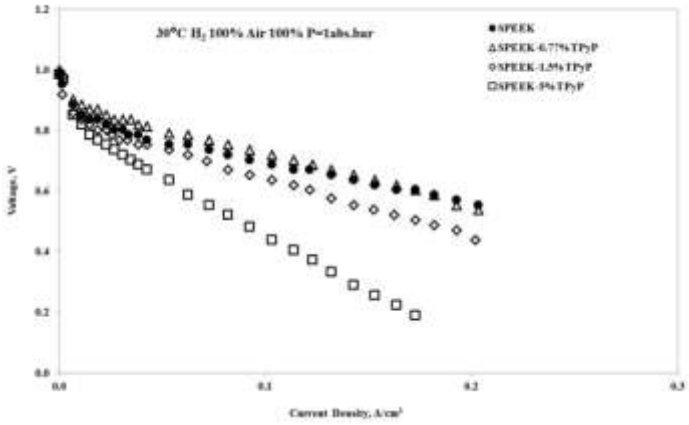

Fig.8 I-V curves comparison at low T, P and 100%RH H_2/air

All the investigated samples present good OCV values (Tab.2), confirming the dense structure of the membranes. The R_s values, obtained from EIS spectra, are in general high and they increase with the amount of TPyP. The power density at 0.7 V is reported in tab.2, it is still evident the benefit of the small amount of TPyP (0.77%) in the polymer matrix, in fact a power density of 80mW was reached against 65mW of SPEEK.

Tab.2 Electrochemical data at 100%RH H_2/air

Membrane	OCV	Rs (EIS)	PD @ 0.7V
	V	Ωcm^2 850mV	mW/cm^2
SPEEK	0.985	0.612	65

SPEEK-0.77%TPyP	1.000	0.672	80
SPEEK-1.5%TPyP	0.999	0.855	50
SPEEK-5%TPyP	1.000	1.852	24

To simulate the real application in portable devices where gases are not humidified, operative conditions were changed in dry H_2/100%RH air, supposing a hydrated cathode for the atmospheric humidity (air-breathing) and the water reaction formation. The polarisation curves are reported in Fig.9.

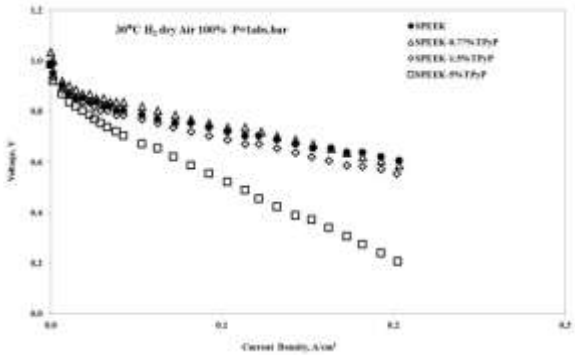

Fig.9 I-V curves comparison at low T, P and dry H_2/100%RH air

Also in this case the trend is similar to the full humidification. The performance slightly increased despite the dry condition of the anode. This behaviour could be probably caused by a not good water management in full humidification operative conditions, that affects the performance.

Tab.3 Electrochemical data at dry H_2/100%RH air

Membrane	OCV V	Rs (EIS) Ωcm^2 850mV	PD @ 0.7V mW/cm^2
SPEEK	0.985	0.590	85
SPEEK-0.77%TPyP	1.018	0.780	93
SPEEK-1.5%TPyP	0.985	0.720	65
SPEEK-5%TPyP	1.000	2.367	29

Also in these operative conditions the OCV data remains good and the power density is increased, with the highest value of 93 mW/cm^2 at 0.7V for membrane containing 0.77wt% TPyP (Tab.3).

Anyhow, the SPEEK-0.77% TPyP membrane represents the best compromise between chemical-physical properties and electrochemical performance. Taking into account that for a portable device, such as smartphone or tablet or handheld radio, could be sufficient a power of about 20W, the SPEEK-0.77 TPyP could be considered a good candidate to be used in a small stack for a real application.

Summary and perspectives

Composite membranes based on sulphonated Polyetheretherketone (sPEEK) and 5,10,15,20-tetra(4-pyridyl)porphyrin (TPyP) were developed for portable applications. A sulphonation degree of 65% and different weight percentages (0-5%) of TPyP porphyrin were used for membranes realization. A complete chemical-physical and electrochemical characterization was carried out. The TPyP introduction does not modify the structural and morphology properties of the polymer while some changes occurs in the IEC, water uptake, dimensional variation and lambda values. This behavior is attributed to the formation of interactions between the sulphonic groups of the polymer and the nitrogenous group of the TPyP. This interaction with a hydrogen sieve material such as TPyP, produces a not aggregated form of the TPyP but a good interaction with the polymeric matrix with a network formation. The proton conductivity of the membrane with the lowest loading (0.77wt% TPyP) does not change respect the pristine SPEEK reference, despite a reduction of water uptake and area % and is maintained in the same order of magnitude in dry conditions. In addition, during fuel cell operation at low temperature, pressure and dry hydrogen, this sample supplies the best power density. The properties of this membrane configuration renders it a good candidate for a real application in portable devices.

References

[1] Fuel Cell Technology Handbook. Edited by Gregor Hoogers. CRC PRESS U.S. 2003.

[2] S. Meenakshi, S. D. Bhat, A. K. Sahu, P. Sridhar, S. Pitchumani, Modified Sulfonated Poly(etheretherketone) Based Mixed Matrix Membranes for Direct Methanol Fuel Cells, FUEL CELLS, 2013, 13, 5: 851–861.

[3] D. J. Jones, J. Rozière, Recent advances in the functionalisation of polybenzimidazole and polyetherketone for fuel cell applications, J. Membr. Sci., 2001,185: 41-58.

[4] G. Alberti, M. Casciola, L. Massinelli, B. Bauer, Polymeric proton conducting membranes for medium temperature fuel cells (110–160°C), J. Membr. Sci, 2001 185: 73-81.

[5] K.D. Kreuer, Hydrocarbon membranes, Handbook of Fuel Cell Technology, ed. W Vielstich, A.Lamm, H. Gasteiger, Wiley & Sons, London, 2003, 420-435.

[6] K. D. Kreuer, On the development of proton conducting materials for technological applications, Solid State Ionics, 1997,97: 1-15.

[7] A. Carbone, R. Pedicini, G. Portale, A. Longo, L. D'Ilario, E. Passalacqua, Sulphonated poly(ether ether ketone) membranes for fuel cell application: Thermal and structural characterisation, J. Power Sources, 2006, 1, 163: 18-26.

[8] J. Kerres, W. Cui, Acid-base polymer blends and their application in membrane processes, Patent US 6,300,381 B1, 2001.

[9] Y. Gao, G.P. Robertson, M.D. Guiver, X. Jian, S.D. Mikhailenko, S. Kaliaguine, Proton exchange membranes based on sulfonated poly(phthalazinone ether ketone)s/aminated polymer blends, Solid State Ionics, 2005,176: 409-415.

[10] Zicheng Zuo, Yongzhu Fu and Arumugam Manthiram, Novel Blend Membranes Based on Acid-Base Interactions for Fuel Cells, Polymers 2012, 4: 1627-1644;.

[11] Yu Fei, ZHOU Zhen-Tao, Zhang Guo Ge, Modified sulfonated poly ether ether ketone (SPEEK) membrane applied to direct methanol fuel cell (DMFC) and preparation method of SPEEK membrane Patent CN 102020781 B, 2012.

[12] Y. Diskin-Posner and I. Goldberg "From porphyrin sponges to porphyrin sieves: a unique crystalline lattice of aquazinc tetra(4-carboxyphenyl)porphyrin with nanosized channels" Chem. Commun., 1999, 1961–1962.

[13] Y. Diskin-Posner, G. K. Patra and I. Goldberg, Supramolecular porphyrin-based materials. Assembly modes of [5,10,15,20-tetrakis(4-hydroxyphenyl)porphyrinato]zinc with bipyridyl ligands, Cryst. Eng. Comm., 2002, 4, 53: 296–301.

[14] Kuan-Jiuh Lin, SMTP-1: The First Functionalized Metalloporphyrin Molecular Sieves with Large Channels, Angew. Chem. Int. Ed. 1999, 38, 18: 2730-2732.

[15] I. Goldberg, Metalloporphyrin Molecular Sieves, Chem. Eur. J. 2000, 6: 3863-3870.

[16] A. Carbone, R. Pedicini, A. Saccà, I. Gatto, E. Passalacqua, Composite S-PEEK membranes for medium temperature polymer electrolyte fuel cells, J. of Power Sources, 2008, 178: 661-666.

[17].I. Gatto, A. Saccà, A. Carbone, R. Pedicini, F. Urbani, E. Passalacqua, CO-tolerant electrodes developed with PhosphoMolybdic Acid for Polymer Electrolyte Fuel Cell (PEFCs) application, J. Power Sources 2007, 171: 540-545.

[18] K. Kalyanasundaram, Photochemistry of water-soluble porphyrins: comparative study of isomeric tetrapyridyl- and tetrakis(N-methylpyridiniumyl)porphyrins, Inorg. Chem. 1984, 23: 2453-2459.

[19] D. L Akins, H. R. Zhu, C. Guo, Aggregation of Tetraaryl-Substituted Porphyrins in Homogeneous Solution, J. Phys. Chem. 1996, 100: 5420-5425.

[20] R. F. Khairutdinov, N. Serpone, Photoluminescence and Transient Spectroscopy of Free Base Porphyrin Aggregates, J. Phys. Chem. B 1999, 103, 761-769.

[21] A. Stone, E. B. Fleischer, The molecular and crystal structure of porphyrin diacids, J. Am. Chem. Soc., 1968, 90, 11: 2735–2748.

[22] N. C. Maiti, S. Mazumdar and N. Periasamy, J- and H-Aggregates of Porphyrin−Surfactant Complexes: Time-Resolved Fluorescence and Other Spectroscopic Studies, J. Phys. Chem. B, 1998, 102: 1528–1538.

[23] M. Castriciano, A. Carbone, A. Saccà, M. G. Donato, N. Micali, A. Romeo, G. De Luca, L. Monsu Scolaro, Optical and sensing features of TPPS4 J-aggregates embedded in Nafion membranes: influence of casting solvents, J. Mater. Chem., 2010, 20: 2882–2886.

Performance Assessment of an Integrated PEFC and an Hydrogen Storage Device Based on Innovative Material

R.Pedicini[1*], F.Matera[1], G.Giacoppo[1], I. Gatto[1], E.Passalacqua[1]

[1]CNR-ITAE, via S. Lucia sopra Contesse 5, 98126, Messina, Italy.
[*]Tel: +39090624277; e-mail: rolando.pedicini@itae.cnr.it

ABSTRACT

Storage of hydrogen in solid materials has the potential to become a safe and efficient way to store energy, both for stationary and mobile applications. An integrated small scale system, integrating a small hydrogen tank and a 25 cm^2 PEFC single cell, has been tested to assess the performance of an innovative hydrogen storage material based on manganese oxide anchored to a polymeric matrix. A prototype small hydrogen tank, with a capacity of 18 cm^3 made of a stainless steel tube, has been filled with the hydrogen storage material, previously characterized and reaching an hydrogen storage capacity of about 1 wt%. The system included a temperature and pressure sensors and a mass flow to control the desorption rate. A Labview software application has been developed for data logging and control of the test set-up. Sorption process has been achieved by fixing the charging time and recording pressure vs time. The electrochemical tests were performed at 80°C (PEFC cell temperature) and several discharge-charge cycles have been performed at different pressure and two discharge rates (i.e. 100 and 200 ml/min). The nominal power produced by the PEFC cell has been between 6-10 W, with an average discharge time of 400-500 s, depending on charging time and pressure. This material, which adsorbs H_2 in no drastic condition and safe as inert when in contact with ambient air, has demonstrated both a good cycle reversibility in terms of H_2 charge and discharge and, moreover, not affected by the packing in the tank

Keywords: Hydrogen storage material; H_2 tank and Fuel Cell integration; electrochemical tests

1. Introduction

The excessive use of energy that exploits fossil fuels has led to an increased environmental pollution and energy crisis. Recently, a deep research has been done on renewable resources in order to eliminate the dependence on fossil fuels. For the characteristics of unlimited supply, zero emissions of greenhouse gas and high energy efficiency, hydrogen has been identified as the principal candidate for the energy industry of the future [1-2]. However, hydrogen has a low density, only 0.0899 g/L at standard temperature and pressure and its storage is one of the predominant barriers to be overcome for its use as an energy carrier. In fact, the main problem is related to the development of safe, compact and high capacity storage systems for molecular hydrogen [3]. In addition, to permit a wide application on board it is necessary to comply the technical and cost requirements of the automotive industry [4-6]. However the possibility to store this gas in a tank depends on its physic form. Actually, three different methodologies to store such a gas are available and consist in: storing as a pressurized gas in steel or metallic alloy tank at high pressure (800bar) [7-8]; storing as a liquid form in tanks able to maintain a cryogenic temperature (77K) [9]; storing onto solid matrices able to adsorb/desorb hydrogen through chemical or physical sorption at given temperature and pressure conditions [10-11]. The last one is the most investigated method due to both the simplicity of the energetic system and the economic advantages. Sever classes of materials are investigated that could be split up in metallic hydrides and their alloys [12-15], metallorganic framework (MOF) [16] and carbonaceous materials [17-20]. Among these materials, the metallic hydride are in a commercial stage and the most used is $LaNi_5$, which storage capacity corresponds to about 1.6wt% in no drastic conditions of temperature and pressure. On the contrary, the limiting steps for its diffusion on a large scale are the high production costs, the difficulty to handle due to its instability in air environment, the need of activation cycles and the high weight. The other classes of materials possess the advantages of light weight, low sensitivity to air and hydrogen storage comparable to metal hydrides but, on the contrary, the storage capacity is activated in drastic conditions of temperature and pressure. Recently, a new class of materials widely investigated is based on transition metal oxides supported on polymeric matrices [21-22]. From previous studies, it was demonstrated that the manganese oxide anchored on a polymeric matrix (functionalized Polyetheretherketone) showed interesting hydrogen storage properties, reaching about 1wt% at 110°C and 60bar. The encouraging results obtained on this material seems to be promising for the development of a prototype, in fact its good hydrogen storage and the light weight render this material promising for real application. In this work, a prototype consisting of a tank with a capacity of 5-8Nl of hydrogen, useful for feeding a fuel cell, was designed, realized and characterized. The electrochemical characterizations were carried out by coupling the prototype to a $25cm^2$ single cell, in order to feed the anode with the hydrogen stored in the tank.

2. Experimental

2.1. Synthesis of the material

A highly chlorosulphonated PEEK, obtained through an electrophilic aromatic substitution reaction [21], was used as polymeric matrix. The precursor PEEK (450PF Victrex) was treated with chlorosulphonic acid at 30°C under stirring for 24 hrs and the resulting polymer had a sulphonation degree around 100%. This polymeric material was successively treated with a $KMnO_4$ solution to obtain a composite material with different MnO_2 in weight percentage. The amount of the oxide was calculated weighting the residual mass at 1000°C, above the decomposition temperature of the polymer. A more detailed procedure for the chlorosulphonation and manganese oxide reaction is reported elsewhere [21]. Following this procedure, a scale-up of the composite material synthesis (from 2 to 20 g) was carried out and a good reproducibility was confirmed by XRD analysis (fig. 1).

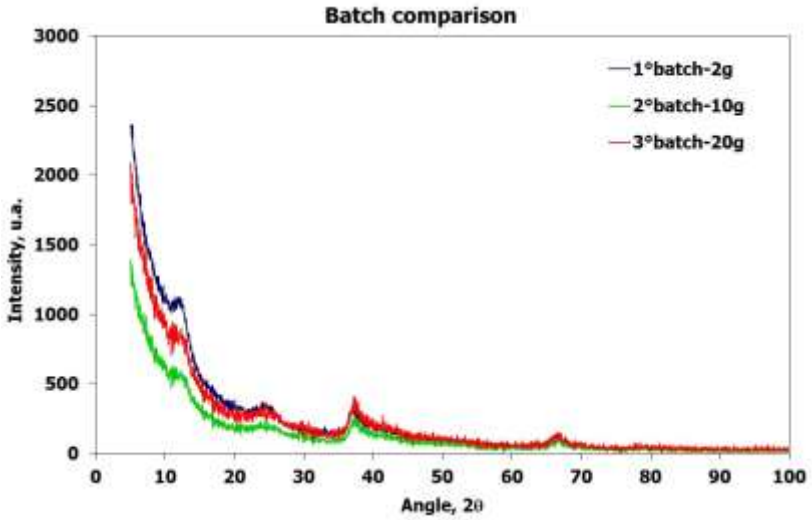

Fig. 1 – XRD batch profiles

2.2 Design of the tank

The synthetized material was already characterised in terms of H_2 storage [21-22] showing a H_2 sorption of 1.1%wt at T = 110°C and P=60 bar. Starting from these features, to feed a 25cm^2 single cell with about 20g of material, the following parameters (Table 1) were considered to size the tank:

Table 1. Theoretical electrochemical parameters with 20 g of sample

Parameter	Amount	Unit
H_2 Stoichiometry	1	-
Composite material amount	20	g
Absorption ratio	1	%mass
Absorbed H_2	0.20	g
PM H_2	2	g/mol
Absorbed H_2 moles	0.10	mol
Constant molar volume	22.41	Nl/mol
Absorbed H2 volume	2.24	Nl
H2 volume at 50 bar	0.04	l
Single cell active area	25	cm^2
Specific Power	400	mW/cm^2
Single cell Power	10	W
Cell Potential	0.60	V
Cell Current	16.67	A
H_2 consumed	8.636E-05	mol/s
Lifetime	1158	s
Lifetime	19.30	Min.

The lifetime of the test was calculated from the molar consumption of reagents (Faraday's law) of the cell at the fixed current, while the potential was chosen to compare the data with other tests performed in a fuel test station. From this data sheet, the cylinder has a H_2 molar volume of 2,24 Nl, able to feed a 25 cm^2 single cell with a 400 mW/cm^2 power density at 0.6 V, corresponding a total power of 10 W. Such system should have a lifetime of about 20 min.
The tank was designed considering three basic experimental parameters: the initial mass of the material (20 g), its apparent density (1.8 g/ml) and the internal tank diameter of the cylinder (1.65 cm).
The design was performed using the Solid Edge program (fig. 2).

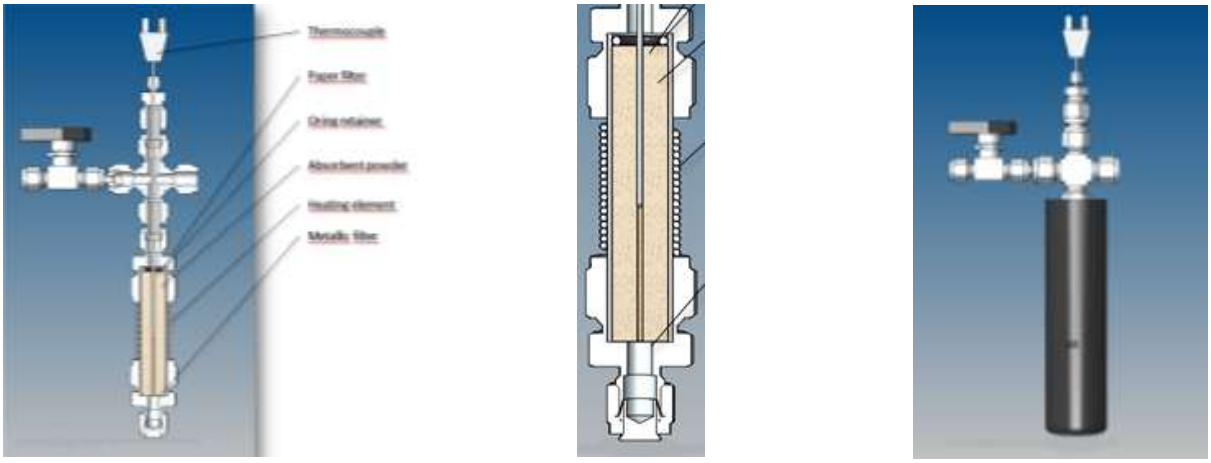

Fig. 2 – Prototype tank design

The prototype tank before and after the loading of the material is shown in fig. 3. The thermal insulation of the cylinder was made using a polymeric material having high temperature resistance.

Fig. 3 – Prototype tank

Having to operate at different temperatures, a thermo resistance was been winded on the cylinder. The assembly cylinder- thermo resistance was thermally insulated to the outside through two layers of insulator, the inner in ceramic sheath (for high T) while the outer one in polymeric material (for T less than 100°C).

2.3 Design and control of the measurement system

The measurement system was realized by interfacing a fuel cell test station and a NI Compact RIO controller connected it to a PC. The monitored signals were:

- the output gas pressure of the thank by means of a pressure transducer;
- the output gas flow rate of the tank and the input gas into the cell, controlled by the fuel cell test station.

3. Results and discussion

Two types of test were performed to measure the performance of the small tank. The first test includes the measurement of the quantity of gas released by the tank filled with the synthetized material. This parameter was recorded through a mass flow controller. The monitored (and recorded) quantities are tank pressure and gas mass flow versus time. The measurements were performed at two constant flow rates, respectively 100 ml/min and 200 ml/min. After each test, the hydrogen tank is recharged at 60 bar(g) and 110°C and different recharge time. The recharge time is recorded to understand the most convenient value relative to desorption performance. The experimental setup for the first test is configured as follows: the hydrogen tank outlet has a shutoff valve and it is connected to a first pressure regulator, which reduces the pressure from the storage value (i.e. 60 bar) down to 10 bar(g); then a second pressure regulator further decreases the pressure to a value compliant to mass flow specification. This latter pressure does not influence the desorption process flow rate because the flow is already limited by the mass-flow controller at the set point. It is necessary to insert a small dead volume between the second pressure regulator and the mass-flow to dump pressure fluctuations generated by the pressure controller and the mass-flow controller regulations, resulting in a fluctuating pressure and unstable flow rate. This added volume, plus piping, connections and controllers volume, false the measurement by giving an additional capacity for hydrogen storage which is not related to the actual storage capacity of the adsorption material. Hence it is needed to estimate this “blank” volume and reduce the measured capacity resulting from the test. This test, made following the same procedure of the complete system test, was performed at 60 bar(g) and ambient temperature (25°C), excluding the hydrogen tank. The result is in an autonomy of approx. 2 minutes (110s), from 60 bar(g) down to 0 bar(g), ambient temperature and at a constant flow of 100 ml/min.
After blank volume estimation, the system was tested as previously described. A total of 6 tests have been performed and their results summarized in table 2.

Table 2. experimental data for charge/discharge of prototype tank

Test	Charge (min)	Discharge (min)	Flow (ml/min)	Net discharge time (min)
1	30	13	100	11
2	120	23	100	21
3	420	25	100	23
4	60	11	200	9
5	120	15	200	13
6	220	12	200	10

Test results show a pretty constant performance in terms of gas output, while the staircase aspect for the pressure plot is caused by the upstream pressure regulator action. The average duration of the gas flow is approx. 15 minutes at a

flow rate of 200ml/min (tests n. 4-6) and 23 min at 100ml/min (tests n. 1-3). Plots of test n.6, performed at 200ml/min, and test n. 2, performed at 100ml/min, are shown respectively in figg. 4a-b.
The non-proportional result of the discharge time at 100ml/min and 200ml/min is related to a leakage, which is obviously more evident at higher pressure and lower flow, while it reduces its influence at lower pressure and higher flow. Despite this issue, the net measured flow is still comparable to the theoretical value as calculated in tab. 1.

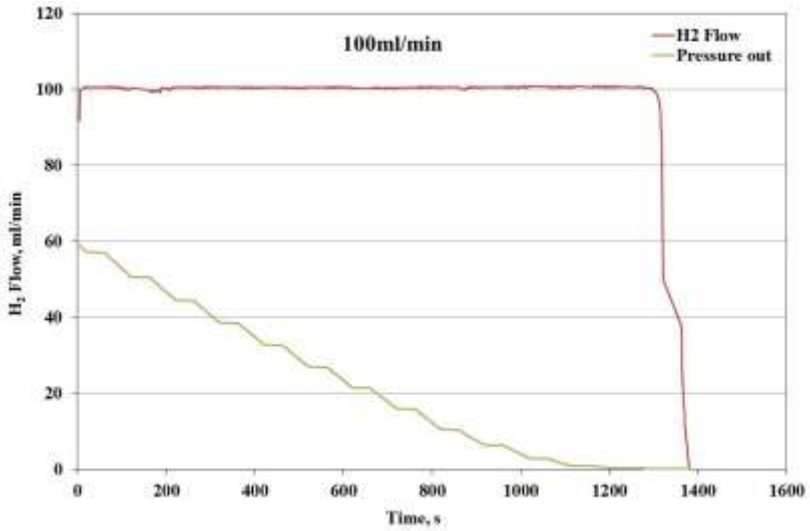

(a)

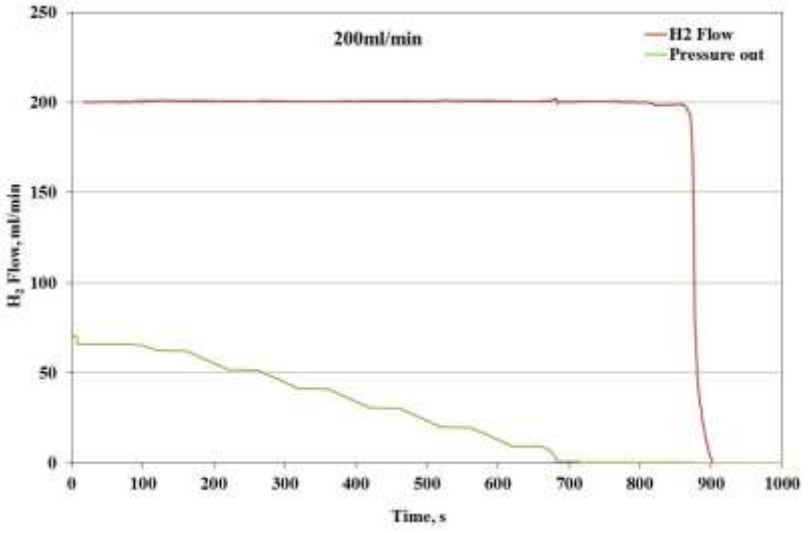

(b)

Fig. 4 – Discharge profile at 100ml/min (a) and 200ml/min (b)

Discharge time versus charge time are then plotted to highlight their correlation (i.e. the tendency to a plateau which shows the end of the absorption process) and any possible anomaly (i.e. significant gas leakage) (fig. 5). As shown in fig. 5, an increase of charge time did neither lead to a proportional increase nor a constant value of discharge time,

confirming that, while the blank volume is promptly filled, the adsorption process requires a longer time while adding a little, but still measurable, more autonomy to the system.

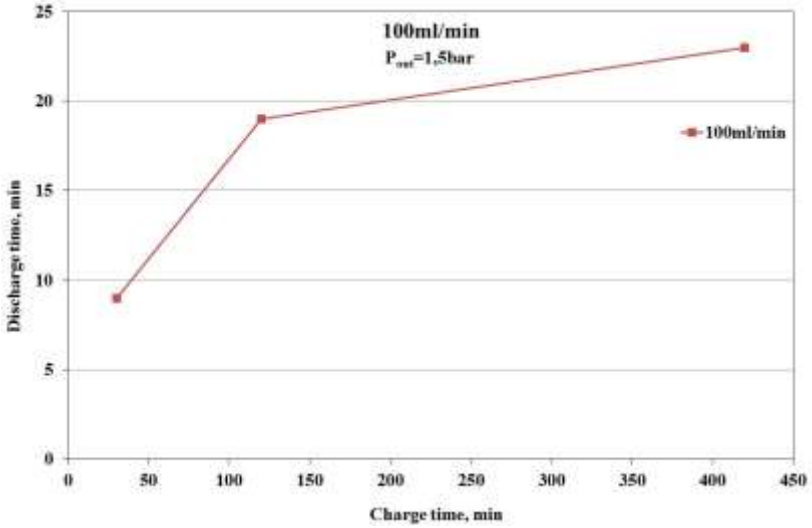

Fig. 5 – Discharge vs charge time at 100ml/min.

A second test was performed by connecting the tank to a Polymer Electrolyte Fuel Cell. This is a 25 cm^2 (active area) single cell operating in dead-end mode, so that the hydrogen desorption and the consumption rate can be measured theoretically by using the Faraday Law and measuring the current of the fuel cell. Previously the cell was tested at 80°C-100%RH by feeding with air and H_2 from the lab pipeline. This is needed to create a performance baseline to be compared with the data obtained from the complete system test. Afterward, the anode was fed with the hydrogen supplied by the prototype tank. In figure 6, an image of the test set up is shown.

Fig. 6 - 25 cm^2 single cell and experimental set up.

In figure 7a) a comparison between the electrochemical test at 80°C 1.5 bar at 0.6V is reported. The blue line represents the performance of PEFC under standard testing conditions while the green line represents the

performance of the actual system. In the latter case, the potentiostatic test shows an unstable behavior while galvanostatic test show a more stable behavior, as reported in figure 7b). This is explained by Faraday's Law, because under galvanostatic condition the gas consumption rate is constant, while under potentiostatic condition any current change leads to a flow instability.

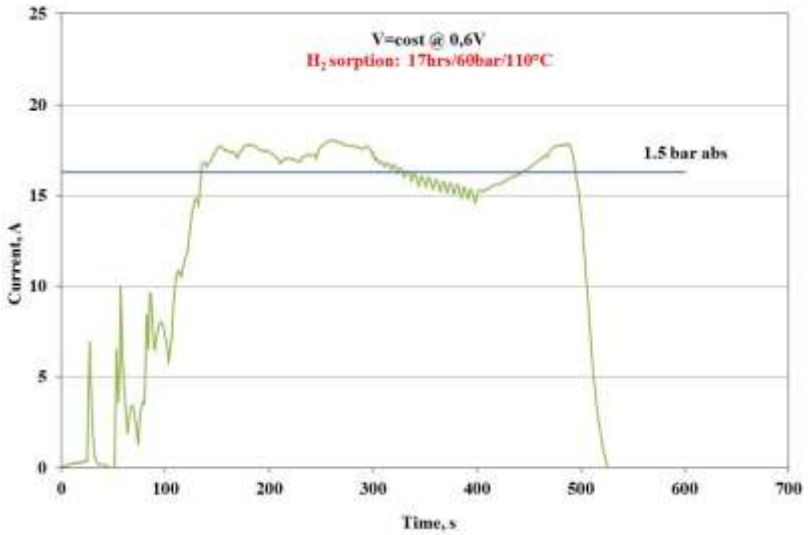

(a)

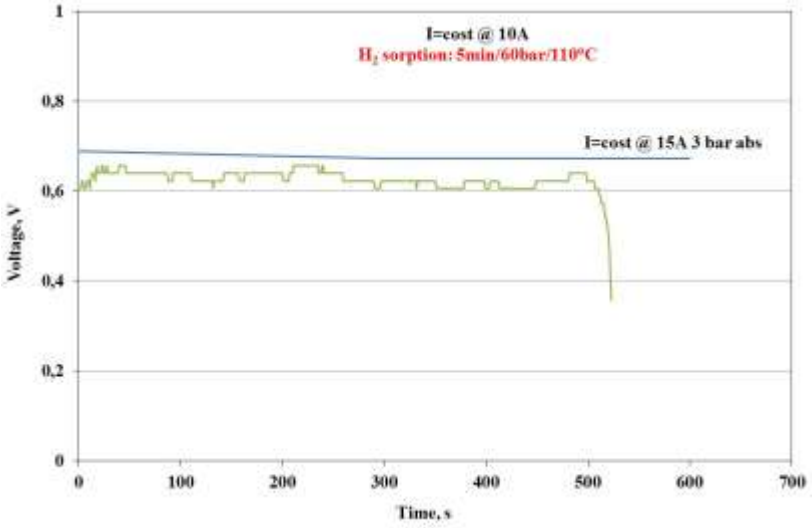

(b)

Fig. 7 - Comparison of fuel cell performance at fixed potential (a) and current (b) by using standard and prototype H_2 feeding

The different performance of the PEFC single cell (blu line vs. green line) is related to the different operative conditions when the cell is fed with the hydrogen from the pipeline (3 bar, 80°C, fully humidified hydrogen, 2.5 stoich at the actual current) or from the tank (80°C, 1.5 bar, dry hydrogen, stoich. value at the actual current). Again,

hydrogen leakage reduced the tank autonomy, this time reducing the duration to 10min instead of the actual discharge time of 20min measured in the first test.

4. Summary and perspectives

This paper shows that, despite its intrinsic simplicity, such a prototype can still be used to demonstrate the feasibility of a simple solid storage system able to operate in a real environment also when connected to a simple load such as a small fuel cell. Leakage problem at higher pressure affects the precision of results, currently losing almost 50% of the storage capacity. This prototype also gives some hints for the next development of such system, for example to avoid to keep two regulation valves (the pressure reducer and the mass flow controller) too close, otherwise resulting in an unstable flow and hence the need to put an additional dead volume to dump pressure variations. The fuel cell performance were comparable to that of a standard testing, showing that the innovative material used for hydrogen storage can be used for practical applications, although still many aspects need to be enhanced such as material storage capacity and system design.

Acknowledgements

This work was developed within the Research Project AdP CNR-MSE and financing from Research Fund for the Electrical System, theme: International Project “Nuclear, Hydrogen, Fuel Cells” e Activity 2.6: Polymeric materials for hydrogen storage.

References

[1] JO’M. Bockris, Hydrogen economy in the future. Int. J Hydrogen Energy 1999;24:1-15.
[2] R. Ramachandran, R.K. Menon. An overview of industrial uses of hydrogen. Int. J Hydrogen Energy 1998;23:593-598.
[3] A. Zuttel, Hydrogen storage and distribution systems. Mitig Adapt Strat Glob Change 2007;12:343-365.
[4] C.E. Thomas, B.D. James, Jr F.D. Lomax, Jr I.F. Kuhn, Fuel options for the fuel cell vehicle: hydrogen, methanol or gasoline? Int. J Hydrogen Energy 2000;25:551-567.
[5] K. Yamane, S. Furuhama, A study on the effect of the total weight of fuel and fuel tank on the driving performances of cars. Int. J Hydrogen Energy 1998;23: 825-831.
[6] U. Eberle, G. Arnold, R. von Helmholt, Hydrogen storage in metalehydrogen systems and their derivatives. J Power Sources 2006;154:456-60.
[7] K.M. Thomas, Hydrogen adsorption and storage on porous materials. Catal Today 2007;120:389-398.
[8] R.E. Morris, P.S. Wheatley, Gas storage in nanoporous materials. Angew Chem Int Ed 2008;47:4966-4981.
[9] J. Wolf, Liquid-hydrogen technology for vehicles. MRS Bull 2002;27:684-687.
[10] B. Bogdanovic, R.A. Brand, A. Marjanovic, M. Schwickardi, J.J. Tolle, Metal-doped sodium aluminium hydrides as potential new hydrogen storage materials. Alloys Compd 2000;302:36-58.
[11] L. Zhechkov, T. Heine, G. Seifert, Physisorption of N2 on graphene platelets: an ab initio study. Int J Quantum Chem 2006;106:1382.
[12] F. Schuth, B. Bogdanovic, M. Felderhoff, Light metal hydrides and complex hydrides for hydrogen storage. Chem Commun 2004:2249-2258.
[13] E.S. Kikkinides, M.C. Georgiadis, A.K. Stubos, Dynamic modelling and optimization of hydrogen storage in metal hydride beds. Energy 2006;31:2428-2446.
[14] M.Q. Fan, S.S. Liu, Y. Zhang, J. Zhang, L.X. Sun, F. Xu, Superior hydrogen storage properties of MgH2e10 wt.% TiC composite. Energy 2010;35:3417-3421
[15] I.P. Jain, P. Jain, A. Jain, Novel hydrogen storage materials: a review of lightweight complex hydrides. J Alloys Compd 2010;503:303-339.
[16] J.L. Rowsell, A.R. Millward, K.S. Park, O.M. Yaghi. Hydrogen sorption in functionalized metal-organic frameworks. J Am Chem Soc 2004;126:5666-5667
[17] C. Liu, Y.Y. Fan, M. Liu, H.T. Cong, H.M. Cheng, M.S. Dresselhaus, Hydrogen storage in single-walled carbon nanotubes at room temperature. Science 1999;286:1127-1129.
[18] M. Volpe, F. Cleri, Chemisorption of atomic hydrogen in graphite and carbon nanotubes. Surf Sci 2003;544:24-34.

[19] Z.Y. Zhong, et al, Nanosized nickel (or cobalt)/graphite composites for hydrogen storage. J Phys Chem B 2002;106:9507-9513.

[20] L. Zhou, Y.P. Zhou, Y. Sun, A comparative study of hydrogen adsorption on superactivated carbon versus carbon nanotubes. Int J Hydrogen Energy 2004;29:475-479.

[21] R. Pedicini, A. Saccà; A. Carbone; E. Passalacqua, Int. J. Hydrogen Energy 2011; 36: 9062-9068.

[22] R. Pedicini, B. Schiavo, P. Rispoli, A. Saccà, A. Carbone, I. Gatto, E. Passalacqua, Energy 2014; 64: 607-614.

Functionalization of Vulcan XC-72 by IMH and its Effect as Support for Pt Electrocatalysts for the EOR

W.J. Pech-Rodríguez[1], D. González-Quijano[1], G. Vargas-Gutiérrez[1,2], J.I. Escalante-Garcia[1,2], F.J. Rodríguez-Varela[2,3,*]

[1]Ingeniería Metalúrgica e Ingeniería Cerámica
[2]Sustentabilidad de los Recursos Naturales y Energía
[3]Programa de Nanociencia y Nanotecnología
Cinvestav Unidad Saltillo, Av. Industria Metalúrgica 1062, Ramos Arizpe, Coahuila, México, 25900.
[*]Tel: +528444389600 Ext. 8526; e-mail: javier.varela@cinvestav.edu.mx

ABSTRACT

In this study, Vulcan XC-72 was functionalized by an intermittent microwave heating (IMH) method in two different soft chemical agents, namely citric acid (CA) and methanol (MeOH). The results showed physical and chemical changes in the structure of functionalized Vulcan. Pt/C electrocatalysts were synthesized by pulse IMH assisted polyol method using the treated carbons as support. The electrochemical activity and stability of the Pt/C materials were investigated by cyclic voltammetry and chronoamperometry measurements. The electrochemical results showed higher catalytic activity and stability of Pt nanocatalyst supported on some of the functionalized carbons for the Ethanol Oxidation Reaction (EOR), compared to a Pt/C electrocatalysts dispersed on non-treated Vulcan. The higher performance shown by Pt/C electrocatalysts dispersed on functionalized supports has been attributed to: i) a better distribution of nanoparticles, and ii) an enhanced interaction between Pt nanoparticles and the oxygenated species formed over the surface of the treated carbon. The results suggest that functionalization of Vulcan with MeOH and CA using the IMH method could become a promising process for the development of highly active Pt/C catalyst for the EOR due to its simplicity and low cost.

Keywords: functionalization of Vulcan; citric acid and methanol; EOR

1. Introduction

Direct Alcohol Fuel Cells (DAFCs) have attracted a great interest as power source for small scale stationary and portable applications due to the simplicity of fuel handling, low operation temperature, high power density, and fuel availability [1-5]. The most common fuels such as methanol, ethanol, ethylene glycol, propanol, and others possess physicochemical properties that make them good candidates for DAFCs [6, 7]. Since it is easily produced from biomass by fermentation of sugar containing raw materials, ethanol (C_2H_5OH) is considered an excellent fuel for low temperature Direct Ethanol Fuel Cells (DEFCs). Ethanol has a relatively low toxicity, high mass energy density, and high availability [8, 9]. However, ethanol molecules have two bonded carbon atoms, and as a result the EOR is complex [10].

At the present, Pt-alone catalysts are still considered to be used as anodes for DEFCs because such catalysts can adsorb and dehydrogenate small organic molecules [11,12]. High surface-area Pt-supports have been proposed to be used in DEFCs because their morphology provide access to a much larger number of active atoms, related to the corresponding bulk metal [13]. The ideal support must have the following characteristics: i) high electrical conductivity; ii) high corrosion resistance under fuel cell operation environment; and iii) must promote the transport of reactants onto the catalysts layer [14]. Carbon materials are recognized as attractive Pt supports because they have high surface area and good chemical stability [15]. Nevertheless, as-received carbon black typically has high ash content and a hydrophobic surface, that results in low capability to anchor Pt nanoparticles [16]. Therefore, several studies have been carried out to modify and functionalize the surface of carbon supports to enhance its interaction with nanoparticles, thus increasing its catalytic activity.

In this study, carbon Vulcan XC-72 was functionalized in CA and MeOH solutions using an IMH process. The functionalized materials were used as support to synthesize Pt/C anodes. Their performance was evaluated for the EOR in acid media.

2. Experimental

2.1. Carbon functionalization

Vulcan XC-72 (Cabot®, specific surface area of 237 $m^2 g^{-1}$) was chemically treated with CA and MeOH as soft chemical agents, in order to create functional groups that enhance the catalytic activity of Pt/C electrocatalysts. Table 1 presents the design of experiment proposed to achieve the functionalization of the support. As can be seen, it considered three different concentrations of the chemical agents (0.05, 0.1 and 0.15 M) with two irradiation time (4 and 8 min).

The procedure to carry out the functionalization is described as follows: Carbon powder (300 mg) was dispersed in a round bottom flask for 1 h in a solution of the corresponding chemical agent, namely CA or MeOH, by ultrasound. Afterwards, the carbon mixture was placed in the center of modified domestic microwave-oven and heated using a 25 s power-on/15 s power-off cycle for 4 or 8 min under magnetic stirring. The resulting solution was allowed to cool down and then was filtered and dried at 200 °C for 30 min, to remove any traces of chemical agent and water.

Table 1. Design of experiments for the functionalization of carbon support.

Catalysts	Chemical agent	Concentration (*mol* L^{-1})	Irradiation time (min)
Pt/C-CA1	CA	0.05	4
Pt/C-CA2	CA	0.05	8
Pt/C-CA3	CA	0.1	4
Pt/C-CA4	CA	0.1	8
Pt/C-CA5	CA	0.15	4
Pt/C-CA6	CA	0.15	8
Pt/C-MeOH1	MeOH	0.05	4
Pt/C-MeOH2	MeOH	0.05	8
Pt/C-MeOH3	MeOH	0.1	4
Pt/C-MeOH4	MeOH	0.1	8
Pt/C-MeOH5	MeOH	0.15	4
Pt/C-MeOH6	MeOH	0.15	8

2.2. Synthesis of Pt/C

Pt/C catalysts having 20 wt. % Pt loading were synthesized by the IMH polyol method as follow: 56 mg of treated Vulcan were dispersed by ultrasound in an EG/H_2O solution (v/v= 90/5) and to this mixture 37 mg of H_2PtCl_6 $6H_2O$ dispersed in an EG/H_2O solution were added drop by drop. The colloidal solution was stirred for 1 h and the pH was adjusted to around 12 using a NaOH/EG solution. After that, the mixture was put in the microwave-oven and submitted to 600 W of irradiation continuously for 58 s, followed by pulses of 4 s power-on/15 s power-off for 40 min. The mixture was left cool off overnight with continuous stirring. Then, the pH was adjusted to 3 using H_2SO_4/EG solution. The final products were filtered and washed with water.

2.3. Catalysts characterization

X-ray patterns were obtained in a Phillips-X´Pert diffractometer using Cukα radiation (λ= 0.15406 nm) source. The scan was from 10 to 100° (2θ).

The chemical composition of catalysts was determined by SEM-EDS in an XL30 Phillips Microscope, operating at 20 kV.

Electrochemical measurement were performed on an Voltalab PGZ 301 potentiostat/galvanostat in a standard three electrode cell using Ag/AgCl as the reference electrode and platinum foil as counter electrode. The working electrode was a thin layer of the synthesized catalysts and Nafion® dispersed on a glassy carbon support (0.196 cm^2 geometrical area). Cyclic voltammetry and chronoamperometric curves were carried out in N_2-saturated 0.5 M H_2SO_4 without and with ethanol. The constant potential during chronoamperometry measurements was 0.87 V vs. SHE.

3. Results and discussion

3.1. Physicochemical characterization

Figure 1 shows the XRD patterns of the Pt/C catalysts synthesized by IMH using carbon supports pre-treated with CA (1a) and MeOH (1b). In both cases, the patterns of Pt dispersed on non-treated Vulcan are also shown as reference. The diffraction peaks at about 2θ= 25° are associated to the graphite structure of Vulcan, plane (002). The diffraction peaks nearly to 39.7, 46.2, 67.4 and 81.2 ° are attributed to the Pt (111), (200), (220) and (311) planes, respectively. The (220) plane was used to calculate the size particle according to the Scherrer´s formula [4] and the results are summarized in Table 2.

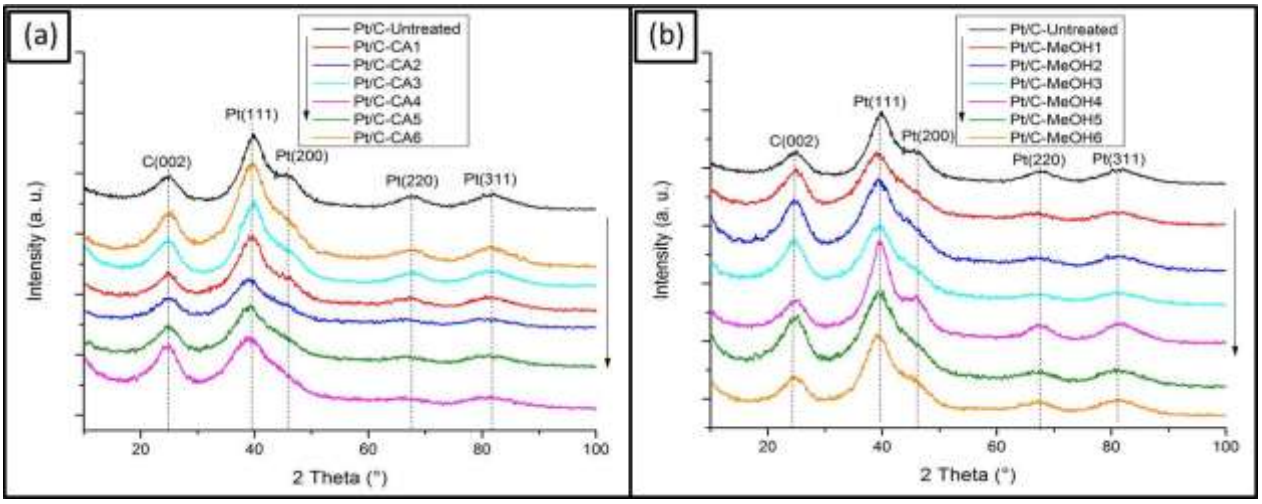

Fig 1. XRD patterns of a) Pt nanoparticles supported on carbon functionalized by CA; b) Pt nanocatalysts supported on carbon functionalized by MeOH.

From Figures 1(a), (b) it can be observed that the patterns corresponding to the Pt/C-CA and Pt/C-MeOH catalysts show some differences related to Pt/C-Untreated, which give as a result dissimilar characteristics regarding crystallinity and particle size. This can be more readily seen in the (220) plane. Overall, the patterns of Pt/C on treated Vulcan show a wider peak. Such characteristic may be due to the interaction of Pt nanoparticles with treated carbon during their nucleation and growth. The particle sizes of the catalysts (2.5 nm and smaller) are given in Table 2.

The results of the EDS analysis show that the metal loading on the Pt/C materials is closed to the nominal composition, i.e., 20 wt. %. Table 2 summarizes the Pt loadings obtained from the catalysts.

3.2. Electrochemical characterization

Figure 2 shows the CVs of the Pt/C nanocatalysts dispersed on Untreated, CA-treated and MeOH-treated Vulcan. The curves have very similar general shapes and current densities characteristics. Only the Pt/C-MeOH4 catalyst shows a noticeable smaller current density profile than the rest of the materials (Fig.

2d). The electrochemically active surface area (EAS) of the synthesized Pt/C materials can be determined by integrating the charge associated with the area of the hydrogen adsorption-desorption region, from the CVs in Figure 2, using the equation (1):

$$\text{EAS} = \frac{Q}{Q_0 \text{ x } Pt_{loading}} \quad (1)$$

were Q is to the integrated charge in the hydrogen adsorption-desorption area from the CVs, Q_0 is the theoretical charge required for the adsorption of a monolayer of hydrogen on polycrystalline Pt (210 μC cm^{-2}) [17], and $Pt_{loading}$ is the amount of Pt dispersed on the working electrode.

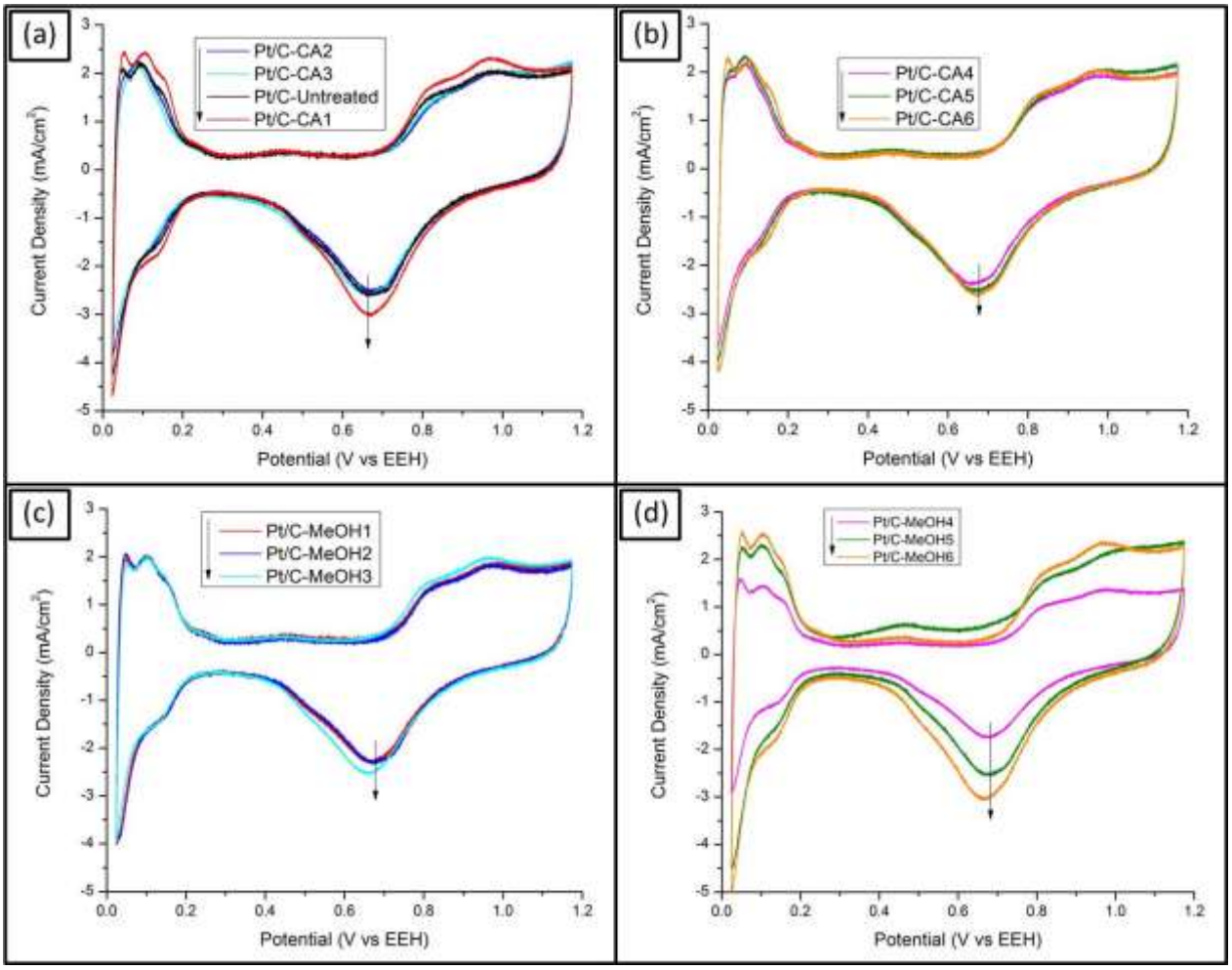

Fig 2. CVs of Pt/C nanocatalysts. (a) and (b) Pt/C (treated by CA) and Pt/C-Untreated; (c) and (d) Pt/C (treated by MeOH). Scan rate of 20 mV s^{-1} at room temperature in 0.5 M H_2SO_4.

The EAS of the catalysts are summarized in Table 2. It can be seen that Pt/C-CA1, Pt/C-CA6, Pt/C-MeOH5 and Pt/C-MeOH6 present higher EAS values than Pt/C-Untreated: 66.9, 65.3 and 63.7, 62.8 $m^2 g^{-1}$, respectively, against 59.6 $m^2 g^{-1}$ of the latter. Meanwhile, Pt/C-CA3 and Pt/C-MeOH4 have the lower EAS values: 48.2 and 42.7 $m^2 g^{-1}$ respectively.

Table 2. Pt content, particle size and EAS values of the Pt/C catalysts

Catalysts	Pt loading (%)	Particle size from XRD (*nm*)	EAS ($m^2 g^{-1}$)
Pt/C-Untreated	20.6	2.1	59.6
Pt/C-CA1	21.5	1.9	66.9
Pt/C-CA2	19.5	2.1	55.6
Pt/C-CA3	20.8	2.0	48.2
Pt/C-CA4	17.9	----	53.5
Pt/C-CA5	20.0	1.8	58.7
Pt/C-CA6	19.9	1.8	65.3
Pt/C-MeOH1	20.1	1.8	56.2
Pt/C-MeOH2	17.7	1.7	58.7
Pt/C-MeOH3	18.8	1.9	52.4
Pt/C-MeOH4	19.9	2.5	42.7
Pt/C-MeOH5	17.74	1.5	63.7
Pt/C-MeOH6	18.64	1.7	62.8

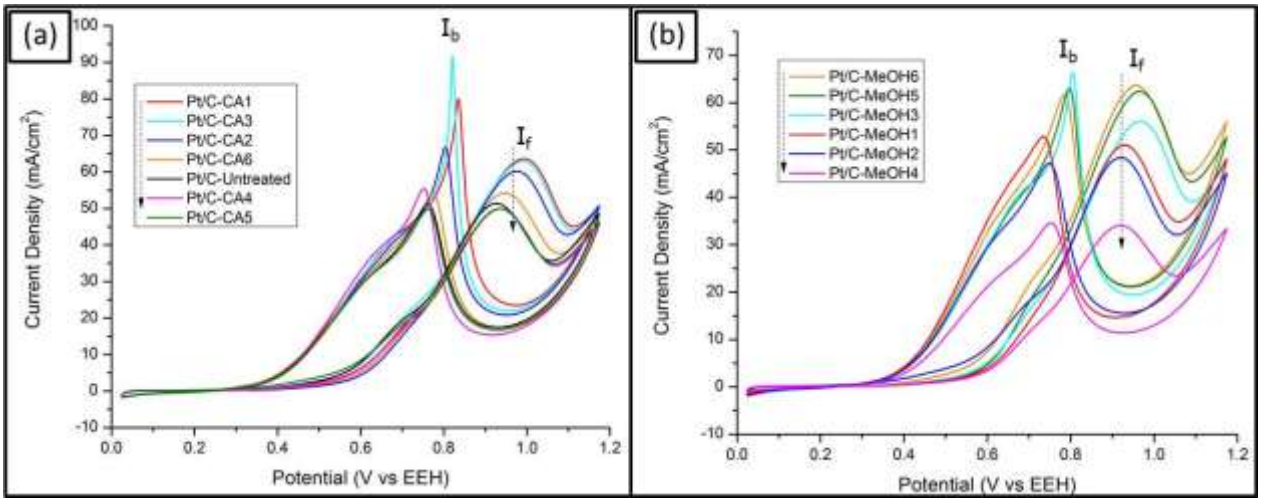

Fig 3. CVs of the EOR. a) Pt/C (functionalized by CA) and Pt/C-Untreated. b) Pt/C (functionalized by MeOH. Electrolyte: N_2-saturated 0.5 M H_2SO_4 + 1 M C_2H_6O.

The polarization curves of the EOR at the Pt/C catalysts are shown in Figure 3. The anodes with the higher catalytic activity for the EOR are Pt/C-MeOH6, Pt/C-CA1, Pt/C-CA3 and Pt/C.MeOH5, with current density values of 63.7, 63.5, 63.1 and 62.3 mA cm^{-2}, respectively (see Table 3). The higher performance for the EOR of some of the Pt catalysts supported on treated Vulcan suggests that its functionalization with CA and MeOH increases the number of surface functional groups, resulting in a more homogeneous dispersion of Pt nanoparticles on the support and therefore on the catalytic activity for the anodic reaction. Most of the catalysts in Table 3 have onset potentials of the EOR roughly around 0.3 V vs. SHE, with the exception of Pt/C-CA3 and Pt/C-MeOH5 with a higher value.

The catalyst tolerance to CO and other reaction intermediaries can be evaluated by the ratio of the anodic current densities in the forward (I_f) and reverse (I_b) scans [18, 19]. A high I_f/I_b ratio suggests that the catalyst efficiently oxidizes ethanol in the anodic scan, producing small amounts of intermediaries that will be oxidized in the cathodic direction. Table 3 summarizes the I_f/I_b ratio of the Pt/C catalysts. It is observed that Pt/C-MeOH6 has the highest I_f/I_b value, followed closely by Pt/C-Untreated, Pt/C-CA5, Pt/C-CA6, Pt/C-MeOH2. However, it should be noted as mentioned before that Pt/C-MeOH6 shows a higher current density of the EOR.

Considering these three EOR parameters, it is clear that Pt/C-MeOH6 is the most active catalyst among those enlisted in Table 3. The performance of Pt/C-MeOH6 may be attributed to the surface composition (presence of functional groups) of the treated Vulcan and its interaction with Pt nanoparticles, thus enhancing the catalytic activity for the EOR.

Table 3. Electrocatalysis parameters of the Pt/C catalysts for the EOR.

Catalysts	Onset potential (*V*)	Peak current density (mA cm^{-2})	I_f/I_b ratio
Pt/C-Untreated	0.30	51.0	1.0
Pt/C-CA1	0.30	63.5	0.80
Pt/C-CA2	0.35	60.2	0.90
Pt/C-CA3	0.31	63.1	0.68
Pt/C-CA4	0.30	49.9	0.90
Pt/C-CA5	0.29	49.8	1.0
Pt/C-CA6	0.30	54.0	1.0
Pt/C-MeOH1	0.31	50.9	0.96
Pt/C-MeOH2	0.28	48.3	1.0
Pt/C-MeOH3	0.28	55.8	0.85
Pt/C-MeOH4	0.29	33.8	0.98
Pt/C-MeOH5	0.34	62.3	0.98
Pt/C-MeOH6	0.30	63.7	1.03

Figure 4 shows the chronoamperometric curves of the EOR at the four most active Pt/C catalysts (supported on CA or MeOH treated Vulcan) and Pt/C-Untreated. The Pt/C-CA1 shows a more stable current density after 600 s. Meanwhile, Pt/C-MeOH6, Pt/C-MeOH5 and Pt/C-CA2 show similar current density-time characteristics. Thus, Pt/C-MeOH6 which has high electrocatalysis values in Figure 3 and

Table 3 also demonstrates a good stability for the EOR. On the other hand, Pt/C-Untreated presents a more important current density decay in the first 100 s and maintains a lower performance over the testing. These results suggest that Pt nanoparticles supported on treated Vulcan have a better stability compared with Pt supported on untreated carbon for the EOR.

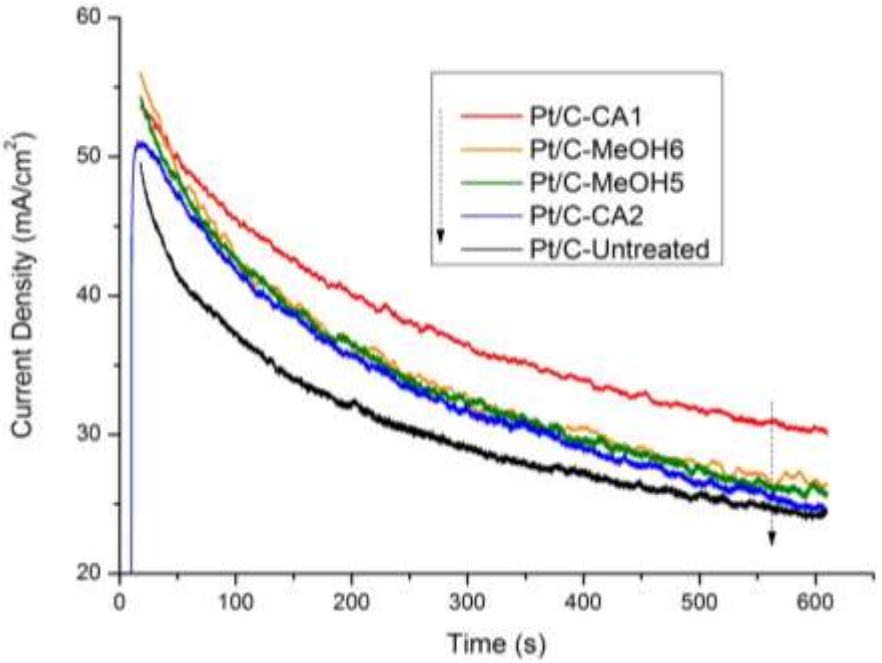

Fig 4. Chronoamperometric curves of the EOR at the Pt/C catalysts. Constant potential: 0.87 V vs. SHE. Electrolyte: N_2-saturated 0.5 M H_2SO_4 + 1 M C_2H_6O.

4. Summary and perspectives

Commercial carbon Vulcan XC-72 was functionalized in different concentrations of MeOH and CA using the IMH process. The treated carbon was used as support for Pt nanoparticles. The electrochemical characterization indicates that the performance of Pt/C catalysts is influenced by the conditions of functionalization and synthesis parameters. The Pt/C-MeOH6 sample, synthesized using carbon functionalized in 0.15 mol l^{-1} methanol for 8 min showed the highest catalytic activity for the EOR among the materials studied in this work.

Acknowledgements

This work was financially supported by the Mexican National Council for Science and Technology (CONACYT). We also thank CONACYT for doctoral scholarships provided to WJPR and DGQ.

References

[1] L. Jiang, H. Zang, G. Sun, Q. Xin, Influence of Preparation Method on the Performance of PtSn/C Anode Electrocatalyst for Direct Ethanol Fuel Cells. Chinese J. of Catal. 2006;27:15-9

[2] E. Antolini, Carbon supports for low-temperature fuel cell catalysts. Appl. Catal. B 2009;88:1-24

[3] J.R.C. Salgado, E. Antolini, E.R. Gonzalez, Preparation of Pt-Co/C electrocatalysts by reduction with borohydride in acid and alkaline media: the effect on the performance of the catalyst. J. Power Sources 2004;138:56-60

[4] Y.-Y. Chu, Z.-B. Wang, D.-M. Gu, G.-P. Yin, Performance of Pt/C catalysts prepared by microwave-assisted polyol process for methanol electrooxidation. J. Power Sources 2010;195:1799-804

[5] S.M.S. Kumar, N. Hidyatai, J.S. Herrero, S. Irusta, K. Scott, Efficient tuning of the Pt nano-particle mono-dispersion on Vulcan XC-72R by selective pre-treatment and electrochemical evaluation of hydrogen oxidation and oxygen reduction reactions. Int. J. Hydrogen Energy 2011;36:5453-65

[6] L. Colmenares, H. Wang, Z. Jusys, L. Jiang, S. Yan, G.Q. Sun, R.J. Behm, Ethanol oxidation on novel, carbon supported Pt alloy catalysts—Model studies under defined diffusion conditions. Electrochim. Acta 2006;52:221-33

[7] C. Lamy, E.M. Belgsir, J.M. Léger, Electrocatalytic oxidation of aliphatic alcohols: Application to the direct alcohol fuel cell (DAFC). J. Appl. Electrochem. 2001;31:799-809

[8] C.M. Silva, R.F.B. De Souza, L.S. Parreira, E.T. Neto, M.L. Calegaro, M.C. Santos, Ethanol oxidation reactions using SnO_2@Pt/C as an electrocatalyst. Appl. Catal. B 2010;99:265-71

[9] S. Rousseau, C. Coutanceau, C. Lamy, J.M. Léger, Direct ethanol fuel cell (DEFC): Electrical performances and reaction products distribution under operating conditions with different platinum-based anodes. J. Power Sources 2006;158:18-24

[10] R.F.B. De Souza, L.S. Parreira, D.C. Rascio, J.C.M. Silva, E. Teixeira-Neto, M.L. Calegaro, E.V. Spinace, A.O. Neto, M.C. Santos, Study of ethanol electro-oxidation in acid environment on Pt_3Sn/C anode catalysts prepared by a modified polymeric precursor method under controlled synthesis conditions. J. Power Sources 2010;195:1589-93

[11] F. Colmati, E. Antolini, E.R. Gonzalez, Preparation, structural characterization and activity for ethanol oxidation of carbon supported ternary Pt–Sn–Rh catalysts. J. Alloys Compd. 2008;456:264-70

[12] M. Sakthivel, A. Schlange, U. Kunz, T. Turek, Microwave assisted synthesis of surfactant stabilized platinum/carbon nanotube electrocatalysts for direct methanol fuel cell applications. J. Power Sources. 2010;195:7083-9

[13] E. Auer, A. Freund, J. Pietsch, T. Tacke, Carbons as supports for industrial precious metal catalysts. Appl. Catal. A 1998;173:259-71

[14] C.L. Wenzhen Li, Weijiang Zhou, Jieshan Qiu, Zhou, Gongquan Sun, Qin Xin, Preparation and Characterization of Multiwalled Carbon Nanotube-Supported Platinum for Cathode Catalysts of Direct Methanol Fuel Cells. J. Phys. Chem. B 2003;107:6292-9

[15] A.D. Taylor, R.C. Sekol, J.M. Kizuka, S. D'Cunha, C.M. Comisar, Fuel cell performance and characterization of 1-D carbon-supported platinum nanocomposites synthesized in supercritical fluids. J. Catal. 2008;259:5-16

[16] J. Ye, J. Liu, Y. Zhou, Z. Zou, J. Gu, T. Yu, High catalytic performance and stability of Pt/C using acetic acid functionalized carbon. J. Power. Sources 2009;194:683-9

[17] S. Yin, P.K. Shen, S. Song, S.P. Jiang, Functionalization of carbon nanotubes by an effective intermittent microwave heating-assisted HF/H_2O_2 treatment for electrocatalyst support of fuel cells. Electrochim. Acta 2009;54:6954-8

[18] Z. Liu, X.Y. Ling, X. Su, J.Y. Lee, Carbon-Supported Pt and PtRu Nanoparticles as Catalysts for a Direct Methanol Fuel Cell. J. Phys. Chem. B 2004;108:8234-40

[19] M.A. Scibioh, S.-K. Kim, E.A. Cho, T.-H. Lim, S.-A. Hong, H.Y. Ha, Pt-CeO_2/C anode catalyst for direct methanol fuel cells. Appl. Catal. B 2008;84:773-82

Thermodynamic and Kinetics Modeling of H_2 Production by dry Reforming of Ethanol With CO_2 Evolution

R. B. Pallares Sámano, M. R. Baray Guerrero, J. Salinas Gutiérrez, V. Guzmán Velderrain, V. Collins Martínez, A. López Ortiz*

Departamento de Materiales Nanoestructurados, Centro de Investigación en Materiales Avanzados, S.C.,
Miguel de Cervantes 120, Chihuahua, Chih., México, 31109, México.
*Tel: 6144394815, Fax 6144394884, mail: alejandro.lopez@cimav.edu.mx

ABSTRACT

A viable alternative to fossil fuels is to make use of H_2 from renewable sources as an energy carrier or as a clean fuel. Steam reforming of hydrocarbons is the conventional process to produce H_2, with the drawbacks that presents low efficiency combined with high operational costs and CO_2 being emitted into the atmosphere. An alternative to this process is the dry reforming of hydrocarbons, which employs CO_2 to produce hydrogen-syngas and the use of ethanol as a renewable feedstock which would prevent CO_2 emission into the atmosphere. One innovative approach is the use of a solid carbonate to serve as a source of CO_2 for this process. Thus, exposing the solid carbonate to high temperatures (reaction temperature), this decomposes emitting CO_2, which is used as raw material along with ethanol (EtOH) to produce hydrogen-synthesis gas. The present work aims to perform a thermodynamic and kinetic simulation study to explore reaction conditions close to equilibrium for a high syngas-H_2 production, under the dry reforming of EtOH. $CaCO_3$ was used as source of CO_2 for the reaction system. The thermodynamic study was performed using the HSC software and the studied conditions were: T = 300-1000 °C, $CaCO_3$/EtOH molar ratio = 1-3. Results showed that at T ≥ 755 °C and $CaCO_3$/EtOH ≥ 2.2, a free carbon formation syngas is produced. Maximum H_2 production was obtained at 855 °C and $CaCO_3$/EtOH ≥ 2.2, while the highest concentration of H_2 was produced at 755 °C. Furthermore, a process and kinetics simulations were performed through ASPEN-Plus and CKS, respectively and based on experimental data taken from the literature for the dry reforming of EtOH. Results indicate that at 900 ºC and $CaCO_3$/EtOH = 2 ratio, the estimated value of H_2 purity was very similar to that obtained by the thermodynamic equilibrium analysis.

Keywords: CO_2 dry reforming, thermodynamic and kinetics modelling

1. Introduction

Today, one of the major technological challenges is the search for energy alternatives to fossil fuels and their impact on the environment. A viable option is to make use H_2 as an energy carrier or as a clean fuel from renewable sources such as biomass, solar energy, etc., and converted to electricity by fuel cells that provide high efficiency electricity with only steam as a clean gas exhaust. However, an efficient generation of hydrogen from the main energy carrier is a key condition for the commercialization of fuel cells [1–5].

Ethanol (EtOH) can be a considered a suitable feedstock to produce hydrogen through many catalytic processes. In comparison with other fuels, ethanol has several advantages. It can be produced through the fermentation of biomass or renewable raw materials, including energy plants, waste materials from agro-industries or forestry residue materials, organic municipal solid waste, etc. Ethanol produced from these raw materials are generally named biomass-derived ethanol or bioethanol. Hydrogen produced from bioethanol presents the significant advantage of being nearly CO_2 neutral, since the carbon dioxide released into the atmosphere during ethanol processing is re-absorbed in the growth of the biomass, and therefore, there is no net release of carbon dioxide into the atmosphere [6].

Ethanol can be converted into hydrogen through steam reforming [7–15], partial oxidation [16–21], autothermal reforming (oxidative reforming) [22–27] and dry reforming (CO_2 reforming, DRE) [28–31]. Although ethanol steam reforming, partial oxidation and autothermal reforming have been extensively studied, dry reforming of ethanol has received much less attention. Furthermore, CO_2 is a greenhouse gas and as a consequence ethanol reforming with CO_2 is an interesting approach for the conversion of CO_2 into syngas or hydrogen, which can further be converted into high value chemicals such as methanol, synthetic fuels, urea, etc.

One innovative approach for the syngas/hydrogen production through the dry reforming of ethanol process (DRE) is the use of a solid carbonate (such as $CaCO_3$) to serve as a source for CO_2 in this process. Thus, exposing the solid carbonate to the high temperatures of the DRE reaction (such as 900 °C), decomposes the solid carbonate through:

$$CaCO_3 \rightarrow CaO + CO_2 \qquad \Delta H^0_{298} = 178 \text{ kJ/mol} \qquad (1)$$

thus, emitting CO_2, which is then used as raw material along with ethanol (EtOH) to produce hydrogen-synthesis gas by:

$$C_2H_6O + CO_2 = 3CO + 3H_2 \qquad \Delta H^0_{298} = 296.70 \text{ kJ/mol} \qquad (2)$$

Then, by combining the CO_2-releasing decomposition of $CaCO_3$ with the CO_2-consuming reforming of C_2H_6O, it is possible to simultaneously coproduce CaO and syngas in a single reaction, represented by:

$$C_2H_6O + CaCO_3 = CaO + 3CO(g) + 3H_2(g) \qquad \Delta H^0_{298} = 649.78 \text{ kJ/mol} \qquad (3)$$

Important advantages that this reaction scheme offers over steam reforming are (a) the formation of a suitable H_2/CO ratio for use in Fischer-Tropsch synthesis and (b) more desirable thermodynamic properties, for example large heat of reaction and reversibility for chemical energy transmission systems such as chemical looping [32].

Moreover, although the dry reforming concept has environmental benefits and economic advantages, there are only a few commercial processes based on the CO_2 reforming reaction such as the CALCOR and SPARG processes [33, 34]. This can be due to the fact that a major limitation of this process arises from the formation of carbon deposits, which can cause a significant deactivation of the reforming catalyst.

One promising approach for the dry reforming concept is the so called "Catforming" process, which consists of two circulating fluidized beds. A downer for the endothermic CO_2 reforming and a riser for the catalyst regeneration. In the process scheme, the transport of the solids between both reactors allows for a period of catalyst regeneration involving coke combustion [35]. Even though the fact that the reforming reactor is to be operated under unfavorable carbon formation conditions, coke will inevitably be deposited on the active sites of the catalyst.

Our proposal is based in the combination of these two new approaches to the dry reforming process that can be used to produce syngas and/or hydrogen in an efficient manner. First, the use of a solid carbonate will provide the necessary CO_2 for the dry reforming of ethanol in a fluidized bed and secondly, the inevitable carbon deposits on the catalyst that characterize this process will be removed by gasification with steam in a separate fluidized bed reactor (riser), and at the same time the CaO will carbonate back to $CaCO_3$ along with the production of additional syngas. Finally, the regenerated catalyst and the sold carbonate will be recycled back to the reforming reactor to complete a full reaction cycle. Details of this process scheme are presented in Figure 1 below.

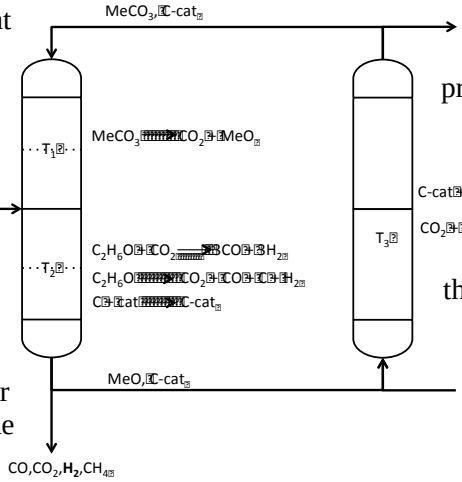

Figure 1. H_2 production by dry reforming of ethanol with CO_2 evolution and catalyst regeneration

In this process MeO (CaO) can be any metal oxide capable to be carbonated at the required conditions of the process. $MeCO_3$ ($CaCO_3$) is any carbonated metal oxide and cat is any dry reforming catalyst. It is important to point out that heat integration plays an essential role for the feasibility of this process. In the dry reforming reactor at least two highly endothermic reactions take place (1 and 2), while at the gasification reactor the carbon oxidation and MeO carbonation are highy exothermic reactions. Therefore, it is expected that presumably, some of the necessary heat for the reforming reactor will be provided by the gasification reactor and their solid carried products (MeO and cat).

Therefore, the present work aims to perform thermodynamic, process and kinetic simulation studies to explore reaction conditions close to equilibrium for a high syngas-H_2 production, under the dry reforming of EtOH, using $CaCO_3$ as a source of CO_2 for the dry reforming reaction system.

2. Simulation Methods

2.1. Thermodynamic Method

Thermodynamic calculations employed the Gibbs free energy minimization technique. In a reaction system where many simultaneous reactions take place, equilibrium calculations can be performed through the Gibbs energy minimization approach (also called the nonstoichiometric method). Details of this technique can be found elsewhere [36]. All calculations were performed using the equilibrium module of the HSC chemistry software for windows [37]. HSC calculates the equilibrium composition of all possible combination of reactions that are able to take place within the thermodynamic system. These equilibrium calculations make use of the equilibrium composition module of the HSC program that is based on the Gibbs free energy minimization technique. The GIBBS program of this module finds the most stable phase combination and seeks the phase compositions where the Gibbs free energy of the system reaches its minimum at a fixed mass balance, constant pressure and temperature. At the ethanol dry reforming system the gaseous species included were: ethanol, ethylene, ethane, acetone, acetaldehyde, acetic acid, C_2H_6O, CO, CH_4, CO_2, H_2, and H_2O, while solid species were: C, CaO and $CaCO_3$.

During the thermodynamic simulation work the reaction temperature was varied in the range of 300-1000 °C at 1 atm. While, carbonate to ethanol molar ($CaCO_3$/EtOH) was varied from 1-5. It is important to notice that all the present simulation calculations are based on theoretical thermodynamic considerations and these are to be taken as a guide to further experimental evaluation of the reaction systems, since no heat and mass diffusional limitations as well as kinetics effects were taken into account for the conformation of the present thermodynamic analysis.

2.2. Process Simulation Method

Process simulation calculations were performed using of Aspen-plus© Engineering Process Simulator. This is a program for simulation of chemical processes in which the analysis of chemical processes as well as heat integration can be made.

Therefore, this simulator was employed for the analysis of the process scheme of Figure 1. The modules of Aspen-Plus that were used to evaluate the reaction system were: the RGibbs (Gibbs Reactor) and RStoic (Stoichiometric Reactor) units, wherein RGibbs method is based on the Gibbs free energy minimization technique for multiphase reactions and material balance, while RStoic is based on known fractional reaction conversions. Cyclone were used to separate solid and gas streams, mixers were also used to combine several gas and/or solid streams, while heat exchangers allowed heat balance and integration.

2.3. Kinetics Simulation Method

Kinetics simulations were performed through the CKS software [38] and based on experimental data taken from the literature. The CKS program conveniently simulates chemical reactions. Its stochastic simulation technique is fast and accurate, and is very suitable for a wide variety of reactions. Specifically the software is based in a stochastic process, which is used to characterize a sequence of random variables (stochastic) that evolve according to another variable, usually time. Each of the random variables of the process has its own probability distribution function and, between them, can be correlated. CKS require the specification of the chemical reaction mechanism in a conventional notation, the rate constants for each step, and the reactions conditions (temperature and pressure). The same program calculates concentration versus time curves as well as the pressure, volume and temperature data. Simulations with CKS are not limited to homogeneous systems; a wide variety of non-homogeneous reactions, for example, between gases and solids or in a fluidized reactors, can be successfully simulated by using this simple technique.

In this the present kinetic simulation a reaction mechanism for the dry reforming of ethanol combined with the CO_2 evolution from $CaCO_3$ was proposed and compared with experimental data for the ethanol steam reforming system, which kinetically behaves similarly to the dry reforming system. Kinetic data results (CKS) from simulation were then compared to the equilibrium data previously obtained in the thermodynamic section of the present study.

3. Results and discussion

3.1. Thermodynamic Analysis

The production of hydrogen and other compounds (CO, CO_2 and C) at a temperature range of 300-1000 °C and $CaCO_3/C_2H_6O$ molar ratios from 1 to 3 were analyzed on the basis of thermodynamic analysis. At the studied conditions the conversion of ethanol was always greater than 99.99% and it can be considered for practical purposes that the conversion is complete. Figure 1 shows the equilibrium content (dry basis) in kmol/mol of EtOH fed as a function of temperature and $CaCO_3$/EtOH molar ratio for H_2, CO, CO_2 and C species.

In this Figure it is evident that H_2 and CO mols at equilibrium increase monotonically with increasing temperature from 300 to 1000 °C and this can be explained in terms of the equation (1), which reflects the temperature dependence of the equilibrium constant as described by Wang et al. [39]. In contrast, CO_2 content at equilibrium is dominated by the combination of reactions (1) and (2), which at temperatures from 300-700°C shows an average of 0.45 kmols of CO_2, thus reflecting the excess of CO_2 being fed according to the stoichiometric $CaCO_3$/EtOH ratio of 1 needed according to reaction (3). However, higher temperatures will produce a greater CO_2 content especially at $CaCO_3$/EtOH molar ratios greater than 2. This can be explained in terms of reaction 2, in which high temperatures (greater than 600 °C) will increase the CO_2 evolution.

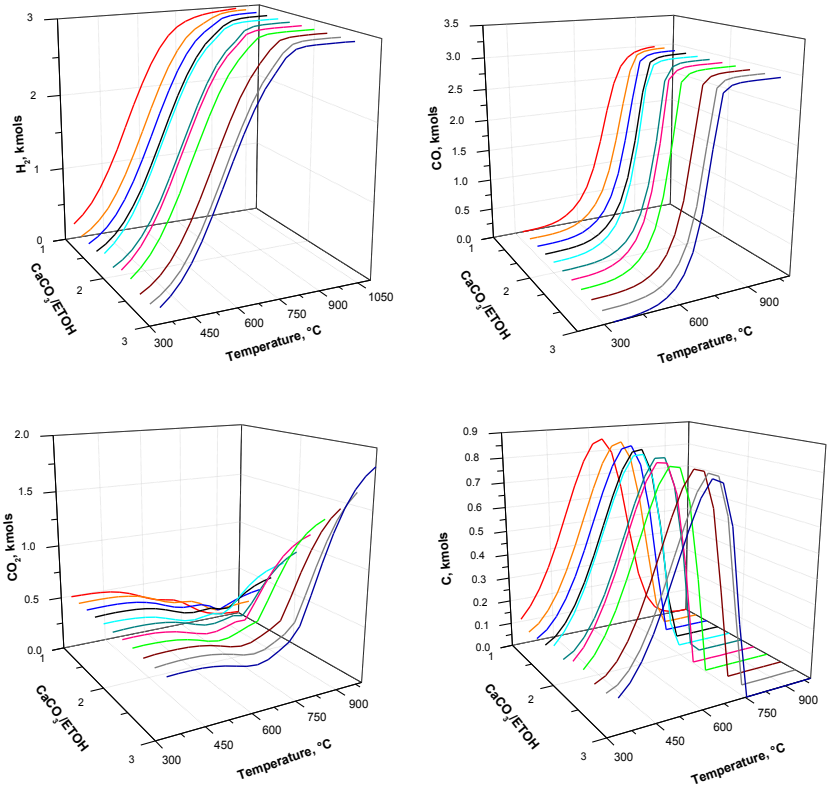

Figure 2. Equilibrium content for the DRE process with CO_2 evolution

This is why the CO_2 content increases to values greater than 1 at temperatures closer to 900 °C and $CaCO_3$/EtOH ratios ≥ 2. Furthermore, CO_2 content at ratios lower than ≈ 1.5 are smaller than the average 0.45 kmols. This is explained by the fact that CO_2 is almost completely consumed by the DRE reaction (2), since the stoichiometric amount of CO_2 needed according to reaction (3) is of 1 mol of $CaCO_3$ per mol of EtOH fed to the reaction system. Also in this Figure the carbon content is plotted as a function of temperature and $CaCO_3$/EtOH ratio. Here, it is evident that lower temperatures than 750 °C will produce carbon with a maximum generated at temperatures around 650 °C. This was expected, since previous thermodynamic analysis using gaseous CO_2 as a feed also confirmed this behavior [39]. Therefore, temperatures greater than around 750 °C and $CaCO_3$/EtOH ratios ≥ 2.2 will insure a carbon free operation region for the DRE combined with CO_2 evolution by a solid carbonate. This behavior can be explained ion terms of the Boudouard reaction:

$$2CO \rightarrow CO_2 + C \qquad \Delta H^0_{298} = -175.81 \text{ kJ/mol} \qquad (4)$$

That is why at temperatures greater than 750 °C the CO content significantly increases, since the above reaction is no longer thermodynamically favoured and consequently no carbon formation is possible.

A more careful analysis of the generated data allows to conclude that according to the previous thermodynamic analysis data optimum conditions in order to produce a maximum hydrogen production and carbon free operation is at temperatures greater than 755 ° C and at $CaCO_3$/EtOH ratios ≥ 2.2.

3.2. Process Simulation

Figure 3 presents a diagram of the process simulation scheme employed during the simulation of the DRE with CO_2 evolution and catalyst regeneration. The catalyst was not included in this simulation due to the fact that this has to be determined based on future experimental research.

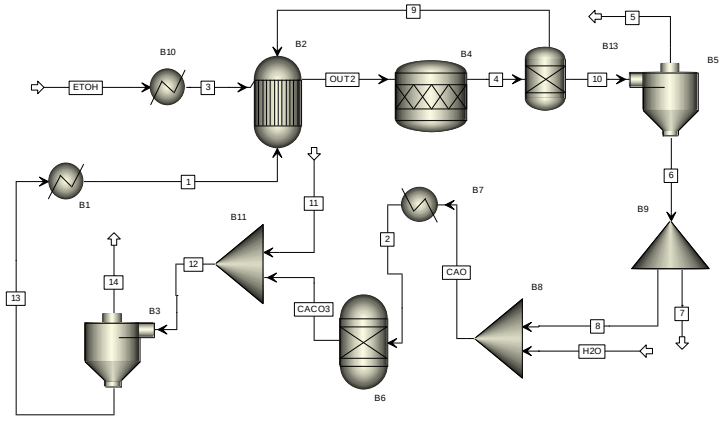

Figure 3. Process simulation diagram for the DRE with CO_2 evolution and catalyst regeneration

This process starts with the EtOH feed of 1 kmol/h to being preheated to 900°C and fed to the DRE reactor, along with a mixture of 1 and 0.83 kmol/h of $CaCO_3$ and CaO, respectively. The reactor duty was 508,034.6 kJ/h at 900 °C and 1 atm. The reactor products were fed to a stoichiometric reactor where carbon was allowed to be formed by reaction (4) using an experimental reaction conversion of 0.6 based on the data from Hu et al. [40] at present DRE reaction conditions. It is important to state that even though at 900 °C and feed $CaCO_3$/EtOH ratio used here, thermodynamically no carbon is formed, experimentally this happens. Therefore, a more realistic result can be obtained by considering the combination of equilibrium results and the corresponding experimental carbon formation. The CO_2 formed by the Boudouard reaction (1.798 kmol/h) were recycled to the DRE reactor (B2). After this reactor a H_2/CO molar ratio of 0.998 was obtained with only negligible amounts of CH_4 and H_2O. Additionally, 0.77 kmol/h of carbon were formed. Then a cyclone was used to separate the gases from the solids and the gas product stream 5 included: 2.223 kmol/h of H_2 and 2.226 kmol/h of CO, while 1.83 kmol/h of CaO were sent to the regenerator along with the carbon. Stream 6 solids were divided at separator B9 and stream 7 was discarded for circulation and balance purposes, while stream 8 containing 1.28 kmol/h of CaO and 0.54 kmol/h of C were combined with 1.2 kmol/h of steam in mixer B8, preheated to 770 °C and then fed to the regenerator reactor, where the carbon gasification and CaO carbonation reactions took place. The product from the regenerator consisted in 0.45 kmol/h of $CaCO_3$ along with 0.83 kmol/h of CaO and 0.913 kmol/h of H_2.Then in mixer B11 0.74 kmol/h of $CaCO_3$ were added to this last stream followed by separation of the gaseous products at cyclone B3, where a mixture of mainly H_2 and steam exited at stream 14. The remaining solids composed by 1 kmol/h of $CaCO_3$ and 0.83 kmol/h of CaO were preheated to 900 °C (B1) to be recycled back to the DRE reactor B2.

Table 1 below summarizes results from the process simulation of selected streams. In this Table it can be seen that the gaseous output stream of the process are streams 5 and 14. Stream 5 presents a H_2/CO ratio of about 1, while stream 14 is almost a pure H_2 stream. This is very convenient, since these two streams can be combined to obtain a specific desired H_2/CO ratio as in the case of the Fischer-Tropsch process for the production of a specific fuel mixture composition.

Comparing the process simulation results with one of the actual commercial dry reforming process called Calcor, the H_2/CO ratio obtained with this process is 0.42 from a natural gas feed [33]. Modifications to this process include a membrane reactor to improve the syngas yield and separation of the CO_2 produced along with the syngas by a standard amine technology and to recycle this stream back to the dry reformer. Furthermore, as stated earlier, the mayor problem of this technology is the carbon formation over the reforming catalyst causing deactivation and constant catalyst replacement or regeneration. Another commercial process is the Sparg that produce a H_2/CO ratio of 1.8 and suppressing the carbon formation by using a partially sulfur poisoned nickel catalyst [34]. However, product synthesis gas from this process still contains about 2.7% of methane.

Moreover, in the case of the present simulation a solution to this problem is offered. Furthermore, it is important to notice that the present process simulation effort in only a first attempt to show the possible advantages of the proposed technology, while production costs and a more deep energy analysis is further needed in order to assess the feasibility the present proposed technology.

3.3. Kinetics Simulation

In order to perform the kinetic simulation of the ethanol dry reforming combined with CO_2 evolution it is required to establish the corresponding reaction mechanism. This was selected according to the following criteria: because there are scarce references of studies related to the kinetics of dry reforming of ethanol and because Jankhah [41] has experimentally found that the kinetic behavior of both the dry and the steam reforming of ethanol follow a very similar kinetic mechanism it was decided that in the present kinetic simulation a reaction mechanism for the dry reforming of ethanol combined with the CO_2 evolution be simulated with kinetic experimental data reported for the steam reforming of ethanol reaction system.

Table 1. Summary of process simulation results of selected streams

Stream Name Mole Flow kmol/hr	ETOH	1	OUT2	4	5	7	CAO	$CACO_3$	11	14
$CACO_3$	0.00	1.00	0.00	0.00	0.00	0.00	0.00	0.45	0.55	0.00
CO_2	0.00	0.00	1.02	1.80	0.00	0.00	0.00	0.02	0.00	0.02
CAO	0.00	0.83	1.83	1.83	0.00	0.55	1.28	0.83	0.00	0.00
C_2H_6O	1.00	0.00	0.00	0.00	0.00	0.00	0.00	0.00	0.00	0.00
CO	0.00	0.00	3.77	2.23	2.23	0.00	0.00	0.04	0.00	0.04
H_2	0.00	0.00	2.22	2.22	2.22	0.00	0.00	0.91	0.00	0.91
C	0.00	0.00	0.00	0.77	0.00	0.23	0.54	0.00	0.00	0.00
CH_4	0.00	0.00	0.00	0.00	0.00	0.00	0.00	0.03	0.00	0.03
H_2O	0.00	0.00	0.78	0.78	0.78	0.00	1.20	0.22	0.00	0.22
Total Flow kmol/hr	1.00	1.83	7.80	7.02	5.23	0.78	3.02	2.51	0.55	1.23
Total Flow kg/hr	46.07	146.84	169.27	159.98	80.83	33.63	21.62	8.30	55.05	8.30
Total Flow l/min	1262.85	0.86	12515.39	11272.81	8386.75	0.18	1778.18	1547.73	0.34	1547.73
Temperature °C	650.00	900.00	900.00	900.00	900.00	900.00	810.46	650.00	650.00	650.00

For this endeavor it was needed to find the experimental data that followed the same reaction mechanism as in the steam reforming system. In the present case it was found that the Eley-Rideal mechanism fulfilled this purpose. Becerra et al. [42] found that an Eley-Rideal type model described adequately the main reaction of the CO_2 reforming of methane, while Akande [43] reported experimental data and found that the steam reforming of ethanol over a Ni/Al_2O_3 catalysts followed also the Eley-Rideal type model resembling the CO_2 reforming of methane mechanism found by Becerra et al. This mechanism is based on the interaction between gas-phase molecules which react directly with adsorbed species; in the present reaction system, not all the reactants were adsorbed on the catalyst surface. Accordingly, the surface reaction involve adsorbed and non-adsorbed substances, so that it is considered a subset of Langmuir mechanisms in which one of the reactants is not absorbed in the catalyst [44].

Because the dry reforming of EtOH and CO_2 evolution is a complex system of reactions and following the above criteria, the combination of the reaction steps of two catalytic mechanisms was proposed; on one side the catalytic dry reforming of methane and on the other the catalytic steam reforming of ethanol, thereby obtaining a catalytic reaction mechanism equivalent to the kinetic process to be simulated. This mechanism is described by the reaction steps given below:

$$C_2H_6O + S \rightarrow C_2H_6O\text{-}S \quad (5)$$

$C_2H_6O\text{-}S + S \rightarrow CH_4O\text{-}S + CH_2\text{-}S$ (6)

$CH_4O\text{-}S \rightarrow CH_2\text{-}S + H_2O$ (7)

$CO + H_2O \rightarrow CO_2 + H_2$ (8)

$CaCO_3 \rightarrow CaO + CO_2$ (9)

$2CH2\text{-}S + 2CO_2 \rightarrow 4CO + 2H_2 + 2S$ (10)

$C_2H_6O + CaCO_3 \rightarrow CaO + 3CO + 3H_2$ (11)

where steps from reactions (5) to (10) represent the proposed mechanism, and the overall reaction is represented by reaction (11), here S represents an active site for the adsorption of species, while C_2H_6O-S represents an adsorbed transient specie. This mechanism was inserted into the CKS program with initial concentrations of C_2H_6O, $CaCO_3$ and S of 1, 2 and 3 mol/L, respectively. Kinetic parameters (e.g. A_o, E_a, etc.) for the above reactions were taken from experimental data on the steam reforming of ethanol reported by Patel et al. [45]. Figure 4 presents results for the kinetic simulation of the dry reforming of ethanol combined with CO_2 evolution at temperature of 900 °C and based on the proposed reaction mechanism.

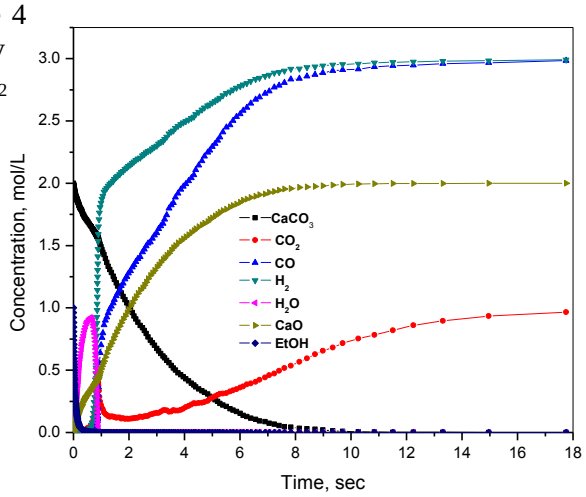

Figure 4. Kinetic simulation re of the diagram for the DRE with CO_2 evolution

Concentration profiles from Figure 4 reflect the nature of the proposed mechanism. Ethanol is fully converted almost instantly, while water is produced from the surface reaction equation (7) to later be consumed at about 1 second by the eater gas shift reaction (8). Hydrogen is formed almost instantly as a consequence of the WGS reaction and then at a slower rate at about 1.5 sec when the CO_2 is being formed by the decomposition of the $CaCO_3$ reaction (9), while CO is initially hindered by the WGS to later be enhanced by surface reaction (10). CO_2 evolution can be clearly observed in Figure 4, since this starts gradually and at about 9 sec the complete conversion of reaction (9) is achieved. This was also reflected in the H_2 and the CO concentrations reaching both 3 mol/L. All these results agree well with the previous

thermodynamic analysis and process simulation results in the sense that at carbon free conditions (900°C and $CaCO_3$/EtOH = 2.2) the H_2/CO molar ratio was almost 1, with also 3 mols H_2 and CO being formed.

4. Summary and perspectives

The present work a thermodynamic, process and kinetic simulation studies were performed to explore reaction conditions close to equilibrium for a high syngas-H2 production, under the dry reforming of EtOH. $CaCO_3$ was used as source of CO_2 for the reaction system, instead of high purity CO_2 employed in the current dry reforming technology. Results showed the feasibility that at $T \geq 755$ °C and $CaCO_3$/EtOH ≥ 2.2, a free carbon formation syngas can be produced. Maximum H_2 production can be obtained at 855 °C and $CaCO_3$/EtOH ≥ 3, while the highest concentration of H_2 was produced at 755 °C. Furthermore, a process and kinetics simulations performed through ASPEN-Plus and CKS, respectively and based on experimental data taken from the literature for the dry reforming of EtOH indicate that at 900 ºC and $CaCO_3$/ETOH = 2 ratio, the estimated value of H_2 purity was very similar to that obtained by the thermodynamic equilibrium analysis. Finally, these results can be taken as a basis for future experimental and theoretical studies in search for a suitable catalyst and conditions to evaluate the present proposed technology.

References

[1] Armor JN. The multiple roles for catalysis in the production of hydrogen. Appl Catal A 1999; 176(2): 159–76.

[2] Joensen F, Rostrup-Nielsen JR. Conversion of hydrocarbons and alcohols for fuel cell. J Power Sources 2002; 105(2):195–201.

[3] Peña MA, Gomez JP, Fierro JLG. New catalytic routes for syngas and hydrogen production. Appl Catal A 1996; 144:7–57.

[4] Goltsov VA, Veziroglu TN, Goltsova LF. Hydrogen civilization of the future a new conception of the IAHE. Int J Hydrogen Energy 2006; 31:153–9.

[6] Velu S, Satoh N, Gopinath CS, Suzuki K. Oxidative reforming of bio-ethanol over CuNiZnAl mixed oxide catalysts for hydrogen production. Catal Lett 2002; 82(1–2):145–52.

[7] Garcia EY, Laborde MA. Hydrogen production by the steam reforming of ethanol: thermodynamic analysis. Int J Hydrogen Energy 1991; 16:307–12.

[8] Vasudeva K, Mitra N, Umasankar P, Dhingra SC. Steam reforming of ethanol for hydrogen production: thermodynamic analysis. Int J Hydrogen Energy 1996; 21:13–8.

[9] Haga F, Nakajima T, Miya H, Mishima S. Catalytic properties of supported cobalt catalysts for steam reforming of ethanol. Catal Lett 1997; 48:223–7.

[10] Mariño FJ, Cerrella EG, Duhalde S, Jobbagy M, Laborde MA. Hydrogen from steam reforming of ethanol. Characterization and performance of copper–nickel supported catalysts. Int J Hydrogen Energy 1998; 23:1095–101.

[11] Liguras DK, Kondarides DI, Verykios XE. Production of hydrogen for fuel cells by steam reforming of ethanol over supported noble metal catalysts. Appl Catal B 2003; 43(4): 345–54.

[12] Aboudheir A, Akande A, Idem R, Dalai A. Experimental studies and comprehensive reactor modeling of hydrogen production by the catalytic reforming of crude ethanol in a packed bed tubular reactor over a Ni/Al_2O_3 catalyst. Int J Hydrogen Energy 2006; 31:752–61.

[13] Cavallaro S, Mondello N, Freni S. Hydrogen produced from ethanol for internal reforming molten carbonate fuel cell. J Power Sources 2001; 102(1):198–204.

[14] Rostrup-Nielsen J, Trimm DL. Mechanisms of carbon formation on nickel-containing catalysts. J Catal 1977; 48: 155–65.

[15] Trimm DL. Coke formation and minimization during steam reforming reactions. Catal Today 1997; 37(3):233–8.

[16] Fierro V, Klouz V, Akdim O, Mirodatos C. Oxidative reforming of biomass derived ethanol for hydrogen production in fuel cell applications. Catal Today 2002; 75(1–4):141–4.

[17] Liguaras DK, Goundani K, Verykios XE. Production of hydrogen for fuel cells by catalytic partial oxidation of ethanol over structured Ru catalysts. Int J Hydrogen Energy 2004; 29:419–27.

[18] Ioannides T. Thermodynamic analysis of ethanol processors for fuel cell applications. J Power Sources 2001; 92:17–25.

[19] Cheekatamarla PK, Finnerty CM. Synthesis gas production via catalytic partial oxidation reforming of liquid fuels. Int J Hydrogen Energy 2008; 33:5012–9.

[20] Hsu SN, Bi JL, Wang WF, Yeh CT, Wang CB. Low-temperature partial oxidation of ethanol over supported platinum catalysts for hydrogen production. Int J Hydrogen Energy 2008; 33:693–9.

[21] Wang WJ, Wang YQ. Thermodynamic analysis of partial oxidation of biomass-derived ethanol for hydrogen-rich gas generation. Int J Hydrogen Energy 2008; 33:5035–44.

[22] Deluga GA, Salge JA, Schmidt LD, Verykios XE. Renewable hydrogen from ethanol by autothermal reforming. Science 2004; 303:993–7.

[23] Cavallaro S, Chiodo V, Vita A, Freni S. Hydrogen production by auto-thermal reforming of ethanol on Rh/Al_2O_3 catalyst. J Power Sources 2003; 123:10–6.

[24] Huang L, Xie J, Chen R, Chu D, Chu W, Hsu AT. Effect of iron on durability of nickel-based catalysts in auto-thermal reforming of ethanol for hydrogen production. Int J Hydrogen Energy 2008; 33:7448–56.

[25] Youn MH, Seo JG, Cho KM, Park S, Park DR, Jung JC, et al. Hydrogen production by auto-thermal reforming of ethanol over nickel catalysts supported on Ce-modified mesoporous zirconia: effect of Ce/Zr molar ratio. Int J Hydrogen Energy 2008; 33:5052–9.

[26] Srisiriwat N, Therdthianwong S, Therdthianwong A. Oxidative steam reforming of ethanol over Ni/Al_2O_3 catalysts promoted by CeO_2, ZrO_2 and CeO_2–ZrO_2. Int J Hydrogen Energy 2009; 34:2224–34.

[27] Youn MH, Seo JG, Park S, Jung JC, Park DR, Song IK. Hydrogen production by auto-thermal reforming of ethanol over Ni catalysts supported on ZrO_2: effect of preparation method of ZrO_2 support. Int J Hydrogen Energy 2008; 33:7457–63.

[28] De Oliveira-Vigier K, Abatzoglou N, Gitzhofer F. Dryreforming of ethanol in the presence of a 316 stainless steel catalyst. Can J Chem Eng 2005; 83:978–84.

[29] Tsiakaras P, Demin A. Thermodynamic analysis of a solid oxide fuel cell system fuelled by ethanol. J Power Sources 2001; 102(1):210–7.

[30] Jankhah S, Abatzoglou N, Gitzhofer F. Thermal and catalytic dry reforming and cracking of ethanol for hydrogen and carbon nano filaments' production. Int J Hydrogen Energy 2008; 33:4769–79.

[31] Ruckenstein E, Wang HY. Carbon deposition and catalytic deactivation during CO_2 reforming of of CH_4 over $Co/g\text{-}Al_2O_3$ catalysts. J Catal 2002; 205(2):289–93.

[32] Halmann M., Seinfeld A., Thermoneutral Coproduction of Calcium Oxide and Syngas by Combined Decomposition of Calcium Carbonate and Partial Oxidation/CO_2-Reforming of Methane, Energy & Fuels 2003, 17, 774-778.

[33] Teuner, St. C.; Neumann, P.; Von Linde, F. The Calcor Standard and Calcor Economy Processes. Oil Gas Eur. Mag. 2001, 3, 44.

[34] Udengaard, N. R.; Bak Hansen, J. H.; Hanson, D. C.; Stal, J. A. Sulfur promoted Reforming Process lowers Syngas Hydrogen/Carbon Monoxide Ratio. Oil Gas J. 1992, 90 (10), 62.

[35] Solh E., T.; Jarosch, K.; de Lasa, H. Catalytic Dry Reforming of Methane in a CREC Riser Simulator Kinetic Modeling and Model Discrimination. Ind. Eng. Chem. Res. 2003, 42, 2507.

[36] Collins-Martínez V. Escobedo Bretado M., Meléndez Zaragoza M., Salinas Gutiérrez J., López Ortiz A. Absorption enhanced reforming of light alcohols (methanol and ethanol) for the production of hydrogen: Thermodynamic modeling, Int J Hydrogen Energy 2013; 38:12539–553.

[37] Roine A. Chemical reaction and equilibrium software with extensive thermo-chemical database. Outokumpu HSC 6.0 Chemistry for windows; 2010.

[38] IBM Almaden Research Center. 1995. Introduction: Getting Started. IBM Corporation. Chemical Kinetics Simulator 1.0 User´s Manual.v-vii.

[39] Wang W., Wang Y., Dry reforming of ethanol for hydrogen production: Thermodynamic investigation, Int J Hydrogen Energy 2009; 34:5382–5389.

[40] Hu X., Lu G., Syngas production by CO_2 reforming of ethanol over Ni/Al_2O_3 catalyst, Catal Comm 10 (2009) 1633–1637.

[41] [X] Jankhah, Sepideh, Ethanol reforming with carbon dioxide, Memory of Masters in applied science with a major in chemical engineering, Université de Sherbrooke, 2007, available at:
http://savoirs.usherbrooke.ca/bitstream/handle/11143/1386/MR37883.pdf?sequence=1&isAllowed=y

[42] Becerra M. A., Iriarte M. E., and Castro-Luna A. E., Catalytic Activity of A Nickel on Alumina Catalyst in The CO_2 Reforming of Methane, React.Kinet.Catal.Lett Vol. 79, No. 1, 119-125, 2003.

[43] Akande A. J., Production of Hydrogen by Reforming of Crude Ethanol, Master of Science Thesis, Department of Chemical Engineering, University of Saskatchewan, Saskatoon, Saskatchewan, Canada, February 2005.

[44] Izquierdo Torres, J. F. Cinética de las reacciones químicas. Barcelona: Universitat Barcelona (2004).

[45] Patel M., Jindal T. K., and Pant K. K., Kinetic Study of Steam Reforming of Ethanol on Ni-Based Ceria−Zirconia Catalyst, Ind. Eng. Chem. Res. 2013, 52, 15763−15771

XIV International Congress of the Mexican Hydrogen Society
Cancun, Mexico, 2014

$W_{1-x}Mo_xO_3 \cdot 0.33H_2O$ Solid Solutions with Tunable Band Gap for Hydrogen Production

A. Arzola-Rubio[a], J. Camarillo-Cisneros[a], V. Collins-Martínez[a], L. De la Torre-Sáenz[a], F. Paraguay-Delgado[a*]

A Departamento de Materiales Nanoestructurados, Centro de Investigación en Materiales Avanzados S. C., CIMAV
Miguel de Cervantes 120, Chihuahua, Chih. México. CP 31109.
*Tel: +526144391107; e-mail: francisco.paraguay@cimav.edu.mx

ABSTRACT

A series of $W_{1-x}Mo_xO_3\,0.33H_2O$ (x = 0, 0.25, 0.50, 0.75) nano/microstructures and $MoO_3\,0.55H_2O$ microamorphous structures have been prepared by hydrothermal synthesis starting from aqueous Ammonium metatungstate hydrate ($(NH_4)_6H_2W_{12}O_{40}\,xH_2O$) and Ammonium heptamolybdate tetrahydrate ($(NH_4)_6Mo_7O_{24}\,4H_2O$) acidified solutions. The $WO_3\,0.33H_2O$ crystal lattice can be substituted with up to 75% Mo without structural alterations of the orthorhombic host structure. With the increase of the Mo content (x) from 0 to 0.75, the band gap of the as-prepared $W_{1-x}Mo_xO_3\,0.33H_2O$ nano/microstructures is narrowed from 2.62 to 2.10 eV. We employed first-principles calculations in the DFT and DFT+U framework as a meaning to confirm our experimental data and we obtained indirect semiconductors up to x=0.75. We suggest that the increasing Mo fraction (25, 50 and 75%), effects of the hydrothermal synthesis (pressure and temperature), hydrogen peroxide and pH are responsible for the narrowing of the band gap and increasing of the superficial area and presumably making hydrogen production feasible through the photocatalytic water splitting.

Keywords: H_2 production; water splitting; W/Mo solid solutions.

1. Introduction

Hydrogen is considered as an ideal energetic vector for the future. Hydrogen fuel can be produced from clean and renewable energy sources and, thus, its life cycle is clean and renewable. Solar and wind are the two major sources of renewable energy and they are also the promising sources for renewable hydrogen production. However, presently, renewable energy contributes only about 5% of the commercial hydrogen production primarily via water electrolysis, while other 95% hydrogen is mainly derived from fossil fuels [1]. Renewable hydrogen production is not popular yet because the cost is still high. Photovoltaic water electrolysis may become more competitive as the cost continues to decrease with the technology advancement; however, the considerable use of small band gap semiconducting materials may cause serious life cycle environmental impacts. Alternatively, photocatalytic water-splitting using unary and binary WO_3 compounds for hydrogen production offers a promising way for clean, low-cost and environmentally friendly production of hydrogen by solar energy. WO_3 compounds can be used for photocatalytic water splitting to produce hydrogen gas using visible solar light, because of its narrow bandgap. Earlier studies of the photo electrochemical behavior of both polycrystalline and monocrystalline WO_3 provided instructive knowledge for the development of photocatalytic water-splitting systems (Hodes et al. 1976; Hardee and Bard 1977). The difficulty in the overall water splitting (both reduction and oxidation of H_20 molecules are to be achieved) by WO3 is that the lower edge of the CB lies below the redox potential of H_20/H_2. This means that the reduction of water molecules to generate hydrogen gas is thermodynamically unfavorable (Gissler and Memming 1977). Applying a bias potential to the system can overcome the energy barrier for the photogenerated electrons to be ejected into the adsorbed water molecules (Santato et al. 2001). Coupling with other semiconductor materials (Abe et al. 2005) and doping by metal ions (Hwang et al. 2002; Hameed et al. 2004) are other alternatives to make use of the oxidation power of WO_3 for water splitting. WO_3 also found interesting applications in electrochromic (Papacfthimiou et al. 2001; Badilcscu and Ashrit 2003; Baeck et al. 2003) and photochromic (Shigesato 1991; Bechinger et al. 1996; Su et al. 1997; Xu et al. 2000; Kim et al. 2006) devices such as large area displays and "smart windows" because WO_3 films can be switched between different optical states under different electro-chemical or optical conditions. The electrochromic effect is caused by the electrochemical reaction between the WO_3 electrode and protons in the electrolyte solution, under the influence of a bias potential to provide charge carriers (electrons in this case). The electrons can then create color centers by reducing the W^{6+} species to W^{5+} species. The photochromism effect of WO_3 is due to the formation of an identical absorption band upon light irradiation (Bechinger et al. 1993). This process is completely reversible by exposing the reduced sample to oxygen gas. DFT has been a handy tool to corroborate gap experimental data and also as a method itself to use in simulate tendencies. Recently, Zhou et al. was capable of modulate the band gaps of the $W_{1-x}Mo_xO_3$ materials by changing the Mo/W ratio [2]. They successfully prepared a series of $W_{1-x}Mo_xO_3$ $0.33H_2O$ micro/nanostructures with controlled stoichiometry (x = 0, 0.25, 0.50, 0.75). They stated that the increase of the Mo content, the band gap of $W_{1-x}Mo_xO_3$ $0.33H_2O$ narrowed from 3.25 to 2.77 eV. In this present work we synthetized a series of $W_{1-x}Mo_xO_3$ $0.33H_2O$ nano/microstructures similar to Zhou et al. from other precursors such as ammonium heptamolybdate and ammonium metatungstate instead of metal powders. We used 2.2M HNO_3 to acidify the solutions instead of forming the peroxopolytungstic and molybdic acid solutions. Our investigation

objective was to study their enhanced band gaps as a function of the Mo content and its capability of hydrogen production.

2. Experimental

For a usual synthesis, y mmol (y = 0, 2.5, 5.0, 7.5, and 10.0) of Ammonium heptamolybdate tetrahydrate and (10 - y) mmol of Ammonium metatungstate hydrate were dissolved in a mixture of 21 mL of H_2O, 9 mL of 30 wt.% H_2O_2 , and 3 mL of 2.2M HNO_3. The solution was then transferred into a Teflon vial then placed in a stainless-steel autoclave and, sealed, and hydrothermally treated at 180°C for 24 h. The solid solutions were collected by centrifugation, washed with Deionized water 3 times, and dried at room temperature. The resultant products with y = 0, 2.5, 5.0, 7.5, and 10.0 were designated as WH1 (WO_3 $0.33H_2O$), WM25 ($W_{0.75}Mo_{0.25}O_3$ $0.33H_2O$), WM50 ($W_{0.50}Mo_{0.50}O_3$ 0.33H2O), WM75 ($W_{0.25}$ $Mo_{0.75}O_3$ $0.33H_2O$) and MH1 (MoO_3 $0.55H_2O$), respectively.

X-ray diffraction (XRD) patterns were recorded on a Philips X'Pert MPD X-ray Diffractometer with Cu KR radiation (ƛ = 1.54056 Å) at 40 kV and a current of 30 mA. Scanning electron microscopy (SEM) images were obtained on a cold field emission JEOL JSM-7401F microscope operated at 5 and 17 kV. An energy-dispersive X-ray spectroscopy (EDS) facility (Oxford INCA X-Sight) attached to the SEM was employed to analyze the chemical composition. UV-vis diffusive reflectance spectra (DRS) were obtained on a Lambda 9 UV-vis spectrometer. The Brunauer-Emmett-Teller (BET) surface areas were measured on a nitrogen adsorption apparatus (Quadrasorb SI, Quantachrome). The samples were degassed at 150-250 C for 12 h before the measurement. All ab-initio calculations were performed using the Quantum Espresso code in the framework of density functional theory (DFT). Due to the known band gap sub-estimation in DFT treatments (by the presence of "d" orbitals in W and Mo) DFT+U method was employed. The models for calculating WH1 and MH1 oxides were to reduce the unit cells from conventional to primitive, while the bimetallic solutions (WM25, WM50 and WM75) were calculated by means of 2x2x1 supercells. In all systems, the hydrated unit cell were employed (to XRD pattern fitting and to DFT calculations), however in both theoretical approach the H atoms are excluded. Hydrogen production was monitored using a gas chromatography Perkin Elmer, Clarus 500, a batch quartz photoreactor and a 250 W mercury lamp.

3. Results and discussion.

For WH1 the indexing corresponds to orthorhombic crystal, space group Aba2 and lattice parameters a = 7.323Å, b=7.690Å, c=12.772Å (calculated from ICSD using POWD- 12++ 228, 695 (1997)). For Mo fraction x = 0:25; 0:50, and 0:75 the space group was maintained, indicating that W in WO3 0.33H2O can be substituted up to 75% by Mo. According to the references [3,4] the appearance of new diffraction peaks in this case is due to the reduced symmetry from an F-centered orthorhombic cell for WO_3 $0.33H_2O$ to a C-centered orthorhombic cell for $W_{0.25}$ $Mo_{0.75}O_3$ $0.33H_2O$ caused by increased distortions induced by Mo substitution. For MH1 (x = 1.00), the XRD pattern can be assigned to hexagonal MoO_3 $0.55H_2O$

(Calculated from ICSD using POWD- 12++ 228, 695 (1997), space group P63/m, lattice parameters a= 1.0584 nm, b = 1.0584 nm, c = 0.3727 nm). All XRD patterns are included in figure 1.

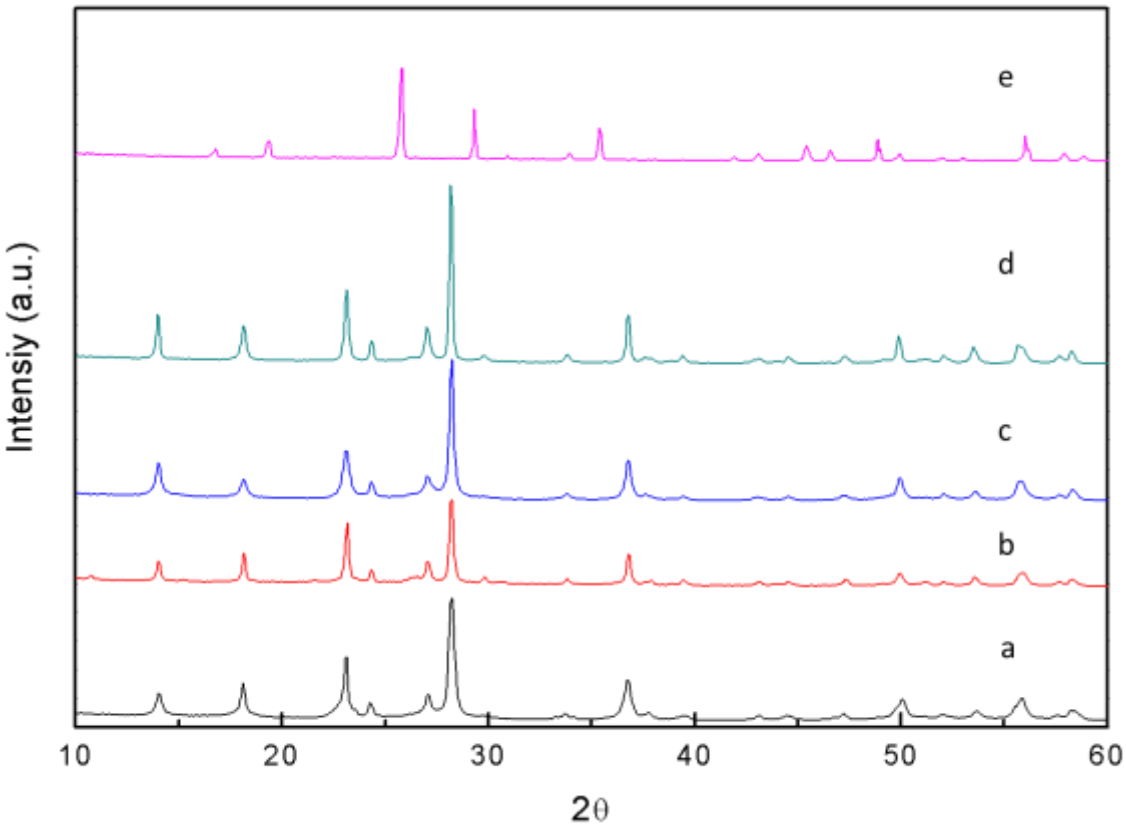

Fig 1. XRD patterns of (a) WH1, (b) WM25, (c) WM50, (d) WM75, and (e) MH1

Table 1. Theoretical and Experimental Mo Content, BET Surface Area and Band Gap

Sample	$X_{theoritical}$[1]	X_{EDS}[2]	S_{BET}[3](m^2/g)	E_g[4] (eV)	Size particle/stddev (nm)
WH1	0	0	68.2	2.62	73 ± 35
WM25	25	21	46.0	2.5	337 ± 223
WM50	50	37	40.1	2.45	103 ± 65
WM75	75	55	15.0	2.10	163 ± 57
MH1	100	100	1.0	2.37	29000 ± 15000

[1]Theoretical Mo content, [2]Mo content determined from EDS, [3]BET surface area, [4]Band gap

There are two major factors that influence the BET surface areas of the products, that is, the particle size and the Mo content. WH1 compound shows the largest BET surface area of 68.50 m^2/g due to the high W content. For the $W_{1-x}Mo_xO_3$ $0.33H_2O$ solid solutions, the particles size (the size of the primary particles) play a more important role. With the increase of the Mo content from 0 to 0.75, the BET surface area of the products decreases from 68.50 to 15 m^2/g, which can be attributed to the increase of the primary particle size deduced from the sharpening of the diffraction peaks shown in the XRD patterns.

Figure 2 represents the SEM images of the solid solutions. For WH1 (2a), WM25 (2b), WM50 (2c) and WM75 (2d), the products are mainly composed of nanometer sized flakes (200 nm in size). We can observe micro irregular particles for MH1 (2e) with widths and lengths of approximately 29000±15000 nm. Measurements values can be found in Table 1

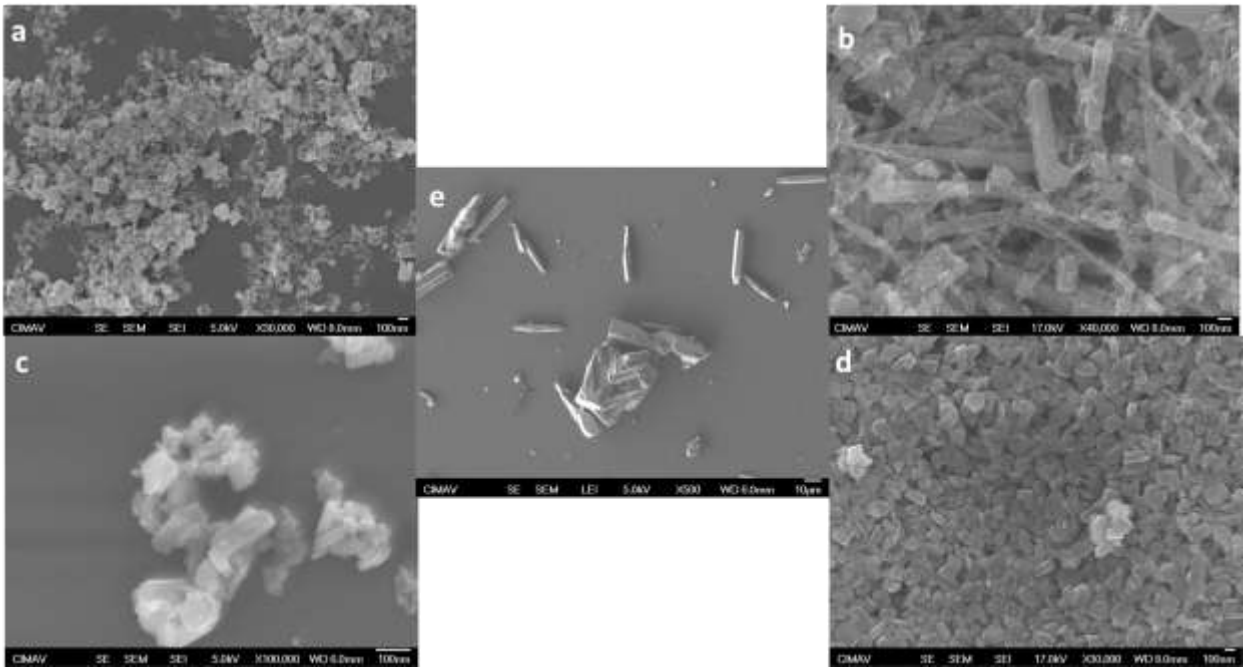

Fig 2. SEM images of (a) WH1, (b) WM25, (c) WM50, (d) WM75, and (e) MH1

From the absorption spectra of the samples, it is under stood that substitution shifts the absorption edge of $W_{1-x}Mo_xO_3$ $0.33H_2O$ from the UV to visible region (figure 3a). Now, we can determine the effective reduction in the band gap (BG) of these solid solutions due to the incorporation of Mo. Figure 3b shows the band gap of all samples. The line drawn on the linear part of [F(R)h]1/2 vs. hcurve at [F(R)h]1/2 = 0 gives the band gap. In pure WO_3, the electronic transition occurs directly from VB to CB. For the W/Mo samples, the results are rather similar to that of WO_3 $0.33H_2O$ except that they show more absorption in the visible range (~440 nm). With the introduction of 25% of Mo, a significant shift can be observed

(compared against WO_3 $0.33H_2O$), indicating a narrowing of the band gap. With even more Mo fraction, shifts can be observed. For x = 0.25, 0.50, and 0.75, the band gaps of the solid solutions are 2.50, 2.45, and 2.10 eV, respectively. The band gap of MH1, which is 2.30 eV, does not follow the trend of the $W_{1-x}Mo_xO_3$ $0.33H_2O$ solid solutions due to its structural difference. The DRS results clearly demonstrate the importance of structure (crystalline phase) in studying the composition-property relationship of the binary $W_{1-x}Mo_xO_3$ materials. We believe that the narrowing of the BG is because of the additional fraction of Mo as Zhou et al. stated: "The increased M^{5+} fraction and thus enhanced intervalency-transition are responsible for the narrowing of the band gap".

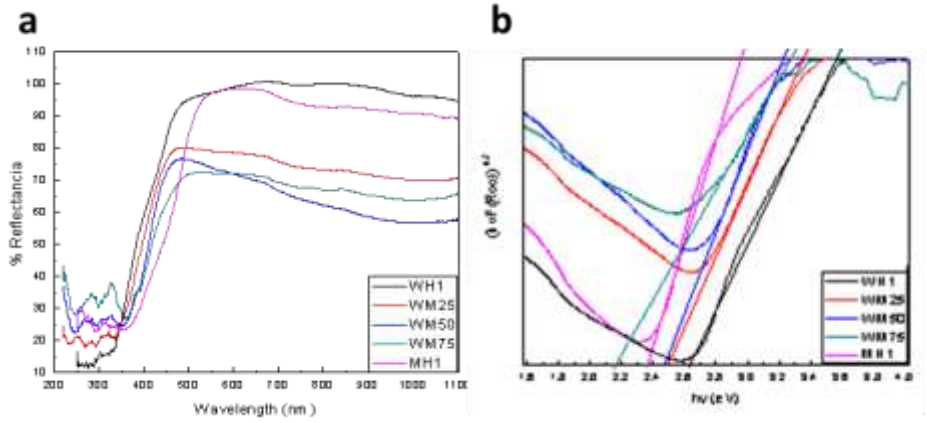

Fig 3. Diffuse reflectance and band gap determination. (a) Diffuse reflectance (%R) spectra of solid solutions (b) Determination of band gap of each samples by drawing a line at [F(R)h]1/2 = 0

DFT calculations resulted in decrease of the electronic gap in function of Mo addition, going from 0.491, 0.435, 0.433 and 0.418 eV to WH1, WM25, WM50 and WM75 respectively. However metallic character was obtained in MH1 compound; in disagree to experimental measured value. The gap trend was also investigated by incorporating the Hubbard correction, optimizing the on-site Coulomb value in WH1 to U = 6 eV. This U value was extended to all other compositions, to take an approach that is independent of the amount of added Mo, the potential was applied over "d" orbital of oxygen atoms. The band structure showed in Figure 4 correspond to our results of DFT+U, which had the same gap trend; i.e. the gap decrease function of the Mo amount, obtaining 2.63eV for WH1, 2.26eV for WM25, 2.04eV for WM50 and 1.98eV for WM75 and indirect gaps. The gap reduction (and the enhanced efficiency in photocatalysis) by adding Mo is because of the extra bands below the conduction bands. Our model correctly captures the current trend WH1 to WM75. Regarding MH1 structure, equal to DFT result, it was not possible to obtain semiconductor character. The clear relationship between band structures of the hydrated compound MH1 and its unhydrated analogy Mo_2O_3, which presents electronic gap (not shown), suggest that the measured gap could result from the combined presence of molybdenum oxide created by

O vacancies. Different MH1 models with O vacancies were tested, despite the metallic character was not modified. In our employed models, it was not possible to investigate the importance of taking into account H atoms (thus dispersive forces) and its effect on the electronic gap, however will be presented in a future work.

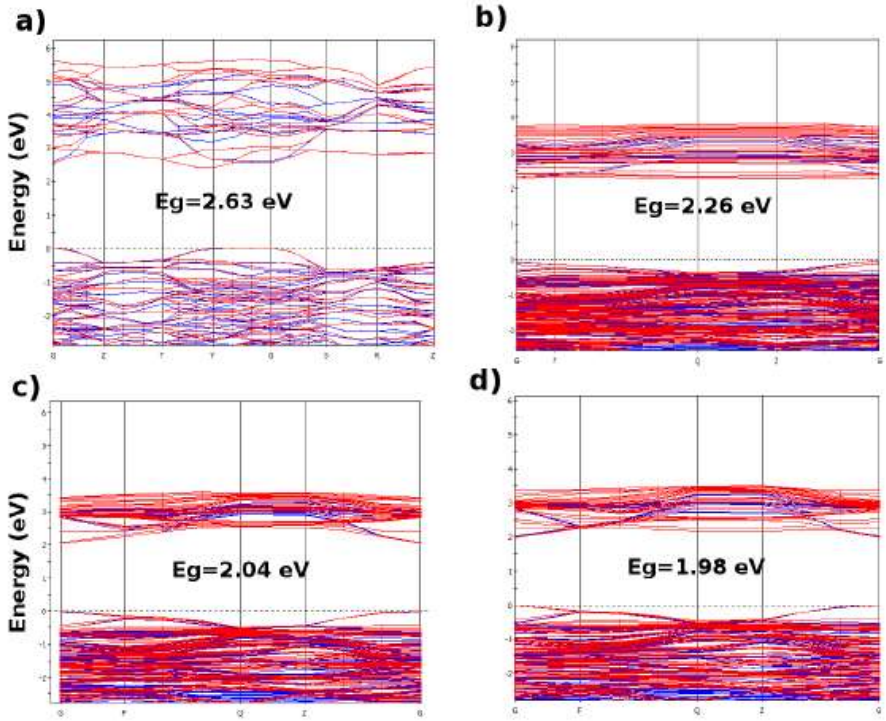

Fig 4. Band structures obtained from the conventional unit cell: a)WH1, and from primitive unit cells: b)WM25, c)WM50 and d)WM75. The U value corresponds to 6 eV.

The photocatalyc activity evaluation of the compounds was monitored through the evolution of the hydrogen produced by the dissociation reaction of the water molecule via photocatalysis. Results are shown in table 2. There was very little production of hydrogen and we believe it is because of the nature of WO_3 itself. We found studies that have shown that WO_3 is a visible light responsive photocatalyst with a relatively narrow band-gap energy (2.4–2.8 eV) and a VB potential similar to that of TiO_2 [5]. Therefore, the oxidizing power of holes in the VB of WO_3 and TiO_2 are considered to be almost the same. However, pure WO_3 is not an efficient photocatalyst because of its low CB level, which limits the photocatalyst's ability to react with electron acceptors such as oxygen [6]. The low CB level also increases the recombination of photo-generated electron–hole pairs leading to lower photocatalytic activity.

Table 2. Photocatalytic hydrogen production

Compound	μmoles H_2/g_{cat}
WH1	10
WM25	11
WM50	15
WM75	20
MH1	5

4. Summary and perspectives

We have synthesized a series of $W_{1-x}Mo_xO_3$ $0.33H_2O$ solid solutions with controlled stoichiometry (x = 0, 0.25, 0.50, 0.75). The lattice of WH1 (WO_3 $0.33H_2O$) can be substituted with up to 75% Mo without structural alteration. When we increase the content of Mo, the band gap of the $W_{1-x}Mo_xO_3$ $0.33H_2O$ structure narrowed from 2.62 to 2.10 eV. We believe that the enhanced intervalency-transitions, pressure, temperature and pH are responsible for the narrowing of the band gap and increasing the superficial area. DFT+U calculations confirmed our experimental data and showed that gap narrow was due to added bands below conductions level of the original WH1 compound. Hydrogen production was reached after 4h of irradiation for each compound. Compound WM75 had the maximum amount produced that was 20 μmoles H_2/g_{cat}. We think that the properties of these enhanced compounds make them suitable for applications like photocatalysis or gas sensing.

Acknowledgments

The authors are thankful with Centro Nacional de Supercomputo (CNS) del Instituto Potosino de Investigacion Cientifica y Tecnologica (IPICyT) for computational resources, with CIMAV NANOTECH and Rodrigo Dominguez for provided support. JCC is supported by CONACYT scholarships 290674 and 290604.

References

[1] Ni M, Leung MKH, Sumathy K, Leung DYC. Water electrolysis—a bridge between renewable resources and hydrogen. Proceedings of the International Hydrogen Energy forum, vol. 1, 25–28 May 2004, Beijing, PRC. p. 475–480.
[2] L. Zhou, J. Zhu, M. Yu, X. Huang, Z. Li, Y. Wang, and C. Yu, The Journal of Physical Chemistry C 114, 20947 (2010).
[3] F. Harb, B. Gerand, and M. Figlarz, C. R. Acad. Sci. Paris 303, 789 (1986).
[4] H. F., Solid State Ionics 32-3, 84 (1989).
[5] M. Miyauchi, M. Shibuya, Z. G. Zhao and Z. Liu, J. Phys. Chem. C, 2009, 113, 10642.
[6] M. Miyauchi, Phys. Chem. Chem. Phys., 2008, 10, 6258.

A hybrid approach based on a solar PV-hydrogen system for household electric energy supply in Mexico

R.G. González Huerta[1], M. Tufiño Velázquez[2,*], A.P. González Arceo[2], A. Yunez Cano[2,3], G.S. Contreras Puente[2], D. Jiménez Olarte[2]

[1] Laboratorio de Electroquímica y Corrosión, ESIQIE- IPN UPALM, México, D.F. 07738
[2] Laboratorio de Física Avanzada, ESFM.IPN, UPALM, México, D.F. 07738
[3]Laboratorio de Energías Alternas CIITEC IPN, Cda. Cecati s/n, Azcapotzalco, Mexico D.F.
*Tel: +525557296000 ext. 46138; e-mail: mitufinovel@gmail.com

ABSTRACT

Mexico as the world has a 90% energy production based on fossil fuels. Therefore billions of CO_2 tons are emitted to the atmosphere; greenhouse gas emissions are generated causing side effects as global warming. On the other hand, Mexico's oil peak production was already reached in 2005 and oil production is decreasing every day. Fossil fuels are non-renewable resources and reserves are being depleted much faster than new ones are being made. Thus the use of renewable energy sources would help to meet increasing energy needs. Besides, every day conventional energy sources increase their cost, while renewable ones become cheaper. In this work we present a hybrid approach based on a solar PV-hydrogen system for household electric energy supply. A mobile house was acquired, designed and dimensioned to be powered by this hybrid system to be used as a demonstration household. A 1 kW PV system was installed in the roof of the mobile house and a hydrogen system made out of an electrolyzer, a hydrides storage tank and a two-500 W fuel cell system will be installed to be used as a back up system. The capacity of the PV-hydrogen system was calculated from the average electric power consumption of a typical Mexican family living in a CFE 01 rated house by the Electricity Federal Agency in Mexico (CFE: Comisión Federal de Electricidad). A direct impact is achieved when renewable energy sources are interconnected to the grid so they cause a reduction in the cost of electricity tariffs, thus benefiting the citizens economy.

Keywords: hybrid approach; PV-hydrogen system; household.

1. Introduction

Mexico has a 90% energy production based on fossil fuels. Its oil peak production was already reached in 2005 and oil production is decreasing every day. As fossil fuels are non-renewable resources, the use of renewable energy sources could help to meet increasing energy needs, making good use of the fact that conventional energy sources increase their cost every day, while renewable ones become cheaper; this goes hand in hand together with technology progress.

In this work we present a hybrid approach based on a solar PV-hydrogen (PV-H_2) system for household electric energy supply. A mobile house was designed and dimensioned [1] to be powered by this hybrid system to be used as a demonstration household. For this purpose a 1 kW PV system was installed in the roof of the mobile house and a hydrogen system made out of an electrolyzer, a hydrides storage tank and a two-500 W fuel cell system will be installed to be used as a back up system.

An estimation of the reduction of CO_2 emission into the atmosphere due to the use of renewable energy sources instead fossil fuels for household electric energy supply is made considering the daily average production of electric power by the PV-H_2 system.

2. Experimental

The mobile house shown in Figure 1 was acquired and designed to be powered by a hybrid system consisting of a PV system and a hydrogen system made out of an electrolyzer, a hydrides storage tank and a fuel cell system, thus it could be used as a demonstration household. This would make possible to show this prototype house to more people as we can move it to different locations for making them aware of the feasibility and benefits of using renewable sources of energy.

Fig 1. Prototype house for household electric energy supply.

The capacity of the PV-H_2 system was calculated from the average electric power consumption of a typical Mexican family living in a CFE 01 rated house by the Electricity Federal Agency in Mexico (CFE: Comisión Federal de Electricidad) [2]. House rating is made according to its bimonthly average energy consumption; CFE 01 rated house has an established baseline day average consumption of 2.2 kW·h/day.

In order to calculate the average daily electric energy consumption of the mobile house we estimated the number of hours that each one of the appliances would be used every day. Considering energy saving

appliances should be used in the house, such as lighting LED's for illumination, a 2 ft^2 refrigerator, a LCD 22 in flat screen TV, a DVD and a Laptop, the estimated average daily energy consumption was 2,253 Wh as shown in Table 1.

Table 1. Average daily energy consumption of house appliances.

Imagen	Appliance	Power [W average]	# of hours Used/day (hours)	Energy Used/day (Wh/day)
	Lighting LED	168	5	840
	LCD TV 22"	70	5	350
	DVD	25	3 4 times/week	43
	Laptop	90	5	540
	Refrigerator 2 ft^3	60	8	480
	TOTAL		⟶	2,253

Due to the good solar irradiance average in Mexico City, we considered 5 hours of effective sunlight per day. Thus a 1 kW PV system was installed in the roof of the mobile house and a hydrogen system made out of an electrolyzer, a hydrides storage tank and a two-500 W fuel cell system is being installed to be used as a back up system.

A direct impact may also be achieved when renewable energy sources are interconnected to the grid so they cause a reduction in the cost of electricity tariffs, thus benefiting the citizens' economy. The main purpose of this investigation is to develop a sustainable housing project intended to be used as a mobile testing laboratory for studying national and ecological technologies developed to produce clean energy, since it is projected to gradually replace each of the existing commercial components with devices developed in our labs.

3. Results and discussion

The PV-H_2 power system of the hybrid approach presented in this work for household electric energy supply is shown in Figure 2. The 1 kW PV system installed in the roof of the house consisted of 8 polycrystalline Si solar modules, a charge controller, a DC-AC electric inverter and a bank of batteries to obtain a fixed time interval of energy autonomy.

PV polycrystalline silicon modules were acquired considering factors such as price, durability and efficiency, since the cost of investment is important for estimating the future savings and recovery cost. On the other hand, the automatic charge controller was chosen to prevent batteries might suffer any damage due to overloading or unloading in excess due to the intermittency of solar radiation and the variable consumption of the energy stored in the batteries bank.

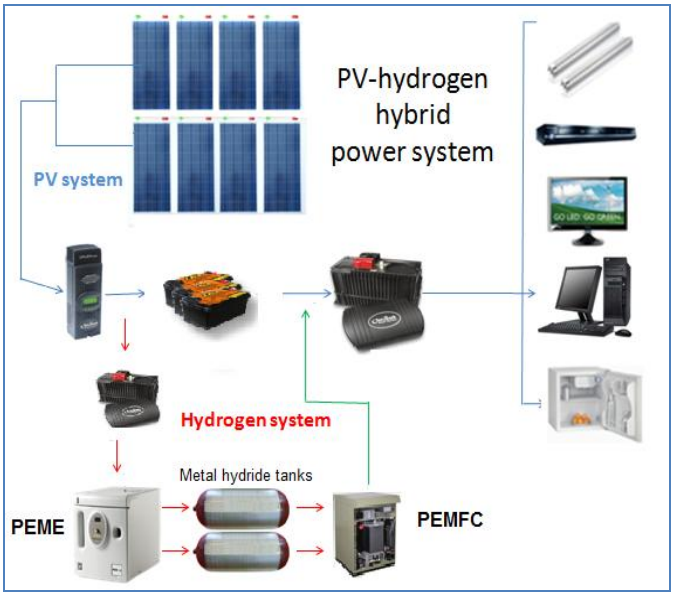

Fig. 2 PV-hydrogen hybrid power system.

The inverter was acquired to operate both in isolated systems, when the electric energy generated by the PV modules is stored in the batteries bank, and in an interconnected system to the grid, with the purpose that the investment may be lower and the cost return takes place in a shorter time delivering power to the federal electric grid. The battery bank provides two days autonomy to the house, when electric energy consumption does not exceeds 2.5 kW·h/day. This is true considering 5 hours of effective sunlight per day, which is an accepted criteria due to the good average solar irradiance in Mexico City.

Electric energy supplied by the PV modules was measured for different weather conditions; that is, measurements were made during sunny, cloudy and rainy days, so the energy output from PV modules could be fully characterized. Thus a more exact estimation of the amount of energy produced during one year by PV modules could be made, as well as an estimation of the reduction of CO_2 emission into the atmosphere due to the use of renewable energy sources instead fossil fuels for household electric energy supply. For this estimation, we considered a daily average production of electric power by the PV-H_2 hybrid system.

PV modules produce electric energy continuously with sunlight so the energy output from them was automatedly monitored using a WinVerter™ Monitor OutBack (OB) Standard software and a Mac Solar V3 sensor which consists in a calibrated solar cell that measures solar irradiance and PV modules temperatures. Measurements were carried out maintaining the PV system operating continuously during 24 hours.

Figure 3 shows the display for the charge controller stage which indicates on the left side the average solar power impinging on the PV modules and the electric power produced by them being sent to the charge controller. On the right side of the display shows the output voltage from the charge controller being sent to the batteries bank. The current-voltage readings at the bottom of the display indicate the input and output power of the charge controller; readings were taken every 10 minutes.

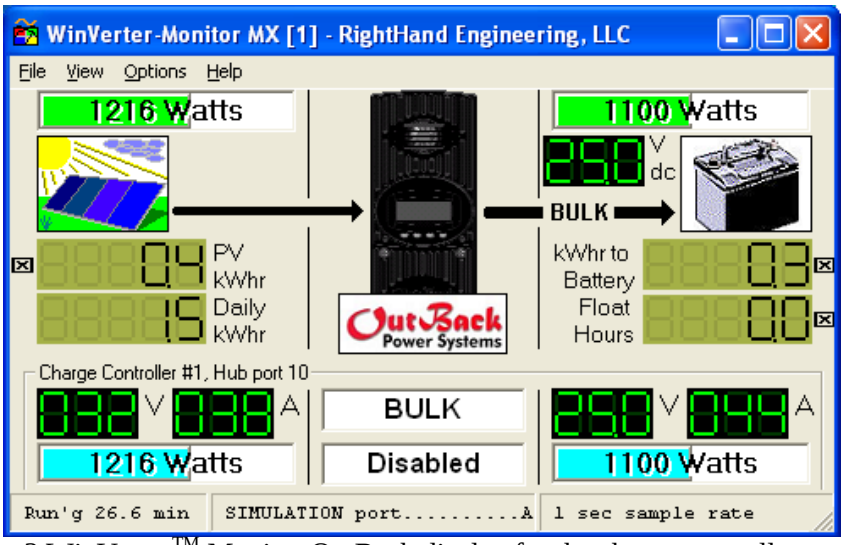

Fig. 3 WinVerter™ Monitor OutBack display for the charge controller stage.

Figure 4 shows the display for the electric inverter stage which indicates in the center below the inverter drawing the direct output voltage from the batteries bank feeding to the electric inverter; the left side is useless. On the right side of the display shows the output voltage from the electric inverter which is used to supply electricity to the house. During daylight electric energy is produced in excess by the PV modules so most energy is stored in the batteries; this energy can be used at night to supply energy to the house, because the house is not connected to the federal electric grid.

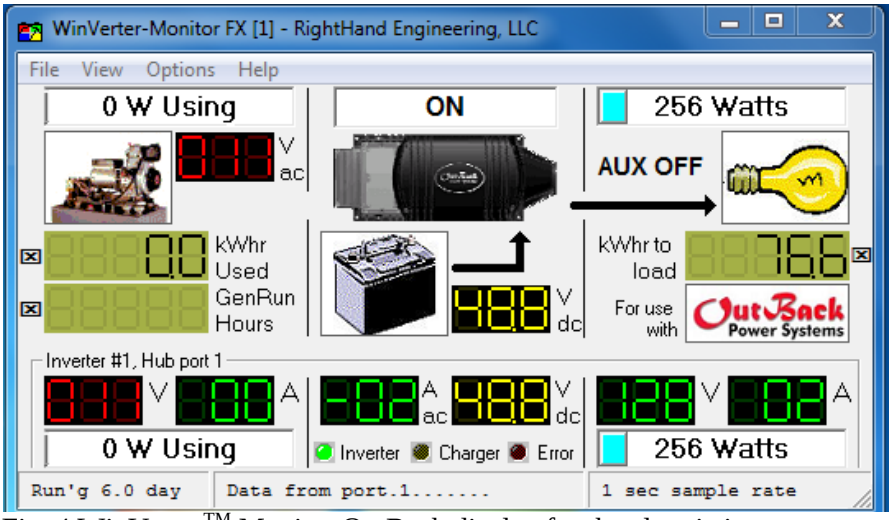

Fig. 4 WinVerter™ Monitor OutBack display for the electric inverter stage.

The average electric power generated by the PV modules is shown in Figure 6 for: a) a typical day, and b) for days under different weather conditions: sunny, cloudy-rainy and cold.

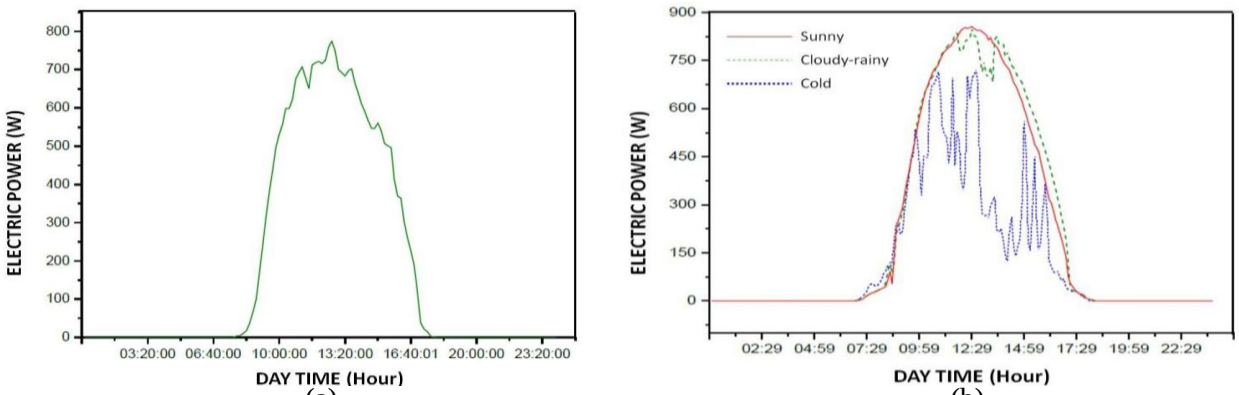

(a) (b)

Fig. 5 Average electric power generated by the PV modules for: a) a typical day, and b) for sunny, cloudy-rainy and cold days.

As expected, electric power produced by the PV modules occur only during daylight, reaching its maximum production at around 13h00. Figure 5b shows that power production during cloudy-rainy days is still high close to power generation for sunny days; this occurs when days are not cold. For cold days power generation decreases dramatically; this is due to the fact that PV modules efficiency decreases with temperature affecting the power generation. In order to obtain the maximum power production by the PV modules, the house was oriented along the east-west direction and the modules placed in the roof of the house inclined an angle of 23°, with the highest side on the north direction.

In order to obtain the total amount of electric energy produced by the PV modules during one day we may calculate the area under the curve of Figure 5. This was done by numerical integration using the OriginPro 8.5 program. The value obtained for a typical sunny day was 4.5066 kW·h, corresponding to the plot of Figure 5a.

On the other hand, the average electric power consumed by all electrical appliances which are used in the house during one whole day is shown in Figure 6.

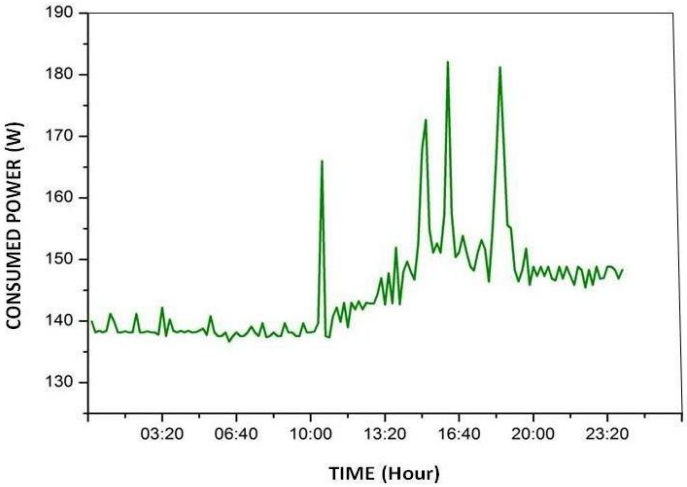

Fig. 6 Average electric power consumed by electrical appliances in the house.

The graph in Figure 6 shows that power consumption is the lowest during overnight until noon, when it starts rising to the maximum power consumption which occurs during night until the moment people goes to sleep. Sharp peaks are due to transient behavior which appear when some appliances are turned on, such as the illumination panels, TV set, DVD device, and others. Small peaks appearing during overnight and superimposing the main curve may be due to the refrigerator working cycle.

In order to obtain the total amount of electric energy consumed by the house electrical appliances during one day we proceed the same way as above by calculating the area under the curve of Figure 6. The value obtained was 3.4782 kW·h. Thus we obtained an excess electric energy produced by the PV modules of 1.0284 kW·h, which means that for sunny and cloudy-rainy days (which are not cold) this energy can be stored in the batteries bank, allowing us to have some autonomy without having to be connected to the federal electric grid. But if this were the case, the electric energy produced in excess would be supplied to the grid causing a reduction in the cost of the electricity tariffs. Due to the good solar irradiance average in most of Mexico´s territory, we can take advantage of this fact to produce electric energy for household by using PV modules. This means also that the use of renewable energies for household electric energy supply would cause an economic impact in benefit of citizens.

Production of electric energy by using renewable energy sources causes a positive impact to the environment as the processes involved do not cause CO_2 or any other contaminant emissions. In order to estimate the reduction of CO_2 emission, in our case due to the use of PV modules for household electric energy supply, we have to know the CO_2 factor (units: kg/KW·h) which indicates the kg amount of CO_2 produced in a country per kW·h of produced electric energy. This factor varies from one country to another and in the case of Mexico it has a value of 0.456 kg/kW·h [3].

The reduction CO_2 emission is obtained by the product of the electric energy produced times the CO_2 factor. In our case we have an average electric energy produced by the PV modules of about 4.5 kW·h and multiplying this by the CO_2 factor we obtain a value of 2.055 kg, which is the daily reduction of CO_2 emission. Thus we obtained a yearly amount of 750.07 kg of CO_2 which are not emitted to the atmosphere thanks to the use of PV modules.

In order to complete the development of this sustainable house prototype powered by a hybrid PV-H_2 system and continue its use as a demonstration household to show the benefits obtained from the use of renewable sources of energy, we are in the process of installing a hydrogen system consisting of: an H_2Planet PEM electrolyzer, model HyPEM XP-300 with an H_2 production of 300 cm^3/min; an H_2Planet hydrides storage tank, model MyH2-900 with an storage capacity of 900 l and two Horizon PEM 500 W fuel cell system, model H-500 (FSC-B500). This H2 system has already been acquired of which and will be used as a back up system, supplying electric power to the house during night or when the batteries power is exhausted.

4. Conclusions

We presented a hybrid approach based on a PV-H_2 system for household electric energy supply, using a mobile house powered by this hybrid system to be used as a demonstration household. We obtained an daily average production of electric energy by the PV modules of 4.5 kW·h, which surpasses the daily average electric energy consumption by the mobile house, thus causing a reduction in the cost of the electricity tariffs to be paid and having an economic impact in benefit of citizens. On the other hand, it has also a positive impact to the environment as there may be an important reduction on the amount of CO_2 or any other gas contaminant emissions.

Acknowledgements

This work has been partially supported by the IPN Energy Network, Secretaría de Ciencia, Tecnología e Innovación (SECITI) under ICYTDF/127/2012 agreement, and CONACYT project 190895.

References

[1] Armando Yunez Cano, (Acta de examen 17740) "Modelado 3D e integración de una casa sustentable solar-hidrógeno", Tesis de licenciatura ESIQIE-IPN, 07/02/2013.

[2] Comisión Federal de Electricidad CFE: http://www.cfe.gob.mx.

[3] Power and productivity for a better world: [http://new.abb.com/energy-efficiency/globaltrends-in-energy-efficiency].

Pt/TiO_2–C Electrocatalysts Prepared by Chemical Vapor Deposition With High Tolerance to Alcohols in ORR

F.M. Hernández-Mendoza[1], M.E. Beltrán-Perez[1], O. Martínez-Alvárez[1], V. Granados Alejo[1], B. Ruiz-Camacho[1,*]

[1]Universidad Politécnica de Guanajuato, Av. Universidad Norte s/n, Juan Alonso Cortázar Guanajuato, México, 38438 *Tel: +52-462-4414307; e-mail: beatrizr@upgto.edu.mx

ABSTRACT

Pt nanoparticles were synthesized by chemical vapor deposition and were deposited on carbon andTiO_2–C substrates. The Pt/C and Pt/TiO_2–C catalysts synthesized were characterized by TEM and XRD techniques. Cyclic voltammetry and rotating disk electrode measurements for the Oxygen ReductionReaction (ORR) were investigated in acid medium in presence of alcohols as methanol and ethanol. A Pt/C commercial sample was tested at the same conditions for comparison purposes. It was found that catalyst nanoparticles were homogenously distributed over the carbon and TiO_2–carbon substrateswith a mean particle size about 3 nm. Significant differences in the electrochemical results and alcoholstolerance are observed in the samples prepared in comparison whit Pt/C commercial catalyst. The methanoltolerance of the catalysts synthesized was higher compared to the ethanol tolerance. The electrochemical activity of Pt/TiO_2–C catalyst prepared with TiO_2 rutile phase was not affected by the presence of alcohols in comparison with Pt/C samples. It is explained by the thermal treatment over Pt/TiO_2–C during the synthesis process that produces a synergetic effect caused by the formation ofthe interface between the platinum and oxide materials where titanium oxide acts as a protecting agent of platinum nanoparticles.

*Keywords:*Pt nanoparticles, chemical vapor deposition, DMFC

1. Introduction

The demand for energy is increasing in our modern society. The dependence on oil-based fuels for transportation is the major cause of air pollution in the growing urban areas of the world. It has generated a great concern to find alternative sources of efficiently generated clean energy [1-2]. Direct methanol fuel cells (DMFCs) are especially attractive for this necessity. It has been considered as one of the most promising energy technologies as an alternative conventional power generating devices. These has several advantages such as high efficiency energy conversion, low emitting pollution, fuel availability as well as the reduction of the cost associated with the production, distribution and storage problems of hydrogen [3]. However, one of the most important impediments in the development of DMFC is the cross-over of alcohol through the proton conduction polymer membrane from the anode to the cathode that reduced the cell performance associated with the competition between the two reactions Oxygen Reduction Reaction (ORR) and Methanol Oxidation Reaction (MOR). The oxidation of methanol involves the formation of intermediate products, mainly CO, which are strongly adsorbed on the surface of platinum blocking consequently the active catalytic sites and thus loss of catalyst activity to the ORR [4-7]. For this reason is necessary to develop new cathode catalysts for DMFC with high catalytic activity and selectivity to the ORR that means with tolerance to the alcohol (methanol, ethanol, propanol, etc.) [8-10].

Nowadays, the best material for the ORR is the platinum nanoparticles; however as was mentioned above its excellent catalytic properties are affected by methanol presence. According to several investigations Pt-Ru alloys exhibit an effective electrochemical activity as anodes for DMFC due to the presence of Ru facilitates the oxidation of CO species, that means Ru nanoparticles confers tolerance to CO poisoning [11-12]. Other recent developments confirm that the addition of metal-oxides (RuO_x[13-14], TiO_2 [1, 13-15-19] and SnO_2 [2, 15, 22-24]) to the conventional Pt/C to produce Pt/MO_x-C composites exhibit excellent properties as cathode fuel cells due to a change of the structural and electronic properties of platinum. Specifically, the TiO_2-C substrate provides high resistance to electrochemical corrosion of carbon [16, 25-27]. Nevertheless, the amount of titanium dioxide and the crystalline phase (TiO_2 anatase/rutile phase) also modifies the strength of the interaction between the substrate and the metal nanoparticles [17, 21]. The positive effect of addition TiO_2 is explained by two effects: (1) changes in the Pt-d electronic properties and (2) a geometric effect that produce the contraction of Pt-Pt bonding distance leading to a favorable condition for the electrochemical reactions [12, 28]. This effect can be controlled by the physicochemical route of synthesis used. The composites are being developed by different routes of synthesis and are considered promising candidates to be used as catalyst for DMFC. Of the different methods reported for the synthesis of Pt nanoparticles, the chemical vapor deposition (CVD) technique produced in a short time (minutes) Pt supported well-dispersed nanoparticles in a range from 1 to 20 nm, depending on the chemical precursors and deposition conditions, which have been definided for different substrates [29]. Based in our previous reports where Pt/TiO_2-C prepared by photo-deposition [2, 16, 17] and chemical vapor deposition [27] methods exhibit an enhancement in the electrochemical stability and activity in the ORR in acid medium. In this paper we explored the electrochemical activity of Pt/C and Pt/TiO_2-C catalysts synthesized by CVD to carry out the ORR in presence of methanol as well as ethanol. All results were compared with a commercial sample (10 wt.%Pt/C-Etek) tested at the same conditions. The results shows significant favorable differences between catalysts prepared in comparison with commercial catalysts.

2. Experimental

2.1 Catalysts preparation by CVD

The synthesis of 10 wt.%Pt / 5wt.%TiO_2-C catalysts was carried out using a thermal horizontal tube quartz reactor by chemical vapor deposition method (CVD). On the preparation, the platinum acetyl acetonate precursor [$(CH_3$-$COCHCO$-$CH_3)_2Pt$], the titanium oxide rutile nanoparticles (TiO_2) and carbon (Vulcan XC-72) were mechanically mixed at room temperature on 10:5:85 weight ratio before impregnation. The mixed powders were heated at 473 K for vapor impregnation during 10 min using a total pressure of 4.5 torr, these conditions evaporated the platinum precursor. Then, the Pt precursor impregnated was moved to a higher temperature zone heated at 523 K in N_2 atmosphere (100 mL min^{-1}) for 10 min inside the tube reactor to achieve the precursor decomposition and to obtain the Pt nanoparticles onto the TiO_2-C nanocomposite [29-30].

The sample 10 wt.%Pt/C was synthesized using the same conditions above mentioned, the load of Pt:C was a 10:90 ratio.

2.2 Physical characterization techniques

X-ray diffraction (XRD) patterns of platinum base electrocatalysts prepared were collected on a Bruker D8 AXS equipment using a Cu anode (K_α, λ=1.5406 Å) and a Bragg-Brentano configuration. The angle 2θ was varied from 30 to 90º with 0.2° min^{-1} and 35 kV. The particle size distribution and the surface morphology of platinum electrocatalysts were obtained with a Transmission Electron Microscopy (TEM) using a JEOL-JEM-2200 field emission operated at 200 kV. The dried samples prepared by CVD (Pt/C and Pt/TiO_2-C) were prepared by dispersion on ethanol by ultrasound and the resulting suspension was deposited onto a cooper mesh and dried at ambient condition before TEM analysis.

2.3 Electrochemical measurements

The electrochemical measurements were performed at 25°C, using a potentiostat in a three-electrode cell. A platinum mesh was used as the counter electrode, and a standard saturated calomel electrode (SCE=0.24 V) as the reference electrode. The potentials in this paper were related to the normal hydrogen electrode (NHE). Glassy carbon disk with a cross-sectional area of 0.19 cm^2 was used as a support for the thin films and used as an ink-type working electrode. The catalytic ink was prepared with 1mg of catalyst, 25 µL of 5 wt% solution Nafion® (Du Pont, 1100 EW) and 125 µL of ultra-pure water. For RDE experiments, 15 µl of this sonicated mixture were deposited on glassy carbon electrode (0.1 mg $_{cat}$).

Cyclic voltammetry (CV) in a nitrogen atmosphere was performed to clean the electrode surface from 0.05 to 1.2 V/NHE at 50 mV s^{-1}. 20 cycles were necessary to stabilize the system. Hydrodynamic experiments were recorded at oxygen atmosphere using an electrode disk rotating in the rotation range of 200, 400, 900, 1600 and 2500 rpm at 5 mV s^{-1} from 1.0 to 0.2 V/NHE. The alcohol tolerance to the ORR at different rotating speed was evaluated at RT in acid medium employing two solutions as electrolyte: a) H_2SO_4 and b) alcohol + H_2SO_4 (0.5 M). Methanol Oxidation Reaction (MOR) and Ethanol Oxidation Reaction (EOR) activity was also measured by potential cyclic between 0.05 and 1.2 V/NHE in the same electrolytes.

3. Results and discussion

3.1 TEM and XRD results

Fig. 1 shows TEM images of (a) Pt/C and (b) Pt/TiO_2-C electrocatalysts prepared by chemical vapor deposition method. According to the micrographs both materials had a similar morphology with uniform distribution onto both substrates (TiO_2-C and Carbon). The mean particle size is between 2 and 4 nm with spherical or globular morphology.

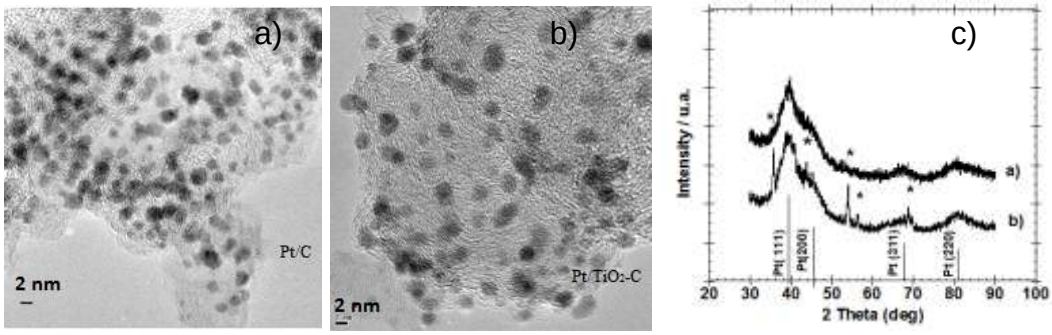

Fig. 1. TEM images of a)Pt/C and b)Pt/TiO_2-C samples synthesized by chemical vapor deposition. c)X-ray diffraction patterns of (a) Pt/C and (b) Pt/TiO_2-C electrocatalyst synthesized by CVD method. (*) referes to reflections from the TiO_2 rutile phase.

Fig. 1 (c) exhibits the X-ray diffraction patterns of Pt/C and Pt/TiO_2-C. Both materials present the crystalline face-centered cubic (*fcc*) structure of platinum. The diffraction peaks of Pt were found at 2θ values of 39.8º, 46.2º, 67.4º and 81.2º ascribed to the (111), (200), (220) and (311). For Pt/TiO_2-C electrocatalysts the presence of some reflections at 2θ vales of 36.1°, 41.2°,44.0°, 54.3°, 56.6°, 69° (indicated by asterisks) can be ascribed to the (101), (111) (210), (211), (220), (301) planes of TiO_2 rutile phase [27].

3.2 Cyclic voltammetry results

CV curves measurements were recorded in the range of potential from 0.05 to 1.2 V/NHE. The results of Pt/C and Pt/TiO_2-C catalysts synthesized by CVD are presented in Fig. 2. The CV curve of commercial Pt/C Etek is also show in the inset of Fig 2 for comparison purposes. All shapes of the voltammograms are very similar and correspond to the typical voltammograms of Pt nanoparticles in acid medium [31-32]. Briefly, Pt samples prepared by CVD exhibit the H-adsorption/desorption peaks at 0.05-0.3 V/NHE and Pt oxide formation/reduction peaks at 0.85/0.75 V/NHE. It can be clearly seen that the Pt oxidation/reduction peaks of Pt/TiO_2-C electrode were considerably enlarged compared to the Pt/C catalysts synthesized. The

electrochemical surface area (ESA) of three catalysts was estimated by integrating the voltammograms corresponding to hydrogen adsorption-desorption area. For calculation of ESA a value of 210 μC cm^{-2} was assumed as the monolayer charge [33-34]. In this study the ESA for Pt/TiO_2-C (5.8 m^2 g^{-1}) was larger than the Pt/C (1.1 m^2 g^{-1}) indicating that more active sites are available at the Pt/TiO_2-C surfaces. According to literature the ESA for Pt increase with the Ti-oxide presence may be due to decreasing particle and because the TiO_2 presence modified favorably the structural and electronic features of platinum to carried out the H-adsorption [2, 13].

3.3 Cyclic voltammetry in presence of alcohol

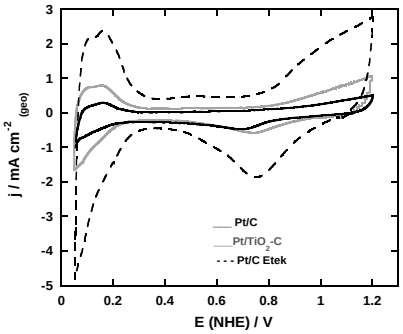

Fig. 2. CV of 10 wt.% Pt/C and 10 wt% Pt/ 5 wt.% TiO_2-C electrocatalysts prepared by CVD compared to the commercial 10 wt.% Pt/C Etek sample in 0.5 M H_2SO_4 at a scan rate of 50 mV s^{-1}at RT.

Fig. 3 displays the CV curves obtained in presence of methanol and ethanol for Pt/C, Pt/TiO2-C and Pt/C Etek. Also the CV curves normalized to the geometric (Fig. 3 (a-b)) and ESA values (Fig. 3 (c-d)) are presented in Fig. 3. Significant differences are observed in the Pt materials prepared compared to the commercial sample. For example in Fig. 3-a is interesting note that CV of Pt/TiO_2-C in presence of 0.5 M methanol remains almost silent, in contrast to the Pt/C and P/C-Etek responses. That is Pt/TiO_2-C not exhibit peaks corresponding to the oxidation and electro-oxidation methanol. This results is confirmed when CV curves are normalized to the ESA values the same observation (Fig. 3-c). Therefore Pt/TiO_2-C exhibit a remarkable methanol tolerance at a methanol concentration of 0.5 M in the same potential interval explored that Pt/C catalysts, it could be explained due to TiO_2 rutile acting as a cover protecting of platinum towards the adsorption of the methanol [21, 35]. This effect is not observed in the CV curves of ethanol presence (Fig. 3-b). That means the samples prepared by CVD including the Pt/TiO_2-C exhibit the typical characteristics of oxidation and electro-oxidation peaks of alcohol. Three samples exhibit smaller tolerance to ethanol compared to methanol presence. Is interesting observed that when CV curves are normalized to the ESA values, Pt/C catalysts exhibit the higher electro-catalytic current than Pt/TiO_2-C and Pt/C Etek materials over the whole scanning voltage range. Also the onset potential of alcohol

oxidation of Pt/C is lower than on Pt/C Etek and Pt/TiO_2-C samples. For example, Fig. 3-d shows that Pt/C electrocatalysts had a peak current of ethanol oxidation of 0.39 mA cm^{-2}_{Pt} which is much higher than on Pt/C Etek sample 0.085 mA $cm^{-2}_{Pt}$and Pt/TiO_2-C catalysts 0.08 mA cm^{-2}_{Pt}. This could be caused also by the thermal (T= 473K) and pressure (P=4.5 torr) treatment during the synthesis method that change the structure and interaction of carbon with platinum.

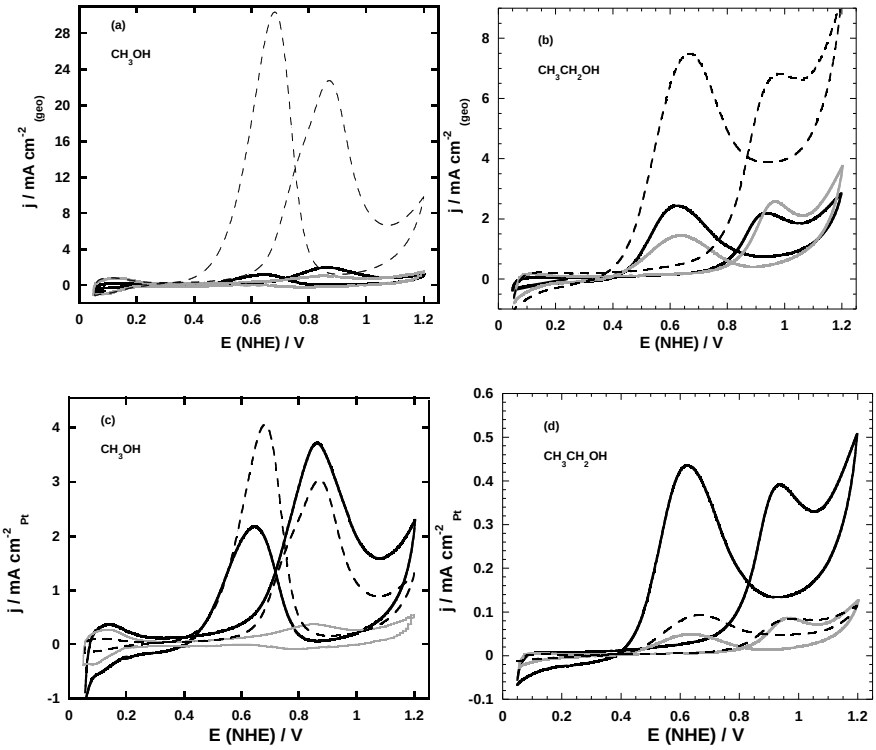

Fig. 3. Geometric (a and b) and ESA (c and d) normalized cyclic voltammograms curves of (—) 10 % Pt/C, (—) 10 %Pt/5%TiO_2-C and (- -) 10%Pt/C Etek catalysts in two electrolytes 0.5 M H_2SO_4 + alcohol ((I) CH_3OH and (II) CH_3CH_2OH). Scan rate of 50 mV s^{-1} at RT.

3.4 Rotating disk electrode studies in presence of alcohol

A rotating disk electrode (RDE) study of Pt/C, Pt/TiO_2-C and Pt/C Etek electrocatalysts to carried out the ORR in presence and absence of methanol (right) and ethanol (left) are presented in Fig. 4. The typical curves on Pt nanoparticles en acid medium exhibit the three distinct regions characteristic: (I) the kinetic region, where the current, i_k, is independent of the rotation velocity; (II) the mixed control region, where the behavior is determined by kinetic as well as diffusion processes; and (III) the mass-transfer region, where the diffusion current, i_d, is a function of the rotation velocity [37-38].

One of the most important results in this study is that the polarization curves of Pt/TiO_2-C sample are practically unchanged by the presence of 0.5 M methanol solution.

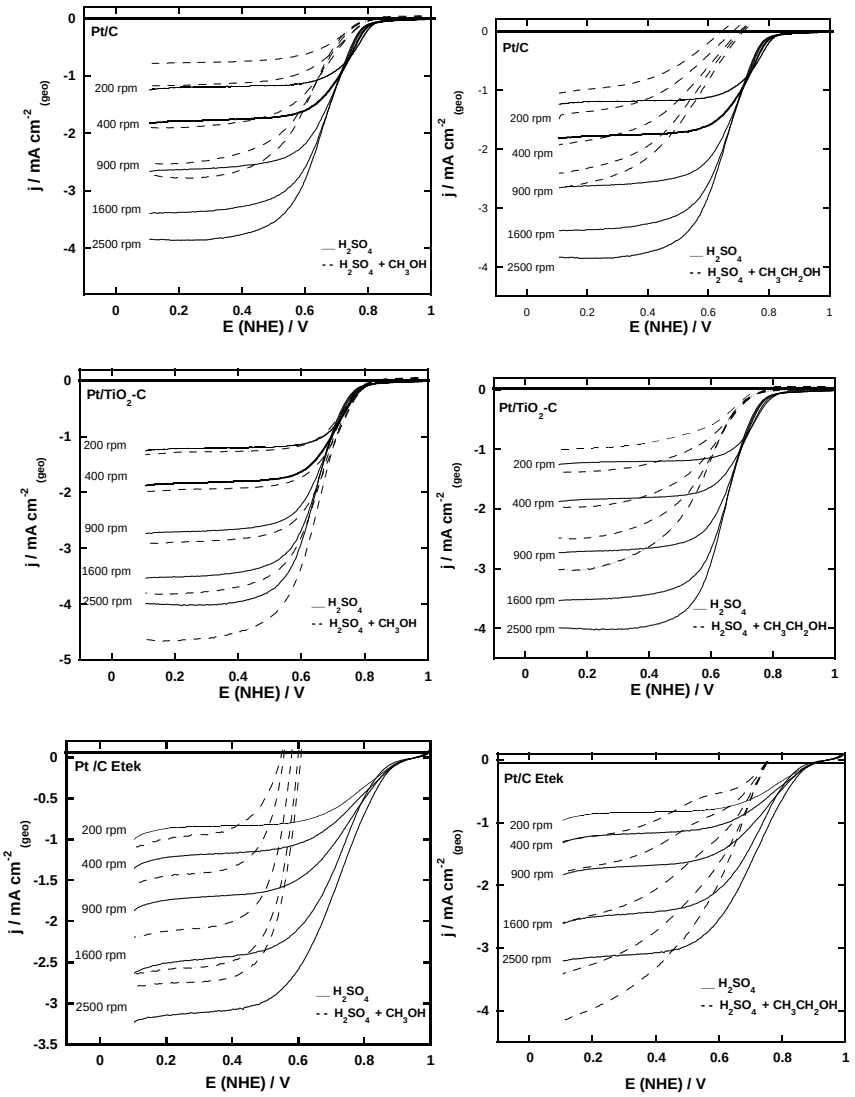

Fig. 4.Oxygen reduction reaction (ORR) curves of 10%Pt/C and 10%Pt/5%TiO_2-C prepared by CVD compared to 10% Pt/C Etek in two electrolytes 0.5 M (I) H_2SO_4 + CH_3OH and (II) H_2SO_4 + CH_3CH_2OH at different rotating speed. Scan rate of 5 mV s^{-1} at RT.

These features are in agreement with the corresponding cyclic voltammograms of Pt/TiO_2-C in presence of methanol in Fig. 3-c. As is expected Pt commercial catalyst shows a mixed potential due to the

simultaneous methanol oxidation and oxygen reaction on its surfaces. In the case of Pt/C catalysts prepared by CVD its polarization curves also showed methanol tolerance, the net cathodic current onset of Pt/C is shifted negatively by 0.15 V/NHE, however this value is lower compared to the over-potential obtained for Pt/C Etek (0.4 V/NHE).

Right of Fig. 4 displays the polarization curves of three samples in presence and absence of ethanol. Important changes are observed compare to the results obtained in methanol. Pt/TiO_2-C sample exhibit the smaller cathodic current shifted of 0.10 V/NHE respect to the results obtained in absence of ethanol. In the case of Pt/C and Pt/C Etek, simultaneous methanol oxidation and oxygen reduction was observed. These results indicated that samples synthesized by CVD (Pt/C and Pt/TiO_2-C) had more tolerance to carried out the ORR in presence of methanol compared to ethanol

The electrochemical activity for ORR and its stability are favorable modified by the TiO_2-carbon substrate and the interaction between Pt. With these results we conclude that the synthesis method produce changes in the Pt electronic and geometric parameters intensely labeled by the presence of TiO_2 for to be used in fuel cells of alcohols.

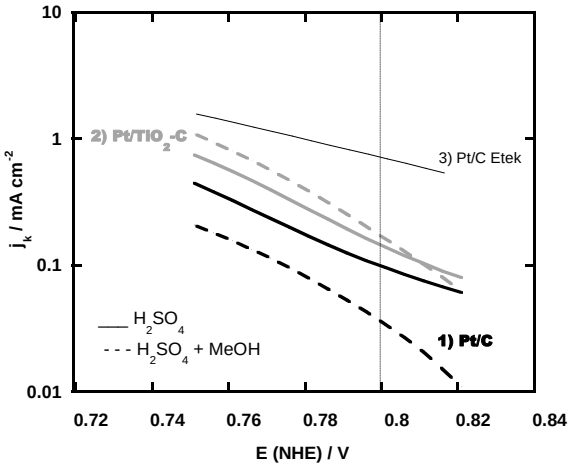

Fig. 5 ORR mass-corrected Tafel plots for the (1) Pt/C, (2) Pt/TiO_2-C and (3) Pt/C-Etek electrocatalysts calculated from the data (mass transfer corrected) in Fig. 5 in (—) H_2SO_4 and (- -) H_2SO_4 + MeOH

ORR mass-corrected Tafel plots for the Pt/C, Pt/TiO_2-C and Pt/C-Etek electrocatalysts calculated from the data (mass transfer corrected) in Fig. 4 are displayed in Fig. 5. For catalysts synthesized by CVD (Pt/C and Pt/TiO_2-C) continue curves were recorded in 0.5 M H_2SO_4 electrolyte, whereas discontinue curves were recorded in 0.5 M H_2SO_4 + MeOH. The Tafel slope (60-70 mV dec^{-1}) of Pt/C and Pt/TiO_2-C was not affect by different electrolyte. That means the kinetic for ORR is not perturbed by presence of methanol in solutions. However, the j-E characteristic of Pt/C is cathodic shifted by 66 μA cm^{-2} at 0.8 V when the

electrolyte contained MeOH. This effect was not observed on the Pt/TiO_2-C sample, the current density remains at 0.8 V. This phenomenon is direct evidence that Pt supported on TiO_2-C is is not affected by methanol presence. The Tafel plot of Pt/C Etek was obtained in 0.5 M H_2SO_4 for comparison proposes. In acid medium, the kinetic current density calculated at 0.8 V/NHE of platinum deposited on TiO_2-C (147 $\mu A\ cm^{-2}$) show and enhancement compared to Pt/C (100 $\mu A\ cm^{-2}$) electrocatalyst prepared with the same methodology (CVD). However, is evident that in acid medium the commercial sample had the higher density current (728 $\mu A\ cm^{-2}$), but its activity is affect drastically by the presence of methanol, in the case of Pt/TiO_2-C sample, it exhibits more tolerance to the methanol to the carried out the ORR, caused by thermal treatment during the synthesis method and the TiO_2 phase rutile in contact with Pt that modified the electronic surface to adsorbed the methanol or intermediates formation during the methanol electrooxidation. For this reason in this work, is necessary to increase the electrochemical activity of Pt/TiO_2-C sample obtained by CVD method.

4 Summary and perspectives

Pt/TiO_2-C and Pt/C catalysts with nanometer size of 3 nm were successfully synthesized by chemical vapor deposition. Cyclic voltammetry as well as the rotating disk electrode for the ORR measurements in presence in alcohols showed that the catalyst synthesized exhibited excellent methanol tolerance for to be used as cathode in a Direct Methanol Fuel Cells. Specifically Pt/TiO_2-C exhibit a higher electrochemical activity to ORR in presence of methanol compared to the ethanol tolerance. The changes in the electronic properties of Pt could be explained by the TiO_2 rutile phase content through its interaction metal-oxide ($Pt\text{-}TiO_2$) obtained by the thermal treatment and the low pressure to be subjected during the synthesis method. A protecting effect of TiO_2 towards Pt that avoid the adsorption of methanol and CO intermediates on the surface of Pt was observed.

Acknowledgements

The authors are grateful to the Universidad Politécnica de Guanajuato (UPG) for the financial support of this work under the project PROMEP No.103.5/12/3400.

References

[1] J. Shim, C.-R.Lee, H.-K.Lee, J.-S. Lee, E.J. Cairns, Electrochemical characteristics of Pt-WO3/C and Pt-TiO2/C electrocatalysts in a polymer electrolyte fuel. J. Power Sources 2001; 102: 172-177.

[2] B. Ruiz Camacho, H.H. Rodríguez Santoyo, J.M. Medina-Flores, O. Martínez-Álvarez. Platinum deposited on TiO2-C and SnO2-C composites for metanol oxidation and oxygen reduction Electrochim. Acta 2014; 120: 344-349.

[3] K.-W. Park, K.-S.Seol, $Nb\text{-}TiO_2$ supported Pt cathode catalyst for polymer electrolyte membrane fuel cells. Electrochemistry Communications 2007; 9: 2256-2260.

[4] G. Selvarani, S. Maheswari, P. Sridhar, S. Pitchumani, A.K. Shukla. Carbon-Supported Pt - TiO2 as a Methanol-Tolerant Oxygen-Reduction Catalyst for DMFCs. J. Electrochem. Soc. 2009; 156 : B1354-B1360.

[5] L. Xiong, A. Manthiram. Synthesis and characterization of methanol tolerant Pt/TiO"x/C nanocomposites for oxygen reduction in direct methanol fuel Cells. Electrochim. Acta 2004; 49: 4163-4170.

[6] Y.Z. Lu, T.H. Lu, C.P. Liu, Y.W. Tang, W. Xing, Chinese Chemical Letters 2005; 16: 1252-1254.

[7] E.A. Franceschini, M.M. Bruno, F.A. Viva, F.J. Williams, M. Jobbágy, H.R. Corti. Mesoporous Pt electrocatalyst for methanol tolerant cathodes of DMFC. Electrochim. Acta 2012; 71: 173-180.

[8] H. Li, Q. Xin, W. Li, Z. Zhou, L. Jiang, S. Yang,G. Sun. An improved palladium-basedDMFCs cathode catalyst. Chem. Commun. 2004: 2776-2777.

[9] R.C. Koffi, C. Coutanceau, E. Garnier, J.-M. Leger, C. Lamy. Synthesis, characterization and electrocatalytic behaviour of non-alloyed PtCr methanol tolerant nanoelectrocatalysts for the oxygen reduction reaction (ORR). Electrochimica Acta 2005; 50: 4177-4127.

[10] J. Wang, G. Yin, H. Liu, R. Li, R.L. Flemming, X. Sun Carbon nanotubes supported Pt–Au catalysts for methanol-tolerant oxygen reduction reaction: A comparison between Pt/Au and PtAu nanoparticles. J. Power Sources 2009; 194: 668-673.

[11] L. Yu, J. Xi. TiO2 nanoparticles promoted Pt/C catalyst for ethanol electro-oxidation. Electrochim. Acta 2012; 67:166-171

[12]M.K. Jeon, P.J. Mc Ginn. Effect of Ti addition to Pt/C catalyst on methanol electro-oxidation and oxygen electro-reduction reactions. Power Sources 2010; 195: 2664-2668.

[13] L. Timperman, A. S. Gago, N. Alonso-Vante. Oxygen reduction reaction increased tolerance and fuel cell performance of Pt and RuxSey onto oxide–carbon composites. J. Power Sources 2011; 196: 4290-4297.

[14] G.-H. An, H.-J. Ahn, Pt electrocatalyst-loaded carbon nanofibre–Ru core–shell supports for improved methanol electrooxidation. J. Electroanal. Chem. 2013; 707: 74-77.

[15]Y. Fan, Z. Yang, P. Huang, Z. Zhang, Y.M. Liu. Pt/TiO2−C with hetero interfaces as enhanced catalyst for methanol electrooxidation. Electrochim. Acta 2013; 105: 157-161.

[16] B. Ruiz Camacho, C. Morais, M.A. Valenzuela, N. Alonso-Vante. Enhancing oxygen reduction reaction activity and stability of platinum via oxide-carbon composites. Catal. Today 2013; 202: 36-43.

[17] B. Ruiz-Camacho, M.A. Valenzuela, R.G. González Huerta, K. Suarez-Alcántara, S.E. Canton, F. Pola-Albores. Electrochemical and XAS investigation of oxygen reduction reaction on Pt-TiO_2-C catalysts. Int. J. Hydrogen Energy 2013; 38: 12648-12656.

[18] L. Timperman, Y.J. Feng, W. Vogel, N. Alonso-Vante. Substrate effect on oxygen reduction electrocatalysis. Electrochim. Acta 2010; 55: 7553-7558.

[19] A. Ignaszak, C. Song, W. Zhu, J. Zhang, A. Bauer, R. Baker, V. Neburchilov, S. Ye, S. Campbell. Carbon-Nb0.07Ti0.93O2 composite supported Pt-Pd electrocatalysts for PEM fuel cell oxygen reduction reaction. Electrochim. Acta 2012; 69: 397-405.

[20] L. Xiong, A. Manthiram. Synthesis and characterization of methanol tolerant Pt/TiOx/C nanocomposites for oxygen reduction in direct methanol fuel Cells. Electrochim. Acta 2004; 49: 4163-4170.

[21] N.R. De Tacconi, C.R. Chenthanmarakshan, K. Rajeshwar, W.Y. Lin, T.F. Carlson, L. Nikiel, W.A. Wampler, S. Sambandam, V. Ramani. Photocatalytically generated Pt/C-TiO2 electrocatalysts with enhanced catalyst dispersion for improved membrane durability in polymer electrolyte fuel cells. J. Electrochem. Soc.. 2008; 155: B1102-B1109.

[22] T. Matsui, K. Fujiwara, T. Okanishi, R. Kikuchi, T. Takeguchi, K. Eguchi. Electrochemical oxidation of CO over tin oxide supported platinum catalysts. J. Power Sources 2006; 155: 152– 156.

[23]M. Wesselmark, B. Wickman, C. Lagergren, G. Lindbergh. Electrochemical performance and stability of thin film electrodes with metal oxides in polymer electrolyte fuel cells. Electrochim. Acta 2010; 55: 7590– 7596.

[24] B. Wickman, M. Wesselmark, C. Lagergren, G. Lindbergh. Tungsten oxide in polymer electrolyte fuel cell electrodes – A thin – film model electrode study. Electrochim. Acta 2011; 56: 9496– 9503.

[25] J. Ma, A.S. Gago, N. Alonso-vante. Performance Study of Platinum Nanoparticles Supported onto MWCNT in a Formic Acid Microcluidic Fuel Cell System. J. Electrochem. Soc. 2013; 160: F859-F866.

[26]W. Vogel, L. Timpermam, N. Alonso-Vante. Probing metal substrate interaction of Pt nanoparticles: Structural XRD analysis and oxygen reduction reaction. Appl. Catal. 2010; A 377: 167-173.

[27] R.G. González Huerta, M.A. Valenzuela, R. Vargas García, N. Alonso-Vante, M. Tufiño Velázquez, B. Ruiz-Camacho. Oxygen reduction performance of Pt/TiO_2-C electrocatalyst prepared by two-step chemical vapor deposition. J. New Mat. Electrochem. Systems 2012; 15: 123-128.

[28] S. Mukerjee, S. Srinivasan, M.P. Soriaga. Role of Structural and Electronic Properties of Pt and Pt Alloys on Electrocatalysis of Oxygen Reduction An *In Situ* XANES and EXAFS Investigation. J. Elecrochem. Soc. 1995; 142: 1409-1422.

[29] J.R. Vargas Garcia, and T. Goto, IOP Conference Series: Materials Science and Engineering 2011; 20-1: 012001

[30] C. Encarnación Gómez, J.R. Vargas García, J.A. Toledo Antonio, M.A. Cortes Jacome, C. Ángeles Chávez. Pt nanoparticles on titania nanotubes prepared by vapor-phase impregnation‑decomposition method. J. Alloys Compd. 2010; 495: 458-461.

[31] K. Tiido, N. Alexeyeva, M. Couillard, C. Bock, B.R. MacDougall, D. Tammeveski. Graphene–TiO2 composite supported Pt electrocatalyst for oxygen reduction reaction. Electrochim. Acta 2013; 107: 509-517.

[32] N.R. Elezovic, B.M. Babic, V.R. Radmilovic, Lj.M. Vracar, N.V. Krstajic. Synthesis and characterization of MoO*x*-Pt/C and TiO*x*-Pt/C nano-catalysts for oxygen reduction. Electrochim. Acta 2009; 54: 2404-2409.

[33] W. Vielstich, A. Lamm, H.A. Gasteiger, Handbook of Fuel Cells, John Wiley & Sons, England, 2003.

[34] T. Biegler, D.A.J. Rand, R. Woods. Limiting oxygen coverage on platinized platinum; Relevance to determination of real platinum area by hydrogen adsorption. J. Electroanal. Chem1971; 29: 269–277.

[35] X.Z. Fu, Y. Liang, S.P. Chen, J.D. Liao. Pt-rich shell coated Ni nanoparticles as catalysts for methanol electro-oxidation in alkaline media. Catal. Commun.2009; 10:1893-1897.

[36] C.-W. Kuo, L.-T.Lu, L.-C.Chang, Y.-C.Hsieh, Y.-C.Tseng, P.-W. Wu, J.F. Lee. Surface modification of commercial PtRu nanoparticles for methanol electro-oxidation. J. Power Sources 2013; 240: 122-130.

[37] X. Li. Principles of Fuel Cell, Taylor & Francis, New York 2006.

[38] E. Borja-arco, R.H. Castellanos, J. Uribe-Godínez, A. Altamirano-Gutiérrez, O. Jiménez Sandoval. Osmium–ruthenium carbonyl clusters as methanol tolerant electrocatalysts for oxygen reduction. J. Power Sources 2009; 188: 387-396.

Enhanced Photocatalytic Hydrogen Production Under Visible Light over Ag Doped TiO_2

V. Guzmán-Velderrain[1], M. Meléndez Zaragoza[1], E. Medina-Henandez[2], P. Gutiérrez Rivera[3], Y. Ortega-López[1], J. Salinas Gutiérrez[1], A. López Ortiz[1], V. Collins-Martínez[1*]

[1]Centro de Investigación en Materiales Avanzados S. C., Laboratorio Nacional de Nanotecnología, Depto. de Materiales Nanoestructurados, Miguel de Cervantes 120, C. P. 31109, Chihuahua, Chih. México
[2]Universidad Autónoma de Chihuahua, Facultad de Ciencias Químicas, Campus Universitario # 2 C.P. 31125, Chihuahua, Chih, México
[3]Universidad Tecnología Junta de los Ríos, Carretera Aldama, Km 3, C. P. 31313, Chihuahua, Chih. México
* Tel: +52 (614)439 11 29, e-mail: virginia.collins@cimav.edu.mx

ABSTRACT

TiO_2 is the most widely used photocatalyst for water and air purification, and for hydrogen production, due to its good properties such as chemical and photo-corrosion resistance and low cost. One disadvantage of this material, resides in its bandgap energy (3.2eV), which lies in the UV spectrum. For this reason, studies have been conducted to modify TiO_2 bandgap into the visible light range. Doping elements used for this purpose are noble metals such as Au, Pt and Ag. However, Au and Pt are expensive and scarce materials, leaving Ag as a preferred candidate. TiO_2 and doped TiO_2 were synthesized via sol-gel/hydrothermal (SGH) named TiO_2-F and TiO_2Ag-F, respectively, while under the sol-gel/hydrothermal/thermal (SGHT) technique was named as TiO_2Ag-C, using titanium butoxide as a precursor and ethanol as solvent. XRD characterization resulted in the presence of the anatase phase in all three synthesized samples as well as the characteristic signals for metallic Ag in TiO_2Ag-F. Samples crystal sizes were determined by the Scherrer equation, and were ~ 10 nm. Light absorption exhibited a shift in the Eg value from 3.05 eV for TiO_2-F to 2.8 eV for TiO_2Ag-F. BET surface area for the SGH and SGHT photocatalysts were of 140 and 95m^2/g, respectively. SEM images presented particle agglomerates of irregular morphology. Photocatalytic evaluation for hydrogen production was performed using a 250 W mercury light lamp, filtering the UV spectrum. TiO_2Ag-F was the only sample that showed activity, producing 180 µmol of H_2/g catalyst over a 4h irradiation period. This activity can be mainly attributed to the ability of this material to be activated under the visible light spectrum and to the silver in a metallic state in TiO_2, which inhibits the recombination of the electron-hole pair generated when the material is activated under light exposure.

Keywords: TiO_2 doped Ag;, Water splitting; Hydrothermal method.

1. Introduction

Today, the main source of energy in most countries, is based on the burning of fossil fuels, which increases each year due to population growth and daily activities. One concern about the excessive use of this source of energy is the amount of pollutants released into the atmosphere, which causes the greenhouse effect and the increase in earth temperature (global warming) [1, 2]. Due to this problem it is important to make use of alternative energy sources such as wind, biomass, nuclear [3] hydrothermal, geothermal and solar [4]. A disadvantage of these type of energy sources are their low efficiency, hence another energy alternative is through fuel cells and hydrogen. Hydrogen obtained through the separation of the water molecule (water splitting), promises to replace fossil fuels as a source of clean energy without the emission of pollutants and greenhouse gases such as CO_2, CO, SO_x, NO_x [5, 6]. By the breakthrough discovery of molecular water splitting, several processes have been developed, among them the photocatalytic. Research interest in hydrogen production via photocatalysis focuses primarily on the study of efficient semiconductor materials under the sunlight spectrum [7].

Titanium dioxide (TiO_2) is one of the most widely used photocatalyst in recent years, some of its uses have been in the degradation of toxic organic pollutants in both water and air and in the dissociation of the water molecule. Main advantages of this photocatalyst reside in its strong resistance to a wide variety of chemicals, as well as to the photocorrosion, besides its low cost [8]. However, a drawback to this material is that it has a band gap value (band gap) in the range of the ultraviolet light (3.2 eV), which within the solar spectrum extents to only 4%. Therefore, its activity is negligible under visible light irradiation and consequently its application is limited [9]. For this reason, studies have been conducted to reduce the bandwidth of TiO_2 into the visible light range through its doping. Among the elements that have been used for this purpose are; noble metals such as gold, platinum and silver (Au, Pt and Ag). Although gold and platinum provide good results towards the decrease of the bandgap, these are very expensive and scarce materials, so that silver can be considered as a potential candidate, because of lower cost and greater accessibility. Several studies where TiO_2 is doped with silver in various fields of application are reported; degradation of dyes (methyl orange, methyl red and crystal violet) as well as the hydrogen production via photocatalysis [10].

The objective of the present work is to synthesize crystalline TiO_2 powders at low temperature doped with silver, to observe the effect of the dopant material on the modification of its band gap, as well as to evaluate the photocatalytic activity towards hydrogen production in the range of visible light.

2. Experimental

2.1. Precursor solutions synthesis

Precursor solutions for doped and undoped TiO_2 powders were prepared by the Sol-Gel/Hydrothermal technique. For the sol-gel synthesis titanium n-butoxide, (ACROS trademark) with a purity of 99% was used as precursor, while for Ag, silver nitrate ($AgNO_3$, DEQ trademark) 99.8%, was employed as precursor and mixed in a 4.5% Ag/TiO_2 a molar ratio and this was dissolved in 5.08 ml of ethanol, 6.44 ml of acetic acid and 0.88 ml of water. A second solution with 8 ml of ethanol and 5.44 ml of titanium

butoxide was also prepared. Both solutions were mixed to form a final solution, which was kept under stirring for 1h. Subsequently, these solutions were subjected to a hydrothermal process at 200 ° C for 2h and finally one of the samples was exposed to a thermal treatment at 200 °C for 3h.

The nomenclature used for the different synthesized samples is presented in Table 1.

Table 1. Nomenclature of synthesized samples

Sample	Doping	Treatment	Temperature °C
TiO_2-F	N/A	Hydrothermal	200
TiO_2Ag-F	4.5%Ag	Hydrothermal	200
TiO_2Ag-C	4.5%Ag	Hydrothermal/Thermal	200/200

2.2. Characterization of Materials

TiO_2 powders were characterized by different techniques, with the aim of studying their physical and chemical features. To determine the crystal structure present in the materials, the powders were analyzed by XRD, using an XPert Pro diffractometer with a wavelength of 1.5406Å and between 15 to 85 ° in 2θ, with a step size of 0.05 and 120s by step. The crystal size of the samples using was calculated by the Scherrer's equation. To obtain the light absorption spectra of the materials the UV/Vis spectroscopy technique was employed, using a Perkin Elmer spectrophotometer (lamda-10) equipped with integrating sphere for diffuse reflectance studies. The particle size of the powders were determined by ultra-high resolution transmission electron microscopy (MET) using a JEM-2200FS that combines an emission gun of 200 kv with an omega filter and equipped with a system for energy dispersive spectroscopy (EDS) for elemental analysis of samples. The surface area of the powders was evaluated by the technique of nitrogen physisorption (BET) to a degassing temperature of 180 ° C, using a Quantachrome Autosorb-1.

2.3. Photocatalytic Evaluation

200 mg of the synthesized TiO_2 powders were suspended in water and methanol, the latter was used as a sacrificial agent; The suspension was placed inside a quartz batch type photoreactor (Figure 1) with a length of 19 cm and a diameter of 5 cm, which was sealed and located 7 cm away from a mercury lamp of 250 W in which 200 ml of distilled water, 4 ml of methanol and 0.2 g of photocatalyst were loaded, all under constant stirring and under illumination for 4h. Hydrogen production was monitored by gas chromatography using a gas chromatograph Perkin Elmer Clarus 500.

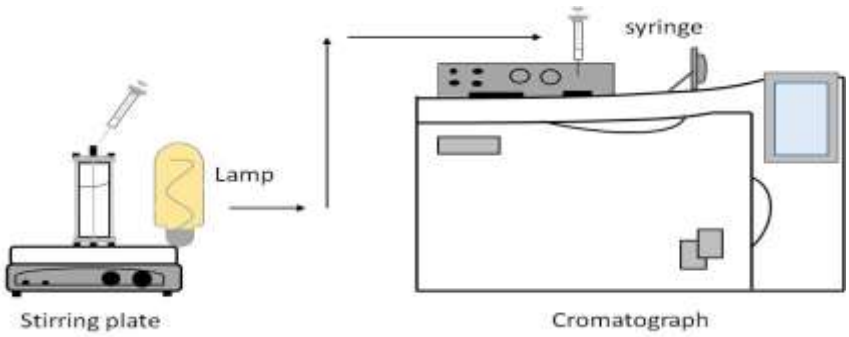

Fig 1. Photocatalytic process evaluation diagram.

3. Results and discussion

3.1. X ray Diffraction

XRD patterns of synthesized undoped and Ag-doped TiO_2 photocatalysts under different treatment conditions are presented in Figure 2. In these diffraction patterns it can be observed main reflections that belong to the anatase phase (characteristic signals (101) at 25° and (004) to 37.8° in 2θ) [11]. However, for TiO_2Ag-F sample a reflection peak at 38.2° in 2θ belonging to the (111) silver can be seen, overlapping with the signal (004) of anatase, reason why this presents a greater intensity in this pattern, besides the presence of the peak at 2θ 44.32° that corresponds to the (200) reflection, confirming the existence of metallic silver in the cubic phase sample [12]. This result can be explained considering that during the sol-gel process, silver was not incorporated into the TiO_2 crystal lattice, producing silver oxide and after review of the thermodynamic data, when this oxide is exposed to the temperature of the hydrothermal process (200 °C) this is converted to metallic silver. While in TiO_2Ag-C sample by applying a heat treatment silver atoms are driven to migrate towards the TiO_2 lattice, thus achieving their entire incorporation into TiO_2 causing silver reflections to disappear [13].

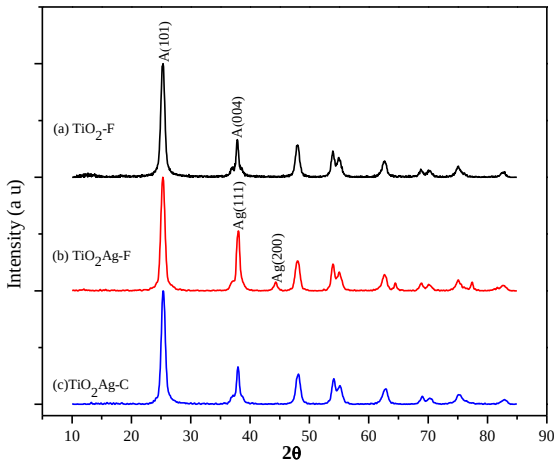

Fig 2. Diffraction patterns of TiO_2-F(a), TiO_2Ag-F(b) and TiO_2Ag-C(c)

3.2. Crystal Size

Table 2 presents calculated crystal sizes obtained from the Scherrer's equation and the diffraction patterns of each material. The synthesized materials present crystal size values of 10.4, 9.8 and 10.1 nm corresponding to the TiO_2-F, and TiO_2Ag TiO_2Ag-C-F samples, respectively. The reduction the crystal size for sample TiO_2Ag-F is associated with the previous explanation: during the sol-gel the Ag^+ ions are converted to silver oxide, so that the later during the hydrothermal treatment are transformed into elemental silver resulting in a physical barrier between the TiO_2 nanocrystals. This phenomenon causes the required movement for the crystals to reach its densifying energy and thereby the growth of these crystals is inhibited [14, 15, 16, 17]. Furthermore, the TiO_2Ag-C sample shows a slight increase in crystal size that can be attributed to crystal growth caused by the heat treatment to which the material was exposed.

Table 2. Estimated crystal size using the Scherrer's equation

Sample	Crystal Size (nm)
TiO_2-F	10.4
TiO_2Ag-F	9.8
TiO_2Ag-C	10.1

3.3. UV-Vis Spectra

Diffuse reflectance spectra (UV-Vis) for doped and undoped TiO_2 in Kubelka Munk units are presented in Figure 3. In order to determine the sample band gap the linear inflection region of the diffuse reflectance spectrum was considered, which represents the energy absorption over the edge. Extrapolating the slope of the linear region to intercept the photon energy axis (x-axis), this point provides the value of optical band gap of the material.

For the spectrum of sample TiO_2-F the estimated value of the energy band gap was ~ 3.05 eV, which is within the reported values of TiO_2 in anatase phase ranging from 3.05 to 3.2eV and outside the visible light spectrum [18].

By doping TiO_2 with Ag, the samples show a decrease in the bandgap. The value obtained for the doped sample TiO_2Ag-F corresponds to 2.8eV. This change in band gap energy is greatly attributed to the localized surface plasmon resonance (465 nm) generated by Ag nanoparticles; the presence of Ag on the surface of titanium oxide drastically creates a disturbance in the dielectric constant of the surrounding matrix and contributes for the material to be able to absorb visible light [19]. While the band gap value for TiO_2Ag-C sample was 2.6eV. This absorption shift towards red ~ 0.5 eV (62 nm) is attributable to the dopant metal, which generate energy states located above the valence band [20].

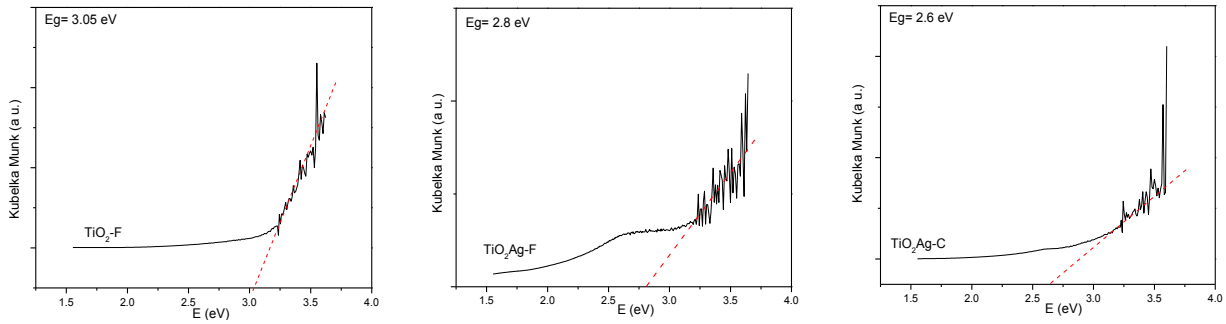

Fig 3. UV-Vis Diffuse Reflectance Spectra for the TiO_2-F TiO_2Ag-F and TiO_2Ag-C samples

3.4. Transmission electron microscopy

Transmission electron microscopy images for the synthesized samples are presented in Figure 4. Morphology of the samples consist in agglomerates of ellipsoid particles of nanometer size. The average particle size was determined by a statistical calculation of the average diameter of about 100 particles. The estimated particle size for the samples was between 12 and 18 nm, as presented in Table 3. Larger particle sizes were exhibited by sample TiO_2-F and this is due to the fact that during the nucleation and growth of the crystals these do not have the presence of the physical barrier of silver. Moreover, image analysis by Energy Dispersive Spectroscopy (EDS) of the TiO_2Ag-F sample, present free silver particles, confirming the results obtained by X-ray

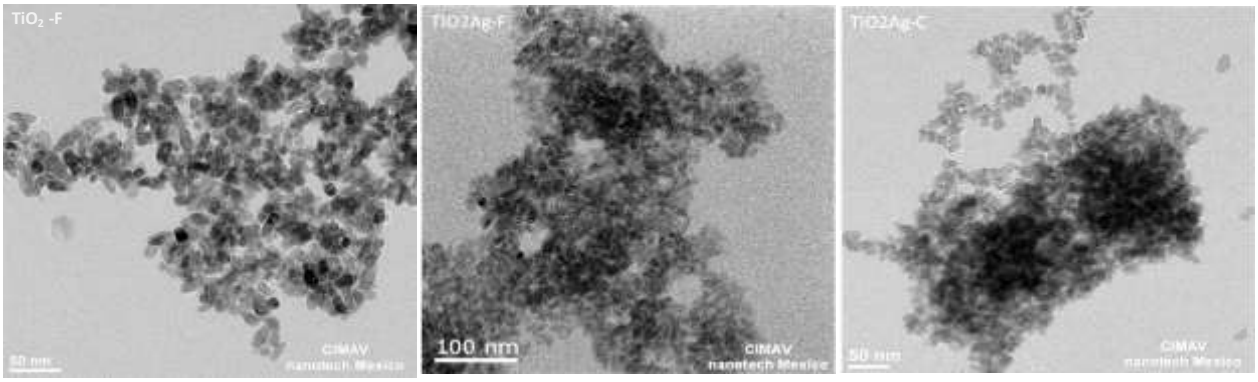

Fig 4. TEM images for the TiO_2-F (a) and TiO_2Ag-F (b) and TiO_2Ag-C (c) sample powders

3.5. BET Surface Area

The specific surface area for each photocatalyst was determined by N_2 physisorption and they were; 124, 138 and 93 m^2/g for TiO_2F, TiO_2Ag and TiO_2Ag-F-C, respectively. These results were expected since the present synthesis method is used to produce nanoparticles and consequently the effect of high surface areas is reflected. Likewise, it can be seen that when doping titanium with silver and after applying only

the hydrothermal treatment, an increase in surface area is reached. This is because the size of the crystal is decreased (as shown and explained in the crystal size section), which causes a decrease in particle size and an increase in surface area. Furthermore, it is noted that the TiO_2Ag-C sample has a reduced surface area and increased particle size. This is associated with this material suffering a sintering process caused by the heat treatment to which this sample was exposed.

Table 3. Surface area and particle size for the synthesized TiO_2 powders

Sample	Area (m^2/g)	Particle Size (nm)
TiO_2-F	125	18
TiO_2Ag-F	140	12
TiO_2Ag-C	95	15

3.6. Photocatalytic Evaluation

Evaluation of the photocatalytic activity for the different synthesized samples by the hydrogen evolution produced by the splitting reaction of the water molecule via photocatalysis is presented in Table 4. Results indicate that the H_2 production that was achieved after 4h irradiation presented the following order TiO_2Ag-F-C > TiO_2Ag > TiO_2-F. This behavior can be explained with the fact that TiO_2 samples that present an increased H_2 production are those doped with Ag, and these being active under the visible light spectrum, this also explains the low H_2 production of undoped TiO_2, as its activation energy is located in the UV region. On the other hand, differences in the performance of silver doped TiO_2 can be explained with studies reported by J. Yu et al. [19]. When silver is present in metallic form (as in the case of TiO_2Ag-F sample), additionally to helping reduce the bandgap through the interaction between the TiO_2-Ag phases, the electrons when excited from the valence band to the conduction band migrate to the Ag clusters, thus preventing the direct recombination of electrons and holes (a large disadvantage that TiO_2 has). When silver is incorporated into the TiO_2 crystal lattice (TiO_2Ag-C), only enter the intermediate states to decrease the bandgap energy, leaving the TiO_2 with its problem; a very fast recombination of electron-hole pair, which is reflected in the low production of H_2.

Table 4. Hydrogen production by the synthesized photocatalysts

Sample	$\mu moles H_2/g_{cat}$
TiO_2-F	15
TiO_2Ag-F	180
TiO_2Ag-C	30

4. Summary and perspectives

- In the present work, it was possible to synthesize undoped and silver doped TiO_2 through the sol-gel assisted hydrothermal treatment.

- X-ray results showed that TiO_2 presents only the anatase phase in all samples. For the doped samples, superficial metallic silver results when the hydrothermal treatment is only applied and by temperature effect (thermal treatment) silver incorporation into TiO_2 lattice is achieved.
- TiO_2 crystal size is affected by metallic silver, which acts as a physical barrier to inhibit the growth of anatase crystals because 10.4nm of sample TiO_2-F is reduced to 9.8nm in sample TiO_2Ag-F and in 10.1nm of sample TiO_2Ag-C. The morphology presented in TiO_2 samples was of ellipsoidal nanoparticles with an average particle size of 18 nm for TiO_2-F and 12 and 15 nm for TiO_2Ag-F and TiO_2Ag-C samples, respectively. Surface areas exhibited by the synthesized samples were affected by the particle size of the materials and these were: 125, 140 and 95 m^2/g for TiO_2-F, TiO_2Ag-F and TiO_2Ag-C, respectively.
- The value of the energy bandgap found for anatase 3.05 eV agrees with that reported in the literature. The shifting to red that silver induce in the TiO_2 bandgap is according to how silver is incorporated into this; when the effect is by interaction between phases (TiO_2-Ag°) as in the case of TiO_2Ag-F this is of 2.8 eV, and when Ag enters the lattice generating the intermediate states as shown in TiO_2Ag-C is of 2.6 eV, since both TiO_2 doped samples were active under the visible light spectrum.
- H_2 production achieved after 4 hours of light irradiation had the following order: TiO_2Ag-F>TiO_2Ag-C-F>TiO_2. The maximum H_2 production was of 180 µmol H_2/g_{cat}. The inhibition in recombination of the electron-hole pair that produce Ag metallic clusters in TiO_2, when attracting electrons, is decisive in the photocatalytic activity of these materials towards the dissociation of the water molecule for H_2 production.

Acknowledgements

The authors thank technicians: Teresa María Chaparro, Enrique Torres, Luis de la Torre and Carlos Ornelas for their contributions to the UV-Vis spectroscopy, BET, X-ray diffraction and scanning electron microscopy results. As well as the Centro de Investigación en Materiales Avanzados for their support in the use of its infrastructure.

References

[1] N. Naseri, H. Kim, W. Choi, A.Z. Moshfegh Optimal Ag concentration for H_2 production via Ag:TiO_2 nanocomposite thin film photoanode international journal of hydrogen energy 37 (2012) 3056e3065.

[2] M. Davoudi, M.R. Rahimpour, S.M. Jokar, F. Nikbakht, H. Abbasfard The major sources of gas flaring and air contamination in the natural gas processing plants: A case study Journal of Natural Gas, Science and Engineering 13 (2013) 7e19.

[3] Manuel Frondel, Nolan Ritter, Christoph M. Schmidt, ColinVance Economic impacts from the promotion of renewable energy technologies: The German experience Energy Policy 38 (2010) 4048–4056.

[4] Ayhan Demirbas Potential applications of renewable energy sources, biomass combustion problems in boiler power systems and combustión related environmental issues Progress in Energy and Combustion Science 31 (2005) 171–192

[5] Surakerk Onsuratoom, Sumaeth Chavadej, Thammanoon Sreethawong Hydrogen production from water splitting under UV light irradiation over Ag-loaded mesoporous-assembled TiO_2–ZrO_2 mixed oxide nanocrystal photocatalysts international journal of hydrogen energy 36 (2011) 5246-5261

[6] Stéphane Abanades, Patrice Charvin, Gilles Flamant, Pierre Neveu Screening of water-splitting thermochemical cycles potentially attractive for hydrogen production by concentrated solar energy Energy 31 (2006) 2805–2822.

[7] Honghui Yang, Liejin Guoa, Wei Yan, Hongtan Liu, A novel composite photocatalyst for water splitting hydrogen production, Journal of Power Sources 159 (2006) 1305–1309.

[8] K. Kocˇi, K. Mateˇju˚ , L. Obalova, S. Krejcˇikova, Z. Lacny´, D. Placha, L. Cˇapek, A. Hospodkova, O. ˇSolcova Effect of silver doping on the TiO_2 for photocatalytic reduction of CO_2, Applied Catalysis B: Environmental 96 (2010) 239–244.

[9] Ali Akbar Ashkarran, Habib Hamidinezhad, Hedayat Haddadi, Morteza Mahmoudi, Double-doped TiO_2 nanoparticles as an efficient visible-light-active photocatalyst and antibacterial agent under solar simulated lightApplied Surface Science 301 (2014) 338–345.

[10] Kenneth J. Klabunde, Dambar B. Hamal, Synthesis, characterization, and visible light activity of new nanoparticle photocatalysts based on silver, carbon, and sulfur-doped TiO_2, Journal of Colloid and Interface Science 311 (2007) 514–522

[11] O.-Bong Yanga, M. Alam Khana, Seong Ihl Woob Hydrothermally stabilized Fe(III) doped titania active under visible light for water splitting reaction international journal of hydrogen energy 33 (2008) 5345–5351

[12] Kiran Gupta, R. P. Singh, Ashutosh Pandey and Anjana Pandey Photocatalytic antibacterial performance of TiO_2 and Ag-doped TiO_2 against S. aureus. P. aeruginosa and E. coli, Beilstein J. Nanotechnol. 2013, 4, 345–351

[13] Chao He, Yun Yu, Xingfang Hu, André Larbot Influence of silver doping on the photcatalytic activity of titania fims Applied Surface science 200 (2002) 239-247.

[14] .I.Y. Tok, S.W. Du, F.Y.C. Boey, W.K. Chong Hydrothermal synthesis and characterization of rare earth doped ceria nanoparticles Materials Science and Engineering A. 466 (2007) 223–229

[15] Chao He, Yun Yu, Xingfang Hu, André Larbot Influence of silver doping on the photcatalytic activity of titania fims Applied Surface science 200 (2002) 239-247

[16] Yongsong Cao, Huihua Tan, Tianyu Shi, Tao Tang and Jianqiang Li Preparation of Ag-doped TiO_2 nanoparticles for photocatalytic degradation of acetamiprid in water Journal of Chemical Technology and Biotechnology 83:546–552 (2008),

[17] Yuanpeng Gao, Pengfei Fang, Feitai Chen, Yang Liu, Zhi Liu, Dahai Wang, Yiqun Dai Enhancement of stability of N-doped TiO_2 photocatalysts with Ag loading Applied Surface Science 265 (2013) 796– 801.

[18] Deanna C. Hurum, Alexander G. Agrios, and Kimberly A. Gray Explaining the Enhanced Photocatalytic Activity of Degussa P25 Mixed-Phase TiO_2 Using EPR J. Phys. Chem. B 2003, 107, 4545-4549

[19] Jiaguo Yu, Jianfeng Xiong, Bei Cheng, Shengwei Liu Fabrication and characterization of Ag–TiO_2 multiphase nanocomposite thin films with enhanced photocatalytic activity Applied Catalysis B: Environmental 60 (2005) 211–221.

[20] Roshan Nainan, Pragati Thakur and Manohar Chaskar Synthesis of Silver Doped TiO_2 Nanoparticles for the Improved Photocatalytic Degradation of Methyl Orange Journal of Materials Science and Engineering B 2 (1) (2012) 52-58.

Synthesis Method Effect of $CoFe_2O_4$ on its Photocatalytic Properties for H_2 Production from Water and Visible Light

Y. Ortega-López[1], J. Salinas Gutiérrez[1], V. Guzmán Velderrain[1], A. López Ortiz[1], V. Collins Martínez[1*]

[1]Centro de Investigación en Materiales Avanzados S. C., Laboratorio Nacional de Nanotecnología, Depto. de Materiales Nanoestructurados, Miguel de Cervantes 120, C. P. 31109, Chihuahua, Chih. México
. Tel: +52 (614)439 11 29 *e mail: virginia.collins@cimav.edu.mx

ABSTRACT

More efficient materials, which work under the visible light spectrum (energy bandgap from 1.5 to 3.0 eV) are the trends for today's new photocatalysts in the field of hydrogen production. Within this criteria, some transition metal ferrites are ideal. Since, the development of a ferrite-based photocatalytic material will help to address the need for a stable photocatalysts, activated under visible light and with high application potential due to their low cost. In particular, this paper reports cobalt ferrite ($CoFe_2O_4$) as a photocatalyst for hydrogen production, activated under visible light. A comparison between two methods of synthesis; chemical co-precipitation (CP) and milling ball (BM) is presented based on its photocatalytic properties. Furthermore, the influence of the synthesis method over the observed activity is presented. Characterization of $CoFe_2O_4$ was performed by X-ray diffraction (XRD), scanning electron microscopy (SEM), transmission electron microscopy (TEM), BET surface area, UV-Vis spectroscopy and water adsorption/desorption tests. Evaluation of the photocatalytic activity under visible light was followed by gas chromatography. Results indicate that crystalline materials with nanometer sizes were obtained (dp < 25nm). BET areas of 21 and 4 m^2/g and band gap energies of 1.3 eV and 1 eV were found for $CoFe_2O_4$ synthesized by CP and BM techniques, respectively. Water adsorption tests shown an adsorption capacity of 39 for and 30 mg-adsorbed-H_2O/g-catalyst for the CP and BM samples, respectively. The substantial decrease in surface area and adsorption capacity of the ferrite obtained by BM is attributed to a possible sintering process that the material undergoes during its synthesis. Photocatalytic activity results showed better activity for $CoFe_2O_4$ obtained through the BM synthesis. These results are associated with the creation of vacancies in the BM sample that generated a higher water absorption capacity and consequently a greater photocatalytic production of hydrogen.

Keywords: cobalt ferrite, visible light photocatalyst, hydrogen producton.

1. Introduction

Recently, hydrogen has received considerable attention as a next generation energy carrier. While several technologies can be used to generate hydrogen, only some of them can be considered environmentally friendly. There is a general perception that hydrogen is obtained through clean technologies, but this may not be necessarily true. If hydrogen is produced from natural gas (steam reforming), coal or biomass (gasification), a large amount of energy is used, not to mention a substantial amount of CO_2 generated as a byproduct. The latter is the main reason to consider as the best option to produce hydrogen from the splitting of the water molecule, either by using an alternative source of energy like hydraulic, wind or solar. From these alternative energies, solar is the most promising approach, since limitations related to the required space are less demanding.

Hydrogen production via the splitting of the water molecule using solar energy can generally be classified into three types: thermochemical, photobiological and photocatalytic. The principle of the water splitting is thermochemically achieved using concentrators to collect heat from the sun, which can normally reach about 2000 °C and using the collected heat to carry out the dissociation reaction of the water molecule in the presence of a catalyst such as ZnO [1-5]. Although this technique seems to be unsophisticated the management/heat control and the quest for heat resistant materials have become a major challenge. In addition, high concentration solar systems are essential to achieve the requirement of high temperature, which makes this technique often expensive. The photobiological water splitting [6-8], basically can be divided into two groups based on the selected microorganisms, the generated products and the reaction mechanisms involved. Hydrogen production by oxygenic photosynthetic cyanobacteria or green algae under irradiation of light and anaerobic conditions is referred to as water biophotolysis while producing hydrogen for anoxygenic photosynthetic bacteria under light irradiation conditions is known as anaerobic organic biophotolysis. Despite being the water biophotolysis a "clean" way to produce hydrogen than in organic biophotolysis still has several problems waiting to be solved, including low hydrogen yield, enzymes poisoning by the presence of oxygen and the difficulty in design and scaling of a bioreactor for the process.

Moreover, the photocatalytic splitting of the water molecule is another promising technology to produce "clean" hydrogen. Compared to the thermochemical and photobiological process, this technology has the following advantages: cost of the process is low, the ability to separate the hydrogen and oxygen evolution during the reaction and suitable systems for domestic applications with small reactors, thus providing a huge market potential.

Currently, TiO_2 is the most common and widely photocatalyst studied. This is because of its high stability and photocorrosion resistance, a phenomenon that occurs with most common semiconductor materials that can be used. However, their efficiency is very low and the process is limited to the use of high-energy radiation (UV) sources. Radiation of these characteristics can only be provided from artificial mechanisms with the consequent energy expenditure, because the UV light occupies only 4% of the sunlight, which is a limiting factor for the photocatalytic technology using TiO_2 as catalyst. This process for hydrogen production is unique in the sense that it is generated from solar energy, which would become a large clean and economic path for energy generation. It is in this sense that the search for photocatalysts activated under solar radiation (visible light occupies 43% of the solar spectrum) and highly effective, becomes one of the most important challenges in this technology.

One of the synthetic methods used for the preparation of photocatalysts is the co-precipitation technique, as it helps in obtaining a powder precursor of greater homogeneity, by precipitation of intermediates (typically hydroxides or oxalates), so it is an economical synthesis technique. Another easy access and low cost synthesis method is by mechanical milling, which uses more available raw materials and cheaper than other methods [9, 10]. Mechanical milling processes not only can produce an alloy but also, can cause chemical reactions, besides obtaining nanometric size particles [11].

Ferrites are viable alternative materials to TiO_2 to be used as photocatalysts for hydrogen production, transition metal ferrites have a number of advantages, mainly emphasizing their low cost, effective catalytic activity corrosion resistance and most importantly their wide bandgap into the visible light spectrum [12-14]. The selection of these materials is based on the redox activity and especially their ability to store oxygen in its crystalline lattice. Ferrites have a tendency, when burned under reducing atmospheres to form compounds with oxygen defects, which facilitates the fixation of oxygen in the existing vacancies. Therefore, these materials are an excellent candidates for the production of hydrogen from water, while providing the solar energy needed for the process.

The main objective of this study is to synthesize cobalt ferrites by chemical co-precipitation (CP) and mechanical milling (BM) and to determine the effect of the synthesis method on the ferrite photocatalytic activity towards the production of hydrogen.

2. Experimental

CP $CoFe_2O_4$ spinel was prepared by co-precipitation starting from nitrate precursors and modifying the procedure reported by Xialing and Hu [15]. In this method $(Fe(NO_3)_3 \bullet 9H_2O$ and $Co(NO_3)_2 \bullet 6H_2O$ solutions were added to NaOH as precipitating agent. The obtained precipitate was filtered and washed to remove any sodium residue. Thereafter, the residue was dried and placed in an agate mortar to obtain a fine and homogeneous powder. Nanosized crystalline oxide powder was obtained by exposing this to a moderate heat treatment at 250 °C by 6 hours, followed by 1 h at 350 °C.

For the preparation of CoF_2O_4 BM nanoparticles by the mechanical milling technique, the procedure consisted of mixing metallic Fe and Co_3O_4 as precursors in a molar ratio of 2:1. Once the material was in stoichiometric amounts, this was mixed and exposed to 700 ° C by 4 hours. Subsequently, in order to both obtain the desired spinel phase and to reduce particle size, the sample is subjected to mechanical milling with an effective time of 12 hours. The milling was carried out in a Spex CertiPrep 8000M Mixer/Mill, using a weight ratio of balls (0.7cm) to powder ($B:P_w$) of 10:1. To perform this synthesis a D2 steel vial was manufactured, and a exposed to a heat treatment; this consisted of an austenitizing temperature of 1010 ° C, oil quenching and tempering at a temperature varying from 300-400 ° C.

In order to determine the temperatures to be used during the calcination of the samples thermogravimetric analyses were needed from the powders obtained during each synthesis. This analysis was performed on a TGA Instrument TA Q500, using an initial sample weight of about 14 to 15 mg placed in a platinum crucible and employing a heating rate of 10 °C/min from room temperature to 980 °C under an air flow.

Characterization of the samples was performed by X-ray diffraction (XRD) using a PANalytical X'Pert PRO diffractometer with X'Celerator model detector, scanning electron microscopy (SEM) and transmission (TEM) using a JSM-7401F and a Philips model CM-200 microspcopes, respectively. BET

surface area was determined employing an Autosorb-1 equipment and Uv-Vis spectroscopy on a Perkin Elmer lambda 10 model.

The water vapor adsorption-desorption tests were performed by TGA; this test was performed by heating about 14 to 15 mg of sample at 130 ° C under nitrogen flow for 20 minutes to perform a surface cleaning of the sample and followed by an isotherm at 35 ° C to monitor the water adsorption-desorption behavior of the samples in a TA Instrument Q 500 TGA. Photocatalytic coatings were evaluated by splitting of the water molecule, using a 250W mercurial lamp and adding methanol to the water reactor system as sacrificial agent (2% vol). The reaction was monitored by gas chromatography using a GC Perkin Elmer Clarus 500. The system setup employed for carrying out the photocatalytic evaluation of the materials is presented in Figure 1. This system is composed by a photoreactor, artificial lighting and GC analysis with a PC data collection.

In order to monitor the photocatalytic reaction, samples were taken at regular time intervals using a 1ml syringe for gases through a septum located at the upper section of the photoreactor. A sample under darkness was taken as the initial concentration and then the sampling was took place every hour up to a total of 10 hours of irradiation.

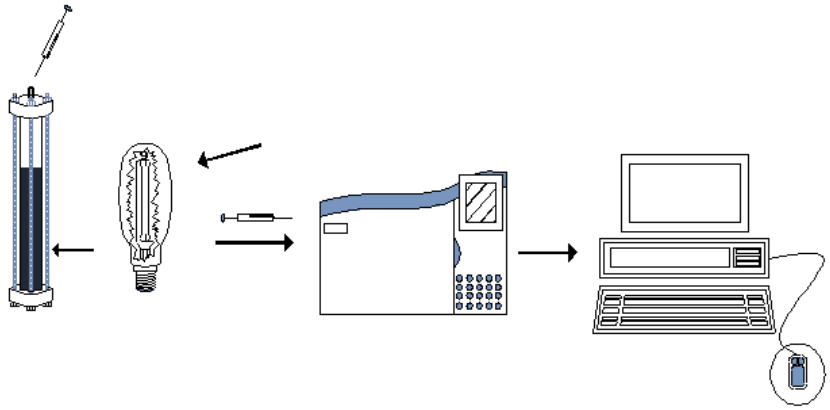

Fig 1. Photocatalytic experimental evaluation setup for the suspension; 0.2 g of $CoFe_2O_4$, H_2O and CH_3OH (sacrificial agent).

3. Results and discussion

3.1. Thermogravimetric Analysis

Determination of the heat treatment temperature of the precipitate product for sample $CoFe_2O_4$ CP during its synthesis was found using a temperature sweep through a thermogravimetric analysis. Figure 2 presents ($CoFe_2O_4$ CP) two signals; both with respect to temperature, one for the weight loss of the sample and the second for the derivative of this. In this Figure it can be observed two slight slope changes at 267 and 350 ° C. In both cases small slopes are observed indicative of slow kinetics. From these data it was considered to establish the temperature and time of heat treatment for this sample, which consisted of keeping the sample for 6 hours at 250 °C and 1 h at 350 °C, this was set in order to achieve the $CoFe_2O_4$ spinel phase, while maintaining a nanometric particle size in the sample, the slower kinetics is compensated by providing a prolonged heat treatment time (6 hours) [16].

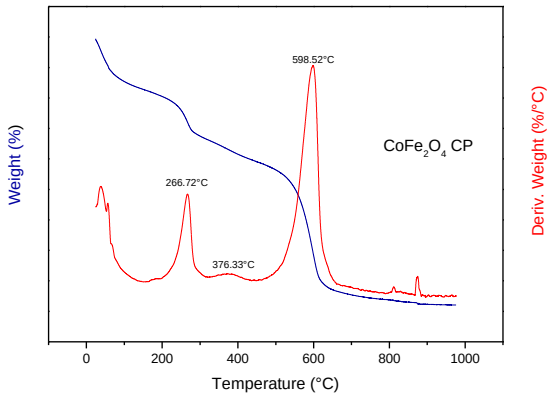

Fig 2. TGA of the precipitate to synthesize $CoFe_2O_4$ CP sample.

In the case of the $CoFe_2O_4$ BM sample determination of the calcination temperature of the Fe and Co_3O_4 mixture was established according to a thermogravimetric analysis. Figure 3 shows the thermogram of the Fe and Co_3O_4 mixture in a stoichiometric ratio ($CoFe_2O_4$ BM), where it is clear that at 700 °C the sample is thermally stable [17]. From the above analysis it was established that the heat treatment was set to 700 °C by 4 hours. Subsequently, the sample was exposed to the mechanical milling process for 12 hours of effective time.

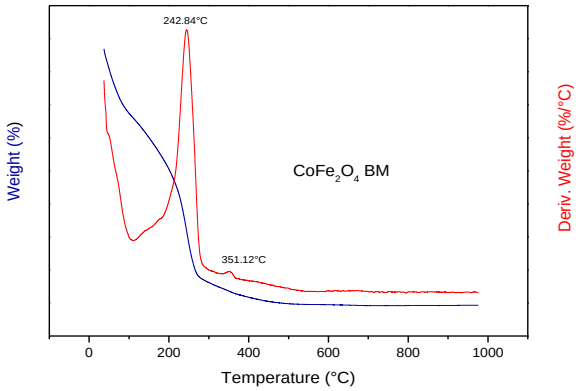

Fig 3. Thermogram for simple $CoFe_2O_4$ BM.

3.2. X-ray diffraction (XRD)

Figure 4 presents the X-ray diffraction pattern for the sample synthesized by chemical co-precipitation, as well as for sample prepared by mechanical milling, $CoFe_2O_4$ CP and $CoFe_2O_4$ BM, respectively. For the data processing, after the proper conversion formats, programs from the Diffrac-Plus package (Bruker AX Systems) were used, including the "Search/Match" identification tool, using the PDF-2 database (ICDD, 2002) ICDD PDF-2 on CD-ROM, Rls 2002, International Centre for Diffraction Data. Pennsylvania, 2002. Analysis of the diffraction patterns indicates that both materials are crystalline, prevailing the $CoFe_2O_4$ spinel phase. However, for the case of the ferrite obtained by chemical co-

precipitation, the Fe_2O_3 phase was also detected, nevertheless that some of the signals from this phase overlap with the $CoFe_2O_4$ phase. This result can be explained considering the phase diagram of Fe-Co-O_2 system (P = atm). For the case of the $CoFe_2O_4$ CP synthesis conditions, which were low temperatures (T < 1400 °C) and stoichiometric ratios of Co and Fe ions; the phase diagram predicts that the solid will consist of a mixture of cobalt ferrite and hematite (Fe_2O_3). While for the sample CoFe2O4 BM, where the initial mixture of metallic Fe and cobalt oxide are exposed to energetic conditions such as high temperature and impact, cobalt spinel is readily possible [18].

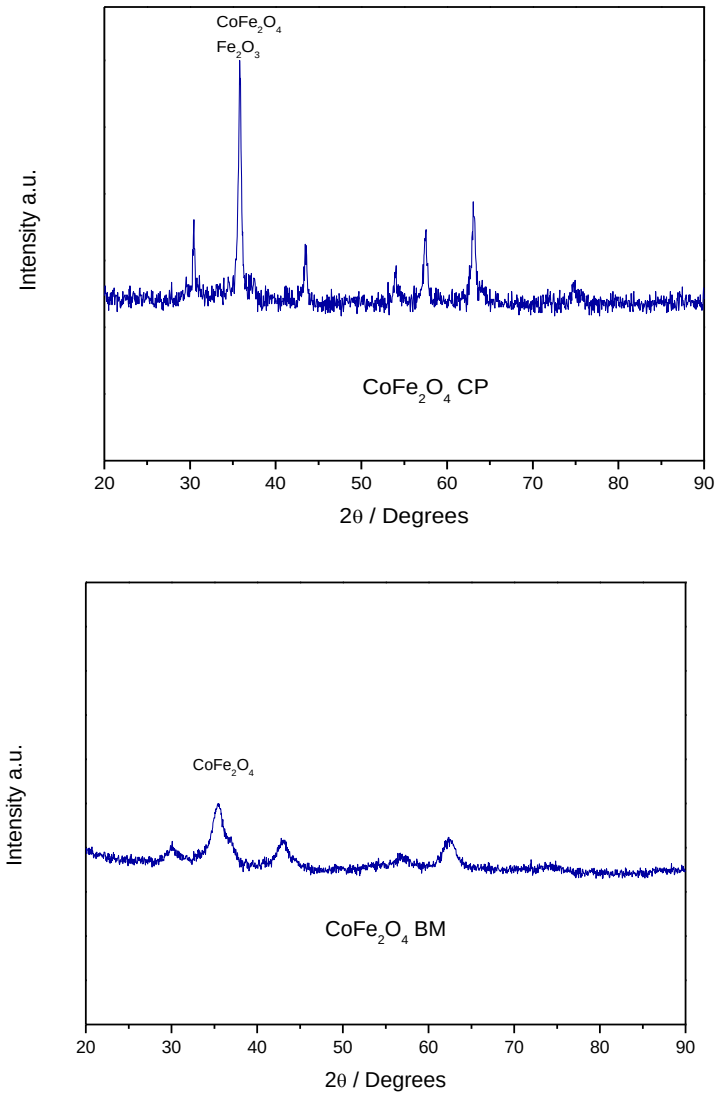

Fig 4. XRD patterns for $CoFe_2O_4$ CP (upper) and $CoFe_2O_4$ BM (lower) samples

Using the information from the X-ray patterns and through the Scherrer equation it was possible to calculate the crystal sizes of the materials. Sample $CoFe_2O_4$ CP present a crystal size of about 20 nm. While, $CoFe_2O_4$ BM sample exhibits a crystal size of around 5 nm, which is extremely smaller than that of

the $CoFe_2O_4$ CP sample. These results are expected, since by comparing the width of the peaks of both diffraction patterns, it can be clearly seen the broadening increase of the XRD peaks for the $CoFe_2O_4$ BM sample, consistent with a decrease of the crystal size, unlike the pattern for the $CoFe_2O_4$ CP sample present narrow and sharp peaks, indicative of a larger crystal size.

3.3. Scanning and Transmission Electron Microscopy

Scanning and transmission electron microscopy were used to determine the morphology and particle size of the samples under study. Figure 5 shows SEM images for samples $CoFe_2O_4$ CP and $CoFe_2O_4$ BM showing that both materials are formed of irregularly shaped agglomerates. Figure 5, CoFe2O4 CP (a) shows the presence of two morphologies. The first is formed by agglomerated nanoparticles, which corresponds to the spinel phase and the second is composed by plate-shaped particles of larger size that corresponds to hematite. These findings were determined according to analyses performed by energy dispersive spectroscopy (EDS), not shown in this work, which in turn confirms the results previously obtained by XRD. While sample $CoFe_2O_4$ BM (b) is formed by large agglomerates, which are composed of particles presenting clear evidence of sintering, which is attributed to the high temperature employed during the synthesis process (700 ° C).

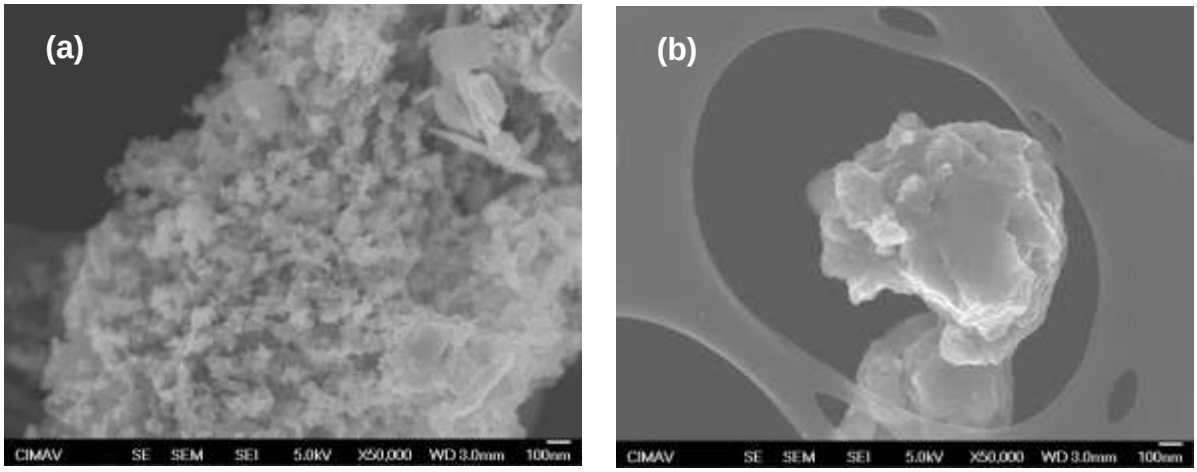

Fig 5. SEM from samples $CoFe_2O_4$ CP (a) and $CoFe_2O_4$ BM. (b)

Figure 6 shows TEM images of the synthesized cobalt ferrite samples. By analyzing the image for $CoFe_2O_4$ CP sample a particle size of around 25 nm can be estimated. This behavior can be associated with the control of the precipitate formation during the synthesis process, which is achieved by strict regulating the flow of the precursor's solutions (both of Co and Fe). Controlled flow induces a slow kinetics behavior for particle nucleation and growth, which makes particles to reach only nanometer sizes. Comparing the above results with those reported by Zhenfa Zi, et al. [19] (who also synthesized cobalt ferrite by co-precipitation) it was found that that research, which reported powders with a particle size between 20 and 30 nm showed very similar behavior to sample $CoFe_2O_4$ CP.

Moreover, also in Figure 6 it can be seen that sample $CoFe_2O_4$ BM exhibits highly compact agglomerates, (where the ultrasonic process was not effective to disperse the sample) with sizes between 100 and 500 nm, and these formed by particles of about 20 nm that apparently were joined together. The

formation of these densified agglomerates is associated with the exposure of the material to the synthesis temperature of 700 °C, confirming the results observed by SEM. However, this sample is nanocrystalline (according to results frm XRD) thus, these highly densified agglomerates tend to behave as a particulate material.

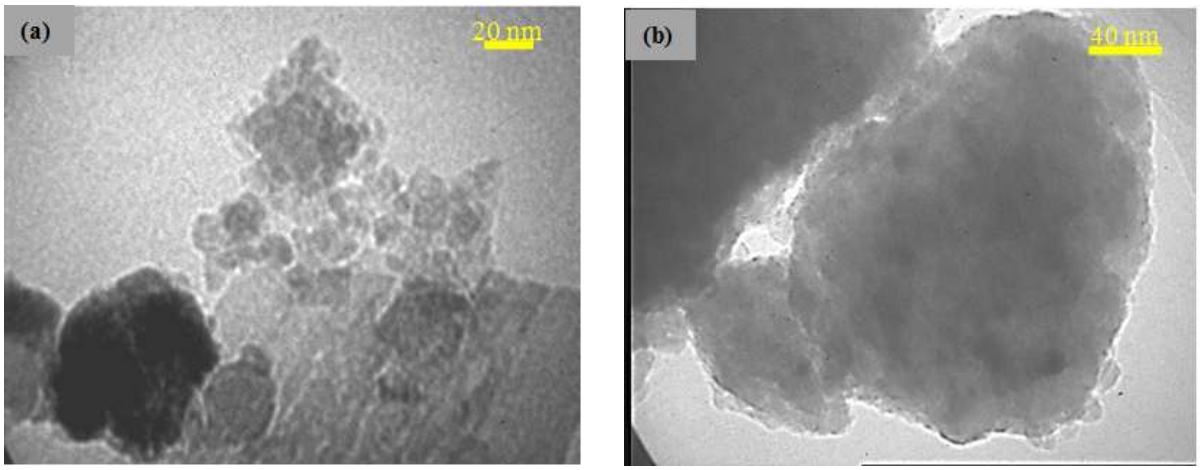

Fig 6. TEM image for samples $CoFe_2O_4$ CP (a) and $CoFe_2O_4$ BM (b).

3.4. BET Surface Area (Brunauer, Emmett y Teller) and Adsorption Isotherms

Values of specific surface areas for the photocatalyst synthesized by chemical co-precipitation and mechanical milling were 20 and 4 m^2/g, respectively. These values can be explained from particle size results determined by transmission electron microscopy.

Sample $CoFe_2O_4$ CP that corresponds to a particle size of 25 nm presented a higher surface area (20 m^2/g) compared to sample $CoFe_2O_4$ BM, which exhibited significantly large particles (agglomerates), ranging from 100-500 nm, which results in a surface area of only 4 m^2/g. The decreasing trend in the specific surface area of materials subjected to mechanical milling can be attributed to a strong aggregation between particles promoted by intensive milling, as reported by Cedeno et al [20].

Figure 7 shows adsorption isotherms for samples $CoFe_2O_4$ CP and $CoFe_2O_4$ BM, where it can be seen that both samples show no hysteresis, suggesting that these samples are non-porous solids. These results are expected since mechanical milling and co-precipitation synthesis methods generally produce non-porous materials.

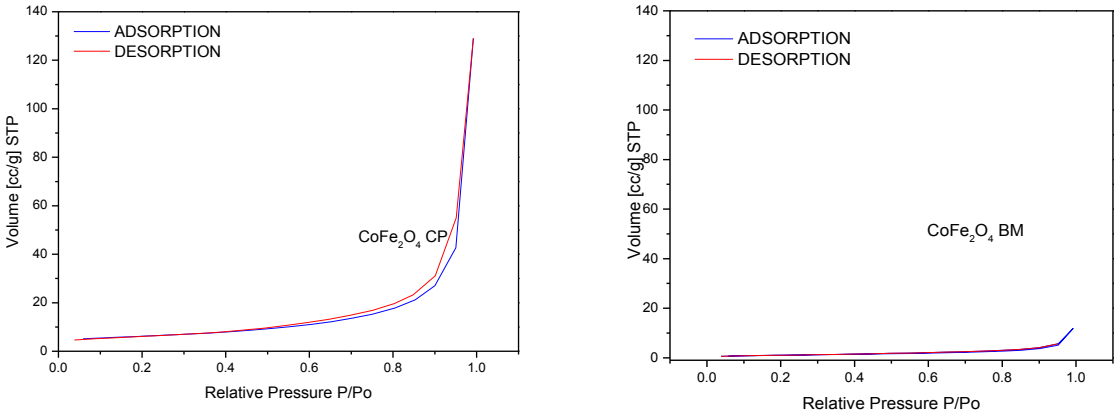

Fig 7. N_2 Adsorption Isotherms for $CoFe_2O_4$ CP and $CoFe_2O_4$ BM samples.

3.5. UV/Vis Spectroscopy

Figure 8 presents the diffuse reflectance UV/Vis spectra for samples $CoFe_2O_4$ CP and $CoFe_2O_4$ BM for an indirect transition employing the Tauc model. These spectra clearly show that values of the energy of the forbidden band are within the visible light spectrum for both cases. The reflectance values were converted in terms of absorption through the Kubelka-Munk function (F(R)) to determine the forbidden bandwidth by extrapolating the linear portion to the abscissa. Obtaining band gap energy value of 1.38 eV for $CoFe_2O_4$ CP and 1.15 eV for $CoFe_2O_4$ BM. Authors like Limei et al. [20] reported very similar values (~ 1.5 eV) to those obtained experimentally. This behavior can be explained with findings reported by Chavan et al, [21], who found that the band gap is highly dependent on the particle size; as the particle size of a ferrite type semiconductor increases its forbidden band decreases and vice versa. Therefore, by comparing the band gap values between the studied samples, it is expected that the $CoFe_2O_4$ CP sample to presents a greater band gap (1.38 eV) than sample $CoFe_2O_4$ BM (1.15 eV). This is because $CoFe_2O_4$ CP is formed by particles of 25 nm size. Whereas, this is opposite for the case of sample $CoFe_2O_4$ BM where the particle size (agglomerates) is significantly higher (100-500nm).

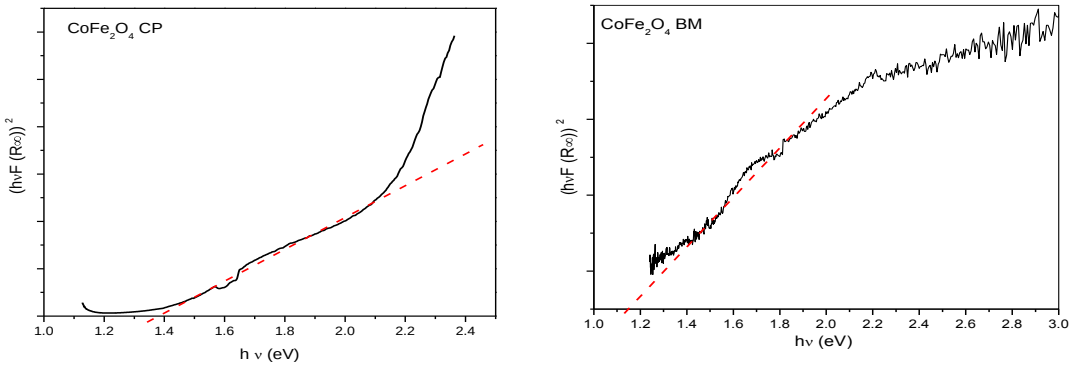

Fig 8. UV/Vis diffuse reflectance spectra (indirect transition model) for $CoFe_2O_4$ CP and $CoFe_2O_4$ BM.

3.6. Water Adsorption and Desorption (Gravimetric Method)

Figure 9 shows graphs of water adsorption-desorption gravimetric isotherms of the synthesized materials. Comparing the water adsorption-desorption capacities of both materials it can be observed that there is a significant difference between the $CoFe_2O_4$ CP sample and the sample one synthesized by mechanical milling (BM $CoFe_2O_4$).

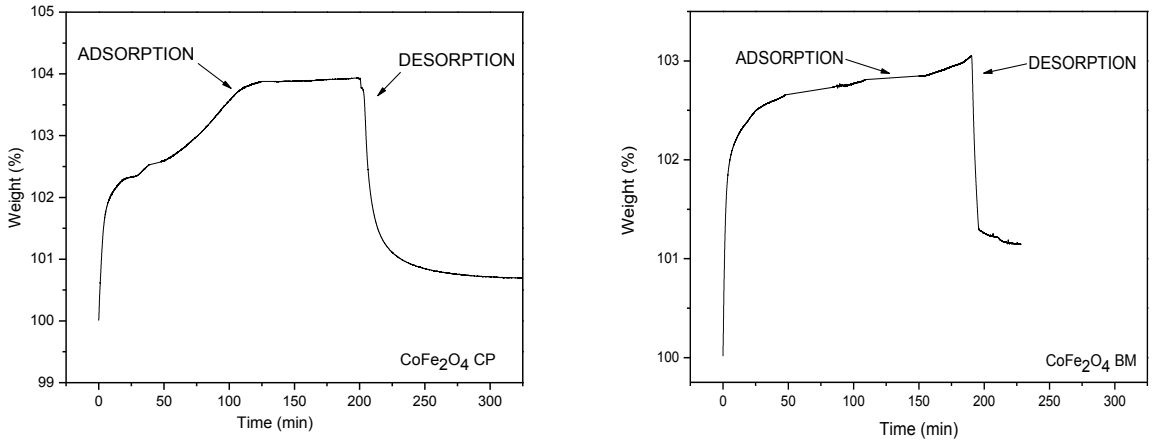

Fig 9. Thermogravimetric analysis for the adsorption-desorption of H_2O for samples $CoFe_2O_4$ CP (left) and $CoFe_2O_4$ BM (right).

Figure 9 shows a thermogravimetric isotherm plot for the adsorption-desorption of water of synthesized $CoFe_2O_4$ CP. Comparing the capacities of both materials, sample $CoFe_2O_4$ CP presented around the double H_2O adsorption-desorption capacity with respect to sample $CoFe_2O_4$ BM (not shown in Figure 9) synthesized by mechanical milling. The water adsorption from the sample synthesized by co-precipitation was about 39 mgH_2O/g, while the sample obtained by mechanical milling had 30 mgH_2O/g. These results are interesting in the sense that if a comparison is made in terms of water adsorption per surface area, it results in a greater water adsorption capacity of the sample synthesized by mechanical milling with 7.5 mg H_2O/m^2 compared to 1.95 mg H_2O/m^2 of sample synthesized by coprecipitation. This behavior can be explained in terms of the activity per unit surface area of each photocatalyst and may indicate that sample $CoFe_2O_4$ BM is photocatalytically more active than CP $CoFe_2O_4$, if a greater water adsorption is associated with an increased formation of OH radicals on the surface of the photocatalyst during the process of formation of the electron-hole pair.

3.7. Photocatalytic evaluation

Figure 10 shows results of the photocatalytic evaluation after 8 hours of irradiation for the samples under study. In this Figure the hydrogen evolution in µmol g^{-1} versus time in h is plotted. An analysis of this figure indicates that the photocatalytic activity towards hydrogen production after 8 hours of irradiation for sample $CoFe_2O_4$ CP exhibited about 2540 µmol g^{-1}, whereas the activity for sample $CoFe_2O_4$ BM was 3490 µmol g^{-1}.

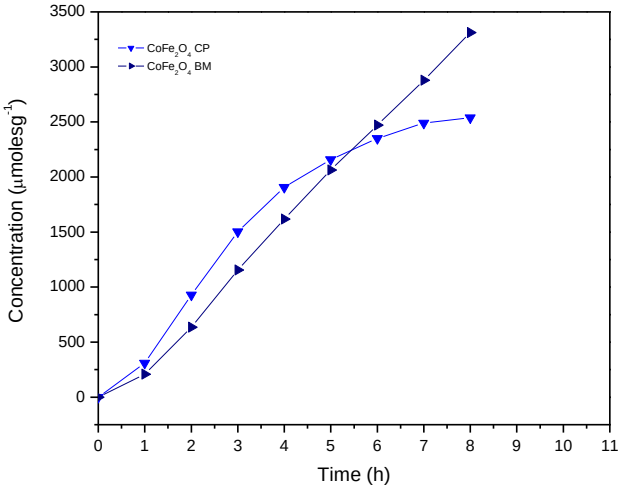

Fig 10. H_2 production after 8 hours of irradiation de H_2 for samples $CoFe_2O_4$ CP and $CoFe_2O_4$ BM

Although both samples can be activated under visible light, photoactivity results can be explained in terms of the morphological, textural, chemical and surface properties that each synthesis method generate on these ferrites. It is important to address that even though some studies are reported for the photocatalytic degradation of contaminants and dyes, so far no studies have been reported using $CoFe_2O_4$ for the production of hydrogen, which makes the activity of this material a significant finding [24,25].

Moreover, the superior photocatalytic activity for sample $CoFe_2O_4$ BM compared to $CoFe_2O_4$ CP can be explained by the findings of Zhang and Geng [26, 27] who reported that the mechanical milling causes a significant increase of vacancies in the solid sample, thus as the density of the vacancies due to collisions increase and these in turn brings about a material that is capable to increase its water adsorption (as reported above) and consequently able to produce a greater amount of hydrogen [28].

4. Summary and perspectives

Cobalt ferrite was successfully synthesized through two different techniques ($CoFe_2O_4$ CP and $CoFe_2O_4$ BM), one by chemical co-precipitation and the other by mechanical milling. These materials presented a band gap energy within the visible range, 1.38 and 1.15 eV, respectively and both exhibiting photocatalytic activity towards hydrogen production. However, sample $CoFe_2O_4$ BM has better photocatalytic activity compared to $CoFe_2O_4$ CP, which is explained by the generation of vacancies present due to hard collisions that occur during the ball milling process, which results in a better photocatalytic activity (3490 µmol g^{-1}) than that obtained through chemical coprecipitation in sample $CoFe_2O_4$ CP (2540 µmol g^{-1}). Even though cobalt ferrite has been used in studies for the photocatalytic degradation of organic pollutants, up to date no studies has been reported the use of $CoFe_2O_4$ for the production of hydrogen under visible light irradiation, which makes the activity found for this material a significant finding.

Acknowledgements

The authors wish to thank to the laboratories of X-ray diffraction, scanning electron microscopy, transmission electron microscopy and catalysis for their help during the progress of the present research.

Our sincere thanks to the Research Center for Advanced Materials (CIMAV) and to the National Council for Science and Technology (CONACYT) for the financial support granted.

References

[1] A. Steinfeld. Solar hydrogen production via a two-step water-splitting thermochemical cycle based on Zn/ZnO redox reactions. Int J Hydrog Energy 2002: 27; 611-619.

[2] R. Fernández-Saavedra, M.B. Gómez-Mancebo, C. Caravaca, M. Sánchez, A.J. Quejido, A. Vidal. Hydrogen production by two-step thermochemical cycles based on commercial nickel ferrite: Kinetic and study. Int J Hydrog Energy 2014: 39; 6819-6826.

[3] A.H. McDaniel, A. Ambrosini, E.N. Coker, J.E. Miller, W.C. Chueh, R. O'Hayre, J. Tong. Nonstoichiometric perovskite oxides for solar thermochemical H_2 and CO production. Energy Procedia 2014: 49; 2009-2018.

[4] F. Fresno, R. Fernández-Saavedra, M. Belén Gómez-Mancebo, A. Vidal, M. Sánchez, M.I. Rucandio, A.J. Quejido, M. Romero. Solar hydrogen production by two-step thermochemical cycles: Evaluation of the activity of commercial ferrites. Int J Hydrog Energy 2009: 34; 2918-2924.

[5] N. Gokon, H. Murayama, A. Nagasaki, T. Kodama. Thermochemical two-step water splitting cycles by monoclinic ZrO_2-supported $NiFe_2O_4$ and Fe_3O_4 powders and ceramic foam devices. Solar Energy 2009: 83; 4 527-537.

[6] I. Akkerman, M. Janssen, J Rocha, R.H. Wijffels. Photobiological hydrogen production: photochemical efficiency and bioreactor design. Int J Hydrog Energy 2002: 27; 1195-1208.

[7] E. Eroglu, A. Melis. Photobiological hydrogen production: Recent advances and state of the art. Bioresource Techn 2011: 102; 18 8403-8413.

[8] I. Akkerman, M. Janssen, J. Rocha, R.H. Wijffels. Photobiological hydrogen production: photochemical efficiency and bioreactor design. Int J Hydrog Energy 2002: 27; 11-12 1195-1208.

[9] O. Kubo, T. Ido, H. Yokoyama. Properties of Ba ferrite particles for perpendicular magnetic recording media. IEEE transactions on magnetics 1982: 28; 6 1122-1124.

[10] R.Valenzuela. Capítulo Preparation of magnetic ceramics. Magnetic Ceramicas. Cambridge 1994: 44-97.

[11] V. Hays. Nanocrystalline Fe-Ni solid solutions prepared by mechanical alloying. Nanostructured Mater 1996: 7; 4 411-420.

[12] N.M. Deraz. Production and characterization of pure and doped copper ferrite nanoparticles. J Anal Appl Pyrol 2008: 82; 212-222.

[13] Y. Haihua, Y Jianhui, L Zhouguang, C Xiang, T Yougen. Photocatalytic activity evaluation of tetragonal $CuFe_2O_4$ nanoparticles for the H_2 evolution under visible light irradiation. J Alloy Compd 2009: 476; 715-719.

[14] A. Kezzim, N. Nasrallah, A. Abdi, M. Tari. Visible light induced hydrogen on the novel hetero-system $CuFe_2O_4/TiO_2$. Energ Conver Manag 2011: 52; 8-9 2800-2806.

[15] X. Hu, P. Guan and X. Yan. Hydrothermal synthesis of nano-meter microporous zinc ferrite. China Particuology 2004: 2; 3 135-137.

[16] D. Nagehan, M. Vedat Akdeniz, O.M. Amdulla. Magnetic monitoring approach to nanocrystallization kinetics in Fe-based bulk amorphous alloy. Intermetallics 2013: 43: 152-161.

[17] A.M. Hamid, A. Abolghasem. Investigation on phase evolution in the processing of nano-crystalline cobalt ferrite by solid-state reaction route. Materials Research 2014: 829: 767-771.

[18] M. Ristic´, B. Hannoyer, S. Popovic´, S. Music´, N. Bajraktaraj. Ferritization of copper ions in the Cu-Fe-O system. Mater Sci Eng B 2000: 77: 73-82.

[19] Z. Zi, Y. Sun, X. Zhu, Z. Yang, J. Dai, W. Song. Synthesis and magnetic properties of $CoFe_2O_4$ ferrite nanoparticles. J Magn Magn Mater 2009: 321: 1251-1255.

[20] Y. Cedeño-Mattei, O. Perales-Pérez, O.NC. Uwakweh. Effect of high-energy ball milling time on structural and magnetic properties of nanocrystalline cobalt ferrite powders J Magn Magn Mater 2013: 341; 17-24.

[21] X. Limei, F. Zhang, C. Bin, X.B. Chen, X. Bai. Preparation of Light-Driven Spinel Nanoparticles $CoAl_2O_4$, $MgFe_2O_4$ and $CoFe_2O_4$ and Their Photocatalytic Reduction of Carbon Dioxide. 2011: ISBN: 978-0-7695-4350-5.

[22] S.M. Chavana, M.K. Babrekarc, S.S. Moreb, K.M. Jadhav. Structural and optical properties of nanocrystalline Ni-Zn ferrite thin films. J Alloy Compd 2010: 507; 21-25.

[23] P. T, Araújo dos Santos, P. T, Araújo dos Santos, A. C. Figueiredo Melo Costa, The Influence Of Calcination Temperature In Ni-Zn Ferrite Doped With Al^{3+}, Proceedings of 21st International Congress of Mechanical Engineering (COBEM 2011), October 24-28, 2011, Natal, RN, Brazil

[24] E. Casbeer, V.K. Sharma, L. Xiang-Zhong. Review: Synthesis and photocatalytic activity of ferrites under visible light. Sep Purif Technol 2012: 87: 1-14.

[25] P.H. Borse, C.R. Cho, K.T. Lim, Y.J. Lee, T.E. Hong, J.S. Bae, E.D. Jeong, H.J. Kim and H.G. Kim. Synthesis of Barium Ferrite for Visible Light Photocatalysis Applications. J of the Korean Physical Society 2011: 58; 6 1672-1676.

[26] B.Q. Zhang, L. Lu, M.O. Lai. Evolution of vacancy densities in powder particles during mechanical milling Physica B 2003: 325; 120-129.

[27] Y. Geng, T. Ablekim, P. Mukherjee, M. Weber, K. Lynn, J.E. Shield. High-energy mechanical milling-induced crystallization in Fe32Ni52Zr3B13 Journal of Non-Crystalline Solids 2014: 404; 140-144.

[28] T. Xia, Y. Zhang, J. Murowchick, X. Che n. Vacuum-treated titanium dioxide nanocrystals: Optical properties, surface disorder, oxygen vacancy, and photocatalytic activities, Catalysis Today 2014: 225; 2-9.

Sociedad Mexicana del Hidrógeno A. C.
Mexican Hydrogen Society

CONACYT

ITC

Photocatalytic Hydrogen Production under Visible Light over Magnesium Ferrite

V. Guzmán-Velderrain[1], M. Meléndez Zaragoza[1], E. Medina-Henandez[2], P. Gutiérrez Rivera[3], L. García Campos[1], Y. Ortega-López[1], J. Salinas Gutiérrez[1], A. López Ortiz[1], V. Collins-Martínez[1*]

[1]Centro de Investigación en Materiales Avanzados S. C., Laboratorio Nacional de Nanotecnología, Depto. de Materiales Nanoestructurados, Miguel de Cervantes 120, C. P. 31109, Chihuahua, Chih. México
[2]Universidad Autónoma de Chihuahua, Facultad de Ciencias Químicas, Campus Universitario # 2 C.P. 31125, Chihuahua, Chih, México
[3]Universidad Tecnología Junta de los Ríos, Carretera Aldama, Km 3, C. P. 31313, Chihuahua, Chih. México
. Tel: +52 (614)439 11 29 *e mail: virginia.collins@cimav.edu.mx

ABSTRACT

Magnesium ferrite ($MgFe_2O_4$) was synthesized by the hydrothermal technique and was found to be an active photocatalyst for hydrogen production from water under visible light. The structural, morphological, and optical properties of the material were characterized by powder XRD, SEM, TEM, and UV-Vis diffuse reflectance spectroscopy. Iron and magnesium aqueous nitrate solutions were used as precursors under hydrothermal conditions of 200 °C for 3.5 h. $MgFe_2O_4$ photocatalytic activity towards the H_2 production was determined by gas chromatography, using a batch-type quartz photoreactor and irradiated using a 250 W mercury lamp. XRD results from the synthesized sample found the $MgFe_2O_4$ crystalline structure. The optical properties revealed semiconducting properties with a band gap energy (E_g) of 2.07 eV (599nm) showing an efficient visible light absorption. SEM images found particles with a morphology in the form of agglomerates composed of hemispherical particles, while TEM images revealed particles with an average of 9.3 nm in size. Furthermore, the solid exhibited a high photoactivity toward the reduction of water, which is attributed to the efficient separation and transportation of the photogenerated charge carriers. This ferrite material exhibited a production of 650 µmol $H_2/g_{catalyst}$ over an irradiation period of 8 h, thus exceeding the H_2 generation obtained by TiO_2, which was of 15 µmol $H_2/g_{catalyst}$. This increase in H_2 production is attributed to the fact that $MgFe_2O_4$ exhibits a band gap, which is activated under the visible light range.

Keywords: Hydrogen production, $MgFe_2O_4$, Water splitting

1. Introduction

In the last decade it has been an increased research interest related to renewable energy, because of environmental constraints and the low efficiency offered by traditional fossil energies. It is thought that the development of a new sources of renewable energy will bring a number of advantages [1]. A promising alternative is the use of hydrogen, because it has so many desirable features such as clean emissions when used as fuel, abundance, accessibility, high efficiency and overall versatility of use [2]. However, the first step in the production of a safe and clean energy, is finding a method for producing hydrogen cheaply and efficiently [1]. Currently, hydrogen is proposed as an energy vector that can be applied to renewable energy source (RES) such as solar, wind, biological, ocean and geothermal. Of these alternative RES it is important to take in to account factors like accessibility, affordability and being environmentally friendly. Based on this the use of water can be considered as an ideal source of hydrogen [3, 4, 5, 6, 7].

In the literature there are reports of hydrogen production from water photo reduction in the presence of semiconductors (SC) as photocatalysts. That is why the exploration of new semiconductors with high photocatalytic activity under visible light irradiation, projected various advantages such as low cost, favorable positioning of the band energy levels and chemical stability in aqueous media [8].

Ferrites with the general formula MFe_2O_4, where (M) represents a metal cation have various applications because of their chemical and thermal stability. Their applications mainly has excelled in electronic devices and circuits, besides their increasing use as absorbers of toxic and hazardous substances to health. Ferrites have shown to be effective photocatalysts under visible light to generate electron-hole pairs on the photocatalytic material surface. However, there is still a great challenge in understanding the mechanisms of water reduction [9].

Magnesium Ferrite ($MgFe_2O_4$) has a band gap energy of 2.18 eV [9], indicating that it can be activated under the visible light range. Literature reports several synthesis methods for preparing the magnesium ferrite spinel, such as ceramic [10-12], hydrothermal [13], sol-gel [14], citrate gel [15], combustion [16 - 17], mechanical alloying [18], coprecipitation [19], etc. However, the coprecipitation method has some advantages such as: simple, fast, easy control of particle size and composition and various possibilities for controlling the state of the total surface of the particles and their homogeneity. Generally, after performing coprecipitation, the material is exposed to a heat treatment to crystallize, but runs the risk of particle growth and then exceed the nanometer scale. Therefore, in the present work the precipitation is to be combined with hydrothermal treatment to obtain a material with all the above mentioned advantages of the coprecipitation method, while keeping the particles in a nanometric size through the use of the hydrothermal treatment.

The objective of this work is to synthesize magnesium ferrite by the coprecipitation combined with hydrothermal treatment, characterize their structural, morphological, textural and optical properties, and to evaluate its photocatalytic activity towards the hydrogen production under visible light.

2. Experimental

2.1. Synthesis of nanoparticles

Precursor solutions were synthesized by the coprecipitation/hydrothermal method, using precursors: Magnesium II nitrate ($Mg(NO_3)_2*4H_2O$) Sigma Aldrich brand with a 98% purity and Iron III nitrate ($Fe(NO_3)_3*9H_2O$) Sigma Aldrich brand with a purity of 98%. The material was prepared in order to obtain 1 g of $MgFe_2O_4$, for that 4.39 g of $Fe(NO_3)_3*9H_2O$ was added in 5 ml of water and 1.39 g of $Mg(NO_3)_2$ in 3 ml of water. These solutions were mixed and placed in a burette and allowed to drip into 20 ml of ammonium hydroxide (NH_4OH) as a precipitating agent and pH regulated to a value of approximately 10. Subsequently, the mixture was exposed to a hydrothermal treatment in an autoclave using a Teflon vial at 200 °C for 3 h.

2.2. Material Characterization

$MgFe_2O_4$ powders were characterized by different techniques in order to study its physical and chemical characteristics. In order to determine the crystal structure of the material, this was analyzed by XRD using a Bruker D8 Advance model X-ray diffractometer with a 1.54060Å wavelength and employing 15 to 85 ° in 2θ with a step-size of 0.05 and 120s by step. The crystal size was estimated using the Scherrer's equation. The light absorption spectra of the material was acquired by UV/Vis diffuse reflectance spectra using a Perkin Elmer (Lambda-10) spectrometer equipped with an integrating sphere. The photocatalyst morphology was examined by transmission electron microscopy (TEM), in addition the particle size thereof was measured by a particle counting on a JEM-2200FS transmission electron microscope of ultra-high resolution that combines an emission gun of 200kV with an omega filter. The surface area of the powders was evaluated by the nitrogen physisorption technique (BET) to a degassing temperature of 180 °C, using a Quantachrome Autosorb-1 BET aparatus.

2.3. Photocatalytic Evaluation

200 mg of $MgFe_2O_4$ nanoparticles were suspended in water and methanol, the latter was used as a sacrificial agent; the suspension was placed inside a quartz batch type photoreactor (Figure 1) with a length of 19 cm and a diameter of 5 cm, which was sealed and located 7 cm away from a 250W mercury lamp. Hydrogen production was monitored using a gas chromatograph Perkin Elmer Clarus 500. Photocatalytic activity was evaluated over a period of time of 8 hours with sampling intervals of every hour.

Since titanium dioxide (TiO_2) is a reference photocatalyst, TiO_2 was synthesized by the sol-gel method assisted with hydrothermal treatment (TiO_2-F), both physical and chemical properties as well as the photocatalytic activity towards the hydrogen production were compared via the dissociation of the water molecule.

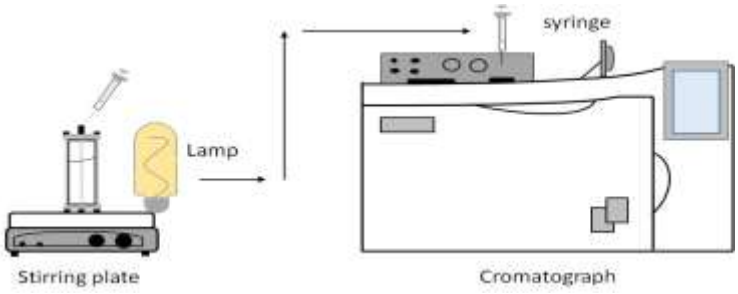

Fig 1. Diagram for the photocatalytic evaluation process

3. Results and discussion

3.1. Difracción de Rayos X

In Figure 2 the X-ray diffractograms of the $MgFe_2O_4$ and TiO_2-F photocatalysts are shown. From them the diffraction angles of the crystalline structures present in the materials can be observed. For the MgFe2O4 sample a mixture of phases was observed; α-Fe_2O_3 and the spinel $MgFe_2O_4$. Observing the diffraction angles of 33.4 °, 42.2 °, 57.5 °, 63 ° which correspond to the reflections (311), (400), (511) and (440) of cubic $MgFe_2O_4$. While angles 24.3 °, 33.1 °, 40.8 °, 49.3 °, 54.1 ° correspond to reflections (012), (104), (113), (024) and (116) that identify the phase α-hematite Fe_2O_3 [20]. The result of the phase mixture can be explained since the phase diagram Fe_2O_3-MgO-O_2 (P, atm) indicates that at stoichiometric ratios and low temperatures a single-phase mixture is reached as presently obtained.

For the case of TiO_2-F peaks located at 25.4, 37.8, 48.0, 54.5 ° of 2 Θ the corresponding to planes (101), (004), (200), (105 and 211) of the anatase phase are observed [22].

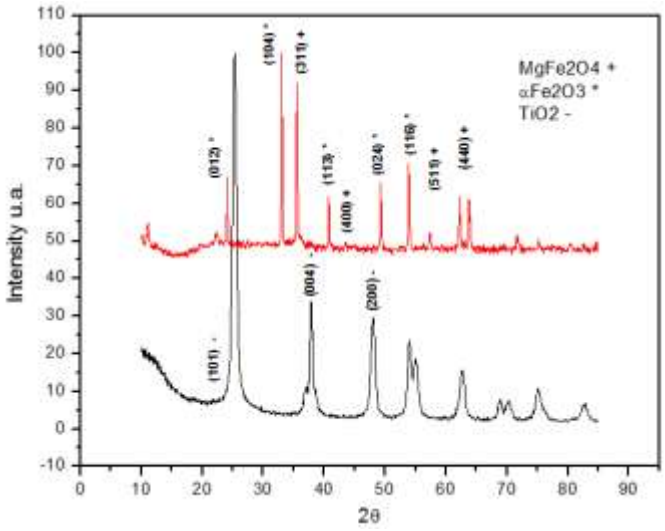

Fig 2. $MgFe_2O_4$ and TiO_2-F sample diffraction patterns.

Comparing the width of the peaks of the TiO_2-F and $MgFe_2O_4$ and sample it can be observed that narrower signals for the ferrite, suggesting a greater crystal size for this sample. To determine the crystal size of the samples X-ray patterns data (characteristic peak of each material) and the Scherrer's equation was employed, thus TiO_2-F presented a crystal size of 10.5 nm, while $MgFe_2O_4$ showed a size of 44 nm, which proves the earlier assumption about the width of the diffraction patterns peaks. This difference in crystal size can be attributed to the different synthesis methods used in each material (different mechanisms of nucleation and growth), coprecipitation for ferrite and sol-gel for the titanium oxide.

3.2. UV-Vis Spectroscopy

UV-Vis diffuse reflectance spectra for $MgFe_2O_4$ and doped TiO_2-F converted to Kubelka Munk units are presented in Figure 3. To determine the sample band gap it was considered a linear trend from inflection region of the spectrum, which represents the energy absorption over the edge. Extrapolating the slope of the linear region to intercept the photon energy axis (x-axis), this point provides the value of optical band gap of the material.

In this Figure it can be seen that the value of energy band gap (Eg) for the TiO_2-F sample is 3.12eV, which is very close to the reported value for the TiO_2 anatase phase of 3.2 eV [22]. On the other hand sample $MgFe_2O_4$ presents an Eg value of 2.07eV. This value is within the values reported for magnesium ferrite spinel which are between 2.0 and 2.18 eV, and these vary depending on the particle size; the smaller the value of the band gap this increases [9].

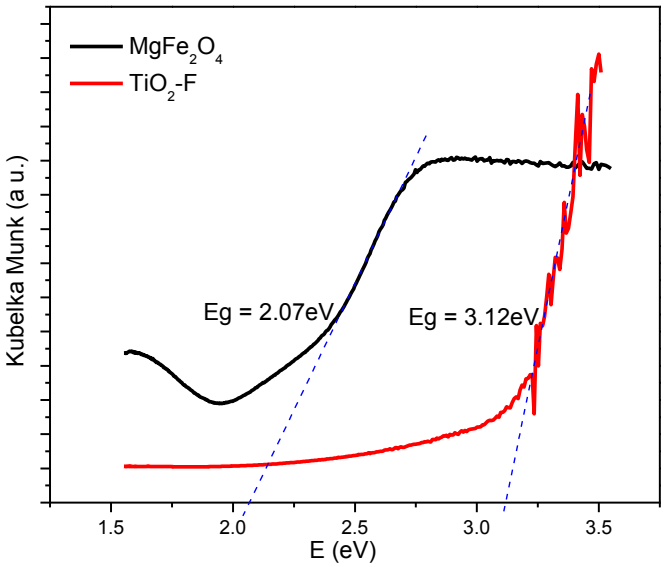

Fig 3. Band gap determination by UV-Vis spectroscopy.

3.3. Transmission electron Microscopy (TEM)

Transmission electron microscopy images for samples $MgFe_2O_4$ and TiO_2-F are presented in Figure 4. In this figure it can be seen completely different morphologies; $MgFe_2O_4$ particles present are cubic shapes with a mean size of 90 nm. While for the TiO_2-F sample ellipsoidal particles with an average size of 20 nm can be observed. These results, as in the case of the crystal size calculations, are to be expected as various methods of synthesis were used, which correspond to different mechanisms of nucleation and particle growth.

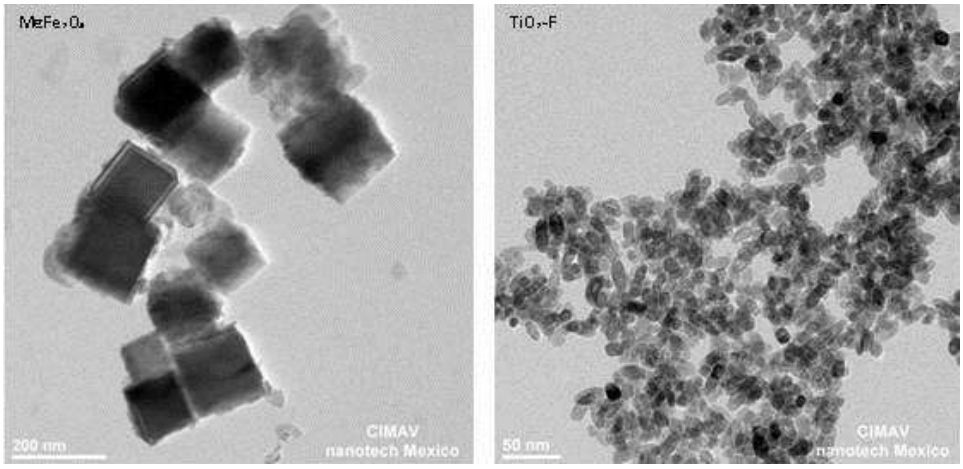

Fig 4. TEM images for the samples $MgFe_2O_4$ and TiO_2-F

3.4. Nitrogen Physisorption (BET)

The method of nitrogen physisorption (BET) was employed for obtaining the surface area of the synthesized materials ($MgFe_2O_4$ and TiO_2-F). Figure 5 shows the adsorption isotherms, where it appears that TiO_2-F isotherm is of type IV according to the classification of the IUPAC, which is characteristic of mesoporous materials, with a H2 hysteresis loop characteristic bottleneck type pores. However, the adsorption isotherm for $MgFe_2O_4$ is of type III characteristic of a hysteresis loop H3 of mesoporous materials with a very wide size distribution [21], which can be associated with interparticle porosity, very characteristic of materials obtained by precipitation.

Moreover, in Figure 5 it can be observed that there is a considerable difference in the amount of adsorbed nitrogen, being higher for the sample TiO_2-F, this is attributed to presenting greater surface area. This result was expected since by size particle (small) as well as by porosity high surface areas are generated. The value of the specific surface area and the particle size obtained by TEM images for each material is presented in Table 1.

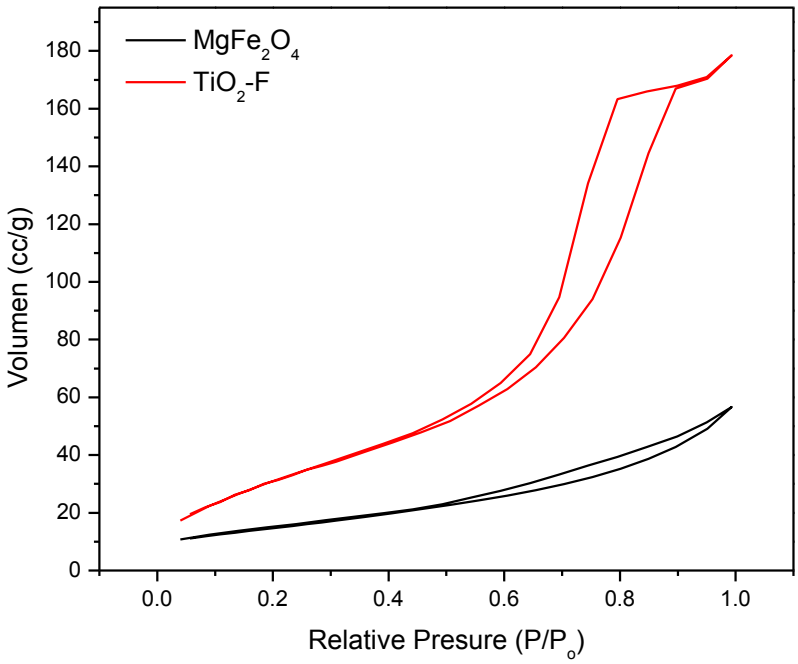

Fig 5. $MgFe_2O_4$ and TiO_2-F adsorption isotherms.

Table 1. BET surface area and particle size for the synthesized photocatalysts

Sample	Area (m_2/g)	Particle size (nm)
TiO_2-F	124	20
$MgFe_2O_4$	53	90

3.5. Photocatalytic Evaluation

In Figure 6 the hydrogen evolution of both $MgFe_2O_4$ and TiO_2-F samples are presented. It is evident that an increased hydrogen production for sample $MgFe_2O_4$ was achieved, although it has less surface area than the TiO_2-F, the photocatalytic activity mainly is attributed to the lower value of Eg, which is in the range of visible light as mentioned in Figure 3. More than 650 $\mu molH_2/g_{cat}$ was reached for sample $MgFe_2O_4$ after 8 h of irradiation against 15 $\mu molH_2/g_{cat}$ produced by the synthesized TiO_2-F.

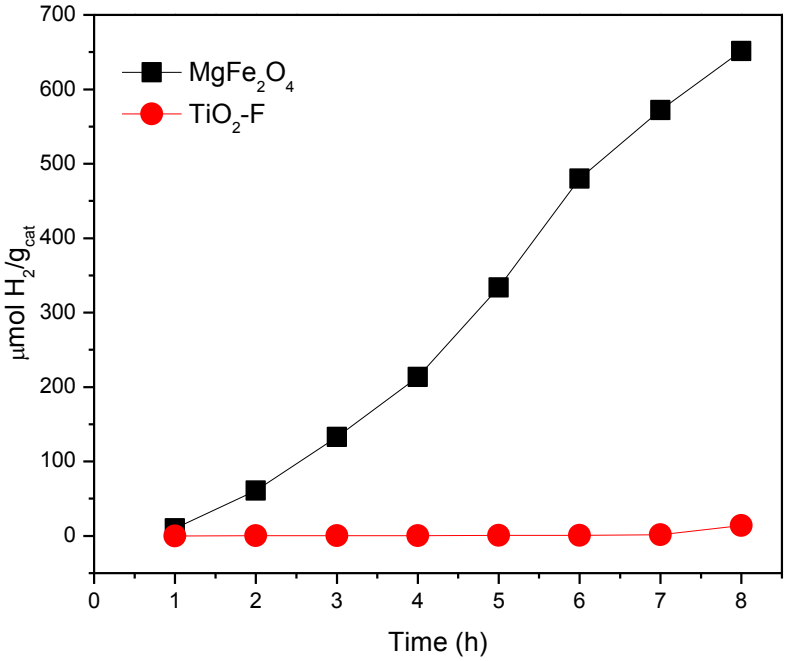

Fig 6. Photocatalytic evaluation for the production of H_2

4. Summary and perspectives

Magnesium ferrite was synthesized by coprecipitation and hydrothermal treatment, resulting in a mixture of phases ($MgFe_2O_4$ and Fe_2O_3), while TiO2-F sample was obtained by sol-gel assisted with hydrothermal treatment, reaching the pure anatase phase. Results obtained by diffuse reflectance UV-Vis spectroscopy showed the Eg value for the ferrite was located in the visible region, 2.07 eV (599nm). TEM results show particle sizes in the nanometer range in both cases, and also indicated a cubic morphology for $MgFe_2O_4$, while ellipsoidal particles for TiO2-F. The photocatalytic evaluation results for the H_2 production indicate a higher activity for the $MgFe_2O_4$ sample, with a maximum production of 650 $\mu molH_2/g_{cat}$ over a period of 8, while TiO_2-F only achieved a production of 15 $\mu molH_2/g_{cat}$. This is due to the fact that magnesium ferrite is able to be activated under the visible light range.

Acknowledgements

Finally, thanks to technicians Maria Teresa Chaparro, Enrique Torres, Luis de la Torre and Carlos Ornelas for their contributions to the of UV-Vis spectroscopy, BET area, X-ray diffraction and scanning electron microscopy results. As well as the Centro de Investigación en Materiales Avanzados S. C. for the support in the use of its infrastructure.

References

[1] Thammanoon Sreethawong, Yoshikazu Suzuki, Susumu Yoshikawa., Photocatalytic evolution of hydrogen over mesoporous TiO_2 supported NiO photocatalyst prepared by single-step sol–gel process with surfactant template. International Journal of Hydrogen Energy 30 (2005) 1053 – 1062

[2] BilgeYildiz∗, Mujid S. Kazimi., Efficiency of hydrogen production systems using alternative nuclear energy technologies. International Journal of Hydrogen Energy 31 (2006) 77 – 92

[3] Jum Suk Janga, Hyun Gyu Kimb, Pramod H. Borsea, Jae Sung Leea, Simultaneous hydrogen production and decomposition of H_2S dissolved in alkaline water over CdS.TiO_2 composite photocatalysts under visible light irradiation. International Journal of Hydrogen Energy 32 (2007) 4786 – 4791

[4] A. Kudo, Development photocatalyst materials for water splitting, International Journal of Hydrogen Energy 31 (2006) 197 – 202

[5] K. Domen, M. Hara, J.N. Kondo, T. Takata, A. Kudo, H. Kobayashi *et al.* New aspects of heterogeneous photocatalysts for water decomposition, Korean J Chem Eng, 18 (2001) 862–866.

[6] Kim, D.W. Hwang, J.S. Lee, An undoped, single phase oxide photocatalyst working under visible light J Am Chem Soc 126 (2004) 8912–8913

[7] H.G. Kim, P.H. Borse, W. Choi, J.S. Lee, Photocatalytic nanodiodes for visible light photocatalysis Angew Chem Int Ed, 44 (2005) 4585–4589.

[8] H. Zazoua, A. Boudjemaa, R. Chebout and K. Bachari, Enhanced photocatalytic hydrogen production under visible light over a material based on magnesium ferrite derived from layered double hydroxides (LDHs), Int. J. Energy Res. (2014)

[9] Erik Casbeer, Virender K. Sharma, Xiang-Zhong Li, Synthesis and photocatalytic activity of ferrites under visible light: A review, Separation and Purification Technology 87 (2012) 1–14

[10] Kullarni RG, Joshi HH, Comparison of magnetic properties of $MgFe_2O_4$ prepared by wet-chemical and ceramic methods, J Solid State Chem 64(2) (1986), 141

[11] Lakshman A, Rao KH, Mendiratta RG, Magnetic properties of In3+ and Cr3+ substituted Mg–Mn ferrites, J Magn Magn Mater 250 (2002), 92

[12] 0. Chhaya SD, Pandya MP, Chhantbar MC, Modi KB, Baldha GJ, Joshi HH, Study of substitution limit, structural, bulk magnetic and electrical properties of Ca^{2+} substituted magnesium ferrite, J Alloys Comp 377 (2004) 155.

[13] Verma S, Joy PA, Khollam YB, Potdar HS, Deshpande SB, Synthesis of nanosized $MgFe_2O_4$ powders by microwave hydrothermal method, Mater Lett (2004) 1092

[14] Oliver SA, Willey RJ, Hamdeh HH, Oliveri G, Busca G Scripta, Structure and magnetic properties magnesium ferrite fine powders**,** Metal Mater 33(10/11), (1995) 1695

[15] Basahel SN, El-Bellihi AA, Gabal M, Diefallah El-HM, Thermal decomposition of iron(III) oxalate-magnesium oxalate mixtures, Thermochim Acta 256(2) (1995) 339

[16] Patil KC, Gajapathy D, Pai Verneker VR., Low temperature cobaltite formation using mixed metal oxalate hydrazinate precursor Mater Res Bull 17 (1982) 29

[17] Rupard RG, Gallagher PK,The thermal-decomposition of coprecipitates and physical mixtures of magnesium-iron oxalates, Thermochim Acta 272 (1996) 11

[18] Sepelak V, Baabe D, Mienert D, Litterst FJ, Becker KD, Enhanced magnetisation in nanocrystalline high-energy milled $MgFe_2O_4$, Scripta Mater 48 (2003) 91

[19] Chen Q, Rondinone AJ, Chakoumakos BC, Zhang ZJ, Synthesis of superparamagnetic $MgFe_2O_4$ nanoparticles by coprecipitation. J Magn Magn Mater 194 (1999) 1

[20] O.-Bong Yanga, M. Alam Khana, Seong Ihl Woob Hydrothermally stabilized Fe(III) doped titania active under visible light for water splitting reaction international journal of hydrogen energy 33 (2008) 5345–5351**.**

[21] Bruno Clair, Shan-Shan Chang, Julien Ruelle, Jacques Beauchene, Francesco Di Renzo, Francxoise Quignard, Guang-Jie Zhao, Hiroyuki Yamamoto and Joseph Gril, Mesoporosity as a new parameter for understanding tensión stress generation in trees Journal of Experimental Botany Advance Access 12 (2009).

[22] Shuxi Dai, Yanqiang Wu, Toshio Sakai, Zuliang Du, Hideki Sakai, Masahiko Abe, Preparation of Highly Crystalline TiO_2 Nanostructures by Acid-assisted Hydrothermal Treatment of Hexagonal-structured Nanocrystalline Titania/Cetyltrimethyammonium Bromide Nanoskeleton, Nanoscale Res Lett (2010) 5:1829–1835.

XIV International Congress of the Mexican Hydrogen Society
Cancun, Mexico, 2014

$KNbO_3$ as Photocatalyst for Hydrogen Production

M. A. Rodríguez-Villa[1,2], A. López-Ortiz[1], M.Y. Luna-Porres[1], K. Aguilar-Collins[1], J. Silva-Aceves[2], R. Farías-Mancilla[2], J. Elizalde-Galindo[2], V. Collins-Martínez[1,*]

[1]Centro de Investigación en Materiales Avanzados S.C., Laboratorio Nacional de Nanotecnología, Depto. Materiales Nanoestructurados, Miguel de Cervantes 120, 31109 Chihuahua, Chih., México.
[2]Universidad Autónoma de Ciudad Juárez, Ave. Plutarco Elías Calles, Alfa, 32317, Ciudad Juárez, Chih. México
. Tel: +52 (614)439 11 29 *e mail: virginia.collins@cimav.edu.mx

ABSTRACT

Semiconductor photocatalytic water splitting to produce hydrogen from solar energy has been considered as one of the most important approaches in achieving an energy based sustainable development. A large number of semiconductor materials have been proposed as photocatalysts for water splitting to hydrogen. The pervoskite-structure compounds have attracted wide attention over the past half a century. $MNbO_3$ (M = Li, Na or K) is a pervoskite oxide with unique physical and chemical properties such as low density, high sound velocity, photorefractive effect and photoactivity. These materials have presented remarkable photocatalytic activity for water splitting and environmental purification. Moreover, potassium niobate ($KNbO_3$) submicro-crystals were prepared by a soft chemical method and characterized by powder X-ray diffraction, nitrogen adsorption–desorption, diffuse reflectance UV–visible spectroscopy, and scanning electron microscopy. The photocatalytic performance was evaluated toward H_2 generation from an aqueous methanol solution (2%Vol) under UV and Vis light using a 250 W mercurial lamp as an irradiation source. XRD results found that synthesized $KNbO_3$ presented an orthorhombic rhombohedral phase. Crystallite size was estimated using the XRD data and the Debye-Scherrer equation, reaching ~ 43.4 nm. From UV–visible spectroscopy it was found that $KNbO_3$ exhibited a band gap energy of 2.98 eV. The BET surface area of the synthesized sample was 1.80 m^2/g. Photocatalytic activity of potassium niobate presented a hydrogen production of 350 µmol/$g_{catalyst}$ using a reactor loading of 200 mg of photocatalyst under a 5 h irradiation time. Results from this study indicate that $KNbO_3$ perovskite is potentially applicable for the production of H_2 through photocatalytic water splitting.

Keywords: $KNbO_3$, Hydrogen production, Photocatalysis.

1. Introduction

The lack of energy resources and increasing pollution associated with energy production by conventional pathways, stimulated the search for cleaner, cheaper and more efficient energy technologies [1]. In recent years the production of hydrogen has received much attention due to its potential application as a clean energy source. Hydrogen can be obtained from renewable resources and produces only water vapor during combustion [2, 3].

Currently, hydrogen is mainly produced by reforming of oil and natural gas at high temperatures [4-7]. The photocatalytic splitting of the water molecule is a promising technology to produce "clean" hydrogen and this process is inexpensive compared to thermochemical or photobiological process [8]. The perovskite structure (ABO_3 where A is a metal, B is a second metal and O is oxygen) is one of the most studied structures among photocatalysts, due to their good photocatalytic as well as physicochemical properties [9-13].

Various compounds photocatalytic such as niobates, tantalates and titanates, have been reported towards the production of hydrogen by the dissociation of the water molecule with reasonable activity [14, 15]. The main objective of this study is to evaluate the photocatalytic activity of commercial and synthesized potassium niobate (KN) samples from three different synthesis methods. The study took place through: (1) the synthesis of KN nanoparticles using three synthesis methodologies; (2) the characterization of the commercial and KN synthesized powders and the; (3) the evaluation of photocatalytic activities of all KN samples.

2. Experimental

2.1. Catalysts Synthesis

$KNbO_3$ nanoparticles were prepared a by soft chemical method, using stoichiometric amounts of $C_4H_4NNbO_9 \cdot xH_2O$ (Aldrich) and KNO_3 (Fermont). Three different synthesis methods were used to prepare powders KN, these methodologies are generally shown in Figures 1 to 3. Furthermore, Table 1 presents the nomenclature used to identify the KN samples studied.

Table 1. Identification KN samples.

Nomenclature	Synthesis Method
KN-c	Commercial sample (Alfa Aesar)
KN-1	Based on the methodology used by Bhattacharyya and Tyagi 2009 [16]
KN-2	Based on the precipitation method employed by Cabrera Lopez et al. 2009 [17]
KN-3	Based on the combination of the methods used to synthesize KN-1 and KN -2.

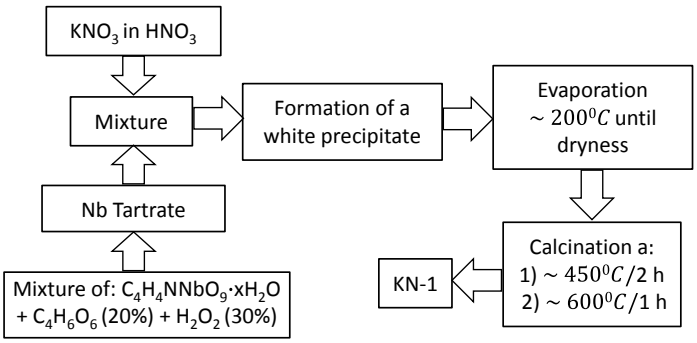

Fig 1. General methodology for the synthesis of KN-1 nanoparticles.

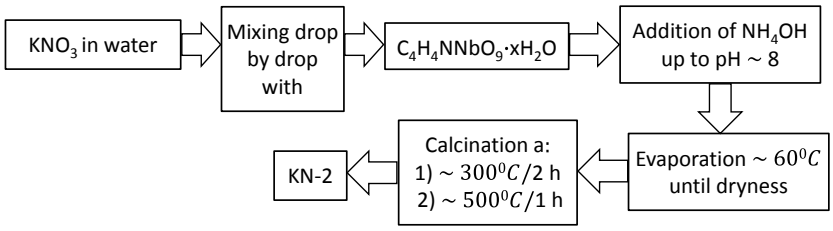

Fig 2. General methodology for the synthesis of KN-2 nanoparticles

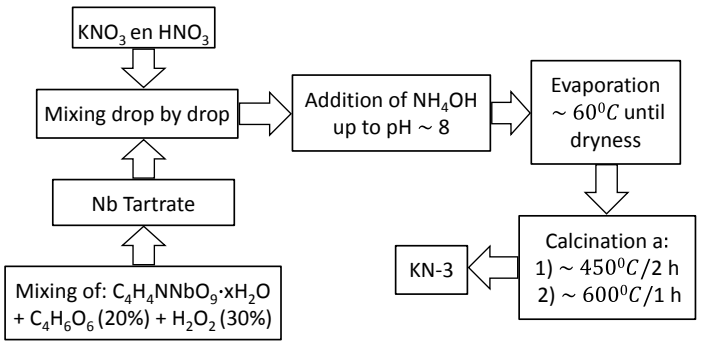

Fig 3. General methodology for the synthesis of KN-3 nanoparticles

The general synthesis methodology of Figure 3 is based on the combination of the methodologies employed for KN-1 [16] and KN-2 [17]. Based on this, the mixed solutions of KNO_3 and tartrate aqueous solution at basic pH were used; besides controlling the addition of nitrate at 0.5 mL/min in aqueous tartaric solution.

2.2. Catalysts Characterization

The phase composition and crystallinity of the sample powders were analyzed by X-ray diffraction in a Panalytical brand, model X'Pert PRO diffractometer with CuKα radiation. Samples morphology were evaluated by field emission scanning electron microscopy in a SEM, JSM-7401F. The bandgap energy of the sample powders were obtained by the UV-Vis diffuse reflectance spectrum using a UV-Vis

spectrometer (Lambda 10, Perkin Elmer) equipped with integrating sphere (Labsphere RSA-PE-20). The specific surface area was determined using the Brunauer-Emmett and Teller (BET) method (Micromeretics Atosorb). The characterization was performed on the synthesized samples: KN-1, KN-2 and KN-3 and commercial: KN-c (see Table 1).

2.3. Catalysts Activity Evaluation

0.2 g of each KN Photocatalyst was evaluated by splitting of the water molecule, using a 250W mercurial lamp and adding methanol to the water reactor system as sacrificial agent (2% vol). The reaction was monitored by gas chromatography using a GC Perkin Elmer Clarus 500. The system setup employed for carrying out the photocatalytic evaluation of the materials is composed by a photoreactor, artificial lighting and GC analysis with a PC data collection. In order to monitor the photocatalytic reaction, samples were taken at regular time intervals using a 1ml syringe for gases through a septum located at the upper section of the photoreactor. A sample under darkness was taken as the initial concentration and then the sampling was took place every hour up to a total of 10 hours of irradiation.

3. Results and discussion

3.1. X-Ray Diffraction

Figure 2 presents XRD diffractograms of the four catalysts in study. Form this Figure it can be seen that the only crystalline phase present in all samples is that one corresponding to the pure $KNbO_3$ phase. With the X-ray patterns information and applying Scherrer's equation the crystallite size of the powders was calculated. The crystallite size of synthesized catalyst was smaller than the commercial catalyst, with values of: 39.3 nm, 48.6 nm, 43.4 nm and 91.7 nm corresponding to KN-1, KN-2, KN-3 and KN-c, respectively.

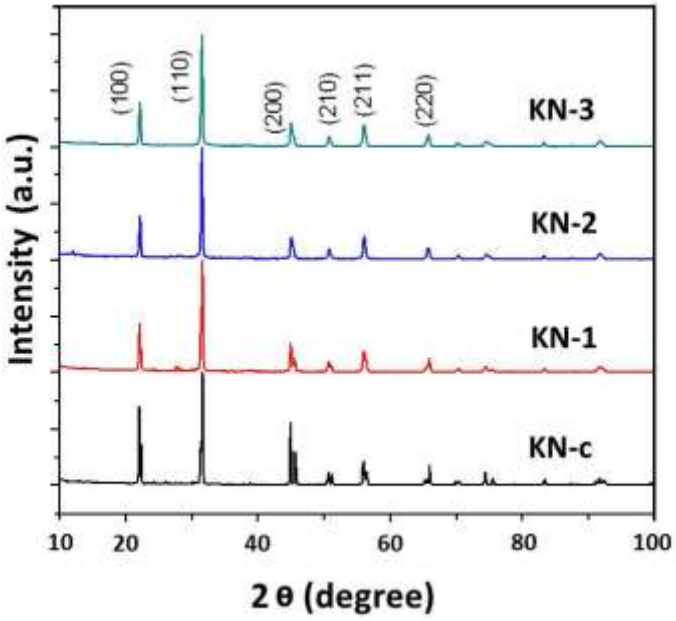

Fig 2. XRD diffractograms of the commercial and synthesized KN powders.

Furthermore, XRD diffractograms of the different synthesized KN samples presented in Figure 2 are similar to those obtained by some other authors such as Shi et al. 2012, Liu et al. 2007, Kinoshita et al. 2012 and Wang et al. 2013 [18-21].

3.2. Morphology and specific surface area

During the sample preparation for SEM analysis, the catalysts particles were previously dissolved in isopropanol and dispersed using an ultrasound machine. Subsequently the catalysts were deposited onto a silica sample holder.

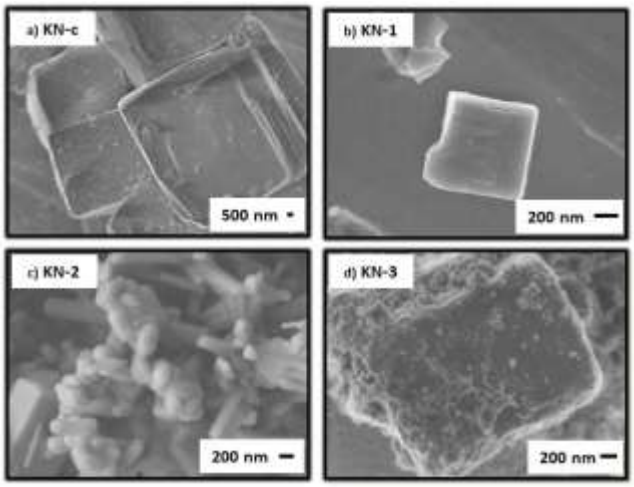

Fig 3. SEM images of the of commercial and synthesized KN catalysts.

Figure 3 shows SEM images of commercial and synthesized KN catalysts. From this Figure It can be seen that the catalysts present a similar morphology, except for sample KN-2 (see Figure 3c) with tubular shape and particles with a diameter of approximately 200 nm. Moreover, the KN-1 and KN-c catalyst (see Figure 3a and 3b) exhibit a particle diameter of 600 nm and 8 µm, respectively. However, catalyst KN-3 (see Figure 3d) involves clusters of small particles with approximate 150 nm, while this is the catalyst having the smallest particle size, compared to the other studied catalysts. The difference in particle size KN synthesized catalysts, can be attributed to the employed synthesis methodology.

Liu et al. 2007 [20] synthesized KN by hydrothermal synthesis and obtained a particle size in the range of 100 to 150 nm, similar to the one obtained in this study for KN-3 (without the presence of agglomerates). In another study Kinoshita et al. 2012 [21] conducted KN synthesis by the solid state technique and similar morphologies to KN-3 were obtained (see Figure 3d), however larger particle sizes (~20 um) for KN samples were produced in this study. Furthermore, using a hydrothermal synthesis of KN Yan et al. 2007 [4] reported similar size and morphology to those obtained in KN-1 sample.

Moreover, the average values of the BET surface area obtained for KN-c, KN-1, KN-2 and KN-3 were 0.47, 0.5, 4.6 and 1.8 m^2g^{-1}, respectively.

3.3. UV-Vis Spectroscopy

The optical properties of the KN nanoparticles were measured through the UV/Vis diffuse reflectance absorption spectrum and these are shown in Figure 4.

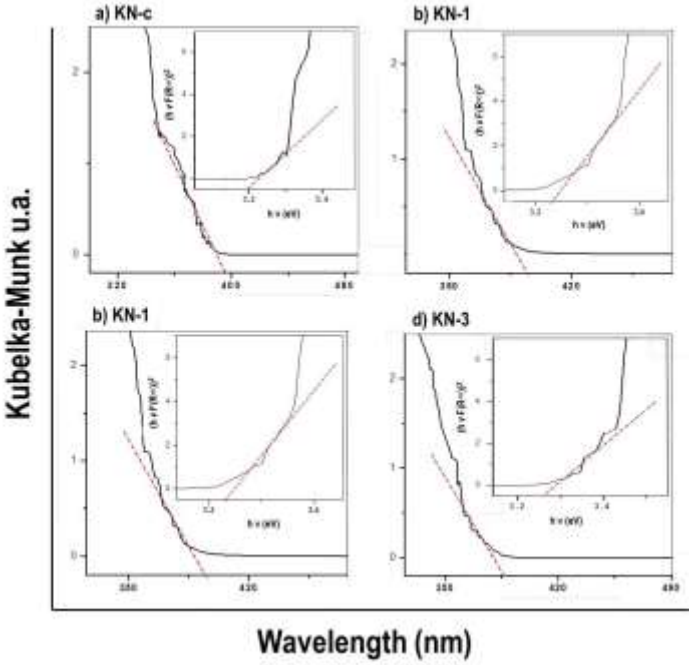

Fig 4. UV-Vis diffuse reflectance spectra and determination of the band gap energy for the different commercial and synthesized KN samples.

UV/Vis diffuse reflectance spectra for the KN powders were converted in terms of absorption using (F (R)) function of Kubelka-Munk to determine in which region of the visible light the material is located; and the forbidden band width. Niobates powders show strong absorption in the visible light region and the optical absorption peaks were very similar to each other (see Figures 4a to 4d), while these were located around 400 nm. Furthermore, the KN bandgap energy was found around 3.2 eV (see Figure 4), with spectra similar to each other (see Figures 4a to 4d). The small differences among the values obtained from KN powders, may be due to the difference in crystallite sizes.

3.4. Photocatalytic Activity

The photocatalytic activity of the commercial and synthesized KN nanoparticles were evaluated through the gas hydrogen production. Figure 5 shows the performance of the photocatalytic activity of the KN catalysts during an irradiation time of 6 h.

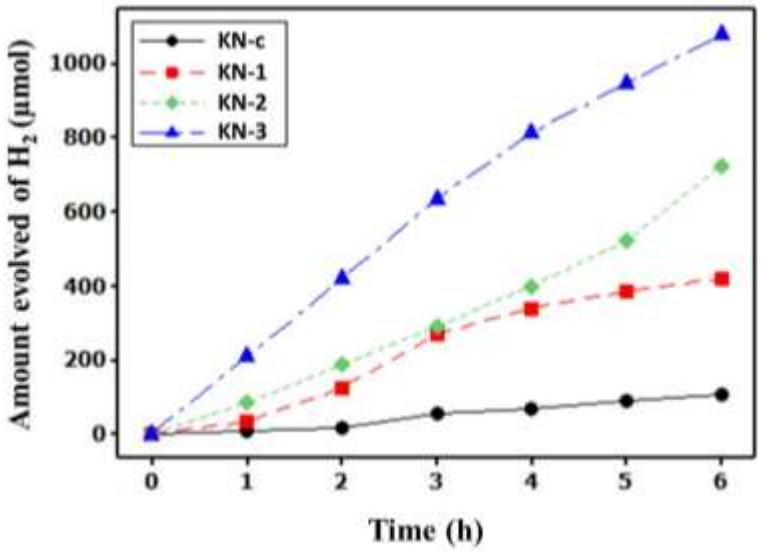

Fig 5. Photocatalytic H_2 production under conditions of visible light irradiation for KN samples.

Table 2 shows a summary of the KN powders photocatalytic activity results carried out under study. The results obtained in a period of 6 h of irradiation (Table 2) show that KN-3 presents a remarkable deference in H_2 production over other synthesized powders in a magnitude of 11 times more than the KN-c powder.

Table 2. Results Summary for the characterization and photocatalytic activity of the KN catalysts.

Catalyst	Surface Area ($m^2 g^{-1}$)	Band Gap (eV)	Crystal (nm)	UV-Vis (nm)	Photocatalytic Activity * (µmol)
KN-c	0.47	3.19	91.7	396	106.54
KN-1	0.50	3.23	39.3	427	421.70
KN-2	1.13	3.27	48.6	412	727.32
KN-3	1.80	3.26	43.4	409	1081.14

***** Photocatalytic activity obtained at 6 h of irradiation and using 0.2 g of photocatalyst.

The value of the band gap energy for different KN samples in this investigation was found to be similar to those reported by Ding et al. 2008, Yan et al. 2013 and Liu et al. 2007 [4, 10, 20]. Also, in order to make a comparison of the H_2 production from this study with other studies in terms of the KN photocatalytic activity, it was found that: Liu et al. 2007 [20] obtained a lower H_2 production compared to the production obtained by using the synthesized catalysts in the present research (see Table 2); Ding et al. 2009 [10] reported twice the H_2 produced as compared to KN-3, but using a two-lamp irradiation intensity than that used in this study and 14 times the same sacrificial agent and Yan et al. 2013 [4] obtained a similar production of H_2, although using Pt as co-catalyst.

4. Summary and perspectives

KN nanometric powders were obtained using different synthesis methods, which showed values of bandgap energies within the spectrum of visible light and showed photocatalytic properties for the dissociation of the water molecule. The KN-3 synthesized material showed the highest hydrogen production, compared to the KN-c (commercial) and synthesized KN-1 and KN-2 samples. Based on the results obtained in this study the photocatalytic decomposition of water may be a promising alternative for the production of hydrogen using as niobates materials as water splitting photocatalysts.

Acknowledgements

The authors wish to thank all the support provided by the Center for Research in Advanced Materials (CIMAV) and the Autonomous University of Ciudad Juarez (UACJ). The authors also give thanks to Eng. Jesús Salinas, MC Karla Campos, Eng. Luis de la Torre, Eng. Enrique Torres and MSc. Wilber Antúnez for sample analysis.

References

[1] A. Borgschulte et al., Journal of Catalysis 235, 353 (2005).
[2] A. Kudo, Catalysis Surveys from Asia 7, 31 (2003).
[3] D. P. Harrison, Department of Chemical Engineering, Louisiana State University, Baton Rouge, Louisiana 70803, 1 (2004).
[4] L. Yan et al., International Journal of Hydrogen Energy 38, 3554 (2013).
[5] A. Kudo, and Y. Miseki, Chemical Society Reviews 38, 253 (2009).
[6] F. E. Osterloh, Chemistry of Materials 20, 35 (2007).
[7] J. Yu, and J. Ran, Energy & Environmental Science 4, 1364 (2011).
[8] Ferritas Nanoestructuradas de Mn y Co como Fotocatalizadores para Producción de H2 a partir de la Molécula del Agua y Luz Visible, Ortega-López Mercedes Yudith, Salinas-Gutiérrez Jesús Manuel, López-Ortiz Alejandro, Collins-Martínez Virginia, 1st latin-American Congress of Photocatalysis (LACP 2012). Photocatalysis: From the treatment of emerging contaminants to energy conversion, September 25-28, Morelia Michoacán, México.
[9] S. N. Tijare et al., International Journal of Hydrogen Energy 37, 10451 (2010).
[10] Q. P. Ding et al., the Journal of Physical Chemistry C 112, 18846 (2008).
[11] L. M. Torres-Martínez et al., Catalysis Communications 12, 268 (2010).
[12] J. Zhu, and M. Zäch, Current Opinion in Colloid & Interface Science 14, 260 (2009).
[13] J. Shi, and L. Guo, Progress in Natural Science: Materials International 22, 592 (2012).
[14] C. Hu, and H. Teng, Journal of Catalysis 272, 1 (2010).
[15] H. Kato, and A. Kudo, Catalysis Today 78, 561 (2003).
[16] A. Zhai et al., Transactions of Nonferrous Metals Society of China 22, 943.
[17] J. J. Cabrera López, J. L. Narváez, and J. E. Rodríguez Páez, Revista Facultad de Ingeniería Universidad de Antioquia 47, 20 (2009).
[18] R. Wang et al., Chemical Engineering Journal 226, 123 (2013).
[19] H. Shi, and Z. Zou, Journal of Physics and Chemistry of Solids 73, 788 (2012).
[20] J. W. Liu et al., International Journal of Hydrogen Energy 32, 2269 (2007).
[21] T. Kinoshita et al., Ceramics International 38, 1897 (2012).

Sonochemical synthesis of Pt/CNT/TiO_2 anode catalyst for direct methanol fuel cells

Z. I. Bedolla-Valdez[1,*], Y. Verde[2], Y. Gochi-Ponce[3], M. T. Oropeza-Guzmán[4], G. Alonso-Núñez[1]

[1]Centro de Nanociencias y Nanotecnología-UNAM, Km. 107 carretera Tijuana-Ensenada, Ensenada, B. C., México, 22800.
[2]Instituto Tecnológico de Cancún, Av. Kabah Km. 3, Cancún, Q. Roo, México, 77500.
[3]Instituto Tecnológico de Oaxaca, Av. Ing. Víctor Bravo Ahuja 125, México, 68030.
[4]Centro de Investigaciones y Desarrollo Tecnológico en Electroquímica, Km. 126.4 carretera Tijuana-Tecate, Tijuana, B.C., México, 22253
[*]Tel: +526461750650 ext. 450; e-mail: zairabe@cnyn.unam.mx

ABSTRACT

Pt/CNT/TiO_2 anode catalyst was prepared by sonochemical method using a high-intensity probe. Multi-walled carbon nanotubes (CNT) was obtained by spray pyrolysis method, purified and then characterized by Raman spectroscopy. The graphitization order of CNT was evaluated by I_D/I_G ratio, the value obtained was 0.39. The CNT/TiO_2 system was synthesized at controlled temperature under ultrasonic conditions. Finally, about 7 wt.% of Pt nanoparticles were incorporated to CNT/TiO_2 using $NaBH_4$ as reducing agent. Pt/CNT and Pt/TiO_2 catalysts were prepared as reference samples. The chemical composition of the systems were determined by ICP and EDS analysis. Structural properties and specific surface area of anode catalysts were examined by XRD and nitrogen adsorption by BET method, respectively. The electrochemical study was performed by cyclic voltammetry in a three-electrode half-cell at room temperature. Pt/CNT/TiO_2 anode catalyst was successfully synthesized by sonochemical method without heat treatment, surfactants or additives. The synthesized catalyst was obtained with a narrow pore size distribution and specific surface area of 193 $m^2\ g^{-1}$. The results of cyclic voltammetry tests for methanol oxidation suggest that the incorporation of TiO_2 improves the catalyst tolerance to carbonaceous species. The Pt/CNT/TiO_2 anode catalyst exhibited better oxidation of methanol to carbon dioxide than Pt/CNT.

Keywords: Carbon nanotubes; Titanium dioxide; Methanol oxidation

1. Introduction

Direct methanol fuel cell (DMFC) is being widely studied in order to satisfy the increasing demand of power systems of portable electronic devices [1]. However, the main obstacles for DMFC commercialization are the high cost of Pt-based electrocatalyst and the sluggish kinetic of methanol electro-oxidation, because of the Pt poisoning surface by CO-like intermediates produced during methanol electro-oxidation. To solve this problem, Pt alloys have been extensively investigated to enhance the catalytic activity or prevent the poisoning problems [2, 3]. Pt-Ru alloy is considered the benchmark anode catalyst for DMFC. The presence of Ru in the catalyst promotes the oxidation of CO by a bi-functional mechanism [4]. Nevertheless, the limited supply and high cost of Ru prevent its use on commercial scale.

The surface structure, electronic properties and catalytic performance of electrocatalysts are related to the preparation methods of the support. Typically, carbon nanotubes (CNT) are used as promising supports for DMFC due to their good electrical conductivity [5], however, the corrosion of carbon support under the harsh reaction conditions would lead to quick loss catalytic activity, and hence the reduction of fuel cell life [6]. In general, the requirements of support materials of Pt-based electrocatalyst are a high surface area to good dispersion of metal loading, good electrical conductivity to facilitate electron transport during electrochemical reaction, mesoporous structure in order to maximize the triple-phase boundary and high corrosion resistance. Recent researches have been reported the use of metal oxides as support for DMFC [7-10], these studies have demonstrated that the incorporation of oxide nanoparticles can enhance the durability and catalytic activity of the electrocatalyst, and also their corrosion resistance. Among many metal oxides (MO), titanium oxide has been attractive as support because of its stability in fuel cell operation conditions, low cost, nontoxicity and commercial availability.

In order to obtain electrocatalytic stability, high CO tolerance and good electrical conductivity, we prepared the Pt/CNT/TiO_2 electrocatalyst by sonochemical method. On the other hand, Pt/CNT and Pt/TiO_2 were prepared as reference samples. Selected materials were characterized by X-ray diffraction (XRD), Raman spectroscopy, Inductively Coupled Plasma (ICP), Energy Dispersive Spectroscopy (EDS) and nitrogen adsorption by BET method. The CO tolerance of Pt/CNT/TiO_2 electrocatalyst due to TiO_2 presence was analyzed by Cyclic Voltammetry (CV) test.

2. Experimental

2.1 Carbon nanotubes synthesis

Multi-walled carbon nanotubes (CNT) were synthesized in a modified spray pyrolysis system, previous reported by Aguilar *et al.* [11]. In our synthesis system an additional valve was added to avoid the access of solution mist inside Vycor tubing (9 mm outer diameter) during the heating and cooling processes. The Vycor tubing was heated into a tubular furnace (Lindberg Blue) up to 925 °C under argon (Infra, 99.999%) flow at a rate of 0.2 L min^{-1}. Once the temperature was stabilized, the argon flow was adjusted at a rate of 4 L min^{-1}. Immediately, a solution with toluene (Sigma Aldrich, 99.8%) and 2.5 wt.% of ferrocene (SigmaAldrich, 98%) was sprayed inside Vycor tubing. Thereafter, the system was cooled up to room temperature under the argon flow at a rate of 0.2 L min^{-1}.

The synthesized CNT were mechanically removed from the Vycor tubing and were purified with nitric acid (Sigma Aldrich, 70%) in a reflux system during 12 h at 90 °C. After that, the CNT were washed with deionized water (Millipore, 18 MΩ) and dried at 100 °C for 12 h.

2.2. Preparation of CNT/TiO_2 and Pt/CNT/TiO_2 catalyst

CNT/TiO_2 and Pt/CNT/TiO_2 were synthesized by sonochemical method employing a direct immersion high-intensity ultrasonic titanium probe with 19 mm diameter (Sonics and Materials, VCX750, 20 kHz).

Sonochemical preparation of CNT/TiO_2 with mesoporous and bicrystalline TiO_2 framework was synthesized at controlled temperature by means of thermocouple attached to VCX750 equipment.

The CNT/TiO_2 was prepared by hydrolysis of titanium isoproxide (TIP) in the presence of isopropyl alcohol and water. The volume ratio of alcohol:water remains constant in 1:2.

Acid treated CNT (75 mg) were dispersed in deionized water during 30 min using a direct immersion titanium probe in the sonication glass vessel (3 s on, 1 s off, amplitude 40%).Meanwhile, 3 mL of TIP (Sigma Aldrich, 97%) were dissolved in isopropyl alcohol (Sigma Aldrich, 99.5%) under magnetic stirring.

During ultrasonic irradiation, the resulting TIP solution was injected into CNT suspension. The sonication was continued for 3 h, in order to complete the crystallization of TiO_2. Once the sonochemical synthesis ended, the mixed solution was aged 10 h. Afterwards, the precipitate was dried in a magnetic mixer-heater at 85 °C. The drying process was performed until the product had dry appearance.

Pt/CNT/TiO_2 composite was synthesized by reduction method under ultrasonic irradiation. The metal loading of the catalyst was calculated to obtain 10 wt.% of Pt. In an ultrasonic bath equipment (Branson, 2510) 90 mg of CNT/TiO_2 were dispersed in 10 mL of isopropyl alcohol during 1 h. Subsequently, a direct immersion high-intensity probe was placed into the solution glass vessel. After, metal precursor solution (H_2PtCl_6, Sigma Aldrich, 99.999%) was added to the mixture, followed by high-intensity sonication for 30 min. To reduce the Pt precursor, 19.4 mg of $NaBH_4$ (Sigma Aldrich, 99%) was added into the solution. The sonication was continued for 30 min. The black precipitate was filtered and washed several times with isopropyl alcohol and then dried under N_2 atmosphere at 120 °C for 3 h.

TiO_2, Pt/TiO_2 and Pt/CNT were prepared as samples references following the procedures previously described.

2.3 Characterization methods

The elemental composition of synthesized electrocatalyst was investigated by dispersive X-ray spectroscopy (EDS) in a JEOL JSM-5300 microscope. In addition, the amount of platinum and titanium in the electrocatalyst was determined by inductively couple plasma-atomic emission spectrometry (ICP-AES) in a Varian Liberty 110 spectrometer. Powder XRD diffraction were performed in a Philips X'Pert MPD diffractometer using Cu K_α (λ=0.154 nm) radiation source. The 2θ angular regions between 20° and 60° were analyzed. Selected samples were analyzed by Raman spectroscopy in a HORIBA Jovin Yvon X'ploRA microscope applying a laser source with wavelength at 532 nm. The porosity of materials was evaluated using a Micromeritics TriStar II 3020. The specific surface area (S_{BET}) of synthesized materials

was calculated by Brunauer-Emmet-Teller (BET) method. Prior to measurement, the samples were outgassed under N_2 flow at 120 °C for 3 h.

The electrochemical experiments were made in a conventional three-electrode half-cell at 25 °C in 0.5 M H_2SO_4 and 0.5 M CH_3OH electrolyte. Glassy carbon electrode (0.3 cm diameter) was used as working electrode (WE); Ag/AgCl [Sat NaCl] and Pt coiled were used as reference and counter electrode, respectively. Inks were prepared with 10 mg of electrocatalyst ultrasonic dispersed in 1 mL of ethanol and 60 µL of a solution 3:1 of Nafion (Sigma Aldrich, 5% in aliphatic alcohols) and deionized water. 10 µL of electrocatalyst ink were placed on the WE surface. The three electrodes were connected to an AUTOLAB PGSTAT302N potentiostat, subsequently, Cyclic Voltammetry (CV) tests were plotted by performing thirty cycles at a scan rate of 0.02 V s^{-1}. Prior to each test, the electrolyte was purged with argon during 30 min.

3. Results and discussion

The crystalline structure of selected samples was analyzed by XRD. Fig. 1a shows the XRD patterns of TiO_2, CNT/TiO_2 and Pt/CNT/TiO_2. In all patterns the presence of anatase (JCPDS, no. 21-1272) and brookite (JCPDS, no. 29-1360) structures are determined. The XRD patters of TiO_2 and CNT/TiO_2 are similar, indicating that the CNT incorporation during the catalyst synthesis did no modify the formation of TiO_2. Pt/CNT/TiO_2 pattern exhibited two Pt diffraction peaks at 39.8° and 46.2° (2θ), demonstrating that Pt is in the metallic form. In CNT/TiO_2 and Pt/CNT/TiO_2 patterns there are no (002) the peak of graphite 2H associated with CNT about at 26° (2θ), due to the CNT peak overlaps with the (101) peak of anatase phase.

The presence of CNT in the system was confirmed by Raman spectroscopy. Fig. 1b shows the Raman spectra of CNT and CNT/TiO_2. The spectra exhibit two characteristic bands at approximately 1572 and 1342 cm^{-1}, corresponding to first order G mode (E_{2g} symmetry) assigned to regular sp^2 graphitic network and D mode (A_{1g} symmetry) corresponds to sp^3 hybridized carbons, indicating the disorder and defects of graphite on CNT surface. The I_D/I_G ratio was used as graphitization degree indicator of CNT [12]. For CNT the I_D/I_G ratio was calculated as 0.39 whereas for CNT/TiO_2 it is equal to 0.48. This indicates that the graphitic order of CNT in the system CNT/TiO_2 is reduced. This effect may be attributed to the ultrasonic treatment during the synthesis and the interaction between CNT and TiO_2. Although the graphitic order was reduced, the crystalline nature of CNT was conserved.

The EDS spectra of CNT/TiO_2 and Pt/CNT/TiO_2 are presented in Fig. 1c, where the presence of C, Ti and Pt is confirmed. In the spectrum of Pt/CNT/TiO_2 also Na is observed as impurity from borohydride reduction method.

The Pt and Ti loadings determined by ICP-AES are presented in Table 1. The synthesis was calculated to obtain 10 wt.% of Pt loading. However, the achieve metal loading was about 7 wt.%. Although the Pt loading was lower than the theoretically calculated, all samples had similar values of metal loading. It is expected that if the amount of $NaBH_4$ as reducing agent increases, more metal nanoparticles will be deposited on CNT surface.

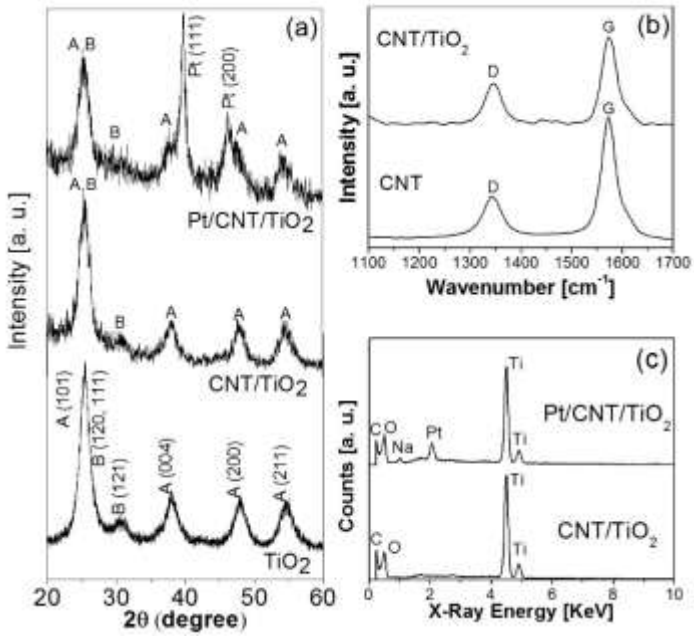

Fig 1. (a) XRD diffraction patterns of TiO_2, CNT/TiO_2 and $Pt/CNT/TiO_2$. (b) Raman spectra of CNT with and without TiO_2. (c) EDS spectrum of CNT/TiO_2 and $Pt/CNT/TiO_2$.

On the other hand, the specific surface area (S_{BET}) of prepared materials is presented in Table 1. Where is observed that $Pt/CNT/TiO_2$ system has larger surface area than Pt/CNT, this fact can improve the dispersion of Pt and enhance the anode catalyst properties.

Table 1. Metal loading of catalysts and specific surface area (S_{BET}) of synthesized materials.

Materials label	Weight % Pt	Weight % Ti	S_{BET} [$m^2\ g^{-1}$]
CNT	-----	-----	42.5 ±6
Pt/CNT	7.1	-----	35.0±6
TiO_2	-----	-----	261±6
CNT/TiO_2	-----	-----	233±6
Pt/TiO_2	7.4	36.2	195±6
$Pt/CNT/TiO_2$	6.9	33.7	193±6

Nitrogen adsorption/desorption isotherms of TiO_2, CNT/TiO_2 and $Pt/CNT/TiO_2$ and inset pore size distribution of TiO_2 and CNT/TiO_2 are presented in Fig. 2. The isotherms for all samples are type IV, characteristics of mesoporous materials. Also, the materials exhibit type H3 hysteresis-loop.

The type H3 loop does not present limiting adsorption at high P/P_0, it is observed with aggregates of plate-like particles to give rise to slit-shaped pores [13].

As show in the insets of Fig. 2a and 2b, TiO_2 and CNT/TiO_2 samples have a narrow pore size distribution with average pore diameter of 4.2 and 5.4 nm, respectively.

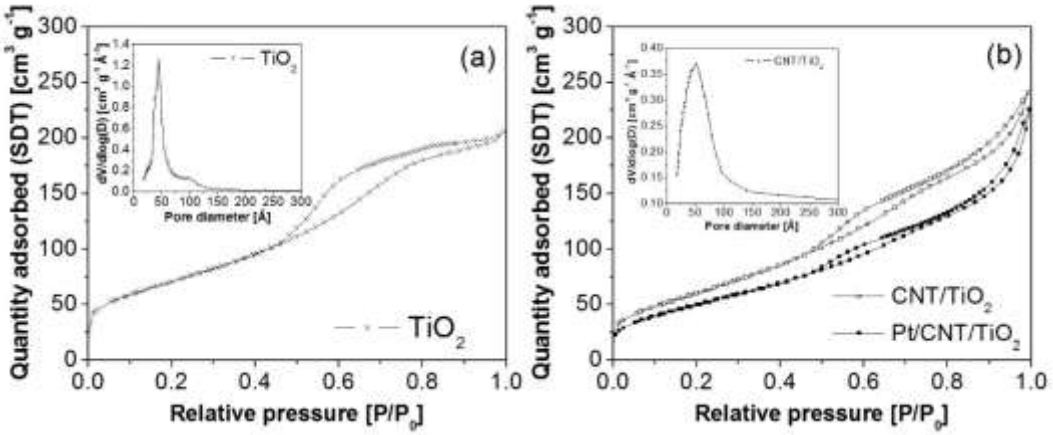

Fig. 2. Nitrogen adsorption/desorption isotherms of (a) TiO_2, (b) CNT/TiO_2 and $Pt/CNT/TiO_2$. The insets shows pore size distribution calculated by Barret-Joyner-Halenda (BJH) method.

In order to investigate the effect of TiO_2 on methanol oxidation, the CV tests of electrocatalysts Pt/CNT, $Pt/CNT/TiO_2$ and $Pt/CNT/TiO_2$ are compared in Fig. 3. The voltammograms of all materials have similar shape, in agreement with previous reports [7, 8]. There are two main anodic peaks in the forward (I_f) and backward (I_b) scans; I_f is associated to methanol oxidation and I_b is related with the oxidation of CO-like intermediates on the pathways of methanol oxidation, such as formaldehyde (HCHO), formic acid (HCOOH), formate ($HCOO^-$) and CO species.

To benchmark CO tolerance performance, current densities I_f/I_b ratio has been used as qualitative indicator of poisoning catalyst tolerance. Lower I_f/I_b value indicates poor methanol oxidation and excessive accumulation of carbonaceous species on catalyst surface. Therefore, a higher I_f/I_b value is indicative of improved CO tolerance [7, 8]. The I_f/I_b ratio was estimated to be 0.98, 1.15 and 1.49 for Pt/CNT, Pt/TiO_2 and $Pt/CNT/TiO_2$, respectively.

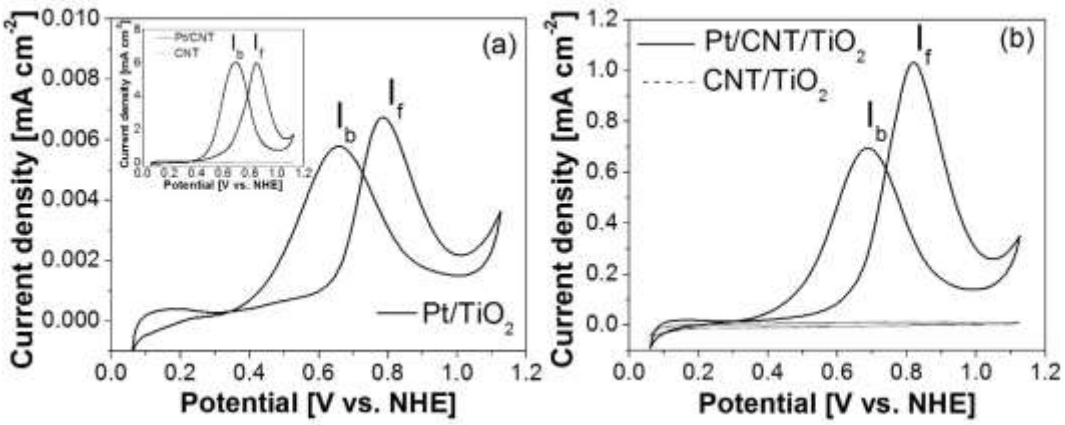

Fig. 3. Cyclic voltammograms of methanol oxidation on (a) Pt/TiO_2, (b) $Pt/CNT/TiO_2$; inset Pt/CNT. The CV test were performed in a mixture of 0.5 M H_2SO_4 and 0.5 M CH_3OH at scan rate of 0.02 Vs^{-1}, thirty cycle is reported.

These results suggest that the materials prepared with TiO_2 have less carbonaceous accumulation, indicating better oxidation of methanol to carbon dioxide and therefore more tolerant towards CO poisoning. $Pt/CNT/TiO_2$ must be activated the H_2O in the electrolyte to form hydroxide species on TiO_2 surface and oxidize CO poisoning species, accordingly to bi-functional methanol oxidation mechanism between Pt and Ru [4, 10].

4. Summary and perspectives

The anodic catalyst $Pt/CNT/TiO_2$ was successfully synthesized without heat treatments, surfactants or additives. The synthesized electrocatalyst was obtained with a narrow pore size distribution and the specific surface area was 193 $m^2\ g^{-1}$. In the other hand, the $Pt/CNT/TiO_2$ showed better methanol oxidation and CO tolerance than Pt/CNT. This effect is directly related with the TiO_2 presence in the electrocatalytic system and clearly observed in the cyclic voltammograms. The inclusion of TiO_2 in electrocatalytic systems for methanol oxidation may be provide some insights to improve the electrocatalysts CO tolerance.

Acknowledgements

This work was supported by CONACyT No. 174689 and PAPIIT IN104714 projects. The authors acknowledge to Eric Flores, Eloisa Aparicio, Israel Gradilla and Mario Vega for technical support.

References

[1] S. Sundarrajan, S. I. Allakhverdiev, S. Ramakrishna, Progress and perspectives in micro direct methanol fuel cell. International Journal of Hydrogen Energy 2012; 37: 8765-8786.

[2] L. Li, Y. Xing, Mathanol Electro-Oxidation on Pt-Ru Alloy Nanoparticles Supported on Carbon Nanotubes. Energies 2009; 2: 789-804.

[3] E. A. Franceschini, M. M. Bruno, F. J. Williams, F. A. Viva, H. R. Corti, High-Activity Mesoporous Pt/Ru Catalyst for Methanol Oxidation. Applied Materials & Interfaces 2013; 5: 10437-10444.

[4] C. Roth, N. Benker, R. Theissmann, R. J. Nichols, D. J. Schiffrin. Bifunctional electrocatalysis in Pt-Ru nanoparticle systems. Langmuir 2008; 24: 2191-2199.

[5] S. Sharma, B. G. Pollet, Support materials for PEMFC and DMFC electrocatalysts-A review.J. Power Sources 2012; 208: 96-119.

[6] R. Borup, J. Meyers, B. Pivovar, Y. Seung, R. Mukundan, N. Garland, D. Myers, M. Wilson, F. Garzon, D. Wood, P. Zelenay, K. More, K. Stroh, T. Zawodzinski, J. Boncella, J. E. McGrath, M. Inaba, K. Miaytake, M. hori, K. Ota, Z. Ogumi, S. Miyata, A. Nishikata, Z. Siroma, Y. Uchimoto, K. Yasuda, K. Kimijima, N. Iwashita, Scientific Aspects of Polymer Electrolyte Fuel Cell Durability and Degradation. Chemical Reviews 2007; 107: 3904-3951.

[7] B. Yu Xia, S. Ding, H. Bin wu, X. Wang, X. Wen, Hierarchically structure Pt/CNT@TiO_2 nanocatalysts with ultrahigh stability for low-temperature fuel cells. RSC Advances 2012; 2: 792-796.

[8] H. Song, X. Qiu, F. Li, Effect of heat treatment on the performance of TiO_2-Pt/CNT catalysts for methanol electro-oxidation. Electrochimica Acta 2008; 53: 3708-3713.

[9] W. Xiuyu, Z. Jingchang, Z. Hong, Pt-Au/CNT@TiO_2 as a High-Performance Anode Catalyst for Direct Methanol Fuel Cells. Chinese Journal of Catalysis 2011; 32: 74-79.

[10] P. Kolla, A. Smirnova, Methanol oxidation on hybris catalysts: PtRu/C nanostructures promoted with cerium and titanium oxides. International Journal of Hydrogen Energy 2013; 38: 15152-15159.

[11] A. Aguilar-Elguézabal, W. Antúnez, G. Alonso-Núñez, F. Paraguay Delgado, F. Espinoza, M. Miki-Yoshida, Study of carbon nanotubes synthesis by spray pyrolysis and model of growth. Diamond & Related Materials 2006; 15: 1329-1335.

[12] J. H. Lehman, M. Terrones, E. Mansfield, K. E. Hurts, V. Maunier, Evaluating the characteristics if multiwall carbon nanotubes. Carbon 2011; 2581-2602.

[13] S. Lowell, J. E. Shields, M. A. Thomas, M. Thommes, Characterization of Porous Solids and Powders: Surface Area, Pore Size and Density, Kluwer Academic Publisher, Netherlands, 2004.

Bioelectricity from Recalcitrant Municipal Leachate in a Microbial Fuel Cell

A.L. Vázquez-Larios[1], H.M. Poggi-Varaldo[1]*, O. Solorza-Feria[2], M.T. Ponce-Noyola[3], R. de G. Gonzalez-Huerta[4], G. Hernández-Flores[1], E. Ríos-Leal[3], N. Rinderknecht-Seijas[4]

[1] Environmental Biotechnology and Renewable Energies Group, Dept. Biotechnology and Bioengineering, CINVESTAV del IPN, P.O.Box 14-740, Mexico D.F., 07000, Mexico
[2] Dept. of Chemistry, CINVESTAV del IPN, P.O.Box 14-740, Mexico D.F., 07000, Mexico
[3] Dept. Biotechnology and Bioengineering, CINVESTAV del IPN, P.O.Box 14-740, Mexico D.F., 07000, Mexico
[4]ESIQIE-IPN, Mexico D.F., Mexico
*Author for correspondence, H.M. Poggi-Varaldo, r4cepe@yahoo.com

ABSTRACT

The objective of this work was to evaluate the effect of several inocula on the treatment and bioelectricity production from municipal leachate in a two-face microbial fuel cell equipped with graphite flakes as anode and (*MFC-G*) and Pt as cathodic catalyst at a dose of 0.5 mg/cm^2 Pt. Inocula tested were: two enriched in Fe(III)-reducing bacteria (i.e., one was started with soil, *In-E*$_{Fe(III)-S}$, the other was started from a sulphate-reducing bioreactorn, *In-E*$_{Fe(III)-SR}$), one enriched in Mn(IV)-reducing bacteria (*In-E*$_{Mn(IV)}$), and a plain sulphate-reducing inoculum (*In-SR*). Each face (I and II) of the *MFC-G* was characterized by separate, in series, and parallel connection. Parallel connection of faces increased the maximum volumetric power up to 14 954, 24 319, 28 112 and 28 113 mW/m^3 for the *In-SR*, *In-E*$_{Fe(III)-S}$, *In-E*$_{Fe(III)-SR}$ and *In-E*$_{Mn(III)}$ respectively. Parallel connection of electrode faces also significantly decreased the R_{int}. In the batch operation where the cells were connected to an external resistance of 100 Ω, the average volumetric powers $P_{V\text{-}ave}$ were 26 424, 25 548, 25 752 and 13 379 mW/m^3 for the *In-E*$_{Fe(III)-S}$, *In-E*$_{Fe(III)-SR}$, *In-E*$_{Mn(IV)}$, and *In-SR* respectively. The high $P_{V\text{-}ave}$ achieved in our work with enriched inocula could be attributed to the combined effects of increased concentrations of exoelectrogenic bacteria as well as the high total anodic surface area by the use of granular graphite. This, in turn, could have improved the electron transfer microbe-to-anode. The power values registered in this work (26 W/m^3) were in the range of power yields typical of the anaerobic digestion of municipal wastewaters (5 to 50 W/m^3). To the best of our knowledge, it is the first time that volumetric powers as high as 26 W/m^3 are reported in the treatment of recalcitrant, actual leachate in *MFC*. Our results constitute a firm step towards sustainable remediation of this recalcitrant and aggressive effluent.

Keywords: enriched inocula; leachate; microbial fuel cell

1. Introduction

A microbial fuel cell (*MFC*) is an electro-biochemical reactor capable of directing converting organic matter into electricity [1-2]. Leachate is heavily polluted wastewater with a complex composition containing four groups of pollutants: dissolved organic matter, inorganic macro-components, heavy metals and xenobiotic organic compounds [3]. Leachate is generated from the landfill, composting and pyrolysis pretreatment of municipal solid waste. This sewage is always mixed with the liquid from microbial anaerobic decomposition, settlement of rainwater and surface water lixivium, which can be named as leaching water or leaching solution. This complex composition and the variance in quality and quantity usually observed, make leachate one of the most difficult of wastewaters to be treated [4]. All kinds of leachate treatment options have been reported such as *(i)* leachate recirculation, *(ii)* co-treatment with domestic wastewater, *(iii)* physico-chemical systems, *(iv)* biological processes, and *(v)* combined treatments [4]. Because of the high costs, generation of waste sludges, as well as emission of objectionable odors of the ordinary treatment, finding an efficient, stable and economic method for municipal landfill leachate treatment is very necessary.

The objective of this work was to evaluate the effect of several inocula on the treatment and bioelectricity production from municipal leachate in a two-face microbial fuel cell equipped with graphite flakes as anode and (*MFC-G*) and Pt as cathodic

catalyst. Inocula tested were: two enriched in Fe(III)-reducing bacteria (i.e., one was started with soil, *In-*$E_{Fe(III)-S}$, the other was started from a sulphate-reducing bioreactorn (*In-*$E_{Fe(III)-SR}$), one enriched in Mn(IV)-reducing bacteria (*In-*$E_{Mn(IV)}$), and a plain sulphate-reducing inoculum (*In-SR).*

2. Experimental

2.1. Microbial fuel cell architecture

The *MFC-G* consisted of a horizontal cylinder built Plexiglass 90 mm long and 57 mm internal diameter. The opposing faces of the cylindrical shell were fitted with corresponding sets of an assemblage of (inside to outside) proton exchange membrane (Nafion 117), a Toray flexible carbon-cloth containing 0.5 mg cm^{-2} platinum catalyst (Pt 10 wt%/C-ETEK), and a perforated plate of stainless steel 1 mm thickness. Each assemblage was corresponded with anodes made of granular graphite and a graphite rod as collector (80 mm long and 5 mm diameter). The average separation between cathode-anode in *MFC-G* was 17.5 mm. The anode chamber volume was 100 mL.

2.2. Municipal leachates

The cells were loaded with 20 mL of municipal leachates sampled from the Mexico City landfill "Bordo Poniente" stage 4. The characterization of the leachate is given in Table 1. The relatively high organic matter content and high value of BOD5/COD ratio indicated that the leachate is biodegradable, and likely not very aged. Interestingly, we expected a lower pH consistent with fresh leachate [4]. That was not the case. It is known that the landfill is emplaced in a site whose soil is sodic-saline soil with pH as high as 11 [5]. The local soil was likely used to cap the landfill cells during the daily operation of the landfill, possibly releasing sodium salts (carbonate, bicarbonate) as well as hydroxides that increased leachate pH. This explanation is supported by the high values of the electrolytic conductivity of the leachate (Table 1).

Table 1. Characteristics of municipal leachate.

Parameters	Value
pH	8.26 ± 0.02
Conductivity (mS/cm)	36.7 ± 0.1
Total Kjeldahl nitrogen (g/L)	2.9 ± 0.03
SO_4^{2-} (g/L)	0.281± 0.01
COD (g/L)	12.3± 0.5
BOD_5 (g/L)	10.6± 0.2
BOD_5/COD	0.86

2.3. Sample collection and enrichment of inoculum

The enriched inoculum was obtained after three serial transfers, described below. Sample from soil was collected in the CINVESTAV-IPN (19° 30´33"N, 99° 07´46"O) to a depth of 2 m. The sample was transferred to an anaerobic bottle. 5 g of soil sample was suspended in 50 mL of anaerobic saline solution; afterwards, a 5 mL of sample was transferred to 50 mL metal-reduction medium with acetate as electron donor and Fe(III) oxide-hydroxide as electron acceptor. A sample of sulphate-reducing sludge was taken from a complete mix sulphate reducing semi-continuous bioreactor that acted as seed reactor [5-7] and handled in a similar way as the soil sample. The enrichment of inoculum were obtained with serial transfers. Duplicate enrichments were incubated at 30 °C for 9 d in the dark condition. The enrichment procedure was repeated 3 times. For the procedure of enrichment Mn(IV) of soil sample was similar way as the enrichment Fe(III). Duplicate enrichments were incubated at 30 °C for 15 d in the dark condition. The enrichment procedure was repeated 3 times.

The culture medium consisted of (g/L): 2.5 $NaHCO_3$, 0.25 NH_4Cl, 0.6 $NaH_2PO_4.H_2O$, 0.1 KCl, 10 mL vitamin solution and 10 mL mineral solution (Lovley & Phillips, [8]; Lovley & Phillips, [9]). The Fe(III) oxide was synthesized as follows: a solution 0.4 M of $FeCl_3.6\ H_2O$ (pH adjusted to 7.0 with 10 M of NaOH) was added, according to the technique described by Lovley & Phillips [8]. The MnO_2 was synthesized by slowly adding a solution of $MnCl_2$ (30 mM) to basic solution of $KMnO_4$ (20 mM) which was stirred with a magnetic stir bar. This procedure is similar to a previously described technique (Lovley & Phillips, [8]).

2.4. Electrochemical characterization and batch operation of the microbial fuel cells

Potential sweep experiments were carried out from open-circuit cell voltage (EOC), to the final potential of 0.02 V at a scan rate of 1mVs-1, performed in a potentiostat/galvanostat Voltalab model PGZ402 [10,11]. Values of R_{int} were estimated from the slopes of corresponding regression lines selected in the linear range of the polarization curves. The current (I_{MFC}), power (P_{MFC}) and volumetric power (P_V) were calculated as previously described [12]. The power density (surface area) was normalized to the projected cathode surface area (surface power density P_S). The cells were loaded with 80 mL of inoculum and 20 mL of actual municipal leachate. The initial biomass concentration in the cell inoculum was *ca.* 1,300 mg $VSSL^{-1}$.

The batch *MFC*s were loaded with municipal leachate and i enriched inoculum. The organic matter concentration in MFCs was ca. 2 g CODL-1. The cells were loaded with 80 mL of inoculum; the initial biomass concentration in the cell inoculum was ca. 1,300 mg $VSSL^{-1}$. The cells were operated for two Periods; in Period I the cells were run until a decrease organic matter concentration was observed. At the end of Period I, the cell was loaded with new municipal leachate (ca. 2.0 g $CODL^{-1}$) although the electrodes and membrane as well as the microbial community remained the same, and further operated for what we denominated In Period II. At the start of Period I the cells were operated for 24 h to open circuit voltage. Afterwards the cells were batch-operated for a total 250 h, at ambient temperature (23°C average) without mixing. The circuit of each MFC was fitted with a corresponding external resistance of 100 Ω for Pt.

The main variable responses of this experiment were the average volumetric power ($P_{V\text{-}ave}$), the efficiency of organic matter removal (η_{COD}), and the coulombic efficiency (η_{Coul}).

2.5. Analytical methods and calculations

The COD and VSS of the liquors of sulphate-reducing seed bioreactor and cells were determined according to the Standard Methods [13]. Manganese (Mn II) contents were analyzed by the method of Brewer and Spencer [14] as modified by Armstrong et al. [15] whereas the presence of Mn (IV) was assessed with a benzidine acetate reagent [16]. The main response variables were calculated as reported elsewhere [2].

3. Results and discussion

3.1. Electrochemical characterization of microbial fuel cells loaded with municipal leachates.

Each face (faces I and II) of the *MFC-G* was characterized by separate (I and II), in series, and parallel connection. Parallel connection of faces increased the maximum volumetric power ($P_{V\text{-}max}$) up to 24,319 and 28,112, 28,799, and 14, 984 mW/m^3 for *In-*$E_{Fe(III)\text{-}S}$, *In-*$E_{Fe(III)\text{-}SR}$, *In-*$E_{Mn(IV)}$ and *In-SR*, respectively (Fig. 1). In general, parallel connection of electrode faces significantly decreased the R_{int} (18, 13, 10 and 19 Ω for *In-*$E_{Fe(III)\text{-}S}$, *In-*$E_{Fe(III)\text{-}SR}$, *In-*$E_{Mn(IV)}$ and *In-SR*, respectively).

The $P_{V\text{-}max}$ for the *MFC-G* for *In-*$E_{Fe(III)\text{-}S}$, *In-*$E_{Fe(III)\text{-}SR}$, *In-*$E_{Mn(IV)}$ and *In-SR* when faces were connected in series and parallel were higher than that reported by Ortega-Martínez *et al.* [17], Vázquez-Larios *et al.* [178, Ortega-Martinez *et al.* [19] and Ieropoulos *et al.,* [20] . Ortega-Martinez *et al.* [17] evaluated the effect of an enriched inoculum on the characteristics of a parallelepiped *MFC*. The values of $P_{V\text{-}max}$ were 1,772 and 5,804 mW/m^3 for the faces connected in series and parallel. Vazquez-Larios *et al*. [18] evaluated a MFC equipped with a cathode painted with Pt as a catalyst, graphite triangular pieces as anodic material, inoculum sulphate-reducing and semisynthetic leachate. The $P_{V\text{-}max}$ for faces I and II connected in parallel and series were 2,094 and 3,098 mW/m^3. Ortega-Martinez *et al.* [19] characterized a multi-face parallelepiped *MFC*; this cell was fitted with a 'sandwich' cathode-membrane-anode assemblage in five of their faces. When the 5 faces of the cell were connected in series and parallel, the $P_{V\text{-}max}$ achieved values of 62 and 570 mW/m^3. Ieropoulos *et al.,* [20] compared the performance of two small size *MFCs* connected in parallel using acetate as the substrate and anaerobic sludge and regiested a $P_{V\text{-}max}$ of 860 mW/m^3.

The relatively high value of $P_{V\text{-}max}$ obtained in our *MFCs* could be attributed to the increase of the total electrode surface area by the application of granular graphite, and this, in turn, could have improved the electron transfer microbe-to-anode process [18]. Also, our work demonstrated that parallel connection of cell faces was more appropriate. On the other hand, the increase of power could be ascribed to the use of the enriched inoculum. Dissimilatory metal reducing bacteria, were capable of the reduction of soil metal oxides have been particularly noteworthy with regard to this ability and to date, many species of electrochemically active bacteria [19].

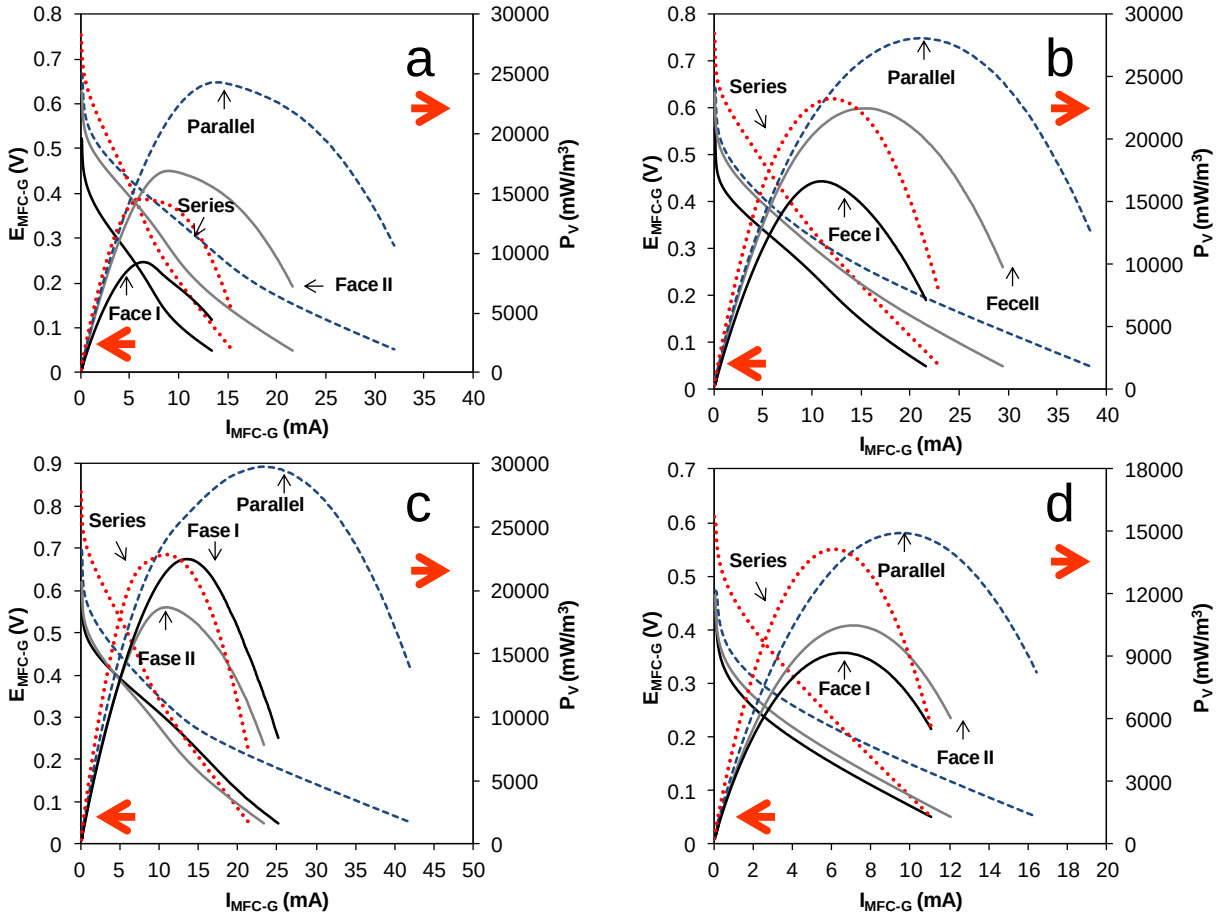

Fig. 1. Polarization curves by linear sweep potential studies in electrochemical characterization of microbial fuel cells, a) *In-*$E_{Fe(III)\text{-}S}$, b) *In-*$E_{Fe(III)\text{-}SR}$, c)*In-*$E_{Mn(IV)}$ and d) *In-SR*. Keys: convex curves stand for volumetric power, read on the right axis; descending parabolic curves represent the E-I relationship, read on the left axis; curve in blue-hyphen stand for parallel connection of the two faces of the cell; red-dot stands for series connection of the faces; continuous gray corresponds to face II alone, and continuous black stands for face I alone.

3.2. Results of batch operation of microbial fuel cells loaded with municipal leachate

Figure 2 shows the time course of cell potential the *MFC-G* in the batch operation of the cells using two enriched inocula, namely, the inoculum enriched in Fe (III)-reducing bacteria (either one soil origin, *In-*$E_{Fe(III)\text{-}S}$ or sulphate-reducing origin, *In-*$E_{Fe(III)\text{-}SR}$), inoculum enriched in Mn (IV)-reducing bacteria, sulphate reducing and *MFC-G* without inoculum. The cells were connected to a R_{ext} of 100 Ω whereas their two faces of each cell were connected in parallel. The gray area in Fig. 2 shows that the open circuit potential (the 21 h and without a resistance in the external circuit) of the cells were 0.516, 0.499, 0.500, 0.358 and 0.061 V for *In-*$E_{Fe(III)\text{-}S}$, *In-*$E_{Fe(III)\text{-}SR}$, *In-*$E_{Mn(IV)}$, *In-SR* and without inoculum, respectively. Two repeated cycles were carried out (Period I and Period II in Fig. 2), where treated leachate was removed and replaced by a new leachate load, whereas the microbial culture and electrodes remained the same.

The $P_{V\text{-}ave}$ for period II the cells *In-*$E_{Fe(III)\text{-}S}$, *In-*$E_{Fe(III)\text{-}SR}$, *In-*$E_{Mn(IV)}$ and *In-SR* were higher than those reported by Zhang *et al.* [21], Puig *et al.* [22], Rikame *et al.* [23], Özkaya *et al.* [24] and Vazquez-Larios *et al.* [25]. Zhang *et al.* [21] evaluated an

upflow air-cathode membrane-free microbial fuel cell (UAMMFC). The experimental results demonstrated that the *UAMMFC* could continuously generate electricity from leachate for an operational period of time (50 h); a maximum volumetric power of 12 800 mW/m^3 was reported. Puig *et al*. [22] operated an air, single chamber *MFC* and Pt catalyst in the cathode to treat landfill leachate in two operation periods. In Period I with 0.507 g COD/L, the authors reported a P_V of 6.1 mW/m^3. In their Period II the organic matter content was increased to 1.48 and 8.51 g COD/L, the P_V were 106 to 344 mW/m^3, respectively.

Rikame *et al*. [23] experimented with a two-chambered *MFC* with carbon electrodes for food waste leachate, the P_V was 15,140 mW/m^3 (η_{COD} = 90%). Özkaya *et al*. [24] assessed the performance of a two-chambered, continuous *MFC* with new Ti–TiO_2 electrodes for bioelectricity generation from young landfill leachate. They found a P_V of 1 920 mW/m^3. Vazquez-Larios *et al*. [25] evaluated a new design with extended electrode surface (larger ξ, specific surface or surface area of electrode to cell volume) and the assemblage or "sandwich" arrangement of the anode-*PEM*-cathode (*AMC* arrangement) and model leachate, similar to that produced in the biological hydrogen production from the organic fraction of the municipal solid waste. A P_V of 606 mW/m^3 was achieved.

The high average volumetric powers achieved in our work could be attributed to the combined effects of increased concentrations of exoelectrogenic bacteria as well as increased total anodic surface area by the use of graphite flakes (Vazquez-Larios *et al*., [18]).

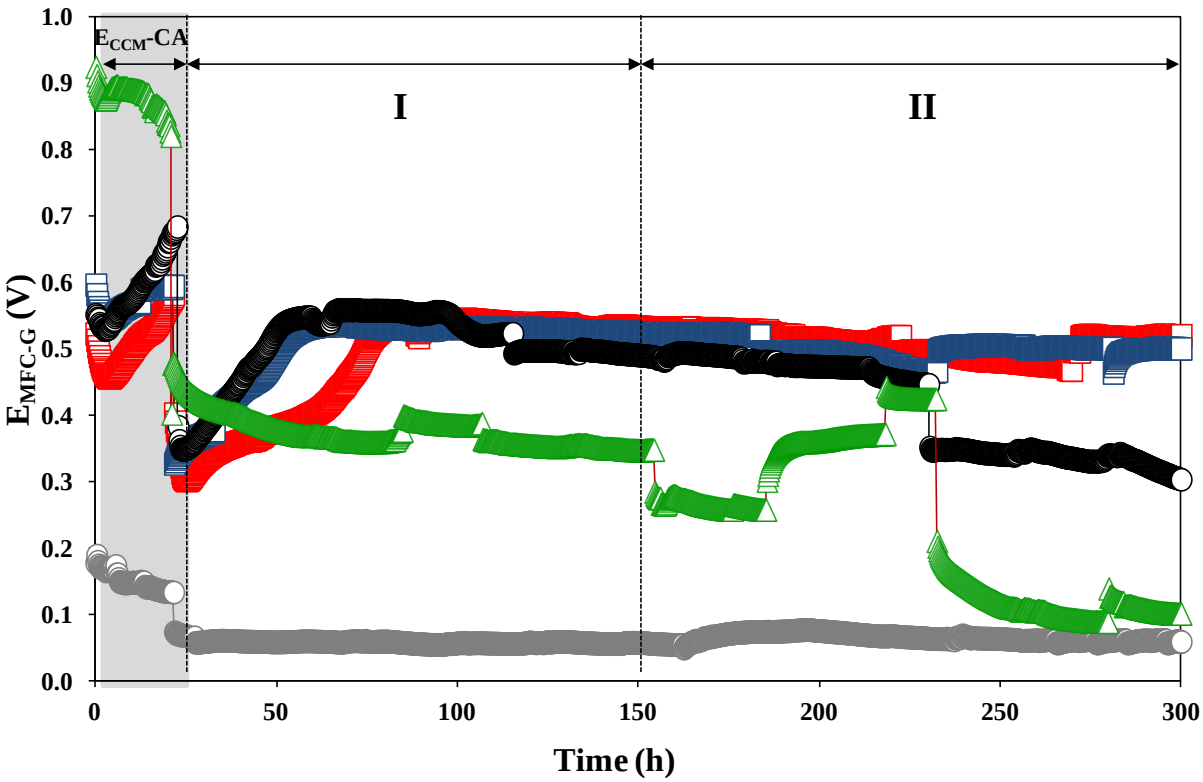

Fig. 2. Time course of voltage outputs of *MFC-G* cell using a inoculum enriched in Fe (III)-reducing bacteria (either one soil origin, *In-*$E_{Fe(III)\text{-}S}$ and sulphate-reducing origin, *In-*$E_{Fe(III)\text{-}SR}$), inoculum enriched in Mn (IV)-reducing bacteria (*In-*$E_{Mn(IV)}$), inoculum sulphate reducing (In-SR) and without inoculum.

4. Summary and perspectives

Two-face *MFCs* fitted with air-cathodes and graphite flakes anodes were characterized and batch operated for bioelectricity generation from an actual leachate. Moreover, the effect of four inocula, the enriched in Fe(III)-reducing bacteria (either one from soil origin, *In-*$E_{Fe(III)-S}$ or sulphate-reducing origin, *In-*$E_{Fe(III)-SR}$) inoculum enriched in Mn (IV)-reducing bacteria (*In-*$E_{Mn(IV)}$), inoculum sulphate reducing (*In-SR*) was assessed.

Each face (I and II) of the *MFC-G* was characterized by separate (I and II), in series and parallel connection. Parallel connection of faces increased the max volumetric power up to 24 319 and 28 112, 289 799, 14 984 mW/m^3 for *In-*$E_{Fe(III)-S}$, *In-*$E_{Fe(III)-SR}$, *In-*$E_{Mn(IV)}$ and *In-SR*, respectively, respectively. In general parallel connection of electrode faces significantly decreased the R_{int} (18, 13, 10 and 19 Ω for *In-*$E_{Fe(III)-S}$, *In-*$E_{Fe(III)-SR}$, *In-*$E_{Mn(IV)}$ and *In-SR*, respectively).

In the batch operation where the cells were connected to an R_{ext} of 100 Ω, the average volumetric power $P_{V\text{-}ave}$ were 26 424 ± 482, 25 548 ± 744, 25 752 and 13 379 mW/m^3 for *In-*$E_{Fe(III)-S}$, *In-*$E_{Fe(III)-SR}$, *In-*$E_{Mn(IV)}$ and *In-SR*, respectively. The high $P_{V\text{-}ave}$ achieved in our work could be attributed to the combined effects of increased concentrations of exoelectrogenic bacteria as well as increased total anodic surface area by the use of graphite flakes. This, in turn, could have improved the electron transfer microbe-to-anode.

The power values achieved in this work (30 W/m^3) were higher or comparable than power thresholds typical of the anaerobic digestion of municipal wastewaters (5 to 50 W/m^3). To the best of our knowledge, it is the first time that volumetric powers as high as 26 W/m^3 are reported in the treatment of actual leachates in MFC. Our results constitute a firm step towards sustainable remediation of recalcitrant leachates.

Acknowledgements

The ICyTDF now SECITI-GDF (PICCO 10-28) and CINVESTAV-IPN (Mexico) financial support to this research is gratefully acknowledged. The authors wish to thank the help of Mr. Rafael Hernández-Vera from the Environmental Biotechnology and Renewable Energies R&D Group of the Dept. of Biotechnology and Bioengineering, as well as the Research Assistants and Technicians from the Hydrogen and Fuel Cell Group, Dept Chemistry, CINVESTAV.

References

[1] R. Barbosa, J. Andaverde, B. Escobar, U. Cano, Stochastic reconstruction and a scaling method to determine effective transport coefficients of a PEMFC catalyst layer. J. Power Sources 2011; 196: 1248–1257
[2] A. J. Bard and L. R. Faulkner, Electrochemical Methods, Fundamentals and Applications, 2nd ed., John Wiley & Sons, Inc., N. Y., 2000.
[3] A.L. Vazquez-Larios, O. Solorza-Feria, G. Vazquez-Huerta, F. Esparza-Garcia, N. Rinderknecht-Seijas, H.M. Poggi-Varaldo. Effects of architectural changes and inoculum type on internal resistance of a microbial fuel cell designed for the treatment of leachates from the dark hydrogenogenic fermentation of organic solid wastes. Int J Hydrogen Energy 2011; 36: 6199-.
[4] H.M. Poggi-Varaldo, A. Carmona-Martinez, A.L. Vazquez-Larios, O. Solorza-Feria. Effect of inoculum type on the performance of a microbial fuel cell fed with spent organic extracts from hydrogenogenic fermentation of organic solid wastes. J New Mater Electrochem Syst 2009;12(1):49-54.
[5] Q-Q Zhang, B-H Tian, X. Zhang, A. Ghulam, C-R Fang, R. He, Investigation on characteristics of leachate and concentrated leachate in three landfill leachate treatment plants, Waste Management 2013; 33: 2277–2286
[6] T.A. Kurniawan, W-H. Lo, G. Y.S. Chan, Physico-chemical treatments for removal of recalcitrant contaminants from landfill leachate, Journal of Hazardous Materials 2006; B129: 80–100
[7] S. Renou, J.G. Givaudan, S. Poulain, F. Dirassouyan, P. Moulin. Landfill leachate treatment: Review and opportunity. J Hazard Mater 2008;150: 468–493.
[8] D.R. Lovley, E.J.P. Phillips. Rapid assay for microbially reducible ferric iron in aquatic sediments. *Appl. Environ. Microbiol.* 1997, 3:1536-40.
[9] D.R. Lovley, E.J.P. Phillips. Novel mode of microbial energy metabolism: organic carbon oxidation coupled to dissimilatory reduction of iron or manganese. *Appl. Environ. Microbiol.* 1988, 54:1472-80.
[10] K. Sathish-Kumar , O. Solorza-Feria, G. Vázquez-Huerta, J.P. Luna-Arias, H.M. Poggi-Varaldo. Electrical stress-directed evolution of biocatalysts community sampled from a sodic-saline soil for microbial fuel cells. J New Mater Electrochem Syst 2012; 15(3): 181-186
[11] K. Sathish- Kumar, O. Solorza-Feria, R. Hernández-Vera, G. Vazquez-Huerta, H.M. Poggi-Varaldo. Comparison of various techniques to characterize a single chamber microbial fuel cell loaded with sulfate reducing biocatalysts. J New Mater Electrochem Syst 2012;15(3):195-201.
[12] A.L. Vazquez-Larios, O. Solorza-Feria, G. Vazquez-Huerta, F. Esparza-Garcia, E. Rios-Leal, N. Rinderknecht-Seijas, H.M. Poggi-Varaldo. A new design improves performance of a single chamber microbial fuel cell. J New Mater Electrochem Syst 2010;13(3): 219-226.
[13] APHA. Standard methods for the examination of water and wastewater. 17th ed. Washington, DC, USA: American Public Association; 1989.
[14] P.G. Brewer, D.W. Spencer. Colorimetric determination of manganese in anoxic waters. Limnol Oceanogr 1971;16:107-112.

[15] P.B. Armstrong, W.B. Lyons, H.E.Gaudette. Application of formaldoxime colorimetric method for the determination of manganese in the pore water of anoxic estuarine sediments. Estuaries 1979; 2(3):198-201.
[16] F. Feigl, Spot tests in inorganic analysis. Elsevier, New York, N.Y.; 1958
[17] A.C. Ortega-Martinez, K. Juarez-Lopez, O. Solorza-Feria, M.T. Ponce-Noyola, J. Galindez-Mayer, N. Rinderknecht-Seijas, H.M. Poggi-Varaldo. Analysis of microbial diversity of inocula used in a five-face parallelepiped and standard microbial fuel cells. Int J Hydrogen Energy 2013;38(28):12589-12599.
[18] A.L.Vázquez-Larios, Solorza-Feria O, González-Huerta R de G, Ponce-Noyola MT, Barrera-Cortés J, Rinderknecht-Seijas N, Poggi-Varaldo HM. Effect of two anodic materials and RuxMoySez as a cathode catalyst on the performance of two singlw chamber microbial fuel cells. J New Mater Electrochem Syst 2013;16(3):163-170.
[19] A. C. Ortega-Martínez, K. Juárez-López, O. Solorza-Feria, M.T. Ponce-Noyola, E. Ríos-Leal, N. Rinderknecht-Seijas, H.M. Poggi-Varaldo. Parallel connection and sandwich electrodes lower the internal resistance in a microbial fuel cell. J New Mater Electrochem Syst 2012;15(3):187-194.
[20] I. Ieropoulus, J. Greenman, C. Melhuish. Microbial fuel cell based on carbon veil electrodes: Stack configuration and acalability. Int J Energy Res 2008;32 (13): 1228–1240.
[21] J. N. Zhang, Q. L. Zhao, S. J. You, J. Q. Jiang, N. Q. Ren. Continuous electricity production from leachate in a novel upflow air-cathode membrane-free microbial fuel cell". Bioprocess Biosyst. Eng. 2008; 36(4): 399-405.
[22] S. Puig, M. Serra, M. Coma , M.Cabre, M.E. Balaguer, J. Colprim. Microbial fuel cell application in landfill leachate treatment. J Hazard Mater 2011;185(2-3): 763-767.
[23] S. S. Rikame, A. A.Mungray, A. K. Mungray. Electricity generation from acidogenic food waste leachate using dual chamber mediator less microbial fuel cell. Int. Biodeter Biodegr. 2012; 75: 131-137.
[24] B. Ozkaya, A.Y. Cetinkaya, M. Cakmakci, D. Karadag, E. Sahinkaya. Electricity generation from young landfill leachate in a microbial fuel cell with a new electrode material. Bioprocess and Biosystems Engineering 2013;36:399-405.
[25] A.L. Vazquez-Larios, O. Solorza-Feria, G. Vazquez-Huerta, E. Rios-Leal, N. Rinderknecht-Seijas, H.M. Poggi-Varaldo. Internal resistance and performance of microbial fuel cells: influence of cell configuration and temperature. J. New Mater Electrochem Syst. 2011; 14(2): 99-105.

Effect of Type of Inoculum and Application of $Ru_xMo_ySe_z$ on Microbial Fuel Cell Performance

A.L. Vázquez-Larios[1], O. Solorza-Feria[2], H.M. Poggi-Varaldo[1*], M.T. Ponce-Noyola[3], R. de G. González-Huerta[4], E. Ríos-Leal[3], J. Barrera Cortés[3], José I. Tapia- Ramírez[5]

[1] Environmental Biotechnology and Renewable Energies Group, Dept. Biotechnology and Bioengineering, CINVESTAV del IPN, P.O.Box 14-740, Mexico D.F., 07000, Mexico
[2] Dept. of Chemistry, CINVESTAV del IPN, P.O.Box 14-740, Mexico D.F., 07000, Mexico
[3] Dept. Biotechnology and Bioengineering, CINVESTAV del IPN, P.O.Box 14-740, Mexico D.F., 07000, Mexico
[4] ESIQIE-IPN, Mexico D.F., Mexico
[5] Dept. Genetics and Molecular Biology, CINVESTAV del IPN, P.O.Box 14-740, Mexico D.F., 07000, Mexico
*Author for correspondence: H. M. Poggi-Varaldo, r4cepe@yahoo.com

ABSTRACT

This research aimed at evaluating the effect of inoculum type and the application of $Ru_xMo_ySe_z$ as a cathode catalyst on the treatment and bioelectricity production of a microbial fuel cell fed with recalcitrant, municipal leachate. The device was an air-cathode, two-face microbial fuel cell fitted with graphite flakes as anodic material (*MFC-G*). The cathode was painted with $Ru_xMo_ySe_z$ at a dose of 0.5 mg/cm^2. The inocula assayed in our work were a plain sulphate-reducing inoculum (*In-SR*), an enrichment in Mn(IV)-reducing bacteria (*In-*$E_{Mn(IV)}$), and two enrichments in Fe(III)-reducing bacteria, namel, *In-*$E_{Fe(III)-S}$ and *In-*$E_{Fe(III)-SR}$.

Each face (I and II) of the *MFC-G* was characterized by separate (I and II), in series and parallel connection. We found that parallel connection of electrode faces lead to significantly lower values of the internal resistnace. In the batch operation where the cells were operated with the faces connected in parallel and loaded with an external resistance of 100 Ω, enrichment of the inocula had a significant, positive effect of cell performance. The average volumetric powers $P_{V\text{-}ave}$ observed were 4 376, 9 555, 11 249, and 13 303 mW/m^3 for the *In-SR*, *In-*$E_{Mn(IV)}$, *In-*$E_{Fe(III)-SR}$, and *In-*$E_{Fe(III)-S}$, respectively. The high $P_{V\text{-}ave}$ registered with the enriched inocula in our work could be attributed to the synergism of increased concentrations of exoelectrogenic bacteria as well as the high total anodic surface area by the use of granular graphite that could have facilitated the electron transport to the anode. The first issue was confirmed by molecular characterization of enriched inocula. In general, values of $P_{V\text{-}ave}$ obtained with the chalcogenide catalyst were 30-40% lower than those registered with Pt catalyst. Yet, the cost of the chalcogenide is 80% lower than that of platinum. We conclude that the application of inocula enriched in Fe(III) and Mn (IV)-reducing bacteria significantly improved the performance of cells that used $Ru_xMo_ySe_z$ as a cathodic catalyst for the ORR

Keywords: ***$Ru_xMo_ySe_z$ cathodic catalyst, leachate, microbial fuel cell, enriched inocula***

1. Introduction

A microbial fuel cell (MFC) is an electro-biochemical reactor capable of directing converting organic matter into electricity [1-2]. Platinum has been commonly used as a catalyst of the oxygen reduction reaction (ORR) in MFCs. Yet the high cost of an MFC is mainly due to the high price of this noble metal. This, in turn, could deter the commercial MFC applications. So, the development of new materials with high catalytic properties to perform oxygen reduction is presently a task of great importance [3-6]. One of the challenges in microbial fuel cells research consists of the application of new electrochemically active catalytic materials (such as RuxMoySez [7]) as alternative electrocatalysts to replace the extensive use of the more expensive platinum. Vazquez-Larios et al. [7] evaluated the application of bimetallic chalcogenide RuxMoySez, as an ORR catalyst and two anodic materials on the performance of two MFCs fed with synthetic substrate. The power delivered by cell the with fitted graphite triangular pieces and chalcogenide catalyst was 43% inferior to that of a similar cell with Pt although the cost of the first catalyst is significantly lower than that of Pt., i.e., 73% lower.

On the other hand, municipal leachate is an aggressive effluent with relatively high concentration of organic matter [8,9]. Leachate from sanitary landfills is of concern in Mexico City, since very recently the Bordo Poniente mega landfill has been closed and it is known that it generates large amounts of both fresh and aged leachates. So far, the available information on treatment of municipal leachate in MFC loaded with inoculum enriched in Mn (IV)-reducing bacteria is still scarce. Previous works have demonstrated the feasibility of using leachate as substrate in MFCs. Yet, the powers delivered were in the low-to-mid side of the range. Greenman et al. [10] demonstrated that it was possible to generate electricity and simultaneously treat landfill leachate in MFC columns, 1.35 mW/m-2 and 43 % BOD removal. Gálvez et al. [11] operated three MFCs hydraulically connected in series for simultaneous leachate treatment and electricity generation. The system when configured into a loop was able to remove 79% of COD and 82% of BOD5 after 4 days. Ganesh & Jambeck [12] operated to treat landfill leachate in cylindrical single air-cathode without inoculation; they observed a volumetric power (PV) of 699 mWm-3 and 74% COD removal. Tugtas et al. [13] investigated treatment of anaerobically pre-trated landfill leachate in a investigated in batch and continuous-flow two-chambered MFCs. They reported a PV of 2 482 mWm-3 and 90 % COD removal. On the other hand, Puig et al. [14] evaluated an air-cathode MFC fed with landfill leachate, the PV was 344 mWm-3 whereas the COD removal was 70 %. It can be seen that, in general, volumetric powers obtained in MFC fed with leachate were in the low-to-mid part of the power range.

This research aimed at evaluating the effect of inoculum type and the application of $Ru_xMo_ySe_z$ as a cathode catalyst on the treatment and bioelectricity production of a microbial fuel cell fed with recalcitrant, municipal leachate.

2. Experimental

2.1.Microbial fuel cell architecture

The *MFC-G* consisted of a horizontal cylinder built Plexiglass 90 mm long and 57 mm internal diameter. The opposing faces of the cylindrical shell were fitted with corresponding sets of an assemblage of (inside to outside) proton exchange membrane (Nafion 117), a Toray flexible carbon-cloth containing 1 mg/cm^2 $Ru_xMo_ySe_z$ (20wt%/C) and a perforated plate of stainless steel 1 mm thickness. Each assemblage was corresponded with anodes made of granular graphite and a graphite rod as collector (80 mm long and 5 mm diameter). The average separation between cathode-anode in *MFC-G* was 17.5 mm. The anode chamber volume was 100 mL. All the cathodes in cell were in direct contact with atmospheric air on the perforate perforated metallic plate side. When the cathodic biocatalyst was the chalcogenide, the cathode had a loading of 1.0 mgcm^{-2} $Ru_xMo_ySe_z$ 20 wt% dispersed in Vulcan carbon XC-72 as it was mentioned above. The catalytic ink was prepared by mixing 11.1 µLcm^{-2} Nafion® 5 wt% and 333.3 µLcm^{-2} of ethanol and the resulting suspension was sprayed onto the *PEM* of a home fabricated electronic semiautomatic device. Afterwards, the *PEM* was pressed the by hot pressing (4.4 kg cm^{-2}) at 120°C for 3 min to improve adherence of catalyst to the membrane [15,16].

2.2. Catalyst synthesis and characterization

The $Ru_xMo_ySe_z$ catalyst was synthesized by decarbonylation of transition-metal carbonyl compounds in organic solvent, under refluxing [17,18]. The $Ru_xMo_ySe_z$ catalyst was synthesized by reacting 0.07 mM $Ru_3(CO)_{12}$ (Aldrich) with 0.20 mM $Mo(CO)_6$ (Strem) and 0.20 mM of elemental selenium (Strem) in a chemical reactor containing 150 mL of 1,6-hexanediol for 3 hours at 230 °C. The un-reacted precursors and the organic reaction medium were eliminated by several washes using organic solvents, and dried overnight at room temperature [19].

The catalyst was composed of uniform agglomerates of nanocrystalline particles with an estimated composition of $Ru_6Mo_1Se_3$, embedded in an amorphous phase. Tafel slopes for the *ORR* remained invariant with temperature at -0.116 V dec^{-1} with an increase of the charge transfer coefficient in $d\alpha/dT = 1.6\times10^{-3}$, ascribed to an entropy turnover contribution to the electrocatalytic reaction. The apparent activation energy was 45.6 ± 0.5 $kJmol^{-1}$. The catalyst generated less than 2.5% hydrogen peroxide during oxygen reduction [18,19].

2.3. Municipal leachates

The cells were loaded with 10 mL of municipal leachates sampled from the Mexico City landfill "Bordo Poniente" stage 4 (Etapa 4). The characterization of the leachate is given in Table 1. The relatively high organic matter content and high value of BOD_5/COD ratio indicated that the leachate is biodegradable, and likely not very aged [6]. Interestingly, we expected a lower pH consistent with fresh leachate [9]. That was not the case. It is known that the landfill is emplaced in a site whose soil is sodic-saline soil with pH as high as 11 [9,19]. The local soil was likely used to cap the landfill cells during the daily operation of the landfill, possibly releasing sodium salts (carbonate, bicarbonate) as well as hydroxides that increased leachate pH. This explanation is supported by the high values of the electrolytic conductivity of the leachate (Table 1).

Table 1. Characteristics of municipal leachate.

Parameters	**Value**
pH	8.26 ± 0.02
Conductivity (mS/cm)	36.7 ± 0.1
Total Kjeldahl nitrogen (g/L)	2.9 ± 0.03
SO_4^{2-} (g/L)	0.281± 0.01
COD (g/L)	12.3± 0.5
BOD_5 (g/L)	10.6± 0.2
BOD_5/COD	0.86

2.4. Sample collection and enrichment of inoculum

The inoculum enrichment was obtained with three serial transfers, described below. Sample from soil was collected in the CINVESTAV-IPN to a depth 2 m that was transferred to anaerobic bottle. The soil sample was moved to the laboratory without oxygen contact, and 5 g of soil sample was suspended in 50 mL of anaerobic saline solution. 5 mL of sample was transferred to 50 mL metal-reduction medium with acetate, Mn (IV) or Fe (III). Duplicate enrichments were incubated at 30 °C for 15 d or 9 d for Mn (IV) and Fe (III), respectively, in the dark condition. The enrichment procedure was repeated 3 times.

Metal-reduction medium consisted of (gL^{-1}): 2.5 $NaHCO_3$, 0.25 NH_4Cl, 0.6 $NaH_2PO_4.H_2O$, 0.1 KCl, 10 mL vitamin solution and 10 mL mineral solution (Lovley & Phillips,[21]). The MnO_2 was synthesized by slowly adding a solution of $MnCl_2$ (30 mM) to basic solution of $KMnO_4$ (20 mM) which was stirred with a magnetic stir bar. This procedure is similar to a previously described technique (Lovley & Phillips, [21]). The Fe(III) oxide was synthesized as follows: a solution 0.4 M of $FeCl_3.6\ H_2O$ (pH adjusted to 7.0 with 10 M of NaOH) was added, according to the technique described by Lovley & Phillips [21]. The MnO_2 was synthesized by slowly adding a solution of $MnCl_2$ (30 mM) to basic solution of $KMnO_4$ (20 mM) which was stirred with a magnetic stir bar. This procedure is similar to a previously described technique (Lovley & Phillips, [21]).

2.5. Electrochemical characterization of the microbial fuel cells

Potential sweep experiments were carried out from open-circuit cell voltage (E_{OC}), to the final potential of 0.02 V at a scan rate of $1mVs^{-1}$, performed in a potentiostat/galvanostat Voltalab model PGZ402 [22,23]. Values of R_{int} were estimated from the slopes of corresponding regression lines selected in the linear range of the polarization curves. The current (I_{MFC}), power (P_{MFC}) and volumetric power (P_V) were calculated as previously described [24]. The power density (surface area) was normalized to the projected cathode surface area (surface power density P_S).

The cells were loaded with 80 mL of enriched in Mn(IV)-reducing bacteria and 20 mL of actual municipal leachate. The initial biomass concentration in the cell inoculum was *ca.* 1 300 mg $VSSL^{-1}$.

2.6. Batch operation of the microbial fuel cells

The batch *MFCs* (with two different inocula) were loaded with municipal leachate and inoculum enriched in Mn(IV)-reducing bacterian inoculum enriched in Fe (III)-reducing bacteria, sulphate reducing and without inoculum. The organic matter concentration in *MFCs* was *ca.* 2 g $CODL^{-1}$. The cells were loaded with 80 mL of enriched in Mn(IV)-reducing bacteria; the initial biomass concentration in the cell inoculum was *ca.* 1 000 mg $VSSL^{-1}$. The cells were operated for two Periods; in Period I the cells were run until a decrease organic matter concentration was observed. At the end of Period I, the cell was loaded with new municipal leachate (*ca.* 3.5 g $CODL^{-1}$) although the electrodes and membrane as well as the microbial community remained the same, and further operated for what we denominated In Period II.

At the start of Period I the cells were operated for 24 h to open circuit voltage. Afterwards the cells were batch-operated for a total 250 h, at ambient temperature (23°C average) without mixing. The circuit of each *MFC* was fitted with a corresponding external resistance of 100 Ω and $Ru_xMo_ySe_z$ catalyts.

The main variable responses of this experiment were the average volumetric power ($P_{V\text{-}ave}$), the efficiency of organic matter removal (η_{COD}), and the coulombic efficiency (η_{Coul}).

2.7. Analytical methods and calculations

The COD and VSS of the liquors of sulphate-reducing seed bioreactor and cells were determined according to the Standard Methods [25]. Manganese (Mn II) contents were analyzed by the method of Brewer and Spencer [26] as modified by Armstrong *et al.* [27] whereas the presence of Mn (IV) was assessed with a benzidine acetate reagent [28].

The η_{COD} was calculated as

$$\eta_{COD}(\%) = \frac{(COD_i - COD_f)}{COD_i} \cdot 100 \quad (1)$$

where COD_i initial chemical oxygen demand and COD_f final chemical oxygen demand.

The volumetric power was estimated with Eq. 2 below

$$P_V = \frac{E_{MFC}^2}{V_{MFC} \cdot R_{ext}} \quad (2)$$

where E_{MFC} is the voltage, R_{ext} is the external resistance, and V_{MFC} is the cell volume. The average value during the batch operation was calculated by numerical integration *versus* time using the Simpson's rule [29].

The η_{Coul} is the ratio between the actual amount of produced electrons (CRS) to the electrons that could be produced from the substrate (CTS), as it follows:

$$\eta_{Coul}(\%) = \frac{CRS}{CTS} \cdot 100 \quad (3)$$

$$CRS = \int_0^t I_{MFC}\, dt \quad (4)$$

$$CTS = \frac{F_i \cdot b_{COD} \cdot (COD_i - COD_f) \cdot V_{MFC}}{M_{COD}} \quad (5)$$

where *F*: Faraday's constant (96 485 Coulombs mol^{-1} e^-), b_{COD}: number of moles of electrons harvested from the COD (4 mol e^- per mol of COD), COD_i: initial COD (g L^{-1}), COD_f: final COD (g L^{-1}), V_{MFC}: *MFC* operation volume (L), M_{COD}: COD's molecular weight (32 $gmol^{-1}$)

3. Results and discussion

3.1.Electrochemical characterization of microbial fuel cells

The first set of experiments consisted of the evaluation of the effect of the type of inoculum (*In-*$E_{Fe(III)\text{-}S}$, *In-*$E_{Fe(III)\text{-}SR}$, *In-*$E_{Mn(IV)}$ and *In-SR*) on the electrochemical characteristics of the MFC-G. Each face of the MFC-G was characterized by separate (I and II), in series, and in parallel electric arrangements.

Parallel connection of faces increased the maximum volumetric power $P_{V\text{-}max}$ up to 14 521, 15 825, 16 359 and 9293 mWm^{-3} (Figure 1), compared with series connection 10 377, 12 778, 10 685 and 6 842 mWm^{-3}. Parallel connection significantly decreased the R_{int} of the cells and almost doubled volumetric power. The $P_{V\text{-}max}$ for the MFC-G (*In-*$E_{Fe(III)\text{-}S}$, *In-*$E_{Fe(III)\text{-}SR}$, *In-*$E_{Mn(IV)}$ and *In-SR*) when faces were connected in series and parallel were higher than those reported by Ortega-Martinez *et al*. [30], Puig *et al.* [14] and Ieropoulos *et al.* [31]. Our $P_{V\text{-}max}$ was superior to that reported by Ortega-Martinez *et al.* [28] for the characterization of a novel, multi-face parallelepiped MFC (Pt for ORR); this cell was fitted with a 'sandwich' cathode-membrane-anode assemblage in five of their faces. When the 5 faces of the MFC-P were connected in series and parallel, the $P_{V\text{-}max}$ achieved values of 62 and 570 mWm^{-3}, respectively. On the other hand, Puig *et al.* [14] also characterized an air-cathode MFC loaded with landfill leachate and estimated a $P_{V\text{-}max}$ of 278.2 mWm^{-3}. Ieropoulos *et al.* [31] compared the performance of two small size MFCs connected in parallel using acetate as the substrate and a seed that consisted of anaerobic sludge; the characterization studies gave a $P_{V\text{-}max}$ of 860 mWm^{-3}.

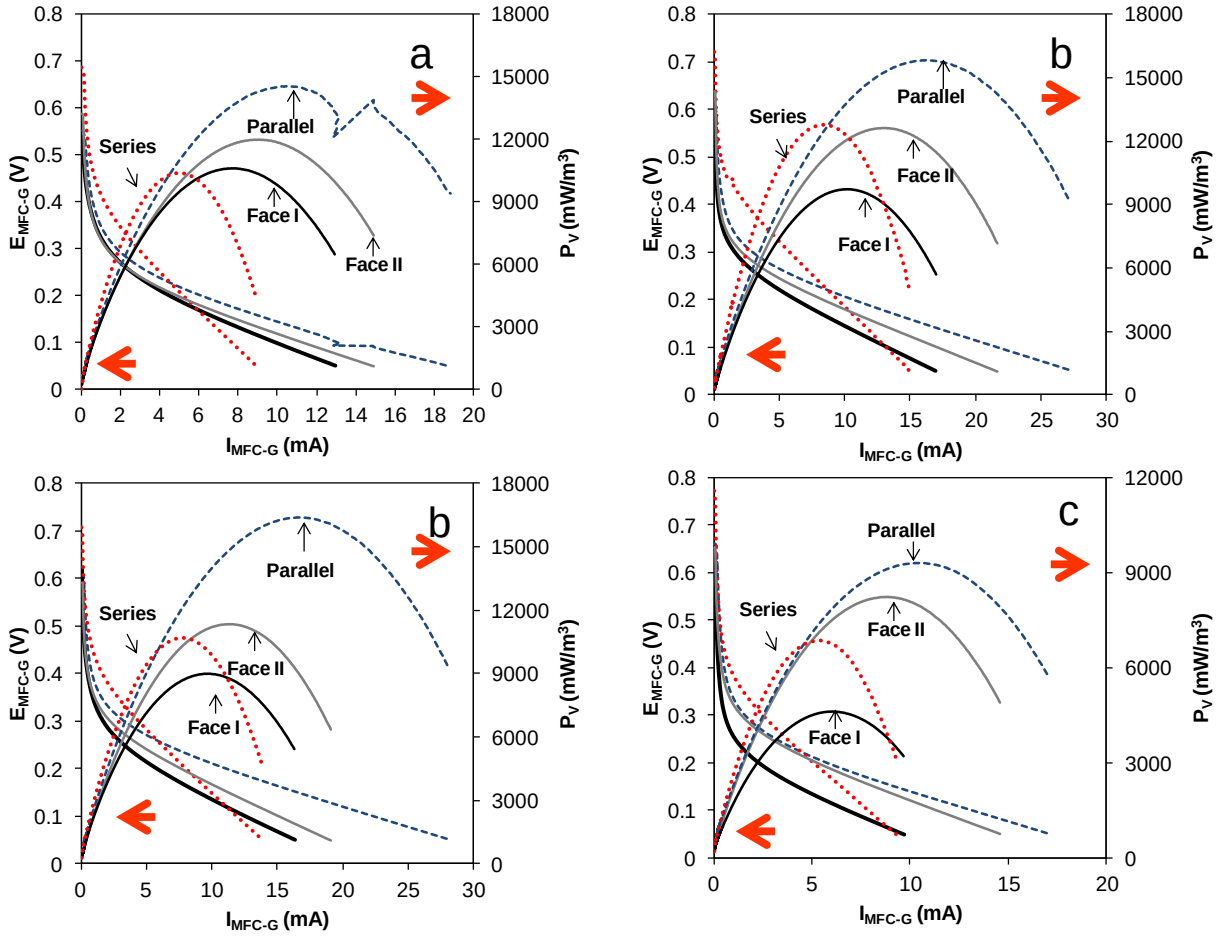

Fig. 1. Polarization curves by linear sweep potential studies in electrochemical characterization of microbial fuel cells, a) *In-$E_{Fe(III)-S}$*, b) *In-$E_{Fe(III)-SR}$*, c)*In-$E_{Mn(IV)}$* and d) *In-SR*. Keys: convex curves stand for volumetric power, read on the right axis; descending parabolic curves represent the E-I relationship, read on the left axis; curve in blue-hyphen stand for parallel connection of the two faces of the cell; red-dot stands for series connection of the faces; continuous gray corresponds to face II alone, and continuous black stands for face I alone.

The relatively higher $P_{V\text{-}max}$ in our MFCs could be attributed to the increase of the total electrode surface area by the application of granular graphite, and this, in turn, could have improved the electron transfer microbe-to-anode process [7]. Also, our work demonstrated that parallel connection of cell faces was more appropriate. On the other hand, the increase of power could also be ascribed to the use of the enriched inoculum. It is known that dissimilatory metal reducing bacteria are capable of the reduction of soil metal oxides such as MnO_2, FeOOH and very often exhibit exoelectrogenic (electrochemical activity) properties [32-34]. This, in turn, is related to improved electron transfer to anode and improved cell characteristics and performance [32,33]

3.2. Batch operation of microbial fuel cells loaded with actual leachate and enriched inoculum

Figure 2 shows the time course of cell potential (MFC-G; either inocula *In-$E_{Fe(III)-S}$*, *In-$E_{Fe(III)-SR}$*, *In-$E_{Mn(IV)}$* , *In-SR* or without inoculum) when their two faces were connected in parallel. The batch runs lasted for *ca.* 250 h. The MFC were connected to R_{ext} of 100 Ω. The gray area in Fig. 2 shows that the maximum, open circuit potential (the 24 h and without a resistance in the external circuit). Two periods or cycles of electricity generation with 2.0 g/L municipal leachate were carried out (Period I and Period II in Fig. 3).

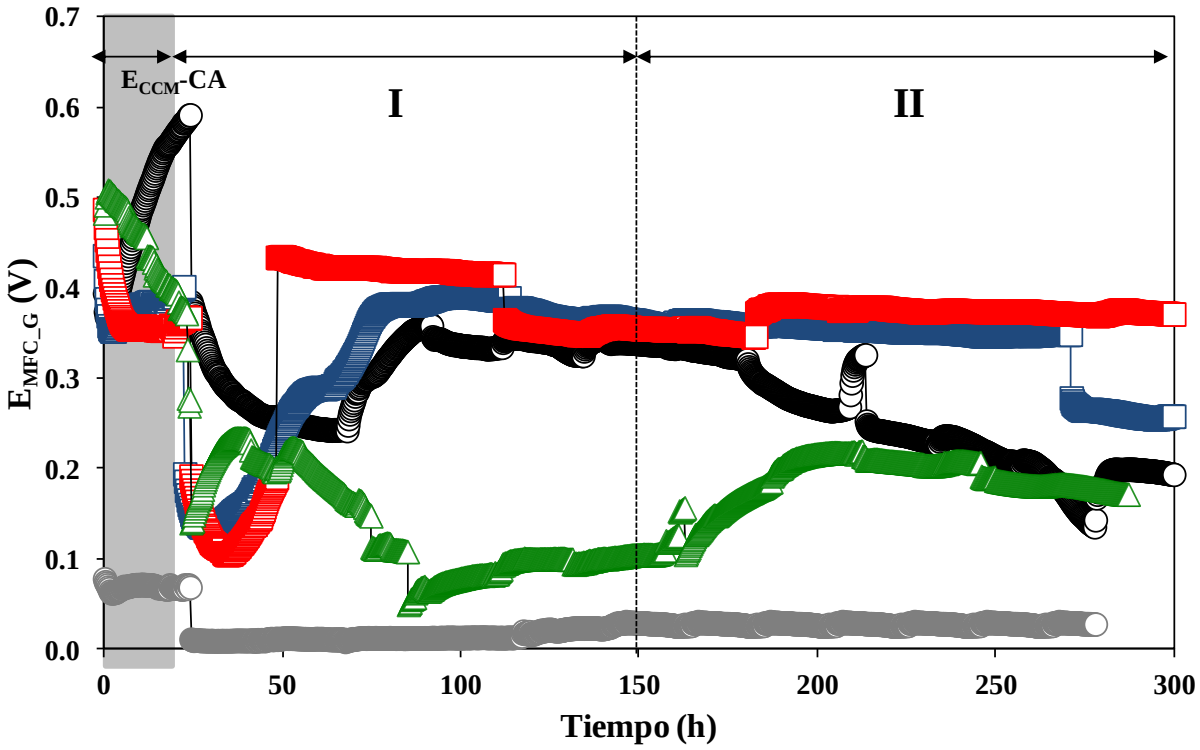

Fig. 2. Time course of voltage outputs of *MFC-G* cell using a inoculum enriched in Fe (III)-reducing bacteria (either one soil origin, *In-$E_{Fe(III)-S}$* and sulphate-reducing origin, *In-$E_{Fe(III)-SR}$*), inoculum enriched in Mn (IV)-reducing bacteria (*In-$E_{Mn(IV)}$*), inoculum sulphate reducing (In-SR) and without inoculum.

The $P_{V\text{-}ave}$ obtained in the cells for the different inocula (*In-*$E_{Fe(III)\text{-}S}$, *In-*$E_{Fe(III)\text{-}SR}$, *In-*$E_{Mn(IV)}$, *In-SR* and without inoculum) were 13 303, 11 249, 9 556, 4 377 and 53 mWm^{-3}. The highest average P_V in our cells were higher than that reported by Puig et al. [14] and Vazquez-Larios *et al.* [24]. Puig *et al.* [14] treated landfill leachate in an air-single MFC fitted with Pt catalyst, for two periods. Indeed, in their Period I the organic matter content of the influent was 0.507 g COD/L and they registered a very low $P_{V\text{-}ave}$ of 6.1 mWm^{-3}. In Period II they increased the organic matter concentration up to 8.51 g COD/L and they found a $P_{V\text{-}ave}$ in the range 106 to 344 mWm^{-3} respectively. Vazquez-Larios *et al*. [24] operated a two-face MFC whose main features were the assemblage or sandwich' arrangement of the anode-PEM-cathode; during the batch operation of the cells loaded with a model extract typical of leachate from the hydrogenogenic fermentation of organic solid wastes and a sulphate-reducing inoculum, the $P_{V\text{-}ave}$ was low to moderate, 479 mWm^{-3}.

4. Summary and perspectives

The values of $P_{V\text{-}ave}$ obtained with the chalcogenide catalyst were 30-40% lower than those registered with Pt catalyst in MFC loaded with municipal leachate as fuel. Yet, the cost of the chalcogenide is 80% lower than that of platinum.
The application of inocula enriched in Fe(III) and Mn (IV)-reducing bacteria significantly improved the performance of cells that used $Ru_xMo_ySe_z$ as a cathodic catalyst for the ORR. In general parallel connection of electrode faces significantly decreased the R_{int}.
Finally, the RuxMoySez can be an attractive alternative cathodic catalyst for MFCs that generate electricity from leachate.

Acknowledgements

ICyTDF now SECITI-DF (PICCO 10-28) and CINVESTAV-IPN (Mexico) financial support to this research is gratefully acknowledged. CONACYT granted a graduate scholarship to ALV-L. The authors wish to thank the help of Research Assistants and Technicians from the Environmental Biotechnology and Renewable Energies R&D Group and the Hydrogen and Fuel Cell Group. HMP-V gratefully acknowledges the use of a free license of software Design-Expert v8.0 from Stat-Ease, Inc.

References

[1] A.L.Vazquez-Larios, O. Solorza-Feria , G. Vazquez-Huerta, F. Esparza-Garcia, N. Rinderknecht-Seijas, H. M. Poggi-Varaldo. Effects of architectural changes and inoculum type on internal resistance of a microbial fuel cell designed for the treatment of leachates from the dark hydrogenogenic fermentation of organic solid wastes. Int J Hydrogen Energy 2011; 36: 6199.
[2] H. M. Poggi-Varaldo, A. Carmona-Martinez , A. L. Vazquez-Larios, O. Solorza-Feria. Effect of inoculum type on the performance of a microbial fuel cell fed with spent organic extracts from hydrogenogenic fermentation of organic solid wastes. J New Mater Electrochem Syst 2009;12(1):49-54.
[3] C. Fuentes-Albarran , A. Del Razo, K. Juarez, A. Alvarez-Gallegos. Influence of NaCl, Na2SO4 and O2 on power generation from microbial fuel cells with non-catalyzed carbon electrodes and natural inocula. Solar Energy 2012;86 (4):1099-1107.
[4] M. Mahmound, T.A. Gah-Allah, K.M. El-Khatib, F. El-Gohary. Power generation using spinel manganese–cobalt oxide as a cathode catalyst for microbial fuel cell applications. Bioresource Technology 2011; (102): 10459.
[5] L. A. Estudillo-Wong, E. M. Arce-Estrada, N. Alonso-Vante, A. Manzo-Robledo. Electro-reduction of nitrate species on Pt-based nanoparticles: Surface area effects. Catalysis Today 2011;166: 201-204.
[6] T. Romero-Castanon, L.G. Arriaga, U. Cano-Castillo. Impedance spectroscopy as a tool in the evaluation of MEA's J Power Sources 2003;118(1-2)179-182.
[7] A.L.Vázquez-Larios, Solorza-Feria O, González-Huerta R de G, Ponce-Noyola MT, Barrera-Cortés J, Rinderknecht-Seijas N, Poggi-Varaldo HM. Effect of Two Anodic Materials and RuxMoySez as a Cathode Catalyst on the Performance of Two Singlw Chamber Microbial Fuel Cells. J New Mater Electrochem Syst 2013;16(3):163-170.
[8] P. Kjeldsen, Barlaz MA, Rooker AP, Baun A, Ledin A, Christensen TH. Present and long-term composition of MSW landfill leachate: a review. Crit Rev Environ Sci Technol 2002;32(4):297–336.
[9] S. Renou, J-G. Givaudan, S. Poulain, Dirassouyan F, Moulin P. Landfill leachate treatment: Review and opportunity. J Hazard Mater 2008;150: 468–493.
[10] J. Greenman, A. Gálvez, L. Giusti, Ieropoulos I. Electricity from landfill leachate using microbial fuel cells: comparison with a biological aerated filter. Enzyme Microb Technol 2009;44: 112–119.
[11] A. Gálvez, J. Greenman, I. Ieropoulos. Landfill leachate treatment with microbial fuel cells; scale-up through plurality. Bioresour Technol 2009;100: 5085–5091.
[12] K. Ganesh, J.R. Jambeck.Treatment of landfill leachate using microbial fuel cells: Alternative anodes and semi-continuous operation. Bioresour Technol 2013;39: 383-387.
[13] A.E. Tugtas, P. Cavdar, B. Calli. Bio-electrochemical post-treatment of anaerobically treated landfill leachate. Bioresour Technol 2013;128: 266-272.
[14] S. Puig, M. Serra, M. Coma , M.Cabre, M.E. Balaguer, J. Colprim. Microbial fuel cell application in landfill leachate treatment. J Hazard Mater 2011;185(2-3): 763-767.
[15] K. Suárez-Alcántara, O. Solorza-Feria. Kinetics and PEMFC performance of RuxMoySez nanoparticles as a cathode catalyst. Electrochim Acta 2008; 53: 4981-4889.
[16] K. Suárez-Alcántara, O. Solorza-Feria. Comparative study of oxygen reduction reaction on RuxMySez (M=Cr, Mo,W) electrocatalysts for polymer exchange membrane fuel cell, J Power Sources 2009;192: 165-169.
[17] R.G. Gonzalez-Huerta, J.A. Chavez-Carvayar, O. Solorza-Feria. Electrocatalysis of oxygen reduction on carbon supported Ru-based catalysts in a polymer electrolyte fuel cell. J Power Sources 2006; 153, 11-17.
[18] R.G. González-Huerta, R. González-Cruz, C. Montero-Ocampo, J. Chávez-Carvallar, O. Solorza-Feria. Development and electrochemical studies of Ruthenium nanoparticles as cathode in a PEMFC. J New Mater Electrochem Syst 2005;8:15-23 (2005).
[19] K. Suarez-Alcantara, A. Rodriguez-Castellanos, R. Dante, O. Solorza-Feria. RuxCrySez electrocatalyst for oxygen reduction in a polymer electrolyte membrane fuel cell. J Power Sources 2006;157(1): 114-120.
[20] T.A. Kurniawan, W.H. Lo, G.Y.S. Chan. Physico-chemical treatments for removal of recalcitrant contaminants from landfill leachate J Hazar Mater 2006;129 (1-3): 80-100.
[21] D.R. Lovley, E.J.P. Phillips. Novel mode of microbial energy metabolism: organic carbon oxidation coupled to dissimilatory reduction of iron or manganese. App Environ Microbiol 1988;54:1472-80.
[22] K. Sathish-Kumar , O. Solorza-Feria, G. Vázquez-Huerta, J.P. Luna-Arias, H.M. Poggi-Varaldo. Electrical stress-directed evolution of biocatalysts community sampled from a sodic-saline soil for microbial fuel cells. J New Mater Electrochem Syst 2012; 15(3): 181-186
[23] K. Sathish- Kumar, O. Solorza-Feria, R. Hernández-Vera, G. Vazquez-Huerta, H.M. Poggi-Varaldo. Comparison of various techniques to characterize a single chamber microbial fuel cell loaded with sulfate reducing biocatalysts. J New Mater Electrochem Syst 2012;15(3):195-201.
[24] A.L. Vazquez-Larios, O. Solorza-Feria, G. Vazquez-Huerta, F. Esparza-Garcia, E. Rios-Leal, N. Rinderknecht-Seijas, H.M. Poggi-Varaldo. A new design improves performance of a single chamber microbial fuel cell. J New Mater Electrochem Syst 2010;13(3): 219-226.
[25] APHA. Standard methods for the examination of water and wastewater. 17th ed. Washington, DC, USA: American Public Association; 1989.
[26] P.G. Brewer, D.W. Spencer. Colorimetric determination of manganese in anoxic waters. Limnol Oceanogr 1971;16:107-112.
[27] P.B. Armstrong, W.B.LyonsB, H.E.Gaudette. Application of formaldoxime colorimetric method for the determination of manganese in the pore water of anoxic estuarine sediments. Estuaries 1979; 2(3):198-201.
[28] F. Feigl, Spot tests in inorganic analysis. Elsevier, New York, N.Y.; 1958
[29] M.G. Salvadori, M.L. Baron. Numerical methods in engineering. Prentice-Hall 4th ed. Englewood Cliffs, NJ, USA. 1959.

[30] A. C. Ortega-Martínez, K. Juárez-López, O. Solorza-Feria, M.T. Ponce-Noyola, E. Ríos-Leal, N. Rinderknecht-Seijas, H.M. Poggi-Varaldo. Parallel connection and sandwich electrodes lower the internal resistance in a microbial fuel cell. J New Mater Electrochem Syst 2012;15(3):187-194.
[31] I. Ieropoulus, J. Greenman, C. Melhuish. Microbial fuel cell based on carbon veil electrodes: Stack configuration and acalability. Int J Energy Res 2008;32 (13): 1228–1240.
[32] A.C. Ortega-Martinez, K. Juarez-Lopez, O. Solorza-Feria, M.T. Ponce-Noyola, J. Galindez-Mayer, N. Rinderknecht-Seijas, H.M. Poggi-Varaldo. Analysis of microbial diversity of inocula used in a five-face parallelepiped and standard microbial fuel cells. Int J Hydrogen Energy 2013;38(28):12589-12599.
[33] K. Sathish-Kumar, O. Solorza-Feria, J. Tapia-Ramírez, N. Rinderkenecht-Seijas, H.M. Poggi-Varaldo. Electrochemical and chemical enrichment methods of a sodic-saline inoculum for microbial fuel cells. Int. J Hydrogen Energy 2013;38(28):12600–09.
[34] A. Wang, D. Sun, N. Ren, C. Liu, W. Liu, B.E. Logan. A rapid strategy for and nodophilic consortium for microbial fuel cells. Bioresource Technol 2010;101(1):5733-5.
[35] B. Ozkaya, A.Y. Cetinkaya, M. Cakmakci, D. Karadag, E. Sahinkaya. Electricity generation from young landfill leachate in a microbial fuel cell with a new electrode material. Bioprocess and Biosystems Engineering 2013;36:399-405.
[36] C. Zhong, B.G. Zhang, L.C. Kong, A. Xue, J.R. Ni. Electricity generation from molasses wastewater by an anaerobic baffled stacking microbial fuel cell. J Chem Technol Biotechnol 2011;86(3):406-413.
[37] T. Shimoyama, S. Komukai, A. Yamazawa, Y. Ueno, B.E. Logan, K. Watanabe. Electricity generation from model organic wastewater in a cassette-electrode microbial fuel cell. Appl Microbiol Biotechnol 2008;80:325–330.
[38] S. Sevda, X. Dominguez-Benetton, K. Vanbroekhoven, H. De Wever, T.R. Sreekrishnan, D. Pant. High strength wastewater treatment accompanied by power generation using air cathode microbial fuel cell. App Energy. 2013;105: 194-206.
[39] E. Martin, O. Savadogo, S.R. Guiot, B. Tartakovsky. The influence of operational conditions on the performance of a microbial fuel cell seeded with mesophilic anaerobic sludge. Biochem Eng J 2010;51(3):132-139.